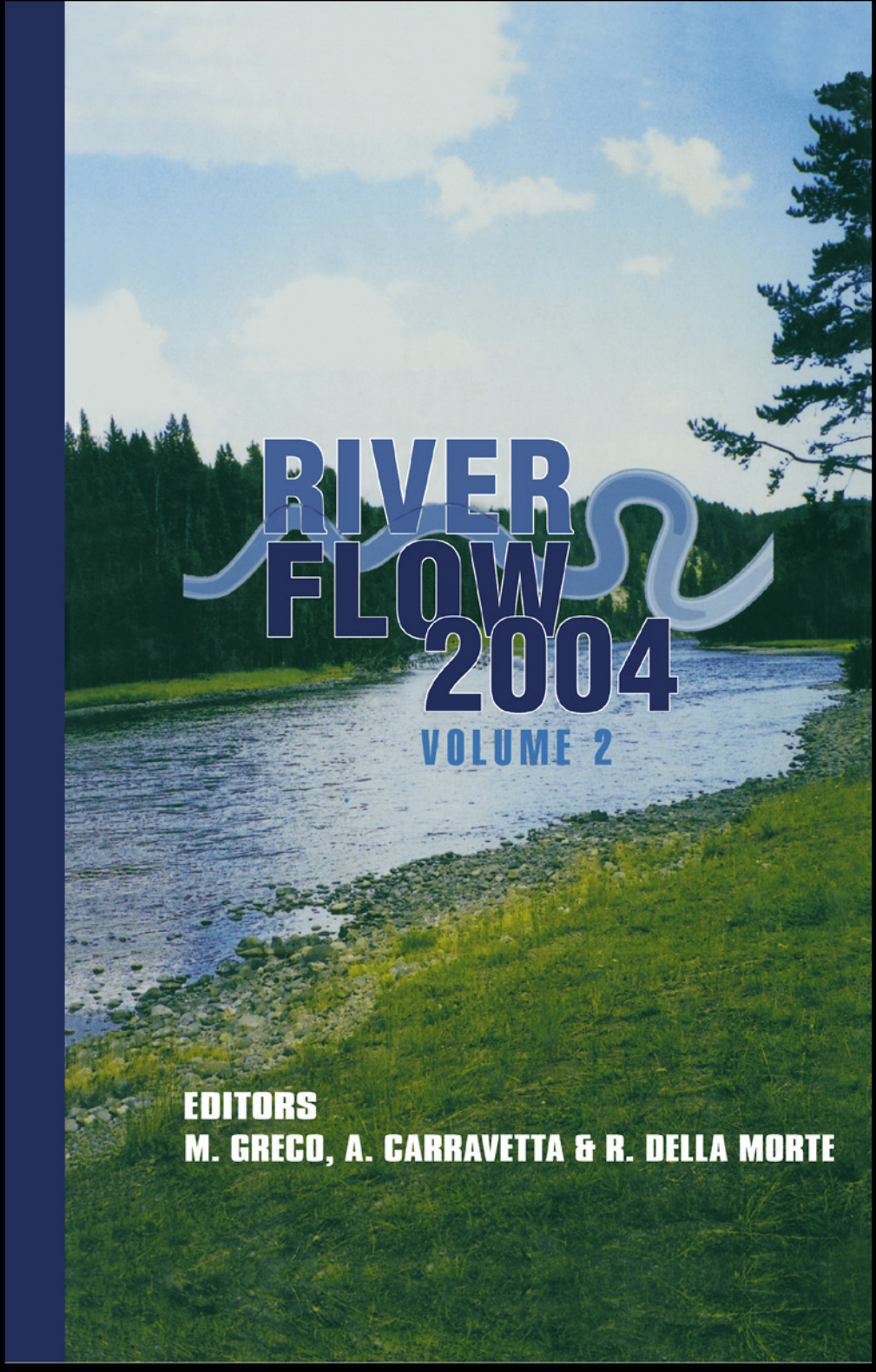

RIVER FLOW 2004

PROCEEDINGS OF THE SECOND INTERNATIONAL CONFERENCE ON FLUVIAL HYDRAULICS, 23–25 JUNE 2004, NAPOLI, ITALY

River Flow 2004

Edited by

Massimo Greco, Armando Carravetta & Renata Della Morte
Federico II University of Napoli, Italy

VOLUME 2

A.A.BALKEMA PUBLISHERS
Leiden/London/New York/Philadelphia/Singapore

Published by: A.A.Balkema Publishers, a member of Taylor & Francis Group plc
mailto:www.balkema.nl and mailto:www.tandf.co.uk
This edition published in the Taylor & Francis e-Library, 2006.

"To purchase your own copy of this or any of Taylor & Francis or Routledge's collection of thousands of eBooks please go to http://www.ebookstore.tandf.co.uk/."

ISBN 0-203-02464-8 Master e-book ISBN

For the complete set of two volumes: ISBN 90 5809 658 0 (Print Edition)
Volume 1: ISBN 90 5809 687 4 (Print Edition)
Volume 2: ISBN 90 5809 688 2 (Print Edition)

Table of Contents

River Flow 2004—Greco, Carravetta & Della Morte (eds.)
© 2004 Taylor & Francis Group, London, ISBN 90 5809 658 0

B.4. Hyper-concentrated flows

B.5. Water pollution and contaminant transport

Preface

River Flow 2004—Greco, Carravetta & Della Morte (eds.)

River Flow 2004 is the second International Conference on fluvial hydraulics and has established the periodicity of the series. Organized as specialty conferences under the auspices of the International Association of Hydraulic Engineering and Research (IAHR) with its Fluvial Hydraulics and Eco Hydraulics Sections, River Flow conferences seem to be an important moment of aggregation for many researchers involved in river modelling and observation.

The intense land use of the last century and the lack of adequate sustainable development policies are probably the most important reasons of river hazards. For the importance of water as a resource in the human well-being we need a better comprehension of river processes and an adequate management of fluvial areas.

Scientists are aware of this necessity and largely contribute with their researches toward this aim. This clearly appears in the number of papers presented at River Flow 2004 (174) and from the number of country represented (43). Papers in this volume are related to the following topics:

- **Fluvial processes** (Morphology and morphodynamics; Bed forms and flow resistance; Over-bank flow and vegetation; Interaction with structures; Sediment supply, entrainment and transport);
- **River hazards** (Dam break and fast transients; Bank failure; Flood propagation; Hyper-concentrated flows; Water pollution and contaminant transport);
- **Hydraulics for river management** (River training and restoration; Habitat management and maintenance flows; Flood management and control; Integration of telemetry and GIS).

As the editors of the Conference proceedings we acknowledge the members of the International Scientific Committee for the in-depth reviewing of the manuscripts. The 70% of the accepted papers have been selected for oral presentation (123), while the 30% have been evaluated as more appropriately presented in the poster session (49). All the accepted papers have been included in this volume.

A grateful acknowledgment is deserved to all the members of the Local Organizing Committee for the intense work related to Conference preparation. Finally we acknowledge the Federico II University of Naples that was strongly involved in the success of River Flow 2004 for hosting the Conference, and the various sponsors for their financial support.

Massimo Greco
Armando Carravetta

Renata Della Morte
G.Ippolito Department of Hydraulic and Environmental Engineering, Federico II University of Napoli

Organization

River Flow 2004—Greco, Carravetta & Della Morte (eds.)
© 2004 Taylor & Francis Group, London, ISBN 90 5809 658 0

International Scientific Committee
M.Altinakar, University of Mississippi, USA
A.Armanini, University of Trento, Italy
A.M.da Silva, Queens University, Canada
P.García Navarro, University of Zaragoza, Spain
W.H.Graf, EPFL Lausanne, Switzerland
W.H.Hager, ETHZ Zurich, Switzerland
W.Hamza, United Arab Emirates University, UAE
J.M.Hervouet, EDF Chatou, France
F.Holly, IIHR University of Iowa, USA
G.H.Jirka, University of Karlsruhe, Germany
G.Klaassen, IHE, The Netherlands
M.Leclerc, Université de Quebec, Canada
D.Lyn, Purdue University, USA
C.Montuori, University of Napoli, Italy
G.Parker, University of Minnesota, USA
N.Tamai, University of Tokyo, Japan
Z.Y.Wang, IRTCES Beijing, China
S.Yalin, Queens University, Canada
Y.Zech, UCL, Belgium

Local Organizing Committee
Massimo Greco, Chairman
Armando Carravetta, Secretary
Giuseppe Del Giudice
Renata Della Morte
Maurizio Giugni
Paola Gualtieri
Domenico Pianese
University of Napoli Federico II

B.
River hazards

B.1.
Dam break and fast transients

Two dimensional modeling of rapidly varying flows by finite volume schemes

F.Aureli, A.Maranzoni & P.Mignosa
Dipartimento di Ingegneria Civile, dell'Ambiente, del Territorio & Architettura, Parma, Italy

River Flow 2004—Greco, Carravetta & Della Morte (eds.)

ABSTRACT: The two dimensional shallow water equations are currently accepted as the mathematical basis for the study of rapidly varying wave propagation phenomena. In the present work, two different TVD second order numerical codes based on a finite volumes discretization of the mentioned system of conservation laws are implemented. The first belongs to the family of MUSCL-Hancock centred slope limiter schemes (SLIC); the second is based on the WAF (Weighted Average Flux) scheme where second order of accuracy is achieved by solving the conventional *piece-wise constant* Riemann problem and averaging it over space and time. Numerical solutions have been validated by comparison with the results of other numerical models for literature test cases and with experimental results obtained by the authors. The comparisons confirm that the models can be reliably used to deal with rapidly varying flows characterized by shocks and by transitions between subcritical and supercritical flow.

1 INTRODUCTION

The time dependent two dimensional shallow water equations are currently accepted as the mathematical basis for the study of rapidly varying wave propagation phenomena such as dam-break flows or levee breakings. For this reason, in the recent years, the efforts of many researchers in the field of hydroinformatics were devoted to the integration of the shallow water equations by means of different kinds of numerical techniques; among these the finite volume approach appear nowadays to be of dominant interest (Toro 1997, Toro 2001, LeVeque 2002).

In the following work, two different TVD second order numerical codes based on a finite volumes discretization of the mentioned system of conservation laws are developed.

The paper is organized as follows. In the next paragraph the 2D shallow water equations are recalled and the details of the two numerical models for solving the

homogeneous part of the equations, together with the treatment of the source terms, are exposed. In the third paragraph the results obtained by means of the two numerical codes are compared with the solutions, close to exact ones, for some test cases widely considered as reference. In the fourth paragraph the capabilities of the numerical codes were tested by comparison with experimental results available in the recent literature.

2 NUMERICAL MODELS

The presented numerical schemes are based on a finite volume discretization of the two dimensional shallow water equations written in the integral form

$$\frac{d}{dt}\int_A \mathbf{U}\,dA + \int_C \mathbf{H}\cdot\mathbf{n}\,dC = \int_A \mathbf{S}\,dA \tag{1}$$

where A represents the area of the integration cell, C the cell boundary, $\mathbf{n}$ is the outward unit vector normal to C, while $\mathbf{H=(F, G)}$ represents the tensor of fluxes. The corresponding conservation differential form of Equation 1 is:

$$\frac{\partial \mathbf{U}}{\partial t}+\frac{\partial \mathbf{F}}{\partial x}+\frac{\partial \mathbf{G}}{\partial y}=\mathbf{S} \tag{2}$$

$$\mathbf{U}=\begin{pmatrix} h \\ uh \\ vh \end{pmatrix},\quad \mathbf{F}=\begin{pmatrix} uh \\ u^2h+\frac{1}{2}gh^2 \\ uvh \end{pmatrix},$$

$$\mathbf{G}=\begin{pmatrix} vh \\ uvh \\ v^2h+\frac{1}{2}gh^2 \end{pmatrix},\quad \mathbf{S}=\begin{pmatrix} 0 \\ gh\left(S_{0x}-S_{fx}\right) \\ gh\left(S_{0y}-S_{fy}\right) \end{pmatrix}$$

In Equations 1 and 2, t indicates time and g is the gravitational acceleration, while S_{0x}, S_{0y}, S_{fx}, and S_{fy} are the bottom and frictional slopes along the x and y axes, respectively.

The Manning equation is used to compute the friction terms:

$$S_{fx}=\frac{n^2uh\sqrt{(uh)^2+(vh)^2}}{h^{10/3}};S_{fy}=\frac{n^2vh\sqrt{(uh)^2+(vh)^2}}{h^{10/3}} \tag{3}$$

in which n is the Manning roughness coefficient.

Both the numerical schemes are shock capturing second order extensions of the Godunov upwind method and are *unsplit* in the sense that the updating of the solution of the homogeneous part of Equation 1 is obtained in a single step, involving flux contributions from all intercell boundaries. In the special case in which the computational domain is composed of Cartesian cells of area $\Delta x\times\Delta y$, an explicit conservative finite volume scheme reads:

$$\overline{\mathbf{U}}_{i,j}^{n+1}=\mathbf{U}_{i,j}^{n}-\frac{\Delta t}{\Delta x}\left(\mathbf{f}_{i+\frac{1}{2},j}-\mathbf{f}_{i-\frac{1}{2},j}\right)-\frac{\Delta t}{\Delta y}\left(\mathbf{g}_{i,j+\frac{1}{2}}-\mathbf{g}_{i,j-\frac{1}{2}}\right) \tag{4}$$

In Equation 4 the *x* and *y* directions are designated by the subscripts *i* and *j* respectively, while the time level is indicated by the superscript *n;* $\mathbf{f}_{i\pm1/2,j}$ and $\mathbf{g}_{i,\ j\pm1/2}$ represent the numerical fluxes in the *x* and *y* directions respectively.

To avoid unphysical or spurious oscillations in the vicinity of high gradients of the solution a TVD constraint was enforced on the schemes by means of different well-known limiter functions.

2.1 *SLIC numerical model*

The scheme is a second order extension of the first-order centred FORCE scheme and results from replacing the Godunov flux by the Force flux in the MUSCL-Hancock scheme (Toro 1997, Toro 2001). It is called SLIC as an acronym for Centred Slope LImiter; it computes the intercell numerical flux in the following steps. The first step requires the definition of a set of boundary extrapolated variables that for the *x* co-ordinate can be expressed as (Hirsch 1990):

$$\mathbf{U}^{L}_{i+\frac{1}{2}j} = \mathbf{U}^{n}_{ij} + \frac{1}{4}(1-k)\boldsymbol{\Phi}^{+}_{i-\frac{1}{2}j}\left(\mathbf{U}^{n}_{ij} - \mathbf{U}^{n}_{i-1j}\right) + \\ + \frac{1}{4}(1+k)\boldsymbol{\Phi}^{-}_{i+\frac{1}{2}j}\left(\mathbf{U}^{n}_{i+1j} - \mathbf{U}^{n}_{ij}\right) \tag{5}$$

and

$$\mathbf{U}^{R}_{i+\frac{1}{2}j} = \mathbf{U}^{n}_{i+1j} - \frac{1}{4}(1+k)\boldsymbol{\Phi}^{+}_{i+\frac{1}{2}j}\left(\mathbf{U}^{n}_{i+1j} - \mathbf{U}^{n}_{ij}\right) + \\ - \frac{1}{4}(1-k)\boldsymbol{\Phi}^{-}_{i+\frac{1}{2}j}\left(\mathbf{U}^{n}_{i+2j} - \mathbf{U}^{n}_{i+1j}\right) \tag{6}$$

where the superscripts *L* and *R* refer to left and right extrapolated variables. In Equations 5 and 6 the parameter *k* represents the amount of *upwinding* that is maximum for $k=-1$: in this case all the information coming from one of the sides of the considered cell is discarded, being the extrapolation applied on the other side only. Always in Equations 5 $\boldsymbol{\Phi}^{+}_{i-1/2,j}$ and $\boldsymbol{\Phi}^{-}_{i+1/2,j}$ represent diagonal *limiter* matrices (3×3) that enforce a TVD constraint in the data reconstruction step in order to limit the slopes of the extrapolating function (Toro 1997, Toro 2001). The kind of bilinear extrapolation performed leads to a second order of accuracy in space. In order to achieve the same accuracy in time, once the boundary extrapolated variables are defined, a new set of boundary variables is obtained evolving on a half of the current Δt the relations 5 and 6 in the following way (Toro 2001):

$$\overline{\mathbf{U}}^{L}_{i+\frac{1}{2}j} = \mathbf{U}^{L}_{i+\frac{1}{2}j} - \frac{\Delta t}{2\Delta x}\left[\mathbf{F}\left(\mathbf{U}^{L}_{i+\frac{1}{2}j}\right) - \mathbf{F}\left(\mathbf{U}^{R}_{i-\frac{1}{2}j}\right)\right] + \\ - \frac{\Delta t}{2\Delta y}\left[\mathbf{G}\left(\mathbf{U}^{L}_{ij+\frac{1}{2}}\right) - \mathbf{G}\left(\mathbf{U}^{R}_{ij-\frac{1}{2}}\right)\right] \tag{7}$$

$$\overline{\mathbf{U}}^{R}_{i+\frac{1}{2}j} = \mathbf{U}^{R}_{i+\frac{1}{2}j} - \frac{\Delta t}{2\Delta x}\left[\mathbf{F}\left(\mathbf{U}^{L}_{i+\frac{3}{2}j}\right) - \mathbf{F}\left(\mathbf{U}^{R}_{i+\frac{1}{2}j}\right)\right] + \\ - \frac{\Delta t}{2\Delta y}\left[\mathbf{G}\left(\mathbf{U}^{L}_{i+1j+\frac{1}{2}}\right) - \mathbf{G}\left(\mathbf{U}^{R}_{i+1j-\frac{1}{2}}\right)\right] \tag{8}$$

The flux is then given by:

$$\mathbf{f}^{FORCE}_{i+\frac{1}{2},j} = \mathbf{f}_{i+\frac{1}{2},j}(\overline{\mathbf{U}}^{R}_{i+\frac{1}{2},j}, \overline{\mathbf{U}}^{L}_{i+\frac{1}{2},j}) = \\ = \frac{1}{2}\left[\mathbf{f}^{RI}_{i+\frac{1}{2},j}(\overline{\mathbf{U}}^{R}_{i+\frac{1}{2},j}, \overline{\mathbf{U}}^{L}_{i+\frac{1}{2},j}) + \mathbf{f}^{LF}_{i+\frac{1}{2},j}(\overline{\mathbf{U}}^{R}_{i+\frac{1}{2},j}, \overline{\mathbf{U}}^{L}_{i+\frac{1}{2},j})\right] \tag{9}$$

where the superscripts *LF* and *RI* refer to *Lax-Friedrichs* and *Richtmyer* intercell numerical fluxes respectively(Richtmyer & Morton 1967,Hirsch 1990):

$$\mathbf{f}^{LF}_{i+\frac{1}{2},j} = \mathbf{f}^{LF}_{i+\frac{1}{2},j}\left(\overline{\mathbf{U}}^{L}_{i+\frac{1}{2},j}, \overline{\mathbf{U}}^{R}_{i+\frac{1}{2},j}\right) = \\ = \frac{1}{2}\left[\mathbf{F}\left(\overline{\mathbf{U}}^{L}_{i+\frac{1}{2},j}\right) + \mathbf{F}\left(\overline{\mathbf{U}}^{R}_{i+\frac{1}{2},j}\right)\right] + \frac{1}{4}\frac{\Delta x}{\Delta t}\left(\overline{\mathbf{U}}^{L}_{i+\frac{1}{2},j} - \overline{\mathbf{U}}^{R}_{i+\frac{1}{2},j}\right) \tag{10}$$

$$\mathbf{f}^{RI}_{i+\frac{1}{2},j} = \mathbf{f}^{RI}_{i+\frac{1}{2},j}\left(\overline{\mathbf{U}}^{L}_{i+\frac{1}{2},j}, \overline{\mathbf{U}}^{R}_{i+\frac{1}{2},j}\right) = \mathbf{F}\left(\tilde{\mathbf{U}}_{i+\frac{1}{2},j}\right)$$

$$\tilde{\mathbf{U}}_{i+\frac{1}{2},j} = \frac{1}{2}\left(\overline{\mathbf{U}}^{L}_{i+\frac{1}{2},j} + \overline{\mathbf{U}}^{R}_{i+\frac{1}{2},j}\right) + \\ + \frac{1}{2}\frac{\Delta t}{\Delta x}\left[\mathbf{F}\left(\overline{\mathbf{U}}^{L}_{i+\frac{1}{2},j}\right) - \mathbf{F}\left(\overline{\mathbf{U}}^{R}_{i+\frac{1}{2},j}\right)\right] \tag{11}$$

2.2 *WAF numerical model*

The second code developed is based on the WAF (Weighted Average Flux) scheme (Toro 1992, Toro 1997). Its key feature is that the second order of accuracy can be achieved by solving the conventional *piece-wise constant* Riemann problem and averaging it over space and time.

Considering the *x*-split homogeneous shallow water equations:

$$\frac{\partial \mathbf{U}}{\partial t} + \frac{\partial \mathbf{F}}{\partial x} = 0 \quad \text{where} \\ \mathbf{U} = \begin{pmatrix} h \\ uh \\ \varphi h \end{pmatrix}, \quad \mathbf{F} = \begin{pmatrix} uh \\ u^2 h + \frac{1}{2} g h^2 \\ \varphi u h \end{pmatrix}, \tag{10}$$

it can be observed that the third equation represents a conservation law for φh where φ plays the role of a passive scalar simply advected by the *x* velocity *u*. This passive scalar can for example represent the modulus of the velocity vector *v* whose direction is trivial, being the co-ordinate direction *y*. By means of the Strang splitting (LeVeque 2002) it is then possible to extend the 1D WAF scheme to two or more space dimensions applying in turn the one-dimensional difference operator to each of the co-ordinate directions. For the general *y* co-ordinate *j* the WAF flux is defined via the *integral average:*

$$\mathbf{f}^{WAF}_{i+\frac{1}{2}} = \frac{1}{t_2 - t_1} \cdot \frac{1}{x_2 - x_1} \int_{t_1}^{t_2} \int_{x_1}^{x_2} \mathbf{F}\left(\mathbf{U}^{*}(x,t)\right) \cdot dx \cdot dt \,, \tag{11}$$

where $\mathbf{U}^{*}(x, t)$ is the solution of the Riemann problem with *piece-wise constant* data $\mathbf{U}_i$, $\mathbf{U}_{i+1}$.

Choosing $x_1 = -\Delta x/2$, $x_2 = \Delta x/2$, $t_1 = 0$, $t_2 = \Delta t$ and approximating the time integration by the midpoint rule it's possible to obtain:

$$\mathbf{f}_{i+\frac{1}{2}}^{WAF} = \frac{1}{\Delta x}\int_{-\frac{\Delta t}{2}}^{\frac{\Delta t}{2}} \mathbf{F}\left(\mathbf{U}_{i+\frac{1}{2}}\left(x, \Delta t/2\right)\right) \cdot dx \tag{12}$$

that becomes the summation:

$$\mathbf{f}_{i+\frac{1}{2}}^{WAF} = \sum_{k=1}^{N+1} w_k \, \mathbf{F}_{i+\frac{1}{2}}^{(k)} \tag{13}$$

where N is the number of conservation laws (in this case N=3), w_k are the weights given by:

$$w_k = \tfrac{1}{2}\left(c_k - c_{k-1}\right), \quad c_0 = -1, \quad c_{N+1} = 1 \tag{14}$$

where $c_k = \Delta t.S_k/\Delta x$ and S_k are respectively the Courant number and the speed for wave k.

To compute numerical solutions by Godunov-type methods, as the one adopted, it is possible to use exact or approximate Riemann solvers. For the shallow water equations in particular, the approximate ones proved to be very robust and simple to compute. The Riemann solver adopted is the approximate HLLC solver (Toro 2001), that is based on a modification of the basic HLL scheme (Harten et al. 1983) to account for the influence of intermediate waves. The HLL solver takes in fact into account a simple wave structure in which only the smallest and largest signal velocities are considered. Intermediate waves, such as shear waves and contact discontinuities that arise when extra equations are added to the basic 1D shallow water equations like in Equations 10, are ignored in this approach. In the HLLC approach the complete three wave structure is considered. It is useful to observe that the third flux component in (10), $\mathbf{f}_{i+1/2}^{(3)}$ can be expressed as the product of the first flux component $\mathbf{f}_{i+1/2}^{(1)}$ and the the variable φ the latter representing they velocity v. Then retaining the HLL fluxes for the first two components of the flux and remembering that the exact solution of the Riemann problem in terms of the advected velocity v is:

$$v = \begin{cases} v_i & \text{if } s^* \geq 0 \\ v_{i+1} & \text{if } s^* < 0 \end{cases} \tag{15}$$

s* being the speed wave in the star region, it is possible to express the numerical flux as:

$$\mathbf{f}_{i+\frac{1}{2}}^{(m)} = \frac{S_{i+1} \cdot \mathbf{F}_i^{(m)} - S_i \cdot \mathbf{F}_{i+1}^{(m)} + S_{i+1} \cdot S_i \cdot \left(\mathbf{U}_{i+1}^{(m)} - \mathbf{U}_i^{(m)}\right)}{S_{i+1} - S_i} \tag{16}$$

where m=1, 2 is the vector component.

The third component of the numerical flux is then obtained as:

$$\mathbf{f}_{i+\frac{1}{2}}^{(3)} = \begin{cases} \mathbf{f}_{i+\frac{1}{2}}^{(1)} v_i & \text{if } s^* \geq 0 \\ \mathbf{f}_{i+\frac{1}{2}}^{(1)} v_{i+1} & \text{if } s^* < 0 \end{cases} \tag{17}$$

Proper estimates of all the three wave speed S_i, s* and S_{i+1} can be obtained by one of the several methods proposed in literature (Toro 1997, Toro 2001).

2.3 *Treatment of source terms*

In both the numerical schemes the treatment of the source term **S(U)** is accomplished by means of a time-operator splitting technique (Toro 1992). The solution procedure is split into the solution of two sub-problems. First the homogeneous problem of Equation 4 with initial data $\mathbf{U}^n$ is solved to obtain a provisional solution $\bar{\mathbf{U}}^{n+1}$ for the next time level, then the solution $\mathbf{U}^{n+1}$ of the system of ordinary differential equations:

$$\frac{d\mathbf{U}}{dt} = \mathbf{S}(\mathbf{U}) = \mathbf{S}_0(\mathbf{U}) + \mathbf{S}_f(\mathbf{U}), \tag{13}$$

with initial data $\bar{\mathbf{U}}^{n+1}$**,** is obtained separately for the slope (Equation 14) and friction effects (Equation 15), by means of an implicit trapezoidal method of second order of accuracy:

$$\mathbf{U}^*_{i,j} = \bar{\mathbf{U}}^{n+1}_{i,j} + \frac{\Delta t}{2}\left[\mathbf{S}_0(\bar{\mathbf{U}}^{n+1}_{i,j}) + \mathbf{S}_0(\mathbf{U}^*_{i,j})\right] \tag{14}$$

$$\mathbf{U}^*_{i,j} = \bar{\mathbf{U}}^{n+1}_{i,j} + \Delta t\, \mathbf{S}_0(\bar{\mathbf{U}}^{n+1}_{i,j})$$

$$\mathbf{U}^{n+1}_{i,j} = \mathbf{U}^*_{i,j} + \frac{\Delta t}{2}\left[\mathbf{S}_f(\mathbf{U}^*_{i,j}) + \mathbf{S}_f(\mathbf{U}^{n+1}_{i,j})\right] \tag{15}$$

$$\mathbf{U}^{n+1}_{i,j} = \mathbf{U}^*_{i,j} + \Delta t\left[\mathbf{I} - \frac{\Delta t}{2}\mathbf{Q}_f(\mathbf{U}^*_{i,j})\right]^{-1}\mathbf{S}_f(\mathbf{U}^*_{i,j})$$

where **I** is the Identity matrix (3×3) and $\mathbf{Q}_f$ is the Jacobian matrix of $\mathbf{S}_f$**.**

3 REFERENCE TEST CASES

In this section the results obtained by means of the two numerical models previously described are compared with reference solutions, close to the exact ones, for some test cases widely considered in the recent literature.

3.1 *Circular dam break problem*

This problem was tested by many Authors in the last decade (Glaister 1991, Alcrudo & García Navarro 1993, Liska & Wendroff 1999, Toro 2001, LeVeque 2002).

A cylindrical water column is placed in the centre of a wet, horizontal and frictionless domain. At t=0 the water column initially at rest is suddenly released and the time evolution of depth and velocity fields is calculated.

Following the example reported by Liska & Wendroff a 10m high water column with radius of

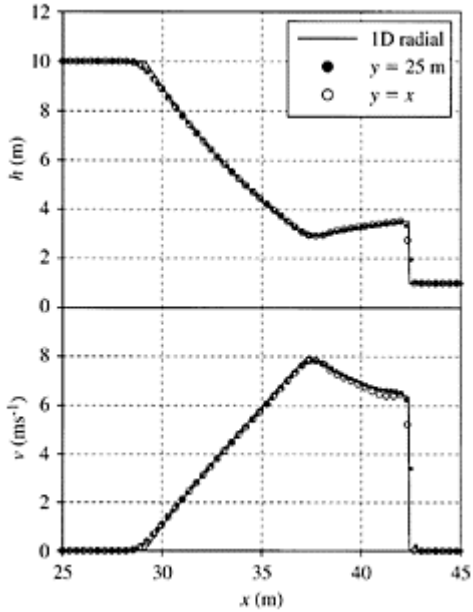

Figure 1. Circular Dam-Break problem. Axial and diagonal results at t=0.69s obtained by the 2D SLIC model (201×201 cells). Radial solution obtained by the WAF model (2000 cells).

11m is placed in the centre of a 50×50m domain wetted with 1m of water.

Since the problem has cylindrical symmetry along the radial direction r, the results of the 2D numerical calculations can be compared with the solution obtained by solving the following one dimensional inhomogeneous system (Toro 2001):

$$\frac{\partial \mathbf{U}}{\partial t} + \frac{\partial \mathbf{F}(\mathbf{U})}{\partial r} = \mathbf{S}(\mathbf{U}) \tag{16}$$

with

$$\mathbf{U} = \begin{bmatrix} h \\ uh \end{bmatrix}, \mathbf{F}(\mathbf{U}) = \begin{bmatrix} uh \\ u^2 h + \frac{1}{2} g h^2 \end{bmatrix}, \mathbf{S}(\mathbf{U}) = -\frac{1}{r} \begin{bmatrix} uh \\ u^2 h \end{bmatrix} \tag{17}$$

where $u=u(r, t)$ represents the radial velocity.

In Figure 1 axial (y=25m) and diagonal ($y=x$) plots of water depth and velocity at t=0.69s (the same presented by Liska & Wendroff) calculated by the SLIC model are shown. Figure 2 reports the same plots obtained with the WAF model.

The domain was halved and cut at x=45m in order to discriminate all the computational points. In both figures the 2D numerical solution is compared with the radial solution obtained by solving Equation 16

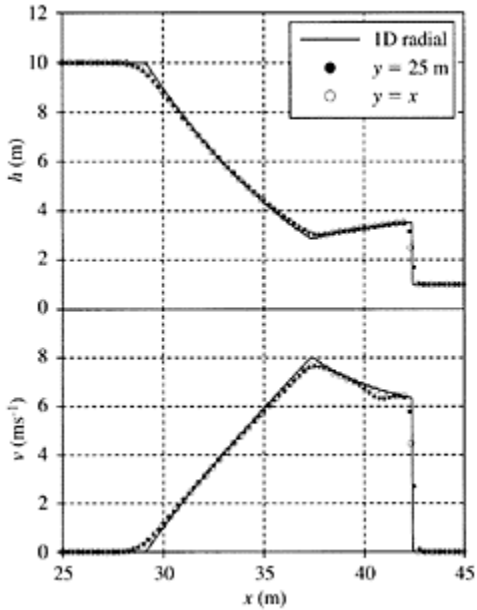

Figure 2. Circular Dam-Break problem. Axial and diagonal results at t=0.69s obtained by the 2D WAF model (201×201 cells). Radial solution obtained by the WAF model (2000 cells).

with the WAF model (Toro 2001) and with a very fine mesh of 2000 cells on the domain $25 \le r \le 50$m. This solution can be considered a good approximation of the exact one.

The figures demonstrate that the radial symmetry of the water depth is very well preserved by both the numerical schemes. Hardly appreciable asymmetries can be observed in the velocity field, just behind the shock. The shock front is captured in two spatial intervals and the overall results fit well the 1D radial reference solution.

3.2 *Shock focusing problem*

More delicate is the shock focusing problem. This rotational symmetric test, solved on an orthogonal Cartesian mesh, causes a lot of difficulties for any kind of numerical method and many 2D models are not able to resolve it well (Billett 1994, Morel et al. 1996, Liska & Wendroff 1999).

In the centre of a square dimensionless domain (−1.5, 1.5)×(−1.5,1.5) is placed an idealized circular wall of radius 0.35. The height is 0.1 inside the wall and 1 outside. Initially the system is at rest. At t=0 the wall is removed, giving origin to a circular

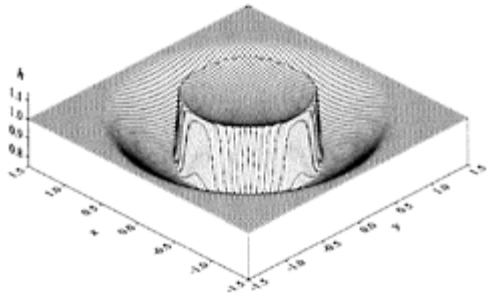

Figure 3. Shock focusing problem. 3D plot of water depth at t=1.00 obtained with the WAF model (161×161 cells).

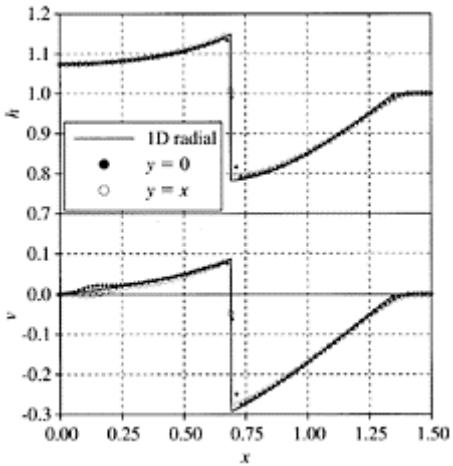

Figure 4. Shock-focusing problem. Axial and diagonal results at t=1 obtained by the 2D SLIC model (161×161 cells). Reference radial solution obtained by the WAF model (5000 cells).

shock that starts to move inward, while a rarefaction wave propagates towards the domain boundaries. The shock progressively concentrates and after passing through the

singularity at (0, 0) expands outwards. In the calculations a mesh with 161×161 points and a dimensionless acceleration g=1 were adopted as in Liska & Wendroff (1999).

In Figure 3 the 3D plot of water depths at t=1.00 obtained by the WAF model is shown. At this time the shock has already passed through the focusing point (0, 0) and is expanding outwards.

In Figure 4 axial (y=0) and diagonal *(y=x)* plots of water depth and velocity at t=1.00 calculated by the SLIC model are shown. A Courant number Cr=0.5 and the *van-Leer limiter* were adopted in the

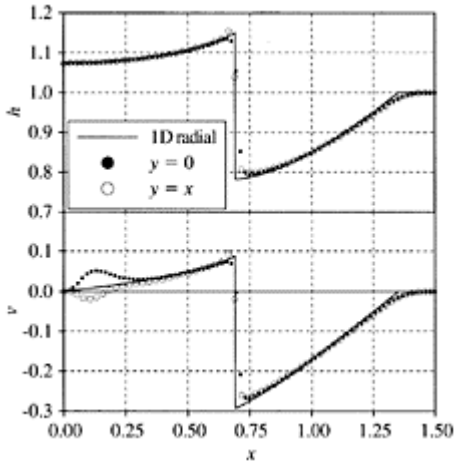

Figure 5. Shock-focusing problem. Axial and diagonal results at t=1 obtained by the 2D WAF model (161×161 cells). Reference radial solution obtained by the WAF model (5000 cells).

calculations. Figure 5 reports the same plots obtained with the WAF model (Cr=0.7 and *van-Leer limiter*). The domain was halved in order to be able to discriminate all the computational points. Note that across the shock there is a change in the sign of the velocity vectors.

Once again both the 2D numerical solutions are compared with the radial solution obtained by solving Equation 16 with the WAF model and with a very fine mesh of 5000 cells on the domain $0<r<1.5$. This solution can be regarded as the reference one.

From the figures it can be deduced that circular symmetry is preserved very well for the water depth, since the axial and diagonal solutions are almost overlapping. For the total velocity, on the other hand, a large difference between axial and diagonal results can be observed. The difference is more evident in the WAF solution but is still present in the SLIC one. As pointed out by Morel et al. (1996) this loss of symmetry is due to errors produced at the focusing point, since until the shock reaches this point the symmetry is

very well preserved. The same authors argued that this behaviour is due to the *limiter* and suggested a strategy to reduce this asymmetry.

3.3 *1D steady flow on a steep bump*

This test is similar to the one reported in Caleffi et al. (2003) except for the height of the bump which was increased from 0.2 to 0.8m as in Liska & Wendroff (1998). The aim is to verify the correctness of the bottom slope source term treatment in presence of critical transitions (from subcritical to supercritical and vice

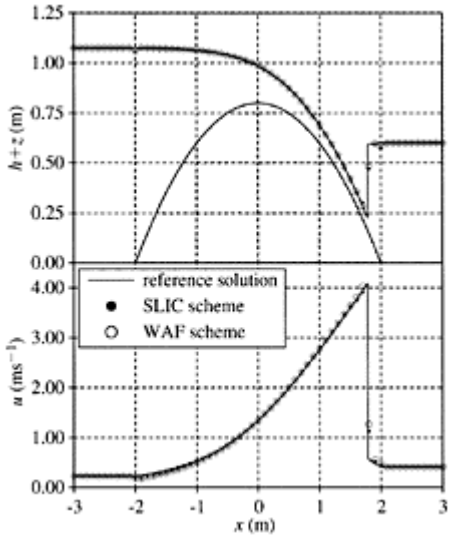

Figure 6. 1D steady flow on a steep bump. Numerical results obtained by the 2D SLIC and WAF models. Reference solution obtained by the application of Bernoulli energy equation and momentum principle through the jump.

versa) together with the shock capturing properties of the two numerical codes.

In a (−10, +10)×1m rectangular horizontal and frictionless channel a bump in the bottom elevation z_b is described by the following profile:

$$z_b(x,y)=\begin{cases}0.8-0.2\cdot x^2 & -2\le x\le 2\ \text{m}\\ 0 & \text{otherwise}\end{cases}. \qquad (18)$$

The domain is discretized with square cells of 0.1m. At the upstream boundary a constant discharge of 0.250m^3/s was imposed, whereas downstream a constant water level of

0.60m was set. These conditions cause a hydraulic jump to locate just upstream the end of the bump. Initial conditions are not important, since they influence only the transition towards the steady state, which was considered reached once the fifth decimal value of the conserved variables *(h, uh)* no longer changed in time (the third variable *vh* is always zero). The reference solution is obtained by solving the cubic algebraic equation derived by the Bernoulli theorem with a spatial discretization Δx=0.005m. The jump was located with the same degree of accuracy by the application of the momentum principle.

Figure 6 shows the numerical solutions obtained by means of the SLIC and WAF models, together with the reference solution in the $-3<x<3$m sub-domain (outside the values are rigorously constant).

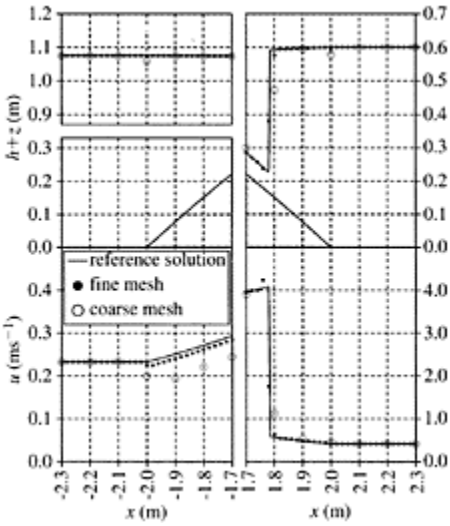

Figure 7. 1D steady flow on a steep bump. Details of water surface elevation and velocity obtained by the SLIC model with two mesh sizes together with the reference solution.

The results obtained by the numerical models are similar, as the same is the treatment of the slope source term in both the codes. Since in this test the source term plays a very important role, the other differences between the two models are masked.

In both the numerical codes, the jump is correctly located and caught in only two spatial intervals. Water surface elevations fit fairly well the reference solution, except for the two grid points located at the beginning and end of the bump, where the profile of the bottom is not smooth. A small dip in water elevation occurs due to the splitting treatment of the source terms that doesn't satisfy the C-property (Bermudez & Vazquez 1994).

The overall velocity profiles computed by the two models compare very well with the reference solution except for some grid points past the beginning of the bump, where the numerical velocity is slightly underestimated.

These differences between computed results and reference solution are strongly highlighted by the height of the bump and by the relatively coarse mesh, and decrease significantly with the mesh size. Figure 7 shows details of the results obtained adopting the SLIC model on a refined mesh (Δx=0.02m), together with those obtained on the coarse mesh (Δx=0.10m) and the reference solution. It can be observed that the dip in the water elevation was reduced to inappreciable size and also the velocity at the beginning of the bump fits better the reference solution.

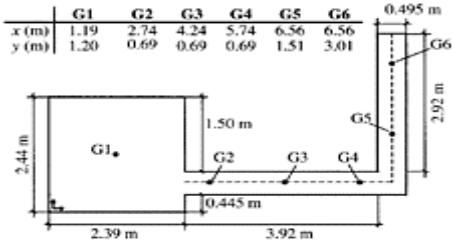

Figure 8. Experimental set-up and gauges location for the CADAM test case on a 90° sharp bend (from Soares Frazão et al. 2001)

4 LITERATURE TEST CASES

At the aim to test the capabilities of the a.m. numerical codes in presence of solid walls, initially dry bottoms and truly 2D flows, their results are compared in this section with two literature experimental tests on rapidly varying flows induced by the removal of a sluice gate.

4.1 *CADAM test case on a 90° sharp bend*

This experimental test was realized in the framework of the CADAM European project in the laboratory of the Civil Engineering Department of the Université catholique de Louvain, Belgium (Soares Frazão & Zech 1999, Soares Frazão et al. 2000, Soares Frazão et al. 2001).

Figure 8 shows the experimental set-up and the location of the six gauges. The bottom of the channel is horizontal. The downstream end of the channel is open. Initially water is at rest in the reservoir with a level of 0.20 m above the bottom of the channel that is initially dry. At t=0 the sudden pull up of the gate separating the reservoir from the channel simulates the dam-break. After about 3 seconds the wetting front reaches the bend, then the reflection at the wall gives origin to a bore which travels upstream, back to the reservoir. Downstream the bend, multiple reflections against the walls occur.

The Manning friction coefficients were estimated by the a.m. authors as n_b=0.0095 $s.m^{-1/3}$ for the bottom and n_w=0.0195$s.m^{-1/3}$ for the walls.

In the numerical description of the channel the end section was slightly modified in order to reproduce the free fall. At this aim a short high slope slide was introduced, at the end of which a far-field condition was set. At the lateral boundaries reflective (free-slip) conditions were imposed. The latest condition does not consider at all the influence of the walls. In order to take into account this effect, although approximately,

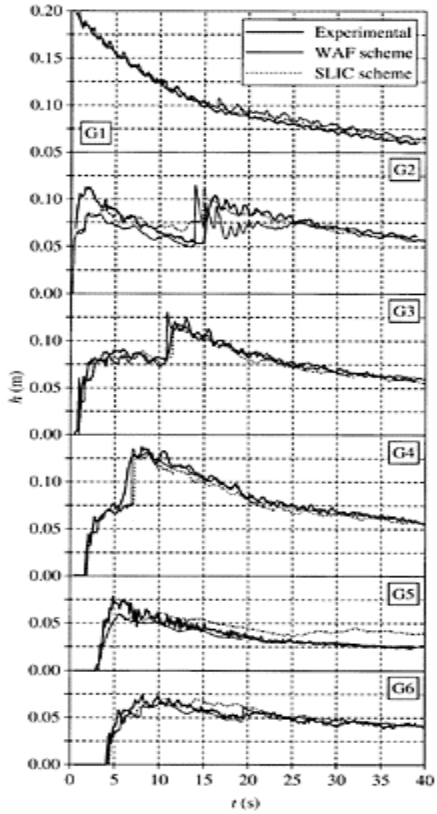

Figure 9. CADAM test case on a 90° sharp bend. Experimental and numerical water depth time series at the gauges locations.

a numerical Manning roughness coefficient was evaluated by means of the formula:

$$\overline{n} = \left(\frac{2 \cdot h \cdot n_w^{3/2} + B \cdot n_b^{3/2}}{B} \right)^{2/3} \qquad (19)$$

where B is the channel width. Equation 19 can be derived from the Einstein's formula by suppressing the wall contribution in the wetted perimeter at the denominator.

Figure 9 shows the water level time series at the six gauges locations. On the whole the comparison

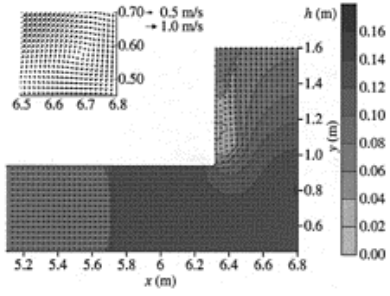

Figure 10. CADAM test case on a 90° sharp bend. Numerical (WAF model) water depth flow field with velocity vectors at t=7s.

between numerical and experimental results is satisfactory, even if at gauges G2 and G5 some significant differences occur between the two models and with respect to the experimental data. The wetting front and the main shock wave are located in time very well. On the other hand both the models are not able to correctly catch the secondary oscillations in the experimental data, due to the multiple reflections at the boundaries.

Figure 10 shows water depth and velocity fields in the bend at t=7s computed with the WAF model. The velocity field seems to fit well the measured one, reported in Soares Frazão et al. (2001); the WAF model is also able to outline the re-circulation region observed experimentally at the outer corner of the bend, as highlighted in Figure 10.

The SLIC model is not able to reproduce this behaviour.

4.2 *Parma experimental tests on a lateral breach*

This experimental test was realized in the laboratory of the Civil Engineering Department of the University of Parma, Italy (Aureli & Mignosa 2002).

In a 10m long laboratory flume (Figure 11) in which is flowing a constant discharge Q=0.01m^3/s a lateral breach is suddenly opened. This causes the sudden inundation of a planar surface, initially dry.

The perturbations rapidly propagate in the flume towards the upstream and downstream boundaries. After about 2 seconds the water in the plane begins to reach the contour, falling into the gutter. At t=5s the water has wetted all the upstream and longitudinal boundary of the plane but not the farther downstream one. About at t=60s the flow is almost steady.

Measurements of water level and velocity histories were accomplished at various places around the breach site by means of ultrasonic distance and velocity meters (for more details see Aureli & Mignosa 2002).

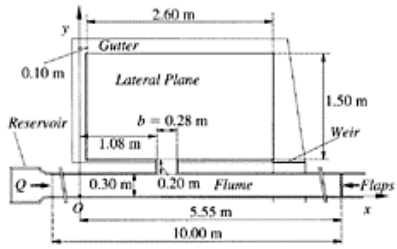

Figure 11. Parma experimental tests on a lateral breach. Picture and dimensions of the experimental set-up.

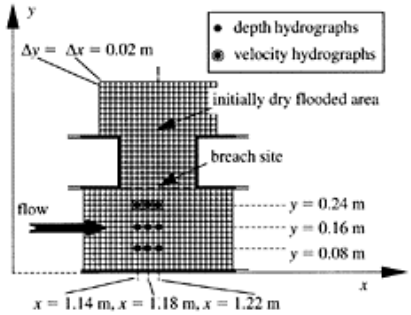

Figure 12. Parma experimental tests on a lateral breach. Particular of the experimental set-up in proximity of the breach zone with reference grid and measurement sites.

In Figure 12 a sketch of the zone of the breach with the reference grid and measurement locations is presented.

The Manning friction coefficient in the flume, experimentally estimated in uniform conditions with different discharge values, was almost the same both for the bottom and the walls and equal to $0.01 s.m^{-1/3}$. Nevertheless, to take into account the walls friction, Equation 19 was applied again in the calculations.

The simulation was performed by means of the WAF model with mesh size $\Delta x=\Delta y=0.02m$ until the final steady-state (t=60s). A far-field boundary condition was set at the downstream end of the channel.

Numerical and experimental water level time series at some significant locations are reported in Figure 13. In the figure a stretching of the hydrographs was made for the first—and more significant—five seconds.

At x=1.14m the three numerical hydrographs are close to the experimental ones. At x=1.18m and x=1.22m the overall behavior is still fairly good, but much more discrepancies between numerical and experimental values are now present. This is essentially due to the strong surface curvatures

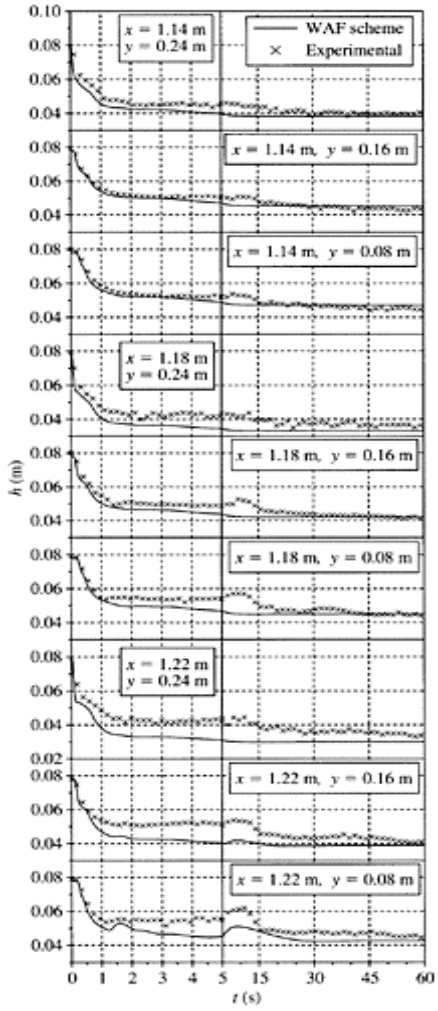

Figure 13. Experimental and numerical results for Parma test cases on a lateral breach.

which make difficult to obtain accurate experimental measurements (the divergence of the ultrasonic beam is about 3.5°) and do not allow to properly interpret the phenomenon—which is essentially 3D—with a 2D depth-averaged numerical model.

In Figure 14 the comparison of three numerical and experimental v_y time series (see Figure 12 for the location inside the flow field) are presented.

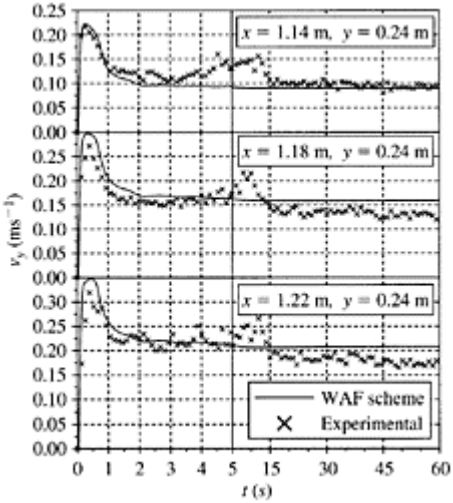

Figure 14. Numerical (WAF model) and experimental velocities (*y*-component) time series.

The measured velocity profiles were acquired at z=0.02m. The calculated values agree well with the measured data in the first seconds, when v_y starts to increase and then rapidly decreases. As for the water level hydrographs, oscillations appear in the experimental values in the middle times (4–15s). They are probably due to wave disturbances originated at the breach location and reflected from the boundaries; these oscillations are not properly caught by the numerical model. Again, final steady-state numerical y velocities agree satisfactorily with observations at x=1.14m, while at the other points the experimental values are overestimated by the computations.

5 CONCLUSIONS

Two finite volumes schemes for the integration of the 2D shallow water equations were presented. The first belongs to the MUSCL—Hancock centred schemes family; the second is based on the Weighted Average Flux method. In both models the source term is treated by means of a time-operator splitting technique.

Numerical results were firstly computed for reference test cases, for which a solution close to the exact one is available. Both numerical models perform well with all the tests,

the only exception being the velocity field of the shock-focusing problem. In this case the numerical results show a lack of radial symmetry, mainly for the WAF model. Also the 1D steady flow on a steep bump is satisfactorily resolved, especially on a fine grid.

Two literature experimental cases were then simulated; the comparisons are more than satisfactory and confirm that the models can be reliably used to deal with rapidly varying flows characterized by shocks, wetting fronts and by transitions between subcritical and supercritical conditions.

For this flows, characterized by a strong variability in space, the evaluation of the capabilities of numerical models could be improved by comparison with high resolution spatial experimental information, instead of local measurements only. At this aim an experimental investigation was presented by the writers in a related paper (Aureli et al. 2004).

REFERENCES

Alcrudo, F. & Garcia Navarro, P. 1993. A high resolution Godunov-type scheme in finite volumes for the 2D shallow water equations. *International Journal for Numerical Methods in fluids* 16: 489–505.

Aureli, F. & Mignosa, P. 2000. Two-dimensional flows due to dam or levee-breaking. *Proceedings Int. Symposium on River Flood Defence.* Kassel: Hercules Verlag.

Aureli, F. & Mignosa, P. 2002. Rapidly varying flows due to levee-breaking, In Bousmar, D. & Zech, Y. (eds.), *River Flow 2002, Proceedings of the First International Conference on Fluvial Hydraulics, Louvain La Neuve, Belgium, 4–6 September 2002.* Lisse: Balkema.

Aureli, F., Maranzoni, A. & Mignosa, P. 2004. Experimental Modelling of Rapidly Varying Flows on wet bed and in Presence of Submersible Obstacles, submitted to River Flow 2004.

Bermudez, A. & Vazquez, M.E. 1994. Upwind methods for hyperbolic conservation laws with source terms. *Computers Fluids* 23(8): 1049–1071.

Billett, S.J. 1994. A Class of Upwind Methods for Conservation Laws, PhD Thesis, Cranfield University.

Brufau, P. & Garcia-Navarro, P. 2000. Two-dimensional dam break flow simulation. *International Journal for Numerical Methods in fluids* 33: 35–57.

Caleffi, V., Valiani, A. & Zanni, A. 2003. Finite volume method for simulating extreme flood events in natural channels. *Journal of Hydmulic Research* 41 (2): 167–177.

Harten, A., Lax, P.D. & Van Leer, B. 1983. On upstream differencing and Godunov-type schemes for hyperbolic conservation laws. *SIAM Review* 25(1): 35–61.

Hirsch, C. 1988–1990. *Numerical Computation of Internal and External Flows.* Chichester: Wiley & Sons.

Glaister, P. 1991. Shallow water flow with cylindrical symmetry. *Journal of Hydraulic Research* 29(2): 219–227.

Lax, P.D. & Wendroff B. 1960. Systems of conservation laws. *Comm. Pure Applied Mathematics* 13: 217–237.

LeVeque, R.J. 2002. *Finite Volume Methods for Hyperbolic Problems.* Cambridge: Cambridge University Press.

Liska, R. & Wendroff, B. 1998. Composite schemes for conservation laws. *SIAM J. Numer. Anal.* 35(6): 2250–2271.

Liska, R. & Wendroff, B. 1999. Two-dimensional shallow water equations by composite schemes. *International Journal for Numerical Methods in fluids* 30: 461–479.

Morel, A.T., Fey, M. & Maurer, J. 1996. Multidimensional high order method of transport for the shallow water equations. Report no 96–09. Zurich: Swiss Federal Inst. of Technology.

Richtmyer, R.D. & Morton, K.W. 1967. *Difference methods for initial value problems.* New York: Interscience-Wiley.

Soares Frazão, S. & Zech, Y. 1999. Effects of a sharp bend on Dam-Break flows. *Proceedings of XXVIII IAHR Congress, Graz, 22–27 August 1999.* Graz: Technical University.

Soares Frazão, S., Morris M. & Zech, Y. 2000."Concerted Action on Dambreak Modelling: Objectives, Project Report, Test Cases, Meeting Proceedings" (CD-ROM), UCL, Civ. Eng. Dept., Hydraulic Division, Louvain-la-Neuve.

Soares Frazão, S., Spinewine B. & Zech, Y. 2001. Digital-imaging velocity measurements and numerical modelling of a dam-break flow through a 90° bend. *Proc. of XXIX IAHR Congress, Beijing, 16–21 September 2001.* Beijing: Tsinghua University Press.

Toro, E.F. 1992. Riemann problems and the WAF method for solving the two-dimensional shallow water equations. *Phil Trans. R. Soc. London A* 338:43–68.

Toro, E.F. 1997. *Riemann Solvers and Numerical Methods for Fluid Dynamics.* Berlin, Springer Verlag.

Toro, E.F. 2001 *Shock-Capturing Methods for Free Surface Shallow Flows.* Chichester: Wiley & Sons.

Experimental modeling of rapidly varying flows on wet bed and in presence of submersible obstacles

F.Aureli, A.Maranzoni & P.Mignosa
Dipartimento di Ingegneria Civile, dell' Ambiente, del Territorio & Architettura, Parma, Italy

River Flow 2004—Greco, Carravetta & Della Morte (eds.)

ABSTRACT: The results of two experimental tests concerning rapidly varying flows, originated by the sudden removal of a gate, are described. In the first the flow expands on a flat plane initially wet for few seconds, then reflects against solid walls. In the second a submersible obstacle is placed in the flat area in order to simulate an abrupt change in the topography. By adding a colouring agent to the water it was possible to obtain a solution with colour intensity increasing together with water thickness. Quantitative information about water depth distribution in the domain was obtained back lighting the Plexiglas bottom of the experimental facility and taking photographs of the area of interest. The tones of the images acquired were converted into water depths by means of transformation functions derived from a preliminary calibration. The test conditions were then simulated with a 2D numerical finite volumes model presented here briefly.

1 INTRODUCTION

Rapidly varying flows such as those resulting from the sudden collapse of a dam are, apart from the first moments, strongly affected by the topography of the region subject to flooding. Valley contractions, irregular bed slopes and obstacles present in the flow field are key factors that can induce the formation of hydraulic jumps, shocks, wave reflections and other sudden changes in the flow behaviour. In modeling this kind of flows, usually accomplished by solving numerically the 2D shallow water equations, the terms related to resistance and topographical influence are synthesized in the so-called source terms. However the capabilities of the numerical schemes are often verified comparing computed results only with analytical solutions in which the source terms are equal to zero. Since for truly 2D unsteady flows analytical solutions are not available—even for

simple geometries and in the absence of the source terms of the equations—it is worthwhile to validate numerical models by comparison with experimental results too (Bechteler et al. 1992, Bellos et al. 1992, Fraccarollo & Toro 1995, Brufau & Garcia-Navarro 2000, CADAM 2000, Soares Frazão et al. 2001).

The paper presents the results of a laboratory investigation having the aim to acquire experimental data of rapidly varying free surface flows induced by the sudden removal of a sluice gate. Two experimental tests are presented here. In the first the flow expands on a flat plane initially wet for few seconds, then reflects against solid walls. In the second an obstacle was placed in the flat area in order to simulate an abrupt change in the topography; the obstacle was chosen thin enough so that it can be submerged by the water but in the meantime enough thick to influence significantly the overall phenomenon. Amongst the available experimental methods to measure water depths, a colorimetric technique applied to the images acquired with a high resolution digital camera was favoured (Braschi et al. 1994). This choice allows to obtain information in the whole area of interest, highlighting the main flow field characteristics, such as shocks and hydraulic jumps, without introducing any disturbance in the flow field.

The results of the experimental investigation were then compared with the numerical results obtained by means of a 2D finite volume numerical code, realised by the authors themselves, whose main features are described here briefly and explained in depth in another paper presented at this Conference (Aureli et al. 2004).

2 EXPERIMENTAL FACILITY AND TEST CONDITIONS

The experimental facility (Figs. 1a, b), set up at the hydraulic laboratory of Parma University, consists of a rectangular tank with a flat bottom made by transparent Plexiglas. The tank is divided by a wall into two portions: the smaller having the function of reservoir and the bigger subject to the flooding consequent to the sudden removal of a gate, placed in the middle portion of the dividing wall. The aluminium gate is seated in a trapezoidal groove for seal reasons and is moved by a pneumatic piston which ensures that the total stroke (0.20m) is released in about 8/100s.

In order to reproduce in a schematic way the effects of an abrupt change in the bottom topography on the flow field, one of the tests was performed placing asymmetrically an obstacle in the floodable area. Likewise the flat bottom, the obstacle itself was realized in a block of Plexiglas so as to be as much transparent as possible. The location and dimensions of the obstacle (Fig. 2) are such that it can be completely submerged by the water flowing from the reservoir after the release of the gate, but in the meantime to significantly influence the overall phenomenon.

At the aim of acquiring water depths in the flooded area via colorimetric techniques, this part of the tank was back lighted with cold fluorescent lamps placed in such a way to obtain a luminance as uniform as possible over the entire investigation area.

Colorimetric information were obtained adding to the water a fixed quantity of a coloring agent (methylene blue) and taking photographs of the back lighted floodable area by means of a reflex digital camera (Canon EOS 10D). The camera is equipped with a 22.7×15.1mm CMOS sensor and is capable to acquire 9 frames at about 3Hz with the

maximum resolution of 3072×2048 pixels; afterwards the filling of the buffer allows to acquire only one frame every 1.8 seconds about.

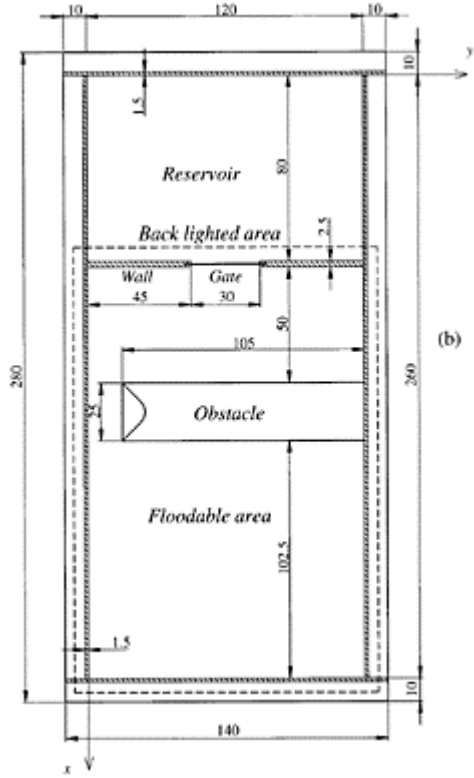

Figure 1. (a) Picture and (b) main dimensions (in cm) of the experimental facility.

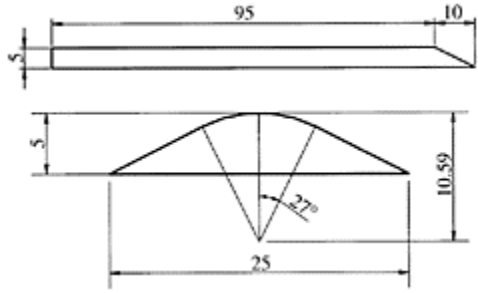

Figure 2. Shape and dimensions (in cm) of the obstacle.

The camera was placed on a tribrach in order to put the optical axis as normal as possible with respect to the bottom of the facility and aligned with the center of the floodable area. To time exactly each picture a 0.01s resolution digital timer was set in a lateral portion of the frame, triggered by the movement of the gate.

The experimental investigation was completed by point measurements of water depth time series accomplished by means of a piezoelectric ultrasonic distance meter. The gauge was located close to the longitudinal wall (x=1.627m, y=0.022m in the coordinate system of Figure 1b), to be out from the perspective projection of the back lighted bottom.

In the following the results of two laboratory tests are reported, whose main characteristics are

Table 1. Main features of the experimental tests.

Test No.	Initial upstream water level (m)	Initial downstr. water level (m)	Obstacle
1	0.15	0.01	Absent
2	0.15	0.00	Present

summarized in Table 1. In the first, due to the presence of an initially wet floodable area, a shock is expected to move downstream and, after few seconds, to reflect against the solid walls of the experimental facility. In the second test the floodable area is initially dry, but the presence of the obstacle induces a complex flow field with the formation of hydraulic jumps and reflections. The aim of the experimentation is to track this two dimensional structures and to reproduce them with the mathematical model.

3 MEASURING TECHNIQUE AND CALIBRATION

The adding of a fixed quantity of colouring agent (methylene blue) to the water permits to obtain a solution whose color intensity, increasing with water thickness, can be translated in quantitative information about water depth distribution in the flow field. This technique allows to obtain water depth information in the whole area of interest avoiding in the meantime any kind of disturbances in the flow (Braschi et al. 1994).

The acquired RAW images were firstly converted in TIFF format (8 bit per channel), avoiding any artifact eventually introduced by compression algorithms or sharpness filtering, and then the three RGB layers were merged in 8 bit grey space. Figure 3 shows an example of the photograph taken at t=4.77s during the Test 2.

Before each test a spatial calibration was performed taking several photographs of the back lighted area submerged with an increasing thickness (from 1 to 15 cm) of water, previously colored, at rest condition. This calibration procedure allows to account for every local disturb that could be caused by a not perfect uniformity of the lighting field, by the light absorption of the Plexiglas block of the obstacle (if present), by the optics vignetting and by all the other external chances.

From the calibration images it was possible to derive for each pixel a transformation function between grey tones, ranging from 0 to 255, and water depths (from 0 to 15cm) and then to estimate indirectly the water depth. The colouring agent concentration

($12.5 g/m^3$) and exposure parameters, of course fixed for all the calibration and test photographs, were chosen in such a way to cover a range of grey tones as wide as possible.

Figure 4 shows three examples of the transformation functions *grey scale—water depth* for a central pixel, for a pixel on the edge of the back lighted area

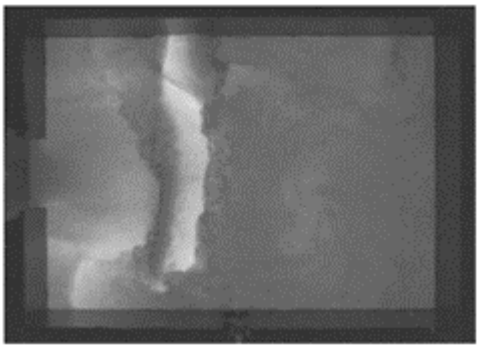

Figure 3. Picture taken during Test 2 at t=4.77s.

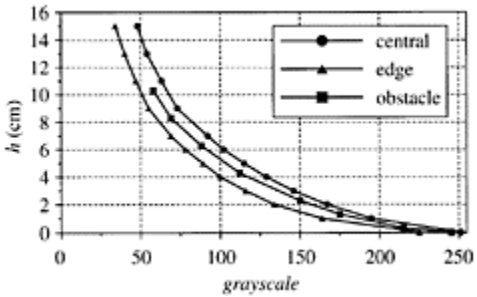

Figure 4. Examples of transformation functions *grey scale-water depth* for a central pixel, for a pixel on the edge of the back lighted area and for a pixel belonging to the obstacle (Test 2).

and for a pixel belonging to the obstacle. From the graph it can be observed that for thin water depths the precision of the conversion is high (about 55–60 grey tones between 0 and 1cm), whereas for thick layers of water the precision decreases significantly (about 6 grey tones in the range 13–15cm). The repeatability error, that is the differences in the grey value for the same pixel in different shots taken at the same conditions, is typically of one or, at most, two grey tones. Then the percentage error in the water depth estimation is almost constant and of about 2%.

Other sources of errors are due to anomalous light reflections against the walls and to the entrapment of air bubbles in the water. To get out of the first source, all the walls and the gate itself were internally blackened. For the second source of errors, no general solution was found. Small air bubbles do not affect very much the images indeed, since the pixel dimension (7.4μm) corresponds to about 1mm in the real field and then all the smaller irregularities are masked; the bigger bubbles, on the other hand, give rise to anomalous reflections which darken the contours sometimes—but sometimes not—below the minimum grey values recorded during the calibration procedure. Since during the test execution water depth values higher than the initial one in the reservoir (15cm) were not expected, it was decided to not extrapolate the transformation function but to discard these data instead.

A post processing routine was set up in order to calibrate the camera and to transform the central projection of each image in a real orthophotograph.

Firstly the inner calibration of the camera and of the lenses was performed, once and for all, by means of a commercial package (PhotoModeler Pro 4.0, 2000). From the calibration the exact focal length *(c)*, the principal point coordinates (ξ_0, η_0) and the radial (k_1, k_2) and decentering (p_1, p_2) lens distortion parameters were derived. To any pixel of the sensor surface, being FC, ξ, η (Fig. 5) the system of image coordinates, the following compensation was applied:

$$\xi_c=\xi+dr_\xi+dp_\xi,\ \eta_c=\eta+dr_\eta,+dp_\eta, \tag{1}$$

where the radial distortion components are:

$$dr_\xi=(\xi-\xi_0)(1+dr),\ dr_\eta=(\eta-\eta_0)(1+dr), \tag{2}$$

with:

$$dr=k_1 r^2+k_2 r^4,\ r^2=(\xi-\xi_0)^2+(\eta-\eta_0)^2, \tag{3}$$

whereas those for decentering distortion read:

$$\begin{aligned} dp_\xi &= p_1\left[r^2+2(\xi-\xi_0)\right]^2+2p_2(\xi-\xi_0)(\eta-\eta_0), \\ dp_\eta &= p_2\left[r^2+2(\eta-\eta_0)\right]^2+2p_1(\xi-\xi_0)(\eta-\eta_0). \end{aligned} \tag{4}$$

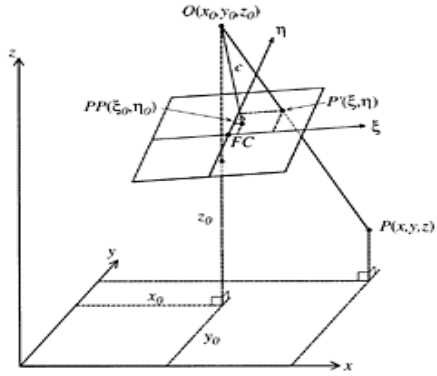

Figure 5. Relation between image and object coordinates (Kraus 1997).

Then the six parameters of the outer orientation, which define the position and attitude of the camera in the object coordinate system (x_0, y_0, z_0 and the angles of rotation ω, ϕ, κ on the primary, secondary and tertiary axis), were derived using three control points with known image and object coordinates. The reconstruction of the orthogonal projection of the water depth field on the object coordinate system, known the water depth z for each pixel and the outer orientation of the camera, was based on the collinearity equations:

$$x = x_0 + (z - z_0)\frac{r_{11}(\xi - \xi_0) + r_{12}(\eta - \eta_0) - r_{13}c}{r_{31}(\xi - \xi_0) + r_{32}(\eta - \eta_0) - r_{33}c}$$
$$y = y_0 + (z - z_0)\frac{r_{21}(\xi - \xi_0) + r_{22}(\eta - \eta_0) - r_{23}c}{r_{31}(\xi - \xi_0) + r_{32}(\eta - \eta_0) - r_{33}c}, \quad (5)$$

where the parameters r_{ij} (i, j=1, 2, 3) are the elements of a spatial rotation matrix which describes the attitude in space of the photograph relative to the object coordinate system xyz (Kraus 1997).

Finally, the scatter data obtained in the object coordinate system were interpolated on a Cartesian grid with $\Delta z = \Delta y$=5mm perfectly superimposable to that adopted in the mathematical model. The interpolation was based on the following inverse distance relation:

$$\tilde{z} = \sum_{i=1}^{N} \frac{z_i}{d_i^2} \Big/ \sum_{i=1}^{N} \frac{1}{d_i^2} \quad (6)$$

where N are the scatter data searched in a circle with 1cm radius around the grid point, each of them characterised by the water depth z_i at distance d_i from the grid point. Anyhow, the high number of scatter points make the interpolation procedure substantially unimportant.

The acquiring and correction procedure, although not free from inaccuracies, allows nevertheless a comprehensive reconstruction of the phenomenon and of its characteristics.

4 NUMERICAL SIMULATION

The adopted numerical code is based on a finite-volumes discretization of the 2D shallow water equations written in integral form:

$$\frac{d}{dt}\int_A \mathbf{U}\, dA + \int_C \mathbf{H}\cdot\mathbf{n}\, dC = \int_A \mathbf{S}\, dA, \tag{7}$$

where A represents the area of the integration cell, C the cell boundary, $\mathbf{n}$ is the outward unit vector normal to C and t is the time; $\mathbf{U}=(h, uh, vh)^T$ is the vector of the conserved variables (water depth and specific discharge in x and y directions); $\mathbf{H}=(\mathbf{F}, \mathbf{G})$ is the tensor of fluxes, being $\mathbf{F}=(uh, u^2h+0.5gh^2, uvh)^T$ and $\mathbf{G}=(vh, uvh, v^2h+0.5gh^2)^T$, with g acceleration due

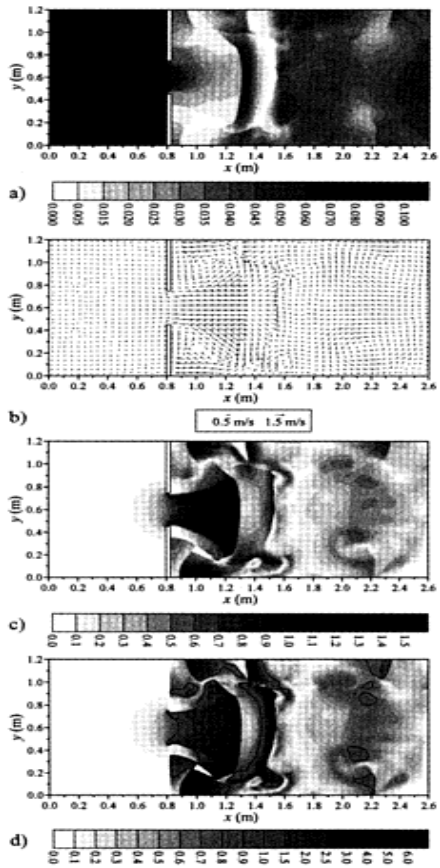

Figure 6. Numerical results for Test 2 at the time t=4.77s: a) contour map of water depths (m), b) vector map of

velocity field c) contour map of velocity norm (m/s), d) contour map of Froude numbers with line at Fr=1 drawn.

to gravity; $\mathbf{S}=(0, gh(S_{0x}-S_{fx}), gh(S_{0y}-S_{fy}))^T$ is the source term,where S_{0x}, S_{0y}, S_{fx} and S_{fy} are, respectively, the bottom and frictional slopes along the x and y axis.

The Manning equation is used to compute the friction terms:

$$S_{fx}=\frac{n^2 uh\sqrt{(uh)^2+(vh)^2}}{h^{10/3}}, S_{fy}=\frac{n^2 vh\sqrt{(uh)^2+(vh)^2}}{h^{10/3}} \quad (8)$$

in which n is the Manning roughness coefficient.

The adopted numerical method for the solution of the homogeneous part of (7) belongs to the class of MUSCL-Hancock centred slope limiter schemes, known in literature under the acronym *SLIC (Slope LImiter Centred)* (Toro 1997, Toro 2001); it is explicit, shock capturing, high resolution, *TVD*, of second order of accuracy both in time and space and it is based on the *unsplit* formula:

$$\overline{\mathbf{U}}_{i,j}^{n+1}=\mathbf{U}_{i,j}^{n}-\frac{\Delta t}{\Delta x}(\mathbf{f}_{i+\frac{1}{2},j}-\mathbf{f}_{i-\frac{1}{2},j})-\frac{\Delta t}{\Delta y}(\mathbf{g}_{i,j+\frac{1}{2}}-\mathbf{g}_{i,j-\frac{1}{2}}). \quad (9)$$

In (9) $\mathbf{U}_{i,j}^{n}$ represents the vector of the integral averages of the conserved variables over the element *(i, j)* at time $t=t^n$, Δt is the time step, Δx and Δy are the mesh sizes, **f** and **g** are the intercell numerical fluxes in x and y directions, respectively.

Numerical fluxes are based on the *FORCE (First-ORder Centred)* (Toro 1997, Toro 2001) method. The source term **S** is treated with a *splitting* technique (Toro 1997, 997, Toro 2001).

A more detailed description of the numerical scheme can be found in a related paper presented at this Conference (Aureli et al. 2004).

The computational domain was described by means of a Cartesian *cell-centred* discretization with square cells of 5×5mm. The computational time step Δt was controlled via the *CFL* stability criterion, with Courant Number Cr=0.95. Reflective, free-slip conditions were imposed on the solid boundaries. The Manning coefficient for the Plexiglas bottom was set at $0.007 sm^{-1/3}$.

As an example, the complete numerical results for Test 2 at t=4.77s are shown in Figure 6.

5 COMPARISON BETWEEN EXPERIMENTAL AND NUMERICAL RESULTS

Figures 7 to 14 show snapshots of experimental and computed water depths in the floodable area at different times for the two tests presented here.

The areas on the borders of the orthophotographs, where not enough information was available to interpolate a reasonable water depth value, were blacked. They of course increase with the water depth. The

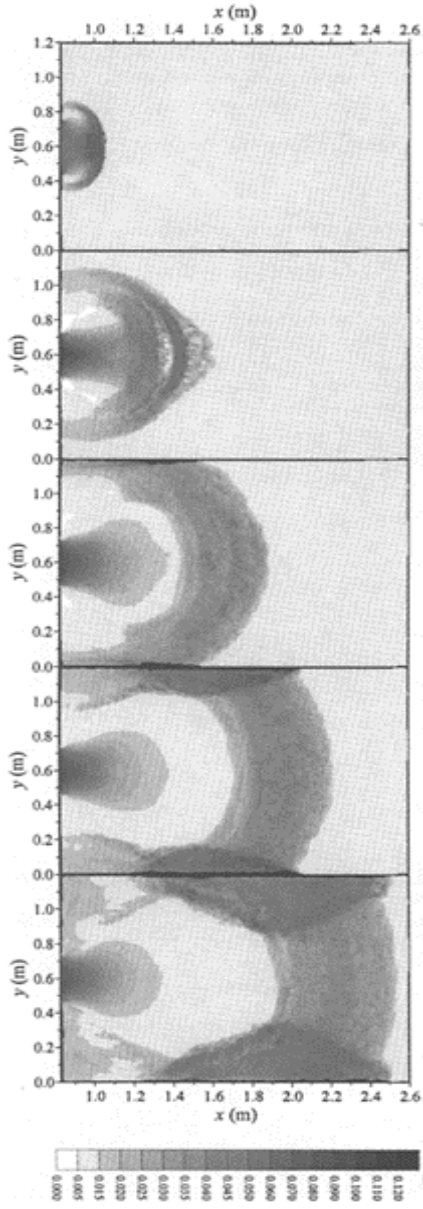

Figure 7. Experimental water depths (m) for Test 1 at t=0.24s, t=0.59s, t=0.94s, t=1.29s, t=1.64s.

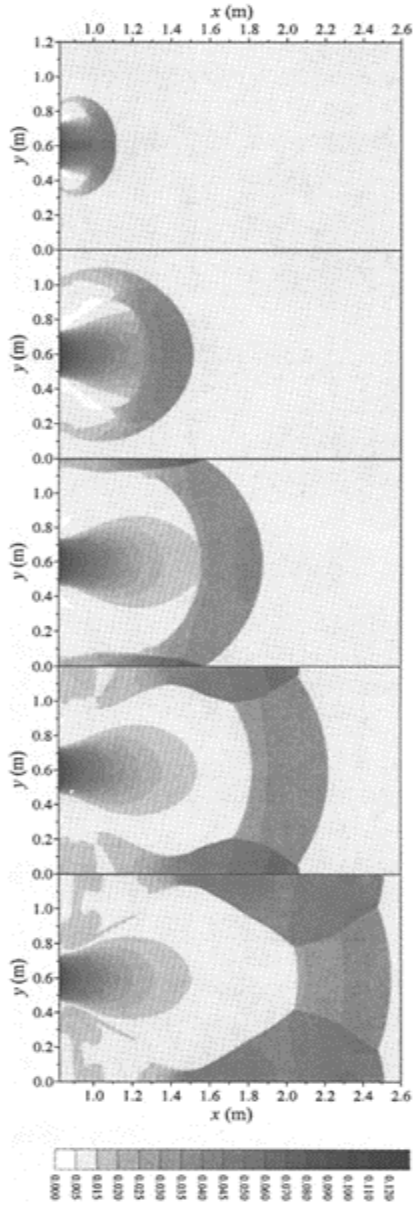

Figure 8. Numerical water depths (m) for Test 1 at t=0.24s, t=0.59s, t=0.94s, t=1.29s, t=1.64s.

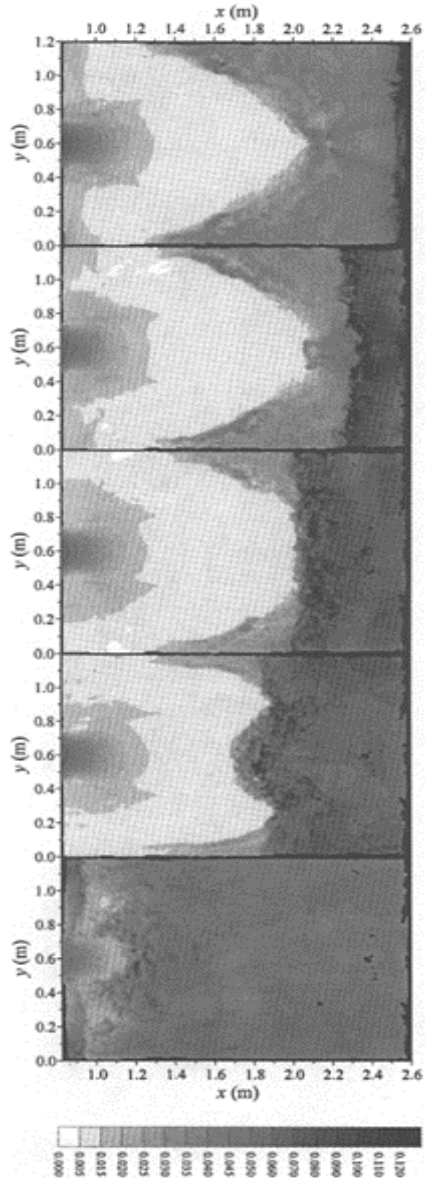

Figure 9. Experimental water depths (m) for Test 1 at t=2.00s, t=2.35s, t=2.70s, t=3.05s, t=4.89s.

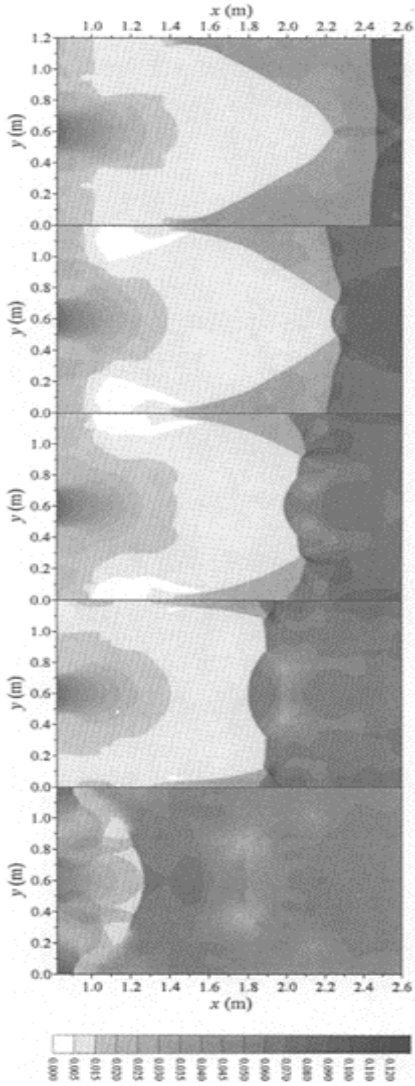

Figure 10. Numerical water depths (m) for Test 1 at t=2.00s, t=2.35s, t=2.70s, t=3.05s, t=4.89s.

blacked areas inside the domain are due to the air bubble anomalous reflections previously discussed.

In Test 1, the shock moving downstream on the still water (Figs. 7 and 8), together with those originated on

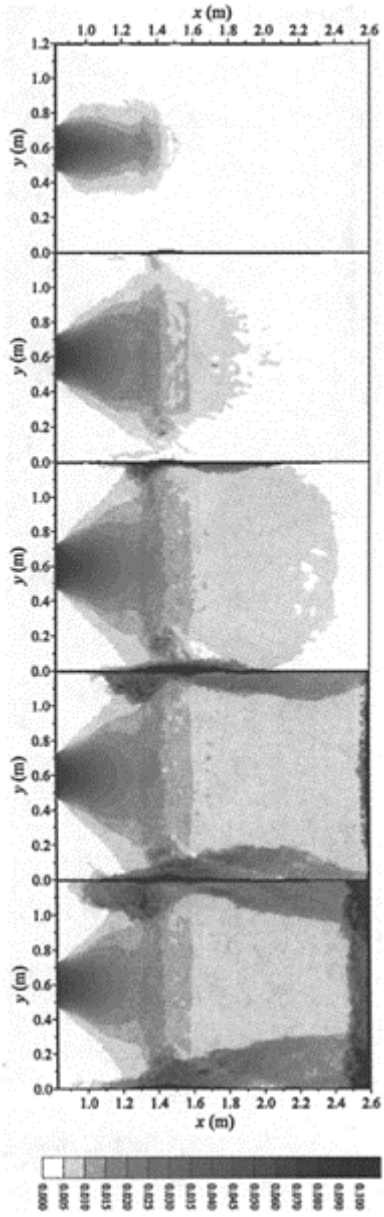

Figure 11. Experimental water depths (m) for Test 2 at t=0.46s, t=0.81s, t=1.16s, t=1.51s, and t=1.86s.

the lateral walls, are caught very well by the numerical model. After the reflection against the downstream wall (Figs. 9 and 10) the position and shape of the moving upstream hydraulic jump is reproduced fairly well, too.

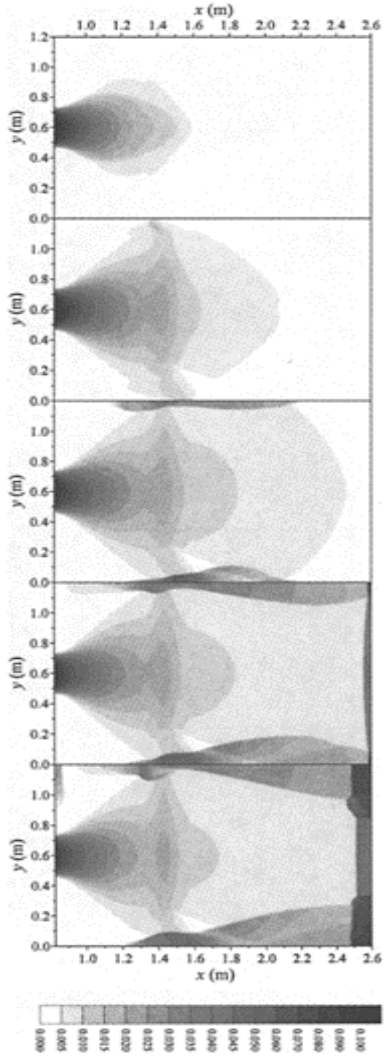

Figure 12. Numerical water depths (m) for Test 2 at t=0.46s, t=0.81s, t=1.16s, t=1.51s and t=1.86s.

In Test 2, the water at first overflows the obstacle, which shows a moderate effect on the overall flow field (Figs.11–12). Then, some complex structures start to develop, mainly upstream the obstacle on the left

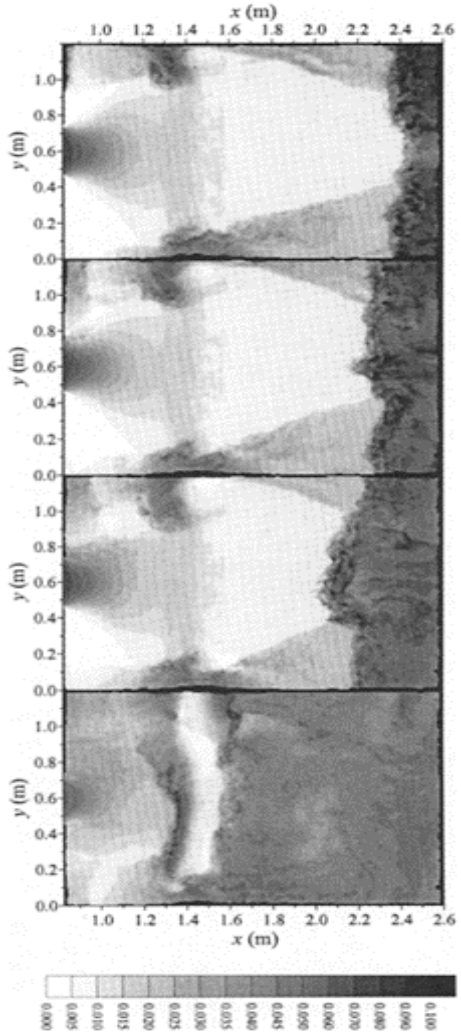

Figure 13. Experimental water depths (m) for Test 2 at t=2.21s, t=2.58s, t=2.93s, t=4.77s.

side (Figs. 13–14). These structures are satisfactorily caught by the numerical model even if during the intermediate times (t=1.86÷2.93s) their dimensions are slightly underestimated.

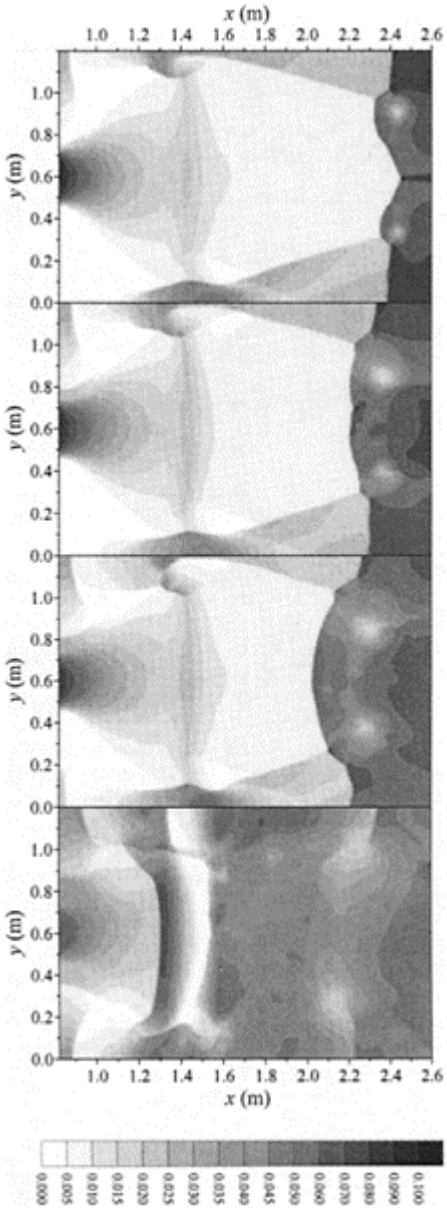

Figure 14. Numerical water depths (m) for Test 2 at t=2.21s, t=2.58s, t=2.93s, t=4.77s.

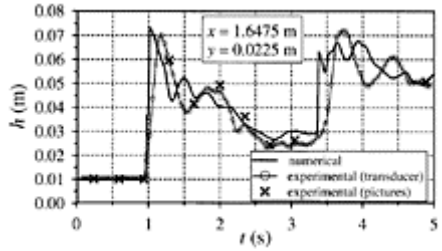

Figure 15. Comparison between experimental and numerical water level time series (Test 1).

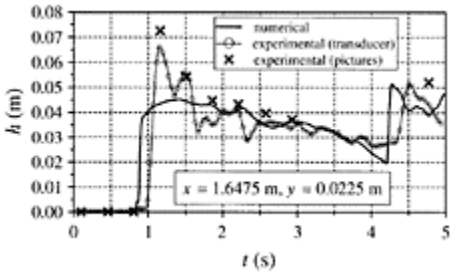

Figure 16. Comparison between experimental and numerical water level time series (Test 2).

At t=4.77s, on the other hand, the experimental water depth flow field becomes again very well reproduced by the numerical model.

Figures 15 and 16 show the water depth time series derived from the ultrasonic transducer, from the orthophotographs and from the numerical model at the location reported in the graphs (cfr. Fig. 1b).

In Test 1 (Fig. 15) the comparison between the results obtained by means of the two experimental techniques is fairly good. The computed results match well the experimental ones too, especially before the second shock at t≈3.5s. The results for Test 2 (Fig. 16) are less satisfactory. The computed water depths show a less peaked value at t≈1.2s with respect to those derived with both the experimental techniques; also, the time location of the first shock is slightly anticipated. In the intermediate times, however, the values deduced by the orthophotographs and those computed fit fairly. It must be stressed that the comparison is made at a very bad location, close to the solid wall, in order to avoid the presence of the transducer body on the acquired images.

6 CONCLUSIONS

Experimental results for two rapidly varying flows due to partial dam break were derived using coloured water and taking photographs of the area of interest. The acquired images were then transformed into orthophotographs and the grey tone of each pixel was converted into water depth by means of a previously calibrated transformation function.

The adopted technique allowed to obtain a high resolution spatial information, avoiding in the meantime any kind of disturbances in the flow field. It proved to be advantageous, with respect to few point measurements, in tracking the several moving structures which often occur in this kind of phenomena due to the superimposition of reflected waves.

The comparison between experimental data and numerical results, obtained by means of a 2D finite volume code realized by the authors, showed an overall good agreement, despite some differences at local scale.

The proposed 2D numerical model seems then to be capable to reproduce in a reasonable way the main characteristics of the phenomena under investigation.

REFERENCES

Aureli, F., Maranzoni, A. & Mignosa, P. 2004. Two dimensional modeling of rapidly varying flows by finite volume schemes, submitted to River Flow 2004.

Bechteler, W., Kulisch, H. & Nujic, M. 1992. 2-D Dam-Break Flooding Waves: Comparison between Experimental and Calculated Results. In A.J.Saul (ed.), *Floods and Flood Management.* Dodrecht: Kluwer Academic Publishers.

Bellos, V., Soulis, J.V & Sakkas, J.G. 1992. Experimental investigations of two dimensional dam-break-induced flows. *Journal of Hydmulic Research*, IAHR 30(1): 47–63.

Braschi, G., Dadone, F. & Gallati, M. 1994. Plain flooding: near field and far field simulations. In Molinaro & Natale (eds.) *Modelling of Flood Propagation over Initially Dry Areas; Proc. intern conf, Milan, 29 June–1 July 1994*. New York:ASCE.

Brufau, P. & Garcia-Navarro, P. 2000. Two-dimensional dam break flow simulation. *International Journal for Numerical Methods in fluids* 33: 35–57.

CADAM, Concerted Action on Dam Break Modelling 2000. Soares Frazão, S., Morris, M. and Zech, Y. eds. Université Catholique de Louvain, Civ. Eng. Depth., Hydraulics Division, Louvain-la-Neuve, Belgium, CD-ROM.

Fraccarollo, L. & Toro, E.F. 1995. Experimental and numerical assessment of the shallow water model for two-dimensional dam-break type problems. *Journal of Hydraulic Research*, IAHR 33(6): 843–864.

Kraus, K. 1997. *Photogrammetry*. Bonn: Dümmler. PhotoModeler Pro Version 4.0 2000., Vancouver: Eos Systems Inc.

Soares Frazão, S., Spinewine, B. & Zech, Y. 2001. Digital imaging velocity measurements and numerical modelling of a dam-break flow through a 90° bend. *Proc. XXIX IAHR Congress, Beijing, 16–21 September 2001. Theme C*: 240–245. Beijing: Tsinghua University Press.

Toro, E.F. 1997. *Riemann Solvers and Numerical Methods for Fluid Dynamics.* Berlin: Springer Verlag.

Toro, E.F. 2001. *Shock-Capturing Methods for Free-Surface Shallow Flows*, Chichester: John Wiley & Sons.

Velocity measurements in dam-break flow using imaging system

A.H.N.Chegini & G.Pender
Department of Civil & Offshore Engineering, University of Heriot-Watt, Edinburgh

A.Slaouti
Department of Engineering & Technology, Manchester Metropolitan University, Manchester

S.J.Tait
Department of Civil & Structural Engineering, University of Sheffield, Sheffield

River Flow 2004—Greco, Carravetta & Della Morte (eds.)

ABSTRACT: An investigation of dam-break flow with dry and wet beds downstream has been undertaken. An image analysis system based on tracer particles was used in the laboratory to record the instantaneous velocity variations in the area of interest in the downstream channel and visualise the flow structure. The experimental measurements of the flow velocity downstream dry and wet-bed were obtained. Higher values of velocity were obtained for the dry-bed case than for the case with downstream water depths. Measurements from the experimental study were used for comparison with analytical solutions, which demonstrates a good agreement with experimental results.

1 INTRODUCTION

Dam-break flows have been studied for a long time, but the flooding caused by the dam rupture only received focused attention during the Second World War due to bombing. These failures and the associated damage have emphasised the importance of evaluating the safety of existing dams for design and planning purposes.

Predictive mathematical model investigations of the effect of dam-break floods have been carried out by several researchers several decades and some important results have been obtained, see for example Su & Barnes (1970), Fread (1977) and Bellos & Sakkas (1987). Since field data for this flow is very difficult to obtain, it is necessary to collect experimental data to verify the mathematical models. Several experimental investigations

of dam-break flow have been reported in the last four decades, see Derssler (1954), Miller & Tschantz (1972), Bell *et al.* (1992) and Lauber & Hager (1998 & 1999).

With the improvement made in computer technology, computational models of flows in dam failures are widely used and have become predictive tools. In addition, physical models are more expensive than a computational equivalent. Examples of computational model studies dam-break flows can be found in Soulis (1992) and Glaster (1993) who compared these with recent experimental data for dam-break flows. On the other hand, a range of novel experimental methods based on signal and image analysis system have been developed for measuring flow velocities which are particularly useful in unsteady flows such as dam-break flow. Such data can be used for the validation of numerical calculations. Traditional velocity measurement methods are laser Doppler anemometry (LDA) and hot-wire anemomerty (HWA) provide single-point measurements (Buchhave, 1989). These methods have high accuracy. Alternative methods are whole field measurement techniques, which should be viewed as complementary measuring tools. In these methods, the flow field is illuminated with a thin light sheet from a powerful source and might be filmed photographically or digitally. Once several particles appear in the illuminated area, then the velocity vectors can be obtained for this area using tracking algorithm techniques based on auto-correlation, cross-correlation or Young's fringe method see Cenedese & Paglialunga (1990), Adrian (1989) and Buchhave (1992).

In this paper, the main objective is to investigate the instantaneous whole-field velocity of the dam-break flows by tracking particles seeded in the flow, after the bore has become established. Previous work concentrated on the initial stages of dam-break flow, theoretically, numerically and experimentally see Stansby, Chegini & Barnes (1998). A measuring system enables individual particles in the flow to be tracked directly. Particle tracking velocimetry (PTV) and particle streak velocimetry (PSV) methods were applied for a digital system. These methods do not need photographic development and processing time, although spatial resolution can be a problem using standard SVHS video equipment. In this study, PSV was used, measuring streaks to obtain maximum average of the particle movements for all the downstream dry and wet bed cases. The automated PTV method was suited to subcritical flows which was assessed by comparing with PSV measurements. Finally, the experimental velocity measurements were compared with computational calculation.

2 EXPERIMENTAL METHOD

The experimental rig was an open channel flume with a horizontal bed. The test facility consisted of a 15.24m length of 0.4m by 0.4m rectangular cross section flume. Part of the upstream and downstream walls of the dam site were made with clear Perspex to view the flow. The upstream end of the flume was closed but the downstream end was open for the dry case and had different level weirs for the downstream wet-bed conditions. These weirs were utilised to form the downstream wet-bed initial conditions. The dam site was set up at 9.76m from the upstream end. A thin movable metal plate (3mm thick) was used to simulate the instantaneous dam-break. This slid in small plastic channels mounted at a section around the flume bed and sides. A rope was attached to the top of the dam plate and loops through a pulley to a 7kg weight which was released from about 0.8m above

the laboratory floor. The experiments were made with an upstream depth (H) of 0.1m and downstream depths of dry, 0.1H, 0.3H, 0.45H and 0.55H.More details of the test facility used to generate the dam-break flows can be found in Chegini (1997).

In this study, an instantaneous whole flow field plane visualisation and velocity measurements of the area of interest were investigated using PTV and PSV techniques. These methods are based on tracer particles which are added to the flow and then illuminated with a powerful light source. The particles were spherical, 80 micron in diameter, solid polystyrene seeding powder with a relative density of 1.0±0.2, which made the particles neutrally buoyant in water and able to follow the flow. The particles were mixed in the flow rig before running each test. The light source for illumination in the field of view was a 4 watt Argon ion laser. The laser beam was transmitted from the laser light source to the light sheet generator by using a 20m long optical fibre link. The light sheet generator produced a vertical plane light sheet with the width of 1–3mm along the flume. A JVC TK-1085E colour CCD camera was used to record a 8.4cm by 6.9cm picture field. The camera operates with PAL standard for video scanning of 25 images/second. The camera was connected to a VCR, PC and TV screen, allowing instant monitoring of the field of vision and enabling the motion of flow to be recorded for further processing. The schematic arrangement of the laboratory set-up is shown in figure 1. In order to analyse an analogue camera output or a standard video signal, this has to be converted to an array of digital information known as a digital image.

A device known as a ‘Frame Grabber’ is used to convert the original analogue signal. This device can be fitted internally into one expansion slot of the standard personal computer or can be externally connected to it. All frame grabbers freeze the analogue signal and discretely sample it to provide an image which is a series of discrete digital values that are then stored in a two dimensional array of numbers. This array of individual element numbers (pixels) with an integer color (grey level) is represented as the digital image. Frame grabber boards are equipped with a minimum of two buffers per image but can have many more, each buffer image having 512×512 pixels with 256 (8 bit) grey levels. The digital image can be processed on the board memory or the host computer from the buffer. Each digital data element (pixel) is denoted by a number, which represents the amount of light intensity of a small area of the visual image. The sampled number of each pixel conventionally gives the level of darkness or brightness of the small area. Zero represents black, the maximum value, 256, denotes white and intermediate values designate various shades of grey. This software was written in parallel C for a 3L compiler to control image capture and processing.

3 IMAGE ANALYSIS SYSTEM

The captured images were cleaned-up by filtering and then thresholding. Therefore, the background becomes black (grey level 0) and the foreground particle images become white (grey level 256). At this stage, all seeding particles appear in the frame image sequence as white colour. The images are now suitable for further processing. The technique of applying image analysis to obtain quantitative velocity flow field information from particle movement encompasses a number of different methods. They are differentiated by the form of the captured image and the analysis technique employed.

The displacement of individual particles within a field of view over the known short time period yields information about the velocity vector field simultaneously over the whole plane for which the particle image data was gathered. The following section describes two techniques PTV and PSV and concludes with a description of their application to a dam-break flow system.

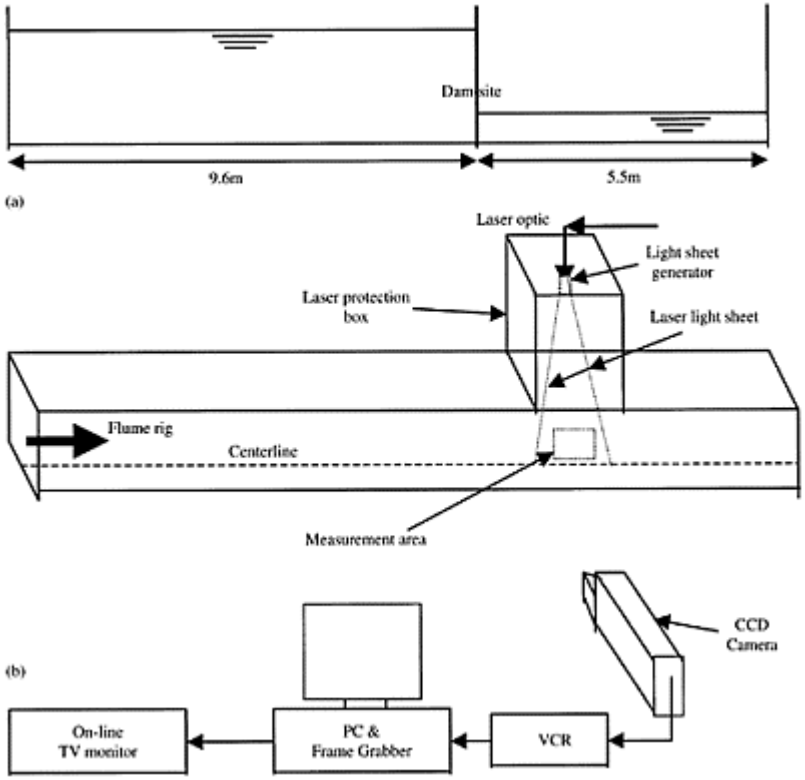

Figure 1. Sketch of experimental facility of dam-break flow (a) side view of the flume; (b) laboratory arrangement.

3.1 *Particle tracking velocimetry*

This method requires individual particles to be located in an image and successive images to be recorded on successive frames. The system analyses pairs of single exposed digital images to produce whole field maps of velocity vectors. Particle images at different times exist on the separate frames. There is no directional ambiguity in the calculated vectors and the direction of particle motion is easily found. There is also no lower limitation on particle motion between frames. The particle tracking technique is used to accurately

determine the position of a particle in an image frame and compare it with its location at a known short time interval later (in a successive frame). The distance traveled by an individual particle is then calculated and the velocity found knowing the time interval between images. This process is repeated for all of the particles appearing in the frame sequence.

In this study, the automated particle tracking system was used for subcritical flows. The digitised images were improved by using image processing techniques, and the particles are tracked by means of a localised correlation function. This technique is based on the comparison of a small window around a particle image in one frame with a series of windows around many particles in a later frame. A match is required between the spatial pattern of neighboring particles around each window with a corresponding window in another frame. The window which gives the best correlation can be used to locate each particle pair. Various correlation algorithms have been developed to allow the tracking of particles from frame to frame. Examples of these are Dalziel (1992), Brucker & Althaus (1992), Hassan *et al.* (1992). A number of complex flow situations has been analysed successfully by using PTV For example, see Nishio *et al.* (1992), Uemura *et al.* (1989).

3.2 *Partide streak velocimetry*

Seeding particles in the fluid medium may be recorded on a single frame of photographic or video film by using a relatively long exposure time. The application of particle streak in fluid mechanics has been used for qualitative flow visualisation as illustrated in Van Dyke (1982). Particle streak images can be digitised for development into the quantitative measuring technique known as particle streak velocimetry (PSV). This method is usually used when the fluid has a seeding particle concentration less than that for PTV This method does not require individual streak images to be overlapped and distinguished from each other. PSV enables accurate individual streak lengths to be determined and then analysed. As the exposure time is known, it becomes possible to obtain the velocity associated with a particle streak. The processing of the streak images includes filtering the images to eliminate noise and thresholding to separate the streak from the background. The white streaks corresponding to the particles can then be located and measured, see Kobayashi & Saya (1988). The image analysis for locating streak images and measuring their lengths with known exposure time to obtain the velocity field has been demonstrated in a wide variety of flow situations, see Utami & Ueno (1987), Green & Gerrard (1993).

The problem with streak image measurements is that in a real flow situation the particles may enter or leave the plane of interest (i.e. the light sheet) during the exposure time. This means that the actually recorded streak length of the particles will be less than the actual distance moved by the particle. Therefore, this will lead to an incorrect estimate of velocity, which is reported by researchers such as Khalighi & Lee (1989) and Adamczyk & Rimai (1988). According to the sensitivity of the recording medium particle streaks may not be recorded at all if they travel too fast. Some attempts have been made to resolve such problems with a degree of success, see Marko & Rimai (1985).

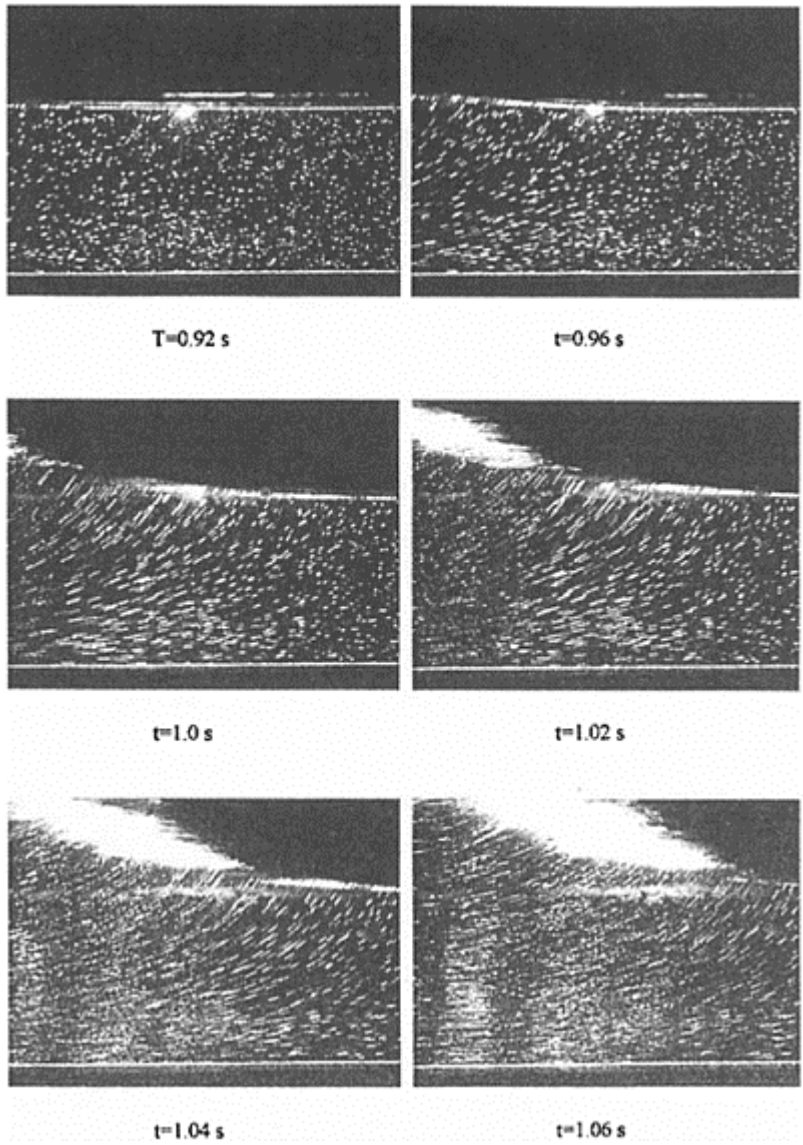

Figure 2. Typical time series of the raw digitised images at downstream of the dam site with initial water depth condition

In this present study, particle images were digitised using equipment that has already been described. A manual method of streak line measurement is used whereby a cursor is carefully moved around the screen to measure the length of streak images. Tests were

performed at a variety of initial conditions with different exposure times. These will be described including some results in the following section.

4 RESULTS

The most interesting of the experimental results will be shown here. More details regarding the experimental data can be found in Chegini (1997). In this paper, visualisation and measured velocity fields are presented by analysing images using PTV and PSV methods. The free surface profiles in the initial stages of the dam-break flow from the digitised images have already been published see Stansby *et al.* (1998). Visualisation and velocity field measurement of dam-break flows over obstacle have also been produced by image analysis methods, Chegini (1997). Surface elevations at various longitudinal positions were also measured using resistance probes and essentially confirmed the results from the digitised images. Details of the surface profile plot with the identified area (8.4×6.9cm) of the recording digitised images at centred 85cm downstream of the dam-site for the downstream dry-bed and wet-bed initial flow conditions can be found in Chegini (1997). Figure 2 shows typical time series of the raw digitised images at location x=85cm downstream of the dam-site for different initial flow depth ratios. These raw digitised images of the flow are processed to obtain the time series of the whole flow field. Note that x=0 corresponds to the dam-site. To aid illumination, seeding powder is dropped on the water around the area of interest. The powder is neutrally buoyant in water. The velocity fields are here defined by the tracking of the particle streaks.

The raw digitised flow field images used to obtain the velocity field for the fixed camera position at 85cm downstream of the dam-site. Some images suggest these regions are in fact a mixture of spray and particles. The results show white long straight and mixed lines with some brighter areas. These are due to high speed and turbulent flow with entrained air. Given the above problems and the fact that the time interval between image is too long the Particle Tracking Velocimetry (PTV) technique cannot match between the two sequence frames. Since the video images were not clear enough as explained, the particle streak velocimetry (PSV) method was applied to obtain the maximum average of velocity. The streak images were measured at several frames on the video play back system whilst the digitising procedure took place. As the relationship between pixels and object distance and exposure time were known the velocity could be determined. Taking the reading of the length of the straight lines, the results can be plotted on a graph, as shown in figure 3, based on streak line measurement technique. This figure shows that the velocity increased quickly at the beginning and then decreased with some variation, to a more or less stable value. This figure also emphasises the bore velocity wave in the front of the flow propagation in the downstream section. The results show that the initial slope of the velocity variation with

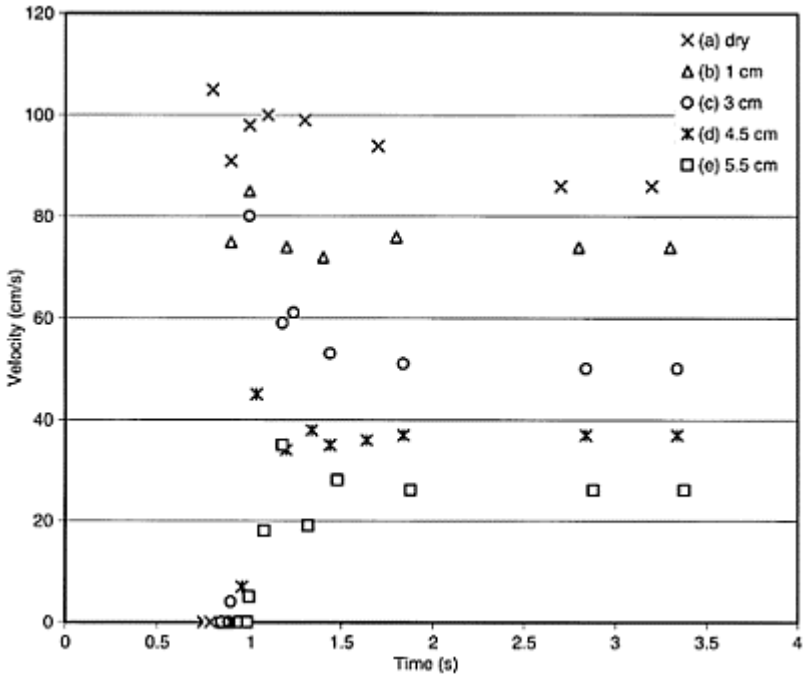

Figure 3. Variation of the streamwise velocity against time obtained by PSV for different initial water depth flow conditions.

time decreases as the downstream initial water depth increases.

Finally, some frames of the digitised flow field images were analysed to obtain the velocity information by the particle tracking technique for a downstream initial depth of 4.5cm and 5.5cm which presents the subcritical flows. The typical results are shown in figure 4 as frames progresses. Observation of the results from the particle tracking technique and digitised images emphasises the similarity as expected. The digitised flow field images of the wave propagation in the downstream initial conditions also show clearly that the flow particles in the stationary area had moved before the wave as confirmed by PTV results. A general comparison between the maximum average of the velocity obtained by PSV (Fig. 3) and PTV (Fig. 4), shows reasonable agreement for the cases with the depth ratios of 0.45 and 0.55.

5 COMPARISON OF ANALYTICAL AND EXPERIMENTAL RESULTS

An analytical solution of the homogenous, incompressible, unsteady, one-dimensional flow, considering flow friction forces but neglecting wind and coriolis force effects, was

applied. A hydrostatic pressure distribution was assumed throughout the flow field. Readers can find the theory in Stoker (1957) and more details of calculation in Chegini (1997). Figure 5 shows the comparisons between analytical solutions and experimental measurements for the test flume under dry-bed and wet-bed flow conditions. For all depth ratios, the velocity fields eventually became quite stable after the bore develops downstream. The experimental velocity fields show the upper limit of the flow including the air/water mixture as compared with analytical results. In general, these comparisons are considered to be satisfactory for the downstream supercritical and subcritical flow region.

6 CONCLUSIONS

An image analysis system has been applied to the dam-break flow for investigation of the instantaneous whole flow field visualisation and measurement of the velocities. The whole flow field velocity data may be used to assess the ability of a computer model to simulate flow structure. The system has limitations which correspond to the high water speed and turbulent flow with entrained air.

Experimental flow visualisation of the dam-break flow has shown interesting movements of the flow particles in the stationary area before the arrival of the wave. These features are confirmed by PTV results and have not been reported previously. As the experiments show, the front wave interaction with the downstream dry-bed or wet-bed flow conditions produce a complex phenomena, but the velocity profiles become established after a front wave. Experimental velocity results after the front wave is consistent with those obtained from analytical solution.

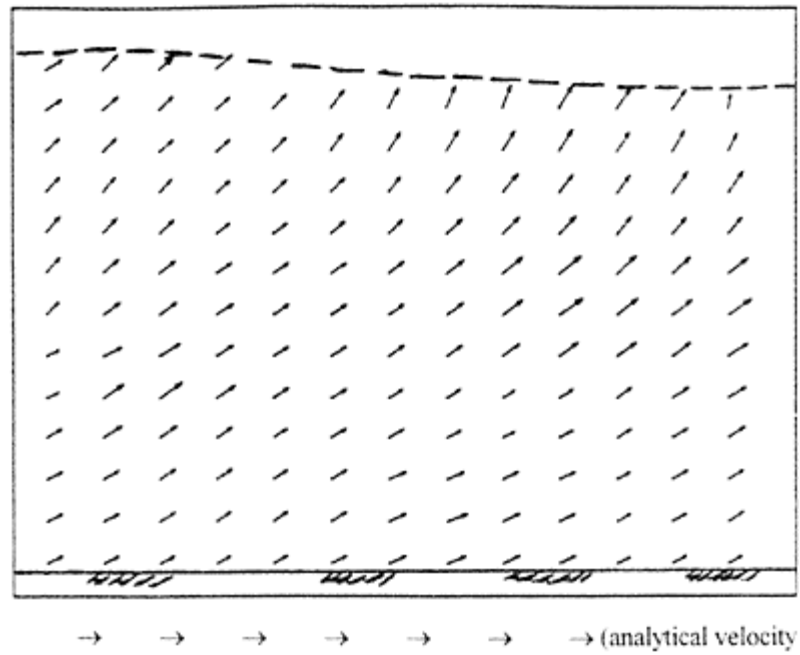

Figure 4. Typical instantaneous interpolated velocity field obtained by

PTV at downstream of the dam site for subcritical flow condition.

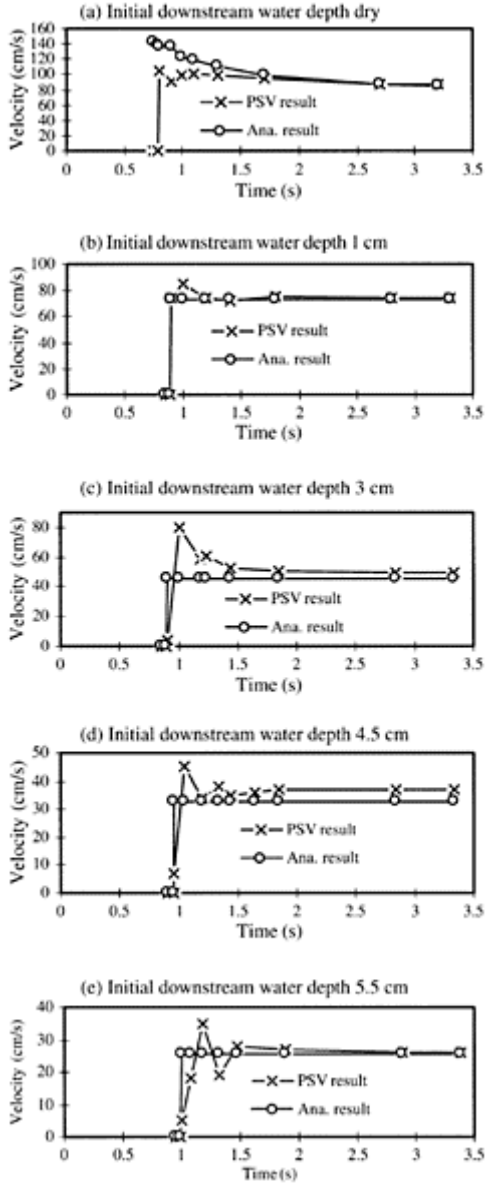

Figure 5. Comparison of the variation of the velocity against time obtained by PSV and analytical calculation.

ACKNOWLEDGEMENT

The help and supervision of Professor P.K.Stansby at UMIST is gratefully acknowledged. The loan of the argon-ion laser from Dr J.T.Turner is also acknowledged.

REFERENCES

Adamczyk, A.A. & Rimai, L. 1988. 2-Dimensional particle tracking velocimetry (PTV), technique and image processing algorithms. *Experiments in fluids* 6:373–380.

Adrian, R. 1989. Engineering application of Particle Image Velocimeters. *Proceeding of ICALOE'89, Laser Institute of America:* 56–71.

Bell, S.W., Elliot, R.C. & Chaudhry, M.H. 1992. Experimental results of two-dimensional dam-break flows. *Journal of Hydraulics Research* 30(2).

Bellos, C.V. & Sakkas, J.G. 1987. 1-D dam-break flood wave propagation on dry bed. *Journal of Hydraulics Engineering* (12):1511–1525.

Brucker, C. & Althaus, W. 1992. Study of vortex breakdown by particle tracking velocimetry (PTV). *Experiments in fluids* 13:339–349.

Buchhave, P. 1989. Advances in turbulence measurement techniques, *Advance in Turbulence.* George, W.K. & Arndt, R. (eds), Hemisphere Publishing.

Buchhave, P. 1992. Particle image velocimetry-status and trends. *Experimental Thermal and Fluid Science* 5: 586–606.

Cenedese, A. & Paglialunga, A. 1990. Digital direct analysis of a multi-exposed photograph. *Experiments in Fluids* 8: 273–280.

Chegini, A.H.N. 1997. Investigation and analysis of dam-break flows. *PhD dissertation.* University of Manchester.

Dalziel, S.B. 1992. Decay of rotating turbulence, Some particle tracking experiments. *Applied Scientific Research* 49: 217–244.

Derssler, R.F. 1954. Comparison of theories and experiments for the hydraulic dam-break wave. *Assemble general de Rome. Int. Assoc. Hydro* 3(38):319–328.

Fread, D.L. 1977. The development and testing of a dam-break flood forecasting model. *Proceeding of dam-break flood modelling workshop.* Washington, D.C. USA Water Resources Council:164–197.

Glaster, P. 1993. Flux difference splitting for open-channel flows. *Inter. Jour. for Numerical Method in Fluids* 16: 629–654.

Green, R.B. & Gerrard, J.H. 1993. Vorticity measurements in the near wake of a circular cylinder at low Reynolds numbers. *Journal of Fluid Mechanics* 246:675–691.

Hassan, Y.A., Blanchat, T.K. & Seeley Jr, C.H. 1992. PIV flow visualisation using particle tracking techniques. *Measurement Science and Technology* 3:633–642.

Imaichi, K. & Ohmi, K. 1983. Numerical processing of flow visualisation pictures measurement of two-dimensional vortex flow. *Journal of Fluid Mechanics* 129:283–311.

Khalighi, B. & Lee, Y.H. 1989. Particle tracking velocimetry, an automatic image processing algorithm. *Applied Optics* 28(20): 4328–4332.

Kobayashi, T. & Saya, T. 1988. A real-time velocity measurement algorithm for two-dimensional flow fields. *2nd International Symposium on Fluid-Control, Measurement, Mechanics and Flow visualisation,* Sheffield, UK: 174–178.

Lauber, G. & Hager, W.H. 1998. Experiments to dambreak wave: Horizontal channel. *Journal of Hydraulic Research* 36(3): 291–307.

Lauber, G. & Hager, W.H. 1999. Experiments to dambreak wave: Sloping channel. *Journal of Hydraulic Research* 36 (5):761–773.

Marko, K.A. & Rimai, L. 1985. Video recording and quantitative analysis of seed particle track images in unsteady ftows. *Applied Optics* 24(21):3666–3677.

Miller, W.A. & Tschantz, B.A. 1972. Laboratory investigation of one-dimensional wave motion in open channels. *Paper presented at the National Water Resources Engineering Meetingm, ASCE,* Atlanta-Georgia:24–28.

Nishio, S., Himeno, Y. & Okuno, T. 1992. Flow measurement around oscillating circular cylinder in uniform flow. *Proceeding of the Workshop on Hull form Design and Flow Phenomena.* Inchon. Korea.

Soulis, J.V. 1992. Computation of two-dimensional dam-break flood flows. *Inter. Jour. for Number. Methods in Fluids* 14:631–664.

Stansby, P.K., Chegini, A.H.N. & Barnes, T.C.D. 1998. The initial stages of dam-break flow. *Journal of Fluid Mechanics* 374:407–424.

Stoker, J.J. 1957. Water wave. *Interscience publishers.* Wiley and sons. New York.

Su, S.T. & Barnes, A.H. 1970. Geometric and frictional effects on sudden release. *J. Hyd. Div. ASCE* 96(11): 2185–2200.

Uemura, T., Yamamoto, F. & Ohmi, K. 1989. A high speed algorithm of image analysis for real time measurement of two-dimensional velocity distribution. *Flow Visualisation* FED 85:129–133.

Utami, T. & Ueno, T. 1987. Experimental study on the coherent structure of turbulent open-channel flow using visualisation and picture processing. *Journal of Fluid Mechanics* 174:399–440.

Van Dyke, M. 1982. An album of Fluid Motion. *Parabolic Press.*

1D model of surface waves generated by a reservoir's bank landslide: a case study

P.García-Navarro, G.Pérez & P.Brufau
Fluid Mechanics, CPS, University of Zaragoza, Spain

M.E.Vázquez-Cendón
Applied Mathematics, University of Santiago de Compostela, Spain

River Flow 2004—Greco, Carravetta & Della Morte (eds.)

ABSTRACT: The work presented is a contribution to the predictive numerical modelling of surface waves generated by bank slides. The study is based on a one dimensional approach assuming that the flow generated is governed by the St, Venant equations. The mechanism triggering the solid slide is out of the scope of the work, therefore the slide properties are set as external parameters. The flow equations are solved with an upwind scheme specially adapted to wetting/drying boundaries.

1 INTRODUCTION

The study of the sliding movement of land volumes is of great complexity. Generally speaking, it can be classified according to several factors such as the time scale associated (from very slow like in glaciers to very fast like in mud or debris flows), the content of water, the slope of the terrain or the characteristics of the involved materials. On the other hand, it can be triggered by another diversity of factors. There is a particular aspect, matter of this study, concerned with the impact of important volumes of sliding materials falling into water volumes, either in movement (rivers) or at rest (lakes, reservoirs). In such events the risk is not precisely associated to the sliding mass but in first instance to the waves generated by the energy transferred to water by collision. A second risk is the possibility of heavy deposition of material in the river bed forming an artificial dam able to accumulate an important volume of water but not for a long time, giving rise to further catastrophic dam failure.

In this work, a one-dimensional mathematical model for water flow and sliding mass movement is presented. The resulting equations are essentially the shallow water equations with time dependent bed level and/or time dependent channel width supplied with an external rule for the time dependencies and a modified friction term. They are

solved by means of an upwind scheme based on Roe's method with special care put on the wet/dry or dry/wet interfaces.

The model is applied to the simulation of a real case. The Santa Liestra reservoir is a project on Ésera River by Santa Liestra village in the Spanish Pyrenees. The project is intended to regulate 81.9Hm^3 at the upper part of the river. There is controversy due to the risk associated to potential land slides in the nearby mountains forming the banks of the future reservoir. With the proposed model, the objective was to simulate the consequences of the described potential slides in their interaction with the reservoir. The starting point for this study were previous geological studies of the area and a former study developed by CEDEX (Centro de Estudios y Experimentación de Obras Públicas).

One of the risk areas identified by geologists is placed on the left bank of the river near a narrow section. It involves more than 50Hm^3 of meteorized and fractured materials. One of the theories describing a possible risk scenario states that the lower part of this solid volume could become saturated when filling the reservoir, leading to instability.

The topology of the area is markedly one-dimensional with the hypothetic falling mass representing a transversal sliding. We have made the hypothesis of rigid sliding, that is, movement of the volume in a block with a falling celerity of 10m/s, according to previous studies.

The sliding volume was characterized by means of six geological cross sections every 250m, estimating the average thickness and volume for each of them.

The river channel was modeled by means of trapezoidal cross sections of variable bottom width and side slope. The simulation was performed using 1000 grid nodes along the river and a time step subject to CFL=0.7 for the transient calculation. The initial water depth in the reservoir was the less favorable corresponding to full reservoir, that is, water surface level h_{in}=642m and water at rest (initial conditions). The friction coefficient for the Manning law used was $n_{Manning}$=0.04. The slide modeling was based on the geometric description of the sliding volume and a special mathematical treatment of transversal sliding described in the main text.

2 GOVERNING EQUATIONS

2.1 *Flow equations*

Flow movement in the longitudinal reservoir considered is assumed to be well described by the 1D shallow water equations. The shallow water equations are an approximation to the three-dimensional reality. The water velocity in a river, for instance, varies from bank to bank and in the vertical direction. However, for many practical applications, these variations may be ignored and the problem be approximated as variable only in the spatial direction along the main flow. In case of continuous solutions the differential form is deduced. In terms of the wetted cross section $A(x, t)$ and the discharge $Q(x, t)$

$$\frac{\partial A}{\partial t}+\frac{\partial Q}{\partial x}=0 \tag{1}$$

$$\frac{\partial Q}{\partial t}+\frac{\partial}{\partial x}\left(\frac{Q^2}{A}+gI_1\right)=gA(S_0-S_f)+gI_2 \tag{2}$$

where S_0 and S_f are bed and energy slope terms and I_1 and I_2 are pressure terms, all of them well described elsewhere (). Equations (1), (2) can also be written in compact differential form

$$\frac{\partial U}{\partial t}+\frac{\partial F(x,U)}{\partial x}=H(x,U) \tag{3}$$

called the conservative form where

$$U=\begin{pmatrix}A\\Q\end{pmatrix},\quad F=\begin{pmatrix}Q\\\frac{Q^2}{A}+gI_1\end{pmatrix},\quad H=\begin{pmatrix}0\\gA(S_0-S_f)+gI_2\end{pmatrix}$$

A different, non-conservative form can be derived

$$\frac{\partial U}{\partial t}+J\frac{\partial U}{\partial x}=H(x,U)-\frac{\partial F(x,U)}{\partial x}=H^*(x,U) \tag{4}$$

where ***J*** is the Jacobian matrix

$$J=\frac{\partial F}{\partial U}=\begin{pmatrix}0 & 1\\c^2-u^2 & 2u\end{pmatrix}$$

with eigenvalues

$\lambda_1=u+c$

$\lambda_2=u-c$

and with eigenvectors

$$e_1=\begin{pmatrix}1\\u+c\end{pmatrix},\quad e_2=\begin{pmatrix}1\\u-c\end{pmatrix}$$

u is the fluid velocity and c is the small water surface waves celerity

$$c=\sqrt{\frac{gA}{\sigma}}$$

Being a hyperbolic system, it admits characteristic formulation and the eigenvalues are equal to the slopes of the characteristic curves in *(x, t)*. This is the property in which Roe's scheme is based.

2.2 *Slide modeling*

The slide movement will be considered solid and compact, formed of the same material as the flow bed or walls, neglecting deformation and infiltration of water into the solid matrix.

The sliding is modeled in the frame of a one-dimensional approach by assuming the sudden motion of either the channel bed or the channel side wall, both conforming the solid-liquid boundary. This involves the assumption of a time and space variable channel geometry. From the mathematical point of view, these effects modify the dynamic equation as time variable source terms inducing transient flow (waves) in the mass of

water. When the slide direction is the same as the channel main direction, the model is based on a channel bed movement (longitudinal slide). The channel bed level *(z)* depends on both position *x* and time *t.* The slide size (volume or thickness) and velocity into the fluid are modeled by means of variations in the function *z (x, t).*

Sliding along a direction normal to the channel main direction is referred to as transverse sliding and the modeling is based on channel breadth variations along distance *x* and time *t, σ_f (x, t).* As in the case of bed variation, the adequate definition of the function σ_f *(x, t),* characterizes the physical parameters of the sliding mass.

This procedure is useful to model sliding shapes entering the channel as a pulse, parabola, triangle, etc, which can be completely submerged or emerge from the water. The movement followed by the shape function is that of the assumed sliding mass. In the longitudinal sliding, the bed movement induces a pressure excess that pushes also in the longitudinal direction. Therefore, a wave traveling in the direction of the perturbation is generated.

However, in the case of a transverse sliding, water is pushed by one of the side walls against the opposite side and forced to climb up. The result is that the initial surface level is raised and two front waves traveling both upstream and downstream are generated. All movements follow a unique direction in the longitudinal sliding case, being adequately modelled by a one-dimensional approach. This is not the case for a transverse sliding, since the transmitted waves are normal to the perturbation direction. The water surface level pattern is complex and the fluid behaviour depends on many factors. The actual phenomenon is locally tridimensional. However, we model it with a one-dimensional approach so that it can be plugged into a 1D river or channel model. The main difficulty associated with naively modelling transverse sliding in 1D is that, at a given cross section, the predicted centroid of the fluid cross section is at a different position than that of the real fluid, hence leading to different waves due to the potential energy accumulated. Channel breadth variation is not enough and should be complemented with channel bed variation. A way to introduce this kind of information into the one-dimensional model is required. The strategy used in this work is described in ( ).

It is customary in shallow water models to use a parametric formulation the energy slope, both in steady and unsteady turbulent cases, either in terms of the Chezy coefficient C_{chezy} or the Manning roughness factor *n(ref).*

$$S_f = \frac{u|u|}{C_{Chézy}^2\left(\frac{D_h}{4}\right)} = \frac{n^2 u|u|}{\left(\frac{D_h}{4}\right)^{4/3}}$$

where D_h represents the hydraulic diameter. This is the accepted friction model for fixed bed problems. When the bed is moving at a celerity $v_d(x, t)$, that is, in the zone where a sliding is taking place, the relative velocity between flow and solid bed $u - v_d$ is the key variable in order to introduce a term containing the shear interaction between the solid mass inmovement and the longitudinal flow. Furthermore, and in order to model the presence of new materials in the channel bed, a friction coefficient different from the channel bed roughness *(n*)* value must be introduced. In these cases, the following is applied [40] [39] for S_f:

$$S_f = \frac{(u - v_d)|(u - v_d)|}{C^{*2}_{Chézy}\left(\frac{D_h}{4}\right)} = \frac{n^{*2}(u - v_d)|(u - v_d)|}{\left(\frac{D_h}{4}\right)^{4/3}}$$

3 NUMERICAL METHOD

The numerical method used in this work is an upwind finite volume method based on Roe's approximate Riemann solver. This technique has proved efficient for unsteady shallow water problems over fixed bed[21].

The computational domain will be divided into a finite number of uniform cells ($\Delta x=cte$) for the numerical resolution of the equations. The time stepping procedure will be based on a variable time step Δt, always determined by the numerical stability requirements. The criterion used is the Courant-Friedrich-Lewy (CFL), which states that the maximum allowable time step, compatible with stability, in this case is given by

$$\Delta t_{Cr} = \frac{\Delta x}{|u| + c}$$

therefore requiring that the dimensionless CFL number

$$\mathrm{CFL} = \frac{\Delta t}{\Delta t_{Cr}}$$

is always less that unity for stability CFL$\leq$1.

The numerical method has been implemented as described in ( ) and ( ) and will not be repeated here.

When modelling landslides and their interaction with water volumes, it is possible and frequent to encounter at the same time wet (h>0) and dry nodes (h=0) in the domain, as pointed before. The limit between a wet node and a dry node will be called a wetting/drying interface and poses a special difficulty from the numerical point of view in the two following situations in which a dry cell is placed next to a wet-dry and has a higher bed level:

h_{i+1}=0 and $z_i+h_i<z_{i+1}$ (Fig. 1)

We need to redefine Δz as $\Delta z=h_i$ instead of $\Delta z=z_{i+1}-z_i$ in order to ensure mass conservation at least in steady state [6].

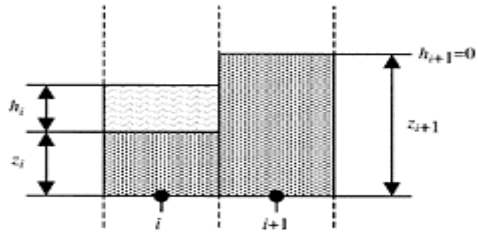

Figure 1. Wet-dry interface (case A).

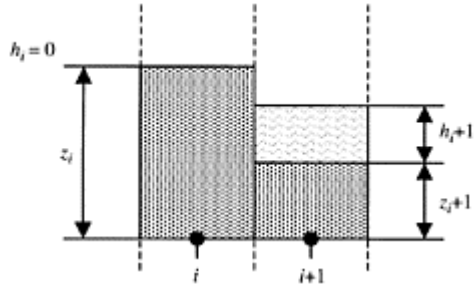

Figure 2. wet-dry interface (case B)

h_i=0 and $z_{i+1}+h_{i+1}<z_i$ (Fig. 2)

We need to redefine Δz as $\Delta z=-h_{i+1}$ instead of $\Delta z=z_{i+1}-z_i$ for the same reason.

4 APPLICATION TO A REAL CASE

After the validation of the model against experimental data for a longitudinal sliding and the calibration of the solutions by means of academic test cases ( ), the numerical method will be applied to a case of practical interest characterized by irregular cross sections and realistic dimensions. The problem consists of the evaluation of the consequences of the potential catastrophic falling of an important volume of solid material into a reservoir. It is the projected Santa Liestra reservoir, on the Ésera river near Santa Liestra village, at the Spanish Pirynees. The construction of a reservoir at that location is intended to regulate 81.9Hm^3, at the upper part of the river. There is an open controversy linked to the dam building due to the potential landslide risk described by a sector of the scientific community. The starting point for the study has been based on a previous report made by the CEDEX (Centro de Estudios y Experimentación de Obras Públicas), and some useful geological data. The more relevant properties will be next outlined; for more geological details, see the references.

Figure 3 shows a sketch of the topographic situation of the reservoir indicating the maximum envisaged water level of 642m and the location of the potential sliding area at the left bank of the Ésera river. The problem in this area is markedly one-dimensional and the sliding can be modelled by means of a transverse sliding model, as the figure suggests.

The volume of the involved materials is bigger than 50Hm^3 according to the geological prospections. Besides, the kind of materials and their fractured and meteorized state, and the fact that the low parts would become saturated when filling the reservoir contribute to the possibility of a sudden and catastrophic failure. This work, however, does not focus on the conditions

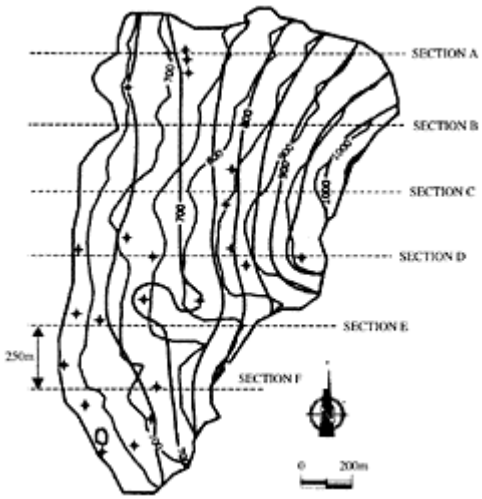

Figure 4. Sliding volume defined by the two bounding surfaces.

Table 1. Sliding volume geometric data.

Section	Location x(m)	Thickness z_0(m)	Area A_d(m^2)	Celerity v_d(m/s)
A	750	5	1000	10
B	500	25	15000	10
C	250	70	50000	10
D	0	80	56000	10
E		50	30000	10
F		50	24000	10

under which the sliding could be triggered. Our study starts from the hypothesis that the sliding takes place and is motivated by the study of the consequences of the impact over the stored water.

Figure 4 shows a detail of the potential sliding volume, with the red lines representing level isolines at the surface in contact with the air and blue lines level isolines at the discontinuity surface. For simplicity, the sliding was assumed rigid, that is, falling in a single block, and with a celerity of 10m/s. This is a maximum risk scenario but follows the hypothesis made in previous studies. Six geological sections as shown on Fig. 4 were used to study the geometry of the sliding volume each of them associated to an average thickness $z_0(x)$ and a surface $A_d(x)$. These values are gathered in Table 1. Any other intermediate value is calculated by interpolation from them.

As the table indicates, the simulation model locates the origin of the x axis at section D. The reason for this was the realization after several simulations that, due to the morphological properties, section D was a split point where the induced water discharge

divided into two opposite directions, one heading towards Morillo de Liena and the other to the opposite direction with no interaction between them. Therefore, as we were interested in the modeling of the North heading waves, the South part was neglected.

The river geometry in the domain under study was based on river cross sectional data approximated to trapezoidal shapes. Table 2 shows their location along the river axis as well as other variables of interest.

Figure 5 represents the longitudinal variation of the top water width at initial conditions, that is, with the reservoir at maximum water level (642m), from the 3500m considered in the simulation. The reach was extended near the tail of the reservoir to include the villages of Morillo de Liena and Navarri into the study in order to evaluate their risk of flooding.

The simulation was performed using 1000 space intervals and a fixed bed roughness $n_{Manning}$=0.04. using the geometric slide data and the transversal sliding model described in **. The speed of the solid

Table 2. Geometry of the river.

Location x(m)	Bed level z(m)	Slope θ(rad)	Bottom width σ_{in}(m)
0	615	1.04	20
250	617	1.22	10
500	620	1.30	40
750	622	1.30	20
1000	622	1.34	40
2250	628	1.16	10
3000	650	0	400
3500	660	0	500

mass movement is assumed constant considering a balance between resistance forces and inertia forces over the sliding volume. The sliding motion at a computational node is finished when all the volume assigned to that point has fallen into the water. Every node has a solid slice of material assigned and the algorithm evaluates the size of transverse sliding at every time step. The numerical results are sumarized and plotted in Figs. 6 to 9.

From the results shown in Figs. 6 to 9 it can be signaled that in the first seconds after the sliding motion starts, very high discharges are produced since water is displaced at a great velocity by the solid materials fallen into the reservoir. The surface wave generated advances towards Morillo against an adverse slope, hence losing energy and celerity. At about t=60s, the sliding area remains dry, acting as a solid obstacle and with all the volume of water moving towards the tail of the reservoir. On the other hand, it can be estimated from the numerical results that the wave celerity, when the wave front is nearly 10m deep, is as high as 14m/s. The wave is rapidly damped at the end of the reach due mainly to the wide section at that location. When the wave reaches Morillo it is still 3m deep and advances at a velocity around 6m/s.

5 CONCLUSIONS

A one-dimensional numerical model has been presented as a tool to simulate landslide movements and their interaction with water volumes. Having been previously proved as adequate for wave propagation problems on rigid bed channels and validated with experimental data, it can also be adapted to situations

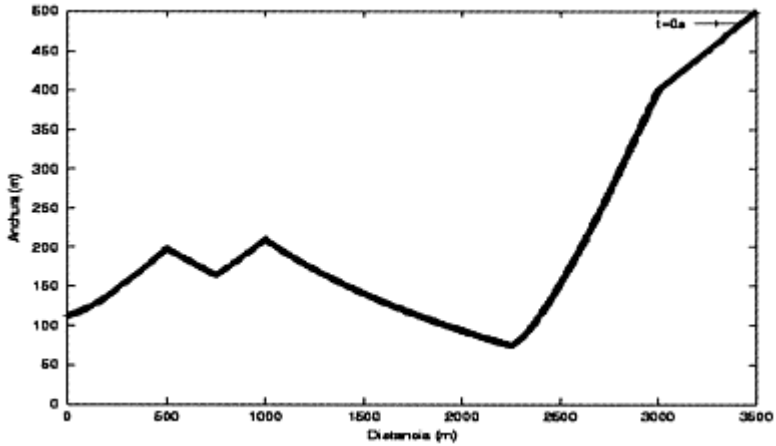

Figure 5. Reservoir top water width at water level 642m.

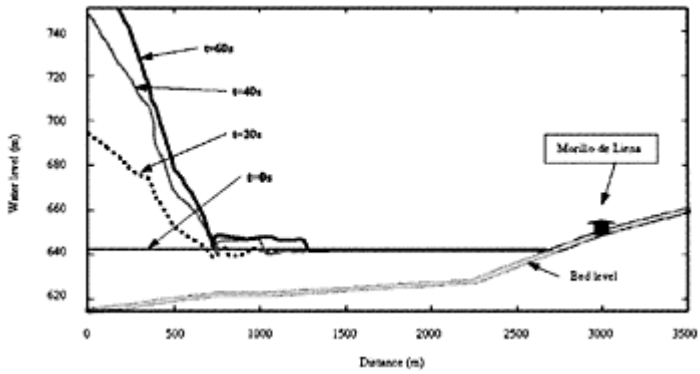

Figure 6. Shock wave propagation towards Morillo de Liena (read arrow at x=3000). Blue line is bottom level at t=0.

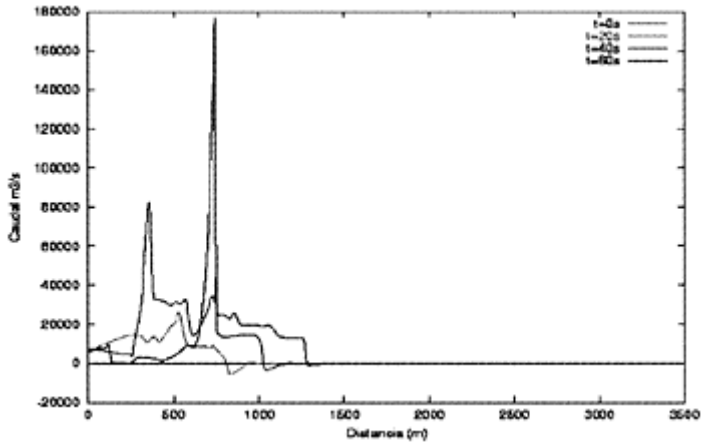

Figure 7. Discharge distribution corresponding to the water depth distributions in Fig. 6.

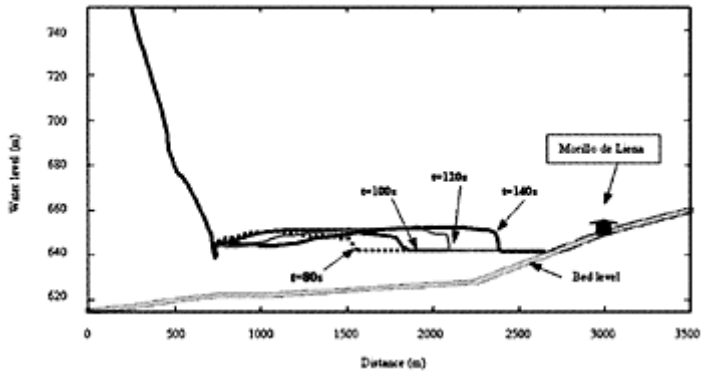

Figure 8. Shock wave water depths (Morillo de Liena at arrow head, x=3000).

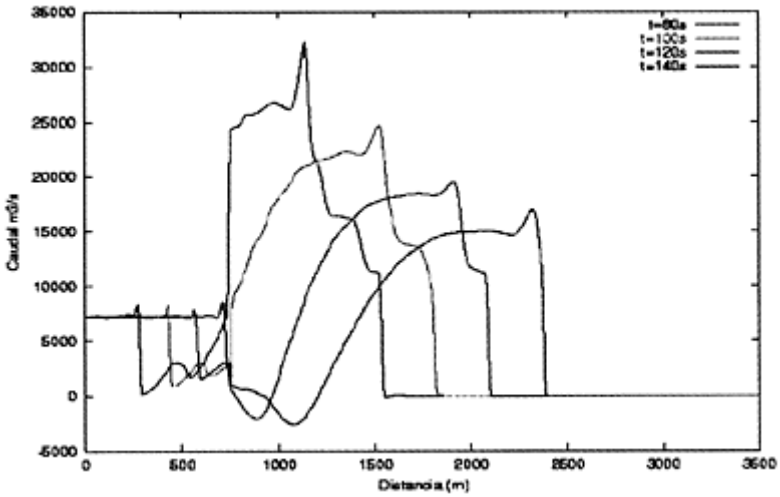

Figure 9. Discharge distributions corresponding to the water levels in Fig. 8.

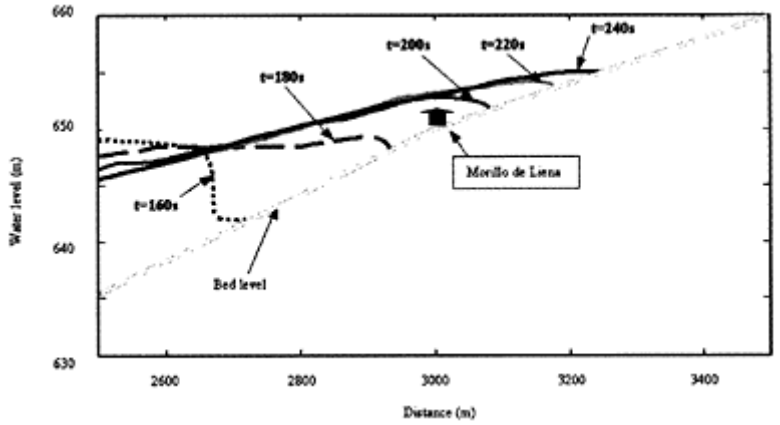

Figure 10. Detail of the water depth evolution near Morillo de Liena.

of channel bed variations in time, allowing for accurate results. The simulation tool developed enables conservative, fast and dynamic calculations of a wide variety of cases including irregular cross sections in presence of different sorts of sliding motions that are characterized depending on their geometry and kinematic properties. From the numerical point of view, it can be concluded that the scheme used, based on the first order explicit Roe's method, is a suitable for this kind of problems.

Longitudinal slides generate both a shock wave traveling in the same sense as the moving solid and a depression wave travelling in the opposite sense. Both the thickness and celerity of the sliding volume are key factors at defining the momentum exchange and hence the wave generated. The particular shape of the solid moving front is less important. Transverse sliding modeling in a one-dimensional approach has to be carefully treated. An algorithm based on the movement of the center mass of the wetted section has been applied to simulate a real case of potential lateral sliding.

The results show the characteristics of the wave generated, magnitude and celerity and the potential risk for the river bank population. This results can be considered the consequence of a preliminary study. It is

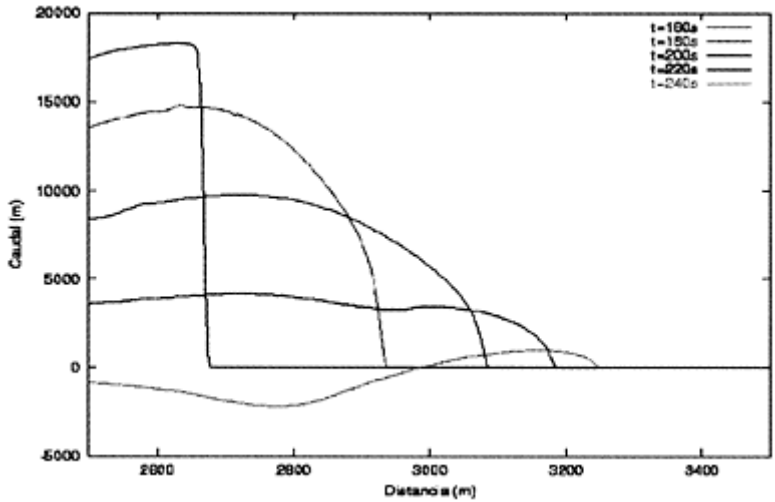

Figure 11. Detail of the discharges near Morillo de Liena.

doubtless necessary to perform more exhaustive and detailed studies of the sliding dynamics, and the river bed geometry since these are the most determinant factors for the wave advance.

REFERENCES

Brufau P., Vázquez-Cendón M.E. & García-Navarro P.A numerical model for the flooding and drying of irregular domains. *International Journal for Numerical Methods in Fluids*, 39, 2002.

Burguete J. & García-Navarro P. Accurate numerical resolution of the shallow water equations using an upwind implicit scheme with large CFL. Technical report, Fluid Mechanics. Universidad de Zaragoza, 2001.

Carracedo J.C., Simon J.Day, Hervé Guillou & Pérez Torrado F.J. Giant Quaternary landslides in the evolution of La Palma and El Hierro, Canary Islands. *Journal of Volcanology and Geothermal Research* 94, May 1999.

Casas Sáinz A.M. Evolución de vertientes y riesgos geológicos en el Ésera medio (tramo Santa Liestra-Morillo de Liena). *Informe técnico. Departamento de Ciencias de la Tierra. Universidad de Zaragoza. Agosto 1997.*

Chow V.T. Open-Channel Hydraulics. *McGraw-Hill*, 1959.

Cunge J.A., Holly F.M. & Verwey A. Practical Aspects of Computational River Hydraulics. *Pitman Publishing*, 1980.

García-Navarro P. & Vázquez-Cendón M.E. On numerical treatment of the source terms in the shallow water equations. *Computers & Fluids* 29, 1999.

Gutiérrez Elorza M. Geomorfología climática. *Ed. OMEGA*, 2001.

Hubbard M.E. & García-Navarro P. Flux Difference Splitting and the Balancing of Source Terms and Flux Gradients. *Journal of Computational Physics*, 165, 2000.

Kiersch George A. Vaiont Reservoir disaster. *Geotimes*, May–June 1965.

Roe PL. Approximate Riemann solvers, parameter vectors and difference schemes. *Journal of Computational Physics*, 43, 1981.

Thomas, M.F. Geomorphology in the tropics. A study of weathering and denudation in low latitudes. *Wiley*, Chichester, 1994.

Vázquez-Cendón M.E. *Numerical solution of the shallow water equations in channels with movable bed. Technical report*, Departamento de Matemática Aplicada de la Universidad de Santiago de Compostela, 2001.

Vila JP. *Étude methodologique des effects d'une avalanche de neige dans une retenue d'eau.* Rapport final. CEMA-GREF, Division Nivologie. 1985.

Numerical simulation for destruction process of rubble stones dam

E.Harada & T.Hosoda
Dept. of Urban Management, Kyoto Univ., Yoshida Honmachi, Sakyo-ku, Kyoto, Japan

H.Gotoh
Dept. of Urban and Environmental Engrg., Kyoto Univ., Yoshida Hnomachi, Sakyo-ku, Kyoto, Japan

River Flow 2004—Greco, Carravetta & Della Morte (eds.)

ABSTRACT: A rubble stones dam is sometimes destroyed at the time of the big flood. It is important for the effective design of the rubble stones dam to understand the destruction mechanism due to the big flood. Interaction between rubble stones is dominant in the destruction process, so key to the detailed understanding of the destruction mechanism is how to evaluate the each rubble stones motion. And also the evaluation of the interaction between solid phase and liquid phase is key too. In this paper, the solid phase is modeled by using the Distinct Element Method, and the numerical simulation based on the solid-liquid two phase flow modeled by Euler-Lagrange coupling is performed to investigate the detailed mechanism for the destruction process of the rubble stones dam.

1 INTRODUCTION

Porous dam is made of rubble stones in consideration of harmony with the nature. By the way, disasters of the destruction of the rubble stones dam due to a big flood have been reported. Hence, to understand the mechanism of the destruction process of the rubble stones dam is important for the effective design of the rubble stones dam. The destruction process of the rubble stones dam is composed of collision between rubble stones, or solid-solid phase, and interaction between rubble stones and fluid, or solid-liquid phase, these processes are very complex, so it is difficult for the detailed investigation of the destruction process of the rubbles stones dam by the measurement of experiments. And also, needless to say, development of the numerical simulation code, which can express

these processes, is an effective tool for detailed analysis of the destruction process of the rubble stones dam. Therefore, the purpose of this paper is investigation of these processes of the rubble stones dam numerically by development of the solid-liquid two phase flow numerical simulation code by the two way method, especially solid phase is modeled by using the Movable Bed Simulator, or MBS, proposed by Gotoh, H. & Sakai, T. (1997), which is based on the Distinct Element Method, or DEM, propsed by Cundall, P.A. & Strack, O.D.L. (1979) which can evaluate the solid-solid interaction. The destruction mechanism of the rubble stones dam is investigated numerically from the driving force acting on the rubble stones. Furthermore, the comparison numerical simulation with experiments is discussed.

2 OUTLINE OF THE SIMULATION MODEL

2.1 *Model of solid phase*

The distinct feature of the destruction process of the rubble stones dam is that the rubble stones shows the transition process from static condition of rubble stones to movement process such as collision and repulsion by the driving force of water flow. So, to evaluate the each rubble stone motion with collision an repulsion, solid phase is calculated by the MBS, or Movable Bed Simulator, proposed by Gotoh, H. & Sakai, T. (1997), which is based on the DEM, or Distinct Element Method proposed by Cundall, P.A. & Strack, O.D.L. (1979). Each particle (=each rubble stone) motion is defined by the following translation and rotational equations:

$$\rho\left(\frac{\sigma}{\rho}+C_M\right)A_3 d^3\frac{d\mathbf{v}_p}{dt} = -A_3 d^3\nabla P+\mathbf{f}_{gr}+\mathbf{f}_{p\,int}+\mathbf{f}_D \tag{1}$$

$$\frac{\sigma\pi d^5}{60}\frac{d\boldsymbol{\omega}_p}{dt}=\mathbf{T} \tag{2}$$

$$\mathbf{f}_{gr}=-\sigma A_3 d^3\mathbf{g} \tag{3}$$

$$\mathbf{f}_D=\frac{(1-c)}{2}\rho C_D A_2 d^2\left|\mathbf{u}-\mathbf{v}_p\right|\left(\mathbf{u}-\mathbf{v}_p\right) \tag{4}$$

$$C_D=C_{D\infty}+\frac{24\nu}{d\cdot\left|\mathbf{u}-\mathbf{v}_p\right|} \tag{5}$$

where p=density of fluid (ρ_{water}=1.0 and ρ_{air}= 0.001); σ=density of particle (σ=2.65); C_M= added-mass coefficient(C_M=0.5); A_2, A_3=two- and three-dimensional geometrical coefficients of particle ($A_2=\pi/4$ and $A_3=\pi/6$); d=diameter of particle (d=0.005m); $\mathbf{V}_p$=velocity vector of particle; t=time; P=pressure of water; $\mathbf{f}_{gr}$=body force vector; $\mathbf{f}_{p\,int}$=particle/particle interacting force vector; $\mathbf{f}_D$=drag force vector; $\boldsymbol{\omega}_p$=angular velocity of particle; $\mathbf{T}$=torque acting on particle; $\mathbf{g}$=gravity force vector; C_D=drag coefficient ($C_{D\infty}$=0.4); and ν=kinematic viscosity. The contacting condition of each particle is looked for at every renewal of the calculation time step (Δt). The acting force between contacting particles is evaluated by spring and dashpot system shown in Figure 1, which is introduced in both of the normal and tangential direction. And also, in this simulation,

particles are non-cohesive, hence the joint, which has no resistance to the tensile force, is assumed in the normal direction. While, in the tangential direction, the friction force(friction coefficient μ=0.577) works. To describe this characteristics, the joint, which slips at the time limit of the shear stress, is assumed in the tangential direction. The detailed model of interaction between particles is mentioned in the paper (Gotoh, H. & Sakai, T. (1997)). The tuning parameters (spring constants in normal and tangential directions *(k_n, k_s)* and damping constants in normal and tangential directions *(η_n, η_s)*) are determined with following the optimization procedure given by Gotoh et al. (2001). The tuning parameter are as follows: $k_{n\ air}$=707.52N/s; $k_{s\ air}$=272.12N/s; $\eta_{n\ air}$=0.70Ns/m; $\eta_{s\ air}$=0.43Ns/m in the air, $k_{n\ water}$=840.82N/s; $k_{s\ water}$=323.39N/s; $\eta_{n\ water}$= 0.83Ns/m; $\eta_{s\ water}$=0.52Ns/m in the water. These parameters are determined to show the good agreement with experiment result. The share of particle concentration *(c)* and the component of drag force ($\mathbf{f}_{Di}$) in each calculation domain cell are evaluated from the position of all particles calculated by the governing equations (1) and (2). And then these values are used in the solid-liquid coupling.

2.2 *Model of liquid phase*

Continuity and momentum equations to the local averaged flow of incompressible fluid are described as follows:

$$\frac{\partial(1-c)}{\partial t}+\frac{\partial}{\partial x_j}(1-c)u_j=0 \tag{6}$$

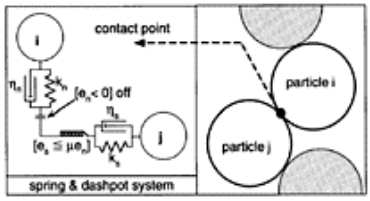

Figure 1. Spring and dashpot system between contacting particles.

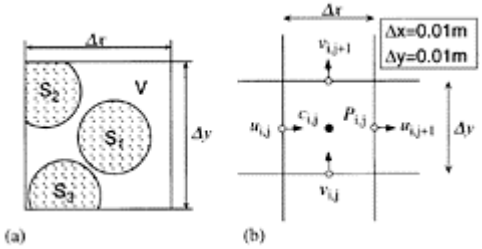

Figure 2. (a) share of the particles in the cell; (b) fluid-variable layout.

$$\frac{\partial}{\partial t}\{\rho(1-c)u_i\}+\frac{\partial}{\partial x_j}\{\rho(1-c)u_iu_j\}= \rho(1-c)g_i-(1-c)\frac{\partial P}{\partial x_i}+\frac{\partial(1-c)\tau_{ij}}{\partial x_j}-F_{Di} \quad (7)$$

$$c=\beta\sum_k\frac{A_k d^2 s_k}{V} \quad (8)$$

$$F_{Di}=\frac{1}{V}\sum_k f_{Di}\,s_k \quad (9)$$

$$\tau_{ij}=\rho(\nu+\nu_t)\left(\frac{\partial u_i}{\partial x_j}+\frac{\partial u_j}{\partial x_i}\right) \quad (10)$$

where β=correction factor for three-dimensional effect (β=0.67); x_i=Cartesian components *x, y;* $\mathbf{u}_i$**;** averaged fluid velocity in Cartesian components *u, v;* $\mathbf{f}_{Di}$=component of drag force of each particle; V=the cell area; S_k=share of *k*-th particle in the cell (shown in Figure 2); τ_{ij}=component of stress tensor; and ν_t=kinematic eddy viscosity. And also, interaction force at interface between solid phase and liquid phase is evaluated by drag force.

2.3 *Model of turbulen t flow*

In this paper, turbulent flow is modeled by standard k-ε turbulent model of second closure model based on the isotropic eddy viscosity. *k* and ε equations including the existence of particles can be written as follows:

$$\frac{\partial(1-c)k}{\partial t}+\frac{\partial(1-c)ku_j}{\partial x_j}= (1-c)P_k-(1-c)\varepsilon+D_k-G_k \quad (11)$$

$$\frac{\partial(1-c)\varepsilon}{\partial t}+\frac{\partial(1-c)\varepsilon u_j}{\partial x_j}= \frac{(1-c)\varepsilon}{k}\left(C_{\varepsilon 1}P_k-C_{\varepsilon 2}\varepsilon\right)+D_\varepsilon-G_\varepsilon \quad (12)$$

$$P_k=-\overline{u_i'u_j'}\frac{\partial u_i}{\partial x_j} \quad (13)$$

$$\overline{u_i'u_j'}=\frac{2}{3}k\delta_{ij}-\nu_t\left(\frac{\partial u_i}{\partial x_j}+\frac{\partial u_j}{\partial x_i}\right);\ \nu_t=C_\mu\frac{k^2}{\varepsilon} \quad (14)$$

$$D_k=\frac{\partial}{\partial x_j}\left\{(1-c)\left(\frac{\nu_t}{\sigma_k}+\nu\right)\frac{\partial k}{\partial x_j}\right\} \quad (15)$$

$$D_\varepsilon=\frac{\partial}{\partial x_j}\left\{(1-c)\left(\frac{\nu_t}{\sigma_\varepsilon}+\nu\right)\frac{\partial \varepsilon}{\partial x_j}\right\} \quad (16)$$

where *k*=turbulent energy; ε=energy dissipation; *Pr*=production of turbulent energy due to shear stress; and G_k, G_ε=term in consideration of components the turbulent fluctuating

caused by the existence of sand particle. The recommend values by Launder, B.E. & Spalding, D.B.(1974) for the constants in the k-ε turbulent model are as follows: $C\mu$=0.09; σ_k=1.0; σ_ε=1.3; $C_{\varepsilon 1}$=1.44; $C_{\varepsilon 2}$=1.92. The evaluation of the G_k and G_ε are neglected for the simplification.

2.4 *Outline of computing method*

The coupling between solid phase and liquid phase is calculated by repeating calculation of liquid phase and solid phase alternately. The marching procedure of calculation from the time $n\Delta t_f$ to the time $(n+1)\Delta t_f$ is as follows. For the first step, the prediction value of velocity (**u***)

$$\begin{aligned}\mathbf{u}^* = \mathbf{u}^n - \frac{\Delta t_f}{\rho(1-c)}\{&\rho\nabla\cdot(1-c)\mathbf{u}^n\mathbf{u}^n \\ &+ \rho\mathbf{u}^n(\nabla\cdot c\mathbf{v}_p) - \rho(1-c)\mathbf{g} \\ &+ (1-c)\nabla P^n - \nabla\cdot(1-c)\boldsymbol{\tau}^n + \mathbf{F}_D{}^n\}\end{aligned} \tag{17}$$

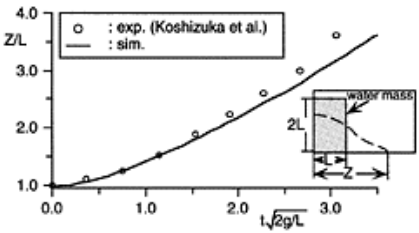

Figure 3. Motion of tip of the broken water.

which is obtained by discretization of equation (7) transformed into the conservative form, is given by using the velocity $(\mathbf{u}^n)$ and the pressure (P^n) at the time $n\Delta t_f$ where Δt_f=time step of the liquid phase (Δt_f=0.00025s); n=marching time step; and τ=stress tensor. The second step, the iterative calculation, which corrects the velocity and the pressure, is performed by the Highly Simplified Marker and Cell method, or HSMAC, proposed by Hirt, C.W. & Cook, J.L. (1972) until the prediction value of velocity **(u*)** satisfies the continuity equation for the multi phase flow,

$$\nabla\cdot\left\{(1-c)\mathbf{u}^* + c\mathbf{v}_p{}^*\right\} = 0 \tag{18}$$

which is derived from sum of each continuity equation of the liquid phase and solid phase, and then the velocity $(\mathbf{u}^{n+1})$ and the pressure (P^{n+1}) at the time $(n+1)$ Δt_f is computed. Next, the particle positions are evaluated from the MBS with using that renewed flow field ($\mathbf{u}^{n+1}$, P^{n+1}). And the drag force and the share of solid phase in each cell of the flow field are computed, and these are used to the next time step of the liquid phase. This series of processes are iterated till the designated calculation time. And also, the governing equations are discretized by the finite volume method, or FVM, on the staggered grid, and also upwind difference scheme is used in the advection term.

2.5 *Boundary conditions and initial conditions*

The upper side of Figure 4 shows the calculated domain. The destruction and the flowing process of the mound (rubble stones dam) is simulated. The mound is formed by arranging the uniform diameter particles in the plover-shaped. To visualize the fluid motion, the Lagrangian massless marker particles are arranged in the fluid mass. The wall boundary conditions of k and ε are given by the wall function, and the velocity profile in the log-law region is given by presuming turbulent flow on the smooth bed.

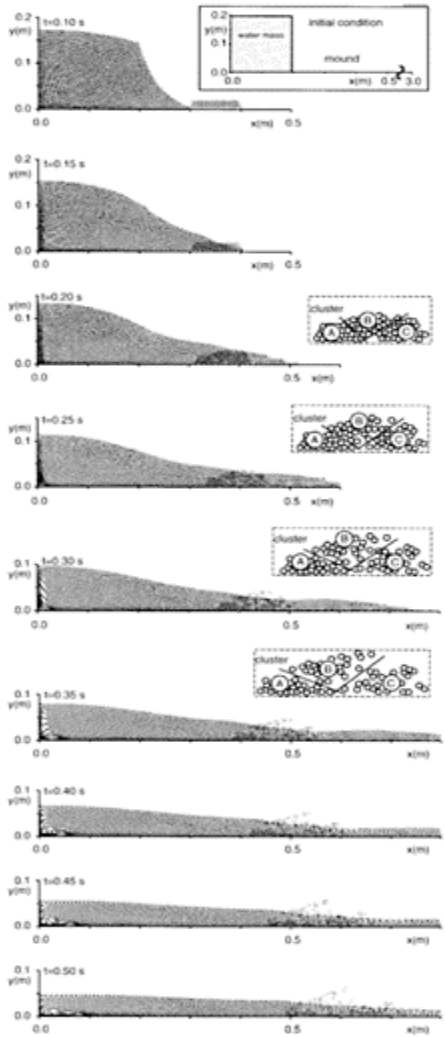

Figure 4. Snapshots of destruction process of the rubble stones dam.

3 SIMULATION

3.1 *Destruction process of rubble stones dam*

The motion of the tip of the water mass running on the bottom wall is shown in Figure 3 to verify the liquid phase of present simulation code. Simulation result shows the good agreement compared with the experiment by Koshizuka et al. 1995. Figure 4 shows the snapshots of the destruction process of the rubble stones dam. The tip of the water mass reaches the toe of the mound (left side of the mound) around the time t=0.1s, and then infiltration of water to the pore of the mound occurs. Increase of the water surface level due to the resistance of the mound is shown around the mound at the time t=0.15s. And also, the mound slides with deflection at its center part by the drag force acting on the mound due to the relative velocity between mound and water mass at the time t=0.20–0.25s. Furthermore, zooming in the deformation of the mound at this stage in detail, two tensile deformation lines occurs inside the mound and separation to three clusters are confirmed. After the time t=0.30s, flow mode of the mound particles are classified by cluster-A, cluster-B and cluster-C. The particles of cluster-B are transported with pushing out into the air, and most of the particles of cluster-C are transported with swelling in the water. While, the particles of cluster-A are transported with slight deformation in comparison with other clusters.

3.2 *Mechanism of destruction*

The driving force concerned in the present simulation code consists of pressure gradient force, inter-particle force and drag force. Under these driving forces, the velocity vector of particles in the early destruction process of the rubble stones dam is shown in Figure 5. The accelerating process of the particles is shown clearly from the velocity vector of particles. The acceleration rate of the cluster-A is smaller than that of the cluster-C, the tendency to the dispersion of the particles between the cluster-A and the cluster-C shown in Figure 4 is reconfirmed. Next, the transport process of the particles due to the pressure gradient force is examined.

Figure 6 shows the time series of the pressure distribution, and also, gauge pressure is used in pressure indication. A high pressure part around the toe of the mound due to the collision with broken water mass at the time t=0.15s gradually permeates inside the mound, and influences the transformation of the mound. Furthermore, a high pressure part from center to back inside the mound is found at the time t=0.20–0.28s, which might be a helpful to generate the cluster of mound. And also, this high pressure part inside the mound might push the particles of the cluster B out of the air.

The transport of the particles due to the drag force acting on the particles and the inter-particle force at the mound is discussed. Figure 7 shows the time series of mean inter-particle force, mean drag force and the total number of the contact points between particles. The mean inter-particle force classified in two

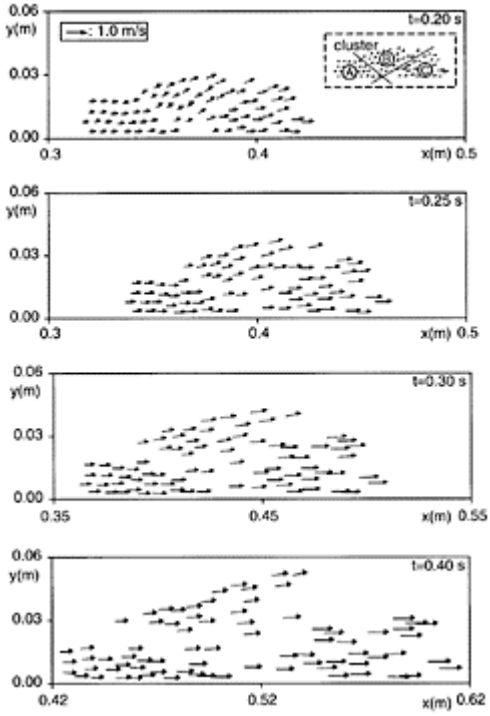

Figure 5. Velocity vector of the rubble stones dam.

blocks of increase section (block-1) and occasional occurrence section (block-2). The abrupt increase of interaction force between particles due to the collision with the collapsing water in the block-1 lead to the destruction of the mound inner structure, and also the energy, which make the mound disperse, would be concentrated. While, in the block-2, the dispersed particles mix with the broken water and transport under the solid-liquid two phase flow. And also, the interparticle force in this block-2 only occurs occasionally, hence the drag force and pressure gradient force dominates to the destruction of the mound. The abrupt increase number of contact points between particles are also shown from the time series of the total number of the contact points between particles, and it is confirmed that the dominant force to the dispersion of the mound particles is the inter-particle force. In the transport process of the block-2, the slight change of the contact points between particles is found, therefore, the driving force by the inter-particle force is comparatively smaller than other factors of driving force. And also, although the number of the contact points between particles show the slight fluctuation, the inter-particle force and the drag force are not shown

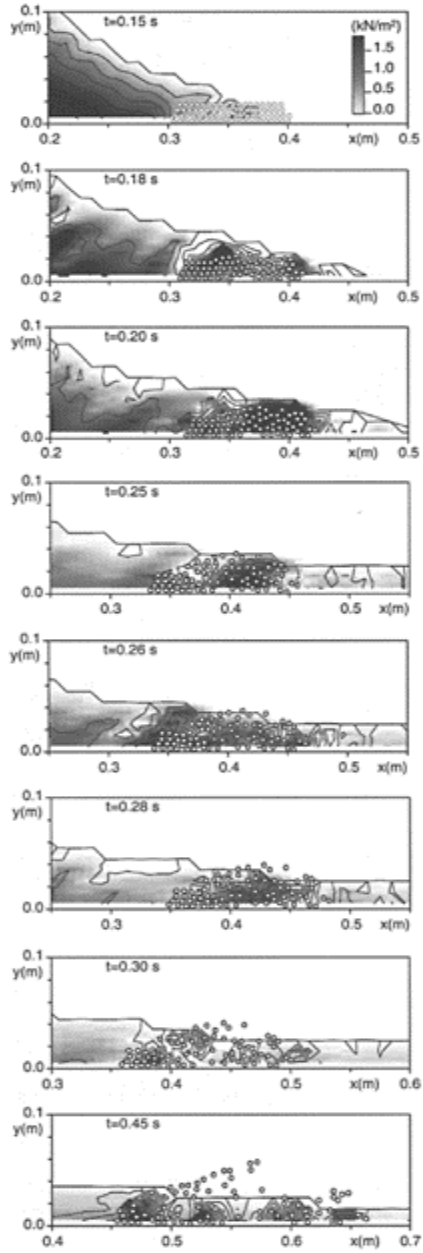

Figure 6. Pressure distribution around collapsing rubble stones dam.

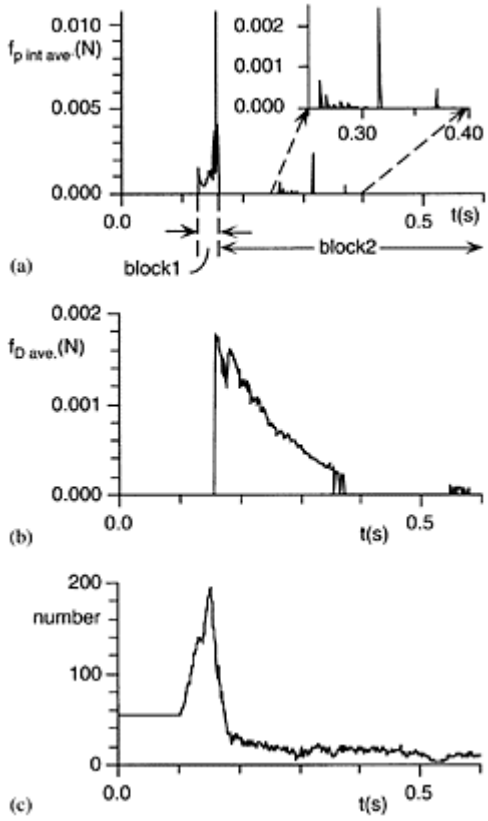

Figure 7. (a) mean inter-paritcle force; (b) middle: mean drag force; (c) total number of contact particles.

at the time t=0.04–0.05s. So, the equilibrium transport process of the dispersed particles, in which the relative velocity between particles and fluid are small, would be shown.

4 EXPERIMENT

4.1 *Outline of experiment*

A destruction of rubble stones dam is reproduced by acrylic open channel, which is 3.0m long, with a slit at 0.5m shown in Figure 8. The cross section of the acrylic open channel is 0.1m width. The driving force of the destruction of rubble stones dam is broken water power, which is reserved in the left side of the slit, due to pulling up the slit. Motion of the mound particles are recorded by the digital video camera, shatter speed of which is

1/4000s, from the side of acrylic-resin-wall. The test mound particle is the glass beads, 2.5 in specific density and 0.005m in diameter. After the

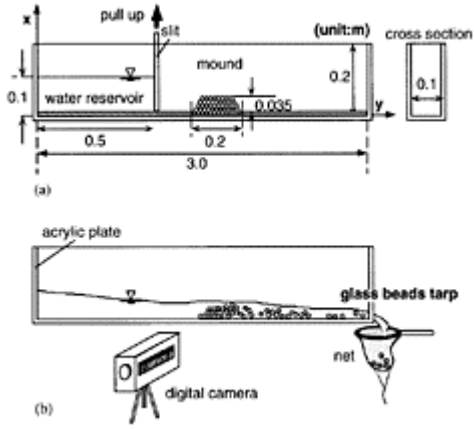

Figure 8. (a) experimental apparatus and setup; (b) schematic of the typical experiment.

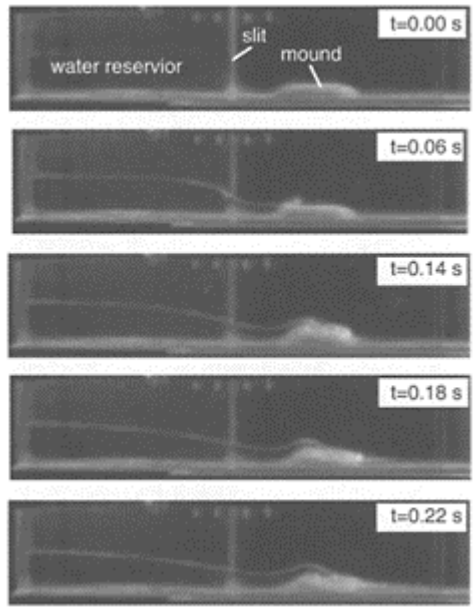

Figure 9. The video frames of destruction process of the rubble stones dam.

destruction of the rubble stones dam due to the broken water, the glass beads are trapped at the right side of the channel by the net.

4.2 *Results*

The video frames of the destruction process of the rubble stones dam are shown in Figure 9. After pulling up

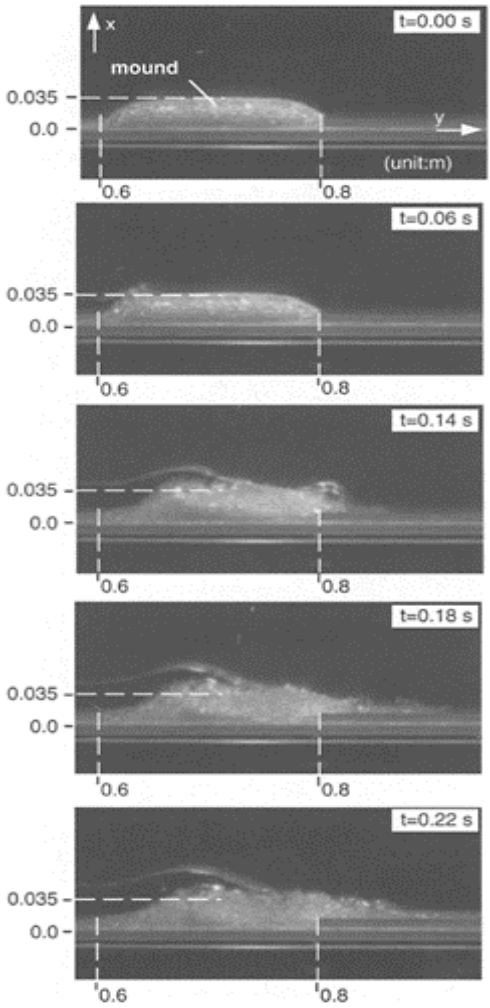

Figure 10. A close-up around the rubble stones dam in experiment.

the slit, the broken water impinges on the left side of the mound edge around the time t=0.06s. And then, the broken water surmounts the mound with eroding the left side of the mound particles, and the mound is transported.

In particular, to focus the destruction process of the rubble stones dam, the video frames around the mound are shown in Figure 10. The broken water catches

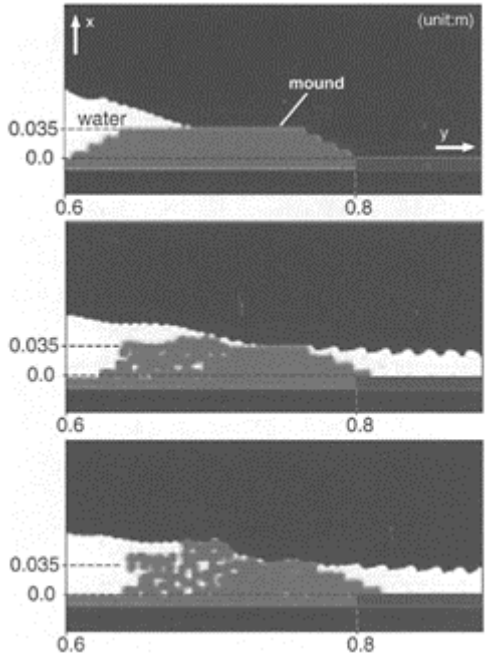

Figure 11. A close-up around the rubble stones dam in simulation.

the glass beads in the left side of the mound, and the glass beads are transported with mixing with the broken water, are observed clearly. Figure 11 shows the destruction process of the rubble stones dam under the same experimental condition. Although the water surface level is different from experiment shown in Figure 10, the eroding process around the left side of the mound due to the force of the broken water is simulated, the same destruction tendency shown in the experiment can be confirmed from the simulation result as well.

5 CONCLUSIONS

The destruction process and mechanism of the rubble stones dam are discussed numerically by using the solid-liquid two phase flow model based on the Euler-Lagrange coupling. The present simulation shows that the static mound particles disperses by the pressure gradient force and inter-particle force in the early stage, and then the equilibrium

state is confirmed that the dispersed particles are mainly transported by the drag force. Although the interface between solid and liquid is expressed simply by the only drag force in this paper, the simulation result about the destruction process of the mound shows good agreement with experiment. So, the validity of the evaluation to the motion of the rubble stones is shown. However, the repeatability of water dynamics are in poor agreement with the experimental data. This might be a reason that the evaluation of the interaction between fluid phase and solid phase is insufficient. In the near feature, unsteady process of the destruction of the rubble stones dam have to be discussed in detail in consideration of the additional force due to the unsteady flow and the modeling of turbulent fluctuation due to the particles laden flow. And also, high accurate numerical simulation about the solid-liquid two phase flow should be developed by comparison with experiments.

ACKNOWLEDGMENTS

Thanks are offered to Mr. S.Senba & Mr. K.Obayashi for help with the experiments.

REFERENCES

Cundall, P.A. & Strack, O.D.L. 1979. Discrete Numerical Model for Granular Assemblies. *Geotechnique,* Vol. 29: 47–65.

Gotoh, H. & Sakai, T. 1997. Numerical Simulation of Sheetflow as Granular Material. *Jour. of Waterway, Port, Coastal and Ocean Engrg., ASCE,* Vol. 123, No. 6: 329–336.

Gotoh, H. et al. 2001. Optimization of Parameters in DEM-Based Numerical Movable Bed Simulator. *Jour. of Hydraulic, Coastal and Environmental Engrg., JSCE,* No. 691/II-57:159–164.

Hirt, C.W. & Cook, J.L. 1972. Calculating three-dimensional flows around structures and over rough terrain. *Jour. Comp. Phys.,*Vol 10: 324–340.

Koshizuka, S. et al. 1995. A particle method for incompressible viscous flow with fluid fragmentation. *Comp. Fluid Dynamics Jour.*, Vol. 4, No. 1:29–46.

Launder, B.E. & Spalding, D.B. 1974. The numerical computation of turbulent flows. *Comp. Meth. Appl. Mech. Engrg.*, Vol. 3:269–289.

Effects of gradient pressure on resistance law in roll waves and effects of tension surface

S.Longo
Department of Civil Engineering, University of Parma, Parma, Italy

River Flow 2004—Greco, Carravetta & Della Morte (eds.)

ABSTRACT: Free surface flow in sufficiently steep channels is unstable and progressive waves develop as periodic distribution of bores connected by smooth profiles. The amplitude of the breakers is higher than the normal water depth. Roll waves in the initial phase development (before overtaking) develop, dissipating for friction less energy than the equivalent uniform stream. Including the gradient pressure effects, an extra saving of energy is computed, which can partially balance the dissipation in the breaker. Assuming different values of the momentum and energy coefficients on the two sides of the breaker, physically acceptable value of the water stream depths are obtained with a limited dissipation rate in the jump. Including the tension surface effects, a new family of roll waves is depicted.

1 INTRODUCTION

Free surface instabilities of flows down inclined channels have been widely observed in Newtonian and non-Newtonian fluids. If there is enough space for the instabilities to grow, in some condition roll waves develop, with several bores having height, period, length and celerity increasing downstream.

The observations of roll waves in a torrent by Maw in the late 19th century were followed by the first description due to Forchheimer (1903) and to Cornish (1934). Observations of roll waves in mud flows are reported by several Authors in many areas. The first study of the phenomenon was based on linear stability analysis of the basic equations written in the long wave approximation. The development of a finite amplitude wave theory is due to Dressler (1949). Dressler's theory, originally developed for fully turbulent flows, was extended to laminar flows for Newtonian fluids by Ishihara et al. (1954) and to power-law fluids by Ng & Mei (1994), who essentially focussed on

pseudoplastic fluids (mud). Recently Prasad et al. (2000) applied Dressler's theory to flowing grains, and Longo (2003) applied Dressler's theory to dilatant fluid.

Roll waves are essentially controlled by Froude number, and can develop in laminar and in turbulent streams. The usual approach is linear stability analysis: the basic flow field (the uniform flow), is perturbed assuming small variations in the water depth and mean velocity. The set of equations in perturbed variables is linearised and solved. If perturbations grow, the basic motion is linear asymptotic unstable, otherwise it is stable. Froude number correspondent to marginal stability (perturbation do not grow nor decay) depends on velocity profile and resistance law. In laminar flow, Yih (1954, 1963) and Benjamin (1957a, b), perturbed Navier-Stokes equations assuming free surface perturbation of sinus shape and recovered Orr-Sommerfeld equation finding a critical Froude number equal to 0.527. Similar result was obtained by Chen (1992), perturbing the shallow water 1-D equation including derivative of Boussinesq coefficient of momentum along the stream motion.

Vedernikov (1945) introduced the so called Vedernikov number to state the necessary condition for roll waves formation. Montuori (1961) state the sufficient condition for roll wave formation.

In turbulent flow in rectangular channels, assuming a Chézy resistance law with a constant coefficient, Jeffreys (1925), Stoker (1957), Liggett (1975) found a critical Froude number equal to 2. Several Researchers as Iwasa (1954); Koloseus & Davidian, (1966); Berlamont & Vanderstappen (1981) put in evidence the strong sensitivity of critical Froude number on velocity profile, Reynolds number, friction law. In particular according to Rouse (1963); Rosso et al. (1990), the Darcy-Weisbach friction factor increases for increasing Froude number in supercritical streams. According to Brock (1966, 1967), no firm conclusion on such a dependence could be drawn because experimental data were not enough accurate, especially the water depth measurements. Moreover an apparent increment of friction factor could better be explained as energy transfer from mean flow to waves.

In addition several laboratory experiments with water streams were conducted by Ishihara et al. (1954), Brock (1967), Julien & Hartley (1985, 1986). Brock (1967, 1969) carried out experiments in a rectangular small channel 40m long and ~12cm wide, and essentially classified two families of roll waves. A first family included natural roll waves, generally non periodic; a second family included artificial periodic roll waves, obtained imposing a controlled disturb at the inlet and characterised by a strong regularity. In both cases there is an initial stage with waves of constant period, and a second stage of growing and with a wave period and length increment. The growth of natural roll waves also happens as coalescence of two or more waves. In the second stage the significant wave characteristics (wave height, celerity and mean wave length) coincide in both natural and artificial roll waves with similar Froude number and channel bottom slope.

Roll waves analysis is a challenging topic from a mathematical point of view and roll waves knowledge has also a practical application. In fact roll waves strongly enhance the maximum water depth (up to 3 times the normal depth) and the maximum fluid velocity, increasing its threatening. Most of the available results refer to the limit condition for roll waves existence, but no one can infer the determination of roll wave parameters (wave length, wave height, celerity) for a given system. There are some experimental

indications due to Ponce & Maisner (1993), who using Brock's data (1967) found that the observed periodic roll waves are those corresponding to the maximum growth rate (in linear stability analysis). Ng & Mei (1994) infer that the observed roll wave has the lowest amplitude corresponding to no energy loss across the shock.

In the present study we analyse the energy balance in permanent periodic roll waves. Dissipation in a free surface flow is generally controlled by wall stress and depends on Reynolds and Froude numbers, wall roughness, shape of the transversal section, channel profile, channel plan and non stationarity parameter. Uniform flow in a channel dissipates energy per unit weight and unit length equal to bottom slope. If bores or jumps are present, part of the energy is dissipated in the shock area with a dissipation depending on the conjugate water depth. Lamberti & Longo (2000) demonstrated that assuming a reliable wave form and resistance law for a free surface flow, in some condition the stream dissipates per unit wave length less energy respect to the uniform stream; the energy excess is then dissipated in the shock. In such a situation the conjugate water depths are obtained imposing the energy balance over a single wave length. They also demonstrated that using the same energy balance criterion and integrating the water depth in a moving reference solidal with the wave form (Thomas, 1939; Dressler, 1949; Brock, 1967), it is possible to evaluate all the waves characteristics for a given water discharge and bottom slope and wall roughness.

In the present manuscript the first part of the analysis is devoted to the boundary layer effects on roll waves. Friction is usually evaluated assuming a quasi-steady motion, neglecting the pressure gradient. If the boundary layer has an adverse gradient pressure, friction is reduced and also dissipation in the stream is reduced.

The second part of the analysis is devoted to tension surface effects. In principle, tension surface can lead to a new family of solution obtained using Dressler's approach. These solution can have practical interest in fluid with a strong tension surface.

The next Section is devoted to deriving the basic equations applying Karman's momentum integral method. In Section 3 we describe the structure of the boundary layer in a roll wave and its effects on resistance law. In Section 4 we describe the 'special solution' with a modified resistance law and in Section 5 we obtain the admissibility conditions for roll waves. In Section 6 the effects of tension surface on admissibility criteria for finite amplitude waves is studied. Sections 7, 8 and 9 are devoted to shock conditions and to energy balance in the discontinuity and in the unstable stream.

2 BALANCE EQUATIONS

Let us consider a 2-D laminar flow of a fluid down a plane of inclination θ. The coordinate system has the x-axis along the bed and the y-axis normal to it (Fig. 1). For long waves, applying Karman's momentum integral method to mass balance and linear momentum balance, we obtain the following set of equations:

$$\begin{cases} A_{,t} + (uA)_{,x} = 0 \\ u_{,t} + \beta u u_{,x} - (\beta - 1)\dfrac{u}{A}\dfrac{dA}{dy} y_{,t} + \\ g\cos\theta y_{,x} + \dfrac{\sigma}{\rho} y_{,xxx} + u^2 \beta_{,x} = g\sin\theta - \dfrac{\tau_b}{\rho R} \end{cases}$$

Figure 1. Schematic of periodic waves with sharp front in shallow fluid flows.

where u is the depth average velocity of flow function of the longitudinal coordinate x and time t, A is the cross sectional area of flow, y is the depth of the flow, β is the momentum flux factor, τ_b is the average boundary shear stress and R is the hydraulic radius of the flow, ρ is the mass density of the fluid, g is acceleration of gravity and σ is the surface tension.

Introducing a moving reference having celerity c and assuming that in the moving reference the chosen state variables U and Y are function of $\xi = x - ct$ only (Fig. 2):

$$u(x, t) = U(x - ct) = U(\xi)$$
$$y(x, t) = Y(x - ct) = Y(\xi) \quad (3)$$

The two equations (1, 2) for a wide channel ($R \approx Y$) become:

$$\begin{cases} (UY)_{,\xi} - cY_{,\xi} = 0 \\ -cU_{,\xi} + \beta U U_{,\xi} + c(\beta - 1)\dfrac{U}{Y} Y_{,\xi} + \\ g\cos\theta Y_{,\xi} + \dfrac{\sigma}{\rho} Y_{,xxx} = g\sin\theta - \dfrac{\tau_b}{\rho Y} \end{cases} \quad (4,5)$$

where the spatial variation of the momentum flux correction term is neglected.

Eqs (4–5) can be rearranged as:

$$\begin{cases} U_{,\xi} = \dfrac{g\left(\sin\theta - \dfrac{\tau_b}{\gamma Y} - \dfrac{\sigma}{\gamma} Y_{,xxx}\right)(U - c)}{\left[(U - c)(\beta U - c) - c(\beta - 1)U - gY\cos\theta\right]} \\ Y_{,\xi} = -\dfrac{gY\left(\sin\theta - \dfrac{\tau_b}{\gamma Y} - \dfrac{\sigma}{\gamma} Y_{,xxx}\right)}{\left[(U - c)(\beta U - c) - c(\beta - 1)U - gY\cos\theta\right]} \end{cases} \quad (6,7)$$

with $\gamma = \rho g$ the specific weight of the fluid. Dividing these two equations and integrating results:

$$U = \frac{(cY - K)}{Y} \quad (8)$$

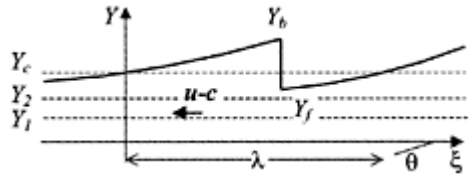

Figure 2. Definition sketch of a roll wave profile in the moving frame.

K is the constant discharge per unit width in the moving frame. It was defined as 'overrun' by Chow (1959) and 'progressive discharge' by Dressler (1949). The discharge in the fixed frame varies with space and time.

3 RESISTANCE AND BOUNDARY LAYER STRUCTURE

Resistance to flow in open channels is function of several independent variables. For a rectangular straight channel of uniform inclination, the force per unit length, intended as that which, when multiplied by the mean velocity of flow yields the rate of energy dissipation, can be expressed as (Rouse, 1965):

$$\frac{\partial F}{\partial x} = f(y, U, k, \varsigma, \rho, g, \mu, \partial y / \partial t) \tag{9}$$

where y is the mean depth, U is the mean velocity, k is a length describing the surface roughness, ζ is a parameter describing the shape of the cross section, p is the fluid density, g is the gravity acceleration, μ is fluid viscosity and $\partial y/\partial t$ is the rate of change of depth with time. Using Buckingham's theorem results in a relation among non dimensional group as:

$$\frac{\partial F / \partial x}{\rho U^2 y} = f\left(\frac{\rho U y}{\mu}, \frac{k}{y}, \varsigma, \frac{U}{\sqrt{gy}}, \frac{\partial y / \partial t}{U}\right) \tag{10}$$

The term on the left hand is essentially a friction factor, the terms on the right hand are Reynolds' number, non dimensional roughness, the cross section shape factor, the Froude number and the degree of unsteadiness. The effects of the Froude number have been widely discussed. According to Rouse (1965) there is an apparent increase in channel resistance as the Froude number exceeds the stability limit, with waves formation. The increase in channel resistance can be intended as a transformation from mean-flow energy to wave energy instead of pure dissipation. Beyond the stability limit roll waves develop and the flow cannot be treated as uniform and steady. In a discussion to Rouse's paper by Brock (1966) the concept of apparent increase in channel resistance is better focused, highlighting that if part of energy gained by gravity is transferred to waves and then dissipated by waves, the apparent dissipation due to boundary friction is higher whenever waves effects are not taken into account in the energy balance. This hypothesis has been supported by detailed measurements (e.g. Rosso et al., 1990).

The dependence of friction factor on the degree of unsteadiness is more complicated. Unsteadiness is usually connected with gradient pressure and it can be verified that self preserving solutions in boundary layers (i.e. solutions invariant respect to horizontal coordinate and function of non-dimensional vertical coordinate and non dimensional velocity) can be obtained only with a careful adjustment of the pressure (Clauser, 1956). As a consequence the dependence of friction factor on unsteadiness parameter is not theoretically available except for specific controlled flow fields. Nevertheless it is interesting to study the effects of the unsteadiness parameter on energy dissipation.

Assuming the wave profile obtained by Dressler as a first approximation, we can demonstrate that the bottom boundary layer has an adverse pressure gradient. Neglecting gravity effects and viscous forces in the outer region, the pressure gradient is simply related to fluid acceleration:

$$\frac{dp_e}{dx} = -\rho\left(\frac{\partial U}{\partial t} + U\frac{\partial U}{\partial x}\right) \tag{11}$$

On using eq.(3) and eq.(8) the pressure gradient in the external flow is expressed as:

$$\frac{dp_e}{d\xi} = \frac{\rho K}{\gamma}\frac{dU}{d\xi} \tag{12}$$

The right hand term in eq.(12) is always positive because fluid velocity increases from the back to the front of the wave and water depth is always positive. The qualitative plot of the external pressure gradient is shown in Figure 3.

The structure of the boundary layer is clearly quite complicate. In the laboratory reference the wall boundary layer has a periodic structure with wave length equal to the length of the roll waves. The adverse gradient pressure tends to grow up the boundary layer thickness behind the moving roller, with increasing efficiency from the front to the back. We can infer that for periodic roll waves the boundary layer attains also

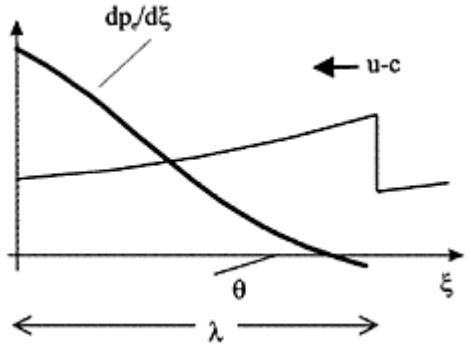

Figure 3. Qualitative plot of the pressure gradient.

a time periodic structure with possible similar solutions. In fact neglecting the time dependent term, the boundary layer can be treated as a stationary boundary layer in

adverse pressure gradient subject to growing thickness and growing bottom tangential stress and decreasing pressure gradient. The Rotta-Clauser parameter:

$$\beta_{RC} = \frac{\delta_1}{\tau_b}\frac{dp_x}{d\xi} \tag{13}$$

where δ_1 is the displacement thickness, can be constant or nearly constant. More experimental activity is necessary in order to assess a friction factor formula depending on unsteadiness parameter but it is plausible that friction factor decreases from the back to the front of the roll waves. However in eq.(10) the non-dimensional group $(\partial y/\partial t)/U$ can be written as:

$$\frac{\partial y/\partial t}{U} = \frac{c}{U}\frac{\partial Y}{\partial \xi} \tag{14}$$

and to investigate the structure of roll waves in presence of a decreasing friction factor, we assume a resistance law as:

$$J = \frac{U^2}{g}\frac{r^2}{R}\left(1 - a\frac{\partial Y}{\partial \xi}\right) \tag{15}$$

with a modified friction factor:

$$r^2\left(1 - a\frac{\partial Y}{\partial \xi}\right) \tag{16}$$

where a is a non dimensional parameter. The modified friction factor collapses to the standard friction factor in uniform flow ($\partial Y/\partial \xi$=0). In presence of roll waves it decreases from the back to the front because $\partial Y/\partial \xi$ is positive and growing. For the sake of simplicity, also considering that this model is not experimentally verified, we assume a constant value for a.

4 THE DISCONTINUOUS SOLUTION WITH THE MODIFIED FRICTION FACTOR AND NEGLECTING THE SURFACE TENSION

On using the modified friction factor in eq.(16), eq.(7) becomes:

$$Y_x = -\frac{gY^3\sin\theta - r^2(cY-K)^2}{K^2 - gY^3 + ar^2(cY-K)^2} \tag{17}$$

where the surface tension term has been dropped. The denominator of eq.(17) admits always at least a real zero named Y_c, which is positive if a>0. The profile would have to be vertical in the neighbour of Y_c if $d^2\xi/dY^2 \neq 0$ in Y_c, otherwise for $d^2\xi/dY^2 \neq 0$ in Y_c a maximum or a minimum is expected. If a=0 Dressler (1949) demonstrated that the function $d^2\xi/dY^2$ cannot be zero in the critical point. It can be demonstrated that:

$$\left.\begin{array}{l}\left.\dfrac{d\xi}{dY}\right|_{Y=Y_c}=0\\ \left.\dfrac{d^2\xi}{dY^2}\right|_{Y=Y_c}=0\end{array}\right\}\ \text{if}\ a=\frac{gY_c^3+2K^2}{2r^2K\left(cY_c-K\right)} \tag{18}$$

In the limit of the present analysis, this profile must be disregarded because the basic equations were derived in the hypothesis of small stream curvature, which is not this case. Hence an acceptable profile can be obtained using eq.(17) eliminating the zero of the denominator, imposing that it is also a zero of the numerator. If Y_c is a zero of the denominator, using eq.(8) results:

$$\begin{cases}gY_c^3\sin\theta-r^2\left(U_cY_c\right)^2=0\\ \left(c-U_c\right)^2Y_c^2-gY_c^3+ar^2\left(U_cY_c\right)^2=0\end{cases} \tag{19,20}$$

that can be reduced to:

$$\begin{cases}gY_c\ \sin\theta-r^2U_c^2=0\\ \left(c-U_c\right)^2-gY_c+ar^2U_c^2=0\end{cases} \tag{20,21}$$

The system admits the two couples of solutions, but only the couple:

$$\begin{cases}Y_c=\dfrac{c^2/g}{\left(\dfrac{\sqrt{\sin\theta}}{r}+\sqrt{1-a\sin\theta}\right)}\\ U_c=\dfrac{c}{1+r\sqrt{\dfrac{1-a\sin\theta}{\sin\theta}}}\end{cases} \tag{22,23}$$

satisfies the condition of roll waves existence $c>U_c$ (Whitham, 1973). The solution is real only if $a<1/\mathbf{sin}\ \theta$.

Using these quantities, the progressive discharge rate necessary for this special case is:

$$K=\frac{c^3/g}{\left(\dfrac{\sqrt{\sin\theta}}{r}+\sqrt{1-a\sin\theta}\right)}\sqrt{1-a\sin\theta} \tag{24}$$

and the following relation holds:

$$Y_c=\frac{K^{2/3}}{g^{1/3}\left(1-a\sin\theta\right)^{1/3}} \tag{25}$$

Introducing the variable $z=Y/Y_c$ and eliminating the pole $z=1$, eq.(17) can be written as:

$$Y_{z=1}=\frac{\sin\theta\left\{\left[z^2+\left[1-\frac{\left(\sqrt{\sin\theta}+r\sqrt{1-a\sin\theta}\right)^2}{\sin\theta}\right]z+\frac{r^2}{\sin\theta}(1-a\sin\theta)\right]\right\}}{\left\{\left[z^2+\left[1-a\left(\sqrt{\sin\theta}+r\sqrt{1-a\sin\theta}\right)^2\right]z+(ar^2-1)(1-a\sin\theta)\right]\right\}} \tag{26}$$

5 LIMITING CONDITION FOR A POSITIVE STEEPNESS OF THE PROFILE

In order to construct roll waves from the previous profile, it is necessary that:

$$\left.\frac{dY}{d\xi}\right|_{Y_e}>0 \tag{27}$$

It can be verified that the numerator in eq.(26) is positive in z=1 if:

$$4r^2<\frac{\sin\theta}{1-a\sin\theta} \tag{28}$$

and the numerator is positive in z=1 if:

$$4r^2<\frac{(2a\sin\theta-3)^2}{a^2\sin\theta(1-a\sin\theta)} \tag{29}$$

Also results:

$$\frac{\sin\theta}{1-a\sin\theta}<\frac{(2a\sin\theta-3)^2}{a^2\sin\theta(1-a\sin\theta)}\ \text{if}\ a<\frac{1}{\sin\theta} \tag{30}$$

As a consequence results:

$$\left.\frac{dY}{d\xi}\right|_{Y_e}>0\ \text{if}\ \begin{cases}4r^2<\dfrac{\sin\theta}{1-a\sin\theta}\\ 4r^2>\dfrac{(2a\sin\theta-3)^2}{a^2\sin\theta(1-a\sin\theta)}\end{cases} \tag{31}$$

However only the first inequality in eq.(31) is acceptable, because the second inequality results in an unphysical wave profile. The denominator in eq.(26) is always positive for physically acceptable values of the parameters, the numerator has two real roots named Y_1 and Y_2:

$$\frac{Y_{1,2}}{Y_e}=\frac{r}{2\sin\theta}\left[r(1-a\sin\theta)+2\sqrt{\sin\theta(1-a\sin\theta)}\right]\mp \frac{r}{2\sin\theta}\sqrt{\left[r(1-a\sin\theta)+2\sqrt{\sin\theta(1-a\sin\theta)}\right]^2-4\sin\theta(1-a\sin\theta)} \tag{32}$$

It can be verified that $0<Y_1<Y_2<Y_c$ if the first inequality (31) is satisfied. The eq.(26) can be integrated in analytical form as $\xi=f(Y)$.

6 THE CRITICAL POINT INCLUDING THE SURFACE TENSION

Including the surface tension term, eq.(17) becomes:

$$Y_{,\xi}=-\frac{gY^3\sin\theta-r^2(cY-K)^2-\frac{\sigma}{\rho}Y^3Y_{,\xi\xi\xi}}{K^2-gY^3+ar^2(cY-K)^2} \tag{33}$$

or

$$\frac{\sigma}{\rho}Y^3Y_{,\xi\xi\xi}+\left[K^2-gY^3+ar^2(cY-K)^2\right]Y_{,\xi}+ gY^3\sin\theta-r^2(cY-K)^2=0 \tag{34}$$

It is a non linear third order equation which can be expressed as a third order non linear autonomous system:

$$\begin{aligned} Y_{,\xi}&=Y_1\\ Y_{1,\xi}&=Y_2\\ Y_{2,\xi}&=\frac{\left\{\left[K^2-gY^3+ar^2(cY-K)^2\right]Y_1+ gY^3\sin\theta-r^2(cY-K)^2\right\}}{\frac{\sigma}{\rho}Y^3} \end{aligned} \tag{35}$$

The system has a singular point at $(Y_s, 0, 0)$, where Y_s is the solution of the equation:

$$gY_s^3\sin\theta-r^2(cY_s-K)^2=0 \tag{36}$$

It can be demonstrated that this equation has three real solutions if

$$c>\left(\frac{27gK\sin\theta}{4r^2}\right) \tag{37}$$

and a single real solution if

$$c<\left(\frac{27gK\sin\theta}{4r^2}\right) \tag{38}$$

In both cases there is always a real positive solution. Near the critical point we let $(Y, Y_1, Y_2)=(Y_s+\varepsilon, \varepsilon_1, \varepsilon_2)$ and we approximate the system of equation as:

$$\underbrace{\left[\frac{K^2-gY_s^3+ar^2(cY_s-K)^2}{\frac{\sigma}{\rho}Y_s^3}\right]}_{f}\varepsilon_1 \tag{39}$$

It is a linear autonomous system of equations in the perturbations of the singular point. In compact form it can be expressed as

$$\begin{Bmatrix} \varepsilon \\ \varepsilon_1 \\ \varepsilon_2 \end{Bmatrix}_{,\xi} = \begin{bmatrix} 0 & 1 & 0 \\ 0 & 0 & 1 \\ d & f & 0 \end{bmatrix} \begin{Bmatrix} \varepsilon \\ \varepsilon_1 \\ \varepsilon_2 \end{Bmatrix} \tag{40}$$

and the eigenvalues are the solutions of the characteristic equation:

$$\lambda^3 - f\lambda - d = 0 . \tag{41}$$

The classification of the singular point is based on the eigenvalues. The eigenvalues are all real if

$$\frac{d^2}{4} - \frac{f^3}{27} > 0 \tag{42}$$

In the present analysis this condition is satisfied for reasonable values of the parameters involved. The singular point is classified as hyperbolic fixed point. A zero eigenvalue is obtained if d=0 or

$$c = \frac{rK + \sqrt{r^2K^2 + 6gY_s^3 \sin\theta}}{2rY_s} \tag{43}$$

and the singular point becomes nonhyperbolic. The analysis on the singular point is in progress but the great variety of singularity suggest different families of solutions if tension surface is non negligible.

7 SHOCK CONDITIONS

The shock condition is obtained from the mass and momentum balance equations for a control volume across the shock:

$$\begin{cases} c\left[Y\right]_f^b = \left[UY\right]_f^b \\ c\left[UY\right]_f^b = \left[\beta U^2 Y + \frac{1}{2} gY^2 \cos\theta\right]_f^b \end{cases} \tag{44,45}$$

where the square brackets are the operator $[<.>]_a^b = <.>|_b - <.>|_a$ and b and f stand for the back and front sections of the shock. The mass balance equation (8) in extended form is:

$$(c-U_b)Y_b=(c-U_f)Y_f=K\equiv K_c \tag{46}$$

with K the apparent discharge in the moving frame. The linear momentum balance equation (6) can be written as:

$$\frac{2c^2}{g}\left(Y_b - Y_f\right) - \left(Y_b^2 - Y_f^2\right)\cos\theta = \frac{2\beta_b}{gY_b}\left(cY_b - K_c\right)^2 - \frac{2\beta_f}{gY_f}\left(cY_f - K_c\right)^2 \tag{47}$$

where eq.(46) has already been used. The usual trivial solution $Y_f=Y_b$ (no shock) holds if in addition $\beta_f=\beta_b$ is assumed. Equation (47) can be solved obtaining $Y_b=f(Y_s)$ and choosing the solution $Y_b>Y_f>0$. Note that in general the momentum correction coefficients should depend on the 'age' of the boundary layer and on the jump height Y_b-Y_f.

8 ENERGY DISSIPATION IN THE SHOCK

The rate of change of mechanical energy across the jump is equal to:

$$\Delta P = -\left\{\begin{array}{l} \frac{1}{2g}U_b^2 Y_b\left(\alpha_b U_b - \beta_b c\right) - \\ \frac{1}{2g}U_f^2 Y_f\left(\alpha_f U_f - \beta_f c\right) + \\ \cos\theta\left[Y_b^2\left(U_b - \frac{1}{2}c\right) - Y_f^2\left(U_f - \frac{1}{2}c\right)\right] \end{array}\right\} \tag{48}$$

where α_b and α_f are the energy flux correction factors. Assuming $Y^*_{<c>} = Y_{<c>}\mathrm{g}/c^2$, eq.(48) reads:

$$\Delta P^* = -\frac{1}{2}\left(1 - \frac{K_c^*}{Y_b^*}\right)^2 Y_b^*\left(\alpha_b - \alpha_b\frac{K_c^*}{Y_b^*} - \beta_b\right) + \frac{1}{2}\left(1 - \frac{K_c^*}{Y_f^*}\right)^2 Y_f^*\left(\alpha_f - \alpha_f\frac{K_c^*}{Y_f^*} - \beta_f\right) - \cos\theta\left[Y_b^{*2}\left(\frac{1}{2} - \frac{K_c^*}{Y_b^*}\right) - Y_f^{*2}\left(\frac{1}{2} - \frac{K_c^*}{Y_f^*}\right)\right] \tag{49}$$

Substituting the expression for discharge in the moving reference and dividing by the discharge per unit width in the moving reference, it is possible to obtain the energy drop across the jump. The expression is cumbersome and is not reported. For $\alpha_f= \beta_f=\alpha_b=\beta_b=1$ the energy drop has the classical expression:

$$\Delta E_j^* = -\cos\theta\frac{\left(Y_b^{*3} - Y_f^{*3}\right)}{4Y_b^* Y_f^*} \tag{50}$$

The assumption of a boundary layer with a gradient pressure is not consistent with the common assumption of constant momentum and energy coefficients. Instead, if we assume $\beta_b>\beta_f>1$ and $\alpha_b>\alpha_f>1$ a domain of acceptable conditions $(Y_b^* > Y_f^*)$ and limited dissipation rate $(\Delta E_j^* \to 0)$ is possible (see Fig.4).

9 DISCUSSION ON ENERGY DISSIPATION IN THE UNSTABLE STREAM

The mean energy dissipated for friction in a wave length is computed as:

$$\Delta E_f = -\int_{Y_f}^{Y_b} \frac{r^2U^2}{gY}\frac{1}{Y_{,x}}dY + \int_{Y_f}^{Y_b} \frac{ar^2U^2}{gY}dY \qquad (51)$$

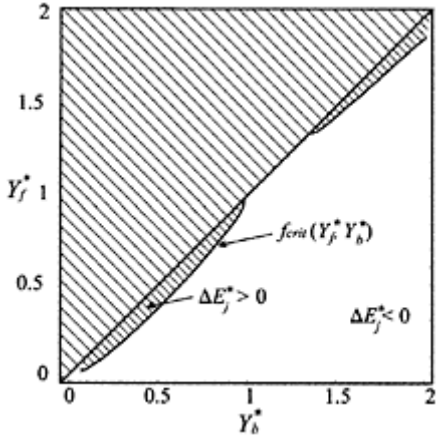

Figure 4. Energy balance in the jump. The hatched area is unacceptable because $Y_f^* > Y_b^*$. The closed hatched area corresponds to energy production in the jump, physically unacceptable. β_b=1.03, β_f=1.02, α_b=1.06, α_b=1.03, θ=10°.

A stream in steady uniform motion obviously results in $\Delta E_f+\lambda$. sin θ=0 for any value of the wave length λ. In the presence of roll waves, including the energy dissipated in the jump, the energy balance over a wave length results in:

$$\Delta E=\Delta E_f+\Delta E_j+\lambda \sin\theta \qquad (52)$$

Assuming the modified resistance, which includes the gradient pressure effects, an energy saving term appears (the last term on the right hand of eq.50), although, on the basis of some numerical experiments, it is still not enough to close the energy budget, i.e. the system dissipates more energy than the energy gained from gravity. The jump enhances dissipation and the stream in unstable motion dissipates more than the equivalent stream in stable steady uniform motion (equivalent means having the same average discharge with identical channel characteristics). All the computations have neglected the finite size of the moving shock, the contribution of the weight of the fluid

in the shock, surface tension effects and the trajectories curvature. It has been demonstrated that inclusion of the weight of the fluid in the jump in linear momentum balance across the shock, tends to reduce the ratio Y_b^*/Y_f^* (Brock 1967) and favors smaller wave lengths. Surface tension contrasts instabilities growth and rounds the wave crest (Hwang et al. 1994). In addition, neglecting dissipation due to friction in the shock (assumed of finite length) it is possible to find a zero energy budget (eq.52) corresponding to a situation where the dissipation by friction in the permanent wave profile plus the dissipation in the jump equals the energy gained by gravity (Lamberti & Longo 2000). The balance is very sensitive to small variations in the parameters. Also the assumption of a different friction law gives different results. According to Kapitza (1948) and Ng & Mei (1994) the observed roll wave has the smallest mean energy averaged over the wave length. Assuming that the momentum and the energy correction coefficients are higher on the back than on the front side of the shock, the energy dissipated in the jump can be zero for $Y_f^* < Y_b^*$. The energy balance criterion holds if and only if the roll waves are assumed permanent and periodic. If a small space variation of the waves is expected, the energy balance should be closed on a group of waves and not on a single wave.

10 CONCLUSION

The proposed solution for finite amplitude roll waves using a modified friction factor is similar to the solution proposed by Dressler (1949) for a Newtonian fluid. The solution is expressed as a discontinuous function obtained by connecting two continuous profiles with a shock. The continuous profiles are obtained in the shallow equations approximation. In order to construct the profile between two shocks, it is necessary that the steepness is finite and positive in the section where critical condition is reached. It results in the limiting value for the pressure gradient factor vs. bottom slope and in a limiting value for the roughness.

Including the momentum and energy coefficients variation in the front and in the back side of the hydraulic jump, a reduced dissipation rate in the jump is obtained for physical acceptable condition $(Y_f^* < Y_b^*)$.

Including the tension surface effects a new family of possible solution is explored. The results on this approach are preliminary and suggest that a limiting value for celerity is imposed by the behavior of the solution near the singular point. The singular point collapses to the critical point if the surface tension is neglected.

ACKNOWLEDGEMENTS

The author acknowledges support for this work from the University of Parma, FIL 2003.

REFERENCES

Benjamin, T.B., 1957a. Wave formation in laminar flow down an inclined plane. *Journal of Fluid Mechanics*, 2:554–574.

Benjamin, T.B., 1957b. Corrections to: Wave formation in laminar flow down an inclined plane. *Journal of Fluid Mechanics*, 3:657.

Berlamont, J.E. & Vanderstappen, N., 1981. Unstable turbulent flow in open channels. *Journal of Hydraulic Divison, ASCE*, Vol. 107, No. HY4:427–449.

Brock, R.R., 1966. Discussion of Critical analysis of open-channel resistance, by H.Rouse. *Journal of Hydraulic Divison, ASCE,* Vol. 92, No. HY2:403–409.

Brock, R.R., 1967. *Development of roll waves in open channels.* W.M. Keck Laboratory of Hydraulics and Water Resources, California Institute of Technology, Report No. KH-R-16, pp.226

Brock, R.R., 1969. Development of roll wave trains in open channels. *Journal of Hydmulic Division, ASCE*, Vol. 95, No. HY4:1401–1427.

Chen, C.L., 1992. Momentum and energy coefficients based on power-law velocity profile. *Journal of Hydraulic Engineering, ASCE,*Vol. 118, No. 11:1571–1584.

Chow, V.T., (1959) 1973. *Open Channel Hydraulics,* McGraw Hill, pp.680.

Chun, F.,, 1982. Stability of flow of a generalized Newtonian fluid down an inclined plane. *Journal of Applied Mathematics and Physics (ZAMP),* Vol. 33: 181–188.

Clauser, F.H., 1956. The turbulent boundary layer. *Advances in Applied Mechanics* IV, 1–51.

Cornish, V., 1934. *Ocean waves.* Cambridge University Press.

Dressler, R.E., 1949. Mathematical solution of the problem of roll waves in inclined open channels. *Communications on Pure and Applied Mathematics,* Vol. 2:149–194.

Forchheimer, P., 1903. Wasserbewegung in Wardewellen. *Zeitschrift für Gewässerkunde* 6(6):321–339.

Hwang, C., Chen, J., Wang, J. & Lin, J., 1994. Linear stability of power-law liquid film flows down an inclined plane. *Journal of Physics D: Applied Physics* 27:2297–2301.

Ishihara, T., Iwagaki, Y. & Iwasa, Y., 1954. Theory of the roll wave train in laminar water flow on a steep slope surface. *Transactions of Japan Society of Civil Engineers* 19: 46–57 (in Japanese)

Iwasa, Y., 1954. The criterion for instability of steady uniform flows in open channels. *Memoirs of the Faculty of Engi-neering,* Kyoto University, Japan, Vol. 16, No. 6:264–275.

Jeffreys, H.J., 1925. The flow of water in an inclined channel of rectangular section. *Philosophical Magazine,* series 6, Vol. 49:793–807.

Julien, P.Y. & Hartley, D.M., 1985. *Formation of roll waves in laminar sheet flow*—Rep. CER84–85PYJ-DMH18. Department of Civil Engineering, Colorado State University.

Julien, P.Y. & Hartley, D.M., 1986. Formation of roll waves in laminar sheet flow. *Journal of Hydraulic Research* 24: 5–17.

Kapitza, P.L., 1948. *Wave flow of thin layers of a viscous fluid.* Collected Papers of P.L.Kapitza, Vol. II, 1938–1964, Pergamon Press (1965), pp. 662–709.

Koloseus, H.J. & Davidian, J., 1966. Free surface instabilities correlations. *Geological Survey Water-Supply* Paper 1592-C, pp. 72

Lamberti, A. & Longo, S., 2000. *Roll waves e dissipazione in correnti idriche ε nei debris flow (Roll waves and dissipation in water streams and in debris flow).* Proc. XXVII National Conference on Hydraulics, GNDCI, Vol. 1:85–94 (in italian).

Ligget, J.A., 1975. *Stability. In Unsteady flow in Open Channels,* Chapter 6, pp. 259–282, WRP.

Longo, S., 2003. Roll waves on a shallow layer of debris modeled as a dilatant fluid. D.Rickenmann & Cheng-lung Chen (eds) *Proc. of the Third International DFHM Conference*, Davos, Switzerland, September 10–12, 2003, Millpress Science Publishers, Rotterdam, Vol. 1, pp. 339–350, 2003, ISBN 90 77017 78 X.

Montuori, C., 1961. La formazione spontanea dei treni d'onde su canali a pendenza molto forte. *L'Energia Elettrica,* N.2:127–141.

Ng, C. & Mei, C.C., 1994. Roll waves on a shallow layer of mud modelled as a power-law fluid. *Journal of Fluid Mechanics* 263:151–183.

Ponce, V.M. & Maisner M.B., 1993. Verification of theory of roll wave formation. *Journal of Hydraulic Engineering,* ASCE, 119(6):768–773.

Prasad, S.N., Pal, D. & Römkens, M.J.M., 2000. Wave formation on a shallow layer of flowing grains. *Journal of Fluid Mechanics* 413: 89–110.
Rosso, M., Schiara M. & Berlamont, J., 1990. Flow stability and friction factor in rough channels. *Journal of Hydraulic Engineering, ASCE,* Vol. 116, No. 9:1109–1118.
Rouse, H., 1965. Critical analysis of open-channel resistance. *Journal of Hydraulic Engineering, ASCE,* Vol. 91, No. HY4:1–25.
Stoker, J.J., 1957. *Mathematical hydraulics,* in Water waves, Wiley Interscience, pp. 451–509.
Thomas, H.A., 1939. The propagation of waves in steep prismatic conduits. *Proc. Hydraulic Conference, Univ. of Iowa,* pp. 214–229.
Vedernikov, V.V., 1945. Conditions at the front of a translation wave disturbing a steady motion of a real fluid. *Comptes Rendus de L'Académie des Sciences URSS* 48(4): 239–242.
Whitham, G.B., 1974. *Linear and nonlinear waves.* Wiley-Interscience Publication, John Wiley & Sons, New York.
Yih, C.S., 1954. Stability of parallel laminar flow with a free surface. *Proc. 2nd U.S. Congress in Applied Mechanics,* pp. 623–628.
Yih, C.S., 1963. Stability of liquid flow down an inclined plane. *Physics of Fluids,* Vol. 6:321–334.

Mathematical simulation of the effects of bridges and structures on flood waves propagation

L.Natale & G.Petaccia
Department of Environmental and Hydraulic Engineering, University of Pavia, Pavia, Italy

F.Savi
University of Roma "La Sapienza", Roma, Italy

River Flow 2004—Greco, Carravetta & Della Morte (eds.)

ABSTRACT: The movement of flood wave in rivers is greatly influenced by channel transitions and controls such as bridges, sills, weirs, sluices or other types of hydraulic structures. The mathematical simulation of the flow conditions through these obstructions often asks for the reproduction of changes from subcritical to supercritical flow and vice versa. This paper presents a suitable technique for simulation of flow through channel controls that uses internal boundary conditions of 1D shallow water mathematical model. The numerical solver is first order finite volume, and is able to reproduce changes of the flow regime through the hydraulic structure and tailwater control. The model was verified simulating experiments on flume reported in literature. Moreover several experiments were performed in the Hydraulic Laboratory of the Department of Hydraulic and Environmental Engineering of the University of Pavia: calculated water profiles fit acceptably observed ones. The 1D mathematical model can not simulate the weir-nappe profiles immediately downstream the structures which are curvilinear and three-dimensional, but it is a practical tool that usefully reproduces the increasing of the water stages and the slowing down of the wave movement caused by structures.

1 INTRODUCTION

The mathematical simulation of flood routing in rivers has been increasingly studied in the last decades. When a flood wave moves along mountain reaches the flow regime varies from subcritical to supercritical and vice versa in space and time due to the

formation of hydraulic surges and control sections. These variations of flow regime are mainly due to abrupt changes in channel geometry and can be simulated only by numerical solvers able to reproduce discontinuities (shocks) of the free surface.

Many numerical solvers have been proposed to integrate the shallow water equations and to schematize the effects of source terms for transcritical flow (Toro, 1997; Hirsch, 1990): their accuracy was verified by simulating experiments on flumes in a wide range of abrupt channel transitions (Morris, 2000; Morris and Galland, 2000; Petaccia and Savi, 2002). Even in natural watercourses, flow regime can be controlled by hydraulic structures such as bridges, weirs or sluice-gates, causing subcritical flow upstream and supercritical flow downstream. The tailwater effects due to these structures must be carefully simulated in order to recognise where levees might be overtopped.

Goutal and Maurel (2002), Rissoan et al. (2002) simulated simple obstacles, such as weirs or constrictions, modifying locally the river geometry (bottom elevation or channel width). Soares Frazão and Zech (2000) simulated flow through bridge with a local constriction of the cross section.

This schematization is not suitable when different hydraulic flow conditions through bridges can occur: free surface flow, pressure flow, pressure and overtopping flow. Moreover minor losses cannot be directly taken into account by shallow water equations. Therefore, as a common practice, internal boundary conditions (rating curves) are adopted. An internal boundary condition relates the flow conditions in the two river reaches, upstream and downstream the structure, where shallow water equations are valid. Usually these rating curves are computed in steady flow conditions taking into account minor losses.

This approach is widely used by models that deal with a single flow regime (subcritical or supercritical): for instance ISIS (Rosu and Ahmed, 1999), NWS FLDWAV (Jin and Fread, 1997; Fread and Lewis, 1998) computer codes. TEVERE (Natale et al, 1999) model, based on Preissmann scheme, simulates in this way flow through a wide range of hydraulic structures.

Some of these models, such as MIKE11 (DHI, 2000), NWS FLDWAV (Fread and Lewis, 1998), RUBAR 3 (Paquier, 1998) simulate flow through structures using numerical solvers able to reproduce subcritical and supercritical flow regimes. However some of these codes simulate in simplified way trans-critical flow: for instance in NSW FLDWAV and MIKE1 1 codes, the convective inertial terms are progressively reduced as Froude number increases, up to neglect them when its value approaches unity. Such models simulate the tailwater effects approximately and do not reproduce changes in time of flow regime, upstream and/or downstream the structure.

García Navarro and Alcrudo (1992) simulated a series of weirs using internal boundary conditions; in their application the flow regime did not change and supercritical flow occurred downstream any weir.

In the following is presented the simulation of the flow across structures taking into account transcritical flow conditions, adopting 1D shallow water equations written in complete form and solved by means of an upwind finite volume scheme. The numerical results are verified on the basis of laboratory tests reported in literature or expressly carried out in the Laboratory of Hydraulic and Environmental Engineering of the University of Pavia.

2 MATHEMATICAL MODEL

Propagation of a dam-break wave can be described by the shallow water equations coming from the mass and momentum balance equations (Cunge et al., 1980):

$$\frac{\partial \boldsymbol{U}}{\partial t} + \frac{\partial \boldsymbol{F}}{\partial x} = \boldsymbol{S} \tag{1}$$

$$\boldsymbol{U} = \begin{pmatrix} A \\ Q \end{pmatrix} \boldsymbol{F} = \begin{pmatrix} Q \\ \dfrac{Q^2}{A} + gI_1 \end{pmatrix} \tag{2a}$$

$$\boldsymbol{S} = \begin{pmatrix} 0 \\ gA(S_0 - S_f) + gI_2 \end{pmatrix} \tag{2b}$$

where x is the spatial co-ordinate measured along the channel, t the time, Q the discharge, A the wetted area, g the gravitational acceleration, S_0 the bottom slope, S_f the friction slope. The terms I_1 and I_2 are related to the hydrostatic pressure force:

$$I_1 = \int_0^h (h-\eta) b(x,\eta) d\eta \ , \quad I_2 = \int_0^h (h-\eta) \frac{\partial b}{\partial x} d\eta \tag{3}$$

h is the water depth and $b(x, \eta)$ the width of the cross section at the distance x and height η, above the channel bed.

3 NUMERICAL SOLVERS

System (1) is solved by means of a first order finite volume numerical solver based on Roe's approximated Jacobian of the flux schematization (Roe, 1981):

$$\boldsymbol{U}_i^{n+1} = \boldsymbol{U}_i^n - \frac{\Delta t}{\Delta x}\left(\boldsymbol{F}^*_{i+1/2} - \boldsymbol{F}^*_{i-1/2}\right) \tag{4}$$

The numerical fluxes F are computed as

$$\boldsymbol{F}^*_{i-1/2} = \frac{1}{2}\left(\boldsymbol{F}_i^n + \boldsymbol{F}_{i+1}^n\right) - \frac{1}{2} \cdot \sum_{k=1,2} \left|\tilde{a}^k_{i+1/2}\right| \cdot \alpha^k_{i+1/2} \cdot \tilde{\boldsymbol{e}}^k_{i+1/2} \tag{5}$$

with

$$\alpha^{1,2}_{i+1/2} = \frac{1}{2}\left[\left(A^n_{i+1} - A^n_i\right) \pm \frac{\left(Q^n_{i+1} - Q^n_i\right) - \tilde{u}^n_{i+1/2}\left(A^n_{i+1} - A^n_i\right)}{\tilde{c}^n_{i+1/2}}\right] \tag{6}$$

and

$$\boldsymbol{e}^{1,2}_{i+1/2} = \begin{pmatrix} 1 \\ \tilde{a}^{1,2}_{i+1/2} \end{pmatrix} \text{where} \quad \tilde{a}^{1,2}_{i+1/2} = \tilde{u}^n_{i+1/2} \pm \tilde{c}^n_{i+1/2} \tag{7}$$

The eigenvalues *a* and the eigenvectors ***e*** of the Jacobian matrix depend on the flow velocity *u* and celerity *c:*

$$\tilde{u}_{i+1/2}^{n} = \frac{\sqrt{A_{i+1}^{n}}\,u_{i+1}^{n} + \sqrt{A_{i}^{n}}\,u_{i}^{n}}{\sqrt{A_{i+1}^{n}} + \sqrt{A_{i}^{n}}} \tag{8}$$

$$\tilde{c}_{i+1/2}^{n} = \sqrt{g\frac{I_{1i+1}^{n} - I_{1i}^{n}}{A_{i+1}^{n} - A_{i}^{n}}} \tag{9}$$

In order to avoid non-physical discontinuities (zero eigenvalues), that are incompatible with the entropy principle, the absolute value of the eigenvalues of ***J*** is modified by defining the quantity:

$$\varepsilon_{i+1/2}^{k} = \max_{k=1,2}\left[0,\left(\tilde{a}_{i+1/2}^{k} - a_{i}^{k}\right),\left(a_{i+1}^{k} - \tilde{a}_{i+1/2}^{k}\right)\right] \tag{10}$$

The new absolute value of each eigenvalue in equation (5) is defined as:

$$\Psi_{i+1/2}^{k} = \begin{cases} \left|\tilde{a}_{i+1/2}^{k}\right| & \text{if } \left|\tilde{a}_{i+1/2}^{k}\right| \geq \varepsilon_{i+1/2}^{k} \\ \varepsilon_{i+1/2}^{k} & \text{if } \left|\tilde{a}_{i+1/2}^{k}\right| < \varepsilon_{i+1/2}^{k} \end{cases} (k = 1,2) \tag{11}$$

4 SOURCE TERMS

The source terms (2b) are schematized in two different ways:

4.1 *Pointwise (Brufau et al., 2002)*

$$S_{0i} = -\frac{z_{i+1} - z_{i-1}}{2\Delta x} \text{ and } S_{fi}^{n} = \frac{n^2 Q_i^{n+1}\left|Q_i^{n+1}\right|}{A_i^{n} R_i^{n\,4/3}} \tag{12}$$

where *n* is the Manning roughness coefficient. The I_2 term is schematized as

$$I_2 = \frac{1}{2}\cdot h_i^2\,\frac{b_{i+1} - b_{i-1}}{2\Delta x} \tag{13}$$

where *b* is the flume width.

4.2 *Upwind (García Navarro and Vasquez-Cendon, 2000)*

According to equation (1), the decomposition of the source terms can be expressed as

$$\boldsymbol{S} = \begin{pmatrix} -\beta_{i+1/2} + \beta_{i-1/2} \\ \beta_{i-1/2}\cdot\left(\tilde{u}_{i-1/2} + \tilde{c}_{i-1/2}\right) - \beta_{i+1/2}\cdot\left(\tilde{u}_{i+1/2} + \tilde{c}_{i+1/2}\right) \end{pmatrix} \tag{14}$$

where the values of β coefficients are chosen in order to produce the balance the momentum equation for rectangular cross sections.

5 INTERNAL BOUNDARY CONDITIONS

Internal boundary conditions were introduced in the unsteady flow simulation in order to reproduce minor losses through structures. Let's focus on the generic structure (i.e. sluice-gate, sharp channel contraction) located at the cross section *(i)* in Fig. 1. Upstream ($i-1$) and downstream ($i+1$) channel cross sections have the same shape of the intermediate section *(i)*. The computational domain is then disconnected in two reaches upstream (from section 1 to $i-2$) and downstream (from section $i+2$ to section N) the structure, where equations (4) are applied and the values of A_i^{n+1} and Q_i^{n+1} are computed.

Considering that no water is stored in the short stretch from ($i-1$) and ($i+1$) since the two sections are very close, the mass balance equation across the structure is considered:

$$Q_{i-1}^{n+1} = Q_{i+1}^{n+1} \tag{15}$$

Further relationships that depend on the flow regime are needed to estimate the three unknowns $A_{i-1}^{n+1}, A_{i+1}^{n+1}$

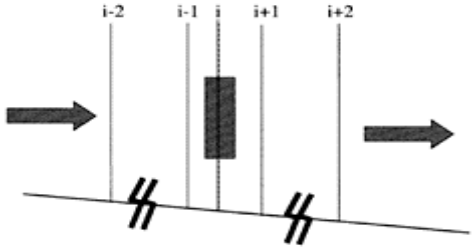

Figure 1. Schematization of an internal boundary condition.

and Q_{i-1}^{n+1}. The model computes both subcritical and supercritical flow solutions and compares the total momentum fluxes plus the total hydrostatic pressures to assess which solution is correct. In the following this procedure will be explained in details.

Supercritical flow through the structure may occur if in section $i-2$ the flow is supercritical. In this case the values of $\hat{A}_{i+1}^{n+1}$ and $\hat{Q}_{i+1}^{n+1}$ (the symbol ^ means that this a possible supercritical solution) are estimated considering a backward schematization of the fluxes, i.e.

$$\boldsymbol{U}_i^{n+1} = \boldsymbol{U}_i^n - \frac{\Delta t}{\Delta x}\left(\boldsymbol{F}_i^n - \boldsymbol{F}_{i-1}^n\right) \tag{16}$$

The energy or the momentum equation in steady state condition is applied between section $i-1$ and $i+1$ to simulate the contraction and the expansion of the supercritical flow through the structure. This equation relates $\hat{A}_{i+1}^{n+1}$ to the values of $\hat{A}_{i-1}^{n+1}$ and $\hat{Q}_{i+1}^{n+1}$ only.

If the flow in section $i+2$ is supercritical no backwater effects occur, then

$$A_{i-1}^{n+1} = \hat{A}_{i-1}^{n+1},\ A_{i+1}^{n+1} = \hat{A}_{i+1}^{n+1} \text{ and } Q_{i\pm1}^{n+1} = \hat{Q}_{i\pm1}^{n+1} \tag{17}$$

Otherwise, subcritical flow condition may exist.

In this case the flow regime depends on the flow conditions both in sections $i-2$ and $i+2$ simultaneously. The following system of 3 equations can be written:

(a) continuity equation between sections $i+1$ and $i+2$, i.e.

$$\frac{\tilde{A}_{i+1}^{n+1} - A_{i+1}^{n}}{\Delta t} - \frac{Q_{i+2}^{n+1} - \tilde{Q}_{i+1}^{n+1}}{x_{i+2} - x_{i+1}} = 0 \tag{18}$$

(b) rating curve in subcritical flow conditions between sections $i+1$ and $i-1$, i.e.

$$\tilde{A}_{i-1}^{n+1} = f(\tilde{A}_{i+1}^{n+1}, \tilde{Q}_{i+1}^{n+1}) \tag{19}$$

(c) continuity equation between sections $i-1$ and $i-2$, i.e.

$$\frac{\tilde{A}_{i-1}^{n+1} - A_{i-1}^{n}}{\Delta t} - \frac{\tilde{Q}_{i-1}^{n+1} - Q_{i-2}^{n+1}}{x_{i-1} - x_{i-2}} = 0 \tag{20}$$

The symbol ˜ means that this a possible (subcritical) solution and it can be computed by solving the above system of equations.

In many cases both subcritical and supercritical solutions do not exist. This means that section i controls the flow with subcritical flow upstream and supercritical flow downstream the structure. Continuity equations are applied to evaluate water depths in $i-1$ and $i+1$ which depends on the rate of discharge only.

If more than one solution exists, i.e. both subcritical and supercritical solutions can be obtained, to check which solution is correct, the momentum functions are compared starting from section $i+1$ and moving upstream.

6 SURGE FORMATION

The equations described in section 2 do not represent properly the dynamics of the surge formation since the volume of water in the roll of the hydraulic jump is neglected.

In fact the model represents a shock discontinuity in the mathematical solution and the numerical solver locates the variations of the flow regimes in a few space intervals (Δx); all in all it does not consider the length of the hydraulic jump.

The backward movement of the surge was simulated as follows: when the supercritical flow impact against the gate the lower part of the current remains essentially undisturbed. Therefore in the model the discharge through the gate is maintained constant in time. The difference between the discharge in the upstream section and the discharge through the gate is stored by the model until it becomes equal to the volume in the roll of the hydraulic jump (V_j).

The upper part of the current impacts against the gate and accelerates vertically generating the roll of the hydraulic jump. The surge does not move until the volume of water in the roll, taking into account a constant value of air concentration in water

(C_w=0.3), corresponds to the hydraulic jump length evaluated by means of the Peterka formula (1958).

Up to this time the lower part of the current and the flow through the gate remains supercritical. The volume of water in the jump *(V_j)*, assuming a linear roll profile, is estimated.

When the hydraulic jump is formed at the upstream face of the gate (section i−1 of Fig. 1) subcritical conditions occur. The model simulates the switch between undisturbed current and under gate flow, described adopting the rating curve in Fig. 4. The surge keeps then to move backward.

7 EXPERIMENTAL VERIFICATIONS

7.1 *WES test case*

The proposed approach was firstly tested comparing the results of the model with the observations of a flume experiment (5.1 test case) carried out at the USACE Waterways Experiment Station (Chen, 1980). The experimental setup consists of a 122m long, 1.22m wide rectangular flume with a slope S_0=0.005. A removable dam, 0.305m high, is located at the midpoint of the flume (x=61m). It involves a constricted breach width of 0.122m, or 1/10 channel width.

The Manning coefficient applied is 0.009ms$^{-1/3}$. This experiment, which constitute a severe benchmark for numerical solver since is characterized by an abrupt variation of the channel width, was simulated by Sanders (2001), that used a II order scheme and more recently by Bradford and Sanders (2002), a 2D approach.

First of all we simulated WES experiments integrating shallow water equations without imposing any internal boundary conditions. In Fig. 2 the observed water depths hydrographs are compared with those computed adopting both pointwise (continuous line) and upwind (dotted line) schematizations of the source terms.

Pointwise schematization is unacceptable since overestimates the outflow so that in the simulation the reservoir empties much faster than real one and the computed wave front celerity is considerably higher than the experimental one. For this reason in Fig. 2 the pointwise simulation of the reservoir emptying is not shown.

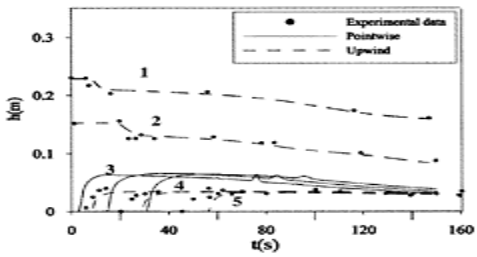

Figure 2. Comparison between upwind and pointwise source term schematizations without internal

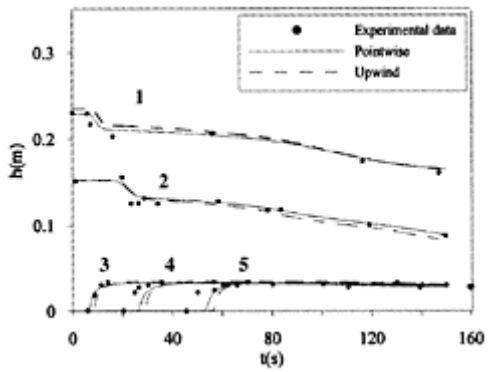

Figure 3. Comparison between upwind and pointwise source term schematizations with internal boundary conditions: (1) at x=30.5m, (2) at x=45.75, (3) at x=68.6m, (4) at x=85.4, (5) at x=106.75m.

The upwind schematization is significantly more accurate.

If internal boundary conditions are introduced, also the pointwise schematization gives acceptable results: the simulations obtained with internal boundary conditions applied to the pointwise treatment are shown in Fig. 3. Similar results are obtained coupling the upwind treatment and internal boundary conditions.

7.2 *Pavia test cases*

In order to investigate more extensively the importance of internal boundary conditions, experimental tests were carried out at Hydraulic Laboratory of the University of Pavia. The flume was 9.30m long, 0.48m wide, horizontal, with a bottom friction coefficient of $0.12 ms^{-1/3}$. The steep wave was generated by the instantaneous opening of a hinged sluice gate placed at x=3.36m. The still water stored upstream the gate was 0.20m deep.

The experiments considered a first sluice-gate, 4 cm open, placed at x=8.40m and a second sluice-gate, 2cm open, at the end of the flume (x=9.3m) to produce evolving tailwater condition in the flume. To estimate the rating curve through the first gate, preliminary experiments in steady state conditions were performed supplying constant discharge and measuring water stages immediately upstream and downstream the gate and fitting the experimental observations using discharge coefficient reported by Ven Te Chow (1959)(Fig. 4).

In the following pictures (5, 6, 7, 8, 9, 10 and 11), the computed (grey and black line) and experimental instantaneous surface profiles taken by a standard video camera (25 frame per second) are compared at various time steps.

x=45.75, (3) at x=68.6m, (4) at x=85.4, (5) at x=106.75m.

The black line represents the simulation I obtained with the surge formation model explained in section 6. The grey line represents the simulation II obtained without the surge formation model.

Both the mathematical models simulate supercritical flow (Fig. 5) when the flow depth is lower than the upstream gate opening.

Figure 6 shows that only a part of the current supplies water to the roll of the hydraulic jump; the computed volume stored by the model at that time is represented by the thinner black line; until the water volume stored by the model I does not equal V_j the model I does not simulate the formation of the surge. The model II (grey line) simulates erroneously the formation of the surge. The stored volume for the

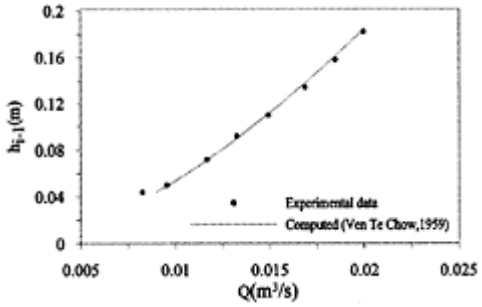

Figure 4. Rating curve for the gate.

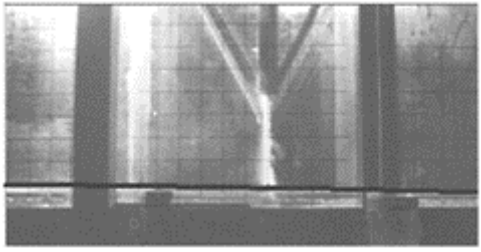

Figure 5. Measured and computed instantaneous profiles at t=4s.

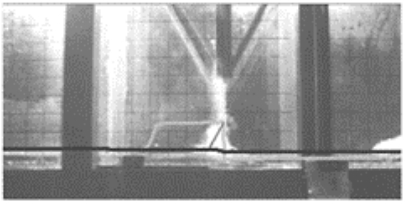

Figure 6. Measured and computed instantaneous profiles at t=5s.

second gate is not represented since is too far from the experimental window.

Figure 7 depicts the instant where the flow regime upstream of the gate changes from supercritical to subcritical.

Figure 8 shows that the downstream surge reaches and submerges the upstream gate.

In Fig. 9 computed and observed water depth after 7.7s are compared. Upstream the gate water depth increases immediately after submergence of the gate becomes effective.

The comparison with the experimental images shows that the model II fails in the simulations of the first instants of the flow impact against the gate (Fig. 6). The discrepancies between the results of the simulation II and experiments mainly depend on the simulation of the bore upstream the gate. It is confirmed that the model does not reproduce correctly

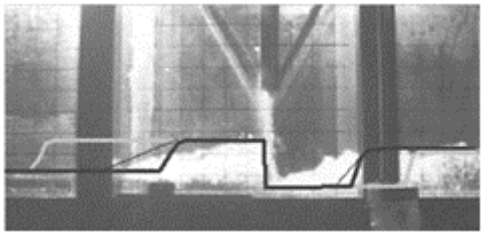

Figure 7. Measured and computed instantaneous profiles at t=6.0s.

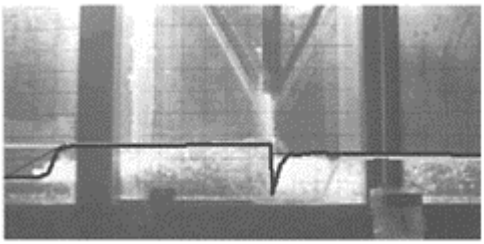

Figure 8. Measured and computed instantaneous profiles at t=6.9s.

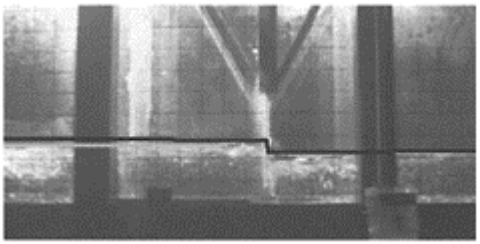

Figure 9. Measured and computed instantaneous profiles at t=7.7s.

the changes of the flow regimes immediately after the impact against the gate (Fig. 6): in this short transient the model simulates subcritical flow although the experiments show that the flow is essentially supercritical. The results of the model II (grey line) underestimate the discharge through the gate and overestimate the celerity of surge moving from the upstream gate. As a consequence the celerity of the surge moving from the downstream gate is underestimated.

As time goes on, the model II reproduces maximum water depths upstream the gate but overestimates the celerity of the surge moving upstream from the gate (Fig. 7). Consequently the model II simulates the submersion of the upstream gate with a short delay in comparison with the experiments (Fig. 8).

Comparing the two simulations can be remarked that the celerity of the surge is not affected by the mechanics of the surge formation, since both the simulated celerities are greater than the observed one.

On the basis of these results some more investigation are going to be performed in the Hydraulic Laboratory of the University of Pavia.

The experimental setup includes a sharp contraction that reduces the cross section to one half of the original one and a bridge.

As an example of preliminary results, the computed and observed water depths profiles for the constriction are compared in Figs. 10 and 11.

Figures 10 and 11 show that the downstream water depths are underestimated due to aeration of the flow and strong surface turbulence induced by the falling

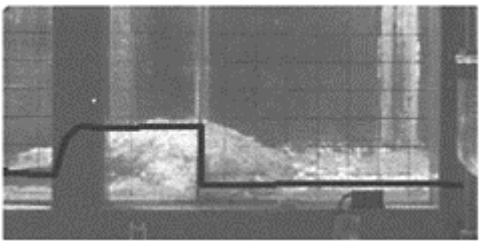

Figure 10. Measured and calculated instantaneous profiles at t=3.2s

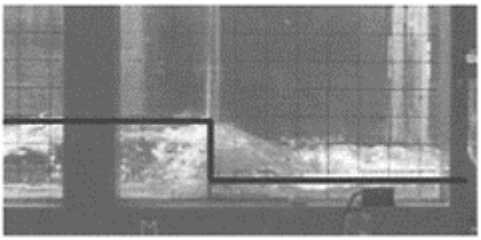

Figure 11. Measured and calculated instantaneous profiles at t=4.0s.

nappe; instead water depths upstream the constriction are described with sufficient detail.

The two dimensionality of the phenomenon will be studied and the limits of the one dimensional model will be analysed.

8 CONCLUSIONS

The flow conditions through hydraulic structures and channel transitions were investigated very extensively, at first working on the schematization of source terms, then inserting internal boundary conditions and modifying the mathematical model. A first order accurate finite volume numerical solver was used and the results obtained with the internal boundary conditions as well as modifying the mathematical model are compared with experimental investigations on laboratory flumes.

The mathematical model that takes into account the volume of the hydraulic jump reproduces satisfactorily the impact of the wave front against the obstacles when the flow is three dimensional and the shallow water model is inadequate. The model simulates satisfactorily the water depth upstream the gate and the change of the flow regime through the obstacle from supercritical to subcritical due to tailwater. More specifically the position of the surge moving upstream and the consequent submergence of the sluice-gate with the increase of the water stage immediately upstream the gate are simulated correctly.

ACKNOWLEDGEMENTS

This work is funded by CNR-GNDCI, Linee 1 and 3.

REFERENCES

Alcrudo F. 1992: *Esquemas de alta resolucion de variacion total decreciente para el estudio de flujos discontinuos de superficie libre,* Ph.d. Thesis, Universidad de Saragoza

Brufau P., Vasquez-Cendon M.E., García Navarro P. (2002): A numerical model for the flooding and drying of irregular domain, *International Journal for numerical methods in fluids*, 39:247–275

Bradford S.F., Sanders B.F. 2002: Finite-Volume Model for shallow water flooding of arbitrary topography, *Journal of Hydraulic Engineering*, 128:289–298

Chen C.I.1980: Laboratory verification of a dam-Break flood model, ASCE, *Journal of the Hydraulic Division:*535–556

Chow V.T. 1959: *Open Channel Hydraulics*, McGraw-Hill Publisher

Cunge J.A., Holly F.M., Vervey A. 1980: *Practical Aspects of Computational River Hydraulics*, Pitman Publ. Inc.

DHI Mike, 11 2000: *A modelling system for Rivers and Channels*, Reference Manual

Fread D.L., Lewis J.M. 1998: *NWS FLDWAV Model: theoretical description and user documentation*, Hydrologic Research Laboratory, National Weather Service, Silver Spring

Garcia Navarro P, Alcrudo F. 1992: High resolution 1D schemes for unsteady open channel flow simulation, *Jornadas de encuentro trilateral para el estudio de la hydraulica de las ondas de submersion*, Zaragoza:1–14

Garcia Navarro P., Brufau P. 1998: One-dimensional dambreak flow modelling: some results, 1st CADAM Meeting, paper 10, Wallingford

Garcia Navarro P, Fras A., Villanueva I. 1999: Dam-break flow simulation: some results for one dimensional models of real cases, *Journal of Hydrology*, 216:227–247

Garcia Navarro P, Vasquez-Cendon M.E. 2000: "On numerical treatment of the source terms in the shallow water equations", *Computer & Fluids*, 29:951–979

Goutal N., Maurel F. 2002: A finite volume solver for 1D shallow water equations applied to an actual river, *International Journal for Numerical Methods in Fluids*, 38:1–19

Henderson F.M. 1966: *Open Channel Flow*, MacMillan Publisher

Hirsch, C. 1990: *Numerical Computation of Internal and External Flows*, Vol.2, John Wiley & Son, Chichester

Jin M., Fread D.L. 1997: Dynamic flood routing with explicit and implicit numerical solution schemes, *Journal of Hydraulic Engineering, ASCE*, 123(3):166–173

Morris M.W. 2000: *CADAM ConcertedAction on Dambreak Modelling, Final Report*, Report SR 571, Wallingford

Morris M.W., Galland J.C. 2000: *CADAM ConcertedAction on Dambreak Modelling, Dambreak Modelling Guidelines & Best Practice*, Report SR 571, Wallingford

Natale L., Savi F, Ubertini L. 1999:Probability of inundation of Rome, *IASTED International Conference on Modelling and Simulation*, Philadelphia

Paquier A. 1998:1-D and 2-D models for simulating dam-break waves and natural floods, *1st CADAM Meeting*, HR Wallingford, march:127–140

Petaccia G., Savi F. 2002: Numerical modelling of shock waves: simulation of a large number of laboratory experiments, *International Conference Riverflow 2002*, 1: 449–458

Rissoan C., Goutal N., Herledan R. 2002:1D hydraulic simulation of a dam break wave on the Rhone river, *ICHE 2002*, Warsav

Roe P.L. 1981: Approximate Riemann Solvers, parameter vectors and difference schemes, *Journal of Computational Physics*, 43:351–312

Rosu C., Ahmed M. 1999: Toce River dam-break test case. A comparison between the ISIS numerical model and the physical model, *4th CADAM Meeting*, Milan

Sanders B.F. 2001: High resolution and non oscillatory solution of the St. Venant equations in non rectangular and non prismatic channels, *Journal of Hydraulic Research*, 39(3):321–330

Soarez Frazão S., Zech Y. 2000: Computation of extreme flood through the Toce valley *4th CADAM Meeting*, Milan

Toro E.F. 1997: *Riemann solvers and numerical methods for fluid dynamics: a practical introduction*, Springer Verlag, Berlin

Soil/water interaction during the breaching process of overtopped embankments

Pickert, G. & Jirka, G.H.
Institute for Hydromechanics, University of Karlsruhe, Germany

Bieberstein, A. & Brauns, J.
Division of Embankment Dams and Landfill Technology, Institute of Soil Mechanics and Rock Mechanics, University of Karlsruhe, Germany

River Flow 2004—Greco, Carravetta & Della Morte (eds.)

ABSTRACT: When a flood exceeds the design level of an embankment dam, the dam will be overtopped and breaching can occur. Consequences are major flooding of the area beyond the dam, which can at least cause high economical damage. Residents, local governmental administrations and environmental agencies are highly interested in knowing the precise description of possible breach development and outflow hydrograph Q(t). Many publications and models are available on this topic and model outputs can vary up to ±50% from the original data. This is due to a limited understanding of the processes involved in the breaching of embankments and the lack of fundamental experimental data. The research presented in this paper has the following aims: First, to generate a reliable data base by carrying out physical experiments (scaled 1:10) and measuring the outflow hydrograph and the erosion of the embankment material per time (erosion curve). Second, to improve the knowledge of the soil/water interactions in partly saturated soils, represented by the water tension in the breach slopes. And third, to provide a 3D elevation picture of a breaching geometry in homogeneous embankments.

1 INTRODUCTION

When a flood exceeds the design level of an embankment dam, the dam will be overtopped and breaching will occur. Consequences are major flooding of the area beyond the dam, which can at least cause high economical damage. Residents, local governmental administrations and environmental agencies are highly interested in knowing the precise description of the breach development and outflow hydrograph Q(t).

Appropriate emergency plans and scenarios could be developed based on this information and the loss of life and/or properties could be minimized.

Existing models, for example the NWS-BREACH-model developed by Fread (1991), describe overtopping events by hydrodynamic equations, erosion equations and simple geotechnical considerations. These simplifications of the breaching process, and especially the processes for the breach widening, have negative influence on the modeling results. Breach widening strongly depends on the neglected soil/water interactions in the soil matrix. These interactions, for example the tension in partly saturated soils have a strong influence on the erodibility of the soil and on the stability of the breach slope.

The present research is focusing an overtopped earthen embankment and has the following aims: First, to generate a reliable data base by carrying out physical experiments (scaled 1:10) and measure the outflow hydrograph and the erosion of the embankment material per time (erosion curve). Second, to improve the knowledge of the soil/water interactions in partly saturated soils, represented by the water tension on the breach slopes. And third, to provide a 3D elevation picture of a breaching geometry in homogeneous embankments.

2 BACKGROUND

2.1 *State of the art*

A comparison of different dam breach models by Morris (2000) done within the EU workshop of Concerned Action on Dambreak Modelling (CADAM) showed the wide variability of model results. Figure 1 shows the computed breach discharges over time (Q [l/s]) of six models. Apart from the results of the Broich2D model which was calibrated against their own measured data, the output variation is rather high.

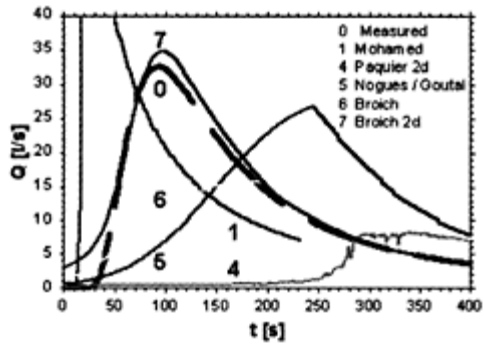

Figure 1. Breach discharges of six models compared to experimetal data (Morris, 2000).

Broich (1998) reports that the accuracy of predicting the peak discharge is perhaps ±50%, and considered the accuracy in predicting the onset of breach formation as even worse.

Morris (2000) published a list of existing dam breach models specifying the implemented breach morphology, flow equations, sediment transport equation and the geomechanics of the breach-side slope. Other summaries and analysis of dam breach models were done by Wahl (1998), Broich (1998), Lecoint (1998) and Mohamed et al. (2000).

During the CADAM workshop Graham (1998) stated that the modeling of breach formation through embankments is done by using process based models. Most breach models are based on steady state sediment equations related to homogeneous banks and adopted breach growth mechanisms. The modelers must therefore make a significant number of assumptions and simplifications in order to model the breach, all of which can greatly affect the modeling results.

The breaching process is dominated by the interaction of these three processes:

– hydraulics of the flow over the embankment and through the breach
– erosion process
– soil properties and geotechnical considerations.

Simplification in one of these processes will certainly affect the overall modelling results. Especially the geotechnical simplification concerning the breach widening processes, affects the modelling results. Breach widening depends mainly on two effects. First the erosion of embankment material due to the transport capacity of the breach flow, and second on the failure of the breach side slopes.

2.2 *Erosion process*

Mohamed et al. (2002) stated that the implemented sediment transport equations are derived for subcritical steady state flow conditions, for a specific type of sediment, and for a certain range of grains sizes. These conditions are likely to be violated during the breaching process since conditions change from subcritical flow to unsteady supercritical flow and back. Soil types do also vary widely in embankment construction. But in the absence of any other method to predict the sediment transport, a careful selection from the existing sediment transport formulas should be done, by considering their applicability to flow on steep slopes and for supercritical flow and additionally their derivation, based on dam breach experimental data.

As stated above, the choice of a sediment transport equation requires professional judgment and knowledge about the breaching mechanisms. In addition to the above stated considerations following verifications of the transport equation can be done:

1. Verify the developed model on very good documented historical dam failures, for example the Teton dam failure 1975 (USA), and compare the results with the actual breach width and depth.
2. Experimental data of the erosion curves for a falling water level in the reservoir. (Bechteler)
3. Explicit breach width and depth for different breaching times. (Coleman, 2000)
4. Carry out experimental models.

2.3 *Key issues for research*

A more accurate failure analysis of the breach side slope, especially the soil/water interactions within the embankment material, would highly improve the understanding of the breaching process.

Experimental data of erosion and transport of embankment material for calibrating numerical models would close the gap between model results and real breaching events.

3 BREACH SLOPE FAILURE

Slope movements are classified in many ways in the geotechnical and geologic sciences, each having some usefulness in emphasizing features pertinent to recognition, avoidance, control, correction or other purpose for the classification.

3.1 *Classification of slope failures*

Among the attributes that are used as criteria for identification and classification of failures, in respect to the subject of breach slope failures, are:

– type of movement
– kind of material
– rate of movement
– geometry of the area of failure.

In geotechnics the following failure characterization (type of movement) is done:

– falls
– topples
– slides
– lateral Spreads
– flows
– complex.

The breaching of an embankment is certainly a complex failure, which has to be simplified based on the experimental research.

3.2 *Causes of slope movements*

The processes involved in slides, movements or failures, comprise a continuous series of events from cause to effect. All slides involve the failure of earth materials under shear stress. The initiation of the process can therefore be reviewed according to (a) the factors that contribute to increased shear stress and (b) the factors that contribute to low or reduced shear strength.

Factors that contribute to increased shear stress can also be classified in different categories:

– the removal of lateral support
– removal of underlying support

– lateral pressure
– surcharge (additional loads)
– transitory earth stresses (e.g. earthquakes)
– regional tilting.

The important factors concerning the breach slope failure are the first and the second.

Factors that contribute to reduced shear strength of rock or soil may be divided in two groups. The first group includes factors based on the initial state or inherent characteristics of the material, such as composition, texture, structure and slope geometry. Organic materials, clays, decomposed rock are inherently weak or become weak upon change in their water content. Additionally, these materials may have a loose structure and/or texture.

The second group includes the variable factors that tend to lower the shear strength of the material. These factors (a) are changes due to weathering and other chemical reactions and (b) changes in inter-granular forces due to water content and pressure in pores and fractures: Water in soils causes an increase in weight of the mass, an increase in pore water pressure, and a decrease in apparent cohesion.

The second factor, changes in intergranular forces (b), has an important influence on the breaching process. Thus, the presented investigations and the current experiments respectively are focused on it.

3.3 *Soil water interactions*

The analysis of the breaches in dams and embankments showed a wide variation of the breach slope, some are very steep others are flat (Bücker, 1998). This is mainly due to the dam material parameters and the effluent water volume.

As stated before the water content of the soil has a great influence on the slope stability. First, as a destabilising factor if the water content is too high, and second, as a stabilising factor in unsaturated soils with a moisture content $w<1[-]$. This stabilising force introduced on the soil matrix by the soil/water interactions is based on the soil-moisture tension.

Soil-moisture tension can take values of a compressive stress (positive) or tensile strength (negative), depending on the water content of the soil matrix. The tensile strength also known as suction power, increases the effective stresses and so the apparent cohesion of the soil.

All water movements in the soil depend directly on the soil-moisture tension, since water will tend to flow from areas of high potential to those with lower potential. The soil-moisture tension reflects the sum of the water holding forces of the soil. With tensiometers, this force can be determined directly:

$$\psi = m \times g \times h \qquad (1)$$

where ψ=water tension [Nm]; m=mass [kg]; g=gravity [m/s^2]; and h=height [m] above level of saturation.

Compared to all other measuring principles, the capillary binding of water to soil is measured with tensiometers directly.

4 EXPERIMENTAL SETUP AND PROCEDURE

In the research laboratory of the Institute for Hydromechanics of the University of Karlsruhe a 1:10 scaled model of a homogeneous embankment has been realized in a flume of 15m length, 1m in width and 0.7m in depth. The model has a height of 0.3m, is 1.9m long and is built over the whole flume width of 1m (Figure 2).

The homogeneous embankment model is built up with three sands on a fixed bed (see Table 1).

With respect to a flood embankment the upstream as well as the downstream slope is 1:3, which ensures the geometrical similarity of the embankment model. In fact the slopes angles are smaller than the angle of friction of the used soil. Thus the slopes are stable.

The embankment is constructed of several layers of sand. In all experiments the mean moisture content of the embankment material is w=0.05 [−] and the mean material compaction factor is D=0.5 [−].

Within the embankment six tensiometer probes are installed during the construction. The tensiometer probes are located in different heights and in different distances from the breach.

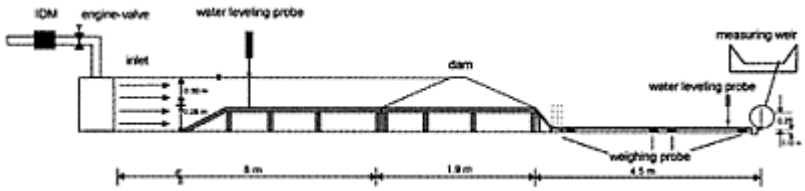

Figure 2. Side view of the experimental setup.

Table 1. Dam materials used in the experimental models.

Label	Type	d_{50}[mm]
Sand 1	Coarse sand	2
Sand 2	Medium sand	0.22
Sand 3	Coarse silt	0.035

A drainage toe ensures that the embankment withstands the hydraulic load and that seepage is discharged safely at the drainage toe. The reservoir level will have no effect on the downstream slope.

Before filling the reservoir, the initial breach plug is located on one of the side walls. This plug is a wooden block with a length of 0.1m (crest width), width of 0.02m. With this plug a rectangular initial breach channel of 0.02m width and 0.02m depth over the total width of the embankment crest of 0.1m is initiated. The plug is used for initialising the overtopping at a defined location at the glass wall.

The reservoir is filled up slowly, so that a constant seepage line will arise in the embankment. The experiment is started by withdrawing the plug, when the reservoir is filled up to water level of 0.29m (0.01m below the embankment crest) and a constant seepage is reached.

During the breaching process the outflow hydrograph, the erosion rate and the suction pressure are measured. Furthermore, the breaching process is recorded for a detailed analysis.

5 MEASUREMENT TECHNIQUE

5.1 *Erosion and flow measurement*

The experimental setup described in Chapter 4 and in Figure 2 is designed in such a way that it is possible to measure the erosion of the dam material with constant water level in the reservoir and no backwater influences on the breaching process.

Right behind the dam toe a sill leads to a channel within the flume where the flow velocity is reduced by three grids in such a way that the eroded dam materials will deposit. This channel is bedded on weighing sensors so that the instantaneous weight of the eroded material and the outflow is measured as W_{total} [kg]. The outflow from the breach is measured at the end of this channel by a measuring weir. The erosion curve is obtained by subtracting the weight of the water W_{wat} [kg] from the total weight W_{total} [kg] for each time step, see equation 2.

$$W_{sed}(t)=W_{total}(t)-W_{wat}(t)[kg] \quad (2)$$

During the calibration phase, a deposition rate of 95% of the eroded material was achieved as well as a measurement error of ±1% of the total weight.

Water leveling probes measure the reservoir water level and the water level in the sedimentation channel. Additional to the reservoir level the inflow to the reservoir is measured with a inductive flow meter (IDM).

5.2 *Fringe projection*

The breaching of an embankment is a highly transient process. Due to that, it is difficult to receive a profile of the breach itself. Coleman (2000) has achieved very good results by stopping the breaching process and mapping the dried breach at certain time steps. But to evaluate or even to model the different stages of collapse of the breach slopes another nonintrusive mapping technique has to be used for continuous measurements.

A technique which is frequently employed in mechanical engineering and in medicine to measure surface distortions or curvations is the Moiré Projection, also named Fringe Projection.

The simplest Fringe Projection for contouring an object is to project interference fringes or a grating onto an object and then view from another direction. Figure 3 shows a definition diagram for Fringe Projection and in Figure 4 the present experimental setup.

From the triangle B-a-b in Figure 3, we find the out-of-plane displacement equation (3) at point B with:

$$W = \frac{g \times N_z}{\tan \alpha} \qquad \textbf{(3)}$$

where W=displacement; N_z=the fringe order at point B, g=grading pitch; and α=angle.

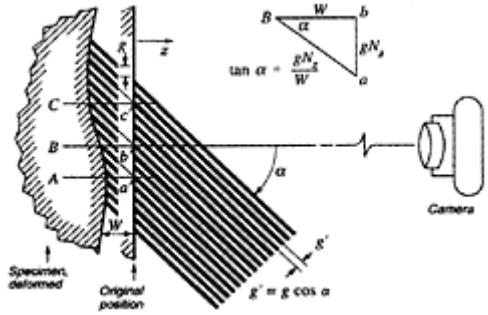

Figure 3. Optical setup for Fringe Projection (Post, 1994).

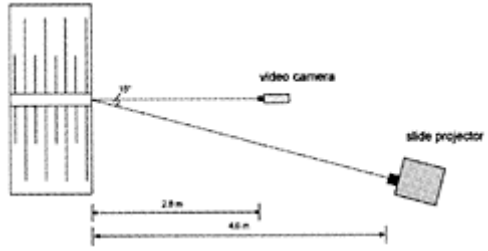

Figure 4. Fringe Projection setup (top view).

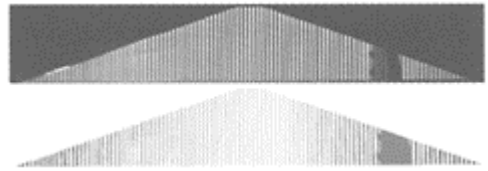

Figure 5. Fringe Projection and extracted fringes.

The easiest way to produce a stripe pattern on the surface is the direct projection using a light source and an alternating black/transparent stripe pattern image and an optical

system to project a sharp image of the stripes onto the surface. Most convenient a slide projector is used with a framed stripe image of black and transparent stripes of a distinct stripe width. As these stripes are projected, however, only nearly parallel light sheets are received, depending on the distance of the projector. The planes of equal light intensity or light phase are—more or less parallel to the axis of the light projector.

The camera must have a distinct angle relative to the projection axis. If the camera has the same axis like the projector and the surface is moved away from the projector, it will not be able to detect any change in the stripe pattern except for a slight change of stripe frequency induced by the not completely parallel light sheets.

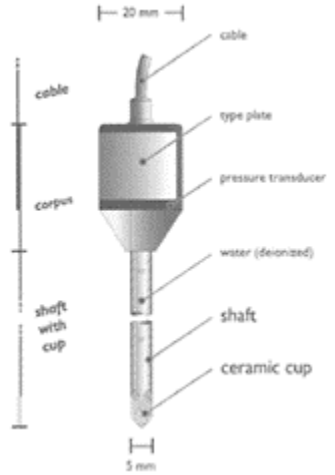

Figure 6. Principle setup of a micro tensiometer probe (UMS, 2003).

As the stripe width is very large compared to the wave length of the light, even very rough surfaces can be inspected. This is the case in the conducted experiments, preliminary experiments showed that the breach slope is rough with overhang. The analysis system consists of a slide projector which produces the pattern of white and black stripes on the dam profile.

The accuracy of all optical methods strongly depends on the knowledge of all geometrical information of the measuring setup. These are projector distance and angle, the optics of the projection system, camera distance and angle relative to the projector and the surface. If all this information is available, the reconstruction of the surface can be done very accurately. Subpixel algorithms, i.e. algorithms that take into account the gradient of gray level changes in the image, provide a much higher resolution than the size of a single pixel. Depending on the pattern and the algorithm used, a resolution of 1/10 of a pixel size can be achieved when looking for edges or the center of gravity of the area of objects.

5.3 *Tensiometer probes*

Tensiometers are inexpensive moisture measurement tools. The accuracy of a well-maintained tensiometer is in the 90–95% range. They use a porous ceramic cup at the end of a long tube which is inserted in the soil, see Figure 6.

The tensiometer is a point sensor because the ceramic cup at the tip of the tube is the contact point with the soil. The measurement is based on a soil tension effect that occurs when the tube is partially filled with water and sealed at the top with a tension measurement device. As the soil drys it absorbs water through the porous ceramic cup and creates a suction (partial vacuum) inside the tube that is proportionate to the change in soil water content.

As the soil water content increases, the ambient soil water pressure increases and forces water back into the ceramic cup, thereby reducing the suction or applying a positive pressure to the sensor. Tensiometers are not affected by salinity or other soil conductivity factors.

5.4 *Data acquisition*

For the data acquisition and experimental setup control a DAQ-PCI-card is used. The 16 analogue input channels are scanned with 100Hz and saved directly to the hard drive. Two digital outputs are used to control the motor gate valve.

The National Instruments software Labview 6.0 is used as control and acquisition software.

An IEEE 1394 CCD video camera with a resolution of 1280*980 pixels records the breaching process through the glass wall of the flume. This system has the advantage that video films can be recorded directly on hard disc up to the maximum hard drive space of 80GBytes, which is very useful for cohesive materials where the breaching process is very long.

6 EXPERIMENTAL RESULTS

The test embankment has a height of 0.3m, a length of 1.9m, a crest width of 0.1m and a total width of 1m. The embankment was built from medium sand with a compaction of D=0.5 [−] and a moisture content of w=0.15 [−], the total weight of the embankment was approximately 650kg.

From removal of the initial breach plug to the end of measurements with an unaffected flow 110sec elapsed. Figure 7 shows a time series of pictures from this test.

At t=0 sec the embankment is intact, the reservoir is filled up to the crest and the initial breach plug is still in place. The second picture (t=40sec) shows the initial breach phase. This phase is dominated by set of vertical steps which are merging together. This type of erosion is introduced by Hanson (1997) as headcut erosion in cohesive materials. The breaching phase begins in picture 3 (t=65sec). All steps are merged and an erosion channel parallel to the downstream embankment slope is formed. The breach channel has been cut upstream, across the total width of the embankment crest.

At t=80sec breach crest is migrating upstream on the embankment slope, whereas the discharge funnel migrates with the breach crest. The breach inclination increases referred

to the downstream embankment slope. At t=110sec the breach crest migrates further upstream and the inclination of the breach increases.

Figure 8 shows the breached embankment viewed from upstream looking downstream after the depletion

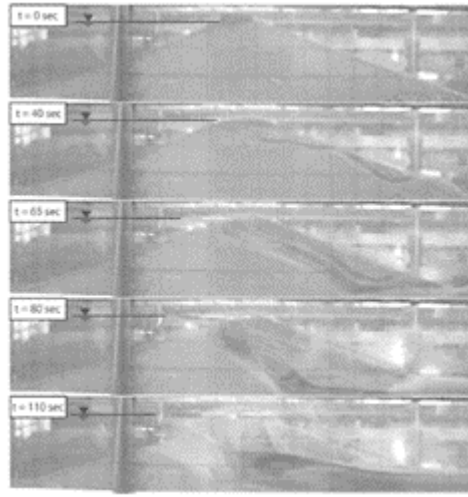

Figure 7. Breaching sequence.

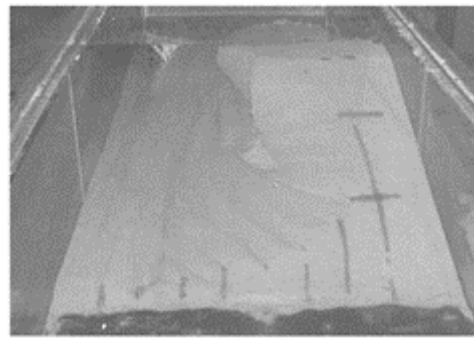

Figure 8. Breached test embankment (view from upstream).

of the reservoir. The hourglass shape with the bottle neck at the embankment crest of the breach well defined by Coleman (2000) is recognisable. Additionally the streamlines of the breach flow are clearly visible in the embankment material.

The geotechnical aspect of this research is also evident. Looking at the bottle neck the overhang of the breach slope is stable due to the negative soil-moisture tension.

A dry medium sand (d_{50}=0.22mm) is cohesionless and has an angle of friction of $\varphi \approx 30°$ with a standard slope stability, which would make an overhang impossible.

But taking the negative soil-moisture tension into account the so-called capillary cohesion stabilizes this overhang. Thus soil mechanical and geotechnical considerations must be included in the understanding of breaching processes.

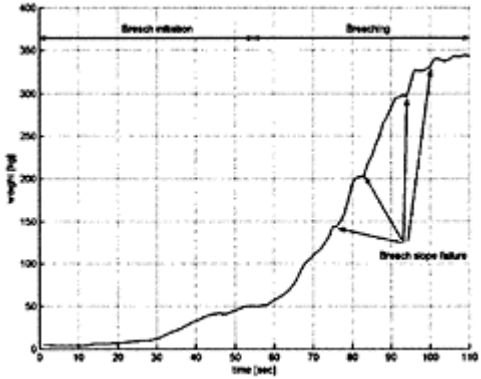

Figure 9. Measured erosion curve of breached embankment.

Figure 9 shows the graph of the correspondent erosion curve. A quantitative comparison of the photograph and the erosion curve indicates that half of the embankment was eroded. The mass of the eroded material was measured in the sedimentation channel.

This graph (Figure 9) with the increasing mean sediment weight per time is in good accordance to the video taped breaching process (Figure 8). The initial breaching phase and the main breaching phase can be identified. Additionally to this, major collapses of the breaching channel due to failure of the breach slope can be correlated in the graph and in the video.

7 CONCLUSION

This paper first results of ongoing work on the understanding of breach development and the aim of developing a fundamental data base for modelers.

The preliminary experimental results show good support for the concept of a breaching process occurring in three phases:

– breach initiation
– breaching
– depletion of the reservoir.

But not only the breaching phases correlate with literature results (Coleman, 2000). The breach development and the breach propagation also show good agreement with results of other experiments (Hanson, 1997; Coleman, 2000).

With respect to the erosion curve it can be stated that the breaching process is measured quite well, but further improvement on the analysis is necessary.

Based on this experiments, the failure mode of the breach side slope can be identified as a fall failure.

The Fringe Projection technique in order to receive a 3D model of a breach and the measurements of negative soil-moisture tension are introduced in this paper, and results will follow.

A drawback of this experimental setup is, that the breaching process herein can only be observed in the initial phase and in the beginning of the breaching phase, which is due to the width of the experimental flume. The further breach development with the possible maximum breach outflow cannot be observed.

REFERENCES

BECHTELER, W. n.a. Bruch eines Deiches durch Erosion, München, Germany

BROICH, K. 1997. Computergestützte Analyse des Dammerosionsbruchs; Universität der Bundeswehr München, Institut fur Wasserwesen, München

BROICH, K. 1998. Conclusions from the test case modelling. Proceedings of the 2nd CADAM workshop, Munich, Germany

BÜCKER, M. 1998. Breschenbildung in Erdämmen—Auswertung historischer Dammbrüche und Zusammenstellung wesentlicher Einflussparameter—Literaturstudie, Institut für Bodenmechanik und Felsmechanik, Abteilung Erddammbau und Deponiebau (unpublished), Karlsruhe, Germany

COLEMAN, S.E., ANDREWS, D.P. 2000. Overtopping Breaching of Noncohesive Homogeneous Embankments, Department of Civil and Resource Engineering, Auckland, New Zealand

FÄH, R. 1997. Numerische Simulation der Strömung in Offenen Gerinnen mit beweglicher Sohle, Mitteilungen der VAW Technische Hochschule Zürich, Zurich, Switzerland

FREAD, D.L. 1991. BREACH: An erosion model for earthen dam failures, Silver Spring, USA: National Weather Service

GRAHAM, W. 1998. Dam failure inundation maps—are they accurate? Proceedings of the 2nd CADAM workshop, Munich, Germany

HANSON, G.J., et al. 1997. Headcut migration analysis of a compacted soil, Transaction of the American Society of Agricultural Engineers

JOHNSON, F.A., ILLES, P. 1976. A Classification of Dam Failures, Int. Water Power and Dam Construction. Vol. 28, Nr. 12

KAST, K., BIEBRSTEIN, A. 1997. Detection and assessment of dambreak-scenarios, Dams and Safety Management at Downstream Valleys, Balkema, Rotterdam, Netherland

LECOINT, G. 1998. Breaching mechanisms of embankments—an overview of previous studies and the models produced. Proceedings of the 2nd CADAM workshop, Munich, Germany

MOHAMED, M.A.A., SAMUELS, P.G., GHATAORA, G.S., MORRIS, M.W. 1999. A new methodology to model the breaching of non-cohesive homogeneous embankments, Proceedings of the 4th CADAM Concerted Action Meeting, University of Zaragoza, Spain

MOHAMED, M.A. A., SAMUELS, P.G., MORRIS, M.W. 2002. Improving the Accuracy of Prediction of Breach Formation through Embankment Dams and Flood Embankments HR Wallingford, Wallingford, UK

MORRIS, M.W. 2000. Concerted Action on Dambreak Modeling Final Report—CADAM, http://blakes.hrwalling-ford.co.uk/projects/CADAM/CADAM/index.html

NISHIMURA, T., et al. 1998. Influence of stress history on the strengh paramerters of an unsaturated statistically compacted soil, Canadian Geotechnique Journal No. 36, p. 251–261

POST, D., et al. 1994. High Sensitivity Moiré, Springer Verlag, New York, USA

SINGH, V P. 1996. Dam Breach Modeling Technology, Kluwer Academic Publisher, Netherlands
UMS GmbH 2003. Datasheet for micro tensiometer T5, Munich, Germany
WAHL, T.L. 1997. Predicting Embankment Dam Breach Parameters—A Needs Assessment, XXVIIth IAHR Congress, San Francisco, California, USA

Experiments of dam-break flow in the presence of obstacles

S.Soares Frazão
Fonds National de la Recherche Scientifique and Department of Civil and Environmental Engineering, Université catholique de Louvain, Belgium

B.Noël & Y.Zech
Department of Civil and Environmental Engineering, Université catholique de Louvain, Belgium

River Flow 2004—Greco, Carravetta & Della Morte (eds.)

ABSTRACT: Dam-break flows are likely to occur in area that are not subject to more common floods. Also, the importance of the wave might be such that the flow route is no more directed by the thalweg of the river. The whole valley is involved, and the roads, bridges and urban buildings become obstacles to the flow. The purpose of the paper is to study the influence of such an obstacle on a dam-break wave, the obstacle being an idealized representation of a single building. The experimental set-up consists in a channel with a rectangular shaped obstacle, representing a building, placed immediately downstream from the dam. The building is not centred in the channel, and is not aligned with the flow direction. Flow observation shows that after the violent impact of the wave on the building, the flow is forced to change its direction to pass the building. This implies the formation of hydraulic jumps with the consequence that the water level is locally more important than without building. Behind the building, a wake zone is observed. Then, further downstream, the flow slowly recovers the structure it would have without the building. Several measurement devices were used to characterize the flow. The water level evolution was measured at five different locations by means of water level gauges. At each gauging point, the velocity was measured by means of acoustic Doppler velocimeter. Then, the surface velocity field was obtained using digital imaging techniques. This study is part of the IMPACT European project which aims at investigating extreme flood processes and uncertainty. The experimental data set presented here was

used in the IMPACT benchmarking programme, as a validation means for numerical models.

1 INTRODUCTION

Flows may be considerably affected by the presence of natural or artificial obstacles. In the case of severe floods, for example due to dam- or dike-break, the influence of such obstacles is even amplified. Neglecting this influence in numerical simulations of such flows could lead to heavy misinterpretation.

The presence of obstacles is common in river as well in minor bed (bridge piers) as in floodplains (abutments, dikes, trees and vegetation, debris from former floods, etc.). Moreover, if the river embankments are overtopped or the flood dikes breached, flow will occur in areas that are normally not subject to inundation, not prepared to support such a hazard, and thus presenting a series of obstacles (roads, railways, dwellings, industrial and commercial structures, etc.).

In steady flows, two major effects of obstacles are observed: an obstruction effect and a wave formation due to nonlinear alignment of the obstacle.

The obstruction effect, even in straight reaches, is best illustrated by the bridge-pier case (see for instance

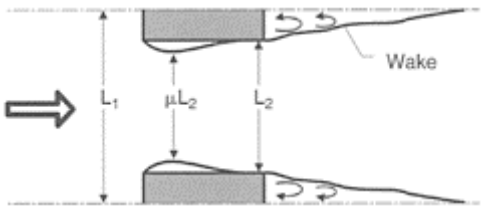

Figure 1. Schematization of bridge-pier constriction.

Chow, 1959). The flow is schematized as represented in Figure 1, where an additional constriction appears due to the limitation in flow-filament curvature.

In uniform-flow channel with mild slope, the flow is mainly subcritical. If the cross-section reduction is limited, the obstruction induces a backwater effect that may extend over a long distance upstream (Fig. 2a).

However, if the relative obstruction is larger, it may happen that the specific-energy curve rises in such a way that its minimum C2, corresponding to the critical

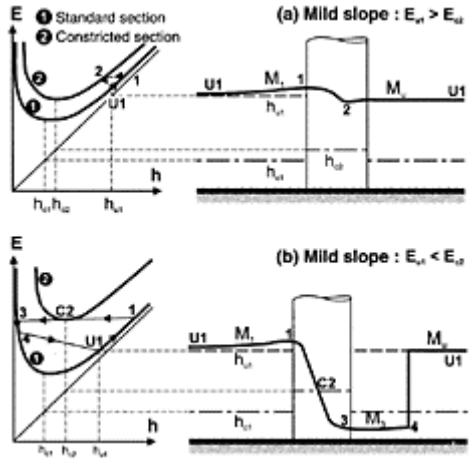

Figure 2. Water profiles along bridge piers in mild-slope cases.

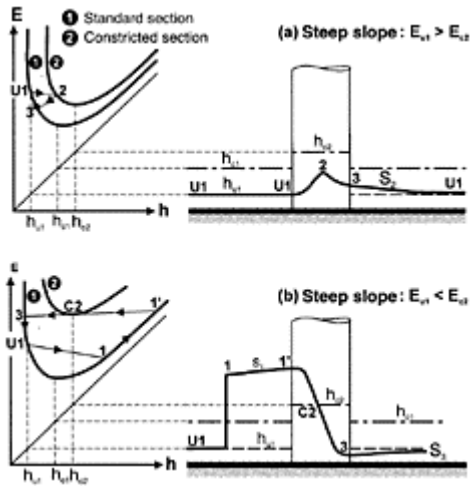

Figure 3. Water profiles along bridge piers in steep-slope cases.

stage, is higher that the uniform condition in the standard section (Fig. 2b). This results in a control section in the constricted section and in the development of a supercritical water profile, which returns to normal conditions through a hydraulic jump.

A similar behavior may be observed in steep-slope conditions, where the flow is generally supercritical. In these situations, the water profile presents the two configurations of Figure 3.

If the constriction is limited, only the water surface close to the constriction is disturbed and the effect

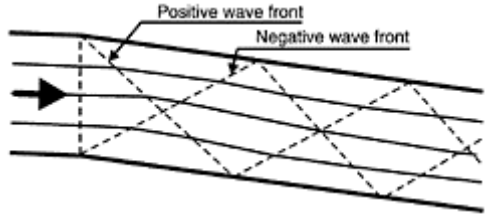

Figure 4. Cross waves in nonlinear alignment (after Chow, 1959).

will not extend farther upstream. If the constriction becomes significant, the minimum possible energy in the constricted section becomes too high to be reached immediately. The specific energy thus needs to increase in the upstream reach, which is only possible in subcritical flow, thus requiring the formation of a hydraulic jump. The resulting upstream water profile extends only over a short distance.

The above description of the obstruction effect caused by the presence of an obstacle is based on a one-dimensional flow modeling. If the resulting constriction is important, two-dimensional aspects may predominate and change significantly the location and shape of discontinuities.

The second observed consequence of an obstacle concerns the effect of nonlinear alignment, which may be rather complex.

In subcritical flows, a transverse superelevation may arise near the outer bank (or along the obstacle). In supercritical case, the outer wall, which turns inward to the flow, will produce an oblique hydraulic jump and a corresponding positive wave front, while the inner wall, which turns away from the flow, will develop a negative wave front, both forming cross waves (Fig. 4).

When the flow is unsteady, and above all in severe transient situations (dam- or dike break for example), this already complex behavior becomes even more complicated. The obstacle now induces reflected waves that in turn may reflect against the banks or other obstacles.

Few descriptions of such transient flow phenomena against obstacles are available. However, they could be of great interest in the modeling of dam-break flow. Above all it is important to evaluate the extension in space and time of the influence of an obstacle to limit accurate and refined computations where they are really needed.

At the large scale of a real flood event, it is not always possible to distinguish between the different features of the flow. Therefore, it was decided to design an idealized experiment that limits the parameters involved in the flow. A single obstacle representing a building is placed in a channel, immediately downstream from the dam. Through appropriate measurements of the flow, it is possible to identify its specific features.

The experiment presented in this paper was used in the benchmarking program of the IMPACT European project (Soares Frazão et al., 2003). This research project, which addresses the assessment and reduction of risks from extreme flooding caused by natural

events or by the failure of dams and flood defense structures (Morris, 2002; Morris and Vaskinn, 2002) has also a special focus on floods in urban areas and in the presence of obstacles.

2 EXPERIMENTAL SET-UP

The experiments were carried out in the laboratory of the Civil Engineering Department of the Université catholique de Louvain (UCL) in Belgium. The channel is sketched in Figures 5–7.

It has a total length of 35.80m and is 3.60 m wide. The upstream reservoir is 6.90m long. The cross section is trapezoidal near the bed (Fig. 7a). The dam is represented by a gate located between two solid blocks; its cross-section is rectangular and it is 1.00m wide (Fig. 7b). To simulate a dam break, the gate is pulled up rapidly. The building, located 3.40m downstream from the dam, consists in a rectangular block with dimensions 0.80×0.40m. It makes an angle of 64° with the channel axis (Fig. 6). After measurement in uniform conditions, the Manning bed friction coefficient is n=0.01sm$^{-1/3}$.

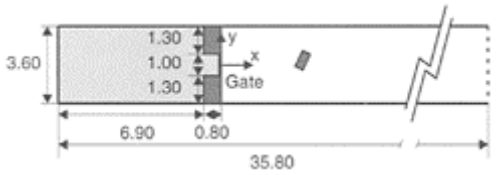

Figure 5. Experimental set-up (dimensions in meters).

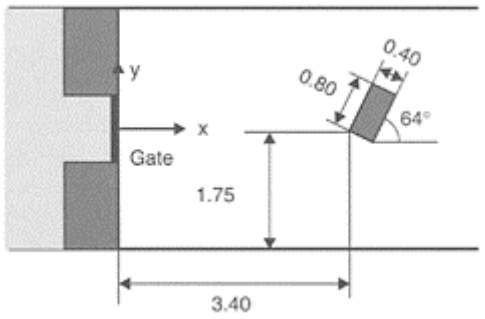

Figure 6. Location and dimensions of the building (in meters).

The channel is closed by a wall at the upstream end. The downstream boundary condition consists in a weir and a chute, but has no influence on the flow during the test duration, which is 30s. The initial conditions consist in a water level of 0.40m in the upstream reservoir and a thin layer of 0.01m of water in the downstream part of the channel.

3 GENERAL FLOW DESCRIPTION

After the rapid opening of the gate, the strong dam-break wave reflects against the building, almost submerging it, and the flow separates, forming a series of shock waves crossing each other. A wake zone can be identified just downstream from the building, surrounded by cross waves. The flow rapidly reaches an almost steady state with a decreasing discharge due to the emptying of the reservoir. Also, re-circulation zones can be identified between the building and the walls.

This description of the flow is illustrated by means of figures obtained from computed results (Noël et al., 2003). Figure 8 shows the free-surface elevation at t=1s, with the two-dimensional spreading of the flood wave.

At t=3s, the reflection of the wave against the building has occurred and results in the formation of

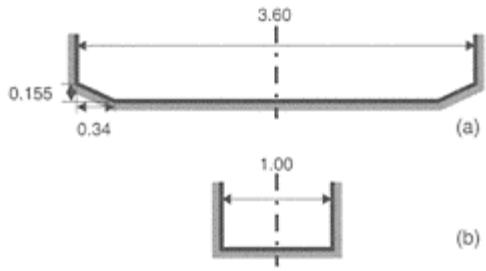

Figure 7. Channel cross section (a) in the reservoir and in the main channel, (b) at the dam location.

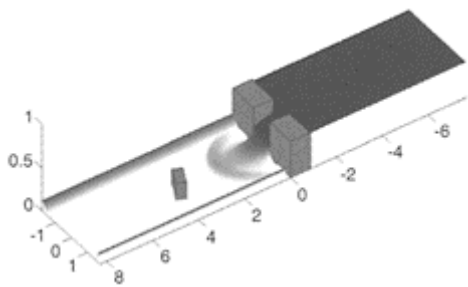

Figure 8. Computed image of the flow at time t=1s.

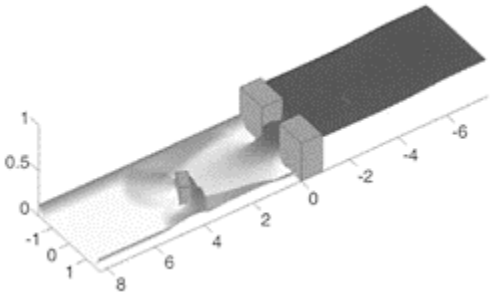

Figure 9. Computed image of the flow at time t=3s.

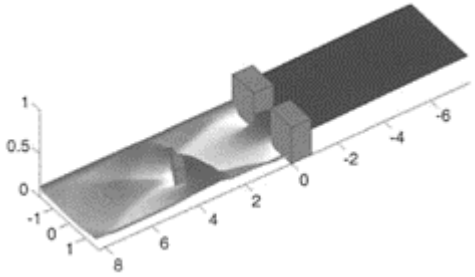

Figure 10. Computed image of the flow at time t=10s.

an oblique hydraulic jump (Fig. 9). The circular front wave also reflects against the side walls of the channel and lateral jumps are formed. Figure 10 shows the flow after 10s: the upstream reservoir empties and the hydraulic jump formed by the reflection against the building migrates in the upstream direction. The separation of the flow around the building and the wake zone can also be identified.

4 FLOW MEASUREMENT

4.1 *Point measurements*

The water level is measured by means of 6 water-level gauges located in the channel as indicated on Figure 11: one gauge in the reservoir to monitor its emptying and thus the inflow discharge, and the others around the building. Their exact position is summarized in Table 1.

The experiment was run several times and showed a very good reproducibility. The velocity was also measured at the same locations by means of an Acoustic Doppler Velocimeter (ADV). However, no complete vertical velocity profiles were measured. Only one velocity data was measured at each gauging point, at a height of 3.6cm above

the channel bed to ensure that the transducers were submerged during the whole experiment. As the flow is a rapid transient with

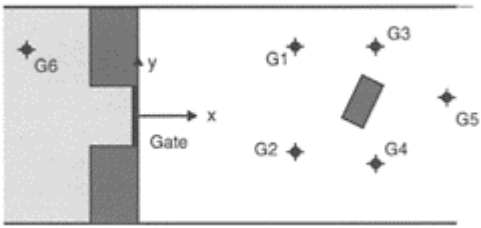

Figure 11. Sketch of the position of the gauging points where the water level and the velocity are measured.

Table 1. Position of the gauges.

Gauge	*x*(m)	*y*(m)
G1	2.65	1.15
G2	2.65	−0.60
G3	4.00	1.15
G4	4.00	−0.80
G5	5.20	0.30
G6	−1.87	1.10

hydraulic jumps and re-circulation zones, it is not fully developed i.e. there is no logarithmic velocity profile. The velocity distribution is closer to a uniform distribution and this kind of "mid-depth" measurement yields good results. This will be detailed in a further section.

4.1.1 *Field measurements*

A complete surface-velocity field was measured by a digital imaging technique yielding high-quality results. High-resolution CCD cameras were placed above the channel to film the flow seeded with tracers at a rate of 38 images per second. This results in a series of images where the white tracers can be clearly identified.

Using the Voronoï technique (Capart et al., 2002, Spinewine et al, 2003) to reconstruct the trajectories of the tracers on the free surface, it is possible to measure the velocity field in the filmed zone.

Thanks to the good reproducibility of the experiment, it was possible to run it several times and to combine the resulting images to cover a large area of the channel. Such a combination of filmed images is shown in Figure 12. The white tracers can be also be identified on the figure.

4.1.2 *Validity of velocity measurements*

By means of the ADV probe, the velocities *u* and *v* in the *x* and *y* directions respectively are obtained at a position 3.6cm above the channel bed. The digital imaging technique provides the surface velocity. Both are different from the depth-averaged velocity in fully developed flows. However, in this rapidly varying

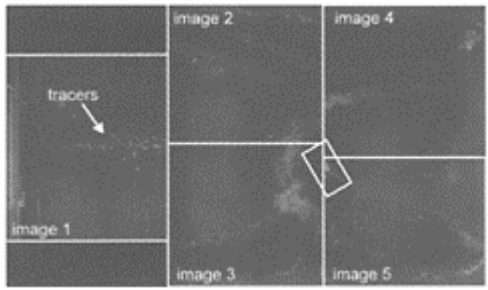

Figure 12. Combination of filmed images from five experiments to cover a whole field around the building (*t*=1.2s).

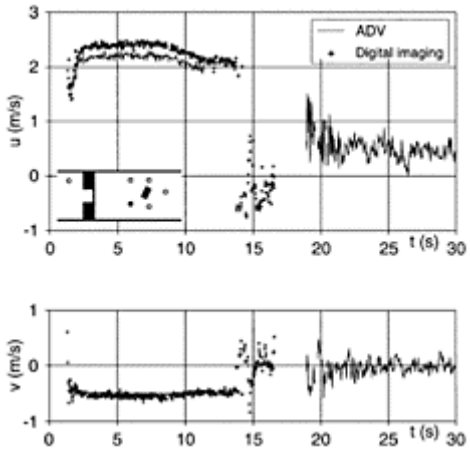

Figure 13. Velocity measurements at gauge G2, (a) *u*- and (b) *v*-component of the velocity.

flow, we can observe that both measurements are in a surprisingly good agreement. Figure 13 compares the ADV and digital imaging data at the location of gauge G2, while Figure 14 shows a similar comparison at gauge G4.

Gauge G2 measures the arrival of the reflected front around time t=15s. Before this time, the flow is supercritical and the u-component of the velocity is high. A difference is observed between ADV and digital imaging measurements, which indicates that the u-velocity distribution is not completely uniform. For the v-component, the correspondence is very good, as well as for the measurements at gauge G4.

5 EXPERIMENTAL RESULTS

5.1 *Digital imaging measurements*

By tracking the tracers on the combined filmed images and applying the Voronoï technique developed by

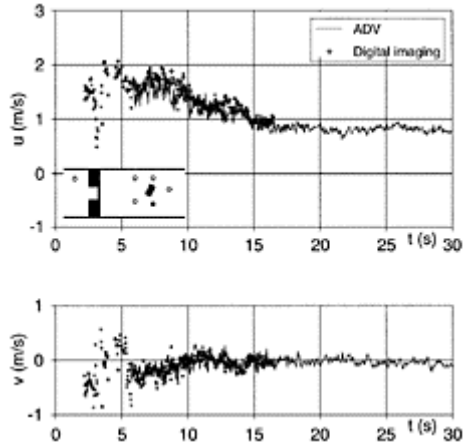

Figure 14. Velocity measurements at gauge G4, (a) u- and (b) v-component of the velocity.

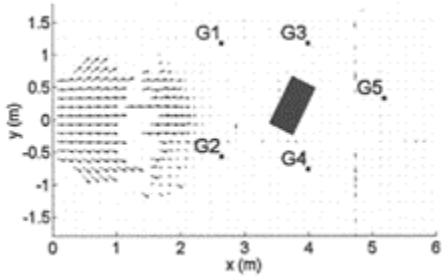

Figure 15. Measured velocity field at t=1s.

Capart et al. (2002) and Spinewine et al. (2003), surface-velocity fields are obtained as shown in the following figures.

Figure 15 shows the flow at t=1s. The two-dimensional spreading of the front wave is clearly visible. Then, at t=2s (Fig. 16), the front reaches the building and also the inclined side walls of the channel where a first reflection occurs. This reflection appears in the figure as a sudden change in direction and in amplitude of the velocity vectors.

At time t=5s, the hydraulic jumps formed by the reflection of the front wave against the building can be identified in Figure 17 as the limit between high velocities upstream from the building and an area of water almost at rest. The lateral hydraulic jump are still present. The flow separates to pass around the building and a wake is formed behind this.

Those latter features then remain and attenuate while the flow reaches an almost steady state as the reservoir empties. Figure 18 shows the velocity field after 10s: the hydraulic jump has propagated slowly

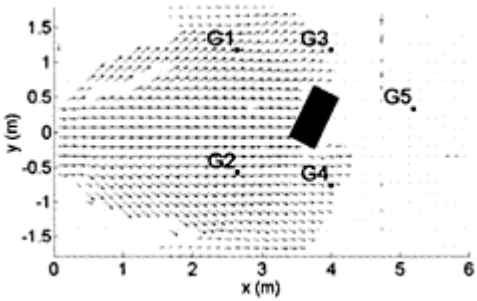

Figure 16. Measured velocity field at t=2s.

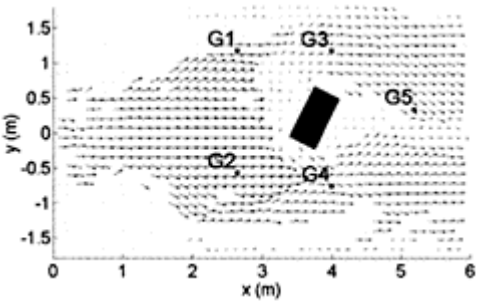

Figure 17. Measured velocity field at t=5s.

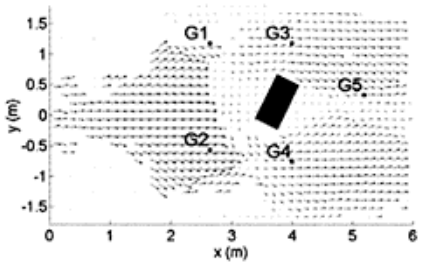

Figure 18. Measured velocity field at t=10s.

in the upstream direction, the lateral jumps take also more space in the flow, the wake zone is still present but the velocities have a decreasing amplitude.

5.2 *Water-level measurements*

The points where the water level was measured are indicated in Figure 11. Gauge G6, located in the upstream reservoir, shows a steady decrease of the water level as the reservoir empties (Fig. 19). Oscillations of the free surface in the reservoir occur as the back wave reaches the borders of the reservoir at

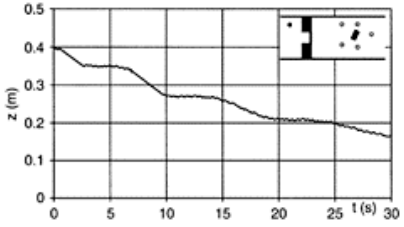

Figure 19. Water level evolution at gauge G6.

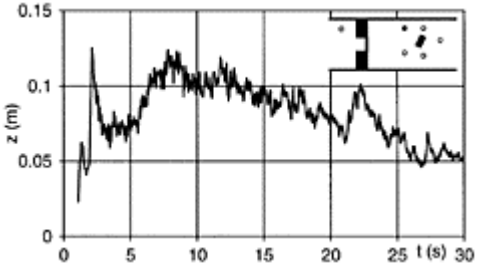

Figure 20. Water level evolution at gauge G1.

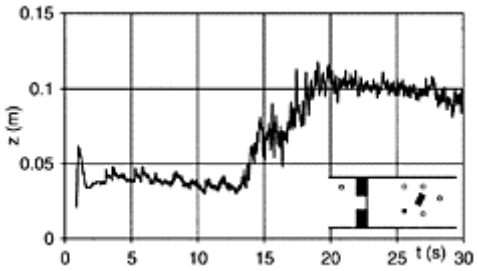

Figure 21. Water level evolution at gauge G2.

different times and reflect, resulting in a superposition of smooth waves.

Gauge G1 (Fig. 20) is located upstream from the building and close to the left bank of the channel. The water level rapidly rises due to reflection of the front wave against the inclined banks of the channel, appearing as a “splash” in the gauge measurements. Then, around t=8s, the oblique hydraulic jump formed by the reflection against the banks reaches the gauge.

The main hydraulic jump formed by the reflection of the wave against the building is well captured by gauge G2 (Fig. 21) around t=15s.

Gauge G4 (Fig. 22), located on the right side of the building, records several reflections of the water. First, there is a kind of “splash” at t=2.5s due to the strong reflection of the water against the building. Then, the

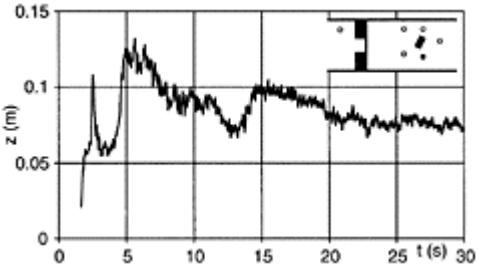

Figure 22. Water level evolution at gauge G4.

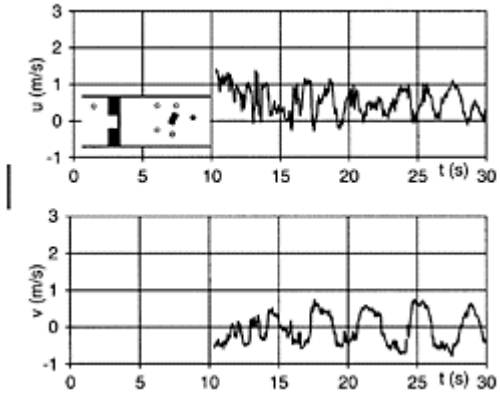

Figure 23. Velocity measurements at gauge G5.

arrival of the oblique hydraulic jump formed by the reflection of the front wave against the side walls of the channel (t=5s) can be observed. Finally a new rise of the water level is observed (around t=15s) when the oblique hydraulic jump and the main hydraulic jump come together and start moving in the upstream direction.

5.3 *ADV-velocity measurements*

The good agreement between both measurements techniques has already been outlined in a preceding section.

Interesting results were also obtained at gauge G5, located in the wake of the building. Figure 23 shows the u- and v-components of the velocity. The oscillations clearly indicate the presence of wake eddies.

6 RESULTS INTERPRETATION

6.1 *Zone of influence of the building*

Dam-break modeling aims at reproducing the water level and the velocity where water rise and/or forces

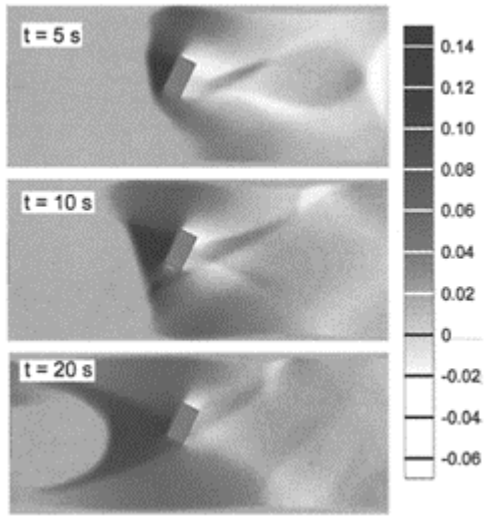

Figure 24. Difference of water depth (in meters) between results computed with and without obstacle.

induced by the current may endanger the population or the properties.

The presence of an obstacle may considerably modify those figures and thus also the associated risks. It is thus beneficial to estimate the changes induced by the obstacle. Figure 24 shows such a result for times t=5, 10 and 20s, respectively.

The upstream part of the flow, between the dam and the obstacle, is practically not influenced by this, which is not the case just in front of the building where significant increase of the water elevation occurs (0.14m above the flow without obstacle, for a water depth of 0.40m in the upstream reservoir). Also along the banks, above all the left bank, the influence of the obstacle is considerable.

Behind the building, the influence is less noticeable. Only a relative depression appears in the wake zones, which is not unexpected.

At t=20s, the influence downstream is very limited, in such a way that a modeling without obstacle would not affect too much the results in the far field.

6.2 *Comparison with steady flow*

If we now compare the longitudinal water profile at a certain distance (0.75m) of the canal axis, at a time (20s) when the first transient effects vanish, it is remarkable to observe that the profile is very comparable to the steep-slope case of Figure 3b, although the flume bed is horizontal. But, in case of dam break, the flow is highly supercritical, which corresponds to the typical steep-slope behavior. For mild

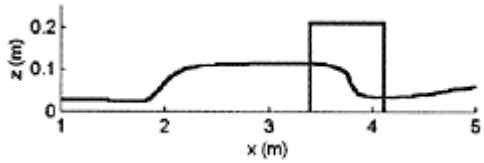

Figure 25. Water profile at t=20s along the line y=0.75m.

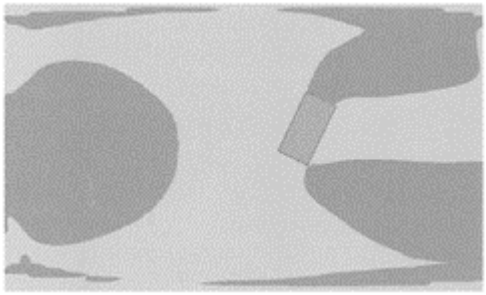

Figure 26. Supercritical (in dark gray) and subcritical-flow (in light gray) regions (t=20s).

or horizontal slopes the specific energy is decreasing along a supercritical water profile whereas this has to increase to reach the minimum energy required by the constriction. Only a passage to subcritical flow through a hydraulic jump may ensure this rise in energy.

Obviously this region just in front of the building would be poorly modeled by a simplified representation without obstacle.

Figure 26 shows the regions where the flow is super- or subcritical. The succession of regimes clearly appears: supercritical upstream, passing to subcritical flow through a hydraulic jump, then a control section near the constricted section and a second jump to return to normal regime.

7 CONCLUSION

The purpose of the paper was to study the influence of an obstacle on a dam-break wave, the obstacle being an idealized representation of a single building.

The measurement of water depths and velocity field were challenging, taking into account the limited thickness of water at many places and the large velocities in those regions. Digital imaging appeared as the best solution at least for surface velocity field.

The measurement confirmed that the flow pattern is deeply perturbed in the near-zone of the obstacle, above all at the front of this, while the far field downstream is less and

less influenced by the presence of the obstacle, which allows to neglect the obstacle influence in the modeling if only the far field is concerned.

ACKNOWLEDGEMENTS

The authors wish to acknowledge the contribution of Benoit Spinewine in the experiments, especially concerning the use of the Voronoï digital-imaging technique.

The authors wish also to acknowledge the financial support offered by the European commission for the IMPACT project under the fifth framework programme (1998–2002), environment and sustainable development thematic programme, for which Karen Fabbri was the EC project officer.

REFERENCES

Capart, H., Young, D.L. & Zech, Y. 2002. Voronoï imaging methods for the measurements of granular flows. *Experiments in Fluids* 32(1):121–135.

Chow, V.T. 1959. *Open channel hydraulics.* New York: McGraw-Hill.

Morris, M. (ed) 2002. *EC Contract EVGI-CT-2001–00037 IMPACT Investigation of Extreme Flood Processes and Uncertainty, Proceedings 1st Project Workshop, Wallingford, UK 16–17 May 2002* (CD-ROM). Brussels: European Commission. Also available at http://www.impact-project.net/

Morris, M. & Vaskinn, K.A. (eds) 2002. *EC Contract EVG1-CT-2001–00037 IMPACT Investigation of Extreme Flood Processes and Uncertainty, Proceedings 2nd Project Workshop, Mo-i-Rana, Norway 12–13 September 2002* (CD-ROM). Brussels: European Commission. Also available at http://www.impact-project.net/

Noël, B., Soares Frazão, S. & Zech, Y. 2003. Computation of the “isolated building test case” and the “model city experiment” benchmarks. In *EC Contract EVG1-CT-2001–00037 IMPACT Investigation of Extreme Flood Processes and Uncertainty, Proceedings 3rd Project Workshop, Louvain-la-Neuve, Belgium 6–7 November 2003* (CD-ROM).

Soares Frazão, S., Noël, B., Spinewine, B. & Zech, Y. 2003. Flood propagation—The isolated building test case—Results from the benchmark. In *EC Contract EVG1-CT-2001–00037 IMPACT Investigation of Extreme Flood Processes and Uncertainty, Proceedings 3rd Project Workshop, Louvain-la-Neuve, Belgium 6–7 November 2003* (CD-ROM).

Spinewine, B., Capart, H., Larcher, M. & Zech, Y. 2003. Three-dimensional Voronoï imaging methods for the measurement of near-wall particulate flows. *Experiments in Fluids* 34(2):227–241.

Sph simulation of dam-break flow in shallow water approximation

M.Gallati & D.Sturla
Hydraulic and Environmental Engineering Dept, University of Pavia, Italy

River Flow 2004—Greco, Carravetta & Della Morte (eds.)

ABSTRACT: This paper reports on the application of the Smoothed Particle Hydrodynamics technique to model 1D and 2D dam-break flows under the shallow water approximation. Following an introduction of the basic equations and a short description of the numerical technique, one dimensional simulations are presented and compared to analytical solutions or to laboratory experiments taken from technical literature. Finally the results of two dimensional dam-break flows are reported: several cases have been simulated comparing results to the ones obtained by an eulerian code (PFP) and experimental evidence.

1 INTRODUCTION

Smoothed Particle Hydrodynamics (SPH) is a meshless lagrangian method for modeling mass flow that was introduced independently by Gingold & Monaghan (1977) and Lucy (1977) in order to model complicated phenomena in astrophysics. Since then the method has been successfully applied to a vast range of problems, including elastic-plastic flow, heat transfer and incompressible flows, to name but a few.

At the Hydraulic and Environmental Engineering Department of Pavia University in 2001 SPH began to be applied to Hydraulics. Several studies and numerical experiments have been performed (Gallati & Sturla 2000, 2001; Braschi & Gallati 2000, 2001, 2003), showing the capability of the method to model rapidly varied unsteady flows with free surfaces.

The aim of the present work is to report on the studies and the experience gained regarding the application of SPH to solve the shallow water approximation of Navier-Stokes equations: the De Saint Venant equations. SPH has already been applied to solve

these equations by Wang and Shen (1999) to simulate the Stoker problem. Here more complex 1D and 2D cases of dam-break simulation are reported.

Several adaptations have been introduced into the original technique (developed to solve Euler equations) in order to adapt SPH to the shallow water context. Another computational skill deals with the treatment of domain boundaries since the original SPH was in an astrophysical context with unbounded domains.

The main part of this paper is devoted to the description of the code, named SW-SPH, developed by the authors. Its performance is shown in 1D cases by comparison to analytical solutions or to laboratory experiments taken from technical literature. In the 2D dam-break simulations results are compared to ones obtained by an eulerian code or laboratory data expressly obtained for this purpose.

2 MATHEMATICAL MODEL

The shallow water equations, also referred to as the De Saint Venant equations, describe two-dimensional unsteady, free-surface flows under the assumption of hydrostatic pressure distribution, small channel bottom slopes and uniform velocity distribution in the vertical direction. These assumptions are usually valid except when the water surface has sharp curvatures.

In lagrangian form these equations are written as:

$$\frac{D\eta}{Dt} + \eta\nabla\cdot\mathbf{v} = 0 \tag{1}$$

$$\frac{D\mathbf{v}}{Dt} = -g\nabla\eta + g(\mathbf{S}_0 - \mathbf{S}_f) \tag{2}$$

where η=water depth; $\mathbf{v}$=flow velocity vector; g=gravity acceleration; $\mathbf{S}_0$=channel bottom slope vector; $\mathbf{S}_f$=slope of energy grade line vector, computed using the steady state friction formula

$$\mathbf{S}_f = n^2 \frac{\mathbf{v}v}{\eta^{1.33}} \tag{3}$$

in which n=Manning's roughness coefficient.

Equation (1) and (2) describe, respectively, the mass and momentum conservation principles. Once specified the boundary conditions their solution allows the state variables ***η(r, t)*** and ***r(v, t)*** to be defined. It is well known that such variables may be discontinuous along moving boundaries (hydraulic jumps).

3 NUMERICAL MODEL

3.1 *The basic idea of SPH*

Standard finite element or finite difference techniques in hydrodynamics follow an Eulerian approach: the space is discretized with fixed grid of cells across which the

inflow and outflow together with the stored mass are computed. A lagrangian approach, as SPH, on the contrary, follows the evolution of selected fluid elements over space and time. We describe in this section the fundamentals of this formalism as it provides sound bases for the SW-SPH code.

The foundation of the SPH is an interpolation theory. The conservation laws of continuum fluid dynamics are transformed into integral equations through the use of an interpolating function that provides the "kernel estimate" of the field variable at a point. The term "kernel" refers to a weighting function and defines how much surrounding field variable values contribute to the value of the field variable at the point **r.**

For a better understanding let's start with the exact relation for any quantity (scalar or vector) *A*,

$$A(\mathbf{r}) = \int_{\Omega} A(\mathbf{r}')\delta(\mathbf{r}-\mathbf{r}')d\omega \tag{4}$$

where Ω is the space domain, δ is the delta Dirac function and dω is the space element.

If we replace δ-function by an interpolating kernel $W(\mathbf{r}, h)$ we obtain an integral interpolation of the function $A(\mathbf{r})$,

$$A_{int}(\mathbf{r}) = \int_{\Omega} A(\mathbf{r}')W(\mathbf{r}-\mathbf{r}', h)d\omega \tag{5}$$

In (5) h is the so-called "smoothing length" that defines the width of the kernel.

The kernel, that mimics a δ-function, has the following two properties:

$$\int_{\Omega} W(\mathbf{r}-\mathbf{r}', h)d\omega = 1 \tag{6.1}$$

$$\lim_{h\to 0} W(\mathbf{r}-\mathbf{r}', h) = \delta(\mathbf{r}-\mathbf{r}') \tag{6.2}$$

The integral interpolation A_{int} can be thought as a smoothed version of the original function *A*. This is the origin of "Smoothed" in SPH.

If $A(\mathbf{r}')$ is known only at a discrete set of N points (particles) $\mathbf{r}_1, \mathbf{r}_2, \ldots, \mathbf{r}_N$, then we can approximate the integral interpolant with a summation interpolant as,

$$A_{sum}(\mathbf{r}) = \sum_j A(\mathbf{r}_j)W(\mathbf{r}-\mathbf{r}_j, h)d\omega_j \tag{7}$$

The final step is to express the differential space element dω as $m_j/\rho(\mathbf{r}_j)$ where m_j is the mass associated with particle j and $\rho(\mathbf{r}_j)$ is the density at point $\mathbf{r}_j$. The crucial point to note is that, if W is a differentiable function, we can calculate the derivatives of A by differentiating (8).

For example the gradient of the function A is,

$$\nabla A_{sum}(\mathbf{r}) = \sum_j A(\mathbf{r}_j)\nabla W(\mathbf{r}-\mathbf{r}_j, h)d\omega_j \tag{8}$$

In SPH the continuum is discretized by particles each one has a defined mass and brings its information in terms of velocity, pressure, etc. distributed around the center according to the kernel function. These particles are free to move under their mutual interaction and

the action of any external body forces. Then, since we have to follow these particles, we are interested in knowing the value of variable A at the particle position $A_i=A(\mathbf{r}_i)$. Eqs. (7) and (8) become:

$$A_i = \sum_{j=1} A_j W_{ij} d\omega_j \tag{7.1}$$

$$\nabla A_i = \sum_j A_j \nabla W_{ij} d\omega_j \tag{8.1}$$

where

$$W_{ij}=W(\mathbf{r}_i-\mathbf{r}_j, h). \tag{9}$$

Once the value at the particle position is computed, using (8) the properties of fluid can be found at any point of the domain.

3.2 *The kernel function*

Theoretically, the choice of kernel is arbitrary, provided that it satisfies equations (6.1) and (6.2). In this paper the cubic spline (figure 1) has been employed,

$$W(r,h) = \frac{\sigma}{h^v}\begin{cases} \left(1-\frac{3}{2}s^2+\frac{1}{4}s^3\right), & if \quad 0\le s\le 1, \\ \frac{1}{4}(2-s)^3, & if \quad 1\le s\le 2 \\ 0, & otherwise \end{cases} \tag{10}$$

where $s=r/h$, v is the number of dimensions and a is the normalization constant with values 2/3, $10/7\pi$, or $1/\pi$ in one, two, or three dimensions respectively. The cubic spline kernel is adopted since it belongs to the family of compact support kernels: a potentially small number of neighboring particles are the only contributors in the sums over the particles (particles belonging to the circular region with radius $2h$ centered at the specific point, see figure 2). This is, of course, a great computational advantage.

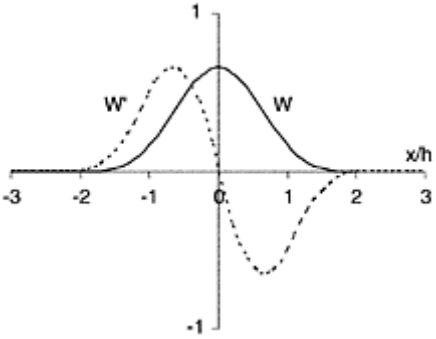

Figure 1. Cubic spline (W) and its derivative (W′) in 1D.

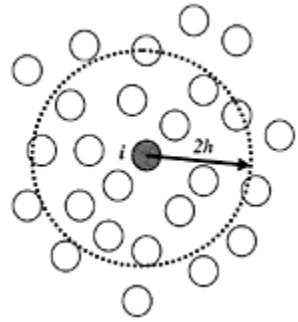

Figure 2. Particle *i* interacts with other particles only out to a distance of 2*h*.

3.3 *Smoothing length*

The smoothing length represents the effective width of the kernel, or the distance at which the particle in question interacts with other particles (figure 2). Changing smoothing length in SPH corresponds to changing the numerical resolution. If the fluid to be modeled does not undergo substantial rarefaction (or compression) constant h is sufficient. If particles become so distant, that they cease to interact (or so close, that a large number are within a smoothing length) h should be changed accordingly. The interpolation precision of SPH depends on having a sufficient number of particles within $2h$ and the speed of the computation depends on this number being relatively small. SPH works best when the number of neighbors is about 5 in one dimension and about 21 in two dimensions. These numbers all correspond to the number of neighbors on a cubic lattice with a smoothing length 1.2 times the particle spacing (using cubic spline).

There are many ways to dynamically change h so that the number of neighbors is kept approximately constant.

In this study the simplest approach is used: each particle has its own smoothing length which varies in space and time according to particle density.

Later, it will be shown that particle density is proportional to water depth, then the following expression is used to calculate smoothing length associated to particle *i:*

$$h_i = h_0 \left(\frac{\eta_0}{\eta_i} \right)^{\frac{1}{\nu}} \tag{11}$$

where h_0 and η_0 are the reference (initial) smoothing length and the reference water depth respectively.

Since each particle has its own smoothing length, each particle pair interaction, must have a smoothing length h_{ij} associated with it. In order to conserve momentum exactly, symmetry of particle interaction is preserved defining:

$$W_{ij}=W(\mathbf{r}_i-\mathbf{r}_j, \boldsymbol{h}_{ij}) \tag{12}$$

where

$$h_{ij} = \frac{h_i + h_j}{2} \tag{13}$$

3.4 *The SW-SPH model*

With the previous basic rules the shallow water equations in the lagrangian form are converted into equations for particles.

The fluid is sampled by a set of particles. A particle *i* has a fixed volume V_i (that correspond to the particle mass m_i in the original SPH context), a position ri, a velocity $\mathbf{v}_i$ and a water depth η_i (that correspond to the density ρ_i in the original SPH context). The differential area element $d\omega_i$ is V_i/η_i.

In the Lagrangian approach we move the particles with the velocity of the fluid, thus,

$$\frac{d\mathbf{r}_i}{dt} = \mathbf{v}_i \tag{14}$$

where $\mathbf{v}_i$ is updated using (2). With (8.1) we can calculate the gradient of η and then we obtain the SPH approximation of the motion equation (2),

$$\frac{D\mathbf{v}_i}{Dt} = \sum_j (g + \Pi_{ij}) \nabla W_{ij} V_j + g(\mathbf{S}_0 - \mathbf{S}_f)_i \tag{15}$$

in which Π_{ij} is the so-called "artificial viscosity". This term is introduced in the computation in order to avoid large unphysical oscillations (particle interpenetration) near to discontinuities (shocks). In this paper the standard artificial equation of Monaghan and Gingold (1983) has been employed and adapted to shallow water context.

$$\Pi_{ij} = \begin{cases} \dfrac{-\alpha\, c_{ij}\mu_{ij}}{\eta_{ij}} & if \quad (\mathbf{v}_i - \mathbf{v}_j)\cdot(\mathbf{r}_i - \mathbf{r}_j) < 0 \\ 0 & otherwise \end{cases} \tag{16}$$

where

$$\mu_{ij} = \frac{h_{ij}(\mathbf{v}_i - \mathbf{v}_j)\cdot(\mathbf{r}_i - \mathbf{r}_j)}{\left\|(\mathbf{r}_i - \mathbf{r}_j)\right\|^2 + \varepsilon h^2} \tag{17}$$

and

$$c_{ij} = \tfrac{1}{2}(c_i + c_j); \quad \eta_{ij} = \tfrac{1}{2}(\eta_i + \eta_j); \quad h_{ij} = \tfrac{1}{2}(h_i + h_j) \tag{18}$$

Here c_i denotes the shallow water wave speed $c_i=(g\eta_i)^{0.5}$; α is an empirical constant commonly=2, ε=0.01 is introduced to keep the viscosity bounded for particles as they approach.

Finally, the SPH representation of the continuity principle is obtained in integral form by means of (7.1) applied to η:

$$\eta_i = \sum_j W_{ij} V_j \tag{19}$$

Shallow water equations have been discretized in space for each particle and for the time interval Δt to get the flow characteristics (velocity, water depth, etc. for each particle) at the advanced time step starting from an initial distribution. The time integration of the SW-SPH equations is explicit thus the time step is chosen to accommodate CFL condition which, keeping in mind that the natural SPH scale length is h, is:

$$\Delta t \le \min_i \left(\frac{h_i}{c_i + |\mathbf{v}_i|} \right). \tag{20}$$

The time integration strategy from time t^N to time t^{N+1} is the following (excluding first time step):

– calculation of time step Δt^N using $h_i^N, c_i^N, \mathbf{v}_i^N$ in (20);
– calculation of particles acceleration at time t^N using equation (15), separated in two parts:

$$\left(\frac{D\mathbf{v}_i^N}{Dt} \right)_1 = \sum_j (g + \Pi_{ij}^N) \nabla W_{ij}^N V_j + g\mathbf{S}_{0i}^N \tag{21.1}$$

$$\left(\frac{D\mathbf{v}_i^N}{Dt} \right)_2 = -gn^2 \frac{|\mathbf{v}_i^N| \mathbf{v}_i^{N+1/2}}{\eta^{1.33^N}} \tag{21.2}$$

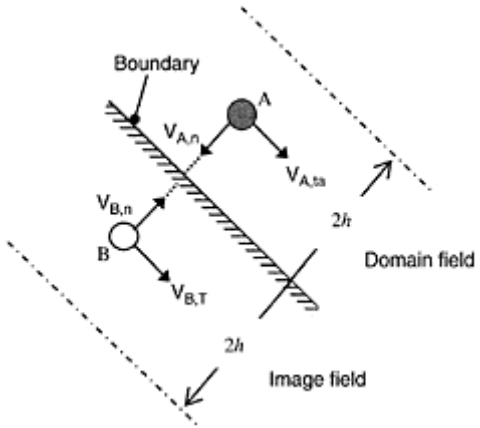

Figure 3. Image (B) of the particle A. Free slip condition: $v_{B,n}=-v_{A,n}$ and $v_{B,t}=-v_{A,t}$.

– velocity updating of each particle at time $t^{N+1/2}$ in a semi-implicit way

$$\mathbf{v}_i^{N+1/2} = \frac{\mathbf{v}_i^{N-1/2} + \left(\frac{D\mathbf{v}_i^N}{Dt} \right)_1 \frac{\Delta t^{N-1} + \Delta t^N}{2}}{1 + gn^2 \frac{|\mathbf{v}_i^N|}{\eta^{1.33^N}} \frac{\Delta t^{N-1} + \Delta t^N}{2}} \tag{22}$$

– position updating of each particle

$$\mathbf{r}_i^{N+1} = \mathbf{r}_i^N + \mathbf{v}_i^{N+1/2}\Delta t^N \tag{23.1}$$

– water depth updating using (19)

$$\eta_i^{N+1} = \sum_j W_{ij}^{n+1} V_j \tag{23.2}$$

– smoothing length updating using new water depth in (11).

In this paper only free slip boundary conditions are considered. They are assigned as follows: the field is extended out of its borders by adding a strip of thickness 2*h* where image particles. To each image particle the values of variables of the corresponding fieldparticle are given except for the velocity component normal to the boundary, which is reversed in sign (figure 3).

4 DAM-BREAK SIMULATIONS

In this paragraph the results of several test problems selected for the validation of SW-SPH code are shown. One dimensional and two-dimensional simulations of the catastrophic failure of a dam have been considered.

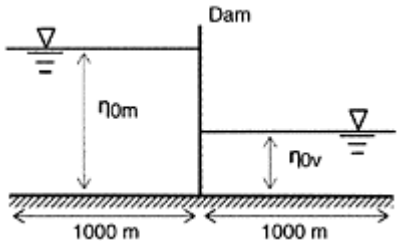

Figure 4. Definition sketch.

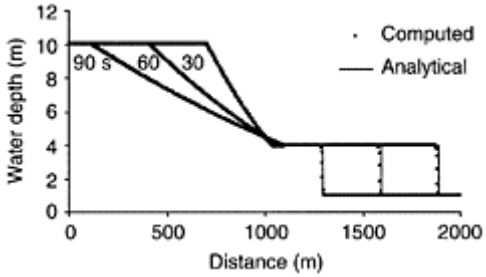

Figure 5. Stoker's problem.

4.1 *One-dimensional simulations*

The first simulations here reported deal with two simple cases for which analytical solutions are available.

At the midpoint of a channel 2000m long a dam separates two basins with different heights of still water (Figure 4).

At time t=0 the dam is instantaneously removed, then a negative wave moves upstream and a surge rushes downstream. For the case of a 1m wide horizontal rectangular channel, with negligible resistance, an exact solution is given by Stoker (1957). This problem, although idealized, is very interesting to test the shock capturing ability of the method.

We consider the case with η_{0m}=10 and η_{0v}=1. In the simulation here presented the initial water mass upstream of the dam is discretized with 1000 particles having a constant volume of $10m^3/m$, placed on a regular grid with a step of 2m. Water mass downstream instead is represented by 100 particles having the same volume but placed on a coarser grid with a step of 20m. The reference water depth, η_0, to be used in (11) is η_{0m}, the reference smoothing length, h_0, has been set 1.5 times the upstream particle distance so that about 7 particles interact. Note that with this initialization eq. (19) gives $\eta_i=\eta_{0m}$ upstream and $\eta_i=\eta_{0v}$ downstream.

The result, as shown in figure 5, is clearly in agreement with the exact solution.

The same problem was run considering the initial tailwater η_{0v}=0 (dry bed test case). In this case the analytical solution is given by Ritter.

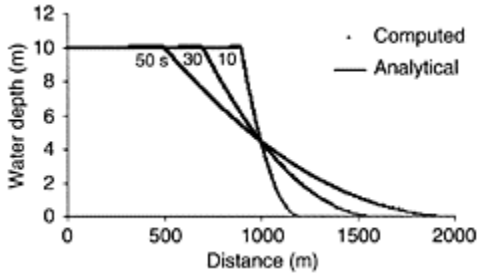

Figure 6. Ritter's problem.

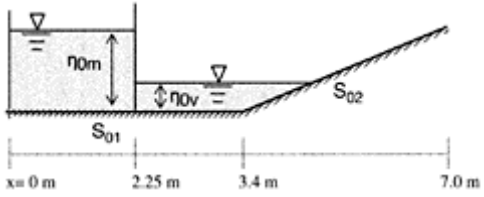

Figure 7. Experimental set-up (from Mignosa et al., 2001).

Table 1. Experimental test conditions.

Test	S_{01} (%)	S_{02} (%)	Manning n	η_{0m} (cm)	η_{0v} (cm)
A	0	−0.1	0.01	25	0.0
B	0	−0.1	0.01	25	4.5

The result, as shown in figure 6, is also clearly in good agreement with the exact solution. Note than no special treatment of dry areas has been employed.

The effect of the "source" term S_0 and S_f have been tested simulating dam-break laboratory experiment. Two sets of experimental data, taken from Mignosa et al. (2001), have been used for comparison. The experimental set up is shown in figure 7. The rectangular flume is 1.0m wide, 0.5m high and 7.0m long.

The instantaneous dam failure is simulated by means of the sudden removal of the gate. The flow field is characterized by shock propagation, reverse flow and wetting and drying conditions.

The experimental conditions of "test A" and "test B"(with and without tailwater depth) are summarized in table 1.

In both the test cases the initial condition is set by placing upstream of the dam 225 particles on a regular grid with step of 1cm. The volume of each particle is 25cm^3/cm and the reference smoothing length 1.5 times the grid step.

In the simulation of test B (non-zero tailwater depth) 32 more particles are placed downstream of the gate on a regular grid with a step of 5.5cm.

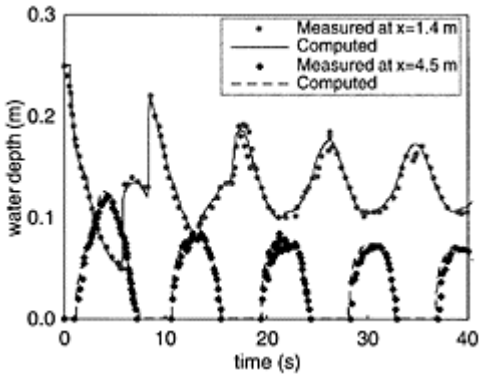

Figure 7.1. Computed and measured stage hydrographs for test case A.

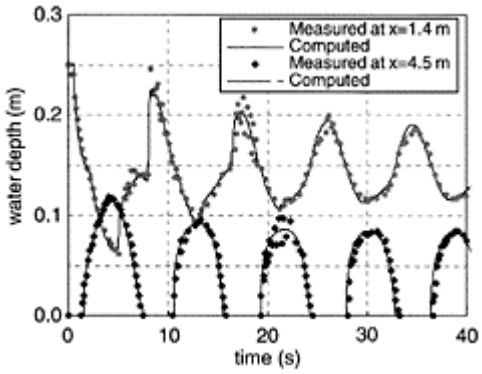

Figure 7.2. Computed and measured stage hydrographs for test case B.

In figures 7.1 and 7.2 the experimental hydrographs are compared to the numerical results. The sections along the flume are set at x=1.4m and x=4.5m. The water depth in those sections is recovered by eq. (7).

A good agreement between numerical results and experimental evidence can be observed.

4.2 *Two-dimensional simulations*

The first test case of two-dimensional simulations is the idealized partial dam breach reported in Fennema et al. (1990). It deals with a partial failure of a dam in a 200×200m basin of simplified geometry depicted in figure 8. The non-symmetrical breach is 75m wide and the dam is 10m thick. The bottom of the basin is horizontal and friction losses are neglected (n=0).

We report the case of initial reservoir depth η_{0m}=10m and tailwater depth η_{0v}=5m.

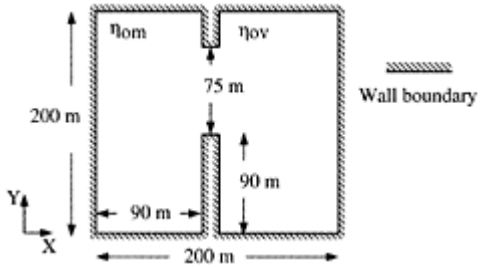

Figure 8. Definition sketch for partial dam-break.

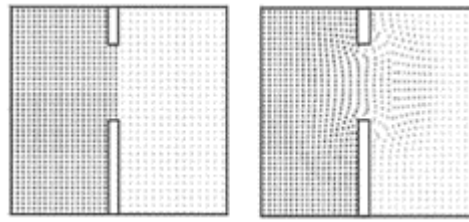

Figure 9.1. Particle position at time t=0s and time t=7.16s.

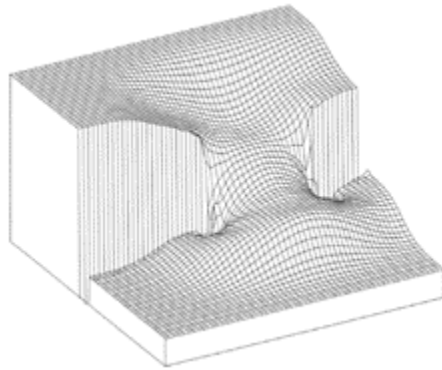

Figure 9.2. Water surface profile computed at time t=7.16s.

In the simulation the initial water mass upstream the dam is modeled with 750 particles with constant volume of 250m^3, placed on a regular grid with step of 5×5m. The downstream water mass is instead represented by 216 particles having the same volume but placed on a coarser grid with step 7.05×7.05m. The reference water depth, η_0, to be used in (11) is η_{0m}, the reference smoothing length, h_0, has been set 1.5 times the upstream particles initialization grid step.

The flow conditions have been computed at time t=7.16s and results are shown in figure 9.1 (particle position) and in figure 9.2 (water surface profile).

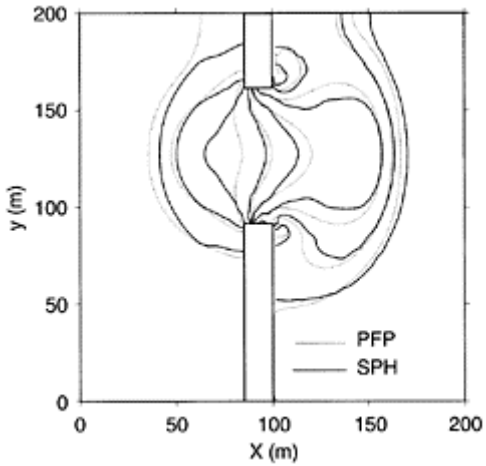

Figure 10. SW-SPH result vs PFP results in terms of water levels (ranging from 5m to 9m with step 0.5m).

In figure 10 the results are compared to the ones obtained by the shock-capturing eulerian code PFP (Braschi & Gallati, 1990). The mesh size of the eulerian simulation is 5m×5m.

After the preliminary tests of the code with simple 1D problems and 2D literature numerical results, a laboratory experiment was decided to get a better understanding of the capabilities of the model.

The scheme and the relevant geometrical data of the experimental setup is reported in figure 11. At the sudden gate opening the reservoir water spreads over the trasparent plane. The boundaries of the plane are plexiglass walls that reflected the flow forming cross shock waves. In order to visualize the characteristics of the flow field the water is colored with methylene blue ink and the plane is lighted from below. By this way it is possible to follow the position of the wave front.

The experiment was shot with a video camera able to record 25 frames per second, fixed 2m above the plane. Using suitable software it is possible to select from the whole film the frames at given times after the gate opening. Although the evaluation of the water depth can be obtained from the color intensity only a qualitative comparison between experimental evidence and simulation is shown in the following.

Two sets of experiments are reported. For both the initial water level in the reservoir is of 8cm and the plane is initially dry.

In the second experiment a rectangular obstacle 10cm high is placed in front of the gate as depicted in figure 12.

The simulation of the flow has been performed modeling the initial reservoir mass water by 333 particles

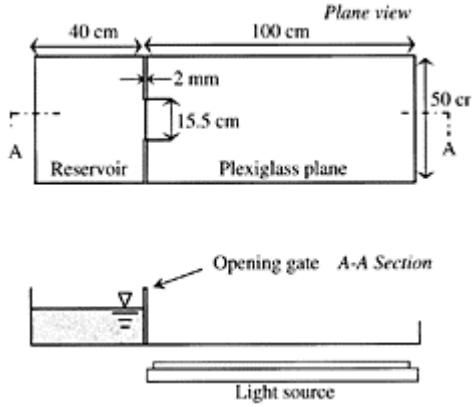

Figure 11. Experimental set-up for experiment 1.

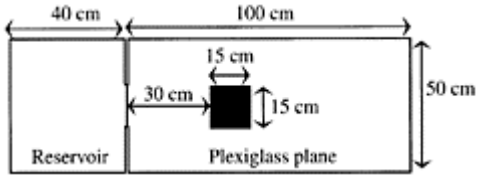

Figure 12. Experimental set-up for experiment 2.

placed on a regular grid with step of 2×2cm; η_{0m} is the initial water depth in the reservoir, h_0, has been set 1.5 times the particles initialization grid step; the Manning coefficient of n=0.01 has been assumed.

In figures 13 and 14 several computed and recorded flow fields are displayed at selected times after the opening. In the first and second column, observed and computed flow fields are reported respectively. The computed results are represented by the particle position in the plane. The particle's color is proportional to water depth associated to it.

In the third column results of the numerical model are displayed in terms of velocity field: in order to obtain these pictures, particle velocities are interpolated on a regular grid using (7).

There is an acceptable agreement between observation and simulation in both the experiments. Qualitatively, the main depth distribution features are retained and the shape and velocity of the two-dimensional hydraulic jumps calculated are in good agreement with the observed ones.

5 CONCLUSION

This paper reports on the application of the Smoothed Particle Hydrodynamics technique to Hydraulics in

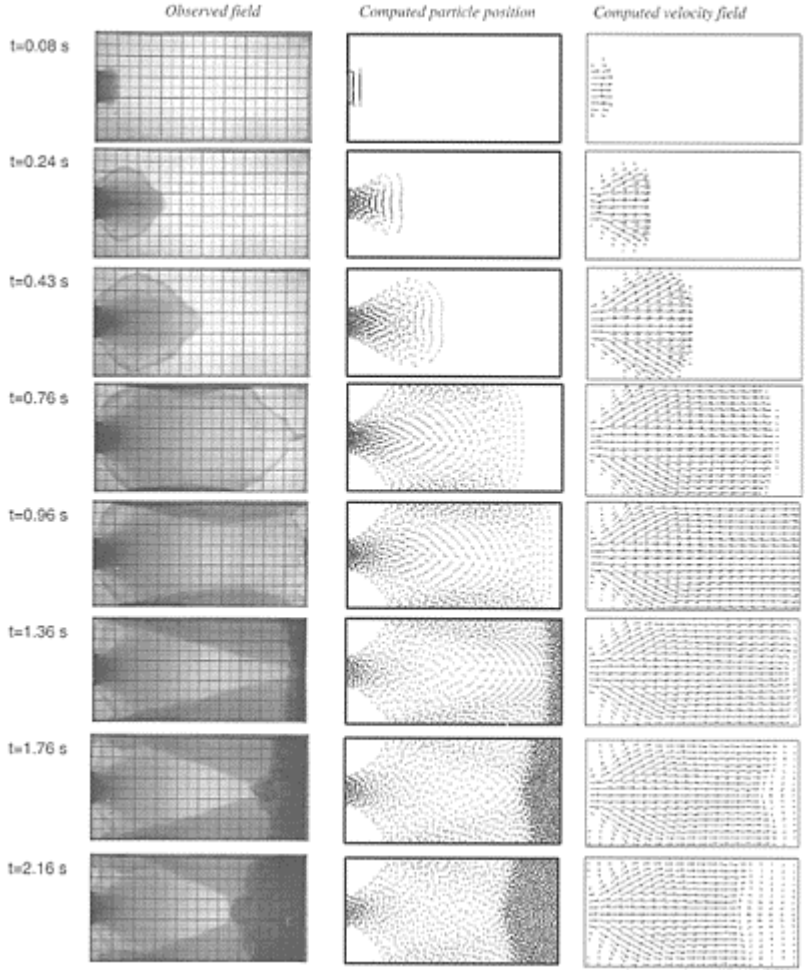

Figure 13. Comparison between computed and observed flow field—Experiment 1.

order to model free surface channel flows under the shallow water approximation. The original technique, born in an astrophysical context, has been adapted to solve the De Saint Venant equations under bounded domains.

Several 1D and 2D simulations of the idealized failure of a dam have been used to validate the code developed by the authors.

The method was shown to be robust and flexible to get realistic results both in 1D simple cases and in

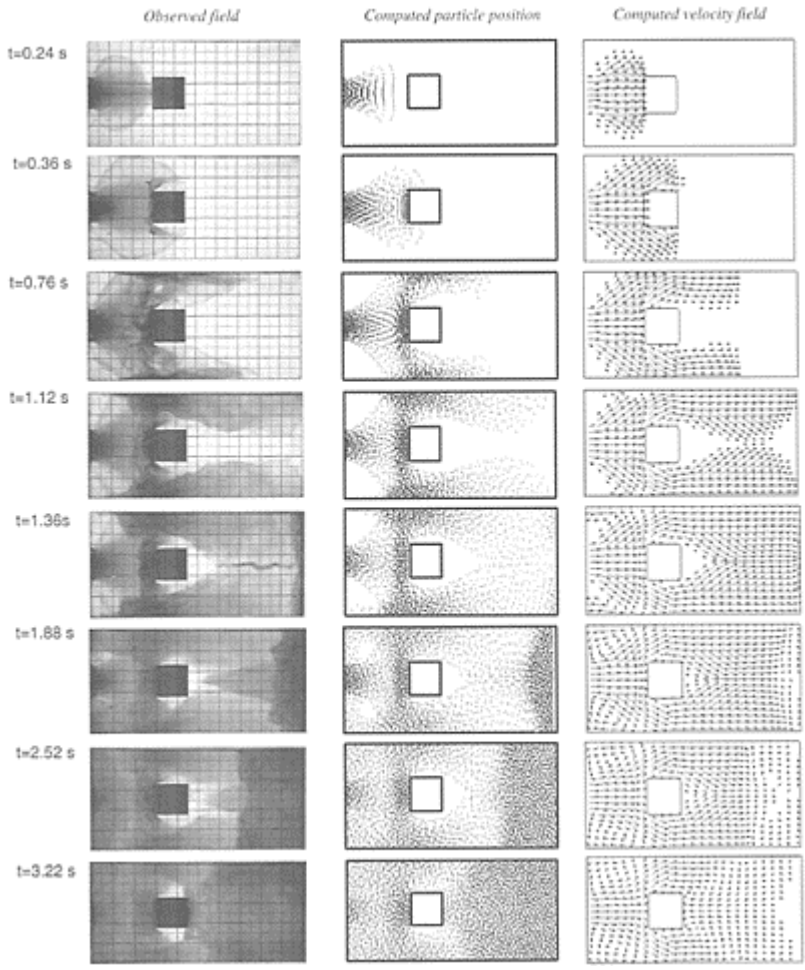

Figure 14. Comparison between computed and observed flow field—Experiment 2.

2D complex problems. It is suited especially to problems with sharp moving fronts since the shock waves can easily be captured and accurately simulated. The method is also able to simulate the propagation of flow over dry areas: no special treatment of dry regions is necessary since field values are computed only where the fluid is.

More complex situations dealing with inflow and outflow boundary conditions and real world dam-break simulations will be the subject of future studies.

REFERENCES

Aureli, F.M., Belicchi, M, Maione, P., Mignosa, P. & Tomirotti, M. 2001. Fenomeni di moto vario conseguenti al crollo di opere di ritenuta II: Indagini sperimentali ε modellazione numerica in presenza di onde di shock. *L'acqua* 5:27–36.

Fennema, R.J. & Chaudhry, M.H. 1990. Explicit methods for 2D transient free surface flows. *Journal of Hydraulic Engineering* 116:1013–1034.

Gallati, M. & Sturla, D. Impiego della tecnica SPH per simulare la dinamica di flussi liquidi con superficie libera in moto rapidamente variato. 2000. *CAPI Calcolo ad Alte Prestazioni in Italia*, Milano, 25–30 September.

Gallati, M. & Braschi, G. 2000. Simulazione lagrangiana di flussi con superficie libera in problemi di idraulica. *L'acqua* 5:7–18.

Gallati, M. & Sturla, D. 2001. Simulazione numerica dei flussi con superficie libera in acque poco profonde con metodo lagrangiano. *XV AIMETA Congress*, 25–30 September.

Gallati, M. & Braschi, G. 2002. Numerical description of rapidly varied flows via SPH method. *IASTED Int. Conf. ASM*, Crete, 25–28 June.

Gallati, M. & Braschi, G. 2002. SPH simulation of 2D shock propagation in shallow water. *IASTED Int. Conf. ASM*, Crete, 25–28 June.

Gallati, M. & Braschi, G. 2003. SPH simulation of the wave produced by a block falling into a water tank. *Int. Conf. On Modelling Fluid Flow*, Budapest, 3–6 September.

Gallati, M. & Braschi, G. 2003. Numerical simulation of the jump formation over a sill via SPH method. *Int. Conf. On Modelling Fluid Flow*, Budapest, 3–6 September.

Gingold, R.A. & Monaghan, J.J. 1977. Smoothed particle hydrodynamics: theory and application to nonspherical stars. *Monthly Notices of the Royal Astronomical Society* 181:275–389.

Gingold, R.A. & Monaghan, J.J. 1983. Shock simulation by the particle method SPH. *Journal of Computational Physics* 52:374–389.

Lucy, L.B. 1977. A numerical approach to the testing of the fission hypothesis. *Astronomomy Journal* 82:1013–1020.

Stoker, J.J. 1957. Water Waves. New York: Interscience publisher, Wiley.

Wang, Z. & Shen, H.T. 1999. Lagrangian Simulation of One-Dimensional Dam Break Flow. *Journal of Hydraulic Engineering* 125:1217–1221.

Simulation of flooding caused by an embankment breaking by means of a 2D finite volume numerical model

F.Aureli, A.Maranzoni & P.Mignosa
Dipartimento di Ingegneria Civile, dell' Ambiente, del Territorio & Architettura, Parma, Italy

River Flow 2004—Greco, Carravetta & Della Morte (eds.)

ABSTRACT: The results of a mathematical simulation of flooding due to the breaking of a railway embankment crossing a river valley are presented. During recent floods, the considered embankment was slightly damaged by piping phenomena. Since two kilometres downstream is located a high risk industrial area the potential flood related with a breaking of the structure would represent an extremely dangerous occurrence. A numerical model was built in order to simulate some catastrophic flooding scenarios. The numerical scheme is based on a finite volume discretization of the 2D shallow water equations. The model was validated performing a simulation of the October 2000 flood event, with good agreement between computed and observed water depths. Then the flooding derived by the failure of the embankment was simulated. The results obtained, together with those derived by the simulation of other possible scenarios, were then utilized in order to design the protection structures for the industrial area.

1 INTRODUCTION

The flood event occurred in October 2000 in northern Italy was a severe test for the embankment system of several rivers, somewhere causing the formation of breaks. Whereas the occurring of catastrophic collapses can be very dangerous for the environment and human lives, the identification of the risk derived by flooding must be evaluated *a-priori* in order to organize civil protection plans. At this aim historical information is essential, but sometimes not enough to understand all the potential hazards, as for dam-breaks or levee-breaks never occurred before. In these cases the risk

evaluation can be performed only with the help of numerical simulations or, more rarely, by means of physical scale models. In order to give reliable results, the mathematical models must be capable to describe the main characteristics of the flooding scenarios such as inundated areas, water depths, velocities, arrival times of the wetting fronts and permanence of the water on the ground.

In this paper the results of mathematical simulation of flooding due to the hypothetical break of a railway embankment crossing the river valley of an important tributary of the Po river (northern Italy) are presented. During two severe floods occurred in the recent past (1993 and especially 2000) the backwater effect due to the valley constriction gave rise to the storage of a considerable water volume just upstream the embankment. This in turn caused high stresses on the structure, which was not designed at this aim, and the beginning of piping phenomena. Since just downstream the railway is located a high risk industrial area, the potential additional flood related with the breaking of the embankment would create an extremely dangerous situation. Due to the impossibility to move in the near future the industrial plants, some catastrophic flooding scenarios were then simulated with a mathematical model in order to obtain design criteria for the protection plans.

The mathematical modelling of the flooding scenarios was accomplished by means of a two-dimensional finite volume numerical code, realised by the authors themselves, whose description and main features are explained in another paper presented at this Conference (Aureli et al. 2004a). Thanks to the information acquired during the recent historical event of October 2000, it was also possible to attempt a calibration of the model parameters and to compare to some extent simulated and historical water levels and flooded areas.

2 DESCRIPTION OF THE STUDY AREA

In order to reproduce the complex flow field in the area of interest it was necessary to describe the main morphological characteristics of the river, of the flood plains and of the structures crossing the river valley such as motorways, railways, waterways and irrigation channels (Fig. 1). It was also essential to obtain a correct representation of the water volume temporarily stored upstream the railway embankment during the floods. At this aim the considered domain was extended far upstream the motorway that determines the upper limit of the backwater effects induced by the railway embankment.

In the meantime the displacement of the upstream boundary from the area of main interest reduces the influence of the approximate representation of

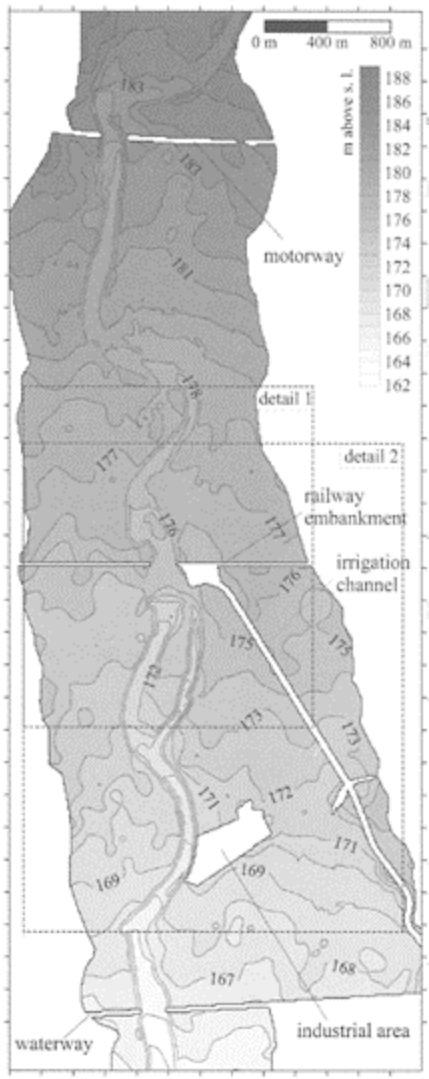

Figure 1. Bathymetry of the domain of interest.

the inflow boundary condition. For the same reason the outflow boundary was assumed beyond the waterway that constricts the river valley downstream the industrial site. On the lateral sides the inundation is naturally bounded by the morphological step of the river valley, so that also the considered domain was prolonged up to there.

Even if the area under investigation is considerably more extended in the longitudinal rather then in the transversal direction, a one-dimensional shallow water model would not be able to represent the complex behaviour of the flow field in this area. The three

consecutive constrictions (from upstream to downstream: the motorway, the railway and the waterway), together with the irrigation channel and its intake structures, influence indeed in a determinant way the flow paths during the floods. Transitions from subcritical to supercritical flows are expected through the constrictions, together with the formation of hydraulic jumps downstream. The hypotesised break of the railway would further complicate the situation, inducing the formation of a steep wave (shock) moving downstream towards the industrial area.

For all these reasons it was considered necessary to perform the simulations by means of a model based on the 2D shallow water equations written in conservation form and solved with a shock-capturing numerical scheme.

The bathymetry of the river and of the floodable region was then described by means of a DEM with a square regular mesh of size 10m, obtained by an interpolation procedure on the available cartographic maps and river cross sections. The dimension of the grid was chosen as a compromise between the estimated computational time and the satisfactory modeling of the region under study. The main constraints were due to the description of the structures such as river crossings, irrigation channels, bridges and so on. A more flexible mesh, such as a structured non-orthogonal Cartesian or a non-structured one, would be helpful for a refined description of the main structures crossing the valley, reducing in the meantime the overall number on grid nodes. Nevertheless, the necessity to track the moving fronts and shocks would require a refined mesh almost everywhere.

The embankment system of the river and the most important structures located in the domain were described as vertical and insuperable boundaries; a check was carried out at the end of the calculations in order to verify that all the embankments were really never overtopped by the waters during the flood. Since the main object of the simulations was to obtain water depths and velocities on the perimeter of the industrial site for design purposes, the area inside was considered as completely unfloodable. At this aim the interior nodes were excluded from the calculations (blanked in Fig. 1).

3 NUMERICAL MODEL

The adopted numerical code is based on a finite-volumes discretization of the 2D shallow water equations written in integral form:

$$\frac{d}{dt}\int_A \mathbf{U}\, dA + \int_C \mathbf{H(U)}\cdot\mathbf{n}\, dC = \int_A \mathbf{S(U)}\, dA \qquad (1)$$

where A represents the area of the integration cell, C the cell boundary, $\mathbf{n}$ is the outward unit vector normal to C, while $\mathbf{H}=\mathbf{(F, G)}$ represents the tensor of fluxes. The corresponding conservation differential form of (1) is:

The solution of the homogeneous part of (1) is based on the Weighted Average Flux (WAF) scheme, where second order of accuracy both in time and space is achieved by solving the conventional *piece-wise constant* Riemann problem and averaging it over space and time (Toro 1992). To avoid spurious oscillations in the vicinity of high gradients of the solution a TVD constraint was enforced on the scheme by means of

different well-known limiter functions (Toro 1997). The solution of the Riemann problem was based on the approximate HLLC solver (Toro 2001), that is a modification of the basic HLL scheme to account for the influence of intermediate waves. A more detailed description of the numerical scheme and of the treatment of the source terms can be found in a related paper presented at this Conference (Aureli et al. 2004a).

$$\mathbf{U}=\begin{pmatrix} h \\ uh \\ vh \end{pmatrix}, \quad \mathbf{F}=\begin{pmatrix} uh \\ u^2h+\frac{1}{2}gh^2 \\ uvh \end{pmatrix}, \quad \mathbf{G}=\begin{pmatrix} vh \\ uvh \\ v^2h+\frac{1}{2}gh^2 \end{pmatrix}, \quad \mathbf{S}=\begin{pmatrix} 0 \\ gh\left(S_{0x}-S_{fx}\right) \\ gh\left(S_{0y}-S_{fy}\right) \end{pmatrix} \tag{2}$$

4 CALIBRATION OF THE MODEL

The value of the roughness coefficients must account for the energy losses due to distributed and local resistance caused, for example, by the interaction of the flow with obstacles of lower dimensions with respect to the elements of the computational mesh. Also the energy dissipation due to the modification of the riverbed, to trees uprooting and to sediment transport have to be implicitly combined in this coefficients. Only two homogeneous regions, the riverbed and the floodplains, were identified in the domain, each characterised by a different behaviour with respect to flow resistance phenomena. The two Manning *n* roughness coefficients were firstly assumed on the basis of literature suggestions and then refined by trials searching for the values that allowed to reproduce at best with the model the maximum water levels observed during the October 2000 flood event. At the inflow boundary a 3000m^3/s constant discharge, corresponding to the estimated peak discharge of the October 2000 flood event, was considered. The discharge was assumed entering the domain orthogonally the inflow section and was distributed amongst the nodes unevenly, with a higher specific discharge on the riverbed.

Downstream the waterway (Fig. 1), at the outflow section of the considered domain, a far-field (non-reflective) condition was introduced, whereas at solid boundaries a free-slip condition was imposed. The simulations were extended in time until the maximum differences between the values of the three conserved variables at two consecutive time steps were less than specified tolerances. Then steady-state conditions were considered reached. From the described procedure a value of Manning n=0.050s.$m^{-1/3}$ for the floodplains was identified, while to the river channels was assigned n=0.033s·$m^{-1/3}$. Figure 2 shows the comparison between computed and observed maximum water depths at some significant points in the neighbourhood of the railway embankment.

The good agreement between observed and computed water depths confirms the suitability of the overall assumptions of the mathematical model concerning topographical description, grid size, roughness coefficient and representation of the main crossings.

5 FLOOD FREQUENCY ANALYSIS AND SYNTHETIC DESIGN HYDROGRAPHS DERIVATION

A gauged river section is located close upstream the area of interest, recording water levels almost continuously from 1925 and with an up-to-date stage-discharge relationship. A reliable flood frequency analysis can then be performed. From the records a 76 years long annual maximum peak flow (Q_0) series was extracted.

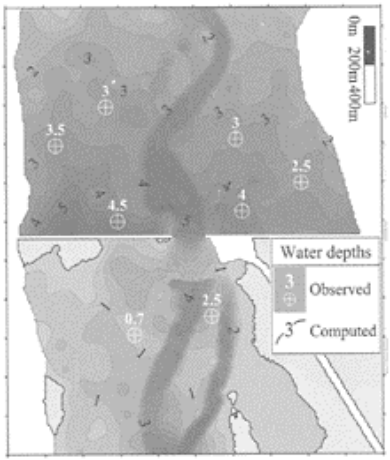

Figure 2. Comparison between observed and computed maximum water depths for October 2000 flood event (detail 1).

Log-normal, Gumbel (EV1) and General Extreme Value (GEV) probability distributions were considered in order to describe $Q_0(T)$. Parameters estimation was based on the Method of Moments for the first two distributions, whereas for the third the method based on L-moments was adopted. Figure 3 shows, on Gumbel probability chart, the data sample (Gringorten plotting position) together with the fitted probability distributions. The Hosking test (Hosking et al. 1985) on the k=0 hypothesis with a significance level α=5%, k being the exponent of the GEV distribution, demonstrates that the choice of the GEV distribution is justified.

From the GEV distribution a peak discharge of 3043m^3/s for T=200 years was derived. This value is close to the estimated peak discharge of the October 2000 flood event, which is also the maximum value of the overall historical series.

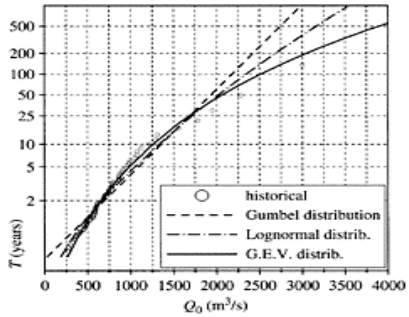

Figure 3. Q_0 data sample together with the fitted probability distributions.

In order to evaluate if a steady state solution would be a reasonable choice as initial condition before the hypothesized railway break occurs, Synthetic Design Hydrographs (SDH) were derived. The methodology (Maione et al. 2000a, b; Aureli et al. 2004b) is based on the statistical analysis of recorded flood waves through the construction of the Flow Duration Frequency (FDF) reduction curves of given return period and the determination of the temporal location of the peak value for each duration. The procedure was applied to a 62 years long historical sub-series, since the older strips have been lost. From the recorded flood waves, the annual maximum average discharges for each duration ranging from 0 to 96 hours were extracted and then processed. The resulting SDHs, for return periods ranging from 5 to 200 years, are shown in Figure 4. From the figure it can be observed that the rising limbs of the SDHs are quite gradual, taking about 22 hours from the starting value to the peak discharge.

The transient induced by the embankment breaking is surely faster than the potential hydrological stress. For this reason it is justified to assume as initial condition the steady state solution obtained by the model with as inflow discharge the peak value of the 200 years SDH. This in turn substantially coincides with the condition assumed for the calibration of the model.

Figure 5 shows the steady state water surface elevations, together with the velocity field (vector map) obtained by the calculations. Figure 6 shows a detail of the Froude values across the railway. The effect induced by the railway constriction is quite evident from the figures: upstream water levels rise up to about one meter below the top of the embankment, whereas downstream a short distance of supercritical flow occurs, abruptly blocked by an impressive hydraulic jump. An analogous, though less marked, effect is caused by the downstream waterway constriction. Close to the industrial area the steady-state results reproduce substantially well what happened during the

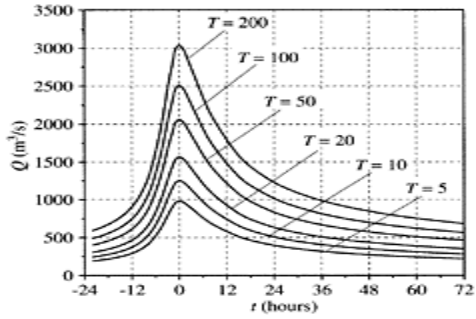

Figure 4. SDHs for the considered gauging station.

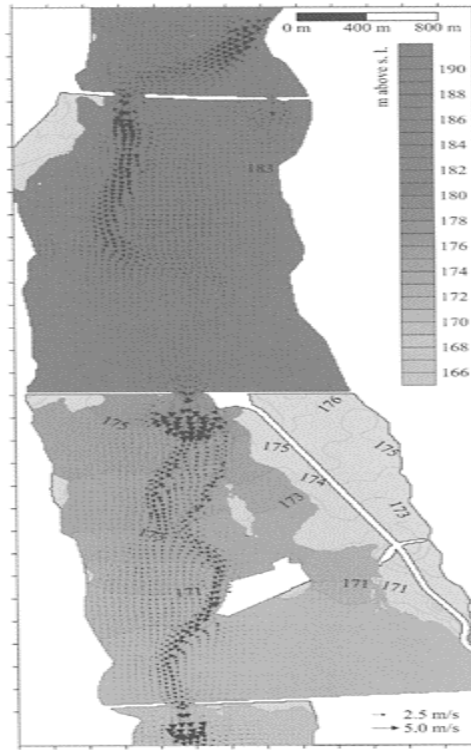

Figure 5. Steady state water surface elevations and velocity field (vector map) before the hypothesized embankment breaking.

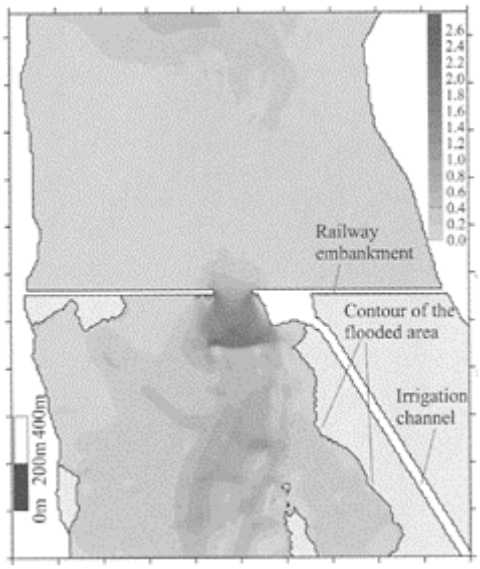

Figure 6. Froude values across the constriction at steady state (detail 1).

October 2000 flood event, when the site was slightly flooded, with water depths of about 0.3÷0.8meters.

6 FLOODING SCENARIO DUE TO THE RAILWAY EMBANKMENT BREAKING

The results obtained from the steady-state simulation were then used as hot-start initial condition for the railway breaking scenario. The collapse was assumed to involve a considerable portion of the left side of the embankment, where the most alarming symptoms of piping occurred during the recent historical floods. Together with the railway embankment also the intake structures of the irrigation channel and a portion of the channel itself were assumed to suddenly collapse. A reasonable bathymetry was reconstructed where the structures were originally located.

Figures 7 to 10 show details of the computed water surface elevations and flooded areas at different times after the breaking. Due to the considerable water volume stored upstream the railway embankment (about $8.5.10^6 m^3$), the sudden collapse of the structure induces the formation of a flood wave that in few minutes reaches the industrial area. Then the flow divides into two branches (Fig. 9): one collides with the top side of the area and then proceeds towards the riverbed; the other follows the right side of the industrial plants and then connects to the flooding due to the

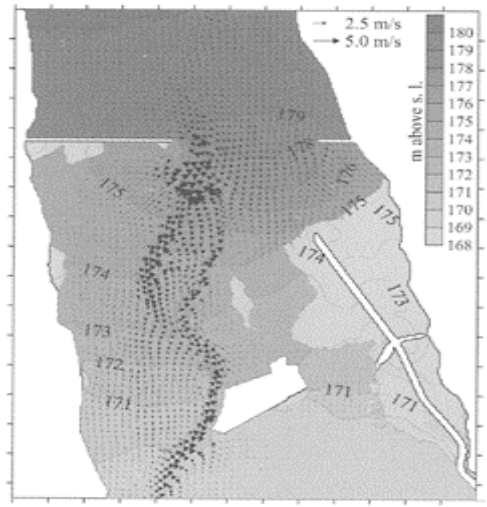

Figure 7. Computed water surface elevations and velocity field (vector map) five minutes after the breaking (detail 2).

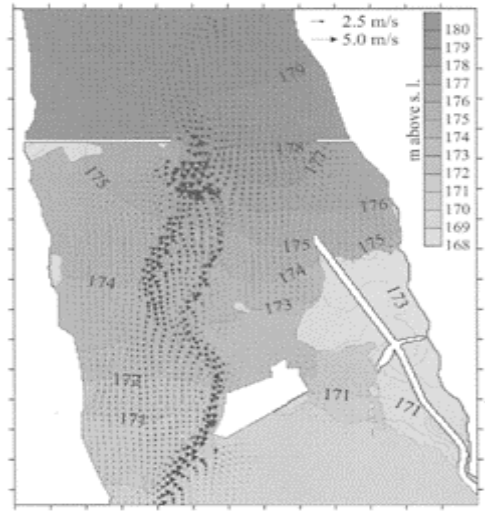

Figure 8. Computed water surface elevations and velocity field (vector map) ten minutes after the breaking (detail 2).

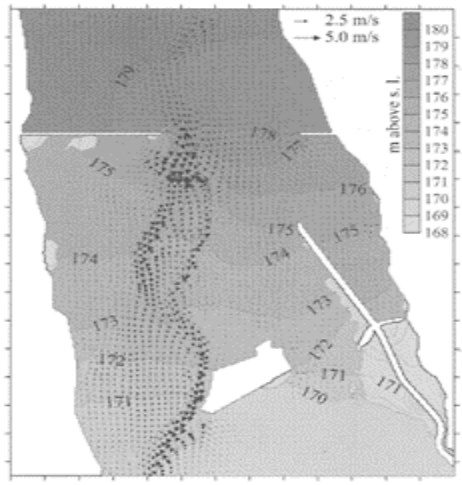

Figure 9. Computed water surface elevations and velocity field (vector map) twenty minutes after the breaking (detail 2).

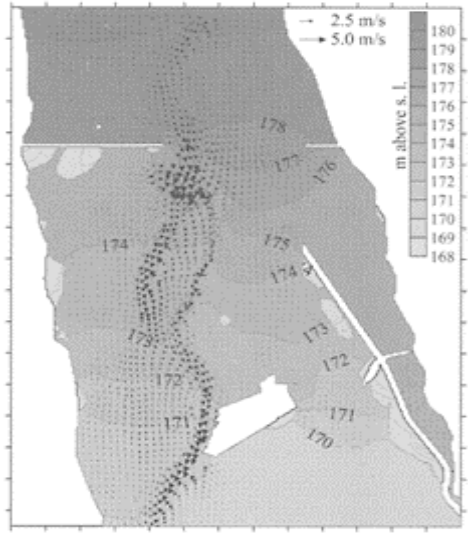

Figure 10. Computed water surface elevations and velocity field (vector map) 60 minutes after the breaking (detail 2).

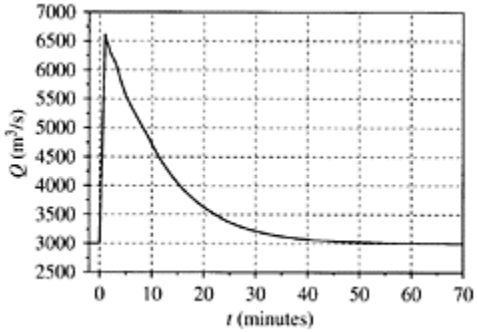

Figure 11. Computed discharge through the original railway line. The break occurs at time zero.

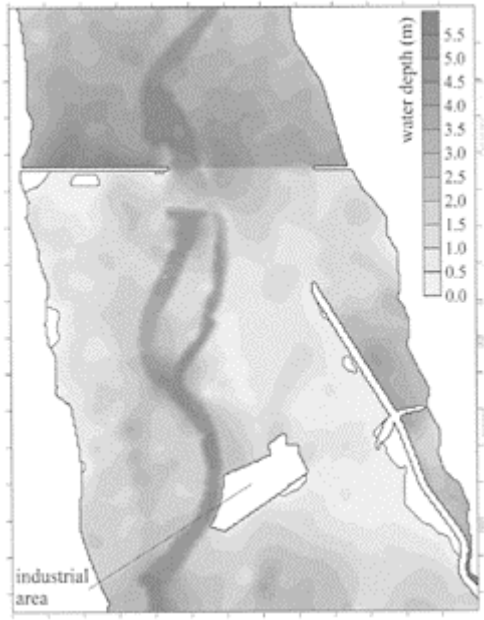

Figure 12. Envelope of computed water depths (detail 2).

backwater effects of the waterways crossing constriction. After one hour (Fig. 10) the flow became again almost steady everywhere. This is also confirmed by the computed discharge flowing through the original railway line, shown in Figure 11.

From the figure it can be easily derived that only a volume of about $2.6.10^6 m^3$ (out of $8.5.10^6 m^3$) was actually released from the storage upstream the railway, the remaining part being necessary for the maintenance of the base flow discharge.

Figures 12 and 13 show details of the envelopes of computed water depths and velocity norm.

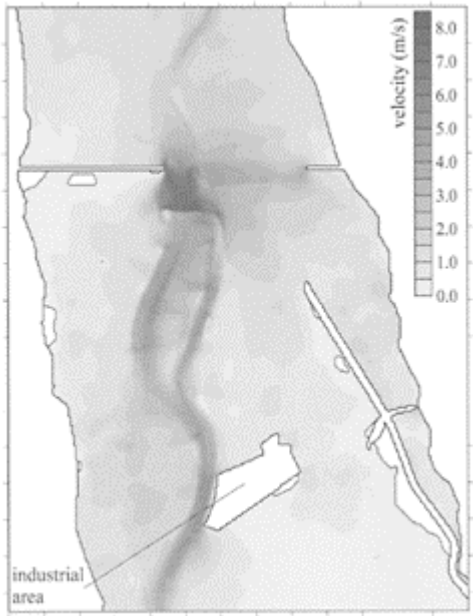

Figure 13. Envelope of computed velocity norm (detail 2).

The maximum of the water depths is reached at the top side of the area, with values of more than two meters. The maximum velocity is attained at the side adjacent to the riverbed with values of about 3m/s. Considerable velocities of more than 1m/s are also reached in correspondence of the right side of the industrial area.

7 CONCLUSIONS

A mathematical simulation of flooding due to the hypothetical failure of a railway embankment crossing the river valley of an important tributary of the Po river (northern Italy) was presented.

Thanks to the information acquired during the recent historical event of October 2000, it was possible to attempt a calibration of the model parameters and to some extent to compare simulated and observed water levels and flooded areas. Also the historical hydrological information was rich enough to perform a reliable flood frequency analysis and a Synthetic Design Hydrograph derivation.

The results of the mathematical model, together with those obtained by the simulation of other catastrophic scenarios, were then utilized to design the protection structures for the industrial plant. In the meantime the railway embankment will be strengthened and a deep diaphragm wall will be realized in order to avoid piping and then reduce failure risks.

ACKNOWLEDGMENTS

This work was developed within a research agreement between the Civil Engineering Department of Parma University and the Po River Basin Authority. The Authors wish to thank the a.m. Authority for the consent to publish the main results of the study.

REFERENCES

Aureli, F., Maranzoni, A. & Mignosa, P. 2004a. Two dimensional modeling of rapidly varying flows by finite volume schemes, submitted to River Flow 2004.

Aureli, F., Maranzoni, A., Maione U. & Mignosa, P. 2004b. Synthetic hydrographs as a design tool for flood routing evaluation, submitted to River Flow 2004.

Gumbel, E.J. 1962. Multivariate Extreme Distributions, *Bulletin of the International Statistical Institute* 39(2): 471–475.

Hosking, J.R.M., Wallis, J.R. & Wood, E.F., 1985. Estimation of the Generalized Extreme-Value Distribution by the Method of Probability-Weighted Moments, *Technometrics* 27(3):251–261.

Maione, U, Mignosa, P & Tomirotti, M. 2000a. Synthetic design hydrographs for flood-control reservoirs and flood-plain management. In U.Maione, B.Majone Lehto, R.Monti (eds.), *New Trends in Water and Environmental Engineering for Safety and Life: Eco-compatible Solutions for Aquatic Environments; Proc. Int. Conf., Capri, 3−7July 2000.* Rotterdam:Balkema.

Maione, U, Mignosa, P. & Tomirotti, M. 2000b. Synthetic design hydrographs for river flood management. In Toensmann F., Koch M. (eds.), *River Flood Defence Proc. Int. Symp., Kassel, 20–23 September 2000.* Kassel: Herkules Verlag.

Provincia di Vercelli 2000. Analisi degli effetti indotti dalla piena del 13–16 ottobre 2000 nel Comprensorio Nucleare di Saluggia, Vercelli (in Italian).

Toro, E.F. 1992. Riemann problems and the WAF method for solving the two-dimensional shallow water equations. *Phil Trans. R. Soc. London A* 338:43–68.

Toro, E.F. 1997. *Riemann Solvers and Numerical Methods for Fluid Dynamics.* Berlin: Springer Verlag.

Toro, E.F. 2001 *Shock—Capturing Methods for Free Surface Shallow Flows.* Chichester: John Wiley & Sons.

Dike-break induced flow: validation of numerical simulations and case study

M.Harms, S.Briechle & J.Köngeter
Institute of Hydmulic Engineering and Water Resources Management, Aachen University, Germany

D.Schwanenberg
WL/delft hydraulics, Delft, The Netherlands

River Flow 2004–Greco, Carravetta & Della Morte (eds.)

ABSTRACT: A TVD Runge Kutta Discontinuous Galerkin finite element method for two-dimensional depth-averaged shallow water equations is used to simulate dike-break induced flows. This paper presents comparisons of experimental data obtained by a physical model to results of the numerical simulation. Furthermore, the numerical method is applied to computations of flood wave propagation initiated by dike-breaks at the River Rhine. The aim of this case study is to evaluate effects of flood protection improvements, which are intended by a partitioning of the area at risk into compartments.

1 INTRODUCTION

Recurring events of extreme rainfall resulting in river hazards have shown the disastrous damages that can be caused by floods. Not only the occurrences of 99 dike-breaks at the River Elbe during the flood in August 2002 indicated that flood protection is vulnerable. A Risk Assessment procedure, subdivided into the three stages Risk Analysis, Risk Assessment and Risk Management, was developed for German dams at the Institute of Hydraulic Engineering and Water Resources Management (IWW), Aachen University, by Rettemeier et al. (2000). The basic principle of the approach can be transferred to rivers and dikes.

To assess the risk provoked by floods and potential dike-breaks within the scope of Risk Analysis the potential damage on people and property has to be determined. Thus, objectives that need to be investigated are the identification of inundated areas as well as flow depth and flow velocities of the initiated wave.

Dike-break induced flood waves are characterized by unsteady, rapidly varying flows over non-trivial bathymetry and by propagation on a dry bed. In contrary to dam-break flows there is a constant discharge in the river and the river will not empty like a reservoir.

A physical model, which takes into account the discharge in the river, the sudden break of the dike as well as wave propagation into an area, has been developed and build at the IWW. Thus, computations can be validated with the measured data of the two-dimensional wave propagation. Similar tests concerning the propagation of the wave into an area were proceeded by Kulisch (2003), Fraccarollo & Toro (1995) and Jovanovic & Djordjevic (1995). All of these authors consider dam-breaks, but not dike-breaks. Aureli & Mignosa (2002) present the single investigation also taking into account the river discharge. They perform computations of the induced wave, while taking measurements in the channel.

A Runge Kutta Discontinuous Galerkin (RKDG) finite element method has been developed and validated for dam-break flow (Schwanenberg & Harms, 2002). Possessing the ability to simulate unsteady, transcritical flow and wave propagation on a dry bed, it will be applied to dike-break flow. As the numerical method has already been presented in detail the following paragraph will merely give a brief outline.

2 RKDG METHOD FOR SHALLOW WATER FLOW

2.1 *Governing equations*

The mathematical description of a depth-averaged incompressible fluid is given by the shallow water equations in the form

$$\partial_t \boldsymbol{U} + \nabla \cdot \boldsymbol{F}(\boldsymbol{U}) = \boldsymbol{S}(\boldsymbol{U}), \tag{1}$$

where

$$\boldsymbol{U} = \begin{pmatrix} h \\ p \\ q \end{pmatrix} = \begin{pmatrix} h \\ uh \\ vh \end{pmatrix}, \tag{2}$$

$$\boldsymbol{F} = \begin{pmatrix} p \\ \beta_{xx}\frac{p^2}{h} + \frac{1}{2}gh^2 \\ \beta_{yx}\frac{pq}{h} \end{pmatrix}, \quad \boldsymbol{G} = \begin{pmatrix} q \\ \beta_{xy}\frac{pq}{h} \\ \beta_{yy}\frac{q^2}{h} + \frac{1}{2}gh^2 \end{pmatrix}, \tag{3}$$

$$\boldsymbol{S} = \begin{pmatrix} 0 \\ gh(-\partial_x z_b - \frac{n^2 p\sqrt{p^2+q^2}}{h^{10/3}}) \\ gh(-\partial_y z_b - \frac{n^2 q\sqrt{p^2+q^2}}{h^{10/3}}) \end{pmatrix}, \tag{4}$$

in which h=water depth; p, q=unit discharge in x-and y-directions; u, v=horizontal flow velocities in x and y-directions; β_{ij}=correction factor for nonlinear momentum flux; g=9.81m/s^2=acceleration due to gravity; ρ=fluid density; and z_b=channel bed elevation. Bed roughness is approximated by the empirical Manning formula with Manning's roughness coefficient n.

Mild bed slope, constant density and hydrostatic pressure distribution is assumed deriving these equations from the three-dimensional Navier-Stokes-Equations. As these assumptions limit the applicability of the equations their effects should be considered.

2.2 *Numerical method*

The presented numerical scheme is based on the RKDG method for hyperbolic equation systems. Detailed introductions to these methods can be found in Cockburn (1999) and Cockburn et al. (2000). Schwanenberg & Köngeter (2000) presented the first implementation of the RKDG method for the shallow water equations and its application to practical problems. The method is divided into three main steps:

– The partial differential equations are decoupled by DG space discretization with a polynomial degree k into a set of ordinary differential equations.
– The ordinary differential equations are integrated in time by a k+1 order TVD Runge Kutta method.
– A slope limiter is applied on every intermediate time step of the Runge Kutta method introducing a selective amount of dissipation in order to obtain stability at shocks.

Due to its explicit TVD Runge Kutta time integration, the method can be efficiently applied to transient and transcritical flows. The method was shown to have sharp representation of shocks. The implementation of source terms and boundary conditions is straightforward. For a in depth presentation see Schwanenberg (2002, 2003, 2004).

3 VALIDATION

3.1 *Physical model*

To validate the applicability of the method to dike-break flows the flow in a physical model (Fig. 1) is simulated. The model in the Institute's laboratory consists of a 1m wide channel with a pneumatically driven gate at one bank and an adjacent propagation area (3.5m×4.0m). The water can fall off freely at the three boundaries of this glass area. Discharge in the channel can be varied from 0 to 390 l/s, while the water level ranges between 30 and 50cm.

The flap gate opens in a minimized time span of less than 0.1s by rotating upwards. It is intended interfere as little as possible with the flow.

Measurements are performed on the propagation area. The water depth is determined by ultrasonic sensors with a measuring frequency of 50Hz in a dense raster. Furthermore a CCD-camera takes 50 pictures per second from top view, thus the propagation of the wave front is recorded.

A detailed description of measuring techniques and the flap gate is given by Briechle & Köngeter (2004).

3.2 *Numerical simulations*

Firstly comparisons of measurements and computations concerning the flow depths on the propagation area are considered. Calculations and measurements are performed on dry bed as well as for a small amount of water on the propagation area. Furthermore, different initial conditions are considered.

Secondly the propagation and shape of the computed wave front is compared to evaluations obtained by the CCD-Camera.

Figure 2 shows computed and measured water depths over time for three points at different distance, 1300, 2300 and 3300mm to the channel on the axis perpendicular to the channel.

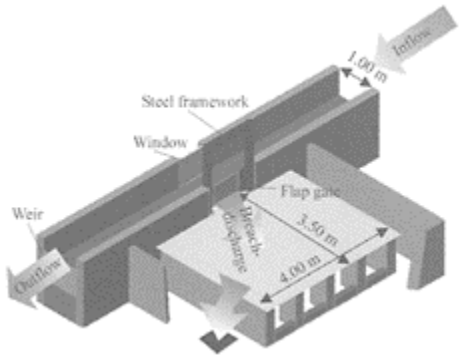

Figure 1. Physical model.

A constant discharge of Q=300l/s is applied. Results are shown for three different initial flow depths, computed on dry ground with a Manning value of n=0.0083s/m$^{1/3}$.

Computations were performed on an unstructured grid with element sizes of less than 5cm. The CFL number was set to 0.3.

Flow conditions in the channel in the different initial states are characterized by initial flow depth and discharge and can be expressed by Froude numbers.

For an initial water depth of 30cm arrival times of the wave differ slightly from the measured values at each gauge, while computed water depths are to low after the wave front passes the gauge. Combining a discharge of 300l/s with a water depth in the channel of 30cm, Froude number before the opening of the flap gate is nearly Fr=0.6. In case of this very shallow flow with high velocities in the channel, the influence of the flow in the channel on the propagation is overestimated. Propagation is not reproduced well on the axis perpendicular to the channel, as the main flow direction is diverted strongly into the direction of the flow in the channel in the simulations.

Better results can be achieved for an initial depth of h=40cm (Fr=0.38) and h=50cm (Fr=0.21) respectively. Arrival times and flow depth of the propagating wave are displayed very well. It can be observed that the wave front at the gauges in 2300 and 3300mm distance is represented to steep, while measurements indicate a slower rising of the water.

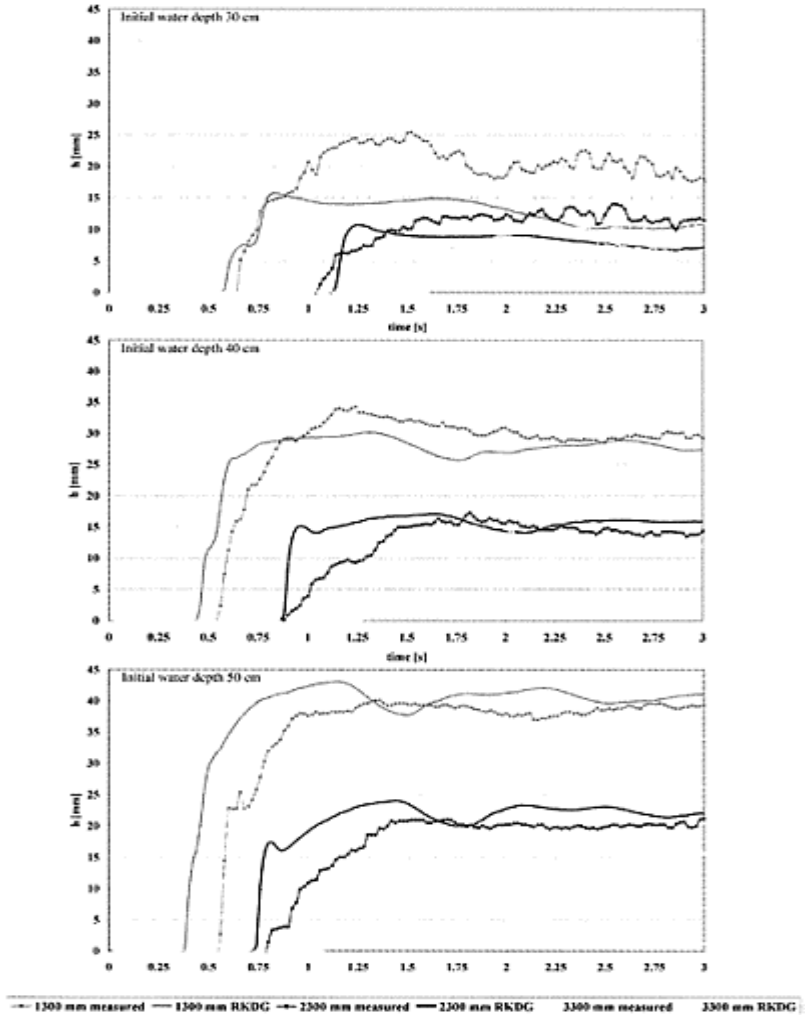

Figure 2. Water depth as function of time for three different initial water depths at three gauges at different distances from the flap gate on the axis perpendicular to the channel. Discharge in channel Q=3001/s.

Results in 1300mm distance from the flap gate are very good for all initial flow depths as regards the maximum flow depth. However, arrival times of the wave front are predicted to early. Possibly, close to the breach vertical components of the flow slow

down the velocity in main flow direction, as indicated by the water surface curvature. The vertical momentum increases with initial water depth, therefore the underestimation of the arrival time increases with flow depth as vertical components are neglected in the computation. Thus, differences can be attributed to the assumption of the shallow water approach.

Additionally, in spite of the rapid opening mechanism it can be presumed that a deceleration of the flow is caused by the flap gate in comparison to the simulations, as the gate is not taken into account. This effect might also be enforced for higher initial flow depths, as a larger part of the water body is in contact to the gate.

Some experiments were undertaken without drying the propagation area before the measurement. It is found that the wave is affected by the water film on the area. Measurements showed that propagation was decelerated by the water on the area and the front of the wave is significantly altered. This effect can be reproduced in the computations by assuming 1 mm of water on the area.

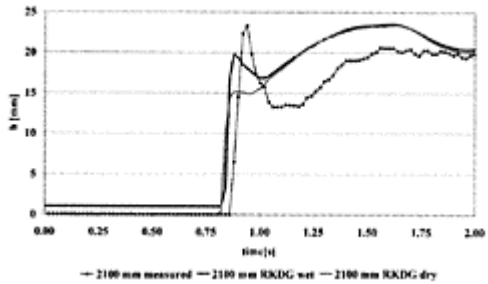

Figure 3. Water depth as function of time for initial water depth of h=40cm and discharge of Q=120l/s measured on a wet propagation area.

Figure 3 indicates that the peak at the wave front can only be displayed, if the thin layer of water on the area is taken into account. Observations during the measurements confirm that the front of the wave is strongly influenced by air entrainment. This explains that the computed water depth does not reach the maximum height of the measurement, as constant density is assumed in the computation.

Flow velocities have not jet been determined in the physical model. Computed maximum flow velocities are detected at a distance of 1m from the flap gate. For an initial water depth of 30cm the resulting velocity is v_{max}=2.15m/s, for 40cm v_{max}=3.11m/s and for 50cm v_{max}=3.5m/s.

Secondly the shape of the wave is considered in plan view to compare it to measurements by the CCD-Camera. The derivation of the wave front from the symmetrical propagation is affected by flow conditions in the channel. Figure 4 shows a comparison of the wave front computed to results obtained by the CCD-Camera for different time steps and a discharge in the channel of 120 l/s (Fr=0.15) and 300 l/s (Fr=0.27).

The figures indicate that the shape of the wave is reproduced quite well. Propagation on the main axis shows good agreement to the measurement. However, the derivation of the flow in the direction of the discharge in the channel is overestimated by the computation for both discharges as mentioned above. Again a reason could be the vertical momentum, which leads the wave to propagate perpendicular to the channel.

Derivation of the wave front increases with discharge in the channel and decreases with an increasing flow depth. Thus is can be found that derivation increases with an increasing Froude number in the channel. The second picture in Figure 4, representing results for higher Froude number in initial state, shows a stronger derivation from the main axis for both computations and measurements. Differences between measurement and computations also increase with an increasing Froude number, as was observed already

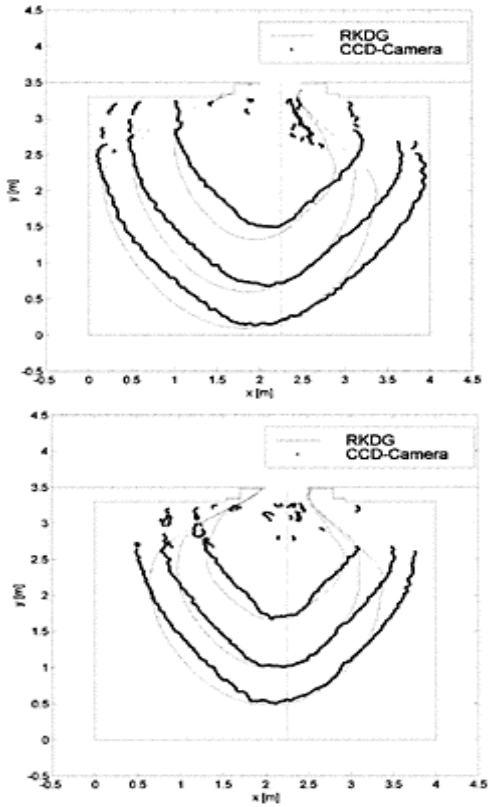

Figure 4. Wave front computed and recorded for Q=120 l/s and h=40cm (Fr=0.15) and Q=300l/s and h=50cm (Fr=0.27).

concerning a discharge of Q=300 l/s and h=30cm resulting in a Froude number Fr=0.58. Lateral Propagation to the side opposed to the channel's flow direction is not represented very well. The flow in the model is constricted and a steep water surface curvature induces a non-hydrostatic pressure distribution. This effect can not be displayed by computations based on the shallow water approach. Some points of the measurement near the gate indicate a borderline between main outflow and water with very strong surface curvatures.

Furthermore, the computed shape of the wave is chubbier and more onion shaped while the recorded one has a clearer apex in the front. Computational results of Aureli & Mignosa (2002) are comparable with the ones presented here. An explanation might be again the neglection of the vertical momentum in the shallow water equations.

We conclude that the shown results indicate a satisfying agreement with the measurement. Arrival time and height of the wave are displayed very well. As the physical model is focussed on the initial phase of dike-breaks, the neglection of vertical momentum is noticed. Conditions in the channel with a flow of high Froude numbers (Fr>0.5) are not computed well. But it can be presumed that in natural rivers Froude numbers are smaller even during floods. For example Froude numbers in the river Rhine are less than Fr=0.4 during a 500 years flood.

4 APPLICATION

4.1 *Flood protection improvement*

Due to mining activities the left polder area of the Rhine north of Cologne suffers from heavy surface settlements. With a height of up to 15m the dikes in this region are among the highest in Europe. Though the construction of the dikes is of high standard resulting in a low possibility of failure, the risk provoked by a dike-break is high as the potentially flooded area is large.

To improve flood protection and reduce the risk, a partitioning of the polder area of 400km^2 into compartments is considered. Thus, it is intended to diminish the risk by decreasing the probability of flooding of the whole region. Furthermore, evacuation times can be extended for areas, which are not directly affected by a dike-break. In this case the risk provoked by a dike-break is lowered because of a reduction of the potential damage.

It is intended to use mainly existing structures like street and railway dam rather than to build a second defense line with the height of the dikes at the river. This case study is a first consideration of the partitioning. The aim is to identify structures, which can be used as borders of the compartments with small effort for construction and at the same time allocate a sufficient volume to detain the water for a certain time. According to information of the German Civil Protection the gained time spans should be more than six hours, to provide sufficient time to evacuate people.

Figure 5 shows a part of the partitioned polder area. The whole area under investigation is separated into 19 compartments utilizing primarily highway and railroad embankments as well as natural given steps in the territory.

4.2 *Assessment of the effects*

To evaluate effects of the partitioning of the polder area into compartments on flood protection and the risk provoked by dike-breaks, different scenarios were computed for actual and design state. Thus enhancement of premonition time spans and reduction of inundated areas can be determined.

Figure 5. Detail of the polder area partitioned into compartments. Labels on the lines indicate the required heights. Compartments are numbered from 1 to 19.

We will consider one of these scenarios located at Rhine km 777 as indicated in Figure 5. After simulating steady state in the river Rhine, an unsteady, synthetic discharge hydrograph of a flood with recovering period of 500 years is applied. Eight days of the nearly 30 days lasting flood are simulated. At the begin of the unsteady computations, two days before the maximum discharge is reached, the complete failure of the dike at a length of 300m on the left bank is assumed.

Computation of this case study on a mesh of approximately 25,000 unstructured triangles with minimum length of 15m are performed setting the CFL number to 0.35. To take into account the flooding of areas of different land use, zones of different Manning values are introduced. For example, flow in urban areas is carried out with Manning values of n=0.2s/m$^{1/3}$. Values are chosen according to references from CADAM (2000) and DVWK (1990) guidelines.

Comparing the discharge through the assumed breach for actual and design state it is found that the discharge is reduced by about 40–80m^3/s due to the retention in the compartments. Thus, the volume of water flooding the area is decreased from 180Mio.m^3 in present state to 130Mio.m^3 in design state.

Analysis of the results show that the main effects of the partitioning are enlarged times of premonition and reduced areas of inundation.

Figure 6 compares results of present and design state for the time two days after the dike-break. It becomes obvious that the propagation in present state is advanced much further into the area at risk. Parts of three more compartments are affected. At this time

Figure 6. Inundation maps at *t*=48 h after the dike-break. Present state on the left, design state on the right.

the difference of the inundated areas is 8km^2. But, it has to be taken into account that due to the reduction of inundation areas in total inside of the compartments the water levels might be higher. Compared to the avoidance of flooding in compartment 5, 14 and 15, this increase of water level can be considered as insignificant.

Analysing the temporal development, it becomes clear that premonition time span for the area inside of compartment 14 is increased from 30 to 50 hours. For the northern area enhancement is even more than 25 hours, while compartment 5 will not be affected by the flood due to partitioning the region.

Another effect is observed considering the arrival time of the flood. In present state the water is spread into the area of three compartments within six hours, while in design state this will take one and a half days.

Considering the maximum water levels that occur during the eight days of propagation, a difference of 23km^2 concerning inundated areas is determined. Figure 7

indicates that the northern part of the area under investigation is not affected as a result of partitioning into compartments.

Summarizing the investigation yields that the calculation of the scenario proofs the achievement of the required aims. For compartments directly affected by the dike-break induced flood wave or located close to the breach premonition time enhancement is determined to be two to three hours. But for further propagation of the flood wave premonition times are enlarged significantly. Results of a different scenario demonstrate that in that case the water could be kept in the first compartment causing a strong decrease of discharge through the breach and a reduction of inundated areas of 85%.

Thus, based on the performed computations the effect of the partitioning can be assessed as positive. However, it has to be considered that results display conditions of specific scenarios. Computations of dike-breaks at different locations along the river Rhine showed that the outgoing discharge through the breach varies highly in dependence on the territory

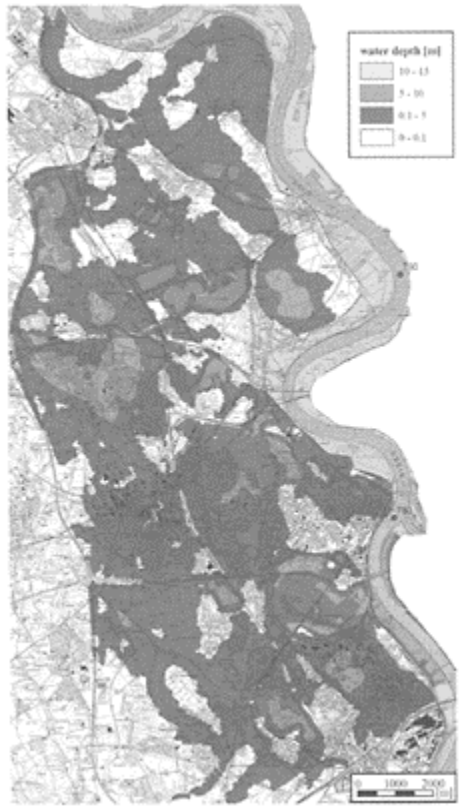

Figure 7. Inundation maps of maximum values during eight days of

flooding. Present state on the left,
design state on the right.

directly behind the dike, to flow conditions and to characteristics of the river.

Furthermore the detailed investigation of damage potentials caused in present state and in case of partitioning allow for well-founded recommendations.

5 CONCLUSIONS

A TVD RKDG finite element method for 2D depth-averaged shallow water equations has been applied to dike-break flows.

Comparisons of numerical simulations to experimental investigations concerning dike-break induced flood wave propagations in a physical model are presented. The aim of the study was the validation of the numerical method. Computed results show good agreement to the measured data in term of water level time series as well as the shape and propagation of the wave front recorded by a CCD camera. Thus, it could be proved that the model is capable to reproduce the main characteristics of dike-break induced flow. Still computations are limited due to the assumptions of the shallow water approach, especially concerning the hydro-static pressure distribution.

These limitations can be overcome using 3D models. But, especially the presented application of the 2D model to dike-break flow at the River Rhine demonstrate that real-world dike-break flows have to be performed for large scales, to which 3D models are not applicable. Actually, in natural dike-break induced flow propagation in horizontal directions is obviously large compared to 3D effects in the flow. Thus, for investigations concerning the far field effects of dike-breaks the shallow water approach is justifiable.

Performing the case study the model is used to evaluate the increase of premonition time spans and the reduction of flooded areas, which is intended by partitioning the area at risk into compartments. It is confirmed that an improvement of flood protection is achieved. At the same time the model is demonstrated to be a useful tool to deliver input data that is needed within the scope of risk analysis for dikes.

REFERENCES

Aureli, F. & Mignosa, P. 2002. Rapidly varying flows due to levee-breaking. In D.Bousmar & Y.Zech (eds.), River Flow 2002, *Proc. International Conference on Fluvial Hydraulics, Louvain-la-Neuve, Belgium, 4–6 September, 2002*. Rotterdam: Balkema:459–466.

Briechle, S., Joeppen, A. & Köngeter, J. 2004. Physical model tests for dike-break induced, two-dimensional flood wave propagation. In River Flow 2004, *Proc. International Conference on Fluvial Hydraulics, Neapel, Italy, 23–25 June, 2004.* Rotterdam:Balkema:in print.

Cockburn, B. (1999). Discontinuous Galerkin Methods for Convection-Dominated Problems, in LNCSE Vol. 9: "High-Order Methods for Computational Physics" (Eds.: T.J.Barth & Deconinck), 69–224, Springer, Berlin.

Cockburn, B., Karniadakis, G.E. & Shu, C.-W. (2000). Discontinuous Galerkin Methods, LNCSE Vol. 11, Springer, Berlin.

Fraccarollo, L. & Toro, E.F. 1995. Experimental and numerical assessment of the shallow water model for two-dimensional dam-break type problems. *Journal of Hydraulic Research* 33(6):843–863.

Jovanovic, M. & Djordjevic, D. 1995. Experimental verification of the MacCormack numerical scheme. *Advances in Engineering Software* 23:61–67.

Kulisch 2003. Ausbreitung von Dammbruchwellen im physikalischen Modell. *Mitteilungen des Institut fur Wasserwesen, Universität der Bundeswehr München,* Heft 79. München:Oldenbourg.

Rettemeier, K., Falkenhagen, B. & Köngeter, J. (2000). Risk Assessment—New Trends in Germany. *Proc. Twentieth Congress on Large Dams Q. 76—R. 41:*19–22 September 2000, Beijing, China. Transactions, Vol. I:Question No. 76. Paris:Commission International des Grands Barrages (ICOLD)—ISSN 0254-0703, 625–641.

Schwanenberg, D. & Köngeter, J. (2000). A Discontinuous Galerkin Method for the Shallow Water Equations with Source Terms, in LNCSE Vol. 11: *"Discontinuous Galerkin Methods"* (Eds.: B.Cockburn, G.E.Karniadakis, and C.-W.Shu), 419–424, Springer, Berlin.

Schwanenberg, D. & Harms, M. (2002). Discontinuous Galerkin Method for Dam-break Flow, In D.Bousmar & Y.Zech (eds.), River Flow 2002, *Proc. International Conference on Fluvial Hydraulics, Louvain-la-Neuve, Belgium, 4–6 September, 2002.* Rotterdam:Balkema: 443–448.

Schwanenberg, D. (2003). Runge Kutta Discontinuous Galerkin method for convection-dominated depth-averaged shallow water problems, PhD thesis, Dept. of Civil Engrg., Inst. Of Hydraulic Eng. and Water Resources Management, Aachen Univ., Germany (in German).

Schwanenberg, D. & Harms, M. (2004). Discontinuous Galerkin Finite-Element Method for Transcritical Two-dimensional Shallow Water Flows, *ASCE Journal of Hydraulic Engineering,* Vol. 130, No. 5 ISSN 0733–9429/2004/5-1-10/$18.00 (in print).

Morris, M. (2000). CADAM Concerted Action on Dambreak Modelling; Dambreak Modelling guidelines & Best Practise, EC contract number ENV4-CT97-0555.

DVWK-Schriftenreihe H 92 (1990). Hydraulische Methoden zur Erfassung von Rauheiten, Verlag Paul Parey.

Surge wave front in a moving reference system

A.Bornschein
Institute of Hydmulic Engineering and Applied Hydromechanics, Dresden University of Technology, Germany

River Flow 2004—Greco, Carravetta & Della Morte (eds.)

ABSTRACT: A surge wave is a very unsteady flow. For better observation and measurement an experimental set-up with a standing surge wave front in a moving reference system was developed. Experimental facilities and instrumentation are presented. Preliminary tests were conducted in order to confirm that the test results are similar to measurements of traditional channels.

1 INTRODUCTION

In its simplest form the dam break wave problem was solved 110 years ago by Ritter (1892) considering a smooth channel bed without roughness. As Hager & Lauber (1996) wrote the results of experimental investigations in test channels confirmed this theoretical solution in the main. One exception is the propagation of a surge wave front downstream of a broken dam which is strongly influenced by bed roughness.

Dressler (1952) and Witham (1955) tried to determine the influence of the bed roughness and found the following equation to determine wave front velocity u_F:

$$u_F = 2 \cdot \sqrt{g \cdot h_0} - a \cdot \sqrt[3]{g \cdot h_0} \cdot \sqrt[3]{g \cdot t} \cdot \sqrt[3]{\frac{g}{C^2}} \qquad (1)$$

where h_0=depth of water at the dam site before failure, g=acceleration due to gravity, C=Chezy roughness parameter and a=coefficient of decreasing of velocity. This equation means that the roughness reduces the propagation of the flood wave, while the start velocity is Ritter's velocity But obviously this solution by Dressler does not reflect the actual influence of the bed roughness exactly.

Lauber (1997) conducted dam break wave investigations in horizontal and sloping channel with smooth bed using advanced measurement techniques. The measured wave

front velocities were compared with calculated values based on Dressler's equation. Lauber had to consider unrealistic low values of Chezy roughness parameter to get satisfactory results.

It seems there is no feasible solution of wave front propagation available. The propagation of the wave front after a certain time due to dam failure is influenced by the bed roughness, bed slope and water surface slope in the front region.

Furthermore the knowledge in the field of surge waves is necessary to predict e.g. the inundation area and destruction potential of a flood wave resulting from dam rupture, to determine the effectiveness of surges which occur when flushing sewers and to design irrigation systems with grooves.

To find out some rules for the propagation of an assumed triangular shaped wave front on a dry bed Martin & Bollrich (1989) treat the wave front in a moving reference system and found out following equation:

$$u_F = h_F^{2/3} \cdot \frac{1}{n} \cdot \sqrt{\frac{1 + b \cdot I}{3b}} \qquad (2)$$

where h_F=height of the wave front at the boundary between turbulent wave-tip and the following flow being approximately as one-dimensional flow, b=shape parameter of the wave-tip, I=bed slope and n=*Manning's* roughness parameter. The formula has still to be verified by experimental results. Other theories consider a stepped wave front (Schoklitsch 1950) or a sine curved wave front (Wackernagel 1962). Experimental investigations of dam break waves often dealt with the dam failure as well as the flood wave propagating downstream of the dam (see Fig. 1). The front created by the flood wave was very small and it was difficult to get detailed measurement results. There is no knowledge available about the velocity distribution in a wave front and about the shear stress caused by a turbulent wave front.

An experimental set-up for investigations at the wave front has to create the turbulent front on its own.

2 EXPERIMENTAL FACILITY

The basic idea of an experimental set-up described by Bornschein (1999) is analogous to theoretical derivation by Martin & Bollrich (1989) to transform the unsteady flow of a surge into be steady from the observers point of view. The experimental set-up with a conveyer belt as the bed depicts the moving reference system.

Up to now experimental facilities with moving-bed were used especially to investigate air flow, debris flow, open channel flow and large eddy flow as for instance described by Tamburrino & Gulliver 1992. The model tests on surge wave front are performed in the Hubert-Engels-Laboratory of the Institute of Hydraulic Engineering and Applied Hydromechanics, Dresden University of Technology, Germany (Fig. 3).

The testing flume has glass sides and is 0.4m high, 0.3m wide and 10m long. It is possible to tilt the flume. The bed slope can be varied from 0 to 0.04.

A frequency-controlled motor drives the moving bed, the conveyer belt. The bed being used currently has a smooth surface. A velocity of the conveyer belt up to 5m/s can be realized.

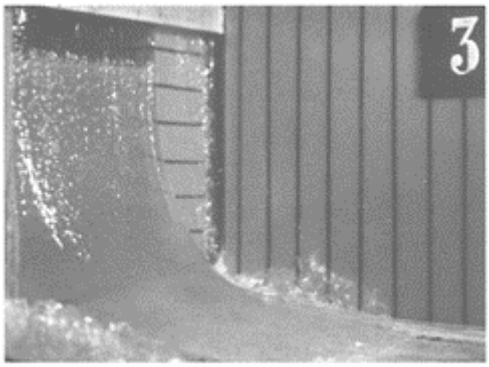

Figure 1. Experimental investigations by Estrade (1967)– dam break wave together with the reservoir outflow.

It is possible to generate waves with different wave heights and different wave velocities.

Ultrasonic sensors measure the wave shape. Three sensors were mounted on a mobile monitoring car, which can drive on aluminium tracks on the top of the glass flume along the channel. The position of the car was recorded together with ultrasonic signals. In this way a continuous touchless measurement of water surface was possible. Because of the steep slope of the water surface at the wave front there were hard requirements to ultrasonic sensors to get satisfactory results of wave shape.

The flow velocity field of the wave front is measured with a 2D Laser Doppler Anemometer System (Fig. 4). As a light source a 5W Argon Ion Laser (Innova 70) manufactured by Coherent is used. The light is separated into 2 times 2 colours in the TSI Color Burst. The 4 beams are focused into optical fibres bringing them to a probe containing transmitting/receiving optics. The optical probes are mounted on a 3 dimensional traversing system to reach all measurement points in the flow computer controlled.

The emitted light signal is detected and transformed to electrical signals in the TSI Color Link. These raw

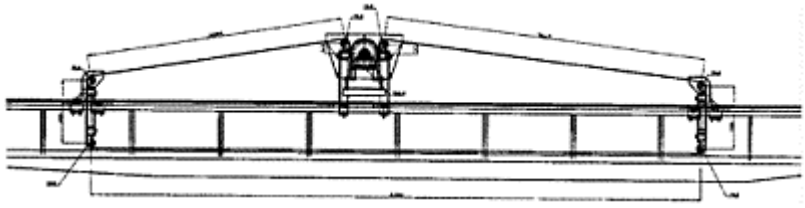

Figure 2. Technical drawing of the experimental set-up.

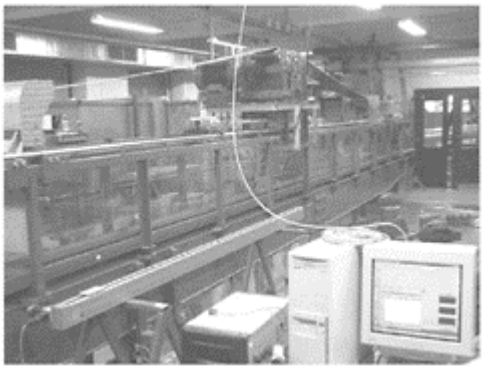

Figure 3. Laboratory channel with the conveyer belt mechanism.

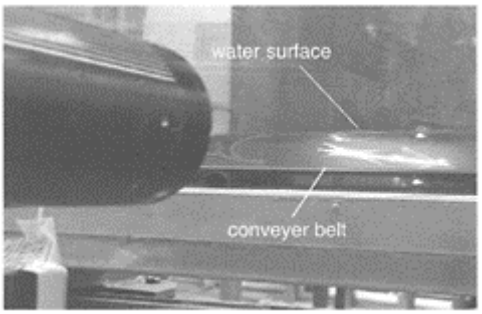

Figure 4. LDA measurement through flume side glass wall (conveyer belt moves to the right side with 2.36m/s, bed slope=0.04).

signals are filtered and processed with the TSI Digital Burst Correlator IFA 650. The final processing of the data is done with the TSI Software FIND for Windows.

Hence it was possible to measure the horizontal flow velocity along the channel as well as the vertical flow velocity.

3 TEST CONDITIONS

The wave front tests were conducted as follow: a certain amount of water was filled into the test flume and the conveyer belt was started. Then the velocity of the belt was adjusted in order to get a steady turbulent wave front near one end of the moving bed. The wave shape (water depth as a function of horizontal coordinate x) and the velocity were measured.

In the context of velocity measurement the vertical distance of measurement volume from bed and from water surface was limited by the distance of the two vertical laser beams. In the optical probe the parallel exit beams from the fibres are focused by a lens into the measurement volume where the beams intersect. In the lens the distance between the two beams is 5cm. Hence good measurement results are only possible when the point in which the two laser beams meet each other located about 0.5 to 1cm above the bed or under the water level. Obviously the determination of surface velocity by LDA was not possible.

Furthermore the surface velocity was conducted by measurement of the time and the path of tracer particles transported on the water surface. In Figure 5 the surface velocity versus the belt velocity for different bed slopes are shown. In average the surface velocity is about 10% of the bed velocity in the moving reference system.

That means in the nature the water particles of the water surface travel faster than the wave body. This depends not clearly from the bed slope.

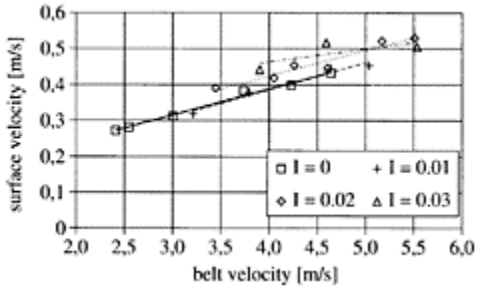

Figure 5. Surface velocity versus belt velocity.

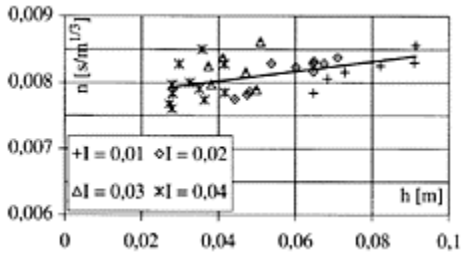

Figure 6. Manning roughness parameter of the smooth conveyer belt.

For further comparison of testing results with different surface roughness, Manning roughness parameter of the smooth belt was determined too. For this test series belt velocity was adjusted that a nearly bed-parallel water surface was resulted.

Since the flow was induced by the moving of the conveyer belt the relevant wetted perimeter was equal to belt wide. Thus the hydraulic radius can be set equal to the water depth. To determine Manning roughness parameter defined by Manning's formula:

$$u_{belt} = \frac{1}{n} \cdot h^{2/3} \cdot \sqrt{I} \qquad (3)$$

water depth **h,** bed slope $\mathbf{I}_B$**,** water surface slope $\mathbf{I}_S$ and belt velocity as the mean velocity of flow were measured in that test series.

In Figure 6 Manning's roughness parameter versus the water depth is shown. There is no significant correlation. The mean value of all test cases is 0.008 and will be used for calculation and comparison with other test results.

The measured distribution of the horizontal velocity indicates a very turbulent flow. In Figure 9 an example is shown, measured under the condition of bed slope=0.01, belt velocity=2.38m/s and mean water

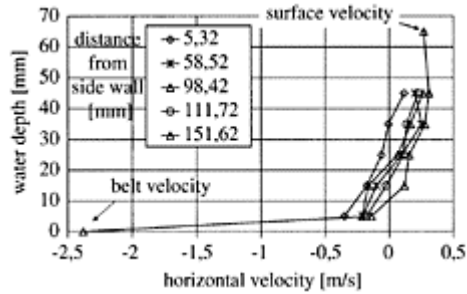

Figure 7. Flow velocity distribution of the horizontal velocity along channel axis due to the moving bed (bed slope=0.01, belt velocity=−2.38m/s, water depth=0.065m).

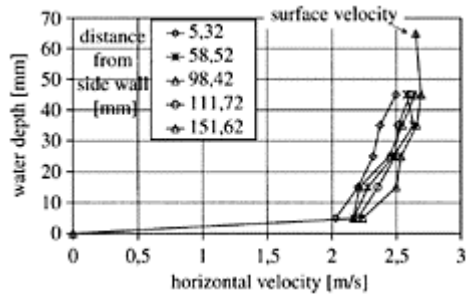

Figure 8. Flow velocity distribution from Figure 8 transformed to the natural reference system.

depth=0.065m. The velocity of the surface was estimated due to Figure 5. For better understanding the belt velocity is displayed in the figure.

To transfer experimental results from moving reference system to nature the Galilean transformation must be used:

$$\bar{u}_n = \bar{u}_{mrs} - \bar{u}_b \tag{4}$$

where u_n=horizontal velocity in nature, u_{mrs}=horizontal velocity measured in the moving reference system and u_b=belt velocity. Transformed data from Figure 7 are shown in Figure 8. Generally this flow profile agrees to flow profile of steady flow in a rectangular open channel.

The measured vertical velocity profile for the same test case as in Figure 7 is shown in Figure 9. The vertical velocity has values near zero except for the region near side wall of the flume.

Hence the main velocity in the case of steady flow condition in the moving-bed flume is the horizontal velocity analogous to the steady flow in traditional channels.

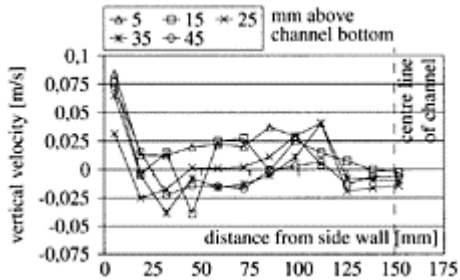

Figure 9. Vertical velocity profile (bed slope=0.01, belt velocity=−2.38m/s, water depth=0.065m).

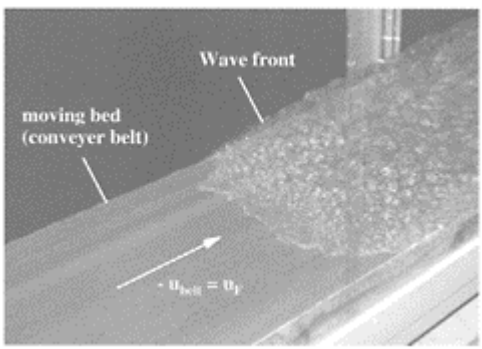

Figure 10. Steady state of wave front in the experimental set-up.

Generally the results from the model tests with an moving-bed flume can be transformed and compared with results from traditional flumes.

4 RESULTS OF WAVE FRONT

The wave front obtained in the experiment is presented in Figure 10. It possesses a very long and flat shape appropriate to the smooth surface of the moving bed. The water surface is very curly. This is similar to waves in standard flumes like at dam break tests by Bell, Elliot & Chaudry 1992.

The slope of the water surface increases until the front where the slope is up to vertical. In traditional dam break experiments with smooth beds the resulting wave front is too small to observe this phenomena. But a steep wave front is observed in channels with a rough bed and in cases of real dam breaks.

Measurement results of the wave head shape shown in Figure 2 and confirms the above description of the shape of the wave front.

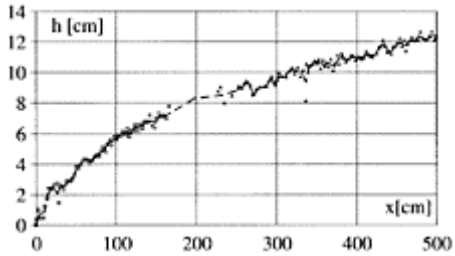

Figure 11. Shape of wave front—dots=measured with ultrasonic sensors, line=mean values (bed slope=0.01, v_{bed}=4.24m/s).

5 CONCLUSIONS

The knowledge in the field of surge waves is necessary to predict the inundation area and potential of destruction of a flood wave resulting from dam failure, to determine effectiveness of surges which occur by flushing of sewers and to design irrigation systems with grooves.

Nevertheless the knowledge about the flow at the wave front and about the propagation of the wave front depending on the bed roughness and turbulence is very limited. A better understanding of these relations is of general importance for the calibration of numerical models to simulate flood waves resulting from breaching dams.

There are various theories about shape and velocity of the wave front. Previous experimental investigations consider wave front together with the whole dam break wave and reservoir outflow.

An experimental set-up was developed basing on the consideration of the wave front in a moving reference system. Thus the unsteady flow of a surge wave was converted to a steady flow from the observer's point of view.

For further comparison is it important that in the case that a flow is induced by a moving bed the wetted perimeter is equal to channel width and the hydraulic radius can be set equal to the water depth.

Due to the velocity distribution and the wave shape it is obviously that the moving-bed flume measurements can compared with test results from traditional flumes.

Further tests with a rough surface belt are in process now.

REFERENCES

Bell, S.W., Elliot, R.C. & Chaudry, M.H. 1992. Experimental results of two-dimensional dam-break flows. In Journal of Hydraulic Research, Vol. 30(2):225–252.

Bornschein, A. 1999. Propagation of surges over initially dry and wet beds. In Proc. Anniversary Scientific Conference 50 Years Faculty of Hydromechanics at the University of Architecture, Civil Engineering and Geodesy, Sofia, Bulgaria, Vol. 1:105−110.

Dressler, F.R. 1952. Hydraulic resistance effect upon the dam-break-functions. In Journal of Research of the National Bureau of Standards, Vol. 49(3):217–225.

Estrade, J. 1967. Contribution á l'étude de la suppression d'un barrage. Direction des Etudes et Recherches, Chatou Serie A Bulletin, 1:3–128.

Hager, W.H. & Lauber, G. 1996. Hydraulische Experimente zum Talsperrenbruchproblem. In Schweizer Ingenieur und Architekt, 114(24):25–38.

Lauber, G. 1997. Experimente zur Talsperrenbruch-Welle im glatten geneigten Rechteckkanal. Dissertation Nr. 12115, Eidgenössische Technische Hochschule Zürich.

Martin, H. & Bollrich, G. 1989. Berechnungsgrundlagen für Schwall- und Sunkwellen sowie Dammbruchprobleme. In Wiener Mitteilungen Wasser.Abwasser.Gewässer, Symposium: Hydraulik offener Gerinne, TU Wien, Band, 79: 139–164.

Ritter, A. 1892. Die Fortpflanzung der Wasserwellen. In Zeitschrift Verein Deutscher Ingenieure, Band, 36(33): 947–954.

Schoklitsch, A. 1950. Handbuch des Wasserbaus. Springer Verlag. Wien.

Tamburrino, A. & Gulliver, J.S. 1992. Comparative flow characteristics of a moving-bed flume. In Experiments in Fluids No. 13:289–298.

Wackernagel, A. 1962. Die Berechnung der Flutwellen bei Bruch von Talsperren. In Schwerzerische Bauzeitung, 80. Jg. No. 22:370–373.

Witham, G.B. 1955. The effects of hydraulic resistance in the dam-break problem. In Proceedings of the Royal Society No. 1170:399–407.

Roll waves evolution in channels

G.F.Maciel
Department of Civil Engineering, São Paulo State University, Ilha Solteira, São Paulo, Brazil

River Flow 2004—Greco, Carravetta & Della Morte (eds.)

ABSTRACT: Flows that process under accentuated steep slopes may develop instabilities called roll waves. Roll waves can be developed in laminar and in turbulent streams. The purpose of this article is to analyze the criteria for the occurrence of roll wave phenomenon in the case of supercritical and turbulent Newtonian and non-Newtonian flows from the engineering point of view. Rewriting the shallow water equations and taking into account the Bingham fluid behavior and fluid viscosity, first, the conditions for the development of roll waves using the stability linear technique are presented; second, it is presented a numerical simulation performed by a finite volume technique using Godunov-VanLeer schemes. Imposing a constant discharge at the upstream of the high gradient channel and superposing very small perturbations (with different frequencies and amplitudes), it was observed that roll waves can be developed more easily for small wavenumbers and for high cohesions of material.

1 INTRODUCTION

Flows that process under accentuated steep slopes may develop instabilities. However, the chaotic aspect present in the nature of these instable phenomena, seem to tend, at the end of a finite time, to a stationary flow, more stable, with the appearance of periodic long waves as a hydraulic jump or “bore waves”. Such perturbations are called “roll waves”. If, on one hand, these waves are rare in natural flows, on the other, they are frequent in artificial canals and in water flowing from dams.

The proposition of this scientific communication is to study, from the theoretical standpoint, with numerical appreciation, instability problems in the fluid flow with rheologic behavior of Bingham fluid type. In particular, it will try to verify the aptitude of the “shallow water” equations, combined to a “Bingham” rheology, to “roll waves” propagation and generation in debris or mudflows. In a first part, the conditions of existence of “roll waves” and formation criteria, either in Newtonian fluids (clean water)

or in non-Newtonian fluids (“debris flow” case) will be analytically verified; in a second part, such instabilities would be numerically generated. The equation system used is a modified shallow water type with and without diffusion terms. The numeric modeling proposed is the finite volume type where the schemes Godunov-VanLeer (1981) (compatible to the hyperbolic non-linear systems) are applied.

2 THEORETICAL MODELLING THROUGH “SHALLOW WATER” EQUATIONS—CONSERVATIVE FORM

“Shallow water” equations with shock used here are obtained from the classic equations of fluid mechanics to which a representative behavior law of a Bingham fluid rheology is added, such as $\tau=\tau_c+\mu.\,(du/dy)$ if $\tau>\tau_c$ and $du/dy=0$ se $\tau<\tau_c$. τ_c represents the critic tension of shearing or initial stress (yield value), μ the dynamic viscosity and du/dy the velocity gradient (shear rate). “Shallow water” system consists of a mass conservation equation (1), a momentum conservation equation (2) and, in this case, two relatives to the hydraulic jump (3 and 4).

$$\frac{\partial h}{\partial t} + \frac{\partial (hu)}{\partial x} = 0 \qquad (1)$$

$$\frac{\partial (hu)}{\partial t} + \frac{\partial (\alpha h u^2)}{\partial x} + g.h.\cos(\theta).\frac{\partial h}{\partial x} = g.h.\sin(\theta) - \frac{\tau_c}{\rho} - \frac{g u^2}{C_h^2} \qquad (2)$$

$$\rho.h.(w-u) = \rho_0.h_0.w \qquad (3)$$

$$\rho_0.h_0.w.u = \frac{1}{2}.\rho.g.h^2.\cos(\theta) - \tau_c.h_0 \qquad (4)$$

In these equations “h” is the flow depth; “h_0” is the uniform flow depth; “u” is the vertical average velocity; “w” is the propagation velocity of the front flow (celerity); “C_h” is Chézy coefficient; “θ” the canal declivity; “ρ” the specific mass of the fluid and “α” the velocity profile coefficient (α=1, by simplification). The Bingham Number considered is this article is high, in order that critical stress dominates largely over viscosity effect.

2.1 *Existence conditions of “roll waves” in the new Bingham fluid rheology, without viscous term*

The proposal of this item is to determine the necessary and sufficient conditions to the generation of “roll waves” as the solution of “shallow water” equations in a Bingham fluid rheology without the diffusion term. At first, the interest variables and thus the work scales should be defined:

length scale: $H = \frac{h}{h_0}$ and $X = \frac{x \cdot tan(\theta)}{h_0}$

velocity scale: $U = \frac{u}{\sqrt{g \cdot h_0 \cdot cos(\theta)}}$ and

$W = \frac{w}{\sqrt{g \cdot h_0 \cdot cos(\theta)}}$

time scale: $T = \frac{t}{\frac{h_0}{tg(\theta)} \cdot \frac{l}{\sqrt{g \cdot h_0 \cdot cos(\theta)}}}$

in which is the propagation speed of the gravitational waves. Introducing the dimensionless variables in the equations (1)–(4), and disregarding the specific mass variations, the following equations are obtained:

$$\frac{\partial H}{\partial T} + \frac{\partial (H.U)}{\partial X} = 0 \quad \textbf{(5)}$$

$$\frac{\partial U}{\partial T} + U \frac{\partial U}{\partial X} + \frac{\partial H}{\partial X} = 1 - \frac{C^*}{H} - \beta.\frac{U^2}{H} \quad \textbf{(6)}$$

$$H.(W-U) = W \quad \text{e} \quad W.U = \frac{1}{2}.H^2 - C^* \quad \textbf{(7)}$$

with $C^* = \frac{\tau_c}{\rho.g.h_0.\sin(\theta)}$ and $\beta = \frac{g}{C_k^2 \tan(\theta)}$

The determination of the “roll waves” formation criterion, demands, first of all, a solution to the free surface equation. First, the equations (5) and (6) are rewritten in a moving system of co-ordinates. By hypothesis $\zeta = X - W.T$, where W represents the dimensionless velocity of the front flow propagation (celerity). Starting from these presuppositions, we obtain two linear equations with two incognitos (U′ and H′). This system resolution will provide two differentials equations with U′ and H′:

$$H' = \frac{\partial H}{\partial \zeta} = -\frac{H.(1 - \frac{C^*}{H} - \beta.\frac{U^2}{H})}{(U-W)^2 - H} \quad \textbf{(8)}$$

$$U' = \frac{\partial U}{\partial \zeta} = \frac{(U-W).(1 - \frac{C^*}{H} - \beta.\frac{U^2}{H})}{(U-W)^2 - H} \quad \textbf{(9)}$$

The relation between (8) and (9) allow to verify that the specific discharge is a constant as described below:

$$\frac{H'}{U'} = \frac{H}{W-U} \quad ; H(W-U) = K = \text{constant} \quad \textbf{(10a,b)}$$

If we apply (10b) in the expression of H′ (equation 8), an equation non-linear of 1st order will be obtained, as shown in equation (11):

$$\frac{\partial H}{\partial \zeta} = -\frac{H.\left(1 - \frac{C^*}{H} - \beta.\frac{(H.W - K)^2}{H^3}\right)}{\left(\frac{K}{H}\right)^2 - H} \qquad \textbf{(11)}$$

The resolution of (11) will provide us the wished profile of the free surface. However, it is verified that there is no solution to this periodic equation. Thus, the proposal would be to try to "build" periodic solutions from continued intercalated solutions by hydraulic jumps.

For this, it is necessary to find continuous solutions presenting the property in which, in a determined section, the flow is supercritical and, in a posterior one, subcritical. By continuity, there should exist an abscissa point ζ_0, a depth point H_0, a speed point U_0, where the Froude number is equal to the unity (critic flow). Thus, $W - U_0 = \sqrt{H_0}$. To this point, especially, the equation denomination (11) is null, which means a discontinuity, except for the case in which the numerator is also null. This critical point is necessarily different of that where the jump occurs, in a way that is only possible to construct the "roll waves" when the numerator and the denominator concomitantly null themselves. Thus:

$$H_0 = \left(\frac{-\beta \cdot W + \sqrt{C^* \cdot (1-\beta) + \beta \cdot W^2}}{1-\beta}\right)^2$$

$$U_0 = \frac{W - \sqrt{C^* \cdot (1-\beta) + \beta \cdot W^2}}{1-\beta}$$

$$K = (W - U_0) \cdot H_0 = (H_0)^{\frac{3}{2}}$$

Substituting (10b) in (11), and after some mathematical developments, the differential equation to the free surface in the continuous interval is obtained:

$$\frac{\partial H}{\partial \zeta} = \frac{H^2 + H \cdot (H_0 - C^* - W^2 \cdot \beta) + \beta \cdot H_0^2}{\left(H_0^2 + H \cdot H_0 + H^2\right)} \qquad \textbf{(12)}$$

Finally, in order to generate "roll waves", starting from the equation (12), it is necessary that $\partial H/\partial \zeta H = H_0 > 0$, implicates in:

$$2.\beta \frac{1 - \sqrt{\beta + \frac{C^*.(1-\beta)}{W^2}}}{-\beta + \sqrt{\beta + \frac{C^*.(1-\beta)}{W^2}}} < 1 \qquad \textbf{(13)}$$

2.2 *Discussing the theoretical results, without diffusion*

The inequality (13) defines a dominion into which "roll waves" can be formed. Such results are illustrated in the Figure 1. It is observed that for an addition of the Bingham term (cohesion effect or critic tension τ_c), "roll waves" can be developed easily, i.e., the increase of this parameter would favour the development of these disturbances. This conclusion agrees, for example, with the experimental observations of Takahashi (1990), who generates "roll waves" in laboratory to Froude numbers F<2. If the fluid cohesion

C* is null, the inequality (13) is given by $\beta<1/4 \Leftrightarrow \tan(\theta)>4.g/C^2$, which agrees with Dressler (1949)-generation of "roll waves" in "clean water".

2.3 *Criterion for "roll waves" generation based on the analysis of linear stability, in the new Bingham rheology and with the inclusion of the viscous term*

The purpose of this paragraph is to evidence the formation criteria of "roll waves" based in the analysis

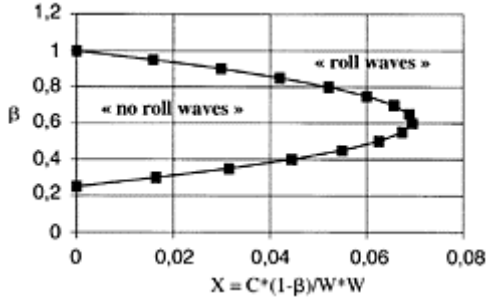

Figure 1. Dominion of existence of "roll waves".

of linear stability. In order to do that, resource will be made to the "shallow water system" (equations (1) and (2)). Adding the diffusion term $\partial/\partial x(h\upsilon\partial u/\partial x$ to the equation (2), throughout the current, in which "ν" represents the average kinematics viscosity; the quantity of movement equation becomes:

$$\frac{\partial(hu)}{\partial t} + \frac{\partial(ahu^2)}{\partial x} + gh\cos(\theta)\frac{\partial h}{\partial x} = g.h.\sin(\theta) - \frac{\tau_c}{\rho} - \frac{gu^2}{C_k^2} + \frac{\partial}{\partial x}\left(h\upsilon\frac{\partial u}{\partial x}\right) \qquad \textbf{(14)}$$

Thus, the second member of the equation (14) takes into consideration four effects: the weight force, represented by the gravity, the shearing due to the Bingham fluid modeling, turbulent dissipation through Chézy coefficient and, finally, the viscous dissipation represented by the term in "ν", adapted to the "shallow water" system.

The parameters that may at times evidence the probable instabilities in the flow curve pass necessarily by a process of system adimensionalization. Taking the uniform flow as a basis in the adimensionalization process, and applying the characteristic scales, such as $x=L\cdot x'$, $h=h_n.h'$ to lengths, $u=u_n\cdot u'$ to velocities and $C^*=\tau c/\rho\cdot g\cdot h_n.\sin(\theta)$ to tensions.

Where L represents the wave length and n an index that characterizes the normal or uniform regime, it is obtained (omitting the character (′)):

$$\frac{\partial h}{\partial t} + \frac{\partial (hu)}{\partial x} = 0 \qquad \textbf{(15)}$$

$$\frac{\partial u}{\partial t} + \alpha.u.\frac{\partial u}{\partial x} - (\alpha-1).\frac{u}{h}.\frac{\partial h}{\partial t} + \frac{1}{F^2}.\frac{\partial h}{\partial x} = \frac{\tan(\theta)}{\varepsilon.F^2}.((1-C^*).\frac{u^2}{h}) + \frac{1}{Re}.(\frac{\partial^2 u}{\partial x^2} + \frac{1}{h}.\frac{\partial u}{\partial x}.\frac{\partial h}{\partial x})$$

with:

$$F=\frac{u_n}{\sqrt{g.h_n.\cos(\theta)}} \; ; \; Re=\frac{u_n.L}{\nu} \text{ and } \varepsilon=\frac{h_n}{L} \qquad \textbf{(16)}$$

Concerning the study of linear stability, it is admitted that heights and velocities are submitted to small perturbations, such as: u=1+û with $\hat{u} \ll 1$ and h=1+ĥ with $\hat{h} \ll 1$.. Introducing the equation (15) in (16) and disregarding the second order terms, the equation system of the perturbed quantities h and u is obtained. Finally, omitting the notation (^):

$$\frac{\partial h}{\partial t} + \frac{\partial h}{\partial x} + \frac{\partial u}{\partial x} = 0 \qquad \textbf{(17)}$$

$$\frac{\partial u}{\partial t} + \alpha.(1+u).\frac{\partial u}{\partial x} - (\alpha-1).\frac{(1+u)}{(1+h)}.\frac{\partial h}{\partial t} + \frac{1}{F^2}.\frac{\partial h}{\partial x} = \frac{tg(\theta)}{\varepsilon.F^2}(1-\frac{C^*}{(1+h)}(1-C^*)\frac{(1+2u)}{1+h}) + \frac{1}{Re}(\frac{\partial^2 u}{\partial x^2} + \frac{1}{(1+h)}\frac{\partial u}{\partial x}\frac{\partial h}{\partial x}) \qquad \textbf{(18)}$$

The equation (17) can be inserted in (18), allowing the elimination of “u” and obtain an equation that only takes into consideration the variable “h”:

$$\frac{\partial^2 h}{\partial t^2} + 2\,\alpha\nu\frac{\partial^2 h}{\partial x \partial t} + (\alpha - \frac{1}{F^2})\frac{\partial^2 h}{\partial x^2} = \frac{1}{Re}(\frac{\partial^2 h}{\partial t \partial x^2} + \frac{\partial^2 h}{\partial x^3}) - (\frac{tg(\theta)}{\varepsilon.F^2})(C^*\frac{\partial h}{\partial x} - (1-C^*)(-2\frac{\partial u}{\partial x} - 3\frac{\partial h}{\partial x})) \qquad \textbf{(19)}$$

With the equation (19), the development criteria of instabilities of wave number k and of frequency *w* are researched. The solutions of the form $\mathbf{h(x,\ t)=H(k)\cdot e^{(ikx-wt)}}$ where $\mathbf{w=w_r+i\cdot w_i}$, are interesting to be obtained, observing that $w_r \geq 0$ in order to assure stability. Introducing h(x, t) in the equation (19), an equation of order 2 with complex coefficients is obtained. From this point, the real and the imaginary parts are separated, thus creating two other equations (one to w_r and another to wi), which allows the obtaining of polynomial $P(w_r)$, having as only incognito w_r. Here, it is interesting to discuss the existence and the nature of the root signals of $P(w_r)$. It is known that stability will only occur if the roots of $P(w_r)$ are positive or null. After some mathematical developments, it is demonstrated that $P(w_r)$ is a strictly monotonous function, decreasing in the interval$]-\infty; 0]$; thus, it is concluded that the condition needed and enough that the roots

of $P(w_r)$ are positive is that P(0) is positive (P(0)>0). After some mathematical developments, the critic Froude number F_c is obtained:

$$F_c = \sqrt{\frac{1}{\left(\frac{1}{2\cdot(1-C^*)+\frac{k^2\cdot\sigma}{Re}}-(\alpha-1)\right)^2-\alpha\cdot(\alpha-1)}} \qquad \textbf{(20)}$$

$$h_p = \frac{\tau_c}{\rho\, g \sin(\theta)} \quad (h_p : \text{depth of the 'plug'})$$

$$\alpha = \frac{9}{15}\frac{(8+7\cdot\frac{h_p}{h_n})}{(2+\frac{h_p}{h_n})^2} \qquad \sigma = \frac{\varepsilon . F^2}{\tan(\theta)}$$

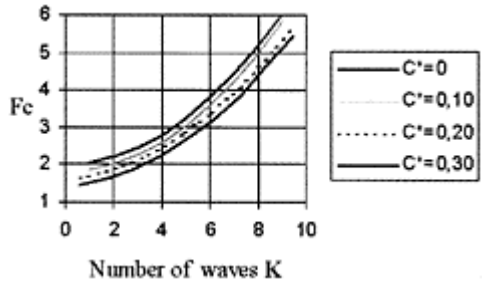

Figure 2. Critic Froude in function of the number k of waves.

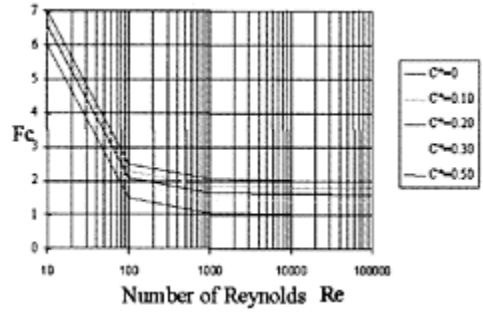

Figure 3. Critic Froude in function of Reynolds' number.

2.4 *Discussing the theoretical results, with diffusion*

From the previous results, some guiding formation criteria and the development of "roll waves" in function of the physic parameters can be illustrated. The following figures show the influence of the Reynolds' number Re and of the wave number k in function of the critic Froude number F_c for various cohesion values C* (Bingham effect). The Figure 2 shows the influence of the number of waves (wavelength) over critic Froude for two fixed parameters, $\zeta=\sigma/R_e=0.05$ and $\alpha=1.00$. It can be deduced from the Figure 2 that roll waves tend to develop more easily or more quickly to a scenery of small wave numbers and high values of critic tension of Bingham (cohesion effect C*). On one hand, it could be asserted that an increase in the cohesion value would guide or favor the appearance of instabilities of roll waves; on the other, long waves would be the first to destabilize.

Figure 3 shows the influence of the adimensional rigidity C* over the Froude number as a function of the Reynolds' number. It can be observed that in the same way that in the result illustrated in the Figure 2, an increase in the fluid cohesion would cause the precocious appearance of roll waves, to fixed Froude and Reynolds numbers.

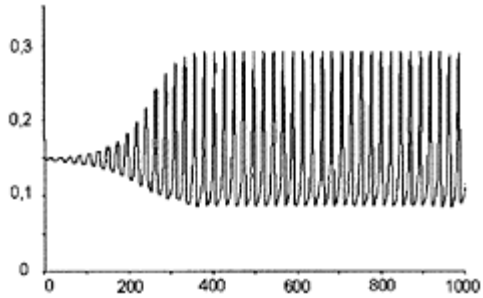

Figure 4. Roll waves amplitudes generated versus longitudinal distances (sinusoidal perturbation of T=3.14s; C*=0 and 1% of discharge).

3 VALIDATION TESTS—NUMERIC RESULTS AND DISCUSSIONS

The purpose of this paragraph is to present some results of numeric order in generating roll waves in Newtonian and non-Newtonian fluids. The simulation program developed had its theoretical formulation in the hyperbolic non-linear systems and its derivations, notedly the resolution of the Riemman problems (Vila, 1985). The numeric simulations were executed from VanLeer numeric schemes (second order in time and space) and effectuated in rectangular section canal of 1000m length (with increment of space $\Delta x=1.00$m) and significant slope of 30%. Working with flow regimes preferentially turbulent and supercritical, two upstream limit conditions could be fixed: discharge of 800l/s/m and depth of 0.15m. On this discharge, small perturbations (of per cent order)

were imposed, so as to generate stable roll waves to the canal downstream, as illustrated by the diagrams below.

A first series of tests were carried out, allowing a more global assessment of the phenomenon, mainly concerning the initial conditions of the perturbation imposed, as described below:

(a) an upstream perturbation on the discharge, sinusoidal perturbation type, was capable of generating well defined roll waves (Figure 4);
(b) a random perturbation was not able of generating well defined roll waves, i.e., with a preferential marked frequency; however, it generated a pulsing free surface, with chaotic aspects, as shown in Figure 5.

Concerning the amplitude of the imposed perturbation (sinusoidal perturbation), the results show that:

(a) to a given frequency, the perturbation amplitude should not influence over the amplitude of the generated roll wave;

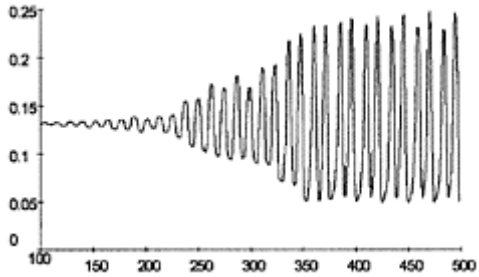

Figure 5. Pulsing surface from random perturbation versus longitudinal distances.

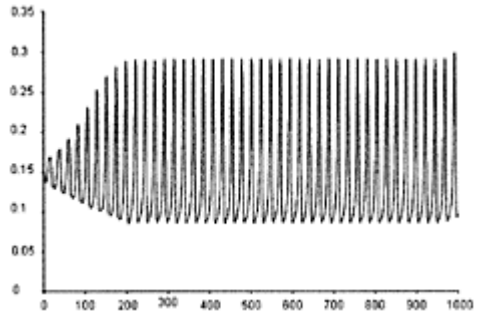

Figure 6. Roll waves amplitude generated versus longitudinal distances (10% discharge perturbation (C*=0).

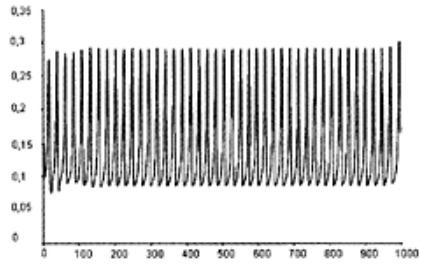

Figure 7. Roll waves amplitude generated versus longitudinal distances (50% discharge perturbation (C*=0).

(b) however, a higher or a lower perturbation amplitude should anticipate or postpone the appearance of the roll wave, as if perturbing the base flow without altering the amplitude of the generated roll wave.

See Figures 6 and 7.

Concerning the wave length of the imposed perturbation, the numeric tests show that the generated roll wave has the same length. A small perturbation of T=3.14s generated a roll wave of the same

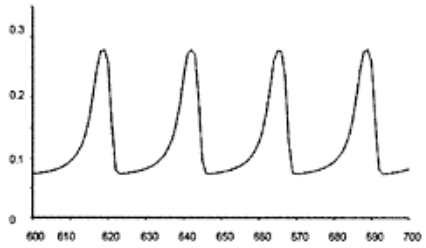

Figure 8. Detail of the roll wave illustrated in Figure 6.

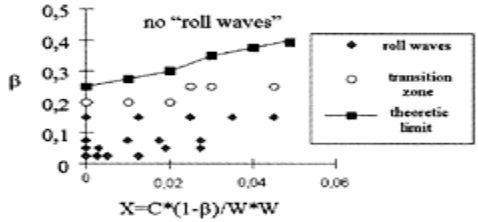

Figure 9. Generation dominions of roll waves in function of the canal declivity and Bingham effects.

period (with respective wave length of 25m). Figure 8 illustrates this result.

A second series of tests were performed, taking into consideration the new rheology and its implication over the generation and characteristics of the produced waves. Various tests were carried out, allowing the establishment of a border or dominion of roll waves formation in function of the parameters being used: β taking into consideration the canal declivity and its resistance; Bingham tension X=C*(1−β)/W*W (Figure 9).

For this case we could certify that for constant β, the Bingham tension effect seems not to influence, in a significant way, the period or the wave length, thus reconfirming the same conclusions for a newtonian fluid. On the other hand, when taking into consideration the cohesive effect (C*), to a given amplitude of perturbation, the roll waves appear earlier and present higher height values. Figures 10 and 11 illustrate these results.

A third series of tests consisted in verifying the sensibility of our system nonlinear when submitted to simultaneous small perturbations and frequencies and amplitude different of $h(x, t)=H_0e^{(kx-w(t)t)}$, where k is the number of waves and w(t) are the frequencies. The diagram below illustrates some results for various configurations: Figures 12, 13 (for Newtonian fluids) and Figures 14, 15 (non-Newtonian fluids).

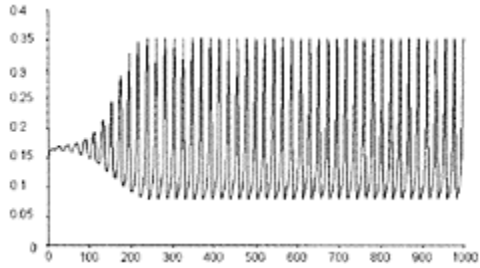

Figure 10. Roll waves with T perturbation of 3.14s (C*=0.10).

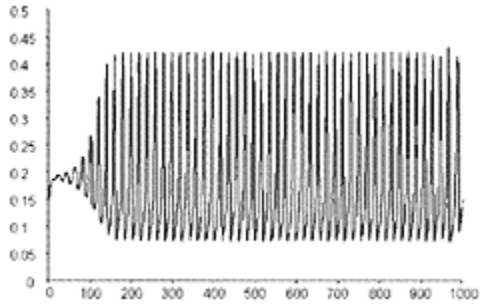

Figure 11. Roll waves with T peiturbation of 3.14s (C*=0.20).

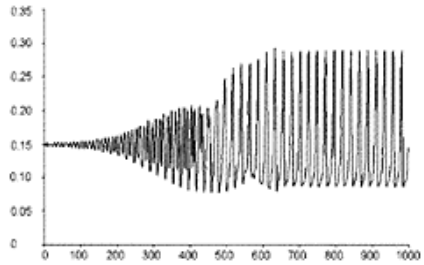

Figure 12. Roll waves with T perturbation=3.14s and different amplitudes (C*=0).

From these results, some comments are in order:

(a) the perturbation amplitude does not intervene in the generated roll wave amplitude;
(b) the generated downstream roll wave presents the wave period or length regarding the bigger wave length of the different perturbations imposed upstream, after passing and capturing other frequencies (lower wavelengths). Another analysis which could be made, confirming such results, is related to the fact that long waves (big wavelengths)

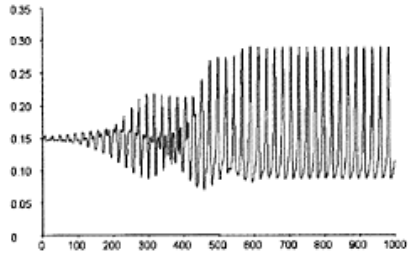

Figure 13. Roll waves with T perturbation=1.00s, 1.57s and 3.14s and constant amplitudes (C*=0).

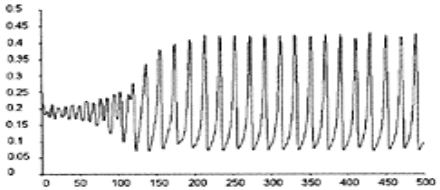

Figure 14. Roll waves with T perturbation=1.00s, 1.57s and 3.14s and different amplitudes (C*=0.2).

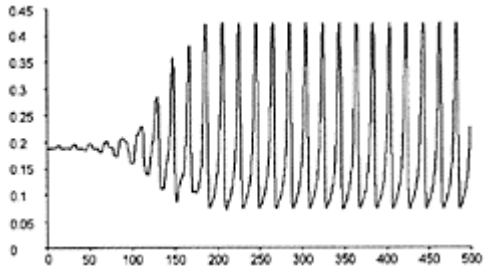

Figure 15. Roll waves with T perturbation=1.00s, 1.57s and 3.14s and constant amplitudes s=0.2).

are almost always the first to destabilize, as illustrated in Figure 2;

(c) to the new Bingham rheology, based in Figures 10, 11, it is proved that the tendencies are the same shown for the Newtonian fluid, i.e., the roll waves appear earlier and with higher height values.

REFERENCES

Brock, R.R. 1966. Discussion of Critical analysis of open-channel resistance, by H.Rouse. Journal Of Hydraulic Divison, ASCE, Vol. 92, No. HY2:403–409.

Brock, R.R. 1967. Development of roll waves in open channels—Report No. KH-R-16. W.M.Keck Laboratory of Hydraulics and Water Resources, California Institute of Technology.

Chen, C.L. 1992. Momentum and energy coefficients based on power-law velocity profile. J. Of Hydraulic Engineering, ASCE, Vol. 118, No. 11, pp. 1571–1584.

Dressler, R.F. 1949. Mathematical solution of the problem of roll waves in inclined open channels. Communs Pure Appl. Math., Vol. 2:149–194.

Godunov, S.K. 1959. A difference method for numerical calculation of discontinuous equations of hydrodynamics. Math.Sb, 47(89):271–300.

Ishihara, T., Iwagaki, Y. & Iwasa, Y. 1954. Theory of the roll wave train in laminar water flow on a steep slope surface. Transactions of Japan Society of Civil Engineers 19:46–57 (in Japanese).

Iwasa, Y. 1954. The criterion for instability of steady uniform flows in open channels. Memoirs of the Faculty of Engineering, Kyoto University, Japan, Vol. 16, No. 6: 264–275.

Jeffreys, H.J. 1925. The flow of water in an inclined channel of rectangular section. Philosophical Magazine, Series 6, Vol. 49:793–807.

Julien, P.Y. & Hartley, D.M. 1985. Formation of roll waves in laminar sheet flow—Rep. Cer84–85pyj-dmhl 8. Department of civil engineering, Colorado state university.

Julien, P.Y. & Hartley, D.M. 1986. Formation of roll waves in laminar sheet flow. Journal of Hydraulic Research 24: 5–17.

Kranenburg, C. 1992. On the evolution of roll waves. Journal of Hydraulic Research, Vol. 245:249–261.

Lamberti, A. & Longo, S. 2000. Roll waves e dissipazione in correnti idriche e nei debris flow (Roll waves and dissipation in water streams and in debris flow). Proc. XXVII National Conference on Hydraulics, Gndci, Vol. 1:85–94.

Mayer, P.G.W. 1957. A study of roll waves and slug flows in inclined open channels. Dissertation cornell univ.

Needham, D.J. & Merkin, J.H. 1984. On roll waves down an open inclined channel. Proc. r. soc. lond a 394:259–278

Ng, C. & Mei, C.C. 1994. Roll waves on a shallow layer of mud modelled as a power-law Fluid. Journal of Fluid Mechanics, 263:151–183.

Roe, P.L. Approximate riemann solvers, parameter vectors and difference schemes, J. Comp. Phys. Vol. 43:357–372.

Saint Venant, B. 1871. Théorie du mouvement non permanent des eaux, Institut de France, Académie des sciences, Comptes Rendus, Paris, Vol. 73:147–237.

Takahashi, T. 1990. Debris flow, Monograph, Iahr, Balkema, Rotterdam.

Vanleer, B. 1981. Toward the ultimate conservative difference scheme. Journal of Comp. Phys. 32, 101–136.

Vila, J.P. 1986. Simplified godounov schemes for (2,2) systems of conservation laws. Siam J.Numerical Anal. Vol. 23 No. 6:1173–1192.

Physical model tests for dike-break induced, two-dimensional flood wave propagation

S.Briechle, A.Joeppen & J.Köngeter
Institute of Hydmulic Engineering and Water Resources Management, Aachen University, Germany

River Flow 2004—Greco, Carravetta & Della Morte (eds.)

ABSTRACT: There is a lack of knowledge about the properties of a flood wave due to dike break and failure of (mobile) flood protection walls, on which a prediction of the implicated risk could be based. Fore this reason a physical model, which takes into account the special boundary conditions of such an incident, was built and measurements were undertaken. The results of a variation of initial water depth and discharge in the river and the eifect of a thin water film on the propagation area are presented and discussed.

1 MOTIVATION AND AIMS

Dikes and (mobile) flood protection walls defend areas used by man from flooding. In case of failure however, the resulting flood wave implicates an extra risk to people and goods in the near field of the breach because of the strong dynamic forces. At the moment it is hard to assess this risk. Due to the rareness and dangerousness of such failures, data from real-world incidents are insufficient to base a prediction of the flood wave propagation on these and there are no analytical solutions for this problem. Attempts to predict the wave numerically are made frequently, but produce uncertain results: Assumptions and simplifications to make the problem computable usually do not reproduce all the complex effects of roughness, turbulence, flow inhomogeneities (e.g. air entrainment) and vertical momentum at places of strong surface slope (e.g. in the near field of the breach or at the wave front). Furthermore validation examples are mostly unavailable. The extend of deviation of the calculation results from the reality is therefore not known unerringly and it is not easy to ascertain how to improve numerical models best.

For this reason experiments are conducted in a physical model. Data of the flood wave propagation are gathered, which later can be used for the validation and improvement of numerical models. Furthermore insight into the wave is gained, especially concerning flow processes, effects of systematically variedparameters, scalability of the results to

other dimensions and as a basis for a simplified projection of the flood wave propagation without an expensive numerical calculation.

2 PROBLEM DEFINITION

2.1 *Comparison of dam- and dike-break*

For the *dam*-break case there can be found several detailed investigations in literature, Hager & Lauber (1996) give a good review. Most physical investigations took place in flumes and therefore reduced the problem to one dimension—propagation takes place only along the flume, lateral propagation is not considered—, in addition breach and reservoir have the same width. Only few investigations allow for a propagation into an area, combined with a breach width smaller than the width of the reservoir. Most recent example is Kulisch (2003), other model tests were conducted by Jovanović & Djordjevic (1995), Fraccarollo & Toro (1995), Naaim & Brugnot (1994), Tingsanchali & Rattanapitikon (1993) and Memos et al. (1983).

However, those findings are not directly transferable to a wave resulting from the failure of a flood protection structure on a river. Figure 1 depicts the

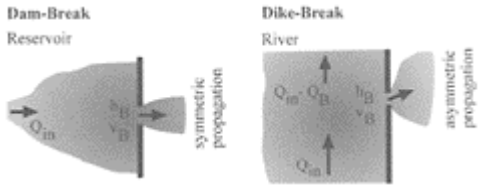

Figure 1. Comparison of flood wave propagation caused by dam- and by dike-break, Q_{in}=discharge into reservoir/river respectively, Q_b=discharge through breach, h_b=water depth in breach, *vb*=velocity in breach.

other two mayor differences: Compared to the reservoir of a dam, in which the water depth converges to zero with time, the discharge Q_{in} in a river can not be neglected—the river bed will not empty completely, but after a certain transitional period a steady state condition will be reached with constant water depth h_B in the breach. Additionally in a river the velocity component parallel to the protection structure has to be considered, since it will deform the wave asymmetrically. The only physical model known to the authors, which accounts for the river flow apart from there own can be found in Aureli & Mignosa (2002).

2.2 *Delimitation of this investigation*

A complete, instantaneous failure is assumed with the chosen mechanism (see section 3.1). A real dike or (mobile) flood protection wall will probably not fail in this idealized way. However, this assumption seems justifiable due to the following reasons:

– Analytical solutions for the dam-break problem and most numerical simulations start from a vertical water front at the breach section. To be able to compare our results with those calculations this idealized scenario seems most appropriate.
– At present knowledge on the various failure mechanisms of dikes and (mobile) flood protection walls and their interaction with the flow is poor, resulting in high uncertainties. To reduce these for this investigation, the failure mechanisms were neglected for the time being.
– It is considered a well defined worst case scenario which corresponds to an instantaneous and total failure at starting time giving the highest factor of safety for risk considerations.

The two-dimensional wave propagation is investigated in the near field of the breach, where the dynamic forces are crucial with respect to the later use of the results in risk assessment procedures. Also in this area (i.e. near the breach) the vertical momentum is likely to become important for the flow process.

The unsteady state immediately after the failure is investigated. Additionally and in contrast to past investigations, the steady state case, reached after a certain time span due to the constant discharge in the river as described above, is examined.

There is no fixed scaling factor applied. Considering initial water depth before break it ranges between nearly 1:1, as would be applicable for small mobile flood protection walls in Germany, to up to 1:30 and more, for example for dikes in the Lower Rhine Area in Germany of up to 15m height. Therefore scalability is of particular interest.

3 EXPERIMENTAL SETUP AND MEASURING TECHNIQUES

3.1 *Physical model*

To satisfy the needs described above a physical model was built at the Institute of Hydraulic Engineering and Water Resources Management (IWW) at Aachen University, which takes into account the special boundary conditions of the dike-break problem.

A channel, 1.0m wide and representing the river, is joined to an area (3.5m×4.0m), on which the propagation of the flood wave can be measured (see fig. 2). Channel and area are separated by the channel wall, i.e. the dike or flood protection wall, in which a pneumatically driven gate is installed for simulation of the breach (see below). The water is allowed to fall freely off the other three boundaries of the area. The floor of the propagation area is made from glass, not only to minimize roughness, but to observe the wave and take measurements from below as well.

In this physical model the following parameters can be varied to study their effect on the flood wave propagation: The initial water depth can be risen to up to 50cm by adjusting a weir at the end of the channel, the discharge in the channel can be set from Q_{in}=0 to 390 l/s and the breach width can be chosen to 30, 50 or 70cm, rectangular in

shape. The area is horizontal and can be covered with different materials to study roughness effects.

The flap initializes the flood wave propagation by opening in a minimized time span of less than 0.1s. The movement of the flap is illustrated in figure 3. The design aimed at the immediate clearance of the entire vertical water front in the breach. This distinguishes the mechanism from the gates used in the past in dam- and dike-break experiments, were the wave propagation was usually initialized by lifting a sliding panel. However, in that case the foot of the wave is

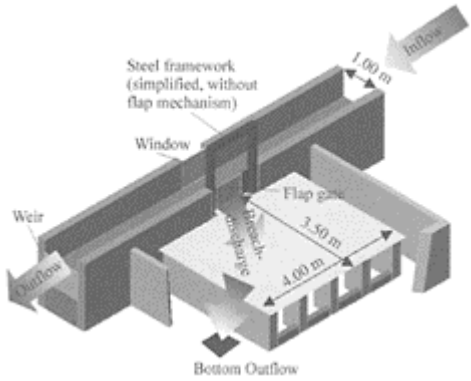

Figure 2. Physical model.

released first, the whole front only after a short delay. This problem is eliminated by the new flap mechanism, but a pull could be exerted on the water body by the horizontal component of its movement. This is however reduced by the hinges on top, which allow the flap to swing. The effect could be shown in comparison to a flap which was fixed to the steel framework.

3.2 *Measuring techniques*

The two-dimensional measuring arrangement is demanding. Strong spatial and temporal changes of the propagating wave, air entrainment and piling up of

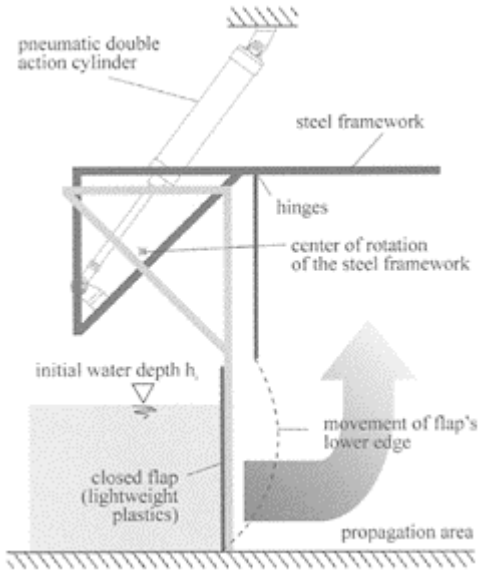

Figure 3. Opening mechanism.

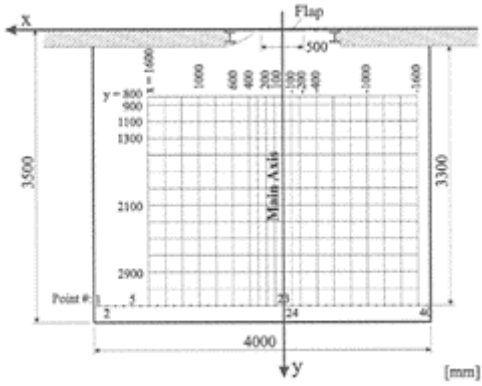

Figure 4. Coordinate system.

water (if the measuring technique is intrusive) entail manifold problems. The wave is difficult to access on the propagation area and all data have to be gathered in two dimensions, which results in a great amount of data.

The water depth is measured by ultrasonic sensors in a dense raster on the propagation area. The measuring locations are the intersection points of the raster lines in figure 4. The sensors have a measuring frequency of 50Hz and are optimized for steep wave fronts. They are not influenced by the vertical momentum of the wave, like pressure gauges installed in the floor would be. Our experience on the physical model indicates that the error is usually less than 2mm. Unfortunately measurement is not possible in the

range of flap movement up to approximately 800mm distance from the breach. However, in the breach itself the water depth can be determined.

Complementary a CCD-camera was installed, recording the whole flood wave from top with a spatial resolution of 756×550 pixels (in gray scales), again giving results with a frequency of 50Hz after de-interlacing of the recorded images. Digital image processing is used to adjust distortion, for automated wave front localization and for post-processing with respect to front velocities, asymmetry etc. When a thin water film remains on the propagation area between the experiments, the entrained air can be used as white contrast for automated digital image processing of the images (see section 4). To detect the wave front in the dried case, the water must be colored to increase contrast, those images can not yet be presented.

Both measuring devices are triggered with the opening mechanism to bear relation to the start of the opening process.

Additionally the wave is recorded by high-speed camera or camcorder to gain an insight into details as the need arises.

3.3 *Measuring program*

The measuring campaign is still under way. Different boundary conditions, namely initial water depth, discharge in the channel, breach width and roughness materials on the propagation area will be systematically tested to be able to quantify their effects. In this paper combinations of Q_{in}=300 l/s discharge in the river and initial water depth of h_i=30 to 50cm are presented. The breach width was 0.5m and the floor of the propagation area was plain glass.

4 RESULTS

4.1 *Effect of initial water depth in the channel*

Figure 5 shows water depth over time on the main axis for a variety of initial water depths at three different distances from the flap. As a first attempt the data

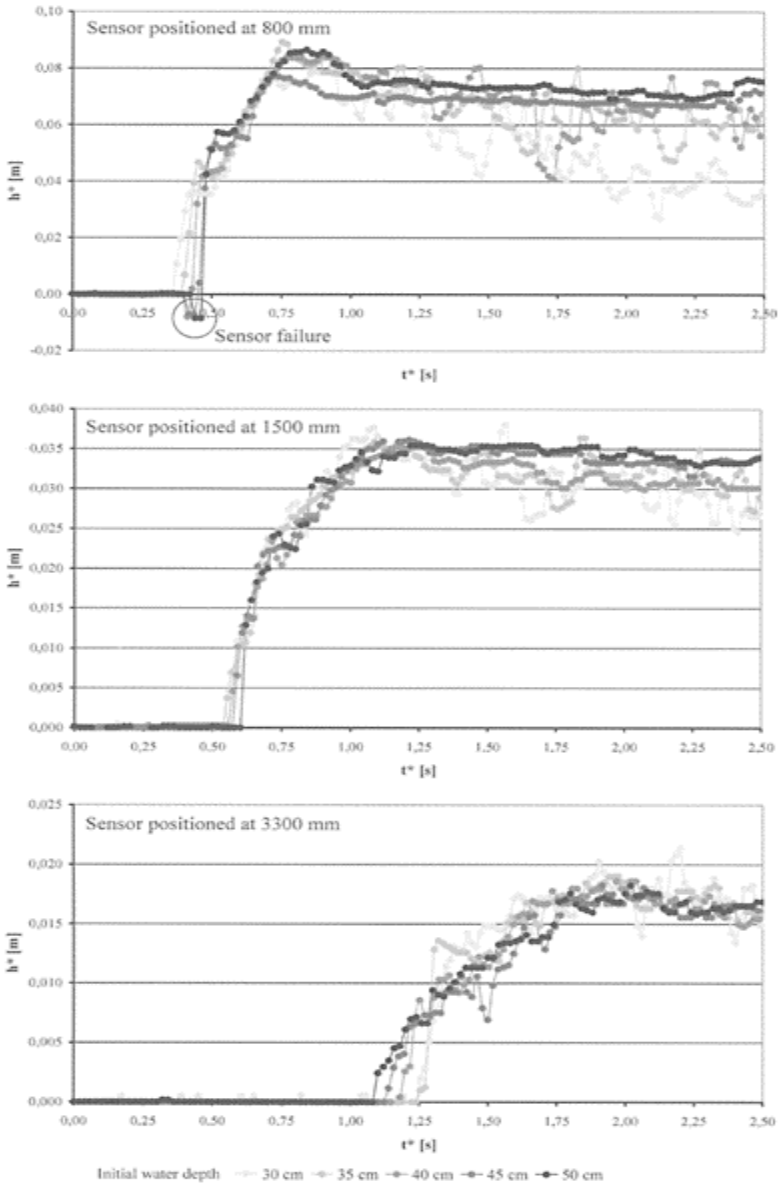

Figure 5. Non-dimensional water depth for five different initial water depths on the main axis at three distances from the flap. Discharge in channel Q_{in}=300 l/s, the propagation area was dried before every experiment.

was scaled by applying Froude's law. For this purpose the model is considered superelevated. In the horizontal directions x and y the scale basis is set to L_{basis}=0.50m (breach width). This width does not change with the modification of the initial water depth, therefore the horizontal scaling factor L equals 1.0. The same would hold for the distances of the sensors from the breach in y direction. As a scale basis in vertical direction the initial water depth of H_{basis}=0.50m is chosen, giving different vertical scale factors H for different initial water depths. Based on Kobus (1978) the following equations can be derived for the superelevation in this case:

$$L = \frac{L_{basis}}{L_{variable}} = \frac{0.50\,\text{m}}{0.50\,\text{m}} = 1.0 = const. \tag{1}$$

$$H = \frac{H_{basis}}{H_{variable}} = \frac{0.50\,\text{m}}{h_i} \tag{2}$$

$$n = \frac{L}{H} = \frac{h_i}{0.50\,\text{m}} \tag{3}$$

$$T = \sqrt{L \cdot n} = \sqrt{n} \tag{4}$$

where n=superelevation factor, T=time scaling factor.

Table 1 assembles the results of the equations (1) to (4) for the different initial water depths.

With these values and the following equation (5) the data for figure 5 were obtained:

$$h^* = H \cdot h = 0.50\,\text{m} \cdot \frac{h}{h_i} \quad \text{and} \quad t^* = T \cdot t = \sqrt{\frac{h_i}{0.50\,\text{m}}} \cdot t \tag{5}$$

where h^* and t^* are the scaled values for the measured water depth and time respectively.

At position 800mm the sensors failed for higher initial water depth, presumably due to the extreme steepness of the front in this place. However, the time the sensor failure occurs can be assumed to be the arrival time.

If the waves were scalable this way, all lines in the graphs should coincide. The water depth h therefore seems to be scalable reasonably well within the

Table 1. Results of the equations (1) to (4) for the different initial water depths.

Initial water depth	Vertical scaling factor	Superelevation factor	Time scaling factor
h_i [m]	H [–]	n [–]	T [–]
0.50	1.0	1.0	1.000
0.45	1.111	0.9	0.949
0.40	1.25	0.8	0.894
0.35	1.429	0.7	0.837
0.30	1.667	0.6	0.775

proximity of the maximum. Differences can be found in a little “step” in the rise before the maximum—the step is lower for lower initial water depths. After the maximum the water depth reduces stronger and fluctuation increases with reduced initial water depth. The reduction in depth is explicable by the fact that the discharge in the channel was not scaled as well, but stayed at 300 l/s and the weir at the outflow of the channel was adjusted accordingly to obtain the different initial water depths and was fixed during the experiments.

Regarding the arrival time of the wave, at position 800mm the wave with the lowest initial water depth arrives first, at position 1500mm the arrival times are nearly identical and at 3300mm the relation is conversed and the wave with the highest initial water depth arrives first.

An explanation for the growing deviation of the measured values with decreasing initial water depth could be, that the simple superelevation rules are only applicable in cases in which the effects of vertical velocity components can be neglected. This is not the case especially near the breach, where all the kinetic energy is derived from the potential difference and the water surface is strongly inclined—this could explain the overestimation of acceleration especially for the lower initial water depth. Additionally a discrepancy of roughness effects can develop—this could be an explanation for the underestimation of the wave velocity in the longer run, where the water depths for the lower initial water depth is less and roughness effects are stronger.

4.2 *Effect of a thin water film*

If a thin water film remains between two tests, i.e. the water drains off over the three free boundaries of the propagation area but it is not dried explicitly, the wave front is significantly altered. Figure 6 shows the differences between the two cases “thin water film” and “completely dried” for a discharge of 300 l/s in the channel and an initial water depth of 50cm. Near the flap the two cases are similar, between 1300 and 1700mm distance however, a difference starts to appear: in the “water film” case the tip of the wave starts to built up a high peak whereas the “dried” case flattens more and more. The envelope of both cases is adumbrated in the figure for orientation. Parallely the arrival time of the wave front at the sensor is increased in the “water film” case compared to the “dried” case, i.e. the velocity of the wave front slowed down by the water film.

The building up of the peak could be due to piling up of the water in the film in front of the strong growing circumference of the wave. However, this can not be the full explanation, since the peak flattens down again after a maximum at about 2500mm distance from the flap. In the photographs in figure 7, recorded by the CCD-camera, strong air entrainment can be perceived as a white band at the wave front, which indicates strong turbulence and roughness effects. The white band is completely absent in the case of a dried propagation area.

A similar peak can be found in Stansby et al. (1998) with a ratio of 0.1 between the water depth on the propagation area and in the reservoir before dam-break. Using a camera, recording through the sides of their flume they observed a “mushroom” shaped wave front.

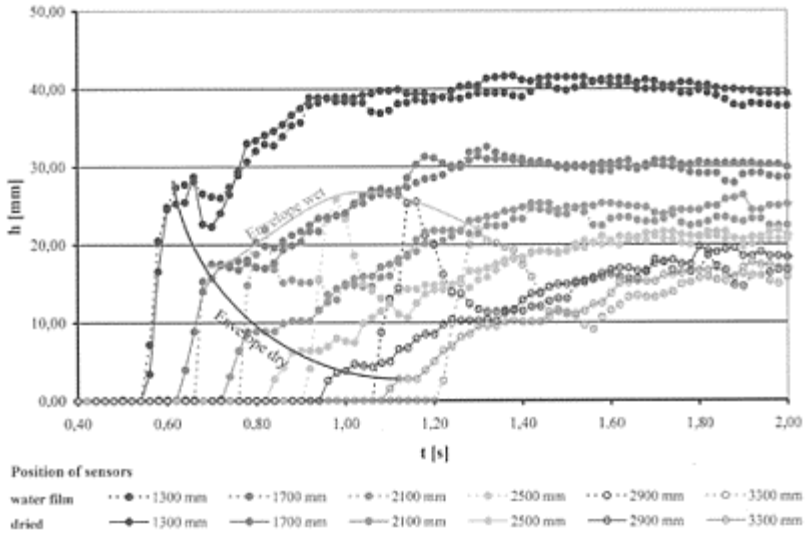

Figure 6. Comparison of the cases "thin water film" and "dried" at six different distances from the flap. Water depth on the main axis over time for intitial water depth h_i=50cm and discharge in channel Q_{in}=300 l/s.

4.3 *Effect of discharge in the channel*

In figure 5 the water depth seems to converge to a constant final value with time. This quasi steady state however lasts only for a short time, since when the negative surge is reflected at the ends of the channel, it causes the water level to drop in progressive stages. In case of higher discharge in the river, the decrease in water level is more even, i.e. the surge reflection is less influential.

Figure 8 shows the position of the wave front with an interval of Δt=0.02s for the cases of no discharge in the channel and, for comparison, with 300 l/s. The sporadic interruptions of the lines at small y-values are caused by the moving flap. The propagation area was not dried, i.e. the thin water film remained between the experiments and air entrainment made the wave visible (see section 3.2).

In the case of no discharge in the top part of the figure, the wave propagation is symmetric and onion shaped. In the bottom part of the figure the trajectory of the wave tips were added. The derivation from the main axis is relatively small. Therefore in the preceding sections the main axis only was considered the water depth discussions.

The deviation of the wave tip is defined by an interaction of initial water depth and the discharge in the channel. The effect of initial water depth and discharge can be combined in the Froude number of the channel before break:

$$Fr = \frac{v}{\sqrt{g \cdot h}} \qquad (6)$$

in which the numerator with the velocity *v* represents the momentum resulting from the discharge parallel to the channel and the denominator with water depth *h* and gravitational constant g represents the momentum from gravitation. The result is shown in figure 9, in which the data points coincide reasonable well with a trend line. The angle of deviation is greater with greater discharge, i.e. velocity in the channel. Furthermore the deviation is greater for lower initial water depth, i.e. lower velocities of the wave front propagation.

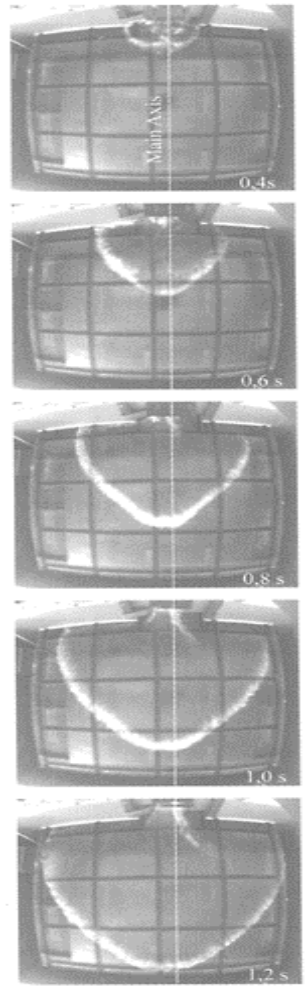

Figure 7. CCD-camera recordings at five different time steps with an

interval of Δt=0.2s. Initial water depth h_i=50cm, discharge in channel Q_{in}=300 l/s.

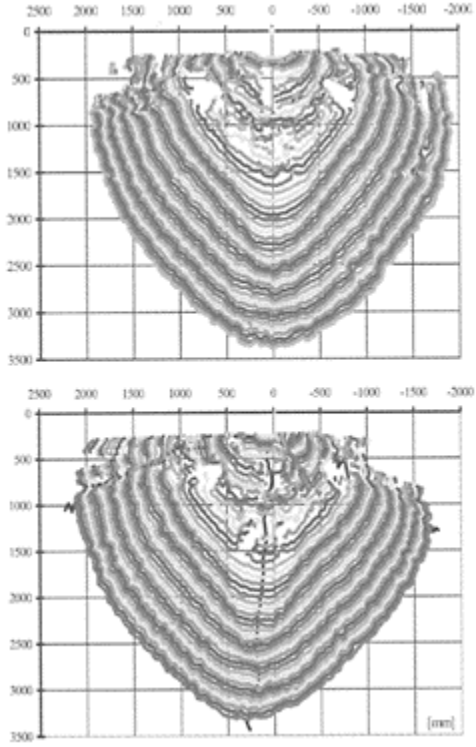

Figure 8. Position of the wave front with an interval of Δt=0.02s. Initial water depth h_i=50cm, discharge in channel Q_{in}=0 l/s (top) and 300 l/s (bottom). In the bottom part of the figure the trajectory of the wave tips were added. The propagation area was not dried, i.e. covered with a thin water film.

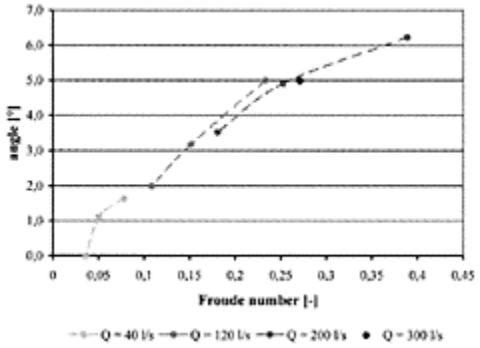

Figure 9. Deviation angle of the wave tip over Froude number before breach. For every discharge (except 300 l/s) the three initial water depths (30, 40 and 50cm) are plotted, the data points with the smallest angle corresponds to the highest initial water depth.

5 CONCLUSIONS AND FUTURE WORK

There are many open questions concerning the flood wave propagation following a dike-break or the failure of a (mobile) flood protection wall. This paper presents first results of a systematic investigation of the influence factors and thereby starts to answer some of those questions.

The analysis of the data shows, that the water depth of the propagating wave is already scalable with respect to the initial water depth by easy means, but there are still some deviations which have to be investigated further. This holds especially in the case of the arrival time, which implies the velocity of the wave front.

A thin water film, which remains when the propagation area is not dried explicitly between the experiments, alters the shape of the wave front significantly by building up a prominent peak and slowing down the wave front velocity.

The sideways deviation of the wave tip position from the main axis is determined by an interaction of initial water depth and the discharge in the channel and can be estimated reasonably well by using the Froude number of the channel before failure.

In the future the physical model tests will be systematically completed, to gain more insight into the flow processes of the flood wave, to be able to quantify the influence factors and to assure accurate scaling of the results to other dimensions.

REFERENCES

Aureli, F. & Mignosa, P. 2002. Rapidly varying flows due to levee-breaking. In D.Bousmar & Y.Zech (eds.), River Flow 2002, *Proc. International Conference on Fluvial Hydraulics, Louvain-la-Neuve, Belgium, 4–6 September, 2002*. Rotterdam: Balkema: 459–466.

Fraccarollo, L. & Toro, E.F. 1995. Experimental and numerical assessment of the shallow water model for two-dimensional dam-break type problems. *Journal of Hydraulic Research* 33(6):843–863.

Hager, W.H. & Lauber, G. 1996. Hydraulische Experimente zum Talsperrenbruchproblem. *Schweizer Ingenieur und Architekt* 14(24):515–524.

Jovanovic, M. & Djordjevic, D. 1995. Experimental verification of the MacCormack numerical scheme. *Advances in Engineering Software* 23:61−67.

Kobus, H. (ed.) 1978. *Wasserbauliches Versuchswesen.* Arbeitsausschuss Wasserbauliches Versuchs- und Messwesen, Deutscher Verband für Wasserwirtschaft, Mitteilungsheft 4. Berlin:DVWW.

Kulisch 2003. *Ausbreitung von Dammbruchwellen im physikalischen Modell.* Mitteilungen des Institut für Wasserwesen, Universität der Bundeswehr München, Heft 79. München:Oldenbourg.

Memos, C.D., Georgakakos, A. & Vomvoris, S. 1983. Some experimental results of the two-dimensional dam-break problem. *Proc. 20th IAHR Congress for Hydraulic Research, Moscow, September 1983:*555–563.

Naaim, M. & Brugnot, G. 1994. Free surface flow modelling on a complex topography. In R.Molinaro & L.Natale (eds.), *Modelling of Flood Propagation over Initially Dry Areas, Proc. of the Specialty Conference at Enel-Dsr-Cris, Milan, Italy, 29 June-1 July, 1994:*298–308. New York: American Society of Civil Engineers.

Stansby, P.K., Chegini, A. & Barnes, T.C.D. 1998. The initial stages of dam-break flow. *Journal of FluidMechanics* 374: 407–424.

Tingsanchali, T. & Rattanapitikon, W. 1993. 2-D mathematical modelling for dam break wave propagation in super-critical and subcritical flows. *Proc. 25th IAHR Congress for Hydraulic Research, Tokyo, Japan, 29 August-3 September* 1993:25–32.

Dispersive effects on linear instability of the Saint Venant flow model

C.Di Cristo
Dipartimento di Ingegneria Idraulica ed Ambientale "Girolamo Ippolito", Università degli Studi di Napoli "Federico II", Napoli, Italy

A.Vacca
Dipartimento di Ingegneria Civile, Seconda Università degli Studi di Napoli, Aversa (Ce), Italy

River Flow 2004—Greco, Carravetta & Della Morte (eds.)

ABSTRACT: A spatial linear stability analysis of the one-dimensional St. Venant flow model, accounting for the dispersive effects, is carried out in the present paper. The theoretical investigation allows to discuss about the influence of channel length on roll-waves occurrence. In order to provide a rigorous justification for selecting the spatial stability theory, a preliminary proof of the convective nature of the flow instability is furthermore performed. The results of the spatial analysis show a non-negligible influence of the disturbance frequency on the perturbation spatial growth rate. As a consequence the semi-empirical criteria commonly employed for predicting roll-waves occurrence, which do not take into account the frequency effects, may lead to overestimate the minimum channel length above which the phenomenon is not perceivable.

1 INTRODUCTION

High velocity flows in steep channels may exhibit surface instabilities, perceivable as a series of water waves. As these waves propagate downstream they increase in amplitude and eventually break forming hydraulic bores. The series of waves just described are the so called "roll waves" and occur usually in man-made channels, such as draining systems and dam spill-ways. Generally, roll-waves presence is undesirable since they may determine a water overflow from the channel sides and excessive intermittency at the outlet. In studying such a phenomenon, two basic issues arise:

– identifying the necessary conditions under which roll-waves appear;
– predicting roll-waves evolution along the channel.

Only the former question will be addressed herein.

From the theoretical point of view, the generation process of roll-waves has been thoroughly and deeply investigated. In what follows we will restrict the discussion on the analyses performed with reference to the linearized one-dimensional flow model (St Venant equations) in which the field variables, mean velocity and flow depth, are assumed to be smooth. Under such assumptions roll-waves generation process has been fruitfully interpreted in terms of instability of the linearized flow model.

Many temporal linear stability analyses have been performed (Brock, 1970; Berlamont, 1976; Ponce & Simon, 1977; Berlamont & Vanderstappen, 1981) in order to individuate the critical values of relevant dimensionless—Reynolds and Froude—numbers corresponding to the appearance of roll-waves. For instance, assuming the channel to be sufficiently wide and expressing the bottom shear stress as a quadratic function of the mean velocity, a critical value of the Froude number, F_{rc}=2, below which roll waves cannot occur, has been found (Brock, 1970). Furthermore all conditions of flow characterized by $F_r>F_{rc}$ are unstable, independently of the perturbation wave-length values. Several experiments (see for instance Brock, 1969) confirmed the absence of roll-waves for $F_r<F_{rc}$, while their presence was not always detected for $F_r>F_{rc}$.

In contrast with the temporal analysis and to take into account the developing character of roll-waves, spatial linear stability analyses have been performed, starting from the hyperbolic character of the St Venant equations (Vedernikov, 1945, 1946; Liggett, 1975; Julien & Hartley, 1986). The point-wise perturbation is assumed to propagate downstream with the celerity of the faster shallow-water wave, according to the hyperbolic wave theory. In terms of stability region the results of the temporal analysis are essentially confirmed, despite the strong different space-time evolution of the perturbation.

Whether the temporal or the spatial technique is more appropriate to investigate the instability of St Venant flow model depends on the nature, *Convective* or *Absolute*, of the instability (Huerre & Monkewitz, 1990). An instability is defined as Convective if a localized initial small perturbation, growing in time, is swept away from the source only in one direction, whereas the instability is Absolute if it spreads in all directions. Only when the instability is Convective, spatial analysis may describe fruitfully its evolution.

The definition of the instability nature allows to verify the theoretical assumptions embodied in some semi-empirical criteria defining the minimum channel length below which the roll-waves presence is not perceivable, even in linearly unstable conditions of flow. These criteria, tested and calibrated using many available experimental data, start from the space-time evolution of perturbations resulting from the spatial linear hyperbolic analysis.

Montuori (1961, 1963), and later Liggett (1975), proposed to relate the critical Froude number value upon the channel length L; for sufficiently small values of L no roll-waves appear. Considering the process as Reynolds independent, the critical Froude number is expressed as a monotone decreasing function of the channel length whose value, for sufficiently large L, is F_{rc}. Similar conclusions have been drawn by Julien & Hartley (1986) who studied roll waves formation process in highly viscous mud-flows observable in steep mountain channels. It is worth of note that the above semi-empirical criteria

share some similarities with the e^n-method, originally proposed by Van Ingen (1956) and by Smith & Gamberoni (1956), commonly used to give an engineering prediction of the boundary layers transition location.

In the present paper the convective nature of the instability is preliminarily proved by examining the linear impulse response of a given uniform base flow. Following the Briggs criterion (Briggs, 1964), an analysis concerning the behaviour of the spatial branches associated with the dispersion equation is carried out in the complex k and ω planes, where ω and k are the complex pulsation and wave-number of the disturbance, respectively.

Furthermore a spatial linear stability analysis in terms of flow response to a point-wise time periodic perturbation is performed. The analysis naturally accounts for dispersive effects. The strict dependence on the source frequency of the perturbation spatial growth rate, whose expression constitutes the theoretical starting point of some criteria commonly employed in hydraulic engineering applications, is finally discussed.

2 GOVERNING EQUATIONS

The system under investigation is an incompressible fluid flowing in a broad rectangular channel without inflow or outflow with a non-erodible plane sloping bed. The one-dimensional equations governing the motion are the well-known St. Venant equations:

$$\frac{\partial u}{\partial t}+u\frac{\partial u}{\partial x}+g\frac{\partial h}{\partial x}+\frac{\tau_b}{\rho h}=gS_0 \tag{1}$$

$$\frac{\partial h}{\partial t}+u\frac{\partial h}{\partial x}+h\frac{\partial u}{\partial x}=0 \tag{2}$$

in which x=streamwise coordinate, t=time variable, g=gravity, ρ=water density, u=depth-averaged velocity, h=depth of the water surface, S_0=bed slope, τ_b=bed shear stress.

Starting from a steady uniform flow $u=u_0$, $h=h_0$, the base state is perturbed by an infinitesimal fluctuation, so that $u=u_0+u'$, $h=h_0+h'$, $\tau_b=\tau_{b0}+\tau_b'$. The substitution of the perturbed variables in equations (1)–(2) leads, after the linearization, to the following problem:

$$\frac{\partial u'}{\partial t}+u_0\frac{\partial u'}{\partial x}+g\frac{\partial h'}{\partial x}+gS_0\left(\frac{\tau_b'}{\tau_{b0}}-\frac{h'}{h_0}\right)=0 \tag{3}$$

$$\frac{\partial h'}{\partial t}+u_0\frac{\partial h'}{\partial x}+h_0\frac{\partial u'}{\partial x}=0 \tag{4}$$

Expressing the bed shear stress in terms of bulk velocity square as $\tau_b=\rho C_f u^2$ and assuming a constant value of the friction coefficient $(Cf=C_{f0})$ equation (3) becomes:

$$\frac{\partial u'}{\partial t}+u_0\frac{\partial u'}{\partial x}+g\frac{\partial h'}{\partial x}+gS_0\left(2\frac{u'}{u_0}-\frac{h'}{h_0}\right)=0 \tag{5}$$

Considering the following non-dimensional variables:

$$\tilde{x}=\frac{xS_0}{h_0};\tilde{t}=\frac{tS_0u_0}{h_0};\tilde{u}'=\frac{u'}{u_0};\tilde{h}'=\frac{h'}{h_0} \tag{6}$$

equations (5)–(4) can be rewritten in dimensionless form as

$$\frac{\partial\tilde{u}'}{\partial\tilde{t}}+\frac{\partial\tilde{u}'}{\partial\tilde{x}}+\frac{1}{F_r^2}\frac{\partial\tilde{h}'}{\partial\tilde{x}}+\frac{1}{F_r^2}\left(2\tilde{u}'-\tilde{h}'\right)=0 \tag{7}$$

$$\frac{\partial\tilde{h}'}{\partial\tilde{t}}+\frac{\partial\tilde{h}'}{\partial\tilde{x}}+\frac{\partial\tilde{u}'}{\partial\tilde{x}}=0 \tag{8}$$

where $F_r=u_0/(gh_0)^{1/2}$ denotes the unperturbed Froude number.

The first order system (7)–(8) can be easily reformulated only in terms of depth and it reads:

$$\frac{\partial^2\tilde{h}'}{\partial\tilde{t}^2}+2\frac{\partial^2\tilde{h}'}{\partial\tilde{x}\partial\tilde{t}}+\left(1-\frac{1}{F_r^2}\right)\frac{\partial^2\tilde{h}'}{\partial\tilde{x}^2}+\frac{1}{F_r^2}\left(3\frac{\partial\tilde{h}'}{\partial\tilde{x}}+2\frac{\partial\tilde{h}'}{\partial\tilde{t}}\right)=0 \tag{9}$$

As the classical linear stability theory prescribes, the perturbation $\tilde{h}'$ is decomposed into elementary waves like $exp\,i(k\tilde{x}-\omega\tilde{t})$, with the complex wave number $k=k_r+ik_i$ and the complex frequency $\omega=\omega_r+i\omega_i$. The substitution of such perturbation into equation (9) leads to the quadratic dispersion equation:

$$D(k,\omega,F_r)=F_r^2i(\omega-k)^2-k^2i-2\omega+3k=0 \tag{10}$$

In performing a *spatial* stability analysis the frequency ω has to be considered real and the instability is related to the occurrence of complex wave numbers k, roots of equation (10), characterized by positive imaginary part. On the other hand, in a *temporal* stability analysis, the wave-number k is assumed to be real and the unstable conditions are related to the existence of complex frequencies ω, roots of equation (10), characterized by negative imaginary part. Performed linear temporal stability analyses (Brock, 1970; Ponce & Simons, 1977) have shown that the flow model (9) is unstable when the Froude number exceeds the limit value 2, independently on the of the perturbation wave-length value.

In order to ascertain which of the two techniques is the most appropriate to describe an unstable process, a study about instability nature can be performed. As mentioned before, instabilities have been distinguished between *Convective* and *Absolute* (Huerre & Monkewitz, 1990). In the Convective instability an initial disturbance, localized in space, is swept away from the source leaving the flow domain unperturbed as time tends to infinity. By contrast, the instability is classified as *Absolute*, if a preferential direction of propagation does not exist. In this case the disturbance spreads both in downstream and upstream directions contaminating the whole domain as time tends to infinity.

A spatial analysis leads to a well posed problem only when the instability is of convective type. Contributions to the theoretical foundations underlying these notions have been brought out in studies concerning plasma (Bers, 1975) and hydrodynamic (see the review of Huerre & Monkewitz, 1990) stability. In a morphodynamic context the nature of bar formation process has been investigated recently by Federici & Seminara (2003).

3 STUDY OF INSTABILITY NATURE

The nature of instability of the linearized St. Venant flow model can be ascertained by studying the impulsive response of equation (9). The usual approach leads to investigate the asymptotic time behavior of the solution (Green's function) of the following initial value problem:

$$\frac{\partial^2 G}{\partial \tilde{t}^2}+2\frac{\partial^2 G}{\partial \tilde{x}\partial \tilde{t}}+\left(1-\frac{1}{F_r^2}\right)\frac{\partial^2 G}{\partial \tilde{x}^2}+\frac{1}{F_r^2}\left(3\frac{\partial G}{\partial \tilde{x}}+2\frac{\partial G}{\partial \tilde{t}}\right)= \tag{11}$$
$$=\delta(\tilde{x})\delta(\tilde{t})$$

where δ=the Dirac delta function. The spatial domain is assumed to be unbounded and homogeneous initial conditions are prescribed. Following Huerre & Monkewitz (1990), the base flow is classified as linearly unstable if there exists a ray $\tilde{x}/\tilde{t}$=cost along which

$$\lim_{\tilde{t}\to\infty} G(\tilde{x},\tilde{t})=\infty \tag{12}$$

A linear unstable condition of flow is convective if, along

ray $\tilde{x}/\tilde{t}=0$, it occurs

$$\lim_{\tilde{t}\to\infty} G(\tilde{x},\tilde{t})=0 \tag{13}$$

whereas it is absolutely unstable when, along the ray $\tilde{x}/\tilde{t}=0$,

$$\lim_{\tilde{t}\to\infty} G(\tilde{x},\tilde{t})=\infty \tag{14}$$

The asymptotic behavior of the Green's function (12)–(14) can be analyzed representing $G(\tilde{x},\tilde{t})$ as double Fourier integral in the complex ω and k planes

$$G(\tilde{x},\tilde{t})=\frac{1}{(2\pi)^2}\int_{BC}\int e^{i(k\tilde{x}-\omega\tilde{t})}\frac{dkd\omega}{D(k,\omega,F_r)} \tag{15}$$

in which $D(k, \omega, F_r)$=the dispersion operator given by equation (10). The contours B and C are placed in the region of absolute convergence of $G(\tilde{x},\tilde{t})$. The application of the steepest descend method to equation (15) allows to analyze the asymptotic conditions (12)–(14) only through the study of both temporal $\omega(k)$ and spatial $k(\omega)$ branches of the dispersion relation $D(k, \omega, F_r)$ in the complex ω and k planes (Briggs, 1964; Huerre & Monkewitz, 1990).

It can be shown (Huerre & Monkewitz, 1990) that condition (12) is not fulfilled, i.e. linearly stable conditions of flow occur, if, for all $k=k_r$ and for all temporal branches $\omega(kr)$, $\omega i(kr)<0$. Therefore, the presence of linearly unstable conditions of flow will be detected if the maximum value ω_i^{max} of $\omega_i(k_r)$ is positive definite.

The simple structure of the dispersion equation (10) allows to deduce in an analytic form the temporal branches $\omega(k)$

$$\omega=k-\frac{i}{F_r^2}\pm\sqrt{\left(k-\frac{i}{F_r^2}\right)^2-k^2\left(1-\frac{1}{F_r^2}\right)+3i\frac{k}{F_r^2}} \tag{16}$$

Setting $k=k_r$ in the right hand side of expression (16), it follows that, according to previous results (Brock, 1970), linearly unstable conditions of flow are permitted only when the Froude number exceeds the limit value $F_{rc}=2$.

In order to ascertain the nature of unstable conditions of flow, occurring when $F_r>F_{rc}$, a careful study of the spatial branches is required. Briggs (1964) proved that the absolute character of the instability can be defined looking for the complex frequencies ω^0 for which two (or more) spatial branches $k(\omega)$ merge (pinch-type singularities). The positive definiteness of ω_i^0 is the necessary condition for the absolute character of the instability. The sufficient condition comes from the analysis, for large enough ω values, i.e. $\omega_i > \omega_i^{max}$, of the spatial branches $k(\omega)$ that coalesce for $\omega=\omega_0$. The instability will be of absolute type if for $\omega_i > \omega_i^{max}$. at least two of such branches are placed on opposite sides of the real k-axis.

The study of the branches location, in condition of spatial evanescence $\omega_i > \omega_i^{max}$, ensures that the instability, corresponding to the pinch, will appear as two waves, propagating in opposite directions, without any discontinuity at the origin of the spatial coordinates. The time growth of these waves, that behave as only one wave (normal mode), will lead to the contamination of the whole domain as time tends to infinity.

Since the spatial branches merging points correspond to the saddle points of the temporal branches $\omega(k)$ (Huerre & Monkewitz, 1990), the necessary condition of the Briggs criterion can be analyzed alternatively looking for the complex wave number k^0 such that $\partial\omega/\partial k=0$, i.e. $\omega^0=\omega(k^0)$.

The last technique is the most useful when many spatial branches are present. The above procedures may be applied only when pinch-type singularities occur at finite values of k^0. If such an instance does not occur the singularities will be defined as essential and the Brigg's criterion cannot be straightforwardly applied. In this case, a direct numerical evaluation of $G(\tilde{x},\tilde{t})$ is needed (Park & Huerre, 1988).

In the St. Venant flow model (9) only two spatial branches exist

$$k=\frac{2F_r^2\omega+3i\pm\sqrt{4F_r^2\omega(\omega+i)-9+8i\omega}}{2\left(F_r^2-1\right)} \tag{17}$$

whose merging points are given by

$$\omega^0=\frac{-i\left(F_r^2-2\right)\pm i\sqrt{\left(F_r^2-4\right)\left(F_r^2-1\right)}}{2F_r^2} \tag{18}$$

The inspection of (18) and of (17) with $\omega=\omega^0$ allows to conclude that the instability of the St. Venant flow model has a convective nature, since only finite pinch-type singularities characterized by negative imaginary part exist, for $F_r>2$.

4 RESPONSE TO A POINT-WISE TIME-PERIODIC DISTURBANCE

The absence of absolute instabilities suggests analysing roll-waves generation process by linear spatial analysis. In this context, considering the dispersive effects, the time-

asymptotic response of the flow model to a point-wise external source oscillating with a prescribed frequency is studied.

The dimensionless pulsation of the oscillation is denoted as $\omega_e=2\pi f_e/S_0$, being $k_2=h_0/(u_0T_e)$ the source frequency and T_e its dimensional period. The time asymptotic response of the flow model can be studied by investigating the time asymptotic behavior of the solution (Green's function) of the following problem:

$$\frac{\partial^2 R}{\partial \tilde{t}^2}+2\frac{\partial^2 R}{\partial \tilde{x}\partial \tilde{t}}+\left(1-\frac{1}{F_r^2}\right)\frac{\partial^2 R}{\partial \tilde{x}^2}+\frac{1}{F_r^2}\left(3\frac{\partial R}{\partial \tilde{x}}+2\frac{\partial R}{\partial \tilde{t}}\right)= \tag{19}$$
$$=\delta(\tilde{x})e^{-i\omega_e\tilde{t}}$$

in which the flow domain is assumed to be unbounded and δ=the Dirac delta function. As in the pulse case, the solution of problem (19) can be described as double Fourier integral in the complex ω and k planes.

$$R(\tilde{x},\tilde{t})=\frac{1}{(2\pi)^2}\int_{BC}\int e^{i(k\tilde{x}-\omega\tilde{t})}\frac{dkd\omega}{(\omega-\omega_e)D(k,\omega,F_r)} \tag{20}$$

being $D(k, \omega, F_r)$=the dispersion operator given by(10).

In unstable condition of flow $(F_r>Frc)$, the time asymptotic behavior of relation (20) can be written as a superposition of two waves traveling both in the downstream direction (Bers, 1975):

$$R(\tilde{x},\tilde{t})=i\sum_{l=1,2}\frac{u(\tilde{x})}{\left(\frac{\partial D}{\partial k}\right)_{k=k_l}}e^{-i[\omega_e\tilde{t}-k_l(\omega_e)\tilde{x}]} \tag{21}$$

where $u(\tilde{x})$==the unit-step function, $k_l(\omega_e)$ with l=1,2 are the two spatial branches, obtained setting $\omega=\omega_e$ in expression (17)

$$k_l(\omega_e)=\frac{2F_r^2\omega+3i\pm\sqrt{4F_r^2\omega_e(\omega_e+i)-9+8i\omega_e}}{2\left(F_r^2-1\right)} \tag{22}$$

and finally

$$\left(\frac{\partial D}{\partial k}\right)_{k=k_l}=2iF_r^2(\omega_e-k_l(\omega_e))+2k_l(\omega_e)i-3 \tag{23}$$

4.1 *Spatial grow rate*

Independently of the ω_e value, the inspection of (22) leads to recognize the existence of only one spatially excited wave ($k_i(\omega_e)$<0); the other one is spatial evanescent. A graphical evidence of such findings is given in Figure 1 in which the imaginary part of the two spatial branches $k(\omega_e)$ for F_r=2.5 is showed.

Let focus the attention on the primary excited wave. Equation (22) indicates that, for a constant Froude number value, the imaginary part of the wave-number, i.e. the spatial grow rate, is a bounded monotone function of ω_e or, equivalently, of the source frequency

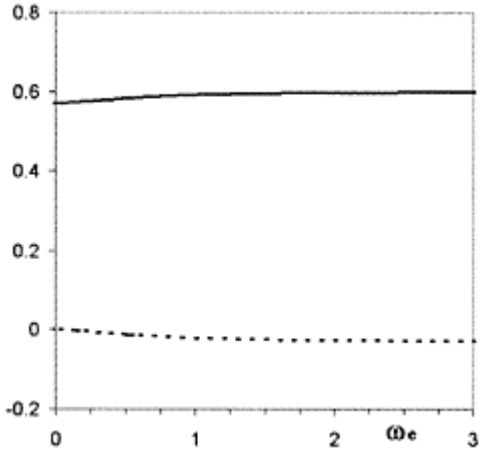

Figure 1. Imaginary part of the wave number: solid line unstable wave, k_1; dashed line evanescent wave, k_2.— F_r=2.5.

f_e, for a fixed bed slope. Independently of the Froude number, very small values of the frequency lead to a vanishing spatial growth rate. On the other hand, the limit process for very high frequencies ($f_e \to \infty$), furnishes the minimum asymptotic value of the k_i, i.e. maximum spatial grow rate, that reads

$$k_i^{\min} = \frac{2 - F_r}{2F_r(F_r + 1)} \tag{24}$$

4.2 *Propagation phase speed*

The analysis of propagation phase speed $c=\omega_e/k_r(\omega_e)$ suggests that the excited waves is the *primary* one (faster) while the evanescent one is the *secondary* one (slower). In Figure 2 the propagation phase speed of both waves versus ω_e is depicted for F_r=2.5. The diagram reveals that the c value of both waves is not constant and strongly depends on the value of the source pulsation. Similar results have been derived by Supino (1960) in studying the evolution of small waves in hydraulic channel, starting from the linearized St. Venant flow model.

For fixed value of the bed channel, the propagation phase speed is a monotone function of the dimensionless source frequency f_e and decreases as the frequency increase, tending to the asymptotic value $1+1/F_r$, which represents its minimum value. The maximum celerity value occurs at f_e=0 and it is 1.5, independently of the Froude number.

4.3 *Distance for roll waves formation*

Spatial growth rates, formally equivalent to the asymptotic value (24), have been deduced from previous

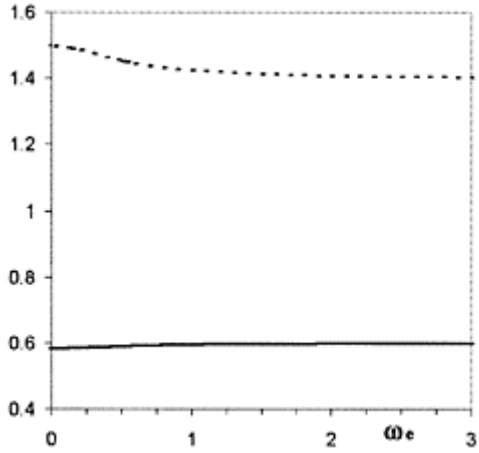

Figure 2. Phase speed: solid line unstable wave, c_1; dashed line evanescent wave, c_2.–F_r=2.5.

linear analyses that do not consider the dispersive effects (Vedernikov, 1945, 1946; Liggett, 1975). More– over, these growth rate expressions have constituted the theoretical justification to semi-empirical criteria for predicting the presence of the roll-waves (Montuori, 1961; Julien & Hartley, 1986).

In particular, Montuori (1961, 1963) related the formation of the roll-waves not only to the Froude number but also to the channel length L. Starting from the results of the spatial linear analysis of Vedernikov (1945, 1946), the author introduced a functional dependence of the critical Froude number value upon the non-dimensional channel length, LS_0/h_0, that, as far as wide rectangular channels are concerned, may be rewritten as follows:

$$\frac{S_0 L}{h_0} = \frac{\ln(\varepsilon)}{k_i^{\min}(F_r)} \qquad (25)$$

The amplification factor $\varepsilon=10^{-4}$ appearing in (25) has been calibrated starting from numerous field data collected in Europe and in Russia. The curve defined by equation (25) individuates two disjoint regions, in the LS_0/h_0–F_r plane. Roll-waves formation is inhibited in flow conditions characterized by LS_0/h_0–F_r pairs laying below the curve.

Figures (3) and (4) depict the deviation of the calculated spatial growth rate from its asymptotic value $(\alpha = k_i/k_i^{min})$ versus the frequency f_e, for two different channel bed slope values (S_0=0.01 and S_0=0.30). In each figure three different values of the Froude number (F_r=2.5, F_r=5 and F_r=1.5) have been considered.

In the S_0=0.01 case (Fig. 3) only for very low frequency values (T_e>500h_0/u_0) substantial deviations from the asymptotic value can be detected. In contrast, for higher bed channel slope value (Fig. 4) considerable differences appear in a broader frequency range. Independently of the bed channel slope, the deviations reduce when the Froude number is increased, even though the Froude number effect appears to be less significant.

From the above results it follows that the spatial evolution of the perturbation, according to the dispersion effects in a linear approximation context, is governed by three dimensionless parameters xS_0/h_0, F_r, f_e/S_0. Therefore the conventional approaches employing only two parameters xS_0/h_0, F_r (Zanuttigh & Lamberti, 2003, 2004; and Montuori, 2004) require an additional constrain on the minimum value of the physical disturbance frequency. We whish to stress that such a lower bound may be particularly severe in presence of channels with huge bed slope (Fig. 4). Furthermore, neglecting the frequency effects leads to overestimate the spatial growth of the disturbance. This final remark provides a theoretical justification for the experimentally ascertained underestimation of the minimum channel length above which equation

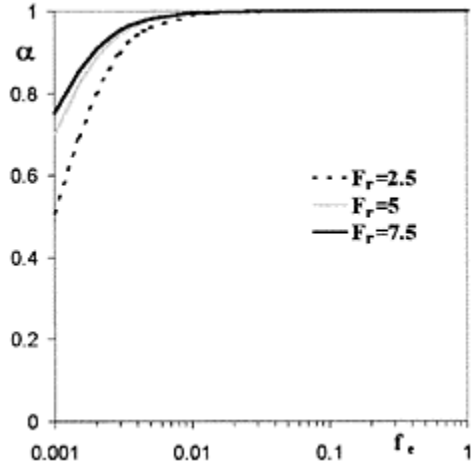

Figure 3. Spatial grow rate $\alpha = k_i/k_i^{min}$ versus the dimensionless frequency f_e,−S_0=0.01.

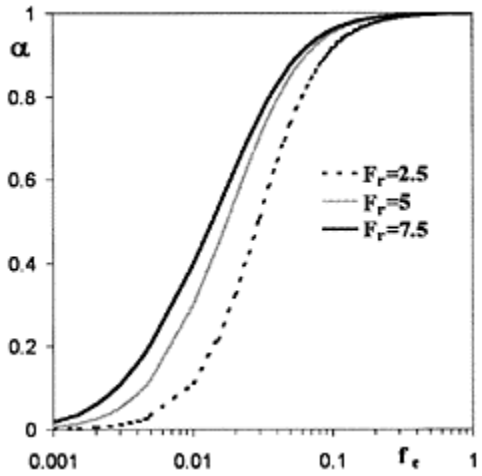

Figure 4. Spatial grow rate $\alpha = k_i / k_i^{min}$ versus the dimensionless frequency f_e,−S_0=0.3.

(25) predicts the presence of roll-waves (Montuori, 1961).

As a matter of fact Figure 4 clearly shows that for large bed slopes the amplification factor is considerably reduced compared to its asymptotic value, in large range of dimensionless frequencies f_e. Therefore equation (25) would correctly account for the above quoted experimental evidences, provided k_i^{min} is replaced by the correct spatial growth rate of the unstable wave given in (22) and the frequency of the disturbance is not excessively large. Which is the appropriate disturbance frequency value is still, as far as the authors are aware, an open question and requires properly design experiments or direct numerical simulations.

5 CONCLUSION

In the present paper, the convective instability property of the one-dimensional linearized flow model has been preliminarily demonstrated. The Briggs criterion, concerning the analysis of the branch-point singularities of the dispersion relation, has been applied. Starting from the ascertained convective character of the instability a spatial linear stability analysis, which naturally accounts for the dispersive effects, has been carried out. Results showed that, in unstable condition of flow, a point-wise temporal oscillating perturbation generates two waves, both propagating in the downstream direction. The primary is spatially growing, the secondary is spatially evanescent. The spatial growth rate of the unstable wave strongly depends on the frequency of the disturbance, particularly as far as high bed slope channels are concerned. It follows that the description of the spatial evolution of the perturbation only through the Froude number and the non-dimensional distance, commonly assumed in hydraulic engineering criteria,

may lead to overestimate the spatial amplification of the perturbation, depending on the temporal frequency of the disturbance and on the bed slope of the channel.

REFERENCES

Berlamont, J.F. 1976. Roll-waves in inclined rectangular open channels. *Proceedings of International Symposium on Unsteady flow in open channels,* BHRA Fluid Engineering, Newcastle, A2:13–26.

Berlamont, J.F. & Vanderstappen, N. 1981. Unstable turbulent flow in open channels. *Journal of Hydraulic Division,* ASCE, 107 (HY4):427–449.

Bers, A. 1975. Linear waves instabilities. In *Physique des Plasmas,* ed. De Witt, C. and Peyraund, J. Gordon & Breach, New York:117–215.

Briggs, R.J. 1964. *Electon-Steam Intemction with plasmas.* MIT Press, Cambridge.

Brock, R.R. 1969. Development of roll-waves trains in open channels. *Journal of Hydraulic Division,* ASCE, 95(HY4): 1401–1427.

Brock, R.R. 1970. Periodic permanent roll waves. *Journal of Hydmulic Division, ASCE,* 96(HY12):2565–2580.

Federici, B. & Seminara, G. 2003. On the convective nature of bar instability. *Journal of Fluid Mechanics,* 487:125–145.

Huerre, P. & Monkewitz, P.A. 1990. Local and global instability in spatially developing fiows.*Ann. Rev. Fluid Mech.,* 22:473–537.

Julien, P.Y. & Hartley, D.M. 1986. Formation of roll waves in laminar sheet flow. *Journal of Hydraulic Research,* 24(1):5–17.

Liggett, J.A. 1975. Stability in Unsteady flow in open channel. Vol. 1, ed. Mahmood, K. and Yevjevich, V., *Water Resources Publications,* Fort Collins.

Montuori, C. 1961. La formazione spontanea dei treni d'onde su canali a pendenza molto forte. L'Energia Elettrica, 2:127−141 (in Italian).

Montuori, C. 1963. Discussion of Stability aspect of flow in open channels. *Journal of Hydraulic Division,* ASCE, 89(HY4):264–273.

Montuori, C. 2004. Discussion: Roll waves Simulation using shallow water equations and Weight Flux Metod. *Journal of Hydraulic Research* (in press).

Park, D. & Huerre, P. 1988. On the convective nature of the Goertler instability. *Bulletin of American Physical Society,* 33:2552.

Ponce, V.M. & Simon, D.B. 1977. Shallow water propagation in open channel flow. *Journal of Hydraulic Division,* ASCE, 103(HY12):1461–1476.

Smith, A.M.O. & Gamberoni, N. 1956. Transition Pressure Gradient and Stability Theory. *Douglas Aircraft Co.,* Rept. ES 26388, California.

Supino, G. 1960. Sopra le onde di traslazione nei canali. *Rendiconti Lincei,* 5–6 (in Italian).

Van Ingen, J.L. 1956. A suggested Semi-empirical Method for the Calculation of the Boundary Layer Transition. *Univ. of Tecn., Dept of Aero. Eng.,* Rept. UTH-74, Delft.

Vedernikov, V.V. 1945. Condition at the front of a translation waves disturbing a steady motion of a real fluid. *USSR Academy of Science,* 48:239–242.

Vedernikov, V V 1946. Characteristics feature of a liquid flow in open channel, *USSR Academy of Science,* 52:207–210.

Zanuttigh, B. & Lamberti, A. 2003. Roll waves simulation using shallow water equations and weighted average flux method. *Journal of Hydraulic Research,* 40(5):610–622.

Zanuttigh, B. & Lamberti, A. 2004. Discussion: Roll waves Simulation using shallow water equations and Weight Flux Metod. *Journal of Hydraulic Research* (in press).

B.2.
Bank failure

Non-intrusive imaging measurements of the morphological evolution of a channel during a dam-break flow

N.le Grelle[1], B.Spinewine[1,2], S.Soares Frazão[1,3] & Y.Zech[1]
[1] *Department of Civil and Environmental Engineering, Université catholique de Louvain, Belgium*
[2] *Fonds pour la Recherche dans l' Industrie et l' Agriculture, Belgium*
[3] *Fonds National de la Recherche Scientifique, Belgium*

River Flow 2004—Greco, Carravetta & Della Morte (eds.)

ABSTRACT: Among the damaging consequences of a dam-break flow on the downstream valley, the morphological changes due to the heavy transport of sediments are not the least. The rapid flow has an important erosive power and a high transport capacity. Besides scouring of the river bed, erosion of the banks can drastically increase the river width and hence completely reshape the valley. Simplified dam-break experiments have been undertaken to investigate this problem at the laboratory scale. They were conducted in an asymmetric horizontal channel with a single bank on one side and a glass side-wall on the opposite side, allowing visual observation of the flow features. The bed and the banks are made of uniform sand. By means of those simplified experiments it was possible to reproduce qualitatively the main features of real events such as the important enlargement of the valley due to the failure of the banks and the deposition of the material eroded from the banks. The major difficulty with such experiments is to obtain reliable data of the rapid evolution of the system. This concerns the water profile, the bed profile and the shape of the cross sections. Indeed, using intrusive probes in rapid flows over movable bed and banks heavily disturbs the system and modifies considerably the results (for example: scouring around a level probe). Furthermore, it provides only a one-point measurement, hence making it unfeasible to obtain a wide set of data given the amount of work required for test preparation. As an alternative we resort to imaging techniques for the non-intrusive characterisation of the flow features over the full coverage of the digital images. The present work relies on an original imaging technique based on laser-sheet technology to track the evolution in time of the whole cross-sectional profiles, both above and below water.

1 INTRODUCTION

Erosion of the bed and banks of a river is usually a longterm and never-ending process that slowly induces geomorphic changes to a valley. In some extreme cases, rapid and important geomorphic changes may occur after a catastrophic event such as a dam or dike break. The debris-flow like rheology of the wave in the early stages of the dam-break flow evolves to intense bed- and suspended-load transport with a particularly high concentration. This flow is highly transient and invades parts of the valley that were probably never inundated in the past. The geological equilibrium of the banks is ruined and dramatic morphological changes can be expected.

In July 1996, the heavy rainfall in the Saguenay region of Quebec induced severe floods in many rivers and a dike-break on the lake Ha!Ha! (Brooks & Lawrence, 1999). The flood wave completely reshaped the alluvial valley and the river Ha!Ha! bed (Fig. 1), with successive reaches of intense erosion and deposition, and an overall increase in channel width that reached 700% in some locations.

In the last years, a number of authors have studied the problem of rapid geomorphic changes induced by a dam-break flow. The problem was first tackled from a 1D perspective with laboratory experiments in idealised conditions and with artificial sediment analogues (see e.g. Capart & Young, 1998, Fraccarollo et al., 2003). In order to get closer to natural valleys, an attempt is now made to investigate the impact of dam-break flows on lateral erosion of the valley flanks. Small-scale laboratory experiments proved to be able to reproduce quite well the behavior observed in real events, at least with non-cohesive material. Recently, experiments were carried out in a half-channel (Spinewine et al., 2002) and imaged in such a way to obtain the time evolution of the water and bed level.

The key problem with such flows is to obtain reliable data without perturbing the flow. Intrusive measuring

Figure 1. Geomorphic changes induced by the lake Ha!Ha! dam-break in July 1996.

techniques can modify the results significantly. For example, local scouring around a bed level probe may completely alter the bed evolution.

As an alternative to intrusive measurements, this paper presents an original non-intrusive imaging technique based on laser-sheet technology. The rapid evolution of a whole cross-section is tracked during the dam-break experiment, both below and above the water surface.

The experiment presented in this paper is used in the benchmarking program of the IMPACT European project (le Grelle & Zech, 2003). This research project addresses the assessment and reduction of risks from extreme flooding caused by natural events or by the failure of dams and flood defense structures.

2 EXPERIMENT DESCRIPTION

2.1 *Experimental set-up*

Dam-break flow experiments in an erodible channel were carried out at the Civil Engineering Laboratory of the Université catholique de Louvain. The experimental set-up is sketched in Figure 2. It consists in a half-width channel with a single erodible bank. The total length is about 3 m. The initial shape of the section is prepared by profiling compacted sand as defined in Figure 3a, where the banks make an angle of 50° with the bed. In the longitudinal direction, the bed and the bank crest are initially horizontal (Fig. 3b).

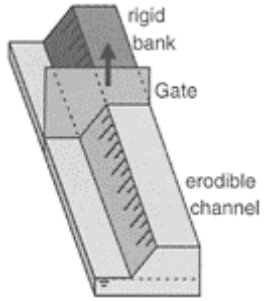

Figure 2. Experimental set-up.

The erodible bed is initially fully saturated while the banks are only partially saturated with water. The important drainage capacity of the sand used in the experiment makes it impossible to maintain the banks in a fully saturated state.

The reservoir upstream from the gate is filled up to 15cm. In the reservoir, the banks are rigid and no erosion is thus possible. The sediments consist in uniform sand with the following characteristics: a median diameter of 1.8mm, a unit mass of 2615kg/m^3, a lose bed porosity of 40.5% and a permeability of 1.5cm/s.

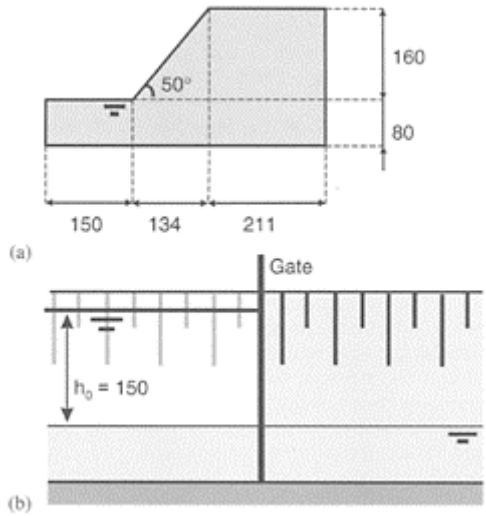

Figure 3. Initial conditions, (a) cross-section and (b) elevation (dimensions in millimeters).

The experimental set-up used here is similar to the set-up used by Spinewine et al. (2002). These authors performed geostatic bank failure experiments to define a stable initial bank slope for the humid sand and to measure the angles of repose of the sand after a bank failure. Their observation is reproduced in

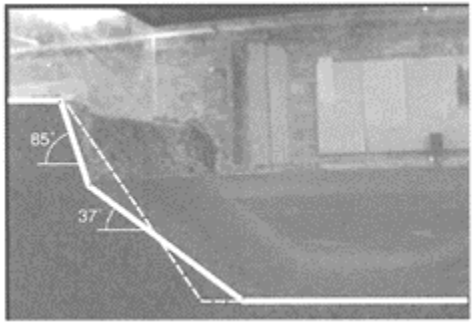

Figure 4. Angles of repose after a bank failure, from the geostatic experiments by Spinewine et al. (2002).

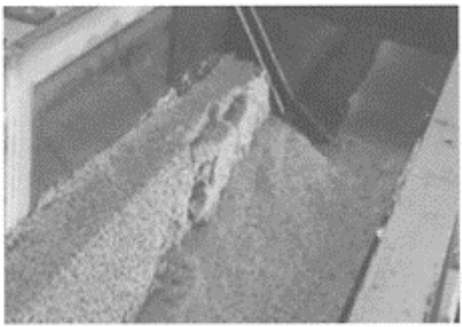

Figure 5. Bank erosion resulting from intermittent block failure.

Figure 4: the angle of the bank is 85° above the water level and 37° under water.

2.2 *General flow description*

The experience is launched by suddenly raising the gate. This releases a dam-break wave which rapidly propagates down the channel and triggers a series of bank failures. The water does not fill the channel up to the top of the embankments and the flow can thus not erode them only by bedload transport. In fact, the rapid erosive flow attacks the toe of the banks with the consequence that they become steeper near the bed and thus destabilized. Bank erosion then occurs in fact as a series of intermittent block failures (Fig. 5) that feed the flow with an important quantity of sediments.

The channel enlargement due to bank failures is the most important in the immediate vicinity of the dam. The water depth there is greater and the flow shows a two-dimensional expansion from the reservoir into the channel.

After about 10s, most of the geomorphic action has occurred. Only light bedload transport can be observed and the banks are no longer affected.

3 LASER MEASUREMENT TECHNIQUE

The overall principle of the method is to use a laser light sheet to enlighten a given cross-section, to localise the trace of the imprinted laser line onto digital images of a remote camera through the transparent side-wall, and to project the line back in 3D space using distinct projective transforms for the immerged and emerged portions.

The method is detailed somewhat further in the next sections. However, a detailed description of the camera calibration method and specific projective transforms goes beyond the scope of the present paper whose objective is to focus on the results of the method. We refer the interested reader to Spinewine et al. (2003) for more details. The companion paper in this conference (Spinewine et al., 2004) applies a similar technique to dike breaching experiments for tracking the evolution of the breach geometry as a function of time.

3.1 *Set-up*

A laser light sheet is used to enlighten a cross-section through the channel side-wall. The flume, the laser-sheet and the camera are sketched in Figure 6. Illumination from above through the water surface would induce uncontrolled refraction effects at the air/water interface. Orthogonal illumination through the side-wall, on the contrary, avoids such alterations.

The trace of the laser light sheet imprinted on the cross-section (Fig. 7) is imaged with a digital camera located more upstream at the same height as the laser source. An example of a resulting image is shown in Figure 8. Two portions of the line are visible on the figure: one profile for the dry bank above water, and one for the submerged part of the bank. The transition between both curves generally escapes to observation. This explains why the resulting profiles shown in further figures present an interruption around the location of the water surface.

3.2 *Treatment of the images*

After the experiment, a series of images of type of Figure 8 are obtained. On each image, the pixel coordinates corresponding to the trace of the laser are identified using an automated algorithm.

Those pixel coordinates are then projected in 3D space using separate geometrical transformations for the above-water and under-water profiles: indeed, the differing refractive conditions need to be accounted for through separate calibration procedures (Fig. 9). Both profiles are merged together to yield the shape of the full cross-section in a given instant. Details about geometrical transformations can be found in Spinewine et al. (2003).

The results were found to be surprisingly reproducible, even though the bank erosion mechanism

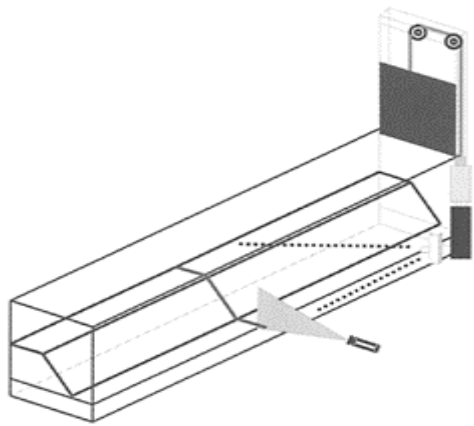

Figure 6. Set-up for the laser-sheet measuring technique.

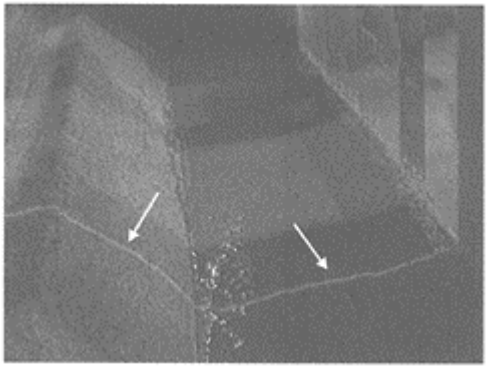

Figure 7. Trace of the laser sheet on the channel.

through intermittent block failures is quite stochastic. Three runs were carried out for each cross-section. An example of the reproducibility (three different runs, same section, same time) is shown in Figure 10.

4 EXPERIMENTAL RESULTS

The experiment was carried out several times to measure the evolution in time of 8 cross-sections located at 0.25m, 0.50m, 0.75m, 0.95m, 1.25m, 1.5m, 1.75m and 2.25m from the gate, respectively (Fig. 11). Those measurements allow to investigate in detail the processes of bank failure and subsequent deposition of the failed material over the channel bed.

The evolution of cross-section S2 located 0.50m downstream from the gate is shown in Figure 12. The

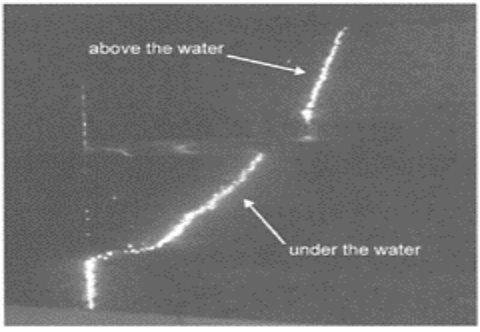

Figure 8. Sample image obtained during the experiment.

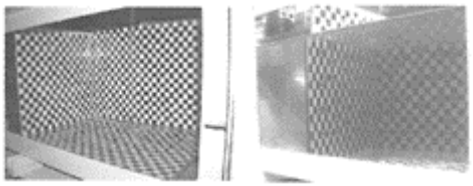

Figure 9. Calibration of above-water and under-water situations.

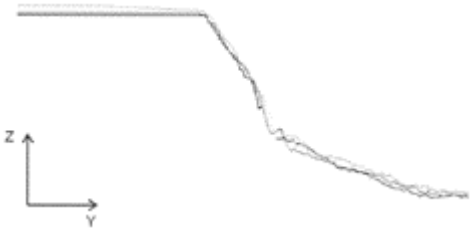

Figure 10. Reproducibility of the experiment—Cross-section at x=2.25m after 5s.

rapid rise of the water level following the dam-break induces rapid and important bank failures. After 2s (Fig. 12b), the water has reached the section and a block failure occurred. The shape of the cross-section indicates deposited sediments at the toe of the bank. After 5s (Fig. 12c), the cross-section has already evolved towards the final shape, with the bank making an angle of 37° with the bed, corresponding to the angle of repose under water. The portion of the bank with a steep slope could not be measured on this image. The flow at this stage is highly transient and the rapid moving water surface induces perturbing reflection effects on these images.

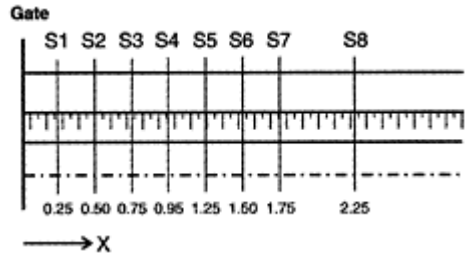

Figure 11. Cross-sections imaged with the laser-sheet technique.

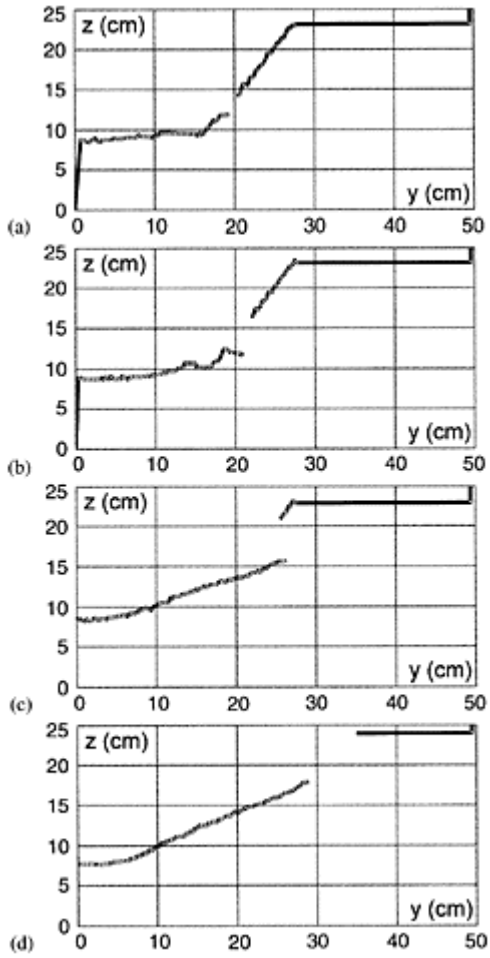

Figure 12. Evolution of section S2 (x=0.50m)—(a) t=1s, (b) t=2s, (c) t=5s, and (d) t=10s.

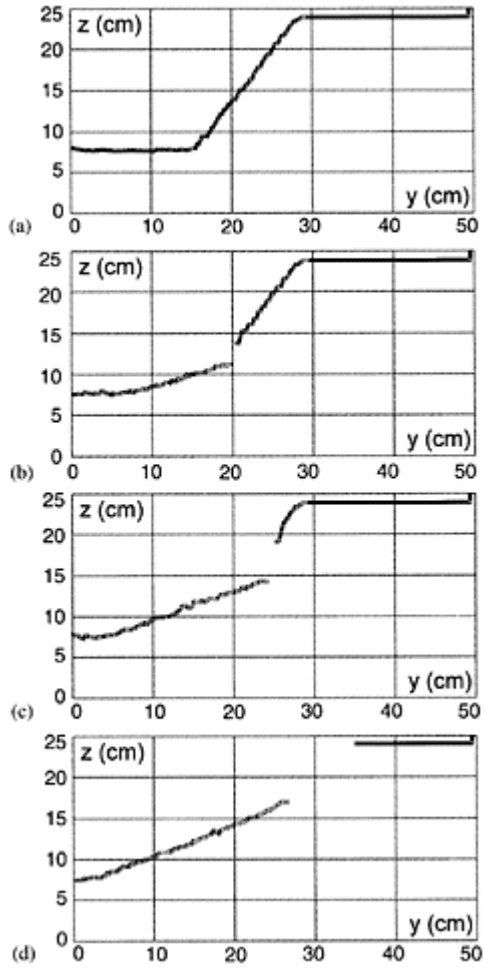

Figure 13. Evolution of section S8 (x=2.25m)—(a) t=1s, (b) t=5s, (c) t=10s, and (d) t=15s.

Figure 13 shows the evolution of section S8 located 2.25m downstream from the dam. The erosion of the bank is more progressive. At t=5s (Fig. 13b), only the lower part of the bank failed due to the arrival of the dam-break wave. Then, after t=10s (Fig. 13c), erosion at the toe of the bank has induced a new failure but the crest of the bank is still not reached. After 15s (Fig. 13d), the width of the valley has increased as a consequence of further failures of the bank.

5 CONCLUSION

For accurately measuring rapid transient flows involving significant geomorphic aspects, it is important to use non-intrusive techniques. Using a laser sheet to enlighten a cross-section of the channel, it was possible to obtain an accurate description of the evolution of this cross-section, both above and under the water surface. Combining this technique with bed elevation and water surface measurements obtained by imaging the flow through the side wall of the channel (Spinewine et al., 2002) yields a valuable characterization of the experiment. This then allows a refined analysis of the ongoing processes.

The bank erosion is driven by a succession of block failures slumping into the water. This feature, observed in the experiments, also appears on the measured profiles. Despite the discrete character of the bank failure mechanism, the measured profiles show a very good reproducibility of the experiment.

ACKNOWLEDGEMENTS

The authors wish to acknowledge the financial support offered by the European commission for the IMPACT project under the fifth framework programme (1998–2002), environment and sustainable development thematic programme, for which Karen Fabbri was the EC project officer.

REFERENCES

Brooks, G.R. & Lawrence, D.E. 1999. The drainage of lake Ha!Ha! River, Saguenay area, Quebec, Canada. *Geomorphology* 28:141–168.

Fraccarollo, L., Capart, H. & Zech, Y. 2003. A Godunov method for the computation of erosional shallow water transients. *Int. J. Num. Meth. Fluids* 41(9):951–976.

le Grelle, N. & Zech, Y. 2003. Presentation of the benchmark on dam-break induced geomorphic changes in a valley with uniform sediments. In *EC Contract EVG1-CT-2001–00037 IMPACT Investigation of Extreme Flood Processes and Uncertainty, Proceedings 3rd Project Workshop, Louvain-la-Neuve, Belgium 6–7 November 2003* (CD-ROM).

Spinewine, B., Capart, H., le Grelle, N., Soares Frazão, S. & Zech, Y. 2002. Experiments and computations of bankline retreat due to geomorphic dam-break floods. *Proc. River Flow 2002 Int. Conf. on Fluvial Hydraulics* (1):651–661.

Spinewine, B., Capart, H., Larcher, M. & Zech, Y. 2003. Three-dimensional Voronoï imaging methods for the measurement of near-wall particulate flows. *Experiments in Fluids* 34(2):221–241.

Spinewine, B., Delobbe, A., Elslander, L. & Zech, Y. 2004. Experimental investigation of the breach growth process in sand dikes. RiverFlow 2004.

Experimental investigation of the breach growth process in sand dikes

B.Spinewine
Dept. Civ. & Env. Engrg., Université catholique de Louvain, Louvain-la-Neuve & Fonds pour la Recherche dans l'Industrie et l'Agriculture, Belgium

A.Delobbe, L.Elslander & Y.Zech
Dept. Civ. & Env. Engrg., Université catholique de Louvain, Louvain-la-Neuve, Belgium

River Flow 2004—Greco, Carravetta & Della Morte (eds.)

ABSTRACT: We present results from a series of laboratory experiments simulating the breaching of a coarse sand dike by overtopping. The focus is set on a range of measuring systems used to gather as much information as possible on the evolution of flow parameters and breach geometry during the tests. In particular, we present an original non intrusive technique involving a sweeping laser light sheet system combined with digital imaging algorithms, whose objective is to obtain full digital terrain models of the evolving breach topography Results are emphasized, and some degree of interpretation is performed in light of other observations and breach modelling frameworks found in the literature.

1 INTRODUCTION

Understanding and preventing the occurrence and development of breaches in dams and/or river dikes has recently attracted widespread interest from both the research community and the civil society. The probable increase in the occurrence of extreme hydrological events resulting from climate changes, combined with the increased industrialization of river valleys, has brought the expected human and economic consequences in case of dike breaches to a critical point at many dams and along large portions of embanked low-land rivers.

However, the development of numerical models for the prediction of breach formation and development is still in the early stage (Wahl, 1998; Singh, 1996). Most available models do rely on crude assumptions for the flow (uniform, gradually varied), breach discharge (weir formulas), cross-section (rectangular, triangular, etc.) and erosion rates (lateral, vertical). Breach width and peak outflow, two utmost important parameters for risk analysis studies, are often derived from semi-empirical relations calibrated against a limited number of data sets (Morris and Hassan, 2002). How such relations are linked to dike characteristics and soil properties remains unclear, and estimation of the associated uncertainty in terms of parameter sensitivity is somehow left over to the rule of thumb.

This comes in contrast with an integrated framework of governing equations able to grasp the underlying mechanisms of the coupling between flow dynamics, breach erosion, sediment transport and lateral bank failures in a unified description. Since recently, such physically-based models try to start from scratch, and to build up evolution equations that do not rely on a-priori assumptions on discharge, breach geometry and erosion rates (see e.g. Froehlich, 2002).

Breach models in general, and the latter class of models in particular, are still facing the lack of reliable data sets for validation. Real failures are not scarce in recent history, but are often poorly documented.

At a different scale, laboratory experiments offer the advantage to control more precisely dike characteristics and to force failure mode (Benoist, 1989; Kulisch, 1994). They also allow the continuous observation of the breach growth process during the whole duration of breach formation and development. However, the measurements performed have, to the knowledge of the authors, mostly been restricted to global parameters such as e.g. discharge and crest width.

The focus of the present paper is precisely set on such measuring techniques. We present results of an experimental campaign of breaching tests in a homogeneous coarse sand dike (Delobbe and Elslander, 2002). A range of measuring systems has been used and cross-validated, with the intention to gain as much information as possible on the evolution of discharges, water levels, and breach geometry. In particular, we present in more details a novel digital imaging technique whose objective is to track the evolution of the entire dike topography as a function of time. The method relies on a sweeping laser light sheet to visualize breach cross-sections, and on 3D projective transforms to merge individual profiles and reconstruct the whole breach topography.

The remainder of the paper is structured as follows: in the next section we present the experimental set-up, including sediment characteristics and initial breach geometry. Section 3 focuses on the various measuring systems, and present in more details the original imaging technique developed for tracking the evolution of breach topography. Results are presented in section 4, preceding some concluding remarks.

2 EXPERIMENTAL SET-UP

2.1 *The flume*

Breaching tests were undertaken in a fixed horizontal flume with a length of 36m and a width of 3.6m, as illustrated in Figure 1. The dike was constructed across the flume with a crest length of 2.4m, the remainder of the flume width being taken over by fixed abutments on both sides. The dike crest is at 15m from the upstream end of the flume, this length providing sufficient volume for acting as upstream storage reservoir.

The upstream part is separated in two parts (indicated as 1 and 2 in Fig. 1) by a large gate. This has two advantages: at first, it allows to store the volume of water in the upper part, keeping the rest of the flume dry for building the dike. Secondly, the level in this upper reach is chosen in such a way that after gradual opening of the intermediate gate the level attained at the upstream side of the dike is at the desired height. Adequate

operation of the gate allows to fill the upstream part of the dike relatively fast, and hence avoid other modes of failure such as piping or seepage through the embankment.

Water in the downstream part of the flume discharges freely in a lower reservoir at the downstream end, and the length of the lower reach is long enough to ensure that the downstream boundary condition does not affect the flow conditions in the breach over the entire duration of the test.

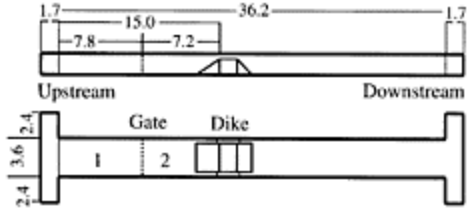

Figure 1. Plane view and elevation of the flume, indicating dike location and upstream gate position.

2.2 *Dike geometry*

The dike itself is built onto the rigid bottom of the flume. It has a length of 2.4m, a crest width of 35cm, and upstream and downstream slopes of 1:2 and 1:3 respectively. The height of the dike is 37cm. In a second series of tests, the whole geometry was raised by 10cm to provide a uniform layer of the same loose material below and downstream of the dike, in order to investigate the potential effect of the creation of a scour hole on the outflow and breach development.

Failure by overtopping was enforced by digging an initial pilot channel in the middle of the dike. This initial breach has a trapezoidal cross-section, with a crest width of 19cm, bottom width of 5cm, height of 7cm and slope angles of 45°. The overall dike geometry is represented in Figure 2.

2.3 *Dike material*

The type of sediments used as dike material and bottom layer is crushed coarse sand with grain sizes uniformly distributed in the range 1 to 2mm. A range of standard tests (Vane test, Casagrande, Proctor) were performed to measure soil properties such as density, void ratio, friction angle, residual cohesion, permeability Results are summarized in Table 1.

Dike stability and seepage flow were simulated with a Finite Element commercial geotechnical package (Geo-Slope). Results, illustrated in Figure 3, were

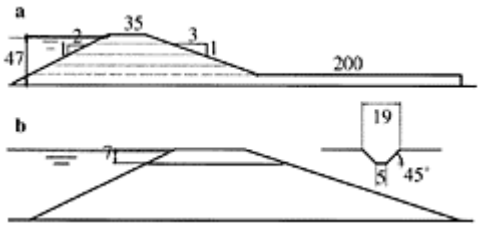

Figure 2. **(a)** Cross-section of the dike for the first and second series of tests, with the presence or not of a loose layer of 10cm below the dike; **(b)** geometry of the initial pilot channel at the centreline. Dimensions in cm.

Table 1. Summary of soil parameters.

Grain size	Uniform 1–2	mm
Shape	Angular, crushed	[−]
Void ratio when compacted	42	[%]
Permeability	1.5×10^{-2}	[m/s]
Saturated volumetric weight	19.74	[kN/m^3]
Friction angle	34	[°]
Cohesion	0	[kPa]

faced with experimental data of a preliminary seepage test. Measured (1.43 l/s) and simulated (2.39 l/s) seeping discharges were close to each other, giving confidence in the soil properties obtained from the various geotechnical tests.

To ensure dike homogeneity and reproducibility of the test, the dike was built in successive layers of 10cm. Each layer was compacted with a given number of strokes with a mass of 10kg falling onto a steel plate of 35×25cm. In-situ soil samples were taken to verify that the same desired degree of compaction was reached. The bottom layer used in the second series of tests was compacted in a similar way.

2.4 *Mode of operation*

Tests were initiated by gradually opening the upstream gate and filling the whole upstream part of the dike up to the desired height, i.e. 2cm below the dike crest level

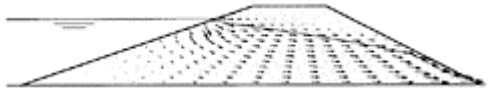

Figure 3. Modelling of the seepage curve and out-flow through the dike, using a finite-element geotechnical software.

or 5cm above the bottom of the initial pilot channel. This smooth filling phase lasts 1.5 minute, in order to avoid water waves reflecting on the upstream slope of the dike and threatening its stability.

The breach then develops in time, and its geometry evolves to an equilibrium as the level in the reservoir decreases. Indeed, no inflow is added to the reservoir during the test.

11 tests were performed in total, 5 identical tests with the dike onto the rigid bottom (tests numbered C1 to C5) and 6 identical tests with a loose layer of sand below and downstream of the dike (tests D1 to D6).

Figure 4 illustrates four characteristic stages of breach development, ranging from initiation to equilibrium.

3 MEASURING SYSTEMS

A range of measuring systems were used during the first and second series of tests, in order to gain as much information as possible on the evolution of breach geometry, water levels, discharges and flow velocities. Those include both intrusive and non-intrusive, and point-wise or full coverage measurements. Not all the devices were used simultaneously. However cross-validation between successive tests confirmed an acceptable degree of reproducibility.

The following system of coordinates is used throughout the remainder of the paper: *x*-, *y*- and *z*-axis are respectively taken along the longitudinal, transverse and vertical directions, and the origin is placed in the middle of the flume at the upstream side of the dike crest, and at the bottom level of the flume.

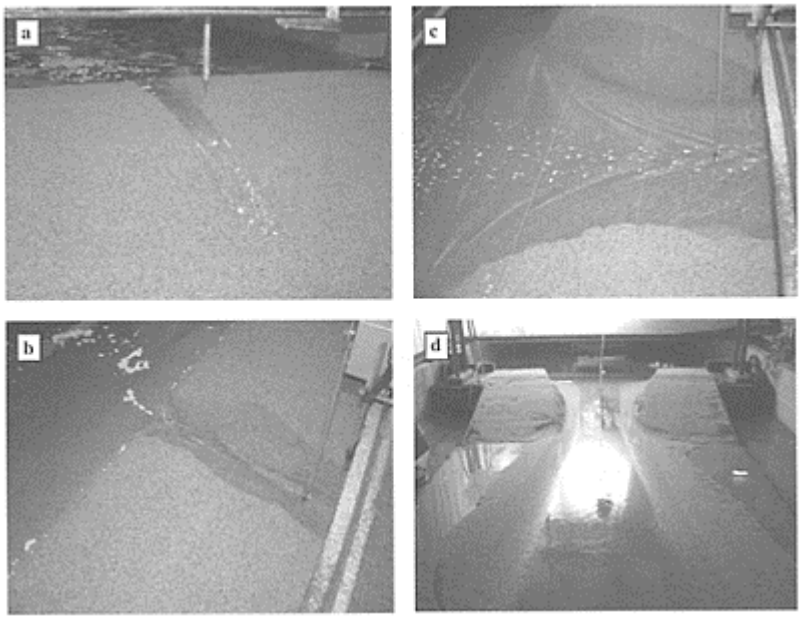

Figure 4. Four stages of breach development: **(a)** initiation; **(b)** erosion along the downstream slope; **(c)** lateral migration; **(d)** equilibrium stage.

3.1 *Standard measurements*

Rather standard measurements are listed first:

– a series of two-wires resistive probes were placed along the flume axis in the upstream reservoir to measure the evolution of water levels. Discharge through the breach was estimated from those water level measurements;
– surface velocities in the breach were obtained through tracking small floating tracer particles with a fast digital camera placed at the vertical of the dike breach, 2.5m above the flume (see Fig. 5). Tracers were expanded polystyrene particles with a diameter of approximately 3mm, and delivered from a vibrated silo in the reservoir. Custom particle identification and tracking algorithms (Capart et al., 2002; Spinewine et al., 2003) delivered the horizontal component of surface velocities;
– the breach width at various locations was manually deduced from the same images of the camera located above the dike crest;
– point measurements of water and bed elevations in the breach were obtained with a level profiler probe, used alternatively for the bed and water levels. The probe was located in the axis of symmetry along the downstream slope at x=59cm;
– the evolution of bed and water profiles along the thalweg were obtained by imaging a thin calibrated checker-board panel buried in the middle of the

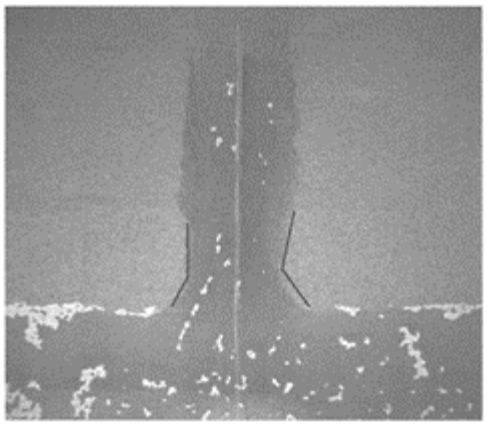

Figure 5. Vertical image and floating tracers used to derive velocity measurements.

breach (see Fig. 6); the perturbation created by this panel was negligibly small, as verified by comparing the results with the point measurements performed independently on a test where this panel was absent.

3.2 *Sweeping laser topography*

A more original technique was developed with the objective to reconstruct the entire topography of the breach using a non-intrusive imaging technique. The principle is to use a laser light sheet to illuminate a particular cross-section of the breach, capture the line imprinted on the dike onto digital images of a remote camera, and ultimately project it in 3D space with appropriate camera calibration. A similar principle was used in a companion paper (Le Grelle et al., 2004) for tracking bank failure events with a fixed laser line. Here, the ambition is to survey the whole dike by sweeping successive cross-sections with an oscillating laser line. The procedure (see Fig. 7) is described in more details here below.

A laser is placed horizontally at the vertical of the dike crest (approximate position x=0.55m, y=0, z=2.50m), and passes through a cylindrical prism to

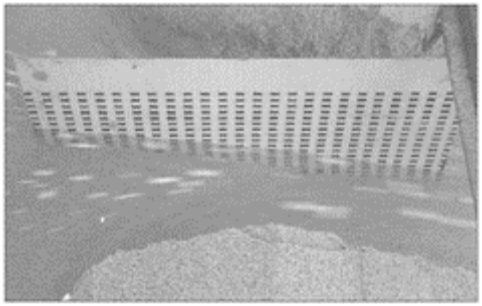

Figure 6. Thin checkerboard panel buried along the breach centreline to visualise water and bed profiles.

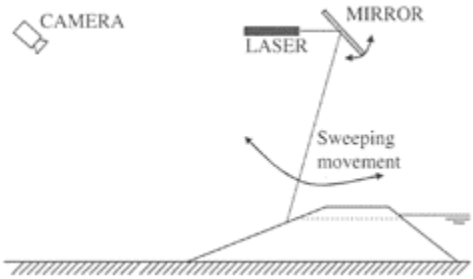

Figure 7. Sketch of the laser surveying technique used for reconstruction of the breach topography.

produce a thin light sheet. The laser used is a red diode laser with 12mW output power, and the light sheet has an opening angle of 39.3°.

The light sheet is reflected towards the dike using an oscillating mirror, adjusted in order to sweep the dike from the upstream slope to about 1m below the downstream toe. The sweeping cycle takes about 5 seconds, which is small enough compared to the speed of breach evolution to be assumed as quasi instantaneous.

A remote camera is placed more downstream (approximate position x=4.4m, y=0, z=2.45m) and oriented to cover the whole range of sweeping laser lines. The camera is a Dalsa CAD4 operating at 40 frames per second for a resolution of 1024×1024 pixels×256 grey scales. Given the covered field of view, one pixel represents less than 2mm in reality.

The images are recorded and processed offline. The contrasted line is automatically detected on the images using a series of filters, following tightly the procedure described in Capart et al. (2002).

The line, expressed as pixel coordinates, must now be projected in 3D space and world coordinates. This requires to know the position (or equation) of the laser light sheet. The

latter is derived from two reference points of the laser line printed on two thin rods fixed above the dike. The procedure also requires a camera calibration transform, from which each pixel may be associated with a 3D ray originating from the camera focal point. Those rays are then intersected with the known plane of the laser light sheet to obtain the 3D position of the line. A detailed description is beyond the scope of the present paper. Nevertheless, we refer the interested reader to Spinewine et al. (2003) where details of camera calibration and projective transforms may be found.

Relying on the above assumption that the sweeping speed of the laser is an order of magnitude faster than the speed of evolution of the breach, the images corresponding to one sweeping cycle are then assembled into a single set of 3D data, from which a digital terrain model of the entire dike may be obtained through standard interpolation techniques.

The advantage of the method is that all the required geometrical information is implicitly encapsulated in the images, and that it is not required to manually measure the respective positions of the mirror, laser lines and camera. The method overall is relatively simple to implement and provides an unprecedented degree of details in the results.

However, it has an advantage that turns out to be a drawback too. Since the laser light passes through the water surface, what is seen from the camera is the line printed onto the sediment bed. On the one hand, this allows to have a detailed perception of the underwater bed geometry and slope angles. On the other hand, the underwater portion of the laser line undergoes alteration at the water surface due to the difference in

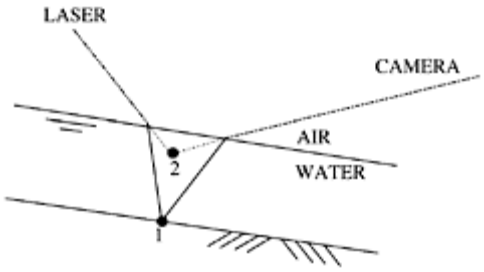

Figure 8. The vertical error due to differing refractive indexes in the air and water regions. Point 2 is actually measured on the image, whereas point 1 is the true position of the bed interface. Note that angles and refractive error is here extremely exaggerated for illustration purposes.

refractive index of air and water. This is illustrated in Figure 8. Consequently the measured bed level has an error proportional to the water depth and slope of the water profile.

While it may not be impossible to account for those refractive effects, this goes beyond the scope of the paper, and would require a measure of the water depth and longitudinal slope of the water profile. As an alternative, what we performed at least is an estimation of an upper bound for the associated error. In the worse conditions corresponding to maximal water depth and inclination of the water profile, the vertical error has been estimated to be in the order of 30mm. Provided that it constitutes an extreme case, this is small but may not be considered as negligible. On the contrary, measurements along the emerged flanks of the breach are not altered by this error, and the accuracy in this region is mainly related to pixel size and camera resolution.

4 RESULTS AND INTERPRETATION

Results obtained with the various techniques described in the previous section are now presented. All results are presented using the system of coordinates outlined in section 3, and with reference time t=0 corresponding to the moment when water starts to enter into the breach. The test to which measurements pertain is also indicated (test C1 to C5 and D1 to D6).

4.1 *Discharge*

A typical curve for the evolution of the discharge through the breach is plotted in Figure 9. Peak outflow was typically close to 65 litres per second, and time to peak is about 3 minutes. The curve is surprisingly smooth and nearly symmetrical, a feature that seem to be related to the failure mode and material characteristics. The breaching development in the present experiments is mainly diffusive and progresses smoothly

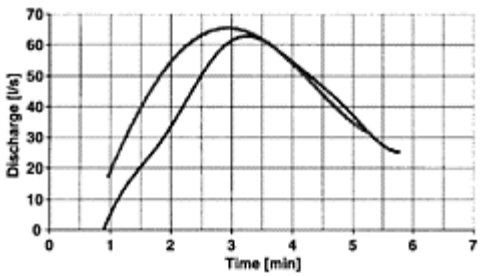

Figure 9. Outflow hydrographs for test C4 (black line) and test D2 (grey line).

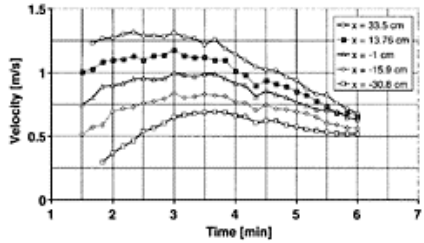

Figure 10. Mean surface velocities, obtained from particle tracking measurements, at selected sections along the dike.

with nearly uniform flow conditions along the downstream slope. This is in accordance with observations by Visser (1998) in largescale breaches of sand dikes, but not with observation of breaches in moraine dams or cohesive dikes (Morris & Hassan, 2002; Temple & Hanson, 1994). In the latter type of breaching, failure is triggered by the upstream migration of a head-cut on the downstream slope, whereby the discharge hydrograph shows a long period of relatively low discharge during the first stage, and then a sudden and drastic increase of discharge as the head-cut reaches the dike crest and the breach fully develops.

4.2 *Surface velocities*

Mean surface velocities were derived from the particle tracking measurements. Selected results for test C3 are presented in Figure 10, showing the time evolution of velocities at selected sections close to the dike crest. The curved profiles reflect somehow the shape of the outflow hydrograph, whereas the intercomparison of the various profiles clearly shows the increase in velocities as one progresses downstream.

We recall that the plotted values are mean surface velocities averaged over the entire width of the breach cross-section. Actual velocities along the centerline are higher than those presented here.

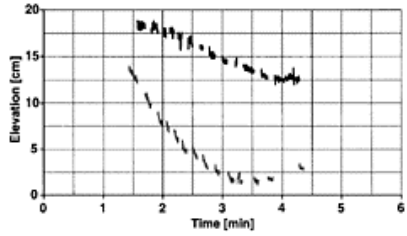

Figure 11. Water level (black line) and bed level (grey line) evolution

obtained from the level profiler located at section x=59cm.

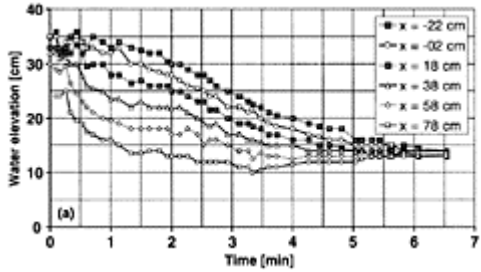

Figure 12. Centreline profiles of (a) water and (b) bed elevations obtained for test C4 with the method of the thin checkerboard panel, at selected cross-sections along the dike.

4.3 *Water- and bed-level profiles at the centreline*

Water and bed levels obtained for test C4 with the level profiler located at x=59cm are plotted in Figure 11. Results for the whole series of C-tests ranged within a margin of less than 10% around those values. Note that the lowest attained bed level corresponds to the time of peak outflow. Past this moment it seems that lateral breach erosion continues whereas the flow has no longer enough transport capacity to evacuate all the sediments eroded from the breach side-walls.

Profiles obtained manually from the observation along the thin checker-board panel buried along the centreline are presented in Figures 12a and 12b for test C4.

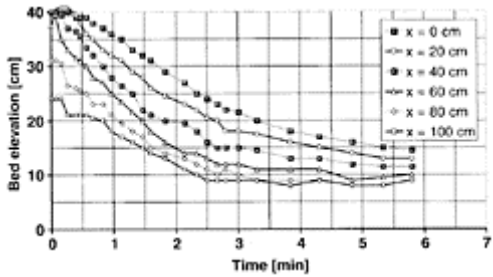

Figure 13. Centreline profiles of bed elevations obtained for test D2 with the same method as for Figure 12.

Figure 13 shows the related bed profiles for test D2, where an additional bottom layer of 10cm of loose material was provided below and downstream of the dike. Comparison with Figure 12b indicates a slower process towards equilibrium, as the various levels have not converged after 6minutes. One may also remark a noticeable influence of the presence of the bottom layer on the vertical erosion, the latter allowing a deeper incision of the breach and a scour hole to develop on the downstream side.

4.4 *Breach width*

Breach width was obtained from the vertical images at three different sections: upstream side of the dike crest at x=0cm, middle at x=17.5cm, and downstream side at x=35cm. Results are illustrated in Figure 14 for test C1. In a first stage, the breach is wider along the downstream slope. After some time however, the breach widening develops faster on the upstream side, and the overall breach adopts a converging shape. Stabilization occurs after about 4.5minutes.

4.5 *Laser topography*

Measurements obtained with the system of sweeping laser light-sheet are now emphasized. Figure 15 shows an example of the set of reconstructed laser line traces corresponding to one full sweeping cycle of the mirror. The instant chosen, at t=45s, corresponds to the first phase of breach development: erosion occurs along the downstream slope, and the transported sediments are re-deposited in the wider reach downstream as flow velocities decrease. This creates a fan-like deposit, which is then later reincised as breach erosion progresses and outflow approaches its maximum value.

Full digital terrain models of the evolving breach topography are then obtained by interpolating between the sets of laser traces. Figure 16 on the following page, compares the results at selected times. The

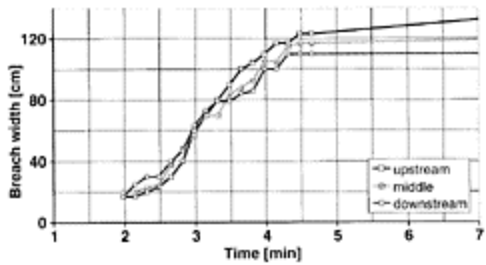

Figure 14. Evolution of the breach width as manually measured on the vertical digital images of run C1. The three profiles respectively refer to the upstream side (x=0cm), the middle

(x=17.5cm), and the downstream side (x=35cm) of the dike crest.

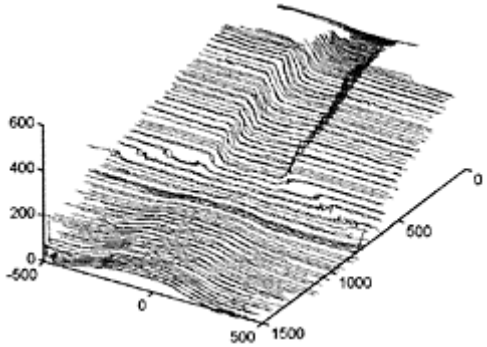

Figure 15. An example of the set of reconstructed laser traces corresponding to one sweeping cycle at time t=45s. These profiles are then used to obtain interpolated digital terrain models, as illustrated in Figure 16.

initial geometry is plotted in Fig. 16**a.** Figures 16**b** and 16**c** correspond to the first phase, as described above. The fan deposit is re-incised starting from Figure 16**d,** and the deepening of the breach progresses from downstream to upstream. Figure 16**e** corresponds approximately to the time of peak outflow, with an important rate of lateral erosion and deepening. The scour hole that develops at the toe of the downstream slope is particularly visible in Figures 16**f** and 16**g.** The breach then reaches an equilibrium stage when the drainage of the upstream reservoir is nearly completed. As seen in Figure 16**h,** the scour hole then gradually fills up again as transport intensity decreases.

5 CONCLUSIONS

We presented results from a series of laboratory experiments involving the controlled overtopping and breaching of a coarse sand dike. Special care has been

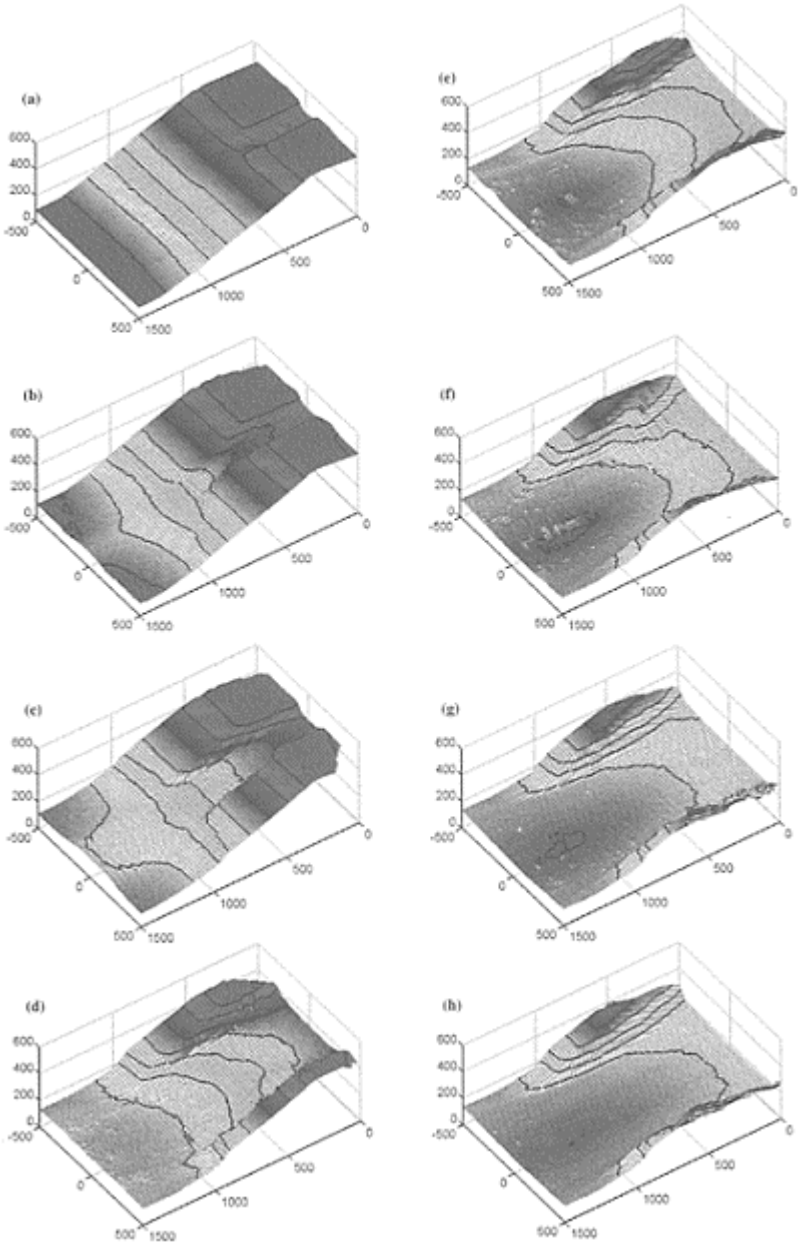

Figure 16. Digital terrain models of the dike at selected times. Respectively from **a** to **h:** *t*=0s, 20s, 45s, 1.75min, 2.9min, 4min, 5min, 6.2min.

Dimensions in mm. Black contours are plotted at levels ranging from 100mm to 450mm in steps of 50mm.

paid to insure well-controlled soil parameters and test reproducibility.

A wide range of measuring systems has been tested on the experiments with success. In particular, the non-intrusive laser imaging technique has proven to provide an unprecedented degree of detail in the evolution of the breach geometry. Such measurements are crucial for the validation of physicallybased breach models that do not rely on any assumption for outflow, breach topology and lateral erosion rates. We have shown how refractive effects at the air-water interface affects the underwater laser measurements, and have quantified an upper bound of the associated error.

Many results were presented, and preliminary experimental findings were briefly discussed and compared with the observations of previous authors. However, much of the interpretation work remains to be done. Further research will be carried out along this line in the future in our research team, including the development and validation of a physically-based mathematical framework and numerical model.

REFERENCES

Benoist, G. 1989. Les etudes d'ondes de submersion des grands barrages d'EDF. La Houille Blanche, 1–1989, 43–54.

Capart, H., Young, D.L. & Zech, Y. 2002. *Voronoï imaging methods for the measurement of granular flows.* Experiments in Fluids **32,** 121–135.

Delobbe, A. & Elslander, L. 2002. *Modélisation expérimentale de la rupture progressive d'une digue à partir d'une brèche.* B. Eng. Thesis, Université catholique de Louvain, Louvain-la-Neuve, Belgium (in French).

Froehlich, D.C. 2002. *IMPACT Project field tests 1 and 2: "blind" simulation by DaveF.* Proceedings of the 1st IMPACT project Workshop, Wallingford, United Kingdom, 16–17 May 2002.

Kulisch, H. 1994. *Physical 3D-Simulations of Erosioncaused Dam-breaks.* International Workshop on and Inundations related to Large Earth Movements, Trento, Italy, 4–7 October 1994.

Le Grelle, N., Spinewine, B., Soares Frazão, S. & Zech, Y. 2004. Non-intrusive imaging measurements of the morphological evolution of a channel during a dam-break flow. River Flow 2004. Proc. of the Second Int. Conf. on Fluvial Hydraulics, Napoli, Italy, 23–25 June 2004.

Morris, M.W. & Hassan, M.A.A.M. 2002. *Breach formation through embankment dams & flood defense embankments: a state of the art review.* Proceedings of the 1st IMPACT project Workshop, Wallingford, United Kingdom, 16–17 May 2002.

Singh, V.P. 1996. *Dam-breach modeling technology.* Kluwer Academic Publishers, Dordrecht, The Netherlands, 242pp.

Spinewine, B., Capart, H., Larcher, M. & Zech, Y. 2003. *Three-dimensional Voronoï imaging methods for the measurement of near-wall particulate flows.* Experiments in Fluids **34**–2, 227–241.

Temple, D.M. & Hanson, G.J. 1994. *Headcut development in vegetated earth spillways.* Applied Engineering in Agriculture, **10**–5, American Society of Agricultural Engineers.

Visser, P.J. 1998. *Breach growth in sand dikes.* PhD thesis and Communications on Hydraulic and Geotechnical Engineering Series, Report 98–1, Delft University of Technology, Delft, The Netherlands.

Wahl, T.L. 1998. *Prediction of embankment dam breach parameters: literature review and needs assessment.* USBR, Water Resources Research Laboratory, PAP-735, Denver, USA.

Monitoring and modelling river bank processes: a new methodological approach

L.Rossi Romanelli & M.Rinaldi
Dipartimento di Ingegneria Civile, Università di Firenze, Florence, Italy

S.E.Darby
Department of Geography, University of Southampton, Highfield, Southampton, UK

L.Luppi & L.Nardi
Dipartimento di Ingegneria Civile, Università di Firenze, Florence, Italy

River Flow 2004—Greco, Carravetta & Della Morte (eds.)

ABSTRACT: Fluvial erosion and mass failure are the two dominant processes causing river bank retreat. In order to investigate the interaction between these two processes and to establish the relative dominance of them under different conditions, research is being undertaken at two diverse study sites: Cecina River (Central Italy) and the River Asker (Southern UK). The study is divided into two main phases: the first phase consists of monitoring bank erosion processes; the second involves numerical modelling of the observed bank retreat. This paper presents a description of the river sites, including relevant geotechnical and hydrological characteristics of the bank materials, a description of the monitoring implementation including the beginning of the monitoring activity, and the methodological approach for the modelling phase.

1 INTRODUCTION

River bank erosion can contribute significantly to the sediment yielded from river catchments. Accordingly, knowledge of the rates and controls on bank erosion events is fundamental to understanding sediment flux. Bank erosion occurs through a combination of mass failures under gravity and fluvial erosion due to the direct action of the flow. While progress has recently been made in understanding the processes controlling large-scale mass failure of stream banks (e.g. Osman & Thorne, 1988; Rinaldi & Casagli, 1999; Casagli et al, 1999; Darby et al, 2000; Dapporto et al., 2001; Simon & Collison, 2002), much less attention has been paid to the role that direct fluvial erosion plays in bank

retreat. This is unfortunate because fluvial bank erosion can be a significant process in its own right, and also is frequently the trigger for a mass failure event.

To address this limitation, the aim of this research is to quantify the controls on fluvial bank erosion, examine the interaction between fluvial erosion and mass failure, and to establish the relative dominance of the two processes under different conditions. One of the key problems that has prevented progress being made on these topics is that it has proved very difficult to obtain reliable empirical data that describe relevant physical controls on the process, particularly during the flood flows that typically generate erosion. Specifically, detailed studies of the erodibility of bank materials, and of near-bank boundary shear stresses, are virtually absent from the literature, primarily due to the problems associated with undertaking accurate fieldwork in the hazardous environment of eroding riverbanks.

In this study we have therefore devised a new methodological approach that involves undertaking a combination of monitoring and hydraulic modelling investigations at two diverse study sites. Our rationale is to employ Computational Fluid Dynamics (CFD) techniques to obtain simulated high-resolution near-bank boundary shear stress data as a substitute for empirical data. The first study site is a reach of the Cecina River (central Italy), a gravel-bed river with large lateral bars and actively migrating outer banks. The second is a reach of the River Asker (southern UK), which is a low-gradient meandering river. These sites were chosen because they represent end-members in a spectrum ranging from very active (Cecina bank erosion rate ~7–17m/yr) to mildly active (Asker bank erosion rate ~0.2m/yr) eroding river meanders. This paper outlines the methodological approach that we are adopting at the Cecina and Asker and includes a description of the monitoring implementation, the monitoring activity since autumn 2003, and the methodological approach for the modelling phase.

2 STUDY AREAS

2.1 *Fiume Cecina*

The Cecina river (900km^2) is situated in Tuscany (Central Italy). The study site is located near Casino di Terra (Pisa) where the tributary Sterza meets the Cecina on its left bank. The main criteria for selecting this site were the high annual bank erosion rate and the availability of river stage and flow discharge data from a gauging station, situated about 2km upstream, at Ponte di Monterufoli. The study reach is about 500m long, though the actively eroding part of the bank (on the left side of the Cecina) extends about 170m upstream from the Sterza confluence. The average gradient of the reach is about 0.0021.

The eroding bank has an average height of about 5–5.5m and it can be defined as a layered type. The stratigraphy has been characterised by grain size analyses of samples collected from the exposed part of the bank in six vertical sections, combined with the results of two static penetration tests (CPT). Six main units, not all of which are present in every section, were therefore identified (Figure 2) as being composed of the following materials: (1) gravel; (2) gravel-sand; (3) well sorted sand; (4) silt-sand-clay; (5) massive sandy-silt; (6) sandy-silt.

A preliminary geotechnical characterization of these sediments were performed on the fine-grained materials (units 4, 5, 6). Samples were collected using a range of *in situ* and laboratory tests. Laboratory tests, in addition to grain size analyses, included phase relationship analyses and triaxial consolidated-undrained tests (CU) (units 5 and 6). *In situ* tests included seepage tests (unit 6) to determine the saturated hydraulic conductivity k_s (Amoozemeter test: Amoozegar, 1989), Borehole Shear Tests (BST: Lutenegger & Hallberg, 1981) (unit 6) and matric suction measurements using a tensiometer. Erodibility parameters (critical shear stress, τ_c, and erodibility coefficient, k_d) were also determined (units 4 and 6) by *in situ* jet tests (Hanson & Simon, 2001) using a non-vertical jet test device recently applied specifically to river banks (Dapporto, 2001). A summary of the grain size analyses, geotechnical and erodibility data is provided in Table 1 and 2.

2.2 *River Asker*

The River Asker (49.1km^2) is situated in Dorset (Southern UK). The study site is located near Bridport.

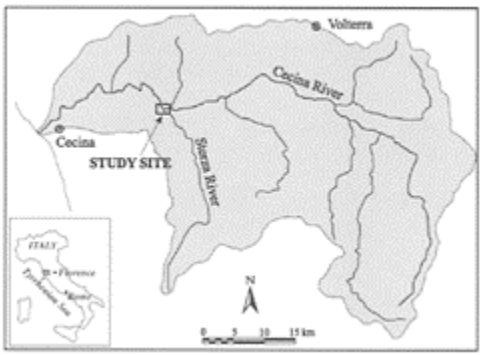

Figure 1. Cecina river basin (Central Italy): location map.

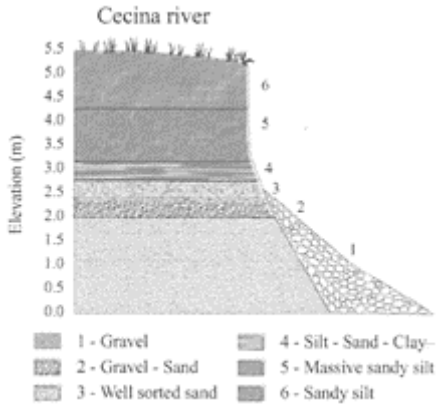

Figure 2. Cecina river: stratigraphy of the bank.

Table 1. Cecina river: grain size analyses.

	1	2	3	4	5	6
Gravel (%)	74.9	44.5	0	0	0	0
Sand (%)	25.1	55.5	100	10.1	18.6	26
Silt (%)	0	0	0	63.9	70.3	65.8
Clay (%)	0	0	0	26	11	8.2
D16 (mm)	11	0.4	0.11	–	0.01	0.02
D50 (mm)	12.6	1.4	0.19	0.011	0.05	0.05
D84 (mm)	41.8	17.9	0.27	0.023	0.07	0.08

This site was selected as river stage and discharge data are readily available from a gauging station, situated about 150m downstream from the bank monitoring reach. Moreover, the Asker site contrasts with the Cecina in that annual bank erosion rates are relatively low, so that the two sites between them cover a wide range of bank erosion rates. The study reach is about 200m long, with an average gradient of about 0.007.

Table 2. Cecina river: geotechnical properties and erodibility parameters for the upper layers.

Parameter	Units	4	5	6
Water content	%	–	–	19.7
Bulk unit weight	kN/m^3	–	–	17.50
Dry unit weight	kN/m^3	26.48	26.09	26.62

Saturated perm.	m/s	–	–	$0.87 \cdot 10^{-6}$
Eff. friction ang. (situ)	°	–	–	37.3
Appar. cohesion	kPa	–	–	4.8
Suction frict. ang.	°	–	–	21.5
Eff. frict. ang. (lab.)	°	–	35.9	38.3
Total cohesion	kPa	–	0	0
Erodibility coeff.	m^3/Ns	$6.61 \cdot 10^{-6}$	–	$4.97 \cdot 10^{-6}$
Critic. shear str.	Pa	0.763	–	1.013

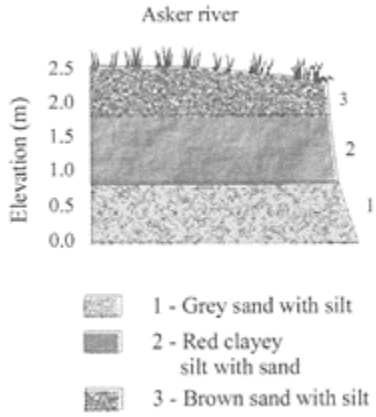

Figure 3. River Asker: stratigraphy of the bank.

The eroding bank has an averaged height of about 2–2.5m and it can be defined as a layered type. The stratigraphy has been characterised by grain size analyses of samples collected from two vertical sections of the bank. Three main units were identified (Figure 3) as being composed of the following materials: (1) grey sand with silt (about 0.8–1m thick); (2) red clayey silt with sand (about 1m thick); (3) brown sand with silt (about 0.4m thick).

A series of samples were collected for laboratory phase relationship analyses. Shear strength parameters were estimated by *in situ* Borehole Shear Tests. Erodibility parameters (critical shear stress, τ_c, and erodibility coefficient, k_d) were determined by *in situ* jet tests as described previously. A summary of the grain size analyses, geotechnical and erodibility data is provided in Table 3 and 4.

Table 3. River Asker: grain size analyses.

	1	2	3
Gravel (%)	0	0	0

Sand (%)	59.4	41.8	57.9
Silt (%)	37.5	52	38.2
Clay (%)	3.1	6.2	2.7
D16 (mm)	0.017	0.008	0.013
D50 (mm)	0.073	0.050	0.064
D84 (mm)	0.135	0.100	0.158

3 MONITORING ACTIVITY

The principles of the monitoring activity are identical at each study site, though there are differences in the actual implementation of these activities at each study site. Nevertheless, in general the monitoring activity is focused on: (1) characterising bed topography of the study reaches, for subsequent use in CFD modelling; (2) evaluating the peak flow discharge and water surface profile of that peak flow discharge along the study reaches for a range of flows, again for subsequent use in CFD modelling; (3) monitoring the magnitude of fluvial bank erosion generated by each flow event.

The magnitude of bank erosion generated by each flow event is monitored using a combination of lowresolution networks of erosion pins together with high-resolution digital photogrammetry (e.g. Lawler, 1993). At the Cecina study site erosion pins have been installed in 6 sections, spaced at about 6m intervals along the reach. At each section a set of 3 horizontal erosion pins, spaced at 0.5m intervals up from the bottom of the bank have been installed. At the River Asker, a total of 19 pin sections are used at approximately 3 m intervals, with 4 pins spaced at about 0.3m intervals up from the base of the bank. In addition, after each flow event a series of ground-based photographs of the eroding banks in each reach are taken for subsequent use in high-resolution digital photogrammetry. This technique, not discussed herein, allows estimates of bank retreat to be obtained across the entire eroding bank face, at approximately $0.2m^2$ spatial resolution.

The hydrological characteristics of each flow event are recorded at the Cecina site in a semi-automated way using a network of pressure transducers and crestgauges. In particular two piezometers and a water level sensor have been installed in a section of the reach. These instruments are connected to a data logger that records at 15 minute intervals. In Figure 4 a flow event recorded by the water level sensor and the piezometers is shown. In addition, 11 crest gauges have been installed at different elevations (to cover a large range of flows) along both the Cecina study reach and the tributary Sterza. These sensors and gauges

Table 4. River Asker: geotechnical properties and erodibility parameters.

Parameter	Units	1	2	3
Bulk unit weight	kN/m^3	18.03	17.93	17.99

Dry unit weight	kN/m^3	13.72	13.72	14.74
Vol. moist. cont.	%	44.0	43.0	33.2
Porosity	–	47.2	47.3	43.3
Deg. of saturation	%	93.1	91.2	76.6
Saturated perm.	m/s	$3.50 \cdot 10^{-8}$	$5.63 \cdot 0^{-10}$	$4.23 \cdot 10^{-6}$
Eff. friction ang.	°	28.1	39.4	38.4
Apparent cohesion	KPa	2.4	2.2	1.6
Erodibility coef.	m^3/Ns	$9.55 \cdot 10^{-5}$	$5.86 \cdot 10^{-6}$	–
Critic. shear str.	Pa	0.296	2.351	–

between them are able to characterise the water surface profile along the reach at peak flows, thereby defining the 'lid' for subsequent use in CFD modelling (see below). The peak flow discharge is available at the gauging station located about 2km upstream at Ponte di Monterufoli. Hydrological monitoring on the Asker is restricted to a network of 10 crest-gauges, spaced at approximately 20m intervals along the study reach. Similar to the Cecina site, peak flow discharge data is available from the gauging station at Bridport, Dorset, located approximately 150m downstream of the bank monitoring reach. At both study sites, efforts are made to acquire flow velocity data across the inlet of the study reach using 2D electromagnetic flow velocimeters during the flood events. These data are helpful in specifying the boundary conditions for use in the CFD modelling.

4 MODELLING PHASE

During the modelling phase, a range of specific flow events that occurred during autumn 2003 are selected for further analysis, using hydraulic and geotechnical data collected during the monitoring phase for the modelling implementation. The first phase of the modelling involves the evaluation of near-bank boundary shear stress distributions through the use of CFD modelling. This allows quantification of the bank erosion rate due only to fluvial erosion, using an excess shear stress formula (see § 4.1). The second phase comprises bank stability analysis to determine the bank erosion rate due to geotechnical failure. This involves the use of the finite element seepage and slope stability analyses SEEP and SLOPE for dynamic simulation of bank pore pressures and mass failure conditions (see § 4.2). The two modelling phases are, however, linked because the bank erosion rate due to fluvial erosion, determined in the first step, is used to provide dynamically adjusting bank profiles during the seepage and stability analyses. The two modelling phases are now described in more detail.

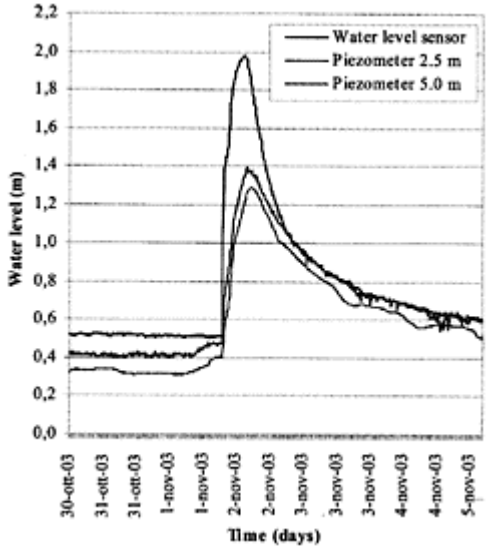

Figure 4. Cecina river: flow event recorded by the water level sensor and the piezometers.

4.1 *Computational Fluid Dynamics simulations*

The shear stress distribution exerted on the bank face by flows of varying magnitude is evaluated by undertaking hydraulic modelling using 3-dimensional Computational Fluid Dynamics (CFD) simulations of monitored flows (e.g. Olsen, 1991; Olsen & Skoglund, 1994; Olsen & Stokseth, 1995; Booker et al., 2001). Models are built using the high resolution topography data sets collected during the monitoring phase, with initial and boundary conditions specified using the flow velocity and water surface profile data obtained during the monitoring.

Preliminary analyses of near-bank boundary shear stress distribution have also been evaluated at low resolution by applying a 1-dimensional HEC-RAS model, which allows determination of hydraulic parameters (water surface profile, flow velocity and mean boundary shear stress) under a steady state flow simulation (Hydrologic Engineering Center, 1997). The near-bank shear stress distribution is then estimated from the 1D simulation data using the results of research from laboratory channels (Leutheusser, 1963; Kartha & Leutheusser, 1972; Knight et al., 1984).

The modelled shear stress distribution allows the deformation of the bank profile caused by fluvial erosion (recall that this is necessary to assess the influence of fluvial erosion on mass bank failure) to be quantified using a simple excess shear stress formula (Partheniades, 1965)

$$\varepsilon = k_d(\tau_0 - \tau_c)^a \quad (1)$$

where ε (m/s) is the fluvial bank erosion rate per unit time and unit area, τ_0 (Pa) is the modelled shear stress distribution, k_d and τ_c (Pa) are the erodibility parameters (defined previously) and a is an empirically-derived exponent. Since the erodibility parameters k_d and τ_c are determined through the jettesting undertaken as part of the field monitoring described previously, and because a can be assumed equal to unity (Dapporto, 2001), the modelled shear stress is the only unknown parameter required to estimated the fluvial bank erosion rate.

4.2 *Geotechnical modelling*

Groundwater seepage and slope stability analysis are undertaken using the off-the-shelf software packages SEEP/W and SLOPE/W (GEO-SLOPE International Ltd, 2000). SEEP/W is a finite element code for determining pore water pressure distributions at the scale of a single flow event, and can model both saturated and unsaturated flow under steady state or transient conditions. By assigning initial and boundary conditions, and defining hydraulic and soil material properties in relation to the field data collected in the monitoring phase, the pore water pressure distribution is computed using the flow equation in conjunction with the continuity equation expressed in generalized form for unsaturated soils (Richards, 1931; Fredlund & Rahardjio, 1993) as follows:

$$\frac{\partial}{\partial x}\left(K_x \frac{\partial H}{\partial x}\right) + \frac{\partial}{\partial y}\left(K_y \frac{\partial H}{\partial y}\right) + Q = \frac{\partial \Theta}{\partial t} \qquad (2)$$

where H is the unknown total head, K_x and K_y the hydraulic conductivity respectively in x and y directions, Q is the external flux and Θ is the water content.

The bank geometry is discretised using rectangular or triangular finite elements and divided into regions

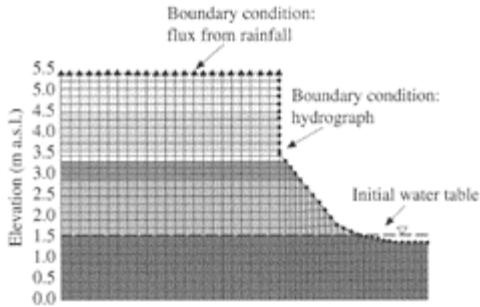

Figure 5. Finite element seepage analyses: geometry of the problem for the Cecina river.

composed of materials with different hydraulic and sedimentary properties. Different volumetric water content and hydraulic conductivity functions, based on the measured grain size distribution, are assigned to each material within the bank. The geometry of the

problem in the case of the Cecina River is shown in Figure 5. For the initial point in the simulation, the water table is set to the same level of the river at the start of the selected flow event. Boundary conditions are then defined for transient simulations. These comprise an infiltration intensity versus time function based on rainfall data available from rainfall stations situated close to the sites and assigned to the nodes on the top of the bank, while the flow hydrograph, based on results of hydraulic analyses or on data measured during the monitoring phase for the selected events (Cecina River), is assigned to nodes along the slope of the bank. The hydrograph is divided into discrete time steps, the model output consisting of the computed pore water pressure in each element within each time step. In the case of the Cecina, these results can be calibrated and compared with observed data from the installed pressure transducers.

SLOPE/W is a software package that performs slope stability analyses by applying limit equilibrium methods (including Morgenstern-Price, Bishop, Fellenius, Janbu and more) to compute the factor of safety of the bank. This software is integrated with SEEP/W in such a way that the results (pore pressure distributions) of the seepage analyses are used as input data for the stability analysis. The bank geometry can be irregular so that changes in bank geometry due to fluvial erosion can be modelled. The slip surface geometry can be planar, rotational and composite, with or without tension cracks. Confining pressure is taken into account by specifying the surface water elevation. The Mohr-Coulomb failure criterion in terms of effective stress is used in the case of positive pore water pressure, while the extended Fredlund et al. (1978) failure criterion for unsaturated soils is used in the case of negative pore water pressure. Geotechnical properties, unit weight and shear strength parameters (c′, ϕ' and ϕ^b), all determined from the field monitoring as described previously, are defined for each different material composing the bank.

In order to address the interaction between mass failure and fluvial erosion, SEEP and SLOPE are used to simulate the evolution of bank stability during and after selected events. Two simulation scenarios are investigated: on the one hand bank deformation by fluvial erosion, previously determined using the CFD modelling and equation (1), is taken into account by updating deformed bank profiles at each time step of the selected flow events; on the other hand control simulations in which the bank has not been deformed are performed. Comparison of the results derived from these two scenarios will enable the effect of bank deformation on bank stability to be isolated.

5 CONCLUSIONS

In this paper we have outlined research being undertaken at two different study sites in order to investigate the interaction and relative dominance between fluvial erosion and mass failure in determining bank retreat.

A description of the study areas and of the main riverbank characteristics sites is provided here. Monitoring activity includes: (a) an initial topographic survey of the study reaches; (b) measurements of water stages and water surface profiles during flow events; (c) measurements of bank retreat generated by each flow event.

A new methodological approach is undertaken for the modelling phase, based on the combination of empirical data collected during the monitoring activity with hydraulic and

geotechnical modelling. This approach involves: (a) the evaluation of a near-bank shear stress distribution by applying 3D CFD simulations to quantify the bank erosion rate due to fluvial erosion; (b) finite element seepage and slope stability analyses for dynamic simulations of pore water pressure changes and mass failures.

REFERENCES

Amoozegar, A. 1989. A compact constant-head permeameter for measuring saturated hydraulic conductivity of the vadose zone. *Soil Science Society of American Journal* 53:1356–1361.

Booker, D.J., Sear, D.A. & Payne, A.J. 2001. Modelling 3D flow structures and patterns of boundary shear stress in a natural pool-riffle sequence. *Earth Surf. Proc. & Lndfrms.* 26:553–576.

Casagli, N., Rinaldi, M., Gargini, A. & Curini, A. 1999. Pore water pressure and streambank stability: results from a monitoring site on Sieve River, Italy, *Earth Surf. Proc. & Lndfrms.* 24:1095–1114.

Darby, S.E., Gessler, D. & Thorne, C.R., 2000. Computer program for stability analysis of steep, cohesive riverbanks, *Earth Surf. Proc. & Lndfrms.* 25, 2:175–190.

Dapporto, S. 2001. *Non-vertical jet testing of cohesive streambank toe material.* School of Geography, University of Nottingham, in collaboration with USDA-ARS National Sedimentation Laboratory, Oxford, Mississippi.

Dapporto, S., Rinaldi, M. & Casagli, N. 2001. Failure mechanisms and pore water pressure conditions: analysis of a riverbank along the Arno River (Central Italy). *Engineering Geology* 61:221–242.

Fredlund, D.G., Morgenstern, N.R. & e Widger, R.A. 1978. Shear strength of unsaturated soils. *Can. Geotech. J.* 15:313–321.

Hanson, G. & Simon, A. 2001. Erodibility of cohesive streambeds in the loess area of the midwestern USA. *Hydrol. Proc.* 15:23–38.

Hydrologic Engineering Center, 1997. *HEC-RAS River Analysis System version 2.0 User's Manual.* Davis, California: US Army Corps of Engineers.

Kartha, V.C. & Leutheusser, H.J. 1972. Distributio of Tractive Force in Open Channels. *J. Hydr. Div.* ASCE 96:1469–1483.

Knight, D., Demetriou, J.D. & Hamed, M.E. 1984. Boundary Shear in Smooth Rectangular Channels. *J. Hydr. Eng.* ASCE 110:405–422.

Lawler, D.M. 1993. The measurement of river bank erosion & lateral channel change: A review. *Earth Surf. Proc. & Lndfrms.* 18:777–821.

Leutheusser, H.J. 1963 Turbulent Flow in Rectangular Ducts. *Proc. Am. Soc. Civ. Engrs.* 89, HY3.

Lutenegger, A.J. & Hallberg, G.R. 1981. Borehole Shear Test in geotechnical investigation. *Special Technical Publ. American Society for Testing and Materials* 740:566–578.

Olsen, N.R.B. 1991. *A Numerical Model for Simulation of Sediment Movements in Water Intakes,* PhD Thesis, The Norweigan Institute of Technology, Trondheim.

Olsen, N.R.B. & Skoglund, M. 1994. Three-dimensional modelling of water & sediment in a sand trap. *J. Hydr. Res.* 32:833–844.

Olsen, N.R.B. & Stokseth, S. 1995. Three-dimensional numerical modelling of flow in a river with large bed roughness. *J. Hydr. Res.* 33:571–581.

Osman, A.M. & Thorne, C.R. 1988. Riverbank stability analysis. I: Theory. *J. Hydr. Eng.* 114:134–150.

Partheniades, E. 1965. Erosion and deposition of cohesive soils. *J. Hydr. Div.* ASCE 91:105–139.

Rinaldi, M. & Casagli, N. 1999. Stability of streambanks formed in partially saturated soils and effects of negative pore water pressures: the Sieve River (Italy) *Geomorphology* 26:253–277.

Simon, A. & Collison, A.J.C. 2002. Quantifying the mechanical & hydrologic effects of riparian vegetation on streambank stability. *Earth Surf. Proc. & Lndfrms.* 27:527−546.

Two-dimensional fluvial channel model with bank erosion on triangular grid

D.Farshi[1] & H.-E.Minor
Federal Institute of Technology Zurich (ETHZ), The Laboratory of Hydraulics, Hydrology and Glaciology (VAW), Switzerland

River Flow 2004—Greco, Carravetta & Della Morte (eds.)

ABSTRACT: A 2D numerical model to simulate the bed load transport and bank erosion in alluvial channels is developed based on shallow water equations (SWE) and Exner equation by Finite Volume (FV) spatial discretization. The Roe Riemann Solver has been utilized for the Flux estimation in SWE and the Local Lax-Friedrich solver is used for the bed load transport. A new formulation of bed shear stress has been presented and the bank erosion simulation been achieved through a new approach. Accuracy and stability of the code are tested against an available set of experimental data.

1 INTRODUCTION

In natural rivers and channels the erosion, sedimentation and bank line migration cause land loss, bridge failure, shoaling of waterways and flooding. In order to obtain maximum benefit and reduce the adverse effects, research on the prediction of the mentioned processes and the effective control strategy has always been a key concern of hydraulic, geological and river engineers. Therefore the analysis of flow, bed level variations and bank erosion is a fundamental prerequisite for many hydraulic engineering problems.

The complicated fluvial phenomenon is dominated by the flowing water, sediment transport, bed forms and bank erosion as well. Hence, numerical simulation of movable bed channels requires the accurate prediction of the flow field, sediment transport and bank erosion. The latter is one of the most difficult points in numerical simulation, therefore many existing alluvial channel models assume that the channel banks are rigid, or adjust bank geometry according to theoretical, but non-mechanical, arguments

regarding energy or stream power expenditure (Chang 1988), (Yang & Song 1986). Although changes in channel depth caused by aggradation or degradation of river bed can be simulated, changes in width cannot be computed by most of the mathematical models. When attempting to model natural systems this is a significant limitation because channel morphology usually changes with time and adjustment of both width and depth are the rule rather than exception.

Developing two-dimensional models for the fluvial process in channel with bank erosion is indeed a new challenge between researchers in recent years. An example is the model of Mosselman (1992), who has extended the model of Olesen (1987) by adding a mechanism for the erosion of cohesive banks, partly using a time averaged description of Osman and Thorne (1988). The model is formulated in a horizontal, channel-fitted coordinate system (s, n) which can be curvilinear and non-orthogonal. Duan et al. (2001) have developed an equation for bank erosion based on the sediment mass balance within a control volume near the bank. They implemented this equation in the enhanced model CCHE2D and simulated meandering process in channels. These models are applied to structured mesh, in which the implementation of the discussed problems is much easier.

From the overview on recent literature it is obvious that there is still no general model to simulate the fluvial process, in particular the bank erosion, on an unstructured grid. The important advantage of unstructured grid is the ability to handle complex geometries with ease. The purpose of this work is to develop a two-dimensional numerical model which is also capable of simulating these processes.

2 GOVERNING EQUATIONS

2.1 *Hydrodynamics equations*

The two-dimensional unsteady flow of water can be described by Shallow Water Equations (SWE). By assuming hydrostatic pressure distribution and neglecting wind shear, Coriolis acceleration and eddy

[1] Formerly at German Armed Forces University, Hydroscience Institute, Neubiberg, Germany.

viscosity, the following form of shallow water equations (SWE) can be derived:

$$\boldsymbol{U}_t + \nabla \boldsymbol{Q} + \boldsymbol{S} = 0 \tag{1}$$

where $\boldsymbol{U}$, $\boldsymbol{Q}$ and $\boldsymbol{S}$ are the vectors of primitive variables, fluxes in the x and y directions and source term respectively, given as:

$$\boldsymbol{U}=\begin{pmatrix}\zeta\\ uh\\ vh\end{pmatrix} \tag{2}$$

$$\boldsymbol{Q}=(\boldsymbol{F},\boldsymbol{G});\boldsymbol{F}=\begin{pmatrix}uh\\ u^2h+\frac{1}{2}gh^2\\ uvh\end{pmatrix};\boldsymbol{G}=\begin{pmatrix}vh\\ uvh\\ v^2h+\frac{1}{2}gh^2\end{pmatrix}$$

$$\boldsymbol{S}=\begin{pmatrix}0\\ \tau_{Bx}/\rho-ghS_{Bx}\\ \tau_{By}/\rho-ghS_{By}\end{pmatrix}$$

Here h represents the water depth, ζ the water elevation, u and v the velocity components in x and y directions and g the acceleration due to gravity. S_{Bx} and S_{By} denote the bed slope in x and y directions. We developed a new formulation of bed stress components in order to consider the bed topography and some of two-dimensional eifect of water flow (Farshi 2002):

$$\boldsymbol{\tau_B}=\frac{1}{\sqrt{1+(\partial z/\partial x)^2+(\partial z/\partial y)^2}} \tag{3}$$
$$\begin{pmatrix}\begin{pmatrix}\rho g n^2 u\sqrt{u^2+v^2}/h^{1/3}\left(1+(\partial z/\partial y)^2\right)-\\ \rho g n^2 v\sqrt{u^2+v^2}/h^{1/3}(\partial z/\partial x)(\partial z/\partial y)\end{pmatrix}\\ \begin{pmatrix}\rho g n^2 v\sqrt{u^2+v^2}/h^{1/3}\left(1+(\partial z/\partial x)^2\right)-\\ \rho g n^2 u\sqrt{u^2+v^2}/h^{1/3}(\partial z/\partial x)(\partial z/\partial y)\end{pmatrix}\\ \begin{pmatrix}\rho g n^2 u\sqrt{u^2+v^2}/h^{1/3}(\partial z/\partial x)+\\ \rho g n^2 v\sqrt{u^2+v^2}/h^{1/3}(\partial z/\partial y)\end{pmatrix}\end{pmatrix}$$

where $\boldsymbol{\tau_B}$=Bed stress vector and z=bed elevation

The first and second component of bed stress vector correspond to $\boldsymbol{\tau_{Bx}}$ and $\boldsymbol{\tau_{By}}$ respectively.

2.2 *Bed load equation*

The bed load continuity or bottom conservation equation can be written in following form:

$$\nabla[(1-p)\rho_s\,\boldsymbol{u}_s]=0 \tag{4}$$

Where

p reperesents porosity, ρ_s bed material density and $\boldsymbol{u_s}$ bed load flow velocity vector.

Introducing the bed load flux vector $\boldsymbol{\Phi}=(1-p)\rho_s\boldsymbol{u_s}$ and after integration, (4) becomes:

$$(1-p)\frac{\partial z}{\partial t}+\nabla \boldsymbol{q_b}=0$$

where z denotes bottom level and $\boldsymbol{q_b}=1/\rho_s\int_{Z_F}^{Z_B}\boldsymbol{\Phi}\,dz$ bed load transport rate vector.

The bed load transport rates (q_{bx}, q_{by}) can be estimated by different equations such as Meyer-Peter and Müller (1948). In order to take the bed slope effects into account, the critical Shields parameter as well as bed load equations have to be modified (van Rijn 1993).

3 NUMERICAL MODEL

3.1 *Hydrodynamic model*

The SWE and sediment flow equation are a nonlinear, coupled partial differential equations system. A unique analytical solution is only possible for idealised and simple conditions. For practical cases, it is required to implement the numerical methods. Keeping this in mind that an unstructured triangular mesh will be used, the Finite Volume (FV) method has been used for the discretization of SWE:

$$\int_{\Omega}\boldsymbol{U_t}\,d\Omega+\int_{\Omega}\nabla\cdot\boldsymbol{Q}\,d\Omega+\int_{\Omega}\boldsymbol{S}\,d\Omega=0 \tag{5}$$

in which Ω=the area of the calculation cell

Assuming $\boldsymbol{U_t}$ is constant over the domain for first order accuracy, it can be written:

$$\boldsymbol{U_t}+\frac{1}{\Omega}\int_{\partial\Omega}\boldsymbol{Q}\cdot\boldsymbol{n_s}\,dl+\int_{\Omega}\boldsymbol{S}\,d\Omega=0 \tag{6}$$

The equation (13) can be discretized as follows:

$$\boldsymbol{U_i^{n+1}}=\boldsymbol{U_i^n}-\frac{\Delta t}{\Omega}\sum_{j=1}^{3}\boldsymbol{Q_{i,j}^{*n}}\cdot\boldsymbol{n_j}\,\boldsymbol{dl_j}-\Delta t\,\boldsymbol{S_i^n}$$

where m is number of cell or element sides, $\boldsymbol{Q_{i,j}^*}=(\boldsymbol{F_{i,j}^*},\boldsymbol{G_{i,j}^*})$ numerical flux through the side of the cell and $\boldsymbol{n_j}$ unit vector of the cell side.

In FV method, the key problem is to estimate the normal flux through each side of the domain namely $\boldsymbol{(Q\cdot n_s)}$. There are several algorithms to estimate this flux. The set of SWE is hyperbolic and, therefore, it has an inherent directional property of propagation. Algorithms to estimate the flux should appropriately handle this property. The *Riemann solver,* which is based on characteristic theory, is such an algorithm. In this work we used an approximate Riemann Solver due to Roe(1981):

$$\boldsymbol{Q^*}=\frac{1}{2}\left[\boldsymbol{Q_R}+\boldsymbol{Q_L}-\left|\tilde{\boldsymbol{J}}^*\right|(\boldsymbol{U_R}-\boldsymbol{U_L})\right] \tag{7}$$

where $|\tilde{J}^*| = \tilde{R}|\tilde{\Lambda}|\tilde{R}^{-1}$, $\tilde{R}$ is the eigenvectors matrix of $\tilde{J}^*$, denoted by $\tilde{e}^1, \ldots, \tilde{e}^m$ with corresponding eigenvalues $\tilde{a}^1, \ldots, \tilde{a}^m$, $|\tilde{\Lambda}| = diag(|\tilde{a}^1|, \ldots, |\tilde{a}^m|)$, subscripts R and L are referred to the right and the left side of the cell interface respectively.

3.2 *Morphodynamic model*

There are three different formulations for the numerical approximation of the bed-updating or Exner equation:

- The SWE and Exner equation are separately and numerically approximated using the same time step
- The SWE is converged to a steady solution and then the bed will be updated. The overall time step of this formulation is the morphological time step of the Exner equation and the SWE is converged to a steady state solution every time the bed is updated. This approach gives inaccurate results and also takes considerably longer computational run times. (Hudson & Sweby, 2000)
- The whole system of the SWE and Exner equations are numerically approximated. Unfortunately in this case the Jacobean matrix of the equation system is singular, which might be expected to create difficulties when implementing a numerical scheme for this formulation. Moreover, it needs an accurate estimation of the wave speed of Exner equation, which is generally not possible, due to the empirical form of bed-load relations.

In this work, the first approach is used, in which; the bed-updating calculation is decoupled from the flow computation. The flow is assumed to be quasi-steady in hydrodynamic model, which might be reasonable due to the explicit simulation method. The FV method has been also utilized to discretize the Exner equation. The bed-updating equation (4) can be rewritten in the following integral form:

$$(1-p)\int_{\Omega}\frac{\partial z}{\partial t}d\Omega + \int_{\partial\Omega} \boldsymbol{q}_B \cdot \boldsymbol{n}_s \, dl = 0 \tag{8}$$

The above equation can be discretized as follows:

$$z_i^{n+1} = z_i^n - \frac{\Delta t}{\Omega}\sum_{j=1}^{m} q^{*n}_{Bi,j}\, \boldsymbol{n}_{s\,j}\, dl_j \tag{9}$$

where $q^*_{Bi,j}$ is numerical bed load flux through the cell side.

A simple flux solver like Local Lax-Friedrich (LLF) solver is used to determine the numerical bed load flux through the computational edge:

$$q_B^* = 0.5\left(q_{BL} + q_{BR} - \alpha_s^*\left(z_R - z_L\right)\right) \tag{10}$$

where α_s^*=max $(|u_{BL}|,|u_{BR}|)$, u_{BR} and u_{BR} are the sediment migrating velocities in left and right side of the calculation edge.

3.3 *Numerical treatment*

The computation of bank erosion can be decoupled from the computation of bed topography if these phenomena occur slowly. Due to the explicit approach and small time steps of computation, this assumption can be reasonable.

The stability of bank strongly depends on the inclination angle. Referring to topography of bed, the maximum slope has to be computed to be compared with critical slope, namely tan γ_{cr}. The maximum slope of a computational cell can be computed by magnitude of gradient vector ***(SD)*** of bed topography at each cell:

$$\tan \gamma_{\max} = |\nabla z| = \sqrt{\left(\frac{\partial z}{\partial x}\right)^2 + \left(\frac{\partial z}{\partial y}\right)^2} \tag{11}$$

After comparing $\gamma_{\max}$ and γ_{cr}, it can be decided whether or not the bank will be deformed. In the case of deformation, the cell will be rotated by $(\gamma_{\max} - \gamma_{cr})$ about the rotational axis. The main task is to find a method to determine the rotation axes, which is appropriate to unstructured mesh such as in Figure 1.

The rotation axis can be represented by rotation vector ***(RA)*** as follows:

$$\boldsymbol{RA} = \frac{\partial z}{\partial y}\,\boldsymbol{i} - \frac{\partial z}{\partial x}\,\boldsymbol{j} \tag{12}$$

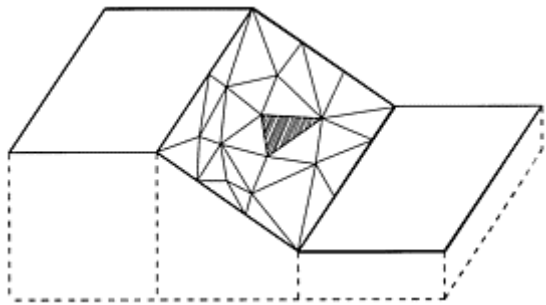

Figure 1. A schematic discretization of a channel bank.

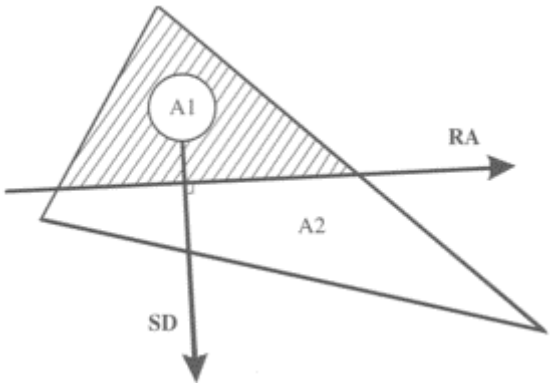

Figure 2. Slope and rotation vectors of a cell A1=A2.

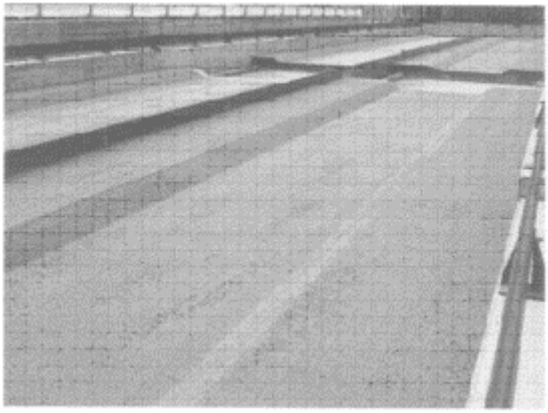

Figure 3. Physical model of TUM.

The rotation axis is located on the cell in such a form that the areas of degradation and aggradation in the cell are equal (Fig. 2).

Each cell is handled individually and rotated to reach the stable angle. Since the individual handling of each cell, it is necessary to implement this method in an iterative approach. Therewith it can be guaranteed that the calculated elevation of common grid nodes of cells has the same elevation.

4 APPLICATION

4.1 *Straight channel with movable bed*

Experiments on a physical model were conducted at the Technical University Munich (TUM) in Germany to understand the fundamental flow behaviour to be used in river restoration activities' planning of two rivers Iller and Isar in Bavaria, Germany (Schmautz, 2003). The experiments took place in different series in a specially established, spread over 100 ms long and 8 ms wide, model channel (Fig. 3).

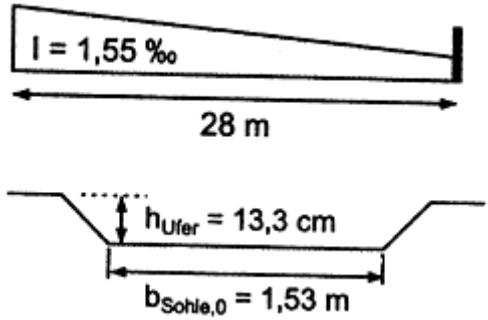

Figure 4. Geometry of the experiment (Q=115.6 l/sec).

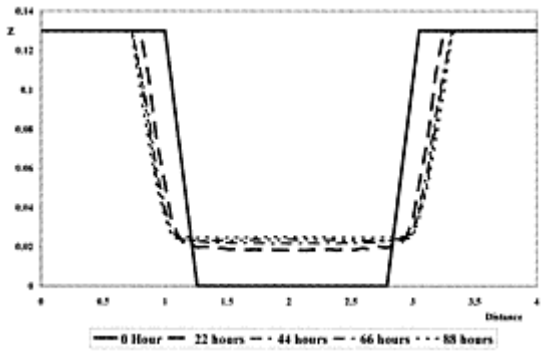

Figure 5. Evolution of bed and bank erosion.

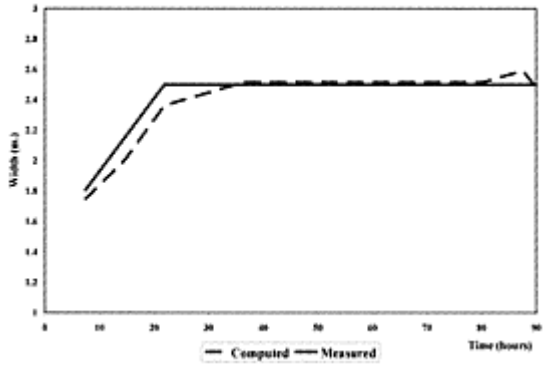

Figure 6. Evolution of width in the half depth.

Between different alternatives we choose the following experiment to validate and test the code (Fig. 4):

The numerical simulation has been made for the above experiment for 87.6 hours. The bank erosion and bed evolution process is computed and compared with the experimental data. Figure 5 shows the simulated bed elevation changes and bank erosion at a cross section. Figure 6 represents the evolution of channel width with the half depth. As it can be seen there is a good agreement between the experiment and computational results.

5 CONCLUSION

This paper reports the research on the development and verification of a two-dimensional model in simulation of alluvial processes in a channel on a triangular mesh, which enables us to handle and define complex geometry, easily.

The bed stress term has been handled in a new form in order to consider the two-dimensional effects of flow and the bed slope effects in bed stress calculation. The bank erosion evolution has been dealt in a form, which is suitable for unstructured grids, especially the triangular mesh. However, this method needs large computational time due to its iterative process.

ACKNOWLEDGEMENT

The first author would like to express his best thanks to Professor Dr.-Ing. Wihelm Bechteler, ex-director of the Hydroscience Institute of German Armed Forces University in Munich, where the main of this work was done.

REFERENCES

Chang, H.H. 1988 *"Fluvial Process in River Engineering"*, Jon Wiley & Sons, Inc., USA.

Duan, J.G.; Wang, S.S.Y. & Jia, Y. 1998 *"The Application of the Enhanced CCHE2D Model to Study the Alluvial Chan-nel Migration Processes"*, Journal of Hydraulic Research, Vol. 39, 2001, No. 5, ppl-12.

Farshi, D. 2002 *"Two-Dimensional Simualtion of Sediment Transport on Unstructured Mesh"*, Ph.D. Thesis, German Armed Forces University, Hydroscience Institute, Neubiberg (Munich), Germany.

Hudson, J. & Sweby, P.K. 2000 *"Numerical Formulation for Approximating the Equations Governing Bed-Load Sediment Transport in Channels and Rivers"*, Numerical Analysis Report 2/2000, The University of Reading, Dept. of Mathematics, Reading, Berkshire.

Mosselman, E. 1992 *"Mathematical Modelling of Morphological Processes in Rivers with Erodible Cohesive Banks"*, Communications on Hydraulic and Geotechnical Engineering, 92, Delft Univrsity of Technology, Delft.

Müller, R. 1943 *"Theoretische Grundlagen der Fluss-und Wildbachverbauungen"*, Mitteilungen der Versuchsanstalt fur Wasserbau, ETH Zürich, Nr. 4.

Olesen, K.W. 1987 *"Bed Topography in Shallow River Bends"*, Communications on Hydraulic and Geotechnical Engineering, 87, Delft Univrsity of Technology, Delft.

Osman, A.M. & Thorne, C.R. 1988 *"Riverbank Stability Analysis, I: Theory"*, Journal of Hydraulic Engineering, ASCE, Vol. 114, pp. 134–150.

Roe, P.L. 1981 *"Approximate Riemann Solvers, Parameter Vectors, and Difference Schemes"*, Journal of Computational Physics, 40, 263–293.

Schmautuz, M. 2003 *"Eigendynamische Aufweitung in einer geraden Gewässerstrecke"*, Ph.D. Thesis, Technical University Munich, Laboratory of Hydraulic and Water Resources Engineering, Munich, Germany (in German).

Van Rijn, L.C. 1993 *"Principles of Sediment Transport in Rivers, Estuaries and Coastal Seas"* AQUA Publication, Amsterdam, The Netherlands.

Wiberg, P.L. & Smith, D.L. 1989 *"Model for Calculating Bed-Load Transport of Sediment"* Journal of Hydraulic Engineering., ASCE, Vol. 115, No. 1.

Yang, C.T. & Song, C.C.S. 1986 *"Theory of Minimum Energy and Energy Dissipation Rate"*, Encyclopedia of Fluid Mechanics, Vol. 1, Chapter 11, Gulf Publishing Company, Ed. Cheremisinoff, N.P.

Yen, C. & Lee, K.T. 1995 *"Bed Topography and Sediment Sorting in Channel Bend with Unsteady Flow"*, Journal of Hydraulic Engineering, Vol. 121, No. 8, pp. 591–599.

Zhao, D.H.; Shen, H.W.; Lai, J.S. & Tabios, G.Q. 1996 *"Approximate Riemann Solvers in FVM for 2D Hydraulic Shock Wave Modeling"*, Journal of Hydraulic Engineering, Vol. 122, No. 12, December, pp. 692–702.

B.3.
Flood propagation

Influencing factors of flow instabilities in steep and stepped channels

T.F.Ganz
Bayerisches Landesamt für Wasserwirtschaft München, Germany

F.Schöberl
Institute of Geography, Natural Hazards Research, Innsbruck University, Austria

River Flow 2004—Greco, Carravetta & Della Morte (eds.)

ABSTRACT: Grade control structures are effective measures for restricting flow energy and bed erosion and therefore frequently applied in steep creeks and torrents. Unfortunately in some cases they seem to be predisposed for initiating hazardous flow instabilities during flood flows, e.g. instable flow waves at the Ruetz river/Tyrol overtopping the river banks and causing dynamic stresses on new bank revetments could be observed, triggered the launch of a systematic model study at the University of Innsbruck. In a first phase limiting discharges for the occurrence of the instabilities were investigated. In a second step influences on the wave height and the development along the channel reach were analysed. Significant parameters influencing the emergence of flow instabilities proved to be the flow discharge and the mean bed slope. In addition to the quantification of these parameters, the experiments focused on determining further influences like bed roughness, geometry of the control structures and concentration of clay suspension. It could be proved that bed roughness and clay concentration do not influence the onset of the instabilities but have a certain effect on the development of the wave height. Wave frequencies turned out to be independent of slope, discharge, bed roughness and concentration of suspension, but proved to be strongly related to the step height of the control structures.

1 INTRODUCTION

Drop structures are effective measures for the control of flow energy and bed erosion and therefore frequently applied in steep creeks and torrents. Unfortunately in some cases they seem to be predisposed for initiating hazardous flow instabilities during flood flows, e.g. instable flow waves could be observed at the Ruetz river/Tyrol, triggering the launch

of a systematic investigation at the University of Innsbruck. When waves develop, channel banks can be overtopped and inundations are the consequence. Furthermore, the dynamic stress of wave-crests on the riverbank may become dangerous for the bank protection. Concerning the design of the river banks it is important to predict the occurrence of waves and the development of wave height along the river reach. To analyse the influence of different boundary conditions on the emergence of flow instabilities, model tests were performed in a stepped laboratory flume. In a first phase, limiting discharges for the occurrence of the instabilities were investigated. In a second step influences on the wave height and the wave development along the channel reach were analysed.

Most of earlier investigations deal with flow instabilities of clear water in smooth channels, e.g. Dressler (1949), Koloseus (1966) and Brock (1969). Whittaker (1982) was one of the first to study the effect of steps and the appearance of unstable tumbling flow conditions when the fully developed submerged hydraulic jump interferes with the physical boundaries of the step-pool system. Recent contributions were for instance provided by De Fessant (2001). Experimental and theoretical evidence for the occurrence of flow instabilities in mudflows goes back to Davies (1988), Savage (1989) and Coussot (1994). Cohesion and increasing viscosity may be seen as factors increasing the possibility of the development of instabilities.

2 EXPERIMENTAL RESEARCH

This study is part of a wider research project analysing and assessing the conditions and dependencies of flow instabilities in stepped channels. In a first stage, limiting discharges for the occurrence of the instabilities were investigated, Ganz & Schöberl (2003). In the recently finished second phase, further factors influencing the wave properties and the development along the channel reach were analysed. Particular focus lay on the effect of bed roughness and the influence of varying water-clay mixtures on the developing wave

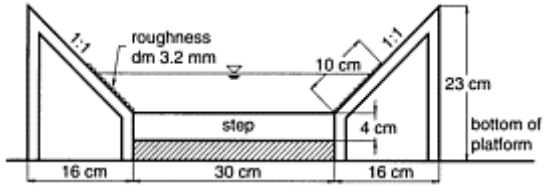

Figure 1. Scale model of the stepped channel, cross-section, example with smooth bed.

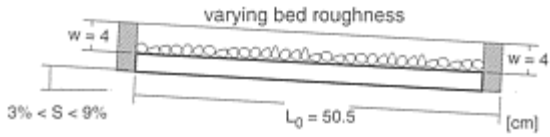

Figure 2. Longitudinal profile of a step-pool sequence, roughness of the bed is produced by pasted grains.

Table 1. Density and viscosity of the used concentrations of water-clay-mixtures.

Concentration C_f (Vol.%)	Densitiy ρ_s (g/l)	Viscosity η_s (mPas)
18	1296	3.89
12	1197	2.33
0	998	1.06

amplitudes. As this research was initiated by a real flood event at the Ruetz river, an alpine river in Austria, the shape of the model channel resembles approximately that of the river reach.

In the experiments, a tilting platform of 12m length with a slope adjustable up to 10% inclination formed the basis for the channel model. The simulated channel (bed width 0.3m and height 0.2m) was straight aligned and had a trapezoidal cross section, (Figure 1). The dimensions of the channel correspond to a model scale of 1:40. At the bottom of the channel cascade-drops with a constant field length L of 0.505m and step height w of 0.04m, were installed, (Figure 2).

Fluid discharges up to 70 l/s with varying concentrations of clay were recirculated. The concentration of the water-clay mixture was stepwise varied from clear water to 18 Vol.%. Results of the determined fluid properties according to Ganz (2003) are given in (Table 1).

The roughness of the side walls was formed by pasted grains (d_m=3.2mm). The flume-bed between the steps was formed by surfaces of varying roughness by different nearly uniform grain mixtures, (Figure 3).

The equivalent bed sand roughness k was evaluated by the concept of Monzavi (1972). In the experiments discharge Q and slope S were systematically varied for a given clay concentration and step-pool geometry.

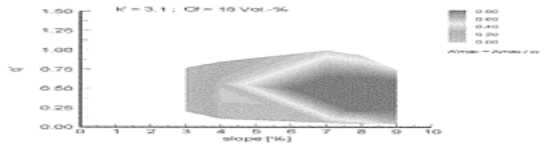

Figure 3. Used roughness categories.

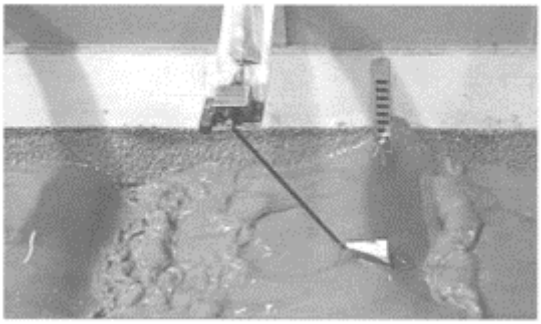

Figure 4. Arrangement of the floating device in the pool field.

The progression of water depths was followed by floating gauges installed in each pool field, (Figure 4).

Based on this equipment, the development of the waves along the channel and the maximum wave amplitudes at the end of the test reach as well as the wave frequency could be recorded for each test run.

3 WAVE FORMATION

The tests demonstrated that beyond a minimum slope instabilities form only between a lower and upper limit of discharge, The step-pool configuration essentially influences the upper flow limit, Ganz & Schöberl (2003), Ganz (2003). Boundary conditions also affect the increment of wave depths along the channel reach. The wave height is strongly related to the flow distance from the inlet section. In Figure 5 the development of the maximum flow depth from gauge to gauge is displayed. As in this example, most of the experiments indicate that the maximum of wave height is reached before the end of the experimental channel. In terms of relative distance from the entrance $x'=x/L$ a maximum is reached for $x'<22$. When hm is the undisturbed flow depth infront of each step and hmax the peak of the water depth generated by the waves, the local wave amplitude A is given by A=hmax—hm. Figure 5 shows the relative maximum water depth hmax/hm against the distance and the discharge for a given step geometry, mean slope and roughness. The maximum envelop of hmax occurs in the central region between the upper and lower discharge limit.

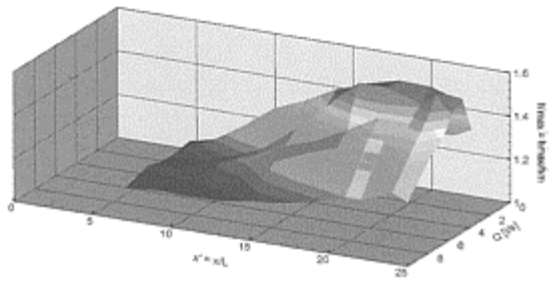

Figure 5. Development of hmax/hm along the channel for a given slope, step geometry and roughness dependent on discharge.

For the generalization of relations and criteria, dimensionless numbers are used. For constant fluid properties, dependencies according to Froude are to be expected, thus discharge is expressed by

$$q' = \frac{q}{\sqrt{g}\, w^{3/2}} \tag{1}$$

with q the specific discharge per width (m^3/s, m), g gravity acceleration (m/s^2) and w the step height of the control structure. Relative bed roughness k∗is given by k/w. Particularly for the analysis of viscosity effects it seems important to cover the whole range between smooth-bed and rough-bed conditions. In this case a combination with the fluid property number

$$\eta_s' = \frac{\eta_s}{\sqrt{g}.\rho_s w^{3/2}} \tag{2}$$

is used, thus the combined term is

$$k' = \frac{k\, g^{1/3} \rho_s^{2/3}}{\eta_s^{2/3}} \tag{3}$$

with k sand roughness of the bed (m), g gravity acceleration (m/s^2), ρ_s density of suspension (kg/m^3), η_s viscosity of suspension (mPas).

A'_{max} represents the maximum amplitude A_{max} divided by the step height w. Mean bed slope S and the volume concentration C_f of the clay mixture are originally dimensionless numbers.

The main object of the investigation was the evaluation of the role of viscosity and bed roughness. Therefore different scenarios of bed roughness and water-clay mixtures were tested to determine effect on the wave formation.

3.1 *Influence of roughness*

The development of wave amplitudes for smooth bed conditions as well as 3 different rough surfaces ranging from k=4.0mm to 13.6mm were tested against

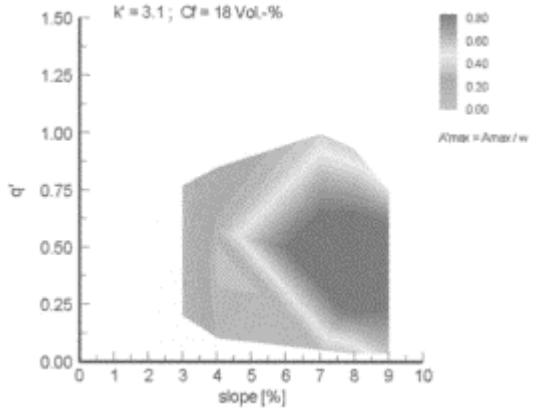

Figure 6. A'_{max} dependent on q′ and slope S for smooth bed conditions; %, k=0.3mm; k′=3.1; C_f=constant=18%.

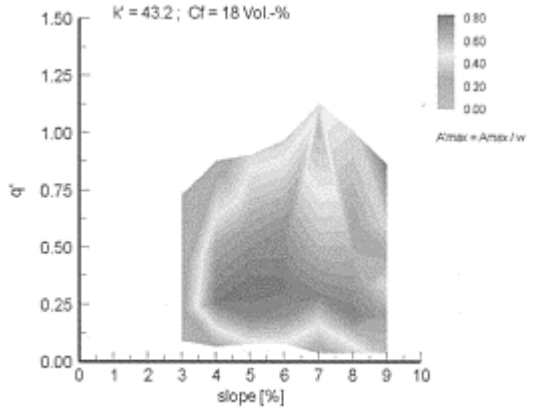

Figure 7. A'_{max} dependent on q′ and slope S, rough bed conditions 1; k=4mm; k′=43.2; C_f=constant=18%.

discharge and slope; k′ of the smooth bed equalled 3.1, compared to rough beds with k′ between 43,2 and 139,9. Step-pool geometry and clay mixture were kept constant. Due to the complex dependencies, results were analysed by 2D colour plots (Figures 6–9).

Distinct differences in the behaviour between the flow in smooth or rough-bed channels are obvious. According to Figure 6, smooth beds lead to higher amplitudes for rising slopes and a pronounced maximum in the range of 6.5%<S< 9% and 0,25<q′<0,70.

For rough beds a clear attenuation of the amplitudes with rising roughness as well as a shift of the area of maximum wave height to higher slopes can be observed. While for the smaller roughness k′=43,2 the maximum area is reached for S=5%, the area broadens for higher k′ and ends up for k′=139,9 at S between 6–9%.

Figure 10 and 11 allow a detailed inspection of A′ dependent on varying roughness k′ and constant slopes of 4% and 8%.

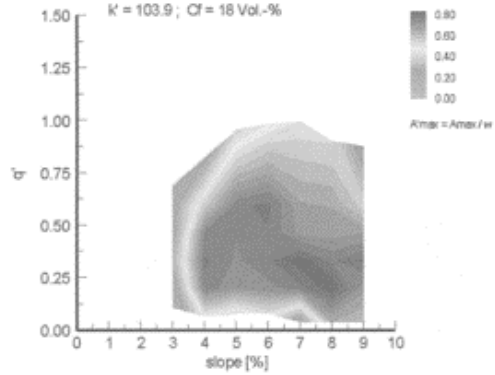

Figure 8. A'_{max} dependent on q′ and slope S, rough bed conditions 2; k=10.1mm; k′=103.9; C_f=constant=18%.

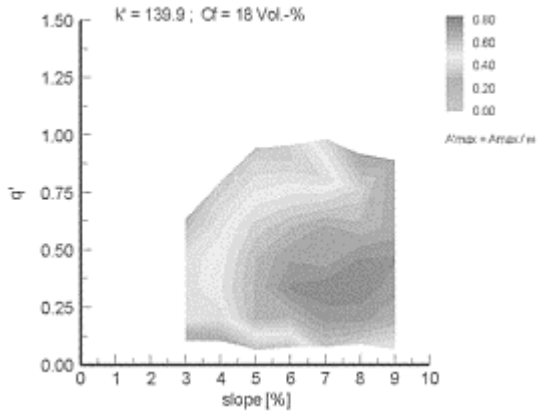

Figure 9. A'_{max} dependent on q′ and slope S, rough bed conditions 3; k=13.6mm; k′=139.9; C_f=constant=18%.

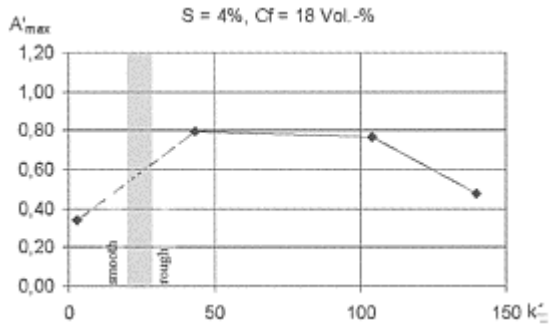

Figure 10. A'_{max} versus varying C_f, S=4%, rough bed conditions 3; k=13.6mm; k′=139.9.

Smooth beds behave contrary to rough beds. With the higher slope A′ is amplified, with the smaller slope attenuated. The grey area marks approximately the transition between rough- and smooth-turbulent flow conditions. For rough beds the dampening effect is

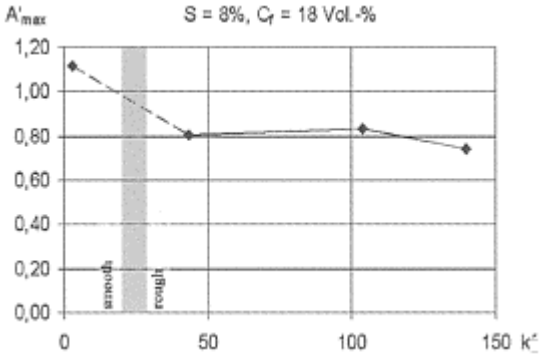

Figure 11. A'_{max} versus varying C_f, S=8%, rough bed conditions 3; k=13.6mm; k′=139.9.

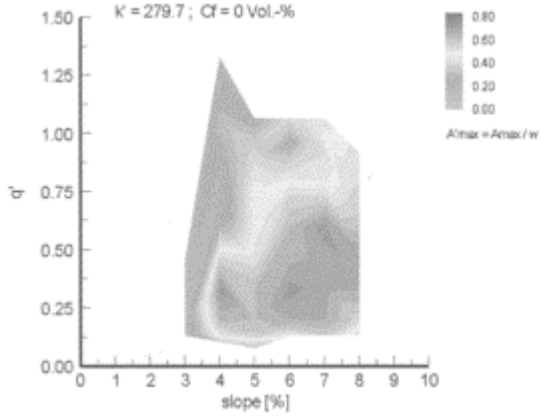

Figure 12. A'_{max} dependent on q′ and slope S, rough bed conditions 3; k=13.6mm; k′=279.7; C_f=0%.

more pronounced for smaller slopes than for higher slopes.

3.2 *Influence of viscosity*

The variation of the concentration of water-clay mixture was investigated in the range of C_f=0%– 18%. Overall, the influence of varying concentrations kept astonishing small and can be neglected for first approximations. A detailed demonstration of the influence of concentration on A_{max} is provided by the 2D colour plots in Figures 12–14. For these test-runs different inflow conditions were applied so that the limits of discharge differs slightly to those given in Figures 6–9.

Figures 15 and 16 allow a detailed inspection of the wave development for constant mean bed slopes. For larger slopes like S=8%, rising concentrations up to C_f=12% produce an increase of the wave amplitude in the range of 10%. With higher concentrations, A′ is reduced even below the level of A′ of clear water conditions. This marked behaviour for higher slopes almost completely disappears for smaller slopes as S=4%.

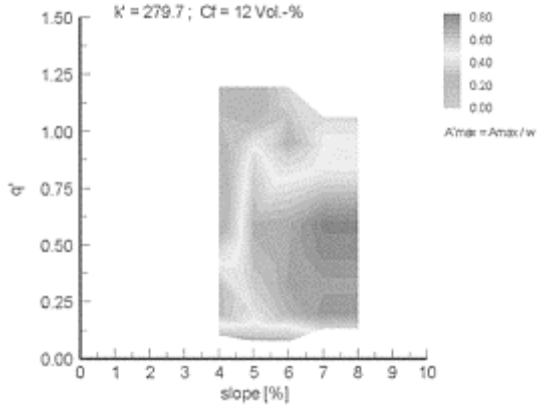

Figure 13. A'_{max} dependent on q′ and slope S, rough bed conditions 3; k=13.6mm; k′=279.7; C_f=12 %.

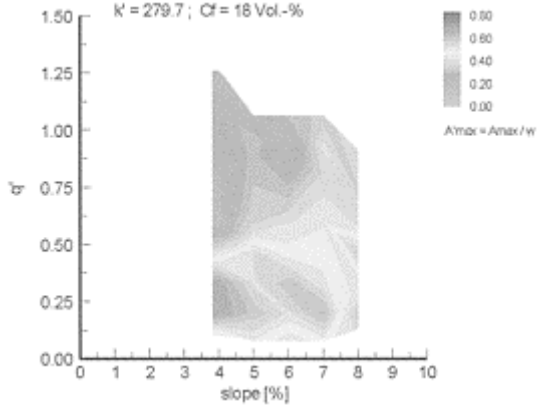

Figure 14. A'_{max} dependent on q′ and slope S, rough bed conditions 3; k=13.6mm; k′=279.7; C_f=18%.

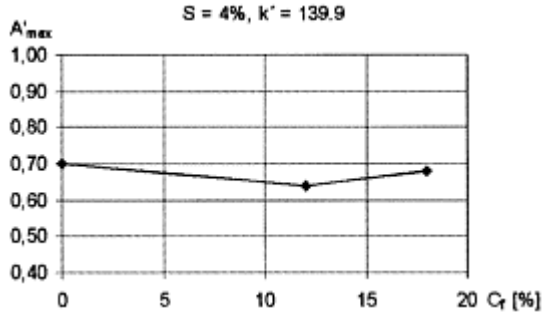

Figure 15. A'_{max} versus variable C_f; constant slope S=4%, roughness 3; k=13.6mm.

3.3 *Wave frequency*

Wave frequencies have been checked downstream from drop to drop in relation to main boundary parameters. Along the channel no change in frequency could

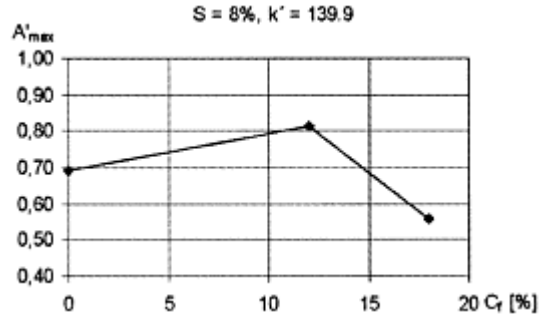

Figure 16. A'_{max} versus variable C_f, constant slope S=8%, roughness 3; k=13.6mm.

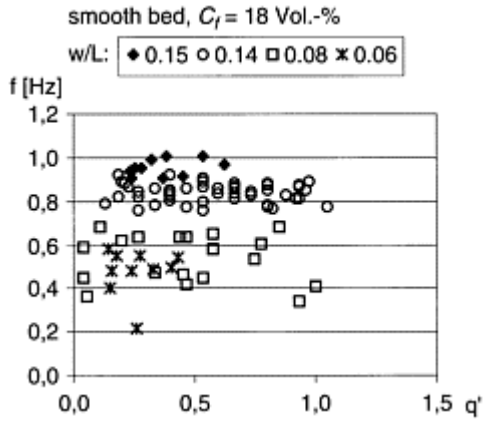

Figure 17. Range of frequencies for different step—pool ratios.

be detected. For the analysis discharge and one further parameter respectively were varied, while all other factors were kept constant. For different discharges, the analysis yielded a certain scatter of data but no definite dependency, (Figure 17).

The same was observed for variations of roughness, slope and clay concentration. However, a clear trend could be determined in relation to the step height of the system. As shown by Figure 18, wave frequency is quasi linearly related to w/L, which further demonstrates the importance of the configuration of the step-pool for the wave formation.

4 CONCLUSIONS AND PERSPECTIVES

The study clearly revealed the high complexity of the formation of instabilities in stepped channels. The wave formation is restricted to a certain range of discharge and slope. Maximum wave heights formed between an upper and lower limit of discharge. For a given step-pool geometry, the investigation

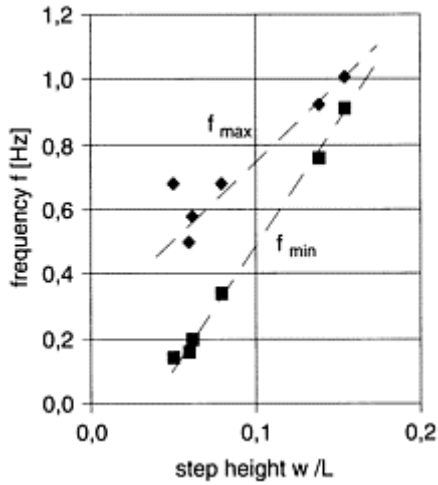

Figure 18. Range of upper and lower envelops of wave frequencies for different step pool aspect ratios.

demonstrated a significant trend of dampening of the maximum wave amplitude with increasing roughness. In addition to this, clear differences in the behaviour between the flow in smooth or rough-bed channels could be observed. Smooth beds lead to higher amplitudes for rising slopes and a distinct maximum in the range of $6.5\%<S<9\%$ and $0.25<q'<0.70$. For the analyses colour plots proved to be valuable tools to illustrate the multidimensional dependencies. The variation of the clay concentration showed only limited effects on the wave formation. The impact of increasing concentration was mainly traceable with steeper slopes. An increase of concentration up to 12% generated a increase of A_{max} while a further increase reduced the amplitudes again. Overall, the effect was not as significant as the change in roughness. Thus in a first approximation, for conditions with concentrations below 18% and rough turbulent beds, a Froude-dependency for the wave formation can be presumed. Wave frequencies turned out to be independent of slope, discharge, bed roughness and the concentration of suspension, but proved to be strongly related to the step height of the control structures.

The determined influences of different parameters are mainly to be seen as a first step for understanding this phenomenon. In order to widen the range of boundary conditions as well as to condense the hydraulic information within the step-pool configuration, numerical simulations have been launched. This additional approach will allow to extend and strengthen the criteria developed in the scale model.

ACKNOWLEDGEMENTS

The Authors wish to thank the “Forsttechnischer Dienst für Wildbach und Lawinenverbauung” for the financial support of the project.

REFERENCES

Brock, R.R. 1969. Development of roll wave trains in open channels. *Journal of the Hydraulics Division,* ASCE, Vol. 95, No. HY 4, Proc. Paper 6704, pp. 1401–1427

Coussot, Ph. 1994. Mud Flow Dynamics. *International Workshop on and Inundations related to Large Earth Movements,* pp. A7.1–A7.12

Davies, T. 1988. Debris Flow Surges—A Laboratory Investigation. Mitteilung der Versuchsanstalt für Wasserbau, Hydrologie und Glaziologie, ETH Zürich

Dressler, R.F. 1949. Mathematical Solution of the Problem of Roll-Waves in Inclined Open Channels. *Communications on pure and applied mathematics.* Vol. 2, pp. 149–194

De Fessant, A.-L. 2001. Étude des instabilités d'un écoulement à surface libre—Sur un fond à géométrie périodique. Ph.D. thesis, Institut National Polytechnique de Toulouse, France

Ganz, T. 2003. Entstehung und Entwicklung von Abflussin-stabilitäten bei Absturztreppen, Dissertation, Institut für Wasserbau, Universität Innsbruck

Ganz, T., Schöberl, F. 2003. Limit of Flow Instability in Steep Stepped Channels, XXX IAHR Congress Thessaloniki

Monzavi, M.T. 1972. Widerstandsgesetz auf statistischer Basis für extreme natürliche Rauheiten, Bericht des Institutes für Hydraulik und Hydrologie der Technischen Hochschule Darmstadt, Nr. 8

Koloseus, H.J., Davidian, J. 1966. Free-Surface Instability Correlation. U.S.G.S. Water-Supply Paper 1592-C

Savage, S.B. 1989. Flow of Granular Materials. In: Germain et al (eds.), *Theoretical and Applied Mechanics,* pp. 241–266. Amsterdam: Elsevier

Whittaker, J.G. 1982. Flow and Sediment Movement in Stepped Channels. Ph.D. thesis, Lincoln College, University of Canterbury, Christchurch, New Zealand

3D calculation of curved open channel flow using physical curvilinear coordinates

Mu-lan Zhu
Hydro-soft Technology Institute Co., Ltd., Tokyo, Japan

Yasuyuki Shimizu
Hokkaido University, Hokkaido, Japan

Mitsuhiro Nakata & Kazufumi Hayashida
Development and Construction office of Ishikari River, Hokkaido, Japan

Kunio Ezaki
Foundation of Hokkaido River Disaster Prevention Research Center, Hokkaido, Japan

Hideaki Mizutani
Hydro-soft Technology Institute Co., Ltd., Tokyo, Japan

River Flow 2004—Greco, Carravetta & Della Morte (eds.)

ABSTRACT: Three difficulties exist in numerical simulations of the flowfield at estuary. (a)Water depths are large and it is difficult to apply a 2-dimensional shallow water model to this kind of flowfield; (b) The boundaries are curved and complex, and do not coincide with coordinate lines in the Cartesian system (x^1, x^2, x^3); (c) It is not easy to generate a grid that varies gradually throughout the whole flowfield. The authors solve these three difficulties by adopting the 3D governing equations and the use of physical curvilinear coordinates ($\xi^{(1)}$, $\xi^{(2)}$, $\xi^{(3)}$) which is a physical counterpart of the generalized curvilinear coordinates and was originally proposed by Truesdell. The proposed model is applied to an experimental channel, and calculated values are compared to observed values and the agreement between them is generally good. Our next step of study is to apply the model to real rivers and include sediment transportation to the model.

1 INTRODUCTION

It is very important to predict flowfield and river-bed deformation for channel planning work. However, there are three difficulties in numerical simulations of the flowfield at estuary First, water depths are large and the flowfield shows a strong 3-dimensional property, thus it is difficult to apply a 2-dimensional shallow water model to this kind of flowfield; Secondly, the boundaries are very complex, they include the external curved boundary of the high-water channel and the internal curved boundary of the low-water channel, and do not coincide with coordinate lines in the Cartesian system (x^1, x^2, x^3). Moreover, the water surface, namely the boundary in the vertical direction keeps varying during a flood; Thirdly, it is not easy to generate a grid that varies gradually throughout the whole flowfield. Usually as shown in Figure 1.1, a significant difference of adjacent mesh size can exist near the boundary between the low-water and high-water channel, unless a complex process for grid generation is employed.

Most existing numerical models in river hydraulics are 2-dimensional, and are unable to deal with the first difficulty Although some existing models are developed in 3D, they use the Cartesian system (x^1, x^2, x^3) and make the imposition of boundary conditions difficult, namely they still retain the disadvantage of the second difficulty Only a few existing models for rivers can solve both the first and second difficulty by adopting the 3D governing equations and the use of generalized curvilinear coordinates (ξ^1, ξ^2, ξ^3).

The generalized coordinate domain is constructed so that a computational boundary in physical space coincides with a coordinate line in generalized-coordinate space (called computational space also). Figure 1.2 shows a 2-dimensional mapping condition from an irregular physical domain to a square generalized-coordinate domain, where the non-uniform curved segments of Δs, Δn which are

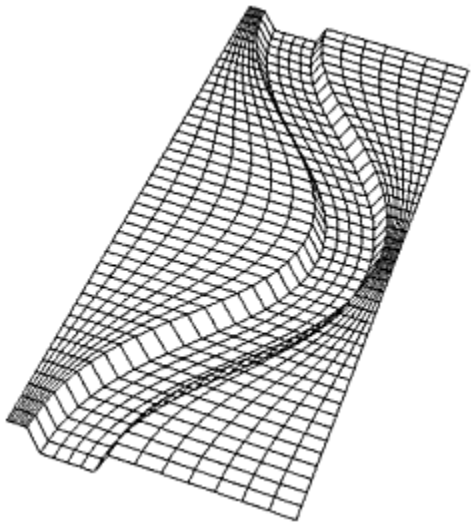

Figure 1.1. An image of generated grid.

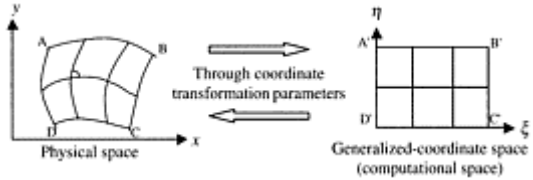

Figure 1.2. A mapping from physical domain to generalized-coordinate domain.

non-orthogonal to each other are mapped to the uniform straight segments of $\Delta\xi^1$, $\Delta\xi^2$ which are orthogonal to each other. The mapping not only deforms the boundaries but also transforms the directions and magnitudes of flow variables, i.e., it also transforms the governing equations. There are many options in formulating the governing equations transformed from Cartesian coordinates (x^1, x^2, x^3) to generalized curvilinear coordinates (ξ^1, ξ^2, ξ^3). The main options can be classified as follows:

(a) The governing equations may be expressed in a semi-contravariant form in terms of generalized curvilinear coordinates (ξ^1, ξ^2, ξ^3), in which the Cartesian velocity of u and the contravariant velocity of U coexist. This is the most extensively used option and most of the numerical models in computational hydraulics are developed in this way. However, this kind of method has two problems. First, the velocity variables should be arranged at the boundary of a control volume in generalized-coordinate space (ξ^1, ξ^2, ξ^3) when using a staggered mesh, but it is impossible to arrange the Cartesian velocity in this way. Secondly, the method suffers from a problem of undesirable mesh sensitivities. According to some theoretical error analyses [1], additional errors associated with the use of generalized curvilinear coordinates (ξ^1, ξ^2, ξ^3) may be significant and consequently, result in a computational stability problem if non-uniformity of the grid in physical space is considerable. Therefore, it is necessary when using this method to have the generated grid in the physical domain grow slowly.

(b) The governing equations may be expressed in a complete-contravariant form in terms of generalized curvilinear coordinates (ξ^1, ξ^2, ξ^3), in which the Cartesian velocity is no longer involved. This method eliminates the first problem stated in (a) which is caused by the coexisting of Cartesian velocity, but still retains the disadvantage of undesirable mesh sensitivities like that in (a). Koshizuka et al. [2] [3] [4] show, theoretically as well as numerically, that stability problems may occur when the mesh size of the adjacent cells differ by more than a factor of 3.

From the above descriptions, it can be seen that the existing 3-dimensional model using generalized curvilinear coordinates can deal with the first and second difficulties, but still suffers from a problem of mesh sensitivities caused by the third difficulty stated above. It is the above weaknesses in the existing models that motivate our studies. Namely, our study objective is to develop a new model applicable to the severe calculation conditions with three difficulties at estuary, and provide the useful prediction results of flowfield for channel planning work. As the first step of our study, the developed model is applied to an experimental channel for the easier program debugging

and the model verification. Our next step of study is to apply the model to real rivers and include sediment transportation to the present model of flow calculation.

2 THREE-DIMENSIONAL FLOW CALCULATION MODEL

As stated in the above, there is a problem of mesh sensitivity when using the generalized curvilinear coordinate. To solve this problem, we must first find out the cause of the problem.

When the governing equations are transformed from the Cartesian coordinate system into the generalized curvilinear coordinate system, the Cartesian velocities in physical space of (u^1, u^2, u^3) are transformed to the contra-variant velocity of (U^1, U^2, U^3) (or co-variant velocity) in generalized-coordinate space. It can be derived out that $U^i=u^{(i)}/\Delta\xi^{(i)}$ where $u^{(i)}$ is identical to the velocity along i mesh-line direction in physical space and $\Delta\xi^{(i)}$ is identical to the mesh width in i direction in physical space. Thus, the field of contra-variant velocity in generalized-coordinate space will be very non-uniform once if the generated mesh sizes are rather non-uniform, even if the field of velocity in physical space is uniform. Especially when the field of velocity is also non-uniform, and its most varying place is the exactly same as that of mesh size, then this kind of variation will be doubled and the calculation stability problem will be aggravated.

To solve this problem, Demirdzic et al. [5], Koshizuka [2–4] and Takizwa et al. [6] introduce the use of physical components to generalized curvilinear coordinates that was originally proposed by Truesdell. The transformed governing equations are expressed in the coordinate system $(\xi^{(1)}, \xi^{(2)}, \xi^{(3)})$ with the velocity of $u^{(i)}$, where coordinate system $(\xi^{(1)},\xi^{(2)},\xi^{(3)})$ is the physical counterpart of the generalized curvilinear coordinates (ξ^1, ξ^2, ξ^3), and the velocity $u^{(i)}$, equal to $U^i\times\Delta\xi^{(i)}$, is the physical counterpart of contravariant velocity U^i in the physical curvilinear space. It can be derived out that $u^{(i)}$ in physical curvilinear space $(\xi^{(1)}, \xi^{(2)}, \xi^{(3)})$ is actually identical to the velocity along the mesh-line direction of i in physical space.

It should be noted that the superscript parentheses are used to denote physical components throughout the paper.

To avoid possible confusion, the coordinate systems and the velocity denotations mentioned in the paper are summarized below. (x^1, x^2, x^3) represents the well-known Cartesian coordinate system in physical space. (ξ^1, ξ^2, ξ^3) represents the generalized curvilinear coordinate system in generalized-coordinate space (called computational space also). $(\xi^{(1)}, \xi^{(2)}, \xi^{(3)})$ represents the physical curvilinear coordinate system in physical curvilinear space which is actually identical to physical space. Figure 2.1 shows these analytical spaces and coordinate systems. (u^1, u^2, u^3) are the Carte-sian velocities in physical space; (U^1, U^2, U^3) are the contra-variant velocities in generalized-curvilinear space; $(u^{(1)}\ u^{(2)}, u^{(3)}\ u^{(3)})$ in physical curvilinear space are identical to the velocities along the mesh-line direction in physical space.

2.1 *Governing equations in the physical curvilinear coordinate system*

(a) Governing equations in the Cartesian coordinate system

• Continuity equation

$$\frac{\partial u^i}{\partial x^i} = 0 \tag{2.1}$$

• Momentum equation

$$\frac{\partial u^i}{\partial t} + \frac{\partial}{\partial x^j}(u^i u^j - \tau^{ij}) = S^i - \frac{1}{\rho}\delta^{ij}\frac{\partial P}{\partial x^j} \tag{2.2}$$

and,

$$\tau^{ij} = \nu_T(\delta^{im}\frac{\partial u^j}{\partial x^m} + \delta^{jm}\frac{\partial u^i}{\partial x^m}) \tag{2.3}$$

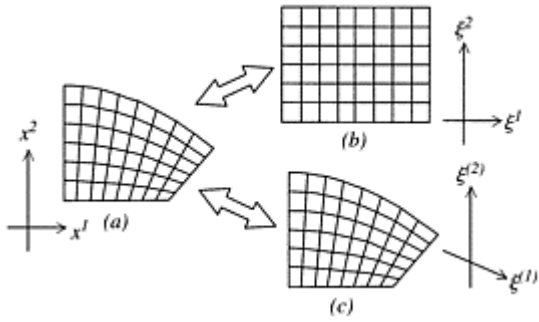

Figure 2.1. Analytical space and coordinate systems (a) physical space, Cartesian coordinate system, (b) generalized-coordinate space, generalized curvilinear coordinate system and (c) physical curvilinear space identical to physical space, physical curvilinear coordinate system.

where, *i, j, k*=1, 2, 3, u^i is velocity in xi direction; *P* is pressure=ρGH, and ρ, *H*, *G* is water density, water level and gravitational acceleration=9.8m^2/s respectively; δ^{ij} is Kronecker's delta defined as δ^{ij}=1 if $i=j$ and δ^{ij}=0 if $i\neq j$; S^i is external forces in x^i direction, τ^{ij} is a tensor representing Reynolds stresses; ν_T is the turbulent viscosity and can be evaluated as follows:

$$\nu_T = \kappa u_* z'(1 - \frac{z'}{h_s}) \tag{2.4}$$

where κ is the Von Karman constant (≈0.4), h_s is the water depth; u_* is the shear velocity at channel bed; and z' is the height from the channel bed.

(b) Basic concepts related to transformation of coordinate system

Chain rule is often used in the transformation of coordinate system. However, when using this method, the contra-variant velocity of U^i and the Cartesian velocity of u^i coexist in the transformed governing equations. In this paper, instead of using chain rule, we transform the governing equations based on the geometric differential calculus. Several fundamental concepts of geometric differential calculus related to the coordinate system transformation are introduced as follows:

(b-1) fundamental co-variant tensor g_{ij}

If the coordinates of two neighbor grid points in computational space are represented by ξ^i and $\xi^i+d\xi^i$ respectively, then their physical distance of *ds* in physical space has an expression as:

$$ds^2=g_{ij}d\xi^i d\xi^j \tag{2.5}$$

The physical meaning of g_{ij} can be explained as follows:

When the mesh width of $d\xi^i$ in computational space is equal to 1, $\sqrt{g_{ii}}$ represents the mesh width in *i* direction in physical space, and $\sqrt{g_{ij}}$ represents the area of *(i, j)* mesh in physical space.

(b-2) Determinant of fundamental co-variant tensor g

$$g=\left|g_{ij}\right|=\begin{vmatrix} g_{11} & g_{12} & g_{13} \\ g_{21} & g_{22} & g_{23} \\ g_{31} & g_{32} & g_{33} \end{vmatrix}=J^2 \tag{2.6}$$

where *J* is the well-known Jacobian which can be also defined by the determinant of coordinate transformation coefficients. The physical meaning of *g* is: if the mesh width in computational space is equal to 1, then $\sqrt{g}$ represents the cubic volume of *(i, j, k)* mesh.

(b-3) Physical fundamental co- and contra-variant tensor $g_{(ij)}$ and $g^{(ij)}$

$$g_{(ij)}=\frac{g_{ij}}{\sqrt{g_{ii}g_{jj}}} \qquad g^{(ij)}=\sqrt{g_{ii}g_{jj}}\,g^{ij} \tag{2.7}$$

(b-4) Christoffel Symbol and Physical Christoffel Symbol

Christoffel symbol can be expressed by coordinate transformation coefficients as follows:

$$\left\{ \begin{matrix} i \\ j \quad k \end{matrix} \right\}=\frac{\partial \xi^i}{\partial x^m}\frac{\partial^2 x^m}{\partial \xi^j \partial \xi^k} \tag{2.8}$$

and physical christoffel symbol has a relationship with christoffel symbol as follows:

$$\left(\begin{matrix} i \\ j \quad k \end{matrix} \right)=\sqrt{\frac{g_{ii}}{g_{jj}g_{kk}}}\left(\left\{ \begin{matrix} i \\ j \quad k \end{matrix} \right\}-\delta_j^i\frac{g_{jm}}{g_{jj}}\left\{ \begin{matrix} m \\ j \quad k \end{matrix} \right\} \right) \tag{2.9}$$

Christoffel symbol represents how many changes of the vector component in *i* direction are caused when the unit vector in *j* direction moves one unit length in *k* direction.

Figure 2.2 shows the cases of $\left\{ {}_{2}{}^{1}{}_{2} \right\}$ *and* $\left\{ {}_{1}{}^{2}{}_{1} \right\}$ which actually represent the curvatures of mesh-line in *j* direction and *i* direction.

(c) Transformation based on geometric differential calculus

The following transformations from the Cartesian coordinate system to the physical curvilinear coordinate system based on geometric differential calculus are introduced:

• Scalars

$$\phi \to \phi \tag{2.10}$$

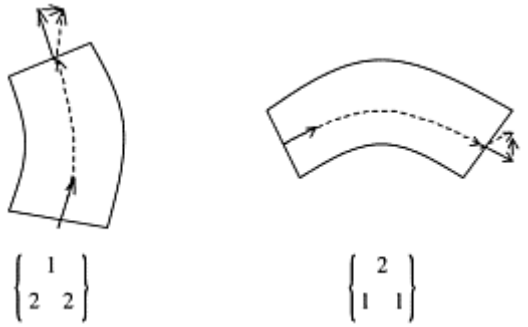

Figure 2.2. Physical meaning of the physical christoffel symbol $\left\{ {}_{2}{}^{1}{}_{2} \right\}$ and $\left\{ {}_{1}{}^{2}{}_{1} \right\}$.

$$\frac{\partial \phi}{\partial x^j} \to \frac{\partial \phi}{\partial \xi^{(j)}} \tag{2.11}$$

• Vectors

$a^i \to a^{(i)}$

(2.12)

$$\frac{\partial a^i}{\partial x^j} \to \nabla_{(j)} a^{(i)} = \frac{\partial a^{(i)}}{\partial \xi^{(j)}} + a^{(m)} \left\{ {}_{m}{}^{i}{}_{j} \right\} \tag{2.13}$$

$$\frac{\partial a^j}{\partial x^j} \to \nabla_{(j)} a^{(j)} = \frac{\Delta a^{(j)}}{\Delta \xi^{(j)}} \tag{2.14}$$

• Tensors

$A^{ij} \to A(\delta^{ij} \to g^{(ij)}\ \delta ij \to g_{(ij)})$

(2.15)

$$\frac{\partial A^{ij}}{\partial x^j} \to \nabla_{(j)} A^{(ij)} = \frac{\Delta A^{(ij)}}{\Delta \xi^{(j)}} + A^{(mj)} \left\{ {}_{m}{}^{i}{}_{j} \right\} \tag{2.16}$$

where, $a^{(i)}$ and $A^{(i)}$ are physical vector and tensor components in the physical curvilinear coordinate system $\xi^{(i)}$, and $\Delta/\Delta\xi^{(j)}$ is the differential operator defined as:

$$\frac{\Delta}{\Delta\xi^{(j)}} = \sqrt{\frac{g_{jj}}{g}}\frac{\partial}{\partial\xi^{(j)}}\sqrt{\frac{g}{g_{jj}}} \tag{2.17}$$

(d) Governing equations in the physical curvilinear coordinate system

Based on the transformation given in (c), the governing equations can be transformed from the Cartesian coordinate system to the physical curvilinear coordinate system as follows:

• Continuity equation:

$$\frac{\Delta}{\Delta^{(i)}}u^{(i)} = 0 \tag{2.18}$$

• Momentum equation:

$$\frac{\partial u^{(i)}}{\partial t} + \frac{\Delta}{\Delta\xi^{(j)}}(u^{(i)}u^{(j)} - \tau^{(ij)}) + \begin{pmatrix} i \\ m \quad j \end{pmatrix}(u^{(m)}u^{(j)} - \tau^{(mj)}) = S^{(i)} - g^{(ij)}\frac{\partial P}{\partial\xi^{(j)}} \tag{2.19}$$

2.2 *Calculation algorithm*

SMAC algorithm is employed in the calculation. The characteristic of SMAC algorithm is that only the velocity derivative term in the continuity equation and the pressure derivative term in the momentum equation are calculated implicitly, while other terms are calculated explicitly, and the time derivative term in the momentum equation is discretized with Euler's method. Besides, a CIP (Cubic-Interpolated Pseudoparticle) originally proposed by Yabe [7–8] is employ to deal with the convective term in the momentum equation. It is well known that a problem of calculation stability is often caused by the convective term when velocity is high, while the CIP method has the advantage of calculation stability in dealing with the convective term with high velocity.

The transformed governing equations shown in Eq.(2.18–2.19) seem very simple, however they are actually complicated when they are unfolded. The momentum equation in the $\xi^{(1)}$ direction unfolded from Eq.(2.19) has an expression as:

$$\frac{u^{(1)}_{n+1} - u^{(1)}_{n}}{\Delta t} + u^{(1)}\frac{\partial u^{(1)}}{\partial\xi^{(1)}} + u^{(2)}\frac{\partial u^{(1)}}{\partial\xi^{(2)}} + u^{(3)}\frac{\partial u^{(1)}}{\partial\xi^{(3)}} = R^{(1)}_{n+1} \tag{2.20}$$

where n denotes time step and $R^{(1)}_{n+1}$ is expressed as:

$$
\begin{aligned}
R_{n+1}^{(i)} = & \sqrt{\frac{g_{11}}{g}}\frac{\partial}{\partial \xi^{(1)}}\left(\sqrt{\frac{g}{g_{11}}}\tau^{(11)}\right)+\sqrt{\frac{g_{22}}{g}}\frac{\partial}{\partial \xi^{(2)}}\left(\sqrt{\frac{g}{g_{22}}}\tau^{(12)}\right) \\
& +\sqrt{\frac{g_{33}}{g}}\frac{\partial}{\partial \xi^{(3)}}\left(\sqrt{\frac{g}{g_{33}}}\tau^{(13)}\right) \\
& +\begin{pmatrix} 1 \\ 1\ 1 \end{pmatrix}(\tau^{(11)}-u_n^{(1)}u_n^{(1)})+\begin{pmatrix} 1 \\ 1\ 2 \end{pmatrix}(\tau^{(12)}-u_n^{(1)}u_n^{(2)}) \\
& +\begin{pmatrix} 1 \\ 1\ 3 \end{pmatrix}(\tau^{(13)}-u_n^{(1)}u_n^{(3)}) \\
& +\begin{pmatrix} 1 \\ 2\ 1 \end{pmatrix}(\tau^{(21)}-u_n^{(2)}u_n^{(1)})+\begin{pmatrix} 1 \\ 2\ 2 \end{pmatrix}(\tau^{(22)}-u_n^{(2)}u_n^{(2)}) \\
& +\begin{pmatrix} 1 \\ 2\ 3 \end{pmatrix}(\tau^{(23)}-u_n^{(2)}u_n^{(3)}) \\
& +\begin{pmatrix} 1 \\ 3\ 1 \end{pmatrix}(\tau^{(31)}-u_n^{(3)}u_n^{(1)})+\begin{pmatrix} 1 \\ 3\ 2 \end{pmatrix}(\tau^{(32)}-u_n^{(3)}u_n^{(2)}) \\
& +\begin{pmatrix} 1 \\ 3\ 3 \end{pmatrix}(\tau_n^{(33)}-u_n^{(3)}u_n^{(3)}) \\
& -g^{(11)}\frac{1}{\rho}\frac{\partial P_{n+1}}{\partial \xi^{(1)}}-g^{(12)}\frac{1}{\rho}\frac{\partial P_{n+1}}{\partial \xi^{(2)}}-g^{(13)}\frac{\partial P_{n+1}}{\partial \xi^{(3)}}+S_{n-}^{(i)}
\end{aligned}
\tag{2.21}
$$

Herein, Eq.(2.21) is expressed in a non-conservation form for using CIP method to calculate the convective terms. To explain the essence of CIP method, considering an one-dimensional momentum equation with free water surface as expressed in Eq.(2.22):

$$\frac{\partial f}{\partial t}+u\frac{\partial f}{\partial x}=g^{*} \tag{2.22}$$

where g^* represents pressure derivative term, friction term, viscous stresses as well as Reynolds stresses and etc.; f represents velocity. Eq.(2.22) can be split into the following two phases which are advection phase and non-advection phase.

Advection phase:

$$\frac{f^{*}-f^{n}}{\Delta t}+u\frac{\partial f}{\partial x}=0 \tag{2.23}$$

Non-advection phase:

$$\frac{f^{n+1}-f^{*}}{\Delta t}=g^{*} \tag{2.24}$$

where n denotes time step. It can be seen that Eq (2.23) is actually a wave motion equation. According to the characteristic of wave motion equation, the value of f at future $t+\Delta t$ time at the place of x_i is actually equal to the value of f at present t time at the place of $x_i-u\Delta t$ as shown in Figure 2.3, i.e.,

$$f(x_i, t+\Delta t)=f(x_i-u\Delta t, t) \tag{2.25}$$

When $u>0$ and Δt is small enough so that the point of $x_i-u\Delta t$ is between the two points of x_{i-1} and x_i, the value of $f(x_i-u\Delta t, t)$ can be estimated based on the known values of $f(x_{i-1}, t)$ and $f(x_i, t)$ by various methods. One of those methods is the CIP method proposed by Yabe [7–8]. The CIP method employs a cubic polynomial function $F(X)$ as expressed in Eq.(2.26) to do interpolation between the two points of x_{i-1} and x_i.

$$f(x_i - u\Delta t, t) = F(X) = a_i X^3 + b_i X^2 + \frac{\partial f_i}{\partial x} X + f_i \tag{2.26}$$

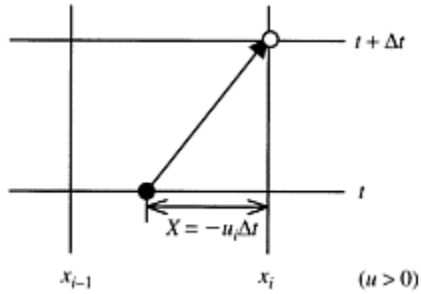

Figure 2.3. Characteristic of wave motion.

where $X=-u_i/\Delta t$, and the coefficients of a_i, b_i can be evaluated based on the known values of $f(x_{i-1}, t)$ and $f(x_i, t)$ at present time of t. Therefore, using the central finite difference method to calculate advection phase shown in Eq.(2.23), and then using the CIP method to calculate non-advection phase shown in Eq.(2.24), we can obtain the answer of original governing equation of Eq.(2.22).

By extending the above approach to 3-D system, we have [8]:

$$\frac{\partial f}{\partial t} + u^{(1)} \frac{\partial f}{\partial \xi^{(1)}} + u^{(2)} \frac{\partial f}{\partial \xi^{(2)}} + u^{(3)} \frac{\partial f}{\partial \xi^{(3)}} = g^* \tag{2.27}$$

The interpolation function within a cubic grid cell is:

$$\begin{aligned}
&F_{i,j,k}(X^{(1)}, X^{(2)}, X^{(3)}) = \\
&[(A1_{i,j,k} X^{(1)} + A2_{i,j,k} X^{(2)} + A3_{i,j,k} X^{(3)} + A4_{i,j,k}) X^{(1)} + \\
&\ A5_{i,j,k} X^{(2)} + \partial_{\xi^{(1)}} f_{i,j,k}] X^{(1)} + \\
&[(A6_{i,j,k} X^{(2)} + A7_{i,j,k} X^{(3)} + A8_{i,j,k} X^{(1)} + A9_{i,j,k}) X^{(2)} + \\
&\ A10_{i,j,k} X^{(3)} + \partial_{\xi^{(2)}} f_{i,j,k}] X^{(2)} + \\
&[(A11_{i,j,k} X^{(3)} + A12_{i,j,k} X^{(1)} + A13_{i,j,k} X^{(2)} + A14_{i,j,k}) X^{(3)} \\
&\ + A15_{i,j,k} X^{(1)} + \partial_{\xi^{(3)}} f_{i,j,k}] X^{(3)} + \\
&A16_{i,j,k} X^{(1)} X^{(2)} X^{(3)} + f_{i,j,k}
\end{aligned} \tag{2.28}$$

where

$$X^{(1)} = -u^{(1)}\Delta t \quad X^{(2)} = -u^{(2)}\Delta t \quad X^{(3)} = -u^{(3)}\Delta t$$

$$\partial_{\xi^{(1)}} f = \partial f / \partial \xi^{(1)} \quad \partial_{\xi^{(2)}} f = \partial f / \partial \xi^{(2)} \quad \partial_{\xi^{(3)}} f = \partial f / \partial \xi^{(3)}$$

and,

$$\begin{aligned}
A1_{i,j,k} &= [-2D_i + \partial_{\xi^{(1)}}(f_{im,j,k} + f_{i,j,k})\Delta\xi^{(1)}] / [\Delta\xi^{(1)}]^3 \\
A2_{i,j,k} &= -[A17_{i,j,k} + \partial_{\xi^{(1)}} D_j \Delta\xi^{(1)}] / [\Delta\xi^{(1)}]^2 \Delta\xi^{(2)} \\
A3_{i,j,k} &= -[A18_{i,j,k} + \partial_{\xi^{(1)}} D_k \Delta\xi^{(1)}] / [\Delta\xi^{(1)}]^2 \Delta\xi^{(3)} \\
A4_{i,j,k} &= [3D_i - \partial_{\xi^{(1)}}(f_{im,j,k} + 2f_{i,j,k})\Delta\xi^{(1)}] / [\Delta\xi^{(1)}]^2 \\
A5_{i,j,k} &= [A17_{i,j,k} + \partial_{\xi^{(1)}} D_j \Delta\xi^{(1)} + \partial_{\xi^{(2)}} D_i \Delta\xi^{(2)}] / \Delta\xi^{(1)} \Delta\xi^{(2)} \\
A6_{i,j,k} &= [-2D_j + \partial_{\xi^{(2)}}(f_{i,jm,k} + f_{i,j,k})\Delta\xi^{(2)}] / [\Delta\xi^{(2)}]^3 \\
A7_{i,j,k} &= -[A19_{i,j,k} + \partial_{\xi^{(2)}} D_k \Delta\xi^{(2)}] / [\Delta\xi^{(2)}]^2 \Delta\xi^{(3)} \\
A8_{i,j,k} &= -[A17_{i,j,k} + \partial_{\xi^{(2)}} D_i \Delta\xi^{(2)}] / \Delta\xi^{(1)} [\Delta\xi^{(2)}]^2 \\
A9_{i,j,k} &= [3D_j - \partial_{\xi^{(2)}}(f_{i,jm,k} + 2f_{i,j,k})\Delta\xi^{(2)}] / [\Delta\xi^{(2)}]^2 \\
A10_{i,j,k} &= [A19_{i,j,k} + \partial_{\xi^{(2)}} D_k \Delta\xi^{(2)} + \partial_{\xi^{(3)}} D_j \Delta\xi^{(3)}] / \Delta\xi^{(2)} \Delta\xi^{(3)} \\
A11_{i,j,k} &= [-2D_k + \partial_{\xi^{(3)}}(f_{i,j,km} + f_{i,j,k})\Delta\xi^{(3)}] / [\Delta\xi^{(3)}]^3 \\
A12_{i,j,k} &= -[A18_{i,j,k} + \partial_{\xi^{(3)}} D_i \Delta\xi^{(3)}] / \Delta\xi^{(1)} [\Delta\xi^{(3)}]^2 \\
A13_{i,j,k} &= -[A19_{i,j,k} + \partial_{\xi^{(3)}} D_j \Delta\xi^{(3)}] / \Delta\xi^{(2)} [\Delta\xi^{(3)}]^2 \\
A14_{i,j,k} &= [3D_k - \partial_{\xi^{(3)}}(f_{i,j,km} + 2f_{i,j,k})\Delta\xi^{(3)}] / [\Delta\xi^{(3)}]^2 \\
A15_{i,j,k} &= [A18_{i,j,k} + \partial_{\xi^{(3)}} D_i \Delta\xi^{(3)} + \partial_{\xi^{(1)}} D_k \Delta\xi^{(1)}] / \Delta\xi^{(1)} \Delta\xi^{(3)} \\
A16_{i,j,k} &= [A17_{i,j,k} + f_{i,j,km} - (f_{i,jm,km} + f_{im,j,km}) + \\
&\qquad f_{im,jm,km}] / \Delta\xi^{(1)} \Delta\xi^{(2)} \Delta\xi^{(3)}
\end{aligned} \tag{2.29}$$

where,

$$\begin{aligned}
D_i &= f_{im,j,k} - f_{i,j,k} \\
D_j &= f_{i,jm,k} - f_{i,j,k} \\
D_k &= f_{i,j,km} - f_{i,j,k} \\
A17_{i,j,k} &= -f_{i,j,k} + f_{im,j,k} + f_{i,jm,k} - f_{im,jm,k} \\
A18_{i,j,k} &= -f_{i,j,k} + f_{im,j,k} + f_{i,j,km} - f_{im,j,km} - f_{im,j,km}
\end{aligned} \tag{2.30}$$

$A19_{i,j,k}=-f_{i,j,k}+f_{i,jm,k}+f_{i,j,km}-f_{i,jm,km}$

and,

$$\begin{cases} im=i-1 & if\ u^{(1)}>0 \\ im=i+1 & if\ u^{(1)}<0 \end{cases} \tag{2.31}$$

$$\begin{cases} jm=i-1 & if\ u^{(2)}>0 \\ jm=i+1 & if\ u^{(2)}<0 \end{cases} \quad \begin{cases} km=k-1 & if\ u^{(3)}>0 \\ km=k+1 & if\ u^{(3)}<0 \end{cases}$$

where $\Delta\xi^{(1)}$, $\Delta\xi^{(2)}$, $\Delta\xi^{(3)}$ are the mesh widths in $\xi^{(1)}$, $\xi^{(2)}$, $\xi^{(3)}$ direction respectively.

The whole calculation procedure can be summarized as the following four steps:

(1) To calculate the pseudo-velocity $\hat{u}_{n+1}^{(i)}$

Eq.(20) can be modified to Eq.(2.32) by substituting the implicit term of $\partial P_{n+1}/\partial\xi^{(i)}$ for the explicit term of $\partial P_n/\partial\xi^{(i)}$ in Eq.(2, 21), then pseudo-velocity $\hat{u}_{n+1}^{(1)}$can be estimated based on Eq.(2.32) using CIP method.

$$\frac{\hat{u}_{n+1}^{(1)}-u_n^{(1)}}{\Delta t}+u^{(1)}\frac{\partial u^{(1)}}{\partial\xi^{(1)}}+u^{(2)}\frac{\partial u^{(1)}}{\partial\xi^{(2)}}+u^{(3)}\frac{\partial u^{(1)}}{\partial\xi^{(3)}}=R_n^{(1)} \tag{2.32}$$

The same procedure can be applied to estimate the pseudo-velocity of $\hat{u}_{n+1}^{(2)}$, $\hat{u}_{n+1}^{(3)}$

(2) To estimate the pressure correction P'

Let,

$$P_{n+1}=P_n+P' \tag{2.33}$$

Then, the following equation can be obtained by subtracting Eq.(2.32) from Eq.(2.20).

$$u_{n+1}^{(1)}=\hat{u}_{n+1}^{(1)}-\Delta t\left(g^{(11)}\frac{\partial P'}{\partial\xi^{(1)}}+g^{(12)}\frac{\partial P'}{\partial\xi^{(2)}}+g^{(13)}\frac{\partial P'}{\partial\xi^{(3)}}\right) \tag{2.34}$$

Also, the similar relationships between $u_{n+1}^{(2)}$and P', $u_{n+1}^{(3)}$and P' can be obtained in the same way. Putting these relationships between $(u_{n+1}^{(1)}, u_{n+1}^{(2)}, u_{n+1}^{(3)})$and P' into the continuity equations of Eq.(2.18), an equation related to P' can be obtained. Thus, the pressure correction of P' can be obtained by solving the equation with TDMA algorithm (Tri-Diagonal Matrix Algorithm).

(3) To calculate the pressure P_{n+1} and the velocities

$$(u_{n+1}^{(1)}, u_{n+1}^{(2)}, u_{n+1}^{(3)})$$

The velocity of $u_{n+1}^{(1)}$can be obtained based on Eq.(2.34), and $u_{n+1}^{(2)}$,$u_{n+1}^{(3)}$ can be evaluated similarly. The pressure of P_{n+1} can be obtained based on Eq.(2.33).

(4) To calculate the water level H

The water level is calculated based on the 2D depth-integrated continuity equation. Concretely, Eq.(2.20) can be split into the following two equations:

$$\frac{\tilde{u}^{(1)}_{n+1}-u^{(1)}_{n}}{\Delta t}+u^{(1)}\frac{\partial u^{(1)}}{\partial \xi^{(1)}}+u^{(2)}\frac{\partial u^{(1)}}{\partial \xi^{(2)}}+u^{(3)}\frac{\partial u^{(1)}}{\partial \xi^{(3)}}=\tilde{R}^{(1)}_{n} \tag{2.35}$$

$$\frac{u^{(1)}_{n+1}-\tilde{u}^{(1)}_{n+1}}{\Delta t}=-g^{(11)}\frac{1}{\rho}\frac{\partial P_{n+1}}{\partial \xi^{(1)}}-g^{(12)}\frac{1}{\rho}\frac{\partial P_{n+1}}{\partial \xi^{(2)}} -g^{(13)}\frac{1}{\rho}\frac{\partial P_{n+1}}{\partial \xi^{(3)}} \tag{2.36}$$

where the difference between $\tilde{R}^{(1)}_{n}$ in Eq.(2.35) and $R^{(1)}_{n+1}$ in Eq.(2.20) is that the former excludes three pressure derivative terms from eq.(2.21).

From Eq.(2.36), the following equation can be obtained:

$$u^{(1)}_{n+1}=\tilde{u}^{(1)}_{n+1} -\Delta t\left(g^{(11)}\frac{1}{\rho}\frac{\partial P_{n+1}}{\partial \xi^{(1)}}-g^{(12)}\frac{1}{\rho}\frac{\partial P_{n+1}}{\partial \xi^{(2)}}-g^{(13)}\frac{1}{\rho}\frac{\partial P_{n+1}}{\partial \xi^{(3)}}\right) \tag{2.37}$$

where $\tilde{u}^{(1)}_{n+1}$ can be calculated based on Eq.(2.35). Similarly, the equations for $u^{(2)}_{n+1}$ and $u^{(3)}_{n+1}$ can be obtained. Putting these equations into the continuity equation, an equation associated with pressure P is obtained. Here, the pressure of P is approximated by the static pressure of P_s which can be expressed by water level of H.

Integrating the equation in depth direction then we can obtain an equation related to the water level of H. The equation is then solved implicitly by TDMA algorithm to obtain the water level of H at the future time $t+\Delta t$.

In the above, we have introduced the 3-dimensional model in the physical curvilinear coordinate system of $\xi^{(1)}\angle\xi^{(2)}\angle\xi^{(3)}$ where the coordinates in three directions can be non-orthogonal to each other. Although many coefficients related to coordinate transformation become 0 once if the coordinates are orthogonal to each other, it is difficult to generate a mesh being orthogonal to each other in all of three directions. Therefore, considering the balance between the difficulty of mesh generation and the complication of calculation, it is more practical to use coordinate system as $(\xi^{(1)}\perp\xi^{(2)})\angle\xi^{(3)}$ in most simulation calculations in river hydraulics.

3 NUMERICAL EXAMPLES

As our first step of study, the developed model is applied to an experimental channel for verifying its correctness. The calculation objective is a meandering channel whose shape is a sine-generated curve expressed as

$$\theta=\theta_{\max}\sin(2\pi x/L) \tag{3.1}$$

Table 3.1. Simulation condition of example-1.

Total width of channel(cm)	20
Length of channel(cm)	220
$\theta_{\max}$	35^0

Discharge *Q (l/s)*	2.15
Slope i_b	0.009
Manning roughness coefficient	0.015

where θ is the angle between the curved centerline and the down-valley axis at an arch distance of *s;* θ_{max} is the maximum value of θ*;* and L is the wavelength measured along the curved centerline. Simulation conditions are shown in Table 3.1.

The initial and boundary conditions are adopted as follows:

- Initial condition: The initial values of velocity $u^{(1)}$, water depth h_s and water level H are defined by the uniform flow calculation. The initial values of velocities $u^{(2)}$, $u^{(3)}$ are defined as 0.
- Boundary condition: At upstream (i=1) and downstream *(i=nend)*, the cyclical conditions of $\phi(1,j)=\phi(nend,j)$, $\phi(nend+1,j)=\phi(2,j)$ are employed.
- At side wall: free-slip condition is employed.

In the calculation, we choose to use the coordinate system of $(\xi^{(1)} \perp \xi^{(2)}) \angle \xi^{(3)}$ by considering the balance between the difficulty of orthogonal mesh's generation and the complication of calculation. The following sigma function σ is employed to generate the boundary-fitted mesh in vertical direction. The divisions in vertical direction are 5 layers as shown in Figure 3.1 and the divisions on plane are 48*10 meshes as shown in Figure 3.2.

$$\sigma = \frac{z - z_b}{H - z_b} \tag{3.2}$$

where z_b, is the elevation of channel bed and H is water level.

Since the water level of H keeps varying during the calculation process toward convergence, the boundary-fitted mesh in vertical direction must be regenerated by Eq.(3.2) with time. The ALE (Arbitrary Lagrangian and Eulerian) [9] method is employed to handle the mesh's moving problem. Concretely, for the momentum equation of $u^{(1)}$ shown in Eq.(2.20), Eq.(2.32) and Eq.(2.35), the convective term of $u^{(3)}\,\partial u^{(1)}/\partial \xi^{(3)}$ is replaced by the term of $(u^{(3)} - w_0)\partial u^{(1)}/\partial \xi$ where w_0 is the mesh moving speed in vertical direction. The same treatment is applied to the momentum equations of $u^{(2)}$ and $u^{(3)}$.

The contours of pressure P calculated at layer of k=1,2 are shown in Figure 3.3 and Figure 3.4 respectively. The contours of the water depth calculated and

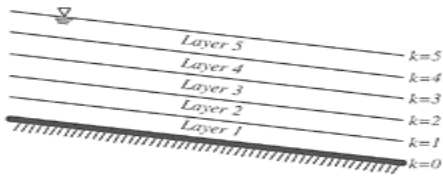

Figure 3.1. The divisions in vertical direction.

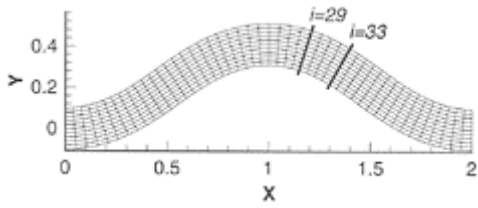

Figure 3.2. The divisions on plane.

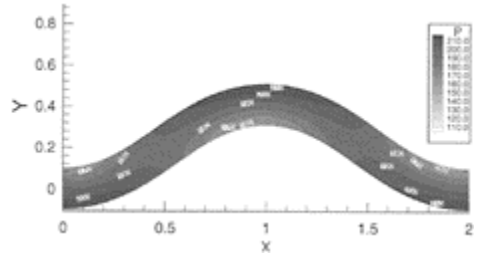

Figure 3.3. The contours of pressure *P* at the layer of *k*=1 (Calculation) (Unit:Pa).

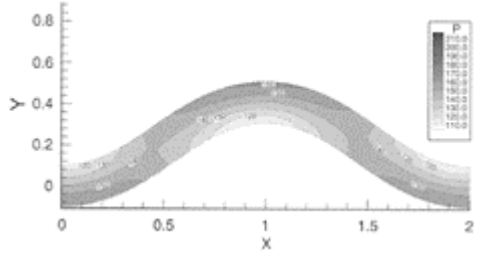

Figure 3.4. The contours of pressure *P* at the layer of *k*=2 (Calculation) (Unit:Pa).

measured are shown in Figure 3.5 and Figure 3.6 respectively. The vectors as well as the contours of the cross velocity calculated and measured in the cross sections of *i*=29 and *i*=33 are shown in Figure 3.7–3.8

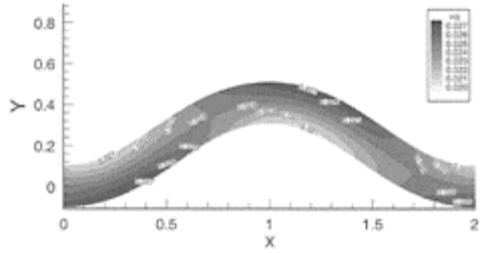

Figure 3.5. The contours of the water depth (Calculation) (Unit:m).

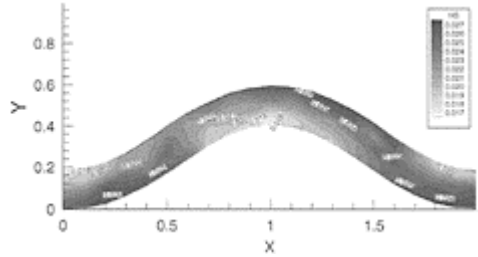

Figure 3.6. The contours of the water depth (Observation) (Unit:m).

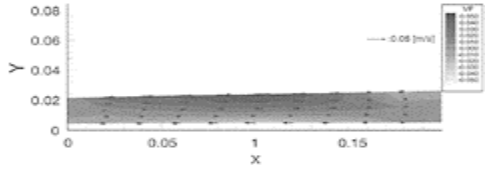

Figure 3.7. The vectors and the contours of the cross velocity in the cross section of *i*=29 (Calculation) (Unit:m/s).

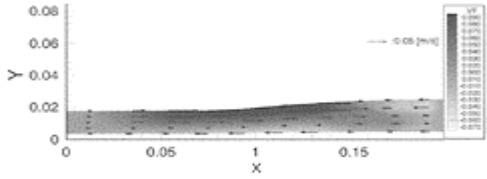

Figure 3.8. The vectors and the contours of the cross velocity in the

cross section of *i*=29(Observation) (Unit:m/s).

and Figure 3.9–3.10 respectively, where the positions of the cross sections *i*=29, 33 are shown in Figure 3.2. The vectors of plain velocity calculated and measured at the layer of *k*=1, 5 are shown in Figure 3.11–3.12 and Figure 3.11–3.12 respectively

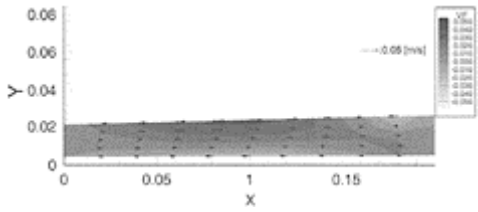

Figure 3.9. The vectors and the contours of the cross velocity in the cross section of *i*=33 (Observation) (Unit:m/s).

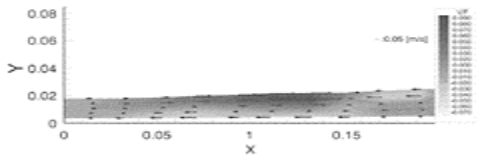

Figure 3.10. The vectors and the contours of the cross velocity in the cross section of *i*=33 (Observation) (Unit:m/s).

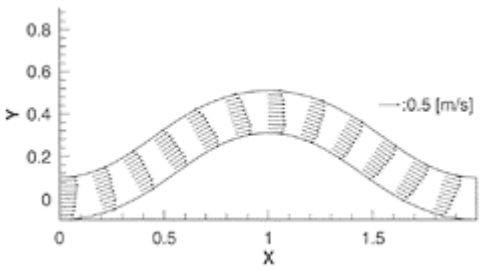

Figure 3.11. The vectors of plain velocity at the layer of *k*=1 (Calculation).

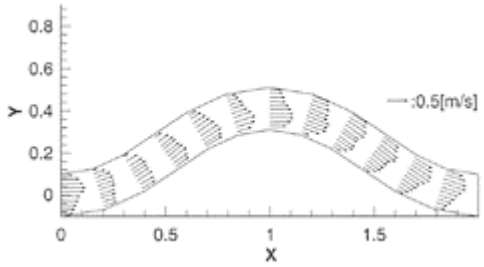

Figure 3.12. The vectors of plain velocity at the layer of *k*=1 (Observation).

Comparing the results between calculation and observation, the agreements between them from the whole condition are generally good, although the cross- and plain-velocities appear smaller than the observed ones.

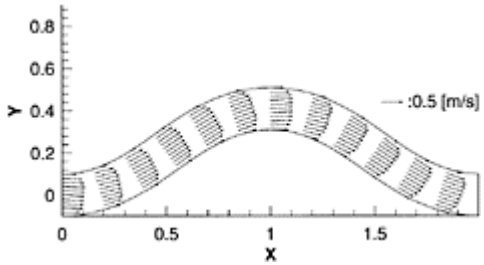

Figure 3.13. The vectors of plain velocity at the layer of *k*=5 (Calculation).

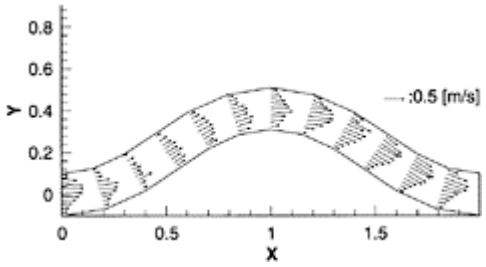

Figure 3.14. The vectors of plain velocity at the layer of *k*=5 (Observation).

4 CONCLUSION

In this paper, a 3-dimensional flow calculation model is developed. The model introduces the physical curvilinear coordinate system to solve the mesh sensitivity problem, and employs a calculation algorithm having the convective term treated by CIP method to improve the calculation stability for the flowfield with high velocity. The developed model is applied to an experimental channel, and calculation values are compared to observation values, and the agreement between them is generally good. Our next step of study is to apply the model to real rivers and include sediment transportation to the present flow calculation model.

REFERENCES

Fletcher C.A.J. *Computational Techniques for Fluid Dynam-ics. Volume II, Fundamental and General Techniques,* Second Edition, Springer-Verlag, 1991; pp.47–78.

Koshizuka S., Oka Y. and Kondo S. "A staggered differencing technique on boundary-fitted curvilinear grid for incompressible Navier-Stokes equation written with physical components", *A Collection of Technical Papers, 3rd Inter-national Symposium on Computational Fluid Dynamics,* Nagoya, Japan, 1989.

Koshizuka S., Oka Y. and Kondo S. "A boundary-fitted staggered difference method for incompressible flow using Riemann geometry", *Proc. 1st Int. conf. On Supercomputing in Nuclear Applications,* Mito, Japan 1990.

Koshizuka S., Oka Y. and Kondo S. "A staggered differencing technique on boundary-fitted curvilinear grids for incompressible flows along curvilinear or slant walls", *J. Comput. Mech.,* 1990; 7: pp.123–136.

Demirdzic I., Gosman A.D., Issa R.I. and Peric M. "A calculation procedure for turbulent flow in complex geometries", *Computers & Fluids* 1987; 15:pp.251–273.

Takizawa A., Koshizuka S. and Kondo S. "Generalization of physical component boundary fitted co-ordinate (PCBFC) method for the analysis of free-surface flow", *Int. j. numer. methods fluids,* Vol. 15, 1992; pp.1213–1237.

Yabe T. "A universal solver for hyperbolic equations by cubicpolynomial interpolation I. One-dimensional solver", *Computer Physics Communications* 66 (1991) 219–232; Elsevier Science Publishers B.V (North-Holland).

Yabe T., Ishikawa T. and Wang P.Y "A universal solver for hyperbolic equations by cubic-polynomial interpolation II. Two- and three-dimensional solvers", *Computer Physics Communications* 66 (1991) 233–242; Elsevier Science Publishers B.V (North-Holland).

Kawahara M, *Analysis of Moving Boundary Flows (Computational Fluid Dynamics Series 4),* University of Tokyo Press, 1995, ISBN4-13-065104-8, pp.46 (in Japaness).

Application of a 2D semi-lagrangian model to unsteady shallow water flow over dry bed

J.Murillo & P.García-Navarro
Fluid Mechanics, CPS, University of Zaragoza, Spain

River Flow 2004—Greco, Carravetta & Della Morte (eds.)

ABSTRACT: The work is devoted to the study of the applicability of a Semi-lagrangian method to the two-dimensional shallow water equations. The method is based on the characteristic formulation of the system and relies on the use of the bicharacteristic curves and a suitable interpolation technique. The interpolation is based on non-oscillatory bicubic Hermite polynomials. The technique is applied to transient problems involving front advance over dry beds with special emphasis put on the treatment of the advancing front.

1 INTRODUCTION

The hyperbolic character of the shallow water or St. Venant equations implies the existence of their characteristic formulation. The related characteristic based numerical methods gained wide acceptance in one-dimensional applications at the early years of Computational Hydraulics due to their conceptual simplicity and the fact that they are physically based and can lead to highly accurate results. Numerical models based on many alternative approaches appeared since then.

In two-dimensional shallow water models, finite differences, finite elements and more recently finite volumes have filled the scientific journals almost from the beginning. Only a few authors have reported experiences using semi-lagrangian methods as applied to 2D flow models. The simplicity of this approach is less evident in 2D than in 1D applications but the fact that the method is physically based remains the same and renders attractive any attempt of validation.

The shallow water equations represent physical laws defined on a domain filled with water and do not describe properly the advance over a dry boundary. This constitutes a moving boundary problem in which the water column goes to zero. The solution proposed in this work is based on the information coming from the interior wet region along the bicharacteristic curves.

2 MATHEMATICAL MODEL

The one-dimensional approximation of open channel flow problems using the Saint-Venant equations gives excellent results in general when the underlying hypothesis are justified. The main limitations of this approach are the cross sectional uniform velocity and horizontal free surface. In many cases, a two-dimensional approach is required in order to be closer to reality. The mass conservation equation and momentum balance in the *x* and *y* directions lead to the following system:

$$\frac{\partial h}{\partial t}+\frac{\partial(uh)}{\partial x}+\frac{\partial(vh)}{\partial y}=0 \tag{1}$$

$$\frac{1}{g}\frac{\partial u}{\partial t}+\frac{u}{g}\frac{\partial u}{\partial x}+\frac{v}{g}\frac{\partial u}{\partial y}+\frac{\partial h}{\partial x}=S_o^x-S_f^x \tag{2}$$

$$\frac{1}{g}\frac{\partial v}{\partial t}+\frac{u}{g}\frac{\partial v}{\partial x}+\frac{v}{g}\frac{\partial v}{\partial y}+\frac{\partial h}{\partial y}=S_o^y-S_f^y \tag{3}$$

where h is the water depth, u is the velocity component in the x direction and v is the component along the y direction, S_o^x and S_o^y are the bottom slopes along directions x and y respectively; S_f^x and S_f^y represent the hydraulic resistance in the two directions and are formulated as [22]:

$$S_f^x=\frac{n^2u\sqrt{u^2+v^2}}{C_u^2h^{4/3}} \tag{4}$$

$$S_f^y=\frac{n^2v\sqrt{u^2+v^2}}{C_u^2h^{4/3}} \tag{5}$$

with n the Manning roughness coefficient and C_u the cubic root of the rate of the acceleration of gravity g in any unit system and its value in the International Unit System.

The partial differential system defined by (1,2,3) is hyperbolic and therefore admits a characteristic formulation. This is next presented and exploited.

2.1 *The characteristic form*

The characteristic form of the equations in a 1D approach leads to a system of ordinary differential equations and therefore to a simpler mathematical formulation. This formulation is associated to the idea that the information propagates in space and time along characteristic surfaces forming a cone. The practical application of the method based on this formulation relies on curves, called bicharacteristic curves, contained on these surfaces.

The polar formulation of the bicharacteristic curves is:

$$\frac{dx}{dt}=u+c\cos\theta \tag{6}$$

$$\frac{dy}{dt}=v+c\sin\theta \tag{7}$$

Eqs. (6) and (7) suggest the linear combination required to eliminate the partial derivatives from the flow equations. If (1) is added to (2) multiplied by $c \cos\theta$ and to (3) multiplied by $c \sin\theta$, we get:

$$\frac{dh}{dt} + \frac{c}{g}\left(\cos\theta\frac{du}{dt} + \sin\theta\frac{dv}{dt}\right) = c\cos\theta(S_o^x - S_f^x) + c\sin\theta(S_o^y - S_f^y) - \frac{c^2}{g}s \tag{8}$$

where

$$s = \sin^2\theta\frac{\partial u}{\partial x} - \sin\theta\cos\theta\left(\frac{\partial u}{\partial y} + \frac{\partial v}{\partial x}\right) + \cos^2\theta\frac{\partial v}{\partial y}$$

A numerical technique can be implemented based on the existence of the bicharacteristic curves. It can be used to supply information at different time levels following an approach similar to the Hartree method. As suggested by Fig. 1, the solution at point (t_o, x_o, y_o), can be found following backward in time the characteristic cone up to its intersection with the plane corresponding to time $t=t_o-\delta t$. Three bicharacteristics are only required to furnish the solution for u_o, v_o, h_o, at (t_o, x_o, y_o). However, if a second order solution is required, the cross derivatives $\partial u/\partial y$ and $\partial v/\partial x$ must also be known at the solution point. One option is to involve four bicharacteristic instead of

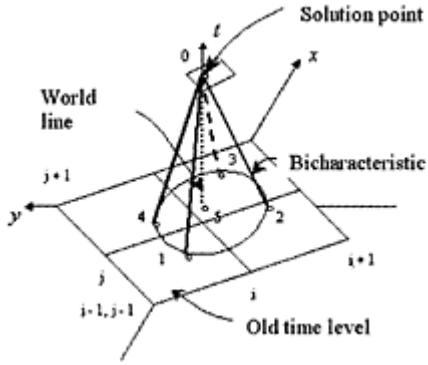

Figure 1. Elements of the bicharacteristic cone.

three and an additional equation called the world line. The four bicharacteristics are chosen at increments of $\pi/2$ in the polar angle φ. The world line is tangent to the vector $(1\ uv)^T$ and corresponds to a streamline in the plane (x, y). The mass continuity equation along the world line can be expressed as:

$$\frac{dh}{dt} + \frac{c^2}{g}\left(\frac{\partial u}{\partial x} + \frac{\partial v}{\partial y}\right) = 0 \tag{9}$$

2.2 *Resolution scheme.*

To solve the system of equations at a time t_o the first step is to know the trajectory of the bicharacteristics, since information propagates along those directions.

The coordinates of the intersections of the bicharacteristics with the plane $t_o-\delta t$ can be found using (6,7) through a first order approximation in δt for the four bicharacteristics.

The intersection of the world line with the plane $t_o-\delta t$ is also found in first order. The flow conditions at points 1–5 and their partial derivatives along directions x and y are detrmined by the interpolation among grid points in the plane $t_o-\delta t$. The final solution is strongly dependent on the interpolation technique used. The knowledge of the flow variables at points 1–5 allows a second order approximation in δt for equation (8).

2.3 *Grid movement at the front wave*

The solution at the advancing wave front is calculated using information from the wet points at the front itself in a previous time step. Katopodes and Strelkoff (1978) and Katopodes and Schamber (1987) defined an integration domain including both interior points and points at the leading front.

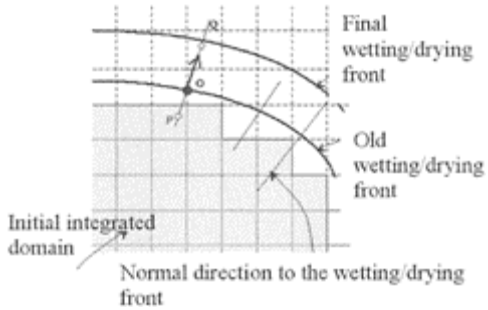

Figure 2. Front wave advance.

A different approach consists of approximating the velocity of the front points using information from the interior points. Taking into account that the front propagation speed must be given by the normal component of the water velocity at the wave frontier (the flow does not cross that boundary), the proposed method is based on the projection onto the direction normal to the front wave, of the flow velocities at the front positions (Fig. 2).

The actual values of the variables at the front position at a new time level are unknown and must be obtained from interpolation based on fictitious values at the outer dry area. The alternative is to neglect all information both from the front itself and from the dry zone and therefore to build interpolation polynomials only over the available information at the wet zone. The calculation is hence simplified.

The stability criterion within the calculation grid is:

$$\delta t \le \frac{\delta x\,\delta y}{\delta x \max\left\{\left|u_{ij}+c_{ij}\right|,\left|u_{ij}-c_{ij}\right|\right\}+\delta y \max\left\{\left|v_{ij}+c_{ij}\right|,\left|v_{ij}-c_{ij}\right|\right\}}$$

for all points *ij* in the plane, where δx, δy are the lengths of the interpolation cells.

2.4 *Wetting-drying condition*

Any numerical model intended to simulate unsteady free surface flows must be able to reproduce moving boundaries separating dry and wet zones. The careless treatment of these boundaries negatively affects the numerical results.

The points chosen for the calculation of the advancing front are not, in general, aligned along a direction normal to it. Being this an essential condition for the correct front simulation, it becomes necessary to introduce some kind of modification in the information relying on them. The projection of the velocity on the direction normal to the front is calculated and the tangential component is elliminated from th predicted

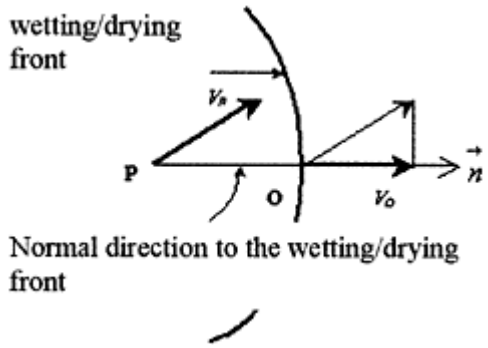

Figure 3. Velocity projection at the wetting front.

solution (Fig. 3). Otherwise, the numerical results are erroneous.

When, on the other hand, the front advances over a positive (adverse) slope, a further point must be taken into account: the local bed slope must be redefined to zero value. If this is not implemented the wave front is not able to advance up the hill as expected leading even to velocity values in the opposite sense to the advancing direction.

3 INTERPOLATION IN TWO DIMENSIONS

The interpolation used in the process of calculation of the variables at the intersection of the bicharacteristics and the plane $t_o - \delta t$ is determinant of the problem evolution and numerical accuracy.

As in one-dimensional problems, the interpolation must be able to supply accurate and smooth results. The accuracy is related to the method used to estimate the derivatives and the smoothness depends on the restrictions imposed on their values. The interpolative polynomial must not present any undesirable minimum or maximum within the computational cell for stability reasons.

In order to achieve the desired properties, the bicubic Hermite interpolation has been used. This procedure requires a refined treatment of the supplied information but produces oscillation free polynomials (Williamson and Rasch 1989). The value of the function as well as an estimation of the derivatives D_{ij} are required at the four cell vertices (Frischt and Carlson, 1980).

4 TEST CASES

Two different problems have been used to assess the suitability of the proposed meted: A flooding wave from a corner and a laboratory dam break problem.

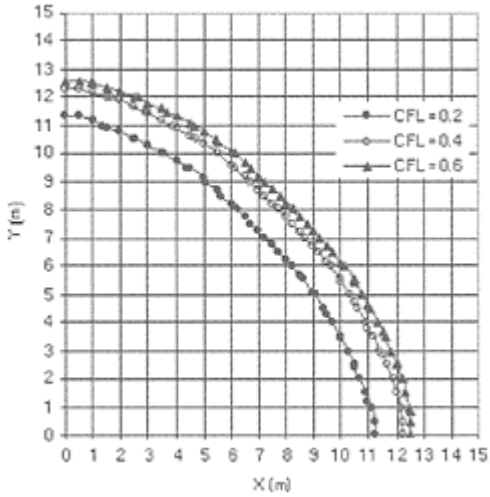

Figure 4. Advancing front position at t=9min using CFL=0.2, 0.4 and 0.6.

If discharge is applied at one of the corner points of a rectangular domain in which there are uniform slope, and roughness, the problem can be considered one-dimensional in the radial direction of a set of polar coordinates. The proposed method will be used on a rectangular structured mesh in order to verify that the solution is well behaved. The flow problem is a challenge for the interpolation scheme in this kind of grid.

In a second stage, the advance of the front in presence of sloping beds will be analyzed.

4.1 *Radial front over flat dry bed*

In order to study the performance of the proposed scheme and the sensitivity to the numerical parameters a first test case is envisaged using two different grids made of squared cells. The first, $M1$, with cell side lengths of 0.5m. The second, $M2$, made of cell side lengths of 1m.

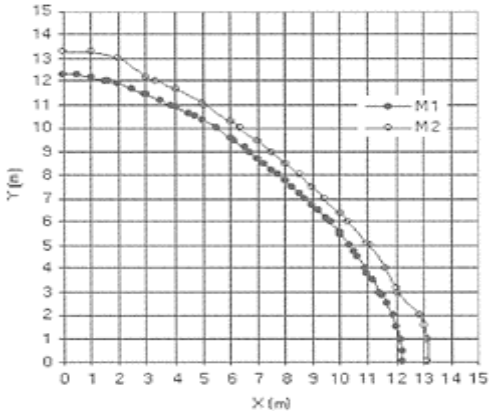

Figure 5. Advancing front position at t=9 min using grids M1 and M2 with CFL=0.4.

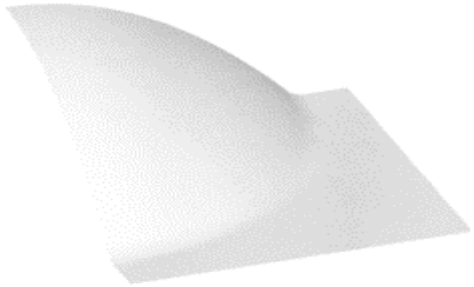

Figure 6. Bottom level for the positive slope radial flow test case.

The test case consists of a radial flooding wave advancing over dry bed from a corner. The inlet discharge is Q=0.00648m^3s^{-1}. The bottom is flat and characterized by a roughness Manning coefficient n=0.04.

The numerical results obtained on grid $M1$ will be compared using different values of the CFL. Fig. 4 shows the advancing front position at t=9min with CFL=0.2, 0.4 and 0.6. The figure indicates that the differences in advance using CFL=0.4 y 0.6 are minimum, and that there is some delay when using CFL=0.2.

The comparison of the results using different grid and the same CFL=0.4 is shown in Fig. 5. This figure contains the plot of the advancing fronts at time t=9min. The radial symmetry is conserved in both grids but the results are of worse quality on the larger grid due to the increment in the size of interpolation cell.

4.2 *Radial flow over dry slope*

The second test case is intended to analyze the behaviour of the numerical solution for the radial flood wave in presence of a slope. The test case is analogous to the previous except for the definition of a slope in both directions *x* and *y* following the shape of an inverted paraboloid as represented in Fig. 6. The radial wave starts at a corner situated on the uppermost

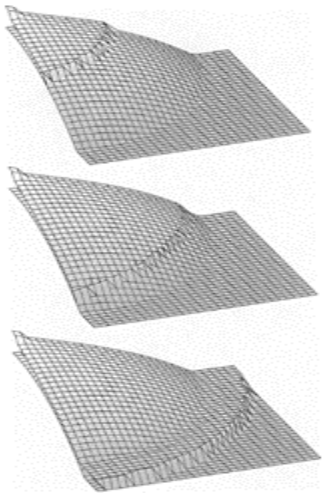

Figure 7. Water and bottom levels at *t*=3,6 and 9min.

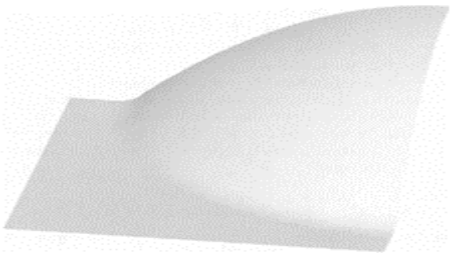

Figure 8. Bottom level for the adverse slope radial wave.

point and the advancing solution progresses without any difficulty and not requiring any special numerical treatment.

Initially, the flow changes very quickly due to the acceleration induced by the slope. Therefore, the water level is reduced as the wave advances. When the front reaches the horizontal part, its advancing speed is reduced and, at the same time, the water level at

the front increases. The leading grid cells of the wetting front do not require special treatments.

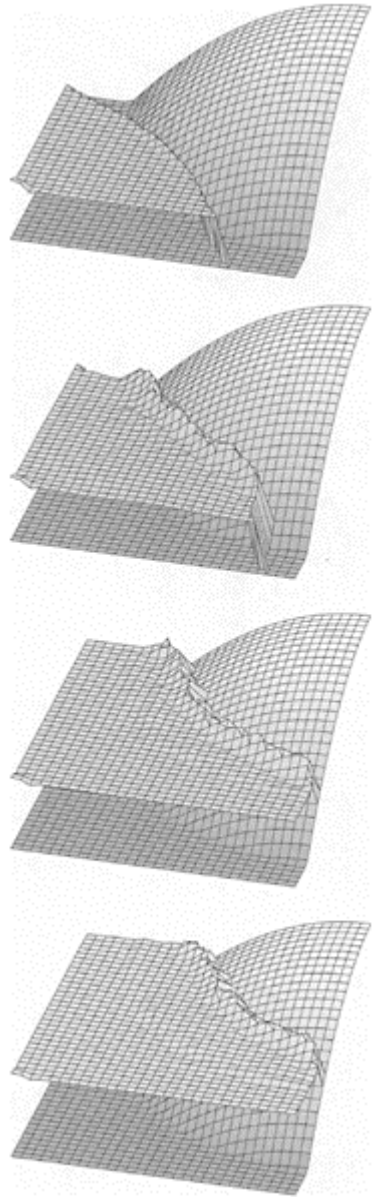

Figure 9. Bottom and water levels at T=3,6,9 and 15min.

4.3 *Radial flow over dry adverse slope*

In this test case, the evolution of the radial flooding wave over a dry adverse slope as the one shown on Fig. 8 is analyzed.

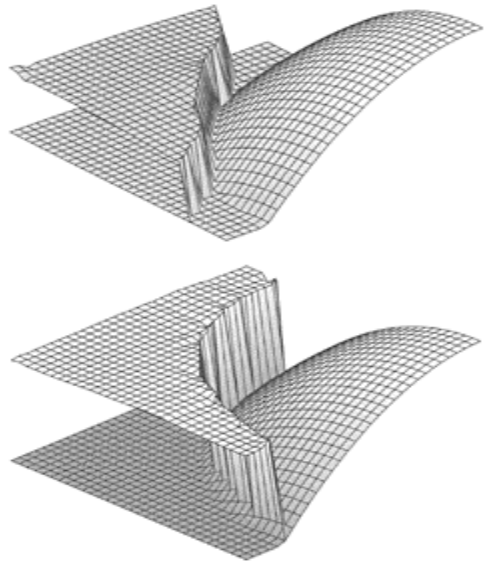

Figure 10. Wrong results due to the incorrect treatment of the wetting/drying front at t=6min and t=7min.

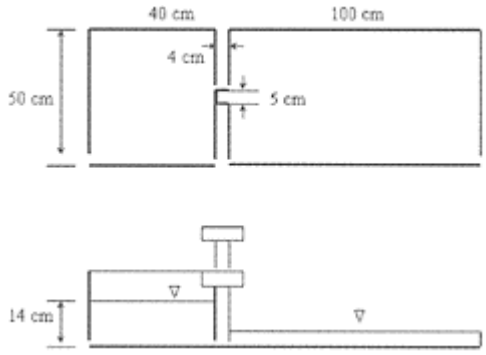

Figure 11. Experimental setup.

The simulation was performed over grid *M*1 using *CFL*=0.4. The wetting front advances with radial symmetry until the base of the slope is reached The flow field is then adapted to the bump progressively flooding it. The numerical results shown in Fig. 9 indicate that the water level rises and the wetting profile changes due to the presence of the adverse slope.

The previously indicated modifications in bottom level and velocity direction at the wetting cells was

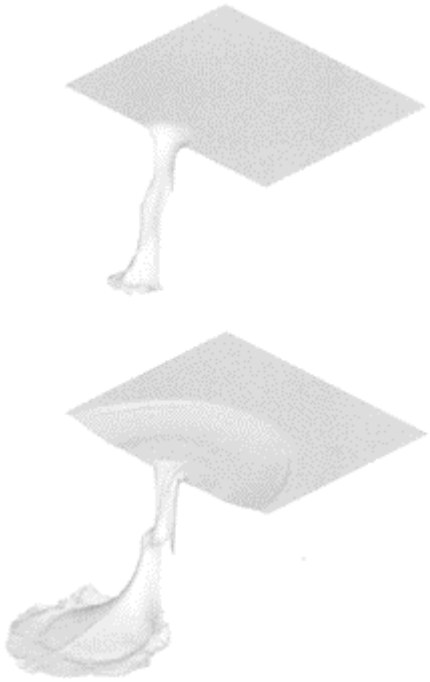

Figure 12. Dam break surface level at *t*=0.08 and 0.24s.

crucial in this example. Fig. 10 displays two samples of the solution obtained at different times in a simulation carried out without the mentioned modifications. The front was stuck at the foot of the slope generating a non-physical growing discontinuity in water levels when the bottom level was not adequately modified at the leading edge grid cells. If the velocity corrections had not been implemented, the results would have been totally incoherent.

4.4 *Validation: Dam break wave*

The last test case presented is the validation of the numerical meted against the experimental data obtained in a laboratory scaled dam break setup. The experiment was carried up as described in (Braschi et al. 1994) and the sketch of the experimental facility

is presentd in Fig. 11. Two reservoirs are connected by a gate. One is dry and the other is full of water up to a horizontal level 0.14m. The sudden removal of the gate is used to simulate an instantaneous dam breaking and releases the water leading to a flooding wave that advances over the dry part.

The simulation of the flow generated was performed using a uniform square grid of size 0.5cm, a *CFL* of 0.45 and a Manning coefficient n=0.01. Variations of this parameter do not influence the results sensibly

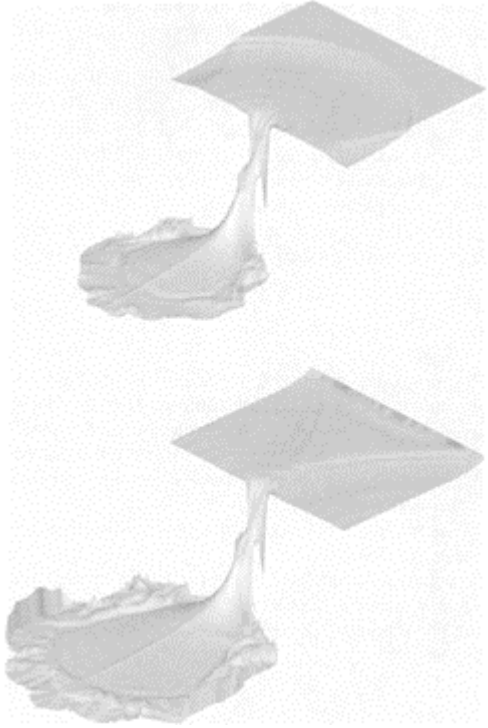

Figure 13. Dam break water levels at t=0, 32, and 0.48s.

since the flow is dominated by inertial and pressure effects.

When the gate is opened, a negative wave propagates into the wet reservoir with a celerity depending only on the unperturbed water level.

Fig. 12 shows the flow water levels 0.08s and 0.24s after the gate removal. The positive wave advances over the dry platform, both in a longitudinal and a transversal direction. As the front advances, two zones can be identified, the inner dominated by inertial effects and the outer more affected by the surface roughness.

At t=0.24s The depresión wave is near the solid walls. At time t=0.32s after the dam breaking, the depression wave has already been affected by reflection at the reservoir lateral walls and progresses towards the interior. This can be seen on Fig. 13.

At *t*=0.40s, the depression wave reaches the upstream end of the initially full reservoir. When time reaches *t*=0.48s the reflection waves in the reservoir cross each other (Fig. 13). On the other hand, at that time the wetting front has reached the side walls of the dry reservoir with an abrupt reflection leading to a considerable rise in water levels. At time *t*=0.56s and later, the wetting front presents a growing tendency of the zone dominated by inertial effects with respect to

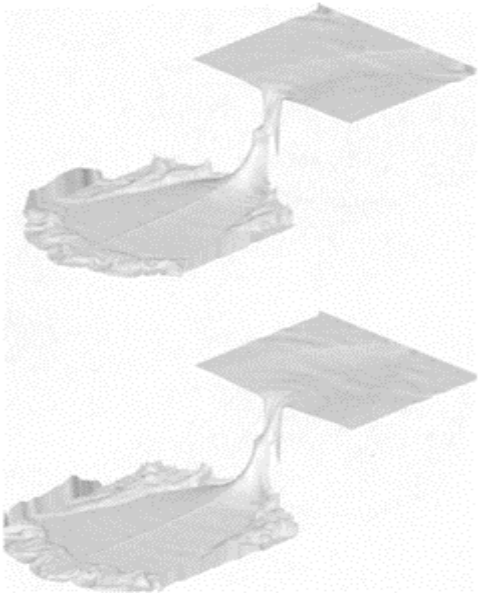

Figure 14. Dam break water levels at *t*=0.56 and 0.64s.

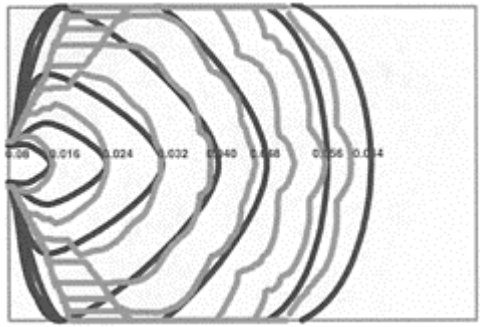

Figure 15. Advancing front positions at times *t*=0.08, 0.16, 0.24, 0.32, 0.40, 0.48, 0.56 and 0.64s. Grey lines:

simulated results. Black lines: experimental results.

the roughness dominated zone. Within the reservoir, several surface waves interact.

Fig. 15 shows a comparison of the computational and experimental results for different positions of the advancing front. Up to t=0.40 seconds, the flow properties are calculated with an excellent agreement. From this time, the numerical front is slower and

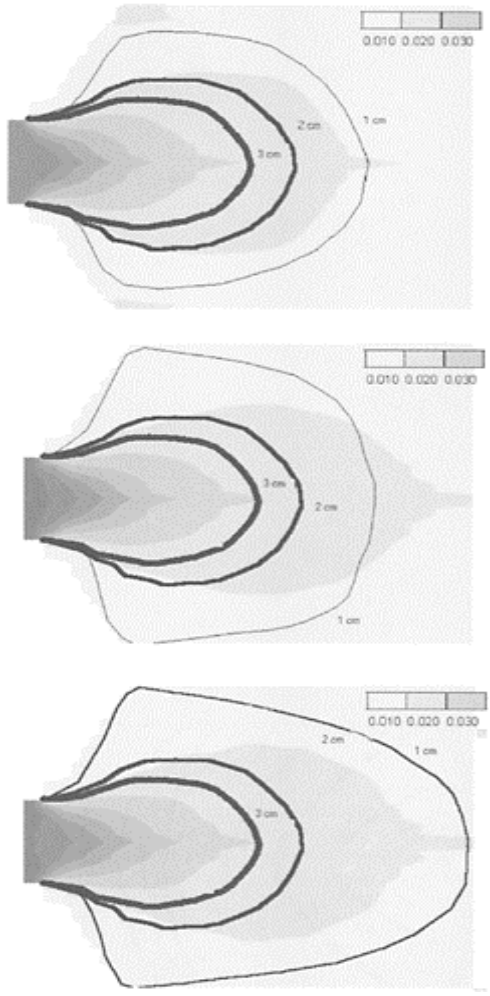

Figure 16. Water level distributions a times t=0.24, 0.40, 0.56s. Thick lines indicate contour lines from the experimental results.

the agreement is worse. On the other hand, the simulated front presents different parts advancing more irregularly than the experimental front.

Fig. 16 displays water level distributions for different times, both measured and calculated. The calculated distribution reproduces well the distinctive characteristics of the real water levels distribution and the agreement is satisfactory despite the underlying hydrostatic pressure assumption.

The water levels at the reflections with the walls does also match properly the measured evolution.

5 CONCLUSIONS

The proposed numerical technique is suitable for the numerical resolution of complex flow problems involving the advance of front waves over dry irregular beds. The front advances conserving the correct shape and the water distribution levels agrees well with experimental results.

The method is able to capture all the wave phenomena in the flow.

A special numerical treatment at the advancing front position is crucial in order to obtain accurate and sound numerical results specially in presence of adverse dry slopes.

REFERENCES

Rasch P.J. and Williamson D.L. On shape-preserving interpolation and semi-lagrangian transport. *Siam J. Sci. Stat Comput.* Vol 11. No 4, 1990.

Fritsch F.N. and Carlson R.E., Monotone piecewise cubic interpolation. *Siam J. Numer. Anal.* Vol 17 No 2, 1980.

Katopodes N. and Schamber R. Applicability of dam-break flood wave models. *Journal of Hydraulic Engineering.* May 1983, 109 No 5, ASCE.

Katopodes N. and Strelkoff T. Computing two dimensional dam-break flood waves. 1987, 14036 HY9. *Journal of the Hydraulics Division.*

Williamson D.L. and Rash P.J. Two-dimensional semilagrangian transport with shape-preserving interpolation. *Monthly Weather Review,* Vol 117, No 1, 1989. American Metereological Society.

Braschi G., Dadone F. and Gallati M. Plain flooding, nearfield and far field simulations, *Modelling of flood over initially dry areas,* ASCE, 1994.

How a 2-D code can simulate urban flood situations

E.Mignot & A.Paquier
Cemagref, R.U. Hydrology-Hydraulics, Lyon, France

N.Rivière
LMFA, INSA de Lyon, Lyon, France

River Flow 2004—Greco, Carravetta & Della Morte (eds.)

ABSTRACT: Numerical codes are being used to simulate flood progress in cities but no real knowledge about the accuracy of these numerical calculations are available. The objective of this study is to check the capabilities of a 2D code to model a flood in an urban area. A simplified city flood was then modelled experimentally and its data were compared with the simulation results. Although results can be considered accurate enough for operational purposes, water depth differences remain, even with a refined mesh. In order to find out which typical urban situations are difficult to simulate by the code, two experimental test cases representing urban details were then modelled and calculated. The first one is the flow around a building where the reflections of the wave on the walls and recirculation behind the building are of major importance. The second one is the distribution of flow discharge in a four branches crossroad with two incoming and two outgoing streets with the same width and same bottom slope of 1%.

1 INTRODUCTION

Various computational fluid dynamics methods have already been used in order to simulate flood scenarios in urban zones (Neary & Sotiropoulos, 1996; Khan et al., 2000; Hervouet et al., 2000; Paquier et al., 2003). The results are encouraging but there is still a lack of knowledge in the accuracy of the risk assessment. In order to check the real capabilities of a 2D numerical code to simulate a urban flood, we use three experimental test cases (two of which are part of the European Project IMPACT (Soares et al., 2004; Soares et al., 2003)) representing a simplified city, the flow around a building and finally

the flow within a four branches crossroad. The comparisons between the experimental and numerical records should permit to check the difficulties remaining when simulating a urban flood numerically.

2 PRESENTATION OF THE CODE

The code we used is Rubar 20. Here below are provided the equations that are solved and the corresponding numerical scheme. The explicit second-order finite volume scheme solves the 2-D shallow water equations.

$$\frac{\partial h}{\partial t}+\frac{\partial (hu)}{\partial x}+\frac{\partial (hv)}{\partial y}=0 \tag{1}$$

$$\frac{\partial (hu)}{\partial t}+\frac{\partial \left(hu^2+g\frac{h^2}{2}\right)}{\partial x}+\frac{\partial (huv)}{\partial y}=-gh\frac{\partial Z}{\partial x}-g\frac{u\sqrt{u^2+v^2}}{K_s{}^2h^{1/3}}+K\left(\frac{\partial}{\partial x}\left(h\frac{\partial u}{\partial x}\right)+\frac{\partial}{\partial y}\left(h\frac{\partial u}{\partial y}\right)\right) \tag{2}$$

$$\frac{\partial (hv)}{\partial t}+\frac{\partial (huv)}{\partial x}+\frac{\partial \left(hv^2+g\frac{h^2}{2}\right)}{\partial y}=-gh\frac{\partial Z}{\partial y}-g\frac{v\sqrt{u^2+v^2}}{K_s{}^2h^{1/3}}+K\left(\frac{\partial}{\partial x}\left(h\frac{\partial v}{\partial x}\right)+\frac{\partial}{\partial y}\left(h\frac{\partial v}{\partial y}\right)\right) \tag{3}$$

The Godunov-type scheme includes 4 steps (Paquier 1998):

1. computing slope of each one of the 3 variables *h* (or *z* water level), *hu* and *hv* in every cell on *x* and *y* axis by the method of the least squares and applying limitations of slopes following in order to obtain TVD (Total Variation Diminishing) scheme.
2. computing values of *W=(h, hu, hv)* at intermediate time $t_{n+1/2}$ in the middle of the edge of cell Mi to obtain second-order scheme.
3. solving a 1-D Riemann problem in the direction normal to the edge at $t_{n+1/2}$ in order to estimate the fluxes through edges for the conservative part of the equations. It is possible to use a Roe type linearization that directly provides an estimate of the fluxes.
4. integrating the terms of the second member of the set of equations (1) to (3) on the surface of the cell in order to add the corresponding contribution and to obtain the final value of the solution.

3 MODEL CITY EXPERIMENT

3.1 *Presentation of the test case*

The aim of this Impact Project (Soares et al., 2004) which took place in Milano (ENEL-CESI) is to simulate the flow within a simplified urban (or semi-urban) area. Cubic impervious blocks (simulating buildings or groups of buildings) are placed within a valley laboratory model upstream, which a flood hydrograph is introduced. Several urban configurations are modelled, based on the same valley topography:

- Two buildings configurations (aligned or staggered blocks)
- Two area widths (a whole valley or use of walls to confine the flow around the buildings area)
- Two discharge hydrographs as upstream conditions.

The case presented here below is the confined valley with 16 aligned buildings. Within the urban area, eight gauges (S3–S10) are used in order to describe the water depth evolution during the experiment.

3.2 *Description of the flow*

During the high upstream discharge period, the flow is rapid in the upstream part of the domain with low water depths. When getting near the building area, the flow slows down and the water depths rise strongly. Then the flow reaccelerates in the streets and the velocity remains low behind the buildings. Downstream from the urban area, the increased passing section leads to high velocities throughout the whole section.

3.3 *Comparison Experimental/Numerical results*

On the one hand, the numerical hydrographs obtained have globally the same shape as the experimental water

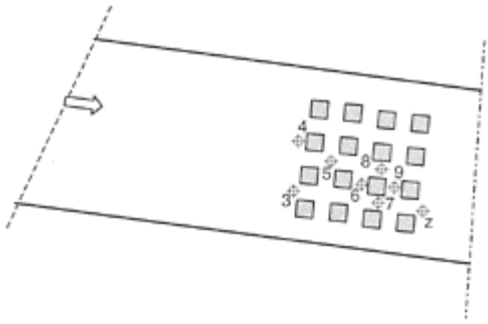

Figure 1. Model city benchmark.

depth curves and the highest and lowest water levels are located at the same places. On the other hand, important hydrograph differences remain.

3.3.1 *Shock against the buildings*

The first difference that can be outlined between numerical and experimental hydrographs is the front wave reflection on the urban area at S3 and S4. The numerical calculation does not simulate accurately this short increase of water depth because of the size of the cells and due to the equations. In a real case, this could be a problem when comparing natural water marks with calculated higher water depths after a flood.

3.3.2 *Hydrographs comparisons*

In term of typical water depth in the urban area, we present the histogram of the water depth at t=30s at all the gauges. We notice that the highest water depths appear upstream

from the urban area (S3 and S4); and within the urban area, the high water depths are in the streets in the centre of the city (S7 and S8) and the lowest are downstream from this area (S10).

The water depths calculated in the urban area (S5 to S9) are very homogeneous, all between h=30.1mm and h=36.5mm, whereas in the experimental conditions, the water depth vary much more between h=28.9mm and h=45mm. This homogeneity could be due to the lack of capability of the equations to model accurately the reflections and recirculations or to a diffusion caused by too large cells within the urban area, which cannot provide a convenient representation of the structures of the secondary flows. Furthermore,

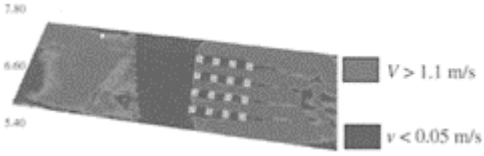

Figure 2. Model city velocity at t=18s.

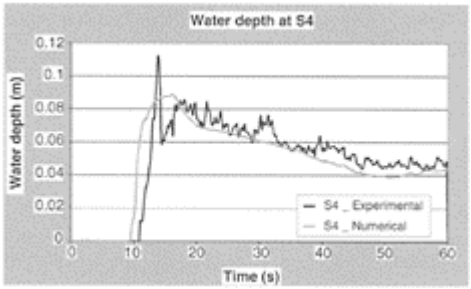

Figure 3. Numerical and experimental water depths at S4.

the water depth is usually higher in the experimental records than in the numerical results except at S5 and S10.

All the numerically calculated water depth curves have a very similar shape and the difference between them is usually only homothetic while the experimental hydrographs have different shapes: for example, the falling curves have different slopes.

3.3.3 *Influence of the friction coefficient*

As the water depths are usually underestimated, we tested an increase of the Manning coefficient from

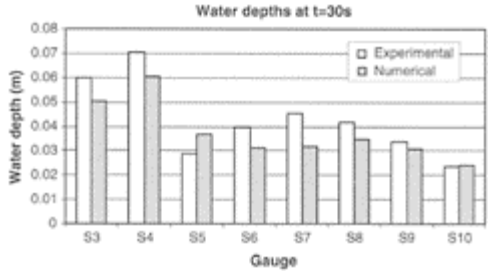

Figure 4. Water depth histogram at t=30s.

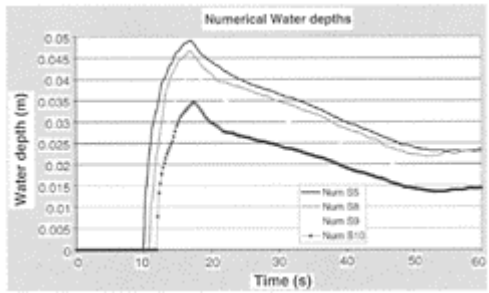

Figure 5. Calculated water depth hydrographs.

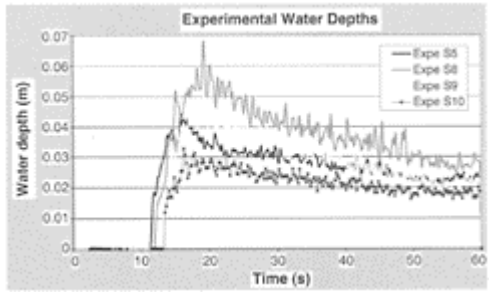

Figure 6. Experimental water depth hydrographs.

n=0.0162 to n=0.025. Of course, this tends to increase the water depth: thus, when the water depth is underestimated (S7 and S8), the high friction hydrograph fits the experimental curve better but, if the hydrograph is well estimated with the experimental friction coefficient, the water depth becomes overestimated with a higher friction.

Increasing the friction coefficient also reduces the front wave propagation and then the delay between the calculation and experimental hydrographs. However, this timing difference is not only reduced upstream from the urban area (S3 and S4), it is also reduced when travelling within the urban area and the propagation velocity is then not as well described as in the original friction coefficient case. The friction coefficient cannot be the right parameter to improve accuracy of calculation results.

3.3.4 *Influence of refining the mesh*

A new mesh with a typical cell size of 1cm is established. Figure 8 shows that the results in term of water depths comparisons are not improved.

The meshing size does not seem either to be the parameter responsible for the lack of accuracy of the flow simulation.

3.4 *Conclusion*

Here above, we presented one configuration among the seven experimental test cases. However, all of them

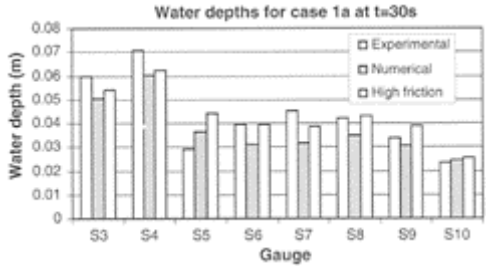

Figure 7. High friction water depth histogram.

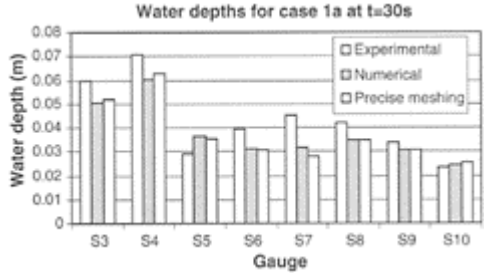

Figure 8. Fine mesh water depth histogram.

lead to the same conclusions: the 2D code can globally simulate the flow within a simplified city, but the errors are locally quite strong:

- The calculated water depths are too homogeneous within the urban area
- The numerical hydrographs are usually underestimated
- The calculated hydrographs do not reproduce exactly the experimental hydrograph shapes.

Thus, it is useful to check the quality of modelling in more detailed situations such as the flow around a building or the flow in a crossroad in order to figure out from what the main errors come.

4 THE ISOLATED BUILDING TEST CASE

4.1 *Presentation of the test case*

The aim of this experiment which took place in Université catholique de Louvian is to investigate the effect induced by a building placed within a sudden dam-break flow. Note that, depending on the working scale, this experiment could also represent the flow around an obstacle such as a parked car within a street during an urban flood. The experimental benchmark (Soares et al., 2003) was carried out within a horizontal open channel with a reservoir where steady water is stored until the beginning of the experiment. At the reservoir downstream boundary, the width of the channel is narrowed to 1 m in order to concentrate the flow and represent a natural dam-break when opening the gate. Further downstream, at around 3.5m from the reservoir, in front of the gate, a 0.8×0.4m impervious building is introduced with a specific angle to the flow direction. The following measurements are taken in order to compare the experimental data with the results of the simulations: water depths at the five gauge points and velocity fields at t=1s, t=2s, t=10s.

4.2 *Description of the flow*

The flow is rapid when getting off the reservoir creating two recirculation zones on the sides of the dam gate due to depression; then, it slows down suddenly (and water depth rises) when arriving close to the building. The flow passes around the building and a clockwise re-circulation zone appears downstream. At around one channel width downstream from the building, the flow tends to become one-dimensional (the velocity magnitude tends to be homogeneous on the channel section). Reflections against the channel sides bottom slopes and against the building are strong, and create complex local secondary flows.

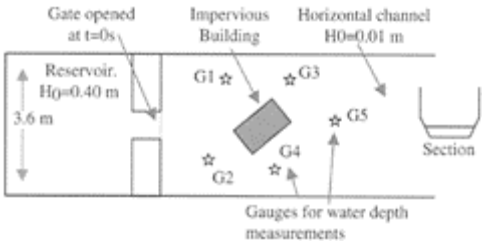

Figure 9. Isolated building benchmark scheme.

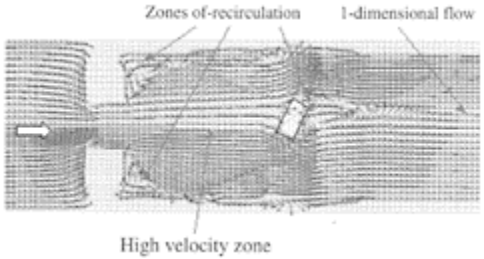

Figure 10. Velocity field at time t=15s.

4.3 *Numerical calculation of single building*

This experimental test case was simulated using a grid based on the regularity of the mesh upstream and downstream from the building, the cells around the building are then somewhat distorted. The typical size of the cells is 10cm for a total number of cells around 10000.

4.3.1 *Influence of the building*

In order to investigate the influence of the introduction of the building (or obstacle to the flow) in the channel, we present gauges G1 and G5 hydrographs with and without the building (plain channel).

Upstream from the building (G1), the water depths are similar in both cases at the beginning of the experiment until the flood wave reflects on the building wall and that backwater effect appears. Then, the original hydrograph rises suddenly, the lager water level being induced by the flow section reduction with the obstacle. Afterwards the hydrographs keep the same shape but the plain channel has lower water depths.

Downstream from the building (G5), Fig. 12 shows a slight wave delay of 0.4 seconds when introducing the building. Furthermore, the wave peak remarkable without the building does not appear with the building, case in which the highest water depth is lower. During the second part of the event (t>15s), the limnigrams are very similar.

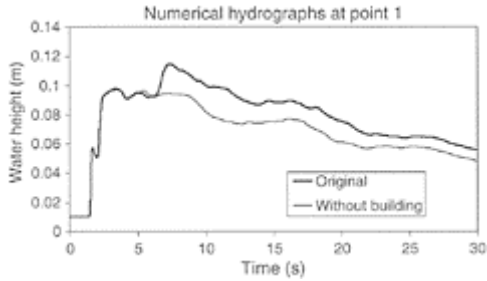

Figure 11. Building influence water depths at G1.

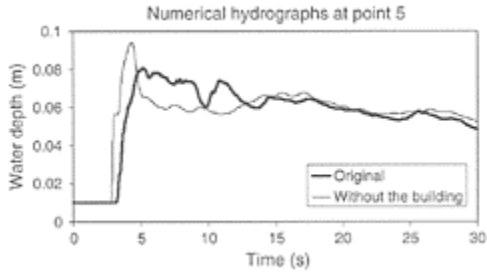

Figure 12. Building influence water depths at G5.

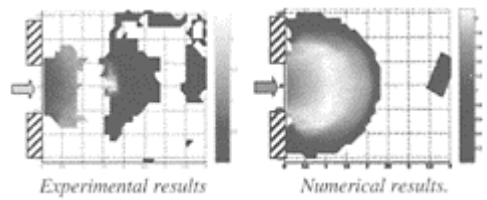

Figure 13. Velocity (m/s) at t=1s.

4.4 *Experimental/Numerical comparison*

4.4.1 *Global comparison*

The experimental velocity field could not be measured in the whole wetted area because of technical difficulties in the most oscillating water level zones (for instance around the hydraulic jumps). Moreover, at t=1s, the velocity was measured both in the area reached by the wave and in the zones where some wind disturbance or channel oscillations created a slight water motion.

T=1s: flood wave propagation

At t=1s, the front wave has an ellipsoid aspect and the front wave has reached the distance x=2.1m. This first wave seems to be well simulated, even if one

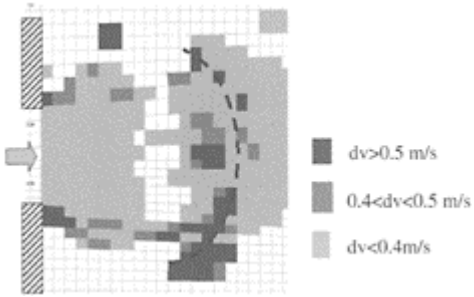

Figure 14. Velocity differences between numerical results and experimental records at t=1s.

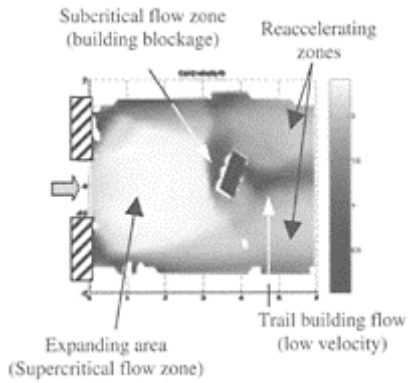

Figure 15a. Numerical velocity (m/s) at t=5s.

main error seems to be related to the shape of the front.

In the experimental record, the maximum water level (white colour) is very close to the front of the wave whereas this distance is larger in the numerical cases. This is confirmed by the image below where the main differences (dash line) are situated in the highest velocity zone (wave front). There seem to be a slight error in the dimension of the expanding front wave; however, this dimension difference is of the order of magnitude of one cell of calculation.

T=5s: developed structures

After 5s of experiment, the front wave has already passed the building area and the flow structure is established. Figure 15 shows that the flow structures appear on the experimental records and numerical results at the same place and with almost the same size.

Figure 16 shows that the main differences between numerically calculated water depths and the experimental records are located in four specific areas:

Zone B: calculation overestimates the velocity values.

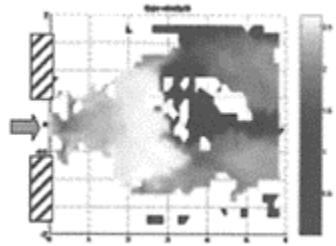

Figure 15b. Experimental velocity records (m/s) at *t*=5s.

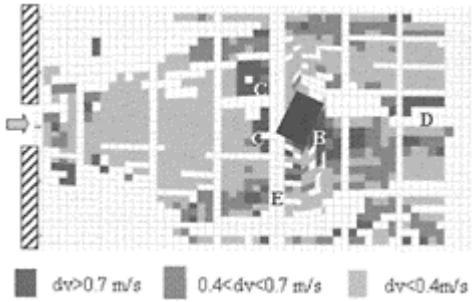

Figure 16. Differences between numerical and experimental velocity results at *t*=5s.

Zone C+C': the low velocity zone is shorter in the numerical calculations compared to the experimental case. This result shows the larger impact of the building on the overall flow in the experimental case compared to the numerical one.

Zone D: The low velocity zone protected by the building, is wider in the calculation compared to the experimental case.

Zone E: We see in both the numerical results and experimental records that there is a frontier near point E between a high velocity zone and a lower one. This frontier is not exactly at the same place in both cases.

4.4.2 *Hydrograph comparison at the gauges*

The 5 gauges were placed in very specific locations within the flow: either next to hydraulic regime change zones (supercritical to subcritical and vice versa: G1, G2, G4), in high wall reflection zones (G3) or finally at the border of the trailing zone behind the building (G5).

In a hydraulic jump location zone (example next to G2), the hydrographs are influenced by the motion of the hydraulic jump. In the experimental conditions, the hydraulic jump passes slowly through the gauge location and afterwards, G2 remains on its subcritical side. In the numerical calculation, at t~19s, the gauge 2 enters the subcritical zone after the displacement of the

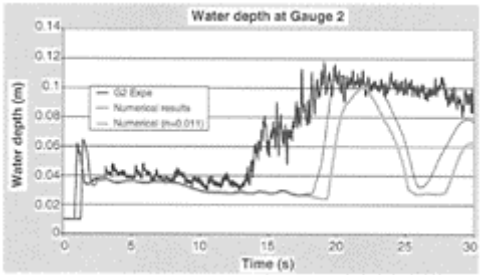

Figure 17. Water depths at G2.

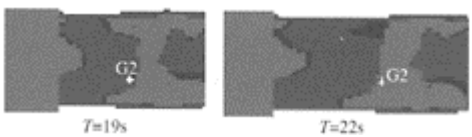

Figure 18. Water depth around G2. In dark: h<5cm, in light grey h>8cm. White cross=G2 location.

hydraulic jump so its water depth increases suddenly. However, shortly after, the hydraulic jump travels back, passes G2 and the water depth decreases again. But, a slight change of a numerical parameter (example Manning increasing from 0.1 to 0.11) can modify the hydraulic jump location slightly but with a large influence on the hydrograph shape at G2. Note that the water depth in both regimes is estimated accurately.

Figure 18 shows that the displacement of the regime frontier implies a displacement of G2 from the supercritical to subcritical zone. However, G2 remains close to the hydraulic jump.

Thus, only errors in the location of the hydraulic jump spoiled the simulation of water depth at G2.

Another difficulty to model locally the water depths is in the areas of high reflections like near G3. Indeed, the shallow water equations cannot integrate the large slope (the slopes of the channel side are 45%) and have difficulties to represent these reflections.

Then, the results are smoother than the experimental data but the shape of the hydrograph is similar.

4.5 *Conclusions*

When comparing calculation results with experimental data, we noticed that the numerical code could provide a convenient overall representation of the flow: high and low velocity areas, hydraulic jumps and trailing zones. However, concerning the water depths and velocities at the five gauge points situated around the building, we found differences corresponding to the difficulties of the code to simulate local flow characteristics accurately. The major differences seem

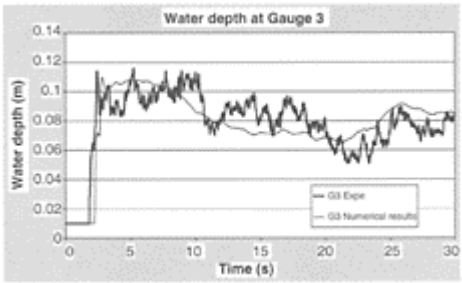

Figure 19. Water depths at G3.

to come from:

- Slight errors in the locations of the hydraulic jumps (spatial errors).
- The difficulty to represent the reflections on the walls (building or banks).
- The size of the trailing zone downstream from the building.

5 FOUR BRANCHES CROSSROAD TEST CASE

In dense urban areas, the flows take place mainly in the streets and the crossroads. The influence of the cross-roads is mostly the distribution of the flow between the different streets joining there. This experiment aims at improving the knowledge of the discharge distribution in a four channels crossroad that is the most popular street junction configuration in a city. In a future study, the capabilities of the numerical code to predict the flow distribution in a crossroad should be tested. Previous studies about open channel junctions mainly focused on three channels junctions either in dividing or combining flows and almost exclusively in subcritical conditions. To the authors' knowledge, the only work with 4 channel junctions was performed by (Nania, 1999); it includes an experimental study of 2 incoming and 2 outgoing flows with equal width concrete channels and for three slope configurations; from the experiments, an empirical relation was built to provide the discharge distribution as a function of the inflow Discharge

Weighted Head ($W=\rho g H_s$, with H_s the Specific Head of the flow). Thus, experiments are performed at LMFA to increase the knowledge in such configurations.

5.1 *Experimental set-up*

The set-up is composed of 4 rectangular channels, made of glass, of length L=2m and of width b=0.3m) oriented perpendicularly to each other, with the *(xy)* frame defined Fig. 18. The channels slope

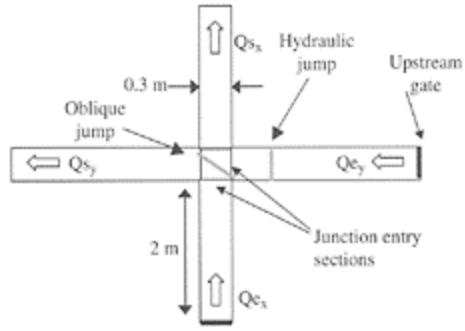

Figure 20. Four channel crossroad.

is 1.27% and the junction is a horizontal square. The water enters the two incoming channels through honeycombs and a gate used to adjust the normal depth, as the flow is supercritical. Both incoming and outgoing discharges are measures thanks to electromagnetic flowmeters. Upstream water depths are acquired thanks to a moveable point gauge, with a reading accuracy of 0.1mm and junction entry section water depths are measured by resistive probes to obtain an average water depth over about ten seconds.

5.2 *Description of the flows*

The upstream flows are usually supercritical and meet within the junction creating locally a very complex secondary flow. The crossroad causes an abrupt flow deviation, resulting in hydraulic jumps. As reported by (Nania 1999) and depending on the upstream discharges, the general flow can be of two types. When the two upstream discharges (Qe_x and Qe_y) are not too different one from another, a hydraulic jump occurs in each inflow channel at specific distances from the junction depending on both discharges: this is called *"type 1"* flow. A *"type 2"* flow is obtained when one incoming discharge is much larger than the other. Then an oblique jump appears in the large discharge inflow channel and a hydraulic jump occurs in the low discharge channel. For a specific discharge rate (one inflow discharge much larger than the other), the flow can become entirely subcritical in the low discharge incoming channel but a virtual hydraulic jump can be located upstream from the gate.

Downstream from the junction, two recirculation zones appear along with two contraction zones. Further downstream, the flow regime becomes supercritical again because of the slope.

5.3 *Choice of parameters*

First aim of the study is to find one single equation providing the part of discharge in each direction as a

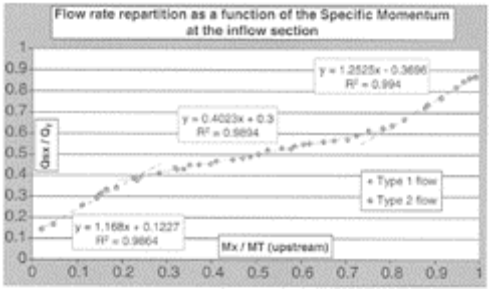

Figure 21. Flow distribution as a function of the upstream Specific Momentum.

function of the inflow conditions. The slope of each channel is constant (1.27%) and should not appear as a parameter. A parameter representing the inflow conditions can be the Specific Momentum:

$$M=\rho\frac{Q^2}{bh}+\frac{\rho g b h^2}{2}$$

where h is the local water depth and Q is the inflow discharge. The Specific Momentum is conserved through the hydraulic jumps, contrarily to the Discharge Weighted Head used by Nania (1999).

In fact, the parameter considered is M_x/M_T (Specific Momentum in the x direction divided by the total Specific Momentum $(M_T=Mx+My)$) calculated using the inflow discharge and the normal water depth set upstream from the hydraulic jump, to express the discharge distribution: Qs_x/Q_T (Qs_x=Outflow discharge along x channel and $Q_T=QS_x+QS_y$). So, the final equation may be written as:

$$\frac{Qs_x}{Q_T}=f\left(\frac{Mx}{MT}\right)$$

5.4 *Experimental results*

The results obtained for 45 different inflow discharge configurations set for the 1.27% slopes are sketched Fig.21.

It seems that two linear regimes exist, a first one concerning the type 2 flow (on the right side, the oblique hydraulic jump is from the x channel, and on the left side, it is from

the *y* channel) and another one, in the centre of the graph, corresponds to type 1 flows. It should be noticed that the configurations where the flow is completely subcritical in one upstream channel fit perfectly with the curve when considering their virtual normal depths upstream from a virtual hydraulic jump. When using the inflow Discharge Weighted Head ($W=\rho g H_s$ instead of the Specific Momentum, the results are quite similar. Hence, further experimental measurements, with different geometric configurations as for example with different slopes, must be performed to underline all the parameters describing the flow distribution.

5.5 *Conclusions*

This test case is the first step of a global experimental benchmark, which should improve the knowledge about the flow distribution at a crossroad. The results presented here permitted to test several parameters to use in order to establish the flow distribution law but more experiments are necessary to validate the various options (Specific Moment, Discharge Weighted Head…).

In addition to this experimental benchmark, simulations using the 2D code presented in paragraph 2 will be performed to check if the flow distribution can be estimated accurately.

6 CONCLUSIONS

We simulated a flood in a simplified urban area with 20 cubic buildings. We noted that the numerical results qualitatively corresponded to the experimental data but that some differences existed and could not be reduced with a finer mesh. Then, we modelled two typical urban flood configurations: the flow around a building and the flow distribution in a four channels crossroad. The numerical simulation of the flow around the building agrees with the experimental data; however, a perfect representation of the flow requires a fine mesh and then the use of many cells. The experimental study of the flow distribution in a crossroad permitted to present a distribution curve for a 1% slope crossroad in which two regimes seem to appear; more experiments are still necessary to validate both this last curve and 2D model in this context.

More generally, the numerical simulations of these test cases permit to improve our knowledge about the capability of a 2D code to model a flood in a dense urban area and the way to define the calculation grid. However, a complementary validation on various field test cases remains necessary.

ACKNOWLEDGMENTS

This research work was partly funded by the European Commission under the fifth framework program as part of the IMPACT project and by the RIO 2 program of the French Ministry of Ecology and Sustainable Development (MEDD) as part of the project “Estimation des écoulements de surface pour une crue extreme en milieu urbanisé”.

REFERENCES

Hervouet, J.-M., Samie, R. & Moreau B. 2000. Modelling urban areas in dam-break flood wave numerical simulations. Proceedings of *RESCDAM* workshop. Seinäjoki, Finland: Finnish Environment Institute.

Khan, A., Cadavid, R. & Wang, S.S.Y. 2000. Simulation of channel confluence and bifurcation using the CCHE2D model. *Water and Maritime Engineering*, 142: 97–102.

Neary, V.S. & Sotiropoulos, F. 1996. Numerical investigation of laminar flows through 90-degree diversions of rectangular cross-section. *Computers and Fluids*, 25(2): 95–118.

Nania, L.S. 1999. PhD thesis: Metodologia numericoexperimental para el analisis del riesgo asociado a la escorrentia pluvial en una red de calles. *Departamento de Ingéniera Hidraulica, Maritima y Ambiental.* Barcelona, Universitat politècnica de Catalunya.

Paquier, A. 1998. 1-D and 2-D models for simulating dam-break waves and natural floods. *Concerted action on dam-break modelling, proceedings of the CADAM meeting, Wallingford, United Kingdom.* M.Morris, J.-C.Galland and P.Balabanis. L2985, Luxembourg, European Commission, Science Research Development, Hydrological and hydrogeological risks.: 127–140.

Paquier, A., Tanguy, J.M., Haider, S. & Zhang, B. 2003. Estimation des niveaux d'inondation pour une crue éclair en milieu urbain: comparaison de deux modelès hydrodynamiques sur la crue de Nîmes d'octobre 1988. *Revue des Sciences de l'Eau*, 16(1):79–102.

Soares Frazäo, S., Noël, B. & Zech, Y. 2004. Experiments of dam-break flow in the presence of obstacles. Submitted to *River Flow 2004.*

Soares Frazäo, S., Noël, B., Spinewine, B. & Zech Y. 2003. Dam-break flow through urban areas—The isolated building test case: review of the IMPACT benchmark. To be published in *EC Contract EVG1-CT-2001–00037 IMPACT Investigation of Extreme Flood Processes and Uncertainty*, Proceedings 3rd Project Workshop, Louvainla-Neuve, Belgium 6–7 November 2003 (CD-ROM).

Detailed validation of CFD for flows in straight channels

N.G.Wright, A.J.Crossley & H.P.Morvan
School of Civil Engineering, The University of Nottingham, UK

T.Stoesser
Institute for Hydromechanics, University of Karlsruhe, Germany

River Flow 2004—Greco, Carravetta & Della Morte (eds.)

ABSTRACT: An investigation has been made into the flow in open channels using a commercial Computational Fluid Dynamics (CFD) package. The study has focused on the ability of the software to correctly predict the complex flow phenomena that occur in channel flows. Previous work (Morvan et al. 2002) has shown the capability of CFD in predicting the flow in natural rivers. In this project, the predictions are contrasted against high quality flume measurements obtained for a trapezoidal channel, and a comparison is made between the different turbulence models available. The results show that whilst all the models generally give similar predictions for the bulk features of the flow, there is a marked difference between the secondary flow characteristics, and that the accuracy of the predictions increases with the level of complexity of the turbulence model used. Results from a LES model confirm the importance of turbulence modelling.

1 INTRODUCTION

The features inherent in open channel flow result from the complex interaction between the fluid and a number of mechanisms including the channel bed and walls, friction, gravity and turbulence. In the past such flows have been modelled using simplified models (for example the Saint Venant equations), which predict mean characteristics of the flow and often contain a high level of empiricism. With advances in computer power, interest has risen in applying more sophisticated techniques providing more accurate results and more in-depth information. In other fluid flow fields such as aeronautics, the implementation of more complex models has mirrored the advances in computer technology and 3D models are now commonly used. However this transition has not occurred as rapidly in open channel flow modelling, and most hydraulics models are either 1D or 2D with very few applications of 3D models. This is, in part, due to the inherent difficulties found in applying CFD in a natural river channel (Wright 2001): inter alia, irregular geometry, vegetation and roughness representation.

In this work the application of a generic commercial Computational Fluid Dynamics (CFD) package to open channel flows is considered. The software includes various models to solve general fluid flow problems and is widely accepted as a modelling tool in other fields. In this study, the Reynolds Averaged Navier-Stokes equations (RANS) are used to represent the fully developed flow in a prismatic trapezoidal channel. The RANS equations are obtained by applying time averaging to the full Navier-Stokes equations, which results in six new terms known as the Reynolds stresses. A turbulence model is then needed to account for the Reynolds stresses in order to close the system of equations. In industry the accepted standard is the two equation k-ε model which assumes that the turbulence is isotropic. More complex models exist which account for the anisotropic nature of turbulence, but at an increased computational cost to the user often making the choice prohibitively expensive. The technique of Large Eddy Simulation does not rely on Reynolds averaging and directly predicts larger eddies whilst using a model for smaller ones (Smagorinsky 1963). In collaboration with researchers at the University of Karlsruhe, LES has been implemented for the channel under consideration here and preliminary results are reported.

In the present study, the very nature of the flow is driven by the anisotropy of the turbulence and several different turbulence models are evaluated including the k-ε model, various standard Reynolds stress models and the new ω Reynolds stress model.

The research programme is being conducted by the Universities of Birmingham and Nottingham and involves detailed CFD experiments for comparison with experimental data collected at Birmingham (Yuen 1989, Knight et al. 1994). The latter encompasses discharge, velocities and shear stresses. So far the investigation has focused on a trapezoidal channel which whilst being a simple geometry involves some complex fluid flow patterns. These patterns are similar to those found in a rectangular open channel (Broglia et al. 2003).

The CFD investigations have examined the influence of grid size and structure, discretisation, turbulence model and wall treatment. The research programme has focused on generating the correct qualitative and quantitative flow features from the CFD software. Bulk quantities such discharge (bulk velocity), maximum velocity and mean shear stress have been used to ascertain the quality of the predictions, in respect to the experimental data. In addition, consideration has also been given to the velocity and bed shear stress distributions, with particular emphasis on generating the secondary flow (recirculation) patterns that should be present in a prismatic channel.

Results to date have demonstrated that the CFD is able to correctly predict the mean shear stress and subsequent shear force on the channel bed and banks. However, with standard turbulence models it is not possible to obtain the correct shear stress profiles. The study has also highlighted the complexities involved in obtaining the correct secondary flow pattern. The currents which are known to be induced by turbulence and the wall effects in open channel flow, should lead to the maximum velocity occurring below the free surface. However in all of the results obtained so far in the study, the maximum velocity has occurred at the free surface. Initial results obtained using a Large Eddy Simulations (LES) model have demonstrated that LES can predict open channel flow phenomena more successfully than RANS based models, and this application is being further investigated.

2 MATHEMATICAL MODEL

The CFD software is designed to solve generic fluid flow problems and the model components are derivatives of the full unsteady Navier-Stokes equations which for an incompressible fluid can be written as

$$div\ \boldsymbol{u}=0 \tag{1}$$

$$\frac{\partial u}{\partial t}+div(u\boldsymbol{u})=-\frac{1}{\rho}\frac{\partial p}{\partial x}+\nu\, div\ grad\ u+\frac{1}{\rho}S_{M_x} \tag{2}$$

$$\frac{\partial v}{\partial t}+div(v\boldsymbol{u})=-\frac{1}{\rho}\frac{\partial p}{\partial y}+\nu\, div\ grad\ v+\frac{1}{\rho}S_{M_y} \tag{3}$$

$$\frac{\partial w}{\partial t}+div(w\boldsymbol{u})=-\frac{1}{\rho}\frac{\partial p}{\partial z}+\nu\, div\ grad\ w+\frac{1}{\rho}S_{M_z} \tag{4}$$

where $\boldsymbol{u}$ is the velocity vector with components u, v and w, p is the pressure, ρ is the density, υ is the kinematic viscosity and the S_M components represent additional momentum source terms such as the effects of gravity. For a complete derivation of the equations see Versteeg & Malalasekera (1995). To fully resolve the Navier-Stokes equations at all length scales would require excessively fine grids and small time steps due to the effects of turbulence. This renders the direct solution of Equations 1 to 4 impractical for all but low Reynolds number flows. However it is possible to model the effects of turbulence on the flow without considering every single eddy, by considering time averaged effects. This is encompassed by defining mean values which when substituted into the full Navier-Stokes equations, give rise to the Reynolds Averaged Navier-Stokes equations which were used in the CFX simulations.

Instead of using these mean values it is possible to use LES to predict the time variation of the larger eddies. The LES code LESOCC developed at the Institute for Hydromechanics (Breuer & Rodi 1996) was used to perform the LES simulations. The code solves the filtered Navier-Stokes equations on a curvilinear, block-structured grid discretised with the finite volume method. A non-staggered grid with Cartesian velocity components was used and both, convective and diffusive fluxes are approximated with central differences of second order accuracy. The SIMPLE algorithm is employed in order to ensure mass conservation and to couple the pressure to the velocity field. Time advancement is achieved by a second order, explicit Runge-Kutta method. LESOCC is highly vectorised and parallelisation is accomplished by domain decomposition and explicit message passing via MPI. The subgrid stress of the filtered Navier-Stokes equations is computed using the dynamic approach of Germano et al. (1991). The linear no-slip ($u^+=y^+$) boundary condition is used for the bottom and the side walls since the first grid point is placed in the viscous sub-layer ($y^+\approx 7$).

3 GEOMETRY AND DATA

3.1 *Experimental data*

To evaluate the performance of the CFD software, a comparison has been made against high calibre experimental measurements obtained from the SERC funded FCF programme (Knight et al. 1994) and by Kenneth Yuen as part of his PhD study at the University of Birmingham (Yuen 1989).

The project has not only been concerned with demonstrating that the CFD is providing solutions that are quantitatively correct with respect to the experimental data, but also that the flow properties are qualitatively in line with expectations, for example the presence of re-circulations. The knowledge gained from this study will also be used to provide guidance

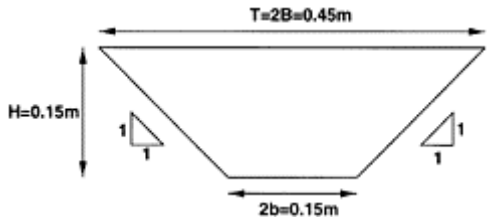

Figure 1. Cross-sectional geometry of experiment 16.

Table 1. Summary of the experimental values.

H	0.15000	2b	0.15000	A	0.04500	P	0.57426
R	0.07836	T	0.45000	D	0.10000	n	0.00990
S_0	0.00100	Q	0.02630	U_{av}	0.58444	F_r	0.59018
Re	0.11564	S_f	0.44130	τ_{av}	0.76846	U*	0.02772

to the hydraulic community on how to apply CFD to open channel flows.

The results presented in this report focus on one particular geometry from Kenneth Yuen's PhD thesis which serves to illustrate the difference in performance between the different turbulence models. In the original experiments various channel geometries were considered including simple and compound channels. Parameters such as the slope and cross-section were altered and the measurements recorded at a given cross-section once a uniform flow had developed. Different flow depths were considered which led to a series of data being collected for different discharges and Froude numbers. In this report Experiment 16 is considered, where the cross-sectional geometry is shown in Figure 1. The channel slope was 0.001 and the discharge was recorded at $0.02630 m^3 s^{-1}$ with the water temperature measured at 14°C. The characteristics of the flow are summarised in Table 1.

3.2 *Model data for the RANS simulations*

A model based on the geometry of Experiment 16 was created with the same cross-section as shown in Figure 1. Periodic boundaries were used at the channel inlet and outlet such that the predicted profile would be the same throughout the channel length. This enabled a much shorter length to be utilised than if a mass flow condition was implemented, whereby the flow profile would need a significant length to develop. Choosing to implement periodic boundary conditions thus reduced the number of cells required in the streamwise direction, enabling more cells to be concentrated on the cross-section. A channel length of 0.1m was chosen and a symmetry plane was imposed along the central plane of the channel (such that only half of the geometry was modelled), as shown in Figure 2 together with

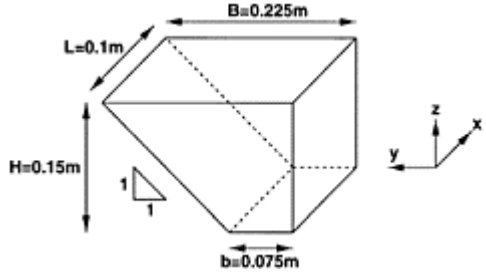

Figure 2. Computational geometry in CFX.

the co-ordinate frame of reference. The channel itself was constructed as half of a flat trapezoidal box with the centreline coinciding with the x axis. The channel bottom was aligned with the y co-ordinate line and z co-ordinate represents changes in the vertical direction. The flow was driven by introducing a momentum source into the equations which accounted for the effects of gravity. This force was resolved into components acting parallel and perpendicular to the channel length to allow for the co-ordinate transformation whereby

$$-\boldsymbol{\rho g}=(\rho g \sin\theta,\ 0,\ -\rho g \cos\theta)^T \tag{5}$$

given that $\tan\theta=S_0$. As the water temperature in the original experiment was measured to be 14°C, a value of 999.25 kg m^3 was used for the water density and together with g=9.8066502 (the internal value of g in CFX) this gave

$$-\boldsymbol{\rho g}=(9.7993,\ 0,-9.7993\times10^3)^T. \tag{6}$$

Additionally the dynamic viscosity of the water was set to $\mu=1.1666\times10^{-3}$N s m^{-2}. Note that in the results presented the z-component of the momentum source was set to zero as it was causing a number of numerical difficulties, whilst having no influence on the flow field. If required, a hydrostatic pressure field can be added as a post-process. The flow

was initialised by setting the initial velocity equal to the mean recorded value in all of the cells i.e.

$$U^0=(0.58444, 0, 0)^T. \quad (7)$$

The free surface was represented as a symmetry plane, and smooth no slip walls were applied at the remaining boundaries.

3.2.1 *Mesh for the RANS simulations*

Two different meshes were constructed based on the requirements of the turbulence models used. Both meshes consisted of structured hexahedral cells. Emphasis was placed upon creating a sufficient use

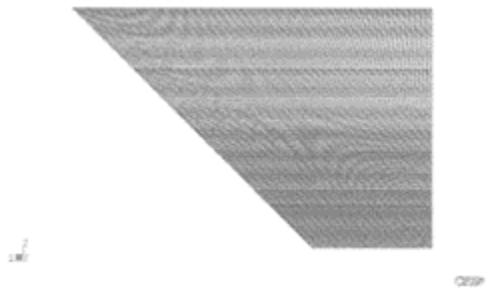

Figure 3. A cross-section of Mesh 1.

of periodic boundary conditions reducing the need for many elements in the streamwise direction. The first mesh consisted of 10×100×200 (200000) cells. A cross-section of the mesh is shown in Figure 3. Note that a biased seeding was used along the spanwise component of the free surface in order to reduce the y^+ variation at the channel wall. Thus the cell at the centre of the channel was three times the width of the cell at the bank. The second mesh followed the same structure as the first but consisted of 10×200×200 (800000) cells.

3.2.2 *Mesh for the LES simulations*

The LES simulation used a mesh of 161×100×100 in the *x*, *y* and *z* directions respectively. It should be noted that in the LES the streamwise length is much greater than for the RANS models. This length is required to allow the eddy structure to develop. This is unnecessary with a RANS simulation as these fluctuations are averaged out. To account for wall effects, van Driest damping functions and the Werner-Wengle wall model were used.

4 RESULTS

Comparative results were obtained using five different turbulence models. The first model considered was the industrial standard *k-ε* model (Versteeg & Malalasekera 1995) which assumes that the turbulence is isotropic and does not solve the Reynolds stresses explicitly. As the name implies, the model is based upon solving the turbulent kinetic energy, *k*, and the turbulence eddy dissipation, *ε*. In contrast to this, the Reynolds stress models solve the six Reynolds stresses directly hence accounting for the anisotropic nature of turbulence and are thus more computationally demanding. Note that *ε* is still present in the standard formulation. Three different variants of the standard Reynolds Stress approach were tested in which the differences were accounted for by different values for the model constants. These models were the Launder, Reece and Rodi Isotropisation of

Table 2. Summary of results from the turbulence model comparison.

Turbulence model	Wall shear (Pa)	Max. velocity (m/s)	Mass flow (kg/s)	Min. y^+	Max. y^+
k-ε	0.7679	0.7767	14.86	9.73	20.44
LRR IP	0.7679	0.7971	15.17	10.27	20.50
LRR-QI	0.7679	0.7900	15.10	11.37	20.71
SSG	0.7679	0.7767	15.02	11.32	20.68
SMC-*ω*	0.7679	0.7527	14.66	5.36	10.26
Theory	0.7679	–	13.14	–	–
Experiment	0.7685	–	13.15	–	–

Production (LRR-IP) (Launder et al. 1975), Launder, Reece and Rodi Quasi-Isotropic (LRR-QI) (Launder et al. 1975) and the model due to Speziale, Sarkar and Gatski (SSG) (Speziale et al. 1991).

Both the *k-ε* and standard Reynolds Stress models use wall functions in the near wall region which relate the tangential velocity to the wall shear stress in the log-law region of the flow. This prevents the need to introduce a fine mesh near the wall, which would be required if the viscous sub-layer was to be resolved.

The final RANS model tested was the Reynolds stress-*ω* or SMC-*ω* model (CFX Ltd. 2003), in which the flow equations are solved right through to the wall without the use of wall functions. The formulation is based on an equation for *ω*, the turbulent frequency as opposed to *ε* in the standard Reynolds stress models. One of the benefits of the approach is that the viscous sub-layer can be resolved with fewer cells than would be required for an *ε* based model such as *k-ε* or the standard Reynolds stress approaches.

The bulk property results from the model comparison are summarised in Table 2 and compared with the theoretical and experimental values. Note that the *k-ε*, LRR-IP, LRR-

QI and SSG results were obtained on Mesh 1, and that the SMC-ω results were produced on Mesh 2.

From Table 2 it can be seen that all the turbulence models predict the correct value for the mean shear stress compared with the theoretical value, which is in close agreement with the value recorded in the experiment. However in all of the simulation cases, the mass flow rate is over-predicted by between 12 and 15%. This may be due to the use of a smooth wall in the CFD as it has been assumed that the low Manning's n value from the experiment represented an almost smooth wall.

Contour plots and vector plots of the secondary flow are shown in Figures 4–13 for the CFX results. Note that to improve clarity not all of the vectors are shown and the display magnitudes have been adjusted for each turbulence model. As expected the results from the *k*-ε model show no indication of the contours bulging towards the bottom corner of the channel, and there

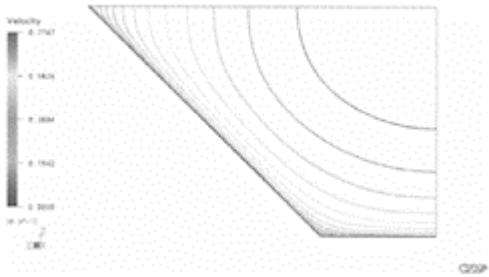

Figure 4. Velocity contours from the *k*-ε model.

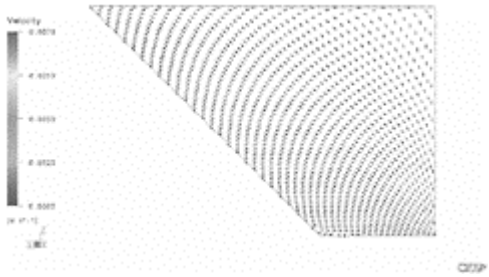

Figure 5. Secondary velocity vectors from the *k*-ε model.

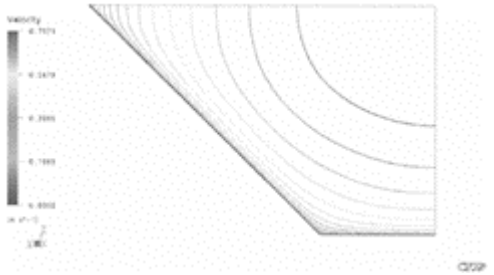

Figure 6. Velocity contours from the LRR-IP model.

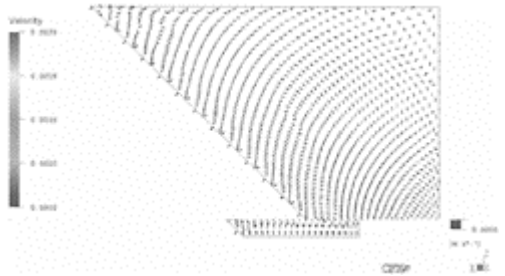

Figure 7. Secondary velocity vectors from the LRR-IP model.

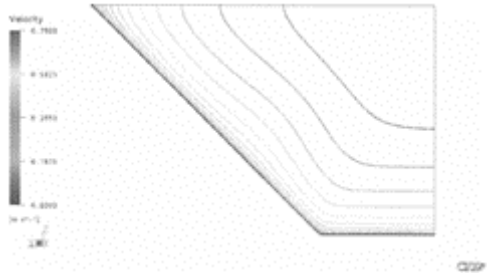

Figure 8. Velocity contours from the LRR-QI model.

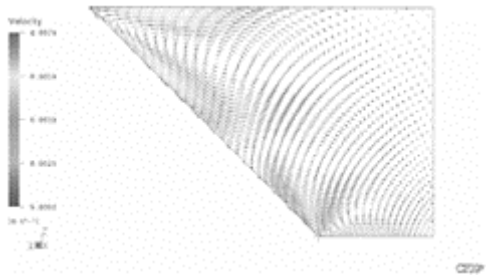

Figure 9. Secondary velocity vectors from the LRR-QI model.

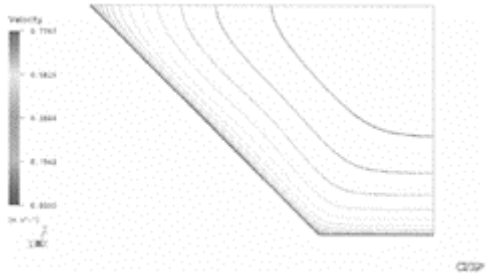

Figure 10. Velocity contours from the SSG model.

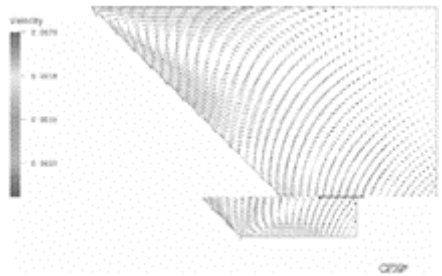

Figure 11. Secondary velocity vectors from the SSG model.

is no evidence of re-circulation currents in the vector plot beyond numerical error. Both features should be evident in the profiles and are thought to be attributed to the turbulence anisotropy and the interaction with

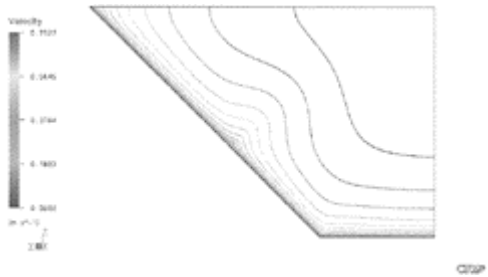

Figure 12. Velocity contours from the SMC-ω model.

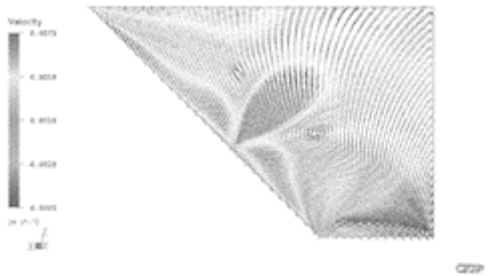

Figure 13. Secondary velocity vectors from the SMC-ω model.

the wall. The results from the LRR-IP model are fairly similar to the k-ε profiles. It is noted by CFX that this formulation does not contain any wall reflection terms which may partially account for the results obtained. The LRR-QI and SSG results both show bulging of the contours and evidence of re-circulation although the magnitudes of the phenomena are less that expected. Typically the scale of the secondary velocity should be of the order of 2−3% of the bulk streamwise velocity (Broglia et al. 2003). The results most in line with expectations are those from the SMC-ω turbulence model which show significant bulging of the contours and strong evidence of secondary flow. A feature of all of the predictions is that the maximum velocity occurs at the free surface, which in reality is not the case.

Consideration has also been given to the shear stress distribution occurring on the channel bed and walls. Figure 14 shows a comparison between the results from the various turbulence models and those measured in the original experiment. All of the results show a characteristic local minimum at the corner of the channel and a decrease towards the free surface in line with expectations and the experimental measurements. The predictions all show the shear stress increasing towards the centre of the channel, whereas the experimental value decreases. In addition the LRR-QI, SSG and SMC-ω models all indicate a decrease at a point approximately two thirds below the free surface, with a marked decline present in the SMC-ω results comparable to that at the channel

corner. Note that this point coincides with where the maximum distortion of the contours is present and the strongest secondary flows occur.

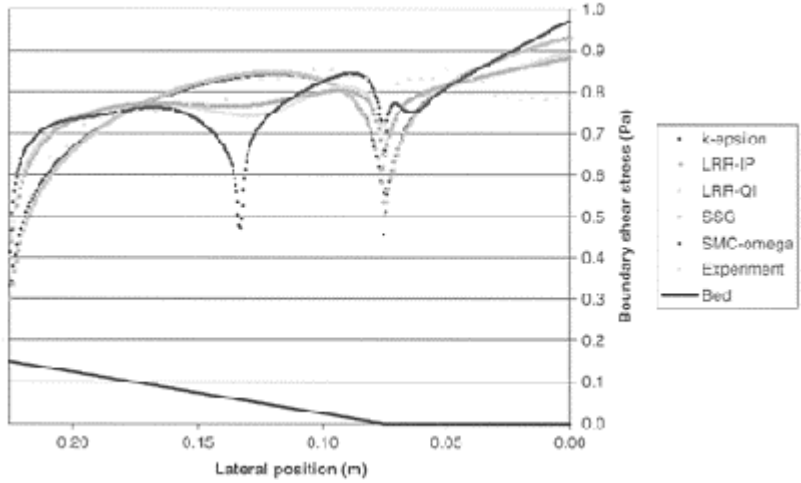

Figure 14. Wall shear stress distribution results from the RANS model comparison.

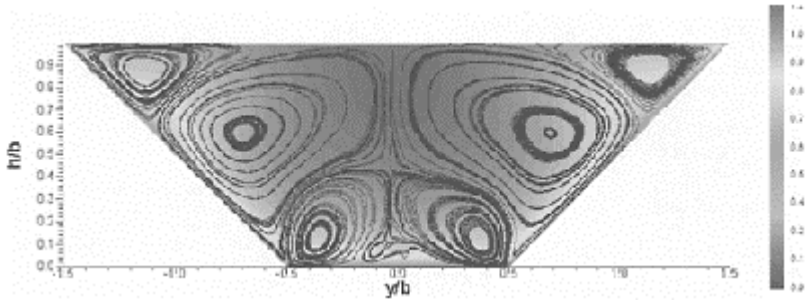

Figure 15. Mean velocity profile from LES simulation.

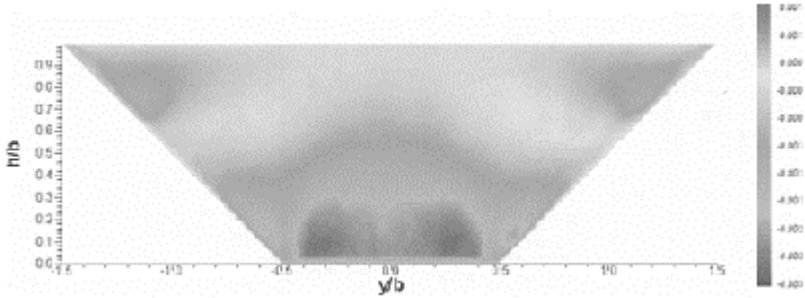

Figure 16. $u'w'$ Reynolds stress distribution from LES simulation.

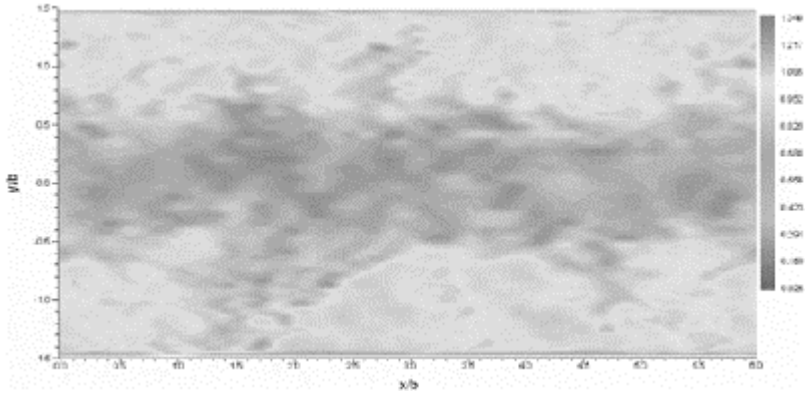

Figure 17. Instantaneous streawise velocity profile from LES simulation.

The LES results in Figure 15 show the bulging of the contours towards the bottom corners in a similar manner to the SMC-ω results. This figure also shows the streamlines which demonstrate a three cell pattern in a similar way to the more complex RANS models. Figure 16 shows the $u'w'$ Reynolds stress. To emphasis the fact that LES can predict time-varying velocities Figure 17 shows an instantaneous velocity field.

5 CONCLUSIONS

The results show that the CFD predictions accurately predict the average shear stress value for all of the turbulence models tested. In all of the cases, the mass flow rate was over predicted, with none of the models appearing significantly better than the others. It was observed that the k-ε model failed to predict any evidence of secondary flow, and that the standard Reynolds stress approaches indicated some re-circulation with varying degrees, but all were below the expected magnitudes. The most realistic results were

obtained using a non-standard Reynolds stress model in which the equations were integrated through to the wall without the use of wall functions. A comparison of the bed shear stress distributions showed that whilst all of the models gave the correct average value, none of the models captured the expected profile, which was observed in the experimental measurements. Whilst the LES results need more analysis the results so far indicate that this approach has considerable benefit compare with the standard RANS models and even the more complex SMC-ω model. However, it must be borne in mind that this technique requires considerably longer run times.

A number of choices had to be made within the modelling strategy that can have a significant effect on the results. These have to be carefully considered, just as in experimental work, and novice users may not always be aware of these.

6 FURTHER WORK

This study has focused on the application of a generic CFD package to a smooth prismatic trapezoidal open channel. Further work will extend the geometries to compound and rough channels. In addition more sophisticated numerical methods will be considered and further work using LES modelling will be conducted.

REFERENCES

Breuer, M. & Rodi, W. 1996. Large eddy simulation of complex turbulent flows of practical interest. In (ed.), Hirschel, E.H. *Notes On Numerical Fluid Mech., Flow Simulations With High Performance Computers II:* 258–274. Braunschweig: Vieweg.

Broglia, R., Pascarelli, A. & Piomelli, U. 2003. Large-eddy simulations of ducts with a free surface. *J. Fluid Mech.* 484:223–253.

CFX Ltd. 2003. CFX user manual.

Germano, M., Piomelli, U, Moin, R., Cabot, W.H. 1991. A dynamic subgrid-scale eddy viscosity model. *Physics of Fluids* 3:1760–1765.

Knight, D.W., Yuen, K.W.H. & Alhamid, A.A.I. 1994. Boundary shear stress distributions in open channel flow. In Beven K. (ed.), *Physical Mechanisms of Mixing and Transport in the Environment:* 51–87. London: J.Wiley.

Launder, B.E., Reece, G.J. & Rodi, W. 1975. Progress in the developments of a Reynolds-stress turbulence closure *J. Fluid Mech.* 68:537–566.

Morvan, H., Pender, G., Wright, N.G. & Ervine, D. 2002. Three-dimensional hydrodynamics of meandering compound channels. *J. Hydraul. Eng.* 128(7):674–682.

Smagorinsky, J. 1963. General circulation experiments with primitive equations Part 1: Basic experiments. *Monthly Weather Review* 91:99–164.

Speziale, C.G., Sarkar, S. & Gatski, T.B. 1991. Modelling the pressure-strain correlation of turbulence: an invariant dynamical systems approach. *J. Fluid Mech.* 277: 245–272.

Versteeg, H.K. & Malalasekera, W. 1995. *An introduction to computational fluid dynamics—the finite volume method*. Essex: Pearson Education.

Wright, N. 2001. Conveyance implications for 2D and 3D modelling. In *Scoping study for reducing uncertainty in river flood conveyance.* Bristol: Environment Agency.

Yuen, K.W.H. 1989. *A study of boundary shear stress, flow resistance and momentum transfer in open channels with simple and compound trapezoidal cross section.* PhD thesis: The University of Birmingham.

Synthetic hydrographs as a design tool for flood routing evaluation

F.Aureli, A.Maranzoni & P.Mignosa
Dipartimento di Ingegneria Civile, dell'Ambiente, del Territorio & Architettura, Parma, Italy

U.Maione
Dipartimento di Ingegneria Idmulica, Ambientale ε del Rilevamento, Milano, Italy

River Flow 2004—Greco, Carravetta & Della Morte (eds.)

ABSTRACT: In this paper the procedure for the determination of Synthetic Design Hydrographs (SDHs), proposed by some of the Authors in previous works, is validated comparing the statistical distribution of peak discharges obtained at the end of a river reach by routing a long series of historical floods and by routing the synthetic floods only. The selected reach is the end branch of the Parma river, a tributary of the Po river (Northern Italy). The mathematical model was calibrated on the basis of three recent historical floods. Then all the historical floods and the SDHs have been routed in the river reach. Historical and synthetic peak discharges at a downstream section were then compared in probability plots. The results show that the distribution obtained by routing the historical floods seems to be correctly described by the results obtained by routing the SDHs.

1 INTRODUCTION1

Peak discharges are significantly reduced in mild slopes river reaches by routing effects due to water volumes temporarily stored in the main channel and in the flood plains. Often these effects are masked by the contribution of tributaries or hill slopes encountered downstream. If concentrated or distributed inputs are negligible, as in the lower reaches of many tributaries of the Po river (Northern Italy), peak discharges really decrease. The amount of reduction depends on a combination of hydrological input and geometry of the reach and flood plains. Flood waves with the same peak discharge but different volumes are of course reduced in different ways.

There is then an interest to define Synthetic Design Hydrographs (SDHs) which are capable to model in a statistically correct way the dumping effect due to routing on the historical floods. In this way it would be possible to derive the peak discharge distribution at a downstream section of a river reach by routing only few SDHs instead of a long series of historical floods.

In previous works (Maione et al. 2000a, b) the Authors proposed a procedure to estimate SDH in gauged river sections where a long series of hydrographs is available. The method is based on the statistical analysis of recorded flood waves through the construction of the Flow Duration Frequency (FDF) reduction curves of given return period and the determination of the temporal location of the peak value for each duration.

In this paper the procedure for the determination of SDHs is validated comparing the statistical distribution of peak discharges obtained at the end of a river reach by routing a long series of historical floods and by routing the synthetic floods only.

2 SYNTHETIC DESIGN HYDROGRAPHS (SDHS) DERIVATION PROCEDURE

SDHs can be derived (Maione et al. 2000a, b) from Flow Duration Frequency reduction curves (FDF) that furnish the maximum average discharge $Q_D(T)$ in a given duration D for each value of the return period T, where

$$Q_D = \max\left(\frac{1}{D}\int_{t-D}^{t} Q(\tau)d\tau\right). \tag{1}$$

The FDF reduction curves are analogous to the IDF curves that relate the maximum average intensity, duration and frequency of rainfall. Their construction is obtained through the statistical processing of historical hydrographs. The analysis can be performed on the annual maximum average discharges for each duration ranging from 0 (corresponding to an instantaneous discharge) to a sufficiently large value, say, D_f representing the characteristic duration of flood events for a given river section. Alternatively, the maximum values of the average discharges that exceed a given threshold value for each duration can be sampled according to the Peaks Over Threshold method (POT).

The estimation of the FDF reduction curve can be conveniently obtained relating the quantiles $Q_D(T)$ to $Q_0(T)$ by means of the reduction ratio $\varepsilon_D(T)$:

$$Q_D(T) = \varepsilon_D(T)Q_0(T), \quad \varepsilon_D(T) = \frac{Q_D(T)}{Q_0(T)}. \tag{2}$$

In the more general case, the reduction ratio is a function of duration D and return period T. The convenience of the position (2) comes from the circumstance that if the $CV(Q_D)$ and the functional form of the probability distribution of Q_D are independent of the duration D, ε_D is independent of return period T and reduces to the ratio of the averages of Q_D and Q_0:

$$\varepsilon_D = \frac{\mu(Q_D)}{\mu(Q_0)}. \tag{3}$$

Under these assumptions the estimation of the FDF curves reduces to the estimation of peak flood discharge quantiles $Q_0(T)$ and of the reduction ratio ε_D.

Some different approaches have been proposed in literature for the identification of the functional form of the reduction ratio ε_D that best fits the experimental data (NERC 1975, Fiorentino 1985, Bacchietal. 1992)

Bacchi et al. (1992) used a deductive approach for the derivation of the reduction ratio based on a formulation that considers the crossing properties of continuous gaussian stationary stochastic processes. From this formulation the following equation for the reduction ratio has been deduced:

$$\varepsilon_D \approx \sqrt{\Gamma(D)} = \sqrt{\frac{\theta}{2D}\left[2 + e^{-\frac{4D}{\theta}} - \frac{3\theta}{4D}\left(1 - e^{-\frac{4D}{\theta}}\right)\right]}, \qquad (4)$$

in which $\Gamma(D)$ is the variance function, i.e. the ratio of the variances of the instantaneous process and integrated one. The parameter θ is the scale of fluctuation, i.e. the integral of the autocorrelation function of the instantaneous process.

Once the FDF reduction curves have been obtained, the construction of the SDH is performed imposing that the maximum average discharge for each duration coincides with the value deduced from the FDF; the shape of the hydrograph is defined by the Peak-Duration values $r_D(0 \le r_D \le 1)$, that are the ratios between the time prior to the peak (in the time interval in which the maximum average discharge of given duration falls) and the duration D. For each duration the value of r_D is calculated from all the historical hydrographs; then the average value is computed and adopted for the construction of the SDH. The data sampling modality is illustrated in Figure 1. The procedure

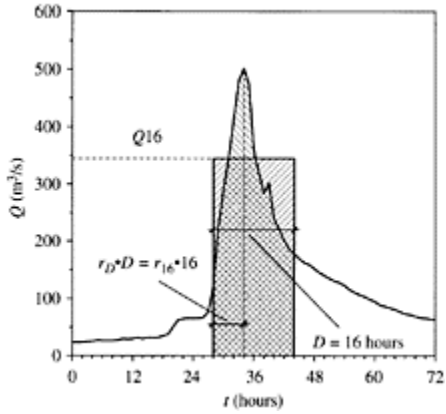

Figure 1. Data sampling of Q_D and r_D from historical hydrographs (in this example D=16 hours).

is similar to that employed for the Chicago Design Storm (Keifer & Chu 1957). However, in the present case the coefficient r_D is a function of D, whereas in the Chicago Design

Hyetograph r is defined as the ratio between the time prior to peak intensity and the total rainfall duration and is made a constant for all durations.

Therefore the following conditions determine the SDH:

$$\int_{-r_D D}^{0} Q(\tau)d\tau = r_D D Q_D(T);$$
$$\int_{0}^{(1-r_D)D} Q(\tau)d\tau = (1-r_D) D Q_D(T). \tag{5}$$

The rising and the falling limbs of the SDH are obtained by differentiating Equation 5 with respect to duration D as follows:

$$Q(t) = \frac{\left.\frac{d}{dD}\left(r_D D Q_D(T)\right)\right|_{D=D(t)}}{\left.\frac{d}{dD}\left(r_D D\right)\right|_{D=D(t)}}, \tag{6}$$

for $t = -r_D D \qquad -r_{D_f} D_f \le t \le 0$

$$Q(t) = \frac{\left.\frac{d}{dD}\left((1-r_D) D Q_D(T)\right)\right|_{D=D(t)}}{\left.\frac{d}{dD}\left((1-r_D) D\right)\right|_{D=D(t)}}, \tag{7}$$

for $t = (1-r_D)D \qquad 0 \le t \le (1-r_{D_f})D_f$

If both FDF and peak duration ratios r_D can be fitted by derivable curves, Equations 6 and 7 can be solved

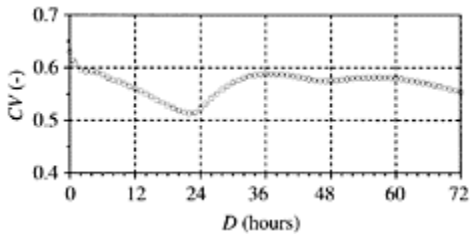

Figure 2. Coefficient of variation $CV(Q_D)$ versus D.

analytically; otherwise numerical methods must be applied.

3 SYNTHETIC DESIGN HYDROGRAPHS FOR PONTE BOTTEGO GAUGING STATION

The mentioned procedure was applied to the 45 years long historical series of floods recorded at the Ponte Bottego gauging station on the Parma river, a tributary of the main italian river Po.

From the 67 recorded flood waves, the 45 annual maximum average discharges for each duration ranging from 0 to 72 hours have been extracted. In some years (10 out of 45) the annual maximum for the selected durations belongs to different flood events.

Figure 2, in which the coefficient of variation $CV(Q_D)$ versus D is reported, shows that the assumption of $CV(Q_D)$ constant with the duration can be reasonably accepted for the considered sample.

Log-normal, Gumbel (EV1) and General Extreme Value (GEV) probability distributions have been considered in order to describe $Q_0(T)$. Parameters estimation was based on the Method of Moments for the first two distributions, whereas for the third the method based on L-moments has been adopted. Figure 3 shows, on Gumbel probability chart, the data sample (Gringorten plotting position) together with the fitted probability distributions.

The Hosking test (Hosking et al. 1985) on the k=0 hypothesis with a significance level a=5%, k being the exponent of the GEV distribution, demonstrates that the choice of the GEV distribution is justified, so that the peak discharge $Q_0(T)$ have been expressed in the form:

$$Q_0(T) = \xi + \frac{\alpha}{k}\left\{1 - \left[-\ln\left(1 - \frac{1}{T}\right)\right]^k\right\} \quad (k \neq 0) \tag{8}$$

The estimation of ε_D has been performed by means of Equation 4, which was demonstrated by Ballarin et al. (2001) particularly suitable to fit the empirical reduction ratios of medium-large catchments.

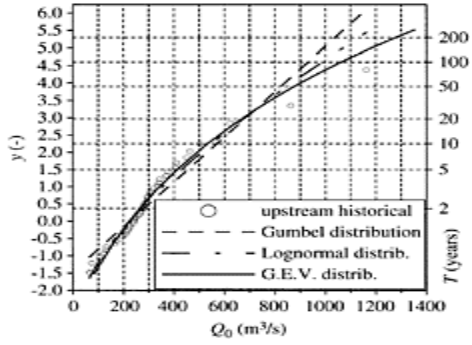

Figure 3. Q_0 data sample together with the fitted probability distributions.

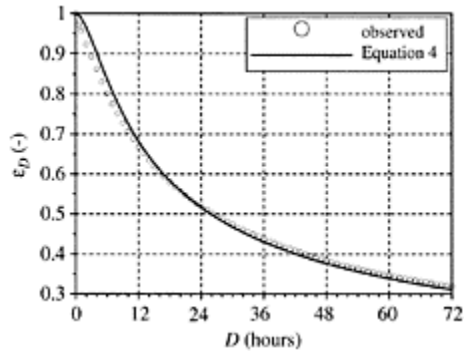

Figure 4. Reduction ratio.

The value of θ=7.2 hours was obtained by a least squares estimation. The corresponding reduction ratio is plotted in Figure 4 together with the empirical ones. Considering that Equation 4 is a one-parameter curve the agreement is quite good for all the durations.

Figure 5 shows the FDF curves for return periods ranging from 2 to 200 years.

The equation of the Peak-Duration curve has been obtained by interpolation of the empirical patterns available for the gauging station. The interpolating function $r_D(D)$ was chosen of the form indicated below together with the least squares estimates of the four parameters:

$$r_D(D) = a + \frac{b}{c + (D)^d}, \tag{9}$$

with a=0.260, b=3.432, c=18.636, d=1.49, D being the duration in hours.

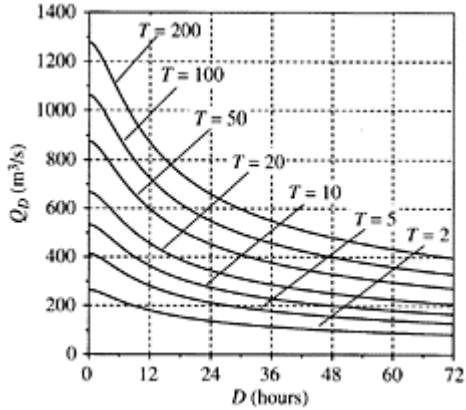

Figure 5. FDF reduction curves at Ponte Bottego gauging station for return periods ranging between 2 and 200 years.

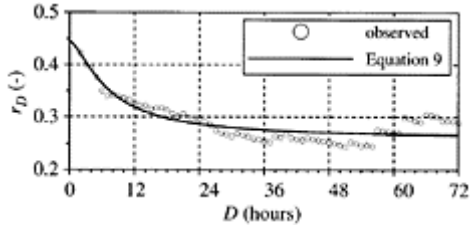

Figure 6. Peak position and interpolating function.

In Figure 6 the interpolating Equation 9 is plotted together with the average values obtained from the historical series. The average absolute difference between the empirical values of r_D and those obtained from Equation 9 is 5%.

Once the estimates of FDF and Peak-Duration curves have been obtained, the SDHs follow immediately by analytical derivation of Equations 6 and 7. Figure 7 shows the SDHs obtained for return periods ranging from 2 to 200 years.

4 TOPOLOGICAL AND MATHEMATICAL DESCRIPTION OF THE RIVER REACH

The selected reach (Fig. 8) is the end branch of the Parma river, starting at Ponte Bottego gauging station and ending at the confluence with the Po river (northern Italy). The total length measured along the thalweg is about 38km with a very mild average slope of 0.06%.

The river is formed by a deep main channel which meanders within two levels that maintain high levels over the surrounding plains. Once flood waters leave

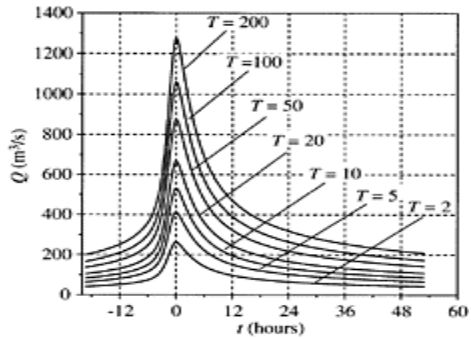

Figure 7. SDHs for Ponte Bottego gauging station.

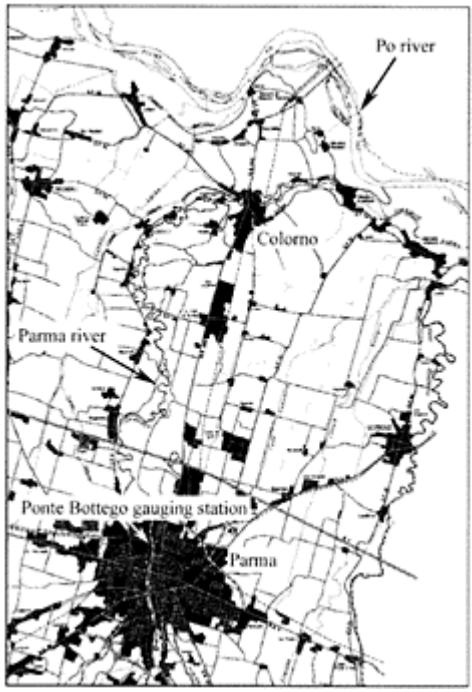

Figure 8. Location of the considered river reach.

the main channel, flood plains of significant width are inundated; in some places floodplains are directly connected with the main channel; elsewhere one or more dikes must be overtopped before the inundation of the flood plain commences; this allows flooding only for high return periods and in the meantime increases the routing efficiency.

The mathematical model adopted for the flood routing is the hydrodynamic module of the software Mike11, produced by the Danish Hydraulic Institute (DHI, 2002). The model solves the vertically integrated equations of conservation of mass and momentum, under the usual St. Venant hypotheses:

$$\frac{\partial Q}{\partial x}+\frac{\partial A}{\partial t}=q$$
$$\frac{\partial Q}{\partial t}+\frac{\partial}{\partial x}\left(\frac{\alpha Q^2}{A}\right)+gA\frac{\partial h}{\partial x}+g\frac{Q|Q|}{C^2AR}=0 \qquad (10)$$

where Q=discharge, A=wetted area, q=lateral inflow, h=stage above datum, R=hydraulic or resistance radius, C=Chezy resistance coefficient, α=momentum distribution coefficient, x=distance along the channel (positive downstream), t=time, g=gravitational acceleration.

The solution of the complete Saint Venant Equations is based on a six-nodes implicit finite difference scheme (Abbott & Ionescu 1967).

Using the cross sections derived from a recent topographical survey a quasi-2D mathematical model of the river reach was implemented.

The topographical description of the area to be modeled is achieved through the introduction of cross sections of the channels and flood plains which lie approximately perpendicular to the direction of flow. The transverse extent l of each cross section depends on whether the flood plain is to be simulated and by what method. In order to describe in a more complete way the characteristics of natural rivers, the presence of flood plains can be represented with several schematizations.

Open flood plains have been directly connected with the main channel and considered to contribute to the total conveyance of the section, even if the roughness is usually higher. Closed flood plains have been described as "pockets" linked to the main channel (and sometimes together) through broad-crested weirs representing length and elevation of the separation dykes. Pocket areas were assumed to contribute only to the storage of the reach.

The existing bridges have been introduced by means of the *culvert structure* available in the model. This was necessary in order to take into account the occurrence that, for high return period flood events, the bridges can result partly full.

5 CALIBRATION OF THE ROUTING MODEL

The November 2000 historical flood was simulated in order to calibrate the roughness coefficients of the main channel and of the open flood plains. The discharge time-series, obtained by converting the

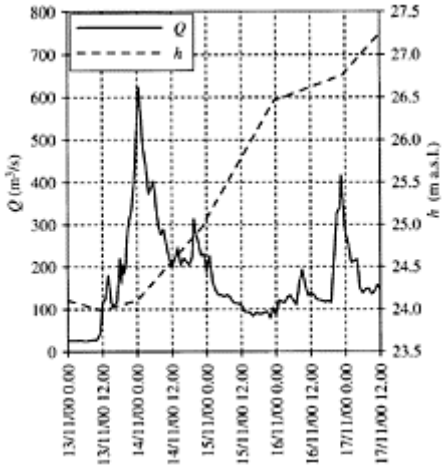

Figure 9. Ponte Bottego discharge and Po water level time-series for November 2000 event.

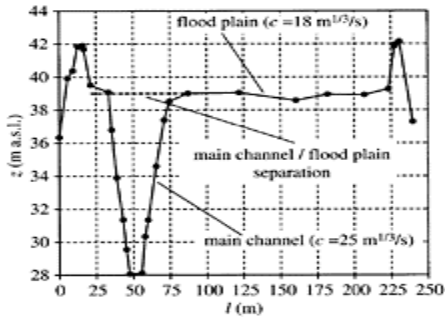

Figure 10. Schematization of a cross section with open flood plains and calibrated roughness coefficients.

recorded hydrograph at Ponte Bottego by means of a stage-discharge relationship, was adopted as upstream boundary condition. As downstream condition the corresponding water level time-series at the confluence with the Po river was considered. Both conditions are shown in Figure 9.

The calibration was performed by trials assuming two different roughness coefficients for the main channel and the open flood plains, constant along the reach. The values that allowed to reproduce at best the recorded water levels at the Colorno gauging station, about 30 km downstream the initial section, are shown in Figure 10, together with the schematisation adopted for a generic cross section with open flood plains.

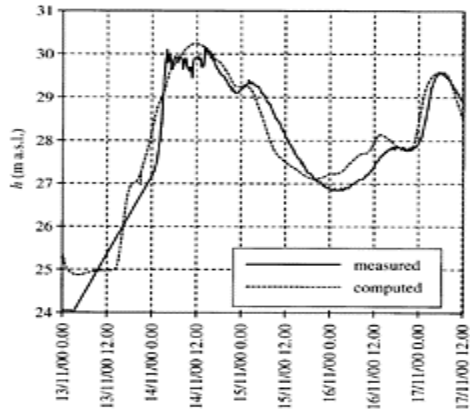

Figure 11. Comparison between recorded and calculated water levels at Colorno gauging station.

Comparison between recorded and calculated water levels at Colorno gauging station is shown in Figure 11. The measured peak water level was probably slightly underestimated

since the gage is located on the downstream face of an arc bridge which was partly full. Apart from the first hours, in which the behavior of the computed level differs significantly from the recorded one, the overall characteristics of the recorded water levels at Colorno station are satisfactorily reproduced. As a validation of the chosen roughness coefficients two further recent historical floods were simulated. Also in these cases the overall characteristics of the recorded hydrographs were satisfactorily reproduced with differences of less then 0.20m in the evaluation of the peak levels.

6 ROUTING OF THE HISTORICAL FLOODS AND OF THE SDHS

The historical series of floods and the SDHs previously derived have then been routed in the river reach.

For each historical flood the discharge time-series obtained by converting the recorded level hydrograph at Ponte Bottego was imposed as upstream boundary condition. The more suitable downstream boundary condition would be represented by the historical water level time-series at the confluence with the Po river. Since these data were not available for all the historical floods, the same constant water level $(\hat{h} = 25\ \text{m a.s.l.})$ for all was assumed in the computations. The negligible influence of this assumption on the discharges at

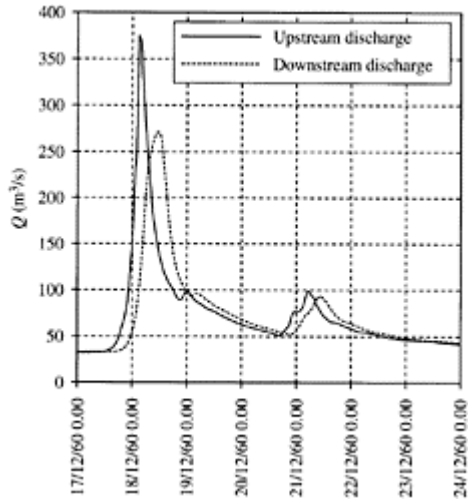

Figure 12. Comparison between upstream (Bottego) and downstream (Colorno) discharges for December 1960 flood event.

the reference section of Colorno was verified by routing the few historical floods for which recorded water levels were available at the confluence twice: once adopting the

recorded water level hydrographs, then imposing the constant water level $\hat{h}$as downstream boundary conditions. Consistently the same boundary condition $\hat{h}$was adopted for routing the SDHs.

In order to obtain the initial conditions (Q and h at t=0 along the river reach) a steady-state profile was computed corresponding to the first value of the discharge time-series and to the $\hat{h}$water level at the downstream section (subcritical flow).

As an example, in Figure 12 the comparison between upstream (Bottego) and downstream (Colorno) discharge time-series for December 1960 flood event is shown.

Figure 13 shows the SDHs in the same sections while in Table 1 are reported the numerical values of the peak discharges Q_0 for the SDHs, together with the routing coefficient $\eta=Q_{0\text{Upstr.}}/Q_{0\text{Dwnst.}}$ for all the return periods considered.

The routing coefficient is high (i.e. the dumping effect is small) for T=2 since for this return period neither open nor closed flood plains are involved by the flow. The routing coefficient then decreases for intermediate return periods (between T=10 and T=100 years) when the inundation of the flood plains by the water leaving the main channel is significant. For the higher value of the return period (T=200 years) the routing coefficient again increases due to the high flood volumes involved.

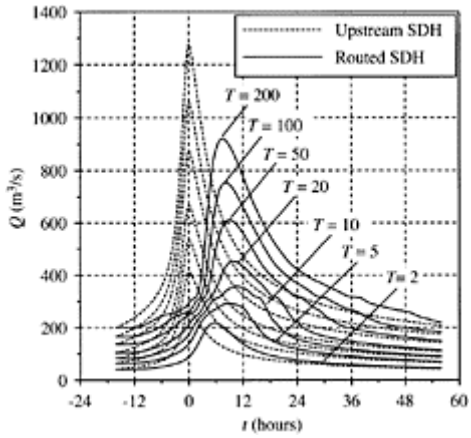

Figure 13. Upstream (Bottego) and downstream (Colorno) SDHs.

Table 1. Upstream and routed peak discharges for the SDHs together with routing coefficients η.

T years	$Q_{0\text{Upstr.}}$ m^3/s	$Q_{0\text{Dwnstr.}*}$ m^3/s	$\eta=Q_{0\ \text{Upstr.}}/Q_{0\ \text{Dwnstr.}}$
2	264	218	0.83
5	412	293	0.71
10	533	357	0.67

20	668	453	0.68
50	876	611	0.70
10	1062	754	0.71
20	1277	922	0.72

*Colorno section.

All the 67 historical floods were considered in order to obtain the annual maximum peak discharge series at the Colorno section (Table 2). For comparable events belonging to the same year it could in fact take place the swap between maximum upstream and downstream peak discharge, the latter depending also on the behaviour of the complete inflow hydrograph (see for example years 1987 and 1998 in Table 2). Considering only one flood event per year could then lead to an incorrect evaluation of the sample of annual maximum peak discharges at the downstream section of Colorno.

From the 67 routed historical hydrographs the sample of the 45 annual maximum peak discharges was extracted and placed on a Gumbel chart according to the Gringorten plotting position. On the same graph the peak discharges of the routed SDHs were placed, attaching to each value, at first in a somehow arbitrary way, the return period of the corresponding starting SDH.

Table 2. Upstream and routed peak discharges for the considered historical events (in bold are highlighted the maximum annual values).

Date dd/mm/yy	$Q_{0\text{Upstr.}}$ m^3/s	$Q^*_{0\text{Dwnstr.}}$	Date dd/mm/yy	$Q_{0\text{Upstr.}}$ m^3/s	$Q^*_{0\text{Dwnstr.}}$
28/04/56	**105**	**101**	11/04/78	**315**	**261**
08/04/57	**134**	**126**	11/10/79	**224**	**164**
07/11/57	120	111	15/10/80	**1162**	**852**
13/12/58	**206**	**158**	31/01/80	194	155
26/03/59	166	157	28/12/81	**245**	**220**
23/12/59	**309**	**244**	08/11/82	**464**	**255**
15/04/60	291	261	02/10/84	**241**	**185**
14/10/60	**450**	**320**	26/04/86	**66**	**56**
15/12/60	375	271	09/04/87	117	**112**
03/01/61	**291**	**252**	05/10/87	**124**	110
23/04/61	276	251	11/02/88	**74**	**53**
25/11/61	215	177	24/02/89	71	60
04/03/62	**189**	**185**	21/11/89	**132**	**123**

04/03/63	**262**	**231**	15/10/90	154	107
24/03/64	**212**	**200**	22/11/90	**283**	**219**
26/11/64	206	189	02/05/91	**164**	**149**
17/11/65	**295**	**254**	16/10/92	272	238
01/12/66	**502**	**346**	16/11/92	**343**	**253**
03/11/67	**334**	**249**	01/10/93	**218**	**154**
20/02/68	231	215	11/06/94	**293**	**269**
14/11/68	**369**	**272**	08/09/94	268	188
13/01/69	**406**	**288**	22/12/95	**247**	**207**
05/01/70	**194**	**178**	02/10/96	**238**	**221**
18/03/71	**268**	**231**	26/06/97	172	101
08/09/72	**278**	**257**	06/11/97	**280**	**180**
21/01/73	234	222	17/12/97	142	131
21/09/73	**409**	**226**	07/04/98	96	77
27/04/74	**340**	**278**	30/09/98	**226**	133
03/04/75	199	180	04/11/98	208	**156**
14/12/75	**270**	**234**	18/10/99	**863**	**374**
16/12/76	**171**	**139**	01/11/00	**623**	**390**
20/02/77	257	235	12/03/01	**306**	**240**
28/08/77	**375**	**261**	15/10/02	**596**	**339**
24/02/78	234	196			

*Colorno section.

Figure 14 shows the comparison between historical and synthetic peak discharges at the Colorno section. For a more immediate comprehension of the appreciable routing effect of the river reach, the upstream peak discharges (historical and synthetic) are also plotted in the same figure.

The overall behaviour of the routed SDHs peak discharges fits satisfactorily those of the routed historical floods: this confirms that the return periods, at first somehow arbitrarily attached to the routed SDHs, are statistically meaningful. Synthetic results are in better agreement with historical ones especially for return periods ranging from 2 to 10 years. In this range the fit can be evaluated at first sight and is besides more reliable due to the less uncertainty in positioning the historical data on the probability chart. For higher return periods (20–200 years) the comparison is much

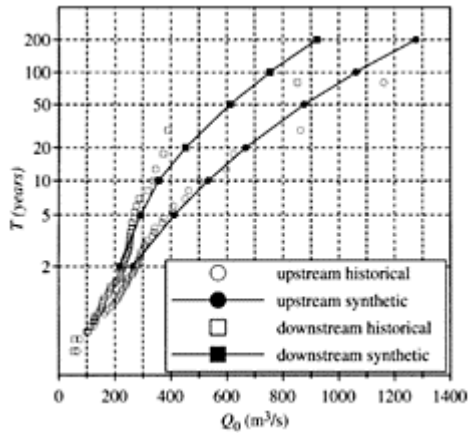

Figure 14. Peak discharges probability plots of historical floods and SDHs for upstream (Bottego) and downstream (Colorno) sections.

more difficult as it would require a deeper statistical interpretation of the historical results. However, the trend of the historical peak discharge distribution seems to be correctly described by the results obtained by means of the SDHs.

7 CONCLUSIONS

A procedure of estimation of Synthetic Design Hydrographs has been proposed in previous works by some of the Authors (Maione et al. 2000a, b). The method is based on the construction of the Flow Duration Frequency reduction curves (FDF), obtained from the statistical analysis of the average flood discharges of given duration and on the determination of the Peak-Duration r_D.

In this paper the SDHs are evaluated and then applied to model the flood routing effect in a mild slope river reach where a long series of historical floods is available.

The statistical significance of the derived SDHs is then evaluated comparing the distribution of peak discharges obtained at a downstream section of a river reach by routing a long series of historical floods and by routing the synthetic floods only.

The satisfactory results obtained suggest that SDHs construction procedure is reliable and the return periods attached, at first in a somehow arbitrary way, to the routed synthetic floods have statistical meaning.

This approach has a twofold advantage. Firstly, whereas a historical series of floods is available, it allows to evaluate the distribution of peak discharges at a downstream section simply routing few synthetic instead of several historical floods. Furthermore, for ungauged sites, regional procedures to determine the SDHs can be applied (Maione et al.

2003) and the derived SDHs consequently used to estimate the routing effect of the considered river reach.

Analogous validations have been performed to confirm the SDHs construction procedure with reference to other river management problems such as flood control reservoirs (Maione et al. 2000a, b) and embankment seepage (Butera & Tanda 2002), with good and satisfactory results, respectively. SDHs seem to be really able to synthesise the main characteristics of the historical floods and can then be applied with confidence to many river flood management problems.

REFERENCES

Abbott, M.B. & Ionescu, F. 1967. On the numerical computation of nearly-horizontal flows. *Journal of Hydraulic research* 5:97–117.

Bacchi, B., Brath, A. & Kottegoda, N.T. 1992. Analysis of the relationships between flood peaks and flood volumes based on crossing properties of river flow processes. *Water Resources Research* 28(10):2773–2782.

Ballarin, C., Maione, U, Mignosa, P. & Tomirotti, M. 2001. Una metodologia di stima indiretta degli idrogrammi sintetici per il progetto di opere di difesa idraulica del territorio. *L'Acqua* (3):9–16.

Butera, I. & Tanda, M.G. 2002. Semi-analytical transient analysis of river embankments with a synthetic design hydrograph. In G.Becciu et al. (eds.), *New Trends in Water and Environmental Engineering for Safety and Life: Eco-compatible Solutions for Aquatic Environments; Proc. Int. Conf., Capri, 24–28 June 2002.* Rotterdam: Balkema.

Danish Hydraulic Institute 2002. *Mike 11 Reference manual.* Hørsholm: DHI.

Fiorentino, M. 1985. La valutazione dei volumi di piena nelle reti di drenaggio urbano. *Idrotecnica* (3):141–152.

Hosking, J.R.M., Wallis, J.R. & Wood, E.F. 1985. Estimation of the Generalized Extreme-Value Distribution by the Method of Probability-Weighted Moments, *Technometrics* 27(3):251–261.

Keifer, C.J. & Chu, H.H. 1957. Synthetic storm pattern for drainage design. *Journal of the Hydraulic Division* 83(HY4):1–25.

Maione, U, Mignosa, P. & Tomirotti, M. 2000a. Synthetic design hydrographs for flood-control reservoirs and flood-plain management. In U.Maione, B.Majone Lehto, R. Monti (eds.), *New Trends in Water and Environmental Engineering for Safety and Life: Eco-compatible Solutions for Aquatic Environments; Proc. Int. Conf., Capri, 3–7 July 2000.* Rotterdam: Balkema.

Maione, U, Mignosa, P. & Tomirotti, M. 2000b. Synthetic design hydrographs for river flood management. In Toensmann F., Koch M. (eds.), *River Flood Defence Proc. Int. Symp., Kassel, 20–23 September 2000.* Kassel: Herkules Verlag.

Maione, U., Mignosa, P. & Tomirotti, M. 2003. Regional estimation of synthetic design hydrographs. *Intl. J. River Basin Management* 1(2):1–13.

NERC (National Environmental Research Council) 1975. *Flood Studies Report.* London.

Surface water modeling of the Biebrza River network

R.Verhoeven & R.Banasiak
Hydraulics Laboratory, Ghent University, Belgium

D.Swiątek, J.Chormański & T.Okruszko
SGGW, Warsaw, Poland

River Flow 2004—Greco, Carravetta & Della Morte (eds.)

ABSTRACT: The Biebrza River, situated in the north-eastern part of Poland, flows through the last extensive, fairly undisturbed river-marginal peatland in Europe. Its valley intensively drains the surrounding plateau and the outwash plain into the river and creates a very complex ground and surface water system. The carried study focuses on the upper and middle basin of the river with a length of about 80km. It aims at the elaboration of a surface water model as a tool for the water resources management in the catchment. During intensive field measurement campaigns a large amount of information on the topography and on the hydraulic characteristics has been gathered. The data is used to provide an accurate and reliable input for a flood-routing model and to guarantee high quality modeling after ample calibration. Special attention is paid to the simulation problems related to storage and flow in the complex network of inundation fields as an important part of the drainage system and to the impact of dense vegetation on the discharge characteristics. Coping with these difficulties, the simulation results show fairly good agreement with measurement data.

1 INTRODUCTION

The Biebrza River and surrounding wetlands are situated in the northeastern part of Poland, in an ice-marginal valley, some 195000 hectares in area (Fig. 1). This region forms the last extensive, fairly undisturbed river-marginal peatland in Europe, containing endangered plant and animal species in a large variety of fully developed ecosystems. It is internationally recognised as a reference area for restoration of deteriorated peatlands.

Biebrza Valley, according to the geomorphologic description, is an extensive depression formed during the last glaciation. It is filled with several thick deposits of fluvioglacial sands. The Biebrza Valley was divided [Zurek, 1984] into basins using a relation of higher order morphologic features such as ancient and young morainic plates, glacier outwash plains or river flood terraces. There are 3 major basins, respectively identified as the Upper Basin reaching from the springs of Biebrza to the mouth of the Netta River; the Middle Basin covering the area from Netta to the mouth of Rudzki Channel and the Lower Basin situated in the southern part of the valley up to the alluvial cone of the recipient Narew River.

The *Upper Basin* has a length of some 40 km (62 km along the river) and a width of 2–3km, with two

Figure 1. Biebrza Valley—site map.

basin-lake widenings: in its middle part and in the transition zone to the Middle Basin.

The *Middle Basin* is the biggest, 40km long and up to 20km wide. It forms a vast, very plat depression paludified by the surface waters of Biebrza and its tributaries flowing from the Lake District, as well as by the ground waters of two aquifers.

The river in *Lower Basin* has a length of 30km and a width ranging from 12 to 15km. The flood plain composes of flat peatlands and a mud zone of 2km along the river border.

The Biebrza river, as a whole, is a typical lowland river. It has mild slopes (in average about 10cm per 1km) and a strongly meandering character. It features varying cross-sections and an irregular longitudinal profile. The variability of the hydrological characteristics along the river is also typical. This is due to the fact that the valley intensively drains the surrounding plateau and the outwash plain into the river. The surface water system is quite complicated consisting of a complex drainage system, network of inundation fields and storage areas. The flow is highly influenced by the dense vegetation.

A comprehensive study has been launched to tackle several water management problems, especially in the Upper and Middle Basin of the river. This happens within a

bilateral project joining efforts of Flemish and Polish research teams. The project is aimed at the development of methods to increase the use and the efficiency of wetland area's, the creation of new artificial area's where the same functions could be implemented and at the study of water management measures to be taken to protect the wetlands ecosystem. Special effort is put on the development of a numerical model, allowing the simulation of the impact of different measures on the water balance of the catchment. For this, starting from the existing data, additional measurement campaigns need to be performed in order to define the input parameters and the boundary conditions of the model.

So far, starting from 1999 several intensive field measurement campaigns have been realised over the vast area of the Upper and Middle Basins, delivering a large amount of data, which can be used to provide an accurate and reliable input for flood routing model.

2 DATA COLLECTION

2.1 *Topographical data*

A Digital Elevation Model (DEM) of the research area is being developed. For this the ArcInfo 7.2 TOPOGRID command is used. This method, originally developed to interpolate DEM for hydrologic modelling purposes, was also several times successfully applied to construct a model of floodplain topography (Cera et al., 1996; Townsend & Walsh, 1998; Chormanski, 2003). For the elaboration of DEM, first, the necessary data were collected by field measurements and map analysis. Consequently, the Digital Elevation Model has been created as a raster model by spatial interpolation.

The main data source for the model generation was a set of contour lines elaborated in digital form on the basis of topographic maps with a scale of 1:25 000. The DEM of the research area was created as a raster network with a cell resolution of 25 meters. Because the topographic maps do not accurately show the flat areas at the valley bottom, the construction of a proper elevation model needs additional measurements. Therefore, the database was extended with topographical data from field measurements. The efforts were focussed on the area close to the river channel. Information was collected along the Biebrza River banks every few hundred meters making use of a precise GPS set working in Differential RTK mode (Hoffmann-Wallenhof et al., 1997). Also, a number of valley cross-sections were measured by traditional levelling. As a result, Figure 2 shows the DEM of Biebrza valley for the section between Jastrzêbna and Sztabin.

2.2 *Hydraulic data*

The hydraulic data collection focuses on the determination of the friction coefficients of the different river reaches and on the steady state calibration of the numerical model to be developed.

Until now, several intensive field-measuring campaigns have been developed in different seasons over the period 1999–2003. Figure 3 gives a schematic overview of the measurement locations along the river over a length of about 80km. The track length of the strongly meandering river between the consecutive cross-sections has been calculated

using the digital topographical maps. In all these locations discharges were recorded from a bridge or from a boat using propeller meters or electromagnetic velocity meters. Usually, the measurements were conducted twice in order to increase the measurement accuracy.

The local water surface has been recorded in multiple, discrete cross-sections along the river leading to a fairly accurate recognition of the longitudinal water surface profile (Fig. 4). From these recordings the friction slope of every reach of the river was calculated. Input of these data into the simulation model lead to the determination of the friction characteristics.

3 NUMERICAL SIMULATION

3.1 *Numerical tool*

The HEC-RAS software package is adopted to model the surface water flow. This tool, developed by Hydrologic Engineering Center (HEC) of the US Army Corps of Engineers (USACE), is a software package intended for calculating water surface profiles in a full network of channels, a dendritic system, or single river reach (HEC, 2000). The HEC-RAS software

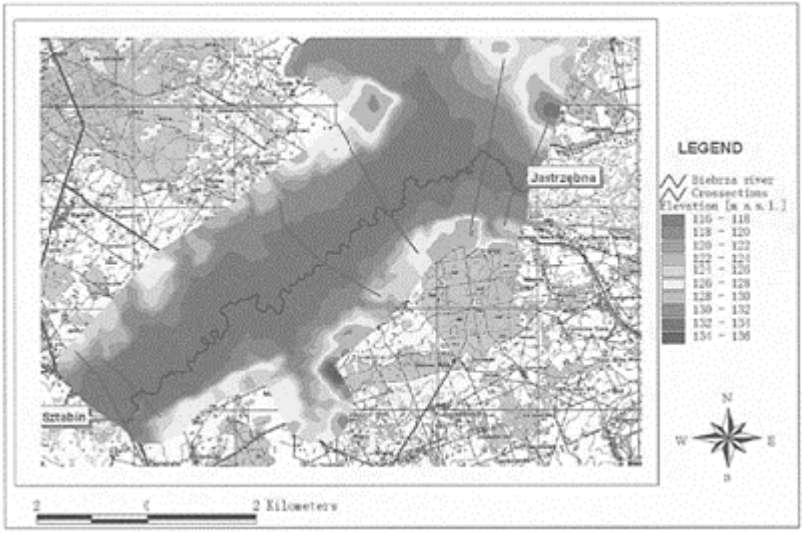

Figure 2. Digital Elevation Model for Biebrza valley—Upper Basin section.

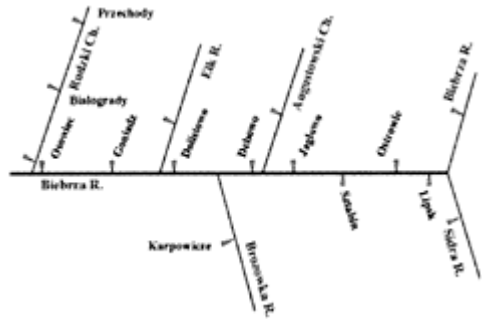

Figure 3. Schematic representation of discharge measurements.

uses the St. Venant equations to compute water surface profiles given cross-section data, roughness coefficients, and flow rates. In addition, the program has a number of special capabilities related to the analysis of culverts and bridges at roadway crossings and to model weir overflow structures, dam-burst and water storage interactions. It can be considered as quasi-two-dimensional software, as it is capable to include off-channel storage and inundation fields. Depending on the flow conditions, inundation fields are simulated as separate channels or as storage cells. The total flow is distributed according to conveyance between the main river channel and the floodplain. The upstream boundary conditions can be a discharge or a stage

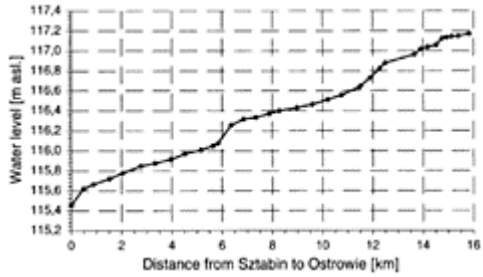

Figure 4. Recorded water surface profile along the section between Sztabin and Ostrowie (14.05.2003).

hydrograph. The available downstream boundary conditions are: a stage hydrograph, a flow hydrograph, a single-valued rating curve or a looped rating curve (Manning's equation).

Furthermore, the software is supported by the inundation fields mapping system, as described above, by the delivery of supplementary topography information in order to construct full flood plain cross sections that reflect accurate channel and overbank data. Inversely, results exported from HEC-RAS may be processed in the ArcView3D analysis

extension for floodplain mapping and analysis. This includes the locations of the cross-section cut lines (Fig. 2) along with water surface profile data and a set of polygons that describe the extend of the modelled floodplain.

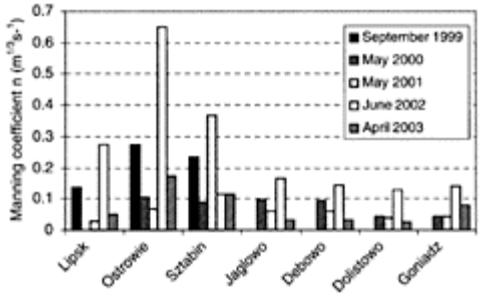

Figure 5. Friction coefficients.

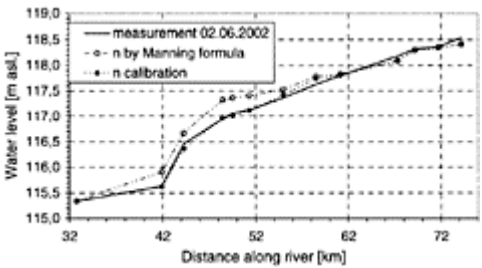

Figure 6. Determination of friction coefficient.

3.2 *Friction coefficients in the steady state model*

Once all discharge data have been processed, the friction coefficient of each part of the river network can be calculated in two different ways: As the field campaigns were performed in periods with stable water conditions, one can suppose the flow regime do be in a steady state with uniform flow and apply the Manning formula in each gauging point to calculate the friction coefficient. The values of the coefficients obtained by this approach are shown in Figure 5.

The strong variation of the friction coefficient as a function of vegetation development is striking. In this region vegetation starts to grow in late April and reaches full growth in early summer. By this it isn't surprising that although the water stages recorded during the campaigns of June 2002 and April 2003 were very similar, the discharges in April were 2 to 3 times higher in April than in June. The alternation of the friction characteristics is particularly strong in the upper section of the river, where the channel is relatively small and where almost the whole cross-section is taken by plants. The growth of the plants not only increases the resistance to flow but also reduces flow velocities and

disturbs the velocity distribution. This important effect has also to be accounted for in the unsteady state flow simulation presented in the next section.

The second method uses the theory of hydraulic water surface profiles: Starting from the data on

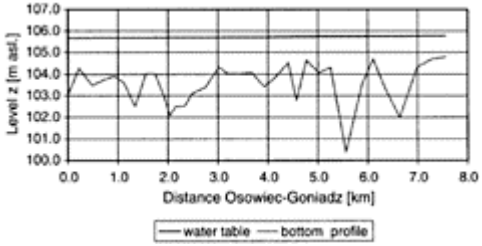

Figure 7. Longitudinal profile.

geometry, water levels and discharge, the Bresse equation allows calculation of the friction coefficient in a river reach between two gauging locations. When looking at Figure 6, it is clear that the second method delivers much better results. The irregularity of profiles, with significant changes in cross-sectional area and longitudinal slope (Fig. 7), that could not be completely recognized, must be compensated by the calibrated friction factor.

3.3 *Extension to floodplains*

The knowledge of the value of the friction coefficients as well as accurate information on the geometry is of primordial importance for the quality of the results of the hydrodynamic models. Up till now only information on the low water level friction characteristics is available. As during flood flow the value of these coefficients might be substantially different, it is also important to focus the field campaigns on high water level situations that normally occur between early and late spring. This is the reason why most field campaigns were planned in this period. Unfortunately, in the last four years springs have been (very) dry in the Biebrza region, leading to a lack of important data concerning the flood routing. Therefore, for a good and reliable reconstruction of the hydraulic flow conditions fluctuations related to different water level and flow regimes in the river catchment, additional field measurement campaigns under high water level conditions need to be elaborated in the (nearby) future.

The actual situation necessitated the use of other data. A flood event recorded in Spring of 1996 has been employed as an auxiliary data set for model development on flood conveyance in the Biebrza valley.

3.4 *Unsteady state simulation*

In the first stage, the modeling of surface water flow is performed for a part of the Upper Basin of the Biebrza River, restricted to the cross-sections between Sztabin (downstream)

and Ostrowie (Jastrzebna). The distance between both these section is 15km. For both cross-sections discharge hydrograms

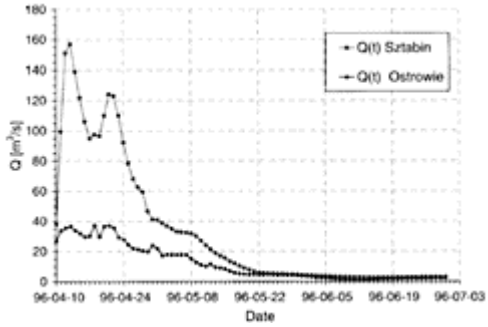

Figure 8. Discharge observed at upstream and downstream gauges.

Q(t) for the period 10.04.1996–30.06.1996, (shown in Fig. 8) are used to define the upstream and downstream boundary conditions. There is a significant difference in discharge rates between these two cross-sections. This is mainly due to the lateral inflow of melting snow during the flood event. The lateral discharge inflow, $Q_{leb}(t)$, from the Lebiedzianka brook is added 12.23km upstream of Sztabin. Next, the uniform lateral inflow is imposed along the river section as $Q_{in}(t)=Q_{Sztabin}(t)-Q\ Q_{Ostrowie}(t)-Q_{leb}(t)$. This solution is obviously a rough approximation of the actual situation, as it does not account for the temporal and spatial variation of the lateral inflow. A more realistic approach on this issue needs to be elaborated in further study.

During flood periods, the river valley consists of parts which mainly act as a storage for flood water and of effective transport areas. The particular areas have been identified according to topography reading and land use. Consequently, the storage areas and friction coefficients for the flow active zones were adapted by calibration for steady and unsteady flow so that the observed and calculated values became congruent.

To obtain a better agreement between observed and calculated water levels in the unsteady flow simulation, the friction coefficient had to be varied in such a way that it takes into account the temporal change of flow resistance due to the growth of vegetation. This appeared of crucial importance for the period under concern. Not only modification of the roughness was incorporated in this step but also the changes in the transport effective area over the cross-section had to be anticipated. The increase of the n-coefficients only to reflect the growth of the plants results in a reduction of the flow velocity and subsequently in a delay of the flood propagation in respects to the recorded event.

Based on all these considerations and on a careful calibration procedure it is possible to develop a reliable numerical model, able to reproduce the natural situation. Figures 9–11 present the calculated and

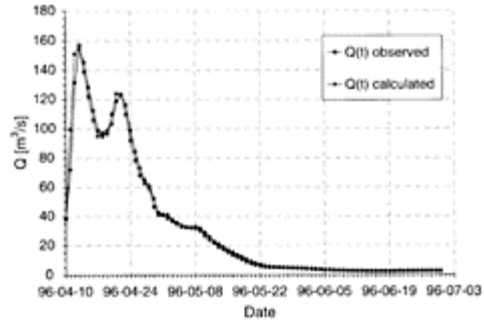

Figure 9. Discharge calculated and observed at Sztabin.

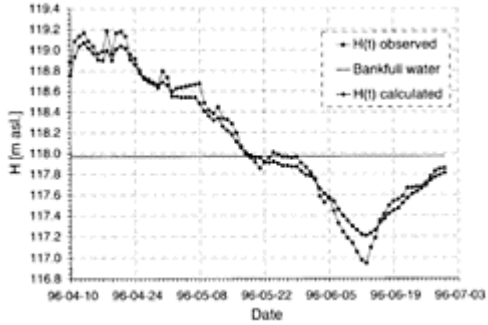

Figure 10. Water stages calculated and observed at Ostrowie.

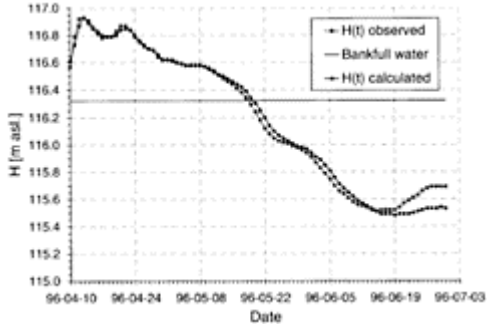

Figure 11. Water stages calculated and observed at Sztabin.

observed discharge hydrographs and water levels at the downstream and upstream cross-sections. The boundary conditions used are those presented in Figure 8 for discharge at

the inlet cross-section and in Figure 11 for water level at the downstream cross-section. As a result the variation of the water levels in both limit cross-sections and the flood wave propagation speed are reasonably well simulated.

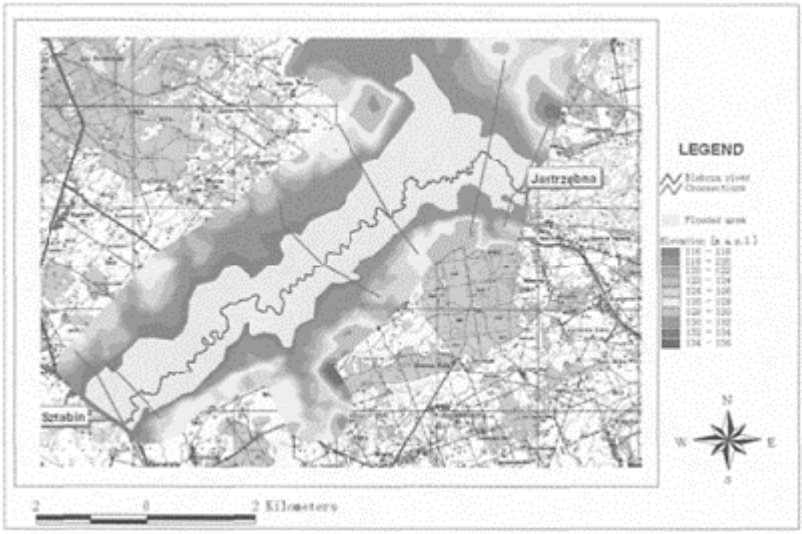

Figure 12. Flood mapping in the Biebrza Valley—Upper Basin (13.04.1996).

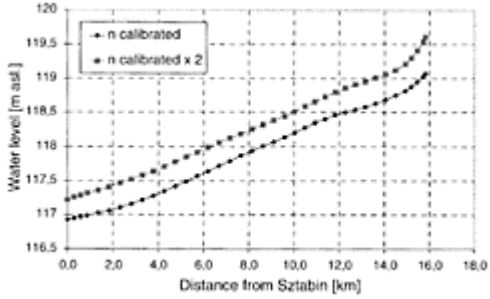

Figure 13. Water stages calculated for 2 different friction situations.

The level of the water surface profile for maximum discharge as generated by the model is used to delineate the flooding boundaries across the valley. The results from this floodplain mapping, as obtained from ArcView are presented in Figure 12.

It is clear that possible flow condition alternations will influence the conveyance of the flow in channel and valley. Therefore, different scenarios need to be tested in terms of

impact of individual or groups of parameters, or changes in the water supply configurations. An example will demonstrate the impact of changing the friction on the flood water stages for the same event as considered above but supposed to happen e.g. in late spring. Therefore the friction coefficients for the floodplain and the channel are increased by a factor 2. Figure 13 shows the water levels along the river for both scenarios. The water levels in the second case rise around 30cm. This results also in an increase of the flooding area from 13.483km^2 to 15.896km^2.

Certainly, this example does not fully reflect the potential changes in the flood plain area of the valley due to the growth of vegetation. In analogy to variation of the friction factor in the main channel, as shown in Figure 5, the variation in flood plain area can be even much more considerable.

4 CONCLUSIONS

The surface water management in the Biebrza valley is under extended and well-designed study. The numerical model for surface water flow is being developed using handsome and effective tools. The numerical modelling approach, although based on some primary assumptions, reveals promising results. The first flooding simulations on a restricted part of the network revealed a good reproduction of recorded field data. The model performance will further be improved given a more extended base of hydrometrical data, especially in terms of overbank flow conditions.

It is obvious that due to the large area to be covered by accurate and reliable data sets and the complexity of the river network, the development of a complete simulation model is a long-term business. However, large progress has been made so far, identifying weak spots of the data acquisition, schematic representation and numerical solution. The feasibility of the numerical model has been well recognized. A right approach combining both field recognition and numerical experience should guarantee the successful realization of the ambitious task to facilitate and encourage the water management and the conservation of the natural beauty of the region, in particular of the Biebrza National Park.

REFERENCES

Byczkowski, A., Kiciński, T. 1984. Surface water in the Biebrza River drainage basin. *Pol Ecol. l Stud.* Vol. 10 (3–4), pp. 271–299.

Cera, T.B., Tremwel, T.K., Burleson, R.W. 1996. Use Arc/INFO, EPA-SWMM, and UNIX text processing tools to determine flood extend.*AWRA Symposioum on GIS and Water Resources.* Sept. 22–26, 1996FT. Lauderdale, USA, pp. 8. http://www.awra.org/proceedings/gis32/cera/index.html

Chormanski, J. 2003. Methodology of flood extent determination in the Biebrza Lower Basin. PhD thesis. Warsaw Agricultural University, pp. 160.

Dodson, R.D., Li, X. 1999. The accuracy and efficiency of GIS-based floodplain determinations. *Proceedings of the 19th Annual ESRI User Conference.* San Diego, California. ESRI, *http://gis.esri.com/library.*

Hoffmann-Wallenhof, B., Lichtenegger, H., Collins, J. 1997. GPS Theory and Practice. Springler, Wien New York.

U.S. Army Corps of Engineers (USACE). 2000. HEC-RAS river analysis system Version 3.0. Users Manual. Hydrologic Engineering Center, Davis, CA.

Verhoeven, R., Van Poucke, L., Huygens, M, Okruszko, T., Ignar, S., Mucka, A., Michalowski, R., Chormanski, J., Swiatek, D., Kardel, I.2003. Surface water management in Biebrza valley. Annals of Warsaw Agricultural University, Land Reclamation, No. 33.

Verhoeven, R., Banasiak, R., Okruszko, T., Swiatek, D., Chormanski, J., Nowakowski, P. 2003. Numerical Modelling of river flow—data collection and problem solving. Key note lecture. *Proceedings of the Conference on Advances in Fluid Mechanics*, in edition, 22–24 March 2004, Lisbon, Portugal.

Townsend, P.A., Walsh, S.J. 1998: Modelling floodplain inundation using integrated GIS with radar and optical remote sensing. *Geomorphology*, No. 21, pp. 295–312.

Zurek, S. Relief, Geologic structure and hydrography of the Biebrza ice-marginal valley. *Pol. Ecol. 1 Stud.* Vol. 10 (3–4), pp. 239–251.

An improved, robust implicit solution for the two dimensional shallow water equations on unstructured grids

S.Komaei
Electrowatt-Ekono AG, Zurich, Switzerland & German Armed Forces University Munich, Neubiberg, Germany

W.Bechteler
German Armed Forces University Munich, Neubiberg, Germany

River Flow 2004—Greco, Carravetta & Della Morte (eds.)

ABSTRACT: In this paper, an implicit unstructured gird algorithm for solving two dimensional Shallow Water Equations (SWE) has been developed. It is based on cell-centred Finite Volume Method (FVM) and can handle cells of triangular and Quadrilateral types. The algorithm includes piecewise linear least-square interpolation and uses Roe's approximate Riemann solver to compute fluxes. In addition, a new technique is introduced to prevent instabilities and oscillations caused from the bed slope terms in the case of problems with arbitrary topography and hydraulic structures. The method results set of nonlinear algebraic equations for the flow variables in each cell. The system of equations can be iteratively solved. Second order accuracy in time and second or higher order accuracy in space can be achieved in this method. The proposed method is validated and verified via solving some examples and comparison of the results obtained from the new method with the other methods.

1 INTRODUCTION

Flows in open channels are often modelled by a set of hyperbolic partial differential equations, i.e. the well known shallow water equations (SWE). Algorithms for solving SWE on structured grids have become widespread in recent years (Delis et al. 2000; Fennema and Chaudhry 1989; Panagiotopoulos and Soulis 2000; Valiani et al. 1999). However, these algorithms have shown difficulties in predicting satisfactory results in complex geometries due to mesh irregularities. As a result, attention has turned to the development of the algorithms on arbitrary unstructured grids. Many current unstructured

algorithms utilize explicit time integration (Anastasiou and Chan 1997; Beffa and Connell 2001; Nujic 1995; Zhao et al. 1996) that can be computationally expensive if a long period of time has to be simulated. On the other hand, the explicit approach is computationally efficient when applied to meshes that are coarse. For cases where finer meshes are used, the time of computations significantly increases. For the sediment transport problem, which is not a high gradient phenomenon and often needs a time range of several years or decades, the simulation takes a lot of time therefore, an implicit scheme could be more useful which allows large time steps to obtain solutions in a computationally efficient manner.

The application of the implicit schemes in SWE is often an extension of the schemes used in computational fluid dynamics (CFD). As pioneers, Fennema and Chaudhry (1989) have used implicit finite difference schemes, developed by Beam and Warming (Beam and Warming 1976; 1978) for hyperbolic systems in conservation law form, for the solution of two-dimensional SWE without source terms. In general, good results are reported, even though quite dissipative. However, these schemes are only first order accurate in space and employ the flux splitting in a nonconservative way. Later, Jha et al. (1996) proposed a modification for achieving full conservation, employing the use of the Roe-average approximate Jacobian (Roe 1981). MacCormack (1982) presented an implicit analog of his earlier widely used explicit method (MacCormack and Paullay 1972) for solving the equations of compressible viscous flow. Panagiotopoulos and Soulis (2000) have extended the implicit MacCormack scheme to integrate the flow equations. They developed a numerical method to solve SWE in generalized coordinates describing the depth-averaged, steady, subcritical and supercritical free-surface flows with the presence of hydraulic jumps. In the other paper, Klonidis and Soulis (2001) have developed another finite volume scheme to calculate steady, two-dimensional SWE. The formulation is based on transformation of the flow equations into a non-orthogonal, boundary-fitted coordinate system. Therefore, the method is suitable for structured grids.

The shortcoming of an implicit finite volume model for two-dimensional SWE on unstructured grids can be seen. This method should have the shock capturing capability and a suitable treatment of bed source terms. In this paper, an implicit robust model for numerical solving of SWE on unstructured grids is introduced. The proposed method has a special treatment of the bed source terms therefore it is able to model flow over an initially dry and irregular bed.

2 SYSTEM OF GOVERNING EQUATIONS, SWE

The system of SWE in the conservative form is given by:

$$\frac{\partial \mathbf{q}}{\partial t} + \frac{\partial \mathbf{f}(\mathbf{q})}{\partial x} + \frac{\partial \mathbf{g}(\mathbf{q})}{\partial y} = \mathbf{S}(\mathbf{q}) \tag{1}$$

with

$$\mathbf{q}=\begin{Bmatrix} h \\ hu \\ hv \end{Bmatrix} \qquad \mathbf{S(q)}=\begin{Bmatrix} 0 \\ gh(S_{0x}-S_{fx}) \\ gh(S_{0y}-S_{fy}) \end{Bmatrix} \tag{2}$$

$$\mathbf{f(q)}=\begin{Bmatrix} hu \\ hu^2+gh^2/2 \\ huv \end{Bmatrix} \qquad \mathbf{g(q)}=\begin{Bmatrix} hv \\ huv \\ hv^2+gh^2/2 \end{Bmatrix}$$

where $\mathbf{F(q)=[f(q), g(q)]}^T$ is the flux vector, h is the water depth, u, v depth averaged velocity in x- and y-direction, respectively, S_{0x}, S_{fx} are bed and friction slope in x-direction and S_{0y}, S_{fy} are bed and friction slope in y-direction. The bed slope is defined in x-direction as:

$$S_{0x}=-\frac{\partial Z_b(x,y)}{\partial x} \tag{3}$$

and the friction slope is estimated using the Manning's formula. For example, in x-direction, it is:

$$S_{fx}=\frac{n^2u\sqrt{u^2+v^2}}{h^{4/3}} \tag{4}$$

S_{0y}, S_{fy} are defined in a similar way.

3 NUMERICAL ALGORITHM

3.1 *Discretization of the governing equations*

The system of governing equations is discretized using the finite volume method (FVM). Integrating Eq. (1)

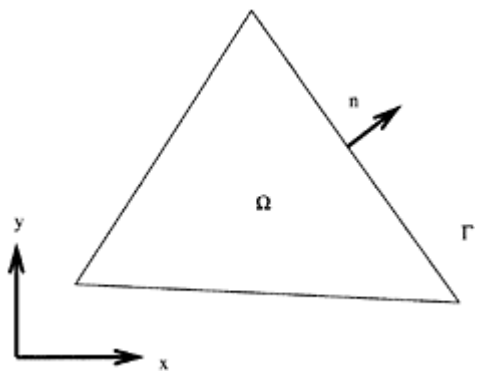

Figure 1. Notation for finite volume method.

over an arbitrary triangular cell Ω and using the divergence theorem, the basic equation of the FVM is obtained as:

$$\iint_{\Omega} \mathbf{q}_i \, dA = -\int_{\Gamma} \mathbf{F}(\mathbf{q}).\mathbf{n} \, dl + \iint_{\Omega} \mathbf{S}(\mathbf{q}) \, dA \tag{5}$$

in which **n** is unit outward vector normal to the boundary Γ (see Figure 1); *dA*, *dl* are area and arc element, respectively. After some manipulation, the semi-discrete form of the equation is:

$$A_i \frac{d\mathbf{q}_i}{dt} + \sum_{m=1}^{N_i} \mathbf{F}_m \cdot \mathbf{n}_m l_m = A_i \mathbf{S}(\mathbf{q}_i) \tag{6}$$

where the subscripts *i* and *m* denote quantities for the *i*-th cell and *m*-th face of the cell, respectively and *N* is the total number of the faces for that cell.

In an implicit scheme, the flux vector F is computed at the new time level *k*+1. Using implicit scheme, Eq. (6) can be rewritten in the following form:

$$A_i \frac{\mathbf{q}_i^{k+1} - \mathbf{q}_i^k}{\Delta t} + \sum_{m=1}^{N_i} \mathbf{F}_m^{k+1} \cdot \mathbf{n}_m l_m = \mathbf{R}_i \tag{7}$$

where $\mathbf{R}_i = A_i \mathbf{S}(\mathbf{q}_i)$ is the right hand side terms evaluated in cell *i* at the known time level *k*. Expanding **F** about a known time level, we get:

$$\begin{aligned} \mathbf{F}^{k+1} &= \mathbf{F}^k + \left(\frac{\partial \mathbf{F}}{\partial \mathbf{q}}\right)^k \left(\mathbf{q}^{k+1} - \mathbf{q}^k\right) + O\left(\Delta t^2\right) \\ \mathbf{F}^{k+1} &= \mathbf{F}^k + \mathbf{J}\,\Delta\mathbf{q} + O\left(\Delta t^2\right) \end{aligned} \tag{8}$$

where $\mathbf{J} = \partial \mathbf{F} / \partial \mathbf{q}$ is the flux Jacobian matrix. Substituting Eq. (8) into (7) leads to:

$$A_i \frac{\mathbf{q}_i^{k+1} - \mathbf{q}_i^k}{\Delta t} + \sum_{m=1}^{N_i} (\mathbf{J}\,\Delta\mathbf{q}) \cdot \mathbf{n}_m l_m = \mathbf{R}_i - \sum_{m=1}^{N_i} \mathbf{F}_m^k \cdot \mathbf{n}_m l_m \tag{9}$$

Following Jameson and Turkel (1981) and Yoon and Kwak (1992), the flux Jacobian matrices are splitted as follows:

$$\mathbf{J}^{\pm} = \frac{\mathbf{J} \pm \mathbf{I}\alpha\lambda_{\max}}{2} \tag{10}$$

with

$$\lambda_{\max} = |\mathbf{V} \cdot \mathbf{n}| + c \tag{11}$$

where **V** and $c = \sqrt{gh}$ are the velocity vector and speed of the wave, respectively and α is a relaxation factor of order unity. Eq. (9) now becomes:

$$\begin{aligned} A_i \frac{\mathbf{q}_i^{k+1} - \mathbf{q}_i^k}{\Delta t} + \sum_{m=1}^{N_i} (\mathbf{J}^+ \Delta\mathbf{q}_i) \cdot \mathbf{n}_m l_m = \\ \mathbf{R}_i - \sum_{m=1}^{N_i} \mathbf{F}_m^k \cdot \mathbf{n}_m l_m - \sum_{m=1}^{N_i} (\mathbf{J}^- \Delta\mathbf{q}_m) \cdot \mathbf{n}_m l_m \end{aligned} \tag{12}$$

or written in matrix form:

$$\mathbf{M}\,\Delta\mathbf{q}_i=\mathbf{RHS}^k \tag{13}$$

in which:

$$\Delta\mathbf{q}_i=\mathbf{q}_i^{k+1}-\mathbf{q}_i^k=[\Delta h,\Delta(hu),\Delta(hv)]^T \tag{14}$$

is the unknown vector. The formulation of the matrix **M** and the vector **RHS** are given by Komaie (2003). To numerically solve the discretized Eq. (12), the major steps of the solution procedure are reconstruction, flux computation and evolution. These steps are illustrated below.

3.2 *Reconstruction*

For the first step, reconstruction, a cell-centered scheme is used. The piecewise linear, least-square reconstruction procedure used here is similar to those used by Barth (1993) and Coirier (1994). Each of the three primitive variables *h; u* and *v* is assumed to linearly vary within a finite volume as:

$$U(x,y)=\overline{U}+U_x(x-\overline{x})+U_y(y-\overline{y}) \tag{15}$$

where *U* can be any of the above variables. The bars in Eq. (15) denote cell-averaged values as defined in the last equations. In high gradient regions, a gradient limiter is normally used in Eq. (15) to ensure that the reconstruction polynomial does not produce new extrema near a flow discontinuity such as a shock wave. Limiters can also control the numerical oscillation that are common with second and higher order numerical schemes. In this paper, the limiter is applied to the gradient terms (Anastasiou and Chan 1997) so that:

$$U=\overline{U}+\Phi\nabla U\,\vec{r} \tag{16}$$

where **r** is the vector from cell centroid to the midpoint of the edge and $0<\Phi<1$ is a chosen limiter.

When Φ is set to zero, the computation domain is characterized by piecewise constant regions resulting in a first-order scheme. The non-linear limiter is given by:

$$\Phi=\max[\min(\beta D_j, 1), \min(D_j, \beta)] \tag{17}$$

where:

$$D_j=\begin{cases}(U_j^{\max}-U_j)/(U_L-U_j) & if \quad U_L>U_j\\ (U_j^{\min}-U_j)/(U_L-U_j) & if \quad U_L<U_j\\ 1 & if \quad U_L=U_j\end{cases} \tag{18}$$

with:

$$U_j^{\min} = \min(U_j, U_i), \quad U_j^{\max} = \max(U_j, U_i) \tag{19}$$

This procedure is carried out sequentially for the two cells separated by the common edge. These values are then used in the Riemann solver to estimate the flux across the edge in the flux computation phase. When β=1, Φ is the *Minmod* limiter and when β=2, the limiter is *Roe's Superbee* limiter. The Minmod limiter is used in this paper.

3.3 *Flux computation*

In the next step, the normal component of the flux vector, i.e. $\mathbf{F}_m.\mathbf{n}_m$ in Eq. (12), should be estimated. With the piecewise linear reconstruction, the unknown variables are continuous and assumed to linearly vary within a finite volume. However, no guarantee exists that the variables will be continuous across adjacent finite volumes because a different polynomial is used in each finite volume. As a result, a flux formula is needed to compute a single flux at a finite volume boundary using fluxes from the adjacent volumes. In this paper the Roe's approximate Riemann solver is used (Roe 1981). Roe's method may be the most famous Riemann solver in CFD and SWE (Brufau et al. 2002; Erduran et al. 2002; Roe 1981; Sanders 2001; Toro 2001; Tseng and Chu 2000). Define the normal component of the flux vector as:

$$\mathbf{F}_n=\mathbf{F}\cdot\mathbf{n} \tag{20}$$

Then $\mathbf{F}_n$ can be computed using the Roe FDS method as:

$$\mathbf{F}_{n,i+1/2} = \frac{1}{2}\left[\mathbf{F}_{n,L} + \mathbf{F}_{n,R} + \left|\hat{\mathbf{A}}_{i+1/2}\right|\left(\bar{\mathbf{q}}_L - \bar{\mathbf{q}}_R\right)\right] \tag{21}$$

where the subscripts L and R denote the flow conditions to the left and right sides of the cell face and $\mathbf{A}_{i+1/2}$ is Roe flux difference splitting matrix.

3.4 *Evolution*

Now it is possible to solve the Eq. (12) for each cell. There is a part of RHS in Eq. (12) that relates to the unknowns of the neighbour cells. Therefore, the system of the algebraic equations should be solved iteratively. The nature of the method enables us to implement it on parallel computer systems. In addition, it is efficient because no block or scalar tridiagonal inversions need to be calculated. After achieving convergence, the solution is updated to find the flow variables at the end of a time step. The main question is whether there is any condition to restrict the time step of the computation for the proposed implicit scheme. It is clear that the CFL condition is not applicable here. But from the mathematics it is well known that to achieve a numerically stable method, the Matrix $\mathbf{M}$=[m_{ij}] should be diagonally dominant. It means:

$$|m_{ii}| \geq \sum_{j \neq i} |m_{ij}| \qquad \forall i \tag{22}$$

3.5 *Treatment of the bed source terms*

Here, the new developed method for numerical implementation of the bed source terms is presented. The proposed method is simple and robust and it is independent of the Riemann solver. It also holds the conservation property that is defined by Bermudez et al. (1998). For the description of the method, two options should be considered:

–How the method deals with the terms $0.5gh^2$ in the flux terms.
–Which scheme is used to numerically compute $\mathbf{S}_b(\mathbf{q})$.

3.5.1 *Flux modification*

The flux vector on the edge can be computed with a desired Riemann solver but after that, the term $0.5g/h^2$ should be recomputed for the sloped edge (Komaie 2003):

$$\frac{1}{2}gh^2 = \frac{1}{2}g\overline{h^2} = \frac{1}{2}g\frac{h_i^2 + h_i h_j + h_j^2}{3} \tag{23}$$

which h_i and h_j are the water depth at the two ends of the edge based on the constant water level assumption over the edge.

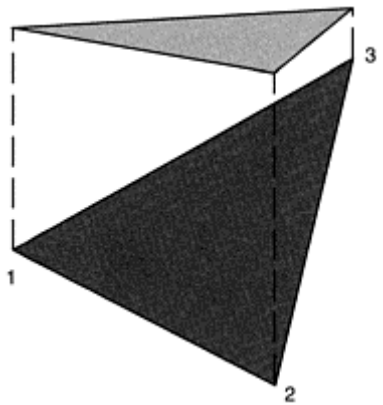

Figure 2. Sloped wet cell and the water surface level, 3D imagination.

3.5.2 *Source terms*

Now it is required to compute the integral of the bed source term vector over a cell Ω:

$$\iint_{\Omega} \mathbf{S}_b(\mathbf{q})\,dA = \iint_{\Omega} \begin{pmatrix} 0 \\ ghS_{0x} \\ ghS_{0y} \end{pmatrix} dA = g\iint_{\Omega} h \begin{pmatrix} 0 \\ -\dfrac{\partial Z_b(x,y)}{\partial x} \\ -\dfrac{\partial Z_b(x,y)}{\partial y} \end{pmatrix} dA \tag{24}$$

If we assume that the bed slope in x- and y-direction in every cell Ω is constant, then we have

$$\iint_{\Omega} \mathbf{S}_b(\mathbf{q})\,dA = g\left(\iint_{\Omega} h dA\right)\begin{pmatrix}0\\ S_{0x}\\ S_{0y}\end{pmatrix} = gVol_{water}\begin{pmatrix}0\\ S_{0x}\\ S_{0y}\end{pmatrix} \tag{25}$$

It means that the bed term integral is converted to the multiplication of two parameters: cell bed slope and the volume of water in the cell between water surface level and bed level. For the case of wet cell, i.e. all three nodes are under the water surface (Figure 2), the volume of water is:

$$Vol_{water} = \left(\frac{h_1 + h_2 + h_3}{3}\right)\cdot A \tag{26}$$

which A is the cell area and h_i(i=1, 2, 3) is the water depth at ith-node of the cell. For the partially wet cell the above Eq. should be modified so that the real volume of water is obtained.

In the case that only one node is under water surface (Figure 3), the location of points "a" and "b" should be

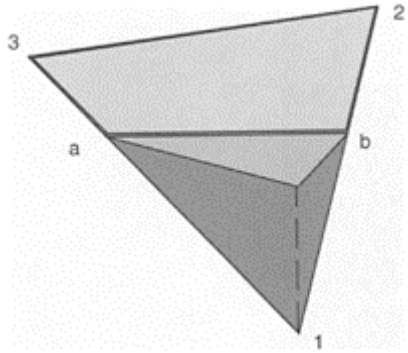

Figure 3. Sloped partially wet cell and the water surface level, 3D imagination.

found at which the water surface plane, i.e.. η=*const.*, intersect the edge lines. At these points, the water depth is zero. With the help of similarity of triangles in, one can easily find for the point "a",

$$\begin{aligned} x_a &= x_1 + \frac{\eta - Z_{b,1}}{Z_{b,3} - Z_{b,1}}(x_3 - x_1) \\ y_a &= y_1 + \frac{\eta - Z_{b,1}}{Z_{b,3} - Z_{b,1}}(y_3 - y_1) \end{aligned} \tag{27}$$

in above Eqs., x_k and y_k are the coordinates of the point k, For the location of the point "b", similar formulations can be found. Now it is possible to compute the wet horizontal area of the element, i.e. A_{ab1}:

$$2A_{ab1} = \det\begin{vmatrix} 1 & x_1 & y_1 \\ 1 & x_a & y_a \\ 1 & x_b & y_b \end{vmatrix} \tag{28}$$

and finally the volume of the water in the cell can be computed as follows

$$Vol_{water} = \frac{A_{ab1} \cdot h_1}{3} \tag{29}$$

In the case that two nodes are under water surface, the same method can be used.

4 NUMERICAL EXAMPLE

Under a research work mainly supported by the central public funding organization for academic research in Germany (DFG), a physical model has been studied at the Aachen University of Technology (RWTH) to understand the fundamental flow behaviour in meandering channels and rivers with overflow into floodplains (Stein 1990).

In order to perform the experiment, a 15.0m long, 3.0m wide and 0.35m deep channel was built from PVC with a variable longitudinal slope in the range of 0 to 0.2% (Figure 4). The channel was equipped by the Laser Doppler Anemometer (LDA) tools to record the velocities.

Stein (1990) has tested two basic variants whose essential difference was the existence or nonexistence of the vegetation on floodplains. The flow behaviour for the dominant flow in floodplain or in main channel could be systematically analyzed through the variation of the vegetation on floodplains. The analysis of the measured data of both variants showed that the mechanisms of flow in the case of dominated flow in main channel exhibits partly strong three-dimensional character (Stein 1990). This experiment has been already used by different researchers to verify their models (Farshi 2002; MinhDuc 1998; Schröder 1996; Stein 1990; Wenka 1992). In this work, we also simulated this experiment with smooth conditions on the floodplains.

In accordance with the statements of Stein (1990) and Wenka (1992) and based on the objective of the current work, it was not expected that our two-dimensional model can simulate the threedimensional flow processes. However, the quality of measured data makes it possible to determine, how far the numerical results are and whether the numerical model is able to approximate the considered phenomena basically and to describe their influence on the averaged flow parameters.

Here the test case A5 with the constant longitudinal slope of 0.05% is considered. For this variant, the average water depth in the main channel at the inlet section is h_m=0.15m, where the subscript "m" means the average in main channel. It is tried to keep the above water depth constant along the channel, as long as this is admitted by the flow conditions. Wenka (1992) used different input velocities for the main channel and the floodplains in variant A5, i.e. V_m=0.23m/sec for the main channel and V_f=0.30m/sec for the flood plains. The subscript "f" represents the average in the flood plains.

To test the ability of the model, a computational mesh has been generated (depicted in Figure 4). It is an unstructured grid that contains triangular and quadrilateral cells. It includes 4802 nodes and 5219 cells in which 4093 cells are quadrilateral and 1126 cells are triangular. The element size ranges between 0.02m and 0.20m. In order to reduce the effect of boundary condition on the results, the simulated channel is longer than physical model (15m instead of 11.34m) but the other geometrical parameters are the same.

The above discharge with the described velocity distribution was applied to the proposed model as inlet boundary condition in the form of the inlet hydrograph.

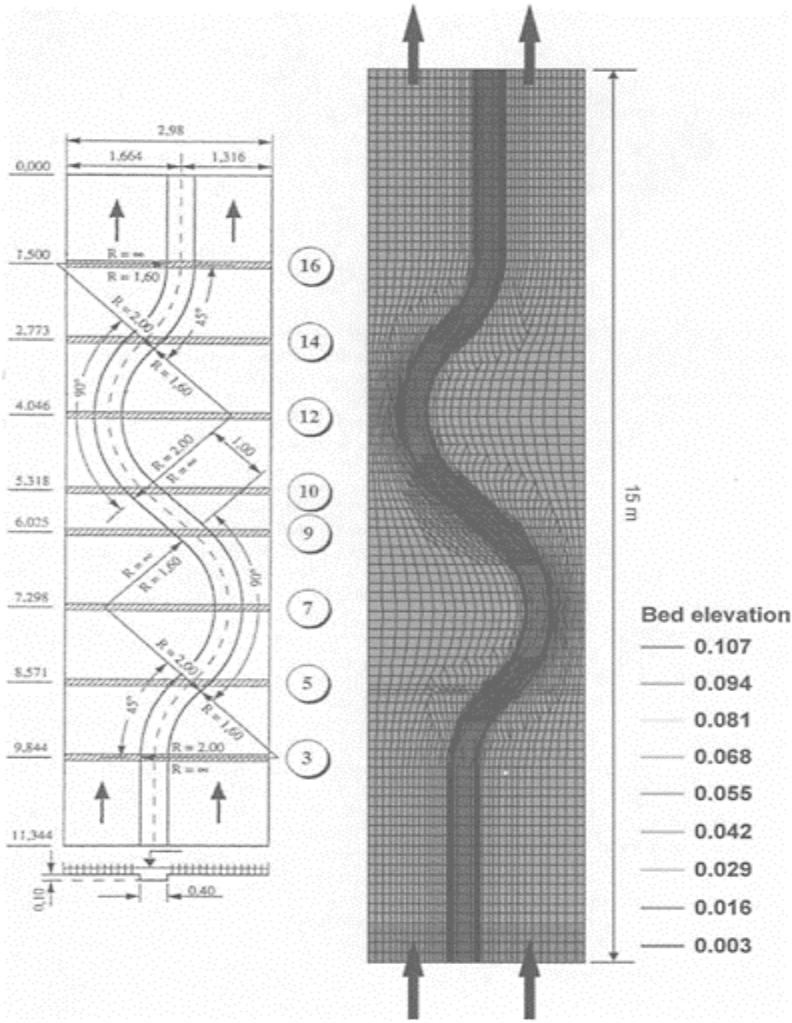

Figure 4. Meandering channel: geometrical dimensions and computational grid.

The outlet boundary condition was selected in the form of critical depth in the wet edges.

After calibration, the constant Manning's coefficient n=0.015 was selected. The time step of 0.015 sec was chosen. After shock capturing the time step and Courant number has been increased. At the end of computation at runtime 850 sec, the time step has reached 1.334sec that corresponds to average Courant number 32.3.

Figure 5 shows the comparison between the computed and the measured values of the resultant velocity at cross-section 7. A very good agreement between

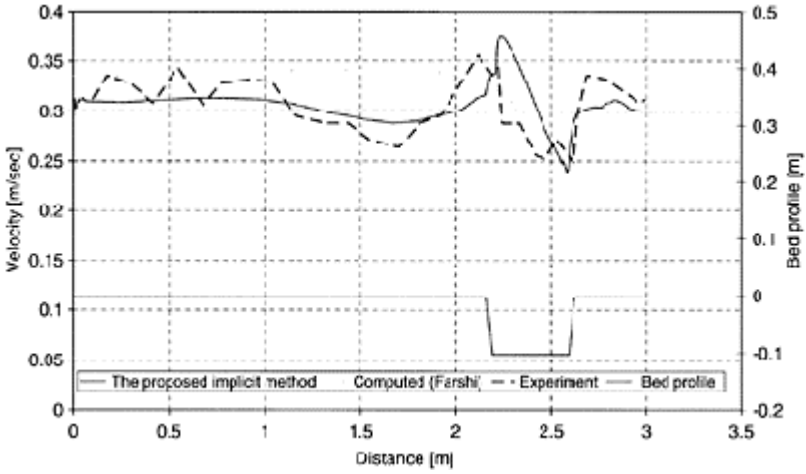

Figure 5. Experiment A5: Velocity distribution in cross-section 7.

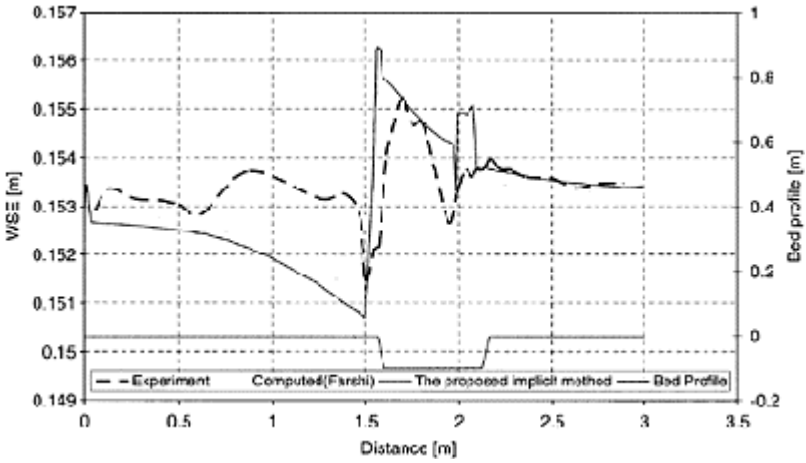

Figure 6. Experiment A5: Water surface elevation in cross-section 5.

the computed and measured results can be seen. Stein (1990) and Wenka (1992) are not successful to simulate the velocity distribution in this region by their turbulence models. Minh Duc (1998) has also simulated this variant and could reproduce the velocity distribution at the right hand side of the main channel well but his model could not achieve good agreement at the left side.

In practical applications, it is most interested to compute the water surface elevation (WSE). In such a complex flow system, correctly computing the WSE is also a difficult task. In Figure 6, the computed values and measured data are compared in cross-section 5 for test case A5.

5 CONCLUSIONS

A new implicit numerical scheme has been introduced and applied for SWE. The method can be applied on unstructured grids with triangular cells. In addition, a new simple treatment of source terms is proposed. The results show a good agreement of the proposed method with the comparable sources. The new method gives a well-computed velocity distribution that could result quite reasonable bed shear stresses. For the high gradient applications, the new method needs more runtime than explicit methods. The main advantage of this method is for the quasi steady state conditions in which the much higher time steps could be used.

REFERENCES

Anastasiou, K., and Chan, C.T. (1997). "Solution of the 2D shallow water equations using the finite volume method on unstructured triangular meshes." *International Journal for Numerical Methods in Fluids*, 24(11), 1225–1245.

Barth, T.J. "Recent developments in high order K-Exact reconstruction on unstructured meshes." *31st Aerospace Sciences Meeting & Exhibit*, Reno, NV

Beam, R.M., and Warming, R.F. (1976). "An implicit finite difference algorithm for hyperbolic systems in conservation law form." *Journal of Computational Physics*, 22, 87–110.

Beffa, C., and Connell, R.J. (2001). "Two-Dimensional Flood Plain Flow. I:Model Description." *Journal of Hydrologic Engineering, ASCE*, 6(5), 397–405.

Bermudez, A., Dervieux, A., Desideri, J.-A., and Vazquez, M.E. (1998). "Upwind schemes for the twodimensional shallow water equations with variable depth using unstructured meshes." *Computer methods in applied mechanics and engineering*, 155, 49–72.

Brufau, P., Vazquez-Cendon, M.E., and Garcia-Navarro, P. (2002). "A numerical model for the flooding and drying of irregular domains." *Int. J. Numer. Meth. Fluids*, 39, 247–275.

Coirier, W.J. (1994). "An adaptively-refined, cartesian, cell-based scheme for the Euler and Navier-Stocks equations," The University of Michigan.

Delis, A.I., Skeels, C.P., and Ryrie, S.C. (2000). "Evaluation of some approximate Riemann solvers for transient open channel flows." *Journal of Hydraulic research*, 38(3), 369–382.

Erduran, K.S., Kutija, V., and Hewett, C.J.M. (2002). "Performance of finite volume solutions to the shallow water equations with shock-capturing schemes." *Int. J. Numer. Meth. Fluids*, 40, 1237–1273.

Farshi, D. (2002). "Two-Dimensional Simulation of Sediment Transport on Unstructured Mesh," German Armed Forces University Munich, Munich.

Fennema, R.J., and Chaudhry, M.H. (1989). “Implicit methods for two-dimensional unsteady freesurface flows.” *Journal of Hydraulic Research*, 27(3), 321–332.
Jameson, A., and Turkel, E. (1981). “Implicit schemes and LU decompositions.” *Mathematics of Computation*, 37(156), 385–397.
Jha, A., Akiyama, J., and Ura, M. (1996). “A fully conservative Beam and Warming scheme for transient open channel flow.” *Journal of Hydraulic Research*, 34(5), 605.
Klonidis, A.J., and Soulis, J. (2001). “An implicit scheme for steady two-dimensional free-surface flow calculation.” *Journal of Hydraulic Research*, 39(4), 393–402.
Komaie, S. (2003). “A Robust Implicit Shallow Water Equations Solver on Unstructured Grids,” German Armed Forces University Munich, Munich.
MacCormack, R.W. (1982). “A numerical method for solving the equations of compressible viscous flow.” *AIAA Journal*, 20(9), 1275–1281.
MacCormack, R.W., and Paullay, A.J. (1972). “Computational efficiency achieved by time splitting of finite difference operators.” *paper 72–15A*, AIAA, San Diego.
MinhDuc, B. (1998). “Berechnung der Stömung und des Sedimenttransports mit einem tiefengemittelten numerischen Verfahren (in German)," Universität Fridericiana zu Karlsruhe (TH), Karlsruhe.
Nujic, M. (1995). “Efficient Implementation of Nonoscillatory Schemes for the Computation of Free-Surface Flows.” *Journal of Hydraulic Research*, 33(1), 101–111.
Panagiotopoulos, A.G., and Soulis, J. V (2000). “Implicit biadiagonal scheme for depth-averaged free-surface flow equations.” *ASCE, Journal of Hydraulic Engineering*, 126(6), 425–436.
Roe, P.L. (1981). “Approximate riemann solvers, parameter vectors, and difference schemes.” *Journal of Computational Physics*, 43, 357–372.
Sanders, B.F. (2001). “High-resolution and non-oscillatory solution of the St.Venant equations in nonrectangular and non-prismatic channels.” *Journal of Hydraulic Research*, 39(3), 321–330.
Schröder, P.M. (1996). “Zur numerischen Simulation turbulenter Freispiegelströmungen mit ausgeprägt dreidimensionaler Charakteristik (in German),” Aachen University, Aachen.
Stein, C.J. (1990). “Mäandrierende Fließgewässer mit überströmten Vorländern-Experimentelle Untersuchung und numerische Simulation (in German),” Aachen University, Aachen.
Toro, E.F. (2001). *Shock-Capturing Methods for Free-Sufrace Shallow Flows*, Wiley and Sons Ltd.
Tseng, M.H., and Chu, C.R. (2000). “Two-dimensional shallow water flows simulation using TVD-MacCormack scheme.” *Journal of Hydraulic Research*, 38(2), 123–131.
Valiani, A., Caleffi, V., and Zanni, A. “Finite Volume Scheme for 2D Shallow-Water Equations Application to The Malpasset Dam-Break.” *CADAM*, Zaragoza.
Warming, R. F, and Beam, R.M. “On the construction and application of implicit factored schemes for conservation laws.” *Proc. Symposium on Computational Fluid Dynamics, SIAM-AMS, Vol 11*, New York, 85−129.
Wenka, T. (1992). “Numerische Berechnung von Strömungsvorgängen in naturnahen Flußläufen mit einem tiefengemittelten Modell (in German),” Universität Fridericiana zu Karlsruhe (TH), Karlsruhe.
Yoon, S., and Kwak, D. (1992). “Implicit Navier-Stokes solver for three-dimensional compressible flows.” *AIAA Journal*, 30(11), 2653–2659.
Zhao, D.H., Shen, H.W., Lai, J.S., and Tabios III, G.Q. (1996). “Approximate Riemann solvers in FVM for 2D hydraulic shock wave modeling.” *Journal of Hydraulic Engineering, AISC*, 122(12), 692–702.

Supercritical flow in channel intersections

N.Rivière & R.J.Perkins
LMFA, Lyon, France

River Flow 2004—Greco, Carravetta & Della Morte (eds.)

ABSTRACT: Experiments have been conducted in a configuration formed by the intersection of four identical channels. Each channel is made from glass and measures 2m long and 0.3m wide; the slope of each channel can be fixed independently, as can the flow rate in the channel. In this configuration the flow enters the intersection through one of the channels, and is evacuated by the other three. The results show that, immediately after entering the intersection, the incoming flow behaves as a free, rectangular supercritical jet. The surface profiles of the jet as it collapses correspond well to the theoretical solution obtained for the classical dam break problem. Close to the exit from the intersection the walls of the side channels have an important influence on the flow in the main channel, and the dam break solution has to be corrected in a way that is still to be precise.

1 INTRODUCTION

During severe flooding of urban areas, the water in the streets can reach a depth of a metre or more, causing severe economic losses, and possible loss of life. We therefore need to be able to predict flood propagation in urban areas, in order to design suitable protection (possibly by directing the flood waters to previously identified sacrificial zones) and to develop reasonable and realistic emergency planning. Because of the complexity of the problem, and the number of different situations that have to be considered, the most suitable approach is by numerical simulation, usually by solution of the St Venant equations. This approach has the additional advantage that as more and more detailed information on street geometry becomes available through GIS databases, this information can be readily—indeed automatically—included in the numerical model. In the simplest possible configuration, the city street can be considered as a rectangular channel with a free surface flow, and there have now been many simulations of flood propagation in urban areas based on this approach. In general, we can conclude from

these studies that the St. Venant equations provide a reasonable model for the flow in individual streets, but that they are not well-suited to flow in street intersections, where the flow is necessarily strongly three-dimensional, and the slope of the free surface can be significant. Unfortunately for these numerical simulations, street intersections often play a crucial role in determining how the incoming flow is distributed between the various outlets, and in determining the corresponding depths. The failure to model these intersections correctly can therefore have serious consequences for the overall quality of the modelling.

There have been very few experimental studies of flow in channel junctions, and even fewer for conditions that correspond to those encountered in city streets. Most studies have been related to flow distribution in networks of irrigation channels, where the intersection is usually formed by the junction of three channels (in the form of a T or a Y), and where the flow regime is sub-critical. They can be divided in two groups: the junctions with two upstream reaches and only one downstream, and the bifurcations, with only one upstream reach.

In urban applications the basic configuration is more likely to be a cross, with one or possibly two of the streets feeding the junction. The slope of a city street can easily be of the order of a few percent, so it is quite common for the flow regime to be supercritical in certain areas.

Most of the available literature describes experimental or numerical studies of subcritical flow in simple channel junctions. For example Weber et al. (2001) provide a complete set of experimental data for a 90° junction, including water depth, surface and bulk velocity fields and turbulence characteristics. The available analytical models are mainly based on mass, momentum and energy balances (see, for example, Gurram and Karki (1997) or Shabayek and Hicks (2002)). Usually, this approach requires additional assumptions such as a uniform depth of the flow in the whole intersection, a critical Froude number in the contraction zone or a hydrostatic pressure distribution.

Such assumptions will not usually be valid for flooding in urban areas. Empirical models have also been proposed, in which several physical phenomena are modeled by a single coefficient, such as a contraction coefficient (Hsu et al., 1998). Again, these methods depend strongly on the experimental conditions and are, as far as we are aware, restricted to the subcritical regime. In the supercritical regime, Greated (1966), and Schwalt and Hager (1994), focus on the development of the surface wave, whereas Hager (1989) also measures velocities but in quasi-constant depth flows.

Even fewer studies have been devoted to channel bifurcations, and the introduction of a third outlet channel complicates the problem considerably, especially for analytical studies. Ramamurthy and Satish (1988) derive an expression for the flow division in short open-channel branches, based on momentum and mass conservation. This gives the upstream/branch discharge ratio as a function of the channel widths ratio and the downstream main channel Froude number. The model assumes a hydrostatic pressure distribution, negligible head losses in the vicinity of the intersection and is restricted to branch Froude numbers higher than 0.35 and upstream Froude numbers smaller than 0.7. For rectangular equal width channels, the model was improved to become independent of the branch channel Froude number (Ramamurthy et al., 1990). To avoid the need for such assumptions, other researchers have proposed empirical models. Krishnappa and Seetharamiah (1963) provide an experimental correlation for the discharge ratio as a

function of the upstream Froude number and the channel depths ratio, which is restricted to 90° angle separations and to subcritical upstream flows and supercritical branch flows. Nougaro and Boyer (1974) provide a diagram giving the discharge ratio valid on a wide range of Froude numbers (sub- and supercritical) and of junction angles, but they show a strong dependency of the results on the downstream conditions (Nougaro et al, 1975). More recently, there have been several 1D and 2D numerical simulations of flow in channel junctions. Shettar and Murty (1996) used a 2D code with a k-ε closure to study a 90° bifurcation. The widths of the main channel and the branch are identical and the depth to width ratio is approximately 0.15. Their results compare well with experimental measurements available in the literature. Khan et al. (2000) adopt a mixing length model, which is more applicable for large-scale problems. All these studies are restricted to subcritical flows, avoiding the problems arising in the application of suitable boundary conditions for supercritical flows. Finally, Nania et al. (1998) simulate flow in the intersection of 4 channels (2 inlets—2 outlets), using 1D and 2D codes, for subcritical and supercritical flows.

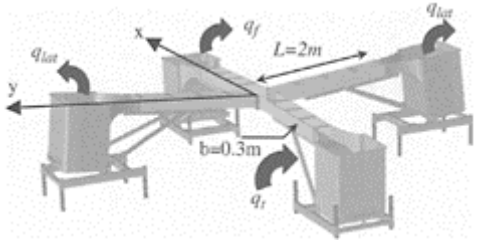

Figure 1. Experimental set-up.

2 EXPERIMENTAL SET-UP

The set-up consists of an intersection of four identical channels (fig. 1). Each channel is made from glass, with a length L=2m and width b=0.3m. The slopes of the four channels can be fixed independently, and each channel can function either as an inlet or an outlet for the intersection. In this study, only one channel functions as an inlet, with a discharge q_t that varies from 2 to 20l/s; the x-axis is therefore aligned with this channel. The flow leaves the intersection via the other three channels—two lateral channels (aligned with the y axis) and one longitudinal channel (x-axis). The flow enters the inlet channel through a honeycomb and then passes under a sluice gate, which serves to impose the upstream water depth and hence the Froude number. The outlet conditions are free. Discharges are measured by electromagnetic flowmeters; the discharge from the longitudinal channel was also calculated by measuring the filling time of the outlet reservoir. Water depths were measured using a moveable point gauge with an accuracy of ±0.15mm. This last technique becomes unusable in the strongly perturbed zones close to the intersection.

3 ANALOGY BETWEEN A SUPERCRITICAL JET DEVELOPMENT AND A DAM BREAK

The flow in the inlet channel is supercritical as it enters the intersection, and it traverses the intersection as a free, supercritical, jet. Hager and Yasuda (1997) studied the development of a supercritical jet in a semi-infinite expansion, and showed that the jet profile was similar to the evolution of the water surface during the breaking of a dam on a dry bed. In their study, the upstream Froude number was greater than 3, and the initial section of the jet was square; as a result the depression wave reaches the centerline of the jet rather rapidly, and the theory becomes rather complicated. In this study the ratio of the upstream depth to

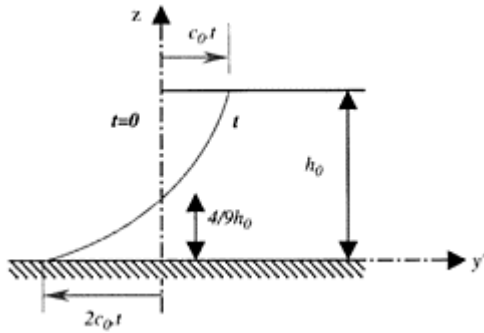

Figure 2-a. The unsteady problem: the dam-break.

the channel width (h_0/b) is much smaller than 1, and so the dam break model is more applicable.

Consider a dam holding back a semi-infinite reservoir of initial depth h_0 (fig. 2-a); at t=0 the dam fails and the water surface then evolves as (Stoker, 1957):

$$z = \frac{1}{9g}\cdot\left(\frac{y'}{t} + 2.c_o\right)^2 \tag{1}$$

where t is the time and c_0 is the velocity of propagation of the depression wave in the reservoir:

$$c_o = \sqrt{g h_0} \tag{2}$$

The water propagates over the dry bed with a velocity $2c_0$, whilst the depth of the water at the site of the dam (y'=0) remains constant, equal to z=4h_0/9 (fig. 2-a). We can apply this model to compute the evolution of the jet in the intersection (fig. 2-b). Upstream of the intersection (x'<0) the flow is confined by the walls of the rectangular channel; within the intersection the water surface is modified by the propagation of dam break waves into the two lateral channels, which we can model using the solution for unsteady case, by making the transformation t=x'/U_0.

To justify the assumption of a semi-infinite body of fluid upstream of the breaking wave we have to ensure that there is no interaction between the two negative waves produced by the flow into each of the lateral channels. This means that $c_0.t<b/2$, or, in other words $x/Fr_0<b/2$; since the length of the intersection (x_{max}) is equal to b we can write: $Fr_0>2$.

Two configurations have been studied, with the characteristics given in table 1.

The surface profile in the side channel is plotted in figure 3, in dimensionless form $(z/h_0$v $y/(x'/Fr_0))$

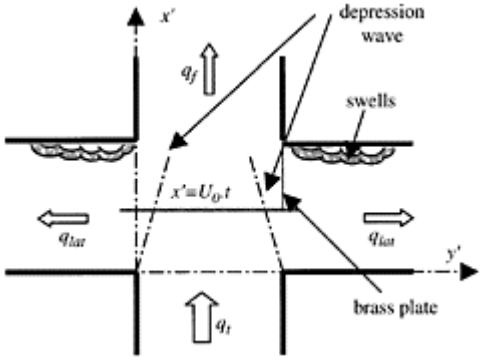

Figure 2-b. The spatial problem: the jet development.

Table 1. Main characteristics of the two jets ($Fr_0>2$).

Configuration	5%–0%	1%−1%
q_t (m^3/s)	0.01	0.01
bed slope S_{0x}	0.05	0.012
bed slope S_{0y}	0	0.012
h_0 (cm)	2.06	2.8
Fr_0	3.6	2.16
h_0/b	0.14	0.2

for different values of the dimensionless distance travelled by the jet (x'/Fr_0). The error bars plotted on the first figure are indicative of the errors for the other profiles. The strong axial velocities in the jet create intense eddying motions on the walls of the side channels (fig. 2-b) which increase the water level and limit the applicability of the model to $x'/b< 0.7–0.8$.

The dimensionless results for the two conditions are in close agreement with each other, and with the theoretical curve based on the dam break model. The increase in z' observed for $y'<0$ in the 5%–0% configuration can be explained by the difficulty of

generating a flow in a horizontal canal; this effect disappears when the canal is inclined (the 1%−1% configuration).

In the following section we will develop a model for the flow distribution in the different channels, based on the surface profiles given by the dam break model.

4 A MODEL FOR THE FLOW DISTRIBUTION

The cross section of the axial flow in the intersection decreases as the jet advances. By continuity, the lateral flow q_{lat} must be given by the flow that has left the jet;

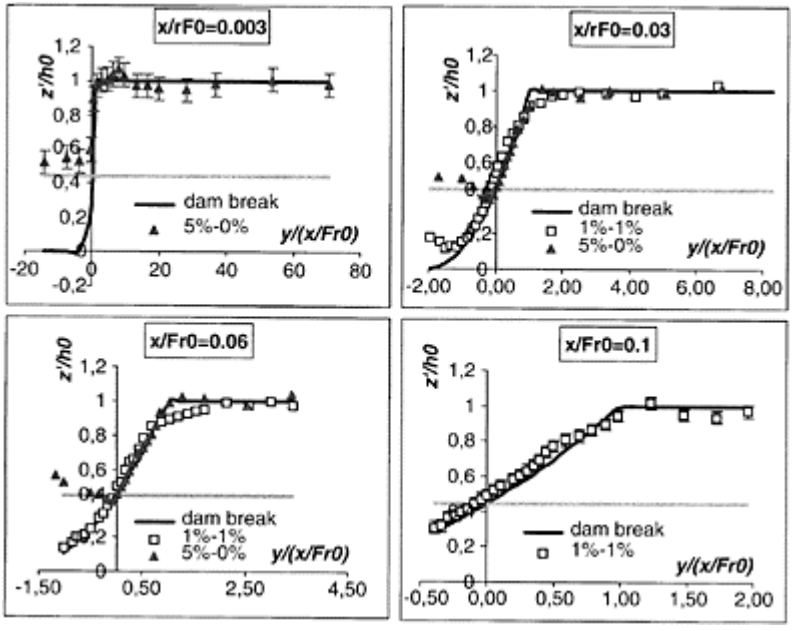

Figure 3. Theoretical and experimental surface profiles at different locations within the intersection (S_0=1, 2% et 5%).

at any distance x' from the entrance to the intersection we can therefore write:

$$q_{lat}(x') = U_0 \cdot \left[\frac{c_0 x}{U_0} h_0 - \int_0^{c_0 x/U_0} \frac{1}{9g} \left(\frac{y'}{x/U_0} + 2c_0 \right)^2 dy' \right] \tag{3}$$

from which we obtain:

$$\frac{q_{lat}(x')}{q_{tot}} = \frac{8}{27} \frac{x'}{b} \frac{1}{Fr_0} \tag{4}$$

The total flow in the lateral canal is given by evaluating this expression for $x'=b$:

$$\frac{q_{lat}}{q_{tot}} = \frac{8}{27Fr_0} \qquad (5)$$

The strong eddying motions around $x'=b$ modify the structure of the jet significantly, and hence tend to invalidate the theoretical model for the lateral flow. To test the influence of these motions thin brass plates were installed at the downstream end of the intersection, so as to extend the walls of the outlet channel and isolate the flow from the influence of the stagnation regions (fig. 2-b). The lateral flow rates were measured for different plate lengths, and the results are shown in figure 4. These curves confirm that the theoretical

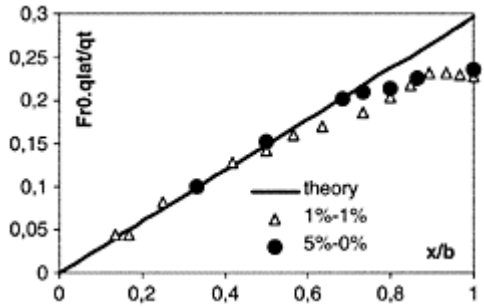

Figure 4. Influence of the stagnation regions on the applicability of the theoretical model.

model provides a good estimate for the lateral flows provided that the stagnation regions do not influence the flow ($x'/b<0.7$). On the other hand, the greater the zone of influence ($x'/b>0.7\rightarrow1$), the more the side flow is diminished, relative to its theoretical value.

The principle explanation for this reduction in flow rate is that the increased surface levels in the stagnation regions serve to drive flow back out of the side channels into the main channel; as a result, equation (5) overestimates the total lateral flow by about 25% in both configurations.

In order to assess the accuracy of equation (5) over a much wider range of flow rates we have compared the measured $q_{lat-exp}$ and theoretical $q_{lat-theo}$ values for a range of different conditions. The results are shown in figure 5, with the measured flow rates plotted as a function of the theoretical value (eq. 5). This figure shows that the different data sets can be grouped together according to the slope of the inlet channel; since the upstream Froude number depends essentially on this slope, this is equivalent to grouping them according to Froude number.

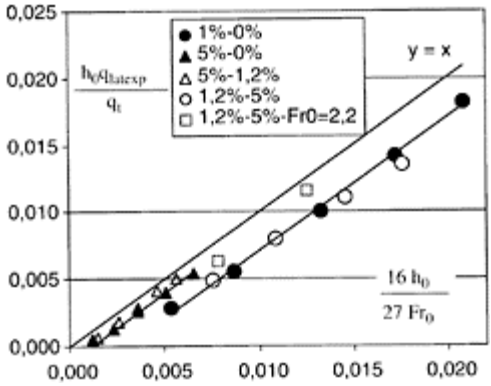

Figure 5. Theoretical (eq. 5) and experimental values of the lateral flow rates for flow conditions in the range 2–20l/s.

The first two data sets are for a longitudinal slope of 5% with an average Froude number $F_{r0}\approx3.5$, and side slopes of either $S_{0y}=0\%$ or $S_{0y}=1.2\%$. The experimental points are very close to the theoretical values, and the difference does not seem to depend on S_{0y}. This probably remains true provided that the water level in the exit canal does not impede the development of the jet within the intersection; this was always observed to be the case for $S_{0y}\geq0$. For any given upstream Froude number the difference between theoretical and measured values varies as α/h_0, where α is a constant. This dependence should be related to the capacity of water in the side channels to flow back into the main channel, above the level $z'=4/9h_0$.

The other data sets correspond to lower values of the longitudinal slope, with Froude numbers less than 2. For $S_{0x}=1\%$, we have $F_{r0}\approx1.6$ and $S_{0y}=0\%$, and for $S_{0x}=1.2\%$, $F_{r0}\approx1.8$ and $S_{0y}=5\%$. The measured flow rates are rather less than those predicted by the dam break model, principally because of the influence of the stagnation regions on the downstream walls of the lateral channels; this effect depends strongly on the upstream Froude number, and increases as the Froude number decreases. For example, for the configuration $S_{0x}=1.2\%$, $S_{0y}=5\%$ the Froude number was increased to $F_{r0}\approx2.2$ (by lowering the upstream sluice gate) and the measured flow rate becomes closer to the theoretical value.

These observations are based on a rather limited number of data sets, and more results are needed, both to confirm these preliminary conclusions, and to develop an expression for the dimensionless coefficient α as a function of the different parameters that characterise the configuration.

5 CONCLUSIONS

Flow rates and water levels have been measured in the intersection of four independent channels. Supercritical flow enters the intersection from one of the four channels, and is

evacuated by the other three. Within the intersection the incoming flow behaves as a super-critical jet. The evolution of the jet can be modelled by the propagation in the side channels of waves similar to those obtained by the solution of the dam break problem. This result has been used to develop an expression for the flow rates in the three channels; the theoretical expression agrees well with the measured flow rates for high inlet Froude numbers, but overestimates the lateral flow rates for lower Froude numbers. The principle reason for this is the development of stagnation regions on the downstream walls of the side channels, which drive fluid back into the main channel. This has been conserved by the installation of vertical plates to isolate the stagnation regions from the flow in the main channel. Further experiments are necessary to determine the exact dependence of this effect on upstream Froude number.

ACKNOWLEDGEMENTS

The experimental installation was designed and assembled by P.Dutheil, and we gratefully acknowledge his contribution to the project. The research was funded by the French CNRS (SPI-ACI jeune chercheur “Hydraulique en milieu urbain”, 2002) and by the French Environment Ministry under the RIO2 Program “Estimation des écoulements de surface pour une crue extreme en milieu urbanisé”.

REFERENCES

Greated C.A. 1968. Supercritical flow through a junction. *La Houille Blanche* 23(8), 693–695

Gurram S.K., Karki K.S. 1997. Subcritical junction flow. *Journal of Hydraulic Engineering* 123(5):447–455.

Hager W.H. 1989. Supercritical flow in channel junctions. *Journal of Hydraulic Engineering* 124(1):595–617.

Hager W.H.,YasudaY. 1997. Unconfined expansion of super-critical water flow. *Journal of Engineering Mechanics* 123(5):451–457.

Hsu D.C., Wu F.-S., Lee W.-J. 1998. Flow At 90° Open-Channel Equal-Width Junction. *Journal of Hydraulic Engineering* 124(2):186–191.

Khan A.A., Cadavid R., Wang S.S.-Y. 2000. Simulation of channel confluence and bifurcation using the CCHE2D model, *Proc. Instn. Civ. Engrs Water and Mar. Eng,* 142: 97–102, June 2000.

Krishnappa G., Seetharamiah J. 1963. A new method of predicting the flow in a 90° branch channel. *La Houille Blanche* 7:775–778

Nania L., Gomez M, Dolz J. 1998. Modelacion de la escorrentia pluvial en cruces de calles, *Proc. XVIII Congreso LatinoAmericano de Hidraulica:* 233–242, Oxaca, Mexico, October 1998 *(in spanish)*.

Nougaro J., Boyer P. 1974. Sur la separation des eaux dans les derivations de canaux a section rectangulaire. *La Houille Blanche* 3:199–203 *(in french)*

Nougaro J., Boyer P., Claria J. 1975. Comportement d’une derivation de canaux lorsque les biefs aval sont pourvus de retenues. *La Houille Blanche* 4:267–275 *(in french)*

Ramamurthy A.S., Tran D.M., Carballada L.B. 1990. Dividing flow in open channels. *Journal of Hydraulic Engineering* 116(3):449–455.

Ramamurthy A.S., Satish M.G. 1988. Division of flow in short open channel branches. *Journal of Hydraulic Engineering* 114(4):428–438.

Schwalt M., Hager W.H. 1995. Experiments to supercritical junction flow. *Experiments in Fluids* 18:429–437.

Shabayek, S., Hicks. 2002. Dynamic model for Subcritical Combining flows in channel Junctions. *Journal of Hydraulic Engineering* 128(9):821–828.

Shettar A.S., Murty K.K. 1996. A numerical study of division of flow in open channels. *Journal of Hydraulic Research* 34(5):651–675.

Stoker J.J. 1957. *Water Waves: the mathematical theory with applications*, New York: Interscience Publishers, Inc.

Weber L.J., Schumate E.D., Mawer N. 2001. Experiments on flow at a 90° open channel junction, *Journal of Hydraulic Engineering* 127(5), 340–350.

Factors on flood problems in Ubon Ratchathani province, Thailand

C.Chinnarasri, U.Israngkura & S.Jarukamol
Water Resources Engineering Research Lab. (WAREE), Department of Civil Engineering,
King Mongkut's University of Technology Thonburi, Bangkok, Thailand

River Flow 2004—Greco, Carravetta & Della Morte (eds.)

ABSTRACT: Lowland areas alongside of Mun River in Ubon Ratchathani Province, Thailand are flooded frequently. The investigation on the significance of the flood causing factors was done by calculating the river water levels at different magnitudes of these factors. The combination of these magnitudes resulted in 108 study cases. Flood hydrographs from river tributaries were constructed by NAM Model using 30 day rainfall over each basin. Mekong River water levels were analyzed from measured data at Kong-Chiam gauging station. The discharges and water levels at different locations along the river reach were computed by MIKE 11 Model covering 30 days period. The results showed that the flood flow at station M7 was the most significant factor as it could produce flooding on the target area when its magnitude was at only 2 year return period or 2,500m^3/s. and when its magnitude was increased the river water level then increased considerably.

1 INTRODUCTION

Ubon Ratchathani is a province in the northeastern region of Thailand. Mun River which is the largest river in this region flows across this province from west to east approximately and discharges into Mekong River at Khong Jeam district. Lowland areas alongside the river reach from the confluence of Chi River to Mekong River as shown in Figure 1 are flooded very frequently.

The latest flood in August 2002 resulted in a damage of about US$ 47 million. The major causes of flooding, apart from the lowland topography, are the large floods from the upstream watershed and from the river tributaries along the river reach and the

backwater effect from Mekong River. In planning a flood mitigation schetne for this area, it is necessary that the boundary of the flooded area and the flood levels under different hydrologic conditions as well as the significance of each hydrologic factor must be identified so that the proper mitigation measure could be established. The objectives of this study are to determine the area which is subjected to severe flooding, the combination of hydrologic events at the commencement of flooding, and the most significant hydrologic factors which causes flooding.

2 METHODOLOGY

2.1 *General*

The flood hydrographs from the upstream watershed, the lateral inflow hydrographs from river tributaries

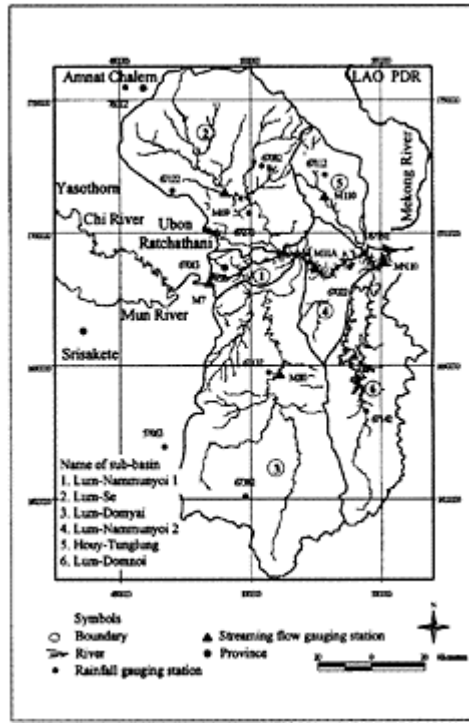

Figure 1. Study area with streamflow and rainfall gauging stations.

Table 1. Peak flow at M7 and peak water levels at Klong Jeam.

Return periods (yr.)	Peak flow at M7 (m^3/s)	Peak WL Khong Jeam (m.MSL)
2	2500.0	102.65
5	3918.0	104.01
10	4856.7	104.50
20	5757.3	105.76
50	6922.9	106.87
100	7796.4	107.70

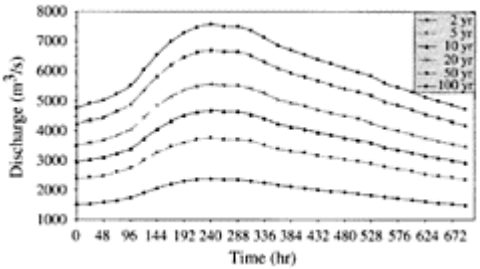

Figure 2. Flood hydrographs from upstream watershed (at M7).

and the stage hydrograph in Mekong River at various return periods were determined then the stage hydrographs along the river reach as caused by several combinations of those three hydrologic factors were derived. The peak stage profiles were then plotted and the areas subjected to frequent floodings were identified. The hydrologic conditions which lead to the commencement of flooding over this area were observed. The hydrologic factor which caused flooding at the lowest return period and which caused the flood stage rising sharply when its magnitude was increased would be considered as the most significant factor.

2.2 *Flood hydrographs from upstream watershed and Mekong River water level*

Flood Hydrographs from the upstream watershed were derived from the recorded flow data at gauging station M7 which is just downstream of Chi River confluence and has a drainage area of about 106,673sq.km. The derived hydrograph of a return period covered a length of 30 days and had the peak discharge equal to the value at that return period. The position of peak discharge and the shape of the hydrograph were made nearly similar to the 30 days hydrograph of large flood in 2001. The peak discharges at various return periods are as shown in Table 1. Figure 2 shows the derived flood hydrographs from the upstream watershed which were used in the study.

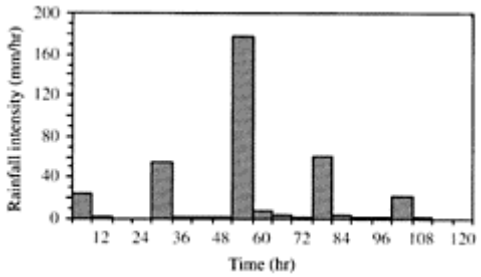

Figure 3. Examples of synthesized rainfall over Lam-Se sub-basin.

The Mekong River water levels at various return periods were derived from the recorded data at Khong Jeam gauging station at the mouth of Mun River. The peak water levels at various return periods are as shown in Table 1. As observed from historical data, during severe flood occurrences the water level varied just slightly so in this study it was assumed to be constant at the value of the specified return period.

2.3 *Flood hydrographs from tributary river basins*

The drainage area of 12,751sq.km. from M7 to Mekong River consists of 6 sub-basins. Their boundaries together with the rainfall and streamflow gauging stations are as shown in Figure 1. Since there were no streamflow gauging stations at the outlets of these subbasins, their outflow flood hydrographs which drain into Mun River had to be determined from a rainfall-runoff model. NAM model developed by the Danish Hydraulics Institute (DHI) was used in this study.

This model was calibrated and verified by the data of three watersheds above stations M69, M80, and M110 (see Figure 1). The model parameters of each basin obtained from these processes were correlated with some physical characteristics of the watershed and the best relationships were used to determine the Nam parameters for each subbasins.

The rainfall of a return period which was used to generate runoff from a sub-basin was the areal average maximum 5-day rainfall which contained maximum 1 day and 3 days rainfall of that return period and had a time distribution pattern similar to the average pattern of heavy storms over this region. Figure 3 is the example of the synthesized rainfall.

2.4 *Computation offlood stages along the river*

The flood stages along the river reach as caused by several combinations of those three hydrologic factors were computed by the one-dimensional hydrodynamic flood routing model which is a module of MIKE 11 computer program package developed by the Danish Hydraulics Institute (DHI 1982). The model

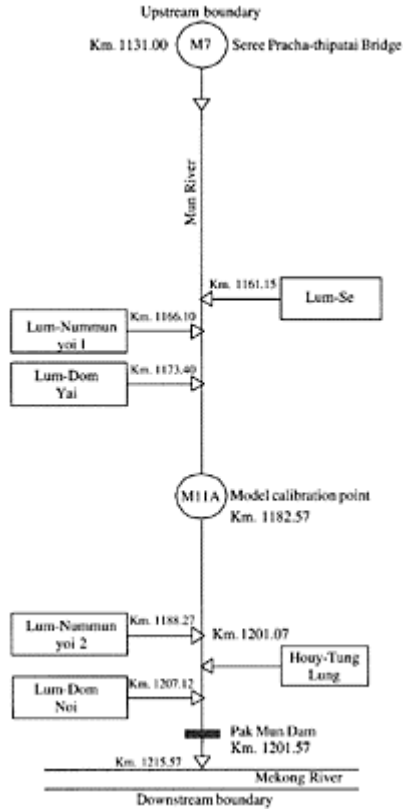

Figure 4. Model configuration.

configuration cover the river reach of about 80km. is as shown in Figure 4. River cross sections spacing at about 3km. interval were used in the computation. River section at Sta. 1131+00km. where M7 is located is the upstream boundary.

The model was calibrated and verified by the observed hydrologic data during August 1 to October 31, 1996 and during July 1 to September 31, 1997 respectively. Figure 5 shows the computed water levels at gauging station M 11 A from model calibration and verification against the observed water levels.

The model was then used to compute the flood stage hydrographs under several combinations of the three hydrologic factors.

3 RESULTS

3.1 *Flood prone area*

The peak flood level profiles under each combination of hydrologic factors were plotted as shown in Figure 6 as an example. From these plots, it could be observed

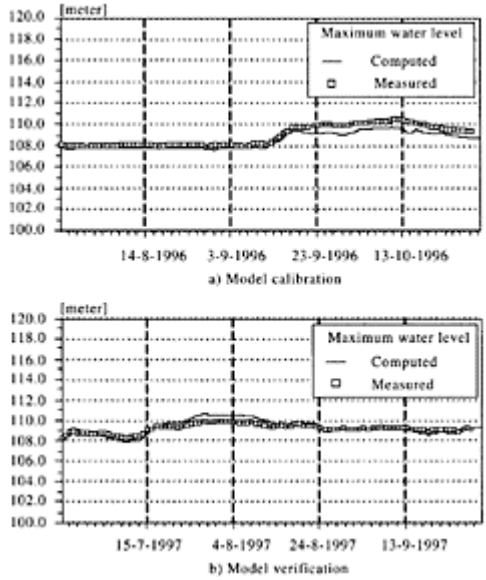

Figure 5. Calibration and verification of MIKE-11 hydrodynamic model.

that the area subjected to severe floodings lies between River Sta. 1133+050km. to Sta. 1161+150km.This flood prone area lies in the urban and semi-urban area in Muang District and Warin Chamrab District.

3.2 *Peak flood stage and flood commencement conditions*

The peak flood stage at River Sta. 1133+050km. which is at the upstream end of the flood prone area was used as the index to indicate the flood harshness over this area. Its values under several study cases are as shown in Table 2. As can be observed from Figure 6, large area on both banks of the river would be flooded when the water level at this station is at +114m.MSL or higher. When the upstream flood hydrograph at M7 is at 2 year return period this condition will commence when the flood hydrographs from tributary watersheds are at 10-year return period and the Mekong water level is at 100-year return period. But when the upstream flood hydrograph increases to 5-year return period, whatever the Mekong water level may be, the flooding would always occur even when the river tributary flood hydrographs were at the return period lover than 2 year. Combinations of hydrologic events on the right and below the bold line in Table 2 are those which will produce severe floodings.

3.3 *Significant level of each hydrologic factor*

As can be seen from Table 2, when the flood at M7 is at a magnitude lower than or equal to the flood magnitude at 2-year return period the chances of the area being flooded is

very rare, i.e., it will occur only when the lateral inflow is at the magnitude of up to 10-year return periods and the water level in Mekong reaches the 100-year return periods level but when the upstream flood magnitude increases to 5-year return period flooding could occur even there in very low lateral inflow. This indicated that the upstream flood is more significant than the lateral inflow flood and the Mekong water level.

Table 2. Peak flood levels at Sta. 1133+050km.

Return Period (yr)		Return Period of Lateral Inflow (yr)					
M7 Flood	Mekong River stage	2	5	10	20	50	100
2	5	113.68*	113.79	113.84	113.92	114.07	114.21
	20	113.71	113.83	113.88	113.96	114.11	114.25
	100	113.82	113.94	113.99	114.07	114.22	114.37
5	5	115.89	115.99	116.03	116.09	116.16	116.22
	20	115.91	116.01	116.05	116.11	116.18	116.25
	100	115.98	116.08	116.12	116.18	116.25	116.32
10	5	117.07	117.16	117.19	117.25	117.30	117.35
	20	117.09	117.18	117.22	117.27	117.32	117.38
	100	117.15	117.23	117.27	117.32	117.38	117.43
20	5	118.09	118.17	118.20	118.25	118.27	118.35
	20	118.10	118.19	118.22	118.27	118.32	118.37
	100	118.15	118.23	118.27	118.32	118.36	118.41
50	5	119.29	119.37	119.41	119.45	119.49	119.53
	20	119.31	119.39	119.42	119.47	119.51	119.54
	100	119.35	119.42	119.46	119.50	119.54	119.35
100	5	120.13	120.20	120.24	120.28	120.32	120.35
	20	120.14	120.22	120.25	120.29	120.33	120.37
	100	120.17	120.25	120.28	120.33	120.36	120.40

Notes. 1)* Water level in m. MSL
2) Flood producing conditions are under the bold line

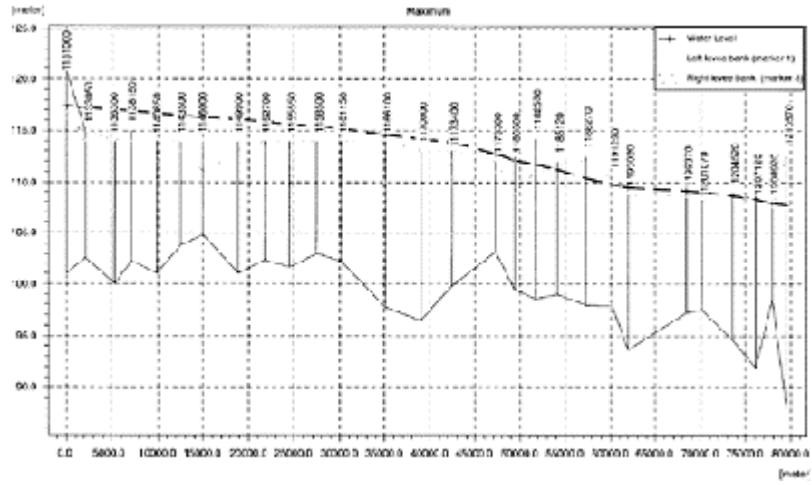

Figure 6. Peak flood level profile: 5-yr flood at M7, 10-yr lateral inflow and 100-yr Mekong River level.

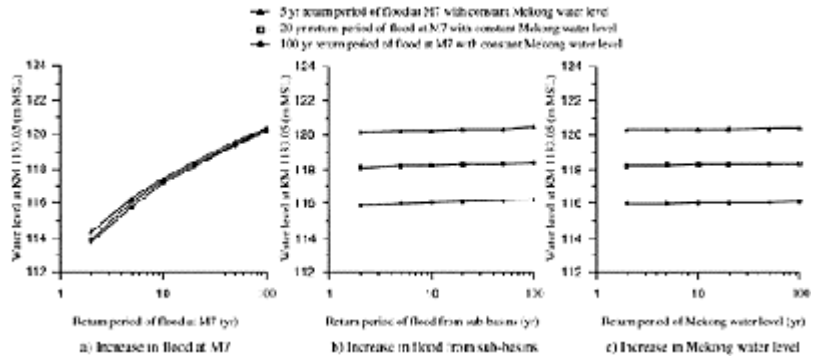

Figure 7. Increase in flood level with increase in return period of a factor.

Figure 7 shows the effects on flood water level as caused by increasing the return period of one factor while holding the other two factors constant at a return period. For the same increase in return period, the increase in upstream flood magnitude resulted in the largest increase in flood level while the increase in Mekong water level yielded the least increment.

From these investigations, it is justified to rank the flood from upstream watershed as the must significant flood causing factors and the Mekong water level as the least significant one.

4 CONCLUSIONS

It could be concluded from this study that:

1) The river flood plain where severe flooding occurred lies between River Sta. 1133+050km. and Sta. 1161+150km. just downstream of gauging station M7. Larger part of this area is the urban or semi-urban area in Muang district and Warin Chamrab district of Ubon Ratchathani Province.
2) Severe floods would rarely occur if the flood magnitude at M7 is lower than or equal to 2-year return period flood but would occur when flood magnitude at M7 is at 5-year return period upward even though there is very small amount of lateral inflow and very low water level in Mekong River.
3) As the flood from watershed area above M7 is the most significant flood causing factors, any flood mitigation plan which can reduce this flood to the magnitude at 2-year return period at the optimum cost would be the most desirable one.

REFERENCE

Danish Hydraulic Institute (DHI). 1992. MIKE 11 reference manual. HØrsholm. Denmark: p.469.

Urban fluvial flood modeling using a two-dimensional diffusion wave treatment

D.Yu & S.N.Lane
School of Geogmphy, University of Leeds, Leeds, UK

River Flow 2004—Greco, Carravetta & Della Morte (eds.)

ABSTRACT: This paper applies a 2-D raster-based diffusion wave model to determine patterns of fluvial flood inundation in urban areas using high resolution topographic data. As this is a new application area, the aim of this paper is to explore the effects of model spatial resolution upon estimated inundation extent. Model response shows that even relatively small changes in model resolution have considerable effects upon the predicted inundation extent as well as the flood wave travel time. This is associated with two connected effects: (1) poorer representation of both cell blockage and the associated surface routing process resultant from the smoother floodplain as the mesh is coarsened, where the flow routing is especially complex; and (2) the effects of (1) upon both the water velocities and water levels which in turn determine which parts of the floodplain the flow can actually travel to. Thus, coupling of high resolution data, which can capture small scale variation in topography, to more sophisticated representation of the inundation process will be required in order to obtain effective predictions of flood inundation extent in urban areas.

1 INTRODUCTION

Fluvial flood modeling usually requires the prediction of flows over complex topography. Flow routing over floodplains is known to be highly two-dimensional and notably where strong shear layer develops between the main channel and the floodplain, even three-dimensional (Knight & Shiono, 1996). Two-dimensional, depth averaged models have been extensively described in the engineering literature for some time and are increasingly being applied to natural river-floodplain systems (see the review in Lane, 1998). Indeed, developments have seen two-dimensional models of floodplain flows come into widespread use (Beven, 2000), including TELEMAC-2D (e.g. Galland et al., 1991, Bates et al., 1995) and RMA2 (e.g. Bates et al., 1992, 1995). Traditionally, two-dimensional models have been constrained by the scarcity of detailed topographic data

(Marks & Bates, 2000, Horritt & Bates, 2001). This constraint is being gradually relieved by the emergence of new data capture techniques, particularly in the field of airborne remote sensing, including interferometric synthetic aperture radar (SAR) (e.g. Brackett et al, 1995, Horritt & Bates, 2001), aerial digital photogrammetry (e.g. Biggin & Blyth, 1996, Lane, 2000, Westaway et al., 2001, 2003) and LiDAR (laser induced direction and ranging) (Krabill et al., 1984, Flood & Gutelius, 1997, Marks & Bates, 2000). These new topographic data sources, which can yield synoptic information at a resolution that in some cases is better than 2.0m and a precision that is better than 0.15m, are providing new opportunities for modeling floodplain inundation from both fluvial and pluvial sources.

More recently, raster-based models have gained credence in the modeling of floodplain flow inundation extent (Bates & De Roo, 2000, Horritt & Bates, 200 la, b). This typically uses a one-dimensional representation of channel flow linked to a two-dimensional treatment of flow over the floodplain, commonly involving a diffusion wave treatment. An application of the diffusion wave approach was first reported by Cunge et al. (1976) and similar methods have been used by Estrela & Quanias (1994) and Bechteler et al. (1994). These approaches use an explicit two-dimensional treatment of mass conservation but a highly simplified representation of momentum conservation, commonly based upon determining the magnitude of flow between any two adjacent cells according to the water surface elevation difference and the Manning equation. Bates and De Roo (2000) developed a raster-based model (LISFLOOD-FP) based on this concept and compared it with a relatively coarse resolution (50–250m) two-dimensional finite element scheme. Unlike other models, this model was specifically designed to predict flood inundation and ignored or minimized the representation of processes that were not considered central to the aim (Bates & De Roo, 2000). Tentatively, these results indicated that topography and a basic process representation was more important than a complete process representation for effective prediction of inundation extent. However, issues such as model calibration, friction parameter representation and the differing resolutions of the two models needed to be addressed before these conclusions are confirmed (Horritt & Bates, 2001b). Horritt and Bates (2001b) compared LISFLOOD-FP with a two-dimensional finite-element model (TELEMAC-2D). Though the raster-based and the two-dimensional finite-element models showed similar performance, insufficiently accurate validation data and the lack of friction parameterization data made it difficult to distinguish between the two kinds of model formulations. More recently, the ability of the LISFLOOD-FP model to predict flood extent and flood wave travel times has been compared with a 1D model (HEC-RAS) and a 2D model (TELEMAC-2D) using independent calibration data from hydrometric and satellite sources (Horritt & Bates, 2002). Results revealed that the LISFLOOD-FP model required independent inundated area data for calibration in order to achieve good predictions of inundation extent. It is also debatable as to whether or not raster-based models can provide an adequate representation of inundation velocities and hence the development of inundation through time. In summary, these results suggest that, compared to fully explicit numerical solutions including finite element (e.g. Bates et al., 1992), finite difference (e.g. Gee et al, 1990) and finite volume (e.g. Lane & Richards, 1998) formulations, raster-based models have major advantages in terms of their ease of formulation, computational efficiency and simplified calibration. However, questions remain over their relatively simple

representation of the flow processes, due partially to the poor representation of momentum transfer on the floodplain.

Much existing research into two-dimensional modeling of flood inundation has focused upon relatively rural areas. Wheater (2002) identified the improved representation of urban flooding at both local and catchments scale as one of the key priorities in current fluvial flood modeling practice. Thus, the aim of this paper is to evaluate the extent to which diffusion wave based models can be applied to situations where there is inundation of relatively urbanized areas. This is an interesting application area because potential flood damage is proportionately greater than rural areas and urban flood inundation receives a relatively high political profile. In modeling terms, these areas may also benefit significantly from the availability of high resolution topographic data as urbanization leads to the presence of structural elements on the floodplain which may have significant impacts upon patterns of flood inundation. These may not be well-represented through traditional treatments of roughness involving up-scaling of sinks in the momentum equations. Thus, the focus of this paper is application of a basic 2D raster-based model to understand inundation in an urbanized area.

2 FLUVIAL FLOOD PROCESSES IN URBAN AREAS

The presence of significant structural features (houses, walls etc.) on a river floodplain is important in relation to both the volume of the floodplain that can be occupied by the flow and the direction that the flow takes across the floodplain. Harnessing high resolution topographic data has appeal as it may reduce the uncertainty into how to parameterize the effects of structural 'topography' upon inundation. In both one- and two-dimensional (both diffusion wave and depth-averaged) models, topographic structure is commonly represented through up-scaling of a roughness parameter with calibration where necessary. This is well-established for representing the effects of individual grains and grain organizations in models of flow in gravel-bed rivers where the roughness length is multipliedupwards (e.g. Lane & Richards, 1998, Lane et al, 1999) and for representing the effects of vegetative roughness in floodplain flow models, where Manning's n is scaled upwards (e.g. Mason et al., 2003). In one-dimensional modeling, using the St. Venant equations, the roughness parameter commonly appears through a friction slope relationship that not only represents bed roughness, but also turbulence effects and dispersion processes, the latter resulting from depth- and width-integrating the full three-dimensional form of the Navier-Stokes equations. One-dimensional models tend to have high sensitivity to roughness and this makes roughness a key focus of parameterization in one-dimensional models. Raster-based flood inundation models have commonly used a uniform roughness coefficient for the floodplain but have treated it as the key calibration parameter (Bates & De Roo, 2000, Horritt & Bates, 2001a, b, Horritt & Bates, 2002). In relation to sensitivity, it has been found that LISFLOOD-FP is insensitive to roughness coefficient on the floodplain (Horritt & Bates, 2002) when inundation area was considered.

In relation to flood inundation, roughness parameterization could become more complex if the required roughness value were allowed to vary spatially as a function of local structural complexity. Horritt (2000) used a simple distributed roughness calibration

scheme in fluvial flood modeling and got a minor improvement over the uniform parameterization. LiDAR data has been successfully used to upscale n in a distributed way for floodplain vegetation (Mason et al., 2003) although this assumes that: (1) vegetative roughness relationships developed from flume experiments can be applied to two-dimensional mapping of n from vegetation height; and (2) the prime control on n is vegetative roughness and there is no need to calibrate roughness to take into account the effects of other processes (e.g. turbulence). However, the extent to which this approach can be extended to urban areas is questionable. First, parameterization of n is based upon manipulation of a sink in the momentum equations, either through the bottom stress term that appears in a full solution of the depth-averaged equations, or through n in the simpler momentum representation in a 2D diffusion model. Structural features such as houses, walls etc. also have a blockage effect which reduces the volume of storage that is possible on the floodplain and which can have a major effect upon routing. Research by Lane et al. (in press) shows that traditional parameterization of high resolution topographic variability in 3D hydraulic models using up-scaling of roughness heights does not necessarily represent mass blockage effects properly. The same conclusion may hold for floodplain structural elements in 2D models. Second, many structural elements have topological properties that create complete barriers to flow (e.g. walls) and which can have a very major effect upon the flow routing process. Upscaling of n may reduce flux across linear sets of grid cells, but will not necessarily recognize the full topological features of a structure.

High resolution topographic data has the capability to deliver sufficient information on floodplain structural elements for modeling purposes. However, as yet, there has been no application of this information to urban flood inundation modeling. In this paper, we focus upon diffusion wave treatments of urban flood modeling as these make it possible to use higher spatial resolution topographic data as compared with more computationally intensive methods such as those based on finite elements. As raster-based fluvial flood modeling gives poor representation of the momentum transfer over the floodplain, there is a related need to describe local wetting and drying processes more adequately to compensate the effect. Various algorithms describing the wetting and drying processes in flood modeling have been developed in finite element methods (e.g. Defina et al., 1994, Bates, 2000). LISFLOOD-FP has no explicit treatment of the wetting process and water is allowed to flow out of the cell as long as the outflow energy slope is positive. This is not realistic in reality in that, in most cases, the water front during wetting will lie within the cell and only part of the cell will be wet at a particular time step. It is also more likely to affect inundation extent in urban areas. As the routing process is strongly controlled by elevation differences between cells, if diffusion across the floodplain is too rapid, water will not necessarily reach higher elevation areas as the spread of flow reduces water surface elevations locally, confining spread to lower elevation areas. In urban areas, the complexity of elevation variation makes this particularly important. The importance of this process will be model resolution dependent: with coarser grid cells, representing this process adequately will become more important. Given the above, in addition to explicit representation of structural elements in a diffusion wave model, we also explore the interaction between model resolution and inundation extent and the role of wetting and drying parameters.

3 MODEL APPLICATION: DATA SOURCES

The model used in this paper takes the same structure as that of the JFLOW model developed by Bradbrook et al. (in review), but modified for the purposes of urban flood inundation modeling. The model is applied to a reach of the River Ouse in Yorkshire, U.K (Fig. 1) near Tadcaster. This reach was chosen because of the availability of a one-dimensional hydraulic model for the main river flow, high quality LiDAR data for the floodplain surface, and remotely sensed data on inundation extent and water levels for a large flood inundation event in November 2000, as well as the dense presence of structural features on the floodplain. The latter data have been used to determine inundation patterns and water levels using digital photogrammetry and image analysis (Lane et al., 2003).

The LiDAR had a resolution of 2 meters. The original LiDAR data had been post-processed to standard data quality requirements using methods set by the U.K. Environment Agency's National Centre for Environmental Data Surveillance in Twerton, Bath. This

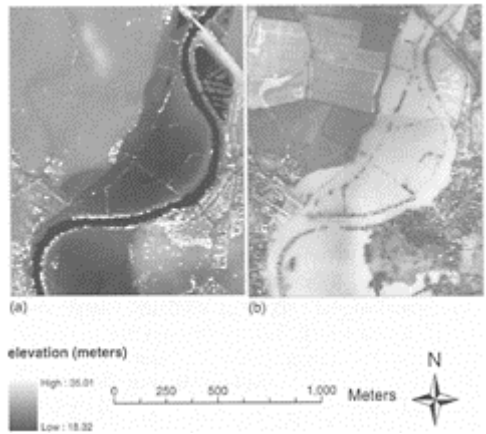

Figure 1. The reach of the River Ouse in Yorkshire, UK, on which the flood event in 2000 was simulated. (a) LiDAR data of 2-meter resolution. (b) Flooding imagery which provides the validation data for the model.

includes standard assessment of data quality to guarantee a precision of ±0.25m throughout, improving to ±0.15m in relatively flat areas with solid reflectance surfaces. The data includes returns from building and trees. For the purpose of urban inundation modeling, some additional image processing was undertaken. Whilst buildings needed to be retained, it was necessary to remove elevations within the LiDAR dataset associated with tree canopies under the assumption that only tree trunks would have a significant

effect upon inundation. The removal of trees was achieved using the same data source used for model validation. Similarly, different surfaces (e.g. grass, road, garden etc.) might need to be allocated different roughness parameters. Spatial distribution of roughness parameters is not addressed in this study. Instead, a uniform roughness value of 0.06 was used based on the typical values suggested by Chow et al. (1988). Although most previous studies use roughness parameters as key calibration parameters, this has not been attempted in this study.

In order to remove tree canopies and also to provide model validation data, 1:4500 scale aerial imagery was obtained. This had been acquired during the falling limb of a major flood event on the 11th November 2000 (Fig. 1). This flood was estimated to be the highest recorded in York since 1625. The imagery was scanned at 21.2μm resolution using a standard desktop scanner. Ordnance Survey benchmark data were used to rectify the imagery to a root mean square error of better than ±2.0m (i.e. commensurate with the resolution of the LiDAR data). Supervised classification was then used to assign the floodplain into functional units: (1) inundated areas, to provide data on flood extent during the falling limb of the hydrograph for model validation; (2) trees, in order to allow correction of the LiDAR data for canopy height effects; and (3) other elevations. Only canopy locations were removed from the LiDAR data.

A one-dimensional hydraulic model of the Ouse from Skelton (upstream of the city) through to Naburn Weir (downstream of the city) is used to provide estimates of flux from the river to the floodplain for a major flood inundation event (estimated to have a return period of greater than 100 years) in November 2000 in the form of a stage hydrograph in 530 hours (Fig. 2). The connectivity between the one-dimensional model and the floodplain is established through a weir equation. This assumes that the flood-plain is protected by an embankment that essentially acts as a continuous, broad-crested weir. This may be identified from topographic data (e.g. LiDAR). The flux to the floodplain is then determined from predictions of water stage in the river channel using a weir equation:

$$q=1.704(H-\Delta z)^{3/2} \quad (1)$$

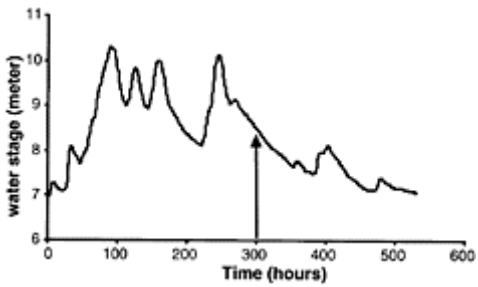

Figure 2. Stage hydrograph in the main river channel. Arrow points to the time when the validation imagery was acquired.

where H is the water surface elevation of the river channel and Δz is the height of the river embankment on the floodplain. Water level hydrographs are interpolated to each river adjacent floodplain cell at each time step and inflow from the river channel occurs once the water surface of the river channel is higher than that of the adjacent floodplain cells. The flow in the river channel at each time step is assumed to be uniform throughout the simulation.

4 MODEL APPLICATION: SIMULATIONS, ACCURACY ANALYSIS AND VALIDATION

The flood event was simulated using three different spatial resolutions: 8-meter, 16-meter and 32-meter and time series of inundation extents for these simulations are shown in Figures 3–5. These show the wetting process for 38 hours. The comparison of the predicted inundation extents obtained using different model resolutions at the time when the validation data was acquired are shown in Figure 6. Comparison of the time series inundation extents obtained using different model resolutions for the first 38 hours shows that model is quite sensitive to spatial resolution with respect to both the inundation extent and the flood wave travel time. Flood inundation is more rapid with a coarser resolution. For example, the model with a 32-meter resolution has roughly the same inundation pattern at around 30.5 hours, as that obtained from the 8-meter resolution model at 38 hours. For the 16-meter case, it took about 32 hours to get the same pattern. This is expected considering the poorly represented inertial processes in a diffusion wave model.

In order to compare the accuracy of the predicted inundation extents statistically, accuracy assessment was undertaken using a method adopted from remote sensing (Congalton & Green, 1999). In this method, an error matrix is set up to express the number of sample units assigned to a particular classification category in one classification relative to the number of sample units in another classification. In most of the cases, one of the classifications is assumed to be correct (reference data). The columns usually represent the reference data and the rows usually represent the classification data. In this application, the validation aerial imagery on the falling limb of the flood event was classified into three classes: dry areas, wet areas and the wetting front. At each time step, the model divides the whole modeling site into three categories to represent the wetness of the grid cells, namely wet cells, wetting front cells and dry cells. The wetness of a particular cell is decided by the wetting parameter. A wet cell is one with a wetting parameter equal or greater than one, a dry cell is one with a wetting parameter equal to zero and a wetting front cell is one with a wetting parameter greater than zero and smaller than one. If temporal validation data in the form of inundation extent at a regular time interval is available, the accuracy of the model prediction can be assessed at each particular time points where the validation data is available. Thus, more insight into how the model behaves in relation to both the flood wave travel time and inundation extent can be gained. However, in this application, as only the validation data at one point on the falling limb of the hydrograph is available, the accuracy of the model prediction was only assessed against the validation data for this point. Once the error matrix has been constructed, the overall accuracy can be computed as the sum of the

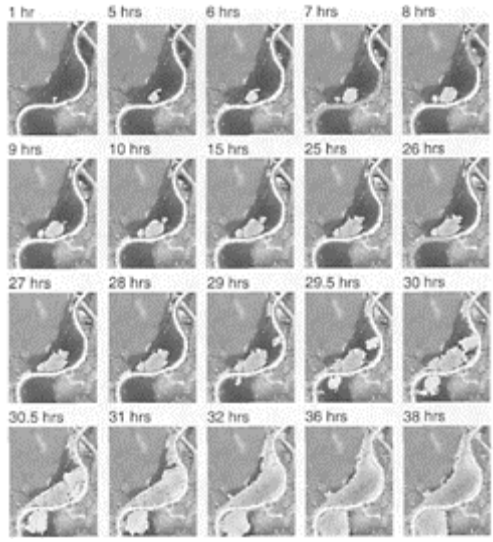

Figure 3. Time series inundation extents (in 38 hours) obtained from model simulation using an 8-meter model resolution.

Figure 4. Time series inundation extents (in 38 hours) obtained from

model simulation using a 16-meter model resolution.

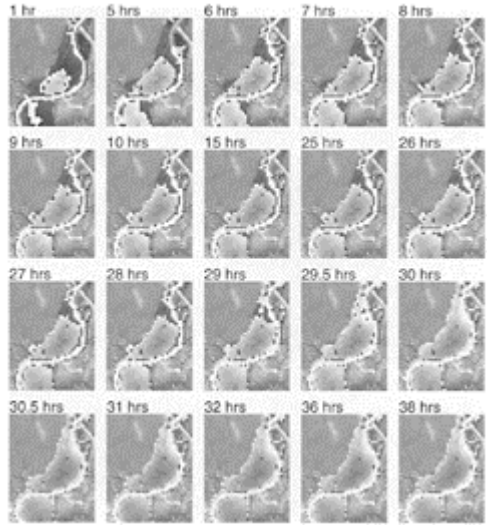

Figure 5. Time series inundation extents (in 38 hours) obtained from model simulation using a 32-meter model resolution.

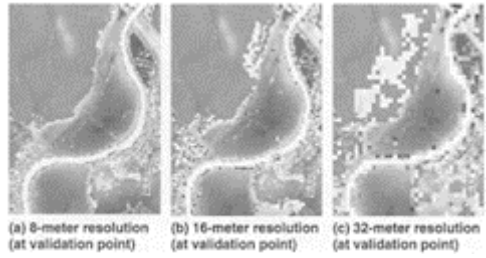

Figure 6. The comparison of the predicted inundation extents obtained using different model resolutions at the time when the validation data was acquired.

corrected classified cells divided by the total number of cells. Besides the overall accuracy, a discrete multivariate technique called Kappa analysis can be used to statistically determine if one error matrix is significantly different from another (Bishop

et al., 1975). The result of performing a Kappa analysis is a KHAT statistic, which is the measure of accuracy or agreement (Cohen, 1960). The KHAT statistic is based on the difference between the actual agreement in the error matrix (i.e., the agreement between the predicted cell status and the reference data as indicated by the major diagonal) and the chance agreement as indicated by the row and column totals (i.e. marginal). A KHAT value can be calculated for each error matrix and is a measure of how well the predicted data agrees with the reference data. Confidence intervals can then be computed using the approximate large sample variance and the fact that the KHAT statistic is asymptotically normally distributed. The significance of the KHAT value for a single error matrix can be tested to determine if the agreement between the predicted data and the reference data is significantly different to no agreement by calculating the Z statistic. In addition to computing the Kappa coefficient for an entire error matrix, it may be useful to look at the agreement for an individual category within the matrix. This can be tested using the conditional Kappa coefficient, resulting in a KHAT statistic which is an estimate of the conditional Kappa coefficient. Similar to the overall KHAT statistic, the variance of the conditional KHAT value and the Z statistic can then be calculated to determine if the classification is significantly better than a random result. The overall accuracy, KHAT value and conditional KHAT value for wet cells at the point when the validation data is acquired for model simulations using 8-meter, 16-meter and 32-meter resolution are compared in Table 1.

Comparison of the inundation extents and the accuracy assessment of the model predictions obtained shows that the model performance is sensitive to spatial resolution when the inundation extent is

Table 1. Overall accuracy for model simulations.

	8-meter	16-meter	32-meter
Overall accuracy	0.87	0.83	0.71
KHAT	0.76	0.70	0.51
Conditional KHAT for wet cells	0.74	0.63	0.41

considered. The overall accuracy of the model prediction decreases as the mesh is coarsened. KHAT statistics give a similar pattern. Landis & Koch (1977) divided the possible ranges for KHAT into three groups: a value greater than 0.80 (i.e., 80%) represents strong agreement; a value between 0.40 and 0.80 (i.e., 40–80%) represents moderate agreement; and a value below 0.40 (i.e., 40%) represents poor agreement. In this application, the simulation with the 8-meter resolution gives a KHAT of 0.76 which represent strong agreement of the model prediction with the validation data. According to KHAT statistics, prediction from simulation with 16-meter resolution also shows strong agreement with the validation data. While the agreement is rather poor for the 32-meter case.

The high sensitivity of model prediction to model resolution is thought to be the causes of two connected effects. First, the effect of resampling a dense mesh onto a coarse one will result in a smoother floodplain. It is found that, for the finite-element method, the two-stage filtration effect of raw data into a digital elevation model and then

into a numerical mesh coarsens the data used in the model (Bates et al., 1996) and will reduce the detail and accuracy of the resultant land surface (Marks & Bates, 2000). This also holds for the resampling process in raster-based modeling. Three commonly used resample methods: nearest-neighbor interpolation, bilinear interpolation and cubic convolution interpolation have some degree of smoothing effect on the input data. Bilinear interpolation determines the value of a cell based upon the weighed distance average of the four nearest input cell centers. It generally causes some smoothing to the data. Convolution interpolation tends to smooth the data more than the bilinear interpolation due to the smooth curve used and the large number of cells involved. The smoothing effect of the nearest-neighbor interpolation is the least among these three methods and was the resample method used in this model.

Second, the representation of small-scale wetting processes will be simplified when the mesh is coarsened. The effect of the wetting treatment in the model is to slow down the flow transfer. The velocity controls the timing of the wetting process for a grid cell and the evaluation of the velocity will be resolution dependent. As the mesh is coarsened, the variance in velocity decreases and the timing of the wetting front migration tends to have a greater possibility of error due to the simplified description of the timing of the flow routing which will otherwise become much more complex in a denser mesh. This explains the high model sensitivity to model resolution in relation to flood wave travel time. Likewise, the difference between water surface elevations of two grid cells determines the direction of the flow routing and the variance in water surface elevations tends to decrease as the mesh is coarsened. The heterogeneity of water surface elevations in the cells will decrease and this may result in a significant chance of errors in terms of the direction of flow. This is especially true for the flow routing in urban areas where structural features on the floodplain can have considerable effect on flow direction and timing. The cell blockage effect associated with structural features will have a less control on the timing and direction of the flow with a smoother floodplain resultant from a coarser resolution. It is expected that the higher resolution the data, the more adequately represented small-scale routing processes and thus the more accurate prediction with respect to both flood wave travel time and the inundation extent.

The effect of mesh resolution will also depend on floodplain configuration in relation to the magnitude of flow associated with a given return period. For a floodplain that is fully occupied with a low return period, mesh resolution will have less effect on high flows. For an unconstrained floodplain, where the lateral extent of a flood continues to increase even at low flows, resolution effects are likely to cause significant error.

5 DISCUSSION

This paper demonstrated the effect of model spatial resolution upon the estimated inundation extent in a two-dimensional raster-based diffusion wave model, with application to a reach of the River Ouse in Yorkshire, U.K to simulate a flood event in the year 2000. Model response shows that the model is quite sensitive to spatial resolution in terms of both the flood wave travel time and the inundation extent. This is thought to be caused by two interrelated effects: (1) the smoothing effect of mesh coarsening on the topological data; and (2) the poorer representation of small-scale flow

routing processes associated with the reduced topological complexity resultant from (1). The local topological complexity due to the presence of small-scale structural features on the floodplain in urban areas makes this even more complex for urban flood modeling, as many of these features have topological properties that may have a major effect upon both the timing and direction of the flow routing. First, the details of the structural features may be reduced as the mesh is coarsened, resulting in a poorer representation of these features in the model. Second, current methods of representing small-scale flow routing processes associated with structural features in flood models have their limitations. Traditional methods of representing structural features usually involves up-scaling of the roughness parameter which, in previous research, has been used as a key calibration parameter to compensate for the poorly represented momentum transfer process in raster-based modeling. This may has the effect of reducing the flux through these features, but will not necessarily recognize the whole topological features of the structure. In this application, the wetting treatment approach that is used has the effect of reducing model dependence upon the roughness parameter. The combined effects of the wetting and roughness parameters can compensate in part for a coarser mesh resolution. However, the coarser the resolution, the lower the ability to control the inundation process as these parameters only partly control the speed and not the direction of wetting. Thus, coupling of high resolution data, which can capture small scale variation in topography, to more sophisticated representation of the inundation process will be required in order to obtain effective predictions of flood inundation extent for urban fluvial flood modeling.

REFERENCES

Bate, P.D. 2000. Development and testing of a subgrid-scale model for moving-boundary hydrodynamic problems in shallow water. *Hydrological processes* 14:2073–2088.

Bates, P.D. and Anderson, M.G. 1996. A preliminary investigation into the impact of initial conditions on flood inundation predictions using a time/space distributed sensitivity analysis. *Catena* 26:115−134.

Bates, P.D., Anderson, M.G., Baird, L., Walling, D.E. and Simm, D. 1992. Modeling floodplain flows using a two-dimensional finite element model. *Earth Surface Processes and Landforms* 17:575–588.

Bates, P.D., Anderson, M.G. and Hervouet, J.-M. 1995. An initial comparison of two 2-dimensional finite element codes for river flood simulation. *Proceedings of the Institution of Civil Engineers, Water, Maritime and Energy* 112:238−248.

Bates, P.D. and De Roo, A.P.J. 2000. A simple rasterbased model for flood inundation simulation. *Journal of Hydrology* 236:54–57.

Bechteler, W., Hartmaan, S. and Otto, A.J. 1994. Coupling of 2D and 1D models and integration into Geographic Information Systems (GIS). In White, W.R. and Watts, J. (eds.), *Proceedings of the 2nd International Conference on River Flood Hydraulics.* Chichester: John Wiley and Sons. pp. 155–165.

Beven, K.J. 2000. *Rainfall-Runoff Modeling: the primer.* Chichester: John Wiley and Sons.

Biggin, D.S. and Blyth, K. 1996. A comparison of ERS-1 satellite radar and aerial photography for river flood mapping. *Journal of the Chartered Institute of Water and Environmental Management* 10:59–64.

Bishop, Y., Fienberg, S. and Holland, P. 1975. *Discrete Multivariate Analysis: Theory and Practice.* Cambridge: MIT Press, MA.

Bradbrook, K.F., Lane, S.N., Waller, S.G. and Bates, P.D., in review. Paper submitted to *Journal of River Basin Management.*

Brackett, R.A., Arvidson, R.E., Izenberg, N.R. and Saatchi, S.S. 1995. Use of polarmetric and interferometric radar data for flood routing models: first results for the Missouri River, Session 36—Planetary Geology: Radar Remote Sensing of Flood Plains, Mountain Belts, and Volcanoes. *Annual Meeting of the Geological Society of America*, 5–9 November , New Orleans.

Chow, V.T., Maidment, D.R. and Mays, L.W. 1988. *Applied Hydrology.* New York: McGraw-Hill.

Cohen, J. 1960. A coefficient of agreement for nominal scales. *Educational and Psychological Measurement* 20: 37−40.

Congalton, R.G. and Green, K. 1999. *Assessing the Accuracy of Remotely Sensed Data: Principles and Practice.* Boca Raton: Lewis Publishers.

Cunge, J.A., Holly, Jr.F.M. and Verwey, A. 1976. *Practical aspects of computational river hydraulics.* London: Pitman.

Defina, A., D'Alpaos, L. and Matticchio, B. 1994. A new set of equations for very shallow water and partially dry areas suitable to 2D numerical models. In Molinaro, P. and Natale, L. (eds.), *Modeling Flood Propagation over Initially dry Areas.* New York: American Society of Civil Engineers. pp. 72–81.

Estrela, T. and Quintas, L. 1994. Use of GIS in the modeling of flows on floodplains. In White, W.R. (eds.), *Proceedings of the 2nd International Conference on River Flood Hydraulics.* Chichester: Wiley and Sons. pp. 177–189.

Flood, M. and Gutelius, B. 1997. Commercial implications of topographic terrain mapping using scanning airborne laser radar. *Photogrammetric Engineering and Remote Sensing* 63:327–366.

Galland, J.C., Goutal, N. and Hervouet, J-m. 1991. TELEMAC-a new numerical model for solving shallwater equations. *Advances in Water Resources* 14(3): 138–148.

Gee, D.M., Anderson, M.G. and Baird, L. 1990. Large scale floodplain modeling. *Earth Surface Processes and Landforms* 15:512–523.

Horritt, M.S. 2000. Calibration of a two-dimensional finite element flood flow model using satellite radar imagery. *Water Resources Research* 36(11):3279–3291.

Horritt, M.S. and Bates, P.D. 2001a. Effects of spatial resolution on a raster based model of flood flow. *Journal of Hydrology* 253:239–249.

Horritt, M.S. and Bates, P.D. 2001b. Predicting flood-plain inundation: raster-based modeling versus the finite-element approach. *Hydrological processes* 15: 825–842.

Horritt, M.S. and Bates, P.D. 2002. Evaluation of a 1D and 2D numerical models for predicting river flood inundation. *Journal of Hydrology* 268:87–99.

Knight, D.W. and Shiono, K. 1996. River channel and floodplain hydraulics. In Anderson M.G. et al. (eds.), *Floodplain Processes.* Chichester: John Wiley and Sons. pp. 139–181.

Krabill, W.B., Collins, J.G., Link, L.E., Swift, R.N. and Butler, M.L. 1984. Airborne laser topographic mapping results. *Photogrammetric Engineering and Remote Sensing* 50: 685–694.

Landis, J. and Koch, G. 1977. The measurement of observer agreement for categorical data. *Biometrics* 33:159–174.

Lane, S.N. 1998. Hydraulic modeling in hydrology and geomorphology: A review of high resolution approaches. *Hydrological Processes* 12:1131–1150.

Lane, S.N., Bradbrook, K.F., Richards, K.S., Biron, P.M. and Roy, A.G. 1999. The application of computational fluid dynamics to natural river channels: three-dimensional versus two-dimensional approaches. *Geomorphology* 29:1–20.

Lane, S.N., Chandler, H.H. and Richards, K.S. 1994. Developments in monitoring and modeling small-scale river bed topography. *Earth Surface Processes and Landforms* 19:349–368.

Lane, S.N., James, T., Pritchard, H. and Saunders, M. 2003. Photogrammetric and laser altimetric reconstruction of water levels for extreme flood event analysis. Paper forthcoming in the *Photogrammetric Record* 18(104): 293–307.

Lane, S.N., James, T.D. and Crowell, M.D. 2000. The application of digital photogrammetry to complex topography for geomorphological research. *Photogrammetric Record* 32:793–821.

Lane, S.N., Hardy, R.J., Ingham, D.B. and Elliott, D.B., in press. Numerical modeling of flow processes over gravelly-surfaces using structured grids and a numerical porosity treatment. Paper forthcoming in *Water Resources Research.*

Lane, S.N. and Richards, K.S. 1998. Two-dimensional modeling of flow processes in a multi-thread Channel. *Hydrological Processes* 12:1279–1298.

Marks, K.J. and Bates, P.D. 2000. Integration of high-resolution topographic data with floodplain flow Models. *Hydrological Processes* 14:2109–2122.

Mason, D.C., Cobby, D.M., Horritt, M.S. and Bates, P.D. 2003. Floodplain friction parameterization in two-dimensional river flood models using vegetation heights derived from airborne scanning laser altimetry. *Hydrological Processes* 17:1711–1732.

Westaway, R.M., Lane, S.N. and Hicks, D.M. 2001. Airborne remote sensing of clear water, shallow, gravel-bed rivers using digital photogrammetry and image analysis. *Photogrammetric Engineering and Remote Sensing* 67: 1271–1281.

Westaway, R.M., Lane, S.N. and Hicks, D.M. 2003. Remote survey of large-scale braided rivers using digital photogrammetry and image analysis. *International Journal of Remote Sensing* 24:795–816.

Wheater, H.S. 2002. Progress in and prospects for fluvial flood modeling. *Philosophical transactions of the Royal Society of London: Mathematical physical and engineering sciences* 360(1796):1409–1431.

B.4.
Hyper-concentrated flows

Morphology of alluvial fans formed by hyperconcentrated tributaries

S.C.Chen & S.H.Peng
Department of Soil and Water Conservation, National Chung-Hsing University, Taiwan

H.Capart
Department of Civil Engineering, National Taiwan University, Taiwan

River Flow 2004—Greco, Carravetta & Della Morte (eds.)

ABSTRACT: This study uses digital image processing to survey the confluence behavior of a tributary with hyperconcentrated flow entering the main river. The experiment has two parts: in the first, digital terrain data were computed via coordinate transformation from profiles extracted by laserlines; in the second, velocity fields were obtained by using Voronoï imaging method to analyze the images through low-pass and high-pass filters when trace-particles were added. The measurement approach is described and preliminary results are presented. Through the discussion of alluvial fan morphology, we can better understand the interaction of this mechanism.

1 INTRODUCTION

With both heavy rainfall and mountainous terrain of weak geological structure, the island of Taiwan is subject to frequent debris flows. In upland basins, torrential river valleys and steep gullies are subject to both flooding and landslides. This study examines various ways in which flow slides and river currents interact, including blocking of rivers due to either accumulated debris or to the formation of landslide dams across the channel width. In other situations, local narrowing of a channel can occur due to partial invasion by a debris fan. At the outlets of debris flow gullies, thick deposits may be left for water currents to slowly transport downstream.

The confluence behavior of a tributary with hyperconcentrated flow into the main river is a common phenomenon in mountainous regions. When the hyperconcentrated flow tributary enters a main river, a natural dam would be formed by the enormous sediment carried by the tributary. Chen (1999) collects and analyzes numerous kinds of natural dams from the literature and field survey after the Chichi earthquake of September 21, 1999 in Taiwan. In addition, a preliminary classification is established

according to the basic concepts of sediment transport (Chen & Peng 2003a). Parker *et al.* (1998a, b) propose a theory and application for alluvial fans and fan-deltas formed by channelized fluvial and sheet flow. Tsai & Shieh (1997) find the morphological similarity of debris-flow fans by laboratory experiments and numerical simulations.

However, previous studies which research the confluence behavior are very limited because it involves numerous factors concerning the confluence mechanism. To study the morphology of an alluvial fan formed by a tributary entering the main river, we did experiments to measure the alluvial fan terrain and confluence velocity field by applying digital image processing. The methods of measurement used in this paper can increase the precision and convenience over previous methods.

2 EXPERIMENTS

2.1 *Experimental device*

The experimental device includes a main channel which is 3.5m long, 0.2m wide and 0.15m high, and a minor branch which is 0.8m long, 0.1m wide and 0.25m high. There is also a gate which can be opened suddenly at the middle of the branch channel to release the mixture of water and sediment as a dam-break type. Besides, in the main channel there are two tanks, one above the upstream end and the other below the downstream end, to construct the circulatory system. To keep the circulatory system working, we used a pump to draw out the water in the downstream tank into the upstream tank which can overflow by controlling two valves to determine discharge of inflow into the main channel and outflow into the downstream tank.

When the hyperconcentrated flow in the branch enters the main channel, it forms an alluvial fan under the water surface of main channel. We measured the morphology of this alluvial fan and the velocity field of confluence to study this mechanism.

The overall experimental process was separated into pre-test and formal-test. The purpose of the pre-test was to determine the physical parameters of experimental materials. Then formal testing was carried out, including several procedures as follows: (1) determine the discharge of main channel in uniform flow; (2) determine the concentration and volume of the hyperconcentrated tributary; (3) calibrate the branch slope and the confluence angle between main channel and branch, when the main channel slope set to zero; (4) release the mixture into the branch and measure the velocity field of confluence; (5) stop the inflow of main channel and survey the topography of the alluvial fan; (6) repeat these steps for different conditions.

2.2 *Methods of measurement*

The experiment included two parts: the first is that the digital terrain data of the alluvial fan was computed using coordinate transformation from profiles extracted by laserlines; the second is that the velocity fields were obtained using Voronoï imaging method to analyze the images via low-pass and high-pass filters when adding the trace-particles. These two methods are illustrated as follows.

2.2.1 *Survey of topography*

The measurement is illustrated in Figure 1. By using a laserline projection above the measured region of the alluvial fan, the profile image was captured via a digital camera set beside the region with an angle of depression. Then the 2D images of various profiles can be transformed into 3D space coordinates, using the method of transformation proposed by Spinewine *et al.* (2003) and illustrated in Figure 2. A transformation is then required to relate the set of 2D image coordinates of any point *P* to its world coordinates. Define $\mathbf{r}_P=[x_P \ y_P \ z_P]^T$ as the world coordinates of point *P* (see Fig. 2), and $\mathbf{R}_P^{(A)}=[X_P^{(A)} \ Y_P^{(A)}]^T$ as the 2D image coordinates of point *P* associated with the camera viewpoint *A*. The transition from camera to world coordinates generally requires a translation and a rotation (Jähne 2002). Thus for each viewpoint *A*, one can specify a matrix $[\mathbf{A}^{(A)}]$ and a vector $\mathbf{b}^{(A)}$ such that

$$\alpha\begin{bmatrix} X^{(A)} \\ Y^{(A)} \\ 1 \end{bmatrix}=\left[\mathbf{A}^{(A)}\right]\begin{bmatrix} x \\ y \\ z \end{bmatrix}+\mathbf{b}^{(A)} \qquad (1)$$

where α is a scalar parameter; matrix $[\mathbf{A}^{(A)}]$ and vector $\mathbf{b}^{(A)}$ must be calibrated from a set of points for which both the world coordinates and the image coordinates are known (see Spinewine *et al.* 2003, Ni 2004 for details). The overall procedures are shown in Figure 3, and the digital terrain data were obtained from executing them.

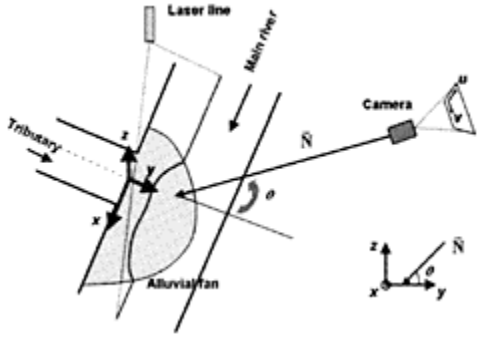

Figure 1. Illustration of the system used to survey topography.

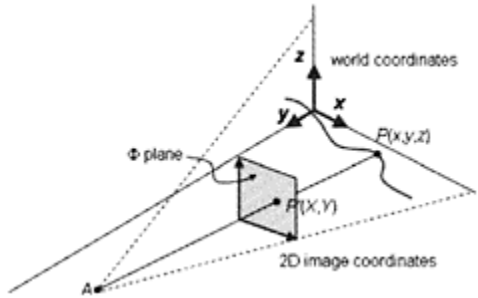

Figure 2. Illustration of coordinate transformation.

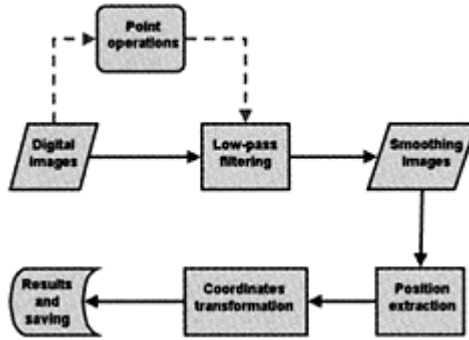

Figure 3. Flow chart of digital image processing.

2.2.2 *Measurement of velocity field*

Consider a 2D velocity field of confluence between the main river and a tributary, which is governed by shallow water equations. If the variation of velocity in vertical direction can be negligible, then the velocity field of water surface will be regarded as the mean velocity field over the flow depth. Therefore the surface velocity field can be measured by

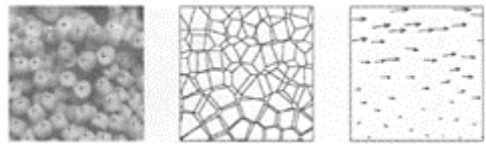

Figure 4. Overview of the Voronoï match algorithm: (left) image of a granular flow abstracted into point-like

particles (+); (center) Voronoï diagrams constructed on these points (thin lines) and on the points of the next image of the sequence (thick lines); (right) displacement vectors (true scale) obtained by matching the Voronoï 1-stars (Capart *et al.* 2002).

Figure 5a. Photo of alluvial fan at the sample site.

using the Voronoï imaging method after adding the trace particles. The Voronoï imaging method was basically developed for the measurement of granular flows (Capart *et al.* 2002). Its principle is to first extract the point-like particle positions of discrete digital images, secondly to construct the Voronoï diagrams for these points at two successive time instants, and finally to compute the velocity vectors by matching the local Voronoï patterns (Fig. 4). Generally, the surface velocity fields can be effectively captured by a digital video camera if they do not have especially large velocities (Chen & Peng 2003b).

2.3 *Experimental materials and conditions*

The experimental materials were sampled from the alluvial fan located on the Cho-Shui River close to 24k+500 of Highway 16 in Taiwan (Fig. 5a) and the particle size distribution diagram of materials is sketched as Figure 5b. Based on these materials, we designed a series of experiments to study the confluence mechanism between a main channel and its tributary. The factors of influencing confluence are generally considered to be the angle of confluence, the ratio of discharge between main channel and tributary, the slopes of main channel and tributary, and

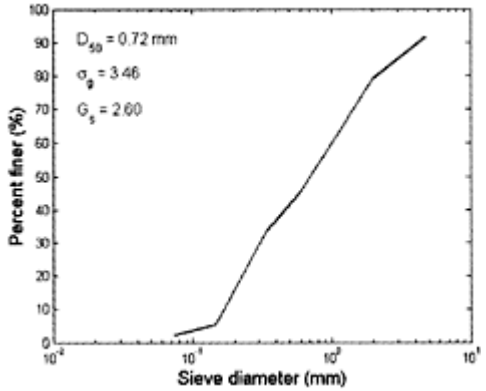

Figure 5b. Distribution of particle size.

Table 1. Experimental conditions.

	Main channel		Branch	
Confluence angle (degree)	Discharge (cms) $\times 10^{-4}$	Flow depth[a] (cm)	Density of mixture[b] (g/cm^3)	Slope[c] (%)
45	0.66	3.8	1.6 and 1.9	10, 20, and 30
	1.99	4.1		
	4.35	4.3		
90	0.66	3.8	1.6 and 1.9	10,20, and 30
	1.99	4.1		
	4.35	4.3		
135	0.66	3.8	1.6 and 1.9	10,20, and 30
	1.99	4.1		
	4.35	4.3		

[a] Used sill downstream to raise the water surface to easily make the alluvial fan.
[b] The total volume of mixture was 4200 cm^3 in each case.
[c] The main channel slope was zero.

the sediment concentration of the tributary, etc. (Zhu *et al.* 2000, Chen 2000, Kao 2003). The experimental conditions are shown in Table 1.

3 RESULTS

We carried out numerous tests based on these experimental methods and obtained the following results. The results include 54 sets of digital terrain data for the alluvial fan and 30 sets of velocity field of confluence.

3.1 *Morphology of alluvial fan*

An example of the results is shown as Figure 6. From these results of digital terrain data, we calculated the

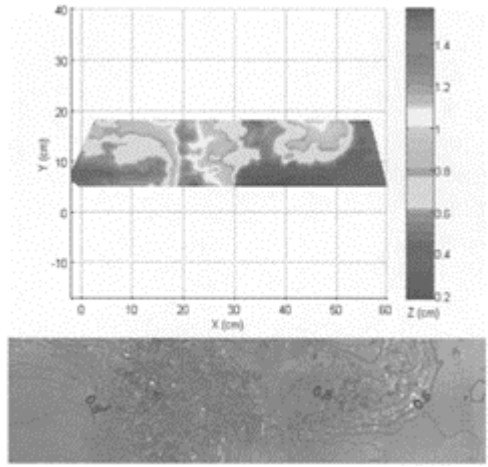

Figure 6. Measurement results in the terrain (where confluence angle is 90 degrees, discharge of main channel is 0.66×10^{-4}cms, density of mixture is 1.9g/cm^3, and slope of branch is 10%): (top) digital terrain data of survey; (bottom) comparison between measurement and actual terrain.

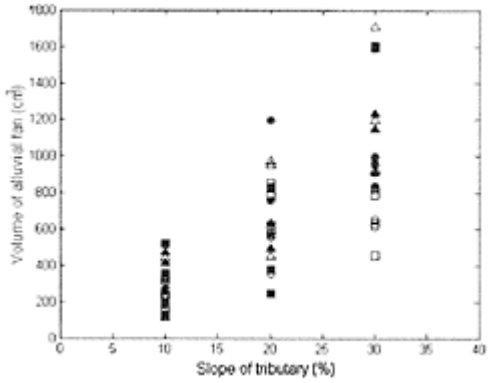

Figure 7. Relation between volume of alluvial fan and slope of tributary (▲: confluence angle=45 degrees; ■: confluence angle=90 degrees; ●: confluence angle=135 degrees; solid and hollow symbols represent density of mixture 1.9g/cm^3 and 1.6g/cm^3, respectively).

residual volume of alluvial fan in the main channel and found the relation between volume and slope of tributary (Fig. 7). Figure 7 indicates that the volume of alluvial fan could not be affected apparently by confluence angle and density of mixture; it is predominated by the slope of tributary. Meanwhile, a high density of the mixture in the tributary also increases the residual volume in main channel when the slope of tributary is 30%. We suggest that the amount of alluvial fan carried by tributary could be determined by gravity force

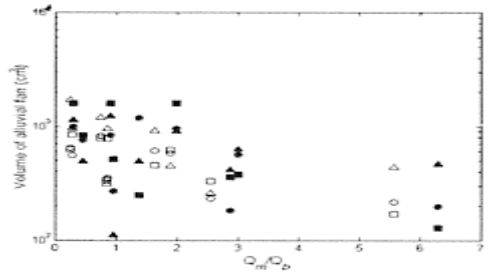

Figure 8. Relation between volume of alluvial fan and ratio of discharge (Q_m: discharge of main channel; Q_b:

discharge of tributary; the others are the same as Figure 7).

induced by the branch slope and the tributary density if the flow intensity of the main channel is neglected.

To realize the effect of main channel flow, we compared the volume of alluvial fan with the ratio of discharge between main channel and tributary (Fig. 8). Figure 8 shows that large ratio of discharge between main channel and tributary (Q_m/Q_b) can decrease the volume of alluvial fan because a portion of the alluvial fan sediment may be carried away by the main channel flow. From Figure 7 and Figure 8, it can be seen that the angle of confluence and sediment concentration of tributary do not markedly relate to the volume of alluvial fan. In fact, the concentration of tributary is one of factors which cause the gravity force to drive the tributary ahead, and the angle of confluence may affect the shape of alluvial fan in our experiment (see Sec. 4.1 for details).

3.2 *Results of velocity field*

Figure 9 indicates an example of the results from measuring the velocity field by the Voronoï imaging method. In this case, the velocity field is initially very disordered because the tributary shoots rapidly across the main channel to reach the opposite bank. About 1 sec later, two vortices form on both sides gradually; at t=1.2sec or so, the vortices fully develop and hold their shapes till about t=2.0sec; they then start to move downstream after t=2.0sec; until t=2.8sec or so, the vortices begin to disperse gradually (Fig. 9). The results of velocity field can be regarded as references for the numerical modeling in the future.

To study the velocity vibration in the x-direction at confluence (x=23.5cm), we took the x-component of the velocity (u) at different y-positions (y) and divided it by the mean velocity of the main channel (U_0) and

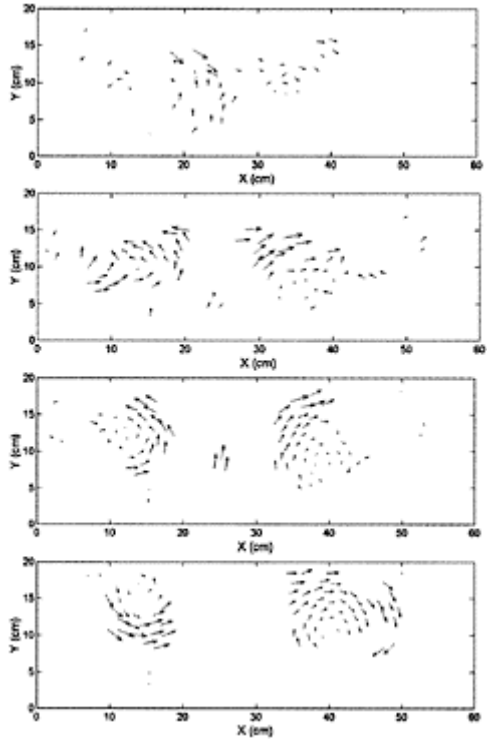

Figure 9. Results of measurement in the velocity field (e.g. fluence angle is 90 degrees, discharge of main channel is 6×10^{-4}cms, density of mixture is 1.9g/cm^3, and slope of branch is 30%): (top) t=0.5sec; (second from the top) t=1.0sec; (second from the bottom) t=1.2sec; (bottom) t=2.0sec.

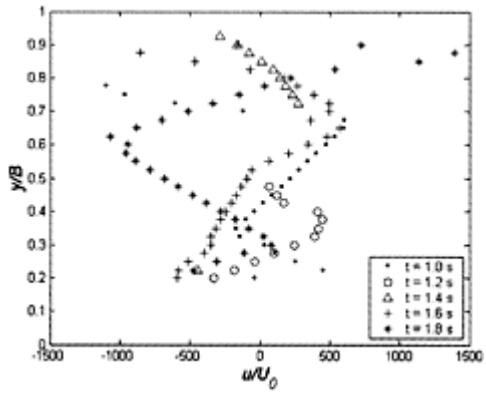

Figure 10a. Relation between u/U_0 and y/B at x=23.5cm (confluence) when t=1.0, 1.2, 1.4, 1.6 and 1.8sec (other conditions are the same as Figure 9).

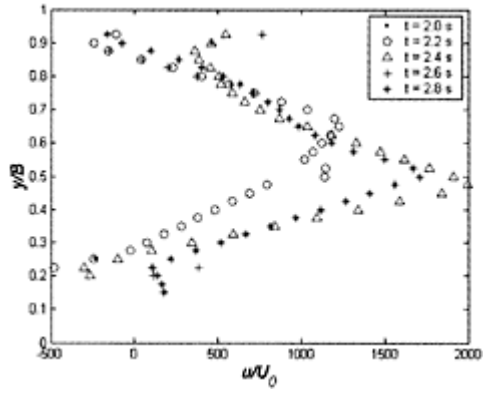

Figure 10b. Relation between u/U_0 and y/B at x=23.5cm (confluence) when t=2.0, 2.2, 2.4, 2.6 and 2.8sec (other conditions are the same as Figure 9).

the width of the main channel *(B)*, respectively, for a dimensionless value (Figs. 10a, b). In Figure 10a, the velocity profiles are unstable with different time instants due to the vortices during t=1.0~1.8sec intervals. In contrast, the dimensionless profiles of the x-component velocity maintain a similar profile during t=2.0~2.8sec intervals because the vortices are affected by main channel flow to move downstream and then to finally disperse. In sum, the velocity field usually determines the motion of sediment, which affects the alluvial fan morphology. In next section, we discuss the morphological details of alluvial fans.

4 DISCUSSION

4.1 *Centroids of alluvial fans*

The volume of alluvial fan is defined by the following integral:

$$V = \iint z(x,y)dxdy \tag{2}$$

Thus, the coordinates X_{CG} and Y_{CG} of the centroid of alluvial fan are equal to the first moments divided by the volume:

$$X_{CG} = \frac{\iint xz(x,y)dxdy}{V} \tag{3}$$

$$Y_{CG} = \frac{\iint yz(x,y)dxdy}{V} \tag{4}$$

Assume that the centroids of alluvial fans can represent their location. To realize the effect of confluence angle,

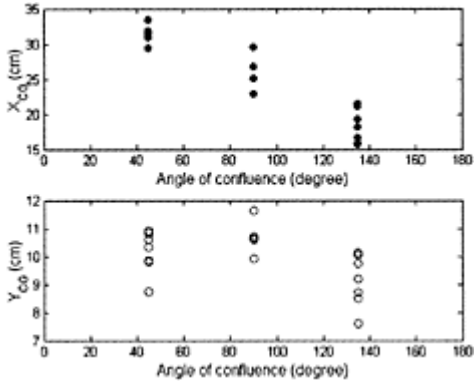

Figure 11. Relation between the centroids of alluvial fans and angles of confluence: (top) when the angle of confluence is larger, the tributary encounters stronger resistance and X_{CG} decreases; (bottom) Y_{CG} is similar to X_{CG}, but Y_{CG} is larger than the others when the angle of confluence is 90 degrees.

we calculated the centroids of 19 alluvial fans which have more complete shapes with different angles of confluence (Fig. 11). Figure 11 shows that the confluence angle could

primarily determine the alluvial fan location. In addition, the “erosion angle” can be also defined by the alluvial fan centroid. If the longitudinal center line of the tributary, called the “axis line”, is extended to the wall of main channel, the line from the confluence point (x=23.5, y=0) to the centroid and axis line forms the erosion angle. Previous research indicates that a positive relation exists between erosion angle and discharge ratio (Q_m/Q_b) (Chen 2000). Our experiments show the similar results, although their relation is not significant.

4.2 *Shapes of alluvial fan*

We extracted the longitudinal profile and cross-section at the alluvial fan centroid (Fig. 12) to analyze shape characteristics of alluvial fans. In these profiles of alluvial fans, the shapes are markedly affected by confluence angle. For example, the peak of the longitudinal profile deflects downstream when the confluence angle is 45 degrees (Fig. 12a). In contrast, the peak of the longitudinal profile deflects upstream when the confluence angle is 135 degrees (Fig. 12c). Furthermore, when the confluence angle is 90 degrees, the shape of the longitudinal profile is shaped like a hat, and the cross-section (Fig. 12b) seems to have two peaks. The reason that there are two peaks might be that the tributary shoots directly to hit the opposite wall of the main channel and to deposit the sediment on the bed.

The alluvial fan contours in different confluence angles are illustrated in Figure 13 as an example.

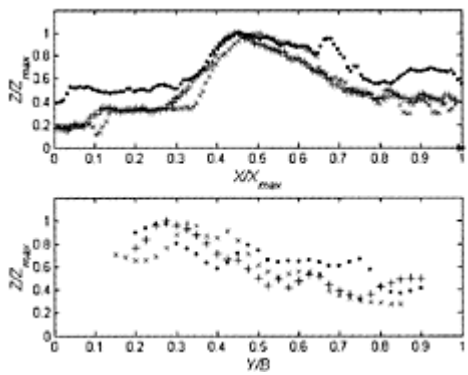

Figure 12a. Extracted profiles at alluvial fan centroid (X_{CG}, Y_{CG}) for confluence angle 45 degrees: (top) longitudinal profile; (bottom) cross-section profile (●: slope of branch=20%, Q_m=0.66×10^{-4}cms; +: slope of branch=20%, Q_m=1.99×10^{-4}cms; ×: slope of

branch=30%, Q_m=4.35×10^{-4}cms; density of mixture is 1.9g/cm^3).

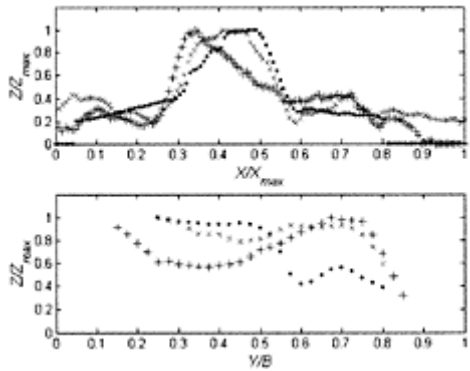

Figure 12b. Extracted profiles at alluvial fan centroid *(X_{CG}, Y_{CG})* for confluence angle 90 degrees: (top) longitudinal profile; (bottom) cross-section profile (●: slope of branch=20%, Q_m=1.99×10^{-4} cms; +: slope of branch=30%, Q_m=0.66×10^{-4}cms; slope of branch=30%, Q_m=1.99×10^{-4}cms; density of mixture is 1.6g/cm^3).

According to these contours, the outlines of alluvial fans in different confluence angles are simplified and summarized as Figure 14. The types of alluvial fan in Figure 14 are similar to the classification, i.e. partial blocks to the main river (Chen & Peng 2003a, Chen 2000). The results of this laboratory experiment can be used for preliminary assistance for numerical simulation. Using either laboratory experiment or numerical simulation, the mechanism of confluence between the tributary and main river can be clarified.

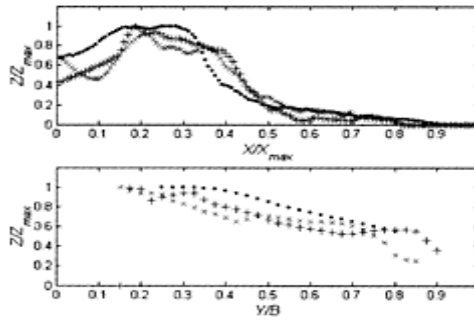

Figure 12c. Extracted profiles at alluvial fan centroid *(X_{CG}, Y_{CG})* for confluence angle 135 degrees: (top) longitudinal profile; (bottom) cross-section profile (●: slope of branch=30%, Q_m=0.66×10^{-4}cms; +: slope of branch=30%, Q_m=1.99×10^{-4}cms; ×: slope of branch=30%, Q_m=4.35×10^{-4}cms; density of mixture is 1.9g/cm^3).

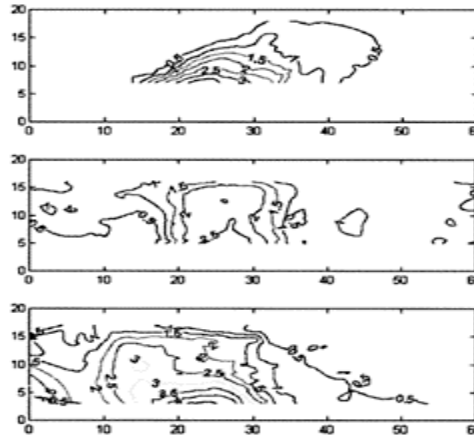

Figure 13. Contour examples of alluvial fans: (top) confluence angle=45 degrees; (center) confluence angle=90 degrees; (bottom) confluence angle=135 degrees.

5 CONCLUSIONS

As stated in the introduction, the major contribution of this study is the measurement of morphological

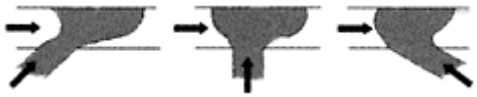

Figure 14. Summary of alluvial fan types: (left) confluence angle of 45 degrees; (center) confluence angle of 90 degrees; (right) confluence angle of 135 degrees.

information on the alluvial fan and the velocity field of confluence between tributary and main flow. We used digital image processing, including topography survey and Voronoï imaging method, to obtain the experimental results. The results show that the methods of measurement in this paper can capture the information precisely and conveniently. From our experiment, the measurement approach is effective and worth advanced research. Besides, through the discussion of alluvial fan morphology, the qualitative descriptions are interpreted for alluvial fan shape, alluvial fan volume, and sediment transportation. However quantitative analysis and further study are still needed.

REFERENCES

Capart, H., Young, D.L. & Zech, Y. 2002. Voronoï imaging methods for the measurement of granular flows. *Experiments in Fluids* 32: 121−135.

Chen, D.M. 2000. *Mechanism of confluence between debris flow and the main river*. Ph.D. thesis, China Inst. of Water Resources and Hydropower Research, China (in Chinese).

Chen, S.C. & Peng, S.H. 2003a. Confluence of debris slides and river flows in Taiwan. In C.F.Lee & L.G.Tham (eds), *Proceedings of the International Conference on Slope Engineering:* 757–762. Hongkong: University of Hong Kong.

Chen, S.C. & Peng, S.H. 2003b. Experiment of confluence between main river and tributary by applying digital image processing. *J. Chin. Soil Water Conserv.* 34(2): 195–205 (in Chinese).

Chen, S.C. 1999. Failure mechanism and disaster mitigation on landslide-dammed lakes. *J. Chin. Soil Water Conserv.* 30(4): 299–311 (in Chinese).

Jähne, B. 2002. *Digital Image Processing.* Berlin: Springer.

Kao, P.S. 2003. *The effects in main river morphology from hyperconcentrated tributary flow*. MSc thesis, National Chung-Hsing University, Taiwan (in Chinese).

Ni, W.J. 2004. MSc thesis, Dept. of Civil Engineering and Hydrotech Research Institute, National Taiwan University, Taiwan (in preparation).

Parker, G. *et al.* 1998a. Alluvial fans formed by channelized fluvial and sheet flow. I: theory. *J. of Hydraulic Engineering* ASCE 124(10): 985–995.

Parker, G. *et al.* 1998b. Alluvial fans formed by channelized fluvial and sheet flow. II: application. *J. of Hydraulic Engineering* ASCE 124(10): 996–1004.

Spinewine, B., Capart, H., Larcher, M. & Zech, Y. 2003. Three-dimensional Voronoï imaging methods for the measurement of near-wall particulate flows. *Experiments in Fluids* 34:227–241.
Tsai, Y.F. & Shieh, C.L. 1997. Experimental and numerical studies on the morphological similarity of debris-flow fans. *Journal of the Chinese Institute of Engineers* 20(6): 629–642.
Zhu, P.Y., Cheng, Z.L. & You, Y. 2000. Research on causes of river blocking by sediment delivery of Peilonggou Gully debris flow in the Sichuan-Xizang Highway. *Journal of Natural Disasters* 9(1):80–83 (in Chinese).

Transient hyper-concentrated flows: limits of some hypotheses in mathematical modelling

D.Berzi & E.Larcan
Politecnico di Milano, Dept. I.I.A.R., Milan, Italy

River Flow 2004—Greco, Carravetta & Della Morte (eds.)

ABSTRACT: A one-dimensional mathematical finite-difference model used for simulation of unsteady hyperconcentrated flow is described. This model is based on the Saint Venant equations, integrated via the MacCormack method. Two mass balance equations and one momentum equation are used, thus, the model can be seen as a quasi-two phase model. In the momentum equation the resistance term is derived from a semi-empirical formulation of shear stress in a generalized visco-plastic fluid (Chen 1996). Bed erosion and deposition effects are also included and numerical results are experimentally verified for high concentration flows in mild slope channel. Though the assumed hypothesis largely simplify the mathematical model, the validity of the model is confirmed, with particular attention on the role of the yield stress. A good agreement between numerical and experimental results is found, but, when the solid concentration is high and the densities of the two phases are significantly different, a quasi-two phase model seems to be unable to simulate the phenomenon. Considerations about the limits of the mathematical approach and the opportunity of more complicated models are underlined.

1 INTRODUCTION

The behaviour of a granular debris flow (flow of rigid spheres in an interstitial fluid) can be analysed through either a microscopic or a macroscopic approach. The former involves statistical mechanics, in particular the kinetic theory (Savage 1984,1989, Jenkins 1987); the latter considers debris flow as a continuum, such as in classical fluid mechanics (McTigue 1982, Chen 1986, 1988). Anyhow, the aim of this paper is to find the constitutive equations of the liquid-solid mixture and define the relation between the resistance terms and the kinematic quantities.

This paper concerns with the mathematical simulation of debris flows due to dam-break. Shear stresses in the mathematical model are approximated following the continuum mechanics approach. The use of formulas of uniform flow for a typical unsteady phenomenon represents another approximation. Nevertheless, a simple model with an empirical approach, such as the mathematical model presented herein, is preferred for practical design purposes. Thus, it seems very important to verify the rightness and the limits of the approximations introduced; hence, numerical results obtained with the model are compared with experimental data. These comparisons are used to define the validity range of the mathematical model, to find the limits imposed by the simplifying hypotheses and to suggest the research guidelines for its improvement.

2 EXPERIMENTAL SET-UP

The parameters of the mathematical model (Section 3) have to be set experimentally; therefore, experimental work has been carried out on a laboratory rig with a 6m long, square section (0.5×0.5m) flume of adjustable slope also for the validation of the results obtained with mathematical model. Failure of the dam can be simulated by means of a pneumatic rising sluice-gate (opening time t=0.3s). Debris flow is modeled by a water-solid mixture, the solid phase is reproduced with either common gravel (ρ=2621kg/m^3, d_{50}=0.005m) or a plastic homogeneous granular material called "vedril" (ρ=1168kg/m^3, d_{50}=0.003). Tests are performed for several solid concentrations, and different channel characteristics: slope (3.2°, 5°, 10°, 15° and 20°) and bottom roughness (zinc coated plate or fixed homogeneous gravel d_{50}=0.005m). A complete list of experimental runs is reported by Bertalli et al. (2002).

Sorting phenomenon are not taken into account because of the use of homogeneous solid material in the mixture. This fact appears to be very important in the dynamics of debris flows, yet too complicated to be implemented.

3 MATHEMATICAL MODEL

Usually models of dam-break waves are based on one-dimensional and two-dimensional schemes, while three-dimensional models are extremely rare. Some of these models consider the liquid-solid mixture as a single phase liquid, while others, more complicated, take into account both liquid and solid phases. Some of the later suppose that solid and fluid are characterized by the same average velocity and introduce only changes in solid concentration, caused by the erosion/deposition rate; other models involve also two different momentum equations, one for each of the two phases, defining, in a some way, the missing interaction component that closes the problem.

Herein the one-dimensional approach to the problem, which is the simplest one (Takahashi 1991, Egashira et al. 1997, Ghilardi et al. 1999, Berzi & Mambretti 2003), is used. The mathematical model presented is a quasi-two phase model that simulates the erosion/deposition phenomenon and uses a single momentum equation. Even if the phenomenon is typically impulsive, modeling is performed by numerical integration of

the well-known Saint Venant equations through a scheme relying on shock-capturing functions.

The equations can be written in matrix notation:

$$\frac{\partial \mathrm{U}}{\partial t}+\frac{\partial \mathrm{F}}{\partial x}=\mathrm{S} \tag{1a}$$

where:

$$\mathrm{U}=\begin{pmatrix} A \\ \rho_M Q \\ cA \\ A_d \end{pmatrix} \qquad \mathrm{F}=\begin{pmatrix} Q \\ \rho_M \dfrac{Q^2}{A}+\rho_M g I_1 \\ cQ \\ 0 \end{pmatrix} \tag{1b}$$

$$\mathrm{S}=\begin{pmatrix} \dfrac{EL}{c^*} \\ \rho_M g A(i-J)+\rho_M g I_2 \\ EL \\ -\dfrac{EL}{c^*} \end{pmatrix}$$

and x is the coordinate along the bottom of the flume; t is time; g is the gravitational acceleration; i is the channel slope; J is the resistance term; A is the cross-section area of the flow; Q is the flow-rate; ρ_M is the mixture density; c is the solid concentration in the mixture; c^* is the solid concentration at the bed; E is the erosion/deposition rate; L stands for the channel width at the interface between the flow and the movable bed layer; A_d is the cross-section area of the movable bed layer.

Here,

$$I_1=\int_0^h (h-\eta)\sigma(x,\eta)\,d\eta \qquad I_2=\int_0^h (h-\eta)\frac{\partial \sigma}{\partial x}\,d\eta \tag{2}$$

where h represents the water depth, while $\sigma(x, \eta)$ represents the channel width at the depth η. Equations la, and 1b represent the mass and momentum conservation laws in the solid-liquid mixture, the mass conservation of the solid phase and the mass conservation of the solid-liquid mixture in the movable bed layer. In these equations pressure distribution is considered hydrostatic, even if the presence of solid material should change the normal stress expression (Bagnold 1954, Chen 1996).

Equations la and 1b are integrated via a second-order precision finite-difference method (MacCormack & Baldwin 1975).

The numerical scheme can be written as follows:

$$\begin{aligned} \mathrm{U}_i^p &= \mathrm{U}_i^n-\frac{\Delta t}{\Delta x}\left[(1-\theta)\mathrm{F}_{i+1}^n-(1-2\theta)\mathrm{F}_i^n-\theta \mathrm{F}_{i-1}^n\right]+\Delta t \mathrm{S}_i^n \\ \mathrm{U}_i^c &= \mathrm{U}_i^n-\frac{\Delta t}{\Delta x}\left[\theta \mathrm{F}_{i+1}^p+(1-2\theta)\mathrm{F}_i^p+(\theta-1)\mathrm{F}_{i-1}^p\right]+\Delta t \mathrm{S}_i^p \\ \mathrm{U}_i^{n+1} &= \frac{1}{2}\left(\mathrm{U}_i^p+\mathrm{U}_i^c\right) \\ \theta &= 0,1 \end{aligned} \tag{3}$$

where subscripts *p* and *c* are predictor and corrector steps respectively and *n* and *i* are the space-time step indices. In order to make computations more stable, θ=1 as it is verified for hyper-concentrated fluids (Berzi & Mambretti 2003).

Like all finite-difference schemes with second order precision, MacCormack scheme is characterized by large oscillations when the flow becomes supercritical and in presence of singularity points. In order to reduce these effects and remove non-physical shocks due to numerical integration, artificial terms simulating viscosity effects are introduced. These terms become negligible when numerical solution are stable. MacCormack scheme written with the introduction of artificial viscosity terms gives:

$$\begin{aligned} U_i^p &= U_i^n - \frac{\Delta t}{\Delta x}\left[(1-\theta)F_{i+1}^n - (1-2\theta)F_i^n - \theta F_{i-1}^n\right] + \Delta t S_i^n \\ U_i^c &= U_i^n - \frac{\Delta t}{\Delta x}\left[\theta F_{i+1}^p + (1-2\theta)F_i^p + (\theta-1)F_{i-1}^p\right] + \Delta t S_i^p \\ U_i^{n+1} &= \frac{1}{2}\left(U_i^p + U_i^c\right) + \frac{\Delta t}{\Delta x}\left(\zeta_{i+1/2}^n + \zeta_{i-1/2}^n\right) \\ \theta &= 0,1 \end{aligned} \tag{4}$$

Jameson (1982) expression is used for evaluating parameter ζ:

$$\begin{aligned} \zeta_{i+1/2} &= \varepsilon_{i+1/2}^{(2)}\left(U_{i+1} - U_i\right) + \\ &- \varepsilon_{i+1/2}^{(4)}\left(U_{i+2} - 3U_{i+1} + 3U_i - U_{i-1}\right) \end{aligned} \tag{5}$$

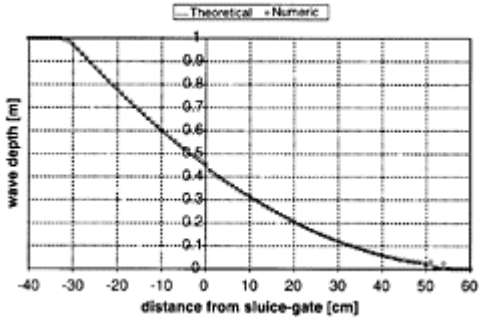

Figure 1. Comparison between Ritter analytical and numerical solution of dam-break wave (10s after dam-break).

where:

$$\begin{aligned} \varepsilon_{i+1/2}^{(2)} &= \max\left(\varepsilon_i^{(2)}, \varepsilon_{i+1}^{(2)}\right) \\ \varepsilon_i^{(2)} &= \alpha^{(2)} \frac{\left|h_{i+1} - 2h_i + h_{i-1}\right|}{h_{i+1} + 2h_i + h_{i-1}} \\ \varepsilon_{i+1/2}^{(4)} &= \max\left(0, \alpha^{(4)} - \varepsilon_{i+1/2}^{(2)}\right) \end{aligned} \tag{6}$$

When clear water is considered in dam-break problems, (Aureli et al. 1998 and references therein) one should set $\alpha^{(2)}$=0.5 and $\alpha^{(4)}$=0.02. In the case of debris flows the best values are different (see Section 4).

The model has been tested for clear-water dambreak (using c=0, E=0 and the Chézy formula for the resistance term J). Figure 1 shows the good agreement between numerical results and Ritter (1892) analytical solution. The global balance of mass seems to be verified too as it is shown in Figure 2.

When debris flow is considered, terms J and E ought to be described for making possible the integration of the equation system la, 1b. If the flow regime is laminar, the resistance term J can be derived from rheology, otherwise some empirical laws have to be considered.

Some expressions based on Bagnold (1954) shear stress and on a Chézy-like formula have been formerly tested (Berzi & Mambretti 2003).

Here, Chen (1996) rheological equation for a simple-shear granular flow is used:

$$\tau = s + \mu_1 \left(\frac{du}{dz} \right)^{\eta_1} \tag{7}$$

where z is the coordinate normal to the flume bottom; u is the local velocity in x-direction; s is the yield stress equal to p sin ϕ; $\phi$is the static friction angle and p the pressure. Equation 7 is valid for an incompressible Stokesian fluid; thus, the solid phase density and

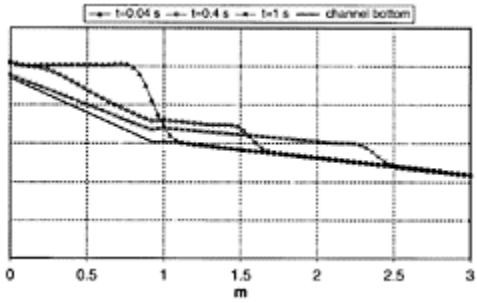

Figure 2. Wave at different times along the channel.

the interstitial liquid density should be the same. This denotes a clear limit of the model. Anyhow, if η_1=1, Equation 7 becomes the expression of a Bingham fluid in a macroviscous regime and if η_1=2 turns into the expression of a dilatant fluid in grain-inertia regime. Hereafter parameters η_1 and μ_1 are defined. For uniform flow in a wide open channel, the relation between the shear stress $\tau(z)$ and the resistance term J is:

$$\tau=\gamma(h-z)J \tag{8}$$

where γ is the specific weight of the mixture. From Equations 7, 8, under the hypothesis of hydrostatic pressure distribution, one can write:

$$\begin{cases} du = \left(\dfrac{\gamma(h-z)(J-\sin\phi)}{\mu_1} \right)^{\frac{1}{\eta_1}} dz & J > \sin\phi \\ du = 0 & J \le \sin\phi \end{cases} \tag{9}$$

The transverse velocity distribution can be obtained by integration of Equations 9:

$$\begin{cases} u(z) = -\dfrac{\mu_1\eta_1}{\gamma(J-\sin\phi)(\eta_1+1)} \left(\dfrac{\gamma(h-z)(J-\sin\phi)}{\mu_1} \right)^{\frac{\eta_1+1}{\eta_1}} + C \\ u(z) = 0 \end{cases} \tag{10}$$

where the first of Equations 10 is valid for $J > \sin\phi$, while the second for $J \le \sin\phi$. The constant C can be evaluated with the no slip condition. Thus, when z=0, $u(z)$=0:

$$C = \frac{\mu_1\eta_1}{\gamma(J-\sin\phi)(\eta_1+1)} \left(\frac{\gamma h(J-\sin\phi)}{\mu_1} \right)^{\frac{\eta_1+1}{\eta_1}} \tag{11}$$

Finally:

$$\begin{cases} u(z) = \dfrac{1}{ab}\left((ah)^b - (a(h-z))^b \right) & J > \sin\phi \\ u(z) = 0 & J \le \sin\phi \end{cases} \tag{12}$$

where:

$$\begin{aligned} a &= \frac{\gamma(J-\sin\phi)}{\mu_1} \\ b &= \frac{\eta_1+1}{\eta_1} \end{aligned} \tag{13}$$

The flow-rate Q is:

$$Q = VA = \int_A u dA \tag{14}$$

where V is the average velocity. Substituting Equation 12 in Equation 14 and dividing by the channel width L:

$$Vh = \int_0^h \frac{1}{ab}\left((ah)^b - (a(h-z))^b \right) dz$$

$$Vh = \frac{h}{ab}(ah)^b - \frac{1}{ab}\left(-\frac{(a(h-h))^{b+1}}{a(b+1)} + \frac{(ah)^{b+1}}{a(b+1)} \right)$$

$$a^{b-1} = V\frac{(b+1)}{h^b}$$

so that:

$$a = \left((b+1) \frac{V}{h^b} \right)^{\frac{1}{b-1}} \tag{15}$$

Now, introducing Equations 13 in Equation 15, the expression of the resistance term J results:

$$J = \frac{\mu_1}{\gamma} \left(\frac{2\eta_1 + 1}{\eta_1} \right)^{\eta_1} \frac{V^{\eta_1}}{h^{\eta_1+1}} + \sin\phi \tag{16}$$

For a Newtonian fluid $(\mu_1 = \mu, \eta_1 = 1, \phi = 0)$, Equation 16 exactly represents the resistance term in laminar flow in an indefinite plain:

$$J = 3 \frac{\mu}{\gamma} \frac{V}{h^2} \tag{17}$$

Equation 16 is valid if turbulent stresses in the interstitial fluid are supposed negligible. Otherwise, when the flow regime is grain-inertial, another empirical term has to be added as suggested by Bagnold (1954).

Concerning μ_1, Chen (1986, 1988) provides the following formula:

$$\mu_1 = \alpha_1 \rho_s^{\eta_1 - 1} d^{2(\eta_1 - 1)} \mu^{2-\eta_1} \mu_*(c) \tag{18}$$

where the parameter α_1 is a function of the solid material characteristics; ρ_s is the solid density; d is a characteristic diameter of solid material; μ is the viscosity of the interstitial fluid; μ_* is the relative viscosity of the granular suspension, function of the solid concentration c (Krieger & Dougherty 1959):

$$\mu_*(c) = (1 - Kc)^{-\frac{B}{K}} \tag{19}$$

with $K=1/c_m$; c_m is the solid maximum concentration and B the intrinsic viscosity, equal to 2.5 for a suspension of very lightly-concentrated rigid uniform spheres but higher for a suspension of heavily-concentrated spheres, in particular if the channel bottom is rough. If turbulent stresses in the interstitial fluid are neglected, only this parameter takes into account the influence on the wave profile of the bottom roughness. This effect is experimentally verified as shown in Figure 3. In this Figure dam-break waves of a hyper-concentrated fluid on smooth and rough bed bottom are depicted. Both tests are performed with a water-gravel mixture (c=0.2) and a channel slope i=20°; wave depth refers to a section placed 1.0m downstream from the sluice-gate.

Coefficient η_1 (Chen 1996) depends on the shear rate number N, similar to Bagnold number, ratio of the inertial stresses due to the particle collisions and the viscous stresses in the interstitial fluid. N can be expressed as (Chen 1986):

$$N = \frac{\rho_s d^2 D}{\mu} \tag{20}$$

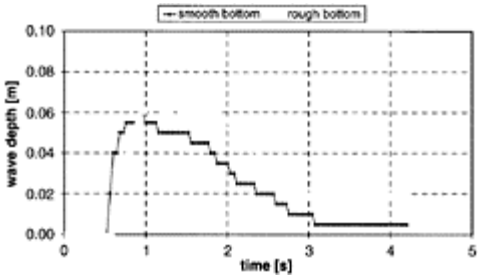

Figure 3. Influence of the bottom roughness on dam-break waves.

where $D=du/dz$. For $N\rightarrow 0$ $\eta_1=1$ (macroviscous regime), for $N\rightarrow\infty$ $\eta_1=2$ (grain-inertia regime). Between these two asymptotic regimes, η_1 assumes intermediate values. On the basis of the tests performed by Bagnold (1954) and Savage and McKeown (1983), Chen (1996) obtained the values of η_1 shown in Figure 4.

Figure 4 shows also the interpolating relation between η_1 and N used in this paper.

A similar relation between a_1 and N doesn't exist because α_1 depends on some material constants, such as a coefficient of restitution.

The experimental tests demonstrate an important solid material exchange between the debris flow wave and the movable bed. Hence, it seems essential to introduce the erosion/deposition rate as a function of some relevant quantities.

Erosion/deposition rate E, defined by Honda & Egashira (1997) and modified by Ghilardi et al. (1999), is here used:

$$\frac{E}{V} = K_E \cdot \tan\left(\vartheta_f - \vartheta_e\right) \tag{21}$$

where:

$$\vartheta_f = \tan^{-1}\left(\frac{J}{\cos i_b}\right) \tag{22}$$

where i_b is the bed slope. θ_e is the equilibrium bed slope. In uniform flow condition θ_e is (Takahashi 1991):

$$\tan\vartheta_e = \frac{\left(\frac{\rho_s}{\rho_l}-1\right)\cdot c}{\left(\frac{\rho_s}{\rho_l}-1\right)\cdot c+1}\tan\phi \tag{23}$$

where ρ_l is interstitial fluid density. In Equation 21 the coefficient K_E is introduced in order to obtain the best fitting with experimental results.

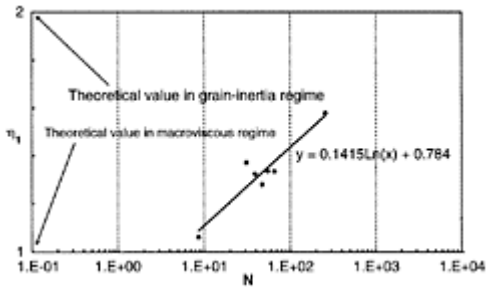

Figure 4. Relation between shear rate number N and coefficient η_1.

4 MODEL SETTING

The mathematical model includes some parameters whose values have to be set. Some of these parameters are introduced in order to reduce the oscillations in the numerical solution due to non-physical shocks. Others are used to calibrate the model and their values can be defined only on the basis of field measurements and best fitting analysis. The latter has been performed by the comparisons between numerical and experimental results of six tests, taken as representative of the whole phenomenon, with different values of channel bed slope, solid concentration, solid material and bottom roughness.

The value of the parameter c^* is chosen by measuring the solid concentration in the deposited material: for the gravel c^*=0.49 and for the vedril c^*=0.54.

The static friction angle $\phi$is equal to 0.5233 rad for gravel and to 0.4815 rad for vedril. The mathematical model provides good results when the solid concentration is low-medium (c=0.2–0.4), without considering the yield stress. The yield stress has to be introduced, when the solid concentration is higher (c=0.6). This fact influences the value of the artificial viscosity term parameters $\alpha^{(2)}$ and $\alpha^{(4)}$. Best results are obtained setting $\alpha^{(2)}$=1 and $\alpha^{(4)}$=4 when the yield stress is neglected, while $\alpha^{(2)}$=5 and $\alpha^{(4)}$=2 are to be considered if the yield stress is introduced. Figure 5 shows several wave profiles for different values of the parameter $\alpha^{(2)}$.

The relation between η_1 and the shear-rate number N is described in the previous Section. Assuming a triangular velocity distribution along the z-direction, Equation 21 becomes:

$$N = \left(\frac{\rho_s}{\rho_l}\right)\left(\frac{d}{h}\right)^2\left(\frac{2Vh\rho_l}{\mu}\right) \tag{24}$$

α_1 is always positive and less than 2 (Chen 1996) but its value depends on the type of the solid material. Since a sensitivity analysis shows that the numerical solution

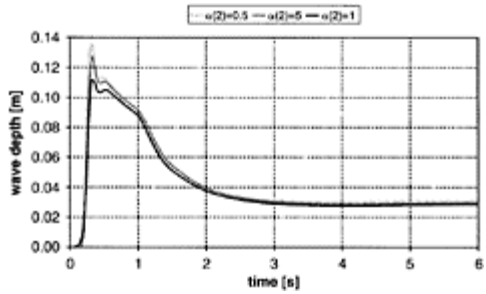

Figure 5. Wave depth versus time in a section at 0.4m from the sluice-gate with different values of $\alpha^{(2)}$.

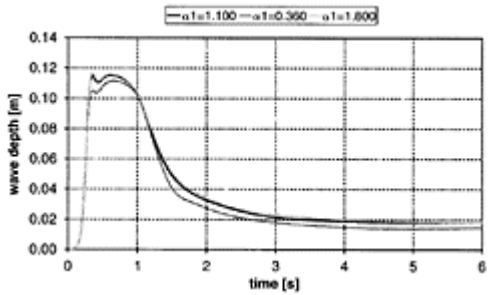

Figure 6. Wave depth versus time in a section at 0.4m from the sluice-gate with different values of α_1.

is weakly influenced by this parameter (Fig. 6), here α_1 is set 1.1 both for gravel and for vedril material.

The intrinsic viscosity B is important because it takes into account the influence of the bottom roughness on the wave behaviour. A thorough study about the value of this parameter could be performed in the future.

Here, when the flume bottom is a zinc coated plate B=3 and, as suggested by Chen (1996) for the granular flow of neutrally buoyant particles, B=4.5 when the flume bottom is an homogeneous gravel bed.

The K_E parameter, introduced in Equation 21, is set equal to 0.1 as indicated by Ghilardi et al. (1999) for unsteady flow.

5 COMPARISONS WITH EXPERIMENTS

The mathematical model involves large simplifications; first, the solid and the liquid phases are characterised by the same average velocity and the same density: hence a

single momentum equation can be employed and the resistance term J can be expressed as described in Section 3. Thus, one can expect that a good agreement between numerical results and experimental data will be obtained only when the solid material is vedril, whose density is similar to water density. Figures 7, 8 show the comparisons between experimental and numerical results: wave depth h versus time t graphs, at a section located 1.0m downstream from the sluice-gate are shown. Figure 7 regards the test performed with gravel-water mixture while Figure 8 that with vedril-water mixture. The solid concentration in both cases is equal to 0.2 and the flume bottom is set rough with a 5° slope.

Figure 7 shows that numerical results of the maximum wave depth as well as the deposit layer thickness (see for $t \geq 3.5$s) are definitely overestimated respect to experimental data; on the contrary, the reaching time to the measurement section is well predicted.

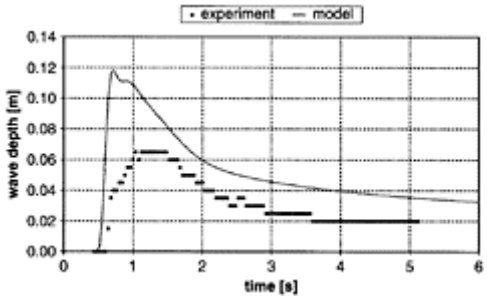

Figure 7. Comparison between numerical and experimental results. Test performed with gravel mixed with water (c=0.2), a rough bottom of slope i=5°, measurement section at 1.0m from the gate.

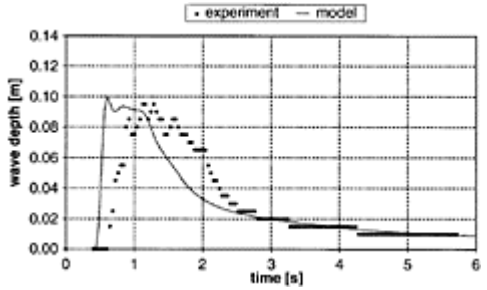

Figure 8. Comparison between numerical and experimental results. Test performed with vedril mixed with

water (c=0.2), a rough bottom of slope i=5°, measurement section at 1.0m from the gate.

In Figure 8 it can be observed that the mathematical model supplies a good estimate of both the maximum wave depth and the deposit thickness. The simulated wave appears to move faster than the experimental wave (around 0.2s), maybe because of the non-zero opening time of the sluice-gate.

These considerations are valid for all the tests performed and at any section of the flume. For example, Figure 9 shows another comparison between numerical and experimental results at a section located 0.4 m downstream from the sluice-gate. The test is performed with vedril-water mixture (solid concentration equal to 0.2) and on a smooth flume bottom with a 5° slope. In this case perhaps a careful analysis of the intrinsic viscosity value B could improve the agreement between the numerical results and the experimental data.

The Saint Venant equations are based on the hypothesis of mild slope; then, its foreseeable that agreement between the numerical and the experimental results should worsen when the slope increases. Indeed, Figure 10 shows the comparison between numerical and experimental results, at the same section of Figure 9

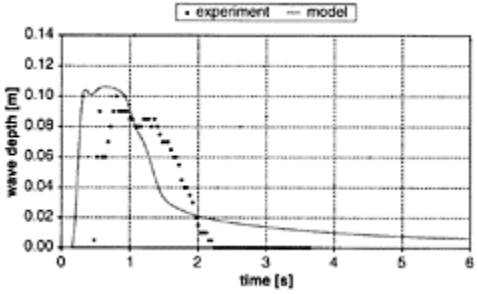

Figure 9. Comparison between numerical and experimental results. Test performed with vedril mixed with water (c=0.2), a smooth bottom of slope i=5°, measurement section at 0.4m from the gate.

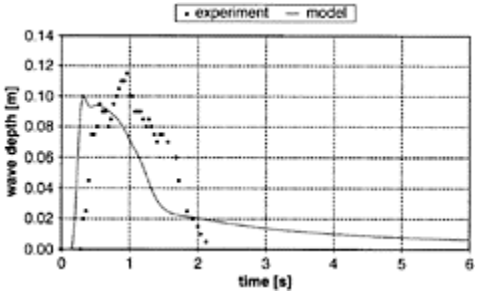

Figure 10. Comparison between numerical and experimental results. Test performed with vedril mixed with water (c=0.2), a smooth bottom of slope i= 15°, measurement section at 0.4m from the gate.

and with the same experimental conditions except that the channel slope. This is set 15° and it can be noticed that the wave depth peak is underestimated (around 20% less than measured one).

The comparisons shown refer to tests performed with mixtures with low solid concentration and neglecting in the mathematical model the yield stress in the resistance term; thus, sin ϕdoes not appear in Equation 16. For high solid concentration, the yield stress has to be introduced in order to avoid results that do not reflect the real phenomenon. Yield stress seems to be present only when continuous friction among the grains develops in high concentration flows.

Figures 11, 12 show the comparisons between numerical and experimental results, at a section located 0.4m downstream from the sluice-gate; whether the yield stress in the model is included or not. Both figures regard tests performed on a rough bottom and a 5° slope with mixtures with a solid concentration equal to 0.6. In Figure 11 the solid material used is gravel, while in Figure 12 it is vedril.

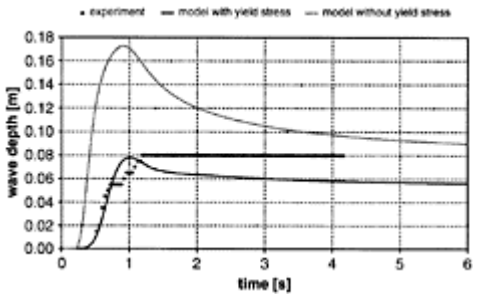

Figure 11. Comparison between numerical and experimental results.

Test performed with gravel mixed with water (c=0.6), a rough bottom of slope i=5°, measurement section at 0.4m from the gate.

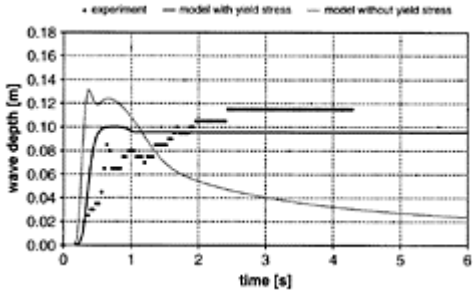

Figure 12. Comparison between numerical and experimental results. Test performed with vedril mixed with water (c=0.6), a rough bottom of slope i=5°, measurement section at 0.4m from the gate.

It can be seen that the wave behaviour is completely misunderstood if the yield stress is not present in the shear stress expression used for the calculation of the resistance term in the model.

Anyhow, even if the yield stress is taken into account, deposit thickness is largely underestimated (about 20–25%).

6 CONCLUSIONS

The matter of the present paper is the analysis of the hypotheses upon which a one-dimensional mathematical model of granular debris flow consequent to dam-break is based. These hypotheses represent a limitation for the application of the model, although their introduction is necessary in order to simplify the problem. The model equations are integrated via a shock-capturing MacCormack scheme.

The main hypotheses considered are the following:

i. the solid and the liquid phase are characterised by the same average velocity;
ii. the water-solid mixture density is constant, that is the solid material is neutrally buoyant;
iii. pressure distribution along the cross-section of the flow is hydrostatic;
iv. the channel slope is mild;

v. the presence of the solid material does not involve changes in the expression of the normal stresses.

The importance of the hypotheses (i) and (ii) is underlined by the comparisons between numerical and experimental results when the solid material is gravel, whose density is much larger than water density. The hypotheses (iii) and (iv) are used to obtain a one-dimensional version of the mathematical model, while hypothesis (v) allows a further simplification. Moreover, some parameters of the model allow its calibration and avoid oscillations in the numerical solution; the values of the parameters for best fitting with experimental data are indicated.

The comparisons between numerical and experimental data show that the mathematical model can satisfactory predict the wave behaviour consequent to dam-break, if the solid concentration is low-medium and the solid material density is similar to the interstitial fluid density. Concerning higher solid concentrations, the introduction of the yield stress term in the shear stress expression allows a quite satisfactory, yet not excellent, agreement with experimental data. The density of the debris in real granular flows is much larger than the water density, therefore the mathematical model employed seems to oversimplify the problem, though it provides useful indications for a first, often safe, evaluation of the wave depths.

It seems that the correct simulation of the unsteady granular flow consequent to dam-break requires a more complex and complete approach. A first improvement can be reached removing the hypothesis of hydrostatic pressure distributions, that means the use of at least, a two-dimensional mathematical model, which will also solve the problem of modelling the complex geometry that characterizes real debris flows. Finally, it is remarkable that only a two-phase mathematical model, employing two different momentum equations, seems to be able to better reproduce the behaviour of a real debris flow.

REFERENCES

Aureli, E, Maione, U, Mignosa, P. & Tomirotti, M. 1998. Fenomeni di moto vario conseguenti al crollo di opere di ritenuta—Parte II: Indagini sperimentali e modellazione numerica in presenza di onde di shock. (in Italian), *L'Acqua*, 5.

Bertalli, L., Larcan, E. & Mambretti, S. 2002. Leggi di resistenza al moto nelle colate di detriti conseguenti al crollo di dighe. 1: Apparato sperimentale e primi risultati. (in Italian), *Atti del XXVIII Convegno di Idraulica e Costruzioni Idrauliche* 3:219–226. Potenza.

Berzi, D. & Mambretti, S. 2003. Mathematical modeling and experimental tests of unsteady flow of non-Newtonian fluids. In D.Rickenmann and C.Chen (eds.), *Proc. 3rd ASCE Int. Conf. On Debris flow hazard mitigation: mechanics, prediction ad assessment.* 447–456. Davos Switzerland.

Chen, C.L. 1986. Bingham plastic or Bagnold's dilatant fluid as a rheological model of debris flow? *Proc. 3rd Int. Symp. On River Sedimentation.* 1624–1636, Univ. of Mississipi. United States.

Chen, C.L. 1988. Generalized viscoplastic modeling of debris flow. *J. Hydr. Engrg.*, ASCE, 114(3):237–258.

Chen, C.L. & Ling, C.H. 1996. Granular-flow rheology: role of shear-rate number in transition regime. *Journal of Engineering Mechanics*, 122(5):469–480.

Egashira, S., Miyamoto, K. & Itoh, T. 1997. Constitutive equations of debris flow and their applicability. In C.Chen (ed.), *Proc. 1st ASCE Int. Conf. On Debris flow hazard mitigation: mechanics, prediction ad assessment,* August 7–9:340–349. San Francisco, California.

Ghilardi, P., Natale, L. & Savi, F. 1999. Two mathematical models simulating a real-world debris flow. *Proc. of the IAHR Symposium on "River, Coastal and Estuarine Morphodynamics"*. Genova.

Honda, N. & Egashira, S. 1997. Prediction of debris flow characteristics in mountain torrent. In C.Chen (ed.), *Proc. 1st ASCE Int. Conf. On Debris flow hazard mitigation: mechanics, prediction ad assessment,* August 7–9: 707–716. San Francisco, California.

Jameson, A. 1982. Transonic Airfoil calculations using the Euler equations. In P.L.Roe (ed.), *Numerical Methods in Aeronautical Fluid Dynamics,* Academic Press. New York.

Jenkins, J.T. 1987. Balance laws and constitutive relations for rapid flows of granular materials. In J.Chandra and R.P.Srivastav (eds.), *Constitutive models of Deformation,* Soc. For Industrial and Appl. Math.: 109–119. Philadelphia, Pa.

Krieger, I.M. & Dougherty, T.J. 1959. A mechanism for non-Newtonian flow in suspensions of rigid spheres. *Trans. Soc. of Rheology,* 3:137–152.

MacCormack, R.W. & Baldwin, B.S. 1975. A numerical method for solving the Navier-Stokes equations with application to shock-boundary layer interaction. *AIAA,* Paper 75–1.

McTigue, D.F. 1982. A nonlinear constitutive model for granular materials: application to gravity flow. *J. Appl. Mech.,* 49(2):291–296.

Ritter, A. 1892. Die Fortplanzung der Wasserwellen. *Zeitschrift des Vereines Deutscher Ingenieure,* vol. 36, n. 3.

Savage, S.B. 1984. The mechanics of rapid granular flows. *Adv. in Appl Mech.,* 24:289–366.

Savage, S.B. 1989. Flow of granular materials. In P.German, M.Piau and D.Caillerie (eds.), *Theoretical and Appl. Mech.:* 241–266. Amsterdam, The Netherlands.

Savage, S.B. & McKeown, S. 1983. Shear stresses developed during rapid shear of concentrated suspensions of large spherical particles between concentric cylinders. *J. Fluid Mech.,* 127:453–472.

Takahashi, T. 1991. Debris flow. *IAHR Monograph Series.* Balkema.

Numerical simulation of hyper-concentrated flows

D.Komatina & D.Đorđević
Faculty of Civil Engineering, University of Belgrade, Belgrade, Serbia & Montenegro

River Flow 2004—Greco, Carravetta & Della Morte (eds.)

ABSTRACT: Numerical modelling of dam-break or dike-break flows of homogeneous non-Newtonian fluids is presented in the paper. One of the most important tasks when formulating such a model is an estimation of friction losses, so that a constitutive equation must be adopted for the fluid under consideration. The constitutive equation introduced into the presented model is based on a general yield-power law (Herschel-Bulkley's rheological model). Numerical model used herein to solve the governing equations of 1D unsteady free-surface flow is based on the MacCormack explicit finite-difference scheme. The proposed model is verified using results of laboratory dam-break tests of mine tailings mixed with water. The mixtures are considered homogeneous, the material being composed mainly of silt and clay and wave propagation being considered of short duration. A comparison between measured and calculated results is given through a number of diagrams, showing the effect of varied parameters both on the wave propagation speed, and the flow depths.

1 INTRODUCTION

Dam-break flow of mine tailings seems to be one of the most dangerous hazards threatening local people, property and the whole environment. Therefore, a considerable attention has been paid to analysis of unsteady free-surface flows of highly concentrated solid-liquid mixtures, which have a non-Newtonian character, such as liquefied mine tailings (Jeyapalan et al. 1983, Komatina 1998), mud and debris (Han & Wang 1996, Huang & García 1997, Hunt 1994, Jin & Fread 1999, Laigle & Coussot 1997, McArthur & Schamber 1986, O'Brien et al. 1993). Few analytical solutions to the problem have been given (Huang & Garcia 1997, Jeyapalan et al. 1983), applying Bingham plastic

rheological model for description of mud and mine tailings flows. Examples of physical modelling of such flows have been presented as well (Coussot 1994, Komatina 1999).

Unsteady dam-break flow of highly viscous solid-liquid mixtures has been numerically studied so far using various constitutive relationships. Newtonian (Aguirre-Pe et al. 1995, Hunt 1994), Bingham (McArthur & Schamber 1986) and Herschel-Bulkley's fluid models (Laigle & Coussot 1997) have been applied to laminar flow modelling, while hybrid models have been employed for turbulent flow modelling—quadratic model (Bingham model, extended to account for turbulent and dispersive stresses) (Liu & Lai 2000, O'Brien et al. 1993), or a model established combining Bingham and Chezy-type relationships (Han & Wang 1996). Explicit numerical schemes of a finite-difference (Aguirre-Pe et al. 1995, Laigle & Coussot 1997) and finite-element type (McArthur & Schamber 1986) have been used in numerical treatments for 1D (Aguirre-Pe et al. 1995, Hunt 1994, McArthur & Schamber 1986) and 2D modelling (Han & Wang 1996, Laigle & Coussot 1997, McArthur & Schamber 1986, O'Brien et al. 1993). Implicit numerical scheme has not been employed to such an extent for modelling unsteady hyper-concentrated flows, due to difficulties when modelling flows having discontinuities (Fraccarollo 1997). It has been accepted as an unconditionally stable, robust and suitable for application to tasks requiring both spatially and temporally huge computational domains (Cunge et al. 1980, Meselhe & Holly 1997), which are likely to occur in nature. Additionally, it has been successfully used in the clear water dam-break subcritical flow modelling (Hicks et al. 1997). However, in a paper of the authors (Komatina & Lalović 2000), where the implicit 4-point finite-difference scheme has been applied, quality of the simulation results decreased due to impossibility of a dry-bed computation—calculated longitudinal profiles of the waves were too smooth and the wave front locations were greater than those measured in laboratory.

In order to improve modelling of discontinuous flows, such as the dam-break hyper-concentrated flow, an application of a shock-capturing scheme, which allows for weak solutions, is analysed in this paper. Therefore, the MacCormack explicit finite-difference scheme, whose good performance in discontinuous Newtonian flow modelling has been reported in literature (Aguirre-Pe et al. 1995, Bellos & Sakkas 1987, Đorđević 2000, Garcia-Navarro & Saviron 1992, Jovanović & Đorđević 1995), is used for 1D numerical modelling of dam-break flows of liquefied mine tailings, previously performed in laboratory canal (Komatina 1998). Friction losses are calculated in the model using the Herschel-Bulkley's rheological equation.

2 FRICTION FACTOR MODELLING

A case of uniform free-surface flow of a homogeneous time-independent incompressible non-Newtonian fluid in a wide channel is considered. It can be shown from momentum equation that the shear stress distribution over the flow depth is linear, see Figure 1:

$$\tau=\tau_o\cdot(1-y/h) \tag{1}$$

where τ is the shear stress at a distance y from the bottom, τ_o is the bottom shear stress:

$$\tau_o=\rho g h\cdot\sin\alpha\approx\rho g h S_o \tag{2}$$

ρ is the fluid density, g—gravitational acceleration, h—flow depth, a—bottom slope angle, S_o—bottom slope, ξ—dimensionless distance from the fluid surface:

$$\xi=\tau/\tau_o=1-y/h \tag{3}$$

and ξ_c—non-dimensional plug flow width, given by:

$$\xi_c=\tau_c/\tau_o=1-y_c/h \tag{4}$$

where y_c is the distance from the bottom where $\tau=\tau_c$.

Evaluation of the friction slope is of a crucial importance in solving the governing equations for a non-Newtonian fluid. For this purpose, a constitutive equation for the material under consideration has to be

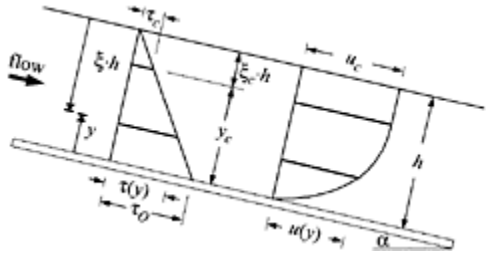

Figure 1. Shear stress *(τ)* and flow velocity *(u)* distribution, shown schematically.

adopted. The Herschel-Bulkley's model is used in the paper:

$$\begin{aligned}\tau &= \tau_c+\eta\cdot\dot{\gamma}^m, \quad \tau>\tau_c\\ \dot{\gamma} &= 0 \qquad\quad , \quad \tau\le\tau_c\end{aligned} \tag{5}$$

where $\dot{\gamma}$denotes shear rate; τ_c, η, and m—rheological parameters of the fluid (yield stress, consistency index and flow behaviour index, respectively). The equation comprises yield and viscous stress components and is valid in laminar flow regime only.

By double integration of Equation 5 over the flow depth, the laminar flow equation can be derived in the following form (Coussot 1994):

$$\frac{3U}{h}=\left(\frac{\tau_o}{\eta}\right)^{1/m}\cdot\Phi \tag{6}$$

where U is the mean flow velocity, which is, for a wide channel, equal to the depth-averaged velocity, and the dimensionless function Φ is defined by:

$$\Phi = \frac{3m}{2m+1} \cdot \left[1 + \frac{m}{m+1} \cdot \xi_c \right] \cdot (1 - \xi_c)^{(m+1)/m} \tag{7}$$

It is well known that standard Newtonian relationships for clear water can be applied for calculation of friction factor for a non-Newtonian fluid, if the Reynolds number is expressed in an extended form, so as to include all the rheological parameters of the fluid (Wan & Wang 1994). For the Herschel-Bulkley's model, the extended Reynolds number is defined as (Komatina 1999):

$$\mathrm{Re}_{ext} = \mathrm{Re} \cdot \Phi^m \tag{8}$$

where the Newtonian Reynolds number is equal to:

$$\mathrm{Re} = \frac{4\rho \cdot U^{2-m} \cdot h^m}{\eta \cdot 3^{m-1}} \tag{9}$$

So, the standard Moody relationship, which can be obtained from Equation 6, is applied in the laminar flow regime (Re_{ext}<2100), (Komatina 1999):

$$f = \frac{24}{\mathrm{Re}_{ext}} \tag{10}$$

and the Blasius formula is applied in the turbulent flow regime (Wan & Wang 1994):

$$f = \frac{0.079}{\mathrm{Re}_{ext}^{1/4}} \tag{11}$$

The bottom shear stress is then determined using the calculated value of the friction factor:

$$\tau_o = f \cdot \frac{\rho U^2}{2} \tag{12}$$

3 GOVERNING EQUATIONS

The 1D unsteady free-surface hyper-concentrated flow is described by the De St.-Venant equations in conservative form:

$$\mathbf{U}_t + \mathbf{E}_x = \mathbf{S} \tag{13a}$$

$$\mathbf{U} = \begin{bmatrix} A \\ Q \end{bmatrix}, \qquad \mathbf{E} = \begin{bmatrix} Q \\ \dfrac{Q^2}{A} + g I_1 \end{bmatrix}, \tag{13b}$$

$$\mathbf{S} = \begin{bmatrix} 0 \\ g A (S_o - S_f) + g I_2 \end{bmatrix}$$

where x and t are space coordinate and time, respectively; A—the flow area; Q—the discharge; S_o—bottom slope and S_f—friction slope. The terms I_1 and I_2 are related to the hydrostatic pressure force:

$$I_1 = \int_0^h (h-\zeta) b(x,\zeta) \mathrm{d}\zeta \ , \quad I_2 = \int_0^h (h-\zeta) \frac{\partial h}{\partial x} \mathrm{d}\zeta \tag{14}$$

in which: the depth integration variable along y-axis is denoted by ζ, the width of the cross-section at the distance ζ from the bottom of the cross-section, which is located at distance x along channel by $b(x, \zeta)$. In prismatic channels I_2=0.

3.1 *Determination of the friction slope*

It is usually assumed that for unsteady flow, the bottom shear stress at a specific point is equal to the value of the uniform flow with a corresponding flow discharge and depth (Aguirre-Pe et al. 1995, Laigle & Coussot 1997). Consequently, application of simple rheological relationships, such as Equation 5, is possible.

The friction slope in Equation 13 is determined using the relationship:

$$\tau_o = \rho g h S_f \tag{15}$$

on the basis of the bottom shear stress, previously calculated from Equation 12.

4 NUMERICAL MODEL

The system of partial differential hyperbolic-type equations 12 is numerically solved using the MacCor-mack explicit finite-difference scheme. The scheme is second order accurate in both the space and time. It consists of a two step predictor-corrector sequence:

Predictor:

$$\mathbf{U}_i^p = \mathbf{U}_i^k - \frac{\Delta t}{\Delta x} \nabla_x \mathbf{E}_i^k - \Delta t \mathbf{S}_i^k, \ 2 \le i \le N \tag{16}$$

Corrector:

$$\mathbf{U}_i^c = \mathbf{U}_i^p - \frac{\Delta t}{\Delta x} \Delta_x \mathbf{E}_i^p - \Delta t \mathbf{S}_i^p, \quad 1 \le i \le N-1 \tag{17}$$

New value:

$$\mathbf{U}_i^{k+1} = \frac{1}{2}\left(\mathbf{U}_i^k + \mathbf{U}_i^c\right) \tag{18}$$

Here, subscript i defines a position of the cross-section along the x-axis, superscripts k and k+1 denote values of the variables at the previous time level *(k)* and the following time level (k+1), whereas superscripts p and c denote values in the predictor and corrector steps, respectively.

The backward and forward difference operators are defined by:

$$\nabla_x \mathbf{E}_i = \mathbf{E}_i - \mathbf{E}_{i-1}, \quad \Delta_x \mathbf{E}_i = \mathbf{E}_{i+1} - \mathbf{E}_i \tag{19}$$

The operator sequence in the predictor and the corrector steps is alternated each time step, which means the operator cycle is concluded in two time steps. In order to provide numerical stability of the scheme, the Courant-Friedrichs-Lewy's criterion is used to determine the time step Δt in Equations 16 and 17.

5 EXPERIMENTS

Mixtures of water and copper tailings taken from the Veliki Krivelj copper mine (Serbia and Montenegro) were used as experimental fluids. The mean diameter of particles is 0.025mm, with 8% of the material finer than 0.002mm, and 70% finer than 0.062mm. The density is 2650kg/m^3, and its chemical composition: 63%SiO_2, 14%Al_2O_3, 3.5%Fe, 3%K_2O, 3% CaO, 3%MgO and 3%Na_2O. Clayey fractions of the material are of kaolinite-illite type.

Rheological parameters of the mixtures were determined using two types of measurements: in a commercial rotational viscometer and in the laboratory canal, illustrated in Figure 2. Measurement errors were estimated to 13% (viscometer) and 16% (canal), (Komatina 1999). The applied procedures provided data on rheological behaviour of the mixtures in different ranges of shear rate: small shear rates (0.5 to 20s^{-1}) in the case of steady-state free-surface flow experiments in the canal, and 50 to 250s^{-1},

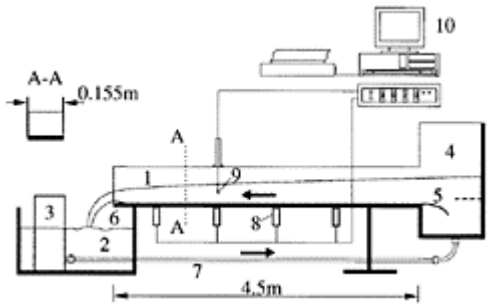

Figure 2. Laboratory flume and measurement equipment: 1—flume, 2—lower tank, 3—pump, 4—upper tank, 5—deflector, 6—control weir, 7—fluid supply rubber tube, 8—membrane probes, 9—electromagnetic probe, 10—data acquisition and processing system.

Table 1. Rheological properties of mixtures.

Mixture	C_V %	ρ kg/m^3	τ_c Pa	η mPas^m	m
1	13.8	1228	0.7	0.52	0.55
2	18.1	1299	1.0	1.58	0.55
3	32.2	1531	60.0	35.50	0.55
4	36.4	1601	120.0	102.00	0.55

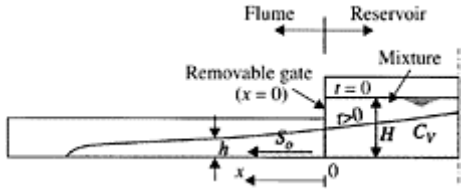

Figure 3. Sketch of a dam-break flow experiment.

using the rotational viscometer. For a mixture, two linear relationships (Bingham model) were defined for each of the shear rate ranges. Finally, a yield power-law (Herschel-Bulkley's model) was defined so as to match the linear relationships. Values of the rheological parameters, obtained in this manner, are listed in Table 1 (where C_V denotes the volumetric concentration of the solid phase).

The dam-break flow experiments were performed in a 4.5m long, 0.15m wide glass-walled laboratory flume, with adjustable bottom slope (Fig. 2). The dam-break type of flow was initiated by releasing mixtures from a 2m long, 0.155m wide reservoir, situated on the upstream part of the flume. A sketch of the experiment is given in Figure 3 (H—initial reservoir depth). Experimental parameters were varied in the following ranges: S_o=0–1%, H=10−30cm, C_V=0–5.6%.

6 RESULTS AND DISCUSSION

Results from the laboratory rig, depicted in Figure 2, were used to verify the results of numerical simulation of one-dimensional unsteady hyper-concentrated flow. The flow was caused by a sudden release of the mixture (induced by an abrupt removal of the gate between the reservoir and the canal), stored in the 2.0m long and 0.155m wide reservoir that had been formed in the upstream part of the flume. The propagation of a positive wave in an initially dry canal was filmed by a video camera with recording speed of 5 images per second. The glass walls had been covered with a square net (Δx=Δz=1cm), thus it was possible to "read" the records—read the flow depths along the canal. Settling

of particles during the propagation was neglected, as the propagation time was short relatively to the settling time of the material composed mainly of silt and clay.

The evolution of the measured and the calculated flow depth profiles of four experiments with different mixtures, in which the initial depth in the reservoir was H=0.3m and the bottom canal slope 1%, are shown in Figures 4–7. The properties of the mixtures are given in Table 1. The initial condition at the opening was defined according to the theoretical Ritter's solution for the one-dimensional dam-break problem: $h=(4/9)H, u=(8/17)\sqrt{gH}$., while for numerical reasons, the initial depth downstream from the reservoir was set to 0.001m. No artificial viscosity was used.

For the sake of easier comparison with the measurements, the time step, used in this simulation, was kept constant Δt=0.01s, which resulted in the maximum Courant's number values of 0.6 for lower concentration mixtures and 0.4 for higher concentration mixtures.

It can be noticed (Figs 4–7), that the wave front propagation speed is generally well reproduced for all the mixtures—the differences between the calculated and the measured wave front locations are less then ±3%. However, discrepancies between the calculated and the measured flow depth profiles expressed in reference to the measured flow depths are somewhat greater for the mixtures with lower concentration of solids (Figs 4–5), than those pertaining to the mixtures with higher concentration of solids (Figs 6–7). The discrepancies for the former mixtures are as high as 45% at the steep front, where it was not possible to read the flow depths from the video tapes accurately. The flow depths were too small to recognize and read easily from the recordings. On the other hand, discrepancies between the calculated and the measured flow depth profiles for the mixtures with higher concentrations of solids (Figs 6–7) are much lesser, since the wave front heights were much greater for these mixtures. Discrepancies for about 90% of the results are within ±15%.

Furthermore, the effect of slowing down the advancing front is readily noticeable for the mixture

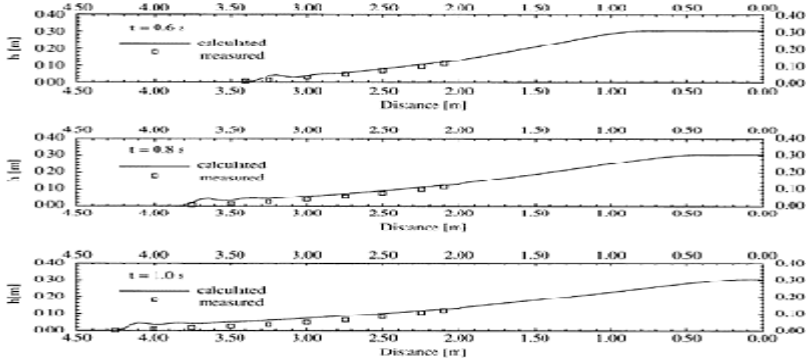

Figure 4. Comparison of the calculated and the measured flow depth profiles for the mixture with C_V=13.8%.

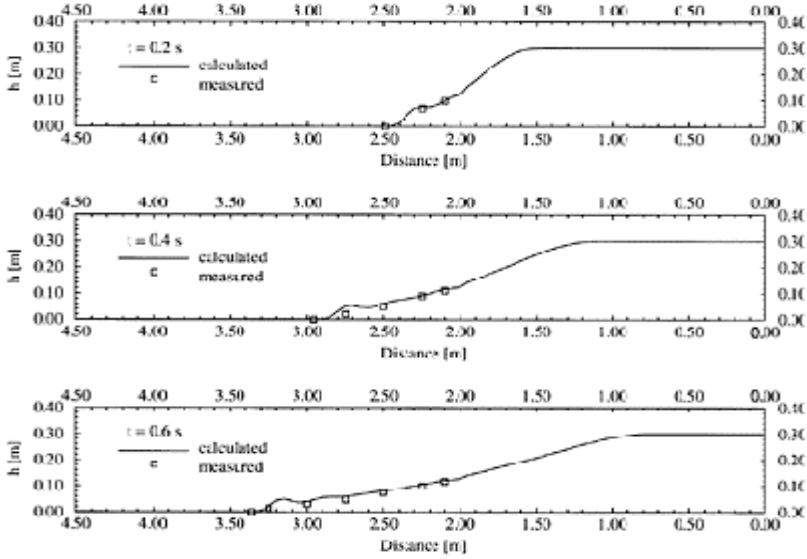

Figure 5. Comparison of the calculated and the measured flow depth profiles for the mixture with C_V=18.1%.

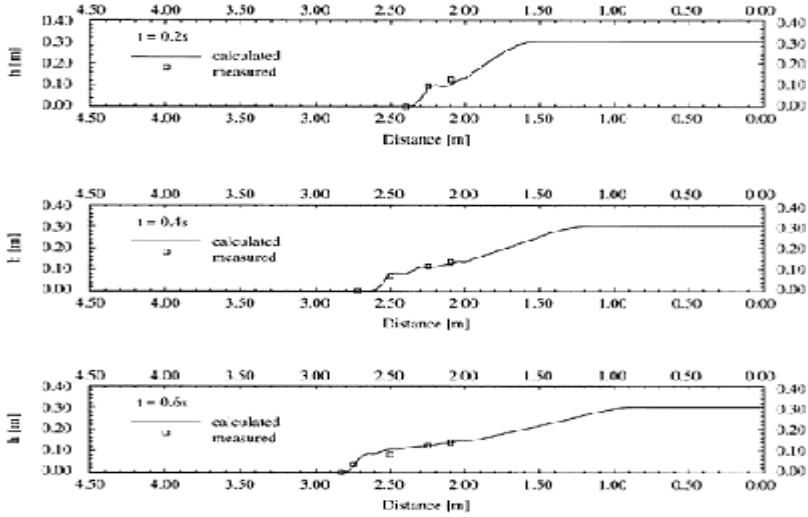

Figure 6. Comparison of the calculated and the measured flow depth profiles for the mixture with C_V=32.2%.

with the highest concentration of solids (C_V= 36.4%)—Figure 7, which is another very important feature of the proposed model. The influence of the concentration of the solid phase on the wave propagation speed is presented in the Figure 8. The higher the concentration, the lower the propagation speed, which is in agreement with the laboratory observations.

As previously explained, the rheological parameters of the Herschel-Bulkley's model were determined by matching the Bingham linear relationships obtained from two different procedures (viscometer and canal). Although the authors are aware of inconsistency of the procedure, it gave good results in this particular case, as can be seen from the plots of advancing fronts of all the mixtures (Figs 4–7). This justifies the applied procedure for determination of the parameters.

With the rheological parameters obtained in this manner, the calculated flow regime was laminar for all the analysed mixtures released from the reservoir, except the one with the lowest concentration of solids (C_V=13.8%), see Table 2. For the mixture having C_V=13.8%, it can be seen that Re_{ext}<10000. According to the findings of Wan & Wang (1994), this means that the flow conditions have not achieved fully developed turbulence, which justifies application of the Blasius formula in the turbulent flow regime.

7 CONCLUSIONS

Dam-break flow computation is a complex task, affected by a number of factors, such as availability and reliability of boundary and initial conditions, and capability of a numerical scheme to reproduce steep front without introduction of additional algorithms for bore tracking. The computation becomes even more complicated when modelling unsteady flows of highly concentrated solid-liquid mixtures. In such a case, estimation of rheological parameters of the mixture, as well as calculation of the friction slope, appear as new sources of errors.

In this paper, a 1D numerical model for hyperconcentrated dam-break flows is illustrated. The main intention is to reproduce numerically dam-break flows already observed in nature or laboratory. As a further objective, prediction of flows due to dam failure or dike

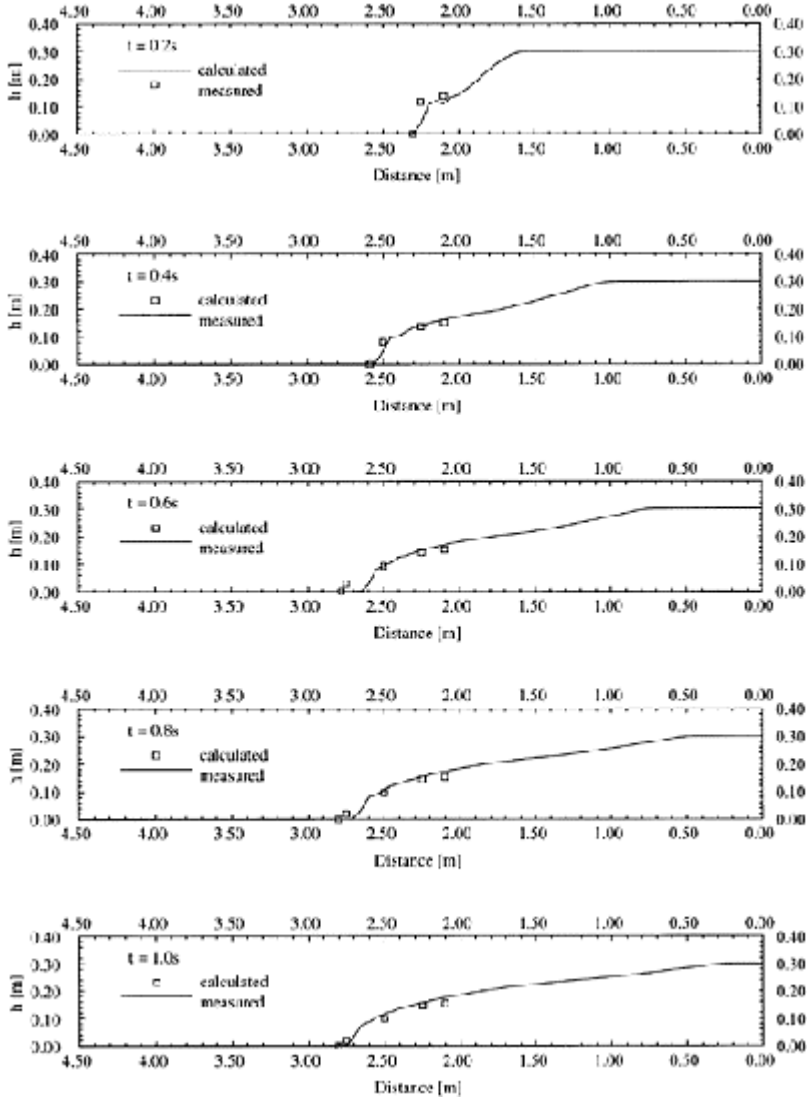

Figure 7. Comparison of the calculated and the measured flow depth profiles for the mixture with C_V=36.4%.

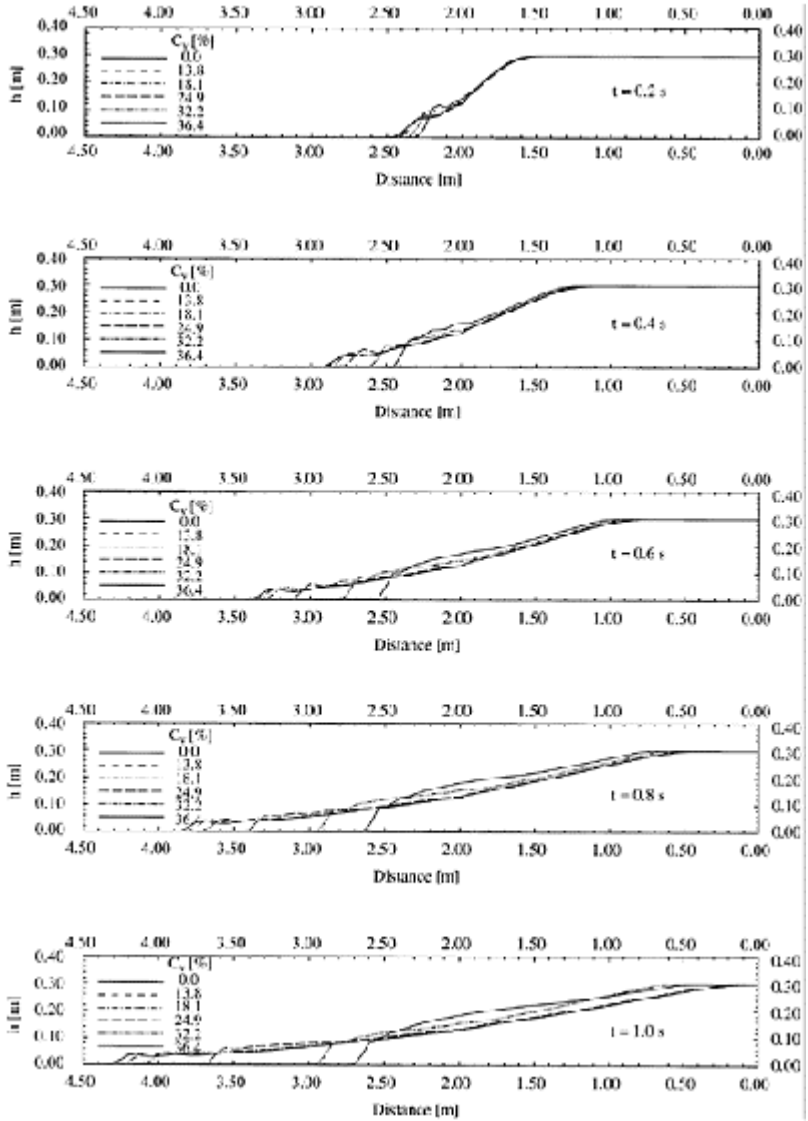

Figure 8. The influence of concentration of solid particles on the wave propagation speed and the flow depths.

Table 2. Values of the Reynolds number and the friction factor.

Mixture	C_V%	Re_{ext}	f
1	13.8	<10000	0.006–0.012
2	18.1	<2000	0.050–0.070
3	32.2	<100	1.20–4.00
4	36.4	<40	5.00–20.0

failure on mine- or ash-tailings deposit sites is planned. The MacCormack explicit finite-difference scheme is used for numerical modelling. As it belongs to the group of shock-capturing methods, it is particularly suitable for solving problems of the main interest to the authors—simulation of flows with a steep front.

Simulation results have shown that the wave front propagation speed is generally well reproduced for all the mixtures. This means that the initial condition at the gate opening, derived for the clear water case, is equally applicable in the case of the hyperconcentrated flow. In addition, the observed effect of slowing down the wave front propagation speed with the increase in the concentration of solid particles is successfully reproduced with the proposed model, which makes it a good predictive tool for solving dam-break or dike-break hyper-concentrated flow problems.

Further, discrepancies between the calculated and the measured flow depth profiles are acceptable. For the mixture with the lowest concentration of solids, the discrepancies at the steep front are high due to the difficulties in reading small depths from the video tapes.

Determination of the rheological parameters of the Hershel-Bulkley's model by matching the Bingham linear relationships obtained from two different procedures (viscometer and canal) is not consistent. However, results from the plots of advancing fronts of all the mixtures justify the applied procedure for determination of the parameters.

With the parameters obtained in this manner, the calculated flow regime was laminar for all the mixtures, except for the one with the lowest concentration of solids (C_V=13.8%). The values of the extended Reynolds number for this mixture show that fully developed turbulence has not been achieved, which justifies application of the Blasius formula.

The proposed model in its present form gives satisfactory results in simulation of flows of homogeneous, hyper-concentrated mixtures in regular channel geometry. In order to extend its application to real problems occurring in industry and nature, improvement of the model by allowing for computations in irregular geometries is necessary.

REFERENCES

Aguirre-Pe, J. & Quisca, S. & Plachco, F.P. 1995. Tests and numerical one-dimensional modelling of a high-viscosity fluid dam-break wave, *Journal of Hydraulic Research,* 33(1):17–26.

Akanbi, A.A. & Katopodes, N.D. 1988. Model for Flood Propagation on Initially Dry Land, *Journal of Hydraulic Engineering,* 114(7):689–706.

Bellos, C.V & Sakkas, J.G. 1987. 1-D Dam-Break Flood-wave Propagation on Dry Bed, *Journal of Hydraulic Engineering,* 113(12):1510–1524.

Coussot, P. 1994. Steady, laminar, flow of concentrated mud suspensions in open channel, *Journal of Hydraulic Research,* 32(4):535–559.

Cunge, J.A. & Holly Jr., F.M. & Verwey, A. 1980. Practical aspects of computational river hydraulics, Pittman Publ., Boston.

Đorđević, D. 2000. *Modelling of free-surface discontinuous flows,* Belgrade, Zadužbina Andrejević (in Serbian).

Fennema, R.J. & Chaudhry, M.H. 1986. Explicit Numerical Schemes for Unsteady Free-Surface Flows with Shocks, *Water Resources Research,* 22(13):1923–1930.

Fraccarollo, L. 1997. Discussion of paper "Numerical modeling of Anhui debris flow", *Journal of Hydraulic Engineering,* 123(10):937–938.

Garcia, R. & Kahawita, R.A., 1986. Numerical Solution of the St. Venant Equations with the MacCormack Finite-Difference Scheme, *International Journal for Numerical Methods in Fluids,* 6:259–274.

Garcia-Navarro, P. & Saviron, J.M. 1992. McCormack's Method for the Numerical Simulation of One-Dimensional Discontinuous Unsteady Open Channel Flow, *Journal of Hydraulic Research,* 30(1):95–105.

Han, G. & Wang, D. 1996. Numerical modeling of Anhui debris flow, *Journal of Hydraulic Engineering,* 122(5): 262–265.

Hicks, F.E. & Steffler, P.M. & Yasmin, N. 1997. One-dimensional dam-break solutions for variable width channels, *Journal of Hydraulic Engineering,* 123(5): 464–468.

Huang, X. & García, M.H. 1997. A perturbation solution for Bingham-plastic mudflows, *Journal of Hydraulic Engineering,* 123(11):986–994.

Hunt, B. 1994. Newtonian fluid mechanics treatment of debris flows and avalanches, *Journal of Hydmulic Engineering,* 120(12):1350–1363.

Jeyapalan, J.K. & Duncan, J.M. & Seed, H.B. 1983. Analyses of flow failures of mine tailings dams, *Journal of Geotechnical Engineering,* 109(2):150–171.

Jin, M. & Fread, D.L. 1999. 1D modeling of mud/debris unsteady flows, *Journal of Hydraulic Engineering,* 125(8):827–834.

Jovanović, M. & Đorđević, D. 1995. Experimental Verification of the MacCormack Numerical Scheme, *Advances in Engineering Software,* 23, Elsevier Science Limited: 61–67.

Komatina, D. 1998. An experimental study on the unsteady dam-break flow of mine tailings, *3rd International Conference on Hydrodynamics:* 481–486.

Komatina, D. 1999. Physical processes and modelling of nonNewtonian free-surface flows, Ph.D. thesis, University of Belgrade, Yugoslavia (in Serbian).

Komatina, D. & Lalović, V. 2000. Numerical simulation of unsteady dam-break flow of mine tailings, *4th International Conference on Hydrodynamics.*

Laigle, D. & Coussot, P. 1997. Numerical modeling of mudflows, Journal of Hydraulic Engineering, 123(7): 617–623.

Liu, K.F. & Lai, K.W. 2000. Numerical simulation of two-dimensional debris-flows, *2nd International Conference on Debris-Flow Hazards Mitigation:* 531–535.

McArthur, R.C. & Schamber, D.R. 1986. Numerical methods for simulating mudflows, *3rd International Symposium on River Sedimentation:* 1615–1623.

Meselhe, E.A. & Holly Jr., F.M. 1997. Invalidity of Preissmann scheme for transcritical flow, *Journal of Hydraulic Engineering*, 123(7):652–655.
O'Brien, J.S. & Julien, P.Y. & Fullerton, W.T. 1993. Two-dimensional water flood and mudflow simulation, *Journal of Hydraulic Engineering*, 119(2):244–261.
Wan, Z. & Wang, Z. 1994. Hyperconcentrated flow, IAHR monograph series, Balkema, Rotterdam.

Probabilistic estimation of debris-flow discharge by Monte Carlo simulation method

J.C.Chen
Disaster Prevention Research Center, National Cheng Kung University, Tainan, Taiwan

C.D.Jan & M.H.Lee
Dept. of Hydraulic and Ocean Engineering, National Cheng Kung University, Tainan, Taiwan

River Flow 2004—Greco, Carravetta & Della Morte (eds.)

ABSTRACT: Equation of debris-flow discharge contains hydrogeological and topographical parameters. Considering the uncertainty of the parameters and using the Monte Carlo simulation method (MCSM), a debris-flow design discharge versus reliability probability at various return period is developed. The method proposed in this paper is used to estimate the debris-flow design discharge in fushing village, Hualien county, Taiwan. The results also compare with that by First-order second-moment method (FOSM).

1 INTRODUCTION

Reliability modeling and other probabilistic techniques are becoming increasingly important tools in design of debris-flow hazard countermeasures. As an example, a discharge design may be based on reliability to assist the engineering in deciding on the most appropriate design parameters under a variety of uncertainties. Once the design discharge was underestimated, the reliability of debris-flow mitigation plan or structures would be doubtable.

Methods in deterministically calculating debris-flow discharge have been proposed by some investigators, such as Takahashi (1978), Kang (1985), Wang & Chang (1985), Chen et al. (2002), among others. Assume that the debris flow peak discharge can be directly related to the peak discharge of the water stream, a semi-empirical relation of debris-flow discharge for a specified return period is given as (Chen et al. 2002)

$$Q = \frac{1}{360}\frac{CA_m(k_1 + k_2 \log T)k_3 I_r}{(1-C_v)}\left[\left(60\frac{l}{v} + \frac{5}{6}\frac{L^{0.6}}{H^{0.6}}\right) + k_0\right]^{-k_4} \quad (1)$$

in which C=runoff coefficient; A_m=watershed area in hectares (ha); T=rainfall return period in years; L=stream length in km; H=elevation difference of stream length in km. C_v=sediment volumetric concentration. The values of C_v for debris flow are in the range of $0.15<C_v<0.9(1-n)$ in which n is porosity of sediment layer; l=the length of over-land flow in km; v=the overland flow velocity in km/hr. Generally, the values of v are in the range of 1.08~2.16km/hr (SWCTC 2000); I_r=reference of rainfall intensity (mm/hr) that is the rainfall intensity at return period of 25 years and duration of 60 minutes; k_0 is a constant and equals 55. The other coefficients (k_1, k_2, k_3, k_4) and the reference rainfall intensity I_r are directly related to the annual rainfall in the concerned watershed, as indicated in Appendix I. The above equation is a deterministic equation if all parameters involved in the equation are evaluated by their mean values. However, the parameters have some kinds of uncertainties. Considering the uncertainties of the random variables in Eq. (1) and using the first-order second-moment method (FOSM), Chen et al. (2002) have been developed a probabilistic equation of debris-flow discharge. For the FOSM, no distribution is required, but the underlying assumption is that the variables are all normally distributed and the function being analyzed is linear. This assumption can present large errors in some cases where the function or equation is highly nonlinear. Therefore, an exact method, the Monte Carlo simulation method (MCSM), in this paper is used to estimate the debris-flow discharge for different reliability probability, and the result is compared with that by FOSM.

2 UNCERTAINTY OF PARAMETERS

The uncertainty of parameters may result from the facts that (1) the topographical parameters, A_m, l, L and H, measured from a topographic map of watershed have inconsistent values for difference persons (engineers)

Table 1. Statistical properties of seven parameters at Fushing village.

Variables x_i	Samples N	Ranges	Mean values μ_{xi}	Variance CV_{xi} (%)
A_m (ha)	31	310.4~396.6	355.6	6.81
l (km)	31	1.36~1.73	1.55	5.22
L (km)	31	1.47~1.90	1.69	5.01
H (km)	31	0.21~0.22	0.216	1.64
C_v	–	0.15~0.56	0.355	28.87
C	–	0.5~0.8	0.65	11.54

v (km/hr)	–	1.08~2.16	1.62	16.67

due to their different experiences on drawing the watershed boundary and the initial point of river upstream; (2) the soil properties, the vegetation and topographic properties vary in space and are highly non-homogeneous, and therefore the overland flow velocity v and the runoff coefficient C are random variables; (3) the sediment concentration C_v of debris flow has high uncertainty also, depending on the property of sediment, slope and the amount of sediment and water. The uncertainties of the above mentioned parameters could be quantified by using statistical parameters, such as the mean value, the standard deviation, the coefficient of variation and probability distribution.

Table 1 lists the statistical result of topographical parameters (A_m, l, L and H) at Fushing village in Taiwan (Jan et al. 2003), basing on the measured data individually conducted by 31 graduate students using same kind of map of watershed. One can see that the variances of the parameters A_m, l and L all are larger than 5%, while variance of H is 1.64%. The mean values and the coefficients of variation for other parameters, C_v, C and v, are estimated from the range of possible values owing to the absence of field data. Given the range of possible values of a random variable, the mean value of the variable and the underlying uncertainty may be evaluated by prescribing a suitable distribution within the range (Ang and Tang, 1984). If the given limits are assumed to be ±cover 2 standard deviations in the normal distribution, the mean values and the corresponding coefficient of variation for parameters C_v, C, v, are also summarized in Table 1. All the seven parameters in Eq. (1), A_m, l, L, H, C_v, C, and v, are treated as random variables and assumed following normal distributions while the rest parameters are treated as deterministic parameters in the present paper.

3 MONTE CARLO SIMULATION METHOD

Many methods have been developed for uncertainty assessment (Harr 1987, Ang & Tang 1984, Rubinstein 1981). Generally, these methods can be classified into approximate and exact. The approximate methods are usually of the moment type, e.g. the first-order second-moment method (FOSM) and the advanced-second-moment method (ASM). The exact methods involve a comprehensive analysis using the probability distribution of all component variables, e.g. direct integration method and Monte Carlo simulation method (MCSM). In this study Monte Carlo Simulation (MCSM) is used to generate random samples of parameters in Eq. (1) based on the specified coefficients of variation and distributions. The probabilistic equation of debris-flow discharge based on FOSM (Chen et al. 2002) is also used for comparison in this paper.

Monte Carlo simulation is a method for obtaining information about system performance from component data. This method has also been referred to as synthetic sampling or empirical sampling. The procedure of Monte Carlo simulation is shown graphically in Figure 1.

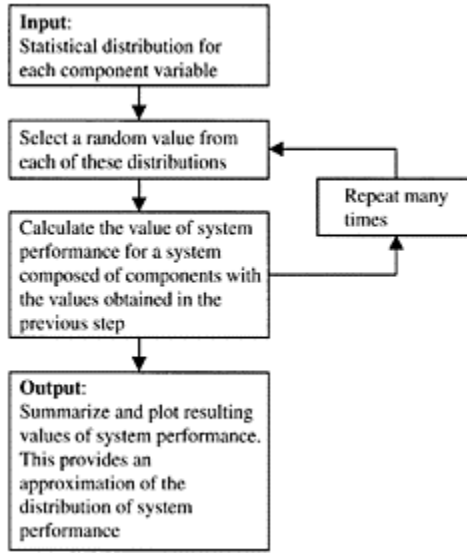

Figure 1. Flow chart of Monte Carlo simulation method.

To obtain a probabilistic debris-flow discharge, the following steps were followed:

1. Values for each of random variables in Eq. (1), including *(C, C_v, A_m, l, v, L, H)*, were generated from their respective distributions for each of N=1000 simulation cycles. All the variables were assumed to be normal with means and standard deviations of Table 1.
2. The debris-flow discharge Q_t was calculated from Eq. (1) based on the generated random variables. This process was repeated for N simulation cycles. Figure 2 shows a frequency histogram of the N=1,000 simulated debris-flow discharge Q_t.

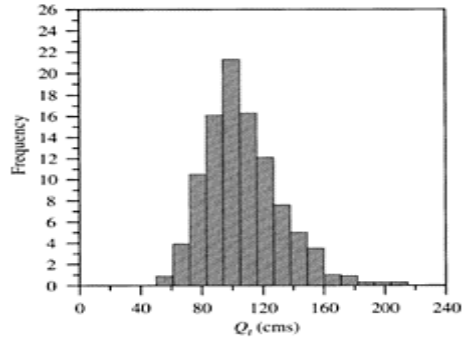

Figure 2. Frequency Histogram for 1,000 simulated debris-flow discharge.

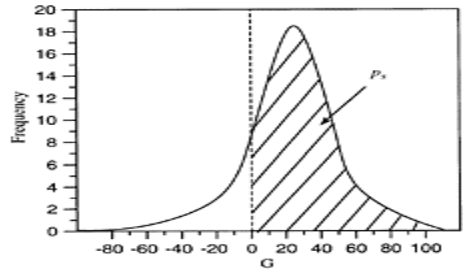

Figure 3. A distribution of sate function G and the reliability probability p_s corresponding for G>0.

3. Given a certain values of Q_d, i.e., a debris-flow design discharge, a distribution of the state function G(=Q_d−Q_t), was calculated based on the N values of Q_t, and the reliability probability p_s corresponding G>0 was obtained, as indicated in Figure 3.

4 PROBABILISTIC ESTIMATION OF DEBRIS FLOW DISCHARGE IN FUSHIHG VILLAGE

Fushing village is located at Hualien county in eastern Taiwan. There were several severe debris flow events in the village during past five years. Figure 4 shows the debris flow hazard in Fushing village on July 31 2001,

Figure 4. During typhoon Troaji period, a large amount of boulders deposited in the village upstream and

damaged the road due to insufficient of bridge crossing section (DPRC 2001).

after typhoon Troaji attacked. A large amount of boulders deposited in the village upstream and damaged the road due to insufficient of bridge crossing section. Hence, how to estimate the debris-flow discharge and determine the design cross section reasonably is an important work in this area.

Given the rainfall coefficients (i.e., I_r=92.332mm, k_1=0.551, k_2=0.305, k_3=18.206 and k_4=0.594), a specified return period T and the parameters listed in Table 1, the reliability probability p_s for a certain value of debris-flow design discharge Q_d which exceed Q_t, i.e. $G=Q_d-Q_t>0$, in Fushing village can be determined by MCSM. Figure 5 shows the relationship of the design debris-flow discharge Q_d against reliability probability p_s for various return period T. The relationship shows that the debris-flow discharge Q_d increases with the increase of T and p_s. This result implies that the larger Q_d is needed if we choose the larger rainfall return period and higher reliability index in design work.

The probabilities of debris-flow design discharge at various return period are also estimated by FOSM (Chen et al. 2002), and indicated in Figure 5 for comparison. Figure 5 shows that Q_d determined by FOSM is trifle greater than that by MCSM in most ranges of reliability probability ($0.2<p_s<0.6$). For example, Q_d=108cms by FOSM and Q_d=103cms by MCSM if we give p_s=0.5 and T=50 years. That is, the determined debris-flow design discharge from FOSM is

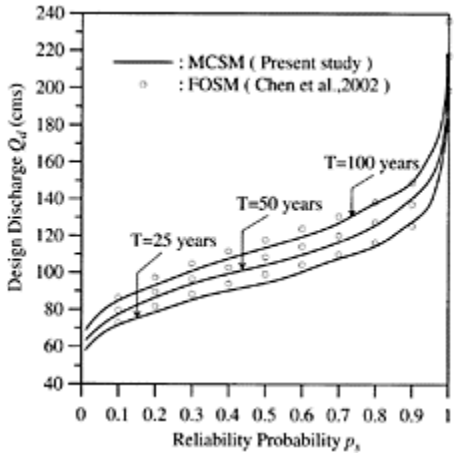

Figure 5. Debris-flow design discharge Q_d versus reliability probability p_s at various return periods T in Fushing village, Taiwan.

more conservative or safety than that from MCSM. Anyway, the debris-flow design discharge determined by FOSM is close to that by MCSM. The relative error is less than

10%. In general, the MCSM may obtain better results than the FOSM, since the MCSM is an exact method. However, the evaluation of p_f by FOSM is much faster than that by MCSM. The comparison in Figure 5 reveals that the debris-flow design discharge obtained by FOSM is indeed a good approximation to that obtained by MCSM.

5 CONCLUSIONS

A debris-flow discharge equation contains three hydrogeological parameters, such as the runoff coefficient, sediment concentration and overland flow velocity, and four topographical parameters, such as the watershed area, the length of overland flow, the horizontal stream length and elevation difference of stream. The uncertainties of the seven parameters in Fushing village in the eastern Taiwan are analyzed and evaluated. Taking into consideration of the parameters uncertainties, we have developed a relationship of debris-flow design discharge versus reliability probability at various return periods by using Monte Carlo simulation method (MCSM). This result obtained by MCSM is also compared with that from previous study by First-order second-moment method (FOSM). These comparisons show that the debris-flow design discharge determined by MCSM is close to that by FOSM.

REFERENCES

Ang, A.H.-S., Tang, W.H. 1984. *Probability Concepts in Engineering Planning and Design, Vol. II: Decision, Risk, and Reliability.* New York: John Wiley & Son.

Chen, J.C., Lee, M.H. & Jan, C.D. 2002. Calculation of Debris-Flow Discharge in a View of Probability. In D. Bousmar & Y.Zech (eds), *River Flow 2002; Proceedings of the International Conference on Fluvial Hydraulics, Louvain-la-Neuve, Belgium, 4–6 September 2002.* Rotterdam: Balkema.

DPRC (Disaster Prevent Research Center). 2001. *Investigation of Debris-Flow Disasters in the Typhoon Toraji.* National Cheng Kung University. Taiwan (in Chinese).

Harr, M.E. 1987. *Reliability-based design in civil engineering.* New York: McGraw-Hill.

Jan, C.D., Lee, M.H. & Chen, J.C. 2003. Reliability analysis on design discharge of debris flow. In D.Rickenmann & C.L.Chen (eds). *The third international conference on Debris-Flow Hazards Mitigation: Mechanics, Prediction, and Assessment. Davos, Switzerland, 10–12 September 2003.* Rotterdam: Millpress.

SWCTC (Soil and Water Conservation Technique Criteria). 2000. *Soil and Water Conservation Technique Criteria,* Soil and Water Conservation Bureau of Committee of Agriculture, Taiwan. (in Chinese).

Kang, Z.C. 1985. *Analysis of Maximum Discharge of Mud-Flow in Jiangjia Ravine, Dongchuan, Yunnan.* Peking: Science Press. (in Chinese)

Rubinstein, R.Y. 1981. *Simulation and the Monte Carlo method.* New York: John Wiley & Son.

Takahashi, T. 1978. Mechanical Characteristics of Debris Flow. *Journal of the Hydraulics Division.* HY8: 1153–1169.

Wang, M.P. 1995. *Hyperconcentrated flow and Debris Flow.* Peking: Hydraulics and Power press (in Chinese)

Wang, W.J., Chang, S.C. 1985. *Characteristics of Debris Flow in Ice Gully, Xichang.* Peking: Science Press (in Chinese).

APPENDIX I

The coefficients, k_1, k_2, k_3, and k_4, and the reference rainfall intensity I_r in Eq. (1) are related to the averaged annual rainfall P (mm), as following relations,

$$k_1 = \left(\frac{P}{42.89 + 1.33P}\right)^2 \tag{A1}$$

$$k_2 = \left(\frac{P}{-65.33 + 1.836P}\right)^2 \tag{A2}$$

$$k_3 = \left(\frac{P}{-189.96 + 0.31P}\right)^2 \tag{A3}$$

$$k_4 = \left(\frac{P}{-381.71 + 1.45P}\right)^2 \tag{A4}$$

$$I_r = \left(\frac{P}{25.29 + 0.094P}\right)^2 \tag{A5}$$

Concentrated mud suspensions flowing in open channels

G.F.Maciel & F.L.Santos
Department of Civil Engineering, São Paulo State University, Ilha Solteira, São Paulo, Brazil

River Flow 2004—Greco, Carravetta & Della Morte (eds.)

ABSTRACT: Mixtures of clay and water exhibit, in general, non-Newtonian property to be up to solid concentration. The purpose of this article is, first, to characterize these mixtures of the physical and rheological point of view. Under controlled conditions, the temperature, pH, and volumetric concentration influence on flow curve of this mixtures, were determined. Second, to carry out dynamic experiments in open channel in order to determine empirical wall stress formula (friction laws) from depths and discharges measured. It can also be obtained, from a global quantity analysis, behavior laws of several rheological parameters due to volumetric concentration. The fitted rheological model was Herschel-Bulkley, $\tau = \tau_c + k(\dot{\gamma})^n$ where τ_c: critical shear stress (yield stress), k: apparent viscosity; n: index of flow; and $\dot{\gamma}$ is shear rate.

Finally, due to rheological properties of material and the dynamic characterization of flow, it was determined the friction law to the hyper-concentrated fluids flowing in wide inclined long channel.

1 INTRODUCTION

Resulting mixtures of Newtonian fluids behavior and solid particle appear with frequency in the nature and industry. Those mixtures exhibit, as a rule, nonNewtonian properties (COUSSOT, 1997). In general, when we approach these mixtures, we identify, first, flows such as wastewater (sewage sludge), slurry coals, mud proceeding of oil explotation, fresh concrete, agroalimentary fluids. Second, we identified phenomena related to sedimentation process in reservoirs, deposition in irrigation channels, transport and finally, the landslides, sand liquefaction, erosive actions and torrential lavas—this real “mud sea” and debris which have banned the life of hundred of people at the world.

From those motivation, came up interests in diagnose, to a better refined way, and with engineering point of view, physic properties of non-Newtonian matrix (water+clay mixture), once characterized, would be insert to flowing studies with laminar behavior (mudflows) or turbulent (mud fronts, urban floods) according to friction laws.

2 WATER+CLAY MIXTURE RHEOLOGICAL CHARACTERIZATION

To the mixtures rheological characterization, R/S rheometer (Figure 2a) was used for controlling shear

Figure 1a. Mud flowing in a river.

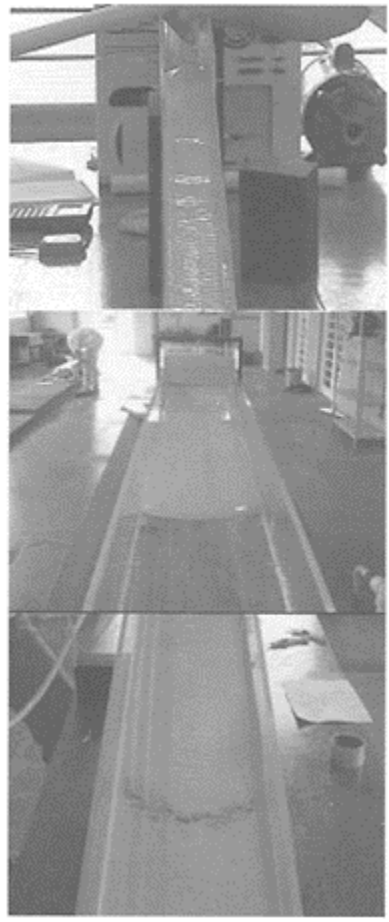

Figure 1b. Mud flowing in small channels at FEIS/UNESP laboratory.

stress and shear rate. The chosen geometry is the kind of that uses coaxial cylinder (Figure 2b) equipped with temperature control (circulating water bath). Supported by Rheo2000 software, could be gauged, to a better refined way, the Herschel-Bulkley parameters, as well the flow curves to each material essayed.

The following results aimed to explain some characteristics of essayed mixtures (water+kaolin clay) related to temperature variation, pH, and volume concentration.

2.1 *Temperature changing analysis*

As it was analyzed (Figure 3), the temperature changing at the sample did not seem to influence to a significant on the flow curve, above all if we consider a zone of temperature that comprises the ambient

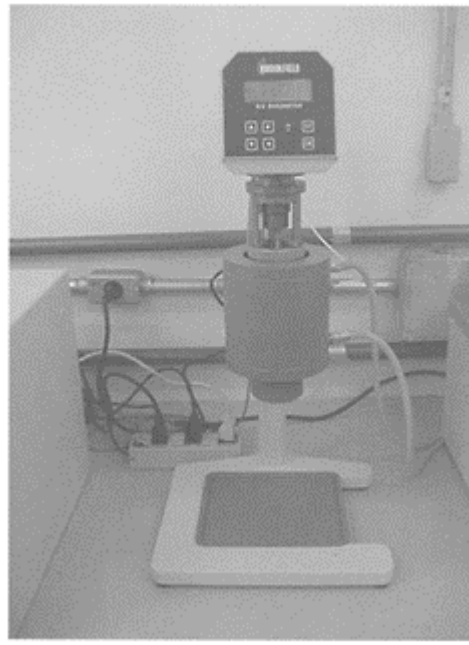

Figure 2a. R/S Rheometer.

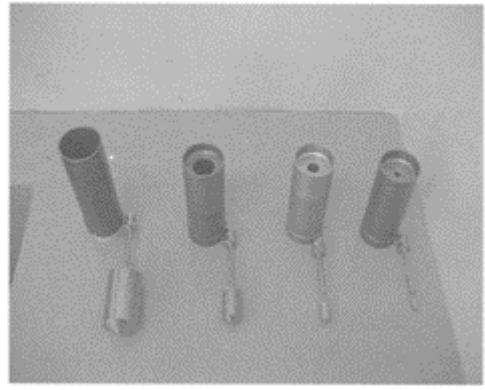

Figure 2b. Coaxial cylinders geometry and spindles.

temperature ($0°C<T<30°C$). So, we can reassure ourselves when the temperature control at the moment of rheometry tests.

2.2 *Ph variation analysis*

It was noticed, as showed results Figure 4, that the pH influence of the mixture at the rheological curve is small in this study. However, the variation of these

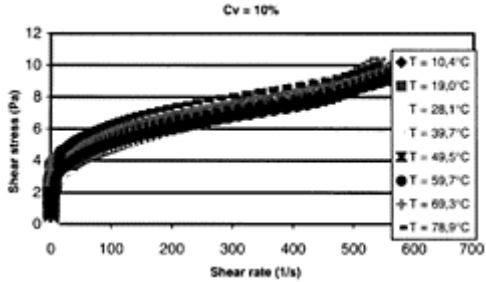

Figure 3. Flow curves in function of temperature.

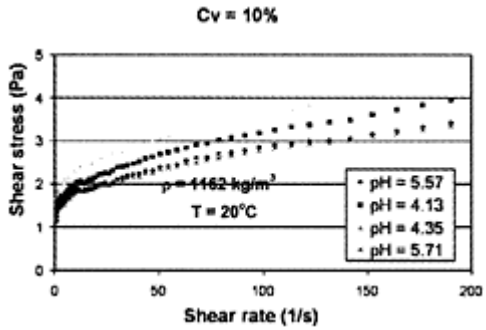

Figure 4. Flow curves in function of pH.

parameters showed itself being more significant than the temperature effect over the shear stress.

2.3 *Concentration variation in volume (Cv) analysis*

It is noticed that hyper-concentrated fluid viscosity goes up due to solid concentration existent to the mixtures. This carry out because as much bigger takes the solid material amount, bigger will be the friction of flowing material, and consequently, it will be larger the stress to produce a certain shear rate.

This way, it also can be noticed that critical stress of fluid increases with the concentration, and, consequently, the minimum stress necessary to produce a deformation is also bigger. Such fact is attested at Figure 5.

2.4 *Comparative global analysis to other rheological models*

Which follows, we show some rheological behavior to some concentrations in volume trying to compare Newtonian, Binghamian and Herschel-Bulkley rheological models to the experimental data. An example of fitting and good adaptability of Herschel-Bulkley is shown at Figure 6, whose data are listed in Table 1.

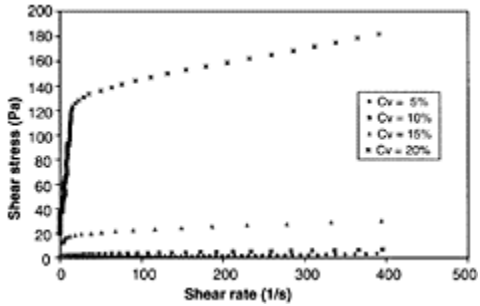

Figure 5. Flow curves in function of Cv variation.

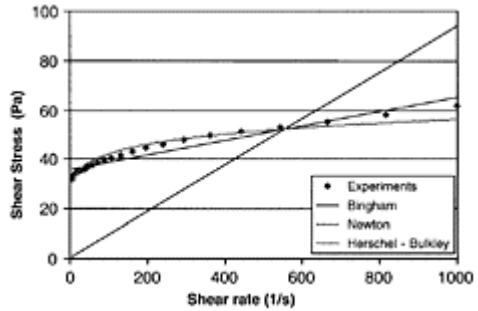

Figure 6. Flow curve of water+kaolin clay−Cv=15%.

Table 1. Rheological models parameters to water+kaolin clay mixtures.

Herschel-Bulkley model				
Cv(%)	τ_c (Pa)	k (Pa.s^n)	n	R^2
10	1,26	0,22	0,47	0,99
15	29,45	1,3	0,46	0,98
20	192,27	46,29	0,27	0,98
	Bingham model		Newton model (τ_c=0en=1)	

Cv(%)	τ_c	μ_B (Pa.s)	R^2	μ (Pa.s)	R^2
10	1,7529	0,01	0,96	0,027	–
15	35,818	0,029	0,929	0,094	–
20	211,66	0,152	0,95	0,515	–

2.5 *Global quantitative analysis of rheological parameters due to Cv variation*

Some scientific works point out that the parameters of rheological model proposed by Herschel-Bulkley follow, to kaoline clays, the following pattern: τ_c values (critical stress) and k (apparent viscosity) increases exponentially with the solid mixture volume concentration. On the other hand, (flowing index n) value lessens to the concentration, obeying to a power law.

From the data of WAN (1982), HUANG & GARCIA (1998), COUSSOT (1992) and MACIEL et al. (2002), we took the following relation:

$$\tau_c = 0{,}0073e^{0{,}4248C_v}$$

$$k = 0{,}0073e^{0{,}3665 \cdot C_v}$$

$$n = 1{,}529C_v^{-0{,}5039}$$

Those relations above all introduce good coefficients of correlation (R^2>0.90), comprised a large range of concentration in volume (5%<Cv<20%), that includes and explains well the results of other authors.

3 DYNAMIC CHARACTERIZATION OF FLOWING IN CHANNELS

Based on works of COUSSOT (1998) and starting by hypothesis of uniform, steady, laminar and incompressible flow, flowing in an infinitely wide inclined plan, we obtained an expression of specific discharge, that is extremely useful at the dynamic characterization to this kind of flowing.

$$q = \frac{\alpha}{(1+m)} z_0^{(1+m)} \left[h - \frac{z_0}{(2+m)} \right] \qquad \textbf{(1)}$$

with:

$$\alpha = \left(\frac{\rho g \sin\theta}{k} \right)^m ; \; z_0 = h - \frac{\tau_c}{\rho g \sin\theta} ; \; m = \frac{1}{n}$$

sin θ*:* declivity of channel; ρ*:* volumetric mass; τ_c, k, n: rheological parameters (Herschel-Bulkley); q: specific discharge.

For calculating the friction coefficient, from a dimensional analysis (using convenient scale), we could determine G and H_b dimensionless numbers that show themselves essential to this study as follow:

$$G = \frac{\rho g h \sin\theta}{\tau_c} \quad \textbf{(2)}$$

$$H_b = \frac{\tau_c}{k}\left(\frac{h}{\bar{u}}\right)^n \quad \textbf{(3)}$$

with:

with:
h: normal depth $\bar{u} = \frac{q}{h}$

The friction at the channel bottom is given according SANTOS (2003) by:

$$\tau_p = G\tau_c \quad \textbf{(4)}$$

Equation to be gauged through experimental data, or in addition;

$$\tau_p = \tau_c[1 + H_b^{-1}] \quad \textbf{(5)}$$

Theoretical friction law—it does not depend on the channel geometry, in this stage.

4 EXPERIMENTAL RESULTS IN ORDER TO DETERMINE FRICTION LAW

4.1 *Experimental apparatus description and methodology of essays*

The experimental apparatus (Figure 7) consists to a 10 meter length channel, with variable width (until 0.60m), and with declivity until 30%. There is a recirculating system where the hyper-concentred flow is warranted by a 7.5 CV motorpump that transport mud to the superior reservoir of constant level. A frequency invertor does the control of discharge. The normal depths were measured with a metallic ruler and ultrasonic sensors in 3 different points of channel. The discharges vary from 1.0 to 10.0l/s.

From characteristic equation of specific discharge, Equation 1, we prepared a sample with concentration in volume Cv=13% and we put it to flow on the experimental channel. The essay was done for three declivity of channel, around 6.3°, 12.2° and 17.4°. In

Figure 7. Mud flowing in channel.

each declivity, there was five variation of discharge. At the same time that took place the flowing essay, it was collected a sample to a rheological test.

All the information obtained at related flow, as well the gauged rheological parameters with Brook-field R/S rheometer, are shown at Table 2.

With: n: flowing index; τ_c: critical shear stress, k: apparent viscosity; Cv: Volume concentration; $\rho 0$: Volumetric specific mass mixture; sin θ: Declivity of channel; h: Normal depth; q (theoric): Theoretical specific discharge (semi-experimental, so it depends of h measure and rheological parameters); L: Width channel; q (exp): Experimental specific discharge; error: Relative error among experimental and theoretical specific discharge.

We can notice that the results present, most of the cases, high errors to the discharges. These errors can be explained by great sensibility of some parameters. Even the normal depth (h), showed at Table 2 be an average took out from several measuring done along the channel, such as, any lack of precision at its measuring, produces a considerable error, so this parameter interferes significantly to the calculus of the theoretical specific discharge (Equation 1). Other procedures of essay have being improved for trying to solve this uncertain.

4.2 *Discussing experimental results*

To the analysis of experimental data, the dimensionless numbers $(G-1)\times H_b$ are illustrated in Figure 8. This way, from comparison among adjusted equation to theoretical points (semi-experimental) obtained through this figure and Equation 5, we can analyze the conformity between the theoretical development and experimental results.

At this analysis, Hb number is obtained by Equation 3, using in the calculus the theoretical specific discharge (semi-experimental). For comparison, it was plotted the data of Hb obtained with experimental values of discharges q (exp), measured by volumetric method.

At this case, we obtained to the following experimental relationship:

$$G=1+1{,}7777H_b^{-0{,}8779} \quad (6)$$

$$G=1+1{,}846H_b^{-0{,}5393} \quad (7)$$

In order to define the influence of geometry on empirical wall stress formula (friction law), we are undertaking additional experiments, varying width of channel and also the section.

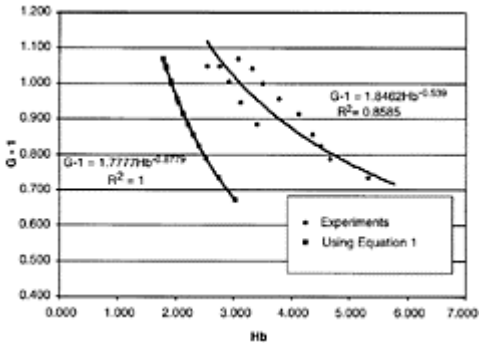

Figure 8. Friction law behavior: G−1 versus Hb.

Table 2. Rheological, dynamic and geometric parameters obtained to water+kaolin clay mixtures flowing in the big channel.

	n	τ_c (Pa)	k (Pa.s^n)	C_v (%)	ρo (kg/m^3)	sinθ	h (m)	q (theoric) (m^3/s/m)	L (m)	q (exp) (m^3/s/m)	error (%)
deciv 1	0.2859	34,545	7,2775	15,4	1249,48	0,0632	0,0746	0,026793	0,6	0,002811	1422,1
	0,2859	34,545	7,2775	15,4	1249,48	0,0632	0,0773	0,040736	0,6	0,004004	1529,0
	0,2859	34,545	7,2775	15,4	1249,48	0,0632	0,0797	0,057555	0,6	0,006765	1251,4
	0,2859	34,545	7,2775	15,4	1249,48	0,0632	0,0813	0,071586	0,6	0,007954	1333,3
	0,2859	34,545	7,2775	15,4	1249,48	0,0632	0,0827	0,086012	0,6	0,009169	1396,8
deciv 2	0,2859	34,545	7,2775	15,4	1249,48	0,1207	0,0447	0,032895	0,6	0,003283	1503,4
	0,2859	34,545	7,2775	15,4	1249,48	0,1207	0,0457	0,041225	0,6	0,004651	1310,5
	0,2859	34,545	7,2775	15,4	1249,48	0,1207	0,0467	0,051181	0,6	0,00629	1189,6

	0,2859	34,545	7,2775	15,4	1249,48	0,1207	0,0477	0,062996	0,6	0,008033	1140,4
	0,2859	34,545	7,2775	15,4	1249,48	0,1207	0,0483	0,071082	0,6	0,010548	956,5
decliv 3	0,2859	34,545	7,2775	15,4	1249,48	0,1714	0,031	0,013915	0,6	0,003105	580,3
	0,2859	34,545	7,2775	15,4	1249,48	0,1714	0,032	0,019303	0,6	0,004392	565,8
	0,2859	34,545	7,2775	15,4	1249,48	0,1714	0,033	0,026262	0,6	0,005967	566,9
	0,2859	34,545	7,2775	15,4	1249,48	0,1714	0,0337	0,032242	0,6	0,007626	537,9
	0,2859	34,545	7,2775	15,4	1249,48	0,1714	0,0337	0,032242	0,6	0,010203	360,0

Table 3. Values of friction tensions.

(1) Friction (Pa) equation 5	(2) Friction (Pa) equations 6 and 4	(3) Friction (Pa) equations 7 and 4	error(%) (1) and (3)	error(%) (1) and (2)	error(%) (2) and (3)
45,95	57,76	59, 33	29,11	25,70	2,72
47,14	59,88	60,43	28,19	27,01	0,93
48,21	61,75	62,35	29,32	28,09	0,97
48,93	63,00	62,88	28,51	28,76	0,19
49,55	64,09	63,35	27,85	29,32	1,16
50,76	66,15	64,27	26,63	30,33	2,93
51,62	67,62	65,70	27,28	31,01	2,93
52,48	69,09	66,96	27,59	31,64	3,18
53,35	70,56	67,99	27,44	32,24	3,77
53,87	71,43	69,29	28,62	32,59	3,09
50,17	65,15	67,54	34,61	29,85	3,67
51,40	67,24	69,01	34,28	30,84	2,63
52,62	69, 33	70,34	33,66	31,74	1,45
53,49	70,78	71,48	33,63	32,33	0,98
53,49	70,78	73,17	36,80	32,33	3,38

4.3 *Determination of friction law*

Theoretical (semi-experimental) and experimental friction values estimated to 0.60m channel of width are presented in Table 3.

5 CONCLUSIONS

The rheological characterization of mixtures and flowing dynamic mud mixture were inferred with success and showed the following conclusions:

–The water+clay essayed showed themselves, such prediction, non-expansible, they did not show thixotropic phenomena (not showed at this article) and changing the basic rheological properties, such as critical shear stress (τ_c), flowing index (n) and apparent viscosity (k) due to volume concentration (Cv);
–The experimental results fitted well to the HerschelBulkley rheological model, noticeable at the determining of critical shear stress and to the large shear rates range ($\dot{\gamma} \sim 100\,s^{-1}$: shear rate observed at field to the mudflow phenomena);
–However, it was also verified a good adaptability to Binghamian model to high shear rates.

This way, based on experimental results obtained at FEIS/UNESP, a new database was established. From this, it was obtained evolution laws of several rheological parameters, according to that was presented at item 2.5 of this article.

–The obtained results for friction of wall at the experiments taken at the channel, showed them-selves highlighting. However, the percentual errors over the specific discharge (Table 2) and on Hb calculus are high, we have found errors to friction, final aim, (Table 3) is satisfactory (order of 3%).

Finally, it is really worth point up during the experiments, under some situations of geometry, discharges and declivities, they were noticed roll waves phenomena with wavelength well defined according to reporting by COUSSOT (1997) in his experiments.

The criteria of generation and numerical analyses, from shallow water equations, have been studied by MACIEL et al. (1997, 2002) and others researchers.

REFERENCES

Bingham, E.C. 1992. Fluidity and Plasticity, McGraw-Hill, New York.
Borges, A.L.O.,Tarqui, J.L.Z. 1999. Determinação das Propriedades Reológicas de Sedimentos Finos em Suspensão Obtidos de Três Tipos de Solos do Estado do Rio Grande do Sul do Brasil. CD ROM do IV Silusba—Coimbra-Portugal.
Chen, C.L. 1988. Generalized viscoplastic modeling of debris flow. Journ. Hydr. Div., ASCE 114:237–258.
Chen, C.L. 1998. General solution for viscoplastic debris flow. Journ. Hydr. Div., ASCE 114:259–282.
Coussot, P. 1988. Rhéologie des boues et laves torrentielles—Etude de dispersions et suspensions concentrées. Tese de doutorado, Institut National Polytechnique de Grenoble.
Coussot, P. 1992. Rhéologie des boues et laves torrentielles—Etude de dispersions et suspensions concentrées, Institut National Polytechnique de Grenoble, 1992.
Coussot, P., Piau, J.M. 1994. On the behavior of mud suspensions. Rheologica Acta, Vol. 33, No. 3, pp. 175–184.
Coussot, P., Proust, S., Ancey, C. 1996. Rheological interpretation of deposits of yield stress fluids. J. Non-Newtonian Fluid Mech., Vol. 66:55–70.
Coussot, P. 1997. Mudflow rheology and dynamics. IAHR Monograph Series.

Huang, X., García, M.H. 1998. A Herschel-Bulkley model for mud flow down a slope. J. Fluid Mech., Vol. 374: 305–333.
Huang, X., Garcia, M.H. 1998. A Herschel-Bulkley model for mud flow down a slope. J. Fluid Mech., Vol. 374:305–333.
Li, G., Wei, H., Han, Y., Chen, Y. 1998. Sedimentation in the Yellow River delta, part I: flow and suspended sediment structure in the upper distributary and the estuary. Marine Geology,Vol. 149, Issue: 1–4, pp. 93–111.
Li, J., Yuan, J., BI, C. & LUO, D. 1983. The main features of the mudflow in Jiang-Jia River. Zeit. Geomorph, 3, 27, 325–341.
Liu, K., Mei, C.C. 1989. Slow spreading of a sheet of Bingham fluid on an inclined plane, J. Fluid Mech. 207, 505.
Maciel, G.F., Vila, J.P., Martinet, G. 1997. Roll wave formation in the non Newtonian flows. XIV COBEM. Bauru, São Paulo, Brasil.
Maciel, G.F. et al. 2002. Project technical report of research FAPESP 00/14853–5.
Piau, J.M. 1996. Flow of a yield stress fluid in a long domain, application to flow on an inclined plane. J. Rheology, Vol. 40:711–723.
Santos, F.L. 2003. Estudo teórico-experimental em via de determinação de uma lei de atrito em escoamentos de fluidos hiperconcentrados, Dissertção de Mestrado, FEIS/Unesp.
Wan, Z. 1982. Bed material movement in hyperconcentrated flow, Ser. Pap. 31 Inst. of Hydrodyn. and Hydraul., Tech. Univ. of Denmark, Lyngby.

Numerical simulation and field observation of debris roll waves in the Illgraben torrent, Switzerland

B.Zanuttigh
University of Bologna, Dipartimento di Ingegneria delle Infrastrutture, Strade, Trasporti, Acque, Rilevamento ε Territorio, Bologna, Italy

B.W.McArdell
WSL Swiss Federal Research Institute, Department of Water, Soil, and Rock Movements, Zuerich, Switzerland

River Flow 2004—Greco, Carravetta & Della Morte (eds.)

ABSTRACT: In natural debris flows, even if the critical Froude number is almost always exceeded, the formation of waves, which eventually develop into surges, is not always observed. This contribution numerically represent a debris flow event occurred in the Illgraben torrent, Swiss Alps, which consisted of a single surge and of about 28 roll waves on the surge tail. Simulations are carried out with two 1-D codes based on Shallow-Water equations and a wide variety of rheological laws (Herschel Bulkley, Bingham, Dilatant Inertial, Generalised Visco-Plastic, Voellmy).

The analysis of flow depth in time, maximum flow depths and velocities along the debris channel shows that a good representation of the main debris features can be obtained with a proper calibration of rheological parameters. More difficult appears to be the representation of flow tail instabilities.

The causes of debris wave development based on literature and interpretation of the model results are examined and an original interpretation is provided.

1 INTRODUCTION

The formation of instabilities in debris or mud flows has been investigated by several authors, among the others Chun (1982), who determined the stability curve for generalised Newtonian flows; Trowbridge (1987), who carried out the same analysis using shallow water equations; Lanzoni and Seminara (1993) experienced that a granular

flow becomes unstable for Froude numbers around 1.0; Coussot (1994) showed that for a Herschel-Bulkley fluid the critical Froude number drops to 0.25 or less; Lamberti & Zanuttigh (2003) extended Trowbridge's method to a Generalised Visco-Plastic flow.

In several cases instabilities should be evident according to theory but do not show-up in nature; moreover, the mechanism of formation of multiple surge events is still unclear and the possibility to predict such features is still uncertain.

This contribution aims to examine through numerical simulations and field observations wave development in debris flows. The numerical model is based on Shallow-Water equations, which are able to capture the position and to reproduce the intensity but not the shape of the debris front. An accurate analytical solution for representing the flow profile at the front as well as at the tail, of two-dimensional unsteady non-uniform Bingham and Herschel-Bulkley flows down a steep slope can be found in Huang and García (1997) and (1998) respectively.

This contribution is divided in four main parts. The first part presents the numerical models adopted. The 1D numerical formulation is adopted since reflections, diffractions and refractions, which are clear in water flows, do not seem to substantially affect debris flows, as it is proven by field surveys (Berti et al., 1999; Mortara et al., 1994; Rickenmann et al, 2001) and several video registrations (Arattano & Trebbo, 2000; Lamberti, 1999; Rickenmann, 2000).

The second part presents the catchment under analysis from a hydro-morpho-geological point of view and the debris flow events, a single-peak and a multiple-surge event.

The third part compares numerical results to available flow depth and velocity registrations for different rheological laws and calibrations of the rheological parameters.

Finally, an interpretation for the formation and development of instabilities is provided, based on the analysis of numerical simulations and on hydrographs measured during debris events (Arattano et al., 1997).

2 NUMERICAL MODELS

2.1 *Numerical scheme*

Both numerical models applied in this study are based on one-dimensional solutions to the conservative form of the shallow water equations, where the frictional resistance term typically used for open channel flow (e.g. a Chézy flow resistance law) has been replaced with flow laws which have been proposed to describe debris flow behavior. The primary unknowns are flow depth and specific discharge. Only the main features are summarized here because both models have been described elsewhere.

The DFEM model from WSL is a finite element solution of the shallow water equations in one dimension and is based on the Finite Element Method TOOL-box (FEMTOOL) libraries developed by Rutschmann (1993). Many research problems using the 1-D, 2-D, and 2-D extended shallow water equations have been addressed using the FEMTOOL codes (Näf, 1997, Krüger, 2001) and a 2-D version of the code for debris flows is under development at WSL. The main modifications for application to debris flow routing are the inclusion of debris flow laws and a treatment of the transition from

wet-to-dry cells involving simple cutoff velocities and depths. When the predicted velocity or depth is below some small user-specified value (a few cm for the flow depth) the bed is assumed to be dry. To increase the numerical stability, it was necessary to introduce an upwind scheme (e.g. Katopodes, 1984).

The WAF-DF model from the University of Bologna (Zanuttigh & Lamberti, 2002) solves the equations using the weighted average flux (WAF) method of Toro (1997). This method is 'shock-capturing' in the sense that discontinuities are automatically treated correctly without the need for a special tracking algorithm. For this reason, the code has been especially useful in interpreting the propagation of roll waves in debris flow surges using data from the Acquabona torrent in Italy (Zanuttigh & Lamberti, 2003).

2.2 *Rheological laws*

Single-phase flow laws can be divided into three major categories (Iverson, 1997), turbulent flow laws (e.g. the Voellmy flow law, Bartelt et al., 1999), laminar flow laws (e.g. the Herschel-Bulkley formulation, Coussot, 1997), and grain-shearing flow laws (e.g. the dilatantinertial formulations, Takahashi, 1991).

The DFEM model has been designed to allow for systematic comparisons of the major categories of flow laws and combinations of flow laws when appropriate (O'Brien et al., 1993). For this paper, one example from each of the three categories of resistance relations has been applied, the Voellmy Fluid (VF), Dilatant-Inertial or Grain Shearing (DI), and Simplified Bingham relations (SB). The relations are incorporated into the model in the friction term and are therefore expressed here in terms of the friction slope, S_f.

The Voellmy Fluid (VF) resistance relation (Hungr 1995) consists of a Chézy-type turbulent friction term and a Coulomb-type dry friction term:

$$S_f = \frac{q\sqrt{q^2}}{h^2 C^2 h_r} + \cos\alpha \tan\delta \qquad \textbf{(1)}$$

where q is the specific discharge, h is the flow depth, h_r the hydraulic radius, $C(\mathrm{m}^{1/2}\mathrm{s}^{-1})$ is the Chézy flow resistance coefficient, α is the slope angle of the channel and δ is the angle of internal friction. The Voellmy relation was developed to describe flow-type snow avalanches (Bartelt et al. 1999) and with the Coulomb term allows the flow to stop on inclined surfaces.

The Dilatant-Inertial (DI) law can be stated in a simple form:

$$S_f = \frac{q^2}{h^5 \zeta^2} \qquad \textbf{(2)}$$

where ζ is a roughness parameter $(\mathrm{m}^{-1/2}\mathrm{s}^{-1})$

The laminar flow relation is the simplified version of the Bingham flow (SB) law (Hungr 1995, Rickenmann 1990). We use the following relation to incorporate the Bingham flow law:

$$S_f = \frac{\tau_0}{\rho g h} \qquad \textbf{(3)}$$

where g is the acceleration due to gravity and p is the bulk density of the flowing debris, and τ_0, the shear stress, is given by the solution to the cubic equation from the Bingham relation:

$$2\tau_0^3 - 3\left(\tau_C + 2\frac{\mu_B q}{h^2}\right)\tau_0^2 + \tau_C^3 = 0 \quad \textbf{(4)}$$

In the DFEM code, the cubic term may be dropped and leading to:

$$\tau_0 = 1.5\tau_C + 3\frac{\mu_B q}{h^2} \quad \textbf{(5)}$$

where τ_C is the yield stress, μ_B is the viscosity. For the case where the stress ratio τ_C/τ_0 is smaller than 0.5, the error in the mean flow velocity is on the order of 6% (Rickenamm 1990).

The rheological behavior of the WAF-DF model is alternatively supposed to follow:

1) the Herschel-Bulkley (HB) model, which is given by:

$$\boldsymbol{\tau=\tau_c+K\gamma^{0.33}} \quad \textbf{(6)}$$

where τ_c is the cohesion or yield stress parameter, K is the consistency index and γ is the shear rate;

2) the Bingham (B) model

$$\boldsymbol{\tau=\tau_c+\mu_b\gamma} \quad \textbf{(7)}$$

where μ_b is the consistency index;

$$\tau = \tau_c \cos\phi + \sigma \sin\phi + \mu_1\gamma^{\eta} = \tau_y + \tau \quad \textbf{(8)}$$

where μ_1 is the consistency index and η is the law's exponent. The sum of the first two terms at the second member of (8) represents the yield stress τ_γ whereas the third term is the stress τ' due to shear rate.

B and HB models are trivial special cases of the GVP model: ϕ=0 and η=1.0 or 1/3 respectively. The GVP model is characterised by two more degrees of freedom than the HB or B models and thus by two more parameters to be calibrated: the exponent of the rheology law η and the friction angle ϕ. Details on the procedure for evaluating flow resistance for this general case can be found in Zanuttigh and Lamberti, 2003.

In both models, the magnitude of the flow resistance term is limited to enhance numerical stability and provide more realistic results. In the DFEM model the magnitude of the friction term (expressed in units of energy) is not allowed to exceed the local kinetic energy of the flow. One implication of this limitation is that the vibrational kinetic energy of a debris flow cannot be converted into translational kinetic energy. In the WAF-DF model the flow resistance for the debris flow is assumed to be not less than turbulent fluid with an appropriate value of the Chézy coefficient, which is assumed equal to $22 m^{1/2}s^{-1}$ following Rickenmann (1999).

3 ILLGRABEN CATCHMENT

The Illgraben catchment (10.5km^2 above the fan apex) contains an unusually large proportion of unvegetated, steep, unstable slopes with abundant colluvium derived from weak carbonate and greywacke bedrock. The channel downstream of the fan apex is 2.6km long, has a mean slope of 10%, and is presently deeply incised.

No information on the geometry of recent debris flow deposits on the alluvial fan is available because all debris flows in the last few years have traveled into the Rhone River where they are immediately reworked by the river flow. In order to stabilize the torrent bed after an avalanche occurred in 1960s, a nearly 50m high sediment retention dam was installed upstream of the fan apex and many check dams were built up downstream this structure.

Several debris flows per year occur generally following intense rainfall in the catchment (Rickenmann et al., 2001) and some presented (McArdell et al., 2003) multiple peak hydrograph that can be interpreted

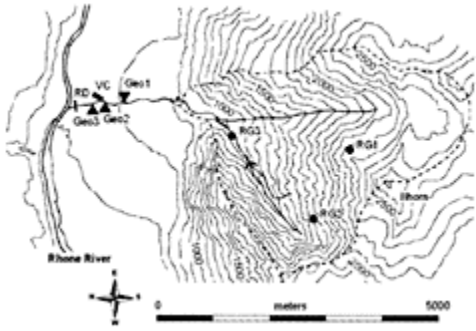

Figure 1. Debris flow observation station at the Illgraben torrent with the location of the geophones (Geo) video camera (VC), radar (RD) and rain gages.

as the result of instability of uniform debris flow conditions.

The downstream 850m of the channel has been instrumented with 3 geophones, a radar flow depth sensor, and a video camera, with data logging triggered automatically by the upstream-most geophone (Figure 1). Observations consist of flow velocities estimated from the travel time between the geophones and a radar sensor and flow depths from the radar. The videos provide additional velocity and depth estimates as well as qualitative observations of the flow behaviour and maximum grain size. An independentlyoperated network of three rain gages was installed in the upper catchment in 2000.

4 NUMERICAL SIMULATIONS

4.1 *The event of June, 2000*

The event of 28 June 2000 was selected because of the availability of several field data as independent field observations of surface velocity, cross section and mud traces collected after the event to reconstruct maximum flow depths and wetted areas.

From the front travel time between the instruments, the flow depth estimated at the radar and the analysis of video images, the total volume of this event can be evaluated around 35,000m^3; the maximum discharge was 125m^3s^{-1}, the front velocity arose 3.9ms^{-1} and the peak flow depth was close to 3m. The flow was observed to have a single coarse granular surge moving over an initially dry bed (Figure 2) carrying boulders more than 2m in diameter. The tail of the debris flow was muddy and low-amplitude roll waves were observed starting about 600 seconds after the passage of the front.

Numerical simulations were carried out on the topography obtained by a field survey performed in

Figure 2. Debris flow front for the 28 June 2000 event from the video tape. The base width of the check dam is about 10m. Mud traces from an earlier event in summer 2000 are still visible immediately downstream of the front.

2000; the channel cross sections were approximated for simplicity to rectangle with variable-width and the base of the sediment retention dam was used as starting point. As no rainfall data was collected, a simple triangular hydrograph was assumed as upstream boundary condition. Based on the downstream observations of total volume, mean flow velocity and depth, the hydrograph is built up so that after 14s flow discharge reaches the maximum value of 14m^2s^{-1} and after 236s returns to zero. Other hydrographs were tested, but in general the differences from plausible alternatives tend to be damped by the

development of near-uniform flow over the more than 3000m long reach from the base of the retention dam to the observation station, so a detailed parametric analysis of input conditions is not included here.

The models were run with incremental changes of the parameters until a “best fit” was achieved. For comparison with the field data, the results are presented by comparing model results with the front velocity measured between instruments in the field and the flow depth determined from the radar. The results can be difficult to interpret because there may not be a unique combination of parameters that allow one to match both the front velocity and the flow depth. The following ‘best’ calibrations were adopted in this contribution:

–for the DFEM: SB, μ_b=130Pa·s, τ_b=100Pa, ρ=2200kg/m^3; DI, ζ=14m$^{-1/2}$ VF, C= 22m$^{1/2}$/s, δ=2.5°;
–for the WAF-DF: HB, K/τ_c=0.1s$^{1/3}$, τ_c/ρ= 0.1m^{2}s^{-2}; B, μ_b/τ_c=0.6s, τ_c/ρ=0.1m^{2}s^{-2}; GVP, η=0.5, μ_b/τ_c=1.3s, τ_c/ρ=0.2m^{2}s^{-2}, ϕ=1°.

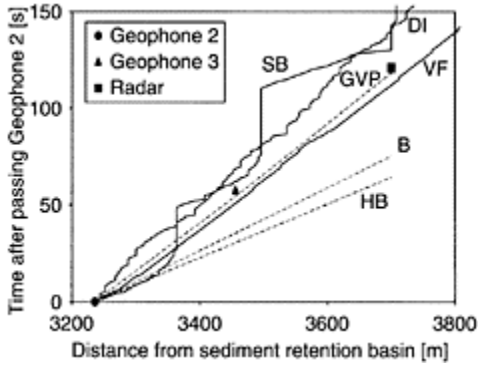

Figure 3. Comparison of front position with field data. Dashed lines indicate WAF-DF results and solid lines indicate DFEM results.

The comparison of front velocity between geophone 2 and the radar (Figure 3) shows a wide variety of flow behaviors for the different flow resistance laws. The curves for the WAF-DF model show a uniform velocity (similar to that observed in the videos), but the flow is too rapid in comparison with the field data for the Bingham and Herschel-Bulkley flow laws. These relatively large velocities are similar to what one would calculate with a Chézy model using C=22m$^{1/2}$s^{-1}, suggesting that the value chosen to limit the magnitude of the friction term may be influencing the results for the flow laws using WAF-DF. However, the slope of the simplified Bingham model during periods of flow, which was run with the exact same set of parameters, is quite similar, so the apparent match with a Chézy model may be a coincidence. The curves for the DFEM model show good agreement for the dilatant and Voellmy resistance laws, but the surge-stop behavior of the simplified Bingham model is probably due to numerical instability and may have no

meaningful physical interpretation. An exact match with the dilatant-inertial model was not possible because numerical instabilities. Additional pairs of simplified Bingham viscosities and yield stress values are also capable of matching the front trajectory; in the absence of flow deposits where one can estimate the yield stress, it is difficult to choose one “best fit” set of parameters. The slopes of the simplified Bingham model, when it is flowing, are similar to the Bingham law predicted with the WAF-DF model, suggesting that a different set of yield stress values (in particular a larger yield stress) may provide a better match with the data. The Voellmy fluid law is always numerically stable with this field case.

A comparison of modeled flow depth with the field data (Figure 4) shows that most of the resistance laws predict too shallow depths compared with field observations. In the simplified Bingham model

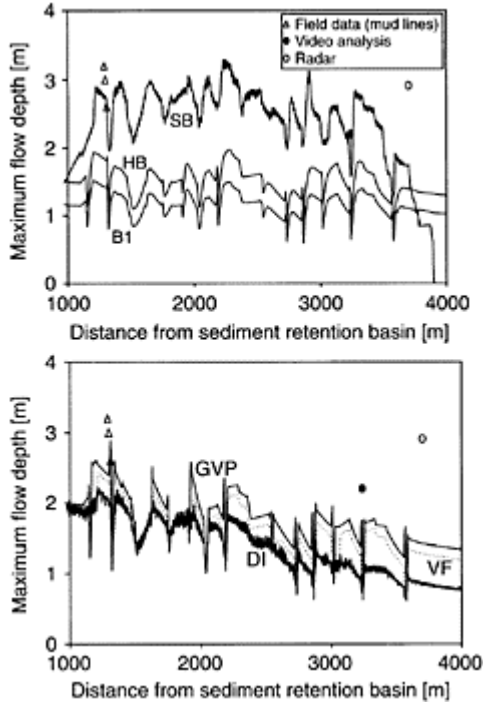

Figure 4. Maximum flow depths (top) obtained from the Simplified Bingham, Bingham, and General Viscoplastic models and the Voellmy Fluid, Dilatant-Inertial and General Viscoplastic model (bottom).

the stop-surge behavior may explain why the simplified Bingham model best reproduces the flow depth near the upstream end of the computational domain (Figure 4). However eyewitnesses did not observe the stop-start behavior and it is not apparent in the video images, suggesting that this is not a reliable numerical result. Perhaps the main difference between the field and model is the downstream diffusion of the wave resulting in lower flow depths downstream. This may be an artifact of simplifying the complex behavior of the debris flow using simple single-phase rheologies with one set of parameters to characterize the entire debris flow wave.

A comparison of the Bingham model results between the two models shows a striking difference in their predicted flow behavior in spite of the fact that the parameters used in the models are identical. Part of the discrepancy can be explained by each model's method of limiting the magnitude of the friction term; another possible explanation is that the Bingham model is inappropriate for such a granular flow. A Bingham Reynolds number, defined as $R_{eB}=4Vh\rho/\mu_B$, where V=the flow velocity, h=the flow depth, ρ=the bulk

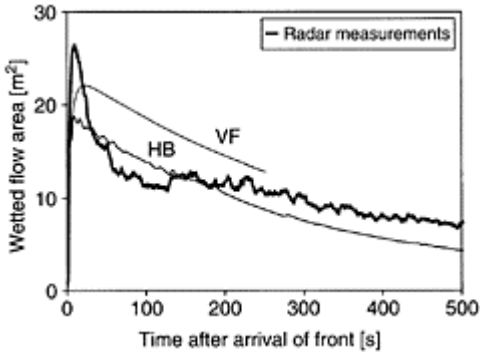

Figure 5. Comparison of field hydrograph for the Voellmy fluid and Herschel-Bulkley flow laws.

density of the debris, and μ_B=the Bingham viscosity of the flow, calculated for the front at the location of the video camera, is estimated to be on the order of 500, or within the laminar range reported by Rickenmann (1990). This suggests that laminar-type flow law (e.g. the SB, B, HB, and GVP models) does not contradict the simulated flow behavior. An analysis of a boulder motion shows roughly 2/3 of the particles showing periods of both rolling and non-rolling behavior over the 50m section upstream of the video camera, suggesting that the qualitative description of a laminar fluid is an oversimplification for this granular debris flow.

The comparison of observed and modeled hydrograph shape shows a generally poor agreement between flow depths or areas, with all numerical simulations failing to match the observed flow depths by nearly a factor of 2. The comparison with wetted flow area at the radar location yields a better match with the tail of the debris flow (Figure 5).

All the 'best' calibrations obtained with the WAF-DF model predict an onset of roll wave activity at flow tail that is characterized by different wave periods and heights depending on the rheological law and calibration, as it clearly appears by Figure 6.

Table 1 compares the summary of numerical and measured wave statistics, showing that the calibration with GVP is the only one that reproduce the period of the onset of roll wave activity observed in nature, whereas none of the calibrations adopted is able to accurately represent roll-waves amplitudes.

4.2 *Discussion*

One major problem with the Illgraben data set is a lack of good data on the cessation of motion of the flow—most debris flows that remain in the channel, like this event, continue moving until they reach the Rhone River downstream where they are destroyed.

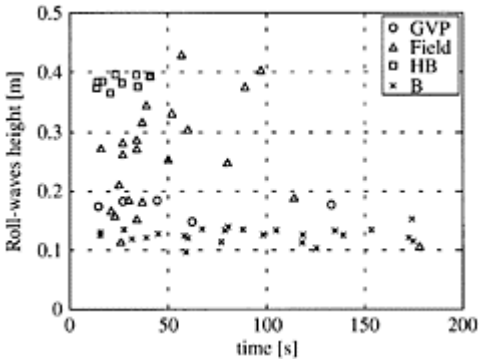

Figure 6. Roll waves height obtained with WAF-DF model.

Table 1. Roll-wave statistics (Results in Figure 6): n is the number of waves, T_m is the mean wave period, H_m is the mean wave height.

	Field	B	HB	GVP
n	24	25	9	8
$T_m[s]$	8	7	4	19
H_m[m]	0.27	0.13	0.39	0.17

Without information on the stopping angle or location of the debris flows, in many cases it may be impossible to find a unique pair of parameters to match the field results. In the case of the Voellmy model, the practical upper limit on the value of the Coulomb dry friction can be determined by the angle of the channel bed, and the best fit envelope of parameters varies linearly between C=14m$^{1/2}$s^{-1}, δ=0.6° and C=22m$^{1/2}$s^{-1}, δ=2.5°.

In general the parameters from the model are realistic in that they are similar for values observed in the Acquabona torrent (Zanuttigh & Lamberti, 2003). The Voellmy parameters are also similar to those calculated for a smaller granular debris flow in the Schipfenbach torrent, Switzerland (Hurlimann et al., 2003), using a snow avalanche simulation program was used (with the density adjusted to represent debris instead of snow). The range of Chézy *C* values is in agreement with empirical values plotted as a function of peak discharge (Rickenmann, 1999).

Regarding the inaccurate representation of roll waves at flow tail for this event and in general the possibility of validated numerical models to accurately reproduce surges and secondary waves in natural events, an important role seems to be played by the upstream input hydrograph. In the case of Acquabona, for which the upstream hydrograph was reconstructed based on available rainfall measurements, it was possible to achieve, by calibrating the rheological parameters, a good match to field data both of wave periods and wave heights (Zanuttigh & Lamberti, 2003).

5 AN INTERPRETATION FOR WAVE DEVELOPMENT IN NATURAL EVENTS

In some cases, debris waves do not develop in nature even if the critical *Fr* is exceeded, as for the event of June 2000 in the Illgraben.

Among basins in which development of surges in debris events is well documented from measurements and observations, we can consider the Illgraben events already shown and the case of the Moscardo torrent, Northern Italy. The Rio Moscardo generates at least one event per year and has been since ten years object of a continuous and accurate monitoring (Arattano et al., 1997). Hydrographs measured along the channel during some events are reported at the left hand-side in Figure 7. Effects of the channel length cannot be appreciated, because the two hydrographs are measured in correspondence of two stations located at a distance of 300m.

In all cases, a first surge is present and secondary waves develop during recession and become more evident with increasing effective duration of the event (top-down in Figure 7), independently on peak discharge. The first surge, mainly composed by boulders and coarser fractions, has an almost symmetrical shape and do last for a relevant time; depending on the event duration, instabilities can show-up as small waves in the descending reach of this first surge or as independent muddy secondary waves with asymmetrical shape, similar to water roll waves in the overtaking phase.

On the basis of these field observations and on numerical analysis (Zanuttigh and Lamberti, 2003) performed along Acquabona channel (Northern Italy), the interpretation sketched at the right hand-side in Figure 7 has been developed. Debris flows tend almost always to develop in theoretically unstable conditions, but debris waves are not always observed. In facts, the front of the event moves with the velocity of masses by which is composed ($dx/dt=u_c$), whereas the unstable perturbations are associated to celerities $dx/dt=u+c$, which are higher than front velocity u_c near the peak of the event. The space allowed for waves to develop is therefore larger the later they origin after peak crossing. When instabilities are not evident, space (length of the channel) and time (duration of the event) are insufficient to allow their development.

6 CONCLUSIONS

Debris waves do frequently develop in nature, whenever a critical Froude number Fr_{cr} is exceeded, causing

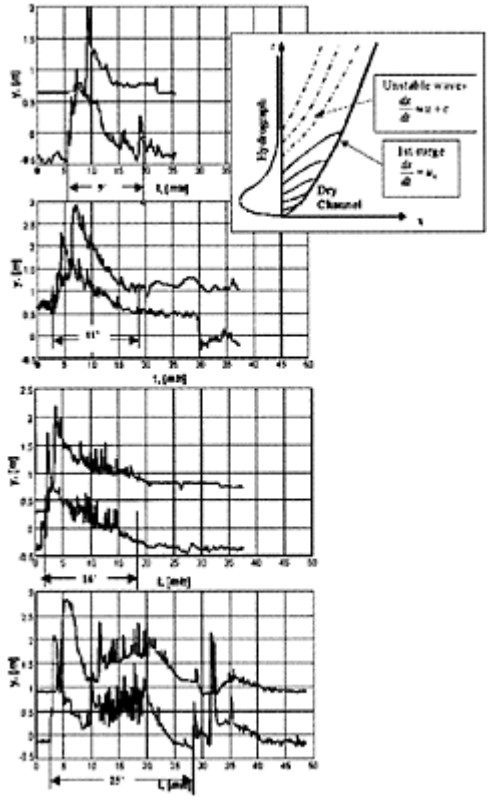

Figure 7. At the left hand side, measured hydrographs at two channel sections (300m distant) of some events occurred in the Moscardo torrent (original plots in Arattano et al., 1997), on which the real duration of the event is highlighted: with increasing duration, instabilities do develop. At the right hand side, the sketch in the *x*-*t* plane graphically represents the interpretation by the authors for debris

wave formation and development in space and time.

a significant increase in peak flow depth and particularly in peak thrust. Debris events are generally composed by a first surge and secondary waves that develop during recession and become more evident with increasing effective duration of the event, independently on peak discharge. When instabilities in nature are not evident, space (length of the channel) and time (duration of the event) may be insufficient to allow their development.

Several flow laws incorporated into two 1D different numerical models, DFEM and WAF-DF, have been compared to field data obtained from a well-documented debris flow event in the Swiss Alps.

The two models, both based on shallow-water equations and on the assumption of a 1-phase flow characterised by a uniform rheology, represent adequately average values of state variables in natural debris flow events.

In general, all flow laws underpredict flow depth in comparison to the field data. By calibrating the rheological flow laws an adequate match of the hydrograph measured at the downstream end of the channel was obtained. The representation of roll wave activity at flow tail is achieved only from a qualitative point of view; further calibrations and in particular an accurate input hydrograph could allow an improvement in numerical results. The travel time of the debris flow front between instruments is 'captured' only by the Generalized Viscoplastic Fluid (for the WAF-DF code) and by the Voellmy Fluid (for the DFEM code) laws.

Discrepancies among computations and field data can be explained with the wide uncertainty on the effective rheology of the flowing material, as the fluid is actually non-homogeneous, the rheological parameters and the concentration vary in space and time, segregation at the front and crushing of stones occur along the stream.

REFERENCES

Arattano, M., Deganutti, A.M. & L.Marchi, 1997: "Debris flow monitoring activities in an instrumented watershed on the Italian Alps", *Proc. 1st ASCE Int. Conf. on Debris-Flow Hazards Mitigation: Mechanics, Prediction and Assessment,* pp. 506–515.

Arattano, M. & P.G.Trebbo, 2000: "Debris flow in ambiente alpino", Video-tape, Consiglio Nazionale delle Ricerche, Istituto per la protezione Idrogeologica del bacino Padano, Turin, Italy.

Bartelt, P., Salm, B. & Gruber, U. 1999: Calculating densesnow avalanche runout using a Voellmy-fluid model with active/passive longitudinal straining. Journal of Glaciology, 45(150), 242–254.

Berti, M., Genevois, R., Simoni, A. & P.R.Tecca 1969: "Field observations of a debris flow event in the Dolomites", *Geomorphology,* 29, pp. 265–174.

Chen, C.L. 1992: "Momentum and energy coefficients based on power-law velocity profile", *J. of Hydr. Eng., ASCE,* 118(11), 1571–1584.

Chun, F. 1982: "Stability of flow of a generalized Newtonian fluid down an inclined plane", *J. of Appl. Math. & Physics*, 33, 181–188.

Coussot, P. 1994: Mudflow rheology and dynamics, Balkema.

Huang, X. & M.H.García, 1997: "A Perturbation Solution for Bingham Plastic Mud Flows," *J. of Hydr. Eng., ASCE,* 123(11), 984–996.

Huang, X. & M.H.García, 1998: “A Herschel-Bulkley Model for Mud Flows Down a Slope”, *J. of Fluid Mech.*, 374, 305–333.
Hungr, O. (1995): A model for the runout analysis of rapid flows slides, debris flows, and avalanches. Canadian Geotechnical Journal, 32(4), 610–623.
Hürlimann, M, Rickenmann, D., & Graf, C. 2003: “Field and monitoring data of debris-flow events in the Swiss Alps”, *Can. Geotech. J.*, in press.
Iverson, R.M. (1997): The physics of debris flows. Reviews of Geophysics, 35(3), 245–296.
Katopodes, N.D. 1984: Two-dimensional surges and shocks in open channels. Journal of Hydraulic Engineering, 110(6), 794–812.
Krüger, S. 2001: Computational contribution to highly super-critical flows, Nr. 167, Versuchsanstalt für Wasserbau, Hydrologie und Glaziologie, ETH Zürich.
Lamberti, A. 1999: “Debris flow Risk Project, Final Report, Videos”, (CD-ROM), University of Bologna, Bologna, Italy.
Lamberti, A., Zanuttigh, B. 2003: “Impact of debris waves” to be published in *IAHR, J. of Hydr. Res.*
Lanzoni, S. & G. Seminara, 1993: “Debris Waves”, *Proc. of XV IAHR Congress, Tech. Sess. B*, pp.79–185.
Mortara, G., M. Cerini & R. Laffi, 1994: “L’evento alluvionale del 22 Luglio 1992 nella conca di Bormio in Alta Valtellina”, *Quaderni di studi e di documentazione CNR*, 17, Supplement to GEAM—Geoingegneria Ambientale e Mineraria. Anno XXIX n.4, pp. 25−33, Torino, in italian.
Näf, D.R. 1997: Numerische Simulation von Stosswellen in Freispiegelströmungen, Nr. 148, Versuchsanstalt fur Wasserbau, Hydrologie und Glaziologie, ETH Zürich.
O’Brien, J.S., Julien, P.Y., & Fullerton, W.T. (1993): Two-dimensional water flood and mudflow simulation. Journal of Hydraulic Engineering, 119(2), 244–261.
Rickenmann, D. (1990): Bedload transport capacity of slurry flows at steep slopes, Versuchsanstalt fur Wasserbau, Hydrologie und Glaziologie der Eidgenoessischen Technischen Hochschule Zuerich, Zurich.
Rickenmann, D. 1999: “Empirical relationship for debris flows”, *Natural Hazards*, 19, pp. 47–77.
Rickenmann, D. 2000: “Debris flows events in Switzerland. Video recordings”, Video-tape, Swiss-Federal Research Institute, Department of Natural Hazards, Birmensdorf, Switzerland.
Rickenmann, D., Hürlimann M, Graf C., Naef, D. & D. Weber, 2001: “Murgang-Beobachtungsstationen in der Schweiz”, *Wasser, Energie, Luft*, 93, Heft 1/2, pp. 1–8.
Rutschmann, P. 1993: FE solver with 4d finite elements in space and time.” VIII Int. Conf. on Finite Elements in Fluids, Barcelona, 136–144.
Takahashi, T. 1991: “Debris Flow”, IAHR monograph series, Balkema, pp.165.
Toro, E.F. 1997: “Riemann solvers and numerical methods for fluid dynamics”, pp. 567, Springer-Verlag.
Trowbridge, J.H. 1987: “Instability of concentrated free surface flow”, *J. of Geoph. Res.*, 92, n. c9, 9523–9530.
Zanuttigh, B. & A. Lamberti, 2002: “Exact Riemann solution and Weighted average flux method for power-law channel section”, *Int. J. of Comp. Fluid Dynamics*, 16, n.3, 155–170.
Zanuttigh, B. & A. Lamberti, 2003: “Analysis of debris wave development with 1-D Shallow Water equations”, *ASCE, J. of Hydr. Eng.*, in press.

B.5.
Water pollution and contaminant transport

Some features of distribution of turbulence parameters of a jet flow in the river mouth

R.Khanbilvardi, B.Shteinman & V.Khazin
International Center for Water Resources and Environmental Research and Department of Civil Engineering, City College of CUNY, USA

O.Ozkurt
The Graduate Center and University Center of CUNY, USA

River Flow 2004—Greco, Carravetta & Della Morte (eds.)

ABSTRACT: The objective of the study was measurement of the turbulence parameters of a jet flow and establishment of some common patterns of their distribution along the current and in the cross section of the flow. In the river mouth, the jet current is an inertial flow smoothly spreading out in the liquid medium, without a direct contact with the bottom or the banks. The most characteristic feature of such flows is gradual attenuation of the runoff current, accompanied by the corresponding decrease in its kinetic energy. Another remarkable feature is intense turbulent mixing of the two water masses—that of the river and that of the receiving water body. The very retardation of the river jet on its boundaries, along with the diminishing flow gradient, are the main causes of its attenuation.

1 BACKGROUND

River mouth areas are specific natural objects that enclose zones of transition of the river hydrological regime to the hydrological regime of the receiving reservoir (seas and lakes). The most important character of this process is a significant change of hydrodynamic, hydrophysical, chemical and biological parameters of the water masses within a comparatively short distance. An external evidence of these river-mouth processes is the formation of rather stable forms of relief, such as the above-water and underwater deltas, the mouth bar and spits. In the river mouth, the jet current is an inertial flow smoothly spreading out in the liquid medium, without a direct contact with the bottom or the banks. The most characteristic feature of such flows is gradual attenuation of the runoff current, accompanied by the corresponding decrease in its kinetic energy. Another remarkable feature is intense turbulent mixing of the two water masses—that of

the river and that of the receiving water body. The very retardation of the river jet on its boundaries, along with the diminishing flow gradient, are the main causes of its attenuation (Mikhailov 1971, Mikhailov 1996, Mikhailov et al. 1986, Shteinman & Kamenir 1998, Shteinman et al. 2000).

A number of empirical, semi-empirical and theoretical methods and models were worked out as an essential part of the assessment of river mouth resources. The publications mentioned deal mainly with the study of mean velocities attenuation along the jet flow in river mouth areas (Mikhailov 1996, Shteinman & Kamenir 1998, Shteinman et al. 2000). Much less studied is the distribution of turbulence characteristics in the jet flows within river mouth areas.

The existing theoretical methods to describe free turbulence observed in jet currents within the river mouths are based on the hypothesis of self-modeling of the respective currents, and on using semi-empirical theories of turbulence. The self-modeling theories are based on some general properties of liquid currents and can also be justified by means of similarity and dimensionality methods. Semi-empirical theories of free turbulence utilize, besides general laws of hydrodynamics, some additional, more specific hypotheses (Monin & Yaglom 1965, 1967, Hintze 1963).

There have been attempts at mathematical simulation when studying turbulence of jet currents (Miligeyev & Sokolov 1986, Svanidze et al. 1984). In these models, in order to choose boundary conditions that would combine turbulence irregularity and statistical orderliness of the averaged motion, boundary conditions from the experiment are introduced (usually the velocities obtained by using quick-response devices).

Although in some cases the theoretical models provide a satisfactory description of the turbulence structure of a river jet flowing into the receiving water body, they do not take into account a number of important effects occurring on the boundaries of water masses of different density. These effects are caused by thinning out of the flow of fresh river water onto the surface of the receiving water body (sea or lake). In such double-circulation conditions, the flows' turbulence structure has a number of essential features that are not described by theoretical and mathematical models.

Here, taking as a sample the measurements performed in the mouth of the Kura River flowing into the Caspian Sea, some features are established of the turbulence structure of a river jet flowing into a sea.

2 SITE DESCRIPTION

The Kura River mouth area is located on the Western coast of the Caspian Sea (Fig. 1), in the Republic of Azerbaijan. The Kura River, by its length (1,515km), watershed area (188,000km^2) and average annual discharge (about 16km^3) is the largest river in Transcaucasia.

The total area of the Kura's delta amounts now to some 75sq. km. The river bifurcates, within its delta, into two branches—northern and southern, and the bulk of river runoff (up to 80%) is entering the sea through the southern one.

The average annual discharge of suspended sediments in the mouth of the southern branch is 280kg per sec. The predominant grain size in the suspended sediments is

<0.05mm, and it is the biggest in the period of high water (April–June), when up to 75% of the annual runoff enters the sea.

The river sediments coming to the mouth coastal waters have formed a crescent-shaped sand bar and mouth spits. The bar crest is at an average distance of about 1km from the mouth, experiencing insignificant seasonal oscillations corresponding to the sediment balance at different stages of the hydrological regime. At the stage of rising high waters, the bar moves seaward, the water depth at its crest falling down to 0.7–0.5m. At the low water stage, the bar is being gradually eroded from its seaward slope.

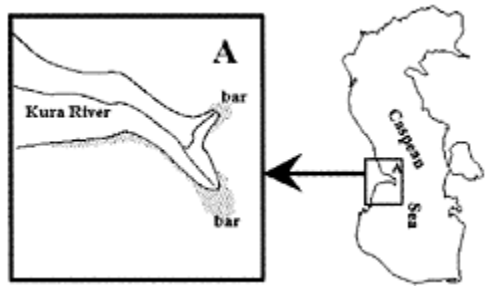

Figure 1. Schematic map of the Kura River Mouth area.

Current velocities at the mouth reach 1.5–2.5m/s in the high-water periods, while in low-water periods they are 0.5m/s on the average.

3 FIELD MEASUREMENTS

Because of the complexity of the process of mixture of the river and sea waters, and accordingly—the restructuring of the river turbulence, the goal of field measurements in the first stage was rather simple: to reveal main physical properties of turbulence—its space-time and spectral characteristics. The measuring tool used in this stage was a micropropeller that records the longitudinal component of flow velocity. This measuring tool is described in Nikora et al. (1994) and Nikora & Shteinman (1996).

The first stage of studies resulted in an information base on statistical characteristics of pulsation of the longitudinal component of velocity at different distances from the mouth section, which allowed making a very general conclusion on the process of restructuring of turbulence of the river flow as it was moving into the sea.

In the following stages of experiments, the tasks became more sophisticated. Now the goal was to obtain information on the flow's velocity structure for 3-D plotting. The measurement system used to record the three velocity components included the three-dimensional velocity fluctuation meter consisting of 3 circular piezoelectric slabs (radius 1m) mounted on a 5cm×5cm×5cm cubic frame interfaced with a computer to give real-time readout. Using this system allows obtaining valuable data on the structure of turbulence (Shteinman et al. 1993, Khanbilvardi et al. 2003a, Ozkurt et al. 2003), and substantially expanding the goals of experiments.

It is worth emphasizing that all measurements were done in calm waters, with almost no waves or alongshore movement of sediments, which made it possible to research various models of free spreading of the river jet on the river mouth area in its pure form.

Measurements were conducted under steady hydraulic conditions and embraced the entire cross section of the flow. The duration of measurements in each point was 15min., so background hydrological and hydraulic conditions were practically unchanged during each experiment.

Measurements were performed at the river mouth cross section and at distances of 25, 50, 75, 100, 150, 200, 300, 400, and 500m from it along the jet's dynamic axis, at its boundaries, as well as in the area of its free spreading beyond the bar.

4 DATA PROCESSING

Quantization of the continuous records of velocity pulsations was done with the step of 1s, and in some cases the quantization step was 0.25s and 0.1s. In accordance with this, the upper frequency of analysis, determined by the quantization step, was accepted as 31.4rad/s.

The main mechanisms used to describe the results were the theory of random processes, the method of structural averaging when studying coherent structures, and the theory of random functions and fields when studying hydrodynamic fields (Grinvald & Nikora 1988, Grinvald 1974, Nikora 1991, Sukhodolov et al. 1998).

When considering jointly the three velocity components, that is the vector fields of velocity, the vectoralgebraic method of analysis was used (Rozhkov 1979), which provides important information under conditions of commensurability of the three velocity components. The main element of this analysis is analyzing the correlation tensor of the vector process

$$K_{\vec{v}}(t,\tau)=\begin{pmatrix} K_{v_1v_1} & K_{v_1v_2} \\ K_{v_2v_1} & K_{v_2v_2} \end{pmatrix} \qquad (1)$$

which is a dyadic tensor function of the arguments *(t, τ)*. This function characterizes the interrelation of the directional changes of the flow velocity vectors at the moments of time *t, t+τ*, and provides numerical assessment of the intensity of these changes and of their orientation in the given system of coordinates.

The invariant *D* of the skew-symmetric part of the tensor K_v, called by Rozhkov (1979) the indicator of spinning (rotational movement of turbulent eddies), can be determined by the relation

$$D_{1,2}=K_{v_1v_2}-K_{v_2v_1} \qquad (2)$$

It is composed of the orthogonal components of the vectors $\vec{v}(t)$and $\vec{v}(t+\tau)$. If $D>0$, then the vector $\vec{v}(t+\tau)$is predominantly oriented to the right of the vector $\vec{v}(t)$,and if $D>0$, then to the left. This means that in the first case the vector's rotation is clockwise, while in the second case it is counterclockwise.

In the equation (2), the basis unit vectors of the tensor $K_{\vec{v}}$depend on the arguments *(t, τ)* and are oriented, with respect to the reference system of coordinates, in the direction

$$\alpha^{(K)} = 0.5 arctg\left[\frac{K_{v_1v_2} + K_{v_2v_1}}{K_{v_1v_1} - K_{v_2v_2}}\right] \quad (3)$$

In our experiments, the spatial structure of the correlation characteristics is conducted successively for the vertical *(u, v)*, horizontal *(u, w)*, and transversal *(v, w)* planes in the left system of coordinates (the X-axis goes with the current, the Y-axis is oriented perpendicular to the gravity vector in the direction of the right edge of the current, and the positive Z-semiaxis goes upward, perpendicular to the bottom plane).

The invariants D_{ij} characterize the intensity of spinning of the velocity vector in various planes.

For a more complete analysis, the so-called linear invariant *J* was considered, which can be determined by the equation

$$I = K_{v_1v_2} + K_{v_2v_2} \quad (4)$$

composed of the collinear vector components $\vec{v}(t)$and $\vec{v}(t+\tau)$. If $J>0$, the collinear vector components are unidirectional, if $J<0$, they have opposite directions, and if $J=0$, the vectors are orthogonal.

A joint analysis of the invariants *J* and *D* allows researching, regardless of the chosen system of coordinates, the structure of collinear and orthogonal alterations of the flow velocity vectors, and finally the intensity of spinning of the turbulent eddies in various planes, as well as the spatial orientation of the axes of such spinning.

5 RESULTS

5.1 *Pulsations of the velocity module and the intensity of turbulence*

As a result of multiple theoretical and experimental studies, it has been established that the intensity of turbulence on rectilinear portions of the river channels with a smooth, poorly erodible bottom is evenly increasing from the water surface to the bottom of the flow, where main generation of the turbulence energy takes place.

At the area of inflow of a jet river flow into a receiving water body, the main factor determining the changes in turbulence intensity is the intensity of dissipation of the longitudinal current velocity (Fig. 2).

Turbulence intensity grows the fastest at the river mouth section, where the flow is abruptly getting wider. The farther from the mouth, relative dissipation of velocity being equal, turbulence intensity is growing slower. It should be emphasized that we are talking only about the longitudinal component of velocity. The type of relationship shown in Figure 2 is caused by the fact that, the farther from the mouth and the wider the flow, the greater part of the pulsations energy falls on the transversal (between the mouth and the bar) and vertical (beyond the bar crest) components of velocity.

Pulsations of the longitudinal component of velocity in the jet flow first grow with the distance from the mouth. At a distance equal to the width of the river channel, the

intensity of longitudinal turbulence on the jet axis is about the same as in the channel, and then grows in the areas of increased longitudinal gradients of velocity.

Levels of turbulence in the diffusion current are significantly higher than in the steady one because of a higher velocity gradient, and, accordingly, higher

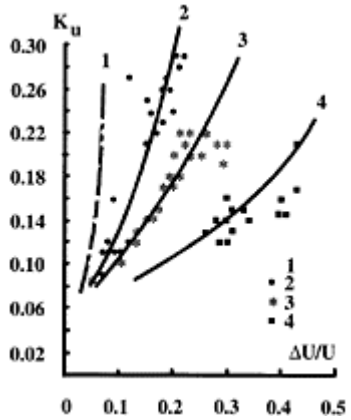

Figure 2. Relationship between turbulence and intensity of attenuation of the longitudinal velocity along the axis of the jet. Flow at various distances from the mouth (1–200m, 2–500m, 3−800m, 4−1,400m)

generation of turbulence. Within the area, 2–3 widths of the river long, in the river mouth, where abrupt flow deceleration occurs, the level of pulsations is observed to grow considerably.

The greater the river water discharge and, accordingly, the flow velocities, the farther from the river mouth gauge occurs the zone of highest turbulent pulsations.

Multiple studies have established the intensity of turbulence in the river flow is getting higher from the water surface to the bottom. However, in the conditions of free spreading of the jet flow, starting from the bar crest where the jet detaches itself from the bottom (so-called detached flow), the highest intensity of turbulence is observed within the contact zone between the upper layer of fresh river water and the underlying layer of denser sea water mass (Fig. 3). As the velocity of the river jet increases, the layer of maximum turbulence is shifting deeper.

The influence of the bottom topography on the velocity pulsations and on the distribution of turbulence intensity is felt in the jet flow in the same manner as in the river channel. As proven by observations (Ozkurt et al. 2003, Khanbilvardi et al. 2003b), in the area between the river mouth gauge and the bar crest, the linear dimensions of the bottom ridges are rapidly diminishing along the flow.

This leads, first, to the faster decrease in the standard deviation of the longitudinal pulsations of velocity, and second, to a more uniform distribution of turbulence intensity over the depth of the flow.

The mouth bar has also the shape of a large ridge composed of river sediments. According to laboratory studies (Petrosyan 1984), maximum values of the

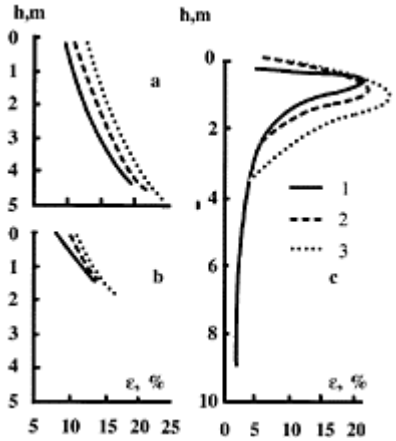

Figure 3. Variability of the intensity of turbulence with the jet flow depth at various distances from the mouth (a—mouth gauge, b—bar crest (500m from the mouth), c—deeping beyond the bar (800m from the mouth—zone of detachment of the river jet from the bottom). Curves 1, 2 and 3 correspond to the flow velocities in the mouth equal to 1.58, 2.10, and 2.46m/s respectively).

standard deviation of pulsations on the vertical lines beyond the bar crest occur at the crest level, and here we see similarity with the channel flow having a ridged bottom. At the same time, the conclusion that the character of changes in turbulence intensity beyond the bar is similar to that of the area below the bar of a moving sand wave, cannot be extrapolated to the field conditions.

In laboratory conditions, an unstratified flow is observed beyond the bar, while in natural river mouths fresh waters are pinching out to the flow surface as the river jet is moving into the sea. This is why the distribution of velocity pulsations and turbulence intensity on the vertical lines beyond the bar crest has specific features as shown in Figure 3 and the river mouth bar, from the point of view of its influence on turbulence, can be considered not as a bottom ridge characteristic of a river, but as a practically

immobile large bottom ridge generating a detached current. Examples of the distribution of turbulence intensity over the cross section of a jet flow at various distances from the river mouth are given in Figure 4.

5.2 *Velocity vector pulsations*

Pulsations of the transversal (w') and vertical (v') velocity differ from the pulsations of the longitudinal component (u'). Within the river area, the ratio $\overline{u'^2}/\overline{v'^2}$ generally displays regular growth from the bottom to the flow surface; the ratio $\overline{u'^2}/\overline{w'^2}$ is also growing, being greater than $\overline{u'^2}/\overline{v'^2}$.

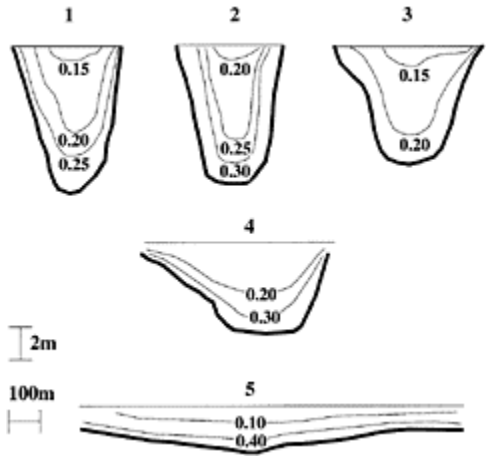

Figure 4. Distribution of Turbulence Intensity over the Cross Section of the Jet Flow at Various Distances from the River Mouth: (1—mouth gage, 2–200m, 3–500m, 4–800m, 5–1,100m)

In the river mouth jet flow, spatial distribution of the velocity components has some specific features. In the jet flow, at the distance from the mouth equal to the width of the river, $\overline{u'^2}$ starts its regular growth with the distance from the bottom. This is related to the fact that friction at the side boundaries of the jet is 6–9 times higher than friction at the bottom (Mikhailov et al. 1986). For this reason, when the river flow exits the mouth gauge, its surface layer acquires intense additional turbulization as compared to the near-bottom layers experiencing basic friction on the bottom because here the transversal velocity gradient is the smallest. For the same reason, is also growing in the surface layer.

Beyond the bar, where the river jet, possessing insignificant energy, is detaching from the bottom and spreading freely, all three components of velocity have the highest values of pulsation in the surface layer. However, if the jet has significant energy, the $\overline{u'^2}$, $\overline{v'^2}$ and

$\overline{w'^2}$ are decreasing from the bottom to the surface, which is due to high vertical gradients of velocity in the near-bottom zone.

Eddy zones on the jet boundaries are the sources of the elevated turbulence, with the velocity of translational motion 5–10 times lower than the velocity in the main body of the jet. Here we observe the highest values of turbulent pulsation and commensurable components u', v' and w'. The intensity of transversal pulsations can be here as high as 60%, while the intensity of longitudinal pulsations is only 25–35%. The transversal pulsations of velocity at a distance equal to 5–6 river widths are 10–20 times higher than those in the jet axis.

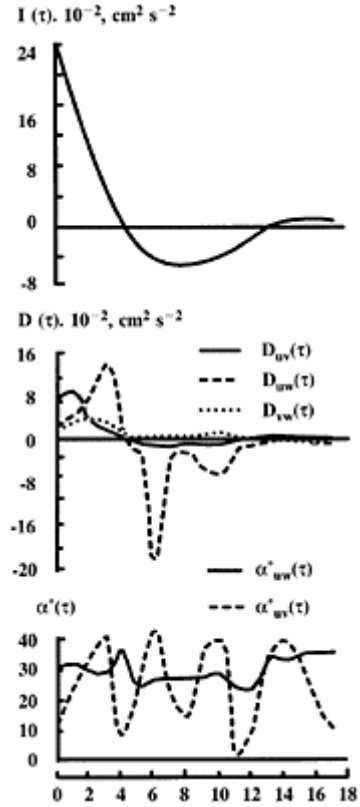

Figure 5. Example of the autocorrelation tensor function invariants.

The above regularities of distribution of the velocity pulsations are the reflection and result of the eddy structure of the flow and of the turbulent eddies spinning in it. Figure 5 presents examples of calculation of the correlation tensor function invariants I and D superposed on various sections of the jet flow.

For functions $D_{uv}(\tau)$, $D_{uw}(\tau)$ and $D_{vw}(\tau)$, corresponding to the channel section, both positive and negative values are present, and lesser than $I(\tau)$ amplitudes of oscillation, the highest ones pertaining to D_{uv} (spinning in a vertical plane), and the smallest to D_{vw}. On the bar, the component D_{uw} dominates other components, testifying to the restructuring of the flow from spinning predominantly in the verticallongitudinal plane *(u, v)* to spinning predominantly in the horizontal-transversal plane *(u, w)*.

Beyond the bar, the component D_{uv} is close to zero (spinning in the *(u, v)* plane is negligible compared to spinning in other planes), powerful spinning occurring in the horizontal plane *(u, w)*.

Analysis of indicators of spinning in different planes has shown that in experiments within the river channel it was in the form of right screw (clockwise), while within the jet part of the flow, as it approaches the bar, toppling and surfacing of eddies occur, with spinning beyond the bar predominantly counterclockwise (in the horizontal plane). Judging by the values of the angle $\alpha^0(\tau)$ given in Figure 5, the direction of the major axis of the tensor curve (direction of the predominant variability of the velocity vector) does not stay constant but is cyclically changing with respect to τ: in the river flow mainly in the plane *(u, v)*, in the jet section up to the bar in the plane (u, w), beyond the bar again in the plane *(u, v)* because here intense mixing of river and sea water masses occurs.

Comparison of the values of the correlation function $I(\tau)$ of the collinear components of the pulsation velocity vector with the function $D(\tau)$ of the orthogonal components shows that $I(\tau)>D(\tau)$ before the bar, and $I(\tau)<D(\tau)$ on the bar. This means that while at the beginning of the jet the interrelation of the collinear components is predominant, around the bar the interrelation of the orthogonal components is stronger, that is the influence of the changing flow direction is greater than the influence of the changing velocity module.

6 CONCLUSIONS

Analysis of the distribution of the standard deviations of the components of the river jet velocity vector at its inflow into the sea has shown that the structure of channel turbulence is rapidly degenerating. Turbulent eddies change their orientation from the predominantly vertical-longitudinal spinning with a horizontal axis to the predominantly horizontal-transversal spinning with a vertical axis. At the same time, substantial additional turbulent energy is being generated in the zones of contact between the jet flow and the adjacent mass of seawater.

REFERENCES

Grinvald, D.I. 1974. *Turbulence of Channel Flows.* Leningrad, Hydrometeoizdat, (in Russian).

Grinvald, D.I. & Nikora, V.I. 1988. *Turbulence in Rivers.* Leningrad, Hydrometeoizdat, (in Russian).

Hintze, I.O. 1963. *Turbulence, Its Mechanism and Theory.* Fizmatgiz, Moscow, (in Russian).

Khanbilvardi, R., Shteinman, B., Khazin, V & Ozkurt, O. 2003a. The influence of surface waves on turbulence characteristics of the jet flow in river mouths. *Proc. 3rd IAHR Symposium on River, Coastal and Estuarine Morphodynamics, Barcelona, 1–5 September 2003.*

Khanbilvardi, R., Shteinman, B., Khazin, V & Ozkurt, O. 2003b. Interaction of flow with mobile bottom in the river mouth. *Proc. 7th International Conf. on Computational Modeling of Free and Moving Boundary Problems, Santa Fe, New Mexico, 4–6 November 2003.*

Mikhailov, V.N. 1971. *Flow and Channel Dynamics in Non-Tidal River Mouths.* Hydrometeoizdat, Moscow, (in Russian).

Mikhailov, V.N. 1996. Methods and models for assessment of hydrological and ecological conditions of river mouth regions. *Proc. Monitoring Tailor-Made II Information Strategies in Water Management, Sept. 1996, Nunspeet, the Netherlands,* 253–262.

Mikhailov, V.N., Rogov, M.M. & Chistyakov, A.A. 1986. *River Deltas. Hydrological/Morphological Processes.* Hydrometeoizdat, Leningrad, (in Russian).

Militeyev, A.N. & Sokolov, B.I. 1986. Mathematical simulation of currents in river mouths of non-tidal seas accounting for real hydrometeorological conditions. *Proc. of the 5th All-Union Hydrological Congress,* 42–43, (in Russian).

Monin, A.S. & Yaglom, A.M. 1965 (Part I), 1967 (Part II). *Statistical Hydromechanics.* USSR Academy of Sciences Publishers, Moscow, (in Russian).

Nikora, V., Rovinski, P., Sukhodolov, A. & Krasuski, D. 1994. Structure of river turbulence behind warm-water discharge. *J. Hydrol. Energy, ASCE,* 120:191–208.

Nikora, V.I. & Shteinman, B. 1996. Turbulence in the Jordan River: A case study. *In: Flow Modeling and Turbulence Measurements,* 1:581–588. Rotterdam/Brookfield.

Nikora, V.I. 1991. A Physical Model of Fluvial Turbulence. Proc. XXIV Congress IAHR, Madrid, 549–556.

Ozkurt, O., Khanbilvardi, R., Shteinman, B. & Khazin, V. 2003. Some characteristics of the interaction between turbulent flows and movable rippled bottom in the river mouth. *Proc. 2nd International Conf. on Computational Methods in Multiphase Flow, Santa Fe, New Mexico, 3–5 November 2003.*

Shteinman, B. & Kamenir, Y. 1998. Decrease in suspended matter concentration with distance from the Jordan River Mouth, Lake Kinneret: Hydrodynamical Aspects. *Adv. in Hydro-Science and-Engineering,* 3:122–136.

Shteinman, B. & Gutman, A. 1993. Flow turbulence and dispersion of different matter in the river mouth. *Wat. Sci. Tech.,* 27:397–404.

Shteinman, B., Gutman, A. & Mechrez, E. 1992. Laboratory study of the turbulent structure of a channel jet flowing into an open basin. *Boundary Layer Meteorology,* 62: 411–416.

Shteinman, B., Mechrez, E. & Gutman, A. 1993. Spatial structure of the jet flow in the river mouth. *Boundary Layer Meteorology,* 62:379–383.

Shteinman, B., Kamenir, Y., Hochman, A. Itzhak, O. & Ben-Dan, T.B. 2000. Sedimentation process in the jet flow of river-lake contact zones. *Advances in Fluid Mechanics,* 3:63–72.

Sukhodolov, A., Thiele, M. & Bungartz, H. 1998. Turbulence structure in a river reach with sand bed. *Water Resources Research,* 34(5):1317–1334.

Svanidze, G., Shteinman, B. & Bronfenbrener, L. 1984. Calculation of turbulent jets in river mouths by mathematical simulation based on the equivalent problem of the theory of heat conductivity. *Proc. of the Conference "Dynamics and Thermal Conditions of Rivers, Reservoirs and Estuaries",* 2:218–210, MGU Publishers, Moscow, (in Russian).

An integrated system for prevention of pollution due to sewage and waste waters into rivers

F.Boccia & D.Postiglione
Enel.Hydro B.U. Ismes Engineer, Centro Direzionale, Napoli, Italy

A.Fusco
Enel.Hydro-Ismes Division & Development Department Director, Seriate, Bergamo, Italy

L.Mancusi
Enel.Hydro B.U. Ismes Engineer, Iside Centre, Prignano Cilento, Salerno, Italy

River Flow 2004—Greco, Carravetta & Della Morte (eds.)

ABSTRACT: In the National Operative Programme (P.O.N.), called AQUATEC "Control, treatment and maintenance innovating technology for water emergency solving", the objective entitled "System for prevention of pollution due to waste waters into rivers" proposes to implement a system for the control and valuation of the effects into the rivers produced by waste waters derived from industrial, human or agricultural activities.

The innovative idea of the project consists in the use, in conjunction with traditional technology of qualitative and quantitative river monitoring and simulation of the pollutants dispersion, of an expert system realized through archives containing both available measurements and simulations of reference scenarios or "classes" of situations. So the system is able to "extrapolate/interpolate" in an intelligent way data in archives to formulate a forecast cause/effect connection of continuous or accidental waste waters.

1 INTRODUCTION

In the last years water ecosystems biotic integrity concept has had a growing importance till to be considered official by Italian regulation 152/99.

This regulation defines general rules for water protection. Its objectives are “to prevent and to reduce water pollution, to recover and to improve water state, to defend special water uses, to assure sustainable uses of the resource and to preserve natural capability of river self-purification, necessary to support wide and well diversified animal and vegetable communities”. “Quality objectives” and “protection plans” are the prescribed tools for these aims.

The use of the presented methodology supposes a continuous monitoring, with all benefits short and long term, for territorial planning, for river quality state evolution control, waste waters delivered into river management, for prevision of impacts, as well as for the possibility of quick decision and prompt intervention in situations of emergency.

To reduce the physical complexity of the continuous survey and data transmission net, we use a virtual sensor system implemented with a fuzzy logic.

The present article describes design and implementation phases in a sample basin of decision support system which consents to interpret qualitative and quantitative data from the river monitoring net. In this way it is possible to analyze causes of the present situation and to interprete short and long term effects into river caused by input of waste waters from industrial, human or agricultural activities.

This objective, focusing attention on the river, is in perfect line with the above-mentioned regulation 152/99, in which the imposition logic respect of the single waste waters or area to protect respect of the quality is exceeded. The problem is dealed within a general hydrogeologic context, according to which environmental quality of river is to be reached in a global way, searching balance between natural water flow and the external contribution due to human presence, avoiding causing qualitative and quantitative irreparable damages. The balance is reached when natural capability of river self-purification remains and so the possibility of supporting wide and well diversified animal and vegetable communities, without pollution processes. The system we want to realize needs continuous monitoring with data acquisition in a S.I.T. from which we get information to execute simulations on different temporal scales. The possibility to get on-line data relative to river state besides assuring real time signalling about critical or warning situations arising, to operate (do) a quick intervention, consents to define initial conditions of the physical environment from which to leave, to get prevision of future scenarios.

2 STATUS OF THE RESEARCH

2.1 *Sensors*

In the last years research in sensors field has had a notable development providing [11] a great number of components suitable for chemical—physical interesting parameters on-line survey. They are founded on potentiometric techniques, for example to measure the

oxygen, ph, etc. or colorimetric ones, for example for determination of nitrogen and phosphorus compounds. Parameters considered for the rivers are typically: temperature, dissolved oxygen, conductivity, redox potential, ph, turbidity, suspended and gravity driver-position solids, ammonia. Automatic sampler which consent to evaluate the pollution stress are available. Moreover they are studying both analytical data validation technics and real-time adjournment methods, with communication systems using wireless techniques (GSM), of the data bank of territorial information systems.

To reduce the physical complexity of the continuous survey and in way to make it more similar data transmission net and to evaluate parameters which don't lend oneself to on-line valutation (BOD), we use a virtual sensor system implemented with a fuzzy logic. The fuzzy logic objective is to generalize classic logic to human thinking way. Some intermediate values which can characterize in a more precise way the real situations are added to the two typical values "true" and "false". The logic inference rules used in this case are calibrated on the particular application field. However they operate simulating the typical "good sense" of the field expert. Moreover virtual sensors [2] consent to estimate the trend of simple and complex parameters on the base of only simple parameter measure acquisitions (flow rate, level, dissolved oxygen, ph, etc.). The system is based on analysis of measures historical knowledge and consents to estimate temporal trend of not directly monitored parameters on the base of others monitored ones. Parameters which we want to estimate temporal evolution must be correlated (fuzzy function) to automatically controlled ones. But it is not required correlation between monitored parameters and estimated ones as, on the contrary, it is required for physically founded models. The use of fuzzy logic for the definition of virtual sensors has as objective to explicit the dependence rules among parameters. This individuation process of inferences between input and estimated ones becomes an explicit knowledge patrimony, and consents to value and control by an expert operator (typical characteristic of an expert system).

2.2 *Quality models*

Fluently river quality study is made by formulation of a mathematical model of the real system to employ with a computer. Model must have the ability to describe in quantitative terms space-time real system evolution, and to give system reply to external solicitations considering internal dynamics. Usually in a software implementing a river quality model the whole of elaborations is organized by functional strictly related modules, which we can usually schematise as follows:

–hydraulic model, which describes water flow field and concentration's distribution of dissolved substances;
–chemical model, which describes inorganic substances kinetics degradation in the river;
–biochemical model, which describes organic substances kinetics degradation;
–ecological model, which reproduces photosynthesis mechanics and dynamic of the river ecosystem food chain;
–thermal model, which describes temperature field into river.

As regard to research, hydraulic models have reached a good maturity and three-dimensional software are available giving reliable results. As regard water quality

models, since very complex phenomena are described, the research is always in evolution for realizing more complete and reliable models. Now many river quality models are available [10] where we notice the difficulty to realize optimum integration between hydraulic and quality models. Some well-known river quality models are: QUAL2E (EPA, 1995), MIKE11 (Danish Hydraulic Institute), WEST (Wastewater Treatment Plant Engine for Simulation and Training, made in Belgium). River quality models are used to produce single elaborations concerning specific environmental conditions; at present it seems that in Italy, except for specific situations, appliances integrating river quality models with on-line obtained data from a territorial scale monitoring net are not available for describing temporal evolutions of phenomena and then to go up to incidental event causes, or to support choice of reclamation actions.

2.3 *Expert systems*

The project wants to realize a decision support system which gives output of simulation with monitoring net data to consent a result interpretation and a prediction of consequent effects. This system cannot use traditional mathematical models whose elaboration time are incompatible with a real-time system, but has to use Artificial Intelligence techniques.

Some expert systems applications are known within the limits of very specific sectors of water treatment, in particular:

–research to establish biological efficiency in active sludge depuration plants [5];
–exploitation well safe yeld control, iron and manganese control in potable water, hydraulic net efficiency control [6];
–nitrogen removal from sludge control [7];
–on-line monitoring of waste waters from purification plant [8];
–optimization of chrome fragmentation in industrial water [9].

Research on Artificial Intelligence gave enquiry tools which are over traditional monitoring limits, consenting to use, with monitoring data, also qualitative, dubious or incomplete information as they are used by an expert of the field. Systems operating in this way are called expert systems. They are founded on the use of “Knowledge Base” considered as a whole of highly structured information and association of concepts and rules.

The central element of an expert system is inferential motor which can be synthetized as a whole of rules and strategies of knowledge elaboration to reach a deduction for the problem solution. But data aren’t precise, so the operative logic can’t be Boolean, but it must consider dubiousnesses and the many shadings of original data; the logic which uses these standards is “Fuzzy Logic”.

3 PROJECT PRESENTATION

3.1 *System structure*

The system is essentially composed by two modules based on a common techniques, and precisely [4]:

System for simulation and prevision of short, middle and long term effects due to incidental waste or continuous ones into rivers or sensitive backwater areas. This system wants to estimate, for incidental sources or continuous waste, river areas interested by waste water, to give in short, middle and long terms a prevision of effects in terms of quality and the possible water recycle. It can also give indication about possible recovery intervention which we can suppose, for example an use of solvents, drawn work closing.

Reconstruction and locating of the original scenarios in connection with water quality control systems. This system wants to elaborate, on the base of monitoring indications, (for example on the confluence in the main river) possible scenarios on the origin of measured values, giving indications on the possible risk areas or letting in zones not in norm.

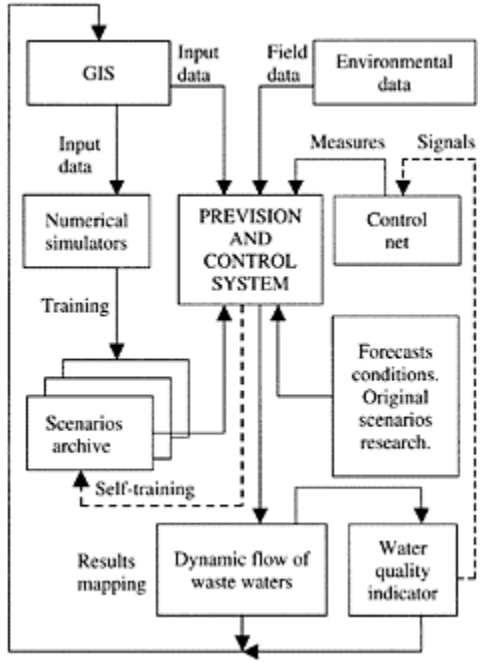

Figure 1. Block scheme of information flux among modules.

Both indicated systems depend on river and territorial characteristics, so we forecast their integration in a GIS from which they will take territorial information, and to which they will give elaboration results for a their mapping in connection with territorial data (waste position, drawn works, effects on bypasses, etc.). Moreover we analyse the possibility to connect the systems with environmental tools (meteo gages flow and/or level meter, current meters, water quality sensors, etc.). All the systems will be “trained” by a series of numerically simulated scenarios able to cover all the possible hydrodynamic situations

which depend on environmental and seasonal parameters, and will increase its knowledge in connection with monitoring date.

3.2 *Choice of the experimental site*

Sarno river basin, considered since many years as a social-economic and environmental emergency area, has been chosen as investigation site for this project. This choice is justified by many factors. First of all at present studies and data are available on Sarno basin and we can use them to study pollution evolution, to have knowledge of the present quality status, as well as to the efficacy of renewal interventions [3].

ARPA Campania, an Institutional Organization employed to environmental controls began two years

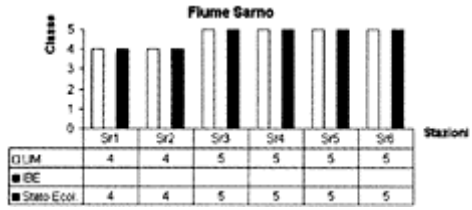

Figure 2. Quality state of Sarno River.

ago sampler and analysis activities for studying quality of rivers in Campania.

Sarno analytical data relative to years 2001 and 2002 have consented operating river first classification according to regulation 152/99. Even if environmental state wasn't defined but pollution level expressed by macro-descripting, it was defined only (LIM). Additional parameters research as organic and inorganic pollutants so far has been limited to metals, measured in all the seven monitoring stations, and to pesticide only in same stations. Since wasn't possible to measure IBE index, the ecological state value (SECA) is strongly conditioned by pollution level expressed by LIM.

From monitoring data analysis and from their elaboration, it is rather clear how strong the Sarno basin decay is, independently from IBE index values and step levels of most important chemical pollutants. The application of mathematical models to study river system behaviour is used whether for the simulation of flow conditions or evaluation of pollutants concentration in the river for convection, dispersive and diffusive transport phenomena. The project forecasts the implementation of mathematical water quality model formed by hydrodynamic, chemical and biochemical modules, open to subsequent integration of ecological and thermal modules. Moreover we forecast to detect, for the realization of a prototype, a part of the river with significant length which is delimited, above and below, by continuous qualitative monitoring station of chemical and physical parameters. The selected zone has a considerable waste inside as pollution load contribution, e.g. the waste of one of the purification of plants of middle Sarno districts. The part which has such characteristics is included between mouth and confluence of Alveo Comune Nocerino, measuring 10km, where effluent of district n°3 purification plant discharges.

3.3 *Choice of the continuous monitoring parameters and qualitative modeling hypothesis*

By considerations made on results of statistics elaborations realized by ARPA Campania, the pollution which causes high BOD and COD values has an industrial origin prevalently. It is caused by heavy metals as nickel, chrome, plumb and mercury, rather then biochemical origin caused by alimentary industries discharge. The method used for Factor Analysis is the Principal Components one (A.C.P.) followed by varimax rotation; Table 1 reports the factor loadings for each parameter, eigen values and the variance percent explained for the first five factors. First of all the analysis has showed that a large part of informations is contained in the first five factors (56.7% of represented variance). Moreover in the table we can notice that:

–1 st factor (16.3% of explained variance) is strongly related to dissolved oxygen, BOD and COD. It essentially expresses the river organic component. It is thought that the organic load represented by this factor comes from industries owing to unimportant correlation with the classical parameters which indicate civil pollution (ammoniacal nitrogen, total phosphorus, Escherichia coli, etc.).
–2nd factor (15.8% of explained variance) is related to total chrome, mercury, nickel and lead. We can say that this factor represents industrial pollution parameters.
–3rd factor (10.3% of explained variance) is characterized by total and ammoniacal nitrogen. We can say that this factor represents nitrogen pollution and it represents reduction state of the system.
–4th factor (7.5% of explained variance) is related to nitrates and total phosphorus. We can suppose that these correlations are due to photosynthesis and nitrification processes and they are representative of system eutrophication.
–5th factor (6.8% of explained variance), difficult to interpret, it seems not containing any directly interpretable information.

Besides we will monitor: dissolved oxygen, BOD, COD, organic, ammoniacal, nitroso and nitric nitrogen, organic and dissolved phosphorus, chromium as organic and conservative substance, Escherichia coli, to consider also biological pollution effects. For each of described parameter their correspondent modules operate the integration of convective-dispersive one-dimensional transport equation in which the space-temporal variation of concentration is due to longitudinal dispersion phenomenon, to dilution with other affluents, to the contribution of other outside distributed and concentrated pollutant loads, to the chemical and physical relations that may influence the examined substance concentration in relation to other state variables (temperature, concentration of other present substances, BOD, dissolved oxygen). In a subsequent phase it is made sensitivity analysis and calibration of the model, assignating to parameters in the model equations values obtained by a monitoring activity. Practically from the sensitivity analysis we can detect parameters whose values influence more

Table 1. Factor loadings.

	Factor 1	Factor 2	Factor 3	Factor 4	Factor 5
pH	−0.315149	−0.052836	−0.472621	0.131181	0.120895
Temperature	0.213251	−0.439654	0.124818	0.410357	−0.253403
Conductivity	0.078933	0.291776	0.020146	0.615537	0.542368
Hardness	0.059501	0.168140	0.468067	0.078384	0.587982
Suspended solids	0.467716	−0.145296	−0.061480	0.056930	−0.134976
Dissolved oxygen	**0.574095**	−0.064111	0.025864	−0.009991	**0.624017**
Dissolved oxygen	**−0.602760**	0.148055	−0.027983	0.014675	**−0.617389**
BOD_5	**0.763772**	−0.020290	0.117071	0.000212	0.157066
COD	**0.827853**	−0.069019	0.170124	0.141501	−0.014045
Total nitrogen	0.028777	0.023086	**0.871325**	0.186921	0.141246
Ammoniacal nitrogen	0.001972	−0.086288	**0.905901**	−0.145075	0.091879
Nitric nitrogen	0.168306	0.076075	0.114658	**0.648997**	−0.080729
Total phosphorus	0.366565	0.050539	−0.004764	**0.613464**	−0.019384
Chlorinolog	−0.094359	−0.005959	0.146972	0.074425	**0.631641**
Sulfate	−0.068915	0.367567	−0.066288	**0.571460**	0.444398
Escherichia Coli	−0.165719	−0.084291	−0.065083	0.425861	0.151964
Cadmium	0.005723	0.138419	−0.123534	0.176760	0.177367
Total Chromium	−0.177116	**0.736187**	0.056414	−0.008926	0.254937
Mercury	−0.087544	**0.789699**	−0.017273	0.060177	−0.177228
Nickel	−0.037159	**0.906849**	0.039098	0.084495	−0.084827
Lead	−0.035849	**0.803166**	−0.029546	0.040662	0.021295
Copper	0.148703	0.410809	0.230934	−0.527335	−0.085502
Zinc	0.025382	0.273601	0.222193	−0.063610	−0.393954
Expl.Var	2.604050	3.416202	2.253429	2.287060	2.485226
Prp.Totl	0.113220	0.148531	0.097975	0.099437	0.108053

Table 2. Eigen values and variance percent explained.

Eigen value	% Total	Cumulative	Cumulative
3.741705	16.26828	3.74171	16.26828
3.639613	15.82441	7.38132	32.09269

2.375607	10.32872	9.75693	42.42141
1.736098	7.54825	11.49302	49.96967
1.552945	6.75193	13.04597	56.72160

the answers of the model in particular initial and contour conditions. On the other hand, from planning of data acquisition activities, which characterize the real system behaviour, we go on to the mathematical model calibration of the system. It is possible to forecast making the model calibration using previously obtained data, supposing stationary contour conditions concerning to the temporal contexts in which data acquisition and model calibration were made and completing our data with a special analytical monitoring activity.

3.4 *Assumptions of hydraulic modelling*

Hydraulic model uses one-dimension equations of a slow stream in variable motion resorting to:

– geometry knowledge any 300 meters of water sections, inclination and roughness of Sarno river;
– water level staff measurements in shallow water;
– the knowledge of waste water localization, tipology and diameter;
– the definition of flow time state in upstream or first section of experimental site and water level in downstream or final section of experimental site.

The river quality model used for tests is arranged in 1997 by ISMES (Mancusi, Barbanti) to study quality of river Serio [1].

In hydraulic and biochemical submodel there is one dimension spatial description. Variable values are averaged or integrated on section.

Equation of mass balance of a general quantity, liquid weight or variable is:

$$\frac{\partial(Ac)}{\partial t}+\underbrace{\frac{\partial(Avc)}{\partial l}}_{\text{Convective term}}-\underbrace{\frac{\partial}{\partial l}\left(AD\frac{\partial c}{\partial l}\right)}_{\text{Diffusive term}}=\overbrace{AS}^{\text{Source term}} \qquad (1)$$

$$\text{with } S=\frac{S_L}{A}+S_c$$

where t=time; c=pollutant concentration; l=spatial coordinate; v=average rate of liquid in cross section; A=cross section area; D=longitudinal dispersion coefficient; S=source term which is addition of two terms: S_L=external contribution or drawing; S_c= contribution by internal dynamics to concentration variations.

Hydraulic submodel

It is made by equations resulting from (1), replacing by respectively water density ρ (mass balance equation and motion quantity density ρv (motion quantity balance equation).

Biochemical submodel

It is made joining conservation equation of water mass and considered compound. In any case there will be a type of equation:

$$\frac{\partial c}{\partial t} + v\frac{\partial c}{\partial l} = \frac{1}{A}\frac{\partial}{\partial l}\left(AD\frac{\partial c}{\partial l}\right) - \frac{S_q}{A}c + \frac{S_L}{A} + S_c \qquad (2)$$

where $S_q c/A$ describes concentration diluition due to water source S_q (dimensionally flow on unit of length).

Model is composed by type (2) equations system, one for any inquired compound. In the S_c term the dynamics of variables are cointained. For any chemical agent can be produced source terms as function of physical and chemical kinetics which control different degradation or concentration addition.

3.4.1 *Nitrogen*

Organic nitrogen N_4

$$S_{N4}=\alpha_1\cdot\tau\cdot A(t)-\beta_3\cdot N_4(t)-\sigma_4\cdot N_4(t) \qquad (3)$$

where a_1=nitrogen fraction present in algae biomass; τ=algae breathing rate; $A(t)$=algae biomass concentration; β_3=organic and ammoniacal nitrogen hydrolisis rate; σ_4=sedimentation rate.

Ammoniacal nitrogen N_1

$$S_{N1}(t) = -\beta_1 \cdot N_1(t) + \beta_3 \cdot N_4(t) - r_N \cdot \alpha_1 \cdot \mu(t) \cdot A(t) + \frac{\alpha_3}{d(t)} \qquad (4)$$

where β_1=ammonia oxidation rate; σ_3=benthic generation ($\sigma_3>0$) or consumption ($\sigma_3<0$) of ammoniacal nitrogen; $\mu(t)$=specific growth rate; r_N=ammoniacal nitrogen fraction in $a_1\cdot\mu(t)\cdot A(t)$ nitrogen used for new algae biomass; α_3=oxygen photosynthetic production rate; $d(t)$=stream average depth.

Nitroso nitrogen N_2

$$S_{N2}(t)=-\beta_2\cdot N_2(t)+\beta_1\cdot N_1(t) \qquad (5)$$

where $\beta 2$=nitrites oxidization rate.

Nitric nitrogen N_3

$$S_{N3}(t)=\beta_2\cdot N_2(t)-(1-r_N)\cdot a_1\cdot\mu(t)\cdot A(t) \qquad (6)$$

where $a_1\cdot\mu(t)\cdot A(t)$=nitrogen used for new algae biomass.

3.4.2 *Phosphorous*

Organic phosphorous P_1

$$S_{P1}(t)=-\beta_4 \cdot P_1(t)-\sigma_5 \cdot P_1(t)+\alpha_2 \cdot \tau \cdot A(t) \tag{7}$$

where β_4=organic phosphorous degradation rate; σ_5=sedimentation rate; α_2=algae phosphorous fraction.

Dissolved inorganic phosphorous P_2

$$S_{P2}(t) = \beta_4 \cdot P_1(t) - \alpha_2 \cdot \mu(t) \cdot A(t) + \frac{\sigma_2}{d(t)} \tag{8}$$

where σ_2=benthic generation ($\sigma_2>0$) or consumption ($\sigma_2<0$) of dissolved phosphorous.

3.4.3 *Algae*

$$S_A(t) = \mu(t) \cdot A(t) - \tau \cdot A(t) - \frac{\sigma_1}{d(t)} \cdot A(t) \tag{9}$$

where $A(t)$=algae biomass concentration; $\mu(t)$=specific growth rate; τ=breathing rate; σ_1=sedimentation rate; $d(t)$=stream average depth.

3.4.4 *BOD*

Carbonic BOD is regulated by degradation and sedimentation processes, described in the following relation:

$$S_B(t)=-k_1 \cdot B(t)-k_3 \cdot B(t) \tag{10}$$

where k_1 and k_3 are respectively BOD degradation and sedimentation rate; $B(t)$=BOD concentration.

3.4.5 *Oxygen*

Oxygen is consumed by a lot of processes already presented and is produced by superficial areation and photosynthesis; dynamics can be described by relation:

$$\begin{aligned} S_C(t) &= -k_1 B(t) - \alpha_5 \beta_1 N_1(t) - \alpha_6 \beta_2 N_2(t) + \\ &+ k_2 (C_s - C(t)) + [\alpha_3 \mu(t) - \alpha_4 \tau] A(t) - \frac{k_4}{d(t)} \end{aligned} \tag{11}$$

where α_5, α_6= oxygen consumption rate on unity of respectively oxidized $NH_4 \cdot NO_2$ concentration; k_2=aeration rate; C_S=saturation concentration; $C(t)$=oxygen concentration; α_3=oxygen photosynthetic production rate; α_4=algae breathing rate; k_4=oxygen demand ($k_4>0$) or production ($k_4<0$) from sediments.

3.4.6 *Fecial coliforms*

$$S_E(t) = -k_5 \cdot E(t) \tag{12}$$

where k_5=death rate; $E(t)$=colibatteri fecali concentration.

3.4.7 *Non conservative indicators* X_{nc}

Equation, which is used to describe non conservative general polluting dynamics X_{nc}, is:

$$S_{Xnc}(t) = -k_i \cdot X_{nc}(t) - \sigma_j \cdot X_{nc}(t) - \frac{\sigma_k}{d(t)} \tag{13}$$

where k_i==degration rate; σ_j=sedimentation rate; σ_k=benthic consumption (σ_k>0) or generation (σ_k<0) of agent; $X_{nc}(t)$=non conservative indicators concentration.

Among non conservative indicators phyto-drugs kinetics is modelled by this form equation.

3.4.8 *Conservative indicators* X_c

Equation, which is used to describe conservative general polluting dynamics X_c is:

$$S_{Xc}(t) = -\sigma_j \cdot X_c(t) \tag{14}$$

where σj=sedimentation rate; $X_c(t)$=conservative indicators concentration.

Chlorine and boron kinetics is modelled by this form equation.

For all considered pollutants is supposed that they behave like dissolved solids and that their diluition don't change water density. In the case of heavy metals the behaviour inside water matrix was described by conservative kinetics, with concentration distribution varying only because of adsorption on colloidal particles and other suspended solid in stream, sedimentation and probable suspension again of dregs:

$$S_{mc}(t) = -\sigma_j \cdot M_c(t) + \sigma_i(v) \cdot M_c(t) \tag{15}$$

where σ_j=parameter sedimentation rate; a_i=suspension again rate, function of cross section average velocity; $M_c(t)$=heavy metals concentration.

3.5 *Expert system*

Data acquisition of a traditional monitoring system, which works in a stand-alone way, usually gives a lot of measures and alarms, but it doesn't give an explanation to the operator about the cause of signals or a general analysis of the situations to suggest the most suitable actions. To pass these limits, the present project uses an expert system, implemented with neural network, which we will realize by creation of a Knowledge Base containing a series of simulation scenarios of reference. So, it is able to extrapolate/interpolate in a clever way data in archive to formulate a forecast of cause/effect connection of a continuous or accidental waste water, leaving from a series

of classes of situations previously detected in the knowledge base, and exhaustive of interesting cases. The building of knowledge base, made of reference scenarios to which the inferential motive will take its elaborations, will be made using the chosen quality model. The system will increase its own knowledge base storing information relative to cases that it is solving. Working way of an expert system is very like the human behaviour, and such is the interactive way with the operator; this important characteristic make its use easy also for not very expert users. Moreover we can see the operative time of an expert system, thanks to the power of elaboration at present available, are perfectly compatible with a real-time use.

3.6 *Input and output of results*

The system is in connecting with field and river characteristics, so we forecast their integration in a GIS from which they will take information about field, and to which they can give elaborations results to realize a mapping in connecting with data of the field (waste waters and sampling works position, effects on bypass channels, etc.). Moreover we forecast the possibility of connecting the systems with environmental tools (meteo gages, flow and/or level meter, current meters, water quality sensors, etc.).

4 CONCLUSIONS

In terms of results, we want to reach the capability of analysing measure and control monitoring data as to be able of previous and in real-time valuing the effect of continuous or accidental waste waters add, and analysing the consequence, on water quality, of regulation intervention or waste waters stop to verify its effectiveness.

ACKNOWLEDGEMENTS

We thank Carelli M., Mainolfi P. and Onorati G. of technical direction of Campania Regional Environment Protection Agency for cluster analysis data of water quality of Sarno river.

REFERENCES

1. Mancusi, L. & Barbanti, A. 1997. Modello della qualità delle acque del fiume Serio. *Rapporto tecnico Prog. STA 9215; Doc. RAT-STA-0053/97 rev.1.* Bergamo, Italy: ISMES S.p.A.
2. Imperiali, P. & Postiglione, D. 2002. Emergenza ambientale nel bacino idrografico del fiume Sarno—Relazione tecnica del Progetto di monitoraggio delle acque sotterranee e superficiali. *Prog. T24200; Doc. RAT-STA-8.1.1.* Bergamo Italy: Enel.Hydro—Business Unit ISMES S.p.A.
3. Postiglione, D., Mancusi, L., Gargiulo, A., Boccia, F., Mainolfi, P., Onorati, G., Carelli, M. & Speranza, P.P. 2003. Progetto di intervento sul fiume Sarno: un sistema integrato per il monitoraggio della qualità delle acque superficiali del bacino idrografico del fiume Sarno. Naples Italy: Enel.Hydro—Business Unit ISMES S.p.A.

4. Mancusi, L. 2003. Sistema di controllo dell'inquinamento dovuto a reflui nei corpi idrici superficiali. *Proceedings of National Conference "Inquinamento del fiume Sarno: il monitoraggio ed i controlli ambientali.* 14 october 2003 Villa Nunziante, Scafati, Italy.
5. Mappa, G. 2000. Microexpert: un sistema esperto per il controllo dei problemi di separazione solido-liquido nei depuratori a fanghi attivi basato sulle metodiche di indagine microscopica. Naples, Italy.
6. Schoorl, J.M. & Mappa, G. 2000. I1 monitoraggio consapevole nella gestione delle risorse idriche. *Proceedings of Study Day "La strumentazione per la gestione degli acquedotti"*. Naples, Italy.
7. Tomei, M.C., Di Iaconi, C., Di Pinto, A.C. & Mappa, G. 1996. Development of an export system for nitrogen removal control. *European Water Pollution Control.* Volume 6 number 6, page 45.
8. Bonvicini, V., Mappa, G. & Sabatino, P. 1999. Monitoraggio della qualità delle acque depurate con l'utilizzo di sensori intelligenti low cost. *In workshop AI*IA99 Intelligenza Artificiale per l'Ambiente. Proceedings of the Sixth Symposium Italian Association for Artificial Intelligence.* 17 september 1999 Bologna, Italy.
9. Caporusso, R.A., Musella, E., Mappa, G. & Sabatino, P. 1999. Sistema di monitoraggio e gestione del trattamento delle acque cromiche. *In workshop AI*IA99 Intelligenza Artificiale per l'Ambiente. Proceedings of the Sixth Symposium Italian Association for Artificial Intelligence.* 17 september 1999 Bologna, Italy.
10. Marsili, S., Giacomelli, V., Cavalieri, S. & Mazzoni, M. 2000. Modellistica fluviale. Florence, Italy: RTI CTN_AIM 2/2000 and ANPA Environment National Protection Agency.
11. A.A.v.v. 2001. Sistema di prevenzione dell'inquinamento dovuto a reflui nei corpi idrici superficiali. *Capitolato tecnico PON AQUATEC.*
12. De Pietro, G. & Graziani, S. 1999. Modelli neurali per la trasformazione afflussi-deflussi in un bacino idrografico. *L'Acqua.* Number 4 page 37. Italy: Associazione Idrotecnica Italiana.
13. Pecora, S. & Veltri, P. 2001. Artificial neural network application for real time forecasting of levels in a natural water course. *L'Acqua.* Number 2 page 11. Italy: Associazione Idrotecnica Italiana.
14. Fiorillo, G. 2002. Stima del trasporto solido nel fiume Po mediante reti neurali artificiali. *Proceedings of 28th Hydraulics and Hydraulic Constructions Symposium.* Volume III, page 129. 16–19 september 2002, Potenza, Italy: BIOS.
15. Cavallo, A., Di Nardo,A. & Di Natale, M. 2002. Lagestione di un serbatoio artificiale mediante una strategia di controllo fuzzy. *Proceedings of 28th Hydraulics and Hydraulic Constructions Symposium.* Volume IV page 431. 16–19 september 2002, Potenza, Italy: BIOS.
16. Di Gianmarco P, Longo, S. & Ferraresi, M. 2002. Un modello di qualità e di trasporto solido per aste fluviali. *Proceedings of 28th Hydraulics and Hydraulic Constructions Symposium.* Volume III, page 443.16–19 september 2002, Potenza, Italy: BIOS.
17. Puca, S., Arena, F. & Tirozzi, B. 2002. Un nuovo approccio per la ricostruzione delle serie temporali dei livelli di altezza significativa con l'impiego di reti neurali. *Proceedings of 28th Hydraulics and Hydraulic Constructions Symposium.* Volume IV, page 3. 16–19 september 2002, Potenza, Italy: BIOS.
18. Cannas, B., Fanni, A. & Di Natale, M. 2002. River flow forecast for reservoir management using neural networks. *Proceedings of 28th Hydraulics and Hydraulic Constructions Symposium.* Volume IV, page 479. 16–19 september 2002, Potenza, Italy: BIOS.
19. Mayr, P., Jugovic, C.J., Koboltsching, G. & Mader, H. 2002. Development of simultaneous measurements of physical parameters in rivers. *Proceedings of 2nd international conference "New Trend and Environmental Engineering for safety and Life: Eco-compatible Solutions for Aquatic Environments.* 24–28 june 2002. Capri, Italy.
20. Chandra Sekhar, M. & Surender Reddy, K. 2002. Modelling stream water chemistry using river basin land use characteristics. *Proceedings of 2nd international conference "New Trend and Environmental Engineering for safety and Life: Eco-compatible Solutions for Aquatic Environments.* 24–28 june 2002. Capri, Italy.

21. Radwan, M., Willems, P., El-Sadek, A. & Berlamont, J. 2002. Modelling of dissolved oxygen and biochemical oxigen demand in river water using a detailed and simplified model. *Proceedings of 2nd international conference "New Trend and Environmental Engineering for safety and Life: Eco-compatible Solutions for Aquatic Environments.* 24–28 june 2002. Capri, Italy.
22. Rauch, W., Henze, M, Koncsos, L., Reichert, P., Shanahan, P., Somlyòdy, L. & Vanrolleghem, P. 1998. River quality modelling: I state of art. *Proceedings of IAWQ Biennal International Conference.* 21–26 june 1998. Vancouver, British Columbia, Canada.
23. Rauch, W., Henze, M., Koncsos, L., Reichert, P, Shanahan, P, Somlyòdy, L. & Vanrolleghem, P. 1998. River quality modelling: III future of art. *Proceedings of IAWQ Biennal International Conference.* 21–26 june 1998. Vancouver, British Columbia, Canada.

A random walk approach for investigating near- and far-field transport phenomena in rivers with groin fields

Volker Weitbrecht[1], Wim Uijttewaal[2] & Gerhard H.Jirka[1]
[1] *Institute for Hydromechanics, University of Karlsruhe, Germany*
[2] *Environmental Fluid Mechanics Section, Faculty of Civil Engineering and Geosciences,*
Delft University of Technology, The Netherlands

River Flow 2004—Greco, Carravetta & Della Morte (eds.)

ABSTRACT: Dead-water-zones in rivers formed by groin fields strongly influence the dispersive mass transport of dissolved pollutants. The cause for this influence is the exchange process between groin fields and main stream. With the help of laboratory experiments the most important parameters, such as storage time, velocity distribution and distribution of the diffusivity have been investigated. A transport model using a Lagrangian-Particle-Tracking-Method *(LPTM)* has been developed, to transfer the locally obtained experimental results for a single dead-water-zone into the global parameters of a one-dimensional far field model that comprises the action of many dead water zones. It is shown that in the presence of large dead water zones at the river banks, an equilibrium between longitudinal dispersion and transverse diffusion can be reached if the morphologic conditions do not change. The simulations result in a cross sectional averaged concentration distribution that converges asymptotically to a Gaussian distribution over the longitudinal coordinate. Due to the presence of dead water zones the distribution of tracer material becomes inhomogeneous in transverse direction.

1 INTRODUCTION

Predicting the transport of dissolved pollutants in rivers is difficult, because of the various effects of the morphological conditions. In rivers with strong morphological heterogeneities, like extensive deadwaterzones, the prediction of transport velocities,

maximum concentration and skewness contains strong uncertainties that need to be reduced. The River-Rhine-Alarm-Model (Spreafico and van Mazijk 1993) has been developed by the “International Commission for the Hydrology of the River Rhine” *(CHR)* and the “International Commission for the Protection of the Rhine” *(ICPR)*. For this kind of predictive models, much effort and money is spent on calibration by means of extensive in-situ tracer measurements (van Mazijk 2002). In the case of the River Rhine Alarm Model, which uses a one-dimensional analytical approximation for the travel time and concentration curve, a dispersion coefficient and a lag coefficient have to be calibrated. The model works well for cases of similar hydrological situations. However, variations in discharge, and thus, changes in water surface levels, lead to increased errors if the same calibrated parameters are used for different hydrological situations. Insufficient knowledge about the relation between river morphology and transport processes are the reason for these uncertainties. Hence, predictive methods that are appropriate for variable flows and changing morphological conditions are needed.

With the present work we focus on the influence of dead water zones, such as groin fields, on the dispersive mass transport in the far field of pollutant releases. Longitudinal dispersion in rivers that can be treated as shallow flows is controlled by two processes. First, the longitudinal stretching due to the horizontal shear, and second, transverse homogenization by turbulent diffusion (Fischer et al. 1979). Detailed velocity and concentration measurements have been performed in the laboratory in order to determine typical flow patterns and local mass transport phenomena. Direct measurements of dispersion coefficients are problematic because the dispersive character of a transport phenomena reaches its final behavior only after a very long travel time (Fischer et al. 1979), which is determined by the width of the flow and the intensity of the transverse turbulent diffusion. In most cases laboratory flumes are far too short, to examine longitudinal dispersion in the far field. To address this problem, laboratory and numerical experiments have been combined in such a way that the effect of local phenomena that have been measured, are translated into the behavior of tracer clouds in the far field with the help of Lagrangian-Particle-Tracking-Method *(LPTM)*.

2 EXPERIMENTS

In the present study the experiments have been performed in a laboratory flume of 20m length and 1.8m width, which has an adjustable bottom slope. In all the experiments only half of the channel width has been modelled, which means that only on one side of the flume groins have been placed. The shape of the groins was chosen to be very simple due to the fact that earlier investigations suggest that there is no significant effect of the groin shape on the exchange processes (Lehmann 1999). Using a simple geometry leads to a small number of parameters, which allows clear understanding of the basic relations between geometry and flow or transport phenomena, respectively.

The flume bottom consists of a plastic laminate with small roughness elements <0.2mm. Level changes in x- and y-direction (Fig. 1) of the flume bottom are smaller than 0.2mm. The flume is connected to a system of a water storage tank and a constant head tank, which is supplied by three different pumps, enabling discharges up to 100ℓ/s. The discharge is controlled by an inductive-flow-meter together with an PC controlled

gate valve. In the present case, only very small discharges of up to 10ℓ/s are needed. Therefore, the gate valve is equipped with a pentagonal regulating orifice, which leads to constant discharges (changes smaller than 0.5%), even if the valve is opened only 5%.

In order to simulate flow patterns under the influence of dead-water zones, respectively groin fields, a series of 15 schematized groins made of PVC with a heavy core were built, so that these elements could be placed at variable positions. The outline of a single groin was chosen to be a combination of a rectangular box (0.45m×0.05m×0.05m) with an attached half cylinder (diameter=0.05m). In the present study experiments have been performed with varying groin field aspect ratio *W/L* (0.17–3.5) and different inclination angles of the groins (Fig. 2).

The velocity measurements were performed using Particle-Image-Velocimetry at the water surface, using the PIV package DaVis from LaVision (Weit-brecht et al. 2002). With the help of a particle dispenser the

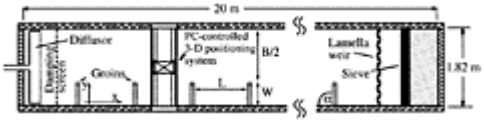

Figure 1. Schematic top view of the laboratory flume showing the groins placed on one side.

water surface is seeded with black Polypropylene particles, such that homogeneous particle distribution on the water surface is achieved. The flow field in the main stream and in the groin field is then recorded with a digital camera at a temporal resolution of 7Hz. The vector fields are obtained by using a cross-correlation technique, leading to spatial resolution of 2cm×2cm.

In Fig. 3 the measured mean velocity profiles are plotted for the different aspect ratios in the case of the standard groins.

The comparison in Fig. 3 shows that, the aspect ratio of the groin field has limited influence on the mean flow properties in the main stream. Above the groin field boundary no significant differences between the normalized velocity profiles can be observed. The velocity profile in Fig. 3 in the main stream part of the flow has the typical shape of a mixing layer velocity profile and can be approximated using a hyperbolic tangent function of the form

$$\frac{u(y)}{U_s} = a \tanh\left(\frac{y}{h_S} b\right) + c \qquad (1)$$

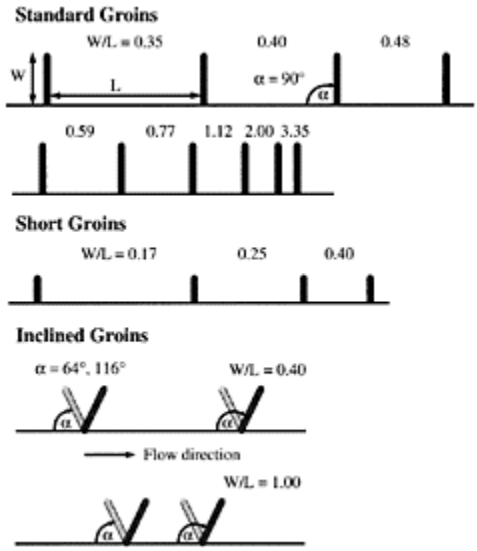

Figure 2. Schematic top view of the different aspect ratios and the different inclination angles that have been analyzed.

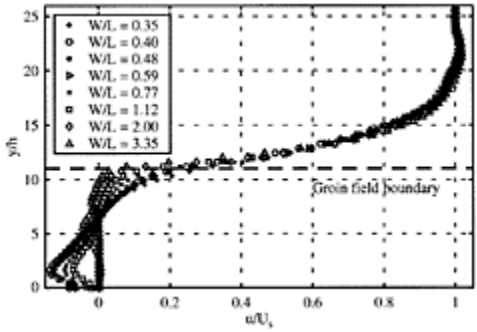

Figure 3. Comparison of the mean velocity profiles for the different *W/L* aspect ratios. The plotted velocities are averaged in space. over the length *L* of the groin fields, and normalized with the maximum velocity at the water surface U_S.

where a, b and c are constants that have to be adapted. In the present case the profile for the reference case W/L=0.4 leads to the following values: a=0.82, b=0.24 and c=0.17. h_s is the water depth in the main stream. This equation represents the velocity profile that is responsible for the stretching mechanism of a tracer cloud in the main stream.

In Fig. 4 the normalized rms-velocities of the transverse component v'/u_* measured with the PIV system are plotted. These values indicate the strength of the transverse turbulent mixing, which is the second important parameter influencing longitudinal dispersion.

Additional concentration measurements have been performed to measure the mean residence time T_D of tracer material in the dead-water-zones (Kurzke et al. 2002) using a depth averaged adsorptive technique. With the help of a multi-port injection-device tracer has been injected instantaneously into one groin field. The evolution of concentration distribution has been recorded with a CCD-camera. Gray scale analysis, which takes into account inhomogeneous illumination and changing background intensities, finally leads to an exponential decay function for every groin field setup

$$C(t) = C_o\, e^{-\frac{t}{T_D}} \qquad \textbf{(2)}$$

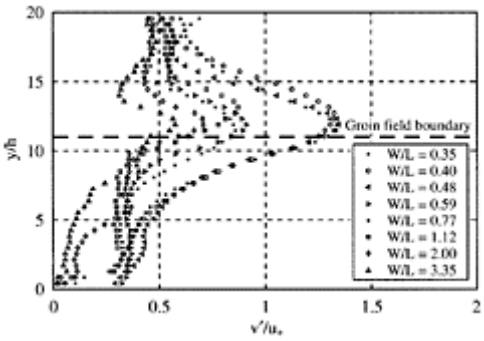

Figure 4. Comparison of the normalized strength of the velocity fluctuations v'/u_* for the different aspect ratios W/L.

where C is the spatial averaged concentration in the dead zone, C_o the initial concentration. The residence time T_D is used in the LPTM transport model to parameterize the influence of dead-water zones on the mass transport in the river.

T_D can be normalized with the width of the groin field W and the main stream velocity U to give a dimensionless exchange coefficient k

$$k = \frac{W}{T_D U} \qquad \textbf{(3)}$$

The resulting exchange coefficients k for the different groin field setups are shown in Fig. 5.

Figure 5 shows that k reduces with increasing W/L, which means that the residence time T_D is longer in the very narrow cases of groin fields. Another results is the increased mass exchange for backward inclined groins compared to downward inclined or regular groins. For short groins Fig. 5 shows also the tendency towards smaller exchange values with increasing W/L. However, the k-values for short groins are noticeably smaller for the same aspect ratio W/L than in the standard case. This shows, that the groin field volume has to be taken into account for the prediction of k.

A slight modification of the scaling factor W/L into $WL/(W+L)$, which can be interpreted as a kind of hydraulic radius R_D of the dead-water-zone, leads to a better normalization shown in Fig. 6. Why the exchange coefficients should scale with the hydraulic radius R_D can be explained by the following: In the case of very long groin fields with $L\rightarrow\infty$ the expression $WL/(W+L)$ tends to W. Therefore, in the case of very long groin fields the recirculating flow is only determined by the width W of the groin field. In the other extreme case for $W\rightarrow\infty$ the hydraulic radius R_D tends to L, which means that the mass exchange in this case is only determined by the length of the mixing layer.

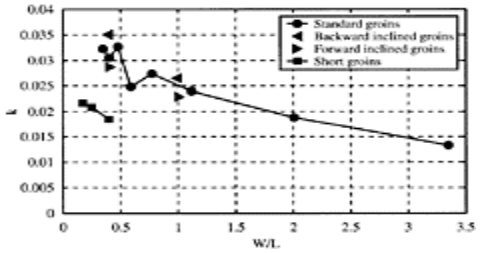

Figure 5. Dimensionless exchange coefficient k against the aspect ratio W/L.

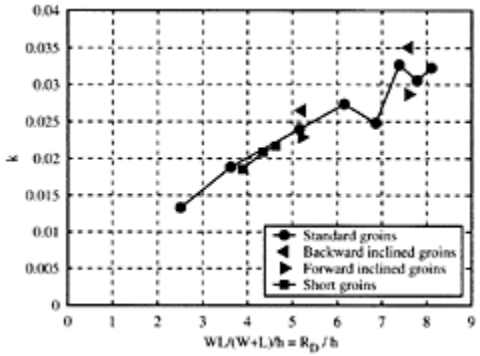

Figure 6. Dimensionless exchange coefficient k versus the normalized hydraulic radius R_D/h.

3 LAGRANGIAN PARTICLE TRACKING METHOD

A transport model based on a two-dimensional Lagrangian-Particle-Tracking-Method *(LPTM)* has been developed to transfer the local results of the laboratory experiments for a single dead-water-zone into the global parameters of a one-dimensional far field model that comprises the action of many dead-water-zones. The method represents a random walk approach as has been used, for example, by Sullivan (1971) to model turbulent shear flow based on statistical mechanical transport theories presented by Taylor (1921).

As the present transport problem is basically a problem of longitudinal dispersion, we assume that the dominating processes in this case are longitudinal shear and transverse diffusion. Thus, the behavior of discrete particles under the influence of advection in longitudinal direction and of transverse diffusion is determined in a two-dimensional domain. The idea is to initiate a cloud of particles that is advected within a known mean flow profile. This advective movement is superimposed on a random movement in transverse direction, representing turbulent diffusion.

The characteristic transport parameters, like dispersion coefficient, transport velocity and skewness coefficient, can be determined by analyzing the statistics of such a particle cloud at any position of the simulation. In addition to one-dimensional information this method yields concentration distributions in transverse direction, in order to describe near-field phenomena.

The influences of dead-water zones are included with the help of extra boundary conditions that represent the mean retention time of particles in the area of dead-water zones. Herewith, the influence of different groin field geometries on the mass transport,

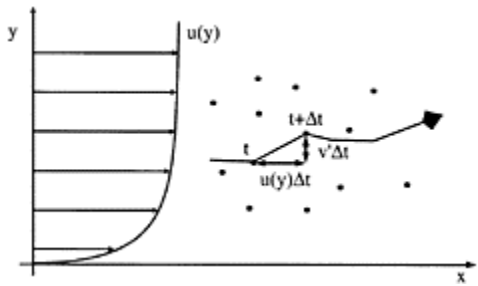

Figure 7. Particle velocity in a two-dimensional flow field with mean velocity in x-direction and turbulent velocities in y-direction.

especially on the mass dispersion, in the far-field of a pollutant spill can be predicted.

The method has been verified with the aid of the analytical solution presented for the Advection-Diffusion-Equation for a Couette-Flow problem (Fischer et al. 1979) and turbulent unbounded vertical shear flow given by Elder (1959). Dispersion coefficients obtained from these solutions are compared with the transport characteristics using the *LPTM* (Weitbrecht et al. 2003).

In the next step the transport model is used to predict the transport parameters for the flow conditions, taken from the experiments. Mean flow quantities and turbulence intensities are determined in pure channel flow and are adapted to the *LPTM*. Finally the influence of dead-zones (groin fields) is implemented.

A random walk simulation can be understood as the tracking of discrete particles, under the influence of the governing flow processes. Typically, the particle displacement dX_i is described by a deterministic and a stochastic part, leading to the so called Langevin equation (Gardiner 1985)

$$dX_i = \underbrace{f(X_i,t)dt}_{deterministic} + \underbrace{Z(t)g(X_i,t)dt}_{stochastic} \quad \textbf{(4)}$$

where X_i is the position *x, y* and *z*. $f(X_i, t)$ represents the advective or drift component, which can be interpreted as the mean flow velocity field. The expression $g(x_i, t)$ describes the diffusive or noise component of the particle movement that describes the strength of the turbulent diffusion in space. The stochastic part is represented by the Langevin force *Z*, which is a Gaussian distributed variate with a mean value of zero and a variance equal to one.

In the present case the governing processes are advection in x-direction and diffusion in transverse direction (Fig. 7), which implies that we can neglect the drift component in y-direction and the noise component in x-direction in Eq. 4. An important part of such a model is the link between the diffusive step size and the length of the time step. Here we use the approach given by Taylor (1921) who stated that the spreading of a particle ensemble measured with the standard can be treated as a Fickian type of diffusion, where $\sigma \sim \sqrt{2Dt}$.. The diffusive step size for a single particle at a certain time step in y-direction is therefore given with

$$v'\Delta t = \sqrt{2D_y\Delta t} \quad \textbf{(5)}$$

where D_y is the turbulent diffusion coefficient in y-direction. Using these assumptions, the position of the particles in every time step Δt can be described by a simplified two-dimensional version of Eq. 4.

$$x_{new} = x_{old} + \underbrace{(\Delta t \cdot u(y))}_{deterministic} \quad \textbf{(6)}$$

$$y_{new} = y_{old} + \underbrace{Z\sqrt{2D_y\Delta t}}_{stochastic} \quad \textbf{(7)}$$

where x_{old}, y_{old} and x_{new}, y_{new} are the spatial locations at times t and $t+\Delta t$ respectively, and D_y is the transverse component of the turbulent diffusion coefficient. The function $u(y)$ denotes the mean flow velocity in relation to the position in transverse direction. Consequently, in every time step, a particle moves *convectively* in x-direction depending on the velocity profile and does a positive or negative *diffusive* step in transverse y-direction.

The reason why there is no diffusive step in the x-direction needed (Eq. 6), can be explained by the fact, that turbulent diffusion in x-direction and longitudinal dispersion are additive processes (Aris 1959), which means that the final dispersion coefficient can be adjusted by adding the turbulent diffusion coefficient. Fischer et al. (1979) showed

that in natural rivers the coefficient of longitudinal dispersion D_L lies in the range of $30<D_L/(u_* h)<3000$, while the longitudinal turbulent diffusion coefficient D_x is considerably smaller. A typical approximation of the turbulent diffusion coefficient is given by $D_x \approx (0.6 u_* h)$, which means that in this approach turbulent diffusion in longitudinal direction can be neglected in comparison to longitudinal dispersion. An advantage of this simplification is a shorter computing time.

Flows with inhomogeneous turbulent diffusion coefficients are treated here, which means that D_y is a function of y. A problem in performing LPTM-simulations is given by the fact that particles segregate into regions of low diffusivity (Hunter et al. 1993). In the stochastic model particles move independently from regions with high diffusivity into regions with low diffusivity. As a consequence the probability of a particle to move from a region of high diffusivity into a region of low diffusivity is higher than vice versa. In order to satisfy continuity an extra advection term in y-direction has to be included, to achieve consistency with the governing Advection-Diffusion-Equation. This extra term is called the noise- drift component. By matching the resulting stochastic transport equations with the Advection-Diffusion- Equation Dunsbergen (1994) showed, that in this case, the noise-induced drift component Δy_n can be formulated as follows

$$\Delta y_n = \frac{\partial D_y}{\partial y} \Delta t \qquad \textbf{(8)}$$

If Eq. 7 is extended with the given expression for the noise-induced drift component (Eq. 8), the transport problem with varying diffusivity is described consistently with the Advection-Diffusion-Equation.

$$y_{new} = y_{old} + Z\sqrt{2D_y(y)\Delta t} + \frac{\partial D_y}{\partial y}\Delta t \qquad \textbf{(9)}$$

Also the boundaries of the calculation domain and their effect on the particles are important. The inflow and outflow boundaries do not affect the particles as in our case the domain has an infinite length. In case of horizontal shear the boundaries representing the channel bank and channel centre line act as reflective walls. Particles which would cross the left or right boundary at a certain time step are reflected into the calculation domain. Consequently, a particle with a calculated y-position outside the calculation domain $y<0$ is re-introduced as follows

$$y_{new} = -y_{calc} \qquad \textbf{(10)}$$

where y_{calc} is the calculated y-position at a certain time step.

With the given equations and boundary conditions transport in open channel flow can be simulated with a depth-averaged velocity profile in transverse direction and a certain distribution of the diffusivity. The next step is to include the influence of dead-water zones (Fig. 8) into the LPTM.

The mean residence time of tracer material in the dead-water zone is the most important parameter to describe the behavior of a dead-water zone. Therefore, it should be possible to model the influence of the mass transport by including this parameter into the LPTM. A possibility is to include the residence time into the boundary condition, such that this boundary simulates the behavior of mass trapping and mass release. Thus,

the interface between main channel and dead-water zone has to act as a transient-adhesion boundary, which means that particles that reach such a boundary are fixed to that position until T_D has passed. This mimics to the real dead-zone behavior. A particle that enters a dead-water zone because of turbulent motion in the mixing layer, does not move on average in x-direction, assuming that the longitudinal extension

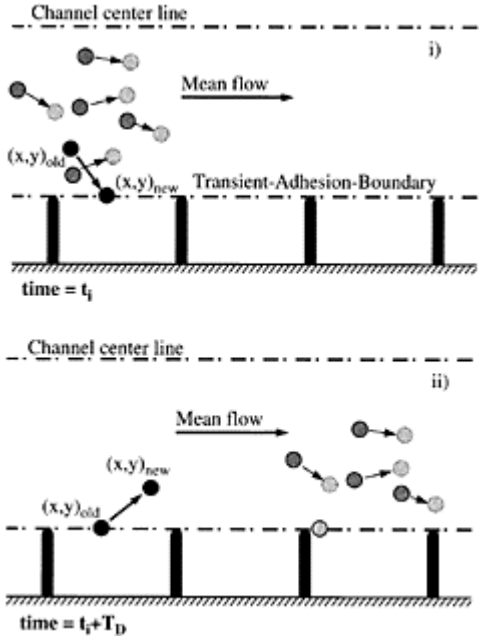

Figure 8. Schematic visualization of a particle approach to a transient adhesion boundary at: (i) time=t_i and (ii) time=t_i+T_D, where T_D is the mean residence time.

of the dead-water zone is small compared to the length of the modeled river section. The particle remains in the dead-water zone on average for time period given by the mean residence time T_D, and after that period it gets back into the main stream.

The outcome of a *LPTM* simulation are *x* and *y*-positions of every single particle at every time step. By analyzing the statistics of the particle positions, information about the transport characteristics can be determined. The one-dimensional longitudinal dispersion coefficient D_L, as a measure of the spatially averaged spreading rate of a tracer cloud, can be determined by calculating the time change of the longitudinal variance σ_x^2 of the particle distribution (Rutherford 1994) as follows

$$D_L = \frac{1}{2}\frac{\sigma_x^2(t_2) - \sigma_x^2(t_1)}{t_2 - t_1} \qquad \textbf{(11)}$$

A second result will be the skewness G_t of the particle cloud. The skewness is defined as the relation between the quotient of the third moment about and the third power of the standard deviation

$$G_t = \frac{\sum_{i=1}^{n}(x_i - \bar{x})^3}{(n-1)\sigma_x^3} \quad \textbf{(12)}$$

where n is the number of particles at the positions x_i with mean position $\bar{x}$and σ_x is the standard deviation of the particle distribution. The skewness of a certain distribution describes the degree of asymmetry of a distribution. The skewness can be used as an indicator for the length of the advective zone, in order to define when it is acceptable to apply the Taylor solution to a pollutant transport problem.

Another parameter of interest is the transport velocity c of the tracer cloud, defined as the velocity of the center of mass of a particle ensemble. In the case of regular channel flow with ordinary reflective boundary conditions c is equal to the mean velocity if the particles are homogeneously distributed over the river cross section. In case of point sources this can be reached after the tracer has passed the advective zone. The transport velocity can be determined as follows

$$c = \frac{\bar{x}(t_2) - \bar{x}(t_1)}{t_2 - t_1} \quad \textbf{(13)}$$

where $\bar{x}$represents the center of mass of a particle cloud.

4 APPLICATION AND RESULTS

In this section the *LPTM* is applied to different flow fields, that have been investigated in the laboratory in order to determine the influence of river heterogeneities on the mass transport properties of a river. Three different cases will be analyzed in detail. First the behavior of the dispersive character of pure channel flow without the influence of groin fields is investigated. In a second step groin fields are implemented, and finally the influence of different residence times on the transport characteristics is determined.

4.1 *Straight open channel flow*

A *LPTM*-simulation has been performed, in order to analyze transport phenomena in regular channels without groin fields. Therefore the measured velocity distribution has been approximated with an analytical function, that can be seen in Fig. 9(i). The diffusion coefficient in this case has been chosen to be constant over the whole river cross section, with a value according to Fischer et al. (1979) for regular channels.

$$D_y = 0.15 u_* h \quad \textbf{(14)}$$

In Table 1 the properties of the flow and the settings of the 2D-*LPTM*-simulation for the case of a straight channel flow are listed.

The equilibrium between longitudinal stretching and transverse diffusion, where the dispersion coefficient does not change any more is reached after about

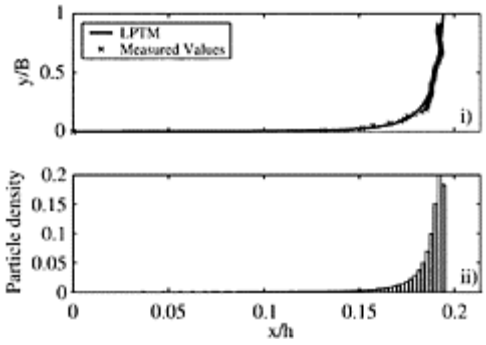

Figure 9. Result of *LPTM*-simulation with pure channel flow, after first time step. (i) Particle position according to the fitted velocity profile and the measured velocities taken from the experiment; (ii) particle density in longitudinal direction.

Table 1. Parameter values for the pure channel flow simulation, taken from the measurements.

Property	Value
Water depth h [m]	0.046
Channel half width B [m]	1
Mean velocity [m/s]	0.19
Horizontal velocity profile	Fig. 9(i)
Channel slope I [%]	0.032
No. of particles	5,000
No. of time steps	40,000
Length of time step Δt [s]	1
Diffusivity D_y [m^2/s]	(Eq. 14)

800 times the channel's half width. The final value of $D_L/(u_* h)$ is 177, and is much larger (30 times) than the dispersion found in a channel with a laterally uniform velocity (Elder 1959).

4.2 *Channel flow with groin fields*

The influence of groin fields is simulated with the transient-adhesion boundary condition (Sec. 3), that represents the mean residence time of a particle in the groin field. These mean residence times have been measured in this study with two different approaches. Concentration measurements have been performed, where concentration decay in a single groin field has been tracked with digital video analysis. Starting with a known homogeneous concentration in the groin field and zero concentration in the main stream an exponential decay could be observed, leading to a typical time scale T_a describing the mean residence time. These experiments are in principle analogous to the measurements that have been performed by Uijttewaal et al. (2001). An improvement could be achieved by the development of a multi-port injection device, that is able to produce reproducible homogeneous concentration fields as initial condition for the concentration measurement (Kurzke et al. 2002). Another possibility to determine the residence times is given by using the velocity fields for the determination of the mass exchange rate between groin field and main stream (Kurzke et al. 2002).

In order to determine the influence of groin fields, a LPTM-simulation has been performed with the same flow properties as in the described case above (Table 1). The difference lies in the transient-adhesion boundary condition at the channel wall. This simulation represents groin fields, where the ratio between the width W of a groin field divided by the length L is 0.4 (Fig. 2). These conditions correspond to laboratory measurements with a groin field length 1.25m and a width of 0.5m. As the water depth in the groin field and the main stream is the same, the ratio between the cross sectional area of the dead water zone and the main stream is 0.5. The mean residence time T_a of a tracer particle has been set to 90 seconds, which corresponds to the measured dimensionless exchange coefficient

$$k = \frac{W}{T_a U} = 0.028 \qquad \textbf{(15)}$$

where W is the width of the groin field and U represents the mean flow velocity in the main channel.

In the case of channel flow with groin fields the velocity profile is slightly changed compared to the pure channel flow, because in the presence of groin fields the velocity profile has to represent the mixing layer between groin field and main stream and can be approximated with a tanh function, where the velocity is still positive at y=0.

The distribution of the diffusivity in that case is not constant over the channel cross section, see Fig. 4. Turbulence measurements showed, that the velocity fluctuations in the region of the mixing layer between groin field and main channel are much stronger than in the undisturbed main channel. Therefore the diffusivity given by Eq. 14 is amplified in the region of the mixing layer, proportional to the increasing transverse velocity fluctuations. This has been done, by fitting a gaussian curve to the transverse rws-values of the channel flow, such, that the diffusivity in the mixing layer is three times larger than in the main channel (Weitbrecht et al. 2002).

In Fig. 10 the *LPTM*-simulation with groin fields is visualized after 200 time steps. The main difference with respect to pure channel flow is found in the particle clouds that travel far behind the main tracer cloud, a phenomenon that is also observed in the

laboratory flume. These small particle clouds arise by the effect of the dead water zones. Particles that have crossed the

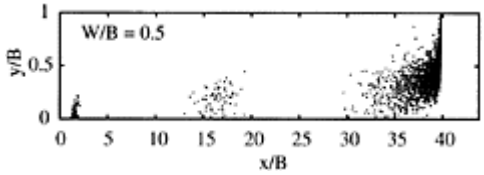

Figure 10. Result of *LPTM*-simulation after 200 time steps with a mean residence time of T_a=90s, that corresponds to a width to length ratio of a groin field of 0.4.

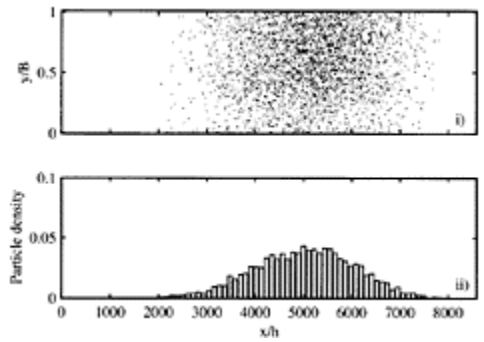

Figure 11. Result of LPTM-simulation after 40,000 time steps with a mean residence time of T_a=90s, that corresponds to a width to length ratio of a groin field of 0.4 and *W*/*B*=0.5; (i) particle position; (11) particle density in longitudinal direction.

lower boundary layer during the simulation, remain at the same x-position for the mean residence time T_a. After T_a has elapsed the particles get back to the flow. The mean distance between those clouds corresponds to the mean residence time T_a.

The final stage of mixing in the case with groins shows again, that after a long period the tracer cloud approximates a Gaussian distribution in longitudinal direction Fig. 11.

The interesting properties of this simulation are the evolution of the dispersion coefficient and of the skewness, as visualized in Fig. 12. The final value of $DL/(u_* h)$ is in that case approximately 24.800 which is a factor 140 higher than in the case of pure channel flow, and about ten times higher than the values common for natural rivers

without groin fields. This can be explained by the exaggerated ratio between the cross sectional area of the dead water zone and the cross sectional area of the main channel, which is 0.5 for this experiment, a value rather high compared to natural rivers.

The equilibrium between longitudinal stretching and transverse diffusion is achieved after approximately 800 times the channel width (Fig. 12), which

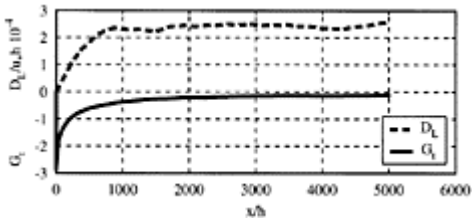

Figure 12. Evolution of Dispersion coefficient $D_L \cdot 10^{-4}$ normalized with the u_* and the water depth h and the evolution of the skewness. D_L is smoothed with a sliding average filter of increasing window size. (W/B=0.5).

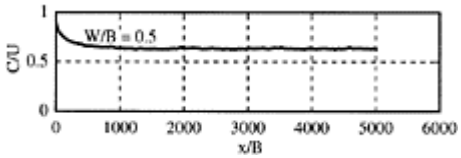

Figure 13. Evolution of transport velocity c of a tracer cloud normalized with mean velocity of the main channel.

indicates that the advective zone has the same length irrespective of the presence of groins.

In the case of a straight channel flow, the transport velocity c, which is defined as the translation velocity of the center of mass of the tracer cloud Eq. 13, always equals the mean flow velocity in the channel. In the case with groin fields the transport velocity of the tracer cloud decreases in time until an equilibrium distribution between the particles in the dead water zones and in the main channel is established, see Fig. 13. In this simulation the transport velocity does not change further after the tracer cloud has travelled approximately 1000 times the channel half width. The final transport velocity is 64% of the mean flow velocity in the main channel.

According to the one-dimensional dead-zone-models by Valentine and Wood (1979, van Mazijk (2002), the transport velocity in the far field can be estimated from the ratio

between the cross sectional area of the dead water zone A_d and the cross sectional area of the main stream A_s

$$c = \frac{U}{1 + A_d/A_s} \tag{16}$$

In the presented case this relation would provide a value of 67% of the mean flow velocity, which is close to the result of the *LPTM*-simulation.

Considering the particle distribution in transverse direction of the river cross section, it can be stated that the initial homogeneous distribution (Fig. 14i) remains homogeneous in the case of a pure channel flow. The distribution is affected in the presence of groin fields

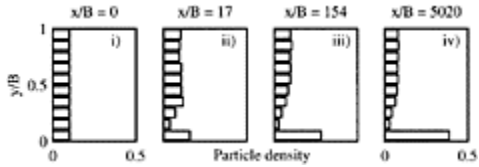

Figure 14. Particle density distribution in river cross-section as a function of the distance *x/B*.

Table 2. Results of *LPTM*-simulations with different exchange coefficients and B/W=0.5, compared with the case of pure channel flow (k=∞).

	k			
	∞	0.035	0.028	0.02
$D_L/(u_* h)$	177	19,800	24,800	32,400
c/U	1	0.68	0.64	0.56

(Fig. 14ii, iii, iv). A substantial part of the particles accumulate in the dead-zone area during the *LPTM*-simulation. In the final stage of mixing (Fig. 14iv) almost 40% of the tracer material is found in the region of the dead water zones. The remaining 60% of the material is travelling in the main stream.

4.3 *Groin fields with different exchange rates*

The dimensionless exchange coefficient k (Eq. 15), can be found in the literature to be in the order 0.02±0.01 (Valentine and Wood 1979; Uijttewaal et al. 2001), with no clear dependency to the shape of the dead water zone. With our laboratory experiments, we could demonstrate that k varies with the width to length ratio of the groin fields within the range of 0.015−0.035. Here the longest groin fields (W/L=0.3) are leading to the highest k-values and the shortest groin fields (W/L=3.5) correspond to the lowest k-value (Weitbrecht and Jirka 2001). In all cases the groin field width W was constant. According

to Eq. 16 the transport velocity is supposed to be the same in those cases. In order to explore the possible influences of the changing *k*-values, two extra *LPTM*-simulations have been performed, where the mean residence time has been set to 75, 95 and 130 seconds, respectively. Consequently, the respective *k*-values used, are 0.035, 0.028 and 0.020.

In Table 2 the results of the simulations with changing *k*-values are summarized. It can be seen that the dimensionless dispersion coefficient $D_L/(u_* h)$ is proportional to the residence time T_a. The longer the residence time, the higher the stretching rate of the tracer cloud.

It can be seen that the influence of the different *k*-values on the transport velocities is at maximum 10% for the presented configuration. According to these simulations, the results of the one-dimensional dead-zone-model mentioned above predicts the transport velocity correctly, for a *k*-value of about 0.035, which corresponds to groin fields with an aspect ratio of about W/L=0.33.

An equilibrium between longitudinal stretching and transverse diffusion is reached in all cases after approximately 800 times the channel's half width *B*. That again indicates that the dominant time scale is not T_a, but the diffusive time scale $B^2/(2D_y)$ associated with the time needed for a particle to cross *B*. If we determine the length x/B that corresponds to this time, we get

$$\frac{x}{B} = \frac{cB}{2D} = 750 \qquad \textbf{(17)}$$

which corresponds very well to the observed behavior of the particle clouds in the LPTM-simulations.

5 CONCLUSIONS

Our approach in which laboratory experiments and *LPTM* are combined, creates the possibility to determine transport characteristics in the far field of a pollutant spill in shallow, predominantly two-dimensional river flows. Detailed velocity and concentration measurements are used to determine local flow and transport phenomena in the presence of groin fields. A translation is made via the *LPTM*, to convert these findings into transport velocities, longitudinal dispersion and skewness coefficients of the cross sectional averaged pollutant cloud in the far field. This information can be used to improve the accuracy of one-dimensional alarm-models, and to reduce the need for calibration with tracer experiments.

The finding, that the transverse tracer distribution is influenced by the presence of dead water zones should be taken into account for the planning of future field experiments, and for the interpretation of existing data. In addition to the concentration distribution it is likely that other properties depend also on the lateral coordinate.

The computationally simple two-dimensional approach allows for studying near field effects as well. Point releases of contaminants near one of the banks and not fully mixed states are impossible to predict with a one-dimensional approach. The same holds for strongly varying flow geometries with confluences, weirs, bends etc.

ACKNOWLEDGEMENTS

The numerical part of the project was funded by the "German Research Council" (DFG, Grant No. Ji 18/8–1) and the "Netherlands Organization Scientific Research" (NWO). The laboratory measurements were sponsored by the German "Federal Ministry for Education and Research" (BMBF, Grant No. 02 WT 9934/9).

REFERENCES

Aris, R. (1959). The longitudinal diffusion coefficient in flow through a tube with stagnant pockets. *Chemical Engineering Science 11*, 194–198.

Dunsbergen, D.W. (1994). *Partide Models Transport in Three-Dimensional Shallow Water Flow.* Ph.D.thesis, TU-DELFT, Faculty of Civil Engineering.

Elder, J.W. (1959). The dispersion of marked fluid in turbulent shear flow. *Journal of Fluid Mechanics 5*, 544–560.

Fischer, H.B., E.G.List, R.C.Y.Koh, J.Imberger, and N.H.Brooks. (1979). *Mixing in Inland and Coastal Waters.* New York, NY: Academic Press.

Gardiner, C.W. (1985). *Handbook of Stochastic Methods.* Springer-Verlag.

Hunter, J., P.Craig, and H.Phillips. (1993). On the use of random walk models with spacially variable diffusivity. *Computational Physics 106*, 366–376.

Kurzke, M., V.Weitbrecht, and G.Jirka. (2002). Laboratory concentration measurements for determination of mass exchange between groin fields and main stream. In D.Bousmar and Y.Zech (Eds.), *River Flow 2002*, Volume 1, Louvain-la-Neuve, Belgium, pp. 369–376. IAHR.

Lehmann, D. (1999). Auswirkung von Buhnenfeldern auf den Transport gelöster Stoffe in Flüssen. Master's thesis, University of Karlsruhe, Inst. for Hydromechanics and TU-Delft, Hydromechanics Section.

Rutherford, J.C. (1994). *River Mixing.* Sussex, England: Wiley.

Spreafico, M. and A.van Mazijk. (1993). Alarmmodell Rhein. Ein Modell fur die operationelle Vorhersage des Transportes von Schadstoffen im Rhein. Technical Report 1–12, Internationale Kommission zur Hydrologie des Rheingebiets, Lelystad.

Sullivan, P.J. (1971). Longitudinal dispersion within a two-dimensional turbulent shear flow. *Journal of Fluid Mechanics 49*, 551–576.

Taylor, G.I. (1921). Diffusion by continuous movements. *Proc. London Math. Soc. 20*, 196–211.

Uijttewaal, W., D.Lehmann, and A.van Mazijk. (2001). Exchange processes between a river and its groyne fields: Model experiments. *Journal of Hydraulic Engineering 127*(11), 928–936.

Valentine, E.M. and I.R.Wood. (1979). Experiments in longitudinal dispersion with dead zones. *Journal of the Hydraulics Division 105*(HY8), 999–1016.

van Mazijk, A. (2002). Modelling the effects of groyne fields on the transport of dissolved matter within the rhine alarm-model. *Journal of Hydrology 264*, 213–229.

Weitbrecht, V. and G.Jirka. (2001). Flow patterns and exchange processes in dead zones of rivers. *In XXIX IAHR Congress*, Beijing, China.

Weitbrecht, V., G.Kühn, and G.H.Jirka. (2002). Large scale piv-measurements at the surface of shallow water flows. *Flow Measurements and Instrumentation 13*(5–6), 237–245.

Weitbrecht, V., W.Uijttewaal, and G.Jirka. (2003). 2-d particle tracking to determine transport characteristics in rivers with dead zones. In *International Symposium on Shallow Flows*, Delft, The Netherlands.

Turbulence of vertical round buoyant jets in a cross flow

M.Ben Meftah & A.Petrillo
Water Engineering and Chemistry Department, Technical University of Bari, Italy

P.A.Davies
Civil Engineering Department, University of Dundee, United Kingdom

D.Malcangio & M.Mossa
Civil and Environmental Engineering Department, Technical University of Bari, Italy

River Flow 2004—Greco, Carravetta & Della Morte (eds.)

ABSTRACT: The paper looks at a vertical round buoyant jet issued in a cross flow and investigates the effect of turbulence in the cross flow upon the structure of the jet. This general problem of the influence of ambient turbulence has been investigated for the case of cross flow turbulence associated with flow over a rough bottom boundary. The results of laboratory investigations of this problem are described and it is shown that the influence of the roughness of the bottom surface is manifested by significant modifications to the buoyant jet trajectory (as compared to the smooth boundary reference case). Preliminary attempts to quantify and parameterize these modifications are presented.

1 INTRODUCTION

One crucial problem in hydraulic engineering concerns the dilution of turbulent thermal discharges in a cross flow. The effects of cross flow turbulence (generated, as in this case, by the presence of a rough bottom boundary) upon the structure of the discharge flow is an important aspect of this problem. The study of a heated water discharge in the form of a turbulent buoyant jet into a channel with a flat bottom and with a cross current is well established in the literature (*e.g.* Lee, 1984; Il Won Seo *et al.*, 2001; Young Do Kim *et al.*, 2002). The flow dynamics of the thermal discharge in the near field are governed purely by the momentum source represented by the high velocity injection. In the far field, instead, mixing is governed by ambient currents and stratification. Moreover, processes at the air-water interface, such as heat exchange towards the atmosphere and

wind stress, can further affect the heat distribution. As regards the ambient turbulence, the visualization study of Grass *et al.* (1991) revealed that powerful vortical structures with a general horseshoe-type configuration occur over smooth surfaces as well as in the turbulent boundary layer near rough walls and that they are similarly linked to bursting events in both the smooth and rough bed cases. The nature of coherent structures and their processes of development over rough surfaces, therefore, appear to be similar to those originating over smooth walls. Furthermore, Grass *et al.* (1991) and Grass & Mansour-Tehrani (1996) observed that a remarkable feature of the rough wall flow is its apparent ability to order itself very rapidly in a small vertical distance above the tops of the roughness elements. Their measurements indicated that for fully rough wall conditions, the near-wall turbulence structures are directly proportional to the bed roughness size for geometrically similar roughness elements and the packing used in their tests.

In order to clarify the dependence of the buoyant jet upon the background turbulence and to improve knowledge of the physical processes that determine its dilution, an experimental study was conducted. Localized background turbulence was generated within the ambient flow by means of two different corrugated plastic surfaces of known "wavelength" λ and "amplitude" ε, fixed at the bottom of a rectangular channel. During this experimental work, the characteristics of the turbulence field produced in the surrounding flow by particular combinations of λ and ε were analyzed, with the aim of finding a typical characteristic length scale of the turbulent eddies associated with flow over the rough boundary and its effect upon the structure of the buoyant jet. Since the study consisted of a three-dimensional buoyant jet interacting with a three-dimensional "patch" of shear turbulence, measurements of velocity and temperature fields were assessed at different vertical levels to obtain the spatial structure of the temperature and the velocity profile of the cross flow. Such an approach required a long time for each run, especially because relevant differences were observed at a distance of mms, and accurate and appropriate techniques to collect data, as described below were necessary.

For each configuration, the objectives of the experiments were (i) to compare the mixing of a buoyant jet discharged into a cross flow with a smooth and rough boundary, (ii) to identify a distortion of the jet structure by the presence of the background turbulence generated by the rough bottom and (iii) to quantify this distortion and parameterize it in terms of buoyant jet and corrugated surfaces characteristics.

2 EXPERIMENTAL WORK

2.1 *Experimental set-up*

The laboratory model was constructed in the Coastal Engineering Laboratory of the Technical University, Bari, Italy (Fig. 1). The system consists of a rectangular steel channel 15m long, 4m wide and 0.4m deep, with lateral walls and base made of transparent glass material (Saint Gobain), 15mm thick. To create a current inside the channel a closed hydraulic circuit was constructed. The fresh water at ambient temperature was supplied from a big metallic tank downstream by a Flygt centrifugal electro-pump, which sucked the water into a steel pipe with diameter 200mm and then

discharged the same water into the upstream steel tank. Into the upstream tank a side-channel spillway with adjustable height was fitted, being made from different plates mounted together. The water that overflowed was directed into a pipe like the one for the water supply and parallel to it, with a 250mm diameter and finally discharged into the tank downstream of the channel. Two different electromagnetic flow meters were mounted on the two parallel pipes described above in order to measure the flow rate in the channel

Figure 1. A view of the channel.

as the difference of the two discharge measurements. The free surface level of the water into the channel, H_a, was maintained at a constant level with a depth of 26cm for all of the experiments, to ensure that the discharge into the channel was constant.

The second part of the laboratory model consisted of a buoyant jet thermal-hydraulic system. The discharged heated water generating the turbulent buoyant jet was pumped into the channel through a round steel tube mounted at the bottom of the channel and within the central longitudinal section. The tube was mounted vertically and it passed through the glass base. The source diameter D=5.0mm of the jet was chosen to satisfy different conditions. Firstly, in all cases to ensure that the jet was fully turbulent, *i.e.* to have the Reynolds number Re, defined for a round jet as $Re=4Q_0/\pi Dv$, with v the kinematic viscosity of the fluid and Q_0 the source discharge, sufficiently high (Re>2000).

Secondly, the value of D was fixed taking into consideration the length scale l_M, defined in terms of the source momentum (J_0) and buoyancy (B_0) fluxes as

$$l_M = \frac{Jo^{3/4}}{Bo^{1/2}} \qquad \textbf{(1)}$$

for a three-dimensional buoyant jet and which represents the distance from the source within which momentum effects are dynamically significant and beyond which the dynamics are dominated by buoyancy. Therefore, when the value of the length scale l_M is high, the momentum flux (J_0) plays a dominant and destabilizing role on the buoyant jet, causing recirculating eddies or mixing over the entire water depth, while when the value of the l_M is low, the buoyancy flux (B_0) is the main and stabilizing element that fosters a stable field in which a buoyant surface layer is formed that does not communicate with

the initial buoyant jet zone (Jirka *et al.*, 1982). Furthermore, because an ambient cross flow existed in the direction of the channel, its momentum flux, defined as

$$J_a = S u_a^2 \quad \textbf{(2)}$$

where S is the transverse surface area of the ambient flow into the channel and u_a is the velocity of the cross flow, was taken into consideration, as destabilizing effect on the buoyant jet development. The values of these three parameters and the relations among them were considered to have a stable flow field; that is, a low value of the length scale l_M was planned so that buoyancy effects were comparable with momentum effects, and a low value of the cross flow momentum flux J_a was chosen so that the position of the free surface level and a cross flow velocity were as low as possible. In particular, for the experiments with a smooth bottom boundary, and with the source diameter D=5mm of the buoyant jet defined, the length scale l_M assumed values between 0.26m and 0.44m, whereas the values of the flow ambient momentum flux J_a was $7.5 \cdot 10^{-3} m^4/s^2$ for all the experimental configurations. For the fresh water supply and its heating, a galvanized iron tank was used, which inside were four resistances of 12,500W for the heating of the water till the fixed temperature (with maximum value 90° C), each one protected by a thermostat, and a temperature transducer for the water temperature measurement. A pump of 1Hp, equipped with manometer and interception key, transferred the hot water from this supply reservoir to a second tank, positioned on a lifting platform, whose different levels were able to define the fixed source discharge. A comprehensive view of all of the buoyant jet generation system described is showed in Figure 2.

A Process Computer and a control software (which task was to store the test data and, if decided by the operator, to supervise all the system) was used to control and manage the buoyant jet system. It was able to generate the discharge of a flow with prefixed and constant pressure, flow rate and temperature into the channel described, and all of the facilities connected with the channel and the jet generation system.

To create a particular turbulence in the ambient cross flow, corrugated plastic elements were positioned on the bottom of the channel, forming a rough bottom boundary (Fig. 3). Three different kinds of roughness elements were used. The first one, was a roll of 10m length and 3 m width, made of polyester resin strengthened with glass fiber, with a "wavelength" λ of 76mm and an "amplitude" ε of 18mm. A hole was made in the center longitudinal section, 6m from the upstream channel section and 4m from the downstream section, located in the trough of the bottom boundary "wave" surface. Each of the other kinds of corrugated elements used during the following experimental configurations, was formed by 11 panels of same dimensions, and with same material and technical characteristics of the previous kind, differing only by the values of λ and ε.

Experimental cases and conditions for vertical round buoyant jet issued in a cross flow with rough bottom boundary are listed in Table 1. In order to cover as wide a range of conditions as possible, experiments were conducted using several different values and

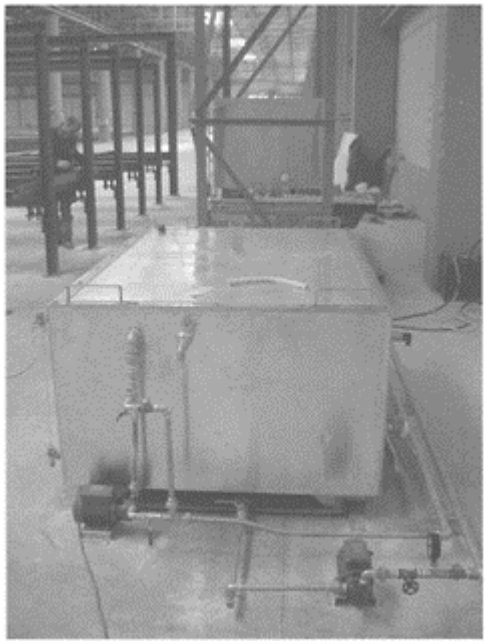

Figure 2. The tanks of the hydraulic circuit of the buoyant jet.

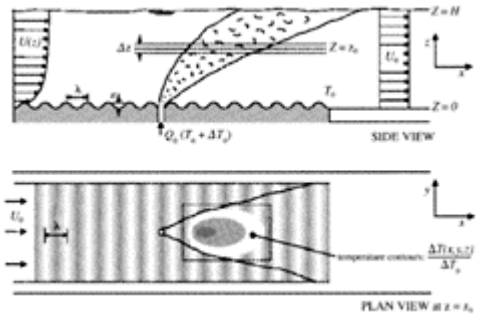

Figure 3. Schematic diagram of the experimental set up with corrugated plastic elements.

Table 1. Summary of experimental conditions.

Test	Q_0 (l/s)	H_a (m)	Q_a (l/s)	T_0 (°C)	T_a (°C)	λ (mm)	ε (mm)
T1	0.3	26	88	52	26	0	0
T2	0.3	26	88	62	27	0	0

T3	0.4	26	88	62	26	0	0
T4	0.4	26	88	52	27	0	0
T5	0.4	26	88	52	27	76	18
T6	0.4	26	88	61	29	76	18
T7	0.3	26	88	53	28	76	18
T8	0.3	26	88	60	25	76	18
T9	0.3	26	88	48	21	146	48
T10	0.3	26	88	54	18	146	48
T11	0.4	26	88	43	17	146	48
T12	0.4	26	88	53	19	146	48

combinations of the buoyant jet and bed-form parameters. Nevertheless, the experiments used the same working fluid (fresh tap water) throughout and the jet source diameter D was kept fixed (5.0mm) for all runs. Different buoyant jet flow conditions were therefore created by changes in Q_0 and T_0. In particular, the jet temperature was changed for each configuration to have two fixed temperature differences $\Delta T=(T_a-T_0$, with T_a the ambient temperature) of 25°C and 35°C between the ambient and the jet. The first configuration provided a smooth flat bottom boundary, while the following three configurations have adopted the different panels with different values of the parameters λ and ε, described above. Eight different thermocouple sensors were utilised to measure the mixing of the heated water into the cross flow, with and without the rough bottom, whereas for the measurement of the velocity the ADV system was used, together with CollectV software for the data acquisition and ExploreV software for the data analysis, both of them products of Nortek, like the ADV

2.2 *Laboratory results*

2.2.1 *Velocity field*

In order to study the turbulence effect upon the jet structure, a set of experiments was investigated with different configuration. The purpose of the experiment is to measure the three-velocity components *(U, V, W)* at different positions around the jet, where, U=mean stream-wise velocity, V=mean transverse velocity and W=mean vertical velocity, the measurement was determined by using an Acoustic Doppler Velocimeter (ADV). Figures 4–6 illustrate some of the experimental tests velocity vector map. It is to be noted that measurements shown in the three figures were made with the same channel discharge, the same source discharge and the same temperature excess at the source, the difference between theme being the nature of the channel bottom, which was a smooth surface bottom

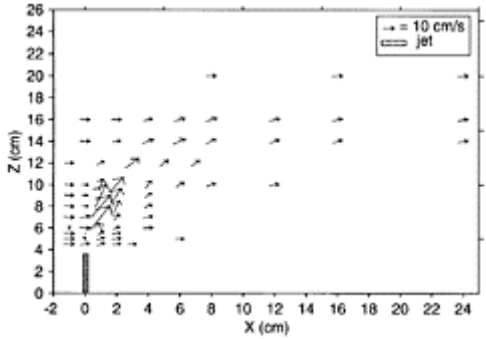

Figure 4. Near field velocity distribution for T1. Side view (y=0).

for Figure 4, corrugated surface bottom of "wavelength" λ=76mm and "amplitude" ε=18mm for Figure 5 and corrugated surface bottom of "wavelength" λ=146mm and "amplitude" ε=48mm for Figure 6.

The flow velocity vectors shown in those figures represent the mean velocity modules of the streamwise and the vertical flow velocity components which were measured along the channel axes where y=0.

As shown in Figures 4–6, it can be seen that the flow velocity vector directions and modules around the jet vary spatially. This variation is considered very rapid and more turbulent. Just for 1 or 2cm in the upstream of the source, the velocity vectors keep the same direction along the vertical axes z and have a uniform distribution for the three bottom configurations.

Over the source nozzle and going toward the downstream end of the channel, the velocity vectors appear to have an upward moving flow area, through which they change their characteristics strongly.

Increasing the spatial coordinates *(x, z)*, the velocity vectors for the three configurations change their

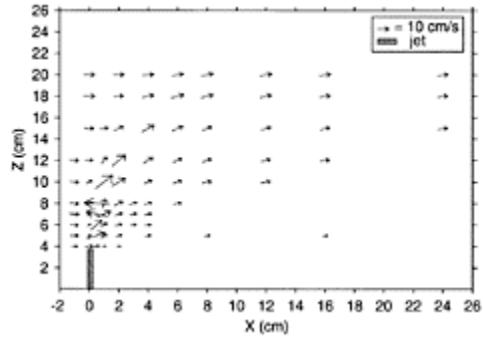

Figure 5. Near field velocity distribution for T7. Side view (y=0).

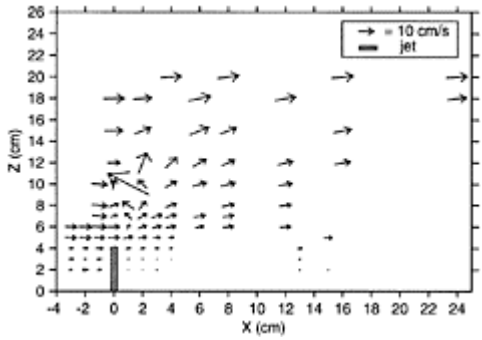

Figure 6. Near field velocity distribution for T9. Side view (y=0).

characteristics step by step, reaching a uniform profile similar to that of the ambient flow.

The other hand, Figures 4–6 show that the ability of the jet to become more vertical depends upon the nature of the channel bottom. In the case when the channel bottom surface was smooth, the jet velocity vectors are deviated more toward the horizontal than the other configurations with the presence of a corrugated channel bottom surface. It can been seen that the velocity vectors direction are influenced by the "wavelength" λ and "amplitude" ε of the corrugated surface. When λ and ε increase the jet velocity vectors become more vertical. This is due to the fact that the jet is confined between the wave crests of the bottom.

2.2.2 *Stress distribution*

As indicated in the previous paragraph, the channel bottom surface nature has a big effect upon the jet structure. In order to study this phenomenon in depth, a Reynolds stress analysis was established. As is well known, the statistical description of a turbulence flow starts by dividing the flow velocity into mean and fluctuating components. So, at each point the three instantaneous velocity components are written as:

$$u=U+u'$$
$$v=V+v'$$
$$w=W+w'$$

where u, v, w are the streamwise, transverse and vertical instantaneous flow velocity components, respectively, and u', v' and w' are the streamwise, transverse and vertical flow velocity fluctuation components, respectively.

The quantities $\overline{u'v'}$, $\overline{u'w'}$, $v'$and $\overline{v'w'}$are the time-averaged streamwise-transverse, streamwise-vertical and transverse-vertical Reynolds shear stresses.

Figures 7–15 show a map of the Reynolds stresses in the x-z plan, with y=0cm, for Test 1, Test 7 and Test 9.

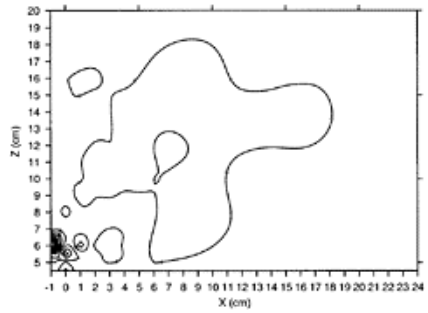

Figure 7. Streamwise-transverse *(u′v′)* stress distribution for T1. Side view(*y*=0).

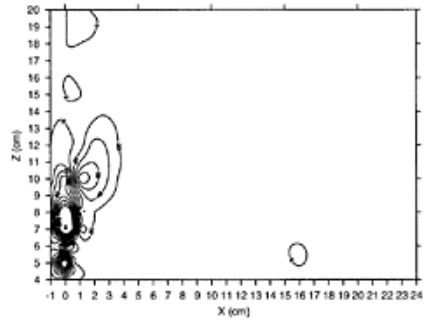

Figure 8. Streamwise-transverse *(u′v′)* stress distribution for T7. Side view (*y*=0).

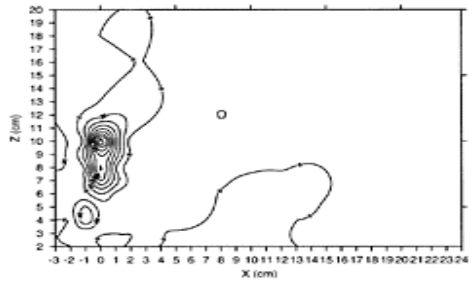

Figure 9. Streamwise-transverse *(u′v′)* stress distribution for T9. Side view (*y*=0).

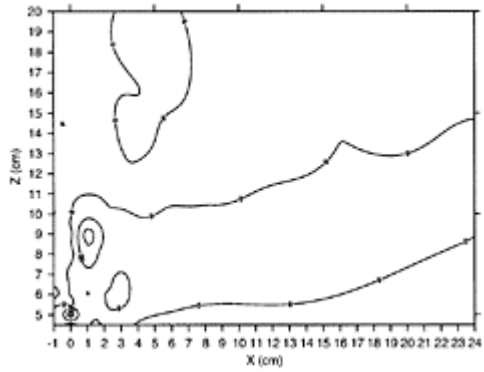

Figure 10. Streamwise-vertical *(u′w′)* stress distribution for T1. Side view (*y*=0).

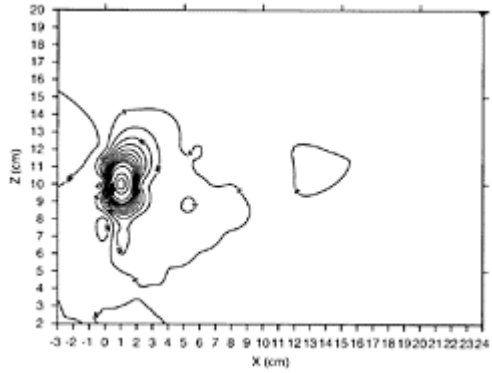

Figure 11. Streamwise-vertical *(u′w′)* stress distribution for T7. Side view (*y*=0).

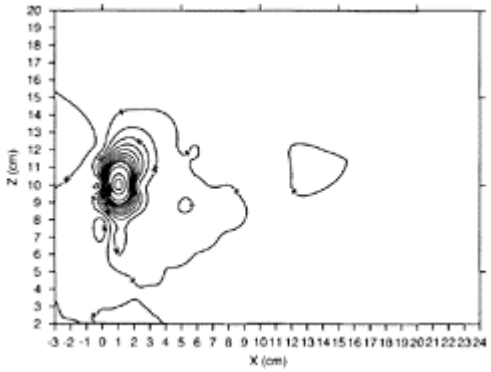

Figure 12. Streamwise-vertical *(u′w′)* stress distribution for T9. Side view (*y*=0).

Test 1 was a configuration with smooth surface channel bottom, Test 7 was a configuration with corrugated surface channel bottom of "wavelength" λ=76mm and "amplitude" ε=18mm, and Test 9 was a configur ation of corrugated surface channel bottom of "wave length" λ=146mm and "amplitude" ε=48mm.

From the figures, it is possible to highlight that the strong $\overline{u'v'}$, and $\overline{v'w'}$ Reynolds stresses are present in the area localized near the jet source, where the velocity vectors change their characteristics strongly, as written in the previous paragraph. Furthermore, both positive and negative values of the Reynolds stresses were present in the same plan. In the measurement points far from the jet source, it was highlighted that the Reynolds shear stresses become small for all configurations. This is due to the small velocity fluctuations in these areas and the dominance of the cross flow velocity components with an absence of the jet stream effects.

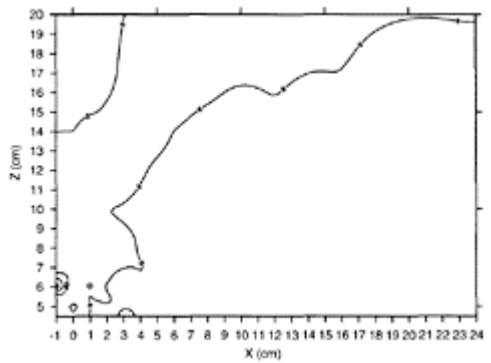

Figure 13. Transverse-vertical *(v′w′)* stress distribution for T1. side view (*y*=0).

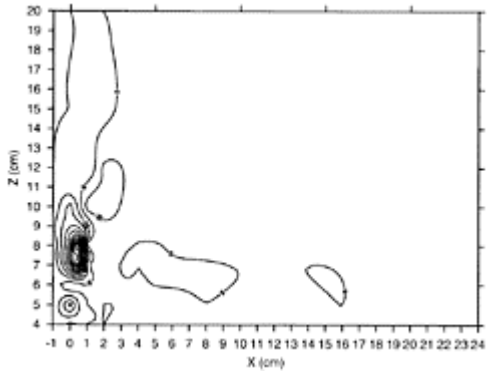

Figure 14. Transverse-vertical *(v′w′)* stress distribution for T7. Side view (*y*=0).

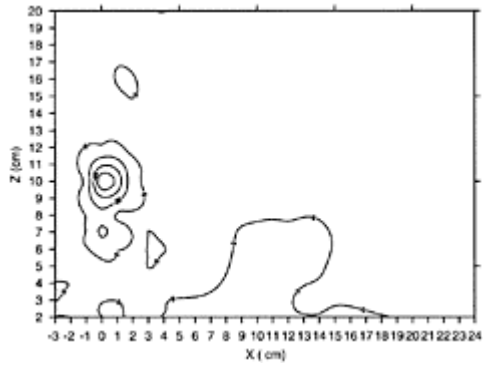

Figure 15. Transverse-vertical *(v′w′)* stress distribution for T9. Side view (*y*=0).

Table 2. Reynolds stress values for Test 1, Test 7 and Test 9.

	$u'v'$(m^2/s^2)		$u'w'$(m^2/s^2)		$v'w'$(m^2/s^2)	
Test	min.	max.	min.	max.	min.	max.
T1	−60	220	−35	60	−80	0
T7	−120	220	−80	160	−220	20
T9	−60	180	−40	460	−80	20

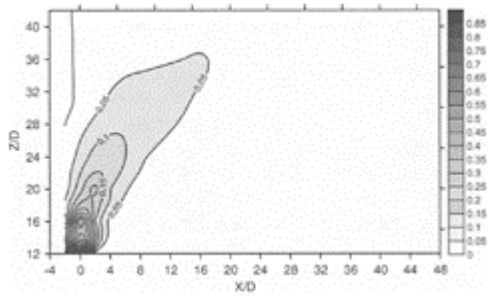

Figure 16. Longitudinal temperature distribution for Test 2.

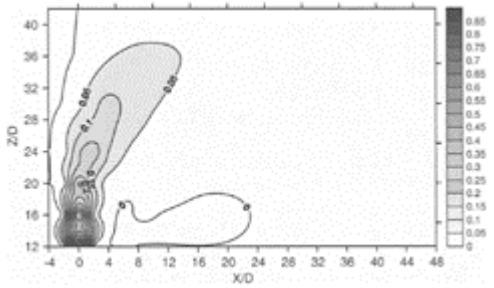

Figure 17. Longitudinal temperature distribution for Test 8.

Furthermore, one can see that there is a difference of the stress distribution between the analysed configurations, depending on the channel bottom surface. The absolute values of $\overline{u'v'}$, $\overline{u'w'}$ and $\overline{v'w'}$ Reynolds shear stresses of the configuration with the smooth channel bottom are generally smaller than those of the other two configurations with corrugated channel bottom, as shown in Table 2. The same table shows also that $\overline{u'w'}$ Reynolds stress component of Test 9 is greater than the ones of Test 1 and Test 7. In addition, it can be seen that Test 9 shows a positive shear stress distribution larger than the negative one, as shown in Figure 12. On the contrary, the $\overline{v'w'}$ Reynolds shear stress component is largely negative.

Examining the different figures, it can be seen clearly that the Reynolds shear stress distributions are more vertical when λ and ε increase.

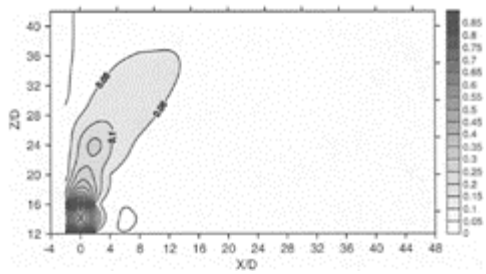

Figure 18. Longitudinal temperature distribution for Test 10.

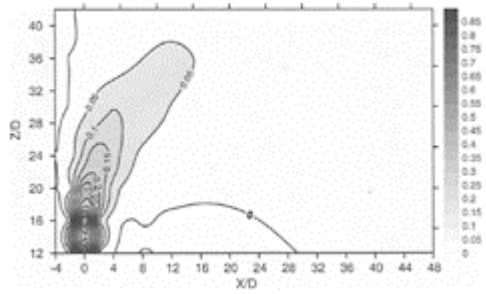

Figure 19. Longitudinal temperature distribution for Test 7.

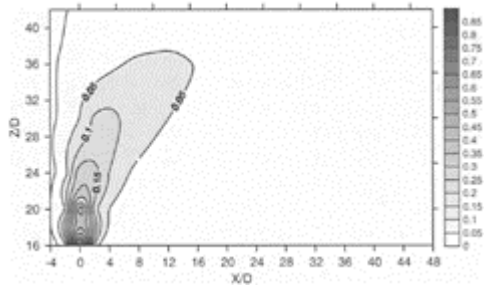

Figure 20. Longitudinal temperature distribution for Test 9.

2.2.3 *Temperature field*

In the present study, another aim was the measurements of the temperature field. The survey was run in a three-dimensional form, taking data at different levels and distances from the source orifice of the heated discharge.

Among the twelve experimental cases, seven typical temperature profiles, at the centre longitudinal section of the channel, are shown in Figures 16–22. In these figures, the ratio $\Delta T/\Delta T_0$ is reported, where ΔT is the difference between the time-averaged temperature in the measurement point and the average ambient temperature, whereas ΔT_0 is the time-averaged excess

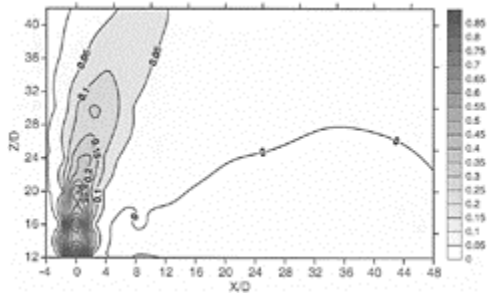

Figure 21. Longitudinal temperature distribution for Test 6.

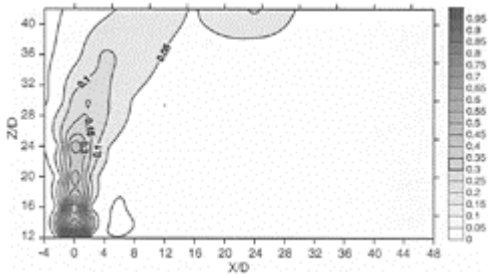

Figure 22. Longitudinal temperature distribution for Test 12.

temperature at the jet nozzle. In other words, this ratio represents the dilution of the buoyant jet into the cross flow. For the sake of brevity, Figures 16–22 were chosen taking into account (i) the three different bottom boundary conditions, which are smooth flat bottom, rough bottom with λ=16mm and ε=18mm, and rough bottom with λ=146mm and ε=48mm, and (11) two different buoyant jets with different density, generated by different own temperatures, and different flow rates Q_0. The purpose is to show the different behaviour of the buoyant jet related to parameters such as λ and ε, and to its own characteristics. Attention was paid also to the horizontal distribution of the temperatures into the ambient, so the measurements were assessed also at different vertical layers.

The analysis of the figures show that the jet is more vertical (i.e. is less deviated towards the cross flow direction) in the case of rough bottom. Furthermore, the jet is less deviated in the case of rough bottom with higher values of λ and ε.

3 CONCLUSIONS

Heated water mixing as the result of discharge from a submerged vertical round source located at the bottom of a channel was analysed, and the smooth and rough bottom boundary cases were compared. Several conclusions were attained from the analysis of the experimental data. Firstly, the experimental results reveal that the roughness elements on the bottom boundary affect significantly the trajectory of the buoyant jet. This result is clear from the figures of the longitudinal distributions of the dimensionless excess temperature. The comparison of the results enable us to highlight that the main effect of the roughness is to elevate the trajectory of the buoyant jet, which becomes more vertical. In addition, the kinematic generation by the roughness elements of a vertical component of the cross flow velocity seems to play an important role in this structural modification of the buoyant jet, as evidenced from the turbulence Reynolds stress distributions. Nevertheless, further work is required to establish and parameterise the relative role(s) of the relevant length scales of the flow and the topographic elements upon the structural modifications to the buoyant jet.

REFERENCES

Lee, J.H.W. 1984. Boundary effects on a submerged jet group. *J. of Engineering Mechanics.* ASCE, Vol. 122, No. 1:19–29.

Seo, I.W., Kim, H.S., Yu, D. & Kim, D.S. 2001. Performance of tee diffusers in shallow water with crossflow. *J. of Hydmulic Engineering,* ASCE, Vol. 127, No. 1:53–61.

Kim, Y.D., Seo, I.W., Kang, S.W. & Oh, B.C. 2002. Jet integral-particle tracking hybrid model for single buoyant jets. *J. of Hydraulic Engineering,* ASCE, Vol. 128, No. 8: 753–760.

Grass, A.J., Stuart, R.J. & Mansour-Tehrani, M. 1991. Vortical structures and coherent motion in turbulent flow over smooth and rough boundaries. Phil. Trans. Roy. Soc. London A336:35–65.

Grass, A.J. & Mansour-Tehrani, M. 1996. Generalized scaling of coherent bursting structures in the near-wall region of turbulent flow over smooth and rough boundaries. Coherent Flow Structures in Open Channels (edit by Phil Ashworth, Sean Bennett, James L.Best, Stuart McLelland): 41–61.

Jirka, G.H., Doneker, R.L. & Hinton, S.W. 1982. User's manual for Cormix: A hydrodynamic mixing zone model and decision support system for pollutant discharges into surface waters. Defrees hydraulics laboratory, School of Civil and Environmental Engineering, Cornell University, Ithaca, New York.

Shallowness and longitudinal dispersion in rivers

Robert Booij
Faculty of Civil Engineering and Geosciences, Delft University of Technology, The Netherlands

River Flow 2004—Greco, Carravetta & Della Morte (eds.)

ABSTRACT: The longitudinal dispersion determines the extent of and the concentration in the cloud of pollutant that descends the river after an accidental spill. It is strongly influenced by the presence of dead water zones along the river. The slow exchange of water and hence of dissolved pollutants between river and dead water zone results in very large values of longitudinal dispersion coefficients. It even leads to the large tails that are often found in the distributions of pollutants. Measurements in a laboratory model of square harbours along a river show that the aspect ratio of dead water zones is important for the residence time of the pollutant in dead water zones. For very shallow dead water zones as common along rivers, with aspect ratios of 20 or more, the flow hardly enters the centre of the zones, leading to very long residence times for the pollutant there. Laboratory models of dead zones along rivers are nearly never deep enough to account for this effect and are hence not useful for the validation of numerical models of longitudinal dispersion.

1 LONGITUDINAL DISPERSION

The spreading of dissolved matter in rivers proceeds in different phases, depending on the distance to the source of the dissolved matter. Because of the shallowness of rivers turbulent mixing over the vertical is the most important process near the source of the dissolved matter. In the next phase turbulent spreading over the width becomes the predominant process. Meanwhile the cloud of dissolved matter undergoes downstream convection by the mean flow and spreading in the longitudinal direction. This longitudinal spreading is more difficult to describe. It hardly depends on direct turbulent diffusion in longitudinal direction, but is mainly due to different convection velocities

over the cross-section (e.g. caused by differences in water depth or curvature effects in river bends), and transverse mixing (Fischer et al., 1979).

When the dissolved matter is sufficiently mixed over the width a relatively simple description of the transport in longitudinal direction, based on the method of Taylor (1953), is possible. In this phase, often called the longitudinal mixing phase, the spreading of the cloud of dissolved matter can be described with a longitudinal dispersion coefficient, while the cloud is displaced downstream by convection with the mean flow velocity averaged over the cross-section, u_{av}. Knowledge of the longitudinal dispersion of pollutants in rivers is important, in particular after accidental spills of harmful matter. The longitudinal

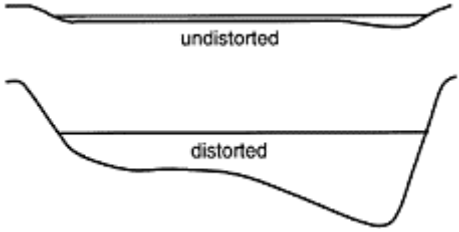

Figure 1. Comparison of a non-distorted plot of the cross-section of a river bend, with a realistic aspect ratio of about 50 (top) and the usual distorted plot of the same bend (bottom).

dispersion determines the extent of and the concentration in the cloud of pollutant that descends the river. The longitudinal dispersion coefficient depends on the transversal exchange of pollutant over the river width and the flow velocity differences over the width.

The flow in a river is a shallow free surface flow. In such a flow the important horizontal length scales of the flow are one or more orders of magnitude larger than the flow depth, h. In rivers aspect ratios W/h, where W is the width of the river, of at least 50 up to a few hundred are observed. This is not always directly obvious from the usual distorted plots of cross-sections of rivers (see Figure 1).

Approximate expressions for the vertical diffusion coefficient, D_v, the transverse mixing coefficient, D_t, and the longitudinal dispersion coefficient, D_L, in rivers are respectively (Fischer et al., 1979)

$$D_v \approx 0.067\ hu^*,$$
$$D_t \approx 0.6\ hu^*,$$
$$D_L \approx 0.011\ u_{av}^2 W^2 / hu^*,$$

where u^* is the average bed shear velocity. For a river with for example

h=2m, W=100m, and u_{av}=15u^*=1m/s

this leads to

$D_v \approx 0.009 m^2/s$, $D_t \approx 0.08 m^2/s$, $D_L \approx 800 m^2/s$.

The times required for a fair mixing of the dissolved matter over the vertical T_v and over the width T_t are respectively (Fischer et al., 1979)

$T_v \approx 0.4/h^2/D_v$ and $T_t \approx 0.4W^2/D_t$

and the distances the cloud is displaced downstream by convection in these mixing times are respectively

$L_v \approx 0.4 u_{av} h^2/D_v$ and $L_t \approx 0.4 u_{av} W^2/D_t$.

For our example river this means

$T_v \approx 180s$, $L_v \approx 180m$, $T_t \approx 5 * 10^4 s$, $L_t \approx 50km$.

Concluding, the longitudinal dispersion coefficient is very large compared to the vertical and transverse mixing coefficients. The vertical mixing is fast, but the transverse mixing takes much more time, because of the large aspect ratio involved. Important for the discussion here is that the transverse mixing takes place more or less within the distance over which the river changes appreciably, e.g. by confluences with tributaries. This would mean that the longitudinal distribution of the concentration of a cloud of dissolved matter would always be more or less Gaussian.

2 INFLUENCE OF DEAD WATER ZONES

In practice many measured concentration distributions even far downstream of the sources of dissolved matter are found to deviate appreciably from a Gaussian distribution. Often a large tail is observed on the upstream side. As most concentration measurements are executed at a fixed position this leads to a tail for the measurement of the concentration φ over time as

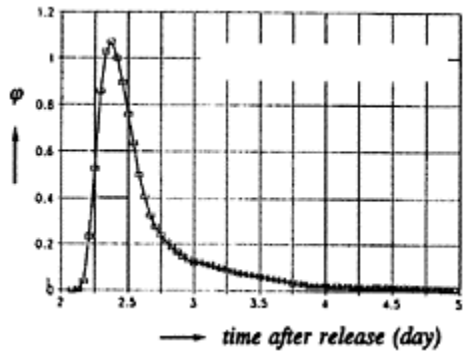

Figure 2. Measured distribution of tracer concentration φ at

Maximiliansau at Rhine-kilometer 362 during the tracer experiment 04/89 (from Mazijk, 1996).

seen in Figure 2. Such a tail points to an insufficient transverse mixing and shows that the description of the longitudinal dispersion as Fickian diffusion is not correct

Such tails are caused by the so-called dead water zones, or stagnant zones, along the river: groyne fields, local broadenings, bordering harbours and lakes, old river branches, etc. These are zones with slow flowing water with low exchange with the main channel of the river. The Taylor method and the resulting approximate expression for the longitudinal dispersion coefficient work well for a river without appreciable stagnant zones. However, when dead water zones are present, then the low exchange with the dead water zones leads to very long transverse mixing times, T_t, and lengths, L_t. When dead zones are present, the mixing length becomes easily much larger than the distance between the important tributaries and the Taylor method is not applicable anymore. A much used approach, the dead zone model, uses in that case a longitudinal dispersion coefficient for the flow in the main channel only and accounts separately for the dead zones (Mazijk, 1996).

To account for the dead zones requires a good knowledge of the exchange flow between dead zones and main channel and of the exchanged concentration. Generally for simplicity well-mixed dead zones are assumed, but more realistic models require knowledge of the flow in the dead zone to compute the concentration of the exchanged water. In principle it is possible to consider the river-dead zones system as a black box. Sufficient measurements of the development of the concentration distributions after earlier spills and tracer experiments may give enough information to predict the concentration development after a new spill. This is however only useful for well-monitored rivers as the Rhine. For other rivers the knowledge will have to be obtained mainly from laboratory experiments where the exchanges between

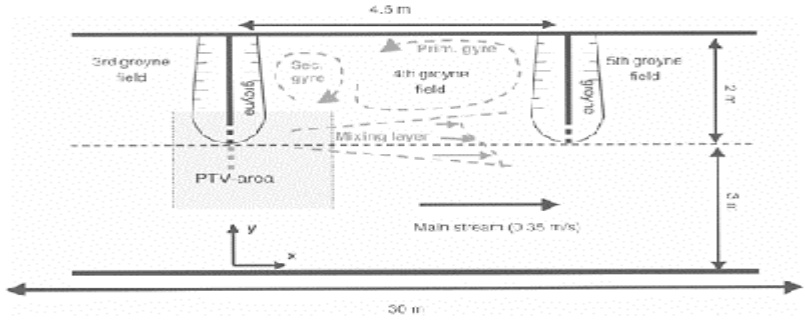

Figure 3. Top view of the experimental setup around the 4th groyne field in the shallow flume of Delft University of Technology used in a experiment of Uijttewaal (2003) for the investigation

of the effects of groyne shapes on the flow around the groynes and in the groyne field and on the exchanges with the river.

river and dead zones and the flow in dead zones is investigated, or by computations with numerical models that in their turn have to be validated with data from such experiments.

3 EXPERIMENTS IN SHALLOW FLOWS

Experimental investigations of shallow flows require large flumes because of the contradictory conditions that play a role in such physical models. The flow has to be turbulent, even in the dead water zones, which requires a sufficiently large Reynolds number. Moreover the value of the Froude number has to remain much below 1 to ensure that the flow is not affected by surface disturbances, e.g. around the tip of groynes or at the corners of a harbour entrance. These two conditions lead to a maximum velocity and a minimum depth, depending on the kind of flow to be modelled. The most severe condition is the aspect ratio of the shallow flow that has to be observed. Together with the minimum depth from the Froude and Reynolds conditions this leads to very wide (and long) flumes. An example is the flume used by Uijttewaal (2003) for the investigation of the effects of groyne shapes on the flow around the groynes and in the groyne fields and on the exchanges with the river (see Figure 3). The dimensions of this flume are:

W=5m, h=25cm, length=30m.

The average velocity in the main stream channel is u_{av}=0.35m/s. An important measure, the ratio of the width of the groyne fields to the mean flow depth between the groynes is between 10 and 15 for the different cases investigated.

Flumes of these dimensions are expensive and hence do not abound. In the chosen compromise between price and performance the aspect ratio is the usual victim. Several experiments in flumes with groyne fields are reported, where the width of the groyne fields is but a few times larger than the flow depth. It is obvious that because of 3-dimensional effects e.g. around the tip of the groynes the flow field will strongly deviate from the shallow flow in a real river. Hence results obtained from those experiments are hardly useful for practical purposes.

In this paper shallow flow experiments in laboratory models of harbours along a river are discussed that suggest that even many experimental flows in wide shallow flumes are not sufficiently shallow. The flow in a shallow harbour along a river resembles in many respects the flow in a groyne field.

4 EXPERIMENTAL SETUP FOR SHALLOW HARBOUR FLOW

Several years ago a series of experiments was executed in a laboratory model of shallow harbours along

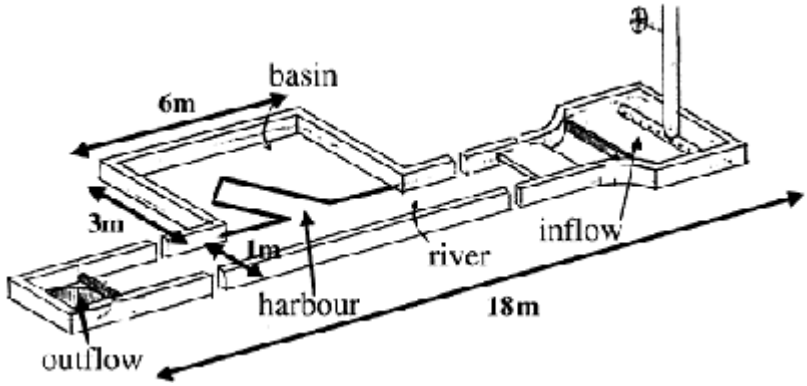

Figure 4. Shallow flume for harbour experiments of Delft University of Technology. The inflow is at the right side, the outflow at the left side. The straight river part has a length of 18 m. Along the river a rectangular basin of 3m×6m allows the construction of different harbours.

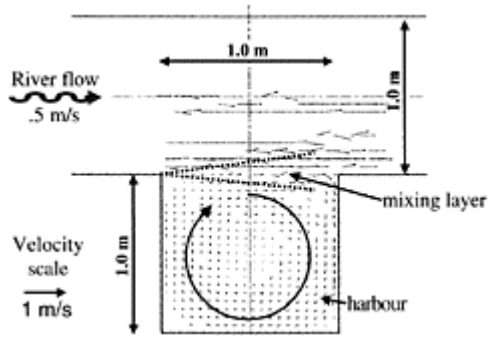

Figure 5. Flow in and around the 1m×1m harbour measured with floats.

a flume to investigate the influence of shallowness and of the layout of harbours and harbour entrances on the flow in the harbours and in the harbour entrance, the exchange through the harbour entrance, etc. (Booij, 1986). A straight flume served as a model for the river. Along this river a basin was made in which several harbours could be constructed (see Figure 4).

The flow in the harbours was driven by momentum transport through the mixing layer in the harbour entrance between river flow and harbour flow. As an example the flow in

and around a square harbour with sides of 1m (the 1m×1m harbour) is shown in Figure 5. In this case the velocities were obtained by measuring the displacements of floats that remained just free from the bottom, in order to yield depth-averaged velocities (see Figure 6). The floats are 10cm

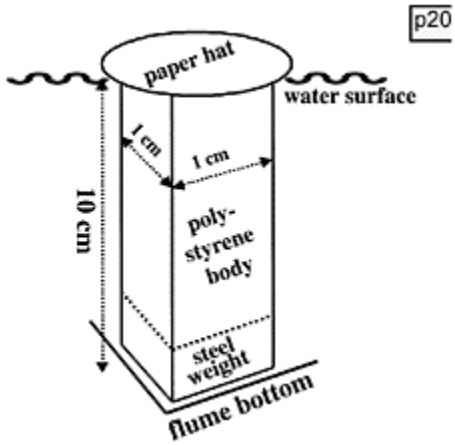

Figure 6. Deep reaching floats, extending to just above the bottom to yield depth-averaged velocities.

long, while the harbours and the river are kept at a depth of just above 10cm.

Another velocity measuring method used was by means of micro-impellers. The micro-impellers were placed at half depth where the velocity is not very far from the depth-averaged velocity.

5 EXPERIMENTAL RESULTS

The aspect ratio of rivers W/h is of the order of 50 to several hundreds generally. Most dead water zones are equally shallow. Hence we concentrate on the shallowest harbours in the investigation (W/h up to 30, where W is the minimum value of length or width here). The shallowest harbour is a square harbour with W=3m hence with an aspect ratio $W/h\approx30$. To investigate the influence of shallowness this harbour is compared with two square harbours with smaller widths, W=1m and 2m (or aspects ratios 10 and 20) respectively.

For the investigation of the influence of shallowness the micro-impellers placed at half depth were used. The measurements show that above an aspect ratio of 10 the character of the flow changes considerably (Booij, 2003). From the measured velocities in a cross-section it can be concluded that in the 1m×1m harbour the water rotates as a whole, which is also obvious from the results of the float measurements reproduced in Figure 5. On the contrary in the larger harbours the flow is concentrated along the sides and the

centre is hardly affected, see Figure 7. This is due to the suppression of large-scale horizontal coherent structures because of the bottom influence, and to a phenomenon called differential advection (explained in chapter 6), which is connected with the secondary flow in the cross-sections. Both lead to a containment of the wall boundary jet and the secondary flow vortex, see Figure 8.

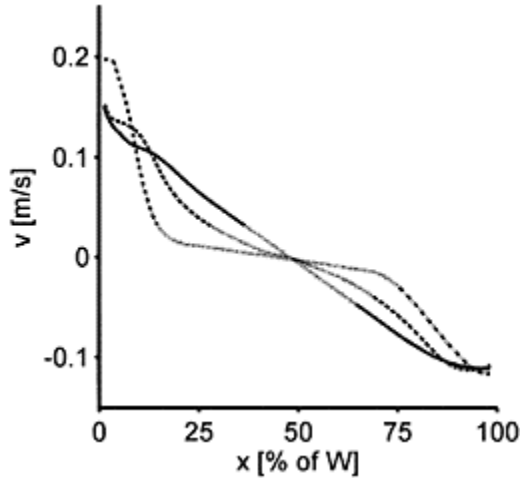

Figure 7. The flow in square harbour models of different shallowness, driven by the river flow. At left the velocity profiles halfway the harbour are plotted. At right the layout and legenda are given.

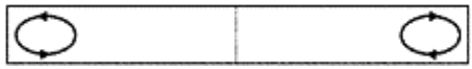

Figure 8. Sketch of the secondary flow vortices restricted to the near wall regions in shallow harbour flow.

6 DIFFERENTIAL ADVECTION

Differential advection makes its appearance in curved shallow flow. Its best known effect is in gentle river bends where the largest velocity is found at the outside bend. The same mechanism drives the curved flow in harbours to the near wall regions.

Generally, the largest flow velocities in mildly curved shallow flow are found at the outside of the curved flow, e.g. the outer bend in curved river flow. The mechanism that

makes the flow velocity at the outside of the curvature increase at the expense of the velocity at the inside is differential advection, which can be understood as follows. In mildly curved shallow flow the main flow velocity profile over the vertical is almost logarithmic. Hence the centrifugal force due to the curvature of the flow is larger in the upper part of the flow than near the bottom. On the average this centrifugal force is compensated by the pressure gradient due to a surface slope towards the outer bend. The resulting force is directed to the outward side in the upper part of the flow and to the inward side near the bottom and hence leads to a secondary flow to the outside in the upper part and to the inside near the bottom (see Figure 9). The main flow and the secondary flow together form the helical flow observed in curved shallow flow.

In mildly curved shallow flow the amount of water flowing outward is more or less equal to the amount of water flowing inward. However the main flow velocity is larger in the upper part of the flow than in the lower part, hence more main flow momentum is transported outwards in the upper part of the flow than inwards in

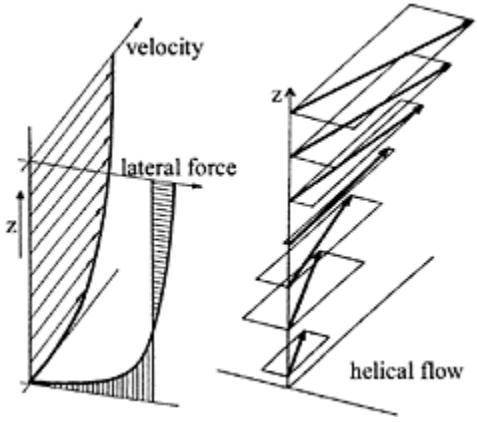

Figure 9. Mechanism of the origin of secondary flow in mildly curved shallow flow and the resulting helical flow.

the lower part. This leads to a net transport of main flow momentum in outward direction and consequently to higher flow velocities at the outer bend.

In the harbour this differential advection leads to a transport of the highest velocities to the outer walls. This counteracts and suppresses the turbulent structures that transport the high velocity from the wall to the centre. This leads to the creation and a containment of a wall boundary jet.

An interesting consequence of differential advection is the poor reproduction of shallow curved flow by 2-dimensional numerical models. In view of the shallowness of rivers and tidal channels the preference for 2-D horizontal models is understandable. However, the momentum transport by differential advection (i.e. from the region of low velocity at the inside bend to the region with high velocity near the outside bend) requires

the implementation of a negative eddy viscosity, which will lead to stability problems. In 3-D computations the secondary flow is computed and hence its advection effects are included, without the necessity of a negative eddy viscosity.

7 BEHAVIOUR OF THE HARBOUR CENTRE

In chapter 5 it was observed that the flow velocities in the centre of the shallower harbours are very low. This means that there is hardly an exchange of water and hence dissolved matter between the centre of the harbour and the outer region. This is also evident from a dye experiment in the 3m×3m harbour. This experiment started with a more or less homogeneous dye concentration in the harbour. After some time the outer region had exchanged all its dye with the river,

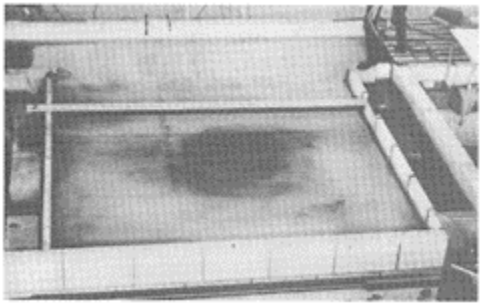

Figure 10. Remaining dye patch in the centre region of the 3m×3m harbour. The river part of the flume is at the top. The river flows from left to right.

whereas the centre region was still strongly coloured see Figure 10.

In less angular harbours the transition from a fully rotating harbour to a harbour with a hardly moving centre appears at slightly lower dimensions, as can be seen in Figure 11. Here a flow in a partly circular harbour is shown, measured with floats. Obvious is the slowly moving centre, although the diameter of the circular part of the harbour is slightly less than the width of a square harbour with corresponding velocity pattern. The angles of the square harbour appear to intensify turbulent disturbances that increase the exchange between centre and outer region.

8 INFLUENCE ON THE LONGITUDINAL DISPERSION

The low exchange of the centre of shallow dead zones with the outer region and hence with the river harbour can have important consequences for the longitudinal dispersion and the tails in the distribution of the dissolved matter. A dead zone influences the

convection and the spreading of the dissolved matter by taking in a part of the dissolved matter as the cloud passes and releasing it gradually over the time, depending on the residence time of the water in the dead zone. In this way it decreases the (average) convection velocity of the cloud, increase the longitudinal spreading and may lead to a tail in the distribution.

For a shallow dead zone the intake of dissolved matter from the passing cloud will be less, as the increase of the concentration of the centre lags behind, because of the low exchange. For a shallow dead zone this will lead to a lower increase of the longitudinal spreading by the fast exchanging outer region of the dead zone. As the dissolved matter from the centre is exchanged back more slowly, this exchange will last much longer and lead to a larger longitudinal spreading and a long tail in the distribution. The magnitude of these

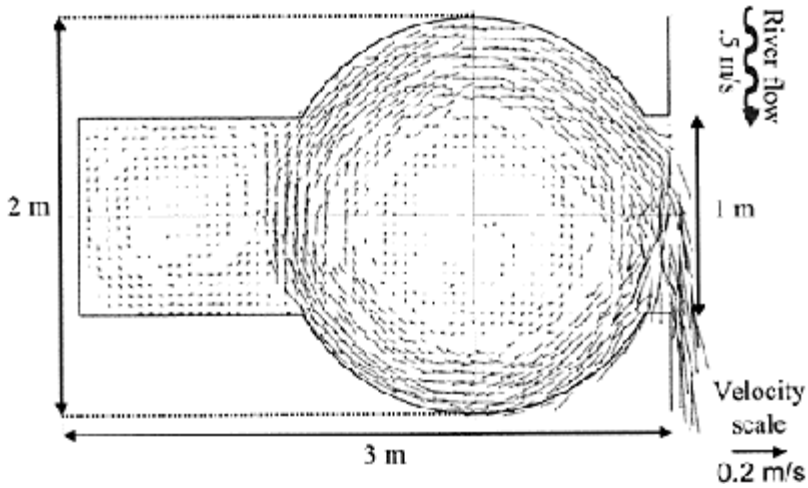

Figure 11. Flow in a partly circular harbour, measured with floats. The river is at right. The flow direction in the river is from top to bottom. Obvious is the slowly moving centre.

different effects depends on the extent of the different parts of the dead zone and of the residence times of those parts in relation to the passing time of the cloud.

Numerical models of the very shallow flow in rivers with dead water zones require ample validation by measurements, for which measurements in laboratory models are used generally. This validation is needed because 2-D models lack a few mechanisms as e.g. differential advection and 3-D models require different momentum exchange coefficients for different directions that are at present not easily predicted. However, the dead water zones in most laboratory models are not sufficiently shallow. Hence the validation is based on too deep flows generally. Consequently most numerical models do

not model the flow in the centre of the dead water zones correctly, leading to too short residence times and hence incorrect predictions of the longitudinal dispersion.

9 CONCLUSIONS

- Knowledge of longitudinal dispersion of pollutants in rivers is important, in particular after accidental spills of harmful matter. The longitudinal dispersion determines the extent of and the concentration in the cloud of pollutant that descends the river.
- The longitudinal dispersion is strongly influenced by the presence of slowly moving (so called dead water) zones along the river, as are present between groynes, in old river branches, harbours, lakes or other bodies of water alongside the river.
- The slow exchange of water and hence of dissolved pollutants between river and dead water zone results in very large values of longitudinal dispersion coefficients.
- Dead water zones also lead to the large tails that are often found in the distributions of pollutants, which show that the description of the longitudinal dispersion as Fickian diffusion is not correct.
- Measurements in a laboratory model of square harbours along a river show that above an aspect ratio of 10 the character of the flow changes considerably. For aspect ratios up to 10 the flow in the harbour rotates more or less as a whole. The flow in shallower harbours, or other dead zones, is more concentrated along the sides and the fluid in the centre moves hardly.
- The low velocity in the centre of shallow dead zones leads to very long residence times and hence much higher values of the longitudinal dispersion coefficients and to long tails in the concentration distributions.
- Laboratory models of dead zones along rivers, even those in wide, shallow flumes, are generally not shallow enough to observe this stagnant centre effect, and hence show a behaviour that is quite different from the shallower dead zones found mostly in practice.
- Measurements in flumes with insufficiently shallow dead zones are not useful for the validation of numerical models of longitudinal dispersion.

REFERENCES

Booij, R. 1986. Measurement of exchanges between river and harbour (in Dutch). *Report 9–86.* Hydr. Engrg. Section, Delft Univ. of Techn., The Netherlands.

Booij, R. 2003. Laboratory experiments of shallow free surface flows. *Proc. Int. Symp. on Shallow Flows* I: 101–108. Delft, The Netherlands.

Fischer, H.B. et al. 1979. *Mixing in Inland and Coastal Waters.* New York: Academic Press.

Mazijk, A. van 1996. One-dimensional approach of transport phenomena of dissolved matter in rivers. *Thesis* Fac. Civil Engrg and Geosc., Delft Univ. of Techn., The Netherlands.

Taylor, G.I. 2003. Dispersion of soluble matter in solvent flowing slowly through a tube. *Proc. R. Soc. London Ser. A* 219:186–203.

Uijttewaal, W.S.J. 2003. Large scale dynamics in groyne field laboratory experiments. Submitted to *J. Hydr. Engrg.*

Pollution transport in the lagoon of Grado and Marano: a two dimensional modelling approach

M.Petti & S.Bosa
Dipartimento di Georisorse e Territorio, University of Udine, Italy

River Flow 2004—Greco, Carravetta & Della Morte (eds.)

ABSTRACT: Pollution and water quality in lagoon areas represent a problem for human health and for the local economy particularly felt by people living nearby. In Italy the lagoon of Grado and Marano, located in the Northeast part of the Adriatic Sea, is subject to mercury pollution. It is held by some that the source of pollution is the river Isonzo that drains polluted sediments from a Slovenian region and partly feeds the lagoon. Others believe that the source of pollutants should be looked for elsewhere, for example in some industrial establishments which, in the past, are believed to have introduced concentrations of polluting material into channels that flow into the lagoon. In this paper a 2D finite volume model is proposed for studying the dispersion of a dissolved pollutant in the lagoon environment and the results obtained in applying the model to the lagoon of Grado and Marano are illustrated.

1 INTRODUCTION

The transport of pollutants is a very complicated environmental problem that involves many disciplines such as ecology, chemistry, toxicology, sedimentology and fluid mechanics. One of the roles of fluid mechanics is to develop hydrodynamic models able to interpret as well as possible the propagation of pollutants in free surface water environments.

A numerical approach to pollutant transport can be based on the classical advection-diffusion equation founded on the passive tracer concept and suitable for a widely dispersed substance. This equation may be integrated by a Lagrangian or Eulerian approach. The first one, known also as particle tracking, is a natural approach in the presence of point sources, but a huge number of particles may be necessary to represent the concentration in each grid box. In the Eulerian approach the concentration equation describes the motion of a substance by numerical advection schemes, but care must be

taken over these to control numerical diffusion or oscillations in the presence of sharp gradient (James 2002). The relative importance of advection and diffusion in the dispersion of a tracer is represented by the Péclet number $P_e=U_0L_0/D_0$, where U_0 is a horizontal velocity scale, L_0 the length scale and D_0 the horizontal diffusivity scale. As observed by Prandle et al. (1993) in southern North Sea studies, in lagoon basins the Péclet number is very high thus the advective transport prevails on the diffusive.

To simulate an advection problem it is very important to have an efficient hydrodynamic and transport model, and care must be taken in the treatment of the advective terms in non-linear hydrodynamic equations (Dragoslav 2001).

In the present work we propose a numerical model based on the Eulerian approach for the simulation of 2D solute transport with unsteady advection-diffusion. A finite volume method is used to solve non linear equations by a Godunov approach supported by a robust and efficient approximate solver proposed by Harten, Lax and van Leer (HLLC) (Toro 1999). The resulting scheme is second-order accurate in space and time and satisfies the Total Variation Diminishing (TVD) condition.

After a number of tests done to check its validity the model was applied to pollution transport in the lagoon of Grado and Marano, affected by serious forms of mercury pollution. Various scenarios of possible sources of mercury pollution have been studied, also keeping in mind the wind, a meteorological factor which is very important in the lagoon dynamics of Grado and Marano. A discussion is reported on the results obtained simulating those considered to be the principal sources of immission of such a pollutant.

Finally, some conclusions are given, along with a very brief account on ongoing and future work.

2 MODEL EQUATIONS

Two-dimensional unsteady solute transport can be described by the depth-averaged equations in the vectorial and conservative form:

$$\frac{\partial \mathbf{U}}{\partial t}+\frac{\partial \mathbf{F}_c(\mathbf{U})}{\partial x}+\frac{\partial \mathbf{G}_c(\mathbf{U})}{\partial y}= =\frac{\partial \mathbf{F}_d(\mathbf{U})}{\partial x}+\frac{\partial \mathbf{G}_d(\mathbf{U})}{\partial y}+\mathbf{S}(\mathbf{U}) \tag{1}$$

obtained coupling well-known shallow water equations with the advection-diffusion transport equation (Ligget 1994). Here *(x, y)* are Cartesian coordinates, **U***(x, y, t)* is the vector of conserved variables, $\mathbf{F}_c$, $\mathbf{G}_c$, $\mathbf{F}_d$ and $\mathbf{G}_d$ the advective and diffusive fluxes respectively in the *x*- and *y*-directions and **S(U)** the source term. Thus:

$$\mathbf{U}=\begin{bmatrix} h \\ Uh \\ Vh \\ Ch \end{bmatrix}, \mathbf{F}_c(\mathbf{U})=\begin{bmatrix} Uh \\ U^2h+g\dfrac{h^2}{2} \\ UVh \\ UCh \end{bmatrix}, \quad (2)$$

$$\mathbf{G}_c(\mathbf{U})=\begin{bmatrix} Vh \\ UVh \\ V^2h+g\dfrac{h^2}{2} \\ VCh \end{bmatrix},$$

$$\mathbf{F}_d(\mathbf{U})=\begin{bmatrix} 0 \\ 0 \\ 0 \\ D_{xx}\dfrac{\partial Ch}{\partial x} \end{bmatrix}, \mathbf{G}_d(\mathbf{U})=\begin{bmatrix} 0 \\ 0 \\ 0 \\ D_{yy}\dfrac{\partial Ch}{\partial x} \end{bmatrix}$$

where U and V are the depth averaged velocities respectively in the x- and y-directions, D_{xx} and D_{yy} the diffusion coefficients of the pollutant, h is the water depth, C the depth averaged pollution concentration, and g the acceleration due to gravity. Source term **S(U)** is defined by:

$$\mathbf{S}(\mathbf{U})=\begin{bmatrix} 0 \\ \left(ghS_{0x}-gn^2\dfrac{U\sqrt{U^2+V^2}}{h^{4/3}}+\right. \\ \left.+fVh+C_D\dfrac{\rho_a}{\rho_w}W_x\sqrt{W_x^2+W_y^2}\right) \\ \left(ghS_{0y}-gn^2\dfrac{V\sqrt{U^2+V^2}}{h^{4/3}}-\right. \\ \left.-fUh+C_D\dfrac{\rho_a}{\rho_w}W_y\sqrt{W_x^2+W_y^2}\right) \\ Qh \end{bmatrix} \quad (3)$$

where S_{0x} and S_{0y} are the bed slopes, n is the Manning resistance coefficient, f a term that takes the Coriolis's acceleration into account, ρ_a the air density, ρ_w the water density, W_x, W_y the wind velocities in the x and y directions and C_D the wind shear coefficient. Q is the depth averaged pollutant source or sink.

Analyzing the advection-diffiision equation in dimensionless form (starred variables) we obtain:

$$\frac{\partial(C^*h^*)}{\partial t^*}+\left[\frac{\partial(C^*h^*)}{\partial x^*}+\frac{\partial(C^*h^*)}{\partial y^*}\right]- \quad (4)$$
$$-\frac{1}{P_e}\left[\frac{\partial^2(C^*h^*)}{\partial x^{*2}}+\frac{\partial^2(C^*h^*)}{\partial y^{*2}}\right]=Q^*h^*$$

where $P_e=U_0L_0/D_0$ is the Péclet number and U_0, L_0 and D_0 are respectively the velocity, spatial and diffusion scales.

A simple analysis of scales in the lagoon of Grado and Marano gives a Péclet number $P_e\approx5000$. This means that the advective transport prevails on the diffusive and therefore particular care must be taken over the choice of the numerical scheme to solve the equations in order to avoid an excessive and unrealistic numerical diffusion.

Moreover, observing that a sudden immission of pollutant represents a real shock phenomenon, a scheme of integration which is not very numerically diffusive is necessary as well as a shock-capturing scheme.

3 NUMERICAL METHOD

In accordance with the observation made, which is the necessity for a numerically little diffusive and shock-capturing scheme of integration, a finite volume method (FVM) was chosen.

One way to solve Equation 1 is to keep the time variable t continuous and consider the equation we obtain by integrating Equation 1 over a two-dimensional generic control volume Ω (Fig. 1):

$$\frac{d\langle \mathbf{U}(t)\rangle}{dt} = -\frac{1}{\Omega}\oint_{\partial\Omega} \mathbf{H}_c \cdot \mathbf{n}\, dl + \frac{1}{\Omega}\oint_{\partial\Omega} \mathbf{H}_d \cdot \mathbf{n}\, dl + \langle \mathbf{S}\rangle \tag{5}$$

where $\mathbf{H}_c=[\mathbf{F}_c, \mathbf{G}_c]$ is the tensor of advective fluxes, $\mathbf{H}_d=[\mathbf{F}_d, \mathbf{G}_d]$ the tensor of diffusive fluxes, $\mathbf{n}$ the outward unit vector normal to the boundary $\partial\Omega$, dl a length element and $\mathbf{H}\cdot\mathbf{n}$ dl the flux components normal to the boundary $\partial\Omega$.<**U**> and <**S**> represent the values:

$$\langle \mathbf{U}\rangle = \frac{1}{\Omega_i}\int_{\Omega} \mathbf{U} d\Omega, \qquad \langle \mathbf{S}\rangle = \frac{1}{\Omega_i}\int_{\Omega} \mathbf{S} d\Omega \tag{6}$$

averaged on the control volume Ω.

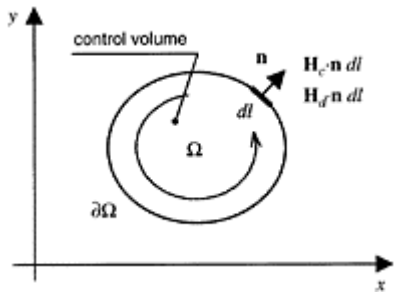

Figure 1. Generic control volume used to integrate Equation 1.

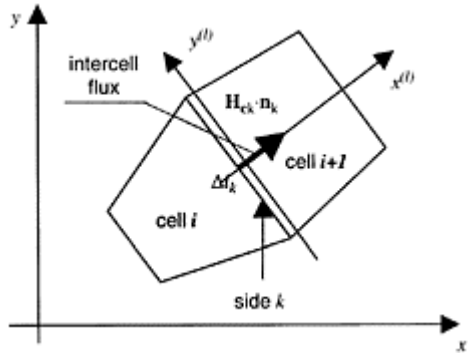

Figure 2. *i*-th control volume and the fluxes associated to its *k*-th side.

In the finite volume approach Equation 5 has to be satisfied on each control volume that results from discretising the physical space into a number of polyhedral control volumes or computing cells; the accuracy of the spatial discretisation depends on the particular scheme with which the fluxes are evaluated.

Assuming quadrilateral finite volume Ω_i, where the subscript *i* identifies a generic cell (Fig. 2), Equation 5 can be discretised as:

$$\frac{d\langle \mathbf{U}(t)\rangle_i}{dt} = -\frac{1}{\Omega_i}\sum_{k=1}^{4}\langle \mathbf{H}_c\rangle_k \cdot \mathbf{n}_k \Delta l_k + \\ +\frac{1}{\Omega_i}\sum_{k=1}^{4}\langle \mathbf{H}_d\rangle_k \cdot \mathbf{n}_k \Delta l_k + \langle \mathbf{S}\rangle_i \tag{7}$$

where *k* identifies a generic side of the cell, Δl_k its length, and $<\mathbf{H}_c>_k$ and $<\mathbf{H}_d>_k$ are the average fluxes across the intercell boundary Δl_k:

$$\langle \mathbf{H}_c\rangle_k = \frac{1}{\Delta l_k}\int_{\Delta l_k}\mathbf{H}_c\, dl, \quad \langle \mathbf{H}_d\rangle_k = \frac{1}{\Delta l_k}\int_{\Delta l_k}\mathbf{H}_d\, dl. \tag{8}$$

For simplicity in the following we omit the parentheses <>.

To solve the semi-discrete Equation 7 we can use a standard split-operator scheme in which the advective and diffusion-source steps are solved separately. To this purpose we write Equation 7 as:

$$\frac{d\mathbf{U}(t)_i}{dt} = \mathbf{L}_i^{(c)}(\mathbf{U}) + \mathbf{L}_i^{(d)}(\mathbf{U}) \tag{9}$$

where:

$$\mathbf{L}_i^{(c)} = -\frac{1}{\Omega_i}\sum_{k=1}^{4}\langle \mathbf{H}_c\rangle_k \cdot \mathbf{n}_k \Delta l_k \tag{10}$$

and:

$$\mathbf{L}_i^{(d)} = \frac{1}{\Omega_i} \sum_{k=1}^{4} \langle \mathbf{H}_d \rangle_k \cdot \mathbf{n}_k \, \Delta l_k + \langle \mathbf{S} \rangle_i \tag{11}$$

are called respectively advection operator and diffusion operator with source term.

Equation 9 can be solved in time by means of standard ODE methods; here we use a splitting scheme that consists in solving (Yanenko 1971, Toro 1999) the two subsequent initial value problems at each time step:

$$\begin{cases} \dfrac{d\mathbf{U}_i(t)}{dt} = \mathbf{L}_i^{(a)}(\mathbf{U}) \\ \mathbf{U}_i(0) = \mathbf{U}_i^n \qquad \textit{initial condition} \end{cases} \Rightarrow \mathbf{U}_i^{adv} \tag{12}$$

$$\begin{cases} \dfrac{d\mathbf{U}_i(t)}{dt} = \mathbf{L}_i^{(d)}(\mathbf{U}) \\ \mathbf{U}_i(0) = \mathbf{U}_i^{adv} \qquad \textit{initial condition} \end{cases} \Rightarrow \mathbf{U}_i^{n+1} \tag{13}$$

$\mathbf{U}_i^n$being the solution at time step t and $\mathbf{U}_i^{n+1}$ the target solution at time step $t+\Delta t$. $t + \Delta t$. $\mathbf{U}_i^{adv}$ is the solution of the first initial value problem (Eq. 12).

It can be seen immediately that system 12 is hyperbolic while system 13 is diffusive and it has a source term. This means that while for the second system it is possible to choose from a relatively ample range of integration schemes, for the first a more careful evaluation is necessary. One way to solve system 12 is to solve the so-called local 'Riemann problem'.

The most delicate aspect in the solution of this problem is the evaluation of the advective intercell flow $\mathbf{H}_{ck} \cdot \mathbf{n}_k$ (Fig. 2) by an appropriate solver.

In this paper we use the approximate Harten, Lax, van Leer (HLLC) solver modified by Toro (1999).

3.1 *The HLLC solver*

The intercell fluxes $\mathbf{H}_{ck} \cdot \mathbf{n}_k$, as $\mathbf{H}_{dk} \cdot \mathbf{n}_k$, can be estimated by exploiting the rotational invariance (Toro 1999):

$$\mathbf{H}_{ck} \cdot \mathbf{n}_k = \mathbf{T}_k^{-1} \mathbf{F}_c(\mathbf{U}_l) \tag{14}$$

where:

$$\mathbf{U}_l = \mathbf{T}_k \mathbf{U} = [h_l \; U_l h_l \; V_l h_l \; C_l h_l] \tag{15}$$

is the vector of rotated conserved variables referred to a local $(x^{(l)}, y^{(l)})$ Cartesian system (Fig. 2), $\mathbf{T}_k$ is the rotation matrix:

$$\mathbf{T}_k = \begin{bmatrix} 1 & 0 & 0 & 0 \\ 0 & n_{x_k} & n_{y_k} & 0 \\ 0 & -n_{y_k} & n_{x_k} & 0 \\ 0 & 0 & 0 & 1 \end{bmatrix} \tag{16}$$

and $\mathbf{T}_k^{-1}$ its inverse. Through Equation 14 the evaluation of the intercell fluxes is reduced to that of an augmented one-dimensional problem and the techniques used for the evaluation of the flow in these systems can be applied. The HLLC solver is one of these techniques.

The HLLC method gives an approximate estimation of the fluxes for solving the Riemann problem (Fig. 3):

$$\frac{\partial \mathbf{U}_t}{\partial t}+\frac{\partial \mathbf{F}_t(\mathbf{U}_t)}{\partial x_t}=0$$
$$\mathbf{U}_t(x^{(t)}=0,t)=\begin{cases}\mathbf{U}_k^{(1)} & \text{if} \quad x^{(t)}<0\\ \mathbf{U}_k^{(4)} & \text{if} \quad x^{(t)}>0\end{cases} \tag{17}$$

across the intercell und er consideration (side *k* of Fig. 2).

Following the 'method of characteristics' proposed by Stoker (1957), and subsequently widely dealt with by Whitham (1974), the Riemann problem is solved by referring to a characteristic diagram $(x^{(l)}, t)$ (Fig. 4). The area $(x^{(l)}, t)$ is divid ded into four regions delimited by the straight lines representing wave speeds S_m (m=1, 4) corresponding to eigenvalues of the hyperbolic problem described by Equation (17).

In the regions 1 and 4 conserved variables ($\mathbf{U}_k^{(1)}$ and $\mathbf{U}_k^{(4)}$) and fluxes ($\mathbf{F}_k^{(1)}$ and $\mathbf{F}_k^{(4)}$) are constant and

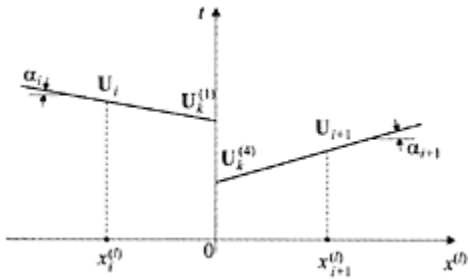

Figure 3. The local Riemann problem solved by the HLLC method and a MUSCL-Hancock TVD scheme.

known. In the regions 2 and 3 mean values of the conserved variables ($\mathbf{U}_k^{(2)}$ and $\mathbf{U}_k^{(3)}$) and fluxes ($\mathbf{F}_k^{(2)}$ and $\mathbf{F}_k^{(3)}$) are obtained integrating Equation 17 successively over the control volumes $[x_i^{(l)}, x_{i+1}^{(l)}]\times[0, \Delta t]$, $[S_1\Delta t, S_*\Delta t]\times[0, \Delta t]$ and $[S_*\Delta t, S_2\Delta t]\times[0, \Delta t]$ (Toro, 1999). Results for fluxes are:

$$\mathbf{F}_G=\begin{cases}\mathbf{F}_k^{(1)} & S_1\geq 0\\ \mathbf{F}_k^{(2)}=\mathbf{F}_k^{(1)}+S_1\left(\mathbf{U}_k^{(2)}-\mathbf{U}_k^{(1)}\right) & S_*\geq 0>S_1\\ \mathbf{F}_k^{(3)}=\mathbf{F}_k^{(4)}+S_2\left(\mathbf{U}_k^{(3)}-\mathbf{U}_k^{(4)}\right) & S_1\geq 0>S_*\\ \mathbf{F}_k^{(4)} & 0>S_1\end{cases} \tag{18}$$

where $\mathbf{F}_{ck}=\mathbf{H}_{ck}\cdot\mathbf{n}_k$ is the target intercell flux and:

$$\mathbf{U}_k^{(m)} = h_m^{(m)}\left(\frac{S_m - U_k^{(m)}}{S_m - S_*}\right)\begin{bmatrix}1\\ S_*\\ V_k^{(m)}\\ C_k^{(m)}\end{bmatrix}, \qquad m=2,3 \tag{19}$$

The wave speed estimates S_1 and S_2 are performed according to elementary wave solutions of the Riemann problem (i.e. rarefaction, shear or shock waves). The wave speed $S_*=S_3=S_4$ is estimated by the equation proposed by Toro (1999):

$$S_* = \frac{S_1 h_k^{(4)}\left(U_k^{(4)} - S_4\right) - S_4 h_k^{(1)}\left(U_k^{(1)} - S_1\right)}{h_k^{(4)}\left(U_k^{(4)} - S_4\right) - h_k^{(1)}\left(U_k^{(1)} - S_1\right)}. \tag{20}$$

Assuming:

$$\mathbf{U}_k^{(1)} = \mathbf{U}_i^n \qquad \text{and} \qquad \mathbf{U}_k^{(4)} = \mathbf{U}_{i+1}^n \tag{21}$$

the intercell flux $\mathbf{F}_{ck}$ estimated by Equation 18 is first-order accurate in space. To solve the problem

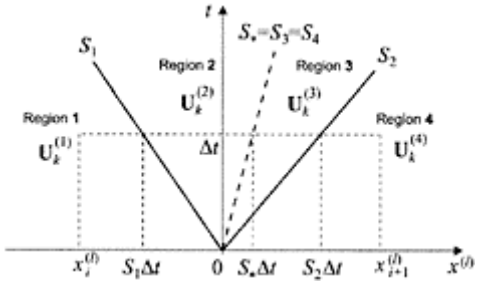

Figure 4. Structure used in the HLLC method to solve the Riemann problem.

at second-order we use a MUSCL-Hancock TDV scheme (Hirsch 1988, Toro 1999) in conjunction with a 'minmod' limiter for slopes α_i and α_{i+1} (Fig. 3).

The solution of system 13 (diffusive with source term) was found by applying a standard finite difference centered scheme which is second-order accurate.

Finally, the second-order time accuracy is obtained using a *split-operator* technique that brings to the scheme:

$$\mathbf{U}_i^{n+1} = \mathbf{L}_i^{(d)(\Delta t/2)}\mathbf{L}_i^{(c)(\Delta t)}\mathbf{L}_i^{(d)(\Delta t/2)}\left[\mathbf{U}_i^n\right]. \tag{22}$$

4 RESULTS OF SOME TESTS

A number of tests were carried out to check the model, here we show the results of a couple of them: one purely advective and one purely diffusive.

4.1 *Advective test*

In this test we analyze the pollutant concentration transport in one-dimensional dam-break problems. The domain, 50m long (x-axis) and 10m wide (y-axis), is discretised by cells of dimensions 0.5×0.5m. The Courant-Friedrichs-Lewy coefficient is C_{cfl}=0.9. The initial conditions (t=0s) are given in Table 1.

In Figure 5 is shown the comparison between numerical and analytical solutions of the pollutant concentration transport at time t=7s.

4.2 *Diffusive test*

In this test we analyze the pollutant concentration transport in a purely diffusive one-dimensional problem.

The domain, 5m long (x-axis) and 2m wide (y-axis), is discretised by cells of dimensions 0.1× 0.1m. The Courant-Friedrichs-Lewy coeffcient is C_{cfl}=0.8. The initial condition is still water, the boundary condition at x=0 is set at a constant immission of pollutant concentration C=1. In this test we assume a constant isotropic diffusion coefficient D= 0.25m^2/s.

In Figure 6 is shown a comparison between numerical and analytical solutions (Fisher et al. 1979) of the pollutant concentration diffusion.

Table 1. Initial conditions for the advective test.

	h	U	C
Variable	(m)	(m/s)	–
x<10m	1.00	2.50	1.00
x>10m	0.00	0.00	0.00

5 APPLICATION OF THE MODEL TO THE LAGOON OF GRADO AND MARANO

The lagoon of Grado and Marano, situated at the most northern point of the Adriatic Sea, between the mouths of the rivers Tagliamento (to the West) and Isonzo (to the East). The lagoon covers an area of around 16,000 hectares, for a length of around 32km and a mean width of 5km. It is connected to the open sea through 6 natural mouths (Fig. 7).

Recent investigations have been carried out for the dredging of the lagoon channels and they have underlined, among the various forms of pollution, a consistent presence of Mercury diffuse more or less throughout the whole Lagoon.

Two hypotheses have been formulated about the origin of this pollution: the former ascribes the polluting

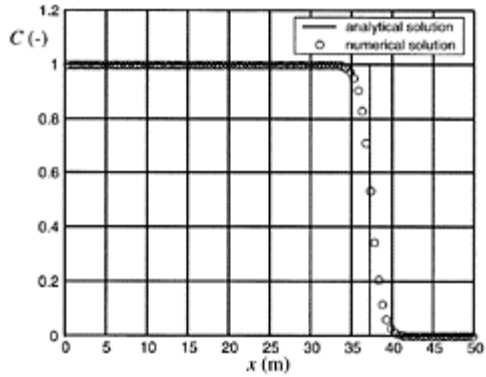

Figure 5. Advective test: comparisons between numerical and analytical solutions of the pollutant concentration transport in one-dimensional dam-break problem (t=7s).

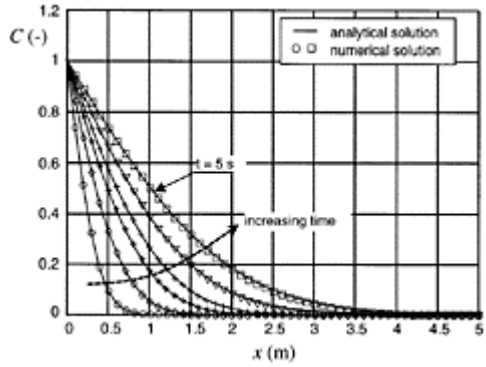

Figure 6. Diffusive test: comparisons between numerical and analytical solutions of the pollutant concentration diffusion in one-dimensional problem.

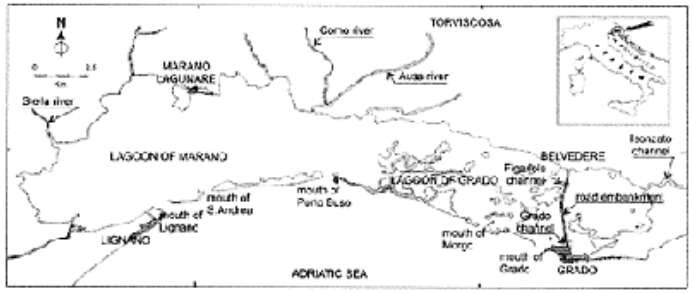

Figure 7. The lagoon of Grado and Marano.

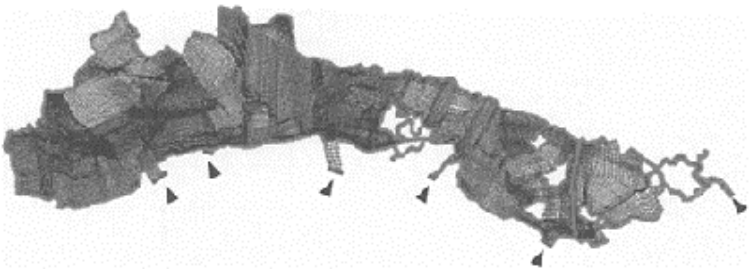

Figure 8. Mesh built for the simulations in the lagoon of Grado and Marano.

source to the mercury area of Idrija in Slovenian territory. This area, close to the Isonzo, nourishes the river that on Italian territory flows into the Lagoon along a channel called Isonzato. The latter hypothesis (Mattassi et al. 1991) ascribes the source to the chemical industries, such as that of chlorine-soda for the production of cellulose in Torviscosa. According to Matassi such chemical industries, located along the river Ausa, have introduced, between 1949 and 1970 around 20kg/day of pollutant and between 1970 and 1984 around 7kg/day. Since 1984, the adoption of more efficient systems of recovery of mercury has led to the substantial disappearance of such sources of pollution.

The two hypotheses have been studied using the implemented model.

5.1 *Mesh*

For the simulations a mesh of 31,041 quadrangular elements was built with mean dimensions varying between 6 and 250m (Fig. 8). The mesh was opportunely thickened in proximity to the lagoon channels.

5.2 *Manning, diffusion and wind coefficients*

A uniform Manning resistance coefficient n=0.020 $m^{-1/3}s$ was assumed on the whole lagoon basin.

This value was obtained by elaborating data from literature and from measurement taken on site, based on the reduction of the wave amplitude and the tidal delay recorded at some measuring points located inside the lagoon (Fig. 9).

As far as concerns the diffusion coefficients D_{xx} and D_{yy}, an isotropic condition was assumed due to the scarce importance of the diffusive process of dispersion in comparison to the advective. The conditions are characterized by a single diffusion coefficient $D=D_{xx}=D_{yy}$=0.25m^2/s deducted from data from literature (Fisher 1979).

The wind shear coefficient was given the value $C_D=1.0\cdot10^{-3}$, obtained from elaborating data found

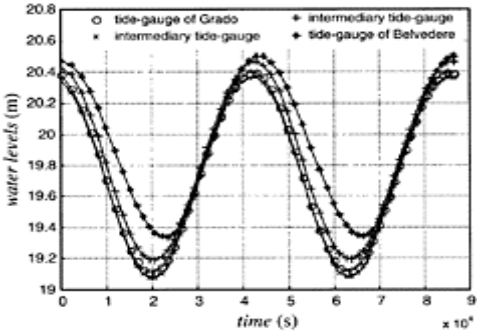

Figure 9. Amplitude reduction and tidal delay between the towns of Grado and Belvedere.

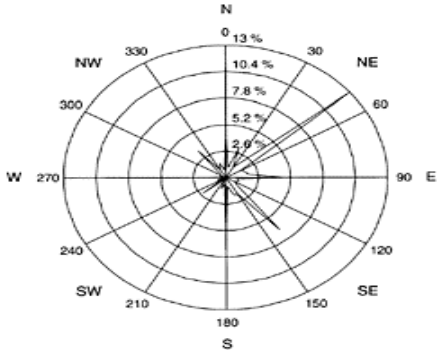

Figure 10. Directional distribution (annual average) of all winds blowing on the lagoon of Grado and Marano.

in literature on the lagoon, which specified changes in the sea water level in correspondence with particular wind event. The value found of C_D agrees with the values proposed by Hicks et al. (1974) in the case of closed basins with reduced water depths.

Finally, to estimate the mean wind velocity W, a statistic analysis was carried out on the data recorded by wind stations considered relevant to the lagoon of Grado and Marano. In Figures 10, 11 are shown the mean directional distribution obtained, this highlight the prevalence of the winds coming from the northeast (Bora) and from the southeast (Scirocco). From this data was drawn out an average occurrence of the Bora

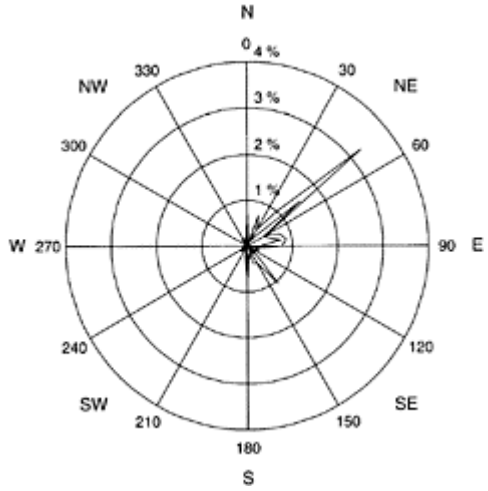

Figure 11. Directional distribution (annual average) of the winds greater than 15m/s blowing on the lagoon of Grado and Marano.

characterized by a speed W=10m/s and direction of origin θ=50°N.

While the Bora blows directly on the free surface of the lagoon water, the Scirocco blowing on the whole Adriatic sea manifests itself with a set-up of the sea due to the wind that increases the tidal level. For this reason the effects of the Scirocco have been included in the amplitude of tidal oscillations.

5.3 *Boundary and initial conditions*

Beach and wall boundary conditions were assumed everywhere except for the six lagoon mouths where tidal oscillations described subsequently were imposed.

As characteristic tides, two oscillations were selected. The first with an amplitude equal to 0.5m and the second 1 m both with periods of 12 hours. These values were deduced by analyses of the data recorded by the tide-gauges of Trieste and Grado keeping in mind the existing correlation between them. The above mentioned values are held

representative of normal oscillations of tides (0.5m) or of medium to high tides (1.0m). These tidal values are already inclusive of the set-up induced by the Scirocco.

As initial conditions the values of velocity and level in the basin are those found after some tidal oscillations.

5.4 *Influx of pollutant from the river Ausa*

The study was conducted for two different tidal amplitudes H with the same period T, in the absence and

Table 2. Characteristic conditions used for the simulation of pollutant coming from the mouth of the Ausa-Corno.

	Tide		Wind		Pollutant	
	H	T	W	θ	Quantity	Time
Test	(m)	(h)	(m/s)	(°N)	(Kg)	(h)
AUS1	0.5	12	0.0	–	20	3
AUS1A	0.5	12	10.0	50	20	3
AUS2	1.0	12	0.0	–	20	3
AUS2A	1.0	12	10.0	50	20	3

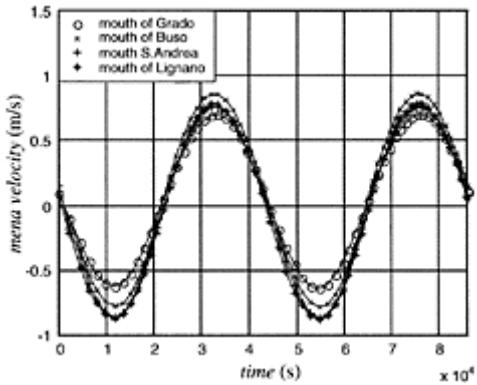

Figure 12. Mean velocities obtained in some lagoon mouths (test AUS1).

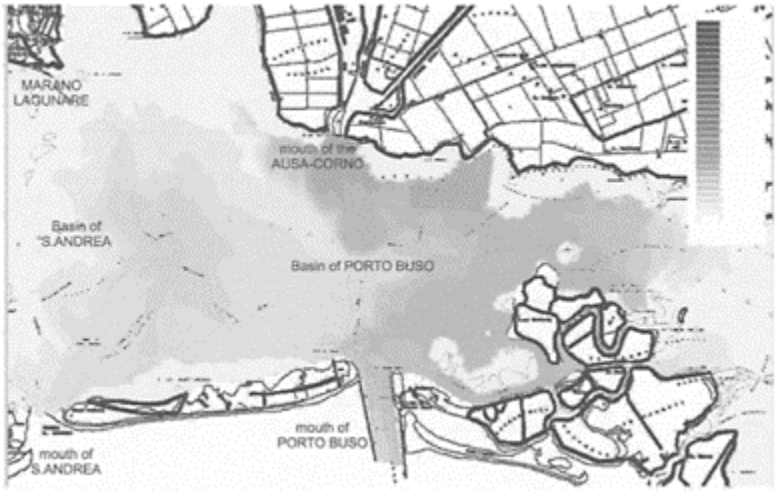

Figure 13. Distribution of the pollutant from the mouth of the Ausa-Corno after 18h of simulation. Tidal amplitude 1m, period 12h, absence of the Bora. Increasing concentration passing from the white tonality to the black.

in the presence of the Bora. The characteristics of the simulation are shown in Table 2. A value of C_{cfl}=0.7 was used for a duration of the simulation equal to 24 hours.

Figure 12 shows the mean velocities obtained in some lagoon mouths with the simulation AUS1. These values like those of the other simulations, are coherent with the only available measures in literature, even if not very recent (Dorigo, 1965).

Figure 13 shows the results after 18 hours of simulation in absence of wind (test AUS2) and Figure 14 shows those in the presence of the Bora (test AUS2A).

In the absence of wind (Fig. 13) a portion of the total mass of pollutant introduced from the mouth of the Ausa-Corno remains as diluted pollutant inside the basin of Porto Buso and the remainder goes out to sea through the Porto Buso channel. Instead, in the presence of wind (Fig. 14) the level of concentration of pollutant remains rather high because the hydrodynamic regime induced by the wind prevents an immediate exit of the pollutant from the Lagoon. Furthermore, the mass of polluted water is pushed towards the west, involving areas such as Marano and Lignano, apparently immune from a phenomenon of this type.

5.5 *Influx of pollutant from the river Isonzo*

In this simulation we assumed an immission of pollutant into the lagoon from the river Isonzo (along the Isonzato channel) equal to 10kg for a duration of 2 hours; this amount is considered to be representative of the mercury coming from Slovenia.

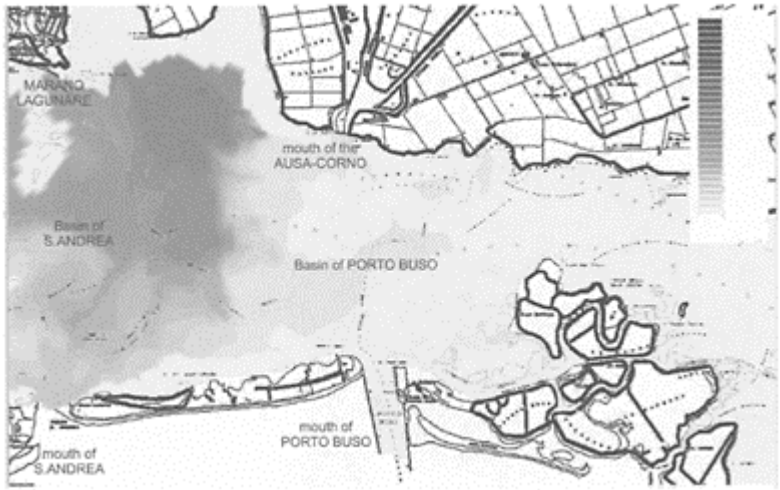

Figure 14. Distribution of the pollutant from the mouth of the Ausa-Corno after 18h of simulation. Tidal amplitude 1m, period 12h, presence of the Bora (10m/s). Increasing concentration going from the white tonality to the black.

Table 3. Characteristic conditions used for the simulation of pollutant from the River Isonzo (through Isonzato channel).

	Tide		Wind		Pollutant	
	H	T	W	θ	Quantity	Time
Test	(m)	(h)	(m/s)	(°N)	(Kg)	(h)
ISO1	0.5	12	0.0	–	10	2
ISO1A	0.5	12	10.0	50	10	2
ISO2	1.0	12	0.0	–	10	2
ISO2A	1.0	12	10.0	50	10	2

Also in this case, after fixing the quantity of introduced pollutant, the study was conducted for two different oscillations of tide (0.5m and 1m of amplitude) both in the absence and in the presence of the Bora (Tab. 3). Also in this application a value C_{cfl}=0.7 was used and the duration of the simulation was 24 hours.

In these circumstances, the results both in the presence or the absence of wind are almost the same due to the embankment of the road that connects Grado to Belvedere. In Figure 15 the results after 18 hours of simulation in the presence of the Bora are shown (test ISO2A).

As can be seen (Fig. 15) in this case, even if the total amount of pollutant introduced is equal to that of the previous simulations (20kg), its concentration remains much higher.

Such a phenomenon can be ascribed to the presence of the Grado-Belvedere road embankment that prevents water exchange between the East (Basin of Primero) and the West (Basin of Grado) part of the lagoon, with the only exception of two small channels (Figariola and Grado). The analysis of the hydrodynamic field also shows the scarce vitality of the basin of Primero, that has low velocity and water level oscillations if compared with the other basins.

Returning to the dispersion of pollutant, this kind of hydrodynamic isolation of the Basin of Primero substantially limits the passage of pollutant from the Isonzato channel over the Grado-Belvedere road embankment. Most of the small amount of pollutant that passes beyond the road remains near the road itself while the rest leaves the lagoon through the mouth of Grado.

6 CONCLUSIONS AND FUTURE WORK

A finite volume numerical model was developed for the study of the dispersion of a pollutant dissolved in shallow water. Many tests of verification showed its reliability and accuracy. Some hydrodynamic tests carried out on the lagoon of Grado and Marano confirmed these characteristics, showing coherence between numerical results and experimental data available in literature.

Subsequently the model was applied to the study of the dispersion of pollutants dissolved in the lagoon of Grado and Marano. The results showed the influence that the Bora and the road embankment that connects the town of Grado and Belvedere have on the dynamics of such a phenomenon.

This study showed that a pollutant, for instance mercury, from the river Isonzo, could cross the road embankment only in a small part, and most of it would anyway laeve the lagoon through the mouth of Grado. Thus, it is not very reasonable to ascribe the pollution of the West side of the lagoon (lagoon of Marano) to the Isonzo river. Moreover, a source of pollutant from the river Ausa could easily propagate towards Marano and Lignano, especially in the presence of the Bora. This could justify the presence of mercury in the lagoon of Marano too, with concentrations similar to those present in the basin of Primero.

Improvements of the implemented model, especially for long periods of simulation, can be obtained using techniques of interpolation ENO and WENO (Jiang & Shu, 1996) that allow a more accurate solution of the local ‘Riemann problem’ (Petti & Bosa 2003).

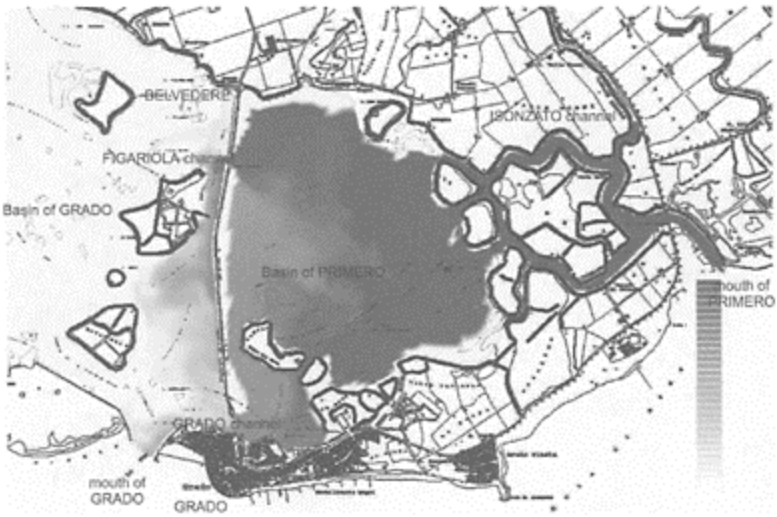

Figure 15. Distribution of the pollutant from the River Isonzo (through Isonzato channel) after 18h of simulation. Tidal amplitude 1m, period 12h, presence of the Bora (10m/s). Increasing concentration going from the white tonality to the black.

REFERENCES

Dorigo, L. 1965. *The lagoon of Grado and Marano and its mouths. Researches and hydraulic measures.* Magistrato alle Acque, Ufficio Idrografico. Venezia: Grafiche Gasparoni. (In Italian).

Dragoslav, L.S. & Heinz, G.S. 2001. Accurate Two-Dimensional Simulation of Advective-Diffusive-Reactive Transport. *Journal of Hydraulic Engineering* 127(9): 728–737.

Fisher, H.B., List, E.J., Koh, R.C.Y., Imberg, J. & Brooks, N.H. 1979. *Mixing in Inland and Coastal Waters.* New York: Academic Press.

Hicks, B.B., Drinklow, R.L. & Grauze, G. 1974. Drag and bulk transfer coefficients associated with a shallow water surface. *Boundary-Layer Meteorol.* 6:287–297.

Hirsch, C. 1988, *Numerical computation of internal and external flows.* Vol. 1 & 2. New York: John Wiley & Sons.

James, I.D. 2002. Modelling pollution dispersion, the ecosystem and water quality in coastal waters: a review. *Environmental Modelling & Software* 17:363–385.

Jiang, G. & Shu, C.W. 1996. Efficient implementation of weighted ENO schemes. *Journal of Computational Physics* 126:202–228.

Ligget, J.A. 1994. *Fluid Mechanics.* Singapore: McGraw-Hill International Editions.

Mattassi, G., Daris, E, Nedoclan, G., Crevatin, E., Modonutti, G.B. & Lach, S. 1991. The water quality of the Lagoon of Grado and Marano. *Regione Autonoma Friuli Venezia Giulia. Trieste: U.S.L n. 8 "Bassa Friulana"* (In Italian).

Petti, M. & Bosa, S. 2003. Accurate shock-capturing finite volume method for advection-dominated flow and pollution transport. *To be submitted.*

Prandle, D., Jago, C.F., Jones, S.E., Purdie, D.A. & Tappin, A. 1993. The influence of horizontal circulation on the supply and distribution of tracers. *Philosophical Transactions of the Royal Society of London* A343:405–421.

Stoker, J.J. 1957. *Water waves.* New York: Interscience.

Toro, E.F. 1999. *Riemann solvers and numerical methods for fluid dynamics, Second Edition.* New York: SpringerVerlag.

Whitham, G.B. 1974. *Linear and Nonlinear Waves.* New York: Wiley.

Yanenko, N.N. 1971. *The Method of Fractional Steps.* Berlin: Springer-Verlag.

Numerical simulation of transport processes in not uniform turbulent streams

I.Cotto & R.Revelli
Dipartimento di Idmulica, Trasporti ed Infrastrutture Civili, Politecnico di Torino
Corso Duca degli Abruzzi, Torino, Italy

River Flow 2004—Greco, Carravetta & Della Morte (eds.)

ABSTRACT: The numerical simulation of the advection dispersion equation with non constant parameters is presented in order to simulate the behaviour of a pollutant in a natural stream with variable geometric and dynamic characteristics, i.e. with a non constant water depth, mean velocity and dispersion coefficient. A collocation-interpolation method based on *sinc* function is used and the results are presented in the form of temporal and spatial moments. Both conservative and non conservative substances are accounted for, this latter with a decay reaction rate both linear and non linear. The results show in particular the behaviour of the centroid, variance and skewness depend on the velocity variation along the river and decay reaction rate. It was also found that the influence of the water depth change is less important than the velocity variation.

1 INTRODUCTION

The presence of pollutants and hazardous substances in a natural stream is a problem of great interest both from the speculative and applicative points of view. It is in fact well known that this problem is important in the environmental economic debate and how a good comprehension and description of the phenomena are necessary to apply correct development and management politics.

Since the early fifties a great deal of work has been devoted to describing the behaviour of the substances in a turbulent stream and natural flow and one of the main theoretical results is the formulation of the advection-dispersion equation (e.g. Taylor 1953, 1954, Aris 1956, Fisher et al. 1979) with the description and formalization of the effect of phenomena such as turbulent diffusion and shear dispersion. This classical

advection-dispersion equation however generally considers a uniform stream and if a non conservative substance is taken into consideration the decay reaction is of a linear type.

Under these assumptions the result of the mathematical problem for an instantaneous release is of a Gaussian type form for the concentration (e.g. Fisher et al. 1979); an integral convolution, therefore, makes it possible to find the mathematical form of the concentration distribution for each form of the release. On the contrary, it is not normally possible to find an analytical solution with a non uniform stream or non linear decay reaction.

Starting from these fundamental results, many studies over the last decades have been dedicated to refining the Taylor model in order to better describe some features that are present in natural streams. This has principally been due to the fact that a great number of laboratory and field studies (dedicated to validating the analytical models or to fitting the appropriate parameters), recognised a bias between the theory and the data (for example, the problem known as “skewness persistence”, etc…).

It is now clear that the presence of transfer mechanisms, of a physical, chemical or biological nature, between the main stream and the boundaries (river bank, bed, free surface), could give rise to discrepancies, in particular due to the occurance of long tails in the concentration distribution (e.g. Hays et al. 1966, Trackston & Schnelle 1970, Day et al. 1975, Valentine & Wood 1977, Benkala et al. 1980, Nordin & Troutman 1980, Kim et al. 1990, Czernuszenko & Rowinski 1995, Hart et al. 1995, Worman 1998, Schmid 2002).

Even sorption-desorption phenomena due to the presence of suspended sediment (e.g. Ng & Yip 2002, Revelli & Ridolfi 2002, 2003) or the kinetics between the river and the neighbouring aquifers (e.g. Kim et al. 1990, Worman 2000) are able to modify the form of the concentration breakthrough.

As in Taylor’s model, a quite general characteristic of the models, that are generated according to the previous considerations (i.e. transient storage equation, aggregated dead zone models, stochastic formulation etc…), is to assume a uniform stream, or at least to describe the river as a sum of different reaches with constant characteristics. The possibilities of a variation in the parameters along the river (Zoppou & Knight 1997, Gupta & Cvetkovic 2000) are not often taken in consideration. This is principally due to the fact that in this case it is not generally possible to find an analytical solution to the problem and methods like moments analysis cannot be applied.

The present work intends to join in the debate with a numerical analysis of a non constant coefficient model. In particular, the advection-dispersion equation will be simulated starting from a stream with quantities such as water depth, mean velocity or dispersion coefficient which are variable along the stream. In addition the chemical, physical or biological transfer mechanisms with boundaries or suspended load will be neglected.

The possibilities of simulating the behaviour of a non conservative substance will also be taken into consideration. In particular both the linear and non linear decay rate will be considered in order to model the common chemodynamic nonlinearities (Schwarzenbach et al. 1993, Brezonik 1996, Schnoor 1996).

The paper is organized as follows: in the next section the model is briefly mentioned, and the solution method is presented. The results of several simulations are given in the last sections and some conclusion are drawn.

2 MATHEMATICAL PROBLEM

Let us consider a one dimensional, steady, not uniform turbulent channel flow with a mild slope i_b. A reference system with the x-coordinate along the channel is introduced. The stream has a depth $H(x)$ and a mean velocity $U(x)$.

Without any lack of generality, we assume that the hydraulic geometry of the channel can be expressed as a power law function along the length of the stream (Leopold & Maddock 1953, Gupta & Cvetkovic 2000), so that

$$H(x) = a_H \cdot \left(1 + \frac{x}{L}\right)^{b_H} \tag{1}$$

$$U(x) = a_U \cdot \left(1 + \frac{x}{L}\right)^{b_U} \tag{2}$$

where a_H, and a_U are dimensional constants; b_H and b_U are dimensionless constants; and L is a reference length, which will be assumed to be equal to the length of the channel.

Let us also suppose that a chemical is dispersed in the stream and let us define $C=C(x, t)$ as the averaged concentration of the chemical per volume of water. If we suppose that there is a local balance between the longitudinal advective transport and the cross-sectional turbulent diffusive transport in any point of the stream, and that the chemical is uniformly distributed along the vertical coordinate, we can write

$$\frac{\partial C}{\partial t} + \frac{\partial}{\partial x}[U(x)C] = \frac{\partial}{\partial x}\left[K(x)\frac{\partial C}{\partial x}\right] + R \tag{3}$$

where $K(x)$ is the dispersion coefficient; and R accounts for the decay reaction.

In order to describe the dispersion phenomena we can write (Elder 1959), for sake of simplicity,

$$K(x) = 5.93 \cdot u_* \cdot H = a_K\left(1 + \frac{x}{L}\right)^{b_K} \tag{4}$$

where $u_*(x)=(gi_bH)^{0.5}$ is the friction velocity and g is the gravity acceleration, therefore so that $a_K=18.57 i_b^{1/2} a_H^{3/2}$ and $b_K=3/2 b_H$.

Rearranging 1 gives

$$\frac{\partial C}{\partial t} = [(K' - U)]\frac{\partial C}{\partial x} + K\frac{\partial^2 C}{\partial x^2} - U'C + R \tag{5}$$

where the prime means the derivative with respect to x. By substituting the Equations 2, 3 and 4 in the Equation 5, the mathematical model is recovered.

The mathematical statement of the problem related to Equation 5 can be obtained by linking the previous equations to suitable initial and boundary conditions. The boundary conditions are defined by

$$C(0, t)=C(L, t)=0 \tag{6}$$

while, as an initial condition, we require

$$C(x, 0)=\varphi(x) \tag{7}$$

where $\varphi(x)$ can be any function, e.g. a Dirac delta, in order to simulate an instantaneous release.

3 NUMERICAL METHOD

The mathematical problem of the Equations 5, 6 and 7 is numerically integrated using an interpolationcollocation method based on *sinc* functions (Bellomo & Ridolfi 1995) that is particularly suitable for nonlinear models and to simulate wave phenomena (Revelli & Ridolfi 2004). Although the method has been presented in several papers let us here recall the main steps while reference can be made to the works by Bellomo & Ridolfi (1995) and Revelli & Ridolfi (2004) for a detailed description and for an extensive bibliographic review.

The method is a modification of the differential quadrature method proposed by Bellman et al. (1972) and Satofuka (1983). It consists of the transformation of the Equation 5 into a system of ordinary differential equation with a spatial discretisation of the variable $C(x, t)$ in a finite number of points and considering the values of the variable itself in the spatial nodes as new unknowns. Let us choose, in the spatial domain, $x \in [0, L]$ a number n of collocation equispaced points

$$x_0=0,\ldots, x_i=ih,\ldots, x_{n+1}=L \tag{8}$$

with $i=0,\ldots, n+1$ and $h=L/(n+1)$. We then collocate an interpolating function $S_i(x)$ in each point so that the solution of the Equation 5 can be approximated with the summation

$$C(x,t) \cong \sum_{i=0}^{n+1} S_i(x)u_i(t) \tag{9}$$

where $u_i(t)=u(t, x_i)$. In this way each term of 9 is given by the product of two functions: the first which depends on space and the second which depends on time. These latter functions $u_i(t)$ are the new unknowns of the problem.

In this work we have choosen a *sinc* as the interpolating function (for alternative possibilities see for example Bonzani 1997)

$$S_i(x) = \frac{\sin z_i}{z_i} \qquad \text{and} \qquad S_i(x_j) = \delta_{ij} \tag{10}$$

with $z_i=\pi(x/h-i)$ and δ Kronecker's delta.

By placing the Equation 10 in the Equation 9 and deriving with respect to x we obtain

$$\frac{\partial u}{\partial x} = \sum_{p=0}^{n+1} a_{ip} u_p \qquad \text{and} \qquad \frac{\partial^2 u}{\partial x^2} = \sum_{p=0}^{n+1} b_{ip} u_p \tag{11}$$

where

$$a_{pi} = \frac{\pi}{h}\frac{z_{pi}\cos z_{pi} - \sin z_{pi}}{z_{pi}^2} \tag{12}$$

$$b_{pi} = \left(\frac{\pi}{h}\right)^2 \frac{(2 - z_{pi}^2)\sin z_{pi} - 2z_{pi}\cos z_{pi}}{z_{pi}^3} \tag{13}$$

with $a_{ii}=0$ and $b_{ii}=-1/3(\pi/h)^2$.

The substitution of the Equations 9–13 in the Equation 5 transforms it into a system of ordinary differential equation that can be solved, linked to the proper boundary and initial conditions, with the aid of classical iterative methods such as the RungeKutta, multi-step Adams-Multon or Adams-Bashforth methods.

4 TEMPORAL AND SPATIAL MOMENTS

The solution of Equations system 5–7 is analysed through the use of the temporal and spatial moments; some features of the solution of the constant coefficient model can in fact be given in terms of the Laplace transform of the solution itself and with the consideration that the moments can be calculated by expanding in Taylor series the Laplace transform itself (e.g. Aris 1956, Nordin & Troutman 1980, Czernuszenko & Rowinski 1995, Schmid 2002).

Temporal (central) moments of the *p-th* order can be defined as

$$\mu_t^p(x) = \int_0^L (t - m_t^1)^p C(x,t)\cdot dt \tag{14}$$

and similarly the spatial (central) moment of the *p-th* order can be defined as

$$\mu_x^p(t) = \int_0^T (x - m_x^1)^p C(x,t)\cdot dx \tag{15}$$

where m_t^p and m_x^p are temporal and spatial noncentral moments of the *p-th* order respectively.

It is important to note that in 14 and 15 we have replaced the usual superior limit $+\infty$ which *T* and *L* which are the time length simulation and the channel length, respectively; this is important for the subsequent discussion of the results.

If we normalize the concentration with respect to m^0 we can find the links between 14 and 15 and the centroid. In this way we are able to find the centroid *m*, variance σ^2, and skewness coefficient *G:*

$$m_x = m_x^1 \quad \text{and} \quad m_t = m_t^1 \tag{16}$$

$$\sigma_x^2 = \mu_x^2 \quad \text{and} \quad \sigma_t^2 = \mu_t^2 \tag{17}$$

$$G_x = \mu_x^3\sigma_x^{-3/2} \quad \text{and} \quad G_t = \mu_t^3\sigma_t^{-3/2}. \tag{18}$$

In the case of the constant coefficient model and $\varphi(x)$ as a Dirac delta it is possible to find an analytical formulation for 16–18 (e.g. Nordin & Troutman 1980). In this case, for the spatial case, it is easily to obtain

$$\begin{cases} m_{x,0} = a_U t \\ \sigma^2_{x,0} = 2a_K t \\ G_{x,0} = 0 \end{cases} \tag{19}$$

while for the temporal case one obtains

$$\begin{cases} m_{t,0} = \dfrac{1}{a_U^2}(xa_U + 2a_K) \\ \sigma^2_{t,0} = 2\dfrac{a_K}{a_U^4}(xa_U + 4a_K) \\ G_{t,0} = (2a_K)^{1/2}\dfrac{(3xa_U + 16a_K)}{(xa_U + 4a_K)^{3/2}}. \end{cases} \tag{20}$$

5 SIMULATIONS AND RESULTS

Using the previously described numerical method, the advection-dispersion equation with nonconstant parameters is simulated. The set of parameters that we kept constant for the whole series of simulations are i_b=0.001, L=33.6km, T=9hr, a_H= 1.27m and a_U=0.48ms^{-1} which means a_K=0.84m^{2}s^{-1}. These parameters are quite similar to the set proposed by Gupta & Cvektovic (2000) and Revelli et al. (2004) so useful comparison can be made. The parameters that we changed are b_H and b_U which we varied from 0 to 0.6. The analytical solution corresponding to the constant coefficient is given by b_H=b_U=0.

The chosen parameters imply a variation of the velocity from the initial value of 0.48ms^{-1}(x=0) to 0.73ms^{-1} for the highest $b_U(x=L)$ and a water depth variation in the river from the initial value of 1.27m (x=0) to 2.22m for the highest $b_H(x=L)$. Correspondingly the variation of dispersion coefficient lies between 0.84m^{2}s^{-1} to 1.94m^{2}s^{-1}

We changed the value of b_H or b_U in every simulation keeping the others identically equal to zero: in this way the influence of each single parameter it easily recognizable.

Regarding the initial condition we always used the same function i.e. a gaussian type form in order to simulate a common source form.

$$C(x, 0) \equiv \varphi(x) = 25.6\exp[-1.8\cdot 10^{-6}(x-3000)^2]. \tag{21}$$

We chose a spatial discretisation grid with n=300 while the system of ordinary differential equations was integrated with the Adam predictor-corrector method with an adaptative time step.

5.1 *Conservative substances (R=0)*

Figure 1 shows the spatial centroid versus time for different values of the parameter b_U. The values were normalized with respect to $m_{x,0}$, i.e. value given by the Equation 19 of

the constant parameter model. The centroid increases regularly and at the end of the simulation it can be greater than at the start by about

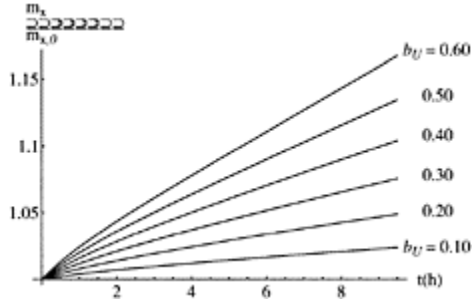

Figure 1. Spatial behaviour of the centroid for different values of b_U(b_H=0). The values are normalized with respect to the constant parameter value $m_{x,0}$.

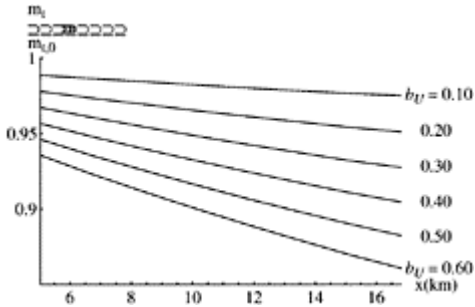

Figure 2. Temporal mean behaviour for different values of b_U(b_H=0). The values are normalized with respect to the constant parameter value $m_{t,0}$.

15–20% for b_U=0.60. The same behaviour occurs if we consider the b_H variation but the change is in the order of 0.1%. This is a characteristic that is almost constant over the whole range of simulations: there is a considerable influence of b_U and a practically nonexisting influence of b_H.

Figure 2 shows the behaviour of the temporal mean for different values of parameter b_U. Even in this case, the influence of b_H is unimportant (a few fractions of unity). The behaviour in this case is different from the previous example, because there is a diminishing value of the rate with respect to time.

The difference, with respect to the constant value model, can be up to 10% and the centroid exhibits a practically linear growth even for non constant coefficient models.

The spatial range in Figure 2 was chosen in order to calculate the temporal moment for the whole cloud; for this reason it results to be lesser than the total spatial considered domain [0, L]. Normally analytical solutions do not suffer from this limitation (see Equation 14) because an indefinite channel length and a simulation time that is greater than the time necessary

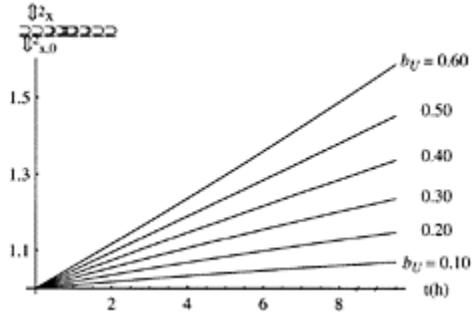

Figure 3. Spatial variance behaviour for different values of b_U(b_H=0). The values are normalized with respect to the constant parameter value $\sigma^2_{x,0}$.

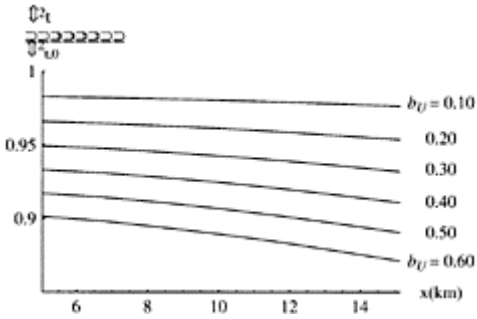

Figure 4. Temporal variance behaviour for different values of b_U(b_H=0). The values are normalized with respect to the constant parameter value $\sigma^2_{t,0}$.

for the whole cloud to reach the prefixed section are often assumed.

The influence on the variance is more marked. Figures 3 and 4 show the spatial and temporal variance respectively, for different values of b_U. The behaviour is similar to that of the corresponding centroids. As expected, there is a general growth in the dimensions

of the clouds and this growth is practically linear for the spatial variance while a deviation from linearity is evident when considering the temporal variance. It is important to note that the influence of b_U is up to 60% for spatial case while for the temporal one we find a difference up to 15% with respect to the constant value model. Even for b_H variations, there is a similar influence but it is less marked: about 5–6% for both cases.

As far as the spatial skewness is concerned, the simulation shows that a change in parameters does not change the value of the form of the cloud: i.e. the skewness remains practically equal to zero and the concentration shows evidence of a Gaussian type form during time evolution.

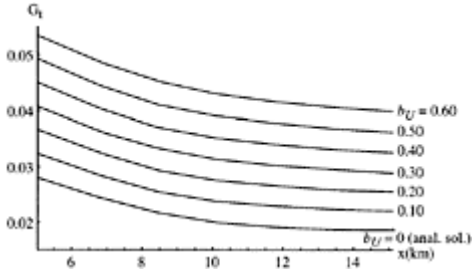

Figure 5. Temporal skewness behaviour for different values of $b_U(b_H=0)$.

However, the temporal skewness, for different values of b_H or b_U exhibits an always decreasing behaviour and tends to $G_{t,0}$ which tends to zero as $x\rightarrow\infty$ as $x^{-1/2}$ (Nordin & Troutman 1980) even though the influence of b_H is very low as in previous cases. The skewness now ever always decreases and the difference between the constant parameter model is of the order of +50% at the start of the considered spatial domain (Fig. 5).

5.2 *Non conservative substances ($R\neq0$)*

The result of the evolution of a non conservative substances is presented as a second series of simulations. In particular, we suppose that a decay rate exists and the most general case is considered in which the decay is nonlinear. The reaction rate, R in the Equation 5 is therefore modelled according to the power law

$$R=-\lambda C^r \tag{22}$$

where λ is the decay rate constants—with units of measure $\mathrm{Kg}^{1-r}\mathrm{m}^{3r-3}\mathrm{s}^{-1}$—and $r\geq1$ in order to model the common chemodynamic nonlinearities (Brezonik 1996, Schnoor 1996, Schwarzenbach 1993).

It is possible to find the analytical formulation for the linear case (r=1), for the constant parameter model, corresponding to the Equations 19 and 20. In particular for the temporal case we found (e.g. Schmid 1996)

$$\begin{cases} m_{t,0,r} = \dfrac{1}{\alpha^2}(x\alpha + 2a_K) \\ \sigma^2_{t,0,r} = 2\dfrac{a_K}{\alpha^4}(x\alpha + 4a_K) \\ G_{t,0,r} = (2a_K)^{1/2}\dfrac{(3x\alpha + 16a_K)}{(x\alpha + 4a_K)^{3/2}} \end{cases} \tag{23}$$

where $\alpha = (a_U^2 + 4a_K\lambda)^{1/2}$, and $\alpha \to a_U$ as $\lambda \to 0$.

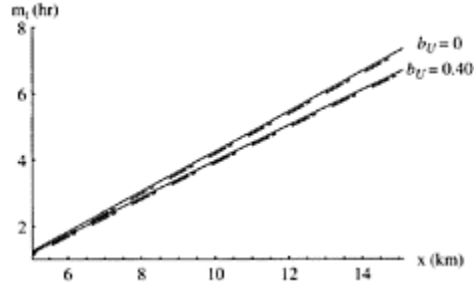

Figure 6. Non conservative substances: temporal centroid behaviour for two different values of b_U·r=1 (dashed line) and r=2 (dotted line). The continuous line represents the conservative substances (no decay).

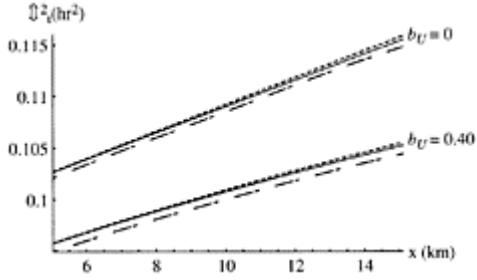

Figure 7. Non conservative substances: temporal variance behaviour for two different values of b_U·r=1 (dashed line) and r=2 (dotted line). The continuous line represents conservative substances (no decay).

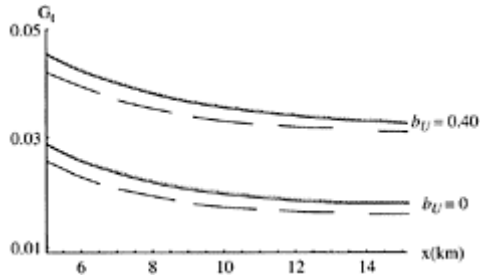

Figure 8. Non conservative substances: temporal skewness behaviour for two different values of b_U·r=1 (dashed line) and r=2 (dotted line). The continuous line represents conservative substances (no decay).

Figures 6–8 show the behaviour of the temporal centroid, variance and skewness respectively for the two cases corresponding to the constant values model (b_U=0) and non uniform stream (b_U=0.40), both for the case with conservative substance, i.e. no decay reaction (r=0), linear reaction (r=1) and not linear reaction (r=2). The decay constant was always kept equal to $2 \cdot 10^{-4} \mathrm{Kg}^{1-r}\mathrm{m}^{3r-3}\mathrm{s}^{-1}$ for each case, which means a half-life time of approximately 1hr for the linear decay. The dashed line in all the figures represents the case r=1, the dotted line represents the case r=2 and the continuous line represents the conservative substances behaviour.

It can be noted that the trend of the curves is the same as the trend of the centroid, variance and skewness without the decay term. This is consistent, for example, with the results found by Schmid (1995) for the transient storage equation whit decay substances.

In particular it can be seen in Figures 7 and 8 that the simulations with r=2 are very similar to the case r=0 (in Figure 6 the two curves are practically coincident), while r=1 implies the same different value of variance and skewness. This is due to the fact that high r means a low disappearing mass (see Equation 22) so it is reasonable to find the same result as the conservative case due to the short observation time interval; in other words, if the decay order r is much greater than 1, the behaviour is like the conservative case so the results of the previous simulations can be retained. In general the centroid and the variance decrease for an increase in b_U while the corresponding skewness is decreases.

As far as the variance is concerned (Fig. 7) the simulation shows that if r=1 the values are lower (1%) than the conservative case, and the opposite occurs for r=2. The same appears for the skewness behaviour (Fig. 8). A first explanation for this unexpected result could be the complex interaction between the nonlinearities present in the coefficients of the model and in the decay term itself, but this requires further studies. In every case, when it exists, the curves exactly match the analytical solution given by 23.

6 CONCLUSIONS

The numerical simulation of the advection-dispersion equation with non constant parameters is presented in this note. In particular, a collocation-interpolation method based on the use of a *sinc* function is used due to its great ability to deal with nonlinear models. The presented results include the case of conservative substances and non conservative substances with linear and non linear decay reactions.

The results are presented in the form of temporal and spatial moments (i.e. centroid, variance and skewness) and, when possible, the comparison with analytical outcomes is also given. In particular, the results show that the behaviour of the centroid, variance and skewness depend on the velocity variation along the river and the decay reaction rate.

In general, for a conservative substance, an increase in velocity along the river causes a decrease in the temporal centroid displacement and variance, while the skewness seems to increase. The same specific considerations are valid for non conservative substances with some additional considerations regarding the influence of the non linear decay rate.

REFERENCES

Aris, R. 1956. On the dispersion of a solute in a fluid flowing through a tube. *Proc. R. Soc. Lon. A.* 235:67–77.

Bellman, R., Kasher, B. & Casti, J. 1972. Differential quadrature: solution of nonlinear partial differential equations. *J. Comp. Phys.* 10:40–52.

Bellomo, N. & Ridolfi, L. 1995. Solution of linear initial-boundary value problems by sinc collocationinterpolation methods. *Comp. Math. Appl.* 29:15−28.

Bencala, K.E. & Walters, R.A. 1983. Simulation of solute transport in a mountain pool-and-riffle stream: a transient storage model. *Water Resour. Res.* 19:718–724.

Bonzani, I. 1997. Solution of nonlinear evolution problems by parallelized collocation-interpolation methods. *Computers Math. Applic* 34:71–79.

Brezonik, P.L. 1996. *Chemical kinetics and process dynamics in aquatic system.* Boca Raton, FL: Lewis.

Czernuszenko, W. & Rowinski, P.M. 1997. Properties of the dead-zone model of longitudinal dispersion in rivers. *Water Resour. Res.* 35:491–504.

Day, T. 1975. Longitudinal dispersion in natural channels. *Water Resour. Res.* 11:909–917.

Elder, J.W. 1959. The dispersion of marked fluid in turbolent shear flow. *J. Fluid Mech.* 5:544–560.

Fisher, H.B., List, E.J., Koh, R.C.Y., Imberger, J. & Brooks, N. 1979. *Mixing in Inland and Coastal Water.* San Diego: Academic.

Guapta, A. & Cvetkovic, V. 2000. Temporal moment analysis of tracer discharge in streams: combined effect of physicochemical mass transfer and morphology. *Water Resour. Res.* 36:2985–2997.

Hays, J.R., Krenkel, P.A. & Schnell, K.B. 1966. Mass transport mechanisms in open-channel flow. *Tech. Rep.* 8. *Vanderbuilt Univ.* Nashville, Tenn.

Hart, D.R. 1995. Parameter estimation and stochastic interpolation of the transient storage model for solute transport in streams. *Water Resour. Res.* 31:323–328.

Leopold, L.B. & Maddock Jr. 1953. The hydraulic geometry of stream channels and some physiographic implications. *U.S. Geol. Surv. Prof. Pap.* 252.

Kim, B.K., Jackman, A.P. & Triska, F.J. 1990. Modeling transient storage and nitrate uptake kinetics in a flume containing a natural periphyton community. *Water Resour. Res.* 26:505–515.

Ng, C.O. & Yip, T.L. 2001. Effects of kinetic sorptive exchange on solute transport in open channel flow. *J. Fluid Mech.* 446:321–345.
Nordin, C.F. & Troutman, B.M. 1980. Longitudinal dispersion in rivers: the persistence of skewness in observed data. *Water Resour. Res.* 14:123–128.
Revelli, R. & Ridolfi, L. 2002. Influence of suspended sediment on the transport processes of nonlinear reactive substances in turbulent stream. *J. Fluid Mech.* 472: 307–331.
Revelli, R. & Ridolfi, L. 2003. Transport of reactive chemicals in sediment-laden stream. *Advances in Water Resources* 26: 815−831.
Revelli, R. & Ridolfi, L. 2004. Sinc collocation-interpolation method for the simulation of nonlinear waves. *Comp. Math. Appl.* 46(8–9):1443–1445.
Satofuka, A 1983. *A new explicit method for the solution of parabolic differential equations.* Numerical methodologies and properties in heat transfer. New York: Hemisphere.
Schmid, B.H. 1995. On the transient storage equations for longitudinal solute transport in open channel: temporal moments accounting for the effects of first-order decay. *Journal of Hydraulic Research* 33: 595–608.
Schmid, B.H. 1997. Analytic solution of the transient storage equations accounting for solute decay. *Proc. 27th IAHR Congress, san Francisco, Theme B*1:15–20. *Journal Hydraul. Res.* 33:595–610.
Schmid, B.H. 2002. Persistence of Skewness in longitudinal dispersion data: Can the dead zone model explain it after all?. *Journal of Hydraulic Engineering* 128:848–854.
Schnoor, J.L. 1996. *Environmental modeling.* New York: Wiley.
Schwarzenbach, R.P., Gschwend, P.M. & Imboden, D.M. 1993. *Environmental organic chemistry.* New York: Wiley.
Taylor, G.I. 1953. Dispersion of soluble matter in solvent flowing slowly through a tube. *Proc. R. Soc. Lond. A.* 219: 186–203.
Taylor, G.I. 1954. The dispersion of matter in turbulent flow through a pipe. *Proc. R. Soc. Lond. A.* 223:446–468.
Thibodeaux, L.J. 1996. *Environmental chemodynamics.* 2nd Ed. NewYork: Wiley.
Trackston, E.L. & Schnelle, K.B. 1970. Predicting effects of dead zones on stream mixing. *Journal of the Sanitary Engineering Division* 96:319–331.
Valentine, E.M. & Wood, I.R. 1977. Longitudinal dispersion *with dead zones. Journal Hydmul, Div. Soc. Civ. Eng.* 103: 975–990.
Worman, A. 1998. Analytical solution and timescale for transport of reacting solutes in river and streams. *Water Resour. Res.* 34:2703–2716.
Worman, A. 2000. Comparison of models for transient storage of solutes in small streams. *Water Resour. Res.* 36: 455–468.
Zoppou, C. & Knight, J.H. 1997. Analytical solutions for advection and advection-diffusion equations with spatially variable coefficients. *Journal of Hydraulic Engineering* 123:144–148.

Estimation of longitudinal dispersion and storage zone parameters

P.M.Rowiński, T.Dysarz & J.J.Napiórkowski
Institute of Geophysics, Polish Academy of Sciences, Warsaw, Poland

River Flow 2004—Greco, Carravetta & Della Morte (eds.)

ABSTRACT: Numerical computations are presented for the longitudinal transport of passive, conservative solutes in an actual river channel with the inclusion of its geometrical complexities. Only one-dimensional conditions after a substance has become fully mixed across the depth and width of the river are concerned. In such case a model describing the processes of advection, longitudinal dispersion, and also temporary storage is suitable for the description of the spread of admixture. A special emphasis is put on the method of the identification of model parameters which is based on a specially designed optimisation procedure using random control search algorithm. The algorithm is one of the random global optimisation techniques and particularly its realization by means of the CRS2 method. Two different situations are considered, namely a linear version in which one can assume that the mean velocity does not vary along the channel course and when the model parameters are constant and the nonlinear version implying channel nonuniformity (and variability of model parameters along the channel). The results of tracer tests carried out in the selected reach of the Wkra river in Central Poland have been used in the analyses. A model taking into account the changes of model parameters along river channel proved to provide better results when compared to the experimental data but the parameter identification in such case is computationally much more expensive.

1 INTRODUCTION

Various versions of the storage-zone models have become increasingly popular for the calculation of the longitudinal dispersion of a solute in a river with irregular cross-sections (e.g. Czernuszenko & Rowiński 1997; Czernuszenko et al. 1998; Manson 2000; Thackston & Schnelle 1970, etc.). On top of the mixing processes (advection and dispersion) this model is the reflection of the existence in the rivers of stagnant zones of water that are stationary relative to the faster moving waters near the center of the

channel. It constitutes a kind of a compromise between data consuming two-dimensional models and the simpler one-dimensional approach. Mathematically similar approach may pertain to the exchange between the streaming water and the subsurface bed sediment, namely to hyporheic exchange causing the retardation of the solute transfer (e.g. Packman & Bencala 2000; Fernald et al. 2001; Jonsson 2003). As is usually the case in physically based models the main difficulty is the estimate of the proper values of the parameters occurring in the model. All those parameters have relatively clear physical interpretation and as such should assume logical values. It should be noted that even in the much simpler case of the application of the Fickian type advection-dispersion equation, the evaluation of the dispersion coefficient constitutes an important problem since usually the information necessary for its estimate is rather scarce. The methods of its evaluation are disputable (Deng et al. 2002; Sukhodolov et al. 1998; Rowiński et al. 2003). It is then not very surprising that a number of methods, often leading to different results, are proposed in respect to the dead-zone types of models. Recently Seo & Cheong (2001) discussed different methods for the estimates of the parameters of the storage zone model and they concluded that the parameters obtained by the methods of moments are in good agreement with the measured parameters, whereas the fit by the maximum likelihood method as well as the existing literature approaches are not. A number of other estimation methods have been elaborated in literature such as physically based empirical method of Pedersen (1977); fitting of the theoretical slope of the Laplace transformed solution for the concentration of the flow zone to the observed slope (Czernuszenko et al. 1998), moments matching procedure (Lees et al. 2000) or even visual determination of the set of parameters yielding the best fit to the concentration data (Bencala & Walters 1983). An obvious element is the relating the computed solute concentrations to some experimentally obtained curves.

Estimation of the parameters has to obviously be proceeded by a proper formulation of the computational procedure. Computational schemes for the simulation of the mass transport equations in cross-sectionally averaged form have been widely used for many years. A wide variety of schemes have been produced encompassing much of what is generally available in computational fluid dynamics: finite difference, finite volume and finite element methods for spatial discretization and explicit and implicit time stepping. Discussion of such methods in respect to the advection-dispersion equations but with the inclusion of temporarily storage zone is rather scarce in literature (Runkel & Chapra 1993; Strauber 1995). In this paper we are concerned with the 1D solute transport equations, which are combined with the process of the exchange of mass between the mainstream and the existing in the flow areas that cause temporary storage of the solute.

The overall aim of the paper is to establish a robust and efficient scheme for modelling of solute transport in natural watercourses and to demonstrate its prediction capability. To achieve this goal a relevant procedure for identification of model parameters is proposed. The results of computations will be compared with selected experimental results obtained by means of a dye tracer test in a lowland river. This study is just a first stab and the performance of the model is demonstrated against the measured data from one dye tracer field study in Central Poland. The emphasis is rather put on the elaborated mathematical approach.

2 MATHEMATICAL MODEL OF LONGITUDINALTRANSPORT OF SOLUTES

We will concern only one-dimensional conditions after a substance has become fully mixed across the depth and width of a river. In such case a model describing the processes of advection, longitudinal dispersion, i.e. the spreading relative to the cross-sectional averaged velocity and also temporary storage is suitable for the description of the spread of conservative, passive pollutants. The transient storage process describes water moving from the flowing stream channel into stagnant areas in which waters are well-mixed but not transported downstream. The detailed description of the transient storage model may be, for example, found in (Czernuszenko and Rowiński 1997; Czernuszenko et al. 1998) and here we will just present the relevant partial differential equations.

Transport of the solutes in the main stream may be described by:

$$\frac{\partial C}{\partial t}+u\frac{\partial C}{\partial x}-\frac{1}{A}\frac{\partial}{\partial x}\left(DA\frac{\partial C}{\partial x}\right)=\frac{\varepsilon}{T}\left(C_D-C\right) \tag{1}$$

where *x*—longitudinal direction, t-time, *C(x, t)*—solute concentration, *u(x)*—cross-sectionally averaged velocity of water, *D(x)*—dispersion coefficient, *A*—cross-sectional area of the channel. It has been assumed that the hydraulic conditions in the channel are steady, i.e. parameters *u, A, D* do not change in time. $C_D(x, t)$ denotes the concentration of solute in the storage zone, parameters $\varepsilon(x)$ and $T(x)$ denote the ratio of the volume of the storage zones to volume of the main stream for unit length and the penetration time of tracer into the storage zones, respectively. In many practical situations we may additionally assume that these parameters do not change along the channel and then the above equation is reduced to the following form:

$$\frac{\partial C}{\partial t}+U\frac{\partial C}{\partial x}-D\frac{\partial^2 C}{\partial x^2}=\frac{\varepsilon}{T}\left(C_D-C\right) \tag{2}$$

where *U, D,* ε and *T* are constant parameters.

The balance of mass in the storage zones is represented by:

$$\frac{\partial C_D}{\partial t}=\frac{1}{T}\left(C-C_D\right) \tag{3}$$

Equations 1 or 2 and 3 describe variations of the solute concentrations in both the main channel and the storage zones. The solution domain is the plane *Oxt* limited by inequalities $0\le x\le L$ and $t\ge 0$, where *L* is the length of the modeled channel reach. The model equations are complemented by the following:

–initial conditions:

$$C(x, t=0)=C_p(x),\quad C_D(x, t=0)=C_{Dp}(x),\ \text{for}\ x\in[0, L] \tag{4}$$

–and boundary conditions:

$$C(x=0, t)=C_0(t),\qquad D\left.\frac{\partial C}{\partial x}\right|_{x=L}=0,\quad t\ge 0 \tag{5}$$

where C_p, C_{Dp} are the initial distributions of solute concentration along the channel reach in both the main stream and the storage zones and C_0 describes the inflow of admixture at the initial cross-section.

The effects of simple shift in time and dissipation in traditional Fickian-type advection—dispersion transport are well known. The source term that occurs in Equations 1 and 2 causes additional effects of pollutant decrease and accumulation (Figure 1). The intensity of the exchange of mass between storage zones and the main stream depends on the difference in concentrations. At the beginning the storage zones accumulate the pollutants which causes the decrease of the admixture concentration in the main stream. However, the stored mass is given back to the channel when the concentration in the main stream is lower than in the storage zone. This process may even cause the shift in time of the peak of concentration temporal distribution (Figure 1).

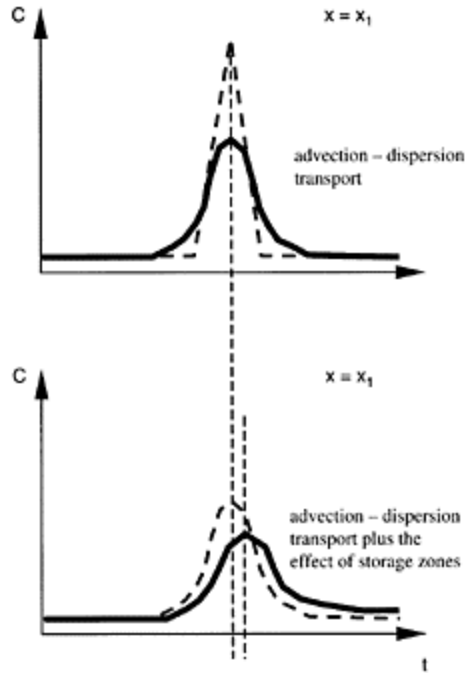

Figure 1. Schematic representation of advection, dispersion and storage zones processes.

3 NUMERICAL SOLUTION

Equations 2 & 3 may be solved analytically only by means of statistical moments (Czernuszenko & Rowiński 1997) and therefore numerical methods are highly demanded. A finite difference method has been applied for the described case. The

scheme is set up with a rectangular horizontal mesh. Equally spaced points along both the *t*- and *x*-axes are chosen with grid spacing Δt and Δx correspondingly, which makes the channel divided into *N* computational cross-sections and *M* temporal levels. A convention is used for which the cross-section denoted by 1 corresponds to $x=0$, and by *N* to $x=L$. The Cranck-Nicholson differencing scheme has been used for the representation of Equation 2–3 which reads:

$$-\left(\frac{U\Delta t}{2\Delta x}+\frac{D\Delta t}{2\Delta x^2}\right)C_{j-1}^{i+1}+\left(1+\frac{U\Delta t}{2\Delta x}+\frac{D\Delta t}{\Delta x^2}+\frac{\varepsilon\Delta t}{2T+\Delta t}\right)C_j^{i+1}-\frac{D\Delta t}{2\Delta x^2}C_{j+1}^{i+1}=$$
$$=\left(\frac{U\Delta t}{2\Delta x}+\frac{D\Delta t}{2\Delta x^2}\right)C_{j-1}+\left(1-\frac{U\Delta t}{2\Delta x}-\frac{D\Delta t}{\Delta x^2}-\frac{\varepsilon\Delta t}{2T+\Delta t}\right)C_j+\frac{D\Delta t}{2\Delta x^2}C_{j+1}$$
$$+\frac{2\varepsilon\Delta t}{2T+\Delta t}C_{Dj}^{i} \qquad (6)$$

for cross-sections $j=2, 3,\ldots, N-1$ and

$$C_{Dj}^{i+1}=\frac{\Delta t}{2T+\Delta t}\left(C_j^{i+1}+C_j^{i}\right)+\frac{2T-\Delta t}{2T+\Delta t}C_{Dj}^{i} \qquad (7)$$

for $j=1, 2,\ldots, N$. Approximation of boundary conditions at each temporal level leads to:

for $j=1$, $C_1^{i+1}=C_0(t_{i+1})$ (8)

for $j=N$

$$-\left(\frac{U\Delta t}{2\Delta x}+\frac{D\Delta t}{\Delta x^2}\right)C_{N-1}^{i+1}+\left(1+\frac{U\Delta t}{2\Delta x}+\frac{D\Delta t}{\Delta x^2}+\frac{\varepsilon\Delta t}{2T+\Delta t}\right)C_N^{i+1}=$$
$$=\left(\frac{U\Delta t}{2\Delta x}+\frac{D\Delta t}{\Delta x^2}\right)C_{N-1}+\left(1-\frac{U\Delta t}{2\Delta x}-\frac{D\Delta t}{\Delta x^2}-\frac{\varepsilon\Delta t}{2T+\Delta t}\right)C_N+\frac{2\varepsilon\Delta t}{2T+\Delta t}C_{DN}^{i} \qquad (9)$$

Equation 9 has been obtained from 6 with the assumption that

$C_{N-1}=C_{N+1}$ (10)

In the case of the model in the form represented by Equations 1 and 3 the situation is much more complex and the application of the Cranck-Nicholson differencing scheme has not led to satisfying results due to the generation of large errors in the process of computations. It has been assumed that the influence of three processes (advection, pure dispersion and transient storage) might best be computed separately as three stages in a three-stage difference scheme. Abbott and Minns (1998) suggest to think about such multi-staging as some processes are being “frozen” or “locked” while the other is implemented. The procedure as described in details below may be schematically presented as in Figure 2.

In the first stage a pure advection process has been considered:

$$\frac{\partial C}{\partial t}+u\frac{\partial C}{\partial x}=0 \qquad (11)$$

In the second stage the results obtained from (11) are corrected by considering the dispersion process:

$$\frac{\partial C}{\partial t} = \frac{1}{A}\frac{\partial}{\partial x}\left(DA\frac{\partial C}{\partial x}\right) \tag{12}$$

Last stage concerns the existence of the storage zones by means of the following equations:

$$\frac{\partial C}{\partial t} = \frac{\varepsilon}{T}(C_D - C) \tag{13}$$

$$\frac{\partial C_D}{\partial t} = \frac{1}{T}(C - C_D) \tag{14}$$

An upwind scheme has been used for approximation of Equation 11

for j=1 $C_1^{i+1}=C_0(t_{i+1})$ (15)

for j=2, 3,…, N

$$-\theta\frac{u_j\Delta t}{\Delta x}C_{j-1}^{i+1} + \left(1+\theta\frac{u_j\Delta t}{\Delta x}\right)C_j^{i+1} = \\ = (1-\theta)\frac{u_j\Delta t}{\Delta x}C_{j-1}^{i} + \left[1-(1-\theta)\frac{u_j\Delta t}{\Delta x}\right]C_j^{i} \tag{16}$$

The Cranck-Nicholson differencing scheme could be applied for the dispersion equation which resulted in the following:

for j=1

$C_1^{i+1}=C_1^{i}$ (17)

for j=2, 3,…, N−1

$$-\frac{\Delta t}{4\Delta x^2 A_j}\left(A_{j-1}D_{j-1}+A_jD_j\right)C_{j-1}^{i+1} - \frac{\Delta t}{4\Delta x^2 A_j}\left(A_jD_j+A_{j+1}D_{j+1}\right)C_{j+1}^{i+1} \\ +\left[1+\frac{\Delta t}{4\Delta x^2 A_j}\left(A_{j-1}D_{j-1}+2A_jD_j+A_{j+1}D_{j+1}\right)\right]C_j^{i+1} + \\ =\frac{\Delta t}{4\Delta x^2 A_j}\left(A_jD_j+A_{j+1}D_{j+1}\right)C_{j-1}^{i} + \frac{\Delta t}{4\Delta x^2 A_j}\left(A_jD_j+A_{j+1}D_{j+1}\right)C_{j+1}^{i} \\ +\left[1-\frac{\Delta t}{4\Delta x^2 A_j}\left(A_{j-1}D_{j-1}+2A_jD_j+A_{j+1}D_{j+1}\right)\right]C_j^{i} \tag{18}$$

and for j=N

$$-\frac{\Delta t}{4\Delta x^2 A_j}\left(A_{j-1}D_{j-1}+2A_jD_j+A_{j+1}D_{j+1}\right)C_{j-1}^{t+1}+$$
$$+\left[1+\frac{\Delta t}{4\Delta x^2 A_j}\left(A_{j-1}D_{j-1}+2A_jD_j+A_{j+1}D_{j+1}\right)\right]C_j^{t+1}=$$
$$=\frac{\Delta t}{4\Delta x^2 A_j}\left(A_{j-1}D_{j-1}+2A_jD_j+A_{j+1}D_{j+1}\right)C_{j-1}+$$
$$+\left[1-\frac{\Delta t}{4\Delta x^2 A_j}\left(A_{j-1}D_{j-1}+2A_jD_j+A_{j+1}D_{j+1}\right)\right]C_j \qquad (19)$$

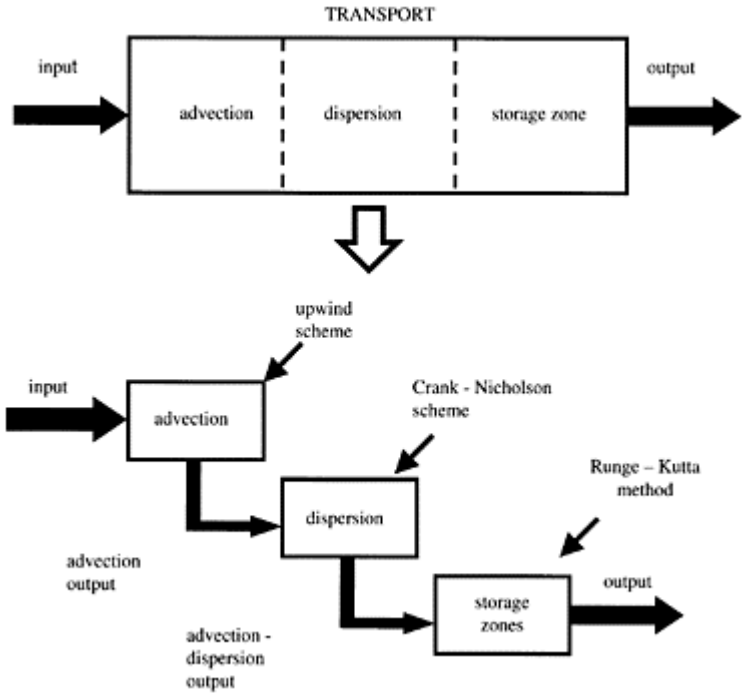

Figure 2. Schematic representation of the applied splitting technique.

It is important to note that in the second stage the input for computations is taken from the first process and not from the actual preceding time level. Equations of the last stage are solved by means of the fourth-order Runge-Kutta method. Let's denote:

$y_1=C$, $y_2=C_D$

(20)

$$f_1(t,\mathbf{y})=\frac{\varepsilon}{T}(y_2-y_1),\ f_2(t,\mathbf{y})=\frac{1}{T}(y_1-y_2) \qquad (21)$$

which allows us to present the problem 13–14 as ordinary differential equation that reads

$$\frac{d\mathbf{y}}{dt} = \mathbf{f}(t, \mathbf{y}) \tag{22}$$

A single step of this method may be represented as:

$$\mathbf{k}_1 = \Delta t \mathbf{f}\left(t_i, \mathbf{y}^i\right), \ \mathbf{k}_2 = \Delta t \mathbf{f}\left(t_i + \frac{\Delta t}{2}, \mathbf{y}^i + \frac{\mathbf{k}_1}{2}\right) \tag{23}$$

$$\mathbf{k}_3 = \Delta t \mathbf{f}\left(t_i + \frac{\Delta t}{2}, \mathbf{y}^i + \frac{\mathbf{k}_2}{2}\right), \ \mathbf{k}_4 = \Delta t \mathbf{f}\left(t_{i+1}, \mathbf{y}^i + \mathbf{k}_3\right) \tag{24}$$

$$\mathbf{y}^{i+1} = \mathbf{y}^i + \frac{1}{6}\left(\mathbf{k}_1 + 2\mathbf{k}_2 + 2\mathbf{k}_3 + \mathbf{k}_4\right) \tag{25}$$

It is proposed that the described method of taking individual consistencies over to component differential forms and adding these differential component forms to obtain a resultant differential form which brings correct results.

4 FIELD STUDY—DYE TRACER TEST IN THE WKRA RIVER

The presented model has been verified based on the tracer test performed in the lowland river reach in Central Poland, namely the Wkra River. The flow rate as well as other hydraulic and topographic characteristics in respect to all the measuring cross-sections are shown in Tables 1a, 1b, 1c. The measurements were repeated three times in the same river reach. A variety of different irregularities along the river banks were observed. The creation of wakes behind the sand waves as well as the areas on the insides of bends with small radius of curvature most likely causing that the flow “overshoots” the bend could be expected and therefore one may assume the existence of different storage zones in the considered river reach.

The method of instantaneous injection of the tracer was applied and it did not require the complex dosing facilities and allowed to obtain high initial concentrations of the tracer. The dye release consisted of 10 liters of alcoholic solution of a fluorescent red dye (Rhodamine). This dye was released at three points at the cross-section just downstream of the stage of fall which speeded up the cross-sectional mixing of the admixture. Concentrations were measured at five cross-sections as indicated in Table 1. First crosssection was established at a distance at which 1D conditions were supposed to be achieved. During the early stages of a test the dye was visible to the naked eye, which facilitated sample collections. The dye was detected by using the field fluorometer Turner Design with continuous flow cuvette system on the one hand and also water samples were collected at sampling points. Measuring data were stored on graphical

Table 1a. Hydraulic and topographic characteristics—Wkra River (case 1).

Characteristic			Cross-section		
Mean flow [m^3/s]			4.18		
Mean water surface slope [‰]			0.318		
	P-1	P-2	P-3	P-4	P-5
Distance from release point [m]	600	1460	2450	3480	4780
Cross-section area [m^2]	8.07	9.72	9.19	10.15	10.35
Width at the surface level [m]	9.82	10.23	9.69	8.89	11.18
Mean velocity [m/s]	0.518	0.430	0.455	0.412	0.404
Mean depth [m]	0.82	0.95	0.95	1.14	0.93
Wetted perimeter [m]	0.77	0.89	0.81	1.01	0.88
Manning roughness [$m^{-1/3}s$]	0.03	0.0413	0.0370	0.0472	0.0419

Table 1b. Hydraulic and topographic characteristics—Wkra River (case 2).

Characteristic			Cross-section		
Mean flow [m^3/s]			3.97		
Mean water surface slope [‰]			0.318		
	P-1	P-2	P-3	P-4	P-5
Distance from release point [m]	600	1460	2450	3480	4780
Cross-section area [m^2]	7.82	9.36	8.81	9.80	10.02
Width at the surface level [m]	9.73	10.1	9.57	8.77	11.07
Mean velocity [m/s]	0.508	0.424	0.451	0.405	0.396
Mean depth [m]	0.80	0.93	0.92	1.12	0.91
Wetted perimeter [m]	0.75	0.87	0.79	0.99	0.86

Table 1c. Hydraulic and topographic characteristics—Wkra River (case 3).

Characteristic			Cross-section		
Mean flow [m^3/s]			4.32		
Mean water surface slope [‰]			0.323		
	P-1	P-2	P-3	P-4	P-5

Distance from release point [m]	600	1460	2450	3480	4780
Cross-section area [m^2]	8.41	9.87	9.22	10.24	10.49
Width at the surface level [m]	9.93	10.29	9.69	8.92	11.22
Mean velocity [m/s]	0.514	0.438	0.469	0.422	0.412
Mean depth [m]	0.85	0.96	0.95	1.15	0.93
Wetted perimeter [m]	0.79	0.90	0.82	1.01	0.89

registers in the form of concentration distributions and then digitized to obtain relevant concentration time series. Concentration temporal distributions as obtained in the measurements are seen in Figures 3 and 4.

5 IDENTIFICATION OF PARAMETERS—PROBLEM FORMULATION

Model calibration problem is formulated as optimization problem
minimize $F(\mathbf{x})$ with respect to $\mathbf{x} \in D \subset R^n$
where $F: R^n \rightarrow R$ is scalar objective function and D is admissible domain with potential solutions $\mathbf{x}$. Many different methods were used to solve such kind of problems, but no one of them may be recommended if we do not know the features of the objective and constraints in the given problem. The most important features are the convexity of function $F(\mathbf{x})$ as well as the convexity of domain D. The form of constraints guarantees that the set of admissible solutions is compact and convex. However, the described problem is a practical and a very complex task. So, we have expected that the calibration criterion may not be convex. This preliminary assumption was confirmed by further numerical tests.

In such case the global optimization techniques should be preferred. These methods have been developed and investigated for several decades and they have been treated as alternative algorithms for problems with many local optimal points. Originally they have constituted the combination of random global search, i.e. Monte Carlo method, and local accurate procedure. Another kind of methods has become very popular during last 30 years. They are based on natural selection and evolution of wild species such as genetic algorithms, evolutionary strategies or evolutionary programming. One of the first descriptions of genetic algorithms was given by Holland (1975). At the same 3 time non-evolutionary methods of global optimization were developed, and among them the methods based on natural and artificial physical and chemical processes. Simulated annealing (Kirkpatrick et al. 1983; Dekkers & Aarts 1991) and particle trajectory method (Griewank 1981) are well known examples in this area. Current knowledge of optimization and classic methods for convex function was the basis for developing new global techniques, i.e. Price (1983), Ali & Storey (1994).

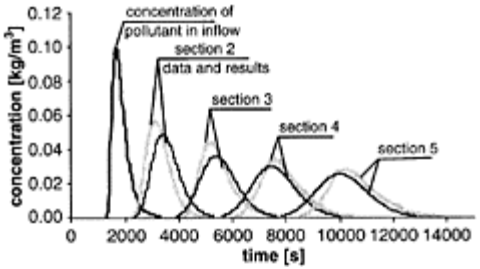

Figure 3. Measured solute concentrations and that obtained by means of linear model.

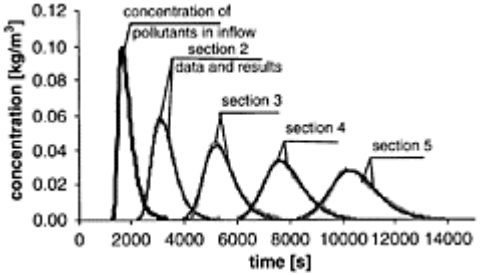

Figure 4. Measured solute concentrations and that obtained by means of nonlinear model.

In the present study the results obtained by means of the dye tracer test in the Wkra River have been used and the time-concentrations distributions $C_m(x_k, t)$ (k=1, 2,…,) at a few selected cross-sections in the main stream have been used for comparisons. As for the boundary condition at the inflowing cross-section the measurement results from the first cross-section $C_m(x_1, t)$ have been taken. The measurements at the remaining cross-sections have been used for the determination of parameters with the objective function taken as:

$$\min_{u,D,\varepsilon,T}\left\{F[u,D,\varepsilon,T]=\sum_{k=2}^{K}\int_{0}^{T_H}\left[C_m(x_k,t)-C(x_k,t)\right]^2 dt\right\} \tag{26}$$

where F is the criterion function, T_H—the optimization time horizon, K—number of measuring cross-sections.

The wetted cross-section has been determined from the mass balance under steady stated conditions given by:

$$Q=u(x)A(x) \tag{27}$$

where Q is the given discharge.

Special constraints have been put on the sought parameters or functions:

$$X_{\min} \le X(x) \le X_{\max} \tag{28}$$

where $X_{\min}$, $X_{\max}$ are the lower and upper bounds for $X(x)$.

The computations of the values of the objective function for the estimated (by the described method) parameters u, D, ε, T have been realized through the simulations of the transport of solutes and the comparisons of the concentration distributions $C(x_k, t)$.

In case of the identification of parameters of the model 1–3 a linear approximation of the sought parameters has been assumed to lower the dimensionality of the problem. The longitudinal variations of $u(x)$, $D(x)$, $\varepsilon(x)$, $T(x)$ have been determined based on their values at the same cross-sections where the solute concentrations had been measured.

6 CONTROL RANDOM SEARCH METHOD

The optimisation problem 26 was solved by means of the global random search procedure (Price 1987) namely the following version of Controlled Random Search (CRS2) described in details by Dysarz & Napiórkowski (2002). The algorithm is one of the random global optimisation techniques. Its basis is well known simplex method used in non-linear optimisation. The set of points from n-dimensional space is processed in following iterations. In each step, new solution is generated by reflection of a simplex vertex. One of a few well known versions of the method was used, namely CRS2.

The algorithm starts from the creation of the set of points, many more than n+1 points in n-dimensional space, selected randomly from the domain. The optimal quantity of set was taken as suggested by Price (1987), equal to 10(n+1). Let us denote the set as S. After evaluating the objective function for each of the points, the best x_L (i.e. that of the minimal value of the performance index) and the worst x_H (i.e., that of the maximal value of the performance index) points are determined and a simplex in n-space is formed with the best point x_L and n points (x_2, x_3,…, x_{n+1}) randomly chosen from S. Afterwards, the centroid x_G of points x_L, x_2,…, x_n is determined. The next trial point x_Q is calculated as the reflection of x_{n+1}, that is $x_Q = 2x_G - x_{n+1}$ (Niewiadomska-Szynkiewicz et al. 1996). Then, if the last derived point x_Q is admissible and "better" it replaces the worst point x_H in the set S. Otherwise, a new simplex is formed randomly and so on.

If the stop criterion is not satisfied, the next iteration is performed. This part of the algorithm was formed

Table 2. Constraints for the sought parameters.

	Steady flow			
	Uniform—Equations 2 and 3		Nonuniform—Equations 1 and 3	
Parameter	Min	Max	Min	Max
u [m^3/s]	0.3	0.7	0.4	0.8

D [m^2/s]	0.5	10.0	3.8	9.0
ε[−]	0.0	0.2	0.0	0.2
T[s]	0.001	200.0	0.001	200.0

in different way then in the Price original concept. The experiments showed that following condition may be taken as the stop criterion

$$F_{ave} - F(x_L) < \varepsilon \tag{29}$$

where F_{ave} is the mean objective function value in the set, $F(x_L)$ the objective function value at the best point xL and ε is the expected accuracy determined empirically (Dysarz & Napiórkowski 2002).

7 NUMERICAL COMPUTATIONS VISA EXPERIMENTAL RESULTS

The results of a tracer test carried out in the selected reach of the Wkra River have been used in the analyses. Three different experimental tests (the discharge

Table 3. Mean values of criterion function and standard error.

Test	1		2		3	
Flow	Linear model	Nonlinear	Linear model	Nonlinear	Linear model	Nonlinear
Mean value	0.1258	0.0049	0.1724	0.0104	0.1216	0.0052
St. error. %	1.529	4.483	1.671	2.677	2.639	2.830

Table 4. Mean values of the determined parameters and the standard errors—uniform flow conditions.

	u [m/s]					
Parameter	Test 1	Test 2	Test 3	D	ε[–]	T[s]
Mean value	0.5592	0.5546	0.5480	4.76127	0.1186	147.99
Standard deviation %	4.313	3.835	3.105	37.086	31.239	23.480

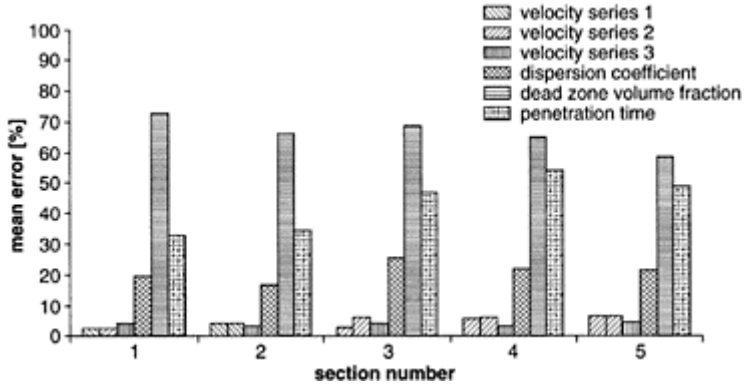

Figure 5. Standard deviations for each determined parameter for nonlinear model.

Q was 4.18, 3.97 and 4.32m^3/s) performed over a 6 kilometers river reach with 5 measuring cross sections are taken into account. As an initial condition for computations a lack of dissolved solutes in the channel was assumed:

$$C_p(x) = C_{Dp}(x) = 0, \quad \text{dla } x \in [0, L] \tag{30}$$

The time horizon for simulations was taken as 4h. Time step is taken as Δt=20s and the spatial one Δx=20m.

Admissible range for model parameters is given in Table 2. Since the differences in the values of the sought parameters are large, a normalization was necessary and it was performed by projecting of the admissible set on the unit cube in R^n by means of expression:

$$\alpha = \frac{X - X_{\min}}{X_{\max} - X_{\min}}, \; 0 \le \alpha \le 1 \tag{31}$$

Examples of simulations of the transport of solutes are shown in Figures 3 and 4. These figures show the measured and computed concentration distributions at five cross-sections.

Performance of both linear and nonlinear models is presented. Table 2 provides the mean values of the objective function as well as the values of standard deviation obtained by means of the expression:

$$\sigma_{\%} = \frac{1}{\overline{X}} \sqrt{\frac{\sum_{i=1}^{N} \left(X_i - \overline{X}\right)^2}{N-1}} 100\% \tag{32}$$

where X_i is the single sample from a series of N samples having the mean value $\overline{X}$.. It is readily seen that the agreement with the measuring data is much better in case when the variability of model parameters along river channel is taken into account, i.e. in case of

Equations 1 and 3. Mean values of the criterion function varied in the range from 0.005 to 0.01 in this case while those values were ten times larger in case of Equations 2 and 3. The values of standard deviation in both cases did not exceed 5% of mean value. However, the increase in the accuracy of results has been obtained at much larger computational cost of parameters' identification. Mean value of the number of runs was 131.4 in case of linear model and it was as large as 4377.6 for the nonlinear model. Table 3 and Figure 5 provide mean values and the standard deviations for each determined parameter for both presented models. The values of the storage zone parameters reflects the relatively simple geometry of the considered channel of Wkra river. Discussion of the performance of these parameters may be, for example, found in (Czernuszenko et al. 1998).

8 CONCLUSIONS

In the study a special procedure was designed for the identification of the parameters of the model of longitudinal transport of pollutants in rivers with the inclusion of the phenomenon of transient storage. A model taking into account the changes of model parameters along river channel proved to provide better results when compared to the experimental data but the parameter identification in such case is computationally much more expensive.

ACKNOWLEDGEMENT

This work was partially supported by The Sendzimir Foundation, USA and by Polish Committee for Scientific Research under grant 6 P04 D 02020.

REFERENCES

Abbott, M.B. & Minns, A.W. 1998. Computational Hydraulics, Ashgate, Aldershot.

Ali, M.M. & Storey, C. 1994. Modified controlled random search algorithms. *Intern. J. Computer Math.*, 53:229–235.

Bencala, K.E. & Walters, R.A. 1983. Simulation of solute transport in a mountain pool-and-riffle stream: a transient storage model. *Water Resources Research,* 19(3):718–724.

Czernuszenko, W. & Rowiński, P.M. 1997. Properties of the dead-zone model of longitudinal dispersion in rivers, *Journal of Hydraulic Research,* 35(4):491–504.

Czernuszenko, W., Rowiński, P.M. & Sukhodolov, A.N. 1998. Experimental and numerical validation of the dead-zone model. *Journal of Hydraulic Research,* 36(2):269–280.

Dekkers, A. & Arts, E. 1991. Global Optimization and Simulation Annealing. *Mathematical Programming,* 50: 367–393.

Deng, Z.Q., Begtsson, E, Singh, V.P. & Adrian, D.D. 2002. Longitudinal dispersion coefficient in singlechannel streams. *Journal of Hydraulic Engineering,* ASCE, 128(10):901–916.

Dysarz, T. & Napiórkowski, J.J. 2002. Determination of reservoir decision rules during flood, *Acta Geophysica Polonica,* 50(1):135–149.

Fernald, A.G., Wigington, P.J. & Landers, D.H. 2001. Transient storage and hyporheic flow along the Willamette River, Oregon: Field measurements and model estimates. *Water Resources Research,* 37(6):1681–1694.

Griewank, A.O. 1981. Generalized Descent for Global Optimization. *J. Optimiz. Theory Appl.,* 34(1):11–39.

Holland, J.H. 1975. *Adaptation in Natural and Artificial Systems.* University of Michigan Press, Ann Arbor.

Jonsson, K. 2003. Effects of hyporheic exchange on conservative and reactive solute transport in streams. Model assessments based on tracer tests. *Acta Universitatis Upsaliensis. Comprehensive Summaries of Uppsala Dissertations from the Faculty of Science and Technology 866,* Uppsala.

Kirkpatrick, S., Geatt, C.D. & Vecchi, M.P. 1983. Optimization by Simulated Annealing. *Science,* 220:671–680.

Lees, M.J., Camacho, L.A. & Chapra, S. 2000. On the relationship of transient storage and aggregated dead zone models of longitudinal solute transport in streams. *Water Resources Research,* 36(1):213–224.

Manson, J.R. 2000. Predicting stream transient storage zone characteristics from tracer data. *Water Resources Research,* 36(2):629–631.

Niewiadomska-Szynkiewicz, E., Malinowski, K. & Karbowski, A. 1996. Predictive Methods for Real-Time Control of flood operation of a Multireservoir System: Methodology and Comparative Study, *Water Resources Research,* 32(9):2885–2895.

Packman, A.I. & Bencala, K.E. 2000. Modeling surfacesubsurface hydrological interactions. In J.B.Jones, R.J.Mulholland (Eds.), *Streams and Ground waters,* Academic Press, 45–80.

Pedersen, F.B. 1977. Prediction of longitudinal dispersion in natural streams. *Series Paper 14, Institute of Hydrodynamics and Hydraulic Engineering,* Technical University of Denmark, Lyngby, Denmark.

Price, W.L. 1983. Global optimization by controlled random search. *J. Optimiz. Theory Appl.,* 40(3):333–348.

Price, W.L. 1987. Global optimization algorithms for CAD Workstation, *J. Optimiz. Theory Appl.,* 55(1), 133–146.

Rowiński, P.M., Piotrowski, A. & Napiórkowski, J.J. 2003. Are artificial neural networks techniques relevant for the estimates of longitudinal dispersion coefficient in rivers?, submitted for publication.

Runkel, R.L. & Chapra, S.C. 1993. An efficient numerical solution of the transient storage equations for solute transport in small streams, *Water Resources Research,* 29(1): 211–215.

Seo, I.W. & Cheong, T.S. 2001. Moment-based calculation of parameters for the storage zone model for river dispersion, *Journal of Hydraulic Engineering,* ASCE, 127(6): 453–465.

Sukhodolov, A.N., Nikora, V.I., Rowiński, P.M. & Czernuszenko W. 1997. A case study of longitudinal dispersion in small lowland rivers, *Water Environment Research,* 69(7):1246–1253.

Strauber, G. 1995. Modified box schemes for pollutant transport in rivers with dead zones, *International Journal for Numerical Methods in Fluids,* 21(12):1123–1135.

Thackstone, E.L. & Schnelle, K.B. 1970. Predicting effects of dead zones on stream mixing. *Journal of Sanitary Engineering Division,* ASCE, 96(2), 319–331.

Impact of riverine and CSO inputs on coastal water quality under different environmental conditions

S.M.Kashefipour

Irrigation Department, Shahid Chamran University, Ahwaz, Iran
B.Lin & R.A.Falconer

Civil Engineering Department, Cardiff University, Cardiff, UK

River Flow 2004—Greco, Carravetta & Della Morte (eds.)

ABSTRACT: Details are given of a hydro-environmental modelling study aimed at investigating the impact of riverine and CSO inputs and several environmental parameters on the bacterial concentration on an EU bathing water (BW) compliance point, located on the Fylde Coast, UK. The several environmental conditions studied including: wind, river discharge, storm flow, and CSO release time in relation to tidal phases, were studied in this project. A series of scenario runs were undertaken to predict BW bacterial concentrations for three continuous riverine inputs, located at the upstream boundaries of the model, and three intermittent CSO inputs, located along the rivers. For each scenario one environmental factor was considered and the inputs were designed to operate separately. To investigate the absolute effect of each factor on the dispersion and distribution of the pollution a zero decay rate was assumed. It was found that increasing river discharges would cause an increase in the bacterial concentration at the BW point. It was also found that the release time of a CSO input would affect considerably bacterial concentration at the considered BW point. Wind direction and storm flows were also found to be important environmental factors that significantly affect pollution distribution in the receiving waters.

1 INTRODUCTION

It is known that many water quality parameters such as the salinity, pH and turbidity levels, solar radiation strength and sediment concentration may affect the bacterial population in coastal waters (Thomann and Muller, 1987; Chapra, 1997). Some other environmental parameters such as tidal conditions, river discharge, wind speed and

direction, and flow velocity may also affect the distribution of bacterial concentration (Kashefipour *et al*, 2000). Moreover, the releasing time of bacterial input in relation to the tidal phases and other environmental conditions (e.g. sunlight intensity) can also be a relatively important factor to the bacterial displacements.

This paper presents a hydro-environmental modelling study of the Fylde Coast and Ribble Estuary, aimed at quantifying the impact of various bacterial sources along the river network on the receiving coastal waters under different environmental conditions. The effectiveness of such environmental conditions on the bacterial concentration distribution was illustrated by evaluating the faecal coliform concentration at an EU designated bathing water point.

2 HYDRO-ENVIRONMENTAL MODEL

Kashefipour *et al* (2002) developed an integrated hydro-environmental mathematical model, in which a one-dimensional (1D) model was dynamically linked with a two-dimensional (2D) model enabled the users to apply this single model for modelling the river networks and coastal waters simultaneously. The 1D and 2D shallow water equations were numerically solved and integrated to form the hydrodynamic module of the integrated model. The 1D and 2D advective diffusion equations were solved and integrated to form the water quality module. This model was able to accurately predict the impact of the river inputs on the bathing water quality along the Fylde coast. More information regarding the calibration and validation of this single model for the Ribble Estuary and its tributaries can be found in Lin *et al* (2001) and Kashefipour *et al* (2002). In this study a series of scenario runs were designed to investigate the effect of wind, river discharge, CSO release time in relation to the tidal phases and flood flows on the bacterial concentration at a bathing water location.

3 MATERIALS AND METHODS

Faecal Coliforms (FC) are mostly used as an indicator of the bacterial population. In this study a zero decay rate was assumed for the FC and this was because the main focus of the study was to investigate the effect of the environmental conditions on the FC distribution. The results obtained from this study can also be extended to other bathing water quality indicators.

Ribble Estuary is located along the North West coast of England, UK. Figure 1 shows the Ribble Estuary and its tributaries, including: the Ribble, Darwen and Douglas rivers. Three continuous inputs were located near the upstream boundaries of the rivers, and three CSO inputs, namely the Upper Ribble CSO, Lower Ribble CSO and Douglas Inter (see Figure 1) operate intermittently. The continuous inputs were assumed to operate for the whole simulation time with a discharge of $0.05m^3/s$ and FC concentration of 1.0e+08cfu/100ml. A discharge of 1.0m3/sand a FC concentration of 3.0e+07cfu/100ml were assumed for all of the CSO inputs and they operated only for three hours. The input sources were set to operate separately for each scenario run, to investigate the effect of each input on the FC concentration at the bathing water location. St Annes Pier, located

at the north of the Ribble Estuary, was an EU designed bathing water point (see Figure 1) and was used in this study as a target location for testing different scenarios. Wind direction, river discharge and storm flow and the CSO release time were four variables tested in this study. To drive the model water elevations predicted for a neap tide were used as the downstream open boundary. Discharges at the upstream boundaries of the three rivers including: Ribble, Darwen and Douglas, were used as the upstream boundary conditions. Fresh water with zero bacterial concentration was assumed for the flow entering to the domain from the upstream and downstream boundaries of the model.

The scenarios tested were listed in Table 1. In this table SW means a wind from south towards north with an angle of 225 degrees to the north and NW was

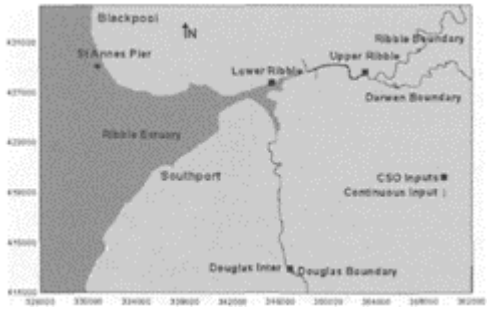

Figure 1. Ribble Estuary and its tributaries.

a wind from the north to the south with an angle of 315 degrees to the north. Rib, Dar and Dug are abbreviations of the Ribble, Darwen and Douglas rivers, respectively. In Table 1 LW, HW, LS and HS are used for low water, high water, low storm and high storm flows respectively. A constant wind speed of 10m/s was applied. The hydrographs of the low and high storms are shown in Figure 2.

It can be seen from Table 1 that the results obtained from the scenarios S1 and S2 were used to evaluate the effect of wind direction on the bathing water quality, S1 and S3 for the CSO release time, S1 and S4 for river discharge, and S1 with S5 and S6 for evaluation of the effect of storm on the FC concentration at the bathing water point.

Table 1. Specifications of the scenarios.

	Wind		Discharge (m^3/s)			CSO release time	
Scenarios	SW	NW	Rib	Dar	Dug	HW	LW
S1	+		12	2	2	+	
S2		+	12	2	2	+	
S3	+		12	2	2		+
S4	+		50	10	10	+	
S5	+		LS	LS	LS	+	

S6	+		HS	HS	HS	+		

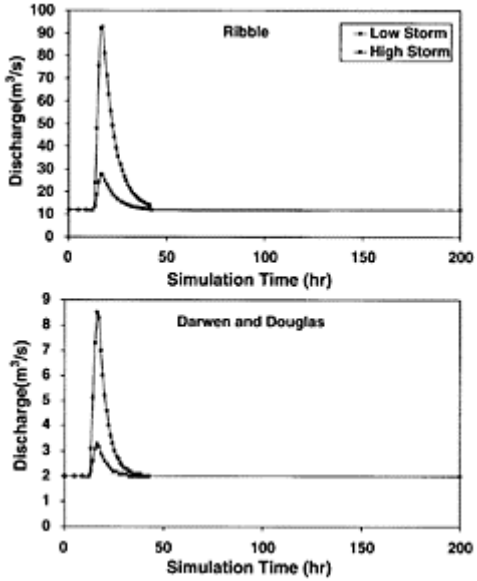

Figure 2. Storm hydrographs for the rivers Ribble, Darwen and Douglas.

It should be noted that the total simulation time for all of the scenario runs was 200 hours, which was about 16 complete tidal cycles.

4 RESULTS AND DISCUSSION

4.1 *The effect of wind direction*

The effect of wind direction on the FC concentrations at St Annes Pier has been shown in Figure 3. As can be seen from this Figure that the south west wind SW225 caused higher FC concentration than that caused by the northwest wind NW315. Since St Annes Pier is located at the northern coastline of the estuary (see Figure 1) these results were expected. The average FC concentrations predicted at the bathing water location due to the continuous and CSO inputs under the above wind directions are summarised in Table 2. This Table shows that for all inputs the FC concentrations for wind direction of SW225 were more than 5 times higher than

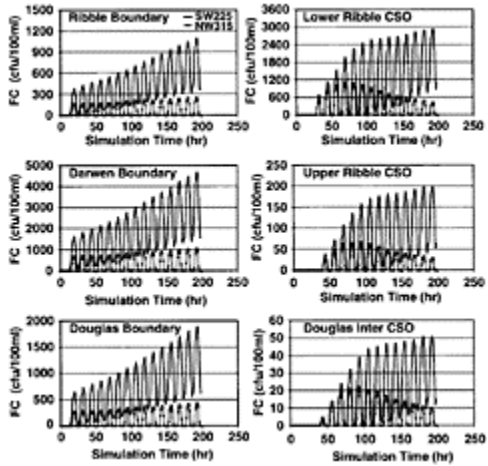

Figure 3. The effect of wind direction on the FC concentration at St Annes Pier.

Table 2. Average FC concentrations at the BW point for different inputs and wind directions.

	FC Concentration (cfu/100ml)	
Input source	SW225	NW315
Ribble boundary	413	71
Darwen boundary	1804	304
Douglas boundary	701	125
Lower Ribble CSO	1076	254
Upper Ribble CSO	66	15
Douglas inter CSO	16	5

the corresponding concentrations obtained for NW315 direction.

It can also be seen from Figure 3 that for all inputs the minimum FC concentrations at the bathing water point occurred at the high waters and the maximum concentrations at low waters. The sinuous shape of the concentration variations in Figure 3 was due to the tidal conditions.

Since the decay rate was set to zero so for the continuous inputs the maximum FC concentration increases after each tidal cycle. Whereas, for the CSO inputs with only three hours operation it was expected that due to the dispersion process, the FC concentration increases initially, reaches a maximum value and then reduces. This trend occurred for the NW315 wind (see Figure 3). It seems that if the simulation time continues more than 200 hours the same trend may also occur for the SW225 wind. The

FC concentrations obtained were generally higher for the inputs closer to the estuary outlet and also for rivers with higher flow velocities (for example Darwen in comparison with Douglas, not shown in this paper).

4.2 *The effect of the CSO release time*

The results obtained for different CSO inputs (see Table 1, scenarios S1 and S3) are compared in Figure 4. In scenario S1 the CSOs discharges were started at the High Water (HW), whereas in scenario S3 the release time was HW plus six hours, or Low Water (LW). As can be seen from this figure different behaviours occurred due to the CSO inputs. For example, for the CSOs located along the Ribble River, including: Upper Ribble and Lower Ribble CSOs (see Figure 1) the FC concentrations at the BW point decreased for scenario S3 in comparison with scenario S1. On the contrary for the Douglas Inter CSO, which is located close to the Douglas boundary, the FC concentrations at the B W point increased when the input was operated at the low water. This phenomenon could be caused by the interaction of river discharge, flow velocity and tide conditions. The travel time for the transport of the pollutants from the Lower Ribble, Upper Ribble and Douglas Inter CSOs to the BW point for scenario S1 were about 14,27, and 28 hours, respectively. The corresponding values for scenario S3 were 23, 23 and 33 hours respectively. This information shows that for scenario S3 the pollutant reached the BW point for the Lower and Upper Ribble CSOs at the starting of the flood-tide phase and this means that a stronger dispersion effect on the FC plumes.

On the contrary for the Douglas Inter CSO the pollutant reached to the B W point at the middle of ebb-tide phase. It should be noticed that with the neap tide, the tidal limit did not reach to the Ribble and Douglas upstream boundaries and between the tidal limit and river boundaries free flow occurs.

These results might be a useful guide to the environmental managers for optimising the release time of the CSOs along the river networks.

4.3 *The effect of river discharge*

Upstream river discharge was another environmental factor considered in this study for investigating the effect of such factor on the FC concentrations at the BW point for different continuous and CSO inputs located along the river networks. In this regard the results obtained for scenarios S1 and S4 were compared and illustrated in Figure 5. As Table 1 shows the upstream river discharges for S4 scenario were about 5 times of the corresponding values for scenario S1. As can be seen from Figure 5 that for all of the continuous and CSO scenario runs the FC concentrations at the BW point will increase significantly when upstream river discharges increase. It seems that the river flow velocity, which is generally affected by upstream flow discharge, could be an important factor affecting the pollution distribution. Higher discharge means higher velocity and as a result the dispersion of the pollutants along the river networks would reduce. For this scenario the travel times for the pollutants to reach the bathing water point were 13, 13 and 15 hours for the Lower and Upper Ribble and Douglas Inter CSOs, respectively.

As it has been explained above that the duration of CSO inputs were only three hours and due to dispersion it was expected that the FC concentrations at the BW point take a maximum value and then reduce with time. This phenomenon has happened for the scenario S4 during the simulation time and it could happen for other scenarios if longer duration of the simulation time was conducted.

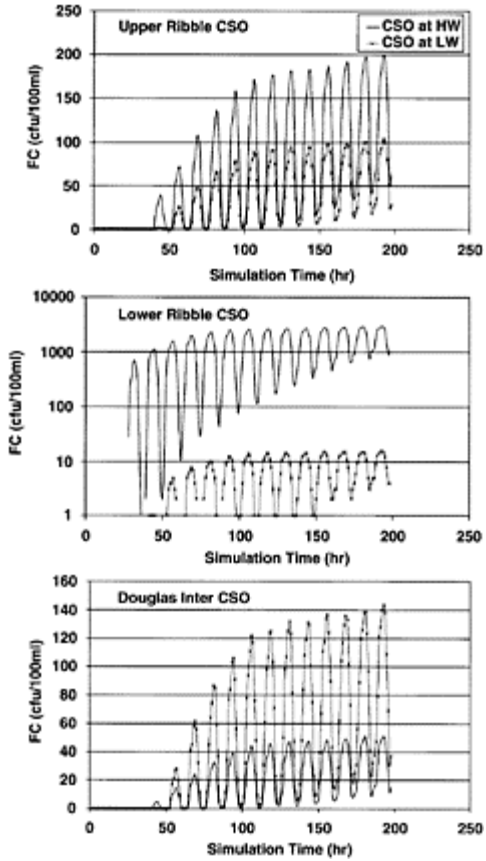

Figure 4. Comparison of the FC concentration for different CSO inputs due to the CSO release time.

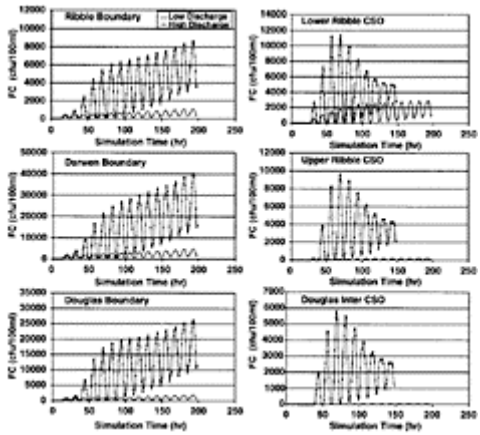

Figure 5. Comparison of the FC concentration for different continuous and CSO inputs due to the river discharge.

The average FC concentrations of the different continuous and CSO inputs for the scenarios S1 and S4 were computed and summarised in Table 3. With an increase of about 5 times in the upstream river discharge (from S1 to S4), the FC concentrations at the bathing water point increased by nearly 10 times.

4.4 *The effect of storm*

Two storms, including: low storm with a small hydrograph and high storm with a big hydrograph, as shown in Figure 2, were considered to investigate the behaviour of the distribution of the bacterial population under different storm flows. The results obtained for scenarios S5 and S6 are shown in Figure 6, together with the corresponding results obtained for scenario S1. The FC concentrations at the BW point for all of the inputs were again increased with the increasing of storm flow. No significant difference was found

Table 3. Average FC concentrations at the BW point for different inputs and scenarios-discharge effect.

	FC Concentration (cfu/100ml)	
Input source	S1	S4
Ribble boundary	413	3133
Darwen boundary	1804	13571
Douglas boundary	701	9430

Lower Ribble CSO	1076	3400
Upper Ribble CSO	66	2663
Douglas inter CSO	16	1585

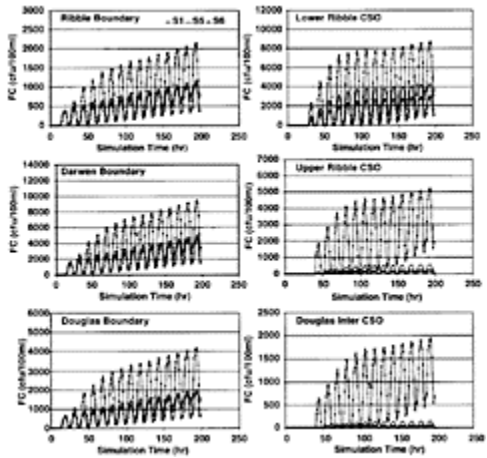

Figure 6. Comparison of the FC concentrations at the BW point for the scenarios S1, S5 and S6.

Table 4. Average FC concentrations at the BW point for different inputs and scenarios-storm effect.

	FC Concentration (cfu/100 ml)		
Input source	S1	S5	S6
Ribble boundary	413	455	815
Darwen boundary	1804	1967	3596
Douglas boundary	701	789	1578
Lower Ribble CSO	1076	1612	3433
Upper Ribble CSO	66	194	1875
Douglas inter CSO	16	48	682

between the low storm (S5) and continuous discharge (S1), and this was due to the small flow and short duration of the storm. The average FC concentrations at St Annes (BW) for all inputs were calculated and summarised in Table 4.

According to Tables 3 and 4 it can be seen that although the peak discharge of the high storm hydrograph was nearly two times of the continuous discharge for scenario S4 the FC concentrations obtained for scenario S6 were less than the corresponding values for S4. This could be due to the short duration of the hydrograph.

5 CONCLUSIONS

In this paper a hydro-environmental model has been used to investigate the effect of several environmental parameters on the bacterial concentration on an EU bathing water compliance point, located on the Fylde Coast, UK. The model was a dynamically integrated 1-and 2-D model, developed by Kashefipour *et al* (2000). Three environmental parameters, including: wind direction, river discharge and storm, and one management factor, namely the CSO release time in relation to the tidal levels, were considered in this study. Three continuous discharges and three intermittent CSO inputs located along the river networks were used as the main sources of pollution. These inputs were assumed to operate separately. The main conclusions drawn from this study may be summarised as follows:

- Wind direction is an important environmental parameter affecting the plume distribution. The bathing water sampling point studied in this project is located at the north of the estuary, thus it is more vulnerable to south-eastern wind.
- The bacterial concentration at the bathing water point decreased considerably when the two Ribble CSO inputs were released at the flood-phase of a tidal cycle including low water. On the contrary, for the same release time the bacterial concentration increased when the Douglas Inter CSO was considered. This phenomenon could be due to the interaction between the flow velocities, pollutant travel time and tidal conditions. This phenomenon could be used utilised by local environmental managers to optimise the release time of the CSOs along the river networks.
- River discharge is another important environmental parameter affecting the bacterial concentrations. Although the concentrations of a continuous input, or a CSO input, was kept the same for all of the scenario runs, the bacterial concentrations at the bathing water point increased significantly with the increase of river discharges.
- The results for the two storm runs showed again that with an increase in the river discharge the bacterial concentrations at the bathing water points also increased.
- Finally it has been concluded that the interaction between river and tidal flows, and interaction between these hydraulic parameters and environmental conditions were the main cause for the fluctuations of bacterial concentration at the bathing water point.

REFERENCES

Chapra, S.C., (1997), *"Surface Water-Quality Modelling"*, McGraw-Hill Companies, Inc., USA, 844pp.

Council of the European Communities, (1976), Council Directive of 8th December 1975 Concerning the Quality of Bathing Water. (76/160/EEC) Official Journal of the European Communities NO. L31, 1–7.

Kashefipour, S.M., B.Lin, E.Harris, and R.A.Falconer, (2000), *"Ribble Estuary Water Quality Modelling"*, Final Report, Cardiff University, UK, 454pp.

Kashefipour, S.M., B.Lin, E.L.Harris, and R.A.Falconer, "Bathing Water Quality Modelling for Ribble Estuary and Fylde Coast", *Water Research*, IWA, Vol. 36, 2002, pp. 1854–1868.

Lin, B., S.M.Kashefipour, E.Harris, and R.A.Falconer, (2001), Modelling Flow and Water Quality in Estuarine and Riverine Waters: A Dynamically Linked 1-D and 2-D Models Approach, *Proceedings of the XXIX IAHR Congress*, September 17–21, Beijing, China, pp. 469–475.

Thomann, R.V, and J.A.Muller, (1987), *"Principles of Surface Water Quality Modelling Control"*, Harper Collins Publishers Inc., New York, 644pp.

River model calibration: a genetic algorithm with evolutionary bottlenecking

J.Russell Manson
The Macaulay Institute, Aberdeen, Scotland

Steve G.Wallis
Heriot-Watt University, Edinburgh, Scotland

River Flow 2004—Greco, Carravetta & Della Morte (eds.)

ABSTRACT: The advection-dispersion equation (ADE) has been used widely to model solute transport in fluvial systems. In this model transport is characterized as having an advective (unidirectional) component represented by the velocity, u, and a dispersion (bi-directional) component represented by the dispersion coefficient, D. A significant body of work has been devoted to enhancing the ADE to include transient storage zones (or dead zones). In these enhanced models two additional parameters (α, A_s) are used to characterize the storage zone. So these enhanced models have four characterizing parameters (u, D, α, A_s). Both the standard and enhanced ADE can be calibrated by fitting the model to experimentally derived solute concentration data. If some objective function is defined, such as the sum of the square residuals between model and observations, then it can be minimized by adjusting the model parameters. There are various algorithms available for doing this. In this research a genetic algorithm (GA) approach was used for this task. This is the first time (to the authors' knowledge) that a GA has been used for this particular application. Clearly, as in any optimization approach, a rapid method of finding the objective function value is required. The objective function was defined in terms of the difference between the "data" and "simulations". The simulations were generated by a numerical method of solution. Since it is well known that numerical solutions to advection-diffusion equations are prone to various deficiencies (e.g. numerical diffusion, grid-scale oscillations), it was important to use a tried and tested numerical method that was known to be free of these problems. Therefore we adopted the semi-Lagrangian method, DISCUS. This method includes an explicit, shape-preserving cubic interpolation update for advection and

fully implicit temporal treatments of dispersion and transient storage. Previous work has shown that DISCUS is accurate, robust and computationally efficient over a wide range of Courant and grid Peclet numbers. The semi-Lagrangian approach is also particularly attractive for optimisation problems because it caters well for the use of large time steps. The GA based optimisation of the DISCUS model was applied to a test case of "data" generated with known characterizing parameter values, again using DISCUS. Thus the expectation was that the optimization would correctly identify these known values as the optimum solution. During initial experiments with the GA it was found that it was very good at finding the rough proximity of the global minimum but then it converged very slowly towards the true minimum. To overcome this difficulty, while retaining the GA framework, evolutionary bottlenecking was introduced to the GA. This involved successively and methodologically refining the parameter space and was found to greatly improve convergence.

1 INTRODUCTION

The advection-dispersion equation (ADE) has been used widely to model solute transport in fluvial systems. In this model transport is characterized as having an advective (unidirectional) component represented by the velocity, u, and a dispersion (bi-directional) component represented by the dispersion coefficient, D. Although widely used this model has several deficiencies. One of these is the inability to capture long tails in observed tracer data caused by transient storage zones. Transient storage zones include recirculation areas, streambed irregularities and bed sediment interstices. These zones are thought to be important for nutrient cycling and stream metabolism, [Kim *et al,* 1992; D'Angelo *et al,* 1993; Allan, 1995; DeAngelis *et al,* 1995; Valett *et al,* 1996; Marti *et al,* 1997; Morrice *et al,* 1997] and they have long been recognised as playing an important role in the transport of dissolved or suspended materials in rivers [Thackston and Schnelle, 1970; Sabol and Nordin, 1978; Valentine and Wood, 1979; Purnama, 1988; Denton, 1990]. The storage zone's size (A_s) and the rate at which solute mass is transferred to and from the zone (α) are thought to be important characterizing parameters. So these enhanced models have four characterizing parameters (u, D, α, A_s).

Both the standard and enhanced ADE can be calibrated by fitting the model to experimentally derived solute concentration data. If some objective function is defined, such as the sum of the square residuals between model and observations, then it can be minimized by adjusting the model parameters. There are various algorithms available for doing this. In this research a genetic algorithm (GA) approach was used for this task. This is the first time (to the authors' knowledge) that a GA has been used for this particular application. Clearly, as in any optimization approach, a rapid method of finding the objective function value is required. Herein the objective function was formulated using a numerical solution to the enhanced ADE model. Indeed, the numerical model was used to create the "data" and the "simulations" on which the parameter optimization was based.

Since it is well known that numerical solutions to advection-diffusion equations are prone to various deficiencies (e.g. numerical diffusion, grid-scale oscillations), it was important to use a tried and tested numerical method that was known to be free of these problems. Therefore we adopted the semi-Lagrangian numerical method DISCUS (Domain of Influence Search for Convective Unconditional Stability). This method has been widely applied to fluvial scenarios, being highly suited to the non-uniformity of flow fields found therein. It is described in several earlier papers that demonstrate the successful application of the method to: pure advection in uniform flow [Manson and Wallis, 1995; Manson and Wallis, 1997]; pure advection in non-uniform flow [Manson and Wallis, 1997]; advection-dispersion in uniform flow [Wallis *et al*, 1998] and advection-dispersion in nonuniform flow [Manson and Wallis, 1999].

This method includes an explicit, shape-preserving cubic interpolation update for advection and fully implicit temporal treatments of dispersion and transient storage. Previous work has shown that DISCUS is accurate, robust and computationally efficient over a wide range of Courant and grid Peclet numbers. The semi-Lagrangian approach is also particularly attractive for optimisation problems because it caters well for the use of large time steps.

During initial experiments with the GA it was found that it was very good at finding the rough proximity of the global minimum but then it converged very slowly towards the true minimum. To overcome this difficulty, while retaining the GA framework, evolutionary bottlenecking was introduced to the GA. This involved successively and methodologically refining the parameter space and was found to improve convergence.

2 MODEL DESCRIPTION

Only the enhanced model will be considered here, in which one-dimensional solute transport in steady, nonuniform flows in rivers with transient storage regions is described by the following mass conservation equations,

$$\frac{\partial m}{\partial t} + \frac{\partial um}{\partial x} = \frac{\partial}{\partial x}\left(DA\frac{\partial c}{\partial x}\right) + \alpha A(s-c) \tag{1}$$

$$\frac{\partial sA_s}{\partial t} = -\alpha A(s-c) \tag{2}$$

where m(x, t) is the solute mass per unit length in the main channel (=cA), c(x, t) is the concentration of solute in the main channel, s(x, t) is the concentration of solute in the transient storage zone, Q(x) is the steady main channel river flow, A(x) is the steady main channel cross-sectional area, $A_s(x)$ is the steady transient storage cross-sectional area, D(x) is the longitudinal dispersion coefficient, $\alpha(x)$ is the solute exchange parameter between the main channel and the storage zones, x is the longitudinal spatial co-ordinate and t is time. The following boundary conditions are frequently used with these equations. At the upstream boundary, $c(0, t)=c_i(t)$, which specifies the solute mass entering the computational domain; at the downstream boundary a zero diffusive flux is assumed which implies that solute is advected out of the domain unhindered.

Equations (1) and (2) were solved using a finite volume approach, evaluating the advection term explicitly in time and evaluating the dispersion and transient storage terms

(fully) implicitly in time. The DISCUS method was used for equation (1). This employs a conservative semi-Lagrangian algorithm that combines a finite volume discretisation, the method of characteristics and a flux-based interpolation scheme. The method is explained in detail elsewhere [Manson and Wallis, 1995; Wallis and Manson, 1997; Manson and Wallis, 1997; Wallis *et al*, 1998; Manson and Wallis, 1999; Manson and Wallis, 2000; Manson *et al*, 2001]. The backward implicit method used for the dispersion term and the transient storage terms is unconditionally stable and robust. It is deficient in the sense that it assumes that the exchange transport rates at the future time prevail over the entire time step: however, it does not suffer from the grid-scale oscillations of the formally more accurate Crank-Nicolson method. Tests have indicated that for the range of parameters investigated here the method appears adequate [Manson *et al*, 2001].

When equations (1) and (2) are solved the solution consists of estimates for c and ε over some discretised spatial and temporal domain, i.e. (c_i^n, s_i^n) for i=1 to N and n=1 to T where N is the number of points in the spatial domain and T is the number of points in the temporal domain. If this model is being fitted to observed data that has been collected at M points in space and time then a fitting parameter may be defined as,

$$R = 1 - \sqrt{\frac{1}{M}\sum_{j=1}^{M}\left(c_j^{obs} - c_j^{model}\right)^2} \qquad (3)$$

so that an R value of 1 indicates a perfect fit. Note that only the in stream concentration has been used for the fitting. Concentrations in the transient storage zone are more difficult to measure and so are rarely documented.

3 PARAMETER ESTIMATION BY GENETIC ALGORITHM

3.1 *Introduction*

As defined in equation (3), R is used as the objective function for the genetic algorithm, which seeks to choose the best combination of parameters in order to maximize R. The genetic algorithm employed is a modified version of secur GA by Carroll [Yang *et al*, 1998] and the reader is referred there for details. Briefly however, a population of individuals is defined. Each individual is characterised by four traits that in the current exercise are simply the fitting parameters (u, D, *a*, A_s). One can think of this as analogous to say traits in humans such as eye colour, hair colour etc. So, for example, one individual could have large u, large D, low α and low A_s. Another might have low u, high D, low *a*. and high As. Now if such a population is defined and then pairs of individuals from the population are allowed to reproduce, the offspring will have certain traits of both parents. For this next generation Darwinian selection is applied to allow survival of only the fittest individuals in the new population. Fitness is based on the value of R for the individual. After many generations the population is made up of only the fittest individuals.

Now when the algorithm was implemented, rather than using qualitative trait descriptors such as high and low, each trait was allocated a value from a pre-specified range of the corresponding parameter. Clearly by choosing the number of values available from the range, the precision of the final answer is defined, since using a finer

resolution (larger number of values) enables a greater number of possible parameter combinations to be explored.

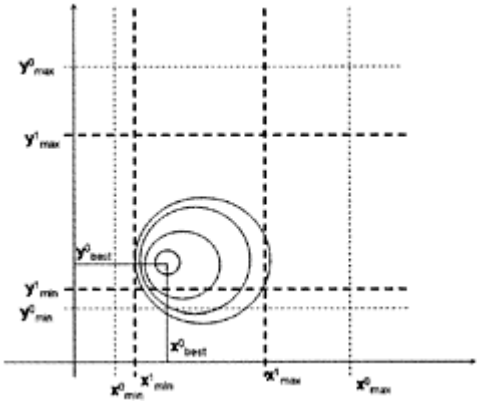

Figure 1. Contours of R over the parameter space (x, y) and important points for the bottlenecking algorithm.

3.2 *Evolutionary bottlenecking*

In evolutionary terminology, "bottlenecking" is defined as a drastic reduction in population size. In the context of the genetic algorithm here we use it to rapidly restrict the parameter search space in a methodological fashion. This has the effect of speeding convergence to the global optimum and is highly effective when convergence is slow, i.e. when the objective function varies very slowly around the optimum point. For ease of explanation let us assume only two parameters (x and y) are involved. If the initial parameter space is defined by the limits: (x^0_{min}, x^0_{max}) and (y^0_{min}, y^0_{max}), see Figure 1, then taking these as the limits of the search space we first use the conventional GA to find the best estimate of the optimum point, let us say this is (x^0_{best}, y^0_{best}). Now we refine our search space to be centred at (x^0_{best}, y^0_{best}) and to extend from x^{i+1}_{min} to x^{i+1}_{max} in the x direction and from y^{i+1}_{min} to y^{i+1}_{max} in the y direction where,

$$x^{i+1}_{max} = x^i_{max} + \zeta_x\left(x^i_{best} - x^i_{max}\right) \tag{4a}$$

$$y^{i+1}_{max} = y^i_{max} + \zeta_y\left(y^i_{best} - y^i_{max}\right) \tag{4b}$$

$$x^{i+1}_{min} = x^i_{min} + \zeta_x\left(x^i_{best} - x^i_{min}\right) \tag{4c}$$

$$y^{i+1}_{min} = y^i_{min} + \zeta_y\left(y^i_{best} - y^i_{min}\right) \tag{4d}$$

This algorithm can be generalized to n parameters as follows:

$$\left.\begin{aligned} {}_j x^{i+1}_{max} &= {}_j x^{i}_{max} - \zeta_j \beta \\ {}_j x^{i+1}_{min} &= {}_j x^{i}_{min} + \zeta_j \beta \end{aligned}\right\} \text{for} \quad j = 1, n \tag{5}$$

where $\beta = \max_j \left| {}_j x^{i}_{best} - {}_j x^{i}_{max} \right|$. The β factor has been introduced to allow a search to move outwith the bottleneck whenever the "best" parameter combination lies at the edge of the bottleneck region.

4 ALGORITHM TESTING

The algorithm was tested by generating some data using the DISCUS model applied to a hypothetical river reach. For this reach the river velocity (u) was set to be 0.05ms^{-1}, the dispersion coefficient (D) was 0.1m^{2}s^{-1}, the exchange rate parameter *(α)* was 0.001s^{-1} and the storage zone size (A_s) was set as 0.05m^2. A tracer distribution was input to the hypothetical river at the upstream end of the reach and allowed to travel for about 2 hours downstream. The simulated concentration versus time curve at the downstream end of the reach was then used as the “data” for the fitting exercise. The genetic algorithm’s goal, therefore, was to find the best fit parameters as [0.05, 0.1, 0.001, 0.05].

To achieve this, a total of 64 possible values for each of the traits were specified from the following initial parameter ranges: (0.0<u<0.1), (0.0<D<0.02), (0.0<α<0.002) and (0.0<A_s<0.1). The traditional genetic algorithm used a population size of 200 and was allowed to evolve for 50 generations, i.e. a random selection of 200 possible parameter combinations was used to generate 200 simulations of the data, using the DISCUS model. This required 10000 simulations and objective function evaluations. For the new (bottlenecking) genetic algorithm the population size was 100 and only 25 generations were used. Therefore only 2500 simulations and objective function evaluations were required. Five bottlenecks were used. The bottleneck fractions were: ζ_u=0.5, ζ_D=0.5, ζ_α=0.5 and $\zeta_{A_s} = 0.9$.

So for the transient storage area the rate of parameter space reduction was restricted. Initial experiments suggested that this prevented premature and erroneous convergence. The results of both the traditional and the bottlenecking genetic algorithms are presented below in Table 1 and Figures 2 and 3. Table 1 shows the final optimum parameters obtained by both algorithms. Note that the traditional GA used four times as many objective function evaluations as the new GA yet three of the four optimum parameters found were still greatly in error, with the transient storage parameters being the most difficult to correctly identify. By increasing the number of generations better estimates could be obtained but convergence was very slow as a direct result of the shape of the optimization surface. The bottlenecking GA, however, which “zooms in” on the optimum achieves a much greater degree of accuracy in many fewer objective function evaluations.

Table 1. Final result of GA searches and % errors.

	Traditional GA		Bottlenecking GA	
u	0.05%	0.00%	0.049959	0.08%
D	0.0976	2.54%	0.099573	0.43%
α	0.00179	−78.90	0.000924	7.60%
A_s	0.091429	−82.86	0.047494	5.01%

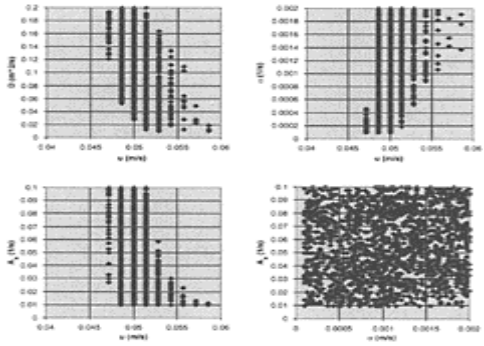

Figure 2. Quasi-confidence regions for traditional genetic algorithm at level R=0.97.

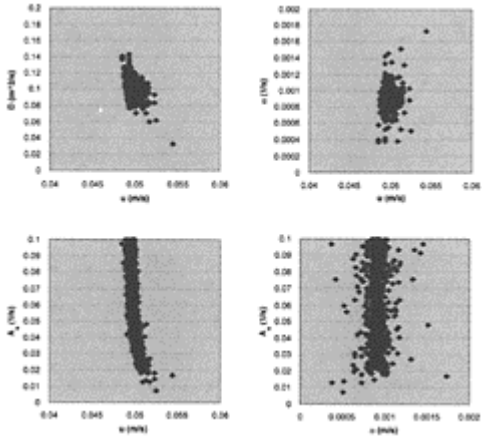

Figure 3. Quasi-confidence regions for bottlenecking genetic algorithm at level R=0.97.

Figures 2 and 3 show the results of the searches in terms of "quasi-confidence" regions, i.e. a point was plotted in the parameter space wherever R was greater than some pre-defined accuracy level. Large regions of widespread points then indicate a highly uncertain parameter estimate. The figures show conditions for an accuracy level of R=0.97 and are particularly informative. The traditional GA (Figure 2) shows very large confidence regions for this test case.

Clearly a great degree of uncertainty surrounds the estimates particularly the transient storage parameters (α, A_s). The smallest quasi-confidence region spread is evident in the velocity parameter. The quasiconfidence region for the transient storage parameters (a and A_s) shows that we can only be confident that the parameters lie within the total parameter space, i.e. little information has been gained by the optimisation process. The bottlenecking GA (Figure 3), however, is much more useful. It manages to establish greater confidence in at least u, D and α. However, at this level (R=0.97) it also has trouble establishing any confidence in A_s, although it does manage to find a good estimate of the point of global maximum R.

5 CONCLUSIONS

This paper has presented a new approach for parameter estimation in river models. The approach has been used here to estimate parameters in an advectiondispersion transient storage model but the technique is not limited to this application. It can be applied in other areas of river modeling. For the application presented here the surfaces of the objective function are often very flat and convergence to the optimum can be very slow. The bottlenecking technique that we have introduced seems to have greatly enhanced the convergence. Clearly this is only one application and further testing of the approach is required. In particular it may be necessary to modify the algorithm to preserve genetic diversity so that interesting search regions are not prematurely excluded.

REFERENCES

Allan, J.D. *Stream Ecology*, Chapman and Hall, 1995.

D'Angelo, D.J., Webster, J.R., Gregory, S.V. and Meyer, J.L. Transient storage in Appalachian and Cascade mountain streams as related to hydraulic characteristics, *J. North American Benthological Society*, **12,** 223, 1993.

DeAngelis, D.L., Loreau, M. and Marzolf, E.R. Modelling nutrient—periphyton dynamics in streams: the importance of transient storage zones. *Ecological modelling*, **80,** 149–160, 1995.

Denton, R.A. Analytical asymptotic solutions for longitudinal dispersion with dead zones, *J of Hydraulic Research*, **28,** 309–329, 1990.

Kim, B.K.A., Jackman, A.P. and Triska, F.J. Modeling Biotic Uptake by Periphyton and Transient Hyporrheic Storage of Nitrate in a Natural Stream. *Water Resour. Res.*, **28,** 2743, 1992.

Manson, J.R., Wallis, S.G. and Hope, D.A. Conservative Semi-Lagrangian Transport Model For Rivers with Transient Storage Zones, *Water Resources Research*, **34**(15), 2000.

Manson, J.R. and Wallis, S.G. A conservative, semiLagrangian fate and transport model for fluvial systems: Part 1—Theoretical Development, *Water Research*, **34**(15), 2000.

Manson, J.R. and Wallis, S.G. Conservative Semi-Lagrangian Algorithm for PollutantTransport in Rivers, *ASCE Journal of Environmental Engineering*, **125**(5), 1999.

Manson, J.R. and Wallis, S.G. An Accurate Numerical Algorithm for Advective Transport, *Communications in Numerical Methods in Engineering,* **11,** pp. 1039–1045, 1995.

Manson, J.R. and Wallis, S.G. Towards an Accurate Fate and Transport Model for Non-uniform Surface Waters, *Advances in Environmental Research,* **1**(1), 1997.

Marti, E., Grimm, N.B. and Fischer, S.G. Pre- and postflood retention efficiency of nitrogen in a Sonoran Desert stream, *J. North American Benthological Society,* **16**(4), 805,1997.

Morrice, J.A., Valett, H.M., Dahm, C.N. and Campana, M.E. Alluvial characteristics, groundwatersurface water exchange, and hydrologic retention in headwater streams, *Hydrological Processes,* **11,** 253, 1997.

Purnama, A. The effect of dead zones on longitudinal dispersion in streams, *J of Fluid Mechancis,* **186,** 351–377, 1988.

Sabol, G.V. and Nordin, C.F. Dispersion in rivers as related to storage zones, *J of the Hydraulics Division,* ASCE, **104,** 695–708, 1978.

Thackston, E.L. and Schnelle, K.B. Predicting effects of dead zones on stream mixing, *J of the Sanitary Engineering Division,* ASCE, **96,** 319–31, 1970.

Valentine, E.M. and Wood, I.R. Experiments in longitudinal dispersion with dead zones, *J of the Hydraulics Division,* ASCE, 105, 999–1016, 1979.

Valett, H.M., Morrice, J.A., Dahm, C.N. and Campana, M.E. Parent lithology, surface-groundwater exchange and nitrate retention in headwater streams, *Limnology and Oceanogmphy,* **41**(2), 333, 1996.

Wallis, S.G., Manson, J.R. and Fillippi, L.A. SemiLagrangian Algorithm for One-Dimensional Advection-Diffusion, *Communications in Numerical Methods for Engineering,* **14,** pp. 671–679, 1998.

Wallis, S.G. and Manson, J.R. Accurate numerical simulation of advection using large time steps, *International Journal of Numerical Methods in Fluids,* **24,** pp. 127–139, 1997.

Yang, G., Reinstein, L.E., Pai, S., Zhigang, X. and Carroll, D.L. A new genetic algorithm technique in optimization of permanent prostate implants, *Med. Phys.* **25** (12). 1998.

Gas-transfer coefficient in a smooth channel. A preliminary assessment of dimensional analysis-based equation

Carlo Gualtieri & Guelfo Pulci Doria
Hydraulic and Environmental Engineering Department "Girolamo Ippolito", University of Napoli "Federico II", Napoli (Italy)

River Flow 2004—Greco, Carravetta & Della Morte (eds.)

ABSTRACT: Recent studies have confirmed that literature equations for the estimation of the reaeration rate are not applicable to all stream hydrodynamic conditions. Since recent efforts have been addressed to develop a comprehensive approach to gas-transfer using dimensional analysis to clearly identify the parameters involved in the process, the present paper provides a preliminary quantitative assessment for this approach using 65 literature laboratory data collected in smooth channels.

1 FOREWORD

The exchange of gases across the air-water interface is important in regulating concentrations of various substances of environmental and water quality concern, such as oxygen, nitrogen, and volatile toxics (Thibodeaux 1996; Chapra 1997). Oxygen transfer at free surfaces has been widely studied since dissolved oxygen (DO) is a key water quality parameter and water quality standards and criteria for DO are provided by environmental regulation of many countries, such as USA, UK, Germany and Japan. Also in Italy, D.L. 152/1999 has, recently, established for streams and lakes a classification system which considers DO as a significant parameter (Ciaravino & Gualtieri 1999). The oxygen transferred from the atmosphere by means of natural reaeration replaces the amount consumed due to the oxidation of organic matter discharged into the water body.

The flux of dissolved oxygen Φ at the air-water interface [$ML^{-1}T^{-2}$] has been quantified according to (Chapra 1997):

$$\Phi=K_L\cdot(C_{sat}-C_w) \quad (1)$$

where K_L is the gas-transfer rate [LT^{-1}], C_{sat} is the equilibrium, or saturation, concentration of DO [ML^{-3}] and C_w is the DO concentration in the bulk water [ML^{-3}]. Accordingly, oxygen is lost to the atmosphere when the upper waters are oversaturated ($C_{sat}<C_w$), and reaeration occurs when $C_{sat}>C_w$. The accuracy of estimates of Φ depends on the accuracies of the specifications of the gas-transfer coefficient, K_L, and C_{sat} and C_w. Reaeration process is often parameterised using the volumetric reaeration coefficient K_a [T^{-1}], given, if h [L] is water mean depth, by (Chapra 1997):

$$K_a = \frac{K_L}{h} \tag{2}$$

Since oxygen has low solubility and high vapor pressure, the exchange process is controlled by the liquid side of the air—water interface (Chapra 1997).

Recent studies have confirmed that available equations for the estimation of the reaeration rate are not applicable to all stream hydrodynamic conditions probably since some parameters involved in the process have been neglected in their formulation (Melching & Flores 1999; Gualtieri et al. 2002). Therefore, recent efforts have been addressed to develop a comprehensive approach to gas-transfer using dimensional analysis to clearly identify the parameters involved (Gualtieri et al. 2002; Gualtieri 2003). This approach has provided a relationship between the reaeration coefficient K_L and some classical fluid mechanics index-numbers (Gualtieri et al. 2002). The present paper provides a preliminary quantitative assessment for that relationship using 65 literature laboratory data collected in smooth channels.

2 DIMENSIONAL ANALYSIS OF GAS-TRANSFER PROCESS

In two previous papers a comprehensive approach to the gas transfer process at the air—water interface based on dimensional analysis was proposed (Gualtieri et al. 2002; Gualtieri 2003).

Gas-transfer is mainly controlled by the turbulence at both side of the air-water interface. Characterizing turbulence influence on gas-transfer across air-water interface has been proved to be difficult since this influence depends on relative phase velocities, roughness of surfaces at the interface, frictional and adhesive forces, surface tensions and several other parameters (Weber & DiGiano 1996). Also, anisotropic turbulent conditions, with significant correlation between the velocity fluctuations and the presence of a velocity gradient and a shearing stress, further complicate modeling effort (Moog & Jirka 1999). However, if the gas-transfer is controlled by the liquid side, the nature of turbulent eddies in the water can affect the parameters influencing the gas-transfer. Therefore, gas-transfer modeling approaches are different in shallow and rapidly flowing waters and in deep and standing waters because the nature of the forcing mechanism is different. In shallow streams, the surface turbulence is mainly due to the water velocity or, more precisely, to the interaction of the water flow with the bottom rugosity and depth variations. At the contrary, the surface of deeper environments is not affected by bottom features, and the shear stress exerted by the wind at the air-water interface is the main physical factor of turbulence (Chu & Jirka 1995). Also, in deep channels isotropic turbulent conditions, where the intensity of the velocity fluctuations in all three directions

is very nearly the same, are more likely to exist (Thibodeaux 1997). The proposed analysis was addressed to turbulence generated by bottom shear stress, where the gas-transfer process is affected by the fluid and gas properties and by the hydrodynamics of the flow. A characteristic feature of turbulent flow is the presence of a wide range of eddy sizes, ranging to the flow domain to smaller sizes. If large eddies break down into multiple smaller eddies, they conserve their kinetic energy, which is efficiently transferred through a cascade of eddy sizes (Pope 2000; Socolofsky & Jirka 2002).

When the eddies become small enough, in the order of Kolmogorov scale in size, viscosity takes over and the energy is finally dissipated into heat. This conversion of energy can be quantified using the kinetic turbulent energy dissipation rate ε [L^2T^{-3}]. In a homogeneous turbulent flow, production and dissipation of kinetic energy are balanced and ε must equal the total turbulent kinetic energy of the flow, k. The rate ε is proportional to the energy line slope J_e as:

$$\varepsilon=gvJ_e \tag{3}$$

Therefore, J_e should be included as key parameter in the dimensional analysis of gas-transfer process. Notably, in steady uniform flow, the energy line slope J_e is equal to the water surface slope J_w and to the bed slope J_b, whereas for steady non-uniform flow, they are generally different (Graf 1998). Consider now that it holds that $R_h \approx h$, where R_h is the hydraulic radius. Also, assume that the gas-transfer process is controlled by the water side concentration boundary layer (CBL). Thus, the dimensional analysis could consider the following parameters:

- natural constants and fluid properties such as the gravitational acceleration constant g[LT^{-2}], the water kinematic viscosity v[L^2T^{-1}], and the water surface tension T_s[MT^{-2}];
- gas exchanged properties, such as the molecular diffusion coefficient D_m[L^2T^{-1}];
- flow properties, such as the mean depth h[L], the mean streamflow velocity v[LT^{-1}], the energy line slope J_e, the channel bed slope J_b and the Manning's roughness coefficient n.

First, the water surface tension, T_s, was transformed into a kinematic parameter as $\tau_s=T_s/\rho$[L^3T^{-2}], where ρ is the water density [ML^{-3}]. Also, the coefficient n can be expressed as:

$$n=n(\varepsilon_{cw}) \tag{4}$$

where ε_{cw} is the roughness coefficient of Colebrook-White equation, that could be applied with good approximation also for streams and rivers. Thus, it holds:

$$K_L=f_1[g, v, \tau_s, D_m, h, v, J_e, J_b, \varepsilon_{cw}] \tag{5}$$

Assuming as fundamental quantities the water mean depth h, [L] and the molecular diffusivity D_m, [L^2T^{-1}], the dimensional analysis leads to

$$Sh=f_2[Sc,We, Re, Fr, J_e, J_b, S] \tag{6}$$

where Sh, Sc, We, Re, and Fr are the classical Sherwood number, Schmidt number, Weber number, Reynolds number, and Froude number, respectively. Sh, Sc, and We are defined as:

$$Sh = \frac{K_L \cdot h}{D_m} \tag{7}$$

$$Sc = \frac{\nu}{D_m} \tag{8}$$

$$We = \frac{U \cdot h}{(T_s/\rho)^{0.5}} \tag{9}$$

where U is water depth-averaged flow velocity [LT^{-1}]. Finally, the relative roughness S is:

$$S = \frac{\varepsilon_{cw}}{4h} \tag{10}$$

Equation (6) is the final form of the dimensionless gas-transfer rate in an open channel for liquid-controlled chemicals. This equation holds whatever is the gas involved in the gas-transfer. Notably, classical Darcy-Weisbach equation provides a relation between Fr, Re, J_e and S; thus, one of these parameters could be expressed as a function of the remaining three of them (Gualtieri et al. 2002). Also, in eq. (6) the temperature influence is directly accounted for through the temperature dependent parameters, such as Sc and We. This represents an advantage respect to the common application of a temperature corrective coefficient, such as the classical θ of Van't Hoff-Arrhenius equation (Chapra 1997).

2.1 *Comparison with large-eddy and small-eddy models*

Classical literature large-eddies and small-eddies models could be compared with the findings of the outlined dimensional analysis. These models start from surface renewal model, which states that rate of gastransfer through the air-water interface depends on the length of time that a certain water parcel coming from the bulk water due to turbulent eddies is exposed to the atmosphere. This time could range from zero to infinity. If r is the rate of surface renewal [T^{-1}], the application of Fick's law leads to:

$$K_L = \sqrt{D_m r} \tag{11}$$

Therefore, r, which is a characteristic of the turbulence, should be estimated. Two different approaches could be used depending on the considered size of turbulent motions renewing the CBL. If renewal process is mainly affected by the largest, integral-scale eddies, the r is proportional to the intensity and to the scale of turbulence. Thus, vertical fluctuation velocity u′[LT^{-1}] and Prandtl mixing length 1[L] are used to define r (O'Connor & Dobbins 1958; Thibodeaux 1997). Also, they are usually related to the

shear velocity u*[LT^{-1}] and to the mean depth h, respectively, to consider that the renewal rate is [T^{-1}]. This is the *large-eddy* model which states that (Moog & Jirka 1999):

$$K_{L\text{-}ND} = \frac{K_L}{u'} \approx \frac{K_L}{u^*} \propto Sc^{-0.5}\, Re^{*-0.5} \tag{12}$$

where $K_{L\text{-}ND}$ is the dimensionless gas-transfer rate and Re* is the shear Reynolds number Re*=(u*4h)/*v*. At the contrary, since the air-water interface tends to damp the eddies as they approach to it closer than their length scale, the contribution of small eddies, at the Kolmogorov scale, in renewing the CBL could be considered. Following this approach, that is called the *small-eddy* model, the renewal rate is $r \propto (\varepsilon\nu)^{0.5}$ and the dimensionless gas-transfer rate is (Moog & Jirka 1999; Socolofsky & Jirka 2002):

$$K_{L\text{-}ND} = \frac{K_L}{u^*} \propto Sc^{-0.5}\, Re^{*-0.25} \tag{13}$$

Therefore, these two models could be generally represented as:

$$K_{L\text{-}ND} = c_1\, Sc^{-0.5}\, Re^{*n} \tag{14}$$

where c_1 is a constant and n=−0.50 holds for the *large-eddy* model and n=−0.25 holds for the *small-eddy* model. Despite to their expressions, these models could be reduced to the proposed dimensional analysis. In fact, both equations (12) and (13) could be transformed into a form similar to (6). In particular, equations (12) and (13), after some arrangements, become:

$$Sh \propto Sc^{0.5}\, Re^{0.5}\, Fr^{-0.5}\, J_e^{0.25} \tag{15a}$$

$$Sh \propto Sc^{0.5}\, Re^{0.75}\, Fr^{-0.75}\, J_e^{3/8} \tag{15b}$$

where, differently than in eq. (6), there are not the Weber number We, the channel bed slope J_b and the relative roughness S. Thus, *large-eddy* and *small-eddy* models should be considered as a particular form of eq. (6) where the effect of the water surface tension, of the bed slope and of the roughness is not accounted for.

3 DATA ANALYSIS AND DISCUSSION

The present paper provides a preliminary quantitative assessment of the eq. (6) using 65 laboratory data collected in smooth channels, i.e. S=0. The considered data refer to different environmental and hydrodynamic conditions, though uniform flow conditions hold, i.e. J_e=J_b. First of all, the Froude number was discarded since it can be expressed using S, Re and J_e. In fact, classical Darcy-Weisbach equation states;

$$J_e = \frac{\lambda}{4h}\frac{v^2}{2g} = \frac{\lambda}{8} Fr^2 \tag{16}$$

where λ is the friction factor, that in a turbulent flow is λ=λ(Re, S). Thus, eq. (17) yields:

$$J_e = \frac{\lambda(Re,S)}{8} Fr^2 = J_e(Fr, Re, S) \tag{17}$$

where Fr, S, Re and J_e=J_b are correlated. Equation (17) could be modified depending on certain;

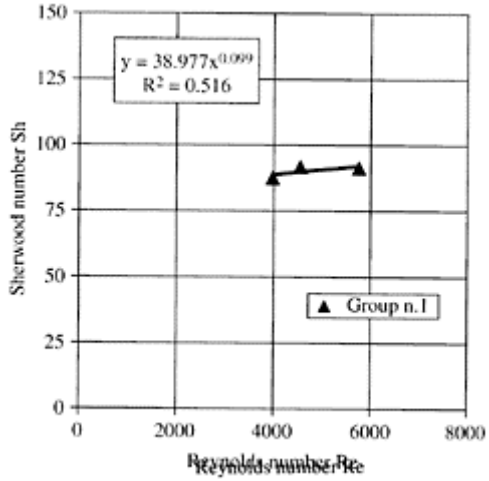

Figure 1. Group n.1.

particularly, each one of the considered parameters could be, in turn, expressed as a function of the others. For example the Froude number could be always expressed as:

$$Fr = \sqrt{\frac{8 J_b}{\lambda(Re,S)}} = Fr(J_b, Re, S) \tag{18}$$

Also, as a first approximation, since for the considered data the variation range of the Weber number is narrow, the influence of We was discarded. Thus, equation (1) yields:

$$Sh=f_3[Sc, Re, J_b] \tag{19}$$

where Sherwood number is affected by only Sc, Re and J_b. Usually, correlations between Sh and Re are in the form (Incropera & DeWitt 1990):

$$Sh=a\cdot Re^b\cdot Sc^c \tag{20}$$

where a, b, and c are constants which are derived from regression on experimental data. Often, c parameter is set c=0.33, whereas the values of b exponent is reported on literature to be 0.87 (Probstein et al. 1972), 0.91 (Harriott & Hamilton 1965), 0.80 (Incropera & De Witt 1990) and 0.89±0.05 (Steinberger & Hondzo 1999).

The data used in the present study are all taken from literature. Particularly, the considered data are those collected in laboratory flumes by Moog and Jirka (Moog & Jirka 1999), by Ran (Ran et al. 2002; Ran 2003), by Lau (Lau 1975), and by Thackston

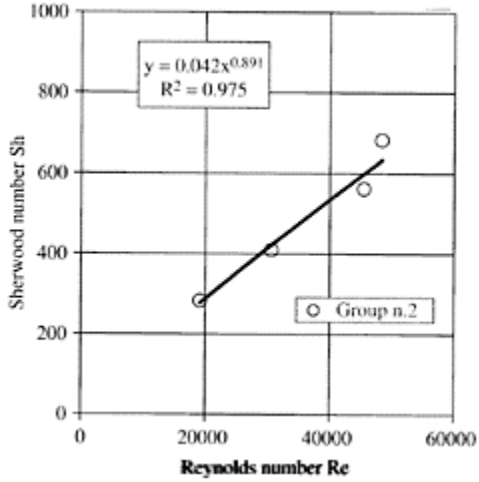

Figure 2. Group n.2.

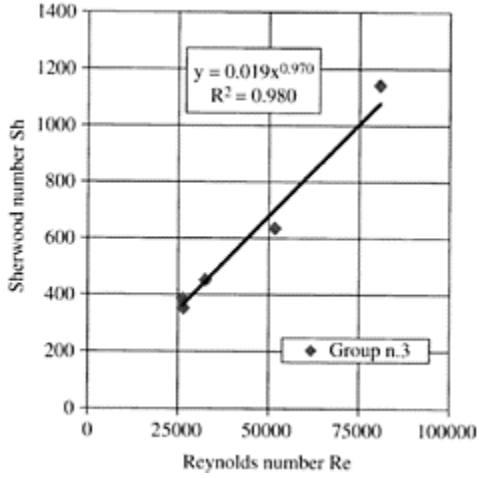

Figure 3. Group n.3.

and Krenkel (Thackston & Krenkel 1969), where well-controlled conditions hold.

These four data sets refer to rectangular smooth-channels where the width ranged from 0.4 to 1.00m. Notably, there is a significant separation in magnitude between the data by Moog-Jirka and the other three flume data sets since the first ones are generally higher (Moog & Jirka 1999).

In the considered experiments the flow velocity ranged from 0.036 to 1.040m/s, while water depth was from 0.011 to 0.145m. The aspect ratio W/h_{avg}, which has a significant influence on gas-transfer process (Gualtieri & Gualtieri, in press), ranged from 5.15

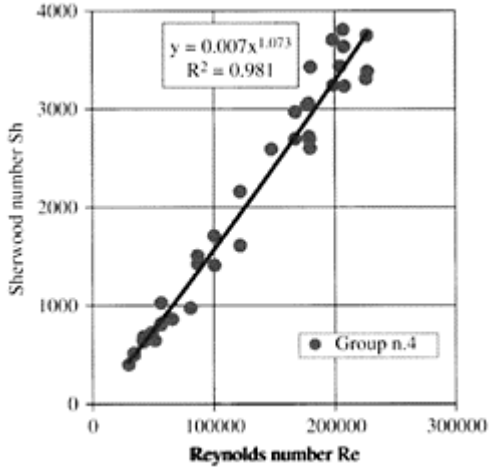

Figure 4. Group n.4.

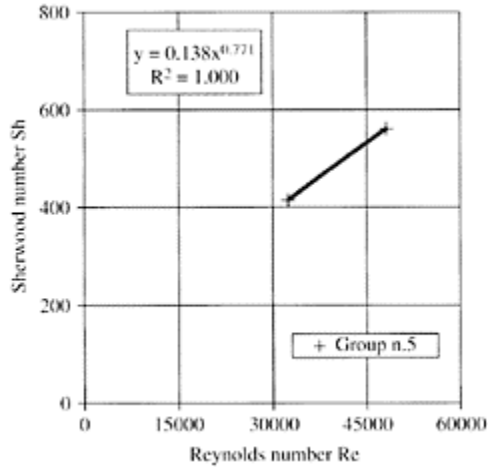

Figure 5. Group n.5.

to 54.15. Interestingly W/h=5 is the threshold value for a “wide” open channel, where the effect of secondary currents or “corner flows” could be neglected (Nezu & Nakagawa 1993).

Finally, water temperature ranged from 11.3 to 25.7°C. Accordingly, Schmidt number was in the range from 419.6 to 890.6, with an remarkable number of data with Sc=548, i.e. Lau data.

The analysis of the raw data has shown that they could be divided in 8 groups according the value of the channel bed slope J_b and the Schmidt number Sc.

The main characteristics of each Groups are listed in Table 1, where the number of data, the average bed

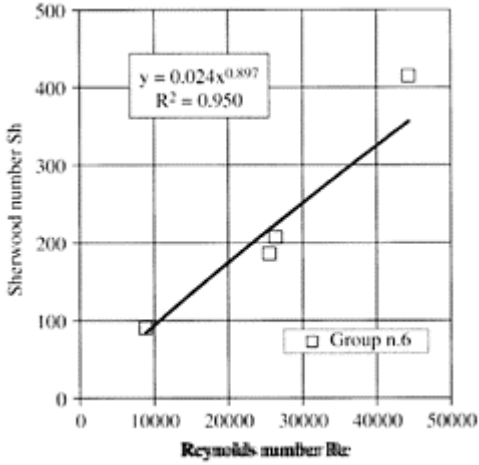

Figure 6. Group n.6.

slope J_b value, the average Sc value, and the average Re value are presented.

Bed slope $J_{b\text{-}avg}$ ranged from 0.00003 to 0.00350. Groups 4 refers to data with the same J_b, which is equal to 0.01. Also, Groups 5 and 6 have similar value of slope $J_{b\text{-}avg}$. while their Sc_{avg} is different. Since the range of water temperature is quite narrow, the average Schmidt number Sc_{avg} of the Groups ranged from 433 to 752. Moreover, Groups 1–5 have the same or very similar values of Sc_{avg} and their overall average Schmidt number is Sc_{avg}=526. Finally, the values of Re_{avg} exhibits an higher range, from 3977 to 227048. Groups 1–3 data belong to Lau set, whereas Group 4 is formed by Ran data. Groups 5 and 6 collect data collected by Lau and by Thackston and Krenkel, respectively. Finally, the higher data by Moog and Jirka are in Groups 7–8. These Groups present the highest Sc_{avg} values, i.e. 704 and 752, respectively.

In the present study a power relation between Sh and Re was proposed as:

$$Sh=\mu_1 Re^{\alpha} \tag{21}$$

where μ_1 parameter depends from Sc and from the channel bed slope J_b as:

$$\mu_1=\mu_1(Sc, J_b) \tag{22}$$

In the proposed model the dimensionless gas-transfer in quiescent water conditions is assumed to be zero. However, in stagnant water, i.e. Re=0, gas-transfer process occurs due to molecular diffusion (Thibodeaux 1997; Li Ran et al. 2002). Thus, a gas-transfer

rate for these conditions should be considered, but the available data does not allow to estimate this

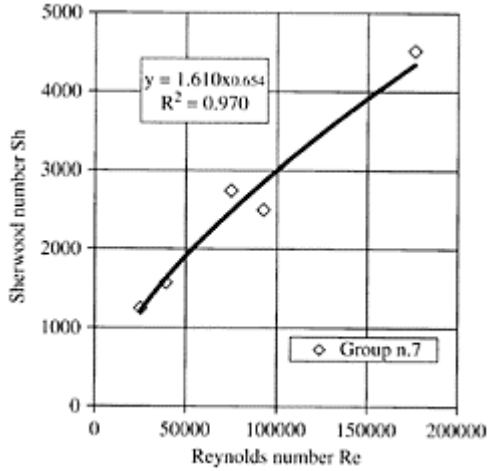

Figure 7. Group n.7.

Table 1. Considered Groups of data.

Group	Data	$J_{b\text{-}avg}$	Sc_{avg}	Re_{avg}	α
1	3	0.00003	548	4759	0.099
2	4	0.00039	548	35909	0.891
3	5	0.00077	548	43491	0.970
4	38	0.00100	518	125004	1.073
5	2	0.00174	548	40322	0.771
6	4	0.00175	433	26260	0.897
7	5	0.00070	752	81550	0.654
8	4	0.00350	704	92659	0.558

rate. Moreover, since gas-transfer process in stagnant water is driven by molecular diffusion, this rate should be a temperature-dependent parameter.

The power relationship, i.e. eq. (21), between Sh and Re is presented for each Group in plots from Fig. 1 to Fig. 8, where R^2 parameter is also indicated.

Moreover, α parameter values are listed in Table 1. These values are mostly close to literature values.

First of all, results demonstrate that eq. (21) provides a general good agreement with laboratory data and the proposed model is supported by the experimental data. Second, since it was assumed that α parameter is independent from Sc, a common value for α

should be adopted. Thus, α values obtained from all Groups were corrected using a weight criterion which considers 3 parameters.

The first one is the number of data belonging to each Group, the second one is ratio $\Delta Re/Re_{avg}$, i.e. the ratio of the difference ΔRe between maximum and minimum Reynolds number to Re_{avg} value in each Group, while the third one is $1/Re_{avg}$. As a result, a value of α=0.78 was estimated. This value was

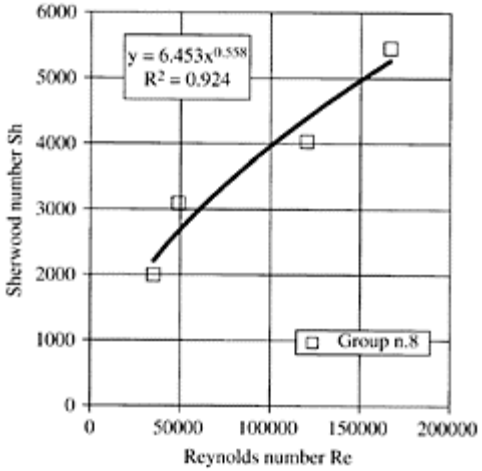

Figure 8. Group n.8.

Table 2. Corrected values for μ_1 and α parameters.

Group	Data	α	μ_1
1	3	0.78	0.119
2	4	0.78	0.138
3	5	0.78	0.153
4	38	0.78	0.233
5	2	0.78	0.124
6	4	0.78	0.087
7	5	0.78	0.368
8	4	0.78	0.466

adopted as α in eq. (21) for all the Groups. Notably, this value is consistent with those previously reported from literature.

As a result, corrected value for μ_1 values were obtained. They are listed in Table 2. The analysis of μ_1 data supports an interesting trend between μ_1 parameter, on one hand, and the bed slope J_b and Schmidt number, on the other hand (Fig. 9).

In fact, Fig. 9 shows that for Sc_{avg}=526 (the open circles) μ_1 parameter significantly increases with increasing slopes J_b. Also, the data for Sc=432 (the diamonds) presents for the same J_b lower μ_1 than those for Sc_{avg}=526. Moreover, the same trend could be observed in the data with higher Schmidt number (the triangle and the cross), i.e. Sc=704 and Sc=752, where μ_1 parameter increases with increasing J_b.

This results demonstrate that gas-transfer process is enhanced by higher channel bed slope J_b for the same value of the Reynolds number. Thus, they confirmed that the bed slope J_b parameter should be included in gas-transfer modeling framework.

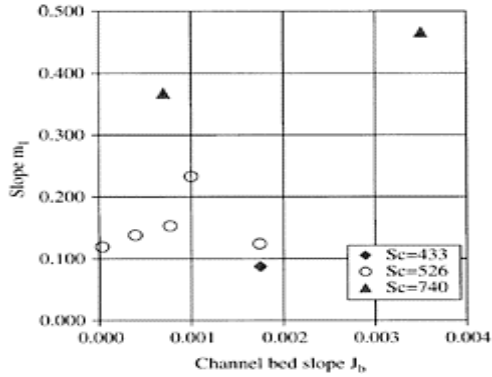

Figure 9. μ_1 parameter vs channel bed slope J_b.

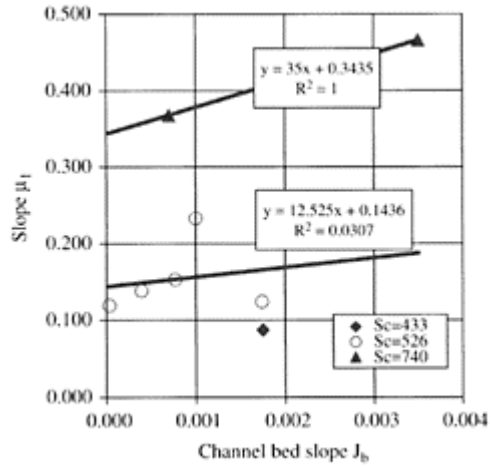

Figure 10. μ_1 parameter vs channel bed slope J_b.

The two data with higher Sc were then regrouped adopting an average Schmidt number, i.e. Sc_{avg}=740. Linear regression of μ_1 parameter on bed slope J_b for both Sc_{avg}=526 and Sc_{avg}=740 is presented in Fig. 10, The Group with Sc_{avg}=526 has 52 data, whereas the Group with and Sc_{avg}=740 has 9 data. Finally, only one data was available for Sc_{avg}=433. Data with lower Sc_{avg} exhibit an higher increase with J_b. Thus, the influence of Sc on μ_1 is supported and it holds:

$$\mu_1=\mu_2 J_b+\mu_3 \quad (23)$$

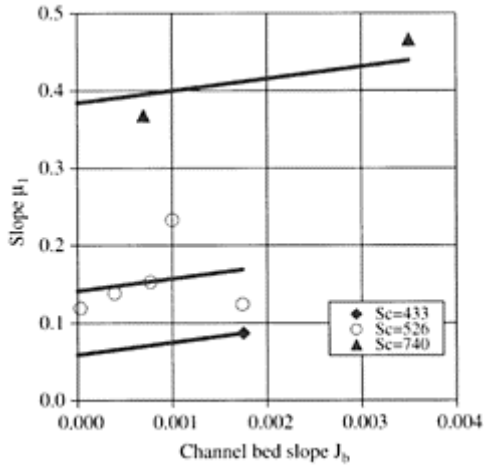

Figure 11. Corrected μ_1 parameter vs channel bed slope J_b.

where μ_2 and μ_3 appear to be both affected by Sc. Fig. 10 shows that μ_3 is 12.52 and 35 for Sc_{avg}=526 and Sc_{avg}=740, respectively. These μ_2 values have been averaged using the number of data with Sc_{avg}=526 and Sc_{avg}=740, i.e. 52 and 9, respectively. A weighted averaged value of μ_2=15.75 has been obtained. Results are presented in Fig. 11. Notably, μ_3 parameter data support Sc influence. Therefore, eq. (21) yields:

$$Sh=[15.75J_b+\mu_3(Sc)]Re^{0.78} \quad (24)$$

4 CONCLUDING REMARKS

Recent efforts have been addressed to develop a comprehensive approach to gas-transfer modeling. The present paper has provided a preliminary quantitative assessment for an approach based on dimensional analysis using 65 laboratory data collected in smooth channels.

The present paper proposed a power relationship between the dimensionless gas-transfer rate and Reynolds number. The slope μ_1 of that relationship was found to be

affected both by the channel bed slope Jb and by the Schmidt number. A linear relationship between μ_1 and J_b was derived for different Schmidt numbers. Its slope was finally averaged for all the data, providing a predictive equation which relates dimensionless gas-transfer rate with J_b, Sc and Re. Further research should be focused to explore the influence on K_L of surface tension and channel roughness developing a predictive equation including also We and S.

ACKNOWLEDGMENT

The paper was prepared as a part of MURST PRIN 2002 research project. *Influence of vorticity and turbulence in interactions of water bodies with their boundary elements and effects on hydraulic design.*

REFERENCES

Chapra S.C. (1997). *Surface water quality modeling.* McGraw-Hill, New-York, USA

Ciaravino G. & Gualtieri C. (1999). *Dissolved oxygen balance in a stream* (in italian). *Water resources utilization and management* Conference, Roma, Italy, March 29, 1999

Graf W.H. (1998). *Fluvial hydraulics.* John Wiley & Sons, Chichester, UK

Gualtieri C. & Gualtieri P. (1997). Hydrodynamic model for reaeration estimation in surface waters (in italian). *AIMETA '97,* Siena, Italy, 29 September/3 October 1997 vol.1 , pp. 155–164

Gualtieri C. & Gualtieri P. (1999). Statistical analysis of reaeration rate in streams. *International Agricultural Engineering Conference (ICAE) '99,* Pechino, China, December 14/17 1999,

Gualtieri C. & Gualtieri P. (2000). Field verification for a reaeration model in streams. *4th International Conference on Hydro Science & Engineering (ICHE 2000),* Seoul (Korea), September 26/29 2000,

Gualtieri C. & Gualtieri P. (in press). Turbulence-based models for gas transfer analysis with channel shape factor. *Environmental Fluid Mechanics*

Gualtieri C., Gualtieri P. & Pulci Doria G. (2002). Dimensional analysis of reaeration rate in streams. *Journal of Environmental Engineering, ASCE,* vol. 128, n. 1, January 2002 , pp. 12–18

Gualtieri C. (2002). Modeling mass-transfer of VOCs in open channels. *5th International Conference on HydroScience & Engineering (ICHE 2002),* Warsaw, Poland, September 18/21 2002,

Gualtieri C. (2003). Dimensional analysis of gas-transfer process in a turbulent flow. *XXX IAHR Congress,* Thessaloniki, Greece, August 24/29 2003,

Gulliver J.S. & Halverson M.J. (1989). Air-water gas transfer in open channels. *Water Resources Research,* vol. 35, n. 8, pp. 1783–1793

Incropera F.P & DeWitt D.P. (1990). *Fundamentals of Heat and Mass Transfer.* John Wiley and Sons, New York

Lau Y.L (1975). An experimental investigation of reaeration in open-channel flow. *Progress in Water Technology,* vol. 7, n. 3/4, pp. 519–530

Melching C.S. (1998). *U.S. Geological Survey reaeration rate database.* Personal communication to the first author, April 1998

Melching C.S. & Flores H.E. (1999). Reaeration equations derived from U.S. Geological Survey database. *J.Environmental Engineering Division, ASCE,* 125, 5, May 1999, pp. 407–414

Moog D.B. & Jirka G.H. (1999). Air-water gas transfer in uniform channel flow. *J.Hydraulic Engineering, ASCE,* 125, 1, January 1999, pp. 3–10

Nezu I. & Nakagawa H. (1993). *Turbulence in open-channel flows.* IAHR Monograph Series, Balkema, Rotterdam, The Netherlands

Pope S.B. (2000). *Turbulent flows.* Cambridge University Press, Cambridge, U.K.

Probstein R.F, Sonin A.A. and Gur-Arie E. (1972). A turbulent flow theory of electrodialysis. *Desalination,* 11, 165–187

Ran L., Lin L., Xiao-Ying F. & Wendian H. (2002). Study on the effect of hydrodynamic characteristic on reaeration process. *Journal of Environmental Sciences,* 14, n. 3, pp. 393–398

Ran L. (2003). *Reaeration data.* Personal communication to the first author, May 2003

Socolofsky S.A. and Jirka G.H. (2002). *Environmental Fluid Mechanics. Part I: Mixing, Transport and Transformation.* Engineering. Lectures. Institut für Hydromechanik, University of Kalsruhe, Germany

Steinberger N. & Hondzo M. (1999). Diffusional mass transfer at sediment-water interface. *J. Env. Eng. Div. ASCE,* vol. 125, n. 2, pp. 192–200

Thackston E.L. & Krenkel P.A. (1969). Reaeration prediction in natural streams. *J.Sanitary Engineering Division, ASCE,* 95, 1, January—February 1969, pp. 65–93

Thibodeaux L.J. (1996). *Environmental chemodynamics.* John Wiley & Sons, Chichester, U.K.

Weber W.J. & DiGiano F.A. (1996). *Process dynamics in environmental systems.* John Wiley & Sons, Chichester, U.K.

A methodological approach for surface water vulnerability assessment

M.Giugni
Dip. di Ing. Idraulica ed Ambientale "G.Ippolito", Università degli Studi di Napoli Federico II, Napoli, Italy

G.Pappalardo & G.Lombardi
Autorità di Bacino Regionale Destra Sele, Napoli, Italy

N.Fontana
Dipartimento di Ingegneria, Università degli Studi del Sannio, Benevento, Italy

River Flow 2004—Greco, Carravetta & Della Morte (eds.)

ABSTRACT: The recently introduced Italian laws (D.L. 152/99 and D.L. 258/00) have drawn attention to the issues of conservation and recovery of the natural environment by defining general guidelines for the protection of surface, ground and coastal waters. A methodological approach has been developed in order to assess the vulnerability of surface waters and to define their environmental quality on the basis of an integrated analysis of the river's ecosystem, which makes it possible for each river (or reach of river) to be attributed with an overall index reflecting its environmental quality *(river's environmental quality map)*. This procedure had been applied to the pilot watershed of the Tusciano river (Southern Italy), by means of a monitoring network comprised of 8 experimental sections. The activities carried out have stressed the substantial validity of the methodology and have made it possible to draw up a preliminary draft of the environmental quality map.

1 INTRODUCTION

The Italian law D.L. 152/99 defines the general framework for safeguarding surface, ground and coastal waters by pursuing the objectives of preventing or controlling pollution, restoring water quality, protecting waters used for special purposes, ensuring

the sustainable use of available resources and preserving the waters' natural ability to cleanse itself of impurities.

These objectives will be met through the use of a variety of instruments, including the targets of environmental quality and Protection Plans. However, before Protection Plans can be defined, the qualitative and quantitative status of water bodies needs to be determined and information has to be acquired regarding the physical, natural, social and economic characteristics of the basins in order to assess anthropic pressure and impact.

This varied set of investigative and planning activities constitutes a totally new approach to environmental policies regarding water resources in Italy.

2 METHODOLOGICAL APPROACH FOR SURFACE WATER ENVIRONMENTAL QUALITY ASSESSMENT

The first step in implementing Protection Plan calls for an environmental quality status to be attributed to the surface waters. Following the investigative surveys previously carried out in the area under the control of the Destra Sele Water Authority (Giugni et al. 2002), a methodological procedure was defined on the basis of assessments made regarding some indicators of the water quality and the Minimum Instream Flow. This allows a preliminary judgement to be made on the river's environmental quality so that suitable safeguards can be adopted and hence contribute to the planning activity regarding water usage.

More specifically the procedure calls for:

a) Physical, chemical and microbiological investigations aiming to assess the Level of Pollution from Macrodescriptors (LPM), which can be obtained by measuring the *macrodescriptor parameters for the classification of surface waters* (dissolved oxygen, BOD_5, COD, ammonium—nitrogen NH_4, nitrate-nitrogen NO_3, total phosphorous, Escherichia coli). This will enable a preliminary quality assessment to be attributed to the river in question. The subsequent measurement of additional parameters regarding organic and inorganic micropollutants (pesticides, organic solvents, aromatic polycyclical hydrocarbons, cadmium, chromium, mercury, nickel, lead, copper, etc.) will provide further information on the system's quality and vulnerability and on the extent of the transported load;
b) Biological Mapping of the river, aiming to assess the Extended Byothic Index (E.B.I.). Biological mapping allows a further assessment to be made, which is complementary to the physical, chemical and microbiological investigation, by assessing the overall effect of pollutants and various other external influences, even if only present sporadically or in very small quantities (Ghetti 1995, 1997, Ruffo 1995, European Environment Agency 1999). Furthermore, the E.B.I. score corresponds to a preliminary quality class;
c) Classification of the River Ecological Status (RECS) achieved by comparing the quality class supplied by the macrodescriptors (LPM) with the result of the EBI, and attributing the reach in question with the worse of the two values. Table 1 reports the quality classes envisaged by Italian law D.L. 152/99;

d) Determination of the definitive River Environmental Quality Status (REQS), by cross-referencing the ecological data with those regarding the presence of organic and inorganic chemical pollutants according to the diagram reported in Table 2;
e) Definition of the River Functionality Index (RFI): the RFI is derived from the RCE-I *(Riparian Channel Environmental Inventory)*. This method was defined by R.C. Petersen (1992) who based it on a 16-question checklist with 4 possible predetermined answers for each one. The main purpose of the proposed model was to collect information regarding the river's main ecological characteristics in order to set up an inventory on the conditions of Swedish rivers and riverbank vegetation. In this framework, although the environmental assessment can be inferred from the scores attributed to the individual characteristics, in actual fact, it was more of a by-product than an explicit goal of the investigation. Its many applications in Italy increasingly brought to light the importance that this methodology could assume not only in helping draw up an inventory of environmental characteristics, but above all as a model for assessing environmental quality. Consequently, the RCE-2 was proposed with a new assessment checklist (Siligardi e Maiolini 1993). When the new index was applied to cases all over Italy, it was seen to be inadequately calibrated with respect to the large number of possible river types, thus fuelling the fear that the RCE was beginning to encompass a heterogeneous family of indices having different contents and goals. Hence the need to update the method so as to make it more general and to allow it to define the goals more rigorously by drawing up guidelines and precise instructions for its users. The modifications made by a working group coordinated by the Italian National Environmental Protection Agency (A.N.P.A.) were so far-reaching that the index was attributed with a

Table 1. River quality classes.

Quality class	Judgement	Colour
I	Not polluted (or not considerably alterated) environment	Blue
II	Environment that shows some pollution's consequences	Green
III	Polluted environment	Yellow
IV	Very polluted environment	Orange
V	Greatly polluted environment	Red

Table 2. River Environment Quality Status (REQS).

Concentration of organic and inorganic chemical pollutants	REQS Class				
	1	2	3	4	5
≤Threshold value	Very good	Good	Suffic.	Poor	Very bad
>Threshold value	Poor	Poor	Poor	Poor	Very bad

new name, the River Functionality Index (ANPA 2000, Siligardi et al. 2000). The RFI checklist comprises 14 questions (with 4 predetermined answers) organised in functional groups:

- questions 1–4 concern the *conditions of plant life along the riverbanks and in the surrounding area*;
- questions 5 and 6 refer to the *relative size of the riverbed* and the *physical and morphological structure of the riverbanks*;
- questions 7–11 consider the *structure of the riverbed*;
- questions 12–14 determine biological characteristics through structural analysis of the macrobenthonic and macrophytic community and the conformation of the substrate.

The answers are specified for each bank of the river and are assigned numerical values in 4 ranges (minimum weight 1, maximum weight 30) which express the functional differences between the individual answers. The total score can assume a value between 14 and 300 and this is associated to a Functionality Level and a Functionality Assessment, as shown in Table 3 which also reports the conventional colours used in the mapping activity.

Therefore, the proposed procedure includes not only the indicators specifically envisaged in the national legislation (LPM, EBI, RECS, REQS) but also the River Functionality Index which, in the authors' opinion, constitutes a further important element for the characterisation of a

Table 3. RFI score.

RFI	Funct. level	Funct. assessment	Colour
261–300	I	very good	blue
251–260	I–II	very good—good	blue—green
201–250	II	good	green
181–200	II–III	good—medium	green—yellow
121–180	III	medium	yellow
101–120	III–IV	medium—poor	yellow—orange
61–100	IV	poor	orange
51–60	IV–V	poor—very bad	orange—red
14–50	V	very bad	red

river's environmental quality as it considers the river ecosystem overall, including its connections with the surrounding area.

Finally, the above described investigations are integrated with the assessment of the Minimum Instream Flow (MIF), which aims to safeguard the physical characteristics of the river, the physical and chemical characteristics of the water and the typical biocenotic communities in natural environmental conditions, as pointed out in the recent Guidelines (a draft copy of which has been published by the Ministry for the Environment) in order

to prepare for the basin's hydrological balance (article 22, paragraph 4, of the law D.L. 152/99).

In order to assess the MIF, reference has been made to the *hydro-biological approach* based on the search for environmental conditions suitable for the development of one or more representative species of the river's wildlife *(biological indicator)* using *in situ* measurement techniques, such as water depth and velocity and characteristics of the bottom substrate, to determine the above mentioned environmental conditions and hence define a habitat quality index as a function of the flow.

In particular, reference is made to the *Microhabitat Method* (Bovee 1978, 1982, Marchetti et al. 1991, Manciola et al. 1994, Santoro 1994, Bovee et al. 1998, Manciola & Neri 2000), using the PHABSIM (Physical HABitat SIMulation system) software (Waddle 2001).

3 SURVEY ON THE ENVIRONMENTAL QUALITY OF THE TUSCIANO RIVER

The methodological procedure briefly illustrated above was applied to the Tusciano river (Campania, Southern Italy), which is under the control of the Destra Sele Water Authority. The waterway's main axis is about 37km long and has a catchment area

Figure 1. Catchment basin and hydrographic network of Tusciano river.

measuring approximately 260km^2. The main tributaries are the Vallone Isca della Serra, the Cornea, the Vallimonio, the Lama, the Rialto. For greater clarity, Figure 1 reports the catchment area and the hydrographic network of the Tusciano river.

In order to enable a reliable assessment of the environmental quality, the informations obtained in the previous surveys were used to set up a monitoring network comprising 8 sampling stations (indicated in Figure 2) located along the Tusciano (station n. 1,2, 3,5,6 and 8), the Cornea (n. 4) and the Lama (n. 7).

As far as the fish population of the Tusciano river is concerned, the lack of time available meant that it was not possible conduct a field campaign to determine the experimental curves for the fish life in the river and so reference has had to be made to suitability curves taken from the scientific literature. In particular, the knowledge of the river's main characteristic features suggested that, for the survey to be complete, reference should be made to both *Salmonidae* (Salmo Trutta Fario) and *Cyprinidae* (Chub), taking into account two developmental stages (adult and fry) for both species.

The field surveys so far conducted have covered a time scale of six months. The results obtained—which should therefore be regarded as preliminary—are summarised in Table 4, which reports, for each sampled reach:

- the order number;
- the waterway in question;
- the watershed area;
- the results supplied by the physical, chemical and microbiological macrodescriptor parameters in terms of the overall score and the classification level (LPM);

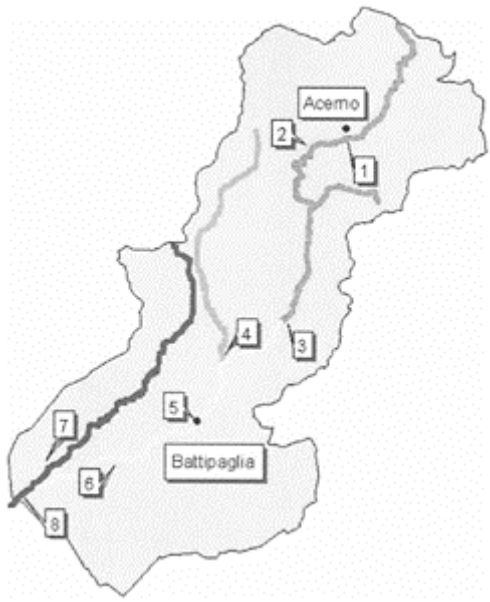

Figure 2. Tusciano river environmental quality map (preliminary draft).

- the results inferred from biological mapping, in terms of the Extended Byothic Index (EBI) and water quality class;
- the Ecological Status (RECS)—which always coincides with the Environmental Status (REQS)—to be attributed to the reach, with the corresponding assessment and the reference colour in the environmental quality map;
- the results supplied by the RFI in terms of the Functionality Assessment and the relative colour;
- the results obtained by applying the Microhabitats method, i.e. the range of the optimal flow ($Q_{op}t$) for the biological indicators considered (salmo trutta fario and chub).

The survey and study showed that the River Environmental Quality Status (REQS) was:

- satisfactory in the mountain reach of the Tusciano river (sampling sections 1 and 2), attributed with a *good* assessment (green);
- acceptable for the foothill and valley sections of the Tusciano river (sections 3, 5 and 6), attributed with a *sufficient* assessment (yellow);
- *very bad* (red) for the final reach of the Tusciano river (section 8);
- unsatisfactory for the tributaries, with *poor* assessment (orange) for the Cornea and *very bad* assessment (red) for the Lama.

In conclusion, the environmental quality status was insufficient for the final reach of the Tusciano river and for the tributaries Cornea and Lama. It was then possible to draw up the Tusciano river environmental quality map, reported in Figure 2, with the hydrographic

Table 4. Results of the field surveys.

			LPM		EBI					RFI		
Sect. (n.)	River	Area (km^2)	Score	Level	Score	Class	RECS	Judgment	Colour	Judg.	Colour	Qopt (m^3/s)
1	Tusciano	38	390	2	10	I	2	good	green	very good—good	Blue—green	0.2–1.2
2	Tusciano	81	390	2	9.5	II	2	good	green	very good—good	Blue—green	0.4–1.8
										Left bank		
3	Tusciano	96	350	2	7	III	3	Sufficient	yellow	good—medium	Green—yellow	0.2–2.0
										Right bank		
										medium—poor	Yellow—orange	

4	Cornea	31.4	145	3	4	IV	4	poor	orange	good—medium	Green—yellow	0.2–1.8
5	Tusciano	148	250	2	6	III	3	Sufficient	yellow	medium	yellow	0.2–2.8
6	Tusciano	154	250	2	7.4	III	3	Sufficient	yellow	medium	yellow	0.2–1.4
7	Lama	22.7	70	4	2	V	5	very bad	red	medium	yellow	0.1–2.0
8	Tusciano	215	100	4	3.5	V	5	very bad	red	poor	orange	0.2–3.8

network marked in the colours corresponding to the environmental quality assessment. However, it should not be forgotten that the conclusions achieved on the basis of the data collected so far should be integrated by other *in situ* surveys so as to extend the field measurements to cover a time scale of at least one year.

Moreover, it must be pointed out that:

- with reference to the Level of Pollution from Macrodescriptors (LPM), in the surveys carried out there was an albeit small reduction in the macrodescriptor values as the flow increased. Measurements taken in periods characterised by low flow values—and hence by a lower dilution of pollutants—could therefore yield higher pollution levels;
- with reference to the Extended Byothic Index (EBI), the results are based on one or two measurements and not on a seasonal cycle (four measurements);
- the surveys carried out with reference to the River Functionality Index (RFI) reveal a slightly better situation for the Tusciano river (sections 1, 2 and 8) and a much better one for the tributaries (in particular for the Lama). The "river ecosystem" overall, thus, appears to be characterised by better environmental status compared to that of the surface waters, in particular for the reaches with a worrying Environmental Status (section 8,Tusciano, section 4, Cornea and section 7, Lama).

As far as the assessment of the Minimum Instream Flow is concerned, it must first of all be stressed that application of the Microhabitat method yielded unsatisfactory results for the fry of the biological indicators considered, and so the data reported in Table 4 refer to the adult species. The data obtained also made it possible to assess the unit optimal flow rate values $q=Q_{opt}/S$ (where Q_{opt} and S indicate, respectively, the optimal flow and the watershed area), summarised in Table 5 for the Tusciano river.

Moreover, the unit optimal flow assumes extremely high values for the tributaries, approximately 45–88 $1/s\cdot km^2$ for the Cornea and 53–571/s·km^2 for the Lama. In this connection it should be pointed out that the Q_{ott} values taken for the tributaries are higher than the flows measured during the *in situ* surveys and hence fall in the area of the simulation performed by the PHABSIM software. There are, therefore, still question marks concerning the advisability of determining the optimal flow of waterways with small-sized basins.

The minimum instream flow, which is obviously much lower than the optimal flow, should on the other hand be determined by assessing the consequences on the biological

indicators of a gradual reduction in the Weighted Usable Area (WUA) corresponding to the optimal flow WUA (Q_{opt}). Calculations carried out to this end, although tentative, have yielded the q values reported in Table 6, which were assessed

Table 5. Unit optimal flow rates (Tusciano river).

	Q (1/s·km^2)	
Section (n.)	Chub (adult)	Salmo Trutta Fario (adult)
1	31.5	31.5
2, 3, 5	16−17	17–21
6,8	8, 17.5	9–11

Table 6. Unit optimal flow rates q50% and q25% (Tusciano river).

	Chub (adult)		Salmo Trutta Fario (adult)	
Section (n.)	$q_{50\%}$ (l/s·km^2)	$q_{25\%}$ (1/s·km^2)	$q_{50\%}$ (1/s·km^2)	$q_{25\%}$ (1/s·km^2)
1	21.3	17.1	21.3	17.1
2, 3, 5	7.5–9.5	4.3–7.1	7.4–10.1	5.1–7.1
6, 8	5.5–7	3.6–4.5	5.3–5.6	2.9−4

with reference to values of 50% and 25% of the WUA(Q_{opt}).

In conclusion, the application of the proposed integrated approach (physical, chemical, microbiological, toxicological, biological, hydraulic and ecological) has made it possible to provide an albeit preliminary definition of the environmental quality status for the watershed of the Tusciano river.

The results obtained, combined with a soil-land use (climate, soil, crop condition) study of the catchment area and with the availability of an updated map indicating water usage and industrial and urban discharge sources, could suggest a preliminary definition of the areas to be safeguarded and the publication of *practical guidelines for environmental restoration* by means of an integrated strategy of non-structural and structural measures.

REFERENCES

Agenzia Nazionale per la Protezione dell'Ambiente. 2000. *Il monitoraggio dello stato dell'ambiente in Italia,* Roma, ANPA.

Bovee, K.D. 1978. *Probability-of-Use Criteria for the Family Salmonidae.* Instream Flow Information Paper n. 4, Cooperative Instream Flow Group, U.S. Fish and Wildlife Service.

Bovee, K.D. 1982. *A guide to stream habitat analysis using incremental methodology.* Instream Flow Information Paper, U.S.D.I. Fish and Wildlife Service, Office of Biological Services.

Bovee, K.D., Lamb, B.L., Bartholow, J.M., Stalnaker, C.B., Taylor, J. & Henriksen, J. 1998. *Stream Habitat Analysis Using the Instream Flow Incremental Methodology.* U.S. Geological

Survey, Biological Resources Division, Information and Technology Report USGS/BRD-1998–0004.

D.L. 11.05.1999, n. 152. 1999. *Disposizione sulla tutela delle acque dall'inquinamento e recepimento della Diret-tiva 91/271/CEE concernente il trattamento delle acque reflue urbane e della Direttiva 91/676/CEE relativa alla protezione delle acque dall'inquinamento provocato dai nitrati provenienti da fonti agricole.* Suppl. Ord. n. 101/L to G.U. 29.05.1999, n. 124.

D.L. 18.08.2000, n. 258. 2000. *Disposizioni correttive ed integrative del D.L. 11.05.1999, n. 152, in materia di tutela delle acque dall'inquinamento, a norma dell'art. 1, comma 4, della L. 24.04.1998, n. 128.* Suppl. Ord. n. 153 to G.U. 18.09.2000, n. 218.

European Environment Agency. 1999. *Environmental Indicators: Typology and Overview.* Copenhagen, EEA.

Ghetti, P.F. 1995. *Indice Biotico Esteso (I.B.E.).* Notiziario dei metodi analitici, IRSA, CNR.

Ghetti, P.F. 1997. *Manuale di applicazione: Indice Biotico Esteso (I.B.E.). I macroinvertebrati nel controllo della qualità degli ambienti di acque correnti.* Ed. Provincia autonoma di Trento—Agenzia provinciale per la protezione dell'ambiente, Trento.

Giugni, M., Celico, P.B., Fontana, N. & Lombardi, G. 2002. A proposed methodology for drawing up water protection plans, In *2nd International Conference New Trends in Water and Environmental Engineering for Safety and Life: Eco-Compatible Solutions for Aquatic Environments, Capri, 24–28 June.*

Manciola, P., Martini, P. & Umbertini, L. 1994. Significato del deflusso minimo vitale e sua determinazione per un corso d'acqua dell'Italia Centrale. *Idrotecnica* (2).

Manciola, P. & Neri, N. 2000. Armouring influence on the estimate of instream flow. In *Proceedings of the IASTED International Conference Modelling and Simulation (MS 2000), May 15–17, Pittsburgh, Pennsylvania-USA.*

Marchetti, R., Crosa, G. & Cotta Ramusino, M. 1991. Applicazione del metodo sperimentale PHABSIM per la valutazione della portata minima: caso del fiume Toce. *Inquinamento* (11).

Petersen, R.C. jr. 1992. The RCE: a Riparian, Channel and Environmental Inventory for small streams in agricultural landscape. *Freshwater Biology*, 27(2).

Ruffo, S. 1995. *Gli ecosistemi fluviali con particolare riguardo alla fauna.* Accademia Nazionale dei Lincei, 90.

Santoro, M. 1994. *Il minimo deflusso vitale.* Idrotecnica (6).

Siligardi, M., Bernabei, S., Cappelletti, C., Chierici, E., Ciutti, F., Egaddi, F., Franceschini, A., Maialini, B., Mancini, L., Minciardi, M.R., Monauni, C., Rossi, G., Sansoni, G., Spaggiari, R. & Zanetti, M. 2000. *Indice di funzionalità fluviale (IFF).* Roma, ANPA.

Siligardi, M. & Maiolini, B. 1993. L'inventario delle caratteristiche ambientali dei corsi d'acqua alpini. Guida all'uso della scheda RCE-2. *Biologia Ambientale.* CISBA, VII, 30.

Waddle, T.J. 2001. *PHABSIM for Windows: User's Manual and Exercises.* On line publication.

Longitudinal dispersion in an extreme meander channel, with changes in shape

J.B.Boxall
Lecturer, Department of Civil and Structural Engineering, University of Sheffield, Sheffield, S1 3JD, UK

I.Guymer
Reader, Department of Civil and Structural Engineering, University of Sheffield, Sheffield, S1 3JD, UK

River Flow 2004—Greco, Carravetta & Della Morte (eds.)

ABSTRACT: Results are presented from a series of experiments conducted on a large-scale laboratory channel with extreme meander planform geometry. The channel had an idealised 'natural' form, with longitudinally variable cross-sectional shape, but constant cross-sectional area. Tracer studies were conducted to investigate the effects of the channel configuration and different discharges on mixing and transport processes. From this new data set, dispersion coefficients are calculated and compared to results for less extreme geometries. The effects of non-dimensionalising are also explored.

1 INTRODUCTION

Understanding and predictive modelling of the fate of soluble pollutants is essential for the efficient management of river environments. Pollutants may originate from either slowly varying inputs, such as sewerage treatment works, or more rapidly varying inputs, such as accidental spills or intermittent discharges from combined sewer overflows during storm conditions. It is desirable to make predictions of both the travel or retention times and the spreading or dispersion of such pollutants, for applications such as environmental impact assessment, protection of abstraction points or aquifer recharge sites. Application of the European Water Frame Water Directive requires quantification of travel times and mixing processes for the estimation of water quality processes at a catchment scale. It is desirable to understand, quantify and to be able to predict the impact of channel form and discharge on mixing processes.

2 BACKGROUND

Solute mixing has been an area of active research since the work of Taylor (1953, 1954), who showed that for pipe full flow, after an initial period, there exists a balance between the effects of shear dispersion (differential velocities) and turbulent diffusion.

Reviews of fundamental theory, and application to open channel flows through laboratory and field studies can be found in Fischer *et al* (1979) and Rutherford (1994).

Vertical mixing is often neglected in open channel flows because of the relatively short length scale. Transverse mixing is of particular interest below continuous sources, and has an inverse relationship to the processes of longitudinal mixing (Fischer 1969). Longitudinal mixing is associated with the temporal and spatial development of a slug of pollutant or tracer once it has become cross-sectionally well mixed, and is the focus of the study reported here.

Previous studies have investigated the influence of many channel properties on longitudinal mixing. Jobson (1997) presented a compilation and regression analysis of field tracer studies in the USA. In particular looking at the relationship of empirical predictors for various channel properties, such as slope, dimensionless drainage area, relative discharge and local discharge.

Rutherford (1994) prefaces his compilation of longitudinal mixing field study data performed on sinusoidal and meandering channels by noting the difficulties of accurately reporting values for hydraulic parameters for field studies. A similar compilation is presented by Fukuoka and Sayre (1973). The conclusion from these compilations is that a wide range of mixing coefficients are obtained from natural channels, and that the non-dimensionalising undertaken was not sufficient to account for all the processes present.

Two parameters, which might be expected to have a major influence on mixing processes, are planform curvature and changes in cross-sectional shape. These two parameters will have a dramatic impact on shear dispersion, which Smith (1992) defines as the dominant longitudinal mixing process by at least two orders of magnitude.

Rozovskii (1957) performed fundamental research into the hydraulics of flow in curved channels, deriving simple predictive expressions and providing field and laboratory validation and verification. Based on this, Fischer (1969) derived an expression to predict longitudinal dispersion coefficients under fully developed secondary flow conditions. The expression was proved for an infinitely long bend in the laboratory, but was shown to have limited validity for natural channel data. The expression includes an inverse relationship between transverse and longitudinal mixing. Hence, increased transverse shear effects, due to secondary currents induced by planform curvature (Boxall and Guymer 2003) reduce the rate of longitudinal mixing.

Fukuoka and Sayre (1973) and Guymer (1998) present results for laboratory studies into longitudinal mixing undertaken in sinusoidal and meandering channels. These studies again show a range of standard and non-dimensionalised longitudinal mixing coefficients. Guymer (1998) also studied the effects of various discharges, suggesting that the observed change in non-dimensionalised mixing coefficient with discharge was due to changes in degree of longitudinal variability of cross-sectional shape (trapping or dead zone effects) of the idealised natural channel form studied. The influence of dead or trapping zones in straight channels with boundary dead zones was explored by Valentine and Wood (1977).

The data reported in this paper was collected on the same experimental facility utilised by Guymer (1998), using a similar idealised 'natural', variable cross-sectional profile with a more extreme meander geometry.

3 ANALYSIS METHODS

Expressions based on Fick's law of diffusion can be theoretically derived to explain the mixing processes occurring in natural channels, provided several assumptions are met: sufficient time has elapsed since injection for equilibrium to establish between diffusion and dispersion, turbulence is statistically independent of time, and the flow cross-section is independent of time and distance. These assumptions are not met in most natural channel situations, however application of mathematical solutions has been shown to provide good representation of measured data, Fischer (1979) and Rutherford(1994).

The one dimensional analytical solution to a Fickian dispersion model may be written as:

$$c_A(x,t) = \frac{M}{A\sqrt{4\pi Dt}} \exp\left(-\frac{(x-u_A t)^2}{4Dt}\right) \tag{1}$$

where C_A is area mean concentration, M mass of pollutant or tracer, A area of flow, u_A area mean longitudinal velocity, x longitudinal distance, t time and D the longitudinal dispersion coefficient. Prior knowledge or prediction of D and t are required to make use of such expressions in a predictive manner.

Taylor (1954) showed that in specific situations the variance of a tracer cloud increases linearly with time, hence D can be defined from the change in spatial variance. Fischer (1966) used a frozen cloud approximation to determine the longitudinal dispersion coefficient through the change in temporal variance:

$$D = \frac{u_A^2}{2}\left[\frac{\sigma_t^2(x_2) - \sigma_t^2(x_1)}{\bar{t}_2 - \bar{t}_1}\right] \tag{2}$$

where σ_t^2 is the temporal variance in the longitudinal direction, and 1 and 2 upstream and downstream sites.

Velocity, u_A maybe evaluated from:

$$u_A = \frac{x_2 - x_1}{\bar{t}_2 - \bar{t}_1} \tag{3}$$

where $\bar{t}_i$ is the time of passage of the centroid of the tracer cloud, given by:

$$\bar{t}_i = \frac{\int_{t=-\infty}^{\infty} t c(x_i,t)\,dt}{\int_{t=-\infty}^{\infty} c(x_i,t)\,dt} \tag{4}$$

and the temporal variance from:

$$\sigma_t^2(x_i) = \frac{\int_{t=-\infty}^{\infty} (t-\bar{t}_i)^2 c(x_i,t)\,dt}{\int_{t=-\infty}^{\infty} c(x_i,t)\,dt} \tag{5}$$

This is often referred to as the method of moments. In most experiments concentrations are monitored using Eulerian measurement techniques, hence temporal variances are most readily obtained.

Expression 2 maybe evaluated by calculating the gradient of change in variance with distance along a study reach, from a sequential of measurement sites. This assumes that the mixing processes are constant over the reach. This assumption can be validated by the quality of the straight line fit obtained, this approach was employed by Guymer (1998). Alternatively the dispersion coefficient can be evaluated between each pairing of tracer measurement sites, and the consistency of mixing processes over a reach evaluated by calculating the mean and standard deviation of the values obtained. This method will be employed in this paper.

Identifying the start and end of the tracer plumes is essential for the above calculations. Variance in particular is highly sensitive to this, since although the concentration maybe low at the plume extremes, the distance from the centroid will be relatively large and this term is squared in the calculation of variance. In the work reported here the plume edges are defined as a sequence of 30 data points with a concentration of less than 0.1% of the peak.

3.1 *Guymer 1998*

Guymer (1998) reports data obtained from the Flood Channel Facility at HR Wallingford in the UK. Two channel were studied one with trapezoidal cross-section and the other an idealised natural channels form. Both channels were based on 60° meander planform geometry and were cast in concrete. The idealised natural channel form had a variable cross-sectional shape with longitudinal distance, but a constant crosssectional area. This data set was available in its raw data format and has been reanalyzed using the method outlined above. The original and recalculated dispersion coefficients for this data set are presented in table 1.

From table 1 it can be seen that the different methods of identifying the start and end of the data and of averaging the dispersion coefficient for each discharge has resulted in a slight decrease in the values obtained. The variation within the repeat injections at each discharge are indicated by the error bars in figure 1. Figure 1 also shows the variation of dispersion coefficient with discharge, showing a possible trend to increase with discharge, although this is small relative to the scatter in the data.

For predictive purposes it is desirable to attempt to normalise the longitudinal mixing coefficient, such that a single dimensionless predictive value, trend or relationship may be obtained. Previous attempts have

Table 1. Dispersion coefficient values for 60° meander channel from Guymer (1998) and from re-analysis.

Channel	Discharge (l/s)	D (1998) (m^2/s)	D (new) (m^2/s)
Trapezoidal	46.1	0.0814	0.0889

Natural	28.6	0.0892	0.0838
Natural	21.4	0.1242	0.0902
Natural	19.1	0.1198	0.1028
Natural	17.7	0.1133	0.1032
Natural	13.7	0.0847	0.0759
Natural	10.5	0.0755	0.0663

utilised bed shear velocity (u*) as a measure of flow resistance generating turbulence. The depth of flow has been adopted as a measure of the maximum length scale of turbulence, or perhaps more applicably to natural or varying channels the hydraulic radius should be used, as a measure of the maximum length scale of turbulence structures and/or as a measure of channel shape. Non-dimensionalising was reported in a tabular form by Guymer (1998), and can also be seen plotted as a function of discharge in figure 2.

Guymer (1998) provides single averaged nondimensionalised values of longitudinal dispersion coefficient for the 'natural' and trapezoidal channel shapes studied. However from figure 2 it appears that there maybe a more complex relationship with discharge for the natural channel.

Dispersion, or differential shear, is thought to dominate mixing. As discharge increases in a straight uniform channel the transverse variation of longitudinal velocity will become more developed, increasing shear effects. Therefore longitudinal mixing might be expected to increase with increasing discharge.

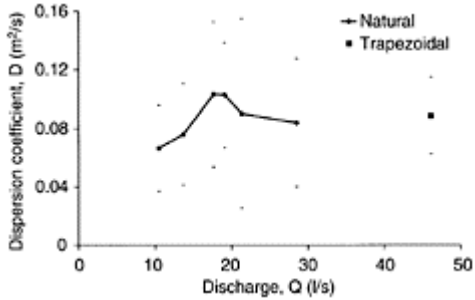

Figure 1. Variation of longitudinal dispersion coefficient for 60° natural and trapezoidal channel data, reanalyzed from Guymer (1998). Error bars represent mean plus and minus standard deviation.

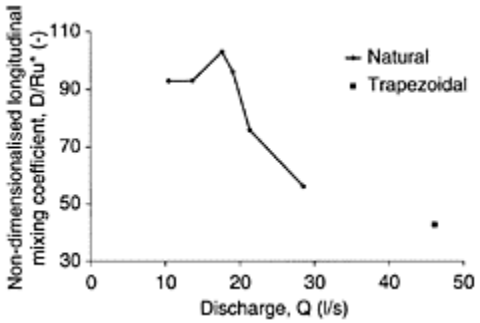

Figure 2. Variation of non-dimensionalised longitudinal dispersion coefficient for 60° natural and trapezoidal channel data, reanalyzed from Guymer (1998).

Guymer (1998) suggests that as discharge and depth decreases the 'tapping' effects of the 'plateaus' on the inside of the bends increases, which could explain the overall increase in non-dimensionalised mixing coefficient with decreasing discharge seen in figure 2.

4 EXPERIMENTAL SETUP

Data is reported from studies undertaken at the Flood Channel Facility at HR Wallingford in the UK. The channel was of the same type of idealised 'natural', longitudinally variable cross-sectional shape as used for study reported by Guymer (1998). This configuration was based on a 110° meander planform. The channel was cast in concrete. The planform geometry can be seen in figure 3 and a representation of 'natural' cross-sectional shape in figure 4. More details of these planforms and cross-sectional forms can be found in Sellin and Greenhill (1992) and Knight *et al* (1992).

Tracer studies were undertaken at a variety of discharges, from bank full (~25l/s) down to a minimum cover on the plateau around the inside of each bed of 10mm (~12l/s). Uniform flow conditions were set and monitored using a series of depth gauges. Short duration pulses of Rhodamine WT dye were introduced as a line source across the bed at the channel inlet through a small diameter pipe with 0.5mm holes at 5mm centres. This was done to promote cross-sectional mixing, reducing the distance to well-mixed conditions. Five Turner Design Series 10 Fluorometers in continuous pump though mode were employed to obtain simultaneous measurements of the temporal variation of the solute cloud at different longitudinal locations, as indicated in figure 3. A further instrument was located upstream of the injection point to monitor the background buildup associated with re-circulating facilities. These instruments where all logged directly to a PC. 6 repeat injections were made at each flow rate.

5 DATA

5.1 *Raw data*

An example plot of the background corrected, calibration applied, concentration time data obtain is

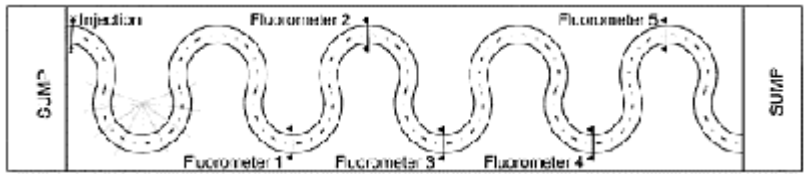

Figure 3. Planform channel layout, injection and monitoring locations.

shown in figure 5. This highlights the reduction in peak concentration and increasing spread with time/ distance.

Figure 6 shows example data from the furthest downstream measurement site for the highest and the lowest flow rates. The traces have been presented relative to the first arrival of tracer at the site and normalised by the peak concentration of each trace. The trace from the lower flow rate shows greater spreading, although it should be remembered that this pulse of tracer has been in the flow for a relatively longer period, and therefore subject to the mixing processes for longer.

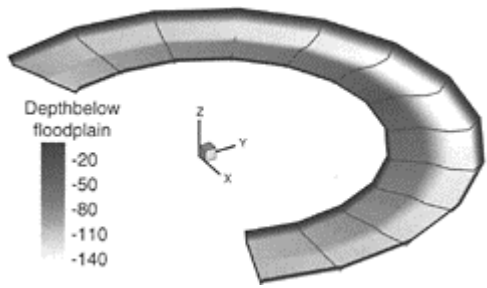

Figure 4. Contour plot of 110° geometry.

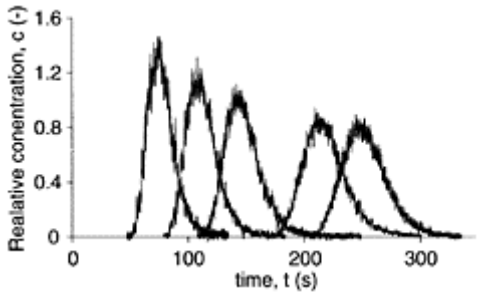

Figure 5. Example concentration time plot from 110° channel at bank full flow conditions.

5.2 *Analysed data*

Figure 7 shows the trend for the mean travel times and velocities calculated from the centroid of the tracer clouds at each flow rate. The plot also includes error bars indicating mean plus and minus the standard deviation for the repeat injections. As expected mean travel time decreases and velocity increases with increasing discharge.

Figure 8 shows the results of calculation for longitudinal dispersion coefficient from the measured tracer data. Again the plot shows mean values, and error bars for mean plus and minus standard deviation of the repeat injections at each flow rate.

Comparing figure 8 with figure 1 suggests that the longitudinal mixing coefficient for the 110° 'natural' channel is of a comparable magnitude to that found for the 60° 'natural' channel, although slightly lower. The longitudinal dispersion coefficients found for the 60° 'natural' channel data set showed a tentative trend, increasing with discharge. Figure 8 suggests that the trend for the 110° is a constant value, or slight reduction with discharge. However, the error bars for each data set indicate that the spread in the data is greater than any of these trends. This spread is associated with the sensitivity of the variance calculation to the definition of the start and end of the measured traces.

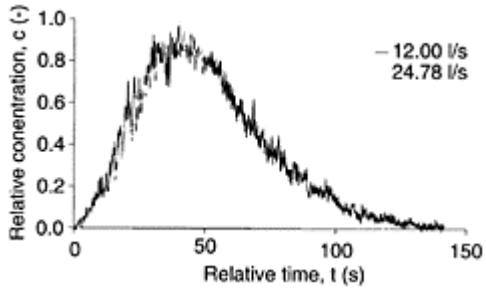

Figure 6. Example concentration time plot from farthest downstream

measurement site (plot relative to first arrival times and peak concentration of each trace).

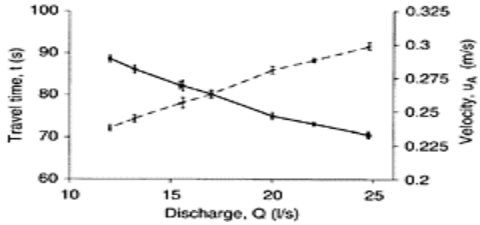

Figure 7. Travel time and velocity for 110° meander channel.

The longitudinal dispersion coefficients found for the 110° degree channel have been non-dimensionalised by the hydraulic radius and the bed shear velocity evaluated from $u^*=(gRS_0)^{0.5}$. The value obtained compares well with the reach average value of the sectional average shear stress presented by Knight *et al* (1992), and recreated in figure 9. This detailed data is only available for bank full flow conditions. Figure 9 highlights the low longitudinal variation in boundary shear stress, with only a slight peak partway into each bend.

Table 2 presents channel properties and average non-dimensionalised longitudinal mixing coefficients as reported by Guymer (1998) with the addition of values for the 110° natural channel form results presented here. As reported by Guymer (1998) the values for the sinuous channels of constant cross-sectional shape are in good agreement, with a slightly greater value obtained for the trapezoidal channel, due to the greater shear dispersion effects associated with such a cross-section. Both the 'natural' channels with constant cross-sectional area, but longitudinally variable cross-sectional shape, show an increase in the value of

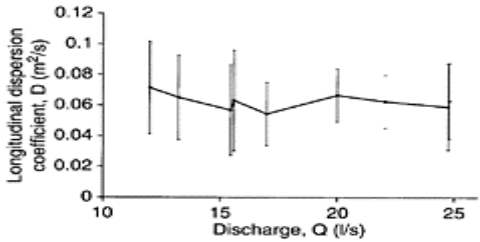

Figure 8. Dispersion coefficient for 110° meander channel.

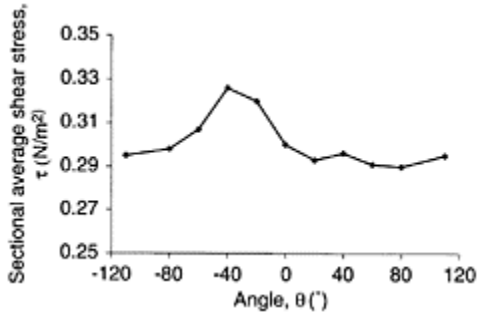

Figure 9. Longitudinal variation in sectional average boundary shear stress for bank full flow in the 110° 'natural' channel, from Knight *et al* (1992). 0° is the apex of the bend.

Table 2. Comparison between Fukuoka and Sayre (1973), Guymer (1998) and present study results.

Study	Channel shape	Sinuosity	Coefficient, D/Ru*
Fukuoka & Sayre (1973)	Rectangular	1.180	28.1±11.4
Guymer (1998)	60°, trapezoidal	1.374	39.2
Guymer (1998)	60°, idealised natural	1.374	99.8±19.99
Present	110°, idealised natural	2.043	63.6±17.94

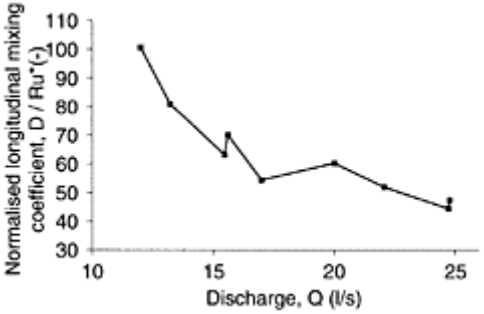

Figure 10. Non-dimensionalised dispersion coefficients for 110° meander channel.

non-dimensionalised longitudinal mixing coefficient, with a greater increase associated with the 60° less extreme meander geometry.

The variation of the non-dimensionalised longitudinal mixing coefficient with discharge for the 110° meander geometry is shown in figure 10. As with the 60° channel it can be seen that the nondimensionalised longitudinal dispersion coefficient is not constant with discharge. Unlike the 60° data the trend for the 110° data appears to be inversely proportional to discharge.

The trends with discharge of the nondimensionalised longitudinal dispersion coefficients resulting from both the 60° and 110° idealised natural channel forms are shown in figure 11. From this it can be seen that for both channel planforms the non-dimensionalised longitudinal mixing coefficient shows a similar decrease.

6 DISCUSSION

For both the 60° and the 110° channel planform data sets reviewed and reported respectively in this paper, it has been shown that as discharge increases the longitudinal dispersion coefficient non-dimensionalised

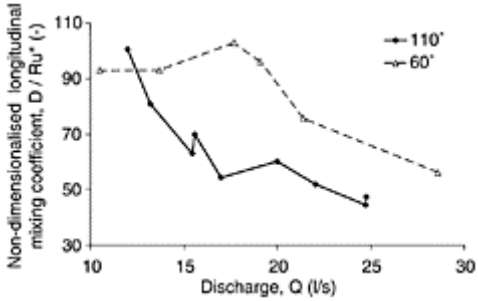

Figure 11. Non-dimensionalised dispersion coefficients for 60° and 110° meander channels.

by hydraulic radius and bed shear velocity, tends to decrease. This suggests that processes other than those accounted for by the non-dimensionalising factors are at work.

Differential shear is thought to dominate longitudinal mixing. Hence as discharge increases in a straight uniform channel, and the velocity profile becomes more developed, the effects of shear dispersion should increase. Therefore longitudinal mixing might be expected to increase with increasing discharge.

According to Rozovskii (1957), the strength of full developed secondary circulation is directly proportional to the mean longitudinal velocity. This taken with the inverse relationship between longitudinal and transverse mixing, highlighted by the expression of Fischer (1969) suggests that as discharge increases in a channel with planform curvature the effects of increasing longitudinal velocity shear will be counteracted by increasing secondary flows. However this trend will be further complicated by the buildup, decay and reversals of secondary circulations associated with meandering channels.

It is suggested that as discharge increases the idealised natural channel shape used for these studies becomes more uniform, hence the trapping effects of the plateau around the bend apexes becomes less, decreasing longitudinal mixing. It is suggested that it is this last trend that dominates the data presented here.

7 CONCLUSIONS

New longitudinal dispersion coefficient values are presented from experiments conducted on a channel with extreme meander geometry and an idealised 'natural' cross-sectional shape. Comparisons of these values with ones from a channel with less extreme geometry, but the same idealised natural cross-sectional form, show close agreement.

Non-dimensionalised longitudinal mixing coefficients from two meandering channels with idealised natural channel forms are shown to be greater than values resulting from straight rectangular and trapezoidal channels. However it has been found that increasing sinuosity does not correlate with increased longitudinal mixing.

Attempts to normalise longitudinal mixing coefficients resulting from the meandering natural channels at different discharges, using bed shear velocity and hydraulic radius, have been shown to be insufficient to produce a single predictive value. However, a trend with discharge is elucidated for these channels.

REFERENCES

Boxall, J.B. and Guymer, I. (2003) 'On the analysis and Prediction of transverse mixing coefficients in natural channels' Journal of Hydraulic Engineering, ASCE. Vol. 129, No. 2 February 2003, pp 129–139.

Fischer, H.B. (1966) "Longitudinal dispersion in Laboratory and Natural Streams", Technical Report KH-R-12, W.M. Keck Laboratory of Hyd. and Wat. Resources.

Fischer, H.B. (1969) 'The Effects of Bends on Dispersion in Streams' Water Resources Research, April, Vol. 5, No. 2, pp 496–506.

Fischer, H.B., List, E.J., Koh, R.C.Y., Imberger, J. and Brooks, N.H. (1979) "Mixing in Inland and Coastal Waters", Academic Press, New York.

Fukouka, S. and Sayre, W.W. (1973) "Longitudinal Dispersion in Sinuous Channels", A.S.C.E., HY1, 99, pp 195–217.

Greenhill, R.K. and Sellin, R.H.J. (1993) "Development of a Simple Method to Predict Discharges in Compound Meandering Channels", Proc. Instn. Civ. Engrs. Wat., Marit. & Energy, 101, Mar., 37–44.

Guymer, I. (1998) 'Longitudinal Dispersion in a Sinuous Channel with Changes in Shape' Journal of Hydraulic Engineering, ASCE, Vol. 124, No. 1, pp33–40.

Jobson, H.E. (1997) 'Predicting Travel Time and Dispersion in Rivers and Streams' Journal of Hydraulic Engineering, ASCE, November, pp 971–978.

Knight, D.W., Yuan, Y.M. and Fares, Y.R. "Boundary shear stress in meandering channels" International Symmposium on Hydraulics Research in Nature and Laboratory, Nov 17–20, 1992, Wuhan, China, pp 102–107.

Rosovskii, I.L. (1957) "Flow of Water in Bends of Open Channels", Academy of Sciences of Ukranian SSR, (translated by Isreal Prog. for Scientific Translations, Jerusalem, Isreal, 1961).

Rutherford, J.C. (1994) "River Mixing", J. Wiley & Sons, Chichester, England.

Smith, R. (1992) ‘Physics of Dispersion’ Coastal and Estuarine Pollution-Methods and Solutions’ Technical sessions, Scottish hydraulics study group, One day seminar 3rd April, Glasgow.
Taylor, G.I. (1953) “Dispersion of Soluble Matter in Solvent Flowing Slowly Through a Tube”, Proc. R. Soc. London Ser. A, 219, 186–203.
Taylor, G.I. (1954) “The Dispersion of Matter in Turbulent Flow Through a Pipe”, Proc. R. Soc. London Ser. A, 223, 446–468.
Valentine, E.M. and Wood, I.R. (1977) “Longitudinal Dispersion with Dead Zones”, A.S.C.E., HY9, 103, 975–990.

Evaluation of longitudinal dispersion coefficients for over-bank flow

Steve G.Wallis
Heriot-Watt University, Edinburgh, Scotland

J.Russell Manson
The Macaulay Institute, Aberdeen, Scotland

River Flow 2004—Greco, Carravetta & Della Morte (eds.)

ABSTRACT: The majority of approaches for predicting pollutant transport in rivers rely on being able to estimate dispersion coefficients. This paper makes predictions of dispersion coefficients for in-bank and over-bank conditions in a two-stage channel, the latter predictions being a new contribution to the field. The work combines a simplified method for predicting the transverse structure of open channel flows with an established technique for evaluating longitudinal dispersion coefficients. The method was applied to an existing hypothetical benchmark channel. For the in-bank case, the dispersion coefficient was very small (less than $3m^2/s$) and increased approximately linearly with flow rate. For the over-bank case, the dispersion coefficient was several orders of magnitude larger and decreased non-linearly with flow rate. The predictions for both flow conditions are consistent with experimentally derived trends reported in the literature, and they provide the first theoretical support for the observations in the over-bank case. The cause of the very large dispersion coefficients in the over-bank case is a strong transverse velocity shear created by areas of low velocity water on the flood plains. The over-bank results have significant implications for users of mathematical models of pollutant transport.

1 INTRODUCTION

Mathematical models are routinely used to predict the fate and transport of pollutants that are accidentally released into rivers. Although several models have been developed for simulating such pollution incidents (Beltaos, 1982, Bencala & Walters, 1983, Wallis et al, 1989, Jobson, 1997, Worman, 2000), the majority are based on the one-dimensional advection-dispersion equation (Fischer, 1967).

The use of this approach requires modellers to estimate dispersion coefficients in rivers. Whereas there is a large body of work devoted to predicting dispersion coefficients in natural and man-made channels for in-bank flows, e.g. McQuiver & Keefer (1974), Jain (1976), Liu (1977), Fischer et al (1979), Rutherford (1994), Seo & Cheong (1998), Deng et al (2002), Wallis & Manson (in prep.), no corresponding work has been undertaken for over-bank flows. The primary aim of this paper is to address this gap in knowledge by making predictions about longitudinal mixing under these conditions that occur when rivers are in flood, with flow taking place in both the main channel and also in the adjacent flood plains. The hydraulics of such flows has been studied extensively in recent years (Keller & Rodi, 1988, Shiono & Knight, 1991, Ackers, 1993, Naot et al, 1993, Lambert & Sellin, 1996, Sofialids & Prionos, 1999, Ervine et al, 2000) primarily because so-called two-stage channels have increasingly been incorporated in the design of flood relief schemes as a means of providing sufficient flow conveyance and/or storage. However, the transport of pollutants that enter these channels during flood conditions has not been extensively studied.

The specific objectives of the paper are to describe a method for predicting dispersion coefficients in channels, to apply the method to in-bank and over-bank flows in a two-stage channel and to discuss the implications of some of the predictions that are made for over-bank flows.

2 THEORETICAL BACKGROUND

The advection-dispersion equation (ADE) for a conservative solute is given below:

$$\frac{\partial C}{\partial t} + \frac{U \partial C}{\partial x} = \frac{D \partial^2 C}{\partial x^2} \tag{1}$$

where C is the cross-sectional average solute concentration, U is the cross-sectional average longitudinal flow velocity, D is the longitudinal dispersion coefficient, x is the longitudinal space co-ordinate and t is time.

In this, longitudinal dispersion is modelled using a diffusion term in which the rate of streamwise spreading of a solute cloud is governed by the magnitude of the dispersion coefficient. As a result of the onedimensional formulation of the ADE the nature of the dispersion coefficient is rather complex because it arises from the interaction of two physical processes, namely differential longitudinal advection and cross-sectional mixing. The former encapsulates the transverse and vertical gradients of the longitudinal velocity that drive the streamwise spreading while the latter continually re-distributes solute within the plane of the cross-section and tempers the streamwise spreading. Both turbulent diffusion and secondary currents contribute to the cross-sectional mixing.

The way in which the dispersion coefficient depends on differential longitudinal advection and cross-sectional mixing is described by the following equation:

$$D = -\frac{1}{A} \int_A U'(y,z) f(y,z) \, dA \tag{2}$$

where A is the cross-sectional area of flow, U′ is the local deviation of the longitudinal velocity from the cross-sectional average longitudinal velocity, f is a function that

describes the cross-sectional distribution of the transverse and vertical mixing coefficients, y is the transverse space co-ordinate and z is the vertical space co-ordinate. Given information on the magnitudes and the distributions of the longitudinal velocity and the mixing coefficients in a cross-section, Equation 2 can be used to evaluate D.

Since the work of Fischer (1967), which was based on the earlier work of Taylor (1954), it has generally been accepted that transverse differential longitudinal advection and transverse mixing dominate the generation of longitudinal dispersion in rivers because they are usually much wider than they are deep. The evaluation of D from Equation 2 is then simplified because only the transverse distributions of depth-averaged longitudinal velocity and depth-averaged transverse mixing coefficient are required. Nevertheless, the practical application of this method is far from simple, requiring the evaluation of the following triple integral (Fischer, 1967, Fischer et al, 1979, French, 1986):

$$D = -\frac{1}{A}\int_0^W hu' \int_0^y \frac{1}{\varepsilon_y h}\int_0^y hu' dy dy dy \qquad (3)$$

where W=channel top width (i.e. width at the water surface), h=h(y) is the local flow depth, u′=u′(y) is the local deviation of the depth-averaged longitudinal velocity from the cross-sectional average longitudinal velocity, $s_y=\varepsilon_y(y)$ is the local depth-averaged transverse mixing coefficient and the other symbols are as previously defined.

Alternative approaches for evaluating dispersion coefficients include the method of moments, Fischer's routing method and the use of empirical equations (Fischer et al, 1979, Rutherford, 1994, Wallis & Manson, in prep.). In the context of the current paper, however, the use of Equation 3 is the most appropriate method because much of the information that would be required to use the other methods is not available for over-bank flows.

To use Equation 3 for any given channel cross-sectional shape, we require information on the transverse velocity profile and the transverse distribution of the transverse mixing. A theoretical method for achieving this is described below.

3 THEORETICAL ANALYSIS OF FLOW STRUCTURE

The two-dimensional depth-averaged shallow water equations may be simplified for the case of fully developed steady flow in a river of general cross-section. In the simplest case, the steady depth-averaged longitudinal momentum conservation equation can be written as (Shiono & Knight, 1991):

$$\rho g S_o h = \tau_b \cos\theta - \frac{\partial}{\partial y}\left(h\tau_{yx}\right) \qquad (4)$$

in which ρ is the fluid density, g is the gravitational acceleration, S_o is the channel bed slope, h=h(y) is the local depth, $\tau_b=\tau_b(y)$ is the local longitudinal bed shear stress, θ is the transverse slope of the bed and $\tau_{yx}=\tau_{yx}(y)$ is the local depth-averaged shear stress in the x-direction on the plane perpendicular to the y-direction. Equation 4 applies at all transverse locations and describes a local balance between the component of fluid weight down the channel slope and the resisting longitudinal shear stresses on horizontal and

vertical planes (caused by bed roughness and transverse turbulent momentum exchange, respectively). Here, the effect of transverse secondary flows has been ignored. Also note that for a transversely horizontal domain, in which h is constant, θ=0.

Using a quadratic friction law the local longitudinal bed shear stress can be re-written in terms of Manning's resistance coefficient, n, giving:

$$\tau_b = \frac{\rho g u^2 n^2}{h^{1/3}} \tag{5}$$

where u=u(y) is the local depth-averaged longitudinal velocity and the hydraulic radius has been replaced with the local depth.

Using the Boussinesq eddy-viscosity concept, the longitudinal shear stress caused by transverse turbulent momentum exchange can be represented in terms of the transverse gradient of local depth-averaged velocity, as follows:

$$\tau_{yx} = \rho \varepsilon_{yx} \frac{\partial u}{\partial y} \tag{6}$$

where ε_{yx} is an eddy-viscosity, which in the simplest case can be written as:

$$\varepsilon_{yx} = \lambda h u_* \tag{7}$$

in which λ is a dimensionless eddy viscosity and u*= u*(y) is the local shear velocity. In the absence of secondary flows it is often assumed that the turbulent mixing of momentum is similar to the turbulent mixing of solutes, i.e. the eddy viscosity, ε_{yx}, is equal to the transverse mixing coefficient, ε_y. Combining Equations 4–7 gives:

$$S_o h = \frac{u^2 n^2 \cos\theta}{h^{1/3}} - \frac{\alpha}{g} \frac{\partial}{\partial y}\left(\lambda h^2 u_* \frac{\partial u}{\partial y} \right) \tag{8}$$

in which α is a binary constant. If α is set to 0 then a laterally varying velocity profile based only on the local application of Manning's equation results. However, when α is set to 1, the role of the transverse momentum exchange is included. In this paper we simplify the problem by considering the case when α=0, since this is sufficient for our purposes here. The more complex case is considered in Manson & Wallis (in prep.).

Having established equations for predicting u′ (Equation 8 with α set to zero) and ε_y (Equation 7), Equation 3 can be solved for D using numerical integration, following the method described in French (1986).

4 APPLICATION TO CASE STUDY

The two-stage channel used here for investigation was based on the hypothetical benchmark channel introduced by Ackers (1993). The channel is shown in Figure 1 and the channel parameters took the following values: B_1=15m; B_2=1.5m; B_3=20m; B_4=1.5m; D_1=1.5m; D_2=1.5m. Manning's n was taken to be 0.03 for both main channel and flood-plains. The bed slope, S_o, was set to 0.003 and the non-dimensional eddy viscosity, A. was assigned the value 0.16—a typical value for straight channels (Rutherford, 1994).

The local shear velocity was evaluated by applying Equation 5 locally, assuming that locally $\tau_b = \rho u_*^2$.

Calculations were carried out for main channel flow depths between 0 and 3 m in 0.15 m increments, thus covering both in-bank and over-bank scenarios.

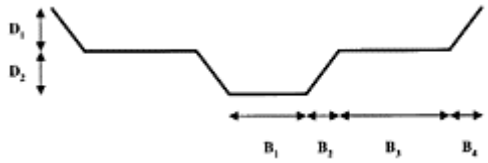

Figure 1. Cross-section of benchmark channel.

Since D was derived from numerical integration, it was essential to study the influence of the transverse discretisation, Δy, on the calculated values. Hence, for each flow depth several evaluations were undertaken with Δy being successively refined until the results became independent of Δy. Only when the results had converged were they deemed to be acceptable. In this application, it was important to capture the shear layers at a sufficiently fine resolution.

5 RESULTS AND DISCUSSION

The results are shown in the form of dispersion coefficient plotted against flow rate in Figures 2 and 3 for in-bank and over-bank flows, respectively. For in-bank flows, the dispersion coefficient increases with increasing flow rate and is very small, being in the range 0–3m^2/s for flows, between 0 and 50m^3/s. The trend is weakly non-linear, but is well approximated by a linear relationship. The magnitude of the dispersion coefficients is supported by the predicted transverse velocity profiles that consist of a wide uniform velocity region with very narrow shear zones at the channel sides. Since dispersion is promoted by gradients in transverse velocity, the very narrow shear zones are only capable of inducing minimal dispersion. As the flow depth increases, the shear zones become wider resulting in a larger dispersion coefficient.

For over-bank flows the results are significantly different. Not only is the size of the dispersion coefficient different, but so is the variation with flow rate. The dispersion coefficients are now in the range 38000–500m^2/s for flows between 70 and 330m^3/s, respectively—several orders of magnitude larger than for the in-bank case. The coefficients decrease rapidly in the flow range 70–100m^3/s and then more slowly at higher flows.

Clearly, the dispersion is being dominated by the role of the strong shear that develops as the flow begins to occupy the flood plains. This shear is easily recognised in the example transverse velocity profile shown in Figure 4, which shows that for this case the velocity in the main channel is about three times larger than the velocity on the floodplains.

Although the influence of the velocity shear decreases as the flood plain flow depth increases, because the velocity becomes more uniform across

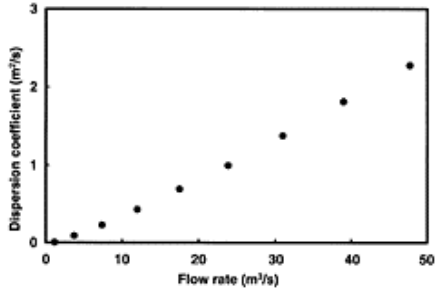

Figure 2. Variation of dispersion coefficient with flow rate for in-bank flows.

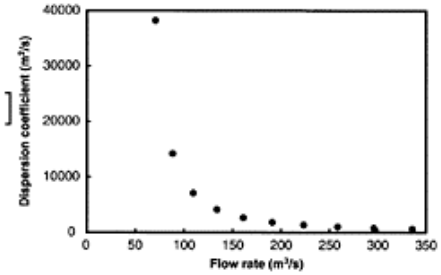

Figure 3. Variation of dispersion coefficient with flow rate for over-bank flows.

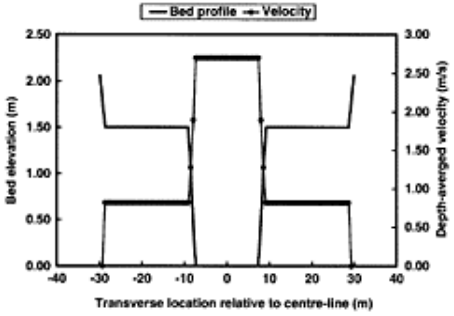

Figure 4. Transverse velocity profile for flow rate of 88m^3/s.

the channel, it retains its dominant role throughout the flow range considered.

Observation of the convergence of the result of the numerical integration as the transverse step size was decreased showed that very small steps were required, particularly when the shear layer was very narrow. Typically, $W/\Delta y$ needed to be of the order of 1000 to achieve satisfactory convergence using a uniform discretisation. Clearly, this very small step size was dictated by the requirement of accurately resolving the shear layer.

The different behaviour of the dispersion coefficient between in-bank and over-bank flows is an important result. Interestingly, these theoretical results are supported by experimental evidence in Rutherford (1994). Firstly, for the in-bank case Rutherford's Figures 4.7 & 4.6 indicate that dispersion coefficients increase with increasing flow rate. The former is directly comparable to the case studied here because it considers conditions at different flow rates in the same reach, for four rivers. In contrast, the latter shows conditions from a very wide range of reaches from about sixty rivers worldwide. For the over-bank case Rutherford's Figure 5.14 shows dispersion coefficients decreasing with increasing flow rates in four reaches of a single river. Rutherford's explanation is resonant of the conditions in the case studied here, namely that bank side areas of shallow flow create strong transverse velocity shear at low flows, but as the flow increases the velocity in the shallows increases causing a reduction in the transverse shear and a concomitant reduction in the dispersion coefficient.

Finally, workers using the ADE to simulate solute transport in open channels should take note that existing methods for predicting dispersion coefficients cannot be used for the over-bank case. For example, many of the published empirical equations and the relationships available within software packages such as MIKE11 (Anon, 1992) and ISIS (Anon, 1998) do not necessarily cater for either, or both, of the magnitude of the coefficients or the nature of its flow dependence, predicted here.

6 CONCLUSIONS

A method has been proposed for predicting dispersion coefficients in a two-stage channel based on a theoretical approach that requires a prediction of the transverse distribution of the longitudinal velocity field. This was achieved using a local application of the Manning resistance equation, although reference was made to an improved method that includes the effect of transverse turbulent momentum exchange (Manson & Wallis, in prep.). Numerical integration of Fischer's flow structure equation then yielded the dispersion coefficient. Results were obtained for the two-stage channel studied by Ackers (1993) under both in-bank and over-bank conditions. The latter results are believed to be the first predictions of dispersion coefficients in such flows. By their very nature, the results are limited to straight channels with negligible secondary flows. The transverse mixing was modelled using a constant dimensionless mixing coefficient of 0.16 and a truly local representation of depth and shear velocity.

For the in-bank case, the dispersion coefficient was very small (being in the range 0–$3m^2/s$ for flows between 0 and $50m^3/s$) and increased approximately linearly with flow rate. For the over-bank case, the dispersion coefficient was very large (being in the range $38000–500m^2/s$ for flows between 70 and $330m^3/s$) and decreased non-linearly with flow

rate. The predictions for both flow conditions are consistent with trends reported in Rutherford (1994).

REFERENCES

Ackers, P. 1993. Flow formulae for straight two-stage channels. *Journal of Hydraulic Research,* 31(4):509–531.

Anon, 1992. *Reference Manual for MIKE 11.* Horsholm: Danish Hydraulics Institute.

Anon, 1998. *ISIS Quality User Manual.* Wallingford: Halcrow/HR Wallingford.

Beltaos, S. 1982. Dispersion in tumbling flow. *Journal of the Hydraulics Division, American Society of Civil Engineers,* 108(4):591–612.

Bencala, K.E. & Walters, R.A. 1983. Simulation of solute transport in a mountain pool-riffle stream: a transient storage model. *Water Resources Research,* 19:718–724.

Deng, Z.-Q., Bengtsson, L., , V.P. & Adrian, D.D. 2002. Longitudinal dispersion coefficient in single-channel streams. *Journal of Hydraulic Engineering, American Society of Civil Engineers,* 128(10):901–916.

Ervine, D.A., Babaeyan-Koopaei, K. & Sellin, R.H.J. 2000. Two-dimensional solution for straight and meandering overbank flows. *Journal of Hydmulic Engineering, American Society of Civil Engineers,* 126(9):653–669.

French, R.H. 1986. *Open-channel Hydraulics.* New York: McGraw-Hill.

Fischer, H.B. 1967. The mechanics of dispersion in natural streams. *Journal of the Hydraulics Division, American Society of Civil Engineers,* 93(6):187–215.

Fischer, H.B., List, E.J., Koh, R.C.Y., Imberger, J. & Brooks, N.H. 1979. *Mixing in Inland and Coastal Waters.* New York: Academic Press.

Jain, S.C. 1976. Longitudinal dispersion coefficients for streams. *Journal of the Environmental Engineering Division, American Society of Civil Engineers,* 102(2):465–474.

Jobson, H.E. 1997. Predicting traveltime and dispersion in rivers and streams. *Journal of Hydraulic Engineering, American Society of Civil Engineers,* 123(17):971–978.

Keller, R.J. & Rodi, W. 1988. Predictions of flow characteristics in main channel/flood plain flows. *Journal of Hydraulic Research,* 26(4):425–441.

Lambert, M.F. & Sellin, R.H.J. 1996. Discharge prediction in straight compound channels using the mixing length concept. *Journal of Hydraulic Research,* 34(3): 381–394.

Liu, H. 1977. Predicting dispersion coefficient of streams. *Journal of the Environmental Engineering Division, American Society of Civil Engineers,* 103(1):59–69.

Manson, J.R. & Wallis, S.G. in prep. On the theoretical prediction of longitudinal dispersion coefficients in two-stage channels. *Water Resources Research.*

Mcquiver, R.S. & Keffer, T.N. 1974. Simple method for predicting dispersion in streams. *Journal of the Environmental Engineering Division, American Society of Civil Engineers,* 100(4):997–110.

Naot, D., Nezu, I. & Nakagawa, H. 1993. Hydrodynamic behaviour of compound rectangular open channel flow. *Journal of Hydraulic Engineering, American Society of Civil Engineers,* 119(3):390–408.

Rutherford, J.C. 1994. *River Mixing.* Chichester: Wiley.

Seo, I.W. & Cheong, T.S. 1998. Predicting longitudinal dispersion coefficient in natural streams. *Journal of Hydraulic Engineering, American Society of Civil Engineers,* 124(1):25−32.

Shiono, K. & Knight, D.W. 1991. Turbulent open-channel flows with variable depth across the channel. *Journal of Fluid Mechanics,* 222:617–646.

Sofialids, D. & Prionos, P. 1999. Turbulent flows in open channels with smooth and rough flood plains. *Journal of Hydraulic Research,* 37(5):615–640.

Taylor, G.I. 1954. The dispersion of matter in turbulent flow through a pipe. *Proceedings of the Royal Society of London*, A223:446–468.

Wallis, S.G., Young, P.C. & Beven, K.J. 1989. Experimental investigation of the aggregated dead zone model for longitudinal solute transport in stream channels. *Proceedings of the Institution of Civil Engineers*, Part 2, 87:1–22.

Wallis, S.G. & Manson, J.R. in prep. A review of methods for predicting dispersion coefficients in rivers. *Water & Maritime Engineering, Proceedings of the Institution of Civil Engineers.*

Worman, A. 2000. Comparison of models for transient storage of solutes in small streams. *Water Resources Research*, 36:455–468.

Evaluation of transverse dispersion coefficient under transient concentration condition

I.W.Seo
Prof., Dept. of Civil Eng., Seoul National Univ., Seoul, Korea

K.O.Baek & S.J.Jeong
Grad. Student, Dept. of Civil Eng., Seoul National Univ., Seoul, Korea

River Flow 2004—Greco, Carravetta & Della Morte (eds.)

ABSTRACT: Laboratory experiments were conducted to investigate characteristics of both the velocity field and the concentration field in the meandering channel having a rectangular cross-section. The S-curved channel has been built considering river morphology and previous experimental studies. The micro-ADV was used to measure the three-dimensional velocity field. The electrode conductivity meter was used to obtain the tracer concentration. The tracer was instantaneously injected into a flow as a vertical line source. Result of the flow experiments shows that the maximum velocity of the primary flow occurs near the inner bank in a bend taking the shortest course along the channel. For the secondary flow, complex flow pattern appears compared to experimental results in a single-bend channel. Throughout the two-dimensional tracer tests, the meaningful concentration versus time versus lateral distance data could be obtained. Using the tracer data, the transverse dispersion coefficient was evaluated by the change of moment method. In addition, the 2-D routing procedure was developed in order to obtain more accurate transverse dispersion coefficient.

1 INTRODUCTION

Dispersion is the spreading out of particles along a stream or channel due to velocity differences. In a mathematical model, the dispersion term occurs as transforming the three-dimensional advection-diffusion equation into the two-dimensional advectiondispersion equation by integration with respect to a depth. Knowledge of the dispersion characteristics of streams and rivers is essential to the understanding and managing of water pollution problems. Furthermore, the transverse dispersion is more important in water quality management than either vertical or longitudinal mixing,

especially, when dealing with the discharge of wastes from point sources or the mixing of tributary inflows. Because of importance to understanding of the pollutant transport in natural streams, many researches including laboratory and field works, and analytical and numerical calculations have been performed on the transverse dispersion. Up to date, many of those researches have concentrated on the mixing in straight, prismatic channels. However, natural streams are rarely straight and prismatic for any considerable distance. The effects induced by non-uniformity and meandering should not be negligible.

When a two-dimensional analysis of the tracer mixing is performed in meandering streams, it is the essential task to determine the transverse dispersion coefficient. There are several methods to determine the transverse dispersion coefficient in case of knowing the concentration versus time data. The change of moment method proposed by Sayre and Chang (1968) has been frequently used. This approach can be obtained by taking the integration with respect to the transverse direction of the steady state conservation equation for two-dimensional flow in a rectangular channel with uniform velocity distribution and no longitudinal dispersion. Holley et al. (1972) suggested the generalized change of moment to overcome disadvantages of the change of moment method. This method can consider transverse velocities, irregular depth, and so on. However, those methods can only be applied to the steady concentration condition, and errors may occur according to inaccurate variance of the concentration curves. In many cases, it would be preferable to perform an instantaneous injection rather than a continuous test. Some of the advantages of the instantaneous injection test are that the amount of tracer needed to perform an instantaneous test is much less than that is required for a continuous test, and an instantaneous test can provide the information on the longitudinal and time spread characteristics as well as the information on the transverse mixing.

In this study, in order to evaluate the transverse dispersion coefficient under the transient concentration condition, the two-dimensional routing procedure was developed. The laboratory tracer tests were conducted in the meandering channel having a rectangular crosssection to observe behavior of the tracer cloud and to obtain the concentration-time data.

2 THEORETICAL BACKGROUND

In most rivers, the aspect ratio is large and the tracer becomes well mixed vertically before well mixed transversely. The vertical mixing is only important close to the tracer source. In the mid-field, the vertical concentration gradients can be neglected, and our attention can be focused on transverse and longitudinal changes of the depth-averaged concentration. The full three-dimensional advection-diffusion equation can be averaged over the depth to yield the two-dimensional equation. Assuming a non-buoyant tracer being transported in an unsaturated incompressible flow, the two-dimensional advection-diffusion equation in the Cartesian coordinates is

$$\frac{\partial C}{\partial t}+u\frac{\partial C}{\partial x}+v\frac{\partial C}{\partial y}=\frac{1}{h}\frac{\partial}{\partial x}\left[hD_L\frac{\partial C}{\partial x}\right]+\frac{1}{h}\frac{\partial}{\partial y}\left[hD_T\frac{\partial C}{\partial y}\right] \qquad (1)$$

where C=depth-averaged concentration; t=time; x, y=Cartesian coordinates systems; u, v=depth-averaged longitudinal and transverse velocities; h=depth; and D_L, D_T=longitudinal and transverse dispersion coefficients respectively.

2.1 *Transformation transient condition into steady condition*

Evaluation of the transverse dispersion coefficient has been associated with continuous injection tests, i.e. tracer is injected into a stream at a constant rate so that a steady-state distribution of concentration is established some time after the commencement of injection. A literature review revealed that the most existing methods are only applicable to steady-state experiments. Extensions to unsteady situations are theoretically possible but they would introduce enormous complexities in the calculation. However, Beltaos (1975) presented a procedure for applying the existing methods to the results of instantaneous tests without increasing the computational efforts or decreasing the accuracy of computations. He introduced the concept of a dosage as

$$\theta \equiv \int_0^\infty C dt \tag{2}$$

Integrating Equation (1) with respect to time, Equation (1) becomes

$$u\frac{\partial \theta}{\partial x} + v\frac{\partial \theta}{\partial y} = \frac{\partial}{\partial x}(D_L \frac{\partial \theta}{\partial x}) + \frac{\partial}{\partial y}(D_T \frac{\partial \theta}{\partial y}) \tag{3}$$

Equation (3) shows that the quantity θ of a slug test behaves exactly in the same manner as the concentration C of a corresponding continuous test. According to the suggestion of Beltaos (1975), the transient test can be converted into continuous test so that the moment method can be applied to the transient test.

2.2 *Routing procedure*

In this study, the new method for evaluating the transverse dispersion coefficient is developed without any conversion procedure. The new method was based on the routing procedure proposed by Fischer (1968). He proposed the one-dimensional routing procedure to calculate the longitudinal dispersion coefficient. In the routing procedure, the dispersion coefficient is calculated by matching a downstream observation of passage of a tracer cloud to the prediction based on an upstream observation. The equation of the onedimensional routing procedure can be derived from the solution of the one-dimensional dispersion equation which is

$$\frac{\partial C}{\partial t} = K\frac{\partial^2 C}{\partial x^2} \tag{4}$$

where K=longitudinal dispersion coefficient which accounts for the effects on the cross-sectional averaged tracer concentration of variations of velocity across the channel cross-section. When it is considered that the solution corresponding to a mass M instantaneously released at time t=0 at the point x=ξ, the solution is

$$C(x,t)=\frac{M}{\sqrt{4\pi Kt}}\exp\left(\frac{-(x-\xi)^2}{4Kt}\right) \tag{5}$$

Suppose that the initial conditions were $C(x, 0)=f(x)$, then the concentration at point x and time t resulting from the slug centered at ξ and of width $d\xi$ and height $f(\xi)$ is

$$\frac{f(\xi)d\xi}{\sqrt{4\pi Kt}}\exp\left(\frac{-(x-\xi)^2}{4Kt}\right) \tag{6}$$

Therefore, the total contribution is the superposition integral as follows

$$C(x,t)=\int_{-\infty}^{\infty}\frac{f(\xi)}{\sqrt{4\pi Kt}}\exp\left(\frac{-(x-\xi)^2}{4Kt}\right)d\xi \tag{7}$$

In order to route a distribution of the downstream concentration from an upstream concentration, Equation (7) can be rewritten as

$$C(x,t_2)=\int_{-\infty}^{\infty}\frac{C(\xi,t_1)}{\sqrt{4\pi K(t_2-t_1)}}\exp\left(-\frac{(x-\xi)^2}{4K(t_2-t_1)}\right)d\xi \tag{8}$$

where $C(\xi, t_1)$=observed concentration as a function of distance at time t_1; and $C(x, t_2)$=predicted concentration as a function of distance at time t_2. Equation (8) requires knowledge of the instantaneous tracer concentration versus distance profile (spatial concentration profile), such as might be determined by an aerial photography. However, it is common to know the tracer concentration as a function of time (temporal concentration profile) at a fixed sampling site downstream. Under the frozen cloud assumption (Fischer, 1968; Rutherford, 1994) which is that no dispersion takes place during passage of tracer cloud past the measuring station, the routing equation of a spatial concentration can be converted into those of a temporal concentration.

$$C(x_2,t)=\int_{-\infty}^{\infty}\frac{C(x_1,\tau)U}{\sqrt{4\pi K(\bar{t}_2-\bar{t}_1)}}\cdot\exp\left(-\frac{U^2(\bar{t}_2-\bar{t}_1-t+\tau)^2}{4K(\bar{t}_2-\bar{t}_1)}\right)d\tau \tag{9}$$

where $C(x_1, \tau)$=observed concentration as a function of time at an upstream site; $C(x_2, t)$=Predicted concentration as a function of time at a downstream site; $\bar{t}_1$, $\bar{t}_2$=mean times of passage at upstream and downstream sites respectively; and τ=a dummy time variable of integration. Through the Equation (9), the concentration profile at a downstream can be calculated, and then by fitting between the calculated concentration and the observed concentration, the longitudinal dispersion coefficient can be obtained.

Based on the one-dimensional routing procedure, the two-dimensional routing procedure is developed in this study. The conceptual diagram of an application of the two dimensional routing procedure at a stream is shown in Figure 1.

The equation of the two-dimensional routing procedure can be derived from the solution of the two-dimensional dispersion equation which is

$$\frac{\partial C}{\partial t}=D_L\frac{\partial^2 C}{\partial x^2}+D_T\frac{\partial^2 C}{\partial y^2} \tag{10}$$

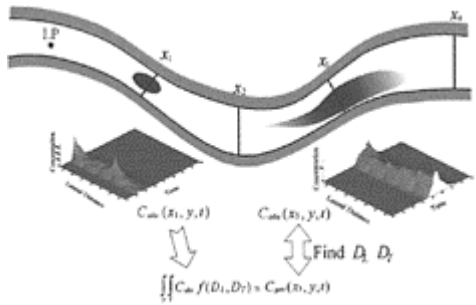

Figure 1. Conceptual diagram of the 2-D routing procedure.

When it is considered that the solution corresponding to a mass M instantaneously released at time t=0 at the points x=ξ and $y=\psi$, the solution is

$$C(x,y,t)=\frac{M}{4\pi t\sqrt{D_L D_T}}\exp\left(\frac{-(x-\xi)^2}{4D_L t}+\frac{-(y-\psi)^2}{4D_T t}\right) \tag{11}$$

Through Equation (11), the spatial two-dimensional routing equation can be expressed as

$$C(x,y,t_2)=\int_0^W\int_{-\infty}^{\infty}\frac{C(\xi,\psi,t_1)}{4\pi(t_2-t_1)\sqrt{D_L D_T}} \cdot\exp\left(-\frac{(x-\xi)^2}{4D_L(t_2-t_1)}\right)\exp\left(-\frac{(y-\psi)^2}{4D_T(t_2-t_1)}\right)d\xi d\psi \tag{12}$$

where $C(\xi,\psi,t_1)$=observed concentration as a function of longitudinal distance and transverse distance at time t_1 and $C(x, y, t_2)$=predicted concentration as a function of longitudinal distance and transverse distance at time t_2. Under the frozen cloud assumption, Equation (12) can be converted into the temporal two-dimensional routing equation which is

$$C(x_2,y,t)=\int_0^W\int_{-\infty}^{\infty}\frac{C(x_1,\psi,\tau)U}{4\pi(\bar{t}_2-\bar{t}_1)\sqrt{D_L D_T}} \cdot\exp\left(-\frac{U^2(\bar{t}_2-\bar{t}_1-t+\tau)^2}{4D_L(\bar{t}_2-\bar{t}_1)}\right)\exp\left(-\frac{(y-\psi)^2}{4D_T(\bar{t}_2-\bar{t}_1)}\right)d\tau d\psi \tag{13}$$

where $C(x_1,\psi,\tau)$=observed concentration as a function of time and lateral distance at an upstream site; and $C(x_2, y, t)$=Predicted concentration as a function of time and lateral distance at a downstream site. Using the Equation (13), the concentration profile at a downstream can be calculated, and then by matching between the calculated concentration and the observed

Table 1. Meander properties of the experiemtal channels.

Researcher	R_C/W	θ	λ/W	λ/R_C	Sinuo.
Leopold & Wolman(1960)	2.3	–	10.9	4.7	–
Chang(1971)	3.6	90	–	–	1.11
Krishnappan & Lau (1977)	0.6~2.2	–	6.3	2.8~10.8	–
Almquist & Holley (1985)	3	125	12	4	1.30
Guymer(1998)	3.5	120	13.7	3.9	1.21
South Han River (Korea)	13.7	86.8	19.7	1.6	1.10
This study	2.4	120	9.7	4	1.32

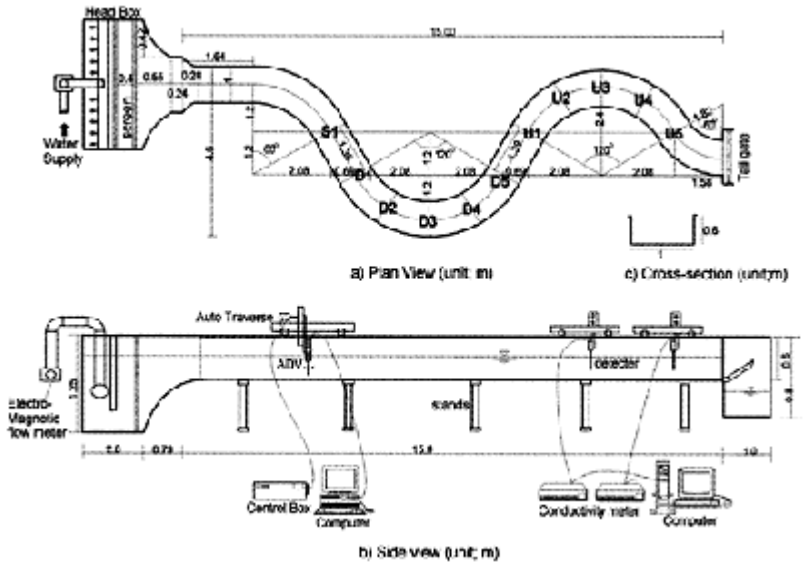

Figure 2. Sketch of the S-curved laboratory channel.

concentration, not only the transverse dispersion coefficient but also the longitudinal dispersion coefficient can be obtained.

The merits of the two-dimensional routing procedure are: (1) dispersion coefficients can be obtained under the transient concentration condition without any conversion procedure; (2) not only the transverse dispersion coefficient but also the longitudinal dispersion coefficient can be obtained simultaneously, whereas only the transverse dispersion coefficient can be obtained through the moment method; and (3) the transverse

dispersion coefficient can be obtained in more detail according to the longitudinal positions.

3 EXPERIMENTS

3.1 *Experimental setup*

The S-curved laboratory channel was constructed to investigate meander pattern of natural streams. Among the various hydraulic factors of the meandering channel, channel width *(W)*, radius of curvature *(R_C)*, arc angle *(θ)*, wavelength *(λ)*, and sinuosity were considered. The properties of meander pattern of the S-curved channel used in this study are shown in Table 1. The S-curved laboratory channel which has a rectangular cross-section is 15m long, 1m wide, and 0.6m deep. It consists of circular arcs connected by straight sections as shown in Figure 2. The radius of curvature is 2.4 m, the wavelength is 9.7m, and the arc angle is 120°. The channel was equipped with instrument carriages, which rested on rails mounted on the flume. One carriage is equipped with an autotraversing system for the velocity measuring sensor throughout the depth and breadth of the flow field.

An electromagnetic flowmeter was installed to continuously measure the discharge of the flow passing through the channel. A point gauge was used to measure the flow depth. A side-looking micro-ADV, developed by SonTek, was used to measure the three-dimensional distributions of velocity and turbulence. The micro-ADV operates on a pulse-to-pulse coherent Doppler shift to provide a three-component velocity at a rate of 50 Hz. The concentration measurements were made with the electrode conductivity meter, which was developed by KENEK. The probe of electrode conductivity meter is very small like ϕ4mm, and there is little influence to the flow. The electrode conductivity meter can obtain concentration data at a rate of 10Hz, the measuring range is 0~30,000ppm, and the linearity is±1.5%.

Six electrode conductivity probes were arranged at each transection by the hand-operated traversing system, and the concentration distributions are measured simultaneously at three transactions. The probe calibration for a response to a concentration was performed by a series of standard salt solutions whose range were from 0ppm to 10,000ppm. The concentration signals were fed into the data acquisition system, which converted the sampled signals to digital voltages. The amplifier unit was adjusted to give zero output in the flume water. A calibration curve of output voltage versus concentration was constructed by immersing the probe in each of the standards and recording the voltage output. The tracer was a salt solution, and a red dye (KMnO4) was added to aid in visualizing the diffusing cloud. The density of the tracer solution was adjusted to that of the flume water by addition of the methanol. The tracer was instantaneously injected into the flow as a full-depth vertical line source using the instantaneous injector. The injector consisted of the fixing plate and ϕ9.0cm cylinder. By lifting the cylinder from the fixing plate, the tracer can be introduced into the water.

3.2 *Experimental conditions*

In the S-curved channel, seven cases of tests on measurements of velocity field were conducted according to flow conditions. The flow experimental conditions are tabulated in Table 2. Measurements of velocity field were conducted at eleven transections whose location was marked at Figure 2. The interval of measuring points at each transection is transversely 7cm,

Table 2. Flow conditions.

Case	*H* (cm)	*V* (cm/s)	*Q (l/s)*	*W/H*	*Fr*
070	7	28.6	20	14.3	0.34
101	10	30.0	30	10.0	0.30
151	15	20.0	30	6.7	0.16
152	15	40.0	60	6.7	0.33
211	21	14.3	30	4.8	0.10
212	21	28.6	60	4.8	0.20
213	21	42.9	90	4.8	0.30

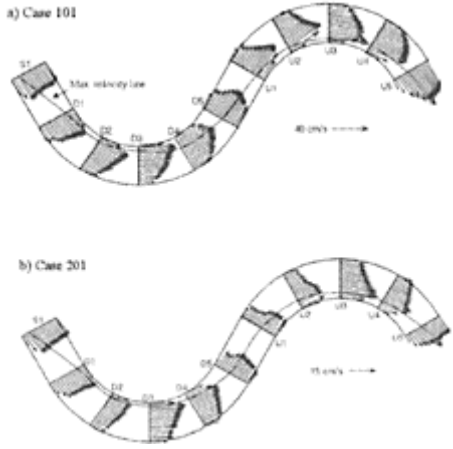

Figure 3. Depth-averaged primary velocity vectors (Case 101).

and vertically 3~5cm. Thus, the number of measuring points at each section varies from 30 to 90, depending on the water depth.

The concentration experiments were conducted in the all flow conditions. The tracer was instantaneously injected into the flow as a full-depth vertical line source at the centerline, left bank, and right bank of the channels. The injection point was marked at

Figure 2. The initial concentration of the tracer was 100,000mg/l (ppm). The interval of concentration measuring points at each transection is 14cm transversely.

4 EXPERIMENTAL RESULTS

4.1 *Velocity field*

One of the purposes of laboratory experiments is to investigate flow patterns in the S-curved channel. In order to observe a primary flow pattern, depth-averaged primary velocity vectors are plotted in Figure 3 for the representative cases. The transverse distribution of the primary velocity skews toward the inner bank at bends and is almost symmetric at the crossovers. The noticeable phenomenon is that the maximum velocity occurs taking the shortest course along the channel, irrespective of flow conditions. In natural streams, however, it has been known that the maximum velocity occurred along the thalweg line which appeared near the outer bank. The reason of this discrepancy in the flow pattern is that experiments were conducted on the rectangular cross-section channel, whereas, the cross-sectional shape of the natural stream is usually triangular, and skewed to the outer bank.

4.2 *Concentration field*

Throughout the tracer test in the S-curved channel, the concentration versus time data could be obtained at six transverse positions in nine transections. The three-dimensional concentration fields, which consisted of concentration, time, and transverse distance from a left bank to a right bank, are drawn for centerline injection of Case 101 in Figure 4.

In order to visualize the behavior of the tracer cloud, the spatial contours of the concentration are plotted through the concentration-time curve using the interpolation technique in Figure 5~7. As shown in Figure 5 (centerline injection), the tracer cloud was somewhat symmetrical shape entering the first bend zone. At the apex, the tracer cloud separated into two parts and the main part skewed toward the left bank which was the inner bank in the first bend. The sub part remained near the outer bank. Passing the crossover, the tracer cloud is skewed toward the right bank, and then high concentration was observed near the right bank through the second bend. It is considered that even though tracer cloud travels following the maximum primary velocity, it separates both in longitudinal and transverse directions due to alternating secondary currents. As shown Figure 6, this mechanism is prominent, for the case of the left bank injection. The core of the tracer cloud was taking the shortest course along the channel following the maximum velocity. However, in the case of the right bank injection (Figure 7), the tracer cloud didn't follow the maximum velocity through the first bend so that high concentration was detected near the right bank along the whole channel. Also, the length of the tracer cloud is longer than others. Not only the transverse mixing but also the longitudinal mixing may increase by the effects of the meander in the case of the right bank injection.

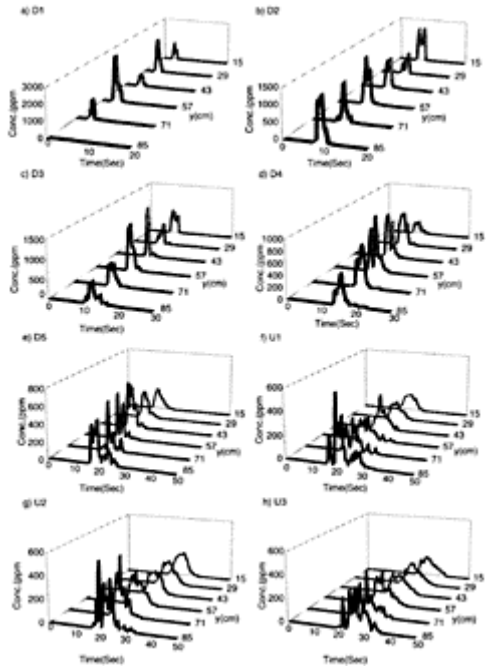

Figure 4. Plots of concentration, time, and transverse distance (Case 101, Centerline injection).

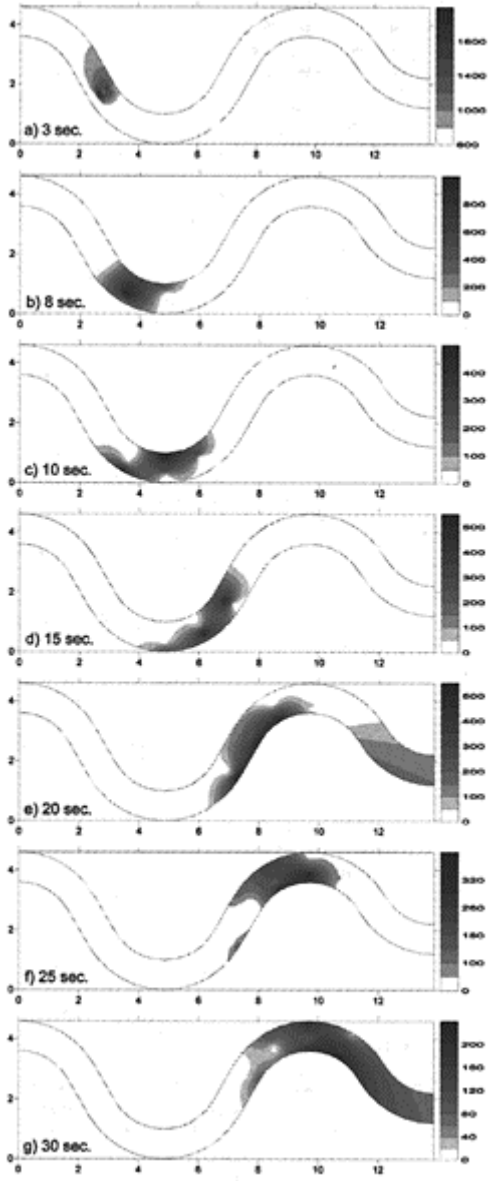

Figure 5. Spatial contour of the tracer cloud (Case 101, centerline injection).

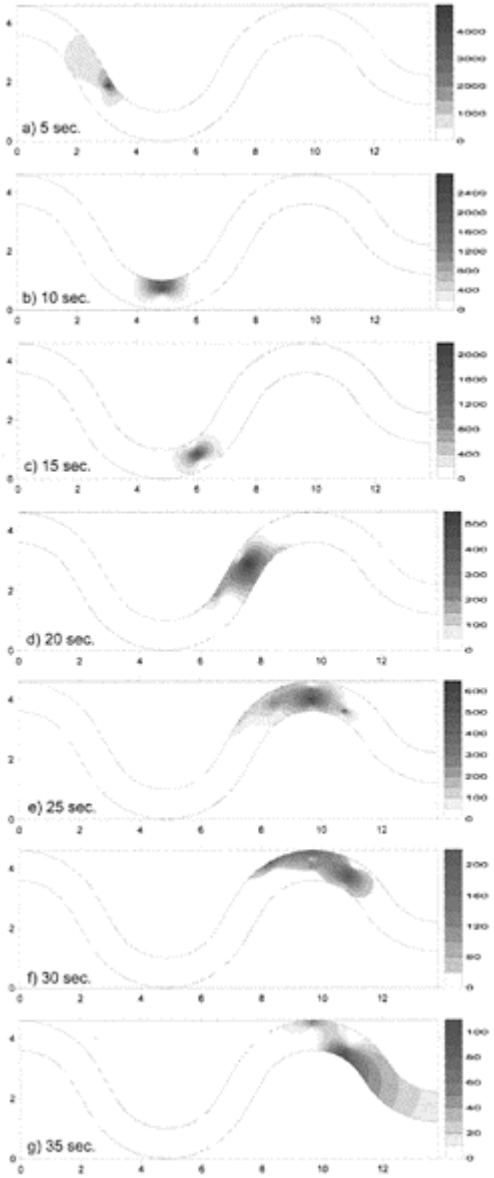

Figure 6. Spatial contour of the tracer cloud (Case 101, left bank injection).

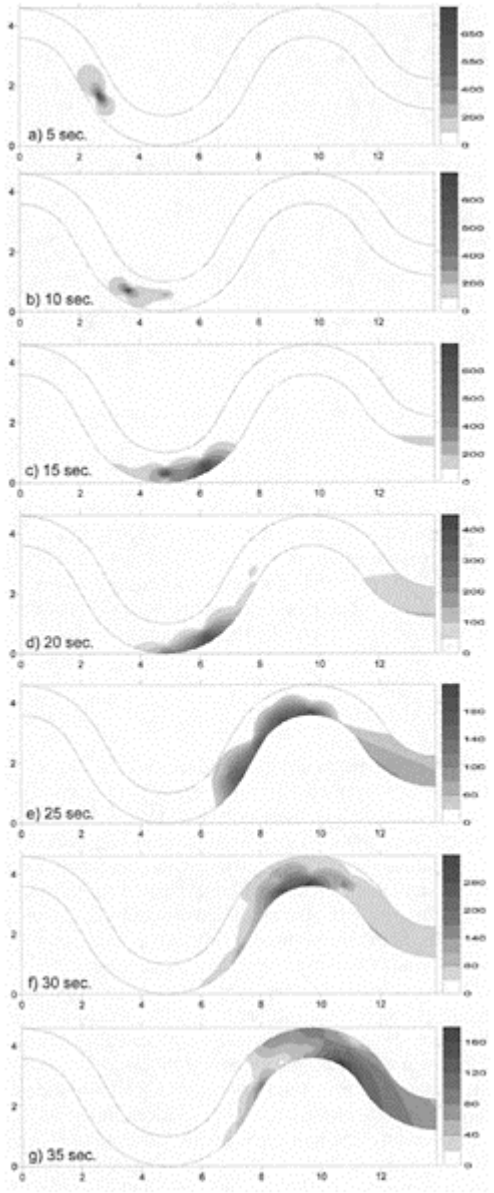

Figure 7. Spatial contour of the tracer cloud (Case 101, right bank injection).

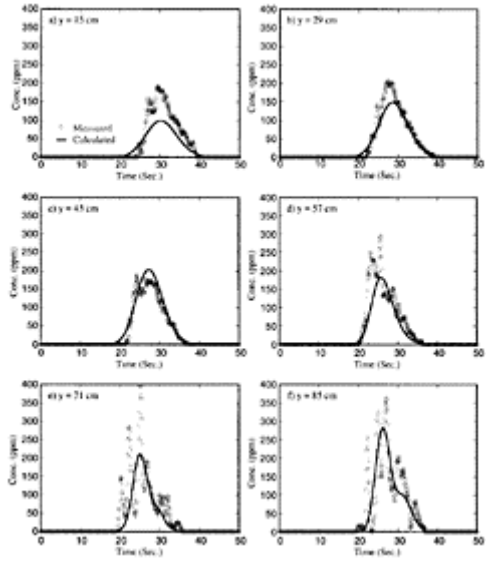

Figure 8. Application of the 2-D routing procedure (Case 101, center injection, Sec. U3).

5 ANALYSIS

In this study, the routing procedure and the moment method were applied to evaluate the dispersion coefficients in the S-curved channel. Using the two-dimensional routing equation (Equation 13), both the longitudinal dispersion coefficient and the transverse dispersion coefficient can be evaluated simultaneously. In order to fit the predicted concentration to the measured concentration, the Gauss—Newton method, which is one of the nonlinear multiple regression techniques, was used. The representative case of applying the two-dimensional routing procedure is depicted in Figure 8. As shown in this figure, the calculated concentration distributions are generally in good agreement with the measured concentration distributions though peak points are somewhat underestimated.

Observed dispersion coefficients calculated by both the moment method and the two-dimensional routing procedure for all cases are tabulated in Table 3. The representative transverse dispersion coefficient was chosen among the several values of the dispersion

Table 3. Comparison of the observed dispersion coefficients.

Inject. cond.	Flow cond.	M-M	2-D routing procedure		
		D_T/HU_*	D_T/HU_*	D_L/HU_*	Up-down
Center	070	0.51	0.29	15.1	D2-U4

	101	0.45	0.70	15.6	D1-U4
	151	0.33	0.46	10.9	D2-U3
	211	0.18	0.19	5.9	D1-U3
Left	070	0.69	0.34	5.2	D1-U3
	101	0.58	0.63	5.7	D2-U2
	151	0.46	0.43	3.4	D1-U2
	211	0.19	0.34	3.1	D2-U4
Right	070	0.43	0.70	32.5	D4-U1
	101	0.45	0.56	37.6	D1-U4
	151	0.42	0.35	21.0	D1-U3
	211	0.17	0.10	38.8	D3-U3

coefficients obtained by the routing procedure for each case. The dispersion coefficient had less RMS error and was computed through long distance between upstream and downstream. For the dimensionless transverse dispersion coefficient (D_y/HU_*), results by the moment method and the routing procedure show little differences. Also, it is found that the dimensionless transverse dispersion coefficient is independent of the injection conditions. However, the dimensionless longitudinal dispersion coefficient varies according to the injection conditions. Especially, results on the right bank injection are larger than others. This is due to the separation of the tracer cloud as shown in Figure 7.

6 CONCLUSIONS

The two-dimensional routing procedure which was based on Fischer (1968) was developed to evaluate the transverse dispersion coefficient under the transient concentration condition. Also, the laboratory tracer tests were conducted in the meandering channel having a rectangular cross-section in order to obtain the concentration-time data.

Result of the flow experiments shows that the maximum velocity of the primary flow occurs near the inner bank in a bend taking the shortest course along the channel. Throughout the two-dimensional tracer tests, it reveals that behavior of the tracer cloud was quite different according to the injection conditions. Using the acquired concentration data, the transverse dispersion coefficients were evaluated via the new developed routing procedure. The evaluated transverse dispersion coefficients by the routing method were in good agreement with those by the moment method.

ACKNOWLEDGEMENTS

This research work was supported by the 21C Frontier project of the Ministry of Science and Technology. This research has been conducted in the Research Institute of Engineering Science of Seoul National University, Seoul, Korea.

REFERENCES

Almquist, C.W. & Holley, E.R. 1985. Transverse mixing in meandering laboratory channels with rectangular and naturally varying cross sections. *Technical Report CRWR-205,* Univ. of Texas, Austin, Texas.

Beltaos, S. 1975. Evaluation of transverse mixing coefficients from slug tests. *J. of Hydr. Res.,* IAHR, 13(4):351–360.

Chang, Y. 1971. Lateral mixing in meandering channels. PhD thesis, Univ. of Iowa, Iowa City, Iowa.

Fischer, H.B. 1968. Dispersion predictions in natural streams. *J. of Sanit. Engrg. Div.,* ASCE, 94(SA5): 927–943.

Guymer, I. 1998. Longitudinal dispersion in sinuous channel wlth changes in shape. *J. Hydr. Engrg.,* ASCE, 124(1): 33–40

Holley, E.R., Siemons, J. & Abraham, G. 1972. Some aspects of analyzing transverse diffusion in rivers. *J. of Hydr. Res.,* IAHR, 10(1):27–57.

Krishnappan, B.G. & Lau, Y.L. 1977. Transverse mixing in meandering channels with varying bottom topography. *J. of Hydr. Res.,* IAHR, 15(4):351–371.

Leopold, L.B. & Wolman, M.G. 1960. River meanders. *Bulletin of the Geological Society of America,* 71:769–794.

Rutherford, J.C. 1994. *River mixing,* New York: John Wiley and Sons Ltd.

C.
Hydraulics for river managementRiver training and restoration

C.1.
Hydraulics for river managementRiver training and restoration

Numerical simulation of bed change under compound channels flow in two-way main channel

H.Yokoyama, Y.Watanabe & Y.Suzuki
Civil Engineering Research Institute of Hokkaido, Sapporo, Japan

River Flow 2004—Greco, Carravetta & Della Morte (eds.)

ABSTRACT: In a river with a two-way main channel the flow bifurcates from the straight channel into a meander channel and then reconverges into the straight channel. A numerical simulation model was developed for estimating flow and bed topography change in such a river using 2-D shallow-water equations. Simulation was applied to an actual river with a two-way main channel, and it was generally able to represent the bed topography Factors of riverbank erosion were then considered by using the simulation results. Velocity and its distribution near the bank were found to affect localized bank erosion. The model was applied to compound flow in a two-way main channel, which was compared to flow in a single meandering main channel. The effects of a two-way channel on flow and bed topography were investigated.

1 INTRODUCTION

River improvement works have been done on many alluvial rivers to lower the water surface level for flood safety and to lower the groundwater surface level for development of agricultural land. Meandering rivers were straightened with cutoffs, which changed the river environment in some cases. Requests for river environmental conservation have been increasing in recent years.

A project to restore the Shibetsu River to its meandering state has been going on since 2000. The river is in the eastern part of Hokkaido, Japan's northernmost prefecture. This project is the first meander restoration in Japan. An oxbow lake was reconnected to the straightened channel in 2002. Currently, flow bifurcates from the straight channel, flows through the restored meander and reconverges with the flow in the straight channel. (We describe such a channel as a "two-way main channel.") In the two years that has passed since the restoration produced the two-way channel, riverbank erosion and change in bed topography have occurred. It is very important to predict the flow and change of riverbed for planning and maintenance of a two-way main channel.

Many studies have addressed flow and bed topography in a meander channel. Development of meander was investigated by linear stability analysis (Ikeda et al., 1981) and nonlinear model (Parker et al., 1982). Struiksma et al. (1985) discussed bed deformation in curved channels by comparing experimental results and mathematical analysis. Odgaard (1989a, b) applied mathematical model to bank scouring and migration in actual rivers. A 2-D simulation model was developed to estimate change of bed topography (Shimizu et al, 1991). Flow in a compound meander channel was investigated experimentally (Fukuoka et al., 1997) and by 3-D simulation (Fukuoka et al., 1999). Channel shift and bank erosion was estimated by using numerical models (Nagata et al., 2000). However, in most of the research on meandering rivers, the main channel was single, and flow in a two-way main channel was not considered.

Sato & Watanabe (2002) conducted experiments on flow in a two-way channel and investigated bed change and the behavior of sandbars. Fujita et al., (2003) developed theoretical analysis and investigated the discharge rate of two-way channel from model experiment and field survey. However, the number of conditions and the number of repetitions is limited in experiments. The development of a computational model that can simulate the flow and change of bed topography would greatly contribute to analysis of phenomena under a complicated river configuration and various hydraulic conditions.

This study aims to develop a numerical model that can solve for flow and bed change in a two-way channel. The simulation model is outlined first. The model is applied to an actual two-way channel on the Shibetsu River. The simulation results are compared to observation data. Factors in erosion in a meander channel are investigated by using the simulation results. After that, simulation is conducted on compound flow in a two-way main channel.

2 NUMERICAL MODEL

2.1 *Equations of flow and sediment transportation*

The flow, which bifurcated and reconverged, had a mixture of horizontal and vertical flow components. In a compound-channel, the difference in flow velocity between the main channel and the flood plain and the complicated boundary shape of the channels causes complex flow. 3-D simulation is desirable for solving flow and bed change because it can consider the effects of vertical flow. However, 3-D simulation takes a very long time, making it difficult to apply. In an actual river, we consider that general hydraulic phenomena can be predicted sufficiently by simulating horizontal flow and bed change. The 2-D shallow-water equations (l)–(3) are transformed to a boundary-fitted coordinate system and used in the model. The upwind differencing scheme is used in the advection term:

$$\frac{\partial u}{\partial t}+u\frac{\partial u}{\partial x}+v\frac{\partial u}{\partial y}=-g\frac{\partial H}{\partial x}-\frac{gn^2u\sqrt{u^2+v^2}}{h^{4/3}} \qquad (1)$$
$$+\frac{\partial}{\partial x}\left(2\nu_t\frac{\partial u}{\partial x}\right)+\frac{\partial}{\partial y}\left\{\nu_t\left(\frac{\partial u}{\partial y}+\frac{\partial v}{\partial x}\right)\right\}$$

$$\frac{\partial v}{\partial t}+u\frac{\partial v}{\partial x}+v\frac{\partial v}{\partial y}=-g\frac{\partial H}{\partial y}-\frac{gn^2v\sqrt{u^2+v^2}}{h^{4/3}} \tag{2}$$

$$+\frac{\partial}{\partial x}\left\{\nu_t\left(\frac{\partial u}{\partial y}+\frac{\partial v}{\partial x}\right)\right\}+\frac{\partial}{\partial y}\left(2\nu_t\frac{\partial v}{\partial y}\right) \tag{3}$$

$$\frac{\partial h}{\partial t}+\frac{\partial (uh)}{\partial x}+\frac{\partial (vh)}{\partial y}=0$$

where t is time, x and y are Cartesian coordinates, u and v are velocity in the x and y directions, H is water surface level, h is water depth, g is gravitational acceleration ($9.8m/s^2$), and n is Manning's roughness coefficient ν_t is kinematic eddy viscosity expressed as follows:

$$\nu_t=\frac{\kappa}{6}U_*h \tag{4}$$

where κ is Karman's constant, and U_* is friction velocity.

The continuity equation of sediment is expressed as follows:

$$\frac{\partial z_b}{\partial t}+\frac{1}{1-\lambda}\left(\frac{\partial q_B^x}{\partial x}+\frac{\partial q_B^y}{\partial y}\right)=0 \tag{5}$$

where z_b is the elevation of riverbed (z_b=H−h), λ is the void ratio of sand (λ=0.4), $q_B^x$and $q_B^y$are sediment discharge in x and y direction.

Mass of sediment transportation is shown in Equation (6), proposed by Ashida & Michiue (1972). In this study, we assume all sediment transportation to be of bed material.

$$q_B=17.0\tau_*^{1.5}\left(1-\frac{\tau_{*c}}{\tau_*}\right)\left(1-\sqrt{\frac{\tau_{*c}}{\tau_*}}\right)\sqrt{sgd^3} \tag{6}$$

where q_B is total sediment discharge per unit time and unit width, τ^* is dimensionless shear stress, $\tau_c^*$is dimensionless critical shear stress (Iwagaki, 1956), s is specific gravity of sediment (1.58), and d is averaged diameter of sediment.

Near-bed velocity vector is needed to distribute total sediment discharge to two directions. Near-bed velocity in the streamline direction $u_b^s$and normal direction $u_b^n$is calculated as follows:

$$u_b^s=\left(u^2+v^2\right)^{1/2} \tag{7}$$

$$u_b^n=-\frac{\left(u^2+v^2\right)^{1/2}N^*h}{r_s} \tag{8}$$

where N* is Engelund's constant (Engelund, 1974), r_s is the radius of curvature of streamline. The effect of secondary flow is considered in Equation (8). r_s is expressed in Equation (9) (Shimizu & Itakura, 1991):

$$\frac{1}{r_s}=\frac{1}{\left(\sqrt{u^2+v^2}\right)^3}\left[u\left(u\frac{\partial v}{\partial x}-v\frac{\partial u}{\partial x}\right)+v\left(u\frac{\partial v}{\partial y}+v\frac{\partial u}{\partial y}\right)\right] \tag{9}$$

Transformation of sediment discharge from Cartesian system to boundary-fitted coordinate system, ξ and η direction, are expressed as follows:

$$q_B^{\xi} = \xi_r q_B \frac{u_b^{\xi}}{\sqrt{u^2+v^2}} \sqrt{\frac{\tau_*}{\mu_s \mu_k \tau_*}} \left(\xi_r \frac{\partial z_b}{\partial \xi} + \eta_r \frac{\partial z_b}{\partial \eta} \cos\theta \right) \quad (10)$$

$$q_B^{\eta} = \eta_r q_B \frac{u_b^{\eta}}{\sqrt{u^2+v^2}} \sqrt{\frac{\tau_*}{\mu_s \mu_k \tau_*}} \left(\xi_r \frac{\partial z_b}{\partial \xi} \cos\theta + \eta_r \frac{\partial z_b}{\partial \eta} \right) \quad (11)$$

where q_B^{ξ} and q_B^{η} are sediment discharge in the ξ and η direction, u_b^{ξ} and u_b^{η} are near-bed velocity in the ξ and η direction, $\xi_r=\Delta\xi/\Delta s$, $\eta_r=\Delta\eta/\Delta n$, μ_s is a coefficient of static friction, μ_k is a kinematic friction coefficient.

2.2 *Conditions of simulation*

The simulation model is applied for calculation of riverbed change in the area of meandering restoration works in the Shibetsu River. Figure 1 shows grids for the calculation. The gray area in Figure 1 is a “dummy” area, where flow and riverbed evolution are not calculated. S is the distance from the convergence point. A low-head dam is set in the straight channel

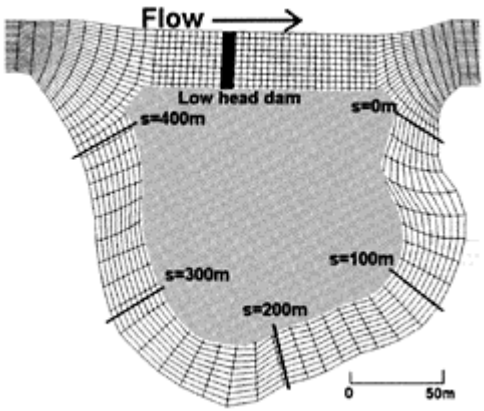

Figure 1. Calculation grid of Shibetu River two-way channel.

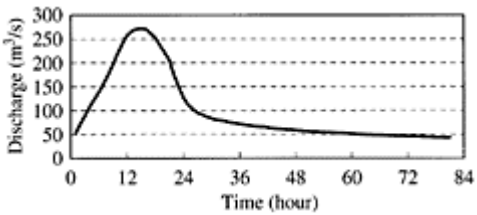

Figure 2. Hydrograph of summer flood on Shibetsu River.

30m downstream from the bifurcation. The dam head elevation is 6.35m.

As a boundary condition, discharge is given at the upstream end. Two typical cases of floods are examined. One case is “snowmelt flood.” Constant discharge of 47m^3/s, which was averaged from values observed in April 2002, is assumed to continue for one week. The other case is “summer flood” (Figure 2): discharge observed from October 2 to 4, 2002. Water depth is given by Equation (12) at the downstream end.

$$h = \left(\frac{nQ}{B\sqrt{i}} \right)^{0.6} \tag{12}$$

where Q is discharge at the upstream end, B is channel width (30m), n is Manning's roughness coefficient of bed, and i is averaged longitudinal bed slope (1/800).

The diameter of bed material is set as 11mm, the diameter averaged from field measurements. Manning’s roughness coefficient is set as 0.017. The initial riverbed configurations in the main channels are from the field measurements obtained in March 2002 for the snowmelt flood and in September 2002 for summer flood. The straight channel upstream and downstream of the bifurcation is assumed to have a rectangular

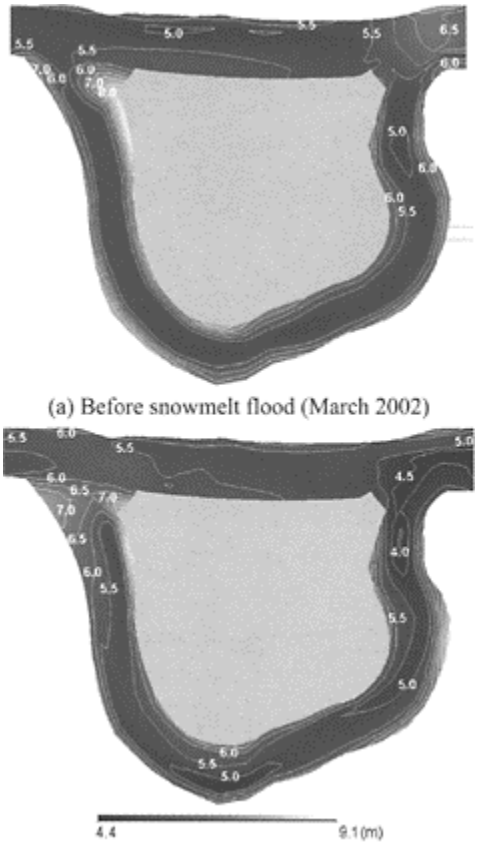

Figure 3. Observed bed topography on snowmelt flood.

cross-section, and the channel profile is assumed to gradually change. The longitudinal bed slope of the channel is 1/800, which is the design bed slope of the Shibetsu River. Upstream and downstream length of model is set as 1.6km each for stabilizing the simulation results.

Bed erosion at the low-head dam is not allowed in calculation of the bed. If bed elevation z_b is lower than the initial value z_{b0} there, then z_b is corrected to z_{b0} automatically.

3 SIMULATION RESULTS FOR THE SHIBETSU RIVER

3.1 *Snowmelt flood*

Figure 3 shows the observed bed topography measured in March 2002 (before the start of snowmelt flood) and in July 2002 (after the flood had ended). Bed form in

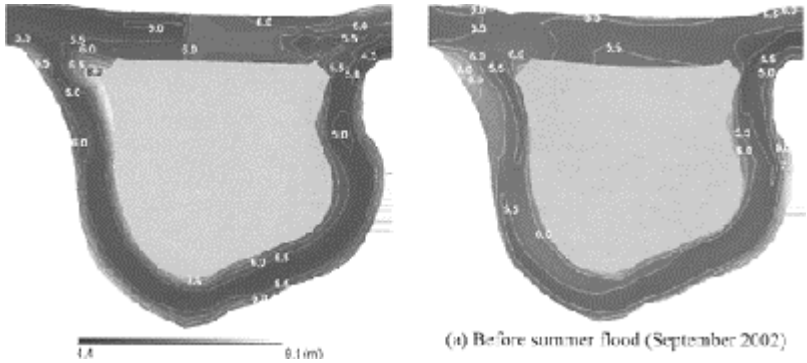

Figure 4. Simulated bed topography after snowmelt flood.

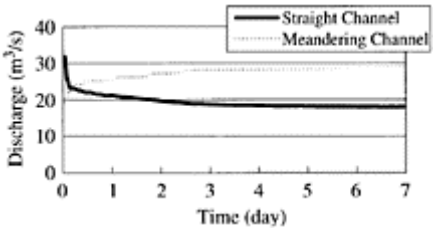

Figure 5. Discharge of two-way channel under snowmelt flood based on simulation results.

March is given as an initial condition in the simulation. Figure 4 shows the simulated bed topography after one week of snowmelt. We compare the calculation results and the observed values.

In the straight channel, deposition on the left bank immediately downstream of the convergence point is washed away after the snowmelt flood in the observation. The simulation also shows a decrease in bed elevation downstream of the convergence point on the left bank. Deposition also appears immediately down-stream of the low-head dam in the simulation. In the meander channel, the riverbed elevation rises around the entrance and scouring occurs in the center of the channel immediately upstream of the convergence point in the actual river. But in the simulation, the bed topography hardly changes in the meander channel except around the bifurcation and the convergence.

Discharge in both channels calculated on the basis of simulation results is shown in Figure 5. Discharge in the meander channel increases over the course of 5 days to

become almost constant. Discharge into the meander channel in snowmelt flood is about 60% of

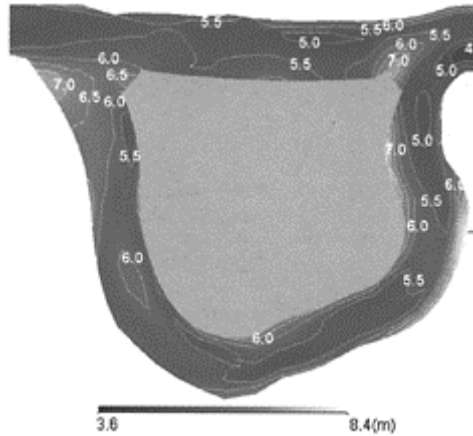

(b) After summer flood (October 2002)

Figure 6. Observed bed topography on summer flood.

the total discharge by field observation. Simulated discharge in the meander channel is 62% of the total discharge at the end of the simulation. The simulation accurately reproduces the observed value.

3.2 *Summer flood*

Figure 6 shows bed topography observed in September 2002 (before summer flood) and in October. Observed bed topography is used as the initial riverbed shape in summer flood simulation. Figure 7(a) shows the calculation results of bed topography at t=15h, when the hydrograph shows peak discharge. Figure 7(b) shows simulated bed topography after the summer flood has finished.

At peak flood discharge, deposition develops at the right bank between the bifurcation and a point 1/4 of the way downstream of that point in the meander

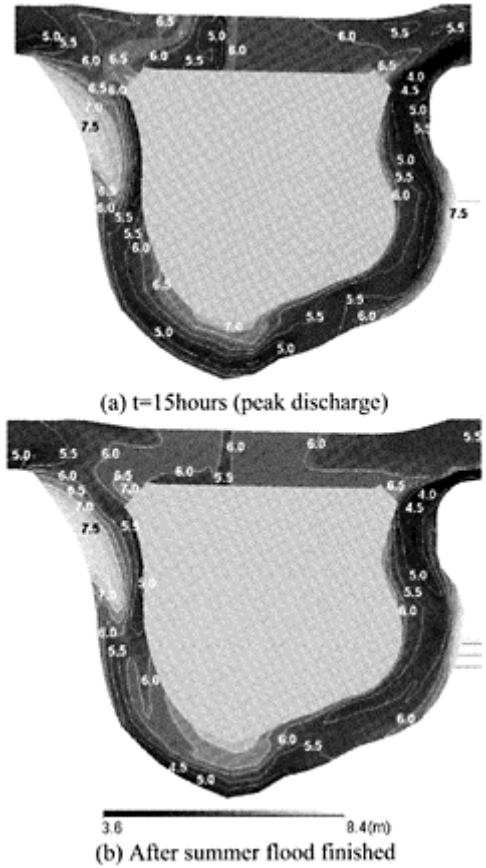

Figure 7. Bed topography of summer flood (simulated).

channel in the simulation. After the summer flood has finished, this deposition remains in roughly the same place. The simulated deposition is larger in scale than the observed deposition. There is bed erosion on the left bank near the bifurcation in actual river. Bed erosion also occurs at roughly the same place as on the simulated riverbed.

In the straight channel, simulated deposition appears immediately upstream of the convergence on the right bank in observation after the flood has finished. Simulated deposition is at the same area, but it is smaller than actual deposition. Bed elevation down-stream of the low-head dam rises in the simulation. However, these trends do not appear in the actual river. In front of the dam, scouring appears at peak discharge. This scouring becomes smaller at the end of the simulation.

Figure 8 shows discharge of a two-way channel under summer flood calculated on the basis of

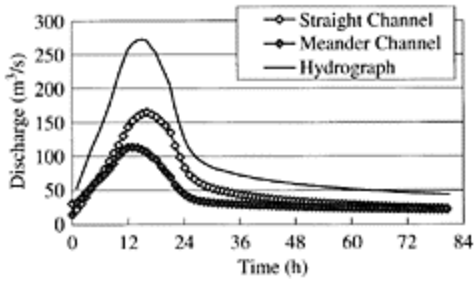

Figure 8. Discharge of two-way channel under summer flood, based on simulation result.

simulation results. The rate of discharge in the meander channel to total discharge is 60% at the start of the flood. It decreases while the total discharge rises. It is about 1/3 at peak discharge and is rising while total discharge is decreasing. It is 45% at the end of the flood. Deposition at the right bank near the bifurcation seems to cause a decrease of discharge in the meander channel.

Through the simulation of bed topography under two floods, simulated results especially differ from the operated value around the bifurcation and low-head dam. Around these areas, the effect of vertical flow is remarkable. 2-D simulation model cannot reproduce near-bed velocity well because vertical distribution of velocity isn't considered well in the model. Accurate estimation of near-bed velocity is one of important factors for appropriate results of simulation.

3.3 *Relationship between velocity and riverbank erosion in meander channel*

Since flow was restored in the meander of the Shibetsu River, bank erosion has been occurring on both banks, mainly near the entrance to the meander channel. We analyze the relationship between hydraulic parameters and bank erosion. The near-bank flow velocity and perturbation velocity, which is defined as the difference between near-bank velocities and cross-sectional averaged velocity, correlates closely with riverbank erosion (Suzuki et al., 2003). We examine the correlation between simulated velocity near the riverbank and observed riverbank erosion quantity.

Figure 9 shows the relationship between longitudinal distribution of observed bank erosion, simulated velocity near both banks and perturbation of simulated velocity near the banks under snowmelt flood and under the maximum discharge of summer flood. The horizontal axis of graphs in Figure 9 is the distance upstream from the convergence point in the meander channel, which is indicated as "s" (unit; meters) and shown in Figure 1. Section s=0m is

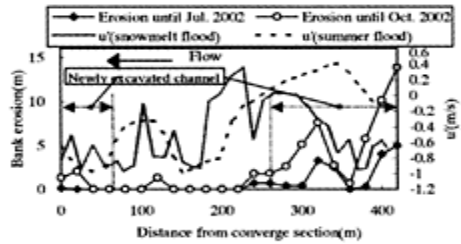

(1) Erosion and perturbation of velocity at the left bank

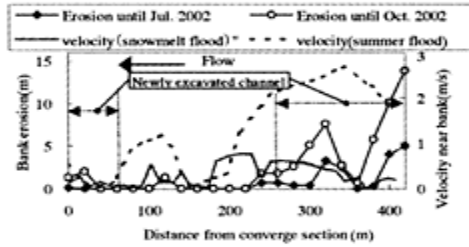

(2) Erosion and velocity at the left bank

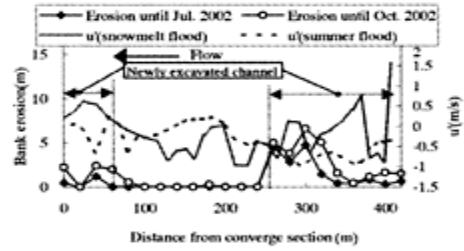

(3) Erosion and perturbation of velocity at the right bank

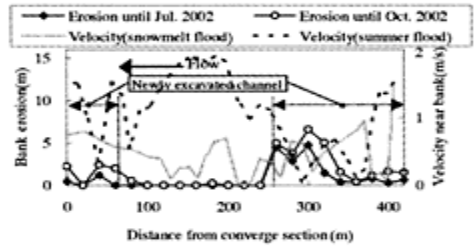

(4) Erosion and velocity at the right bank

Figure 9. Longitudinal distribution of perturbation of velocity, velocity near both banks and erosion.

the convergence point and s=420m is the bifurcation point. The perturbation of velocity near the bank, u', is defined by Equation (13):

$$u' = u_{wall} - u_m \tag{13}$$

where u_{wall} is near-bank flow velocity, and u_m is cross-section averaged velocity. Bank erosion is defined as the change from the riverbank measured in March 2002. Erosion until July is the change caused by snowmelt flood, and erosion until October is the summation of change caused by snowmelt flood and summer flood. This meander channel can be regarded as having two kinds of sections: (1) a section from s=60m to s=260m (the previous oxbow lake), and (2) a section from s=0m to s=60m and another from s=260m to s=420m (the newly excavated parts of the meander channel).

In the meander section between s=100m and 240m, the riverbank erosion is generally less than in the other sections. This section is in the previous oxbow lake and the erosion-resistance of the riverbank seems stronger in this section than in the sections excavated upstream and downstream of the oxbow. The right riverbank from s=60m to s=260m occurs particularly little change during the two floods.

First, we examine erosion caused by snowmelt flood. Riverbank erosion appears around the convergence point and on the meander section between the bifurcation and s=250m. The erosion is remarkable between s=240m and s=300m on the right bank and between the bifurcation and s=350m on the left bank. There isn't clear correlation between riverbank erosion quantity and near-bank velocity. Erosion is particularly remarkable from s=350m to the bifurcation on the left bank actually, although simulated near-bank velocity is small. Around this area, flow in the vertical direction is supposed to be strong and bank erosion there may have advanced from causes other than shear stress induced by the near-bank flow. The perturbation velocity is generally small in the meander channel and does not correlate with riverbank erosion quantity in snowmelt flood.

Second, bank erosion after the summer flood is examined. Erosion make progress on the area where the bank had been eroded until July and is noticeable on the left bank of section between the bifurcation and s=350m. In this section near-bank flow velocity is large, suggesting that the flow velocity near the riverbank affects the erosion. Also on the right bank, near-bank velocities seem to relate closely to the bank erosion. There isn't clear relation between perturbation velocity and bank erosion quantity around the bifurcation. But around the convergence, there seems to be a little relation between two factors. Simulation doesn't seems to be reproduce the velocity well around the bifurcation and it may be one of the factor that there is little relation between near-bank velocity, perturbation velocity and bank erosion quantity.

In summary, the calculation results of summer flood suggest that river erosion tends to occur in sections with greater near-bank flow. The near-bank flow velocity or perturbation velocity is somewhat related to riverbank erosion in summer flood. However, little correlation is found between near-bank flow velocity or perturbation velocity and erosion in snowmelt flood or the area where effects of vertical flow cannot be ignored.

4 EFFECTS OF LOW-HEAD DAM ON THE RATIO OF DISCHARGE IN THE MEANDER CHANNEL

The longitudinal slope of the meander channel bed is milder in the two-way channel than in the straight channel bed. The entrance of meander channel may become obstructed by sediment deposition if its discharge is insufficient. Therefore a low-head dam was set in the straight channel to secure proper flow in the meander. In a two-way channel, it is important to establish the proper dam height. We investigate the ratio of discharge in the channels using a simulation to examine the effect of the low-head dam on flow in a two-way channel.

Simulation is carried out on a fixed-bed. Each section of channels is set as rectangular. Longitudinal slope is 1/800 in straight channel. Plane geometry of the channel is same to Figure 1. Three cases of discharge are set: Q=20m^3/s, 40m^3/s and 270m^3/s. Froude number immediately upstream of the bifurcation is 0.47 (Q=20m^3/s) and 0.51 (Q=40m^3/s).

Figure 10 shows the relationship between height of low-head dam and simulated discharge rate in the

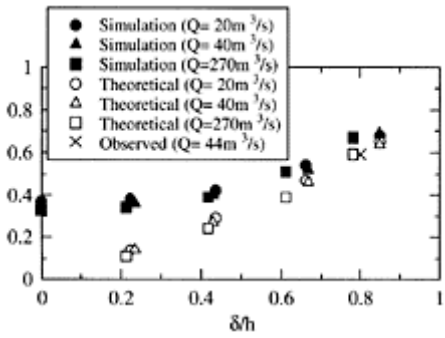

Figure 10. Comparison of ratio of discharge in meander channel to total discharge among simulation, theoretical analysis and observed value.

meander channel. (Observed value in Figure 10 is quoted from the research by Fujita et al. (2003).) δ/h is is the ratio of height of low-head dam to water depth upstream of the bifurcation. “r” is the ratio of discharge in meander channel to total discharge. That ratio determined by theoretical analysis depending on the momentum conservation law (Fujita et al., 2003) is also shown in Figure 10, which can express actual phenomena under the condition of complete overflow and submerged overflow on the dam. Observed value is good agreement with theoretical analysis and simulated value. Under the complete overflow condition (δ/h>0.6), simulated discharge is in good agreement with theoretical value. Under submerged overflow conditions, there is a difference between theoretical value and simulated value. In theoretical analysis separation streamline is set to divide

bifurcation area so cross-sectional velocity distribution is assumed to be uniform around bifurcation. This is one of the factors of the difference between both values. According to the simulation, at least 30% of the total discharge goes into the meander channel. Ratio of discharge in meander channel becomes large slowly with increase of height of low-head dam. Ratio seems to be determined by δ/h and little affected by discharge.

5 EXTENSION TO COMPOUND FLOW WITH TWO-WAY MAIN CHANNEL

5.1 *Introduction of the calculation*

The discussions in the previous section are limited to hydraulic phenomena in a main channel and do not consider flow on the floodplain. However, in a large-scale flood, inundation of the floodplain will occur and a more complicated flow regime and riverbed evolution can arise. For river planning and management of rivers with compound channel flow, it is very important to include the effects of floodplain flow in calculations of flow and bed topography.

We discuss characteristics of compound flow in a two-way main channel by using a simulation. To examine how flow characteristics in a two-way main channel influence flow and bed topography, simulation is done for main channels of two different shapes: (1) meander channel, and (2) meander channel plus straight channel (i.e., two-way main channel). Simulation results of these two cases are compared. There are neither experimental nor field measurement data for comparison and examination, so we discuss the flow only from the simulation data.

5.2 *Conditions for the calculation*

Figure 11 shows calculation grids of compound flow with two-way main channel. We set the dimensions

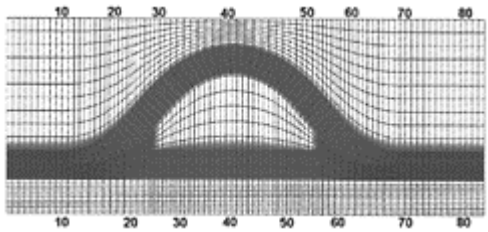

Figure 11. Calculation grid of compound channel with two-way main channel.

of simulation area considering a reduced scale to the Shibetsu River (1:167): The width of the main channel is 0.3m. The depth of the main channel below the floodplain

elevation is 0.03m. The whole channel width is 2m. The maximum meandering angle of the meander channel is 50 degrees. Wavelength of the meander channel is 4.2m. Bed slope in the longitudinal direction is 1/800. For bed friction, Manning's roughness coefficient is set as 0.013 in the main channels and 0.02 in the floodplain. Riverbed evolution is assumed to occur only in the main channels. The diameter of the bed material is 0.75mm. Total discharge is 0.00167m^3/s, which is based on planning discharge of the Shibetsu River. Constant discharge is set at the upstream and uniform flow water depth (Equation (12)) is set at downstream ends. To increase calculation stability, the effects of secondary flow are not considered in the simulation of compound flow. We investigate the calculated values three hours after the beginning of water passage.

5.3 *Calculation results*

The distributions of water level and velocity in a two-way main channel under compound flow are shown in Figure 12(1). The results for a compound channel with a single-meandering main channel are shown in Figure 12(2). We see that resistance is smaller for a straight main channel. In a two-way main channel, the maximum flow velocity occurs longitudinally in the straight main channel, where flow is concentrated. In a one-way main meander channel, flow is also concentrated in main channel. But discharge in main channel is smaller than one in two-way channel. The straight main channel reduces the water level and discharge on the floodplain. It is expected to improve the safety of flood control.

Figure 13 shows riverbed changes. Bed change is generally more active in straight main channel than in meander channel. In the straight channel, bed elevation rises from the bifurcation to the convergence and decreases in other section. Around the entrance of meander channel, deposition can be seen.

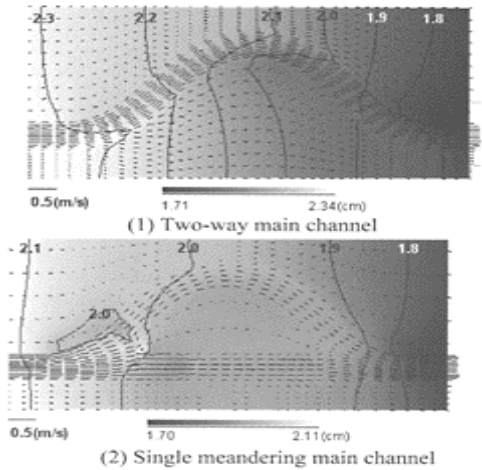

Figure 12. Water surface contour and velocity.

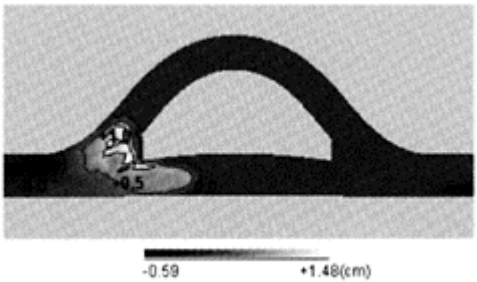

Figure 13. Bed change of compound flow with two-way main channel.

6 CONCLUSION

Simulation was performed for snowmelt and summer floods on the Shibetsu River. The calculation results partly reproduced the changes in bed topography. However, the calculation results did not accurately reproduce the bed topography in some cases, especially around the bifurcation, where near-bed velocity should be affected by vertical flow.

Velocity and perturbation velocity near the river-banks somewhat correlated with riverbank erosion in the summer flood. The method of predicting erosion using the calculated velocity seems to be effective in some cases. However, it needs more improvement for estimating near-bank velocity with satisfied accuracy.

The compound flow with two-way main channel was experimentally simulated. Straight channel would be expected to improve safety for flood control.

ACKNOWLEDGEMENTS

The Hokkaido Development Bureau, Ministry of Land, Infrastructure and Transport of Japan, provided a grant for this research. Field measurement data of the Shibetsu River were provided by the Kushiro Development and Construction Department of the Hokkaido Development Bureau. We would like to express our appreciation for this assistance.

REFERENCES

Ashida, K. and Michiue, M. 1972. Study on Hydraulic resistance and bedload transport rate in alluvial streams. *Proceedings of JSCE,* No. 206:59–64 (in Japanese).

Engelund, F. 1974. Flow and bed topography in channel bends. *Journal of Hydmulic Engineering, ASCE,* Vol. 100, No. HY11.

Fujita, M., Hasegawa, K., Watanabe, Y. and Kuwamura, T. 2003. Bifurcated discharge rate to the oxbow meandering channel regulated by a small dam with overflow condition in the Shibetsu

River, *Proceedings of 3rd IAHR Symposium on River, Coastal and Estuarine Morphodynamics, Balcelona, 2003*, 831–844.

Fukuoka, S., Ohgushi, H., Kamura, D. and Hirao, S. 1997. Hydraulic characteristics of the flood flow in a compound meandering channel. *Journal of Hydraulic, Coastal, and Environmental Engineering, JSCE,* No. 579. 83–92 (in Japanese).

Fukuoka, S., Watanabe, A. and Okada, S. 1999. Analysis of bed topography in a compound meandering channel using a 3-D numerical model with assumption of hydrostatic pressure. *Journal of Hydroscience and Hydraulic Engineering, JSCE,* Vol. 17, No. 2, 99–105.

Nagata, N., Hosoda, T. and Muramoto, Y. 2000. Numerical analysis of river channel processes with bank erosion. *Journal of Hydraulic Engineering, ASCE,* Vol. 126, 243–262.

Ikeda, S., Parker, G. and Sawai. K. 1981. Bend theory of river menaders. Part 1. Linear development, *Journal of Fluid Mechanics,* Vol. 112, 363–377.

Iwagaki, Y. 1956. Hydraulic study of critical tractive force: *Proceedings of JSCE,* No. 41:1–21 (in Japanese).

Odgaard, J. 1989a. River meander model 1: Development, *Journal of Hydraulic Engineering, ASCE,* Vol. 115, No. 11, 1433–1450.

Odgaard, J. 1989b. River meander model 2: Application, *Journal of Hydraulic Engineering, ASCE,* Vol. 115, No. 11, 1451–1464.

Parker, G., Sawai, K. and Ikeda, S. 1982. Bend theory of river menaders. Part 2. Nonlinear deformation of finite amplitude bends, *Journal of Fluid Mechanics,* Vol. 115, 303–314.

Sato, K. and Watanabe, Y. 2002. Influence of bars in river channels with bifurcation and convergence, *Proceedings of River Flow 2002, IAHR, Louvain-la-Neuve, Belgium,* Vol. 2:741–750.

Shimizu, Y. and Itakura, T. 1991. Calculation of flow and bed deformation with a general non-orthogonal coordinate system, *Proceedings of XXIV IAHR Congress, Madrid, Spain,* C-2:41–48.

Struiksma, N., Olesen, W.K., Flokstra, C. and De Vriend, J.H. 1985. Bed formation in curved alluvial channels, *Journal of Hydraulic Research,* Vol. 23, No. 1, 57–79.

Suzuki, Y., Watanabe, Y., Hasegawa, K., Mori, A. and Kuga, T. 2003. Changing of two-way river course in restoration project at the Shibetsu River, *Annual Journal of Hydraulic Engineering, JSCE,* Vol. 47, 703–708 (in Japanese).

River meandering restoration—case study and laboratory experiments

R.Banasiak, R.Verhoeven, L.De Vos & S.Verfaille

Hydraulics Laboratory, Ghent University, Belgium

River Flow 2004—Greco, Carravetta & Della Morte (eds.)

ABSTRACT: In the frame of a pilot project a multidisciplinary study concerning the evaluation of the feasibility and sustainability of river re-naturalisation has been conducted. Special emphasis was put on the hydraulic aspects of the restoration of a natural meandering river course degraded by engineering works in the past. Firstly, an outline is given of several predictions for the river meander pattern. Most formulas however, are of empirical nature, which makes them less suitable for case studies with specific local conditions. Secondly, a case study, performed in order of the environmental department of the Flemish government, is highlighted. Thirdly, a laboratory investigation, performed in a flume set-up, is described. During several tests the development of the meander patterns was recorded using discharge, slope of the river bed and initial channel bed configuration as variable parameters. The influence of artificial interventions, such as deflectors, to promote meander development, has been tested as well.

1 INTRODUCTION

Meandering is a basic feature of natural rivers. In the past many natural watercourses have been trained to meet different economical needs. These training works often neglected ecological aspects in such a way that the transformed rivers were straightened and thus lost their ecological value. Moreover, even the original aim of anti-flood protection has failed since the river straightening and flood plain cutoffs led to a decrease in river storage capacity and faster propagation of flood waters and higher flood peaks. In Flanders this has caused frequent flooding in both rural and urban areas, in particular in the downstream parts of water-courses. The results became clear: wet or water filled cellars, more frequent agriculture losses and streets under water.

To meet these problems the Flemish Administration for Environmental, Nature and Landplanning (AMI-NAL) has recently conducted a pilot project aiming at the evaluation

of the feasibility and sustainability of river restoration. In particular the restoration of meandering river courses is considered. A preliminary study indicated several sites, which are suitable for meandering, taking into account a variety of different aspects. This article mainly investigates several aspects of the hydraulic changes that occur in rivers subjected to meander restoration.

The overall idea behind any restoration is to create a stable channel. In order to avoid potential problems, it is important to understand the changes that a river will experience when different control or regulation schemes are applied. The prediction of these changes is an important aspect of every restoration project

A brief description of a physical model study, performed in the Hydraulics Laboratory, Ghent University, is included. This model study was performed to gain more information on the mechanism of meander development. The influence of obstacles on the meander development is a specific part of this study.

2 PREDICTORS ON RIVER MEANDERING

The meandering forms that are created even across a range of spatial scales and environmental boundary conditions display often startling regularities. The sinuous shape of the meandering planform has led scientists to look after the factors responsible for shaping river meanders. So far, several theories have been proposed and many, in majority, empirical formulas based on some sets of data have been derived.

In many empirical formulas the discharge is regarded as the dominant independent variable to which the dependent variables, such as width, depth, velocity and meander wave length, adjust. Dependant variables are usually expressed as power functions of bankfull discharge,

$$B=C_B Q^{\alpha} \tag{1}$$

and the meander parameters are related to the channel width, e.g. (Leopold & Wolman, 1964):

$$\lambda=11B^{1.01} \tag{2}$$

$$a=3B^{1.1} \tag{3}$$

$$r_c=2.4B \tag{4}$$

where B=bankfull channel width (m); λ=meander wave length (m), a=meander amplitude (m), r_c= maximum meander radius (m), and C_B and α= constants.

The physical explanation for the selection of the bankfull discharge as bed forming parameter is that with smaller discharges less sediment transport occurs, which hardly affects the river bed transformation. For discharges larger than bankfull the water masses are conveyed over the flood plains with as a consequence presumable lower bed forming activity. The empirical relations obviously do not include many other important factors

such as bed and bank material, sediment load, slope, etc. Therefore, the empirical coefficients are usually specific site dependent.

Chitale (1970) investigated meandering patterns of more than 40 rivers in India. Using field data consisting of depths and widths for bankfull discharge, slope and bed material size, single and multiple correlations were performed resulting in the following equations for shape and relative size of meanders:

$$\frac{L_{thalweg}}{L_{valley}} = \frac{M}{\lambda} = 1.429\left(\frac{d_{50}}{D}\right)^{-0.077} S_*^{-0.052}\left(\frac{B}{D}\right)^{-0.065} \quad (5)$$

$$\frac{a}{B} = 48.299\left(\frac{B}{D}\right)^{-0.471} S_*^{-0.453}\left(\frac{d_{50}}{D}\right)^{-0.050} \quad (6)$$

in which S_*=slope in feet per 10,000ft length of the channel, d_{50}=mean bed material diameter, D=average depth of channel, B=surface width of channel, M=meander length. The percentage errors of estimation using this equations were 18.69 and 58.05 respectively. Accuracy did not improve much by increasing the number of variables in Eq. 5 against other single correlation. Significant scatter between the observed and estimated values for the equations were supposed due to omission of the definition of the nature of bank material, sediment concentration, sediment gradation and the inevitable limitation of data. In addition, as both depth and width vary along a meandering channel from bend sections to transition sections, the ratios of d_{50}/D and B/D vary along the channel. Furthermore, the bankfull discharges often had to be estimated, resulting in significant uncertainties.

Stability theories have been applied to delineate the origin of meanders. Analysis by Ikeda et al. (1981) and Parker et al. (1983) using a dynamic equation for longitudinal velocity and a kinematic equation for bank erosion have provided the mechanistic founding of the meander path. An expression for the wavelength was

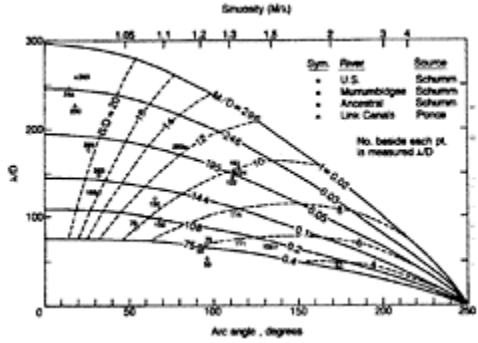

Figure 1. Plan geometry of river meanders (Chang, 1984b).

derived as:

$$\frac{\lambda}{D} = 8\left(\frac{\pi B}{fD}\right)^{1/2} \quad (7)$$

where D=flow depth, f=friction coefficient from Darcy-Weisbach formula.

The meander curvature and other geometric features for rivers were analysed by Chang (Chang, 1984a, Chang, 1984b). Chang uses an energy approach combined with relations for flow continuity, sediment load, resistance to flow, bank stability and transverse circulation in channel bends to obtain a mathematical formulation for the equilibrium river state. The analysis establishes the maximum equilibrium curvature, stated as the radius-of-curvature to channel-width ratio, which has an average value of 3; it shows only minor variation within the meandering range:

$$\frac{r_c}{B} = 2.2 + 0.15\left(\frac{B}{D} - 4\right) \tag{8}$$

From the regular meander path model Chang obtained a graphical relationship for the plan geometry of river meanders as shown in Figure 1.

3 MEANDERING RIVERS—CASE STUDY

3.1 *Historic and present river courses*

In this section five selected rivers in Flanders showing a typical lowland character, are considered. These rivers are the Kleine Nete, Grote Nete, Marke, Warmbeek and Kemmelbeek. The first data of implemented modifications date from the 19th century. The rivers were subjected to training works, over which the first data found are dated from 19th century. In that time attempts to control frequent flooding and to meet the rising demands for agriculture led to significant changes in the structural quality of most watercourses and reservoirs in the region. Later on,

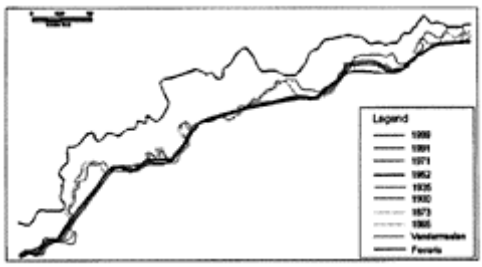

Figure 2. The Kleine Nete river course changes in time (van Wallons, 2002).

the training works were continued, in particular in the 60- and 70-ties of last century. Most of these rivers were channelised and straightlined to their the present far-to-nature state.

As an example, Figure 2 shows the river course changes throughout the time for the river Kleine Nete. For this evaluation more recent and old maps, dating from the eighteenth century, were used.

From this Figure, it is clear that the Kleine Nete indeed was a meandering river. Comparable results were obtained for the 4 other rivers. A large amount of wave lengths has been calculated for each river, in order to determine the predominant wave length, together with other meander characteristics. The old maps show the natural state of the river and thus are valuable sources for determining an equilibrium river pattern. They can serve as a reference for the restoration project However, some problems were encountered while trying to assess the meander patterns.

It is assumed that the oldest maps by Ferraris (1771–1778) aren't reliable for the determination of the meander characteristics, as significant deviations in the river trajectory were found compared to the later elaborations. Presumably, the topographical methods of that time were not accurate enough. Therefore the first evaluation goes back to the years 1846–1854, to the military maps by Vandermaelen.

Furthermore, due to the irregularity of the river course, instead of immediately determining the meander wavelength, it was mostly calculated as twice the distance between two inflection points, as this was easier to determine.

Finally, the sinuosity of the rivers was determined as the ratio between the actual length of the river over a section to the distance between the begin and the end of the sections (Fig. 3). This was done in a careful way, as it appeared that the section length differs from map to map depending upon the map scale and the number of details included.

3.2 *Geometry and hydraulic parameters*

Parallel with morphologic studies a large amount of geometrical and hydraulic data has been gathered

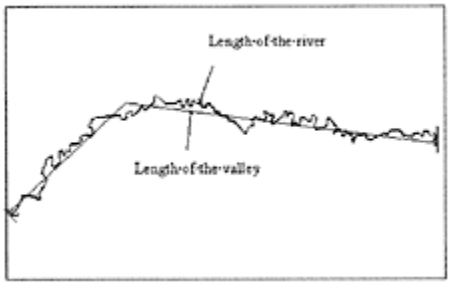

Figure 3. The Grote Nete river—determination of the sinuosity.

during field measurements. Representative parameters for the selected sections of the rivers were derived from a large set of cross sections. Friction coefficients were established based on discharge and water surface measurements. The river bed material was collected in several points along the rivers and analysed to determine the grain size distribution. The formation of the banks consists mostly of fine graded sand, locally with significant silt-clay content. The main hydraulic parameters of the studied rivers are collated in Table 1.

3.3 *Predicted meander size*

The set of morphologic and hydraulic data is used to determine the meander patterns according to the above presented formulas. Then they are compared with the meander patterns read from historic sources.

The results of these calculations and the average values from map reading are summarised in Table 2.

One can see that significant differences for meander parameters are obtained by different methods, which needs some comments.

The results derived by the Chitale formula are realistic concerning the prediction of the sinuosity of the rivers. On the other hand, the sizes of meanders are significantly overestimated; the predicted amplitudes are 3–4 times larger than those found in the maps.

The determination of the meanders using Chang's graphical method was somewhat problematic. The studied rivers feature relatively small width-depth ratios, as a result of which the values B/D fall in the right-bottom part of the graph were accurate reading is difficult. This results further in very high values for the sinuosity, especially for the Warmbeek and the Grote Nete river, where M/λ is higher than 5. Chang believes that smaller width-depth ratios associated with cohesive properties of channel forming material promote the development of very sinuous channels. The corresponding values for meander wave length are relatively good. However, when using the sinuosity from the maps, the λ/D ratio from the graph would be around 100–120, which is much more than the actual values for the studied rivers.

Table 1. Hydraulic parameters of studied rivers.

		Warmbeek	Grote Nete	Kleine Nete	Marke	Kemmelbeek
Bankfull discharge (m^3/s)	Q_b	4.6	11.1	29.2	18.1	18.6
Depth (m)	D	1.3	2.4	2.5	2.0	2.2
Width (m)	B	4.5	8	14	13	10
Hydraulic radius (m)	R	0.94	1.44	2.26	1.38	1.34
Slope (−)	S	0.00067	0.0005	0.0003	0.00075	0.00145
Friction coeff. (−)	f	0.073	0.09	0.078	0.078	0.091
Sediment size (mm)	d_{50}	0.35	0.18	0.18	0.14	0.25

Table 2. Comparison of different methods for meander shape determination.

			Warm-beek	Grote Nete	Kleine Nete	Marke	Kemmel-beek
Sinuosity (−)	M/λ	Maps	1.24	1.58	1.48	1.37	1.51
		Leopold & Wolman	1.22	1.25	1.27	1.27	1.26

		Chang	5.8	5.8	2	1.7	2.9
		Chitale	1.43	1.63	1.62	1.5	1.49
Length (m)	λ	Maps	50	43	146	150	100
		Leopold & Wolman	50	90	159	147	113
		Chang	30	60	175	170	110
Amplitude (m)	a	Maps	16	33	43	31	32
		Leopold & Wolman	16	30	55	51	38
		Chitale	56	128	221	140	99
Curvature radius (m)	r_c	Leopold & Wolman	11	19	34	31	24
		Chang	10	17	34	33	23

Similarly, overestimated values for meander length are obtained with the relationship suggested by Ikeda & Parker.

The 'best' results are obtained using formulas by Leopold & Wolman. These simple formulas, based on bankfull channel width only, produce the meander amplitude, length, curvature radius that comes reasonable close to the natural development of the studied rivers.

The differences in results are not surprising, as in the reported studies the scatter of the measured meander patterns, to which the formulas were fitted, was also significant. An explanation for the geometrical variations, despite those already mentioned in previous paragraph, is the heterogeneity that exists in natural rivers. The heterogeneity, which includes factors such as vegetation, cohesive sediment content, variation of sediment size, fallen trees, rocks, etc., may inhibit the development of a self-formed meander geometry. That is why more sophisticated formulas, that use some selected factors can produce misleading results.

From this one can conclude that the choice and use of any formula must be done carefully and at best proceeded by verification to the local conditions using reference meander patterns. It is evident that the understanding of the meander development is still far from satisfactory.

4 LABORATORY STUDY

Because of the incompetence of the existing formulas, a physical model study was launched to gain more information on the mechanism of meander development. Hereafter, several laboratory tests are discussed. Considering the complexity of the simulated process, the test should be regarded as a preliminary stage of the ongoing study.

4.1 *Test conditions*

The laboratory experiments were conducted in a test flume that is 15m long and 2.6m wide and is enclosed in a circulating water system. The flume was filled with a mixture of sand and caolinite clay. The characteristic diameters of the sand are d_{10}=0.17mm d_{50}=0.23mm d_{90}=0.315mm. The cohesive fraction was added in order to increase the stability of the channel banks. Its content in the sediment mixture was 3%. The sediment was leveled to obtain a flat plain with an average thickness of 15cm. The longitudinal slope was situated between 0.7mm/m and 7mm/m. In the centre of the flume a straight trapezoidal channel was formed. The channel has a depth of 6 or 8cm, a 15cm bottom width and a bank slope of 1:1. The initial geometric parameters were chosen in respect to the Warmbeek river, one of the studied meandering rivers.

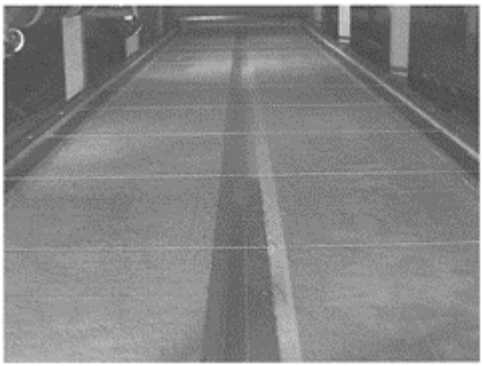

Figure 4. Testing set-up.

The morphologic changes that occurred during the tests were recorded on a video camera. The horizontal and vertical geometry was measured with a laser interferometer. The interferometer was mounted on a carriage that could shift over the flume. No sediment was added in the current test.

4.2 *Test performances*

Test 1

In the first test a slope S=0.00067 was applied. The straight channel had a depth of 8cm and a width of 31cm. The bankfull discharge was initially 5.7l/s but was during the test reduced to 2.75l/s (1cm below the banks) because water started to flow over the banks in the downstream section. Since after 30 hours no meander patterns were observed to develop, the discharge was increased again to about 3.7l/s. After another 50 hours of test run no meander patterns were developed.

Test 2

The slope was the same as in Test 1. The channel depth was smaller, 6cm and had an initiating bend (with λ/2 2.6m and a=0.35m). Also in this test no meander formation was obtained, see Figure 5.

From these initial conditions, it could be concluded that the flow had not enough potential to transport the sand along the bed and to erode the banks.

Test 3

In this configuration the slope was significantly increased to S=0.007. The channel had a depth of 8cm and an initiating bend with λ/2=2.6m and a=0.3m. The discharge was set to 3.33l/s. At 17 hours, the bed topography was measured for the first time. The total duration of the test was 86 hours. During this test, significant sediment transport and bank erosion was observed. The obtained transformation is shown in Figures 6 and 7 respectively representing an intermediate and the final meander pattern.

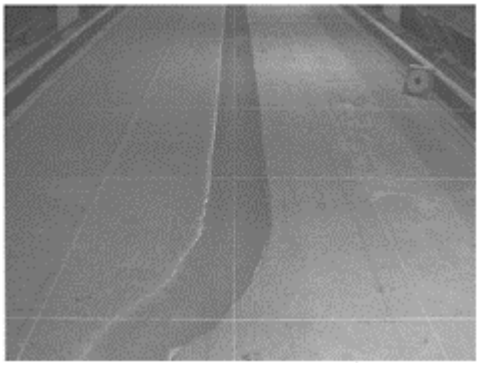

Figure 5. Channel after the end of Test 2.

Figure 6. Test 3: Channel development after 20 hours.

Figure 7. Test 3: Channel development after 86 hours.

Although the channel becomes wide and shallow, a deeper sinuous talweg and an extended downstream wave migration can be easily recognized. In Figure 8, the recorded cross-sections through the top of

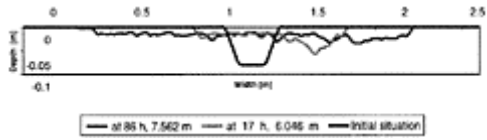

Figure 8. Test 3: Channel cross-section.

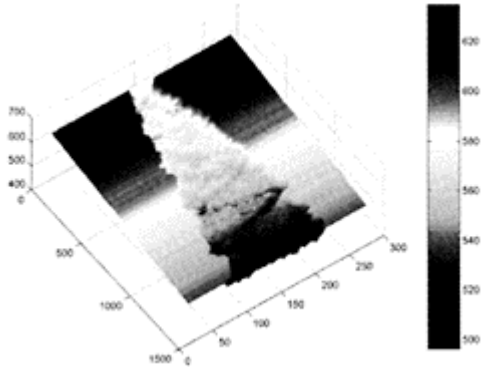

Figure 9. Test 4:3D-channel development after 29 hours (length and width in cm, depth in mm).

a sinuous wave are shown. The asymmetrical character of this section is remarkable.

At 17h, the meanders had a wavelength of 2.63, 2.63 and 2.81m, and an amplitude of about 0.6m, which was nearly constant along the channel. After 86h the meanders evolved to 3.41, 4.0 and 4.09m in length and the amplitude varied from 0.6 to 1.5m, increasing along the channel. Smaller meanders in the upstream channel section were due to the lack of sediment supply at the entrance, which caused erosion of the bed, consequent flatter slope and loss of capacity to erode the banks.

Test 4

In Test 4 the initial conditions were the same as in Test 3 except for the initiating bend; the channel was straight over the entire length. The discharge of 3.33l/s was maintained constant throughout 29 hours of testing. The resulting channel configuration is shown in Figure 9. The talweg extends in the downstream direction with a sinuous shape and increasing depth. The width of the meandering channel belt increases linearly from 0.31m to 1.45m. The meander length varied from 1.2 to 4.03m, and the sinuosity reached a value of 1.27.

Test 5

In this and in the following test it was intended to check the influence of an obstacle in the straight channel on the initiation of meander formation. The use of such obstacles, known as deflectors, is a recommended measure to recreate meandering patterns in degraded

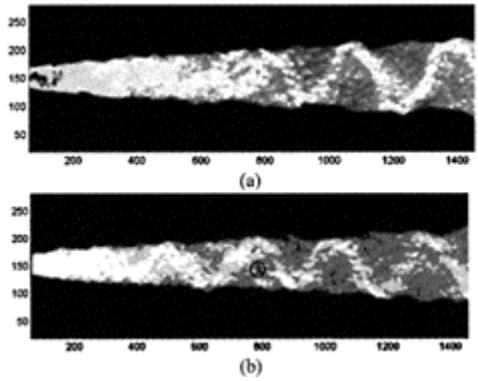

Figure 10. Final channel development in (a) Test 4, (b) Test 5 (units in cm; circle indicates the position of the obstacle).

straight rivers, FISRWG (1998). In this test a single permeable obstacle was placed in the right bank of the channel, at 7.2m from its beginning. The other channel characteristics remained the same as in Test 4.

During the test it appeared that the deflector had little impact on the development of the meander pattern. Only at the very beginning of the test the deflector influenced the erosion of the opposite bank. Later on, local turbulence caused erosion of the bank around the obstacle, which led to a deflector cut off from the bank it was built in. The deflector lost its significance quite soon and in the end it was just an unnecessary obstacle in the channel.

After 23 hours, the meandering talweg reached a length varying from 2 to 3.2m and an amplitude up to 1.1m. The sinuosity reached a value of 1.2 in the most downstream section.

Figure 10 represents the final channel state for the last two tests, which had the same initial configuration except for the deflector, used in Test 5. The larger size of the meandering talweg in Test 4, in comparison with Test 5, is due to the longer duration of the test. Remarkable in Test 4 is the deviation of the sinuous meander pattern. The meander transverses appear to be convex, facing downstream. This is comparable with natural rivers, which usually develop intrinsically asymmetric meanders too (Sun & Parker, 2000).

Test 6

This time, the impact of three thin wall defectors built in the right bank and oriented in different ways towards the channel axis, as shown in Figure 11, were examined.

The deflectors, in particular the two upstream ones, reflect the stream towards the opposite bank causing its almost immediate erosion. Thereby, the speed and magnitude of meander growth was considerably higher than in previous tests. The perpendicular orientation

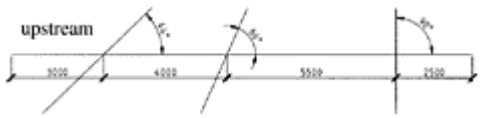

Figure 11. Deflectors orientation.

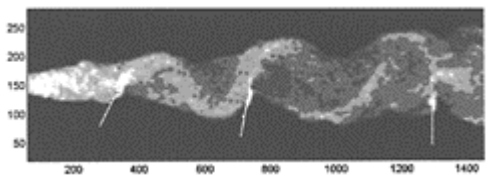

Figure 12. Channel development in Test 6 (units in cm).

of the deflector resulted mainly in local scoring and had a smaller effect on the formation of a meander. In the course of test, it appeared again that the remaining deflectors form an undesired obstacle to further meander development. While the amplitude and length of the meanders increased, the meander also shifted downstream. The deflectors were the

cause of the resulting meander pattern, which consists of 1 meander between two successive deflectors, see Figure 12. The discontinuity in the talweg between deflector 2 and 3, was also caused by the presence of the deflectors. This is because the deflectors maintained the position of the first top, that was formed behind each deflector.

4.3 *Discussion*

In the performed tests, the caving banks are the source of the transported material within the meandering channel. The rate of bank erosion appears to be important, not only for determining the meandering state, but also for the determination of depth and width of the cross-sections. Easily eroding banks result in wide and shallow sections. The increased slope or discharge causes rising velocities, through which the bank erosion grows and the channel widens and shoals.

In these experiments, the resulting channel pattern appears to be more like a sinuous talweg than a truly meandering channel. Although a curved channel did develop from an initially straight channel, the sinuosity was rather low. The shoaling of the channel is due to the easily erodible banks, whereas the stream is 'overloaded', having a to steep slope. A next step in the testing should include the use of another type of bed material and the variation of the slope. Slowly eroding banks are supposed to result in deeper and narrower channel cross-sections. As it was already noted, rivers with a small width/depth ratio promote the development of very sinuous channels. Various combinations

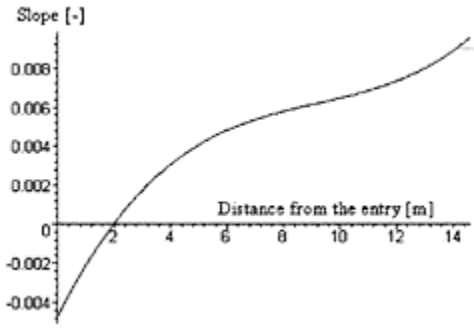

Figure 13. Bottom slope of the channel after Test 4.

of fluvial materials have been recently tested with the aim of reproducing meandering rivers in the lab. The preliminary results show that e.g. a mix of diatomaceous earth and kaolinite clay is able to produce a meandering channel with a sinuosity of almost 2.0 (Smith, 1998).

The initial cross-section of the channel had no significant influence on the meander development. The tests confirm that when an erodible material is used, a river will shape its cross-sections in accordance with its flow, slope and bank materials, irrespective to its initial cross-sections. A river deepens or shoals until it reaches an equilibrium configuration, for which the rate of sediment supplied to the cross-section from the

adjacent banks is balanced by the rate of transport towards the downstream sections. The tendency to attain this equilibrium can be illustrated by the elevation of the channel, recorded in Test 4 (Fig. 13). In the upper section, the channel deepens and the slope flattens until the flow no longer has the power to erode the banks. When erodible material is used, the channel shoals, and the slope steepens until the transport capacity of the channel equals the rate of bank erosion. The development of a meandering talweg is also a result of the dissipation of excessive energy. The higher the valley slope is, the higher the rate of meandering will be. The prerequisite is to have stable, not easily erodible banks.

The most remarkable result is that the use of deflectors as an artificial measure to initiate meandering is not a suitable solution for recovery of meandering watercourses. The deflectors need to be removed after the meander has started to develop, otherwise it will disturb the ongoing development of river course. Instead of constructing and removing such deflectors, a deflector which is eliminated by the meander process itself, is a simple and recommendable solution for restoration projects. Test 3 and Test 5 demonstrate that an initiating bend or a permeable deflector does not influence the meander pattern but only the speed of its development.

5 CONCLUSIONS

A comparison between calculated meander geometry and the geometry deducted from old maps of naturally meandering rivers has been performed. This comparison shows that it is hard to find reliable formulas that approach the meander characteristics. The quality of the prediction seems to depend rather on the set of data to which the formulas were fitted, then on the amount of variables in the formulas. Simple relations obtained by Leopold & Wolman (1964) reveal meander patterns close to those found in the considered sites.

The physical experiments provide a better insight in some practical aspects concerning the performance of laboratory tests. They give an idea of the feasibility of artificial interventions to promote the meander restoration in degraded straight rivers. The next testing program will include the change of the sediment strength configuration to reach a higher sinuosity in the small laboratory flume.

REFERENCES

Chang, H.H. 1984a. Analysis of river Meanders. *Journal of Hydraulics Engineering*, Vol. 110, No. 1, pp. 37–50.

Chang, H.H. 1984b. Regular meander path model. *Journal of Hydraulics Engineering*, Vol. 110, No. 10, pp. 1398–1411.

Chitale, S.V. 1970. River Channel Patterns. *Journal of Hydraulics Division*, ASCE, Vol. 96, No. HY1, pp. 201–221.

De Vos, L., Verfaille, S. 2003. Remeandering of small rivers—theoretical and physical model study (in Dutch). Thesis UGent, 187 p.

FISRWG 1998. Stream Corridor Restoration: Principles, Processes and Practices. By the Federal Interagency Stream Restoration Working Group (FISRWG). ISBN-0-934213-59-3.

Friedkin, J.F. 1945. A laboratory study of the meandering in alluvial rivers. In: Schumm, S.A. 1972. *River morphology.* Stroudsburg (Pa), Downden, Hutchinson and Ross, pp. 238–281.
Hansen, H.O. (Ed.) (1996). River Restoration—Danish experience and examples. National Environmental Research Institute, Denmark. 99 p.
Ikeda, S., Parker, G., Sawai, K. 1981. Bend theory of river meanders 1. Linear development, *Journal of Fluid Mechanics*, Vol. 112, pp. 363–377.
Leopold, L.B., Wolman, M.G., Miller, J.P. 1964. *Fluvial Processes in river engineering.* John Wiley & Sons, 432 p.
Nielsen, M.B. 1996. Lowland stream Restoration in Denmark. In: Brookes, A. & Shields Jr., F.D. (Eds.): *River Channel Restoration—Guiding Principles for sustainable projects.* John Wiley & Sons, pp. 269–289.
Parker, G., Diplas, P, Akiyama, J. 1983. Meander bends of high amplitude. *Journal of Hydraulics Engineering*, Vol. 109, No. 10, pp. 1323–1337.
Van Liefferinge, C., De Weerdt, B., De Smedt, D. 2002. Investigation of the feasibility, needs and relevance for remeandering of different river courses. *Intern. Report*, (in Dutch) Ghent University.
Vallons, A. 2002. Study on the historic and current topology of Flemish rivers: case studies (in Dutch). Thesis KUL Leuven, 121 p.
Schumm, S.A., Khan, H.R. 1971. Experimental study of channel patterns. *Nature*, 233:407–409.
Smith, C.A. 1998. Modelling high sinuosity meanders in a small flume. *Geomorphology*, 25:pp. 19–25.
Sun, Y., Parker, G. 2000. Meandering rivers. St. Anthony Falls Laboratory, University of Minnesota: 126 p.
Yang, C.T., Song, C.S. 1979. Theory of minimum rate of energy dissipation. *Journal of Hydraulics Division, ASCE*, Vol. 105, No. HY7, pp. 769–784.

Small river re-naturalization and cultural heritage

G.Müller

Department of Civil Engineering, The Queen's University of Belfast, Belfast, UK
G.Himmelsbach

Spessartprojekt, Aschaffenburg, Germany
C.von Carmer

IFMW Karlsruhe, Germany
P.Fröhle

University of Rostock, Civil Engineering Dept.

River Flow 2004—Greco, Carravetta & Della Morte (eds.)

ABSTRACT: Until the advent of modern power sources such as steam and combustion engines, the small rivers in Middle Europe played a central part in the economy as suppliers of mechanical power, water and means of transport. As a result, virtually all small rivers host a variety of remains of previous industrial activities such as weirs, mill races, ponds etc. which were built in the era ranging from the Middle Ages to the beginning of the 20th Century. Today, these remains are often not even recognized as such any more by hydraulic engineers, planners and the general public. The canalization of many rivers during the 1960s and 70s destroyed many remnants of the pre-steam age industries along the small rivers. As a result of the increasing ecological awareness, the concept of re-naturalization was developed in the 1980s. The current 'ideal' aim of re-naturalization, of re-creating a 'natural' river, does not take the historical context of our rivers into account, so that re-naturalization as well as the 'hard' engineering solutions can both result in the irretrievable loss of the cultural heritage. A current research project conducted by the authors tries to raise awareness of the historical context and to develop concepts of how to integrate the remains of the industrial past into the

changing demands on our small rivers whilst contributing to the overall quality of the environment.

1 INTRODUCTION

Before the advent of steam power, the small rivers played a vital part in the economy of the Central European countries as well as in North-America. Rivers supplied mechanical power for industry, irrigation water for agriculture, drinking water for the population, water for defense systems and they were used as transport ways for bulk goods. In order for the rivers to fulfill all these duties, and to ensure that the course of the river remains stable, man made very significant changes to the small rivers ever since the Middle Ages. These changes include the construction of weirs, fortification of banks, change of river course, addition of diversion or transport canals, creation of lakes for water storage, and many other items. With the development of first steam power and then electricity and the internal combustion engine, the use of the small rivers by man declined until it reached a point where they are hardly used at all.

Following the decline of usage, and the increasing demand for rural and urban space, many small rivers were forced into straight beds, concrete channels or even underground, changing the river from an ecosystem into a lifeless drain. This happened in particular during the 1960s and 70s. With the development of an increasing consciousness for our environment, other ecologically acceptable solutions for the small rivers were sought for. The solutions principally include the *re-naturalization* or return of the river to its natural state, using traditional construction methods and natural materials. The river would therefore be allowed to develop its own dynamics and ecosystem. Re-naturalization is today seen by many scientists, engineers and landscape architects and subsequently the public as the most desirable development strategy for rivers.

Many hydraulic engineers are not fully aware of the extent of the former use of the small rivers, or of the purposes they were used for. Quite often the redevelopment of a river—be it a ‘hard’ engineering solution or a ‘soft’ re-naturalization—therefore destroys the remnants of forgotten industrial activities not by intention but by lack of knowledge and awareness. These remnants however constitute a significant part of our cultural heritage and indeed of the development of engineering, which are subsequently and irretrievably lost.

The authors of this article, engineers and an archaeologist, are currently conducting a research project where the character and the importance of this heritage is investigated with the aim to raise awareness of the situation and to develop integrated solutions.

2 CULTURAL HERITAGE AND CULTIVIZED LANDSCAPE

2.1 *Introduction*

When engineers in Germany talk about *‘Kulturlandschaft’* (cultivated landscape), they invariably mean the landscape shaped by man’s current activity like agriculture, construction, infrastructure and so on. Archaeologists however have a rather different

definition of this term. For them, *'Kulturlandschaft'* means the landscape which was shaped by man for hundreds and thousands of years, and which—for today's inhabitants often invisibly—contains significant parts of our cultural heritage. Very often the remains of this field of agricultural and industrial activities are overlooked simply for lack of knowledge about our pre-steam era industrial past both on the side of engineers and the general public. In addition, the question arises as to how far an ecosystem which developed within a man-made environment for up to eight centuries can not be considered as natural. Modern textbooks on river hydraulics and river re-naturalization often completely omit the historical context, e.g. Patt et al. (1998). Only very recently has the term *'Kulturlandschaft'* been introduced into the engineering field, Hintermeier (2003). Today, the extent to which the small rivers were formerly used, and the importance this usage had to society, is hardly known even to specialists working in this field such as hydraulic engineers. Therefore the remains of the former usage are often not even recognized as such.

A small comparison may illustrate the importance of rivers as power source and means of transport in times before steam or combustion engines existed: a typical water wheel of 10kW provided more, cheaper and more reliable power than 30 to 40 horses or one hundred men; a horse drawing a boat on a canal could shift 40–50 times the weight it could move on a road. Water courses were therefore of prime importance. In the following, some of the principle uses of small rivers and their features will be presented in order to illustrate the way and the extent to which rivers were changed.

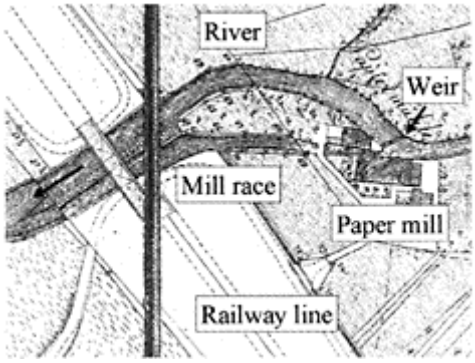

Figure 1. Typical mill installation (WWA Aschaffenburg, 1889).

2.2 *Cultural heritage 1: power production*

The water wheel is one of man's oldest hydraulic machines; water wheels were already described by the Roman architect Vitruvius (in *'De Re Libri Architecturi X'*). A water wheel installation required a head difference in the river, which was usually provided for by a weir. The wheel installation itself was located at a mill race (today it would be called a 'diversion canal'). Apart from wind mills, water wheels were the only mechanical prime movers before the advent of steam engines and drove flour mills, textile and

mechanical machinery, powder and mineral mills, water pumps for drinking water supplies etc., Reynolds (1983). It is estimated that in 1850 there were 25–30,000 water wheels in operation in England, 6,400 in Ireland and around 40,000 in Germany. Even as late as 1925, there were still 33,500 water wheels in operation in Germany with individual capacities of 1–75kW and an overall capacity of approximately 200MW. This technology eventually disappeared in the 1950s and is today already virtually forgotten. Figure 1 shows a typical mill installation (River Aschaff/Bavaria 1889) with a weir, inflow detail, mill race, mill building with water wheel and outflow. Water wheels are today regarded as an outdated technology belonging to the romantic ages. Some recent research has however shown that water wheels had been developed into very efficient energy converters. Figure 2 shows some typical water wheels and the measured efficiency curves which indicate the surprisingly high efficiencies of 75− 85%. More technical information about water wheels can be found in Müller & Kauppert (2002, 2003).

2.3 *Cultural heritage 2:17th century fortifications*

Traditionally, city fortifications are envisaged by most people as walls with towers, possibly with a water filled ditch in front of the wall. This type of fortification was in use until, at the end of the 15th century, modern cannons were introduced which simply shot stone walls apart in a very short time. As a result, fortification design changed dramatically during the 16th century and a system of earthen ramparts, bastions, outworks and major hydraulic elements, some of which are still visible today, evolved. The City of Braunschweig in Northern Germany is one of the few German cities where even the river course was changed in order to create a wet ditch for the artillery fortification, and where this altered course is still in existence. Today, not even the name of the river branches (*'Umflutgraben'*, flood diversion canal) recalls their original purpose. Figure 3 shows two maps of the City from 1650 and from today. In Figure 3a the original course of the River Oker through the city centre is still visible. The river channel running through the city center was maintained, probably for transport purposes, and weirs and mill races were built in order to power mills inside of the city in case of a siege. These canals are also visible, as is the very narrow wet ditch of the mediaeval fortifications (thick dark line). In Figure 3b, most of these items have disappeared and only small sections of the medieval ditch and the wet trench of the 17th Century fortification still exist.

2.4 *Cultural heritage 3: transport and irrigation*

The use of rivers for transport did not only mean navigation, but also e.g. the floating of timber. Often, special float canals were built alongside the river to provide sufficient depth and width of water for floats; as can be seen in Figure 4 for the River Aschaff. Apart from transport, in particular very small water courses were often used for irrigation purposes. The run of such small water courses was therefore frequently changed from its typical location at the lowest point of a valley to a zig-zag course running from the low point to the edge of the valley further downstream. This new and higher course enabled

parts of the valley to be irrigated from above, and reduced the river's gradient and dynamics.

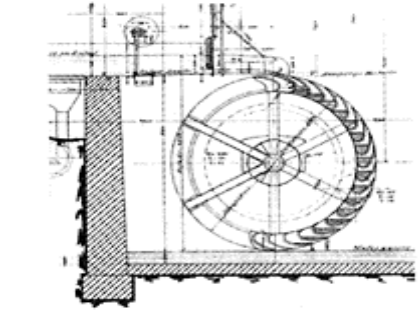

a. Overshot water wheel

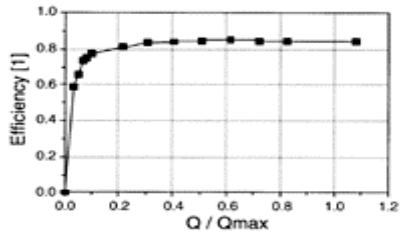

b. Efficiency curve for a 3.60 m diameter overshot wheel

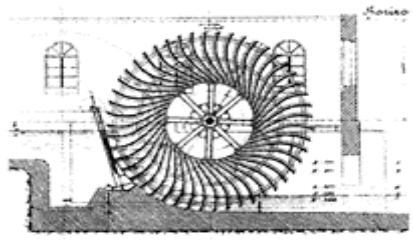

c. Undershot (Zuppinger) wheel for textile mill

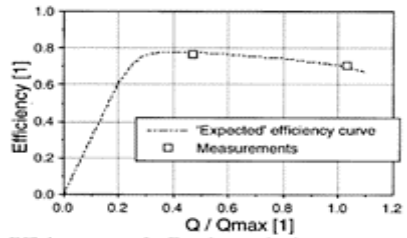

d. Efficiency curve for Zuppinger wheel

Figure 2. Typical water wheels for head differences of 1.0–5.0m, Müller & Kauppert (2003).

In addition, ponds were created for purposes such as storage of logs, provision of water to float logs downstream, fish farming, provision of additional water for mills during daytime etc. In many instances rivers were made navigable by building weirs and possibly side canals; this aspect is also very interesting both from the point of view of cultural heritage and the re-use today for leisure boating. This topic is however beyond the scope of this article.

3 RENATURALIZATION AND EXISTING WATER COURSES

3.1 *Re-naturalization*

One characteristic of historic (i.e. before the 1900s) alterations of river courses was that usually only those

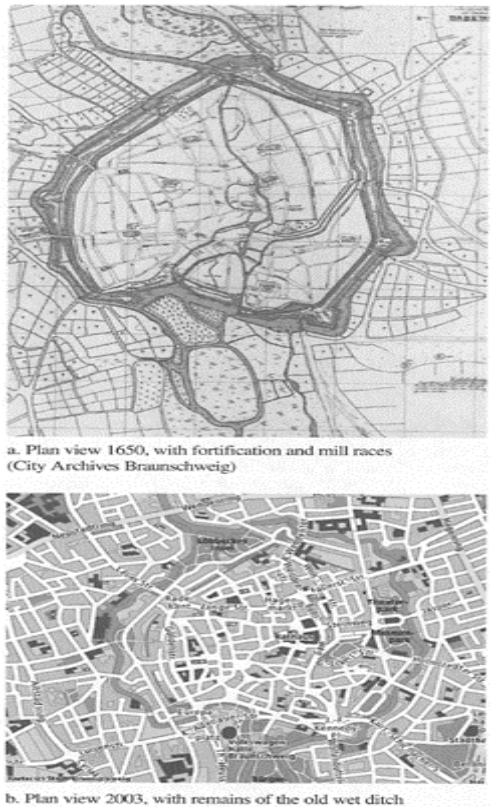

a. Plan view 1650, with fortification and mill races (City Archives Braunschweig)

b. Plan view 2003, with remains of the old wet ditch

Figure 3. The City of Braunschweig, Northern Germany, in 1650 and today.

small sections were changed where a change was absolutely required, such as the addition of a mill race. The development of hydraulics as an engineering discipline led to a situation where small rivers were perceived by engineers purely as channels for

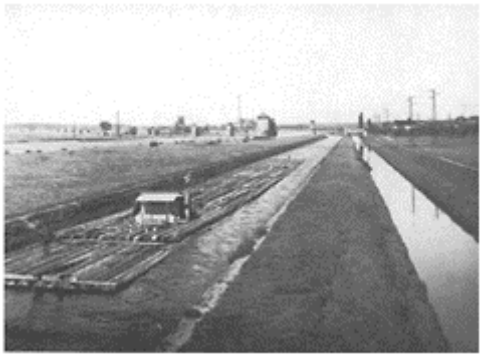

Figure 4. Floating logs (Aschaff, ca. 1920, Spessartprojekt).

rain- and groundwater. During the 1960s and 70s many small rivers were subsequently straightened over long stretches, often using concrete linings, in order to minimize the land required by the river (e.g. to maximize farmland or inner city land usage) or to protect roads and railway lines. This straightening generated a number of very undesirable side effects, such as a deepening of the river bed and the unfavorable superposition of flood waves caused by their accelerated propagation. The rivers running in concrete channels could not support eco-systems or even trees any more, and degenerated into lifeless drains. Following the increasing ecological awareness of the public, engineers tried to develop a concept for an ecologically and hydraulically acceptable alteration of water courses.

The re-naturalization of rivers is a concept which is today regarded by biologists, ecologists, landscape planers, by the public and by many engineers as the most desirable development. The main goal of renaturalization is to bring the river as close to its original or 'natural' state as possible by removing artificial obstacles such as weirs, by changing of canalized sections, by provision of fish passes, of space for flood plains etc., e.g. Patt et al. (1998). In addition, renaturalization tries to create a water-land interface to create a living space for aquatic and an access area for land based animals and to increase flood retention areas, although the latter aim is difficult to achieve due to the high demands for space. For these purposes, 'soft' construction techniques using natural material like willow branches, wood and rock were developed.

'One of the primary aims of the national and international effort for the protection of rivers is the creation or re-creation of a free passage; …therefore weirs and barrages can be regarded as a significant anthropogen disturbance of the ecosystem', Schrenk (2003). The German recommendations for the management of small rivers which are currently being developed give a 'potentially natural state of the water course' as the development aim. The 'potentially natural state' is

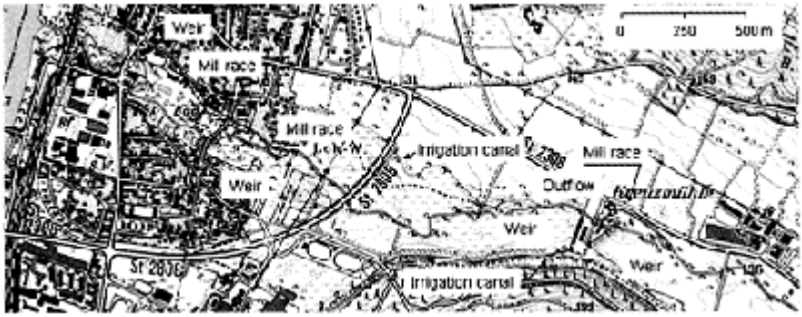

Figure 5. River Elsava.

defined as an ideal conceptual state of future development of the water course which is undisturbed by man. Although this ideal is defined, current practice is to bring water courses 'close to a natural state' rather than creating a truly natural state. The latter concept is very difficult to achieve due to a variety of reasons such as land interests, the proximity of infrastructure installations such as roads, railways, gas, water, sewage and electricity lines etc. which must not be interfered with, recreational use and other reasons.

A review of the interference of man with the rivers since the 1960s however shows that 'hard' engineering solutions and current re-naturalization concepts have one peculiar aspect in common: the historical context is completely omitted, and the implementation of either concept implies the destruction of all historical artefacts along the river.

In the following, three examples will be given in order to illustrate the complexity of the problem of defining what constitutes the natural state of a small river, and which effects the various man-made alterations had or have and to define what constitutes a desirable development.

3.2 *Existing water courses 1: River Elsava*

The River Elsava (NW Bavaria) is a typical small European river with a length of approximately 15km, a drained area of 142km^2 and an average flow rate of 1.23m^3/s. This river has been used by man since the middle ages for power production and irrigation and a large number of man-made features still exist along the river. A water mill at the old monastery of Himmelthal (Elsava) was first mentioned in 1232, water rights for the extraction of water for irrigation purposes were recorded in 1435 (Elsava). It can therefore safely be assumed that weirs and side channels have existed for 600–750 years. Figure 5 shows a stretch of around 3000m of the river Elsava in North-West Bavaria (flowing into the River Main). On this figure alone, 3 mill races and two irrigation canals are visible. In all, the Elsava once had 12 mills of which one, a saw mill *(Kreuzmühle),* is still in operation. Both irrigation channels are also still in use, one of them to supply cooling water to a chemical factory. The Elsava today constitutes a small river reasonably unaffected by dramatic changes, which has preserved the main features it has had for many centuries. The *Archeological Project Spessart* (see internet references) is trying to raise the consciousness within the population about this heritage of the age of small hydropower and early industry in order to prevent the disappearance

of mill races by accident or re-naturalization and possibly to discover new usages for the existing hydraulic systems.

3.3 *Existing water courses 2: River Aschaff*

This river, a tributary of the River Main (NW Bavaria) with length of 8.4km, a drained area of 144km^2 and an average flow rate of 1.34m^3/s once powered nine water mills and was also used as a way to transport logs by floating them down river. For these purposes, weirs were built and artificial lakes created to store wood under water or to provide a mass of water to float the stored wood downstream over shallows and obstacles. When a weir and power station was constructed in the river Main in 1920, the estuary of the Aschaff had to be relocated downstream of the weir in order to maintain the gradient and the water rights connected with the Aschaff, see Figure 6 (Aschaff 1917–1970).

The old estuary was subsequently replaced *('Mündung bis 1920')* and the lower course of the Aschaff was straightened in 1970, whereby all the old mills, weirs, diversion canals, mill ponds and mill races were destroyed and disappeared, see Figure 7a. Figure 7b shows the canal-cross section then built. The *Archeological Project Spessart* has documented the changes of the river and established a 'Heritage Walking Course' with display boards to familiarize people with the ongoing changes, the previous

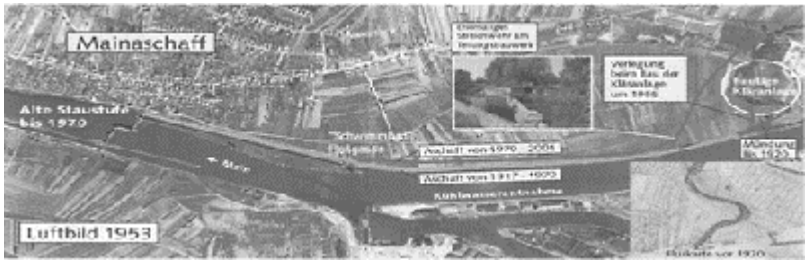

Figure 6. Aerial photography of the confluence of the River Aschaff with the River Main, with alterations from 1917 to 2001.

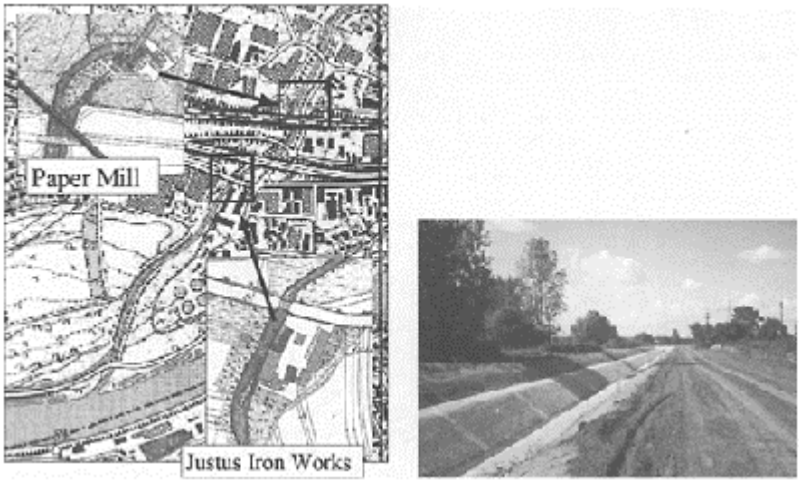

Figure 7. River Aschaff, changes of the estuary section.

importance of the river and thus the reasons for today's situation (including the loss of many aspects of the heritage).

From 2001 to 2002, an upstream section of the River Aschaff was re-naturalized, giving it a meandering plan view with ragged banks and shallow water zones which provide an suitable environment for aquatic animals. The course of the River had to be fixed in order to avoid interference with a newly built motorway and a variety of other infrastructure installations. Figure 8 shows today's course of the river with plan views of the two mills which existed before the re-naturalization with mill races, side channels and weirs. Again it can be seen that all remnants of the previous use of the river have disappeared in favor of a naturally-looking river. The River Aschaff demonstrates visibly the effect of the alterations of the last 40 years which were implemented following the prevailing river development philosophy but disregarding the historical context.

3.4 *Existing water courses 3: the Wallensteingraben*

The *Wallensteingraben* in North-Eastern Germany today looks like a natural water course, draining Lake Schwerin towards Wismar and the Baltic Sea. In reality, it constitutes the remains of a small canal

Figure 8. Re-naturalized section of the Aschaff with former mills(WWA Aschaffenburg, 1889).

built at the end of the 16th century to further Wismar's salt trade. The canal was finished in 1580, with a total length of 15.5km and a height difference of 37.60m which was overcome with 12 locks. Due to political developments, mainly caused by the 30 Years War (1618–1638) and the fact that Wismar became Swedish, depriving the city of its hinterland, the trade and with it the requirement for the canal practically disappeared. Subsequently the canal fell into disrepair. It still acted as a drainage for the lake, and powered water mills. In Figure 9, the course of the *Wallensteingraben* between Lake Schwerin (bottom) and the City of Wismar is shown. Today's remains of the artificial waterway (Goldammer, 1997) are indicated by circles, the locations of old mill races along the natural river (Hohensee, 1989) by water wheel symbols. Some remnants of the channel are still visible, though much of the canal was destroyed during railroad construction. Figure 10a shows a part of the summit reach excavated up to 10m deep. In parts, the earthworks of the locks can still be identified, as well as stones and bricks originally used for the sluices can be found which were re-used later in other buildings, Goldammer (1997). A small natural stream which drains the hinterland of Wismar and provided fresh water, fish and water power for the local population and eventually became part of the canal.

Along this small river and the *Wallensteingraben*, 14 water mills were situated which produced mechanical energy from hydro power. Some of the mills can be traced back to the 1250s. At the beginning of the 20th century, the operation of the mills ended at all mill races.

Turbines were installed at some of the historic mill sites to produce electric energy, but only two turbines still utilize this renewable energy resource. Over the centuries a, new biological and morphodynamic equilibrium has established itself in such man-used

Figure 9. The *Wallensteingraben:* Map, (BUGA, 2000).

and -made ‘river’ reaches. The development strategies, where weirs and mill races are removed, often mean that the historical remains of early hydraulic and cultural engineering activities are destroyed. Figure 10 illustrates the state of the old canal as it can be seen today.

Currently the *Wallensteingraben* is used for flood control and to stabilize the water level in Lake Schwerin. The average discharge at the northern outflow of the lake is about $0.8 m^3/s$. Dating back to the times of the former GDR, parts of the river are designated Nature Preservation Areas. Concerning the channel, plans are currently emerging to again connect Lake Schwerin to the Baltic Sea, thus, to reactivate or rather rebuild the canal along a new, slightly changed course not for the transport of salt, but for

a. The 10 m deep cut of the *Wallensteingraben* through a hill

b. Typical view of the *Wallensteingraben*

Figure 10. *Wallensteingraben* (IFMW).

leisure boating and recreation to further the economic development of the region once more (Buga, 2000).

4 DISCUSSION

4.1 *General*

A study of some small rivers in Central Europe indicated that these water courses have been altered by man for many centuries for varying purposes ranging from power production over transport to fortification. One additional aspect of the changes often was the reduction of the gradient and therefore the dynamics of the river. The geometry and functionality of our small rivers can therefore not be understood without their historical context. The ecosystems which evolved around the rivers are subsequently adjusted to an 'artificial' situation, but have sometimes been established for a very long time. Although the ideal aim of a 'natural river' is under discussion, it appears that in today's world the constraints imposed by infrastructure and settlement are too severe to allow for a river to develop its own natural state again.

4.2 *The Canadian River Heritage System*

The removal of all historical artefacts which usually is a consequence of re-naturalization deprives our society of a part of its cultural heritage and therefore of a part of its identity. In Canada, this has been realized some time ago and the Canadian Government has designated a number of river sections as 'Heritage Rivers', which are protected river sections of (amongst others) special ecological, geological, archeological, historical or recreational interest. The aim is to systematically create and maintain a Canadian River Heritage so that Canada's nature, history and society is reflected in the river system without which the development of the country had been impossible. Within the Canadian River Heritage System (CHRS) these sections are administrated and managed, Nagel & Goldhammer (1997). This system by now comprises nearly 6000km of rivers, amongst them a long stretch of the Grand River. CHRS incorporates a large variety of nearly 100 organizations ranging from Universities to representatives of the indigeneous people (Six Nations Council), cities, government authorities, newspapers etc. which all have an interest in their river. It appears that the idea of the 'cultivized landscape', as a system not just with hydraulic and environmental aspects but also with a historical context which is worth preserving has been taken to a practical conclusion by CRHS and may serve as a model for further developments in other countries.

4.3 *Re-naturalization and cultural heritage*

Re-naturalization is today considered to provide a natural environment for the development of an ecosystem as well as an area for recreation. The inclusion of the cultural heritage in the management of small rivers today would imply that the river would have to retain some usage apart from recreation. The development of rational strategies of usage of the available power and water which are compatible with the historical usage could present a new area of activity. Some progress in the field of power production has been made recently, where it could be shown that water wheels are not the out-of-date inefficient machines they are usually considered to be. A detailed literature review revealed that water wheels can be regarded as very efficient and ecologically acceptable energy converters for low head hydro power conversion, Müller & Kauppert (2003). This means that even our small rivers can—as renewable energy sources—contribute to the overall aim of carbon-dioxide reduction.

4.4 *Outlook*

The authors are convinced that the re-naturalization in particular of canalized sections of small rivers is of great benefit to our environment. The re-naturalization of rivers which are still in a state where the old usage is recognizable (see section 3.2) would however destroy the cultural heritage. With the inclusion of the historical context, and the preservation and purposeful re-use of the resource river as e.g. a renewable energy source, it becomes possible to preserve our cultural heritage as well as to develop a functioning eco-system (influenced by man of course to some degree) around our small rivers. In a re-naturalization (or river restoration) project therefore the *'added value for nature'* of the restored river and the *'historical value'* of the river (and a possible further use by man within the context given by history) should be weighed against each other in

order to obtain an acceptable solution. An existing water mill e.g. could be protected and, preferably, be operated again and integrated into an overall solution. A very small old canal which can never be used again however, may currently only provide a poor natural environment and should therefore be 'restored' or rather upgraded to create a functioning and ecologically diverse solution with the emphasis on the ecosystem rather than the historical value. In conclusion it can be said that the 'cultivized landscape' as perceived by engineers should be expanded to include another dimension, namely time.

5 CONCLUSIONS

From the Middle Ages onwards the small rivers in Central Europe were re-built and used by man for a variety of purposes. Before the 20th Century, the small rivers formed a vital part of the economy. The remains of these activities are still in existence, but often not even recognized as such for lack of knowledge and awareness. Examples for such remains are:

a. Weirs and mill races belonging to old mills which constituted the nuclei of modern industrial developments.
b. Wet ditches which formed parts of the cities' defensive system.
c. Irrigation canals, storage ponds, canals for floating logs.

In addition, some old artificial waterways built for transport are today considered as being natural. Past and current re-development strategies for small rivers (canalization and re-naturalization) very often neglect the historical context and therefore result in the loss of historical artifacts and a diminution of our cultural heritage. An integrated solution for the development of small rivers which includes and weighs ecological as well as cultural aspects, and possibly incorporates a re-use of the historical installations such as micro hydropower, should therefore be sought. The scope of an engineering evaluation of our environment or, *Kulturlandschaft'* should be expanded to include another dimension, namely time.

ACKNOWLEDGEMENTS

The authors would like to acknowledge the help from Mr. Pfeiffer *(Wasserwirtschaftsamt Aschaffenburg),* the City Archive of Braunschweig, Mr.Höhn *(Pro Schwerin),* and the critical comments from Dr.-Ing. K.Koll (Technical University of Braunschweig) and thank them for their support.

REFERENCES

BUGA Planungsgruppe. 2000. *Wallensteingraben Schwerin Wismar,* Schwerin/Germany.
Goldammer, G. 1997. *Der Schaale-Kanal. Relikterforschung historischer Binnenkanäle zwischen Elbe und Ostsee.* Mitteilungen der Geographischen Gesellschaft in Hamburg (87) (in German).

Hintermeier, K. 2003. Zeitgemäße Gewässerentwicklungsplanung erfordert auch kultur-historische Landschaftsanalyse—Kommentar (Timely river development planning requires the analysis of cultural and historical aspects—commentary, in German), *Wasserwirtschaft.* No. 9:3.
Hohensee, F. 1989. *Der Wallensteingraben. Geschichte, Gegenwart und Zukunft eines mecklenburgischen Gewässers.* Ostseedruck Rostock (in German).
Müller G. & Kauppert K. 2002. Old water mills—Britain's new source of energy?. *Proc. ICE Civ. Eng.* Vol. 150. No. 4:178–186.
Müller, G. & Kauppert, K. 2003. Die Wasserraäder als hydraulische Kraftmaschinen (The water wheels as hydraulic energy converters, in German), *Bautechnik.* Vol. 80. No. 3:181–189.
Nagel, F.N. & Goldammer G. 2001. Wasserwege als Gegenstand der Kulturlandschaftspflege (Waterways as part of the preservation of the cultural heritage, in German), in: Schenk, Fehn & Denecke. 1997. *Kulturlandschaftspflege.* Gebr. Borntraeger, Berlin & Stuttgart: 275–285.
Patt, H., Jürging, P. & Kraus W. 1998. *Naturnaher Wasserbau. Entwicklung und Gestaltung von Fliefigewässern* (Natural hydraulic engineering, development and design of water courses, in German). Springer-Verlag. Berlin.
Reynolds,T.S. 1983. *Stronger than a hundred men,* J.Hopkins University Press. Baltimore & London.
Schrenk, G. 2003. Wehre und Staue an kleinen und mittelgroßen Fliefigewässern (Weirs and barrages at small and medium rivers, in German), *Wasserwirtschaft.* No. 7–8: 71–79.

INTERNET REFERENCES

http://www.ifmw-ka.de/
http://www.spessartprojekt.de/

Stability of reinforced block ramp

S.Pagliara & P.Chiavaccini

Department of Civil Engineering, University of Pisa, Italy

River Flow 2004—Greco, Carravetta & Della Morte (eds.)

ABSTRACT: Block ramps are structures able to produce high dissipation energy, ensuring a stable stream bed and are usually used in naturalistic stream restoration projects as alternative method for grade control. A way to increase ramp stability consists in covering the base ramp blocks with boulders. In this work the results of tests performed in a flume located in the Hydraulic Laboratory of the Civil Engineering Department of the University of Pisa are presented. The ramp was founded on a geotextile where two or three layers of the base material were placed. The rocks were angular and crashed with an almost uniform granulometric curve. The stability tests were conducted evaluating the failure discharge as a function of base diameter, boulders concentration and their planimetric arrangment.

1 INTRODUCTION

Block ramps are structures able to produce high dissipation energy, ensuring a stable stream bed and are usually used in naturalistic stream restoration projects as alternative method for grade control because they succeed in putting together hydraulics and ecological exigencies. In fact, they modify the longitudinal profile of the river and, at the same time, guarantee correct biological exchanges between the downstream and upstream reaches. From the hydraulic point of view experimental researches (Pagliara et al., 2000, 2002) have pointed out that block ramps act as an excellent energy dissipator, giving place to strong energy losses. From the environmental point of view block ramps do not act as barriers, as the hydrodynamic conditions on the ramp can be generally compatible with the characteristics of dynamism of the stream fauna. The functionality of the ramp can be ensured only if the structure for the design discharge is stable that means that the shear stresses are not able to move the bed material. Some relations express the link among the diameter of the base rock, the unit discharge and the slope of the ramp to ensure the stability (Whittaker & Jaeggi, 1996, Robinson et al., 1998). Armanini & Scotton (1995) evaluated the stability in term of Shields parameter. The critical part for the ramp stability is the downstream one, in which the shear stresses are greater and the

ramp failure is generally sudden; in this part the movement of few elements brings to the total failure of the structure (Pagliara & Chiavaccini, 2003). The present study better investigates the hydraulic conditions which characterize the different failure types of the ramp and the effects on the stability of boulders placed over the ramp. The use of boulders gives different advantages: they can increase the energy dissipation caused by the ramp acting as macroroughness elements and can facilitate stream fishes passage across the ramp, as their presence create on the ramp an alternance of swifter and slower flow zones more favorable to the biologic exchanges (Pagliara & Pozzolini, 2003).

2 MATERIALS AND METHOD

The experimental flume was 0.5m wide by 9m long. Ramp height was 0.25m. The ramp was based on a geotextile where two or three layers of the base material were placed. A sill at the downstream end of the ramp prevented the skidding of the ramp ensuring a stable toe during tests. The rocks were angular and crashed with an almost uniform granulometric curve. The tests were conducted on ramps of different slopes ε (1:4,1:8 and 1:12) covered with rocks having medium diameter of 0.011, 0.022 and 0.032mm (Figure 1), where boulders in different concentration (up to 40%) were placed. Boulders projected from the base ramp for half diameter.

A schematic drawing describing the experimental apparatus is presented in Figure 2.

The concentration R of the boulders was measured by the following relation (Armanini & Scotton, 1995):

$$R = 100\frac{S_b}{S_{tot}} \tag{1}$$

where S_b is the surface of the boulders and S_{tot} is the total surface of the ramp. The diameter of the boulders

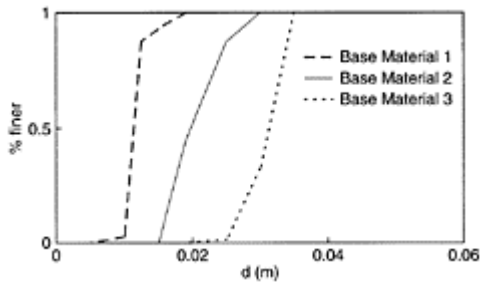

Figure 1. Granulometric curves of the base materials.

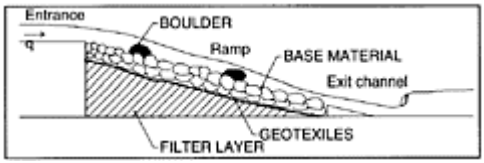

Figure 2. Definition sketch of the studied ramp.

were three times bigger than the base material. Boulders projected from the base material of about half diameter.

The tests were conducted increasing the flow until the reaching of the discharge that provokes the ramp instability. Flow rates were measured with an hydrometer placed upstream of the ramp.

3 FAILURE MECHANISMS

Tests pointed out that the failure of the ramp is characterized by 4 steps:

– the initial movement of the base material, in which the rocks begin to vibrate;
– the entrainment of some isolated elements.
– the local failure in which a group of elements leave their position simultaneously, producing a circular or semicircular scour hole; in some case (for the highest boulder concentrations) the initial movement can happen for the boulders instead of the base material;
– the global failure of the ramp (Figure 3) in which different local failures happens: the ramp presents longitudinal holes and the layers of the base material are completed removed, especially in the downstream part of the ramp.

In this paper the third step has been considered the significant step in order to define the ramp failure. This choice is due to the fact that the condition of local failure modifies the geometry of the ramp, its hydraulic

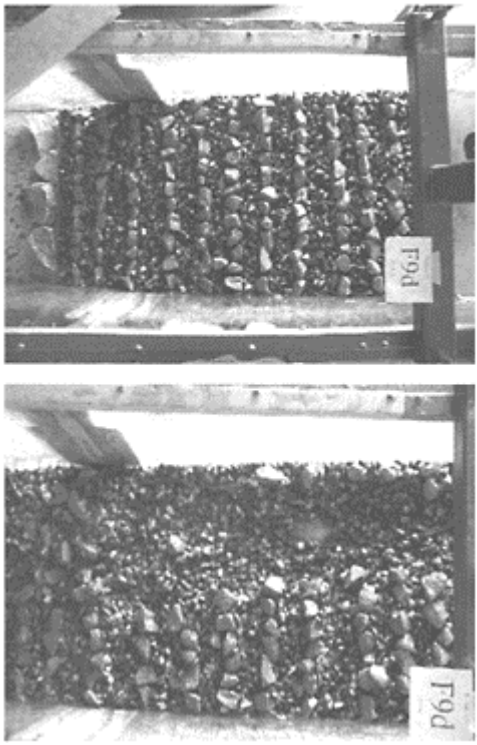

Figure 3. Ramp before and after global failure.

behavior and its functionality. For prototypes this situation means that is necessary to repair the structure itself with burden of costs.

In the base condition, without the use of stabilizing systems the local failure happens in the downstream part of the ramp.

In order to verify the validity of the experimental model, the values of failure discharge measured for the base condition were compared with the values calculated using the block ramp stability formula of Whittaker and Jaeggi (1996):

$$q = 0.257\sqrt{\frac{\rho_s - \rho_w}{\rho_w} g}\,\alpha^{-7/6} d_{65}^{3/2} \qquad (2)$$

where q is the unit critical discharge (m^2/s), ρ_s is rock density (N/m^3), ρ_w is water density (N/m^3), α is the slope of the ramp and d_{65} is the nominal diameter of the material for which 65% of the sample is finer by weight (m).

The results (Figure 4) point out that there is a good correspondence between calculated and measured values with differences generally minor than 20%.

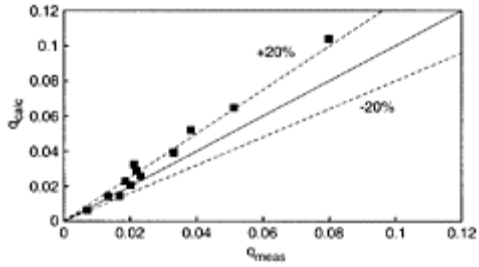

Figure 4. Calculated and measured failure discharge (q) in the base condition.

Figure 5. Boulders placed over the ramp (upstream view).

4 THE USE OF BOULDERS TO INCREASE STABILITY

Tests conducted on the base material have shown that the failure of the ramp is sudden and the weakest part of the ramp is the downstream half. To increase the stability of the ramp, the use of boulders disposed with different concentration has been investigated (Figure 5).

The stability tests were conducted evaluating the failure discharge as a function of boulders concentration and of their position. Boulders placed in rows, random and in arch forms were examined (Figure 6) in order to evaluate what is the best choice for the design of these structures. For each condition at least 3 failure tests (for a total of 108 tests) were performed, increasing incrementally the flow until the identified failure mechanism was reached.

The presence of the boulders improves the stability conditions. The effect depends not only on the concentration but also on the planimetric arrangment used.

In particular arc forms appear less stable than other forms (Figure 7 and Figure 8) because water flow is concentrated to the center of the flume, while there

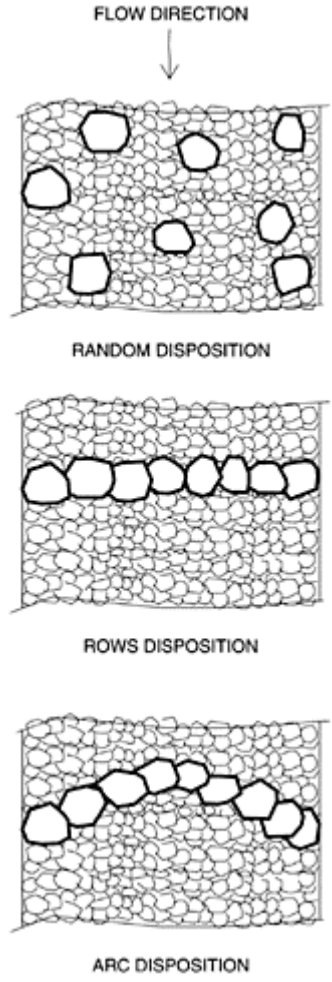

Figure 6. Disposition of the boulders (plan view).

are no evident differences between the random and the rows disposition (Figure 9 and Figure 10).

Besides in the arc form, the weakest part of the ramp are the boulders themselves, because the scour hole formed downstream provokes their instability. Rows and random disposition are different only for the way in which failure is reached. The rows of boulders create a series of little hydraulic jumps downstream each row where the initial movements verify, while for random disposition the flow is uniformly disturbed and the

initial movement happens randomly. In Figure 11 the effect of local failure for random arrangement is shown. As evident a little scour hole is formed and consequently boulders has moved downstream.

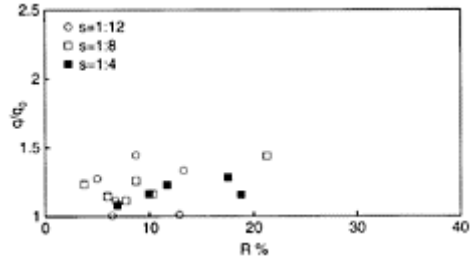

Figure 7. Increase of failure discharge with boulder placed in arc disposition.

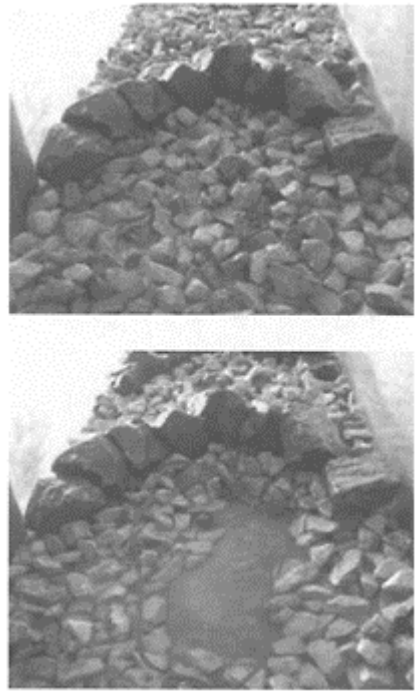

Figure 8. Local failure for boulders in arc arrangement.

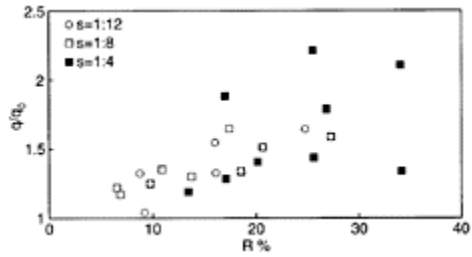

Figure 9. Increase of failure discharge with boulder placed in rows disposition.

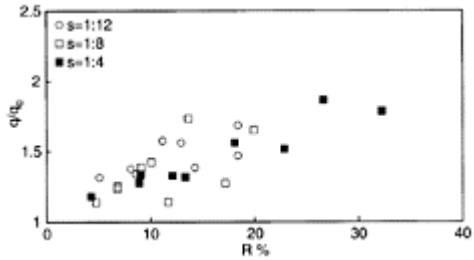

Figure 10. Increase of failure discharge with boulder placed in random disposition.

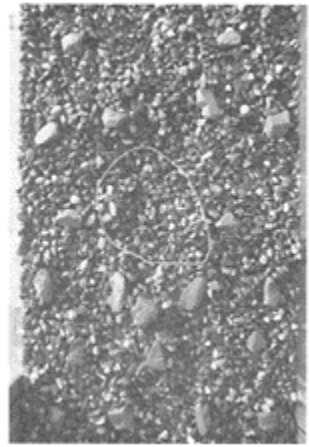

Figure 11. Local failure for boulders in random disposition.

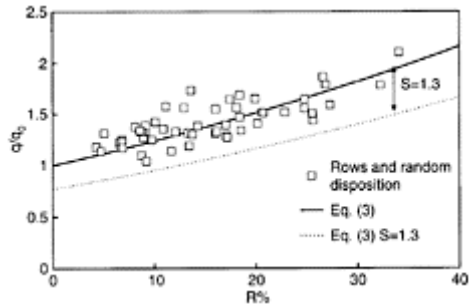

Figure 12. Increase of stability as a function of boulder concentration and fitting curve.

However, the effect of the disposition (rows or random), referring to the values of failure discharges, appears negligible in according with the results obtained for other kinds of stability system such as micropiles (Pagliara & Chiavaccini, 2003).

The increase of stability for random and rows disposition reach values up to 180–190% for concentration of 30–35%. Results show that the slope of the ramp and the dimension of the base material has a little influence on stability (Figure 12).

A new relationship for block ramp stability covered with boulders can be derived. This equation links the increase of stability (the ratio of failure discharge of the ramp with boulders q and the failure discharge of the ramp with only the base material q_0) to the boulders concentration, expressed by means of the parameter R.

The best fitting is obtained with the following equation:

$$\frac{q}{q_0} = (1 + aR)^{1/b} \tag{3}$$

where:

a=0.008

b=0.36

This curve presents a correlation coefficient r=0.76.

The parameters a and b are defined for a ratio of the boulder diameter and the diameter of the base material equal to 3. Therefore Eq. (3) cannot be used for other ratios.

A safety coefficient S=1.3 is recommended for practical uses.

When R=100% the ramp is all covered with boulders and its behavior is the same of a ramp where the base material is bigger. In this case stability can be determined using expression (2) in which d_{65} for the ramp all covered with boulders is expressed by d_{65B} while for the ramp in base condition it is expressed by d_{65f}. The test were conducted for d_{65B}=3d_{65f}, thus for R=100%

$$\frac{q}{q_0} = \frac{0.257\sqrt{\frac{\rho_s - \rho_w}{\rho_w} g\alpha^{-7/6} d_{65R}^{3/2}}}{0.257\sqrt{\frac{\rho_s - \rho_w}{\rho_w} g\alpha^{-7/6} d_{65f}^{3/2}}} = 5.11 \quad (4)$$

The Eq. (3) for a value of R=100% gives q/q_0=5.11

5 CONCLUSIONS

The present study analyses the mechanisms of failure of different block ramps. The effect on stability of boulders placed over the ramp is accounted. Failure of the ramp happens in four different steps: *initial movement, initial leaving, local failure and global failure.* Local failure can be considered as the effective instability condition, because ramp changes geometry and looses the original configuration. The disturbance on the flow provoked by the boulders tends to diminish the shear stresses acting on the base material, increasing its stability. This condition happens when boulders are placed in a manner that flow passing over them does not converge. In fact the boulders placed in an arc form don't guarantee an increasing of stability. This is because flow is concentrated downstream of the arc and the shear stresses can be greater than in the base configuration. Besides in this case the weakest part of the ramp are the boulders themselves, while for rows and random disposition the base material moves before boulders, except at higher boulder concentrations.

With the boulders the increase on stability reaches values up to 180–190% in respect to the base condition, and the relation (3) can be used to express analytically this amount.

ACKNOWLEDGEMENTS

The present research was founded by grant PRIN 2001 "Sistemazioni idrauliche non convenzionali a basso impatto ambientale" U.O.Università di Pisa. The authors are grateful to A. Chines for assistance with measurements and for the support in the realization of experimental apparatus.

REFERENCES

Armanini A. & Scotton P. 1995. Criteri di dimensionamento e di verifica delle stabilizzazioni di alveo e di sponda con massi sciolti e massi legati, *Quaderni del dipartimento di Ingegneria Civile ed Ambientale, Università di Trento,* IDR 1/1995.

Pagliara S. & Dazzini D. 2002. Hydraulic of block ramp for river restoration, In *2nd International Conference New Trends in Water and Environmental Engineering for Safety and Life: Eco-compatible Solutions for Aquatic Environments,* Capri, Italy.

Whittaker W. & Jaeggi M. 1996. Blockshwellen, *Mitteilungen der Versuchsanstalt fur Wasserbau, Hydrologie und Glaziologie,* Zurich.

Pagliara S. & Chiavaccini P. 2003. The use of piles to increase block ramp stability. In *XXX IAHR International Conference*, Thessaloniki, Greece, ISBN 960-243-597-6: 449–456.

Pagliara S. & Pozzolini S. 2003. The effects of large boulders on the hydraulic of unsubmerged block ramps. In *XXX IAHR International Conference*, Thessaloniki, Greece, ISBN 960-243-597-6:199–206.

Pagliara S. & Peruginelli A. 2000. Energy dissipation comparison among stepped channel, drop and ramp structures. In *Workshop on Hydraulics of Stepped Spillways, Zurigo*, Rotterdam, Balkema.

Robinson K.M., Rice C.E. & Kadavy K.C. 1998. Design of rock chutes, *Transactions of the ASAE*, Vol. 41(3): 621–626.

Three dimensional hydrodynamics of pool-riffle sequences for urban stream restoration

J.F.Rodríguez

School of Engineering, University of Newcastle, Australia
M.H.García, F.M.López & C.M.García

V.T.Chow Hydrosystems Laboratory, University of Illinois at Urbana-Champaign, USA

River Flow 2004—Greco, Carravetta & Della Morte (eds.)

ABSTRACT: A set of laboratory experiments was carried out to investigate the 3D flow structure of pools and riffles in constricted streams. The experiments included four different bed configurations: flat bed (FB), centered pool-riffles (CPR), alternate pool-riffles (APR) and alternate pool-riffles with vegetation (APRV). The CPR configuration was included since centered pools minimize the possibility of scour near the banks, and are thus particularly suitable for urban settings where bank erosion is unacceptable.

1 INTRODUCTION

The present research was motivated by a concrete problem: the restoration of a channelized, low-gradient, urban stream using in-channel structures of the poolriffle type (Rodríguez et al., 2000). In-channel solutions are preferred in restoration projects on urban settings due to the limitations in planform alignment imposed by the existing infrastructure. If carefully designed, pools and riffles can enhance the aquatic habitat and achieve the restoration goals. Designing artificial pools and riffles is not easy, since knowledge of their 3D hydrodynamic behavior is limited. Most of the analysis to date has been 1 or 2D, and mostly qualitative, despite the fact that 3D flow patterns are fundamental in the development and maintenance of pools and riffles. Past restoration practices have tried to reproduce features of natural pool-riffles based on observations, with limited success.

A set of laboratory experiments was carried out to investigate the 3D flow structure of pools and riffles. The experiments included four different bed configurations: flat bed (FB), centered pool-riffles (CPR), alternate pool-riffles (APR) and alternate pool-riffles with vegetation (APRV). The CPR configuration was included since centered pools minimize the possibility of scour near the banks, and are thus particularly suitable for

cases in which bank erosion is unacceptable. The sequence FB-CPR-APR-APRV not only represents an incr ease in hydrodynamic complexity; it can also be seen as different steps in the restoration process of a degraded stream. The FB series represents the behavior of the channelized stream with no geomorphological diversity, the CPR experiment describes a naturalization alternative with man-made in channel structures, the APR set gives insight into the hydrodynamics of in channel structures that are more likely to be found in a natural stream, and finally the APRV configuration includes the effect of vegetation. Each series included low (run 1) and high (run 2) flow conditions.

2 METHODS

3D velocity measurements were collected using an Acoustic Doppler Velocimeter in a laboratory flume (0.0025 slope) where the four bed configurations were successively set up (Figures 1 and 2). The flume was 12.5m long, 0.9m wide and 0.6m high, with 1-cm diameter crushed stone on the bed to provide a fixed, hydraulically rough surface. The simulated vegetation of the VAPR test was flexible (plastic aquarium plants) and was placed in a hypothetical seasonal flooding zone (Figure 2). The data was collected at five

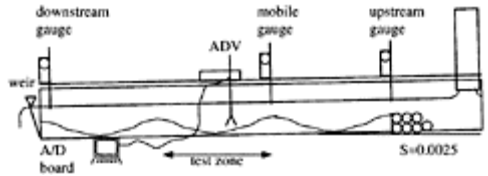

Figure 1. Experimental setup.

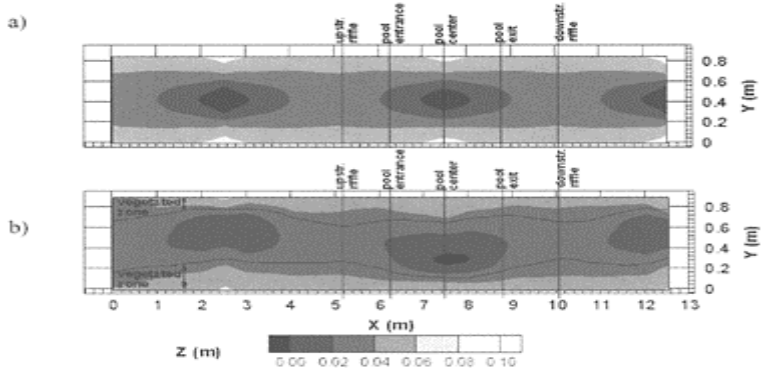

Figure 2. Bed topography and measurement sections for pool-riffle experiments: a) CPR and b) APR and APRV

Table 1. Summary of experimental conditions. Q, h, U, U_*, Re and Fr respectively denote reach-averaged values of discharge, hydraulic depth, velocity, shear velocity, Reynolds number and Froude number.

Run	Q (m^3/s)	h (m)	U (m/s)	U_* (m/s)	$Re \times 10^{-3}$	Fr
FB1	0.05	0.11	0.48	0.047	44	0.45
FB2	0.10	0.15	0.72	0.053	82	0.60
CPR1	0.03	0.09	0.37	0.045	30	0.38
CPR2	0.11	0.19	0.64	0.068	90	0.47
APR1	0.05	0.09	0.66	0.044	53	0.64
APR2	0.11	0.15	0.80	0.055	97	0.71
APRV1	0.05	0.16	0.35	0.055	55	0.28
APRV2	0.11	0.25	0.49	0.064	121	0.31

cross sections: upstream and downstream riffles and pool entrance, center and exit. At each cross section, measurements were spaced 5cm and 1cm in the transverse and vertical directions, respectively. Wall shear stresses were computed using a bed-normal law of the wall. Experimental conditions are shown in Table 1.

3 RESULTS

3.1 *Low flow*

The FB1 test (Figure 3) shows three cores of high streamwise velocity that are evenly spaced. These high velocity zones are about 10% faster than the surrounding flow and are associated with regions of downwelling and high wall shear stress. Secondary circulation is characterized by the presence of six circular cells. All these features are typical of secondary currents produced by turbulence anisotropy at the flow boundaries (Nezu and Nakagawa, 1993).

In the CPR1 experiment, convergence and divergence patterns affect the streamwise as well as the transverse velocity distributions. The streamwise velocity presents two cores of high velocity at the riffles (Figure 4) as a result of transverse flow divergence. Transverse flow convergence consolidates the cores towards the center of the channel at the pool center. The high velocity cores are associated with flow downwelling, and the resulting recirculation pattern is surface divergent on the riffles and surface convergent on the pools, as usually observed in natural pool-riffle sequences.

The wall shear stress distribution shows a concentration towards the centerline of the pool center with a maximum at the pool entrance.

The APR1 test (Figure 5) shows the effect of thalweg curvature generating centrifugal forces. Transverse velocity components are now clearly superimposed to convergence at the pool entrance. This effect is felt only moderately by the streamwise velocity, which has two high velocity cores that remain throughout the pool. The cores are associated with four major cells. At the riffle centerline the cells are surface divergent and at the deepest part of the pool they are surface convergent, as occurs in natural pool-riffle sequences. Shear stresses are higher at the pool entrance. At the pool center cross section shear stresses are higher in the shallower side.

The effect of vegetation in slowing down the flow and raising water levels is observed in the APRV1 test (Figure 6). The streamwise velocity is always concentrated on the vegetation-free central zone, with little

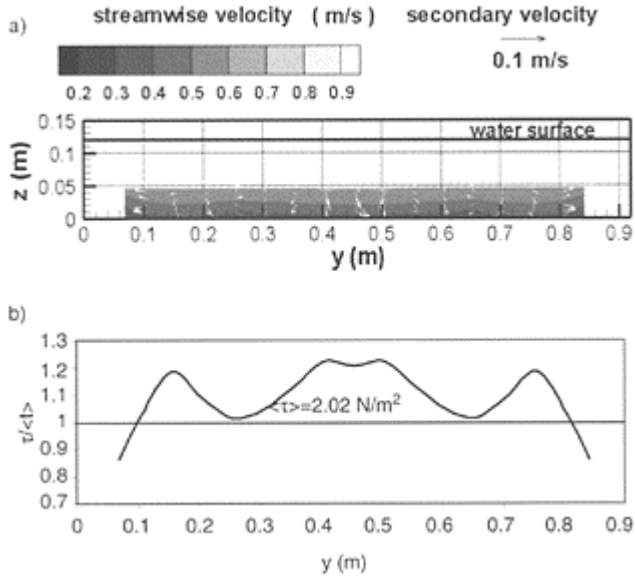

Figure 3. FB1 test: a) velocities, b) dimensionless wall shear stresses.

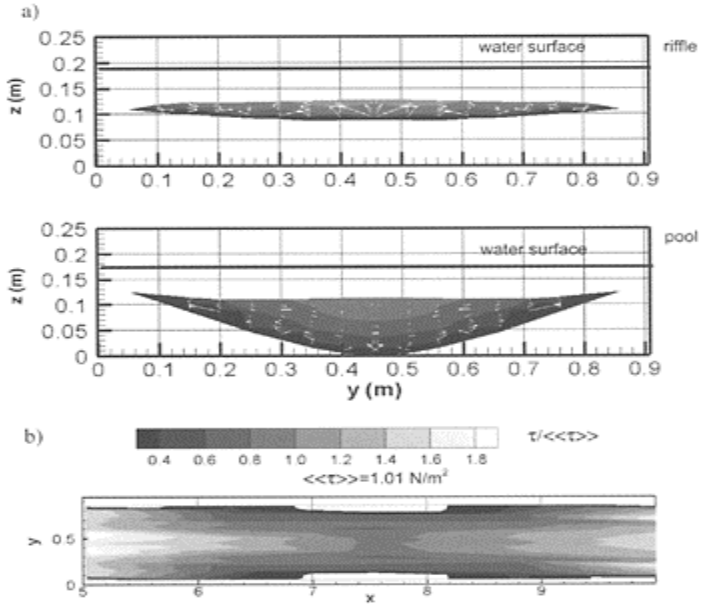

Figure 4. APR1 test: a) velocities (color as as in 3a), b) dimensionless wall shear stresses.

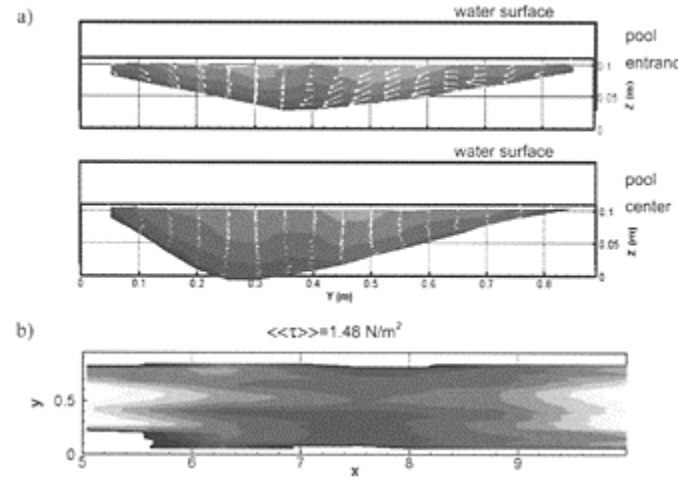

Figure 5. APR1 test: a) velocities (color as as in 3a), b) dimensionless wall shear stresses (color as in 4b).

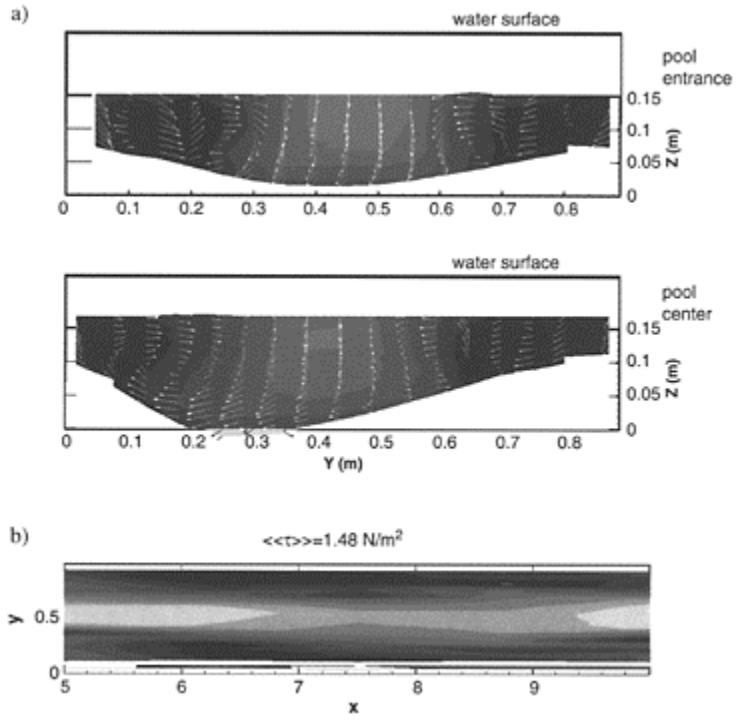

Figure 6. APRV1 test: a) velocities (color as in 3a), b) dimensionless wall shear stresses (color as in 4b).

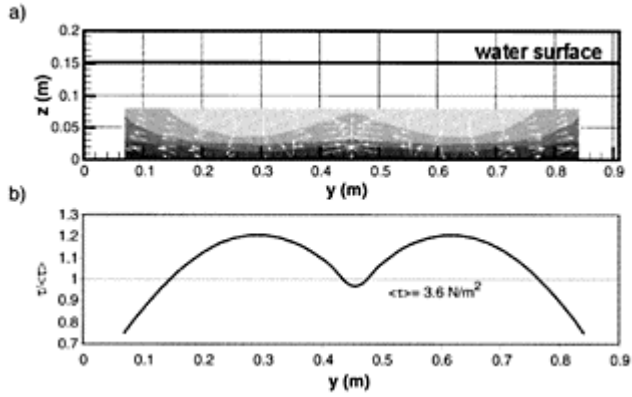

Figure 7. FB2 test: a) velocities (color as in 3a), b) dimensionless wall shear stresses.

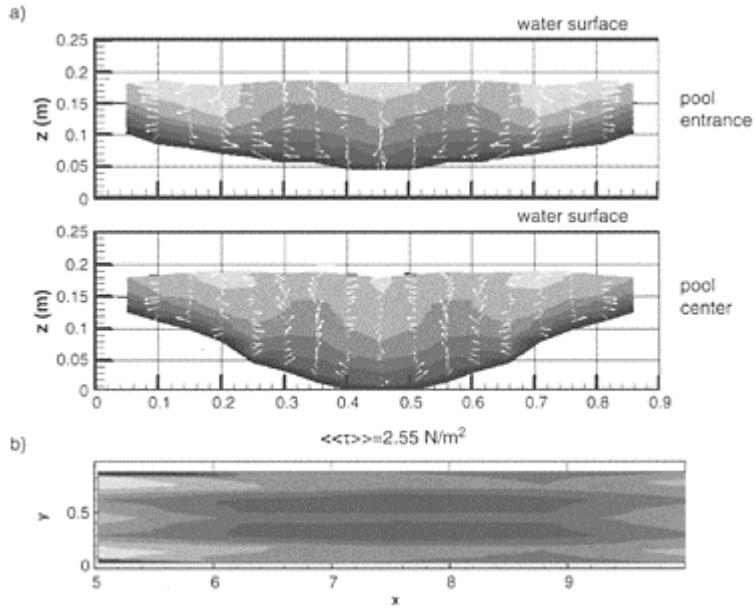

Figure 8. CPR2 test: a) velocities (color as in 3a), b) dimensionless wall shear stresses (color as in 4b).

effect of thalweg curvature. Two central circulation cells are defined by downwelling on the centerline (associated with the high-velocity core) and upwelling at the borders of the vegetation zone. Shear stresses are concentrated along the centerline.

3.2 *High flow*

The FB2 test (Figure 7) shows a structure similar to that of FB1, but with two cores of high velocity only. This is because the secondary circulation cells scale with flow depth, and only four cells can fit in the whole channel width. Wall shear stresses are greater under the high velocity cores. As with the FB1 test, the pattern is characteristic of secondary circulation due to turbulence anisotropy at the flow boundaries.

The similarity between the CPR2 (Figure 8) and the APR2 (Figure 9) tests is remarkable. Velocities are slightly higher in the APR2 experiment, which also has a shallower depth. Three high velocity cores are present throughout the structure, corresponding to six cells. The agreement with the wall shear stress is also very

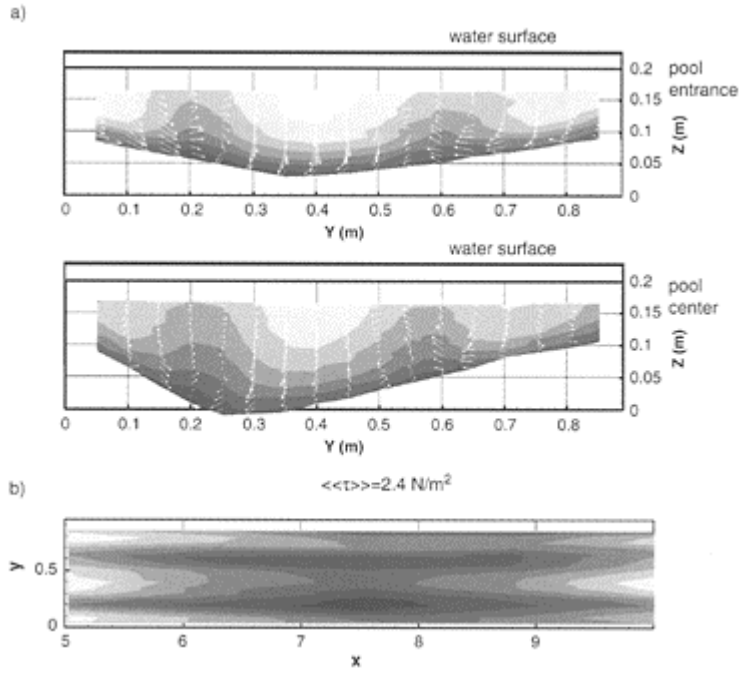

Figure 9. APR2 test: a) velocities (color as in 3a), b) dimensionless wall shear stresses (color as in 4b).

good. The cells scale approximately with the depth of the riffles and stretch down to occupy the whole cross section at the pool. Besides this stretching, the shape of the geometry does not seem to affect the secondary circulation patterns. Compared to the FB2 test, the CPR2 and APR2 tests present two more circulation cells. This difference is due to the fact that cells scale with the flow depth at the riffles, which are considerably shallower than the depth of the FB2 test. In fact, the flow patterns of the pool-riffle experiments correspond better with the FB1 test, which has a depth of the order of the riffle depth.

The APRV2 experiment (Figure 10) has a different pattern, which is similar to the APRV1 test. The vegetation directs the flow towards the center, with only one velocity core and two well defined cells. However, there is some indication of the presence of two incipient high velocity cores at the sides. Wall shear stresses are concentrated on the centerline, with a slight increase towards the shallower side of the pool.

4 ANALYSIS AND DISCUSSION

4.1 *Topographic effects*

The previous section has shown important differences between the high and low flow behavior of the pool-riffle configurations without vegetation (series CPR and APR). For low flow, the geometry of the bed plays an important role in determining the three dimensional hydrodynamics. This is more obvious in the CPR1 case than in the APR1 case, probably due to differences in discharge. The CPR1 case has the lower discharge, and geometric effects are expected to be more effective under this condition.

The bed geometry produces lateral divergence and acceleration on the riffles and lateral convergence and deceleration on the pool. In the APR1 case it also produces lateral shoaling at the pool entrance and exit. The combination of lateral divergence and acceleration generates the splitting of the maximum velocities into two cores at the riffles. These cores induce an undulating pattern on the bed shear stresses, which results in secondary circulation.

As the flow enters the pool, lateral convergence displaces the velocity cores towards the deepest part of the pool, generating a different secondary flow pattern (this effect is less evident in the APR1 case). The velocity cores are associated with surface convergent secondary circulation and downwelling, so they produce surface convergence/near bed divergence in the pool deepest part and surface divergence/near bed convergence at the riffle centerline. The pattern described is in total agreement with the ideas of Thompson (1986) based on field observations and is related to Prandtl's first kind secondary currents.

The high flow situation shows no apparent effects of the pool-riffle geometry. The flow behaves essentially like in a uniform flow situation, with turbulence anisotropy in the bed and channel walls generating secondary circulation and associated high-velocity cores. The walls are important in constricting the flow, producing a narrow channel effect. The riffle controls the secondary circulation patterns and the position of the high velocity cores, since the cells scale with the riffle depth. At the pool, the cells stretch vertically to cover the whole cross section. Downwelling or upwelling can occur in the pool and riffle centerlines depending on the width/depth relation. The description resembles a uniform flow situation and is associated with secondary currents of Prandtl's second kind (Nezu and Nakagawa, 1993).

The difference in low and high flow behavior is reflected in the relative magnitudes of the shear velocities at the pool and at the riffle. The high flow situation (CPR2 and APR2) is more uniform, and so the difference between the riffle and the pool shear velocities is smaller than in the low flow case (CPR1 and APR1).

This is evident from Figure 11, in which $<U_{*r}>$ and $<U_{*p}>$ are the riffle and pool cross sectional shear velocities, respectively. The convergence with discharge shown by the figure is often observed in natural pool-riffle sequences and has important implications for the self-maintenance of the structures. According to the figures, the CPR case has a higher convergence rate than the APR configuration.

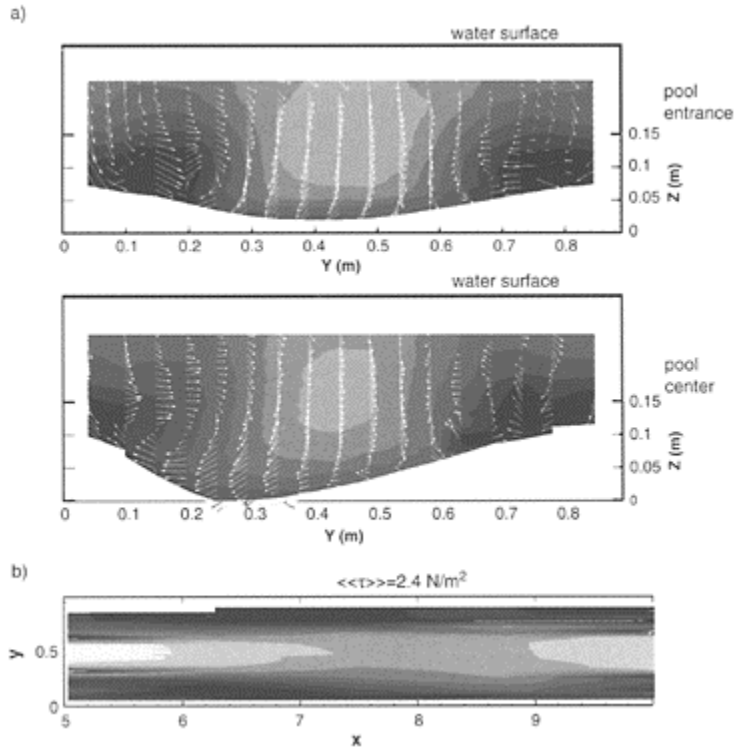

Figure 10.

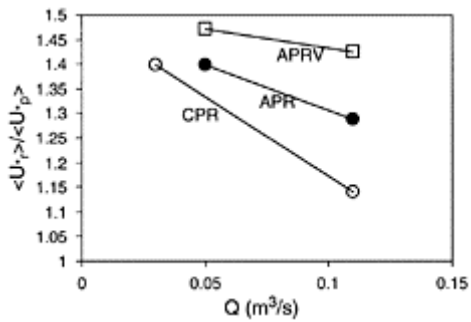

Figure 11. Ratio of riffle to pool wall shear stresses.

Consequences of this difference in behavior for high and low flow conditions may have other implications for the design and maintenance of pools and riffles in urban streams. The constriction of the walls starts playing an important role when the flow

depth raises to more than 1/5 the width, which is not uncommon. Under this condition, higher shear stress zones are located approximately at 1, 3, and 5 times the depth from the walls and may or may not coincide with the position of an artificially placed pool. If the bankfull discharge is regarded as the one responsible for the pool maintenance, the placement of the pool can be done in order to match one of the high shear stress zones for bankfull flow.

4.2 *Vegetation effects*

Vegetation inhibits to some extent the topographic effects. Increased roughness raises the water levels and slows down the flow velocities. The plant zones force the flow towards the centerline both for low (APRV1) and high (APRV2) flow, generating only one high velocity core. Two strong circulation cells are located in the central zone but secondary flow patterns over the plants are less defined. For the APRV2 case, two incipient high velocity cores at the channel sides suggest that the effect of the plants may decreases for higher flow.

The similitude between the APRV1 and APRV2 experiments can be seen in Figure 11. The figure shows that the ratio $<U_{*r}>/<U_{*p}>$ changes considerably less than in the CPR and APR cases.

5 SUMMARY AND CONCLUSIONS

Detailed 3D velocity measurements on a laboratory model have provided important information regarding the effects of topography and vegetation on the flow dynamics of pool-riffle sequences in constricted waterways. After analyzing flat bed (FB), centered pool-riffles (CPR), alternate pool-riffles (APR) and vegetated alternate pool-riffles (VAPR) bed configurations, the following conclusions can be drawn:

- The pool-riffle configurations without vegetation showed low flow patterns qualitatively different than high flow patterns. Low flow characteristics were affected by the bottom geometry while high flow patterns were independent of the shape of the bed.
- The configuration with vegetation showed similar low and high flow patterns, obviously dominated by the vegetation distribution.
- All configurations tested showed a convergence of the pool and riffle shear stresses towards a common value, as observed in natural pool-riffle sequences.
- The location of high velocity cores (and thus high shear stresses) tends to be independent of the bed geometry as the flow increases. This position may not coincide with the position of an artificially placed pool and may not promote self maintenance.
- Vegetation can be used to direct the flow, diverting it from the banks and concentrating it on the central part of the channel.

ACKNOWLEDGEMENTS

Partial financial support came from the project “Development of an Integrated Scientific and Technological Framework for Stream Naturalization,” Grant 98–NCERQA-M1, U.S. EPA.

REFERENCES

Nezu, I. and Nakagawa, H. (1993). Turbulence in open-channel flow. IAHR Monogr.

Rodríguez, J.F., García, M.H., Bombardelli, F.A., Guzmán, J.M., Rhoads, B.L. and Herricks, E. (2000). “Naturalization of urban streams using in-channel structures.” Proc. Joint Conf. on Water Res. Engrng and Water Res. Plan. and Man., ASCE, Minneapolis, MN.

Thompson, A. (1986). “Secondary flows and the pool-riffle unit: a case study of the process of meander development”. Earth Surf. Process. Landforms, 11, 631–641.

Morphological rehabilitation and flood protection by controlled river dynamics—a physical model

U.Stephan & M.Hengl

Institute for Hydraulic Engineering and Calibration of Hydrometrical Current-Meters, Vienna, Austria

River Flow 2004—Greco, Carravetta & Della Morte (eds.)

ABSTRACT: According to the results of a physical model it is shown, how to change the state of a gravel bed river from erosion to a morphological dynamic river system connecting again river and wetlands. The basic idea is to raise the bed level with help of a ramp and to initiate a self-acting bank erosion process increasing the river width. In addition, the currently straight river morphology is converted into a meandering one. The physical model provided valuable experiences regarding self-acting bank erosion and meander development. These measures might be used for river restoration, but must be analyzed in each specific case regarding their suitability for improving a river-wetland-system.

1 INTRODUCTION

Many rivers in Central Europe such as the Salzach, Isar, Inn, Danube or Drau, show a heavy degradation process which has evolved from various human activities in the past such as straightening and constricting the river or bed load entrapment in the catchment. As a typical consequence the river system adjusts in a long-term geomorphologic manner to these human influences with various awkward effects. Bed erosion of many rivers has progressed to such an extent that bank structures as well as bridge piers have become endangered. The groundwater table has decreased remarkably. The river wetlands have been cut off from the river itself, which is closely connected to a loss of habitats and of population diversity in the wetland ecosystems. In addition, the flood run-off occurs chiefly on the main channel. Thus, wetlands are flooded less and tributaries are detached

from the main river. Loss of retention areas deteriorates the downstream flood protection as well as the wetland ecosystems.

Even more unfavorable, if not dangerous, is a phenomenon called *"Sohldurchschlag"* or sudden river-bed break-down, which could be observed in many alpine rivers such as the Inn or the Salzach, e.g. Hengl (2000), WRS (2000). The term describes a change in the erosion process due to the presence of fine sediment layers below the gravel bed of a river. If the mean river bed intersects the gravel bed because of the progressive erosion process and reaches these fine sediment layers below the gravel bed, the geomorphologic consequences can no longer be predicted. The erosion process is increased tremendously because of the greatly increased erosion potential of these fine materials. The extent of damage from the above mentioned effects, i.e. endangering of buildings near the river bank and in the river, decreasing groundwater table, destruction of bank protection works, among others, is intensified.

Therefore, the river restoration planning stage of the river Salzach downstream of Salzburg is presented as an example of how to change a state of a river from erosion to a morphological dynamic river system connecting again river, tributaries and wetlands. The main goals of the river restoration measures are to sustainably stabilize the river bed regarding bed load input from the catchment, to guarantee flood risk protection, to raise the river bed, to provide a dynamic river morphology and, finally, to connect again river and wetlands.

2 BASIC CONCEPT

Within the Water management frame study Salzach, a concept for a solution was developed meeting morphological, hydraulic as well as ecological demands (WRS 2001a)

The main idea is to raise the bed level with help of a ramp. The ramp axis is directed towards the river bank and, thus, initiates self-acting bank erosion which, finally, leads to a dynamically curved river morphology. This construction combines a few important solutions: On the one hand, the river bed is raised while bed load transport fills the deposition wedge upstream

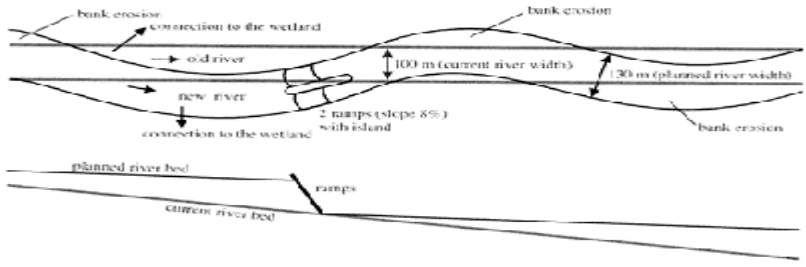

Figure 1. Principles of the solution concept for raising the river bed and

improving the morphological state of the river

of the ramp. Hence, the mean water level is also raised as well as the groundwater table. The former leads to a more frequently flooding of the wetland system and, thus, to an improved connection between river and wet- land. In addition, the river width is increased due to the self-acting bank erosion process. This, first, compensates the raised water level due to the raised river bed in case of a floods and, secondly, causes an improved mor- phological as well as ecological diversity of the river bed. During the filling process of the deposition wedge upstream of the ramp, the bank erosion temporarily enables continuous bed load transport downstream of the ramp and, thus, prevents further bed erosion. On the other hand, raising the river bed reduces the risk of *"Sohldurchschlag"* due to a thicker gravel layer covering the fine sediments layers below the gravel bed. The principles of the concept are shown in Figure 1.

For each measure, which is brought to be a solution for a problem, it has to be considered that the guidelines for the future morphological situation of the river-wetland-system are reasonable and realistic (Stephan et al. 2003). On the other hand, the selection of suitable solutions must be based on both past and the current morphological situation of a river. On the other hand, any contemplated measures must take natural morphological processes into account. Thus, natural Bed load input, river geometry as well as discharge of the current river must be suitable for a meandor morphology in the future.

To analyse the current morphological situation of a river, the approach developed by da Silva (Yalin & da Silva 20001) may be used (Fig. 2). This method suggests that the morphology (macro bed forms) of a river depends on the factors: the ratio of bed width to flow depth (B/h) and the ratio of flow depth to mean grain size (h/d_m). When the bed width changes, flow depth changes also, as do the ratios B/h and h/d_m. Figure with B as the river width, h the flow deapth, J the slope and d_m as the mean grain size of the mat shows that the current possible morphological situation of the river ranges between alternate bars meanders for the whole extent of dischargess, that is discharge for beginning sediment transport up to design discharge with a return period of 100 years. to the recommended river width of B=130m, a damental morphological change of the river is not to expected. For the proposed solution, the morpho will not change essentially. But the planned meas would be doomed to fail, if these geomorphol boundary condition were not considered.

3 DESCRIPTION OF THE MODEL

The main components of the plannet river training works were tested in a physical model scaled 1:50. The physical model mainly focused on

– a proper ramp geometry to initiate the self-acting bank erosion process and to ensure a proper hydraulic the function for energy dissipation and scour protection;
– needed measures to control the erosion process;

– analyses of time variability of the sediment input downstream of the ramp due to the bank erosion process;
– analyses on the development of the meanders in longitudinal direction and the needed bank protection measures;
– bed load transport capacity of a meandering river reach in equilibrium.

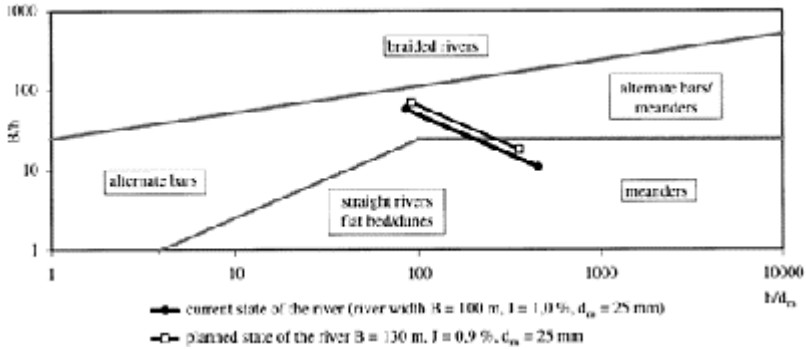

Figure 2. Macro bed forms of the river Salzach—current and planned state of the river (adapted from Yalin & da Silva 2001).

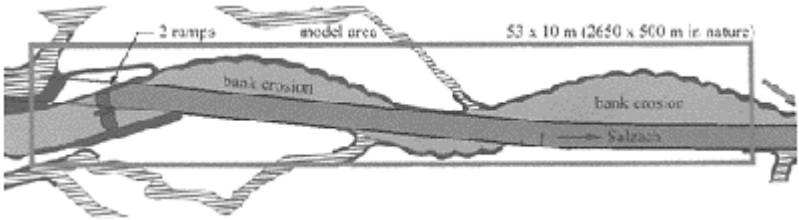

Figure 3. Plan view of the physical model.

A numerical sediment transport model simulating the long term bed level changes of the whole, 60km long river reach was based on the latter. The design discharge with a return period of 100 years amounts to some 3100m^3/s. An important part of the concept is the contribution of wetland areas and tributaries as flood retention areas to the flood run-off. Thus, only 2000m^3/s of the design discharge remain in the main channel, 1100m^3/s flow in the wetland areas as it resulted from a 2d-flow model. Therefore, the model area was limited to the river itself and the river-adjacent areas and the flood run-off in the wetlands was neglected.

Due to limited space, the physical model was 53m long and 10m wide reproducing 1.5 meander wave lengths downstream of the ramp. Figure 3 shows the model section including both the final state of the river and the straight river how it appears today.

Meander wave length and width were planned to 1500m and 130m, respectively. Thus, the meander angle resulted in 18.6° and the meander amplitude for the inner and outer curve in 80m. To limit the self-acting bank erosion in advance, a bank protection was built according to this meander geometry.

The ramp building consisted of two parallel ramps sloped 1:12 separated by an island. Each of the ramps was 60m wide. Ramp curvature and ramp size were defined according to Platzer (2000). Due to fine sediment layers below the gravel bed of the river, the need for an extensive scour protection right behind the ramps arose.

The initial state of the model shows a 100m wide straight river with a trapezoidal cross section, two parallel ramps and a control groyne to initiate the bank erosion process (Fig. 4). The downstream boundary condition for the physical model regarding the stage-discharge-relationship resulted from the 2d-flow model.

The sand used in the physical model was quartz sand with a mean grain size of d_m=33.4mm, calculated according to Meyer-Peter & Mueller (1948). 18 sample at different locations of the model were analyzed regarding the sieve curve. The results are shown in Figure 5a. The remarkable scattering of the samples

Figure 4. Initial state of the physical model.

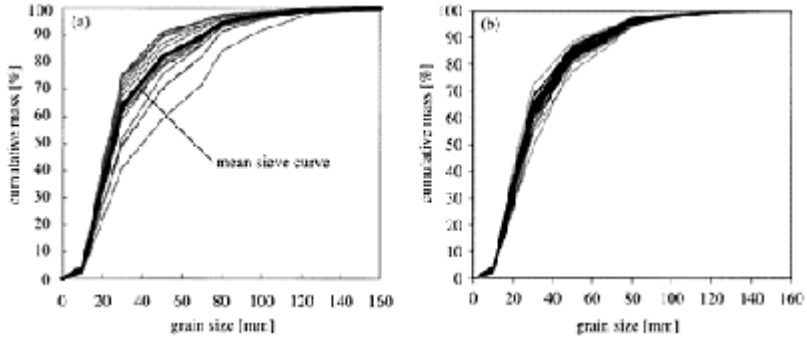

Figure 5. Sieve curves of the model sand (a) and the bed load input (b) (nature size).

might be explained by the method of how the sand was brought into the model area, since the sand was blown into the model. Figure 5b shows the sieve curves of the sand used for bed load input being almost the same as the bed material.

The bed load was added continuously using a conveyer belt (Fig. 6), but was not distributed equally over the river width, since the ramps were situated in a curve. The input ratio between left and right part of the river width was 3:2. The input rates were calculated according to Jäggi (1992) for a 130m wide river with a bed slope of 0.9%.

The measurement program comprised measurements of water and bed levels as well as bed load measurements. The former were conducted within 54 cross sections covering a channel reach of 2.35km in nature using ultrasonic probes. The bed load was collected in a sedimentation trap mounted on four pressure gauges at the model outlet and weighed continuously considering buoyancy effects.

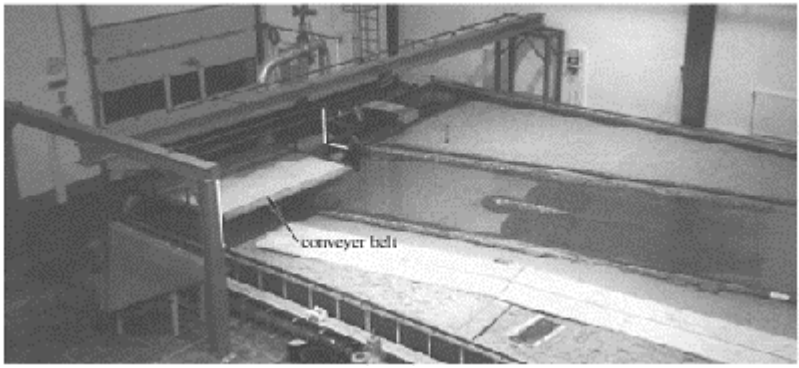

Figure 6. Conveyer belt for bed load input upstream of the ramps.

The experimental program was divided into two main parts: The first part contained the self-acting bank erosion and development of the meanders without bed load input at the model inlet simulating the situation after putting up the ramps. This part took 700 hours. During the second part, the longitudinal changes of the river bed depending on bed load input into the river reach as well as the bed load transport capacity of a curved river morphology were investigated. The total experimental duration amounted to 3608 hours. A detailed description of the physical model is given in WRS (2001b).

4 RESULTS

4.1 *Changes of the ramp building and scour protection*

The right part of the double ramp had to be turned to the left by 8° to improve the flow downstream of the ramp for better initiating the self-acting bank erosion. In addition, the height of the ramp head was reduced by 30cm.

The hollow shaped scour protection right behind the ramp was 1.1m deep and 1.5 times the length of the ramp. The hollow itself was lined with two rip-rap layers. Following the hollow, a river reach of, again, 1.5 times the ramp length was covered with stones sized 300 to 500kg with a stone density of one stone per $2m^2$. Despite of the solid scour protection, scour depths up to 5m are to be expected.

4.2 *Bank protection and controlling of flow*

The morphological development of the river reach downstream of the ramp is mainly influenced by groynes. Depending on the extent of bank erosion of the outer bank the length of the flow directing control groynes at the inner bank is increased to regulate the bank erosion process. Thus, the formerly straight river develops into a meandering one. Figure 7 shows the final state of the first meander curve behind the ramp building.

At the inner bank of the meander, generally no bank protection measures are needed. From the ford to the vertex of the meander curve, the groyne distance at the outer bank was 100m and the length of the groynes was 25m. From the meander vertex to the following ford, the flow direction must be turned. Thus, the flow attack at the outer bank was increased and the groyne distance reduced to 75m as well as the groyne length increased to 30m. The groyne heads should be protected separately due to occurring deep local scours. The groynes at the outer bank of the meander stabilize the curved morphology of the river and prevent further bank erosion as well as a fundamental shift of the main channel. Consequently, there is no need to set up the groynes at the outer bank unless the maximum extent of bank erosion is reached.

4.3 *Morphological development (bank shift, volume of bank erosion, depth variation)*

The development of the curved river morphology in the physical model resulted from experimental runs with varying discharges. The return period of the discharges ranged from 1 to 100 years with intermediate low discharge phases and, consequently, little

sediment transport. 700 experimental hours, which correspond to 19 years in nature, almost finished the meander development and bank erosion process. The meander geometry, derived from the Farguesch laws

Figure 7. Control groynes at the inner bank to direct the flow to the outer bank and bank protection of the outer bank (final state of the measures).

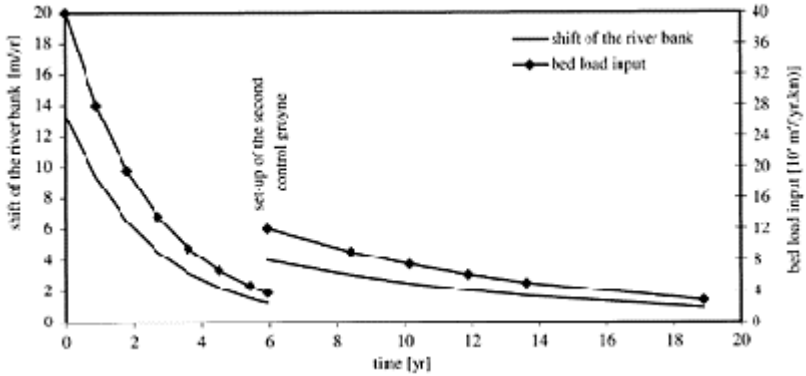

Figure 8. Mean shift of the river bank and volume of bank erosion in a meander assuming a 3m gravel layer height in the river-adjacent areas.

(Schaffernak 1950), emerged to be too small regarding both the meander wave length and the meander amplitude and had to be increased by 10% and reduced by 20%, respectively. The groynes in the outer bank may be used for adapting the meander geometry.

Bank shift due to the bank erosion process mainly depends on the flow shear forces acting on the banks as well as on the bank material. In the physical model, the same material was used for both the river bed and the river banks. The shift velocity (Fig. 8) was calculated

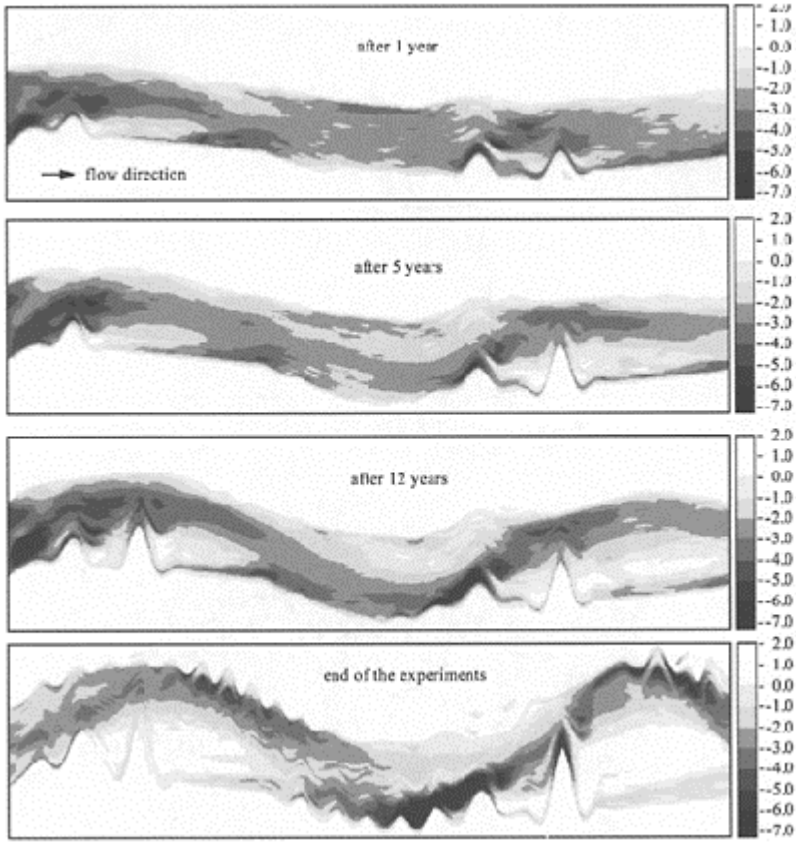

Figure 9. Flow depths [m] for a discharge of Q=500m^3/s.

assuming the height of the gravel layer in the river-adjacent areas being not larger than 3m considering fine sand deposition in the wetlands. The bank shift caused an increase of the river width from formerly 100m to 130m.

Figure 8 also shows the volume of bank erosion resulting from the bank shift. Putting up a ramp leads to a temporary deficit in bed load transport downstream of the ramp due

to the filling of the deposition wedge upstream of the ramp. Unless the bed load material from the catchment passes the ramp, the self-acting bank erosion process needs to balance the downstream bed load deficit. Therefore, it is important to know grain size, type and layer height of the material of the river-adjacent areas, since the bed load input downstream of the ramp mainly depends on the geological characteristics of the river banks. To meet this demand in the frame study of the Salzach, extensive soil investigations in the river-adjacent areas were performed.

During the experiments as mentioned above, the bed levels were measured regularly within 54 cross sections. Analyses on meander development and bed level variations were based on these measurements. In particular, the latter are an important morphological pattern, since the ecological diversity is strongly enhanced by a morphological diversity of the river bed. Figure 9 shows the meander development with groynes being at the outer banks in four steps from the beginning until the end of the experiments. The dark areas mark the flow concentration at the outer banks. With progressive meander development, bed level variations and, hence, the morphologic diversity is increased.

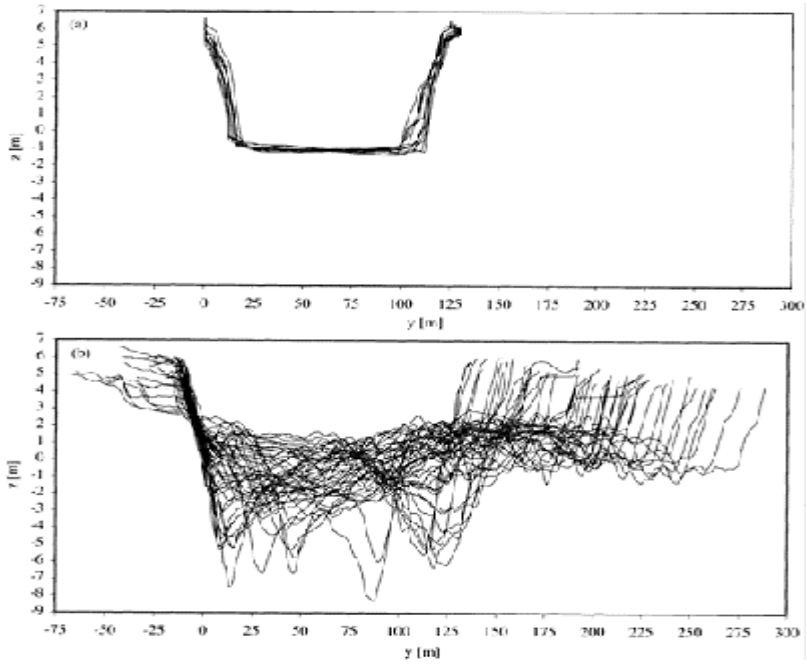

Figure 10. Bed level variations of a river reach of 2.2km for the current (2001) (a) and the planned (physical model) (b) state of the river Salzach.

In addition, Figures 10a and b show various cross sections of a 2.2km long river reach of the Salzach comparing the current and the future state of the river. The current state of the river (a) with a straight river morphology in a 100m wide channel bed does not show any bed level variations for the river reach at all. An ecological diversity is not supported by this obvious monotonous situation. Unlike the current state, the planned meandering state (b) exhibits a wide variety of different channel widths as well as different channel depths caused by longitudinal changes of bends and fords. Both, shallow, low flowing cross sectional parts and deep parts with high flow velocities occur in this channel reach. Depending on discharge and bed load transport, the local morphological pattern of the river changes with space and time.

4.4 *Bed load transport capacity*

The final series of experimental runs focused on investigating the bed load transport capacity of a meandering river reach, which was expected to differ from a straight one. To calculate the bed load transport capacity, the channel reach has to be in equilibrium,

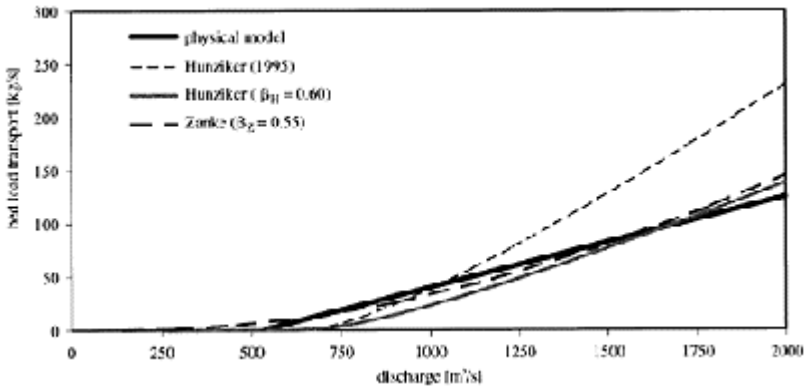

Figure 11. Transport equation of the physical model compared to transport equations of Hunziker (1995) and Zanke (1999).

i.e. the quantity of bed load input and output is to be the same within a certain period. The difference between input and output should not exceed 2%.

The results of the physical model were compared to the transport equation of Hunziker (1995), which also was used in the numerical sediment transport model, as well as of Zanke (1999) (Figure 11). Both transport equations were derived for a straight channel. To achieve the same bed load transport for both the physical model and the theory, the calculated bed load transport had to be reduced by a constant β. The slightly different values of β result from different methods of analysis of Hunziker (1995) and Zanke (1999).

However, the transport capacity of a meandering channel turned out to be less than the transport capacity of the straight one with the same channel width. This might be explained by the increased sinuosity of the meandering channel causing longer flow paths for the bed load, a reduced channel slope and, hence, a reduced shear force at the channel bed.

5 CONCLUSIONS

According to the results of the physical model, the planned river restoration measures turned out to be suitable for sustainably stabilizing the degrading river bed and, thus, ameliorating both the morphological and the ecological state of the river-wetland—system. The river can adjust to changing boundary conditions such as discharge and modify its bed. The ramps stand up to the design discharge and raise the river bed in front of the ramps to better connect river and wetlands. In addition, raising the river bed reduces the risk of *"Sohldurchschlag"* due to a thicker gravel layer covering the fine sediment layers below the gravel bed. Due to energy dissipation on the ramp, the downstream river reach is strained less. The self-acting bank erosion is initiated and directed mainly by control groynes. It leads to an increased river width and, thus, to a reduced bed load transport capacity as well as water levels in case of floods. Compared to mechanical river widening, self-acting bank erosion is a cost-saving method providing varying bed load input as required, i.e. high bed load input due to high bank erosion rates in case of floods and less bed load input in case of low flow periods.

The concept is based on the idea that the meander morphology corresponds to the current as well as future boundary conditions and does not change the current morphological state of the river fundamentally.

REFERENCES

Hengl, M. 2000. An Ecological and Hydraulic Redevelopment—Case Study Untere Salzach. *Kongress Wasser Berlin 2000.* Berlin.

Hunziker, R. 1995. Fraktionsweiser Geschiebetransport. *Mitteilung der Versuchsanstalt fuer Wasserbau, Hydrologie und Glaziologie.* ETH Zuerich. Nr. 138.

Jäggi, M. 1992. Sedimenthaushalt und Stabilitaet von Flussbauten. *Mitteilung der Versuchsanstalt fuer Wasserbau, Hydrologie und Glaziologie.* ETH Zuerich. Nr. 119.

Meyer-Peter, E. & Mueller, R. 1948. Formulae for Bedload Transport. *Proceedings of the 2nd Congress IAHSR. Stockholm.*

Platzer, G. 2000. Dimensionierung muldenfoermiger Blocksteinrampen. *Schriftenreihe des Bundesamtes fuer Wasserwirtschaft.* Wien. Band 9.

Schaffernak, F. 1950. *Grundriss der Flussmorphologie und des Flussbaues.* Wien: Verlag Springer.

Stephan, U., Hengl, M. & Schaipp, B. 2003. River restoration considering geomorphological boundary conditions. *Proceedings of the XXXth IAHR Congress.* Thessaloniki. C(II). 457–464.

WRS 2000. *Wasserwirtschaftliche Rahmenuntersuchung Salzach. Untersuchungen zur Flussmorphologie der Unteren Salzach.* Muenchen: Bayerisches Landesamt fuer Wasserwirtschaft.

WRS 2001a. *Wasserwirtschaftliche Rahmenuntersuchung Salzach—Zusammenfassende Darstellung und Bewertung der Loesungsvarianten.* Salzburg: Amt der Salzburger Landesregierung.
WRS 2001b. *Wasserwirtschaftliche Rahmenuntersuchung Salzach—Physikalisches Modell Sohlrampe mit Maeanderstrecke.* Salzburg: Amt der Salzburger Landesregierung.
Yalin, M.S. & da Silva, A.M.F. 2001. Fluvial Processes. Delft: IAHR Monograph.
Zanke, U. 1999. Zur Physik von stroemungsgetriebenem Sediment (Geschiebetrieb). *Mitteilungen des Instituts fuer Wasserbau und Wasserwirtschaft.* TU Darmstadt. Heft 106.

Destruction of herbaceous vegetation by flood flow on a floodplain in a recovery process

S.Sugio

University of Miyazaki, Miyazaki, Japan
K.Watanabe

Saga University, Saga, Japan

River Flow 2004—Greco, Carravetta & Della Morte (eds.)

ABSTRACT: This research focuses on examining the destruction of the herbaceous vegetation on an excavated floodplain in the recovery process. The methods of examination were (i) drawing the distribution chart of the vegetation on the floodplain, (ii) surveying the physical condition of the floodplain, (iii) testing the tensile load to cut off the caulis and the pullout load to extract the roots of the vegetation, (iv) simulating the two dimensional steady flow at the peak of the flood and (v) estimating the maximum size of the transported bed material on the floodplain and the drag force acting on the canopy of vegetation. From these investigations we found that some parts of the vegetation clusters on the floodplain may be destroyed by transport of the bed material. However, almost all of the other parts can be destroyed by the tensile load due to the drag force on the canopy.

1 INTRODUCTION

The vegetation in a river channel plays an important role in the ecosystem. However it becomes an obstacle to flood flow and affects the transport of riverbed material. Therefore, the growing situation of the vegetation becomes an important aspect in river management. Up to the present, although the destruction of woody vegetation due to floods has been examined in various ways, the examination of herbaceous vegetation has been minimal.

The Kita River is a first class river, which flows in the northern part of Miyazaki Prefecture in Japan. In this river, the heavy rainfall of Typhoon No. 19 in 1997 caused a

severe river disaster and severe damage in the basin. A special emergency project to protect from further severe flood disasters was executed for the channel of the Kita River. In this project, it was requested that the excellent natural environment of this river be conserved, and a fixed degree of safety against flooding secured. Lowering the flood levels in a river reach by increasing the discharge capacity of the river channel is possible by enlarging the conveying cross section and by reducing the roughness of the river. In the Kawasaka district of the Kita River, the cross section was enlarged by excavating the floodplain and the trees in the channel were removed. In excavating, the water zone and the river banks were to be disturbed as little as possible in order to conserve the natural environment.

The revegetation has been monitored to clarify the recovery process of the vegetation after excavation. In monitoring, the destruction of the herbaceous vegetation was observed on the floodplain in the Kawasaka district. This paper describes the monitored results of the revegetation and examines the mechanism of the observed destruction of vegetation.

2 RESEARCH FIELD

A point bar formed on the left convex side of the bend of the Kawasaka district in the Kita River, has developed and become a floodplain. This floodplain between the 14km and 13km sections was selected as the research field. This floodplain was excavated on average by a thickness of two meters and flattened in March 2000 according to the execution plan for the river improvement of the special emergency project for the Kita River. A check field of this research is the floodplain between the 12.2km and 11.4km sections in the Honmura district which was not excavated. These locations are shown in Figure 1.

2.1 *Vegetation in Kawasaka*

In the Kawasaka district, woods of *Quercus acutissima* and *Rosa mulfiflora Thunb*. thrived before the excavation of the high ground on the floodplain, and the river

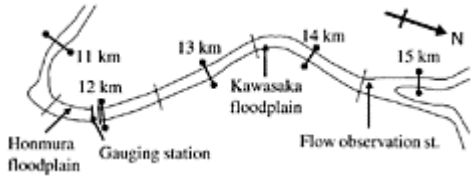

Figure 1. Location of the research field.

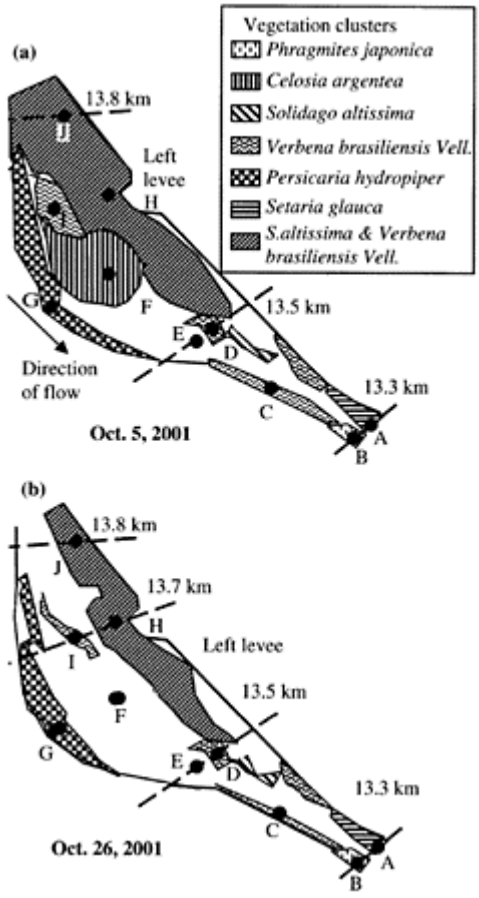

Figure 2. Vegetation distribution chart on the floodplain in Kawasaka.

banks had clusters of *Phragmites australis* or barren ground. Though the floodplain became barren ground overall in March 2000 due to the excavation, herbaceous vegetation germinated in the spring of 2001, and grew up smoothly to the state where the vegetation cover was 20–45% in the summer. Exotic vegetation such as *Verbena brasiliensis Vell*. and *Solidago*

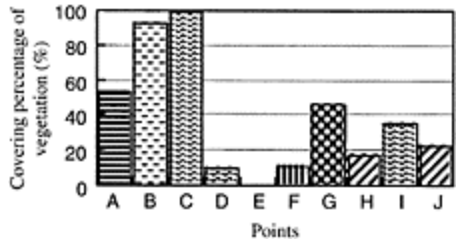

Figure 3. Percentage vegetation cover on the floodplain in Kawasaka.

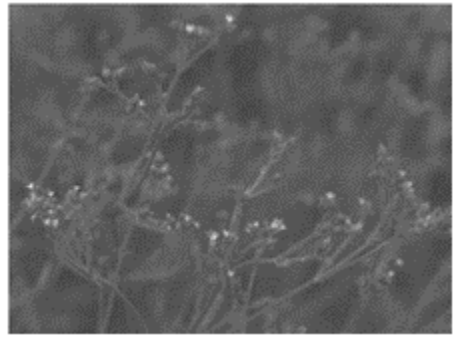

Photo 1. *Verbena brasiliensis Vell.*

Photo 2. *Solidago altissima Linn.*

altissima Linn. grew about 0.5–2m high in clusters in the whole area of the floodplain. Figures 2a and 2b show the vegetation distribution chart surveyed on October 5, 2001 and October 26, 2001, respectively. Figure 3 shows the percentage vegetation cover on the floodplain on October 5, 2001. Photos 1–6 show the photographs of the vegetation.

2.2 *Vegetation in Honmura*

It was observed from the monitoring, that most of the vegetation on the floodplain in the Honmura district

Photo 3. *Persicaria hydropiper.*

Photo 4. *Phragmites japonica Steud.*

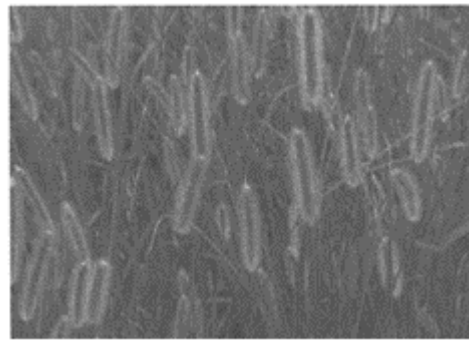

Photo 5. *Setaria glauca.*

was destroyed by the severe floods in 1997, however several woods remained. Subsequently, vegetation recovered gradually, and the floodplain was mostly covered with vegetation by the autumn of 2001. Clusters such as *Rosa mulfiflora Thunb.*, *Celtis sinensis var. japonica*, and *Salix eriocarpa Fr. Et Sav*, were distributed as woody vegetation, and clusters such as *Phragmites japonica Steud*, *Reynoutria japonica*

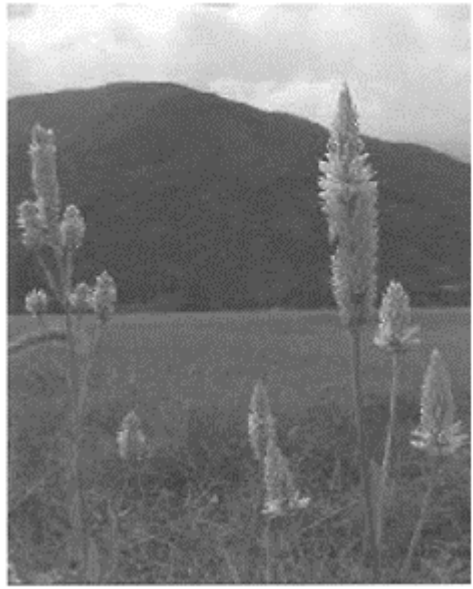

Photo 6. *Celosia argentea Linn.*

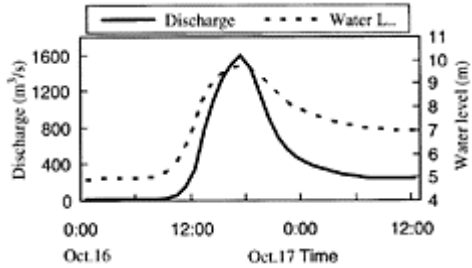

Figure 4. Flood discharge and flood water levels on October 16, 2001.

Houtt, and *Artemisia capillaries Thunb.* as herbaceous vegetation.

3 FLOODING

Floods caused by Typhoon No.21 greatly damaged the basin of the Kita River on October 16, 2001. The flow discharge was observed at the flow observation station at the 14.5km section, and the water level was observed at the gauging station at the 12km section. These observed results are shown in Figure 4. The maximum discharge of this flood was 1,600m^3/s. Figure 5 shows the elevations on the floodplain at a typical cross section before and after the flood. A clear change of bed elevation due to the flood did not take place in

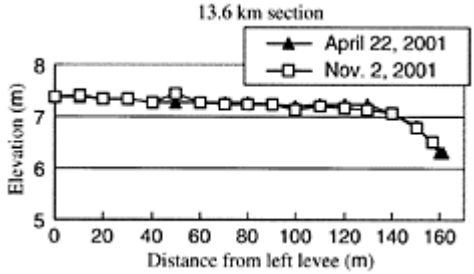

Figure 5. Observed elevation on the floodplain.

Photo 7. Floodplain in Kawasaka district after the flood.

the Kawasaka district. However, the vegetation was destroyed in half of the floodplain due to the flood as shown in Photo 7.

4 VEGETATION DESTRUCTION AND VEGETATION DISTRIBUTION AFTER FLOOD

Figure 2b shows the vegetation distribution chart surveyed after the flood. Comparing this chart with that for before the flood shown in Figure 2a, it can be seen that vegetation

disappeared in half of the floodplain, though some parts remained on the low water channel side of the floodplain.

As for the vegetation destruction situation, the following four types were found.

(i) Vegetation disappeared by the roots
(ii) Only the roots remained
(iii) The canopy disappeared, but caulis and roots remained
(iv) Vegetation was buried in river bank area.

In the drawing of Figure 2b, the areas of vegetation where only the roots remained are included in the barren ground assuming that the vegetation was destroyed. Though the composite cluster of *Solidago altissima Linn.* and *Verbena brasiliensis Vell.* remained on the levee side of the floodplain, many canopies of

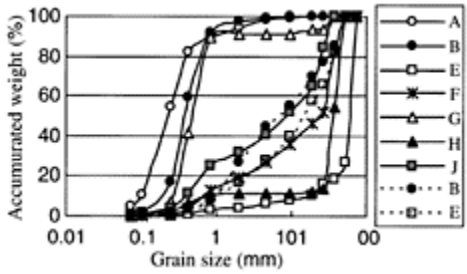

Figure 6. Grain size distribution curves.

Verbena brasiliensis Vell. were cut off. On the other hand, no significant vegetation destruction occurred on the floodplain in the Honmura district.

The grain size distribution curves are shown in Figure 6 by the solid line for the bed material on the floodplain after the flood and by the dotted line for one before the flood. Though the grain sizes are almost the same at the various points on the floodplain before the flood, a significant difference in the grain size distribution was caused in these points after the flood. Gravels larger than 26.5mm in size occupy the major portion of the grain size distribution at Points E and H. Soils smaller than 0.5mm in size are the major component at Points A, B and G where the percentages vegetation cover are high.

5 NUMERICAL ANALYSIS

5.1 *Basic equations*

The flow at the peak of the flood was numerically investigated. Two-dimensional St. Venant shallow water equations in a generalized curvilinear coordinate system used were;

$$\frac{\partial(uh)}{\partial\xi}+\frac{1}{r}\frac{\partial(rvh)}{\partial\eta}=0 \qquad (1)$$

$$u\frac{\partial u}{\partial \xi}+v\frac{\partial u}{\partial \eta}+\frac{uv}{r}=-\frac{1}{\rho}\frac{\partial p}{\partial \xi}+2\frac{\partial}{\partial \xi}\left(\varepsilon\frac{\partial u}{\partial \xi}\right)+\frac{\partial}{\partial \eta}\left(\varepsilon\frac{\partial u}{\partial \eta}\right)-\frac{\tau_\xi}{\rho h}-\frac{NF_\xi}{\rho h} \tag{2}$$

$$u\frac{\partial v}{\partial \xi}+v\frac{\partial v}{\partial \eta}-\frac{u^2}{r}=-\frac{1}{\rho}\frac{\partial p}{\partial \xi}+\frac{\partial}{\partial \xi}\left(\varepsilon\frac{\partial v}{\partial \xi}\right)+2\frac{\partial}{\partial \eta}\left(\varepsilon\frac{\partial v}{\partial \eta}\right)-\frac{\tau_\eta}{\rho h}-\frac{NF_\eta}{\rho h} \tag{3}$$

where ξ, η=axes in curvilinear coordinates; r=radius of curvature; u, v=velocities in the ξ, η directions; $p=\rho g(h+z)$; ρ=water density; g=gravitational acceleration; h=flow depth; z=bed elevation; ε=coefficient of eddy viscosity; τ_ξ, τ_η=bed shear stresses in ξ, η directions; F_ξ, F_η=drag forces acting on a dead grass lump in the ξ, η directions; and N=number of grass clumps per unit area. The bed shear stresses were expressed by using the coefficient of Manning's roughness n, as

$$\frac{\tau_\xi}{\rho h}=\frac{gn^2}{h^{4/3}}u\sqrt{u^2+v^2} \tag{4}$$

$$\frac{\tau_\eta}{\rho h}=\frac{gn^2}{h^{4/3}}v\sqrt{u^2+v^2} \tag{5}$$

The coefficient of eddy viscosity was expressed as

$$\varepsilon=\frac{\kappa}{6}u_*h\ ,\quad u_*=\sqrt{(\tau_\xi+\tau_\eta)/\rho} \tag{6}$$

where κ=Karman constant=0.4; and u_*=shear velocity.

5.2 *Drag force*

Many clumps of dead grass twined around canopies of *Verbena brasiliensis Vell.* were observed after the flood in October 2001 and also after a small flood in July 2002. Therefore, the force acting on each canopy is regarded as the drag force acting on the dead grass clump. Regarding a circular plate with diameter of D as a grass clump, the drag force can be expressed as

$$F=\frac{1}{2}\rho C u_\delta^2\frac{\pi}{4}D^2 \tag{7}$$

where u_δ=velocity at the height δ of the clump from the bed; and C=drag coefficient=1.0. The velocity u_δ can be given from the Manning-Strickler equation as

$$u_\delta/q=1.17(\delta/h)^{1/6},\quad q=\sqrt{u^2+v^2} \tag{8}$$

The scale of the grass clumps in the flood frow is uncertain. The diameters of clumps ranged from 6cm to 12cm in the survey after the floods. In this study, each clump is considered to be a circular plate with diameter of 10cm. Since the water depth on the

floodplain was over 4.0m and the length of the vegetation was 45cm to 190cm, roughly 70cm on average, all of the vegetation must have been submerged and the height of each clump δ is assumed to be half of the vegetation length, δ=45cm herein. By using this value of δ, F_ξ and F_η are expressed finally as, respectively,

$$\frac{F_\xi}{\rho h} = \frac{0.00376}{h^{4/3}} u\sqrt{u^2+v^2} \tag{9}$$

Table 1. The number of dead grass clumps.

Cluster	Value of N ($1/m^2$)
Phragmites japonica Steud	0
Celosia argentea Linn.	2
Solidago altissima	0
Verbena brasiliensis Vell.	10
Persicaria hydropiper	0
Setaria glauca	0
Verbena brasiliensis Vell. and Solidago altissima	2

$$\frac{F_\eta}{\rho h} = \frac{0.00376}{h^{4/3}} v\sqrt{u^2+v^2} \tag{10}$$

The numbers of dead grass clumps are different from each other due to the kind of vegetation and thier density. For example, the grass clumps in the cluster of *Verbena brasiliensis Vell.* numbered about ten per $1m^2$ from the survey after the flood. Based on this value, the number N at each analytical point was estimated from the distribution and density of vegetation before the flood in 2001 as shown in Table 1.

5.3 *Analytical conditions and velocity distributions*

The analytical domain including the floodplain at the Kawasaka district was selected between the 13.0km and 14.4km sections. The domain was divided by 50m in the ξ direction and each cross section was divided into 24 meshes with intervals of 7.5m to 10.5m. Values of the coefficient of Manning's roughness were taken as 0.031 for the main channel and 0.035 for the floodplain according to the results of a 1-D simulation of the flood in 1997.

Taking the flood on October 16, 2001 as the flow to simulate, the peak discharge of $1{,}600m^3/s$ was taken as the boundary condition at the upstream end. The water level of 10.63m at the 13.0km section was taken as the downstream boundary condition. This value was obtained from a 1-D simulation of the flood by using the measured peak water level of 9.74m at the 12.0km section.

Figure 7 demonstrates a numerical result of the flow velocity vector. It can be seen that the low water channel deviates to the right levee between the 14.0km and 13.4km sections and velocities are increased there due to the floodplain formed on the convex side of bend. Velocities were 2.2m/s to 2.8m/s in the low water channel and 0.8m/s to

1.8m/s on the floodplain. In particular, velocities near the center part of the floodplain were significantly decreased due to the cluster of *Verbena brasiliensis Vell.*

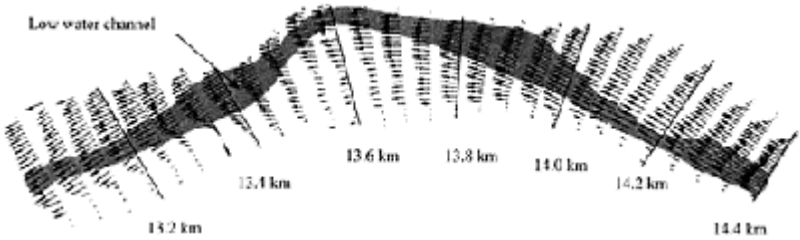

Figure 7. Velocity vector distributions.

6 DESTRUCTION OF VEGETATION

6.1 *Mechanism of destruction*

The effects of flooding on the vegetation have been classified by Ishikawa (1996) into the following four kinds: (1) destruction by the transported bed material, (2) destruction of the physical condition by the flow, (3) burying by the transported bed material, and (4) adverse effect to the physiological activity caused by submergence. The vegetation in the Honmura district was destroyed due to the flood in 1997. Main cause was burying by the bed material. This type of destruction should be considered by the estimation of tractive shear stress related to bed material transport under flood.

Many clumps of dead grass twined around canopies were observed after the flood due to Typhoon No.9 in July 2002. A photograph of a dead grass clump is shown in Photo 8. It is considered that these dead grasses were washed away in the upper reaches and twined around canopies of vegetation on the floodplain during the rising of the water level. When the drag force acts on each grass clump, vegetation is constrained to the flow direction. A comparison between the drag force and tensile load should be considered.

6.2 *Movement of bed materials on the floodplain*

From the simulated results, the values of shear velocity u_* on the floodplain were 11.0cm/s to 12.6cm/s. This means that the maximum size of gravel moved by the shear stress can be estimated to be 1.5cm to 2.0cm. Therefore, it is considered that gravels smaller than this size moved during the flood. According to the grain size distribution curves shown in Figure 6, the percentage of gravels with diameters greater than 2cm at Point E was almost 50% before the flood. This is the reason why the bed elevation was not

Photo 8. Dead grass clump twined around canopies of *Verbena brasiliensis Vell.*

significantly deformed by the flood as shown in Figure 5.

6.3 *Distribution of dragforce acted on grass lump*

Figure 8 shows the distribution of the simulated combined drag force F acting on a grass clump twined around a canopy of vegetation on the floodplain. The horizontal axis denotes the distance from the top of left levee. The value of F is roughly 1N to 10N. In the figure, the vegetated areas before and after the flood are also shown.

7 TENSILE LOAD OF HERBACEOUS VEGETATION

A tension test for various kinds of vegetation was carried out to clarify the tensile load to cut off the caulis and the pullout load to extract the root. A schematic diagram of the testing method is shown in Figure 9. The caulis of the vegetation was bound with a string, and a load was attached to the other end of the string. The load when the caulis was cut or the root was extracted was measured. Strings were bound at the joint of the

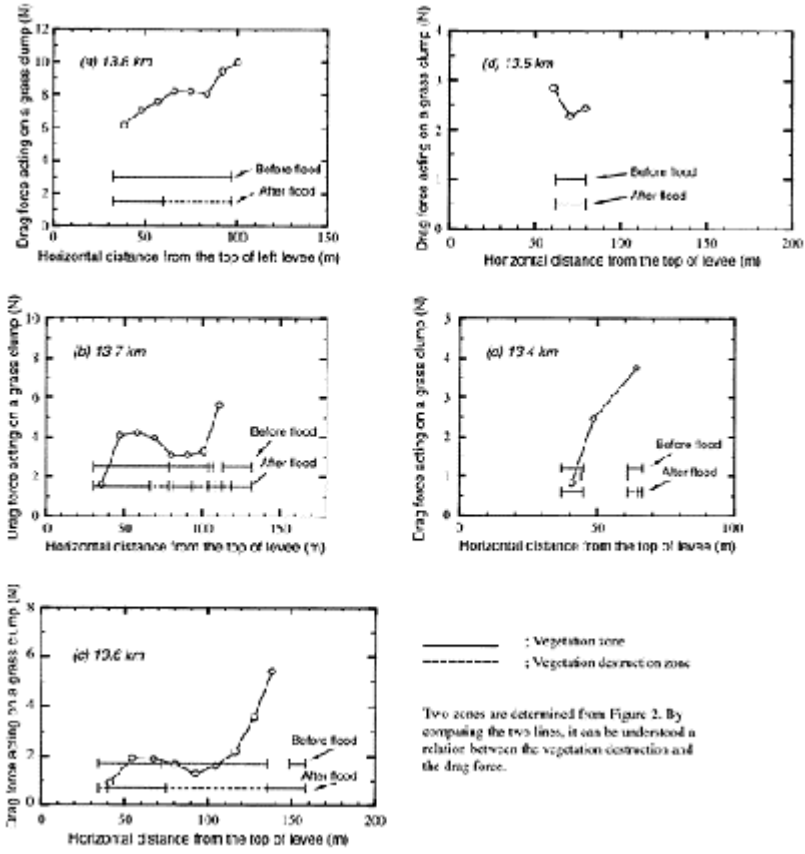

Figure 8. Distributions of combined drag force acting on a dead grass clump at each cross section of the floodplain in the Kawasaka district.

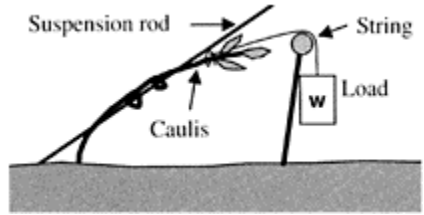

Figure 9. Schematic diagram for tension test method.

Table 2. Results of tension test.

Plants	Loaded position	Tensil load (N)	Height of plant (cm)
Verbenabrasiliensis Vell.	Canopy	9.8~4.3	95~164
	Root	over 186.2	95
Phragmites japonica Steud	Root	58.8~156.8	45~56
Persicaria hydropiper	Canopy	14.7~29.4	43~56
	Root	over 137.2	56
Celosia argentea Linn.	Canopi	24.5	61
	Root	24.5~58.8	56~61
Solidago altissima	Canopy	49	80
	Root	68.6	57
Setaria glauca	Root	49~63.7	51~53

canopy for the tension test of the caulis and at the lowest part of the caulis for the root pullout test. In addition, in the test of tensile load, the lower part of the caulis was rolled in a suspension rod to prevent the load from acting on the root part.

The measured results are shown in Table 2. The results show the tensile load of the joint of the canopy is smaller than the pullout load of the root for many kinds of vegetation. From this result, it is understood that cutting the caulis is easier than extracting the root.

8 DISCUSSIONS OF VEGETATION DESTRUCTION

In the composite cluster of *Solidago altissima Linn.* and *Verbena brasiliensis Vell.* between the 13.7km and 13.8km sections, many canopies of *Verbena brasiliensis Vell.* were lost in the flood. Since the drag force acting on a dead grass clump is greater than the tensile load as shown in Figure 8a, it is considered that the drag force caused the destruction of *Verbena brasiliensis Vell.* by cutting canopies in this area. At the 13.7km section (Figure 8b), the drag force decreased because of the decreased velocity due to the resistance of the cluster of *Verbena brasiliensis Vell.* Then, the destruction of this cluster was only partial.

The cluster of *Celosia argentea Linn.* between the 13.6km and 13.7km sections almost disappeared by the roots as shown in Figure 2b. According to the simulated results for the tractive force, it is considered that gravels with diameters smaller than 2cm were transported in the barren ground and in the low density vegetated area. Since the percentage vegetation cover was small in the cluster of *Celosia argentea Linn.* as shown in Figure 3, it can be presumed that gravel movement destroyed the physical condition in this cluster and the root pullout load of *Celosia argentea Linn.* must have decreased. On

the other hand, the tensile load of the caulis is larger than the drag force. Therefore, it is reasonable to consider that the caulis of *Celosia argentea Linn.* was not cut and its cluster was washed out by the roots.

At the 13.6km section, the composite cluster of *Solidago altissima Linn.* and *Verbena brasiliensis Vell.* was not destroyed, because the drag forces were smaller than the tensile load as shown in Figure 8c. The cluster of *Verbena brasiliensis Vell.* at the 13.5km section was also not destroyed for the same reason, as shown in Figure 8d.

The cluster of *Persicaria hydropiper* along the edge of the floodplain almost survived as shown in Figures 2b. It can be considered that the large drag force near the low water channel could not destroy *Persicaria hydropiper* because of the flexibility of the caulis. Values of root pullout load for *Phragmites japonica Steud* and *Setaria glauca* are larger than the drag forces as shown in Figure 8d. Therefore, both clusters at the 13.3km section were not destroyed and survived as shown in Figure 8e.

9 SUMMARY

As mentioned above, various field investigations were carried out on the herbaceous vegetation of the floodplain of the Kita River. The destruction of the herbaceous vegetation due to the flood flow was then examined. The results obtained are as follows:

(1) Part of the herbaceous vegetation on the floodplain in the recovery process was destroyed due to a flood flow with a maximum discharge of 1,600m^3/s caused by Typhoon No. 21 on October 16, 2001.
(2) The destruction situation can be classified roughly into the following four types: (i) vegetation disappeared by the roots, (11) only the root remained, (iii) the canopy disappeared, but the caulis and roots remained, and (iv) vegetation was buried in the river banks.
(3) Many clumps of dead grass twined around canopies of *Verbena brasiliensis Vell.* were observed after a small flood in July 2002.
(4) Through a numerical analysis of the flood flow on the floodplain, it is recognized that the reason why a clear change of riverbed elevation did not take place on the floodplain in the Kawasaka district was due to lack of movement of gravel larger than 2cm in size in floods.
(5) It was found from simulated results that a drag force of 2–10N acted on canopies of the vegetation in large parts of the floodplain.
(6) Through tension tests for various kinds of vegetation, it became clear that cutting the caulis is easier than pulling out the root.
(7) It is confirmed that the disappearance of the canopy of *Verbena brasiliensis Vell.* was caused by cutting the caulis due to the drag force acting on a dead grass clump.
(8) It is inferred that disappearance of vegetation by the root is due to both movement of gravels with small diameters and the action of the drag force.
(9) It can be presumed that the vegetation on the low water channel side of the floodplain was prostrated by the flow-induced force and survived the flood because of the flexibility of the caulis.

ACKNOWLEDGEMENT

The investigation in this paper was partially supported by research funds from the River Ecology Research Group of Japan. The authors would like to thank the Nobeoka Construction Office of the Ministry of Land, Infrastructure and Transport and the Nobeoka Engineering Works Office of Miyazaki Prefecture for supplying the hydrological data.

REFERENCES

Ishikawa, S. 1996. Characteristics of Riparian Vegetation. In Okuda, S. & Sasaki, Y. (eds). *River Environment and Riparian Vegetation:* 116–139. Tokyo: Soft Science.

Kyushu Regional Development Bureau, Ministry of Land, Infrastructure and Transport & Miyazaki Prefecture (ed.) 1999. *Report on the examination of river improvement in the Kita River.* Tokyo: Riverfront Improvement and Restoration.

River Bureau, Ministry of Land, Infrastructure and Transport (ed.) 2002. *Rivers in Japan.* Tokyo: Infrastructure Development Institute-Japan, Japan River Association.

River Ecology Research Group of Japan (ed.) 2002. *Understanding the Natural Environment of Rivers—Perspectives of River Ecology Research.* Tokyo: Riverfront Improvement and Restoration.

River Environment Division, River Bureau, Ministry of Land, Infrastructure and Transport (ed.) 2002. *Renaturalization of rivers—Restoring natural rivers.* Tokyo: River Environment Division, River bureau, Ministry of Construction.

Sezaki, T., Hattori, A., Kondo, K., Tokuda, M., Fujita, K., Yoshida, M. 2000. Field Study on the Destruction Processes of Herbaceous Vegetation on Gravel Bars due to Flood Flows. *Annual Journal of Hydraulic Eng., JSCE.,* 44, 825–830.

Shimizu, Y., 1991. A study on Prediction of Flows and Bed Deformations in Alluvial Streams. *Report of Studies, Civil Engineering Research Institute, Hokkaido Development Bureau,* 93, 1–109.

Shimizu, Y. & Osada, K. 2002. Study on the Destruction Mechanism of Riparian Trees in a Gravel-bed River caused by Flood Disturbance. *Advances in River Eng., JSCE.*, 8, 301–306.

Sugio, S., Watanabe, K., Tanoue, A. 2003. Research on the Destruction of Herbaceous Vegetation by Flood Flow on Sand Bar in Recovering Process. *Annual Journal of Hydraulic Eng., JSCE.,* 47, 1003–1008.

A new bed for the river Inde: a case study with special view on the risk of depth erosion

P.Kamrath, C.Schweim, S.Briechle & J.Köngeter

Institute of Hydmulic Engineering and Water Resources Management
Aachen University,
Aachen, Germany

River Flow 2004—Greco, Carravetta & Della Morte (eds.)

ABSTRACT: This paper presents the results of research about a river relocation in a German coal mining area. The river Inde resides in the lignite dismantling area called the "Rhineland", which is enclosed by the three towns Aachen, Cologne and Mönchengladbach. In the year 2005 the contemporary riverbed will be intersected as a result of the brown coal mines forward movement to the east and the continued use of lignite as energy source for the neighbouring power plants. Long time enduring critical shear stresses throughout flood events could cause depth erosion, which would damage or eventually destroy the sealing layer and therefore flood the pit mine as a worst-case scenario. Hence, the aim is to give the new river as much freedom as possible and to eliminate any uncertainties regarding the flood protection of the coalmine at the same time.

1 INTRODUCTION

The planned riverbed consists of a variable geometry and cross sectional shapes separated in one main channel and two flood plains. According to modern aspects of river-design a partly meandering river was chosen where diverse flow patterns are beneficial to the river ecology.

The new part of the river will cover a reach of 12.0[km] (Fig. 1). The river Inde has a mean discharge of 4.3[m^3/s]. Its new riverbed shows a bed slope of 1.2[$‰_0$] and a mean width of the channel of 13.70[m]. The riverbed of the new Inde is denoted by a wide bandwidth of different roughness regions. For numerical simulations a one-dimensional view is not sufficient, because the lateral resolution of the results would not be detailed enough for erosion forecasting purposes.

The transport of the bed material was tested in the institute's laboratory. Hence, the main influencing parameters regarding the bed load are the materials critical shear stress τ_c and the mass erosion capacity respectively. In addition to the bare materials critical

shear stress the influences of sparse vegetation and ripples caused by the construction method are important aspects to consider in the model (Fig. 2, top). For this purpose a vegetation-erosion algorithm is applied to the numerical model.

As a consequence to the sparse and slow growing vegetation the shear stresses are computed for varying scenarios. At first a scenario for the time immediately

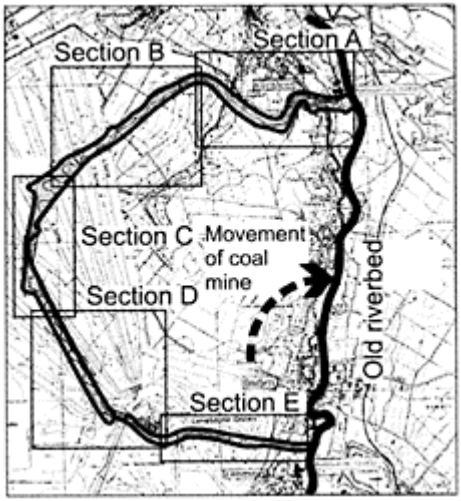

Figure 1. The relocation of the river Inde.

after flooding the new part of the river is predicted when settlement processes are not finished yet and plants are sparse. Secondly at another point of time in the far future when settlement is finished and vegetation is dense. Except of erosion stability forecasting during annual repeating floods, the initial bed load during an only every one hundred years occurring event is interesting, too.

2 THE MODEL

2.1 *Simulation of flow characteristics*

The flow processes in the river are dominated by a very heterogeneous river geometry and roughness distribution. To assure the hydromechanical efficiency as well as to get information about the occurring shear stresses at different flood events the two-dimensional depth averaged model RISMO is used. RISMO has been developed at the Institute of Hydraulic Engineering and Water Resources Management and has been applied for several two-dimensional simulations (Rouvé & Schröder 1993).

The numerical model solves the shallow water equations with the finite element method. The shallow water equations are obtained by vertical integration of the Navier-Stokes equations and the continuity equation (Kuipers & Vreugdenhill 1973):

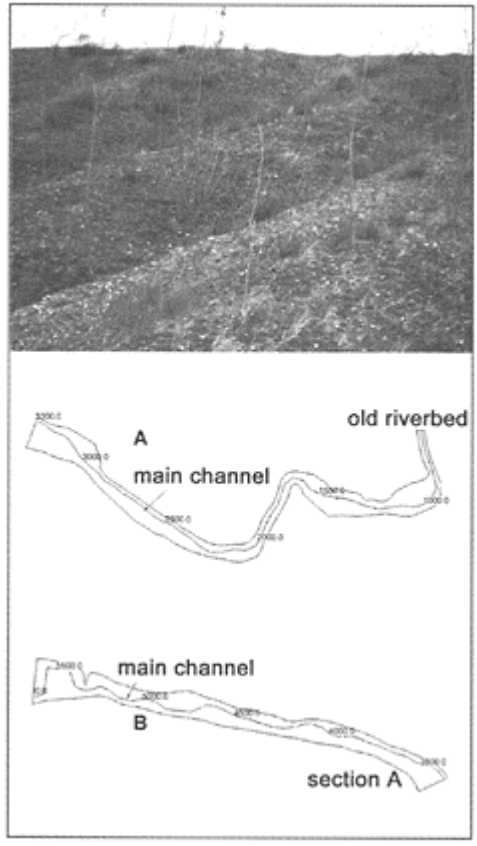

Figure 2. Sparse vegetation and ripples on flood plains (top) and overview of sections A and B (river km 5^{+800}–0^{+600})

$$H\left(\frac{\partial U_i}{\partial t}+\frac{\partial U_i U_j}{\partial x_j}\right)=H\left(-g\frac{1\partial S}{\rho\partial x_i}+\frac{1\partial}{\rho\partial x_j}\left(V_{ij}+T_{ij}+D_{ij}\right)+F_i\right) \quad (1)$$

$$\frac{\partial H}{\partial t}+\frac{\partial\left(HU_i\right)}{\partial x_j}=0 \quad (2)$$

with

$$V_{ij}=\rho\nu\frac{\partial U_i}{\partial x_j} \quad (3)$$

$$T_{ij}=-\rho\overline{u_i u_j} \quad (4)$$

where H is the flow depth, U_i are time-averaged horizontal velocities, x_i are the Cartesian coordinates, S is the water surface elevation, F the outer force, ρ the density of water and v the cinematic viscosity.

A wet-dry algorithm considers bank overflow and partly submerged regions. The flow calculation yields the velocity and the depth of flow for each node for a given discharge and for a set of boundary conditions like the bottom roughness and outflow water level. The simulation is carried out from downstream to upstream to use the results from one section as the outflow boundary condition to the next one. When the flow calculations are completed a decoupled sediment transport module is used to calculate transport rates. The influences of the ripples and the sparse vegetation are all covered into Manning's roughness parameter *n.* The whole reach of the new riverbed is divided into sections with about 8000 elements each.

2.2 *Applied roughness*

The open pit mine offers a material as a side product which is used for the new riverbed. It consists of a mixture of gravel, sand and loess with a characteristic diameter d_{ch} of 15[mm]. Resistance to flow is typically characterized by a roughness coefficient. The most commonly used equation for flow resistance is the Manning equation. All other forms of resistance parameters as the Chezy C parameter or the Darcy—Weisbach friction factor f can be converted into Manning's coefficient n.

The roughness of the bare material was tested in an earlier physical experiment in order to transfer the results into the numerical model (Baur et al. 1997). From a series of tests the roughness was determined to be n=0.019[s/m$^{1/3}$]. The estimation of roughness is very precise, as long as no heterogeneous influences are considered. Unfortunately, the flood plains of the new river Inde consist of ripples and a very sparse vegetation layer (Fig. 2, top). The ripples width is approximately 2.0[m] and their height about 0.6[m].

To take these structures into account, an approach recommended by van Rijn (1993) is chosen:

$$\frac{1}{n^R} \approx \frac{26}{k_s^{1/6}} = 26 \cdot \left(20 \cdot \gamma_R \Delta_R \cdot \left(\frac{\Delta_R}{\gamma_R} \right) \right)^{-1/6} \qquad (5)$$

In Equation 5 above n^R [s/m$^{1/3}$] is the added Manning roughness resulted by ripples or dunes, k_s[mm] is the equivalent sand roughness parameter, γ_r[–] is called a presence factor (γ_r=1.0 for ripples and γ_r=0.7 for dunes) and Δ_r[m] is the height of the structures.

2.3 *Influence of sparse vegetation*

The influence of the sparse vegetation on the ground is neglected. Only larger plants e.g. willows and shrubs are simulated. Plants on the floodplain and along banks can increase or even decrease the effective flow resistance. The Manning's resistance coefficient for vegetation is calculated in conformity with the Cowan (1956) method for additive resistance and based on the work of Copeland (2000). According to his research, the modulus of plant stiffness E_s is critical to the calculation of resistance because of the flexibility of the plants and the deformation of leaf masses due to the flow forces. The modulus of plant stiffness is calculated by:

$$E_s = \frac{F_{45} \cdot h^2}{3 \cdot I} = 6,791 \cdot \left(\frac{F_{45} \cdot h^2}{D_s^4} \right) \tag{6}$$

where F_{45} is the force to bend the plant to an angle of 45°, D_s is the thickness of the stem and h the plants heights as to see in Figure 3. With the typical stiffness of willows the roughness for submerged vegetation can be computed by following equation:

$$n = 0,183 \cdot \left(\frac{E_s \cdot A_s}{\rho \cdot A_i \cdot u_\tau^2} \right)^{0,183} \cdot \left(\frac{h}{Y_O} \right)^{0,243} \cdot \left(M \cdot A_i \right)^{0,273} \cdot \left(\frac{\nu}{u_\tau \cdot R_h} \right)^{0,115} \cdot \left(\frac{1}{u_\tau} \right) \cdot R_h^{2/3} S^{1/2} \tag{7}$$

with:

A_s	Total cross sectional area of a plant	[m2]
Ai	Frontal area of a plant blocking flow	[m^2]
u_τ	Shear velocity	[m/s]
YO	Flow depth	[m]
M	Plant density	[$1/m^2$]
R_h	Hydraulic radius	[m]

Equation 7 is applicable only for submerged flow defined by depth $Y0 > 0.8\ h$. At present time, approximately one willow or shrub for each 50 [m^2] with E_s=1.5 • 10^8 [N/m^2] can be found on the flood plains. Hence, the resulting Manning's roughness coefficient for the river Inde is chosen to be $n=0.05$ [s/m 1/3]. The ripples are obviously the parameter with the highest influence. For the moment when the new part of

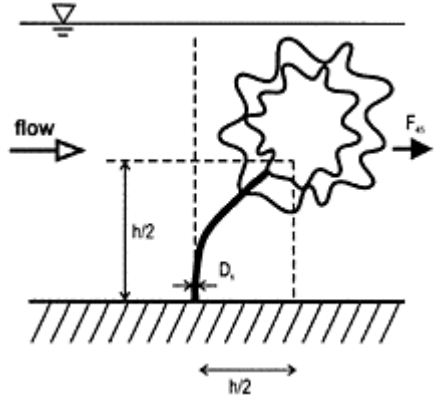

Figure 3. Methodology for measuring the force F_{45} to calculate plant stiffness E_s.

the river is flooded, the influence of sparse vegetation is insignificant.

2.4 *Critical shear stress value*

The value of the critical shear stress relies on the degree of fractional ground cover *V*, which ranges from zero to one. V_{max}=1 is the maximum percent cover that can be supported in a given environment. Unfortunately, only few data sets exist to constrain the relationship between the critical shear stress τ_c and *V*. In the absence of better information, a linear relationship is a good approximation (Tucker 1999).

$$\tau c(V)=\tau cs+V\tau ct \tag{8}$$

where τ_{cs} is the critical shear stress for an unvegetated surface and therefore primarily a function of the grain size and τ_{cv} is the added critical shear stress under 100% vegetation cover. The transport capacity then depends mainly on vegetation cover and is commonly written like:

$$q_s = k(\tau-\tau_{krit})^p \tag{9}$$

The transport capacity q_s depends on the difference of the fluid shear stress τ and the critical shear stress τ_c. At present time, the coverage *V* is about 10%. With τ_{cs}=*6* [N/m^2] as resulted by experiments in a flume and τ_{cv}=50 [N/m^2] as the maximum value under full coverage the critical shear stress immediately after flooding the Inde is assumed to be approximately 11[N/m^2].

2.5 *Erosion processes*

The rate of erosion is calculated with one of the common sediment transport formula. It is the method of Meyer-Peter & Müller (1949) which derives the sediment transport capacity:

$$q_S = 8 \cdot \rho_F \cdot u_\tau \cdot d_{ch} \cdot Fr^* \cdot \left[\frac{Q_S}{Q} \left(\frac{k_{St}}{k_r} \right)^{3/2} - \frac{Fr_c^*}{Fr^*} \right]^{3/2} \tag{10}$$

with:

q_s	transport capacity	[kg/m·s]
ρ_F	bulk density of material	[2650kg/m^3]
u_τ	shear velocity	[m/s]
d_{ch_m}	characteristic particle size	[15mm]
Fr	Froude number due to particle= $f(\tau, d_{ch})$	[−]
Fr_c^*	critical Froude number due to particle	[−]
Q_s	flow rate with effect on	[m^3/s]

k_{St}	transport roughness coefficient due to flow	[$m^{1/3}/s$]
k_r	roughness coefficient due to particle	[$m^{1/3}/s$]

By comparing the rates at two following cross sections the model predicts erosion or deposition within the element. By dividing the difference of one sections inflow and outflow with their distance one gets the change in bottom elevation for each time step:

$$\frac{\partial z_g}{\partial t} = \frac{q_s^{in} - q_s^{out}}{\rho_F \cdot d} \tag{11}$$

In Equation 11, d is the distance between the cross sections. Therefore, the derivative of the bottom elevation in time is equal to the derivative of the transport capacity in x-direction. There are no long-term changes in river morphology predicted by the numerical model, because there is more demand on the local accuracy of the estimated initial shear stresses than on long-term prediction.

3 APPLICATION

3.1 *General*

The main intend is to predict depth erosion and the total area with shear stresses above the critical value with the help of a numerical model. Therefore different vegetation coverage levels and specific times are investigated.

In 2005 the old riverbed will be finally intersected and the new one will be flooded. Thus, another aspect is to study the influence of the ripples to the computed shear stress values and to suggest, whether a removal is needed for flood protecting reasons or not. Hence, one main thought is central: minimization of the total area with shear stresses above a critical value. This chapter presents the results and compares the different scenarios. The focus is set on sections A and B which are built in the next year (Fig. 2, bottom).

3.2 *Influence of settlement*

Especially in the first years after cutting the old river and flooding the new part in the year 2005 any flood events could produce great damage, because there is no protection by any vegetation. Because the new riverbed is being built close-by the open pit mine which was refilled with material just a few years ago, the bottom elevation will change over the next 20 years between 0.1[m] and 0.6[m]. Thus, as a first step, the influence of the unfinished settlement on the shear stresses should be examined.

Figure 4 shows the computed shear stresses at river km 5^{+400} for two different moments at a discharge of 111.0[m^3/s]. On the left the computed values for the year 2005 are shown as predicted and on the right the results for the year 2020 are plotted.

It is obvious for this section, that values of shear stresses are minor in the year 2005, when vegetation coverage is little. Table 1 compares the total critical area. For the summation a critical shear stress value of τ_c=11[N/m^2] is assumed for both cases.

Growing of vegetation between the year 2005 and 2020 is therefore neglected. During an every one hundred years occurring flood the size of the area where erosion is possible increases due to the settlements about 50%. It is important that the risk is not higher in the beginning compared to a later specific time.

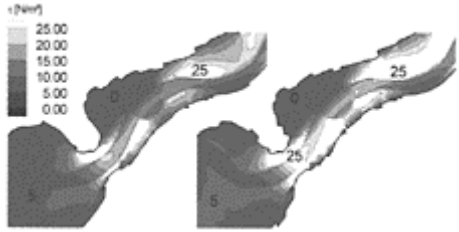

Figure 4. Influence of the unfinished settlement: Computed shear stresses for 2005 (left) and 2020 (right) at km $5^{+40}0$.

Table 1. Summation of critical area for section “B" at two different specific times.

Section B [km 3^{+300}–5^{+800}]		2005 [m^2]	2020 [m^2]
Scenario	SHQ*	7961.4	13,534.2
	HQ^{**}_{100}	53,751.3	76, 157.1

*Q=22.35m^3/s, summer flood (approximately 5 times a year).
**Q=111.00m^3/s.

3.3 *Influence of ripples and dunes*

The ripples on the flood plains are caused by the construction method of the new riverbed. The ripples result from the construction equipment which consists of the typical machines in open pit mines, normally used to remove the enormous quantities of earth. A comparison of calculated shear stresses with and without ripples should help to decide, whether the ripples should better be removed or not. Figure 4 shows the shear stresses at the same Inde km 1^{+750} for both cases.

Figure 5 and Table 2 clearly illustrate the great influence of the ripples at the flood plains. Although water depth becomes smaller and velocities are computed bigger for the case without ripples, the calculated shear stresses are in general of higher values. The influence of the strong roughness dominates. After virtually removing any ripples, the summated critical area is diminished to 29.8% for the HQ100 (111.00m^3/s) case and 70.9% for the SHQ (22.35m^3/s) case.

3.4 *Influence of vegetation*

The vegetation coverage on the flood plains is central to avoid depth erosion. Thus, when the relocation of the Inde was planned in the early 1990s and first experiments were carried out, it was assumed that the flood plains are covered with a dense layer of vegetation by 100% after a very short period of time. This prediction was wrong. The used material is a side product and was located at a depth of approximately 200 m below

Figure 5. Influence of the ripples: computed shear stresses for removed ripple roughness (left) and with ripples at the flood plains (right) at km 1^{+750}.

Table 2. Summation of critical area for section "A" for the scenarios with and without ripples.

Section B [km 3^{+300}–5^{+800}]		With ripples [m^2]	Without ripples [m^2]
Scenario	SHQ	30,639.2	8924.5
	HQ_{100}	99,258.3	69,705.4

the surface. Therefore the percentage of nutrient substances is very little and flora needs more time to grow than usual.

That's why it is of great interest to predict the degree of fractional ground cover which is needed to bisect the total area with supercritical shear stresses. In Figure 6 the critical area A_{Ero} is plotted against the degree of fractional ground cover V and the critical shear stress τ_c respectively. The vertical line at V=10% (τ_c=11N/m^2) denotes the present state. When the plants grow, the figure yields clearly that the critical area becomes smaller. The point when the area is bisected differs for every case. But in general a critical shear stress about 20.0[N/m^2] and a degree of ground cover about V=28% is sufficient to reduce the endangered area by 50%. Anyway, this is the total critical area which is endangered that depth erosion can occur. But because erosion and sedimentation are conditional to the derivative in x of the transport capacity and the shear stress (see Equation 11) respectively, both only occurs when the shear stress values change rapidly.

3.5 *Depth erosion*

Figure 7 shows, that the initial depth erosion velocities are varying between 0 and 2.0[cm/min]. Typical floods at the river Inde last between one and four days, but the duration of discharges above 25[m^3/s] is less than half a day. Extrapolating an initial velocity of 0.1[cm/min] results to depth erosion about 0.77[m] in 12 hours. The alteration of the riverbeds bottom due to erosion has effects on the hydromechanics and therefore on depth erosion velocity, too. But nevertheless for flood protection reasons higher velocities should not be permitted during a flood event. Thus, even when the growth of vegetation helps keeping the

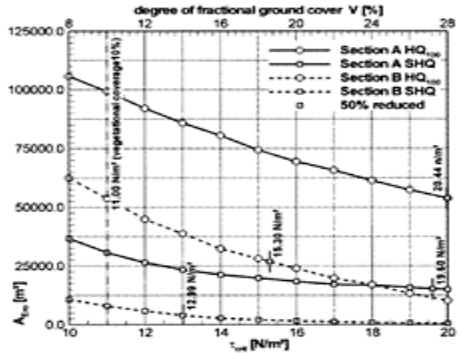

Figure 6. Influence of the degree of fractional ground cover to the total area with supercritical shear stresses.

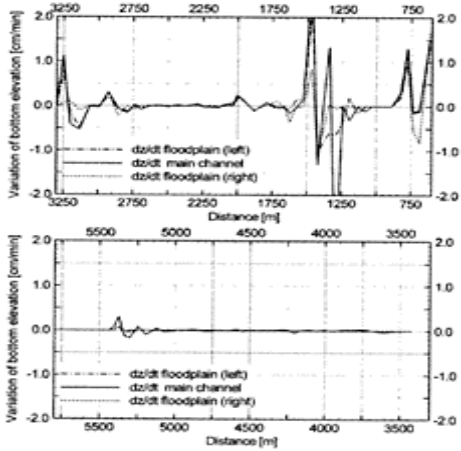

Figure 7. Variation of initial bottom elevation due HQ100 for section A (top) and section B (bottom).

Table 3. Sections to stabilize by widening or covering.

	Distance [m]	Left flood plain	Main channel	Right flood plain
1	5500–5100	×	×	×
2	2950–2850	×	×	×
3	2000–1875	×	×	×
4	1725–1650			×
5	1580–1525	×		
6	1525–1420	×	×	×
7	1340–1280		×	

total endangered area small, some cross sections need to be stabilized to increase τ_c.

Conventional stabilization methods (e.g. bed covering layers) as well as local widening of the riverbed geometry as an alternative are suggested operations to eliminate the risk at the identified points. For all sections with velocities higher than 0.1[cm/min] an enhancement of vegetation is not sufficient, but is suggested as well, because it improves stability for the whole reach of the new Inde. Thus, the new part of the river still keeps its natural character, except for those sections listed in Table 3.

4 CONCLUSIONS

This paper presents the results of numerical modeling the relocation of the river Inde. The aim is to predict influences of ripples, vegetation coverage and the unfinished settlement process.

The results yield, that combining erosion safety and conservation of a natural character is a challenge. A detailed investigation of critical areas and sections endangered by depth erosion is important to estimate the risk of an uncontrolled flooding of the coalmine.

The effects of ripples and slowly growing vegetation during different flood scenarios and specific times between today and the far future were analyzed taking into account the settlement of the river-beds bottom. It is evident, that the best protection against depth erosion is a dense vegetation. Supporting the flora to grow leads to an increase of the critical shear stress and diminishes the total endangered area.

Ripples reduce mean velocities on the one hand but increase shear stresses and prevent a homogenous vegetation layer to grow on the other. The flood plains should be leveled by removing the ripples before the final relocation.

The simulations reveal, that local operations are needed to stabilize regions with initial mass transport rates above 0.1[cm/min].

Finally, it will be interesting to compare the predicted numerical results with measurements made after the flooding in the beginning of the year 2005.

REFERENCES

Baur, T., Lukowicz, J.von & Köngeter, J. 1997. Numerical Optimization of a Riverbed-Geometry with Special Regard to Erosion. In J.Watts (ed.), *Proc. 3rd int. Conf. on River Flood Hydraulics, November 5–7,* Stellenbosch, South Africa: pp. 285–290.

Copeland, R.R. 2000. *Determination of Flow Resistance Coefficients due to Shrubs and Woody Vegetation.* USACE, ERDC/CHL HETN-II-3.

Cowan, W. 1956. Estimating hydraulic roughness coefficients. *Agricultural Engineering* 37(7):473–475.

Kuipers, J. & Vreugdenhil, C.B. 1973. *Calculations of Two-dimensional Horizontal Flow,* Delft Hydraulics Laboratories, Report no. S163–1.

Meyer-Peter, E. & Müller, R. 1949. Eine Formel zur Berechnung des Geschiebetriebes. *Schweizerische Bauzeitung* 67(3), Zürich, Switzerland.

Rijn, L.C.van 1993: *Principles of Sediment Transports in Rivers, Estuaries and Coastal Seas.* Amsterdam: Aqua Publications: 13.

Rouvé, G. & Schröder, M. 1993. One-dimensional vs. two-dimensional prediction of compound open channel flow. *Advances in Hydro-Science and Engineering; Proc. of the ICHE-'93, June 7–11, Vol. 1* Washington DC, USA.

Tucker, G.E. & Bras, R.L. 1999. *Dynamics of Vegetation and Runoff Erosion.* Final Technical Report USACERL, Massachusetts Institute of Technology, Cambridge, MA 02139.

The complex flow in groyne fields: numerical modelling compared with experiments

W.S.J.Uijttewaal

Environmental Fluid Mechanics Section, Faculty of Civil Engineering and Geosciences,
Delft University of Technology, Delft, The Netherlands
S.A.H.van Schijndel

WL\Delft Hydraulics, Delft, The Netherlands

River Flow 2004—Greco, Carravetta & Della Morte (eds.)

ABSTRACT: Groynes are effective as river training structures. At low water levels the main stream is confined, keeping the navigation channel at a proper depth. The relatively high flow velocities at the tip of a groyne cause strong separation effects with possible consequences for the stability of the bed. At higher water levels groynes are submerged, providing more space for the river in lateral direction up to the river banks. In those circumstances groynes also act as an extra flow resistance. In order to explore possible optimization of the effectiveness of groynes at various stages the flow around different groyne types is investigated. Experiments are performed concurrently with numerical simulations. It turns out that the dynamics of the flow structures which are generated downstream of the groyne have a big influence on the circulation dynamics in the groyne field. This paper focuses on the large-scale flow structures in relation to flow separation. The large scale motion causes the instantaneous flow fields to deviate strongly from the mean flow fields emphasizing their role in the momentum and mass transfer from the main stream to the groyne fields. The importance of the large scale dynamics suggests that these should be included in order to model the flow properly. To that end horizontal large eddy simulation (HLES) is applied to the experimental cases. When compared with standard turbulence models like k-ε, HLES performs much better in predicting the overall flow pattern including separation as well as the areas of high turbulence intensities. However, the submerged cases with flow separation in the horizontal and

in the vertical plane caused bigger problems to be modeled accurately. Apparently, the stronger three-dimensionality requires a more detailed analysis with a high vertical resolution. Apart from the conclusions regarding the numerical simulations of such complex flows also conclusions regarding the optimal groyne shape could be drawn. The shape of the groyne tip can be adapted such that the horizontal shear is minimized causing a weaker vortex shedding. This can be done by decreasing the slope of the groyne tip in cross-stream direction or by making the groyne permeable.

1 INTRODUCTION

The large variability in river discharge and the expected problems associated with climate changes, increases the demand for a proper regulation of the water level especially with respect to flooding at high stages and navigation in periods of drought. An effective way to fix and confine the flow in a narrow and deep part is by applying groynes. Groynes are usually constructed in the form of impermeable dikes perpendicular to the river bank. At normal discharges the flow is deflected from the erodible bank and confined by a relatively narrow cross section resulting in high flow velocities. Such an arrangement allows for the formation of a channel with the proper navigable depth even at low discharges. At high discharges the groynes are submerged and the lateral confinement is governed by the dikes which are generally located on the flood plane, sufficiently far away from the river axis. The shape and the arrangement of groynes as they are frequently found in North-Western Europe is the result of decades of what could be called evolutionary design. Given the available construction materials the design has been adapted to the predominant flow conditions United Nations (1953). With the changing climate and the changing viewpoints with respect to the environment and the increasing importance of the ecology a reconsideration of the current river environment appears appropriate. Considerations in this respect are:

- Increasing the discharge at high stages.
- Keeping the navigation channel at proper depth.
- Increasing the biodiversity.

In order to explore the possible improvements that can be made to the river, it is necessary to have the disposal of a realistic and accurate way of modeling the flow. Naturally the flow is not the only important property, but a proper insight in the flow is a prerequisite for the forecasting of e.g. sediment transport and ecological developments, Przedwojski (1995), van Mazijk (2002), Arlinghaus et al. (2002).

Unfortunately it is not always possible to perform a full scale analysis in comparing field measurements with numerical simulations. The intermediate step of a physical scale model is therefore an approved way to validate the proper representation of the physical processes as implemented in the numerical model.

For the purpose of investigating new groyne designs as well as determining the suitability of numerical simulation techniques, a number of experiments has been performed and compared with numerical simulations Uijttewaal (2004). The complexity

of the flow in a groyne field provides a test case with respect to many properties. For the groyne designs used in this study the relevant properties are:

- Flow separation in the horizontal and vertical plane, at a sharp edge as well as a straight smooth wall.
- Large vortex structures and gyres.
- Flow through a permeable obstacle.
- Inhomogeneous distribution of turbulent kinetic energy and shear stresses.

A satisfactory representation of these properties will be a hard requirement for a numerical model. Once the reliability of the numerical simulation is established, it can straightforwardly be used for a number of other applications.

2 PROBLEM DESCRIPTION

Accurately modeling the complex flow in groyne fields requires a proper representation of the relevant physical processes in both the physical and the numerical model. Especially in a flow dominated by separation and vortex shedding, the turbulence and its dynamics are considered as very important.

Until now little systematic research has been performed on the effects of the groyne shape on the flow field and its dynamics. The possible advantages of a new groyne design should be known in advance in order to justify modifications to be made on the prototype scale. With the present knowledge and means it is hardly possible to make reliable predictions and to explore new groyne designs.

3 AIMS

In this study we would like to find out what modifications in the groyne design can lead to a more smooth and quiet flow field. This to provide the means to manipulate the flow and to prevent scour.

With respect to the numerical modeling it is important to know how well the present models perform. In view of new developments with respect to Horizontal Large Eddy Simulation (HLES) it is especially important to explore the possibilities of this promising technique in civil engineering applications. An important aspect in this respect is the implementation of the relevant geometrical details determining the properties of the groyne. Given the large scale applications and high Reynolds numbers encountered in practice, performing a full three dimensional LES with sufficient resolution to justify a standard sub-grid model appears unlikely for the coming decades. We therefore have to deal with numerical models with a limited resolution and some remaining degrees of freedom, like the implementation of sub-grid phenomena and boundary conditions and the grid dimension in the vertical direction.

4 APPROACH

Four different groyne designs were tested in laboratory experiments on a schematized and scaled physical model. For a few cases the observed mean flow field and turbulence properties were compared with the results obtained from a numerical model.

4.1 *Experiments*

In order to test the groynes and validate the numerical model, a number of flow conditions and geometries were implemented. These cases were also used in an earlier study on groyne optimization (Uijttewaal et al. 2002, Uijttewaal 2004).

In a physical model scaled 1:40 with respect to a prototype river reach, a schematized bathymetry was realized consisting of an array of groynes situated on a shallow part near the bank. Since the simulated river width was much larger than the range influenced by the groynes it appeared sufficient to mimic only one half of the river. A top view of the flow facility is sketched in figure 1.

Five groyne fields were built in a flume 30m long and 5m wide. The bed of the main channel was 8cm lower than at the transition to the groyne fields. The level rises towards the bank to an elevation of 15cm. With a water level of 25cm in the main channel, the most shallow part in the groyne field was 10cm deep and the groynes are just emerged. For the submerged cases presented here a water level of 30cm was used, providing a 5cm thick water layer flowing over the groyne crest. With a mean velocity of 0.35m/s in the main channel and an estimated velocity of approximately 0.1m/s in the groyne fields, the flow can be considered as fully turbulent everywhere in the domain.

The various types of groynes that were tested were designed with respect to minimization of the shear induced vortex formation downstream of the groyne tip. Four different groynes are depicted in figure 2. Type A is considered to be the reference case and represents the design as it is found in many rivers with a slope of the groyne tip of 1:3. With type B the slope at the groyne tip has been adjusted to make it more gentle (1:6) in order to broaden and weaken the mixing layer thereby reducing the formation of large vortex structures. Another way to achieve this is by making the groyne permeable. Type C consists of a pile sheet made of square rods with sides of 1cm spaced such that in the near bank area the blocking fraction is 50% and 40% near the main channel. Combining the possible advantages of type B and C results in a hybrid groyne D which is partly permeable. An extensive measurement programme has been performed in order to test the design with respect to the required flow properties (Uijttewaal et al. 2002). Measurement techniques used to comprise particle tracking velocimetry (PTV) and laser Doppler anemometry (LDA). The focus is on the area around and downstream of the groyne tip, the location containing the largest shear and highest turbulence intensity. This area is indicated by gray squares in figure 1 and covers 1.5m by 1.5m. Floating particles of 3mm diameter were distributed homogeneously over the domain and recorded with a 1kx1k digital camera at 30Hz during 5 minutes. Adjacent areas were recorded in separate experiments. The small differences in camera calibration and orientation, in experimental conditions and lens distortion, impeded a seamless connection between the different

areas. The observed errors are however sufficiently small to allow conclusions in the comparison with the numerical model.

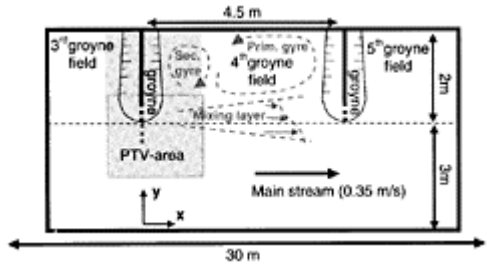

Figure 1. Sketch of the flow facility (top view) including the main flow features.

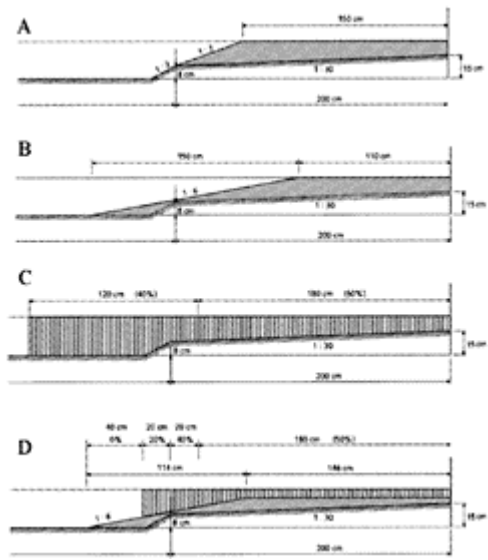

Figure 2. Cross-sectional views of the four groyne types as used in the experiments.

4.2 *Numerical model*

Given the complexity and the dimensions of the domains that have to be dealt with when used for fullscale applications, a two-dimensional depth averaged description of the flow is the starting point. The results of the simulations should therefore be seen as a test as to what extent the efficient depth average modeling is suitable for our applications. It will

be clear in advance that strongly three-dimensional features as occurring with submerged groynes are not likely to be fully covered by the model.

The numerical hydrodynamic modelling system Delft3D-FLOW approximates the non-linear shallow water equations in two or three dimensions. These equations are derived from the fully three dimensional Navier Stokes equations for incompressible free surface flow, assuming hydrostatic pressure. The contribution of 3D turbulent eddies to the vertical exchange of horizontal momentum and mass is usually modelled through a vertical eddy viscosity computed by means of a k-ε turbulence model.

Present questions in river engineering, however, require a more detailed description that resolves the dynamics of the flow, covering a range of turbulence scales, that reaches from the small scale 3D turbulence, through quasi-2D turbulence up to the largest geometry scale. A proper description of quasi-2D turbulence is especially important when dealing with flow dynamics in groyne fields. The classical approach would be to follow the concepts of unsteady Reynolds-averaged Navier-Stokes as mentioned above and accordingly design a closure for quasi-2D turbulence. Previous work however has shown the disadvantages of such an approach (Nassiri et al. 1999, Bijvelds et al. 1999). We therefore prefer to simulate the quasi-2D turbulence and still model the 3D turbulence with the well known closures. To this end we have applied the depthaveraged option of Delft3D-FLOW in combination with horizontal large eddy simulation, further referred to as HLES. This concept will be used to describe the important dynamical variations of the flow which are necessary to obtain a better understanding of complex processes such as erosion and sedimentation in a groyne field and around a groyne tip.

A particular type of turbulence closure is required for representing the action of the unresolved part of quasi-2D turbulence. The latter turbulence closure is called subgrid-scale (SGS) model as it depends on lowpass filtering of the spatially varying flow field by the choice of the mesh size. The sub-grid scale model as applied in this study has been described extensively in Uittenbogaard & van Vossen (2003). In brief the SGS eddy viscosity accounts for the direct energy loss by bed friction. Rather than spatial filtering, a simple temporal recursive high-pass filter is applied on the resolved velocity field. This filter removes the slow or steady large-scale contributions to the strain rates that enter the sub-grid model. It has been successfully tested in shallow and stratified flows.

To be able to compare the measurements in the physical model directly with the simulations, the numerical model was applied to the same geometry. The mesh size Δx of the model sets limits to the scales that can be resolved, typically of the order of $6\Delta x$. The important energy containing horizontal eddies should typically be larger than this size. Further restrictions are imposed by the geometry of the groynes that can be represented and the details of the flow pattern around them. It is important in this respect to avoid influences of the grid implementation on the separation of the flow at the head of the groyne. An advantage of the geometries as used here is that flow separation occurs at the relatively sharp groyne tip. Because of the combination of a straight flume with groynes perpendicular to the flow a curvilinear grid does not have an added value. A choice is made for a very fine rectangular grid with a typical mesh size of 5–10cm, being of the order of the water depth, and yielding about 68,000 active horizontal grid points. In the depth averaged case we have obviously used only one layer.

At the upstream boundary we defined a Riemann boundary with the velocity of the main channel (0.35 m/s) and the downstream boundary condition is formed by a constant

water level corresponding to the water level in the scale model. The roughness of the main channel and the groynes is characterised by a Nikuradse roughness $k_{nikuradse}$=0.6mm, and is based on measurements in the main channel in the scale model. Friction caused by the side walls in the groyne field was accounted for.

Because of the fine grid it was possible to include the shape of the groynes of type A and B in the bathymetry. In the emerged situation we placed socalled 'thin dams' at the crest to prevent numerical disturbances caused by overtopping of the groynes. To be able to simulate the dynamics in the case of permeable groynes of type C and D we prefer to model them as dry points in the numerical grid, but this is only possible if the groynes are not submerged. In case of submerged permeable groynes an additional roughness value needs to be defined to account for the effect of the groynes.

5 RESULTS

In this section the velocities as measured at the free-surface with the PTV-method are compared with the depth-averaged results of the numerical simulations. Although the flows can be considered as shallow different results are expected due to this method of comparison. It will however be clear that the gross features of the flow should be similar.

As a starting point the standard groyne, type A, is considered in non-submerged conditions. For that case the groyne field can be considered as a shallow cavity where the flow separates at the upstream groyne tip as sketched in figure 1. The mixing layer that develops between the main stream and the groyne field plays a role in the momentum transfer to the groyne field circulation. For the chosen width to length ratio of the groyne field a circulation pattern is expected consisting of two counter-rotating gyres which causes a second separation point along the straight side wall. These characteristics are well reflected in the results shown in figure 3, which shows the magnitude of the flow velocities in an area that ranges in streamwise direction from 0.5m upstream of the groyne to 4m downstream and in y direction from the bank (y=5m) into the main stream. In the lower part of the graph the main stream direction is from left to right as indicated by the arrow. The agreement between the numerical and experimental data is good. The same holds for the characteristic enhanced turbulence intensity as found in the mixing layer downstream of the separation point and around the stagnation point at the upstream side of the groyne. In the numerical simulation the mixing layer turbulence is more pronounced while the fluctuations in the upstream part of the groyne are underestimated. Despite this mismatch, the large scale motion appears sufficiently two-dimensional to be represented by a depth averaged model.

As soon as three-dimensional effects start to play a significant role the discrepancies between the experiments and the depth averaged model increase. For groyne B the wake of the submerged groyne tip (with

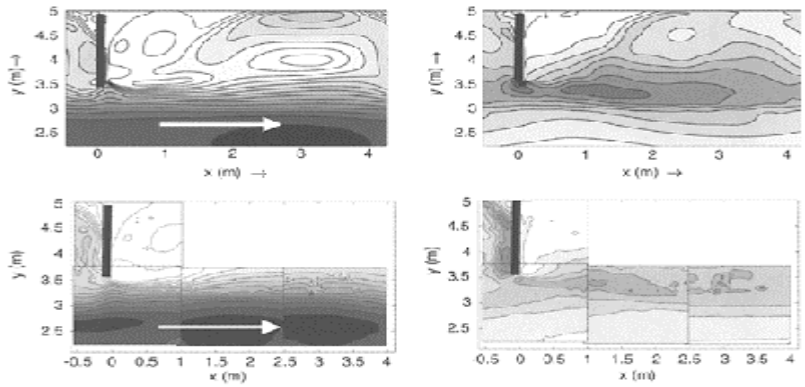

Figure 3. Magnitude (left column) and standard deviation (right column) of time-averaged flow velocity in fourth groyne field of type A in emerged situation, magnitude ranging from 0 m/s (white) to 0.35m/s (black) in intervals of 0.025m/s and standard deviation ranging from 0m/s (white) to 0.1m/s (black) in intervals of 0.01m/s. Numerical simulations (upper row) experiments (lower row). Thick line indicates groyne crest.

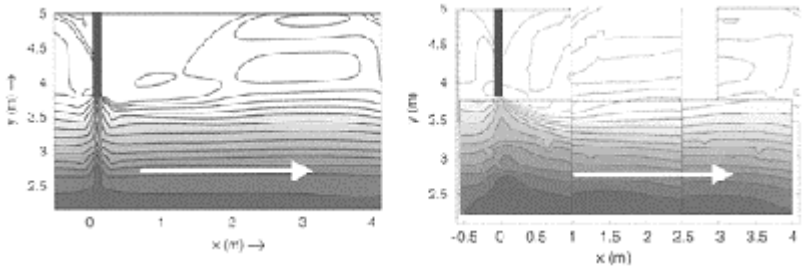

Figure 4. Magnitude of time-averaged flow velocity groyne B in emerged situation, magnitude ranging from 0m/s (white) to 0.35m/s (black), a comparison between numerical

simulations (left) and experiments (right).

slope 1:6) typically contains strong vertical velocity components. In both the mean flow pattern and the turbulence intensities clear differences are found. Comparing figure 4-left with 4-right, the flow pattern around x=0m is symmetric. The flow over the groyne tip is asymmetrical in the experiment because of the flow separation in the vertical plane. The separation downstream of the groyne tip gives also rise to an enhanced production of turbulent kinetic energy in this area which can obviously not be reproduced by the numerical model (not shown).

Similar effects are found with the submerged case of groyne A, figure 5. The flow over the groyne crest gives rise to separation in the vertical plane with clear consequences for the effective resistance of the obstacle. Important differences between the experiment and the

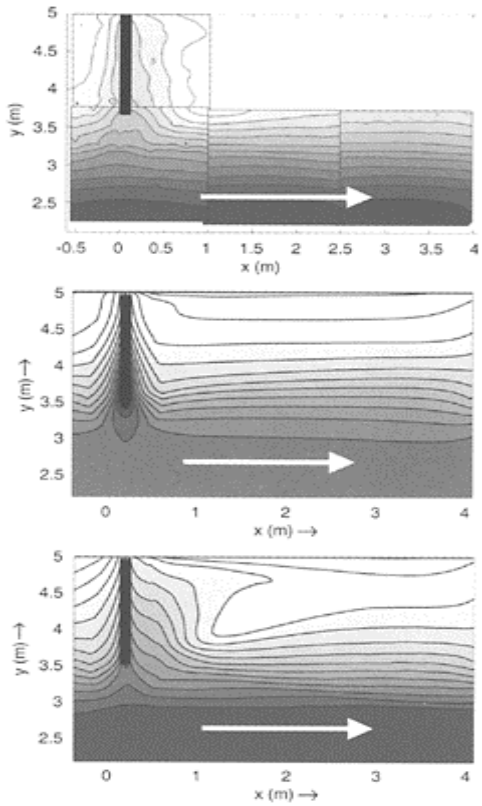

Figure 5. Magnitude to time-averaged flow velocity for the sumberged groyne A. A comparison between

experimental data (top) a depth-averaged numerical approach (bottom-left) and a 3D-approach with 20 layers (right).

simulations are therefore found in the mean velocities over the groyne which are generally overestimated by the numerical model (see figure 5-top and 5-bottom-left), in the asymmetry in the flow pattern upstream and downstream of the groyne and in the production of turbulent kinetic energy which is clearly underestimated. A clear improvement is obtained with a 3D-approach of 20 layers (figure 5-right). The asymmetry in the flow over the groyne is clearly reproduced and the maximum velocity is significantly reduced. Such computation are rather expensive and not feasible for general applications. An even more realistic solution is expected from the use of a non-hydrostatic model.

Further complications appear when the groyne is made permeable as in the cases of types C and D. The amount of water that flows through the groyne field is determined by the effective resistance of the pile sheet. It is however far from trivial to implement the effective properties in a realistic manner, since the resolution does not allow the simulation of all flow details around the piles.

A few tests have been made on the configuration of the partially permeable groyne D, for which the experimental results are depicted in figure 7-left. The gradual increase of the area blocked by the groyne going from the channel towards the bank, combined with the permeable part on top gives also rise to a smooth velocity profile. The mixing layer extends over more than 1m, resulting in a horizontal velocity gradient half of that with groyne A. Still the velocity near the bank($y>3.5$m) is small with a small recirculation zone in the downstream part of the groyne field. The obstruction by impermeable part and the turbulence production by the flow through the groyne give rise to these low velocities, in combination with a relatively high turbulence level downstream of the groyne. The simplest implementation of this flow impediment, is an additional surface roughness on top of the nonpermeable part of the groyne. In figure 6-left it is clearly seen that this leads to an unrealistic solution. The roughness hardly affects the flow and the major effects are caused by the bathymetry around the impermeable base of groyne D. The alternative implementation of the permeable part of the groyne in the form of dry points is an improvement but there still is a significant discrepancy with the experiments. Blocking the flow through the groyne has a clear eifect on the flow through the groyne field and the formation of a mixing layer at the interface with the main stream. A combination of both the increased roughness and the dry points leads to a more satisfactory solution, figure 7-right. Clearly the resistance of the groyne and the disturbances generated by the piles are both necessary ingredients that govern the flow field. The comparisons with the experiments of figure 7-left show that not only the pattern of the mean velocity is similar in shape and amplitude, but also the distribution of the turbulence intensities. The most important difference is found just downstream of the grid. The extra turbulence produced by the flow through the goynes is not well represented by the model, partly due to insufficient resolution.

6 CONCLUSION

This study shows that the different groyne designs used, give rise to a variety of flow phenomena where flow separation and turbulence production are important. The lateral transport of momentum from the

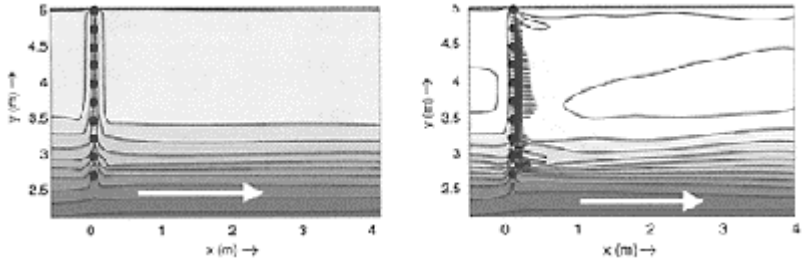

Figure 6. Mean velocity magnitude for hybrid groyne D emerged. Results for hybrid groyne defined as additional roughness in the left graph and results for hybrid groyne defined as dry points in the right graph.

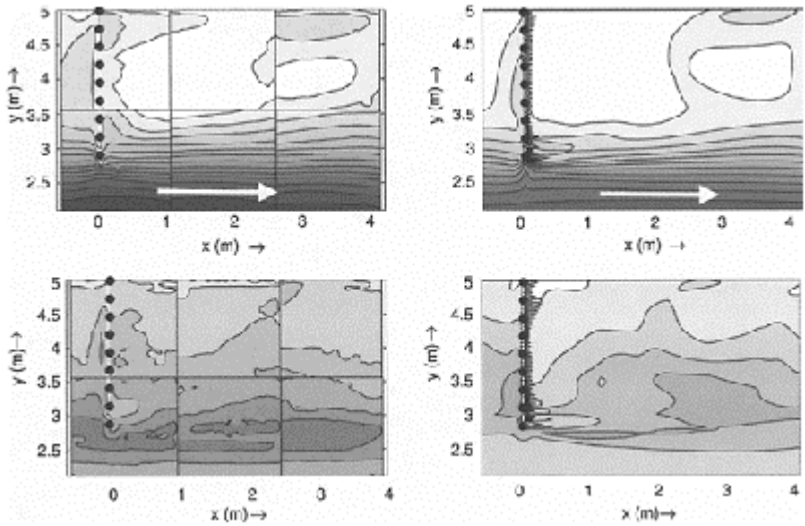

Figure 7. Mean velocity magnitude for hybrid groyne D emerged (upper row) and standard deviation (lower row). Scale model results in left column and

computations in right column, where the hybrid groyne is represented as dry points with additional roughness between piles.

main stream drives a circulation in the groyne field. The horizontal velocity gradient in this area gives rise to the enhanced production of turbulent kinetic energy. The strength of the velocity gradient depends on the velocity inside the groyne field and the shape of the groyne tip. By adapting the shape of the groyne, the turbulence properties in the mixing layer can be manipulated. Making the groyne permeable suppresses the recirculation and weakens the shear in the mixing layer. At high water stages the flow over the submerged groynes separates downstream of the groyne crest resulting in an increased flow resistance and small velocities in the groyne field. Knowledge with respect to the relationship between the geometrical properties of the groyne and the hydrodynamical consequences provides us with clues for e.g. optimising the conditions for a certain envisaged habitat for biological species; high versus low exchange rates with the main stream, high versus low velocities and turbulence intensities etc. The different turbulence production mechanisms associated with the horizontal and vertical flow separation as well as the wall and bottom boundary makes a numerical simulation of such flows troublesome. It is clear that we have tested the numerical model against a number of cases, which are known beforehand to cause difficulties. Especially the submerged case containing typical three-dimensional effects is not very likely to be properly represented by a depth averaged model. Also the permeable and hybrid groynes are problematic when the resolution does not allow for resolving the flow in the wake of the rods and in between the rods. Nevertheless, the important phenomena of the complex flow in groyne fields could be reasonably well simulated after sufficient adaptation of the simulation configuration and boundary conditions. Obviously, it is preferred to have a model that does not need tuning of certain boundary conditions or an unrealistic implementation of an obstacle in the form of roughness elements.

This study has however helped us in finding the important aspects that have to be taken into account when modelling complex flows as found in groyne fields. It is expected that with this knowledge further improvements to our modelling approach can be made, leading to a simulation tool that is of help for a detailed optimisation of the hydrodynamics in groyne fields and its consequences for morphology and ecology. Important properties in this respect are: exchange between main stream an groyne field, velocity magnitude, turbulence intensities, local bed shear stresses, etc.

ACKNOWLEDGEMENTS

The Road and Hydraulic Engineering Division of the Ministry of Transport, Public Works and Water Management is gratefully acknowledged for supporting this research financially. The authors are indebted to M.Berg for her contribution to the experimental work.

REFERENCES

Arlinghaus, R., Engelhardt, C., Sukhodolov, A. & Wolter, C. 2002. Fish recruitment in a canal with intensive navigation: implications for ecosystem management. *J. Fish Biology* 61, pp. 1386–1402.

Bijvelds, M.D.J.P., Kranenburg, C. & Stelling, G.S. 1999. 3D numerical simulation of turbulent shallow-water flow in square harbor. *J. Hydr. Eng.*, 125(1), pp. 26–31.

Mazijk, A.van, 2002. Modelling the effects of groyne fields on the transport of dissolved matter within the Rhine Alarm Model. *J. of Hydrology* 264, pp. 213–229.

Nassiri, M, Babarutsi, S. & Chu, V.H. 1999. Wall Boundary Conditions on Recirculating Flows Dominated by Bottom Friction. *Proceedings XXVIII.* Proceedings XXVIII, IAHR congress, Graz, Austria. 1–6.

Przedwojski, B. 1995. Bed topography and local scour in rivers with banks protected by groynes. *J. Hydr. Res.* 33(2), pp. 257–273.

Uijttewaal, W.S.J., Berg, M.H. & van der Wal, M. 2002. Experiments on physical scale models for submerged and non-submerged groynes of various types. Int. Conf on fluvial Hydraulics, Louvain-la-Neuve, Belgium. pp. 377–383.

Uijttewaal, W.S.J. 2004. Large scale dynamics in groyne field flows: laboratory experiments. *submitted.*

Uittenbogaard, R.E. & Vossen, B. van 2001. 2D DNS of quasi-2D turbulence in shallow water, *DNS/LES Progress and Challenges. Third AFOSR International Conference, Arlington, Texas* (Greyden Press, Columbus, Ohio, USA), pp. 577–588.

Uittenbogaard, R.E. & Vossen, B. van 2003. Subgrid-scale model for Quasi-2D turbulence in shallow water. *Proc. Int. Symposium on Shallow Flows*, Balkema (to appear).

United Nations 1953. Economic commission for Asia and the far east “River training and bank protection”, *Flood control series* 4, Bangkok.

Groyne optimisation and river hydrodynamics

G.J.Akkerman & M.A.van Heereveld

Royal Haskoning Consultants, Architects and Engineers, Nijmegen, Netherlands
M.van der Wal & J.M.T.Stam

Ministry of Transport, Public Works and Water Management, Directorate-General of Public Works and Water Management, Road and Hydraulic Engineering Institute, Delft, Netherlands

River Flow 2004—Greco, Carravetta & Della Morte (eds.)

ABSTRACT: Groynes are widely used in the Netherlands, mainly to promote or maintain nautical depth and a stable main channel. Most of them have been designed and constructed more than a century ago. Since then damage to the groyne head, settlement of the crest or outflanking of some groynes has occurred. A mathematical model study, with a 1-dimensional morphodynamic model, has been carried out to examine the average sedimentation that may be caused by damaged groynes. Based on the work presented in this paper, our understanding of the rate of sedimentation, the effects on the flood water levels and the effects of groyne repair has increased. A challenging outcome is that, although repair should be carried out for river stretches where nautical depth is critical, in other stretches we may consider delaying repair to reduce flood levels. The paper ends with suggestions for further research.

1 BACKGROUND

During the last 150 years, approximately 3600 groynes have been constructed in the main Dutch rivers and channels. Groynes in Dutch rivers have four functions:

– reducing the risk on the formation of ice dams;
– maintaining nautical depth for inland navigation;
– riverbed fixation;
– bank protection and land reclamation between groynes.

The present design method of groynes is mainly done using ‘rules of thumb’, some of them dating from the 19th century and mainly based on trial and error. Up to now groynes have fulfilled their functions fairly well. However in recent years, extreme river floods have raised the priority for flood protection measures including optimisation of groynes. These extreme floods caused us to regard groynes as obstructions which increase the extreme flood levels. Long term trends such as climate change, increase in size and engine power of inland navigation, as well as the increasing need for maintenance efficiency, compel us to reassess groyne design and groyne maintenance.

2 RESEARCH OBJECTIVES

In this research we seek to develop practical rules for the optimisation of groyne design and groyne maintenance. The most important function groynes have at present is to maintain nautical depth in the fairway. Therefore any changes in groynes might have effect on sedimentation, and as a consequence may bring about costly dredging. A second important aspect is that flood waves should pass the river smoothly with a minimum of resistance so as to avoid flooding. This means that the flow channel should preferably have as few obstacles as possible. Obviously these are two conflicting aspects. From the point of view of flood management, there is a tendency to lower existing groynes. However, this leads to sedimentation of the navigation channel which is undesirable from nautical point of view.

By experimenting with different groyne designs we seek to provide the best design for these two main functions. Another approach is to focus on groyne maintenance. Groynes may sometimes have deteriorated in height, the groyne head may have steepened or the attachment of the groyne with the floodplain may be lost (outflanking by which a bypass channel may develop). An example of the ouflanking is shown in Photograph 1.

The attendant reduction of flow obstruction is favourable for flood wave passage. However, as a secondary effect the reduced obstruction will cause sedimentation of the main channel, which in turn affects the nautical depth. The question rises which of the two effects is most dominant. The present paper will address this question and will deal with the prediction of the potential sedimentation for the damage types mentioned before.

3 RESEARCH METHOD

3.1 *Typical sedimentation and erosion pattern*

The bed pattern near groynes is strongly 3-dimensional, as illustrated in Figure 1 in which multibeam measurements are depicted for a characteristic section of the Waal river in the Netherlands. The complex bed pattern is due to the complicated flow pattern near the groynes and in between the groyne fields.

A precise method for prediction of these patterns of erosion and sedimentation is not available up to now. However, damaged groynes will cause an overall sedimentation in the main channel in between the groynes on both sides of the fairway. With a 1-dimensional morphodynamic model such an overall sedimentation can

Photograph 1. Outflanked groyne in the Waal river.

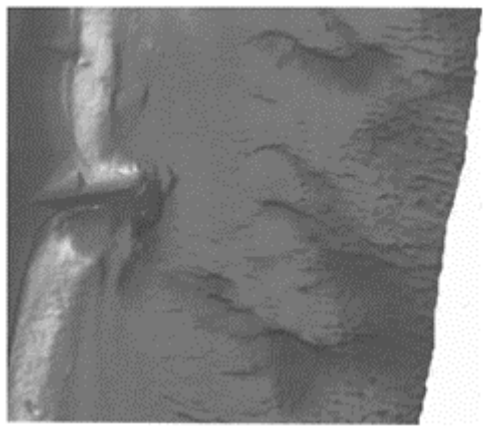

Figure 1. Multibeam measurements of bathymetry near groynes.

be computed rather well. In such a model the sedimentation width can be specified, as well as the pattern of sedimentation, i.e. evenly distributed over the width or linearly with the depth, the latter being the default situation.

3.2 *Mathematical model*

A 1-dimensional morphodynamic model, based on the SOBEK program package, was used in the present study. To this, a 90km stretch of the Waal river was schematised, taking one characteristic cross-section, including a main channel section, a groyne section and a floodplain section, see Figure 2.

The hydraulic performance of the model was calibrated and validated against measurements at different flow rates. A morphologic validation was beyond the scope of the present investigation. Rather, tests have been performed to check the effect of grid

spacing, the required time to arrive at a morphological stable bed, the influence of the time-step and the influence of numerical parameters. The sediment influx to give a stable bed condition in the reference situation (with no damaged groynes) was determined by trial and error. The sediment influx was set at values of $0.021m^3/s$ and $0.0312m^3/s$ for Q_{50} (50% exceedence discharge=$1467m^3/s$) and Q90 (10% exceedence discharge=$2400m^3/s$) respectively. These were the two steady-state discharges with which the model was operated. Furthermore a schematised flood wave was applied, starting with a steady-state flow rate of $2000m^3/s$ (corresponding to Q_{60}) and a subsequent flood wave with a peak discharge of $3000m^3/s$ (corresponding to (Q_{95}); after the flood wave the Q_{60} was maintained for 10 years.

3.3 *Damage situations applied to the model*

In this model three types of groyne damage have been modelled with two damage intensities:

– groyne head steepening: the standard slope is 1:3.5 (vertical to horizontal). Damaged slopes were 1:2 and 1:1;

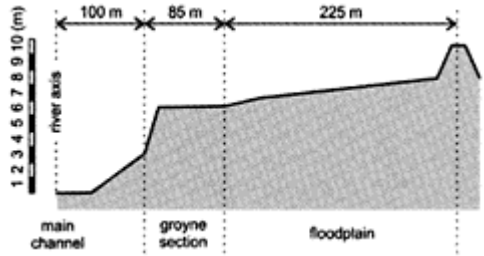

Figure 2. Characteristic cross-section (vertical scale strongly exaggerated).

– groyne height decrease: a decrease of 0.1m and of 0.2m was applied;
– groyne outflanking: a shortening of the groyne of some 15m and 30m has been applied.

Each damage pattern was introduced in the model as a corresponding increase in flow area of the main channel at the cost of the flow blocking area of the groyne section.

The simulations have been done with one, four and eight successively damaged groynes. It was assumed that the groynes opposite the main channel were damaged as well in the same manner. In total 48 model runs have been made, combining the aforementioned flow rates, types of damage and number of groynes. In each of these cases groyne damage resulted in sedimentation in the cross-sections with the damaged groynes. Just downstream of it, a scour hole develops which gradually extends downstream in time.

Another effect of groyne damage is the water level reduction near the damaged groynes. This reduction extends upstream as a backwater curve. This effect is favourable for extreme flood levels. However, as a secondary effect sedimentation will occur which

will decrease river depth and will negatively affect flood level reduction. Simulations are required to indicate the net effect.

3.4 *Repaired damage*

Once damaged groynes are being repaired, related sedimentation migrates as a shoal downstream. At downstream locations the temporary sedimentation will be accompanied by a slight increase in water level. For the repaired groynes, the water levels will increase substantially and will attain the original equilibrium levels.

4 RESULTS

4.1 *Sedimentation rates*

The simulations yielded equilibrium sedimentation rates as shown in Table 1.

These results have been obtained for a permanent discharge of Q_{90} and are independent of the number

Table 1. Review of equilibrium sedimentation rates.

Damage type	Intensity	Sedimentation ($m \times 10^{-2}$)
Head slope steeepening	1:2	6
	1:1	10
Crest height	−0.1m	4
	−0.2m	7
Outflanking	≈15m	14
	≈30m	27

of subsequently affected groynes. The sedimentation area, obviously, is directly related to the damaged groyne fields and extends from the downstream affected groyne to the upstream one.

The results show that for the damage types under consideration considerable sedimentation may occur. Especially outflanking causes serious sedimentation, but the consequences of the other damage types cannot be ignored either. In case of an unfavourable combination of damages and discharges, sedimentation might reach up to about 0.5m.

It should be remarked that the flow rate influences the sedimentation. The equilibrium sedimentation for Q_{90} is 2 to 4 times as large as for Q_{50}. Sedimentation for the schematized flood wave was in between the results for the permanent Q_{90} and Q_{50} discharges. We consider the outcome for the Q_{90} discharge as most realistic, albeit possibly somewhat conservative.

Further analysis showed that the sedimentation rates can be expressed very well in terms of an increase in cross-sectional flow profile. The computed sedimentation show a

nearly linear increase with the increase in flow profile (see Figure 3). In Figure 3 the dependency on the flow rate is also clearly visible. It should be remarked that groyne height reduction is not relevant for the Q_{50} flow condition, as the water level does not exceed the crest of the groynes in that situation. The results show that for damage intensities other than have been considered here, a good prediction can be made based on linear interpolation.

4.2 *Development of sedimentation*

The development of the sedimentation pattern, upon the occurrence of damage, is important as it may take a considerable time to reach equilibrium. The simulations, basically carried out for steady-state conditions (with Q_{50} and Q_{90}) give no definite answer to this. Reaching equilibrium for the Q_{90} discharge took less

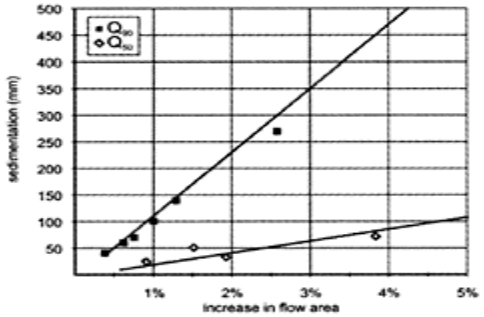

Figure 3. Sedimentation against flow area increase.

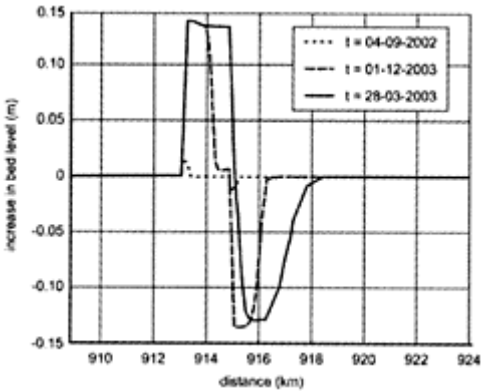

Figure 4. Illustrative example of sedimentation development.

than 1.3 years in the model. Taking into account the relatively high discharge of Q_{90}, the true time for reaching equilibrium in the Waal river will be in the order of magnitude of maximum 10 years. Consequently, sedimentation is likely to occur within a relatively short time. An illustration of the timely development of the sedimentation and the temporary scour hole downstream is shown in Figure 4.

4.3 *Sediment migration after repair*

The sand wave that migrates downstream after repair of the groyne(s) has been simulated in the model for the permanent Q_{90} discharge. Together with the migration of the sand wave, the scour hole migrates farther downstream, starting from the downstream end of the damaged groyne field. The travel time of the sediment wave was found to be about 3.5 years over a distance of 5km. Measurements of sand wave propagation in the Waal river show travel speeds which are in the same order of magnitude.

Both types of waves show a clear decrease of intensity during downstream migration, as can be seen in Figure 5. After migration over 5km, the height of the sand wave reduces to half the original value.

4.4 *Consequences for flood levels*

The increased flow area after groyne damage, as well as the incidental sedimentation pattern, affects the flood levels.

Groyne damage results in an increase of flow area which causes the flood level to decrease. The sedimentation however, increases the flood levels. This effect is however smaller than the flood level decrease. The implications on the flood levels have been checked for the most serious damage, i.e. for the case of outflanking by some 30m. In the equilibrium situation

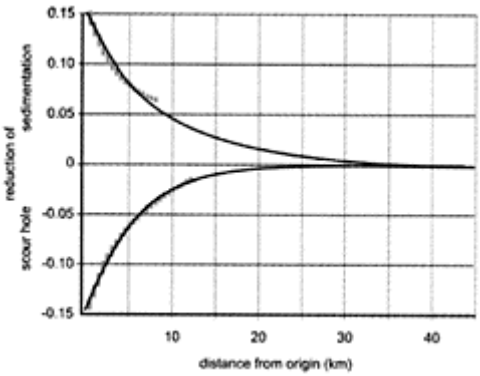

Figure 5. Typical decrease of sedimentation and scouring during downstream migration, after groyne repair.

the net effect on the flood levels is some −5mm for the arrangement with 4 damaged groynes. This flood level reduction tends to increase for a larger number of damaged groynes. For the Waal river this reduction is of significance, as regards the costs involved to arrive at such a reduction by measures in the floodplain.

5 CONCLUSIONS

The sensitivity analysis with a 1-dimensional morphodynamic model yielded practical results as regards the effects on sedimentation and flood water levels after the occurrence of groyne damage. Three types of groyne damage have been considered: steepening of the groyne head, reduction of groyne height and outflanking of the groyne.

Major conclusions are summarized as follows.

1. Groyne damage results in significant local sedimentation and lower flood water levels. The sedimentation ranges from some centimeters to some decimeters, depending on the type of damage. Hence, a combination of damages may potentially cause up to 0.5m sedimentation as an average in the stretch with damaged groynes.
2. The sedimentation may require additional dredging to maintain nautical depth.
3. After repair, the sediment that accumulated during the period that the damage exists, migrates downstream as a shoal over some 10 tot 20km and gradually reduces in height.
4. The flood level reduction may increase to about centimeter for an arrangement of more than 4 groynes (in the case of major outflanking). For less intensive damage it may be in the order of magnitude of millimeters.
5. The findings lead to a challenging concept for groyne maintenance: take action for repair at river stretches where the nautical depth is critical and consider delay of repair at the remaining river stretches. The objective of the latter is to reduce flood levels. This can be a realistic option when the damage is not progressive, as can be expected for head slope damage and groyne settlement with the protective layers still intact.
6. The dependency of sedimentation and flow rate stresses the need to apply realistic discharge scenarios to the model for proper predictions to be used in a strategy for optimized maintenance of groynes.

6 FUTURE WORK

Study on groyne design for the Dutch rivers will continue. The following studies are foreseen:

– A case study on a characteristic groyne damage event in the Waal river, to analyse the effects of the maintenance strategy applied in the past and to verify the bed level changes with the predictions from the present model. When positive, this case can be extended to a major part of the Waal river and a longer maintenance period.
– Verification of the present 1-dimensional morphodynamic model with a 2-dimensional (depthaveraged) morphodynamic model.

– Identification of potential hazardous sedimentation events, i.e. by combining unfavourable flow events and accumulated groyne damage.
– Development of an optimised maintenance strategy for the Waal river based on actual groyne conditions and realistic discharge scenarios. Herein also the effect of vegetation growth on the groynes has to be considered, as well as the present maintenance strategy of cutting willow trees at the groynes after some 5 years. At river stretches with critical navigation depths, the repair costs of the groynes can be balanced against the costs of maintenance dredging. Alternatively, the latter may possibly be skipped at the cost of reduced ship freight.
– Implementation of field tests of innovative concepts of groynes, e.g. with an adjustable crest, in a pilot stretch of the Waal river.
– Extension of the above for other major rivers in the Netherlands.

C.2. Habitat management and maintenance flows

The environmental impact of dams and weirs: technical issues related to the minimum vital flow release

C.Comoglio

Dipartimento di Georisorse e Territorio, Politecnico di Torino, Torino, Italy

River Flow 2004—Greco, Carravetta & Della Morte (eds.)

ABSTRACT: The awareness about impacts on fluvial ecosystems caused by dams and weirs has recently increased in the Italian regulatory framework and the release of the minimum vital flow is now going to be introduced as compulsory for all the new projects and existing sites.

In this paper are identified and discussed the main technical issues that this new legal requirement will determine (technical adjustments in old structures, discharges monitoring and modulated release, flow availability in downstream reaches, release through fish passes, environmental monitoring programme, etc.) and that should be managed through appropriate institutional guidelines and adequately analysed and solved for each site in order to effectively pursue the quantitative and qualitative safeguard of water resources.

1 INTRODUCTION

The use of river water for electricity production, irrigation and other purposes can influence the rivers hydrological balance and cause significant environmental impacts involving directly and indirectly many components of the fluvial ecosystems. Generally the more relevant impacts take place in the downstream reaches because of the alterations of the river hydraulics due to the withdrawal of significant discharges. In particular the reduction (or in many cases the absence) of the discharge in the downstream river sections and, consequently, the alteration of the hydraulic parameters (water level, stream velocity, flow area and wetted perimeter), can alter the water quality and cause significant impacts upon the river biocoenoses.

The release of a limited water discharge from dams and weirs in the downstream river reaches, the so-called minimum vital flow (or instream flow or environmental flow) is the

main and essential mitigation measure that can be adopted in order to reduce the environmental impacts and safeguard the involved ecosystems.

The concept of minimum vital flow *(MVF)* appeared for the first time in the Italian regulatory framework in 1989 with the article 3 of the National Law 183/1989: it stated that a rational use of water resources at watershed level must guarantee a minimum constant vital flow in downstream reaches despite the existing system of water abstraction.

Afterwards, the article 5 of the Decree 275/1993 stated that the release of the minimum constant vital flow must be considered in the water abstraction licences, taking into account the requirements of river water quality and seasonal balance safeguard and the opportunities of saving, reusing and recycling this natural resource.

The Law 36/1994 introduced new elements which developed the definition of the concept of *MVF* towards ecological criteria: sites with significant withdrawals must be regulated in order to guarantee the flow required for the life in the downstream reaches and to safeguard the involved ecosystems balance.

This regulatory scenario and the absence of explicit criteria for the minimum vital flow calculation led different authorities (mainly the Regions of Northern Italy) to the definition of own local technical rules aimed at quantifying the discharge to be released downstream the abstraction sites, mainly based on hydrological criteria. An interesting definition of the minimum vital flow was given by Regione Piemonte in 1995: it is the flow which, inside a watercourse, has to be released in order to keep vital at any time the efficiency and quality conditions of the concerned ecosystems. The new legal requirement became compulsory for new projects and on the occasion of the renewal of the water abstraction licence of existing sites.

Afterwards, in 1999, two regulations introduced new elements for a uniform and systematic application of this release requirement, realigning the wide variety of local initiatives. With the article 12 of the Decree 79/1999 the release of the minimum constant vital flow in downstream reaches for new water abstraction sites (only for hydroelectric use with a mean annual nominal power higher than 3.000kW) became compulsory and a necessary element to be specified in the water abstraction licences.

The Decree 152/1999 introduced a new approach in the water resources safeguard, previously associated only to pollution problems, stating that the qualitative and quantitative aspects must be managed in an integrated way at hydrographic basin level, fixing specific targets of environmental quality for each significant watercourse. The minimum vital flow must be a fundamental element of the future Plans of watershed safeguard and must be taken into account while defining the measures aimed at ensuring the water balance of each basin. Furthermore all the existing sites must be regulated in order to release a discharge calculated using national guidelines.

While the above mentioned guidelines have not been yet defined (making formally inapplicable the legal requirement) and the local technical rules are still in force, recent initiatives are being developed by the Watershed Authorities (institutions composed of State and Regions to manage the watersheds of national importance). In particular the River Po Watershed Authority (widest italian hydrographical basin with a surface of 71.057km^2) defined, with the Decision 7/2002, new criteria that will have to be applied to the whole territory. The minimum vital flow is made up of an hydrological component and an environmental component:

$$MVF = MVF_{hyd} \cdot MVF_{env} = k \cdot q_{MEDA} \cdot S \cdot MVF_{env} \quad (1)$$

where k=experimental hydrological parameter defined for each watershed; q_{MEDA}=average annual specific natural discharge [l/s-km^2]; and S=basin surface [km^2]. The criteria for the calculation of the environmental component MVF_{env} and its range of application shall be defined by each Region inside every Plan of watershed safeguard taking into account the watercourse morphology, the interaction with groundwater, the anthropic pressures upon water quality, the presence of naturalistic, touristic or social interests. All the new projects shall comply with the previous release requirements, while for the existing sites two relevant deadlines have been fixed: all sites must respect the release of the hydrological component by the end of year 2008 and the release of the environmental component, where defined, by the end of 2016.

While the regulatory framework is developing towards the gradual application of the minimum vital flow release to the whole territory, the number of existing dams and weirs currently subject to this requirement is still not relevant: in Regione Piemonte, which has been one of the first local authorities to face the problem and to define specific rules, less than 13% of the total number of existing sites is releasing a compulsory flow.

2 TECHNICAL ISSUES RELATED TO THE MINIMUM VITAL FLOW RELEASE

Especially in the environmental field the attempt to fix univocal criteria and rules often conflicts to the wide variety of different situations and problems which can occurr in reality. This remark applies also to the definition of the criteria for the minimum vital flow calculation, where, even despite accurate hydrological and environmental models, the real availability of natural discharges and the sensitivity of the involved fluvial ecosystems can significantly vary along the same watercourse. Therefore, the hydrological and environmental criteria for the *MVF* calculation should be adequately adapted and calibrated on every site. In this way, through a detailed analysis of the natural peculiarities of the site and the definition of an adequate monitoring system, the value obtained applying the criteria fixed by law can be assessed in terms of efficiency in guaranteeing and safeguarding the fluvial ecosystems. Despite its usefulness in terms of environmental safeguard, this approach is costly and would be unlikely accepted by the owners of the sites unless imposed by law, especially considering that it can lead to an increase of the discharges that should be released and, consequently, to a further reduction of productivity and proceeds.

A preliminary analysis of the environmental scenario and an assessment of the environmental impacts of a dam or a weir is required as compulsory only during the authorization phase for new projects, according to national and regional laws concerning the environmental impact assessment (EIA) procedures, and, in some cases, for the renewal of expired concessions. The environmental impact study (EIS) targets are the evaluation of the most probable environmental impacts caused by the project and the definition of appropriate mitigation measures and monitoring systems to be implemented after the site construction. Within the authorisation phase some efforts should be usefully

made by the competent authorities in order to address the scope of the EIS also towards the prediction of the real environmental effectiveness of the value of *MVF* obtained through the mere application of the criteria defined by the current regulations: in this way regional or national guidelines could better define the contents of the EIS and the analysis to be developed for new projects of dams and weirs.

Finally, when the criteria for *MVF* calculation will be defined by law and applied to the whole territory, two main key-issues will have to be faced: the technical adjustments to be implemented in existing sites (especially in old structures) and, in every site, the evaluation of the calculated *MVF* capability to guarantee the efficiency and the quality of the involved ecosystems. For the second issue specific technical aspects to be considered and solved for each site will be:

– discharge monitoring;
– flow availability in downstream reaches;
– modulation of the releases;
– release through fish passes;
– environmental monitoring programme.

While the provision for releasing the minimum vital flow can be quite easily managed during the project phase, before the infrastructure construction, the technical problems which have to be faced in adapting existing sites to the new legal requirement can be relevant and are mainly related to the typology of the considered structure (concrete dam, earth dam, movable weir with sluice-gates, fixed weir, temporary weir, etc.), to the local geomorphology, to the amount of water to be released and to the possible need to release the discharge through a fish pass. It has to be outlined that if the "natural" discharge coming from upstream is lower than the fixed value of *MVF* adequate devices and settings will have to be implemented in order to guarantee the downstream release of the whole flow. In fact, in the regulatory framework the release of the minimum vital flow is considered a requirement to be respected at local level (in the section immediately downstream the dam/weir) and in every instant (if the "natural" discharge coming from upstream is lower than the fixed value of minimum vital flow nothing will have to be withdrawn and all the flow will have to be released downstream).

All the previous elements contribute to the technical and economic feasibility of the structure adjustment and, together with the loss of productivity due to the *MVF* release, can determine a relevant economic effort by the sites managers. In order to achieve an homogeneous and efficient implementation on the whole territory appropriate technical guidelines should be defined by the competent authorities adressing the sites managers towards the best available technologies and the most suitable and economically viable solutions to be applied depending on the different typologies of water abstraction sites. In this way Regione Piemonte is now operating, with a specific research developed by Politecnico di Torino, through a preliminary review of the main characteristics of all the existing sites and inspections on representative cases and interviews and discussions with their managers: the results will be a technical guideline which will help the sites managers in complying with the new legal requirement.

While the obligation to measure the abstracted discharges and the consequent periodical data transmission to the competent Authorities has recently become compulsory for all sites, there is not a similar precise legal requirement to assess the

compliance to the *MVF* release, which, nevertheless, can be controlled by the competent Authorities through direct inspections in every moment, especially if anomalous flow conditions inside the watercourse are observed. In this scenario the site manager could usefully install adequate devices for the measurement and the recording of both the discharges (abstracted and *MVF*) and the consequent transmission of the recorded data, even in real time. In this case the previous continuous measures could adequately integrate the existing institutional monitoring network, providing new elements for the knowledge of the watershed hydraulic balance. The choice and installation of such devices should be discussed with the competent authorities (or addressed through specific guidelines) and their periodical calibration should be carried out with the supervision of institutional personnel in order to guarantee the reliability of the measures. Furthermore the constant respect of the *MVF* release should be easily verifiable on site by anybody through proper devices showing in real time the value of the flowing discharge.

The measurement of the *MVF* released at the dam/weir section proves the compliance to the legal requirement but not the discharge availability in the downstream river reaches. In fact, depending on the geomorphological and hydrogeological characteristics of the watercourse, the flow could split in many canals or be drained by a river-bed substratum of high permeability, becoming unavailable for the ecosystems needs. The river aptitude to keep in every downstream section the flow distribution of the released discharge in conditions compatible with the environmental safeguard targets is strictly linked to the river slope and width, the sequence of riffles and pools, the granulometry and permeability of the substratum and to the interactions with the surrounding aquifers. All the previous elements should be assessed during the project and operational phases in order to evaluate the adequacy of the calculated *MVF*, implementing, if necessary, adequate mitigation measures such as the increase of the value of released discharge or the setting of a channel inside the watercourse aimed at guaranteeing the constant presence of flow and hydraulic conditions sufficient for the biocoenoses needs. The Plans of watershed safeguard will contain useful elements regarding the basin water balance which could be helpful in outlining the relationships between surface and groundwater and in defining the river reaches more critical in terms of flow availability due to local geomorphologic characteristics.

Since fluvial ecosystems are dynamic, in order to maintain viability and resilience, a range of natural variation in the hydraulic regimen is required and consequently the release of a constant discharge, even if complying with the law, can lead to significant impacts upon the river biocoenoses (fishes and aquatic macroinvertebrates, aquatic and riparian vegetation, etc.). For this reason, especially in reaches of particular naturalistic interest, a preliminary analysis of the watercourse peculiarities could address to a release modulation depending on the more critical period for the involved species, particularly taking into account the ichthyofauna critical/sensitive periods (migrations, spawning and juvenile phases). In this sense the knowledge of the main peculiarities of the fluvial ecosystems is essential and should be seeked not only during the project phase but also for the adjustment of existing sites. Specific analyses should be addresed to identify the most sensitive species and the period where proper caution should be taken in managing the site in order to avoid negative influences upon the biocoenoses. The previous information can be used both for the management of the releases and for the scheduling

of the maintenance operations which can cause an increase of water turbidity and solid transport that usually can affect the survival of eggs, larvae and juveniles.

In some cases, particular needs for increasing the released discharge in limited periods of time can be related to a punctual anthropic presence, such as, for example, when the influx of tourists increases the pressures on water quality and consequently a proper dilution of the pollutants is required, or when the touristic use of the river (canoeing, kayaking, etc.) needs an additional flow.

Then, because of the afore mentioned reasons, the installed hydraulic devices will have to be capable to adequately modulate the downstream release for every circumstance with a consequent increase of the related costs. However, in case of modulated releases, the annual schedule of the additional flows should be included in the water abstraction licence and controlled through the installed monitoring system of the abstracted and released discharges.

The impact of dams and weirs on the river biocoenoses is also relevant because the interruption of the fluvial ecosystem continuity due to the infrastructure can affect fishes migrations and drift phenomena with consequent loss of biodiversity and alterations of the population structure of the involved species. Since the most of the Italian ichthyc species, especially in Alpine streams (Northern Italy), are potamodromous and do not have a significant economical value, except for some interested by sportfishing (mainly Salmonids), fish passes are uncommon (in Regione Piemonte the previous devices are adopted by about 8% of the total number of existing sites) and, where applied, compensatory (e.g. periodical restocking) rather than mitigatory measures were prescribed. A recent local initiative has to be outlined: in 2000 Provincia di Torino defined a regulation which imposed as compulsory the installation of fish passes for the new projects of water abstraction and also for the existing sites on the occasion of licence renewals or extraordinary maintenance works; the requirement applies also to hydraulic works which can interrupt the fluvial continuity.

Nevertheless, due to the fact that existing dams and weirs shall soon face adaptation works in order to comply with the *MVF* release, the competent authorities should seize the opportunity to reorganize the whole sector evaluating if the previous discharge, or part of it, must be released through a fish pass in order to restore the river longitudinal connectivity. This approach should be related to an appropriate knowledge of the watercourse fishes populations and of the characteristics of each species in terms of migratory behaviour during their life cycle. The analyses should consider the whole watershed identifying the potential contribution of each river reach upstream every dam/weir in terms of biological significance for the involved species (availability of spawning grounds, trophic availabilities, etc.) in order to evaluate the real usefulness of such devices and to plan priorities in restoring the ecosystems continuity. A specific section of the Plans of watershed safeguard could usefully deal with the previous aspects. Appropriate technical guidelines could provide the main criteria for the fish passes design, specifying the preliminary hydrobiological and hydrological analyses to be carried out in the project phase, the elements on which the choice of the fish pass typology (artificial by-pass channel, rock-ramp, vertical slot, denil, weir fishways, etc.) should be based (with particular regard to the infrastructure characteristics and local peculiarities), including its location in the infrastructure (on or near the riverbank, in the most upstream point reachable by migrating fishes, etc.), the attractivity of the facility

(hydraulic conditions at the downstream entrance, etc.) and the devices available for its protection (screens, deflectors, etc.), its efficiency monitoring (direct inspections during migration periods, installation of counting devices, etc.) and its maintenance.

If the design discharge of the fish pass, defined through hydrobiological and technical considerations, is lower than the *MVF* value, an additional flow shall be released in order to comply with the legal requirement: in this case the site owner should manage two different hydraulic devices, and provide for an adequate measurement system of the two discharges. Although the total or partial release of the *MVF* through a fish pass will certainly increase the costs (construction, maintenance, monitoring) that the sites owners shall face, the restoration of both the flow availability in downstream reaches and the fluvial ecosystem continuity can be considered a necessary measure which shall be no more ignored.

Finally, the efficiency of all the previous measures should be periodically checked and verifed through an appropriate environmental monitoring programme. While the implementation of a specific monitoring system is compulsory for projects subject to the environmental impact assessment procedure, for existing sites it could be essentially addressed to evaluate the fulfilment of the environmental targets for which the *MVF* has been set and a fish pass has been required; then it could be included as a specific requirement in the water abstraction licence. This approach should not release the competent authorities from their institutional duties charging the sites owner of excessive costs. The definition of adequate indicators, parameters, methods and frequencies should take into account the local peculiarities and be consistent and integrable with the institutional monitoring network of the watershed qualitative and quantitative characteristics. In this way, virtuous initiatives adopted by the sites managers, such as the voluntary adhesion to environmental management systems (ISO 14001 and EMAS), could be appropriately stimulated by the competent institutions since now through the introduction of specific incentives and facilitations.

3 CONCLUSIONS

The release of the minimum vital flow can be considered the main measure for the mitigation of the environmental impact of dams and weirs and the Italian legislation is going to introduce it as compulsory for all the sites. For a useful implementation of this requirement the discharge values obtained applying the normative criteria should be assessed for every site in order to check their efficiency in terms of guaranteeing and safeguarding the fluvial ecosystems. Specific technical issues to be considered and solved for each site are the monitoring of the released discharges, the evaluation of the flow availability in downstream reaches, the modulation of the releases to support ecological and anthropic needs, the release through fish passes and the definition of an environmental monitoring programme. A detailed preliminary analysis of the watercourse natural peculiarities and the subsequent implementation of an adequate monitoring system are fundamental and useful tools to achieve the previous targets.

Since a reorganization of the whole system of water abstractions is necessary for pursuing the quantitative and qualitative safeguard of the water resources it is absolutely desirable that the competent authorities will define appropriate technical guidelines

addressing the sites managers towards the best available and economically viable technologies trying to achieve a sustainable use of this precious natural resource.

REFERENCES

Baron, J.S. et al. 2003. Sustaining healthy freshwater ecosystems. In ESA (ed.), *Issues in ecology*, 10/2003.

Comoglio, C. 2002. EMAS implementation in hydropower plants. In Becciu et al. (ed.), *New trends in water and environmental engineering for safety and life: eco-compatible solutions for acquatic environments. Proc. 2nd International Conference, Capri, Italy, 24–28 June 2002*.

Comoglio, C. & Mattalia, W. 2002. River water abstraction environmental compatibility assessment: the Regione Piemonte (Italy) approach. *Environmental Flows for River Systems. Proc. Fourth International Ecohydmulics Symposium, Cape Town, South Africa, 3–8 March 2002.*

Larinier, M., Travade, F. & Porcher, J.P. 2002. Fishways: biological basis, design criteria and monitoring. In FAO, CSP, Cemagref (co-ed.), *Bull. Fr. Peche Piscic., 364 suppl, 208 p.*

Calculation and visualization of fish movement in the flow with artificial structures

Hiromichi Ohashi & Yasuyuki Shimizu

Hokkaido University, Hokkaido, Japan

River Flow 2004—Greco, Carravetta & Della Morte (eds.)

ABSTRACT: From the engineering and biological view point, it is important to understand the movement of fish in the flow with artificial structures (e.g. fishway) or natural bed topography (e.g. bar and pool). There have been a large number of works on river flow with structures or fishway including numerical computational studies, however, the interaction between real river flow and fish movement have not been clarified. In this paper, an attempt is made to understand the fish movement in the flow by numerical experiment and flow visualization technique. Flow field is calculated by 2-dimensional unsteady, non-compression continuity equation and momentum equations. Momentum equations are separated into the advection phase and non-advection phase. CIP numerical scheme, known as high accuracy numerical calculation, is used in advection phase and central difference method is used in the non-advection phase and diffusion phase. The fish movement is calculated based on the momentum equation of fish derived by the characteristics of fish (e.g. drag and thrust of fish, relation between body length and swimming speed, and relation between swimming speed and sustained time). According to these calculations, the movement for fish in the flow is indicated and visualization of result is shown.

1 INTRODUCTION

In Japan, river improvement works are often made to increace flow capacity, especially in urban area. After river improvement, the ascent of fish is interrupted because bed slope becomes steep or by the influence of artificial structures. Therefore in order to make ascent easy, fishways are installed in rivers where the channel is difficult for fish to ascend. There are a large number of and many kinds of fishways in Japan including Makomanai river, Hokkaido, Japan. Figure 1 is the example of fishway in Makomanai river, Hokkaido, Japan. There are a large number of researches and studies about

fishway, fish habitat and fish characteristics. A study of hydraulic characteristics in fishway was made by Izumi et al (1999), an analysis of fish habitat model in relation to the factor that our humanbeings cause was made by Franzin et al (2003) and an experiment to investigate biological evaluation of fish in fishway was made by Wada et al (1999). Characteristics of fish movement was, however, never indicated by the numerical calculation considering the realation with unsteady flow in the fishway.

In this study, the fish movement when the artificial structures, especially fishways, are set in the flumes is indicated by the numerical calculation. Specifically, each fish is calculated in the flow using the momentum equations of fish after flow calculation is made.

Figure 1. Fishway in the Makomani River.

Furthermore verification of fish movement by the difference of conditions in the fishway (e.g. exist or not the non-submerged obstacles) was made.

2 NUMERICAL CALCULATION OF FLOW

2.1 *Calculation model*

Flow field is calculated by two-dimensional, unsteady, incompressible flow. The continuty equation and momentum equations are showed as follows.

$$\frac{\partial h}{\partial t} + \frac{\partial (hu)}{\partial x} + \frac{\partial (hv)}{\partial y} = 0 \tag{1}$$

$$\frac{\partial (uh)}{\partial t} + \frac{\partial (hu^2)}{\partial x} + \frac{\partial (huv)}{\partial y} = -hg\frac{\partial H}{\partial x} - \frac{\tau_x}{\rho} + D^x \tag{2}$$

$$\frac{\partial (vh)}{\partial t} + \frac{\partial (huv)}{\partial x} + \frac{\partial (hv^2)}{\partial y} = -hg\frac{\partial H}{\partial y} - \frac{\tau_y}{\rho} + D^y \tag{3}$$

where, t is time, x and y are co-orthogonal coordinates, u and v are depth averaged velocity components in x and y directions, respectively. h is flow depth, H is water surface elevation ($=h+\eta$). τ_x and τ_y are bed shear stress in x and y directions, respectively. ρ is water density and g is acceleration due to gravity. τ_x and τ_y can be written using Manning's Equation as follow.

$$\tau_x = \frac{\rho g n_m{}^2 u\sqrt{u^2+v^2}}{h^{1/3}} \tag{4}$$

$$\tau_y = \frac{\rho g n_m{}^2 y\sqrt{u^2+v^2}}{h^{1/3}} \tag{5}$$

where, n_m is Manning's roughness coefficient. D^x, D^y are given by the following equations.

$$D^x = \frac{\partial}{\partial x}\left[\nu_t \frac{\partial(uh)}{\partial x}\right] + \frac{\partial}{\partial y}\left[\nu_t \frac{\partial(uh)}{\partial y}\right] \tag{6}$$

$$D^y = \frac{\partial}{\partial x}\left[\nu_t \frac{\partial(vh)}{\partial x}\right] + \frac{\partial}{\partial y}\left[\nu_t \frac{\partial(vh)}{\partial y}\right] \tag{7}$$

where, v_t, kinetic eddy viscosity is written as follow.

$$\nu_t = \frac{\kappa}{6} u_* h \tag{8}$$

where, κ is Karman constant, u_* is shear velocity and calculated by

$$u_* = \frac{g n_m{}^2 (u^2+v^2)}{h^{1/3}} \tag{9}$$

Flow equations of (1)–(3) are calculated numerically using finite difference method with computational grids in co-orthogonal coordinate system. From Eq. (1) and (2), momentum equation in x direction can be expressed as follow:

$$\frac{\partial u}{\partial t} + u\frac{\partial u}{\partial x} + v\frac{\partial u}{\partial y} = -g\frac{\partial H}{\partial x} - \frac{\tau_x}{\rho h} + \frac{D^x}{h} \tag{10}$$

To solve momentum equations, these equations are separated into two phases of adveciton and nonadvection. A high-order Godunov scheme known as the CIP(Cubic-Inrepolated Pseudo-Particle) method, proposed by Yabe & Ishikawa (1990) and modified for the calculation of open channel flow by Nakayama et al (1998), is adopted for advection phase. An assumption is made that at very small time increasements, the change in time of the velocity components at a point in space can be broken down into the time evolution of the inhomogeneous terms and the time evolution at a point due to the advection of the field. Eq. (10) is separated into three phases of advection, nonadvection and viscous term as follows.

$$\frac{\partial u}{\partial t} + u\frac{\partial u}{\partial x} + v\frac{\partial u}{\partial y} = 0 \tag{11}$$

$$\frac{\partial u}{\partial t} = -g\frac{\partial H}{\partial x} - \frac{\tau_x}{\rho h} \tag{12}$$

$$\frac{\partial u}{\partial t} = \frac{\partial}{\partial x}\left[\nu_t \frac{\partial u}{\partial x}\right] + \frac{\partial}{\partial y}\left[\nu_t \frac{\partial u}{\partial y}\right] \tag{13}$$

The solution of Adveciton phase for small Δt is simply approximated as:

$$u(x, y, t+\Delta t) \approx u(x - u\Delta t, y - v\Delta t, t) \tag{14}$$

The trick then is to find the value of u at points in space which generally do not lie on the numerical grid points, as specified by the right hand side of Eq. (14). If liner interpolation is used to fine u at points not on the grid, the first order Godunov method is attained. A more accurate solution requires higher order interpolation, and thus high order Godunov schemes. In the CIP method, a cubic interpolation of u is proposed, and when the interpolation is combined with Eq. (14) the resultant equation for u at grid point i, j and time $t+\Delta t$ is given by:

$$\begin{aligned} &u(i, j, t+\Delta t) \\ &= \{(a_1 X + c_1 Y + e_1)X + g_1 + u_x(i, j)\}X \\ &+ \{(b_1 Y + d_1 + f_1)Y + u_y(i, j)\}Y + u(i, j) \end{aligned} \tag{15}$$

in which,

$$\begin{aligned} X &= -u\Delta t \quad , \quad Y = -v\Delta t \\ u_x &= \frac{\partial u}{\partial x} \quad , \quad u_y = \frac{\partial u}{\partial y} \end{aligned} \tag{16}$$

And coefficients $a_1 - g_1$ are expressed as follows:

$$\begin{aligned} a_1 = \frac{1}{i_s \Delta x^3}\Big[& i_s \{u_x(i_m, j) + u_x(i, j)\}\Delta x \\ & -2\Delta \{u(i, j) - u(i_m, j)\}\Big] \end{aligned} \tag{17}$$

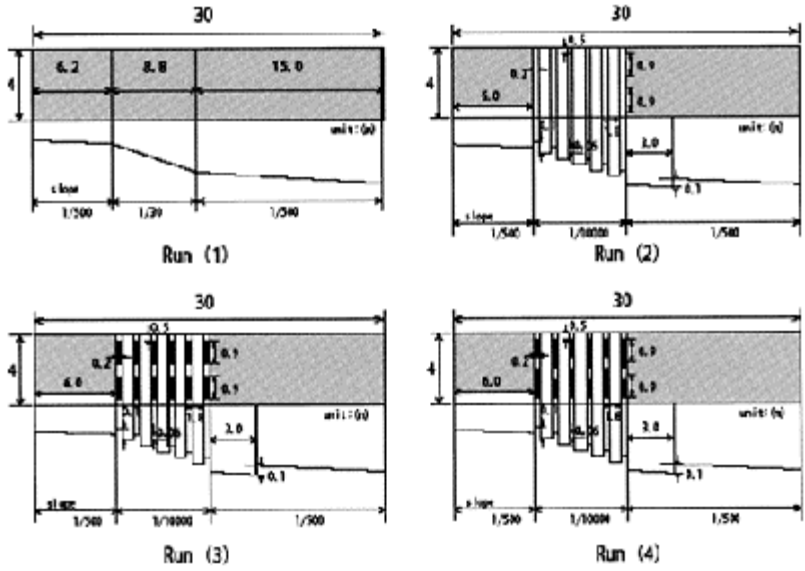

Figure 2. Calculation flume.

$$b_1 = \frac{1}{j_s \Delta y^3}\Big[j_s\{u_y(i,j_m)+u_y(i,j)\}\Delta y - 2\Delta\{u(i,j)-u(i,j_m)\}\Big] \tag{18}$$

$$c_1 = \frac{1}{j_s \Delta x^2 \Delta y}\Big[u(i,j)-u(i,j_m)-u(i_m,j) + u(i_m,j_m) - i_s\{u_x(i,j_m)-u_x(i,j)\}\Delta x\Big] \tag{19}$$

$$d_1 = \frac{1}{i_s \Delta x \Delta y^2}\Big[u(i,j)-u(i,j_m)-u(i_m,j) + u(i_m,j_m) - j_s\{u_y(i_m,j)-u_y(i,j)\}\Delta x\Big] \tag{20}$$

$$e_1 = \frac{1}{i_s \Delta x^2}\Big[i_s\{u_x(i_m,j)+2u_x(i,j)\}\Delta x + 3\{u(i_m,j)-u(i,j)\}\Big] \tag{21}$$

$$f_1 = \frac{1}{j_s \Delta y^2}\Big[j_s\{u_y(i,j_m)+2u_y(i,j)\} + 3\{u(i_m,j)-u(i,j)\}\Big] \tag{22}$$

$$g_1 = \frac{1}{i_s \Delta x}\{u_y(i_m,j)-u_y(i,j)+c_1\Delta x^2\} \tag{23}$$

in which,

$i_s=sign(u)$, $j_s=sign(v)$

$i_m=i-j_s, j_m=j-j_s$ (24)

In Eq. (24), Sigmoid function is employed. Eq. (12) is calculated from the continuity equation by taking the divergence of the momentum equations and solving for depth as a Poisson equation. And Eq. (13), the viscous term, is approximated using central finite differences.

In the same way, velocity component of transverve direction can be computed. Each velocity component is defined in the center of two faces of the computational cells, and depth is at the center of the cell. This method has been explained in detail by Shimizu et al.

2.2 *Flume for calculation*

In this study, flow field in 4 flumes are calculated. Figure 2 shows the detail of the flumes for each case. These flumes are decided based on the real condition of Makomanai River in Hokkaido, Japan. In all flumes, the length and the width are set as 30*m* and 4*m*, respectively. In Run (1) it is assumed that the middle part of the flume became steep after river improvement. In Run (2), (3) and (4), fishways are set in the steep part in Run (1), respectively. Flume in Run (2) corresponds to the weir and pool fishway. In Run (3) and Run (4), addition to Run (2), non-submerged obstacles are set regularly and irregularly, respectively.

The slope in Run (1) is set as 1/30, and 1/500 in the middle part which became steep and in the flume except for the middle part. In Run (2), (3) and (4) the slopes in upstream and downstream are, as well as Run (1), set as 1/500 and in the middle part the vertical drops are made. The total of drops is equal to the difference of middle part in Run (1).

2.3 *Boundry conditions*

As boundry conditions, the discharge and depth are given in the upstream and downstream, respectively. The velocities are set as 0 in and around obstacles which are not submerged.

2.4 *Hydraulic conditions*

The discharge is given as $0.15m^3/s$ based on usually condition in the Makomanai river. The Manning's roughness coefficient is set as 0.014.

2.5 *Numerical conditions*

Computational grids in the downstream and transverse directions are 100 and 30, respectively. The time steps for computations are set to be 0.01 seconds. Calculations are continued for 200 seconds from the beginning.

The calculation is made by these calculation model, calculation method and conditions. The computational flows are created by repeating the later half (from 50sec to 100sec) of the flow for 6 times in the 4 flumes, respectively, after calculation because calculation time, 100*s*, is not enough to grasp the fish movement completely and initial flow is unstable.

Figure 3 shows the result of calculation in Run (4) by neutually tracer. It is shown that the complicated flow occured around non-submerged obstacles.

3 CALCULATION OF FISH MOVEMENT

In this study, the calculation of fish movement is carried out by the characteristics and calculation method of fish movement shown as follow.

The following characteristics are proposed by Itazawa et al (1991) and Hirose et al (1994).

3.1 *The characteristics of fish swimming*

It was assumed that the fish always tries to keep its body parallell to the flow direction, as it cannot swim perpendicular to the flow. Therefore the fish always ascends the river along with the flow but in the opposite direction.

3.2 *The characteristics of muscles*

In general, fish has 2 kinds of muscles known as the “ordinary muscle” and the “red muscle”, respectively. The red muscle can keep being used for a long time as long as the oxygen is supplied without becoming tired. The ordinary muscle can put out to burst up the speed momentarily, but cannot be maintained for a long time because of generating the lactic acid. Fish usually swims in the river using only the red muscle without using ordinary muscle. Ordinary muscle is used only, for example, to avoid danger or to ascend rapid stream. Consequently, the speed of the fish can be characterized as crusing speed (U_{cur}) when only red muscle is used, and Maximum swimming speed (U_{max}) when both muscles are used. Furthermore, these speeds depend on the size of the fish. The value of cruising speed and the maximum swimming speed are usually considered to be about 2–5*BL/s* and 10*BL/s*, respectively, where *BL* is the length of the fish. Moreover, the maximum swimming speed is assumed to be maintained only for a few seconds, since fish can use the ordinary muscle only momentarily. In this study, the maximum swimming speed is able to be adapted for fish swimming even after swimming completely at

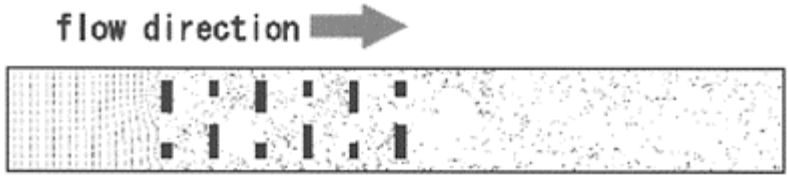

Figure 3. The result of flow calculation.

U_{max} for maximum maitained time based on the above mentioned characteristics in the case that fish swims at cruisig speed or stops moving for constant time.

3.3 *Calculation method*

The method to estimate the fish swimming speed by the momentum equation for fish movement based on the Newton's Second Law was adapted for calculation of fish movement in this study. Because in the case that fish swimming speed are estimated from flow velocity directly, fish turns for many times by the influence of flow rapidly changing at the place where flow is highly fluctuated (e.g. behind obstacles) as the result that direction of fish movement only depends on the flow direction on its moments. Hovever, the swimming direction depends not only on the present flow direciton but also previous direction of fish movement as a result of using the momentum equation for fish. The momentum equation for fish movement is shown as follows.

$$m\frac{\partial \vec{u}}{\partial t} = \vec{T} - \vec{D} \tag{25}$$

where, T and D are the trust and drag of fish, respectively. The acceralation of fish is computed by difference of the trust and drag. The drag of fish D is written as follow.

$$D = \frac{1}{2}\rho C_d U^2 \tag{26}$$

where, ρ is water density, C_d and U are the drag coefficient and relative velocity of fish, respectively. In general, the drag is the sum of the skin friction and pressure drag. In this study the pressure drag, however, is ignored because the pressure drag of streamlined body is small relative to the skin friction. The drag coefficient is decided based on the shape of fish, it is set to be 0.008 in this study. For the trust of fish, T, is separated into 2 kinds by the difference of muscles fish using as previously mentioned. In the case of using both muscles, the red muscle and ordinary muscle, the output is maximum and the trust is written as follow with assumption that the trust is equal to the drag if fish swims at constant speed.

$$T_{max} = \frac{1}{2}\rho C_d {U_{max}}^2 \tag{27}$$

where, U_{max} is the maximum swimming speed. In the case of using only the red muscle, the trust is written as follow because the trust is equal to the drag if fish swims at constant speed.

$$T_{cru} = \frac{1}{2}\rho C_d {U_{cru}}^2 \tag{28}$$

where, U_{cru} is the cruising speed. Seleciton of equation depends on the strength of the flow. In the case that the flow velocity is larger than $0.8U_{cru}$, then the ordinary muscle is used, T_{max} is used and T_{cru} is used in the other case (flow velocity is less than $0.8U_{cru}$).

3.4 *Initial condition of fish movement*

Initial conditions of fish movement for calculation are set as follow. In this study the calculating fish is assumed to be the Sweetfish that inhabits in Makomanai River. The length of fish is 20cm. The maximum swimming speed (U_{max}) and crusing speed (U_{cru}) of fish are 12*BL/sec* and 4*BL/sec*, respectively. The maximum swimming speed can be used for 8 *sec*, after that it can be used for 1 *sec* every 10 *sec*. Five fishes are assigned in calculation and they are placed at downstream location when calculation begins.

4 RESULT OF CALCULATION

Figure 4 shows the result of calculation in each four flumes. Solid lines and dotted lines in each rectangles represent the paths of fish movement in the flume. In Run (1) the paths are stopped at the middle way.

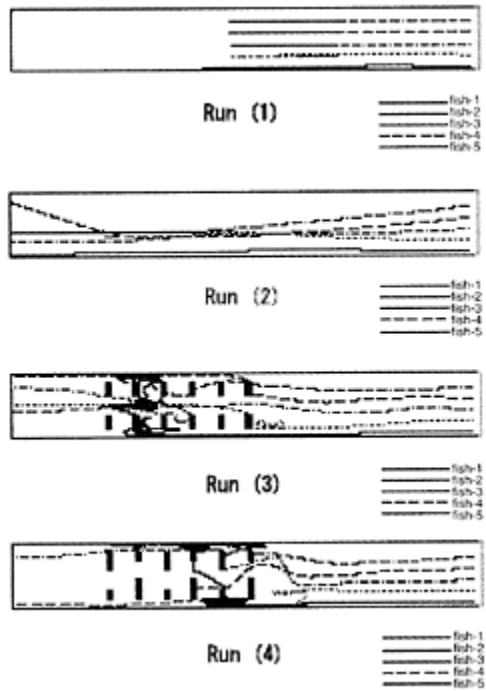

Figure 4. The result of calculation.

It means that fishes could not travel to upstream. In Run (1), compared between the leftside and rightside in the flumes, it is found that the paths in the leftside became thicker. It means that repetition of ascent and descent of fish by the flow in the steep part. In Run (2) all five fishes can ascend because all paths reached upstream oppositely. It is shown in Run (3) that four fishes out of five can reach upstream and each fishes

meandered around the non-submerged obstacles different from Run (2). In Run (4), two fishes out of five can go to upstream and meandered around the non-submerged obstacles as well as Run (3).

5 CONCLUSION

It is indicated that not only the ability of fish to ascend, but also the difference of flume configurations. At first the effect of fishway is clarified because no fish which could ascend at all in Run (1). However, fishes are able to ascend in Run (2), (3) and (4) which structures (e.g. vertical drops, pool, non-submerged obstacles) are set.

Next there are two big differences in Run (2), Run (3) and (4). Firstly, one is that fishes meandered for many times in Run (3) and (4) because the flow is constantly changing in transverse direction by the influence of non-submerged obstacles. Secondly, some fishes can reach upstream, while others could not in Run (3), (4). There are several reasons. Fish could not ascend by the influence of turbulence around non-submerged obstacles, and fish cannot go beyond non-submerged obstacles, because flow velocity becomes fast here. It is not clealy indicated that the ascent of fish is difficult in the narrow place from the Figure 4, but we could verify it from the animation from calculation.

There are no outstanding difference compared to Run (3) and Run (4), but it is found that flow which non-submerged obstacles are set irreguraly make fish difficult to ascend because of the number of fishes which can reach upstream.

Characteristics of parallel ascent and two kinds of muscles are not shown from the paths of result, but they are shown at animation from calculation and numerical analysis of fish movement is made based on the characteristics of fish movement.

REFERENCES

Izumi, M., Kudo, A. and Azuma, N. 1999. Flow characteristics and ascending of fishes in Ice Harbor type fishway of Mitumenai-headworks. *Proceedings of Hydraulic Engineerings, JSCE,* 989–994 (in Japanese)

Wada, K., Koizumi, N., Ishikawa, M. and Nakamura, S. 1999. Upstream migrating route of juvenile Ayu in a modified larinier pass fishway. *Proceedings of Hydraulic Engineerings, JSCE,* 983–988

Franzin, W.G., Nelson, P.A. and Cooley, P.M. 2002. Erosion, transport and deposition; a hydraulics-based approach to fish habitat. *Proc: River Flow* 2002, Louvain-la-Neuve, Belfium

Yabe, T. and Ishikawa, T. 1990. A numerical cubicinterpolated pseudoparticle (CIP) method without time splitting technique for hyperbolic equation, *Journal of the Physical Society of Japan,* Vol. 59, No. 7, 2301–2304

Nakayama, K., Sato, T. and Horikawa, Y. 1998. A numerical study on a shallow water flow using CIP method, *Proceedings of Hydraulic Engineering, JSCE,* Vol. 42, pp.1 159–1164 (in Japanese)

Shimizu, Y., Fujita, M. and Hirano, M. 1999. Calculation of flow and bed deformation in compound channel with a series of vertical drop spillways. *Proceedings of Hydmulic Engineering, JSCE,* 683–688

Hirose, T. and Nakamura, T. 1994. The design of the fishway (in Japanese)

Nakamura, S. 1994. The story of the fish way (in Japanese)
Itazawa, T. and Habu, I. 1991. Fish physiology (in Japanese)
Blake, R.W. 1983. Fish locomotion

An experimental study of velocity fields and flow patterns in aligned deep slot fishways

L.Pena & L.Cea

CITEEC, A Coruña University, A Coruña, Spain
J.Puertas

Civil Engineering School, A Coruña University, A Coruña, Spain
T.Teijeiro

Environmental Engineering School, Santiago de Compostela University, Lugo, Spain

River Flow 2004—Greco, Carravetta & Della Morte (eds.)

ABSTRACT: This paper is a study of the flow pattern taking place in a specific design of aligned deep slot fishways. The analysis is based on an experimental study in which the flow velocities and the water depths were measured in a laboratory model of the fishway. A spatial 3 dimensional mesh was used to measure the 3 velocity components. To measure the water depth a bidimensional mesh was used. Sills of different heights were placed in the slot in order to analyze its influence in the flow pattern. For each different sill, several discharges were used. As a result of the study, the relationship between the discharge and the different characteristic water depths (medium, maximum and minimum depths in the pool) as well as the discharge equations were obtained for each different sill. Three different flow patterns were observed in function of the height above the bottom of the pool. Finally, the slot velocity and the maximum velocity in the pool were analyzed.

1 INTRODUCTION

One of the most important direct effects of the hydraulic constructions in rivers is the perturbation of fish circulation, which, in some cases, can lead to the disappearance of some migratory specimens (Larinier, 1998, Zhong & Power, 1996).

The most common solution to this problem is the construction of fishways to allow the upstream migration of the fish. The aligned deep slot fishways, which are studied in this paper, are a new design which is still not used at the present time in practice. This new design is an hybrid between the aligned vertical slot design and the deep slot design. The difference with the vertical slot design, in which the slot goes down straight to the bottom, is that a sill is placed in the bottom of the slot. In this way a strong vertical velocity component appears in the slot, destroying the quasi bidimensional behaviour of the vertical slot fishways. The object of this study is to analyze the modifications introduced in the flow pattern by the sill and to characterize the hydraulic behaviour of this new kind of fishways.

A basic design which will be referred to as configuration T1 (Fig. 1) was chosen to perform the study (Teijeiro, 2001; Pena, 2003; Puertas, 2004). In Table 1

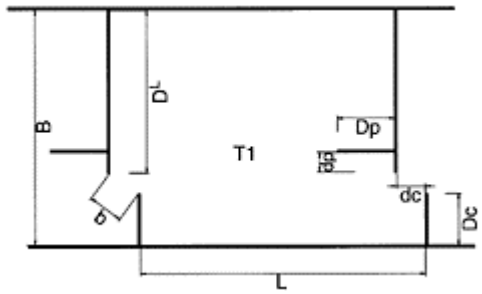

Figure 1. Basic design and dimensions of a configuration T1 pool.

are shown the real and the parametric dimensions of the pool. The bottom slope is 10%.

The height of the different sills placed in the bottom of the slot are 100, 200, 300, 400 and 500mm.

2 EXPERIMENTAL PROCEDURE

The experimental work was carried out at the CITEEC (Centro de Innovación Tecnolóxica en Edificación e

Table 1. Real and parametric dimensions.

	Real (mm)	Parametric (function of the slot width b)
b	160	1.00b
L	1213	7.58b
B	1000	6.25b
D_L	680	4.25b
D_c	217	1.36b

d_c	121	0.76b
D_p	243	1.52b
d_P	86	0.54b

Table 2. Height of the different sills which were placed in the bottom of the vertical slot.

Sill (mm)	Parametric dimension (function of width b)
100	0.625b
200	1.250b
300	1.875b
400	2.500b
500	3.125b

Enxeñería Civil) at the University of A Coruña (Spain). The fishway model consisted on a metallic structure of 12m long with a $1\times1m^2$ rectangular section. The fishway was divided into eleven pools: a head tank receiving the water from an upstream reservoir, nine active pools and a tail tank. The experimental measurements were recorded in pool number 7.

A conceptual state of uniform flow (Rajaratnam et al., 1986, 1992) was used, so that the mean depth measured at the middle transversal section was the same in all the pools. At the lower end of the flume a tailgate causing overflow was used in order to impose the necessary boundary condition to obtain a uniform flow for each different discharge.

A cartesian positioner was placed over the experimental pool in order to automate the positioning of the measurement instruments. Two measurement devices were placed on the cartesian positioner, but not simultaneously: a depth probe and ADV velocimeter.

Velocities were measured by means of a Doppler effect velocimeter (MicroAcoustic Doppler Velocimeter SonTek).

Velocity measurements were carried out in planes parallel to the flume bed with 10cm in between, starting at 5 cm from the channel bed up to as close as possible to the water surface. In each plane, data points were distributed forming a 10×10cm mesh, reduced to 5×5cm in critical zones. Therefore a three-dimensional mesh of 10×10×10cm for the measurement of velocity was maintained.

Table 3. Sills and discharges used.

	Water depth		Velocity	
Sill (cm)	Q (m^3/s)	Number of points	Number of levels	Points per level
10	0.025	111	2	140
	0.035	111	3	140
	0.045	111	3	140

	0.055	111	4	140
	0.065	111	4	140
	0.075	111	5	140
	0.084	111	6	140
	0.094	111	7	140
20	0.024	111	3	140
	0.035	111	4	140
	0.045	111	4	140
	0.055	111	5	140
	0.065	111	5	140
	0.075	111	7	140
30	0.026	111	3	140
	0.035	111	4	140
	0.045	111	5	140
	0.055	111	5	140
	0.065	111	6	140
	0.075	111	7	140
40	0.025	111	4	140
	0.034	111	5	140
	0.044	111	6	140
	0.055	111	6	140
	0.065	111	7	140
50	0.025	111	5	140
	0.035	111	6	140
	0.045	111	6	140
	0.055	111	7	140

Water surface height in the pools was measured by means of a conductivity-based depth probe, DHI Wave Gauge Type 202. Depth measurements in the pools were evaluated following a bidimensional mesh with data points at a 10×10cm maximum separation in between. Calibration tests were performed prior to each working day.

After a previous experimental test, a measurement frequency of 15Hz was chosen.

2.1 *Sills and discharges studied*

In Table 3 are summarized the different cases which were tested. In all cases the bottom slope of the fishway was 10.054%.

2.2 *Discharge equations*

The discharge equations, which relate the adimensional water depth and discharge, were evaluated. The

Table 4. Discharge equations for the different sill heights. The adimensional discharge is related to the adimensional water depth. r^2 is the correlation coefficient.

$Q^A_{210}=0.7939y_0/b-0.583$	$r^2=0.9956$
$Q^A_{220}=0.8185y_0/b-1.040$	$r^2=0.9862$
$Q^A_{230}=0.8571y_0/b-1.666$	$r^2=0.9746$
$Q^A_{240}=0.8174y_0/b-1.981$	$r^2=0.9968$
$Q^A_{250}=0.7741y_0/b-2.264$	$r^2=0.9978$

water depth is adimensionalized by the width of the slot, while the discharge is adimensionalized as:

$$Q^A = Q/\sqrt{g\,b^5} \tag{1}$$

where Q^A is the adimensional discharge, Q is the experimental discharge, g is the gravitational constant and b is the real width of the slot. The discharge equation can be expressed as:

$$Q^A=\alpha(y_0/b)\beta+\mu \tag{2}$$

where y_0 is the mean water depth in the transversal section of the middle of the pool and α, μ and β are proportionality coefficients.

The discharge equations obtained from the experimental data are shown in Table 4, where $Q^A_{210}, Q^A_{220}, Q^A_{230}, Q^A_{240}, Q^A_{250}$ account for the adimensional discharge corresponding to each different sill height: 10, 20, 30, 40 and 50cm.

It was verified that the discharge and the water depth are linearly correlated (β coefficient is equal to 1) and that the proportionality constant a, as well as the coefficient μ depend on the basic design of the pool and on the height of the sill.

All the discharge relations are almost parallel to each other, which shows that, independently of the sill used, the sensitivity of the design to variations in the discharge remains invariable.

2.3 *Characteristic water depths*

The characteristic water depths are those by which the free water surface can be represented. As it was done in the analysis of the vertical slot fishways (Puertas, 2004), the following characteristic water depths are defined: maximum water depth in the pool, y_{max}, water depth in the vertical slot, y_b, mean water depth, y_m, minimum water depth, y_{min}. The water depth in the vertical slot is defined as the difference between the free water surface and the upper part of the sill. Therefore, the depth at both sides of the sill is bigger than the depth in the slot, being the difference of the same order of magnitude than the height of the sill. For the calculation of the minimum water depth it is not considered the slot depth.

Table 5. Relation between the characteristic water depths and the adimensional depth y_0/b. In all cases a good correlation was found, being the minimum correlation coefficient equal to 0.98.

Sill (mm)	y_{max}/b	y_b/b
100	$1.0156y_o/b+0.458$	$0.9984y_o/b-0.538$
200	$1.0432y_o/b+0.324$	$0.9788y_o/b-1.027$
300	$1.0673y_o/b+0.221$	$0.9032y_o/b-1.268$
400	$1.0962y_o/b+0.063$	$0.8233y_o/b-1.565$
500	$1.1072y_0/b-0.042$	$0.9464y_0/b-2.656$
	y_m/b	y_{min}/b
100	$0.9844y_0/b+0.070$	$0.9618y_0/b-0.356$
200	$0.9849y_0/b+0.086$	$0.9499y_0/b-0.303$
300	$0.9903y_0/b+0.064$	$0.9914y_0/b-0.454$
400	$0.9893y_0/b+0.074$	$1.0206y_o/b-0.565$
500	$0.9848y_o/b+0.103$	$0.9096y_0/b-0.080$

A general relation between the mean water depth in the central transversal section and any of the characteristic depths was used:

$$\frac{Y}{b} = \alpha'\left(\frac{y_o}{b}\right)+\beta' \qquad (3)$$

where Y is any of the characteristic water depths defined above (y_{max}, y_b, y_m, y_{min}), b is the width of the vertical slot, y_0 is the mean water depth in the central transversal section and α' and β' are proportionality coefficients.

The computed equations are shown in Table 5.

The values of the characteristic water depths are proportional to the flow discharge, as well as to the height of the sill. The water height over the sill depends on the discharge but it is independent of the height of the sill.

2.4 *Free water surface*

In general it can be found a certain similitude between the patterns found for the free water surface and those to the vertical slot fishways (Puertas, 2004):

– There is an area of high water depths upstream the slot.
– There is a strong diminution of the water depth in the slot.
– The minimum water depth occurs downstream the slot, where a circular depth depression exists.
– After this minimum, in the downstream direction, another area of high depths exists next to the transversal vertical wall which separates the pools.

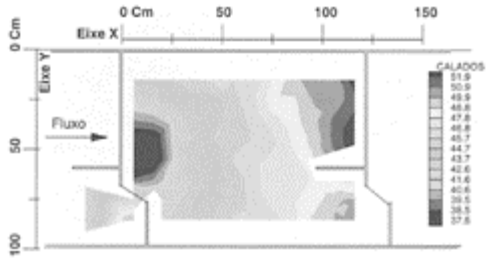

Figure 2. Isodepth lines in the aligned deep slot fishway. The plot corresponds to a discharge of $Q=0.055 m^3/s$ and a sill of 0.10m height.

Apart from these general similitude between the vertical slot and the deep slot designs, there are two mainly differentiating characteristics:

– The position of the circular water depth depression which occurs downstream the slot.
– The distribution of the isodepth lines.

For the vertical slot design, the position of the water depth circular depression is downstream the slot in the direction of the opposite corner of the pool. In the aligned deep slot design, the depression moves upstream towards the transversal pool separation wall.

The second difference is the distribution of the isodepth lines. In the vertical slot design the isodepth lines are approximately perpendicular to the diagonal which goes from the slot to the opposite pool corner, while in the deep slot design they are almost perpendicular to the fishway longitudinal axis (Fig. 2).

Another important property observed is that the free water surface pattern remains invariable to the height of the sill. Each design has a characteristic pattern which depends only on the configuration of the vertical walls that define the pool and which does not depend on the sill placed in the slot.

Finally it was verified that the pattern of the free water surface is also independent of the flow discharge. This behaviour was observed for all the experimental discharges used.

3 VELOCITY FIELDS

3.1 *Horizontal velocity fields*

The introduction of the sill in the vertical slot has a great importance in the velocity field. In the vertical slot design, the flow is quasi bidimensional, the vertical velocities are almost zero and there are not important differences in the velocity fields which occur at different vertical levels. This allows to characterize the flow pattern independently of the level over the bottom of the fishway (Puertas, 2004). When the

Figure 3. Flow pattern of the horizontal velocity field in a plane situated at 5cm above the bottom of the pool.

Figure 4. Flow pattern of the horizontal velocity field in planes located between 5cm above the bottom of the pool and the upper border of the sill.

sill is introduced, this behaviour is no longer true. The horizontal velocity field varies with the height over the bottom and the vertical velocity cannot be neglected, specially near the slot.

One of the aims of this study was to find several flow patterns which allow to describe the flow independently of the discharge and the sill used. Different flow patterns must be defined in order to be able to represent the velocity field in horizontal levels below the sill as well as in horizontal levels above the sill.

Three different flow patterns at three different levels were found after analyzing the experimental data.

The first one (Fig. 3) occurs at 5cm above the bottom of the pool, no matter which discharge neither which sill is used.

A second pattern was found (Fig. 4) which represents the velocity field in levels higher than 5cm but lower than the upper border of the sill.

The horizontal velocity field pattern occurring in levels situated over the sill up to the free water surface varies with height. The strongest difference takes place near the sill. Nevertheless, it can be defined a general flow pattern which represents quite accurately the flow field. This third pattern is shown in Figure 5. It is in the slot section where the velocity direction varies most strongly with height. In Figure 5 two directions are defined in the slot. At the deepest levels, the velocity direction turns left, being almost parallel to the transversal wall, while in the most superficial levels the velocity remains perpendicular to the slot.

As it has been said, in the deep slot design, the vertical velocities are not negligible. Near the slot the flow

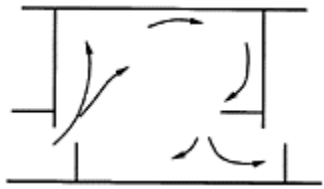

Figure 5. Flow pattern of the horizontal velocity field in levels situated over sill.

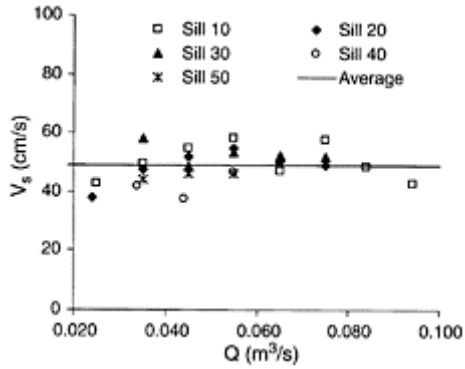

Figure 6. Experimental values of the mean velocity in the slot for different discharges and different sills.

moves up, it is then propelled away from the slot, and when it reaches the opposite vertical wall it moves down. The absolute value of the vertical velocity is usually smaller than the horizontal components, being usually smaller than 20cm/s. However, as it is shown by the experimental results presented, it is of great importance in the global behaviour of the flow in the fishway.

3.2 *Slot velocity*

The velocity in the slot *(V_s)* was calculated at different heights. For each height three different experimental points were used to compute the mean value of the velocity.

In Figure 6 it is represented the mean velocity in the slot for each different discharge and each different sill. As it can be seen, all values are quite similar independently of the discharge and the sill used. A mean velocity of 48.82cm/s can be considered as representative of all situations.

3.3 *Maximum velocity*

The maximum velocity *(V_{max})* is another characteristic velocity that can be used to define the hydraulic behaviour of a fishway.

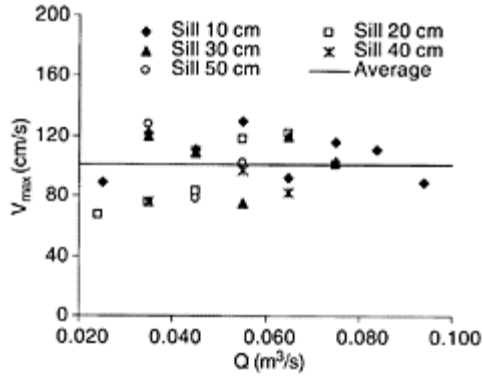

Figure 7. First maximum velocities. Maximum velocities for each different discharge and sill, computed as the mean value of the maxima at the different measurement planes situated above the sill.

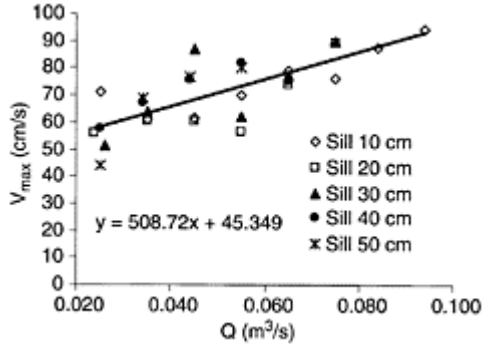

Figure 8. Second maximum velocities. Maximum velocities for each different discharge and sill, computed as the mean value of the maxima at different measurement planes situated below the sill.

As it was expected, it was necessary to define two different maximum velocities. The first maximum corresponds to the points situated above the sill and the second maximum to points situated below the sill. The maximum velocity is defined as the mean of the different maxima occurring at different measurement planes. For the first maximum, only

the planes situated above the sill are considered while for the second maximum the planes considered are those ones situated below the sill.

The first maximum velocity is shown in Figure 7. Different discharges and sills are represented. As the maximum velocity is almost independent of the discharge, a mean value was calculated, obtaining a velocity of 101cm/s.

The second maximum velocities (planes situated below the sill) are plotted in Figure 8. As it can be seen, the maxima increase with the discharge up to a highest value which is very near to the first maximum (planes situated above the sill) represented in Figure 7. For all discharges, the second maximum is smaller than the first maximum. It should be expected that for bigger discharges both maxima agree.

The velocities measured oscillate in a very wide range. The biggest value measured was 174.7cm/s. The location of the biggest velocities is always near the slot.

4 CONCLUSIONS

The aligned deep slot fishways are an hybrid design between the so called deep slot fishways and the aligned vertical slot fishways. Therefore, its hydraulic behaviour has common points with the two original designs.

The discharge equations which relate the discharge and the water depth are linear, as it happens in the vertical slot design. However, the equation depends on the height of the sill placed in the slot. The bigger the sill, the bigger the water depth in the pool.

The configuration of the free water surface is independent of the discharge and of the sill used.

It has been found three different flow patterns which allow to represent the horizontal velocity field. Depending on the level over the bottom of the pool, one pattern or another appears. The three patterns found can be summarized as follows:

(1) Independently of the sill used, at a level of 5cm over the bottom of the pool, the streamlines follow the pattern shown in Figure 3.
(2) For planes situated at a higher level than 5cm but below the upper border of the sill, the flow pattern is represented in Figure 4.
(3) The planes situated at a higher level than the upper level of the sill follow the pattern shown in Figure 5. The velocity direction is perpendicular to the slot for planes near the free water surface. At lower levels, the velocity direction turns left.

Although the vertical velocity component is much smaller than the horizontal components, it has a great importance in the development of the flow pattern in the pool.

The mean velocity in the slot can be considered almost constant and independent of the discharge and of the sill used.

Regarding the maximum velocities, two different behaviours were observed. In planes located above the sill, the maximum velocity is constant and it does not depend on the discharge neither on the sill used. In planes situated below the upper border of the sill, the maximum velocity is independent of the sill height but it increases with the discharge.

ACKNOWLEDGEMENTS

The authors would like to thank the CITEEC staff (Centro de Innovación Tecnolóxica en Edificación e Enxeñería Civil) at the University of A Coruña (Spain), without whose help the development of experimental work essential to this research would not have been possible, as well as the Spanish Ministry of Science and Technology, which funded this research project (CICYT-HID-1999–0297).

REFERENCES

Larinier, M., Porcher, J.R, Travade, F., Gosset, C. 1998. *Passes a poissons. Expertise conception des ouvrages de franchissement.* Collection Mise au Point, Conseil Superieur de la Pêche, Paris. 336 p.

Pena, L., Teijeiro, T., Puertas, J. 2003. *Experimental study of depth discharge equations and velocity patterns on vertical slot fishways.* Proceedings XXX IAHR Congress, August, 2003. Theme C. p. 433–440. Thessaloniki. Greece.

Puertas, J., Pena, L., Teijeiro, T. 2004. *An experimental approach to the hydraulics of vertical slot fishways.* Journal of Hydraulic Engineering, Vol. 130, No 1.

Rajaratnam, N., Van de Vinne, G., Katopodis, C. 1986. Hydraulics of vertical slot fishways. *Journal of Hydraulic Engineering*, vol. 112, No 10, p. 909–927.

Rajaratnam, N., Katopodis, C., Solanki, S. 1992. New designs for vertical slot fishways. *Journal of Hydraulic Engineering* 19, p. 402–414.

Teijeiro, T. 2001. *Citerios de diseño de escalas de peces de hendidura vertical.* Tesis doctoral. Dpto. de Ingeniería Agroforestal, Universidad de Santiago de Compostela. Lugo.

Zhong, Y., Power, G. 1996. Environmental impacts of hydroelectric projects on fish resources in China. *Regulated rivers: research and management.* Vol 12:81–98.

Estimating effect of navigation on fish habitats in inland waterways

C.Engelhardt, A.Sukhodolov & C.Wolter

Institute of Freshwater Ecology and Inland Fisheries, Berlin, Germany

River Flow 2004—Greco, Carravetta & Della Morte (eds.)

ABSTRACT: The swimming performance of juvenile fishes can be insufficient to overcome return current velocities induced by navigation in inland waterways. A method to assess habitats of fish on the basis of return velocity computations is introduced using general physical principles. A simple analytical model is presented to determine the return velocities in a canal of known dimensions and for a vessel of certain draught and speed. Field measurements were performed in the Oder-Havel canal to evaluate the mathematical model. Comparing predicted values of return velocity for the investigated waterway with thresholds of maximum swimming speed for juvenile fishes a habitat bottleneck could be shown. Suggestions are given as to how the navigation impact on fish can be minimized by canal shoreline design.

1 INTRODUCTION

Navigable inland waterways were always important for the economic development of society; nowadays their total length exceeds half a million kilometers worldwide (Kubec & Podzimek 1996). Aside from their primary functioning as navigation routes, inland waterways provide habitats for sundry species of aquatic animals and plants. Although the necessity of limiting the cruising speed of vessels because ofchannel protection considerations became an exploitation policy long ago, the ecological aspect of the problem was not considered rigorously either in design of channel or in navigation rules hitherto. In part this situation accounts for the lack of knowledge about the effects of navigation on dynamics of populations for species inhabiting inland waterways.

A vessel propelling in a canal expends energy to overcome the resistance of fluid. That energy is mainly transformed into a complex pattern of currents and waves trailing astern. Helmholz fan, propeller wash (U_p), slope supply flow (U_s), and return currents (U_r)

moving in opposition to the direction of the vessel's motion (Figure 1) are the principal constituents of the pattern. In width-restricted canals, when commercial tugs towing loaded barges cruise with the speeds close to navigation limits, the return currents maintain extremely large velocity values (Simons et al. 1981; Mazumder et al. 1993). The magnitude of these currents may greatly exceed the swimming abilities of larval and juvenile fishes and thereby cause high larvae mortality (Wolter & Vicinskas 1997; Arlinghaus et al. 2002). As the young-of-the-year fishes are important

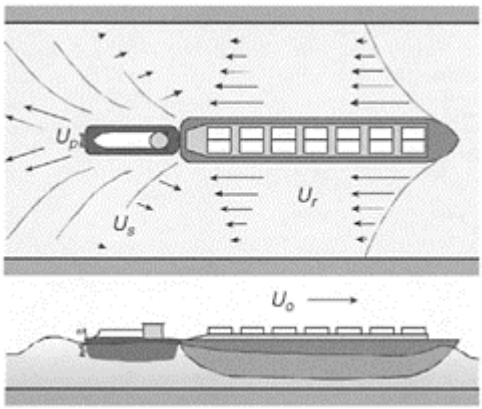

Figure 1. Schematic representation of currents generated by a vessel cruising in a canal (after Blaauw et al. 1984).

indicators of habitat quality (Schiemer et al. 2001), it seems possible to establish quantitative relationships between side effects of navigation and habitat quality by means of comparison of return current velocity and swimming abilities of juvenile fishes. To develop this relationship to the level of a practical computational scheme therefore requires predicting the return velocity for the given characteristics of the canal as well as for typical vessels in addition to predicting swimming abilities of juvenile fishes as a function of the body length.

Although vessel-induced waves and currents have been intensively studied in the shipbuilding applications (Jiang 2001), available computation schemes are either complex (Stockstill & Berger 1999) or rely heavily on purely empirical approaches (Maynord & Siemsen 1991; Maynord 1996). Moreover, both advanced numerical models and empirical methods require that significant amount of data be collected prior to computations. Numerical models need detailed data sets pertaining to the geometry of the channel and a vessel, characteristics of hydraulic resistance and eddy viscosity (Stockstill & Berger 1999), while development of empirical relationships requires numerous observations. Therefore, there is a need to develop a simplified computational scheme based on fundamental physical laws which can be operated upon a few parameters.

Fish swimming performance depends on a variety of biological and physical factors. Observations undoubtedly indicate that the principal factor is the body length (Wardle

1975; Videlar 1993; Haefner & Bowen 2002). Correspondingly, swimming performance was assessed by a model for maximum swimming speed on the basis of the white lateral muscle's contraction time and the relation between tailbeat frequency and forward motion (Wardle 1975).

Present study is focused on the development of a simplified model of return velocity in a straight prismatic canal with still water and its applications to describe effect of navigation on fish habitats. The model was derived from advection-diffiision equation and tested on the original data set of field observations.

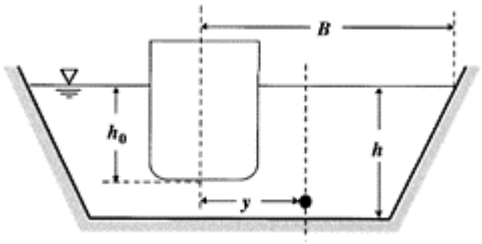

Figure 2. Schematic representation of canal's crosssection with a vessel.

2 RETURN CURRENT MODELING

A moving vessel expends energy to overcome resistance of water while propelling in a waterway. The kinetic energy gained by water from the interaction with the vessel has to be transported away and dissipated during the transport. This energy transfer can be described by the advection-diffusion equation

$$\frac{\partial k}{\partial t}+\mathbf{u}\frac{\partial k}{\partial \mathbf{x}}-\frac{\partial}{\partial \mathbf{x}}D\frac{\partial k}{\partial \mathbf{x}}=0 \qquad (1)$$

where t=time, $\mathbf{x}$=vector of coordinates, $\mathbf{u}$=vector of characteristic velocity of the kinetic energy transfer, D=coefficient of kinetic energy diffusion, and k=dimensionless kinetic energy $= U^2h/U_0^2h_0$, $U_0$and U=velocities of the vessel and water, h_0 and h=draught and the canal depth respectively (Figure 2).

In inland waterways the canal widths are usually comparable or smaller than the length of commercial vessels (Figure 3) while their draughts at load are slightly smaller then the canal depth. Therefore, accounting for significant cruising speeds of vessels, the ship-induced disturbances occupies the whole water column and reach the banks so quickly that the maximum of return velocities is observed in a cross-section while a ship still passing by. These circumstances allow significant simplification for equation (1). Thus, it is reasonable to consider only depth averaged, steady state energy transfer with constant coefficient of diffusion which for the transverse direction writes to as

$$\frac{\partial^2 k}{\partial y^2}-a\frac{\partial k}{\partial y}=0, \quad a=\frac{u}{D}, \qquad (2)$$

where y=cross-canal distance counted from the centerline of the ship's hull. The condition of steadiness is

$$T >> \frac{y}{u}, \tag{3}$$

here T=period of drawdown wave.

Figure 3. Commercial navigation in the Oder-Havel canal in Germany.

Substituting the variable $\zeta=\partial k/\partial y$ yields

$$\frac{\partial \zeta}{\partial y} - a\zeta = 0, \quad \frac{d\zeta}{\zeta} - a\,dy = 0, \tag{4}$$

and after integration converts to

$$\text{In } \zeta - ay + C = 0, \tag{5}$$

where C=constant of integration. Applying an inverse transformation to (5), one obtains

$$\zeta + C_1 e^{-ay} = 0, \text{ or } dk + C_1 e^{-ay}\,dy = 0,\ C_1 = e^{c}, \tag{6}$$

that with a substitute for the distance $\eta=y/B$ writes as

$$dk + C_1 e^{-aB\eta} d\eta = 0, \tag{7}$$

where B is waterway-width. Integration of equation (7) yields

$$k = \frac{C_1}{aB} e^{-aB\eta} + C_2, \tag{8}$$

where C_2=constant of integration. C_2 is a small and can be neglected at long distances in still water $k\approx 0$. Now substituting expressions for kinetic energy into (8), one obtains

$$\frac{U^2}{U_0^2}\frac{h}{h_0} = \frac{C_1}{aB} e^{-aB\eta}, \quad \frac{U}{U_0} = \sqrt{\frac{C_1}{aB}}\sqrt{\frac{h_0}{h}}\, e^{-\frac{aB}{2}\eta}. \tag{9}$$

Finally, one can rewrite equation (9) to as

$$\frac{U}{U_0} = \alpha \sqrt{\frac{h_0}{h}} e^{-\beta \frac{z}{B}}, \tag{10}$$

where $\alpha = \sqrt{\frac{C_1}{aB}} = \sqrt{\frac{C_1 D}{uB}}$, and $\beta = \frac{aB}{2} = \frac{uB}{2D}$.

Despite that general relationship of the coefficients α and β to the parameters of the flow are known, their values have to be determined experimentally because of lack of a suitable mathematical description for diffusion coefficient D, and the unknown value of C_1.

Equation (3) can be rewritten to account for a specific case $\sqrt{gh}$

$$T = \gamma \frac{L}{U_0} >> \frac{y}{\sqrt{gh}} \tag{11}$$

which is a well recognized group velocity limit in the shallow water canals. The value of coefficient γ is expected to equal 1, and the practical threshold to satisfy condition (11) is an order of magnitude, that means that the period of ship passage should be at least 10 times longer then the time of disturbance wave travel from the ship to the bank.

Equations (10) and (11) comprise a simple model allowing predictions of return velocities in a canal of known dimensions for a vessel with the certain draught and speed. The model requires, however, some parameters that can be obtained experimentally for the certain geometry of the canal (for example trapezoidal shape) and similar types of vessels.

3 FIELD MEASUREMENTS

3.1 *Study reach*

The artificially constructed Oder-Havel canal is a 150km long inland waterway connecting watersheds of the Oder and the Havel rivers in the northeastern lowlands of Germany. It was opened for navigation in 1620, last modified in 1914; its channel is 34m wide and 3m deep, with a steep bank (slopes of 33%) protected by rip-rap embankment. The field measurements were performed in a reach of the canal located at 63.5km (52°85′N; 13°73′E).

3.2 *Measuring system and equipment*

During the passage of vessels in the study reach the records of instantaneous velocity vectors were collected using acoustic doppler velocimeter (ADV) manufactured by Sontek, Inc. This instrument consists of an ADV probe mounted to submersible field electronics. The sampling volume of the probe is located 10cm from the sensors and is $<0.25 cm^3$ in size. The resolution of the ADV is 0.1mm/s with a noise level of 1% of the velocity range at a sampling frequency of 25Hz. A special moveable platform was constructed to enable accurate and stable positioning of the measuring systems (Figure 4).

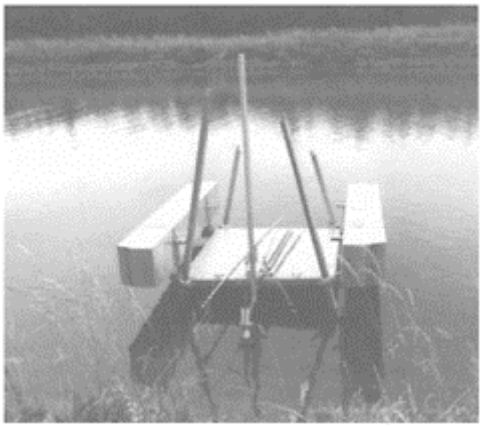

Figure 4. Moveable platform for ADV sensors mounting installed in the cross-section of the Oder-Havel canal, 63.5km.

Hydrographic survey of the waterway reach, positioning of ADV sensors and the determination of coordinates for vessels were performed with a total station Elta® R55 (Carl Zeiss Geodetic Systems, Germany, distance 5mm, range 1300m). The draught was recorded from the draught scale of the vessels, and the length, width and capacity were obtained from the official calibration registers. Speed of vessels was calculated from time consumed by each vessel to pass a defined reference reach. Water levels were recorded using pressure loggers (DL/N, STS Co., Sirnach, Switzerland) mounted into perforated steel pipes and placed close to the locations of ADV probes.

3.3 *Measurements and data processing*

For altogether 17 commercial tows the flow velocities were measured close to the bottom (0.15m) at three locations across a transect of the Oder-Havel canal simultaneously at sampling rate of 25Hz. The recording started as soon as a vessel became visible from the site and continued until the water surface became practically calm.

The software package ExploreV 1.5 (NortekUSA) was used to process the results of ADV measurements. Prior to computations of the statistical characteristics of turbulence, each record was inspected visually to identify possible problems such as spikes, trends, or abrupt discontinuities in the time series. Post-processing of the data involved removal of the defective portions of the time series using the data clipping capabilities of the software, spikes detection with a set of criteria implemented in the ExploreV and the recovering of bad samples with linearly interpolated values. Editing of time series thus allowed to exclude errors associated with spurious signals emerging from interaction of acoustic signal with large floating particle in the stream such as woody debris.

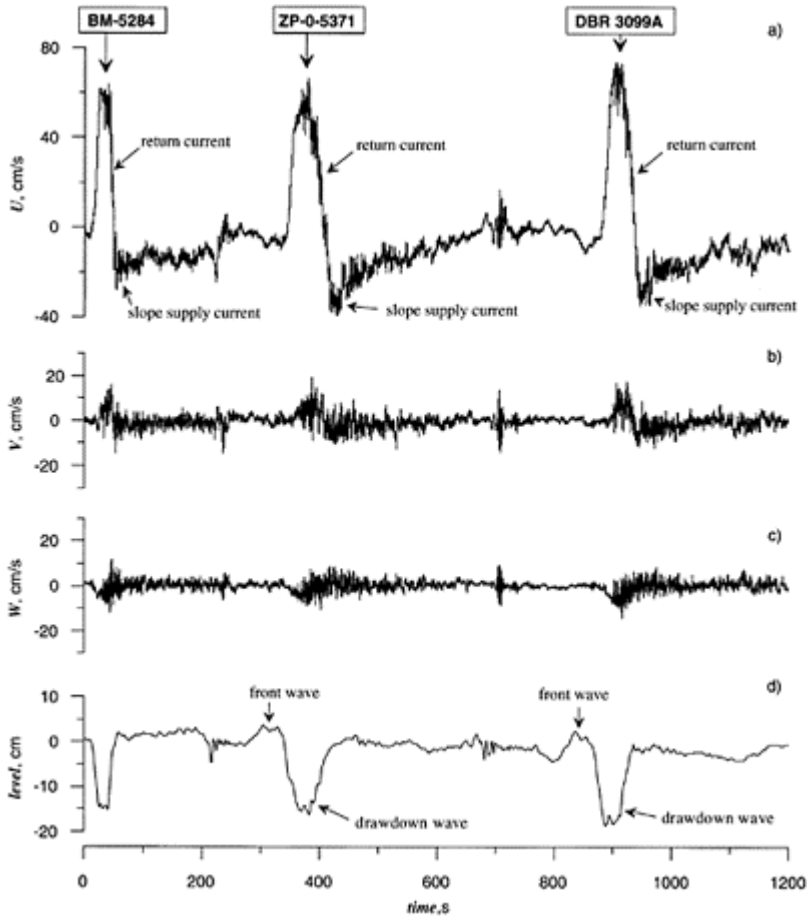

Figure 5. Example of velocity records sampled with ADV in the Oder-Havel canal during the passage of three commercial tows (the registration numbers of tows are displayed in textbox).

4 RESULTS

A coordinate system with a streamwise *x* direction aligned with the direction of vessels motion, a transversal *y* direction, and a vertical direction *z*, originating at the canal bed and directed toward the free surface is adopted herein.

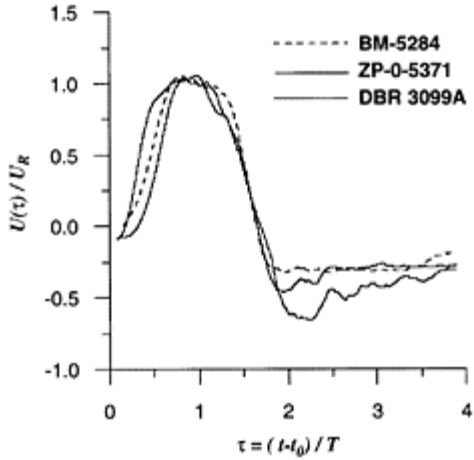

Figure 6. Dimensionless velocity records.

An example of measured velocities and water levels is shown in Figure 5. Analysis of velocity fluctuations and changes of water level allows to unambiguously determine different elements of the vessel's wake pattern. It can be also seen that velocity patterns display apparent similarity, though there are definite differences in length, load and speed of vessels.

Records of velocity and water level were processed to obtain the periods of drawdown waves and mean values for return currents U_R (calculated as an averaged value for the time interval corresponding to the period of drawdown wave). The measured velocity patterns can be scaled with those two parameters (Figure 6).

The data plotted in Figure 6 were smoothed using boxcar procedure to eliminate fluctuations of higher order. Close correspondence between return velocity and small scatter in the data thus confirm that vessel length and speed are the most valuable parameters controlling the formation of return currents. At the same time records exhibited larger scatter for slope supply currents that most probably included the effect of a tug hull and peculiarities of propeller-generated currents individual for different types of tugs.

Close examination of individual patterns of return velocity as the result of zooming and resizing (Figure 7) supports the acceptance for the condition of steadiness (3). Comparison of measured pattern and accepted in the model (10) is presented in Figure 7b.

Periods of drawdown waves and their approximates calculated from length and speed of vessels are shown in Figure 8. A line corresponding to the linear regression between these parameters outlines the area of perfect agreement. These plots reveal that the period of drawdown wave can be simply estimated for a vessel with a certain size.

Transverse distributions of dimensionless return velocities and their comparison with model (10) are presented in Figure 9. Standard least squares procedure yielded values for

parameters α=2.24 and β=2.52 (R^2=0.92). The data indicate close agreement with the solution by model (10) indicated as the solid line in Figure 9.

5 DISCUSSION AND CONCLUSIONS

A simplified analytical model for predicting return currents developing in the area of drawdown wave accompanying the passage of large commercial vessels in the canals is presented. The comparison of the model's prediction with the results of field observations indicated a good performance of the model. This allows recommending the model for use in ecological studies as a tool of estimating the effect of navigation on different species of the aquatic life. Below we present an example of the model application for characterization of fish habitats.

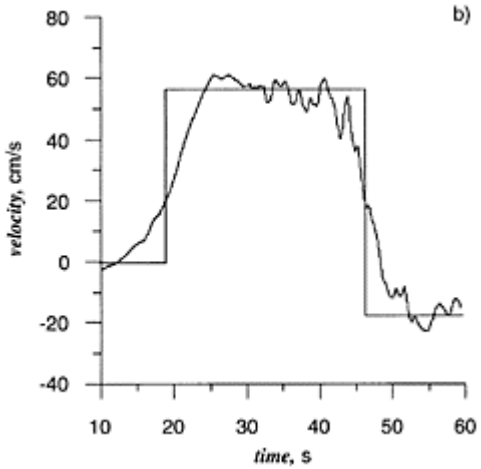

Figure 7. Zoomed velocity record and its approximation in the model (thick line).

Fish swimming performance was assessed according to a general model of maximum swimming speed on the basis of white lateral muscle's contraction time and the relation between tailbeat frequency and forward motion (Wardle 1975). According to this estimation, a 15mm long fish larvae swims with a maximum speed of 0.22m/s, that is considerably below the navigation-induced return current velocity. The lower level of return current for the Oder-Havel canal of 0.7m/s would be performed by a 47mm long fish for less than 20s (Wardle 1975). However, when larvae of common freshwater fish species hatch at total length of less than 10mm and swim free between 6–15mm (Koblickaya 1981; Pinder 2001),

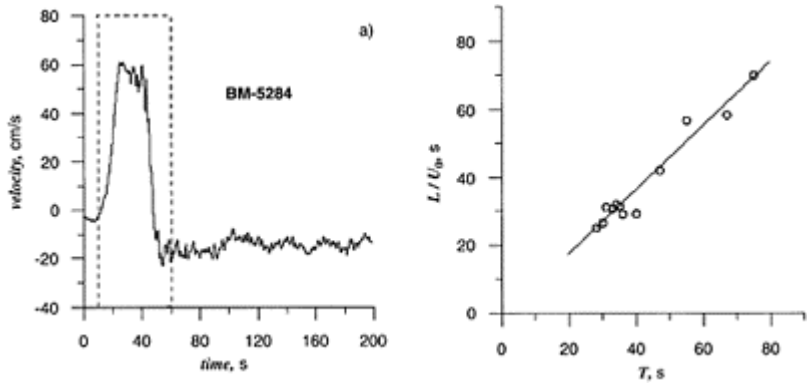

Figure 8. Comparison of measured *(T)* and computed periods for drawdown waves.

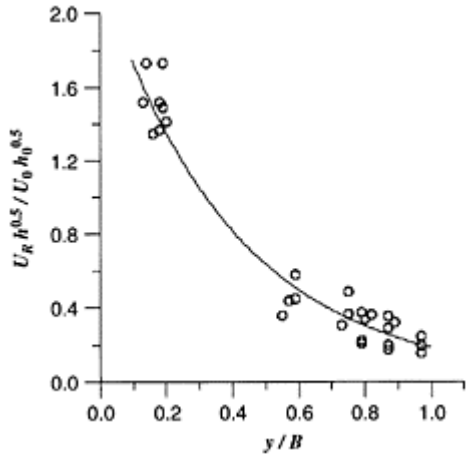

Figure 9. Measured (circles) and predicted (line) values of return velocities.

their maximum swimming performance covers only a split of the physical threshold conditions (Figure 10).

To conclude, sustainable management of inland waterways requires minimizing the navigation impact by enhancing ecotone diversity and shoreline structures. This can be achieved by (1) preserving existing and creating additional embayments; (2) revitalizing submerged and emerged macrophytes or similar microhabitat structures; and (3) establishing temporal lowered speed limits for commercial tows for the periods especially dangerous for juvenile fishes.

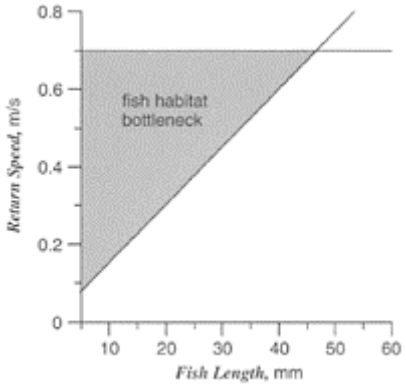

Figure 10. Maximum swimming speed of fish (according to Wardle 1975) in relation to the return velocities.

ACKNOWLEDGEMENTS

The authors wish to express their appreciation to R.Arlinghaus, H.Bungartz and W.Sauer for their participation in field studies. H.Zwadlo is thanked for his help with preparation of the submersible mount for ADV probes.

REFERENCES

Arlinghaus, R., Engelhardt, C., Sukhodolov, A., & Wolter, C. 2002. Fish recruitment in a canal with intensive navigation: implications for ecosystem management. *J. of Fish Biology* 61: 1386–1402.

Blaauw, H.G, van der Knaap, F.M.C., de Groot, M.T., & Pilarchyk, K.W. 1984. Design of bank protection of inland navigation fairways. *Transactions of Delft Hydraulic Lab.* 320.

Haefner, J.W., & Bowen, M.D. 2002. Physical-based model of fish movement in fish extraction facilities. *Ecological Modelling* 152:227–245.

Koblickaya, A.F. 1981. *A key for identifying young freshwater fishes.* Moscow: Light- and Food Industry Publishing.

Kubec, J., & Podzimek, J. 1996. *Wasserwege.* Hanau: Verlag Werner Dausien.

Maynord, S.T. 1996. Return velocity and drawdown in navigable waterways. *Technical Report of US Army Eng. Waterways Experimental Station*, HL-96–7, Vicksburg. Maynord, S.T., & Siemsen, T.S. 1991. Return velocities induced by shallow-draft navigation. In: *Hydraulics Engineering*, ASCE, New York: 894–899.

Mazumder, B.S., Bhowmik, N.G., & Soong, T.W. Turbulence in rivers due to navigation traffic. *J. of Hydraulic Eng.* 119(5): 581–597.

Pinder, A.C. 2001. *Keys to larval and juvenile stages of coarse fishes from fresh waters in the British Isles.* Cumbria: Freshwater Biological Association.

Simons, D.B., Li, R.M., Chen, Y.H., Ellis, S.S., & Chang, T.P. 1981. Investigation of effects of navigation trafic activities on hydrologic, hydraulic, and geomorphic characteristics. *Report of Environmental Work Team*, Minneapolis.

Stockstill, R.L., & Berger, R.C. 1994. *HIVEL2D: a two-dimensional flow model for high-velocity channels. Tech-nical Report of US Army Eng. Waterways Experimental Station,* REMR-HY-12, Vicksburg.

Vardle, C.S. 1975. Limit of fish swimming speed. *Nature* 255:725–727.

Wolter, C., & Vilcinskas, A. 1997. Perch *(Perca fluviatilis)* as an indicator species for structural degradation in regulated rivers and canals in the lowlands of Germany. *Ecology of Freshwater Fish* 6:174–181.

C.3. Flood management and control

River flow forecast by means of selected black box models

A.Piotrowski, P.M.Rowiński & J.J.Napiórkowski

Institute of Geophysics, Polish Academy of Sciences, Warsaw, Poland

River Flow 2004—Greco, Carravetta & Della Morte (eds.)

ABSTRACT: Performance of two different types of approaches were investigated with respect to the daily river flow predictions. The first approach is Multi-Layer Perceptron Artificial Neural Network, the second one, based on the deterministic chaos concept, is so called Phase-Space Reconstruction (PSR) model. Both models were applied to daily river flow data collected from several gauges, located in river reaches in western Canada. Each data set consists of more than 10000 consecutive daily measurements. The method based on the phase-space reconstruction theory has been applied despite the fact that the authors doubt in the existence of deterministic chaos in the river system. Classical phase-space method may be applied only to single time series data. In the present study an extension was proposed, in which time series from additional gauge stations added to the system. Comparison of models' performance was made for this extended and classical approaches for both phase-space reconstruction and Artificial Neural Networks models.

1 INTRODUCTION

An accurate forecasting of river flow is a fundamental problem in hydrological sciences. In recent years application of black box type models to runoff prediction has been gaining more popularity due to their easiness of employment and relatively low number of variables involved. Multi-Layer Perceptron Artificial Neural Networks (ANN) are probably most broadly used for forecasting (Hsu et al. 1995, Campolo et al. 1999, Campolo et al. 2003, Dolling & Varas 2002, Chibanga et al. 2003 and many others). They are the simplest among the non-linear neural network models, nevertheless they are capable of making very accurate forecast, when proper set of input variables is taken into account. On top of that they are easy to be trained, contrary to, for example, radial basis functions networks. ANN approach is sometimes called global approximation approach as it deals with all set of historical data values to optimise network weights, which means that all known information about the system is used to make a relevant forecast.

A methodologically different approach, though still quite popular, pertains to phase-space reconstruction (Jayawardena & Lai 1994, Porporato & Ridolfi 1997, Sivakumar et al. 2002). It is a local approximation approach and it has been developed in the framework of the deterministic chaos theory. The presence of low-dimensional chaotic behaviour in the rainfallrunoff process is a matter of an ongoing debate (see e.g. Schertzer et al. 2002) and it will not be discussed in detail herein. Let us only note that the main idea of this approach corresponds to the possibility of the reconstruction of the phase-space from a discrete set of values for a given observable scalar such as water stages at a given gauge station. The authors of the present study will benefit from the phase-space reconstruction method which in fact is a way of finding the most similar situations in historical data and applying only these selected parts of data set for forecasting. It seems that this method may stand alone as a reliable tool without linking it to the existence or nonexistence of a hypothetical deterministic dynamical system leading to disordered solutions. According to Sivakumar et al. (2002), the phase-space reconstmction method is better than ANN approach when dealing with autoregressive forecast problem. Further in the paper it will be shown that such conclusion is premature and in case of the selected Canadian river reaches both ANN and phase-space reconstruction methods boast similar performance of forecasting daily runoffs. Additionally an extension, further called as quasi-phase-space reconstruction method, will be proposed and this method will allow for the use of the data from more than one gauge station. As expected this method will improve the results considerably.

The comparison of the results of two black box models will be presented according to the following scheme:

– version A: as inputs only historical runoff data from the same gauge are applied for both ANN and phasespace reconstruction approaches;
– version B: forecast is made for the same gauge as in version A, but input data set consists of data from 2 or 3 gauges. Additional gauge for version B is selected at the same river where the forecasting gauge or its main tributary is placed.

For each case 3 consecutive measurements from particular gauge were treated as input variables which means that we have 3 input variables in version A, and 6 or 9 in version B.

2 FLOW DATA

Long enough data sets collected in 5 western Canadian rivers (Figure 1) are applied in the analyses (Environment Canada 2003). Table 1 presents the duration of daily data sets, location of the main gauge (used for the forecasts, denoted by number 1) and the additional gauges (applied in version B only, denoted by number 2 or 3). Each data set contains more than 10000 daily measurements, and 5 river reaches are considered in the study. It seems to provide sufficient information to

Figure 1. Location of gauge stations.

Table 1. Description of data sets.

River	Gauge sites	Length
Athabasca*	1. Hinton	71.01.01–
	2. Jasper	02.12.31
Fraser*	1. Above Texas Creek	55.01.01
(upper part)	2. Shelley	02.12.31
Fraser*	1 . Mission	65.05.01
(lower part)	2 Above Texas Creek	92.12.31
South	1 . Medicine Hat	65.01.01–
Saskatchewan** *	2. Bow river	02.12.31
	3. Oldman river	
North	1 . Prince Albert	70.01.01
Saskatchewan**	2. near Deer Creek	01.12.31

* mountainous terrain, ** steppe.

compare the performance of all the considered models. In each case the daily river flow forecast was made for last 5000 measurements. Those 5000 measurements were not taken into account during ANN training process, but they were only used to compare performance of both models at each river reach. The ANNs were trained with the use of the earlier records (larger than 5000 elements in each case).

3 MODELS APPLIED

In this section attention is focused on the implementation of some anticipatory nonlinear methods based on Deterministic Chaos and Artificial Neural Networks for prediction of the inflows.

3.1 *Artificial Neural Network approach*

Multi-Layer Perceptron Artificial Neural Networks have become widespread in recent years and the researchers often claim that they provide a useful tool for the predictions of river flow. Three layer networks with sufficient number of hidden nodes are usually applied due to the continuity of the relevant function. Every network contains an appropriate number of input and output nodes which is equal to the number of input and output variables, and the assumed number of hidden nodes. There is no effective rule for the estimate of the number of hidden nodes. In this study it usually turns out to be close to the number of input nodes, but in each case it is experimentally verified.

The ANN nodes in neighbouring layers are linked via weighted connections. The values of those weights can be adaptively modified during the process of training the network. In this study, due to the relatively simple architecture of all the networks, Levenberg-Marquardt nonlinear optimisation algorithm was adopted (Press et al. 1989).

Shortly the Multi-Layer Perceptron network (see Figure 2) operates in the following way: signals si (i=1, …, N) from the input nodes (e.g. values of input variables normalized to 0–1 interval) are multiplied by

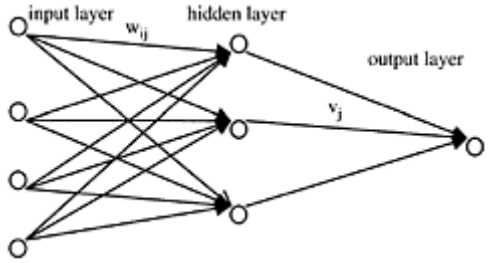

Figure 2. Multi-Layer Perceptron Artificial Neural Network scheme.

proper weights W_{ji} (j=1,... K), connecting the neuron from which signal has been dispatched and a suitable neuron in the second layer.

In the second layer the weighted sum of all the inputs are computed and then transformed by logistic function

$$f(x) = \frac{1}{1+e^{-\alpha x}} \tag{1}$$

giving the output value of a neuron in the second layer:

$$z_j = f\left(\sum_{i=1}^{N} s_i w_{ji}\right) \tag{2}$$

Afterwards the weighted signals z_j (multiplied by proper weights v_j), are transferred to the neuron of the third layer. In the neuron of the third layer the new weighted sum is computed

$$y = \sum_{j=1}^{K} v_j f\left(\sum_{i=1}^{N} s_i w_{ji}\right) \tag{3}$$

and after de-normalization of the output, the sought (forecasted) value may be determined. This is a feed-forward network, which means that there is only one direction of the flow of information, from the input to the output layer.

3.2 *"Phase-space reconstruction" approach*

Another method used in runoff forecasting studies is motivated and based on the theory of dynamical systems (Kantz & Schreiber 1997), i.e. the time evolution is defined in some phase-space. For a purely deterministic system, once its present state is fixed, the states at all future times are determined as well. So it is essential to establish a phase-space for the system such that specifying a point in this space specifies the state of the system and vice versa. Then one can study the dynamics of the system by studying the dynamics of the corresponding phase-space points.

Characteristic for chaotic systems is that in many cases the corresponding attractors turn out to be strange attractors of the fractal structure with a non-integer dimension (Kudrewicz 1993, Ott 1993).

Since it is natural to describe a deterministic dynamical system as an object in phase-space, it is also most natural to use a phase-space description for approximation of the dynamic of the system. Such approximate dynamics can be useful for prediction.

The reconstruction of a vector space which is equivalent to the original state space of a system from a scalar time series is the basis of almost all nonlinear methods. Scalar measurements is a projection of unobserved internal variables of a system onto an interval on real axis. It is obvious that even with a precise knowledge of the measurements it may be impossible to reconstruct the state space of the original system from the data. Fortunately, we are rarely keen of obtaining a whole, precise description of the process. It is usually enough to determine its good approximation. Hence a reconstruction of the original space is not really necessary for the data analysis. It is sufficient to construct a new space such that the attractor in this space is "equivalent" to the original one (Kantz & Schreiber 1997).

The classical situation, as treated in hydrological sciences, though being a matter of serious debate (e.g. Schertzer et al. 2002) is the following. A sequence $\{x_i\}$, $x_i \in R^1$, i=1, …, N, of measured values is given. In order to find an approximation of the deterministic system one considers the function F defined by the following relationship

$$y_m^{l+\Delta} = F(y_m^l) = F(x_i, x_{i-1}, \ldots, x_{i-(m-1)}) \tag{4}$$

with a properly adjusted number m, called *embedding dimension* and a given time delay Δ. Hence, the so-called quasi phase-space composed of m-element subsequences y_m^l is considered

$$y_m^l = (x_i, x_{i-1}, \ldots, x_{i-(m-1)}) \tag{5}$$

The function F in Equation (4) is a dynamical process in the space R^m, which according to the embedding approach (Takens 1981) forms an attractor in R^m, if the original process is a deterministic chaos. To determine proper embedding dimension from a finite sample of points one determines, for example, correlation integral $C_N(m, r)$ for several embedding dimensions (Grassberger & Procaccia 1983). Then correlation dimension D is determined as the slope of function In $C_N(m, r)$ with respect to ln(r), in a respective range of sufficiently small r, such that the function behaves as a linear one (one expects C to scale like power law, $C(r) \propto r^D$). Now using Takens theorem, one can put m=2D+1 as the searched embedding dimension.

One can proceed then to the stage of determining the prediction model for the relationship F in Equation 4. It is possible for deterministic chaos case: as the process is really deterministic and due to existence of an attractor. The considered prediction model has the form of a function such that it approximates the function F, or even less—a "acomponent" of F, being prediction of a future value of state.

$$x_{i+T}=f_T(x_i, x_{i-1}, \ldots, x_{i-(m-1)}) \tag{6}$$

where T is a prediction horizon. Such a function depends on the time instant i of making prediction, and on the horizon T of this prediction. Thus, one can seek for a function

$$f_T^i(y_m^i) = f_T^i(x_i, x_{i-1}, \ldots, x_{i-(m-1)}) \tag{7}$$

that would determine a good approximation of the value x_{i+T} of the given sequence $\{x_i\}$.

Our computations do not confirm the straightforwardness of the application of the described approach and we become skeptical about its correctness. Correlation integral for data described in Section 2 revealed no obvious scaling region as the indicator of self-similar geometry. The saturation value of D (which is just the lower bound of box dimension) with increasing m was not clear at all. We are also aware of the occurrence of noise in the applied data, so the question arises whether those data can be analyzed within the deterministic system.

As a consequence of the above we applied a part of the method derived within the deterministic chaos theory, but as mentioned in Introduction there is no need to decide whether the chaos exists in the system under consideration. We keep the name of the method as the "phase-space reconstruction" approach (Jayawardena & Lai 1994, Sivakumar et al. 2000) to show its origin but we do not claim we have applied the embedding theorem. A method of delays as a realization of the "phase-space reconstruction" approach has been selected for the purpose of the present study. In order to make a forecast one constructs m-dimensional data vectors from measurements spaced equidistant in time (temporal sequence of measured values at the selected gauge) which creates an analogy to the phase-space.

Further the principle of the applied method lies in the search of K-points from the d-dimensional point set that are placed at the smallest distance (according to some assumed measure) from the points representing the current situation. In other words we are interested in finding K vectors of the length m from the past, most of all resembling the current situation. We do assume one day time delay which allows us to use the consecutive recordings from the gauge station. Thus we obtain an autoregressive forecast

for each day (version A). In the present study it was assumed that m=3 which proved to produce reasonable results.

3.3 *Quasi "phase-space reconstruction" approach*

We proceed similarly as in Section 3.2 but this time we test whether the similar forecast is possible using data collected from more than one gauge. Intuitively more information should lead to a better forecast. Being remote from the rigorous treatment of the deterministic chaos we may "extrapolate" the previous considerations from scalar observables (water stages) to vectors. This time we build 2m-dimensional quasi "phase-space" where the first d-vector is made of the consecutive measurements from the first gauge and the second d-vector is made of the consecutive measurements in the second gauge station (time delay is again assumed as one day).

One should note that the measurements from different gauges may have different standard deviations, so the scale related to the first three components and the last three components may be heterogeneous, that can impact the search for N closest neighbours in this space. Fortunately in our case the performance of forecast made using data sets divided by standard deviation is almost the same as for raw data and therefore no normalization was necessary. The above describes the technique for daily runoff forecast in version B.

4 COMPARISON OF APPLIED METHODS

The comparison will be made for both versions A and B by means of correlation coefficient applied to measured and predicted daily or (in one case) 4-daily runoff volume increments (seeTable 2). Such approach shows the performance of the model much better than the correlation applied to just actual runoff volumes where almost all results are close to unity independently of the quality of results.

As it was expected inclusion of additional gauge station (version B) improves the results quite significantly for both "phase-space reconstruction" as well as ANN (Figures 3–8). The only exception is the lower Fraser river. The addition of data from the gauge station at Texas Creek did not help the "phase-space reconstruction" technique. The exemplification of this fact is seen in Figure 4. Note that all the Figures 3–8 are prepared for a selected period of about one month only, out of 13 years time series. For clarity the relevant period was chosen to reveal especially large changes in the daily river runoff.

This is worth mentioning that in version A all ANN and phase-space models show similar performance.

Table 2. Correlation coefficients of forecasted and measured (daily, except noted case) runoff changes.

	Version A		Version B		
River	ANN	PSR	ANN	Quasi PSR	No. of gauges
Athabasca	0.674	0.667	0.904	0.899	2

Fraser(upper part)	0.738	0.735	0.928	0.922	2
Fraser (lower part)	0.478	0.512	0.660	0.507	2
South Saskatchewan	0.518	0.507	0.979	0.796	3
North Saskatchewan (1 day forecast)	0.601	0.603	0.736	0.760	2
North Saskatchewan (4 day forecast)	0.364	0.317	0.856	0.847	2

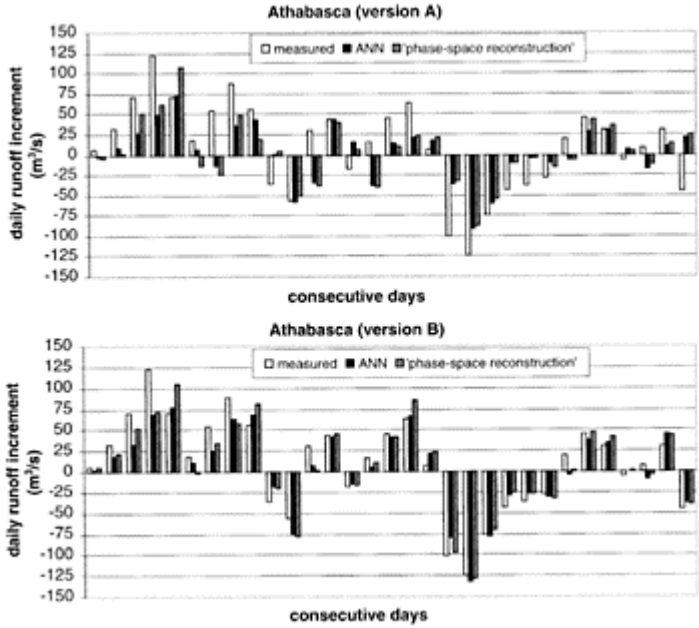

Figure 3. Comparison of one lead day runoff forecast for Hinton gauge station, on Athabasca river, obtained from ANN and quasi “phase-space reconstruction” models in versions A and B.

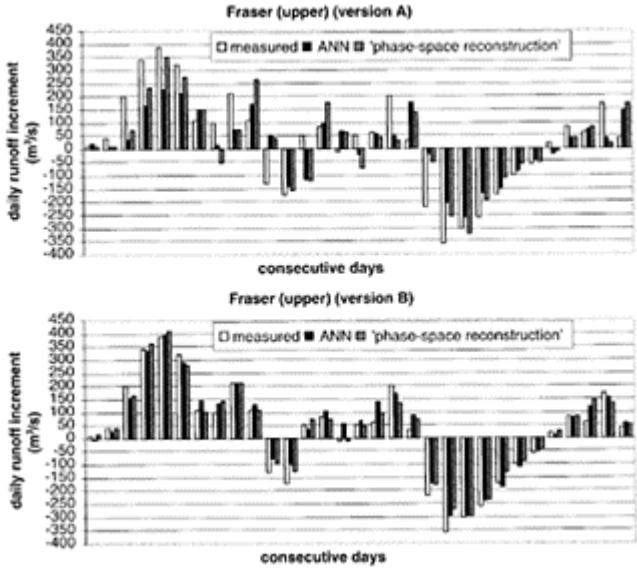

Figure 4. Comparison of one lead day runoff forecast for gauge station near Texas Creek (BC), on upper part of Fraser river, obtained from ANN and quasi “phase-space reconstruction” models in versions A and B.

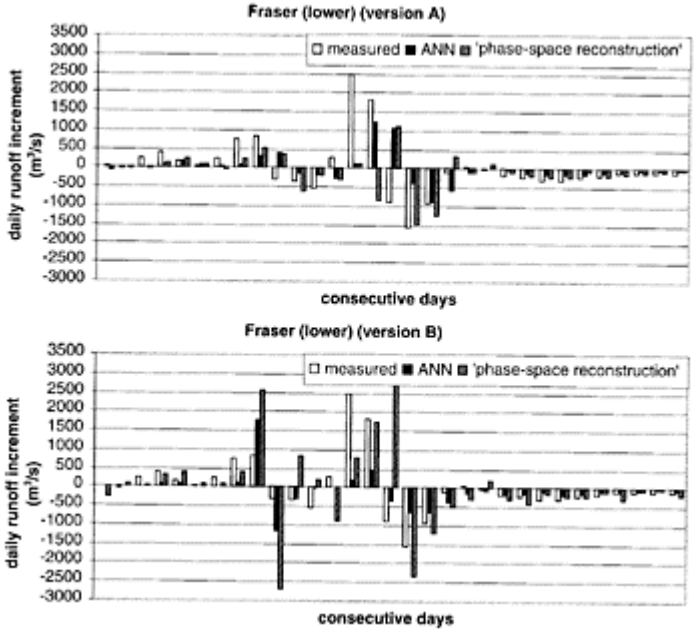

Figure 5. Comparison of one lead day runoff forecast for gauge station near Mission (BC), on lower part of Fraser river, obtained from ANN and quasi "phase-space reconstruction" models in versions A and B.

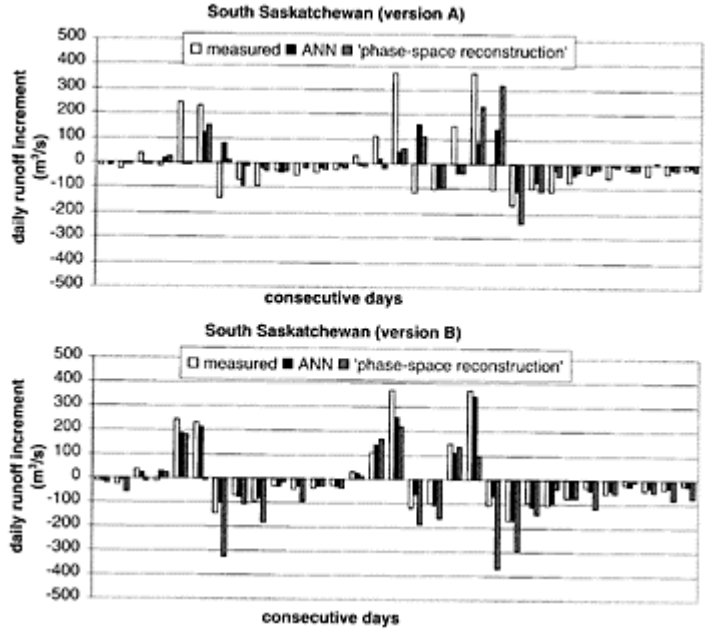

Figure 6. Comparison of one lead day runoff forecast for Medicine Hat gauge station, on South Saskatchewan river, obtained from ANN and quasi "phase-space reconstruction" models in versions A and B.

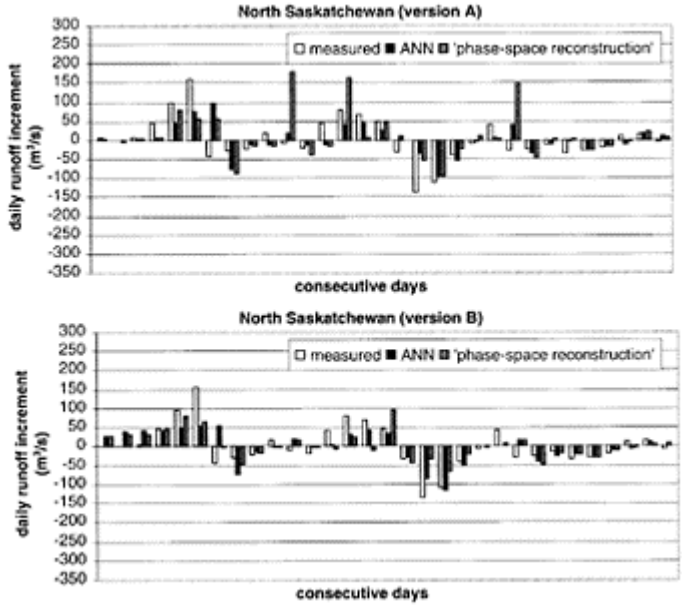

Figure 7. Comparison of one lead day runoff forecast for Prince Albert gauge station, on North Saskatchewan river, obtained from ANN and quasi “phase-space reconstruction” models in versions A and B.

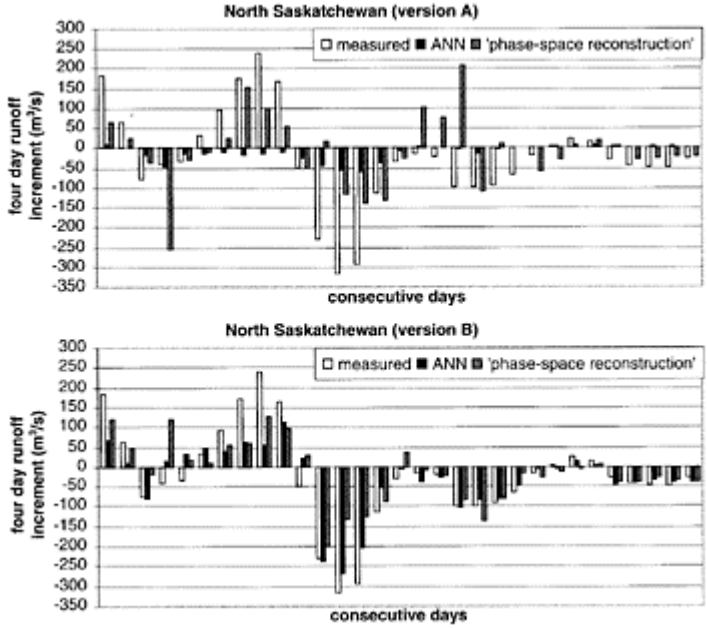

Figure 8. Comparison of four lead day runoff forecast for Prince Albert gauge station, on North Saskatchewan river, obtained from ANN and quasi "phase-space reconstruction" models in versions A and B.

This result is different from the one of Sivakumar et al. 2002 who considered daily river flow data set from only one gauge station in Thailand. A very short time series was analysed in that study, and the authors removed half of the data set because large differences were observed in those two parts of time series. In that study the phase-space model performance was much better than ANN.

Note that in version B in case of South Saskatchewan river prediction made by ANN is very good indeed and better than that by quasi "phase-space reconstruction" (see Figure 6). In case of quasi "phasespace reconstruction" the difficulty lies in the fact that it is quite hard to find enough vectors (3 delayed data from three gauges) in 9-dimensional space similar to the current data allowing for the evaluation of relevant linear regression coefficients.

An astonishing fact is that in version B in respect to North Saskatchewan River, 4-daily runoff forecast (Figure 8) proves to be better than the daily predictions (Figure 7, Table 2). It is the result of the selection of additional gauge at the distance corresponding to flow routing during the time period of 4 days.

5 CONCLUSIONS

The present study that was based on long enough time series from five river reaches shows that the method analogical to the phase-space reconstruction derived in the framework of deterministic chaos theory is useful for runoff predictions even if we have no evidence about the existence or non-existence of chaos in the considered river systems. It has also been shown that contrary to what is suggested in some hydrological articles, Artificial Neural Networks may provide accurate enough forecasts, in many cases even better than those based on "phase-space reconstruction". On top of that it has been shown that the use of additional information from other gauges improves significantly the forecasts based on both ANNs and "phase-space reconstruction". Such proposal has not been considered in respect to "phase-space reconstruction" in literature so far.

REFERENCES

Campolo, M., Andreussi, P. & Soldati, A. 1999. River flood forecasting with a neural network model. *Water Resources Research,* 35(4):1191–1197.

Campolo, M., Soldati, A. & Andreussi, P. 2003. Artificial neural network approach to flood forecasting in the River Arno. *Hydrological Sciences Journal,* 48(3): 381–398.

Chibanga, R., Berlamont, J. & Vandewalle, J. 2003. Modelling and forecasting of hydrological variables using artificial neural networks: the Kafue River sub-basin. *Hydrological Sciences Journa,* 48(3):363–379.

Dolling, O.R. & Varas, E.A. 2002. Artificial neural networks for streamflow prediction. *Journal of Hydraulic Research,* 40(5):547–554.

Environment Canada web page: http://citech.pyr.ec.gc.ca/aterweb/

Grassberger, P. & Procaccia, I. 1983. Measuring the strangeness of strange attractors. Physica 9(D): 189–208.

Hsu, K-L., Gupta, H.V & Sorooshian, S. 1995. Artificial neural network modeling of the rainfall-runoff process. *Water Resources Research,* 31(10):2517–2530.

Jayawardena, A.W. & Lai, F. 1994. Analysis and prediction of chaos in rainfall and stream flow time series. *Journal of Hydrohgy,* 153:23–52.

Kantz, H. & Schreiber, T. 1997. Nonlinear Time Series Analysis. Cambridge University Press, Cambridge.

Kudrewicz, J. 1993. Fractals and Chaos, *WNT,* Warsaw.

Ott, E. 1993. Chaos in Dynamical Systems. Cambridge University Press.

Porporato, A. & Ridolfi, L. 1997. Nonlinear analysis of river flow time sequences. *Water Resources Research,* 33: 1353–1367.

Press, W.H., Flannery, B.P., Teukolsky, S.A. & Vetterling, W.T. 1988. Numerical recipes: The art of scientific computing (Fortran Version). Cambridge University Press.

Schertzer, D., Tchiguirinskaia, I., Lovejoy, S., Hubert, P, Bendjoudi, H. & Larcheveque, M. 2002. Discussion of "Evidence of chaos in the rainfall-runoff process". *Hydrological Sciences Journal,* 47(1):139–148.

Sivakumar, B., 2000. Chaos in hydrology: important issues and interpretations. *Journal of Hydrology,* 227:1–20.

Sivakumar, B., Jayawardena, A.W. & Fernando, T.M.K.G. 2002. River flow forecasting: use of phase-space reconstruction and artificial neural networks approaches. *Journal of Hydrology,* 265:225–245.

Takens, F. 1981. Detecting strange attractors in turbulence. In: R and, D., A. & Young, L.S. (Eds.), *Dynamical Systems and Turbulence*, Lecture Notes in Mathematics, 898:366–381. Springer, Berlin.

Merging of river training and restoration in river basin management

N.Tamai

Kanazawa University, Kanazawa, Japan

River Flow 2004—Greco, Carravetta & Della Morte (eds.)

ABSTRACT: River training works have been executed for flood control or flood damage mitigation and water resources development. Human impacts, for instance, reservoirs, flood levees, straightening of channels, intake structures and so on, have altered natural rivers to great extent. Now river engineers are requested to cope with ever increasing flood peaks and to work for restoration of altered rivers. In some cases river training works and restoration are understood as a choice between two things. But the author points out that this is a fault of dualism.

When our target is to make basin-wide utility maximum, we cannot resort to conventional flood control schemes. We need to pay much attention to non-structural means including floodplain management and river restoration. Floodplain management is one of tools for demand control in land use. River restoration is one of ways for human demand control. In river restoration it is essentially important to give more space or freedom to rivers. This will be accomplished by human demand control. River restoration is a symbolic slogan to accomplish a multiple purpose project considering flood damage mitigation and conservation of ecosystems for river basin management.

1 INTRODUCTION

River training works have been executed for flood control or flood mitigation and water resources development. Human impacts, for instance, reservoirs, flood levees, straightening of channels, intake structures and so on, have altered natural rivers to great extent. Now river engineers are requested to work for restoration of altered rivers. In some cases river training works and restoration are understood as a choice between two things. But the author points out that this is a fault of dualism.

Human impacts on natural environment becomes bigger and bigger since industrial revolution. One clear example is global warming. Human activities developed to exceed capacity of natural environment. Human impacts have reached to an extent to exceed a righting moment of environment in the latter half of the 20th century. Then nature cannot recover its original state and entered into an irreversible process of deterioration. Under such conditions we need asset management to conserve nature as finite resources.

When we understand the essential features of natural asset of a river basin, we will obtain a unified view of entity of a river basin including natural disturbances, human impacts and responses of a basin system, and succession of ecosystems in a basin. We need to change paradigm from selection by dualism to coexistence by consensus among all stakeholders.

2 FLOOD CONTROL AND A NEW CONCEPT OF BASIN MANAGEMENT

At first interaction between human activities and their consequences in river basins is summarized in the area of flood control. The goal of this chapter is to establish a new concept for amalgamation of flood control/flood mitigation and river restoration.

2.1 *Does flood control investment bring about safer society?*

Design flood discharge increases as flood control works develop. In Figure 1 the historical increase of the fundamental design discharge in case of the Tone River that has the largest basin area in Japan is shown. In the present Master Plan authorized in 1980 the fundamental design discharge is 22,000m^3/s in which peak cut 6000m^3/s is planned by reservoirs and a diversion channel.

The river channel and flood levees are designed to cope with the allotted discharge of 16,000m^3/s to the river channel. In this master plan a probabilistic approach was adopted for the first time in determination of the fundamental design flood. Starting from the basin-wide river improvement work planned in 1901, observed maximum discharge was adopted as the design flood until the master plan of 1949. It is clear that the design discharge increased as we make efforts for flood control works and total investment to flood control increases. In other words flood control works brought about larger amount of peak discharge.

The design flood of the Yodo River that plays a major role for water resources in Osaka area experienced a similar increase. Why does this anomaly happen? The key factor of this anomaly is feedback from human activities in a river basin to a river channel. When flood control works succeed into a certain level, human settlement to a river basin increases and economic activities develop under safer situation from threatening of flooding. Higher rate of urbanization and economic activities tend to develop with positive feedback with each other.

Comparison of the variation of the design discharge with societal items, population and gross domestic product, is shown in Figures 2 & 3. We can recognize good correlation of an increasing rate between the design flood and GDP. But we had sharp reduction in GDP just after the World War II. Therefore, tendency in GDP curve shows

unusual disturbance around 1945. Flood control works creates safer living conditions in a river basin. Goals of investment for flood control are to protect floodplain from flood for more safe space for human beings and higher economic products. In this sense Figure 2 shows that goals of flood control projects are accomplished in Japan because GDP showed good growth in the 20th century.

But urbanization and higher economic activities generate negative side effects on a river channel. Urbanization means decrease of forest areas and agricultural land, and increase of non-permeable areas. These changes cause larger amount of runoff and faster convergence of water into river channels. In parallel with higher economic activities human society needs much wider space and in consequence, rivers are confined into a narrow space between flood levees. Infiltration in forest and agricultural land reduces and temporary storage capacity in river basins is lost by housing projects and industrial activities. Consequently, the fundamental design flood from a river

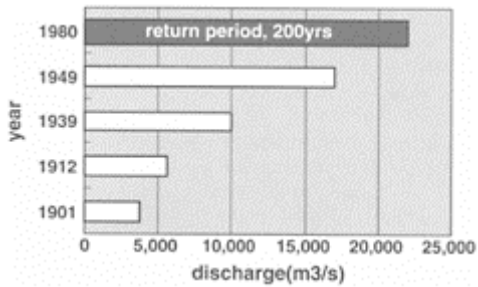

Figure 1. Historical variation of the fundamental design discharge of the Tone River in the Master Plan.

basin increases and arrival time of floods becomes short as we develop river improvement works. Ironically river channels receive bigger flood and water stage becomes higher as a consequence of river improvement works. Therefore, advanced level of flood control projects and larger return period do not necessarily mean that our life becomes safer.

2.2 *How can we create comprehensively safe society?*

As we see in the section 2.1 series of flood control works generate larger design flood. This means that a flood control project needs another flood control works of a larger scale in the future. A typical chain to show the consequences is as follows. In this expression an arrow shows resulted changes of social and hydrological factors in a river basin. A flood

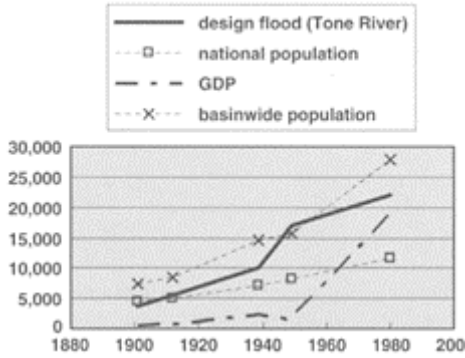

Figure 2. Comparison of the variation of the design discharge of the Tone River with societal items (Unit is as follows: design discharge, m^3/s; national population, 10 thousand persons; GDP, 10 billion yen, adjusted as of 1980; basin-wide population, thousand persons).

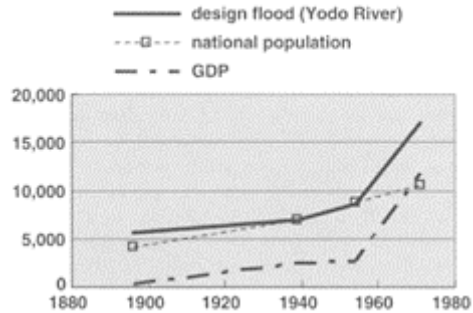

Figure 3. Comparison of the variation of the design discharge of the Yodo River with societal items (Unit is as follows: design discharge, m^3/s; national population, 10 thousand persons; GDP, 10 billion yen, adjusted as of 1980).

control project is executed.→The river channel has larger conveyance of flow and becomes safer against flooding.→Increase of population in river basins occur.→Urbanization develops.→Higher industrial activities develop.→Land use in

riparian zones develops.→Increase of peak discharge is generated by the change of hydrological processes in a river basin.→Riparian zones become vulnerable to flooding again.→A new project for higher level of flood control becomes necessary.

We need to remind that flood is a consequence of human settlement. There is no damage even if the water stage becomes extremely high in a river basin under purely wild conditions. Under wild situation a high flow is only a scene of natural disturbances and we recognize no flood damage. This fundamental characteristic is shown in Table 1.

The development of projects and recent tendency related with flood control are summarized in Table 2. Traditionally river engineers were engaged in flood control projects or flood protection projects. Engineers hoped that they were able to control peak discharge and water stage by constructing regulating structures of a flood in a river basin. Engineers tended to consider that when the objectives of the master plan were accomplished, safety level for residents in a river basin was satisfied according to their calculation. But most of engineers considered only behavior of flood in river channels that they constructed. They did not pay much attention to human reactions in a river basin. Human behavior in a river basin is more dynamic than that engineers considered in a planning stage. Once society is given a safe condition in a river basin, land use is altered to satisfy people's desire that never stops expanding.

Developments of human activities in a river basin continuously require additional flood protection works

Table 1. Difference in high flow and a flood by human factor.

	Natural condition	With human settlement
High flow	High flow	Flood, damage

as described in a previous section. Through experiences we gradually understand the following facts in river basins. Firstly, even if a mater plan is completed, a larger flood that exceeds a project level is possible as natural phenomena. Secondly, development of river basin makes damage potential in flood-affected area higher and higher. Thirdly, judgment of safety level by that of each facility, for instance, levee height, reservoir capacity, conveyance of river channels and diversion channels, is insufficient. Safety level of facilities is calculated for a single purpose of the facility and it does not explain safety level for residents.

Voices to require real safety of residents not the safety of facilities became strong during recent decades and importance of "non-structural means" is recognized in society. We understand that we cannot control flood that occurs as a natural event but we can only mitigate flood damage by "structural means" combined with "non-structural means". The target of non-structural means of flood control is to decrease damage potential. For example, in 1997 executive order by the President of the US already requested to avoid further development activities in floodplains below the water stage of a flood the return period of which is 100 years.

3 AMALGAMATION OF RIVER RESTORATION WITH FLOODPLAIN MANAGEMENT

3.1 *Dilemma caused by human impacts*

The discussion stated above is summarized schematically in Figure 4. The figure shows that development of river improvement works, which is shown by a thin solid line in Figure 4, steadily increases safety. A safer river basin is quite attractive for land developers and industrialists. They start turning forests and agricultural fields into residential and industrial areas. Land use change is accelerated by population increase in urban areas. Due to increase of non-permeable land surfaces in a river basin, peak discharge increases and arrival time of flood decreases. According to our experience urbanization occurs explosively as shown in

Table 2. Classification of projects related with floods.

Project	Objectives	Basic strategy	Typical facilities or systems
Flood control	● Reduction of the peak discharge	Structural means	● Reservoir
	● Reduction of the water stage		● Retarding basin
			● Diversion channel
Damage mitigation	● Flood plain management	Non-structural means	● Insurance
	● Evacuation from flood plain		● Hazard map
			● Rescue systems

Figure 4 where solid squares stand for human impacts and their consequences, such as, population, urbanization, peak discharge, etc. When urbanization rate exceeds certain level, say 50%, river improvement works become very difficult because available land is quite limited and land price becomes too expensive although we suffer from frequent floods with higher damage potential. Reducing factors shown by triangles in Figure 4 show reduction of redundancy with hazards, such as, arrival time of flood, resilience for evacuation, etc. Reduction of these factors corresponds to the increase of vulnerability of urban areas against flood.

In Figure 4 a bold solid line shows basin-wide utility or safety. The basin-wide utility is not a simple increasing function like safety by river improvement works. Safety of river improvement works indicates safety of a river channel. Once better condition is achieved, “increasing factors” and “decreasing factors” in a river basin emerge as human or social responses as are

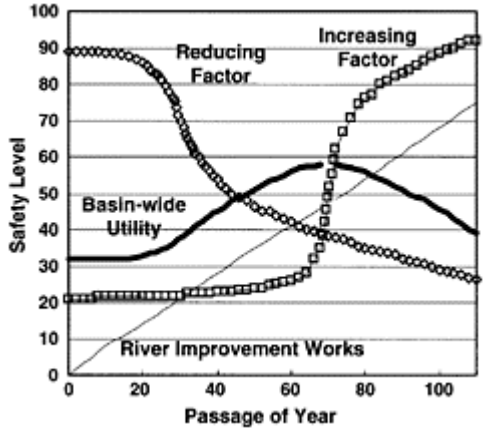

Figure 4. River improvement works and basin-wide utility (Modified from a figure in the final report of the Forum for Public Involvement and Basic Plan of Yoshino River (2001).).

discussed in this section. Therefore, a manager of a river basin needs to consider not only conditions of a river channel (a thin solid line in Figure 4) but also non-linear social responses (triangle and square symbols in Figure 4) at the same time. If adverse effects by other factors on flooding in a river basin as a whole become very large, basin-wide utility or safety begins to reduce with normal river improvement works as shown by a solid bold line in Figure 4. We are facing with such situations in many countries, regardless of developed and developing countries. I want to show that similar discussion can be applied to discussion in water resources and river environment later. Therefore, let me suggest you to pay attention to the point that general terms are used in Figure 4 to explain essential factors in the problem instead of specific terms in flood control.

Feedback loops in basin development projects in river engineering and their social influences are summarized in Table 3. Impact and response by projects for flood control, water resources development, and natural environment in a river basin are listed up in the table and the similar discussion and categorization can be applied to all of them.

Figure 4 shows a dilemma that the optimum condition for a part of a system is not the optimum for the whole system. We understand that flood control projects are not the optimum solution to secure comprehensive utility or safety of a whole basin and the mechanism of interaction of major components in a river basin is described in Figure 4.

When we recognize that pressure of urbanization is difficult to suppress and in urbanized area it is very difficult to raise safety level only by conventional means. We need to resort to non-structural means for flood mitigation in parallel with structural means. This phase corresponds to the peak in basin-wide utility in Figure 4. Through structural means for flood control we constructed many structures in a river basin and

consequently altered natural conditions of a river basin. Therefore, structural means of flood control stands for alteration of a river channel and a basin.

Table 3. Summary of a feedback loop in basin development projects and their social influences.

Project	Objectives of a single project under conventional institutional structure	Associated changes in a river basin	
		Reducing or deteriorating factor	Increasing factor
Flood control	Lower probability of flooding	Forest, agricultural field, arrival time	Urbanization, non-permeable land, peak discharge
Water resources	Larger reservoir capacity	Water quality	Eutrophication (retarding time), affected area
Safe and prosperous life in river basins	Larger gross domestic product	Natural resources, Biological diversity	Impacts on environment

3.2 *Toward basin-wide consensus—farewell to dualism*

Non-structural means include floodplain management. For floodplain management we need a council that is composed of all stakeholders, typically, managers of governments, water users, residents, and audits or experts. In floodplain management final conclusion may require conservation of hydrological mechanism, conservation of wetlands, conservation of agricultural fields, etc. Conservation can be said a core part of river restoration. Therefore, river restoration is re-presented by conservation of natural conditions. Conservation principles introduce certain constraints to land developers, farmers, recreational activities and so on. In other words floodplain management is demand control in land use. In this sense river restoration is a synonym of floodplain management.

Demand control in water resources and human activities are easily understood using Table 3. Demand control is not to maximize objectives of each single project in the first column of Table 3. In other words demand control is required to derive balance between increasing factor (human needs) and reducing factor (natural assets).

There is delicate difference in terminology. “Floodplain management” was conventionally used in the area of non-structural means of flood mitigation. In this paper the conventional concept is called as “floodplain management conventional”. “Floodplain management conventional” was introduced only for flood damage mitigation and considered quantity of water only. But floodplain management in this paper includes wider aspects. This is called as “floodplain management new”. “Floodplain management new” includes management of all water related systems in a river basin, for instance,

quantity, quality, riparian ecosystems, aquatic recreation, water ethics, local traditions of water related events and so on. River restoration in a broader sense means restoration of all aspects in water related systems. Frequently river restoration is used for enhancement of natural components for ecosystems in a river basin. But natural components are used symbolically for easy understanding of new aspects. It is emphasized that "river restoration" is a synonym of "floodplain management new".

Flood mitigation and river restoration are not conflicting two factors in "floodplain management new". Let me give two examples to explain one project can contribute both to river restoration and flood mitigation. Example 1 is re-meandering of a straightened channel. Re-meandering is a symbolic project in restoration works. A meandering river channel provides less water surface gradient and reduces flow velocity. At downstream of re-meandering reach concentration of river water is avoided and consequently we can deduce flood peak. Example 2 is conservation and restoration of wetlands. Wetlands serve as retarding basins for flood mitigation, provide various habitats to ecosystems, and can contribute to natural conservation in a river basin. We need to deepen the concept of "floodplain management new" and basic principles to guide actual projects in a river basin under "floodplain management new". In order to reach to consensus among all stakeholders we need to apart from dualism. Furthermore, we need to develop a decision support system that is able to evaluate ecosystems and value of environmental assets quantitatively.

4 A NEW HORIZON FOR ECO-COMPATIBLE BASIN MANAGEMENT

4.1 *What is eco-compatibility?*

It is difficult to give a rigorous definition to ecocompatibility in one sentence like "turbulence". Therefore, examples are introduced in the following paragraphs, in which eco-compatibility is satisfied.

In this paper we saw several cases that a single purpose project tends to confront with conservation of natural environment. Then we consider that a multiple stakeholder approach is necessary. In this multiple stakeholder approach ecosystems or nature restoration takes part in the discussion as one of players. A multiple stakeholder approach is one of examples of eco-compatible way in river basin management.

We already discussed tensions between flood control or flood mitigation and nature restoration, and water resources development and nature restoration in previous chapters. It is shown that merging of flood mitigation with nature restoration is possible and balance between water resources and nature restoration brings about comprehensive optimum condition in a river basin. These are examples of eco-compatible basin management.

4.2 *Economic aspects in eco-compatible basin management*

From Figure 4 we can obtain an important result on a basic economic aspect in "river basin management new". The peak in utility curve in Figure 4 appears in a middle level

of investment for flood control project (The abscissa corresponds to investment to a flood control project.). This means that a single-purpose flood control project cannot attain a bigger utility even though we increase the amount of investment after the investment level reaches to this optimum point. This means safety level of a conventional flood control project need not to be very high. It should be reasonably high by a plan, say, FC. Let us denote the safety level of this FC is FC-year flood. In order to obtain higher safety level than FC-year flood we need to adopt combination with flood mitigation by non-structural means. The additional cost for higher safety than FC-year flood should be used not for structural means but for non-structural means. Usually a cost curve for flood control facilities increases nonlinearly with increase of safety level. Adoption of eco-compatible techniques has ample room to seek for less costly flood mitigation.

4.3 *Examples of eco-compatible basin management*

How can we cope with or live with floods? In order to accomplish this goal we need to change the principle of our activities from "flood control" to "eco-compatible basin management". Examples are recent projects in the Mississippi and the Yangtze. After the great floods in 1993 and 1998, respectively, we understood that human beings could not control big floods with manmade facilities and we need to give more space for rivers. Under natural conditions whole alluvial plain is space for rivers and swollen water during floods can move into floodplain freely But recently rivers are confined into very narrow space between flood levees. Consequently, water stage during flood becomes higher and higher in a river channel as we want rain water to disappear around us as fast as possible.

In the Mississippi basin after the great flood of 1993 major emphasis is laid on flood mitigation or floodplain management. In this new plan buy out, restoration of wetlands, set back of flood levees, and others are core programs for flood mitigation. "Buy out" means a program to stimulate residents in floodplain in danger of inundation to buy alternate land in a higher location out of floodplain for movement. In the Yangtze basin similar principles were introduced after the great flood of 1998. Major projects are re-forestation in mountains, removal of farmers' dikes in reclaimed land along Dong Ting Lake, move of people in floodplain or islands in the river course to higher location and so on.

In these two biggest class river basins in the world amalgamation of nature restoration and flood mitigation takes real form in many actual projects. They are examples and proofs of effectiveness of the concept of "floodplain management new" or "eco-compatible basin management".

5 CONCLUDING REMARKS

It is shown on actual proof that design flood discharge increased with the increase of gross national product. Consequently, we learned that more investment to flood control projects does not guarantee safer condition for residents when the flood control proceeds to certain level due to social response in a river basin. Non-structural means are necessary to secure very high level of safety for flood mitigation. Amalgamation of flood control with restoration or nature conservation provides better solution from basin-wide aspects.

The analysis developed for flood control applies to water resources development, similarly Based on experiences in flood control and water resources development the concept of eco-compatible basin management is clarified and is shown practical even from economical point of view. Consequently, ecocompatible basin management provides one solution for sustainable basin management.

REFERENCES

Editorial Committee of 100-Year Modern History of Training Works of the Tone River 1987. 100-year modern history of training works of the Tone River, 114–115.

Editorial Committee of 100-Year Modern History of Training Works of the Tone River 1987. 100-year modern history of training works of the Tone River, 166–168.

Forum for Public Involvement and Basic Plan of Yoshino River 2001. For Better Solution of the Renovation of the Weir No.10, Tokushima Work Office (http://www.tokumlit.go.jp/)/Library of Yoshino River/Weir No. 10/24pp. (in Japanese).

Interagency Floodplain Management Review Committee: Sharing the Challenge: Floodplain Management into the 21st 1994, 189pp.

Yodo River Work Office, Kinki regional Office, Ministry of Construction, Japan 1998. Brochure of projects in the fiscal year 1998.

Floods management in Uruguay. The case study of Tacuarembó city

A.Capeluto, L.Teixeira & G.López

Instituto de Mecánica de los Fluidos e Ingeniería Ambiental (IMFIA). Facultad de Ingeniería. Universidad de la República, Montevideo, Uruguay

River Flow 2004—Greco, Carravetta & Della Morte (eds.)

ABSTRACT: Tacuarembó city may serve as a paradigm for several province capital cities of Uruguay with respect to floods. As a consequence of this, the presented method of analysis as well as the developed solutions can be used for many other cases. This paper summarizes the results of the work developed at the IMFIA in order to diagnose and evaluate alternatives of flood management in the city of Tacuarembó. The problem approach is based on an integrated watershed management scope, considering different dimensions of present problems. Hydrologic and hydrodynamic models of the river basin were implemented, which allowed the analy sis of different alternatives of flood management. A multi-objective decision-making analysis was used as a complementary tool for the determination of the most suitable solution. Particularly the possibility of combining structural and nonstructural measures was analyzed. The reliability of proposed flood control structures was analyzed by techniques of probabilistic methods.

1 INTRODUCTION

For Uruguay, floods mean not only a very important economical problem (about two million dollars per year of losses as a direct consequence) but also a socioenvironmental one that hits mainly on lower socioeconomical layers and have several repercussions on cities' activities.

Almost every important city in our country has suffered floods and assume them as one of their main structural problem.

Since its origins Uruguay has shown a typical urban population distribution, living nowadays in the cities about 90% of the total population in the country.

The rising number of people settling on risky areas is a consequence of a complex process mainly influenced by the migratory country-city process as well as the expulsion of poorest people from consolidated areas of the cities. These people settle down in a very precarious way, consolidating areas of great vulnerability when occupying floodplains.

Additionally, in recent years, particularly since 1990 this problem has become even more relevant as a result of the detected increase of floods frequency and intensity, reaching even consolidated areas, what can be related to the notorious increase of rainfall frequency and intensity. The last could be probably connected with climate changes or climatic variability cycles longer than a year.

Given the explained situation, as well as the lack of specific studies for this kind of problem, and the scarcity of specific management and protection initiatives, it has become evident the need of developing a local analysis methodology that should fit local tools and resources in order to control or reduce impacts produced by this kind of events.

This article summarizes the obtained experience in the case study of Tacuarembó city floods. As a riverside city, and because of its topographic and population characteristics, Tacuarembó turns to be a paradigmatic case of many other important cities in our country.

In this way, a methodological approach is presented here, to analyze floods problem in Uruguay. The results point out the importance several tools like hydrodynamic models, multi-objective decision-making analyses and probabilistic reliability analyses. The applied approach provides a better understanding of the problem, what gives the chance to find the most suitable solution.

2 METHODOLOGY

The basic analysis tool used in the present study were the hydrologic and hydrodynamic models of the case study system. In this way, a diagnosis of the present situation as well as the analysis of several flood protection and control alternatives were possible, considering both structural and non-structural measures.

By implementing a multi-objective decision-making analysis, a systemic approach was intended in order to select an optimal alternative, considering not only the classic technical and economical dimensions of the problem, but also its environmental dimension.

Finally, reliability of the selected flood control measures was estimated by probabilistic analysis techniques, using level II methods. These methods make it possible to analyze the failure of a work as a system by considering the uncertainties of every involved variable, as well as compare their respective incidence on reliability results.

2.1 *Diagnosis tools*

First, a diagnosis of the present situation was done, considering on one side the territorial occupation reality, and on the other a statistical analysis of rainfall data in order to detect

a possible raising tendency of extreme events parameters related to climate changes or hyper-annual climatic cycles. This analysis was performed over existing data series of Tacuarembó city.

As it is well known, annual accumulated rainfall records have been increasing in recent years in Uruguay. This accumulated rainfall increase does not necessarily implies an increase of potential flood cases, because these ones depend on maximum rainfall records whose durations are similar to the basin's concentration time. Consequently, it becomes particularly interesting to observe what happens to annual maximum daily rainfall, discharge, and stages records (behavior and evolution), what results to be representative information of extreme events in this case.

Statistical information of rainfall data of Tacuarembó city was also compared with similar statistical information of Artigas city, being able in this way to determine if the observed phenomena at Tacuarembó was just a particular case or we could find a larger area with similar behavior.

2.2 *Hydrologic and hydrodynamic modeling*

For this case study, hydrologic and hydrodynamic models were implemented for the analyzed basin, whose scheme is presented in figure 1.

The topographic information employed in this study was based, on one hand, on existing information (basically 1/50000 topographic maps with level curves each 10m), and on the other hand on a specially carried out survey. The last involved a special flight, and several field measurements including 21 flood plain cross sections, 9 of the riverbed, and the bridges geometry, gathering enough information so as to generate a digital terrain model.

Daily rainfall data was available for the period 1940–2001 at Tacuarembó, having also available statistical rainfall information of Artigas city, Genta (2003).

Hydrometric and gauge information as well as the estimated discharge—stage curves were supplied by

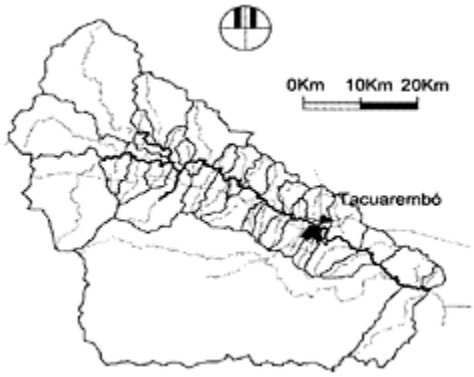

Figure 1. Sub-basins of the modeled stretch.

the national office of river management (DNH). From available information (previous inspection), only the 1986–2001 period stage data and its corresponding gauged discharge were taken into account.

The hydrological model of the upstream border subbasin as well as those of tributary sub-basins allowed to define the border conditions of the hydrodynamic model except for the downstream border. Hydrological modeling would finally supply the corresponding hydrographs at each border point.

Hydrographs were obtained by applying the Triangular Unit Hydrograph method on the synthetically generated storm. The storm was configured by following the Alternate Block method which uses the IDF curves information.

With respect to the hydrodynamic model, it can be outlined that a 49km stretch was represented, taking also into account the hydrologic modeling of 36 tributaries. The involved catchment area is 1378km^2, being 663km^2 of them situated downstream Tacuarembó city. The downstream border condition that best fitted the gauged data turned out to be a Q-h relationship given by Manning's equation, considering the last cross section geometry and a hydraulic slope equal to the riverbed slope (So=0.0003). It was demonstrated by this model that flow conditions in this border section does not affect flow characteristics in the area of interest, what leads to conclude that the model was large enough to study this area.

Part of model results, obtained after calibration and validation are presented in figure 2.

Looking at model outputs of maximum river stages at those cross sections associated to the city's stretch, encroached areas of the city were identified for several return period floods. Superimposing the identified areas over the streets and estates plans of the city, damaged families and blocks were quantified for each return period event.

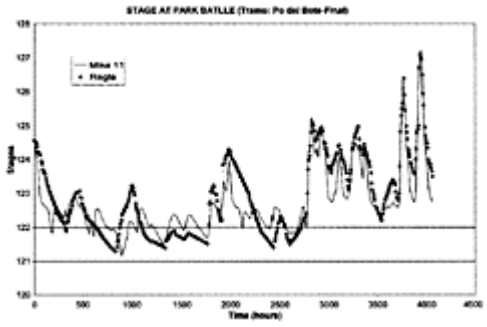

Figure 2. Comparison between modeled and measured stages at Parque Batlle station.

Based on this information and the statistical study results, present situation was described and evaluated.

2.3 *The alternatives*

Several flood control alternatives were also studied by representing different structural measures in the model. Effects of each alternative on floods was determined by noticing the stage decreasing at "Paso del Bote" cross section with respect to the present situation. Damages were quantified in the same way it was done for the present case, counting affected estates and blocks and finally identifying the relieved cases.

The evaluated structural alternatives arise not only from the working group, but also from interaction of this group with local people, turning it necessary to evaluate some alternatives that even being technically unsuitable, they were present in the collective thought. In this way, it was possible to quantify the negligible relevance of these structural solutions and show them to local people so that they could finally approve the resulting alternative. This interaction experience can be outlined itself as a relevant aspect.

The evaluated alternatives were the following:

- Dredging of the riverbed along a 6.5km stretch downstream the city.
- Removal of two existing bridges at the city.
- Construction of riverside levees
- Construction of regulating dam upstream Tacuarembó city.

2.4 *Multi-objective decision-making analysis*

Aiming to select an optimal solution among the studied group of alternatives, a special approach would be necessary in order to methodically evaluate each alternative from different points of view in accordance to several dimensions, and mark them to allow a comparison.

Technical, economical and environmental aspects where considered as the relevant criteria or analysis dimensions in order to value the different alternatives.

To compare every alternative, valuation scales were established for each dimension, depending on the fulfillment of certain requisites inherent to the considered dimension, the mark assigned to the alternative. Taking an example, from the technical point of view a solution would be valued depending on the offered protection (temporally and spatially), if it tends to a definitive solution (as it could be land use regulation), or if it protects in a transitory way, etc. In a similar way, certain requirements were established for the economical (costs and financial feasibility) and the environmental (different kinds of impacts and degrees of incidence).

Every alternative was marked in a range from 1 to 10 according to each criteria. Weighting coefficients were assigned to each dimension in order to outline their relative importance. A calibration process was required to establish the weight coefficients in order to properly reflect the assumed relevance order.

This methodology allowed to order the alternatives in a systematic way, taking simultaneously into account several analysis dimensions and their relative importance.

2.5 *Reliability calculations methodology*

Goodness of design as well as suitability of the proposed flood control measures will depend on how well predicted the behavior of these structures is in occasion of flood events along their service period.

In a traditional analysis uncertainty is just attributed to rainfall. This information is represented in the way of IDF curves or probability density functions for each rainfall duration. By considering this information, service life and admissible risk criteria, the control structure is traditionally designed. It must be outlined that in this approach, reliability is just estimated as the probability of rainfall records of exceeding certain value.

However, random character can also be attributed to many other design variables. Probabilistic methods of reliability calculation, particularly level II methods, Nowak (2000), Thoft-Christensen (1982), consider these other uncertainties. They work with the probability density functions associated to the respective variables and a mathematical expression of the studied failure mechanism, the so called failure function.

Level II methods operate assuming every variable as normally distributed and doing some approximations when estimating their associated probability. Among their advantages, it must be outlined that they allow to evaluate the relevance of each variable on reliability results. In this way it is possible to obtain a more balanced design by pointing out whisch are the critical variables with reference to reliability.

Table 1. Considered cases in reliability analysis.

	$P_{3,Tr}$	N_r	N_A	T_c
Case A	X	X	X	
Case B	X	X	X	
Case C	X			X
Case D	X			X
Case E	X	X		X
Case 0	X			

In the case study a regulating earth dam was selected as a flood control measure. Its reliability with respect to the overtopping failure mechanism was calculated by means of level II methods, considering several design variables as probabilistic and comparing results to those calculated by the traditional analysis.

Overtopping failure mechanism can be represented by the following reliability function:

$$g=H_c-H_{máx} \tag{1}$$

where failure domain is defined as that which leads to negative values of g, being H_C the height of the dam embankment and $H_{máx}$ the maximum height of the reservoir water raised by an occurrence of a flood.

The variables considered with an associated random character were: rainfall intensity (3 hours, T_r years) $\mathbf{P_{3,Tr}}$, roughness coefficient of the riverbed **Nr,** roughness coefficient of the culverts $\mathbf{N_A}$, and one of the dam's upstream sub-basin's concentration time **Tc**. These variables were not all simultaneously considered as probabilistic, proposing different case studies depending on which variable was considered in a probabilistic way. In Table 1 the studied cases are defined, marking with a cross when the variable was considered in a probabilistic manner.

3 RESULTS

3.1 *Diagnosis*

This case study may serve as a paradigm for many of most important cities in Uruguay, that similarly to Tacuarembó, have historically developed beside rivers.

Land use pattern and its evolution have been related to the migratory and urban expansion processes, which have given as a notorious result the occupation of Tacuarembó Chico's and some of its tributaries' flood plains all over the city. This people settle down in a very precarious way converting the riversides in really vulnerable areas to recurrent floods.

In conclusion, flood plains occupation turn to be one of the obvious causes of flood related damages that Tacuarembó city has historically endured.

On the other hand, as a result of the statistical study, a notorious increase of the maximum rainfall intensities as well as of the accumulated rainfall depth in the last 30 years must be pointed out. A concomitant variation was also observed when analyzing maximum river stages.

Table 2. Results for 10, 25, 50, and 100 years return period.

Event	Stage (m)	Affected blocks	Affected properties
T_r=10 yrs	128.63	55	326
T_r=25 yrs	128.96	86	613
T_r=50 yrs	129.30	107	871
T_r=100 yrs	129.62	123	1133

Concentration time of Tacuarembó Chico river's basin at Tacuarembó city is about 24 hours.

On the other hand the used accumulated rainfall depth data are daily. Consequently the detected increasing tendency of the daily maximum registries is coherent with the increasing tendency of the annual maximum discharges.

3.2 *Hydrodynamic model Present situation and analyzed measures*

Present situation is described in a precise manner by analyzing the following results of the hydrodynamic model.

Table 3 summarizes relevant information and behavior of present situation and the analyzed alternatives for a 10 year return period event. The alternatives are compared in terms of the maximum stage at Paso del Bote, quantity of affected properties, consequences, quantity of alleviated properties, economical cost, environmental cost and how the measure protects for larger return period events.

The multi-objective decision-making analysis is summarized in Table 4. Punctuation assigned to each alternative according to different analysis dimensions, weight coefficients (first column) as well as total punctuation per alternative, all of them are presented in this table.

In spite of the fact that weight coefficients, scales and marks are established in a quite subjective way, this method helps to set up the implicit designer's criteria in a clear manner by quantifying them, and so making it possible to compare different alternatives. Furthermore, it also helps to re-evaluate the relative relevance attributed to each dimension.

This method does not bring new results that were no implicit in designer's or decider's mind, but will help to present and see them in a clear way.

From multi-objective decision-making analysis it was clearly set that a regulating earth dam would be the most adequate alternative as a flood control measure for Tacuarembó. Dam's location is shown in figure 3. In addition to this measure, non-structural

Table 3. Summary of results for present situation and different flood control alternatives.

	Present situation	Dredging	Bridge opening	Riverside levee	Regulating dam
Stage (m)	128.63	128.58	128.28	127.18	127.22
Affected properties	326	326	248	89	89
Consequences	–	–	–	Urban drainage	Bridge affection
Relieved properties	–	0	78	237	237
Cost (million dollars)	–	4.5	12	3	1.75
Environmental cost	–	Very high	Medium	High	Medium
Degree of protection	–	Low	Medium	Medium	High

Table 4. Multi-objective decision-making analysis.

		Alternatives			
Dimensions	Weight coefficients	Dredging	Bridge opening	Levee	Dam
Technical	1	2	2	5	6
Economical	0.8	3	1	6	8
Environmental	0.9	3	10	3	6
Total marks		7.1	11.8	12.5	17.8

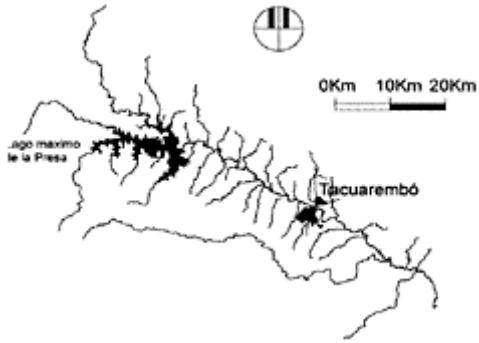

Figure 3. Location of the regulating dam.

measures should also be implemented, being of prior consideration land use policies and regulations. Other non-structural measures were also evaluated, being worth pointing out that of people transfer away from risk areas.

The recommended measure consists on a regulating earth filled dam 15 meters high, with an estimated retaining capacity of 85 000 000m^3, and a maximum pool area of about 1800 hectares. The discharge is automatic, by means of rectangular culverts.

The proposed structural measure must necessarily be complemented and coordinated with land use regulations that would gradually tend to remove the established housings from the flood plain.

Particular emphasis is required to control indiscriminate land occupation on protected areas. The accomplished damage reduction that results from floods frequency reduction can eventually be equaled or reversed as a result of an increased investment on protected areas. Structures are designed to endure up to specific return period events. Being these surpassed, works will not cope with them, leaving then protected areas again exposed to damage. The larger is the allowed investment, the larger is the potential damage. Civil works inspire false confidence feelings, and planners must be aware of this.

3.3 *Reliability of the proposed dam*

Reliability results can be summarized by the following tables.

Table 5. Reliability of dam for different cases and different service periods.

Service period (years)	Case 0	CaseA	Case B	Case C	Case D	Case E
1	0,9999305	0,9999302	0,9999082	0,9999254	0,9999028	0,9998728
10	0,9993052	0,9993022	0,9990824	0,9992543	0,9990284	0,9987287
30	0,9979171	0,9979081	0,9972497	0,9977644	0,9970881	0,9961910
50	0,9965309	0,9965160	0,9954203	0,9962768	0,9951516	0,9936598

Table 6. Return period of the event that leads to failure (annual reliability).

	Return Period (years)
Case 0	14388
Case A	13693
Case B	8715
Case C	12256
Case D	7736
Case E	5000

On Table 5, variation on reliability results can be noticed for annual values as well as for different service periods when considering different combinations of variables with probabilistic behavior.

On Table 6 annual reliability results are shown in a more familiar way by showing the return period associated to that event that will induce to failure of the dam for each case. Special attention must be paid to the fact that, while according to the traditional analysis failure could be expected for a 14 000 years return period event, probabilistic methods would demonstrate that the dam will fail just for a 5000 years return period event when considering the larger number of probabilistic variables.

In order to apply these methods, it becomes a basic requirement to gather statistical information of design variables. In this way, a better representation of the corresponding uncertainties can be achieved by fitting probability density functions to finally obtain more certain reliability results.

4 CONCLUSIONS

A diagnosis of urban floods problem in Uruguay is presented, concluding that the notorious raise in frequency as well as in intensity of these kind of events in the last decades, is clearly associated with two reasons. On one hand, changes in land use occupation pattern have been happening, particularly flood plains encroachment, and on the other hand a notorious raise of rainfall parameters was detected, particularly on its intensity, giving as a result a decrease of the associated return periods for extreme events.

The particular case of a city that may serve as a paradigm for several important cities in Uruguay was analyzed. In this case, based on a multi-objective decision-making analysis and aided by modern risk evaluations, structural flood control measures were defined (regulation dam), complemented also with non-structural ones (land use regulations and policies).

Probabilistic analysis methods, which incorporate consideration of other variables than rainfall in a probabilistic manner, show that the associated values to flood control structures' safety are notoriously inferior than those calculated according to the traditional method. The last leads to conclude about the necessity of reviewing design norms by incorporating the methodology used in this case.

The applied methodology as well as the obtained results, situate this study as one of the pioneers of this kind of analyses in Uruguay, showing the way that modern and internationally applied concepts and methodologies can be adapted to third world's local tools and resources.

A relevant experience to point out is the interaction with local people along the whole study, who participated in different stages of the project, particularly when setting the diagnosis of present problem and finally when identifying and selecting the optimal alternative.

REFERENCES

Genta & Teixeira (2003). *Inundaçoes Urbanas na América do Sul*. Chapter: Inundaciones y Drenaje Urbano en Uruguay. WMO, WGWP, ABRH, 2003. ISBN: 85-8868607-04.

Nowak & Collins (2000). *Reliability of Structures*. McGraw Hill Company.

Thoft-Christensen & Baker (1982). *Structural Reliability Theory and its Applications*. Springer Verlag, Berlin.

New trends in flood risk analysis: working with 2D flow models, laser DEM and a GIS environment

P.Archambeau, B.Dewals, S.Erpicum, S.Detrembleur & M.Pirotton

Laboratory of Applied Hydrodynamics and Hydraulic Constructions, University of Liege, Belgium Second author: Research Fellow of the National Fund for Scientific Research (Belgium)

River Flow 2004—Greco, Carravetta & Della Morte (eds.)

ABSTRACT: This paper outlines the integration of new and accurate laser DEM into the determination of floodplains. Global and robust GIS environment is absolutely necessary to manage this very large amounts of topographic data. The development and interaction of 2D flow models, simplified or not, ensures to offer more accurate and flexible physically based tools to the decision-makers.

1 INTRODUCTION

Floods control, risk mapping and more generally river management are topics on which a wide range of decision-makers focus a permanently increasing attention. The first step in flood hazard analysis and management, prior to any mitigation policy, is a thorough understanding and assessing of the level of risk. Though lots of work has been carried out for decades in the field, a genuinely reliable and efficient modelling of the corresponding flows remains a challenge. In spite of improved computation capacities, collecting, handling and validating large sets of topographic data as well as simulation results are still challenging tasks for hydro-modellers and practitioners.

The present paper covers a description and a detailed comparison of two state-of-the-art numerical models to be used as strategic tools in the process of flood risk assessment and mitigation. The first one is a 2D model for hydrodynamics, simplified according to the diffusive assumption (DM), quickly generating initial flow fields for the second one, a complete model based on the shallow water equations (SWE).

Those two models are integrated in the software package WOLF, which has been developed for almost ten years at the University of Liege. WOLF includes a complete set of numerical models for simulating free surface flows (process-oriented and spatially distributed hydrology [1], 1D and 2D hydrodynamics [2, 3], sediment transport [4, 5], air entrainment [6] ...) as well as optimisation algorithms. This optimisation tool, based on the innovative Genetic Algorithms, allows an objective calibration of friction coefficients [7].

A user-friendly GIS interface, entirely designed and implemented by the authors, makes the pre–and post-processing operations very convenient. Import and export operations are easily feasible from and to various classical GIS tools. Different layers of maps can be handled to analyse information related to topography, ground characteristics, vegetation density and hydrodynamic fields.

The validation of the model has been performed continuously for many years and is still running. Two cases studies on Belgian rivers are presented to illustrate inundation applications in a urban area.

2 MATHEMATICAL MODEL DESCRIPTION

The SWE model simulates any steady or unsteady situation, possibly taking into consideration air transport or sediment-laden flows, in Cartesian or curvilinear coordinates. It is in addition coupled to a turbulence model based on the Prandtl mixing length concept. The DM model is restricted to a specific range of Froude and kinematic numbers, but requires significantly less CPU resources.

In the shallow-water approach (SWE) the only assumption states that velocities normal to a main flow direction are smaller than those in the main flow direction. As a consequence the pressure field is found to be almost hydrostatic everywhere. In the diffusive model (DM) a similar depth-averaging operation is combined to the following hypothesis: the purely advective terms can be neglected. As a consequence the free surface slope is simply balanced by the friction term.

The divergence form of the SWE include the mass balance:

$$\frac{\partial H}{\partial t} + \frac{\partial q_i}{\partial x_i} = 0 \tag{1}$$

and the momentum balance:

$$\underbrace{\left[\frac{\partial q_i}{\partial t} + \frac{\partial}{\partial x_i}\left(\frac{q_i q_j}{h}\right)\right]}_{\text{inertia terms}} + gh\left(S_{fi} + \frac{\partial H}{\partial x_i}\right) = 0; \quad j = 1,2 \tag{2}$$

where Einstein's convention of summation over repeated subscripts has been used. H represents the free surface elevation, h is the water height, q_i designates the specific discharge in direction i and S_{fi} is the friction slope.

The *diffusive assumption* leads to a considerable simplification of the momentum equations:

$$S_{fi} = -\frac{\partial H}{\partial x_i}. \tag{3}$$

A friction law is needed for closure of both the SWE and the DM models. Its general formulation can be stated as a relation between the discharge, the water height and the slope:

$$q = \alpha h^{\chi} S_f^{\gamma} = \alpha h^{\chi} \left(\frac{\partial H}{\partial s} \right)^{\gamma}, \tag{4}$$

where α, γ and χ are coefficients suitable for the description of floodplain flows.

A more detailed description of the mathematical formulation can be found in the recent paper by Archambeau et al [3].

3 NUMERICAL IMPLEMENTATION

A finite volume scheme is used in all models to ensure exact mass conservativity. An upwind schetne is exploited for space discretization of the SWE model and extended to the DM.

An implicit pseudo-time integration scheme, suitable for solving non-transient problems, is implemented in the SWE model. In the DM model the GMRES or Conjugate Gradients (CG) algorithms are used for evaluating iteratively the solution of the symmetric linearized system.

3.1 *Space discretization and boundary conditions*

An original upwind scheme is applied for space discretization of the complete set of equations. The stability of this second order upwind scheme has been demonstrated through a theoretical study of the mathematical system as well as a von Neumann stability analysis. Much care has been taken to handle correctly the source terms representing topography gradients. A fitted spatial upwinded scheme is developed similarly to the previously described DM.

The models allow the user to specify any inflow discharge as an upstream boundary condition (BC). The downstream boundary condition can be a free surface elevation, a water height, a Froude number or even no specified condition if the outflow regime is supercritical (SWE only).

3.2 *Resolution of the DM model*

The primary goal of the diffusive formulation is the quick computation of steady-state approximate solutions. Those first estimations of the final solution are intended to serve as fairly good initial condition for the complete SWE model.

A first approach for solving the DM might be a pseudo-time evolution, starting from a user-defined initial condition. In order to prevail the possibility of using large time steps, this pseudo-time integration would need to be performed in an implicit way.

A second approach is to disregard the time derivative term and to solve a non-linear system of time independent equations. Both methods are obviously very similar if the time step becomes very large. Various iterative techniques are available for solving such

very large linear systems. Among them are the methods “by point”, such as Jacobi, Gaus-Seidel, … [8, 9] or full implicit such as ADI [10–14], GMRES [15], CG [16–19].

3.3 *Time integration for the SWE model*

An implicit pseudo-time integration scheme, suitable for solving steady-state problems, is implemented in the SWE model. This technique allows much larger time steps than those acceptable for an explicit time integration. On the other hand the resolution procedure is more intricate. A Newton method is exploited to solve the large non-linear system. The successive linearized systems are solved with the powerful GMRES algorithm, which is advantageously coupled to a preconditioner. For this purpose an incomplete LU decomposition is applied. The Switched Evolution-Relaxation technique by Van Leer has been used to continuously optimise the time step.

In the DM model the GMRES or CG algorithms are also used for evaluating iteratively the solution of the symmetric linearized system. In both cases the resolution procedure represents a very challenging step because of the complexity of a cost-effective evaluation of the Jaobian matrix. WOLF performs this job effectively, by storing only non-zero elements and their location in the large sparse matrix.

3.4 *Friction modelling*

River and floodplain flows are mainly driven by topography gradients and by friction effects. The total friction includes three components: bottom friction (drag and roughness), wall friction and internal friction.

The bottom friction is classically modelled thanks to an empirical law, such as the Manning formula. The DM and SWE models allow the definition of a spatially non uniform roughness coefficient. This parameter can thus easily be distributed as a fimction of soil properties, vegetation and sub-grid bed forms.

The friction along vertical boundaries, such as bank walls, is introduced thanks to a physically based model developed by the authors. This modification of the classical friction law presents the advantage of leading to a correct hydraulic radius of the 2D cross-section in case of sufficiently shallow flows.

The internal friction is properly reproduced by the turbulence model.

3.5 *More features of the numerical codes*

In addition an automatic mesh refinement is used to enhance the convergence rate towards accurate steady-state solutions [3]. The computations are performed on several successive grids, first very coarse and then gradually refined. The hydrodynamic fields are almost stabilized when the computer code automatically jumps onto the next grid. This fully automatic method considerably reduces the number of cells in the first grids. Then, the successive so-called initial solutions are interpolated from the coarser towards the finer grid in terms of both water heights and discharges.

In case of an explicit pseudo-time evolution: the stable time step is significantly larger since it depends linearly on the size of the mesh. For an implicit evolution, the benefits of the quadratic convergence are reached since the initial solution is sufficiently close to the

steady state solution. In spite of extra computation time to re-mesh and linearly interpolate the initial solution the overall CPU time saving is clearly appealing.

4 LASER DEM

Very recently, the Belgian Ministry of Facilities and Transport (MET) and most particularly the Service of Hydrology Studies (SETHY) acquired a very accurate DEM on the floodplains in the whole Walloon Region.

A method of airborne laser was used for the proximity inundation zones of the entire rivers network. An echo-sonar was applied for measuring the bathymetry of the main channel, exclusively on navigable rivers (Fig. 1).

Consequently, the poor and inaccurate 3D information that has been available for many years, 30m square and an error of several meters in altitude, is replaced by an exceptional DEM since the precision in altitude is 15cm and, on top of that, the information density is one point per square meter.

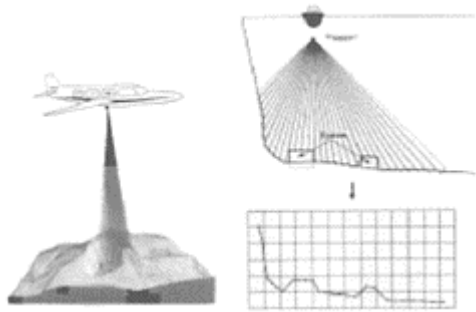

Figure 1. Principle of the DEM acquisition by airborne laser and echo-sonar ship.

Figure 2a. Béthane: IGN topography (digitalized contour line map).

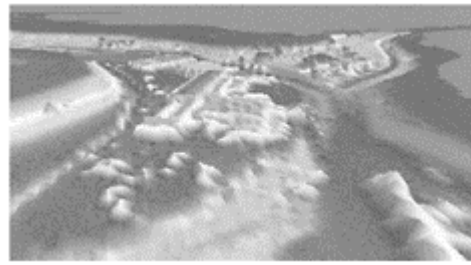

Figure 2b. Béthane: laser data including buildings.

To illustrate the accuracy of the DEM, (Figs. 2 and 3) two comparisons of data on the same regions are presented, the towns of Bethane and Eupen (Belgium).

Generally, specific features of flows in urban area (such as blockage by buildings, slowing down of the wave front propagation, etc) were taken into account by a local modification of the roughness coefficient. While, with this new set of topographic data, irregularities of the topography influence directly the inundation flows. This permits to refocus the roughness coefficient to more proper physical values.

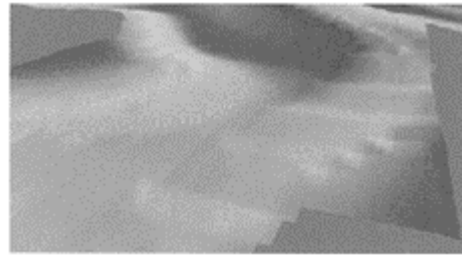

Figure 3a. Eupen: IGN topography (digitalized contour line map).

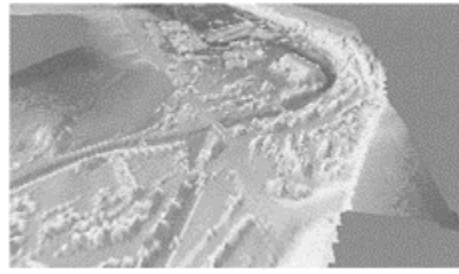

Figure 3b. Eupen: laser data including buildings.

5 GIS ENVIRONMENT

Management and operations on such a large set of data requires a robust and efficient pre- and postprocessing. A GIS environment, entirely designed and implemented by the authors, performs this tools. Several databases containing topographic data, pictures of historic floods, characteristics of structures along the rivers (dams, bridges, weirs, …) are stored on a single data server with their geographic coordinates to be easily downloaded by any modeller.

A difficult task for the preprocessing is the interpolation of the minor river bed when no distributed data are available. It's the case on the non-navigable rivers where the airborne laser is the only source of the DEM. In fact, the laser beam doesn't cross the water surface. Therefore, the only available information are based on cross-sections and thus must be interpolated in 3D to recompose a global DEM. Original methods were developed by Detrembleur [20] to fulfil this job and are implemented in the WOLF package.

6 CASES STUDIES

6.1 *Flood induced inundation on the river Ourthe*

The first case proposed is a flood event on the river Ourthe that occurs 14 February 2002 (study commissioned by the MET-SETHY).

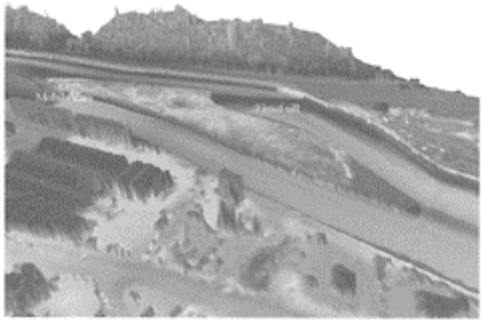

Figure 4. Example of DEM interpolation of the river bed and aggregation with the airborne laser data (river Ourthe, Tilff; Belgium).

Figure 5. Comparison between water heights and aerial picture of the flood event (football field).

Characteristics of the simulation are:

- Discharge: 570 m^3/s
- Length of the real computed river: 7.35km
- Total number of computations cells: 300.000
- Uniform size of the cells: 2×2m
- Two hydraulic structures: a mobile dam and fixed sill.

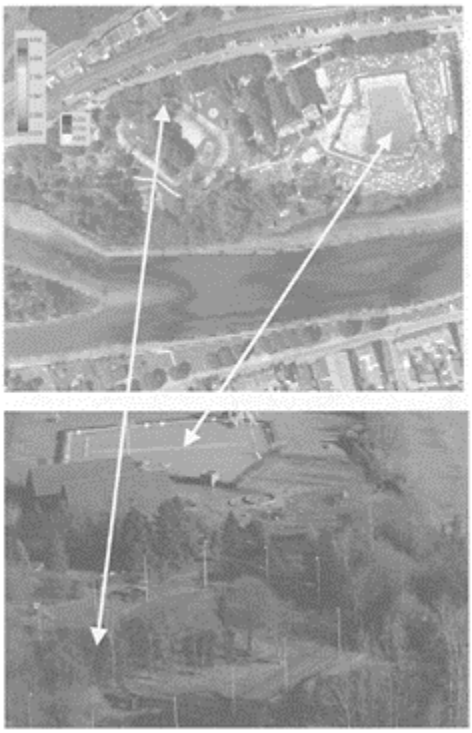

Figure 6. Comparison between water heights and aerial picture of the flood event (water-pool of the “Prés de Tilff”).

In this case, there were discrepancies between the first simulation and the real observations. Actually, the interpolation of the main river bed was computed based on cross sections taken in ’70 years. Actually, major modifications of this bed were realized to mitigate floods in the town of Tilff. The right bank was newly designed to a vertical wall when it was computed with a slope of 4:4. A complete dredging was performed too.

After the introduction of the different modifications in the topography, the results improved significantly as demonstrate the comparisons between numerical water heights and aerial pictures of the floods (Figs. 5–6).

6.2 *Flood inundation on the river Lesse*

The second case presented in this paper consists in the verification of the works protecting from floods in Han-sur-Lesse on the river Lesse, Belgium (study commissioned by DGRNE, Walloon Region).

This town, which attracts tourists, is located at the downstream of geological caves that divert the free surface flow of the Lesse trough underground flow. A maximum discharge of about 25m^3/s can

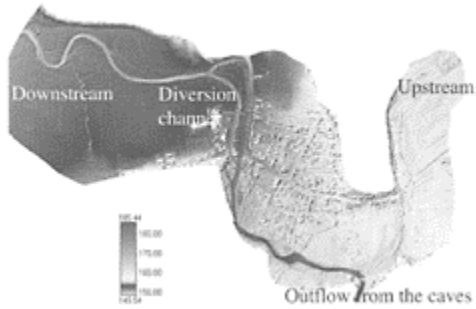

Figure 7. General topography of Han-sur-Lesse.

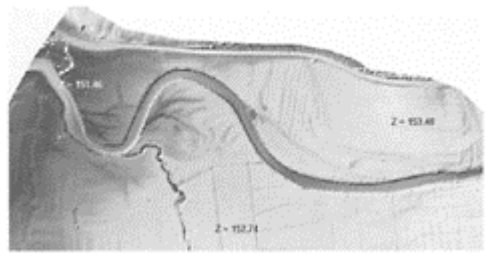

Figure 8. Enlargement of the downstream topography.

pass by this way. The rest is forced to return to the historical bed.

A first stage was the building of a diversion channel to increase the natural discharge capacity of the river. A side-weir creates a separation between the two channels. Thus, the normal discharge only flows in the natural river. In addition, a second stage consists in the building of walls and small dyke to prohibit the overflow in the urban zone.

Figures 8 and 9 illustrate the precision of the laser DEM. The drainage channels of farm fields, residual erosion of historical floodings, current small dyke and the interpolated topography of the main river bed can be observed.

Characteristics of the simulations are:

- Discharge: 150m^3/s
- Length of the real computed river: 4km
- Total number of computations cells: 450.000
- Variable size of cells (Fig. 10)
- Hydraulic structures: a mobile dam and several fixed sills.

A multibloc discretization is used in this problem to limit the total computation time. The finest information is conserved along the river trough the town but a progressive increase in the cells size is performed towards the extremities of the computation domain to ensure evanescent boundary conditions.

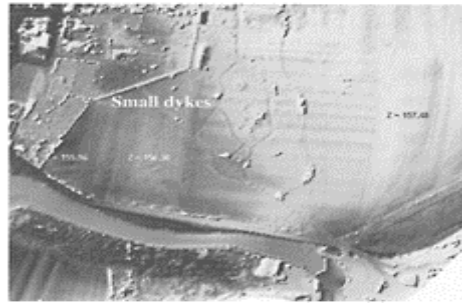

Figure 9. Enlargement of the topography around the exit of the caves.

Figure 10. Multiblocs discretization.

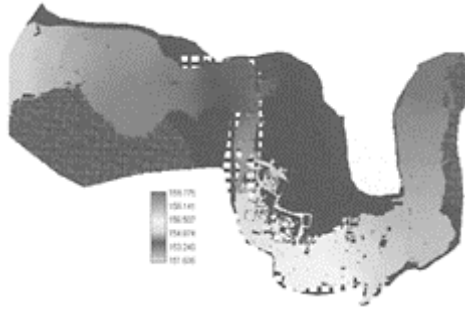

Figure 11. Free surface elevation for the flood of January 2003.

The reference event dates from Jannuary 2003 because it's the only flood after the building of the diversion channel. Figures 11 and 12 illustrate the results in terms of free surface elevation and water heights. A good concordance is obtained between computed results and field observations, and thus both in extension of the flood and in water heights.

An observation of the results in terms of Froude numbers (Fig. 13) permits to indentify a critical

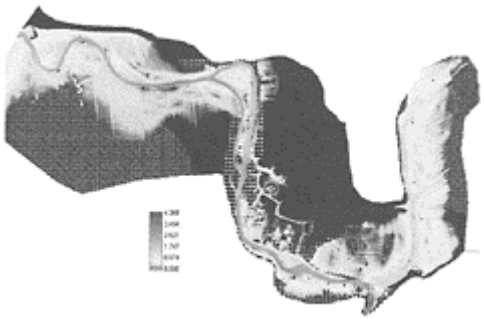

Figure 12. Water heights for the flood of January 2003.

Table 1. Comparison of water height for the flood of January 2003.

Observation (cm)	Computed (cm)
82	86
5	15–30 center of street
25	5 along the houses
20	30
94	95
113	117
100	100

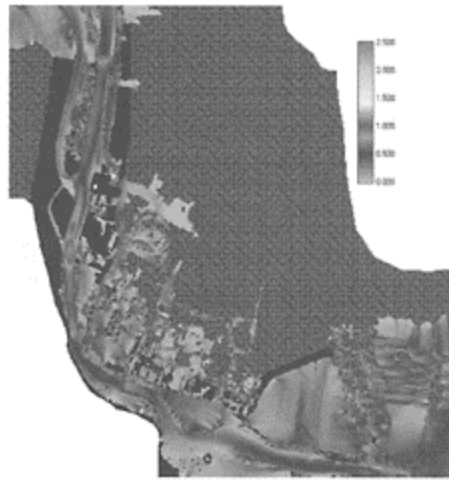

Figure 13. Froude number for the flood of January 2003.

section, just before the side-weir, in an obvious place. The real nature of the problem consists in a rise of the bottom topography due to an outcrop. This critical section reduces significantly the favourable effect of the stage 1 on the upstream. Furthermore, stage 2 doesn't modify this place bacause the buildings just stop at the upstream. Thus, recommendations were made to

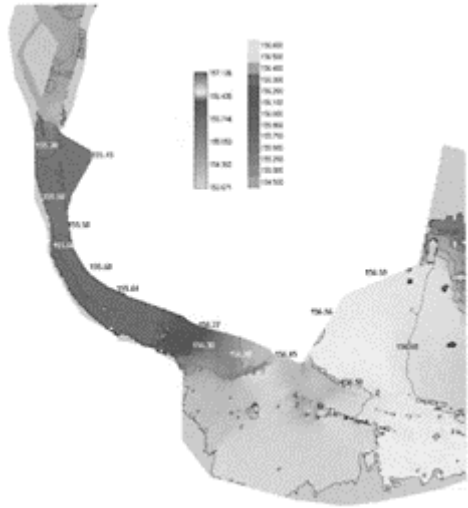

Figure 14. Free surface elevation after the building of stage 2 (m).

the manager to extent the works to redraw this portion of river.

The check of the stage 2 consists in a simulation where the town is untouchable by the floods. Thus, impermeable boundary conditions are applied on the outline of the town. A comparison of the final water heights with the heights of walls and dykes concludes to a good design of the works.

7 CONCLUSION

The present paper offers a comprehensive comparison between both numerical models (DM and SWE) for very practical applications such as floodplains modelling and inundation maps plotting. The key advantages brought by the GIS environment are also illustrated, focusing on the major contemporary requirements of decision-makers in the field of flood control.

Further research is currently undertaken for investigating sediment transport effects and their simulation.

REFERENCES

1. Archambeau, P, et al. Impact studies and water management with WOLFHYDRO: a new physically based hydrological solver. in International Symposium on Environmental Hydraulics. 2001. Arizona State University, USA.
2. Mouzelard, T., et al. Water management of large dams. in International Symposium on Environmental Hydraulics. 2001. Arizona State University, USA.
3. Archambeau, R., et al. A set of efficient numerical tools for floodplain modeling, in Shallow Flows, G.H. Jirka and W.S.J. Uijttewaal, Editors. 2003. IfH & TU Delft: Delft. p. 141–158.
4. Dewals, B., et al. Coupled computations of highly erosive flows with WOLF software. in 5th International Conference on Hydro-Science &–Engineering. 2002. Warsaw University of Technology.
5. Dewals, B., et al. Dam-break hazard mitigation with geomorphic flow computation, using WOLF 2D hydrodynamic software, in Risk Analysis III, C.A. Brebbia, Editor. 2002. WIT Press.
6. André, S., et al. Quasi 2D-numerical model of aerated flow over stepped chutes. in XXX IAHR Congress. 2003. Thessaloniki, Greece: IAHR.
7. Erpicum, S., et al. Optimising a cascade of hydroelectric power stations with the WOLF package, in Water Resources Management, C.A. Brebbia, Editor. 2003. WIT Press. p. 65–74.
8. Hirsch, C., Numerical Computation of Internal and External Flows, Computational Methods for Inviscid and Viscous Flows. Vol. Volume 2. 1990. Wiley. 691.
9. Young, D.M., Iterative solution of large linear system. Englewood Cliffs. 1971, New York: Academic Press.
10. Kim, S. and J. Douglas, Fractional time-stepping methods for unsteady flow problems, http://citeseer.nj.nec.com/382490.html
11. Malhotra, S., Douglas, C. and Schultz, M. Parameter choices for ADI-like methods on parallel computers, 2000, http://citeseer.nj.nec.eom/11073.html
12. Douglas, J. and S. Kim, On accuracy of alternating direction implicit methods for parabolic equations, 1999, http://citeseer.nj.nec.com/douglas99accuracy.html
13. Molls, T. and G. Zhao, Depth-averaged simulations of supercritical flow in channel with wavy sidewall. Journal of Hydraulic Engeneering. 2000. 126(6): p.437–445.

14. Panagiotopoulos, A. and J. Soulis, Implicit bidiagonal scheme for depth-averaged free-surface flow equations. Journal of Hydraulic Engeneering. 2000. 126(6): p. 425–436.
15. Saad, Y. and M. Schultz, GMRES: A generalized minimal residual algorithm for solving non-symmetric linear system. SIAM Journal of Scientific and Statistical Computing. 1986. p. 7.
16. Jones, M. and P. Plassman, An improved incomplete Cholesky factorization. 1991. Mathematics and Computer Science Division, Argonne National Laboratory: Illinois. p. 12,
17. White, D., Solution of capacitance systems using incomplete Cholesky fixed point iteration. Journal for Numerical Methods in Engineering, 1998.
18. Lin, C.-J. and M. J, Incomplete Cholesky factorizations with limited memory. 1997.
19. CACR, C.f.a.c.r., NAG Libraries. 2000, http://www.cacr.caltech.edu./
20. Detrembleur, S., Elaboration d'outils intégrés de gestion des données topographiques et morphologiques pour la modélisation des crues et inondations, in Applied Hydrodynamics and Hydraulic Constructions. 2003. University of Liège: Liège. p. 110.

Floods control in Argentina: learning from the experience

R.A.Lopardo & R.Seoane

INA (National Water Institute), Ezeiza, Argentina

River Flow 2004—Greco, Carravetta & Della Morte (eds.)

ABSTRACT: This paper deals with flood control and mitigation in large flatland valleys in Argentina and describes the advances, mistakes and omissions over the last twenty years. The authors analyse the advances made and the problems encountered when developing a hydrological measurement network for planning and designing hydraulic structures and a hydrological early warning system. The paper focuses on flood problems along the Paraná River, which affected urban areas, the Southern Salado River, which inundated rich lands in the flatland region of the Province of Buenos Aires, and the Northern Salado River, that caused a severe flood event in 2003. Historically, Argentina has sought to tame floods through the construction of infrastructure works to protect the people of the floodplains. Recent disasters and the need to protect the environment call for non-structural measures, such as floodplain zoning, development control, flood warning and disaster mitigation planning.

1 INTRODUCTION

Flood disasters are a major issue in the life of societies. The objective of this paper is to describe different aspects of flood-related problems, to stress the importance of warning systems, to assess the impact of climate change in Argentina, and to perform a hydrological analysis of the significant rise in the Salado River basin that affected the city of Santa Fe.

Integrated water resources planning, through a basin level Master Plan for flood protection that links and binds structures and protection works with non-structural solutions to control and mitigate emergencies, is a critical and urgent task not only in Argentina and other Latin American countries but also in other parts of the world. Such a plan must be designed when waters are still. Even if the population “forgets about the water problem” because there are no floods, local authorities must take basic needs into account and implement a flood control and disaster prevention policy.

Located in the southern region of the Americas, Argentina has a population of 37 million and a total area of 2,500,000km^2. Because of their uneven distribution, water resources in Argentina cause both floods and droughts.

Humid regions represent 24% of the country's total area and account for 68% of the total population. On the other hand, arid regions represent 61% of the country's total area but account for only 6% of the population. Mean discharge in Argentina is 25, 836m^3/s (22,000m^3 per inhabitant per year), i.e., 22 times higher than the "water stress level" adopted by the United Nations.

The Plata River Basin, including the lowland "Pampas" region, accounts for 86% of the total discharge in Argentina. This basin is the most important in terms of human concentration, urban development and economic activity in the country. The waters of the Bermejo, Paraná, Paraguay and Uruguay rivers, which are part of the Plata system, are shared with Bolivia, Brazil, Paraguay and Uruguay.

The Northern Salado River rises in the northwestern region of Argentina and is a tributary of the Paraná River. The Southern Salado River Basin, in the heart of the agricultural and cattle region of the "Pampas" region, forms the southern border of the Plata River Basin.

Heavy convective rains in the "Pampas" Central Region are expected to aggravate actual physical conditions (reservoirs that are already full and groundwater levels that are already high). are likely to cause damages, particularly in areas with vertical drainage processes, as is the case of the sandy soils in the NW region of the Province of Buenos Aires. This situation may seriously affect sowing and harvesting activities that are intensively carried out in the region.

2 THE LOWLAND "SOUTHERN" SALADO RIVER REGION

The Central "Pampas" (Area Pampeana Central) comprises part of the provinces of San Luis, La Pampa, Buenos Aires, Santa Fe and Córdoba. The Salado River Basin extends over an area of 168,100km^2 comprising 58 districts of the Province of Buenos Aires with a population of 1.3 million. The area's main economic activity is agriculture, accounting for 25% of the country's total farm crops, 30% of total beef production, and 18% of dairy produce.

Irregular rains and summer rainfall deficit are some of the climate conditions prevailing in the basin. In the last 25 years there have been periods of very heavy rainfall resulting in extensive floods, such as those which affected the north-eastern sub-region in 1986, 1987, 1993, and the recent floods in Lake La Picasa's command area, among others.

There is neither natural drainage nor important waterways. The region's average slope is 3.5cm/km; it lacks a systematized drainage network; and floods are caused by excessive rainfall. Unplanned construction of canals has transferred the problem from upstream to downstream areas.

In the last few years the area has been subject to an intensive agricultural development process whereby it shifted from cattle raising to grain and crop farming activities.

Water management is crucial for the region's development. Lack of a sustained policy to manage flood problems is one of the main obstacles to their solution. It should be

noted that each province in the basin has embarked upon solving their own flood problems. Only two studies (1985, 1999) have attempted a comprehensive diagnosis of the region as a whole.

In order to provide a general view of the case under analysis, we may break down the system into three layers: the natural system, the socio-economic system, both of them interacting and generating mutual actions and reactions, and an institutional subsystem or layer which is closely linked to the other two.

Physically, the NW region of the Province of Buenos Aires is not a standard river basin. Since 1900, when records began to be kept, annual evaporation exceeded rainfall. Downstream from the Salado River, tributaries and other rivers flowing into the sea were channelized (1920) to flush water out and render the land suitable for human occupation.

The natural system is described using the conceptual hydrological model for flatland areas which refers to a landscape with low energy to drain water flows and to the lack of defined basin limits and of major drainage structures or waterways. Consequently, there is a strong predominance of vertical variables, such as infiltration and evaporation, over horizontal variables, which relate to drainage. Surplus rainfall water is stored in shallow surface areas and drainage is generated by accumulation of water and the creation of a hydraulic gradient.

Environmentally, the rainfall regime has great space and time variability and an uneven seasonal distribution though the amount of rain has increased since 1971.

The socio-economic subsystem is characterized by low population density, extensive grain and crop farming and cattle raising activities—depending on the suitability of the soils—little infrastructure—both in terms of road and canal networks—and unplanned land use. Flood problems have increased due to inadequate agricultural practices and poorly designed canals and embankments which sometimes affect downstream areas.

As regards the political-institutional subsystem, Argentina has adopted a federal system for administering its natural resources. According to the National Constitution, natural resources are owned by the provinces and it is them who manage and supervise their water resources without the participation of the national government.

Lack of a long-term active policy for flood management is another issue affecting the region. In the absence of a policy for the entire hydrological system, each province in the basin seeks to find its own solutions to their water problems.

3 THE SALADO RIVER MASTER PLAN

To mitigate the damages caused by torrential floods and severe droughts, the Integrated Master Plan for the Salado River Basin seeks to promote sustainable use of water resources, improve economic conditions, and preserve environmental parameters in the Salado River.

Local roads as well as provincial and national highways have been flooded causing serious economic restrictions that had a strong impact on the transportation of agricultural and dairy products. Not only fields that were not flooded but also important urban and rural areas experienced production losses for they were isolated from the rest.

Estimates show that the value of agricultural production will rise by 10% as a result of drainage works and reservoir construction. The area protected by the Plan represents almost 35% of the basin's total area (6 million hectares).

Maximum annual benefits to be derived directly from the construction of works for the whole basin are estimated to be in the order of U$55 million for grain and crop farming; U$93 million for cattle raising; U$19 million for dairy products; U$10 million for land-holding infrastructure; U$60 million from changes in land use; and U$9 million for public rural infrastructure. This makes up an annual total of mean direct benefits of almost U$250 million once the whole hydraulic infrastructure included in the Plan has been executed.

The total cost of investments in hydraulic drainage and storage works, rural roads and environmental mitigation measures is in the order of U$1.5 to U$1.8 billion. Investment in the said works is planned to take place over a fifteen to eighteen year period, i.e., an annual investment of around U$100 million per year. The Net Present Value of the investment at a 10% rate is U$193 million and the Economic Internal Rate of Return for the whole project is 14.3%.

Finally, it is important to note that the Province of Buenos Aires has enacted Law No. 11257 fostering the creation of Basin Committees and Management Consortia to manage resources and monitor infrastructure construction. The Provincial Government, together with the respective districts, has started outreach and consultation tasks in the belief that dissemination and consultation of the Plan among farmers and potential beneficiaries is a key factor for its success.

From a technical point of view, the Integrated Master Plan is based on analytical tools that facilitate the understanding of the basin's operation and make it possible to predict how it will react to planned interventions. The plan will provide a well-balanced social and environmental development framework by implementing a range of different measures that supplement one another and are coordinated by a flexible execution scheme. Non-structural measures in the Master Plan are:

(a) An Institutional Program that includes institutional restructuring, legal and fiscal measures, capacity building, transparent management tools, and public education and awareness.
(b) An Environmental Program that includes management of wet and inundated areas, environmental analysis and monitoring, regulation of fishing, integrated natural resources management, and wildlife and habitat management.
(c) A Sustainable Economic Development Program that includes soil conservation, improvement of natural pastures, intensive cattle breeding activities, promotion and development of small- and medium-sized tourism businesses, and rural employment opportunities.

4 FLOODS IN THE DOWNSTREAM AREA OF THE PLATA RIVER BASIN

The Plata River Basin comprises an area of some 3,150,000km^2 over the territories of Bolivia, Paraguay, Brazil, Uruguay and Argentina. It is made up of the following river

basins: Alto Paraná, Paraná, Paraguay, Uruguay, Iguazú, Pilcomayo and Bermejo (Figure 1).

The total population in the basin is over 80 million that contribute 70% of the gross domestic product of these five countries. More than forty hydroelectric dams, that produce 60% of the region's total energy, have been built on the rivers flowing in the basin (the well-known Itaipú Dam among them). Some rivers are navigable, and implementation of the "Paraná-Paraguay Hidrovía" navigation scheme is under way. The Paraná River Basin, between 16° and 34° of southern latitude, covers an important part of Brazil, the entire territory of Paraguay, part of Bolivia, and an important part of Argentina. The catchment area in the Delta upstream from the Plata River is 2,600,000km^2.

The Paraná River Basin comprises four distinct rivers: the Paraguay River, the Iguazú River, the Upper Paraná River and the Paraná River (downstream from the confluence with the Paraguay River). The present analysis focuses on that final stretch of the Paraná River. The town of Paso de la Patria (Argentina) is on the confluence of the Upper Paraná and Paraguay rivers, 687km downstream from the left bank of the Iguazú River. The Paraná River section at Paso de la Patria is 3,500m wide, with plenty of islands and sandy banks. This section is 1,240km from the city of Buenos Aires, where the river rises (Soldano, 1947). Downstream from the confluence with the Paraguay River, the Paraná River turns into a typical "flatland river with movable bed": permanent discharges and low slopes, dune translation on a fine sand bed, and a big floodplain that is inundated only during copious discharges, with the exception of some islands. Downstream from the city of Corrientes, the river slope decreases gradually reaching some 0.01m/km.

Systematic water level measurements in the Paraná River started in 1901. As noted by Aisiks (1984), if the Paraná River does not reach the 5.5m level mark in the city of Corrientes (discharging some 25,000m3/s), there will be no flood damages in the valley upstream and downstream from that section. An analysis of historical data shows that the Paraná River floods every three or four years and although floods can occur in any season, they are more likely to take place in February and March with a secondary rise in June. The most severe floods occurred in 1905, 1966, 1982–1983, 1992 and 1998. A discharge was gauged in June 1905 (Q=43,000m^3/s); in March 1966 the discharge was 41,000m^3/s. The 1983 flood had special characteristics because it had started in 1982 after heavy rainfall saturated the soil in the basin. A high discharge was recorded at the Corrientes section (Q=51,300m^3/s) on May 30th, there was a second peak on July 12th (Q=45,000m^3/s), and the maximum discharge took place on July 18th (Q=61,000m^3/s).

A large-scale coupled ocean-atmosphere oscillation in the Pacific Ocean, known as the El Niño-Southern Oscillation (ENSO), is related to interannual variations in precipitation and streamflow in several region of the world. Sea Surface Temperature index (SST) and the Southern Oscillation Index (SOI) are used to

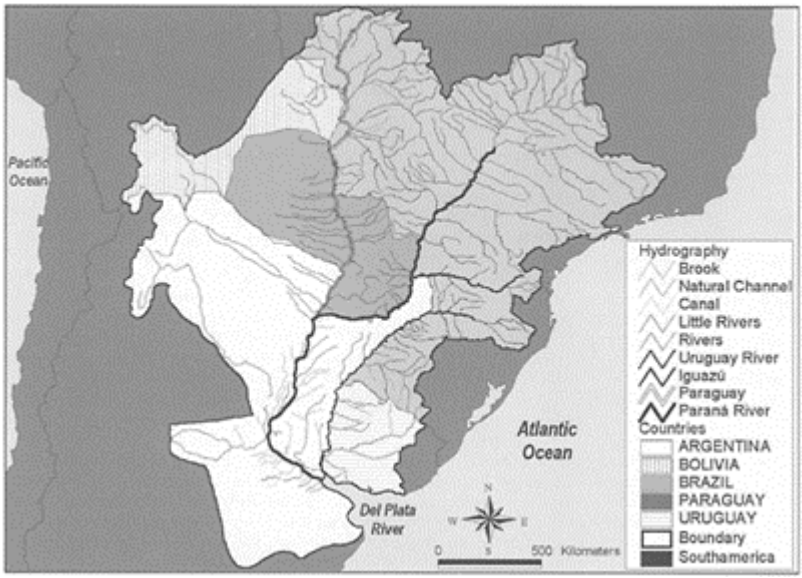

Figure 1. La Plata river basin.

quantify ENSO. SST anomaly is the sea surface temperature departure from the long term mean, averaged over a eastern and central equatorial Pacific Ocean. The warm El Niño phase is associated with high SST anomalies and the higher annual discharge in River Paraná at Corrientes and Posadas (Amarasekera et al., 1997). Floods related with warm phase of El Niño observed during 1982/83, 1992/93 and 1997/98 and the median of daily discharges are shown at the figure 2 for the period 1884/2002.

In 1992 a devastating flood in the city of Santa Fe reached a discharge of $Q=54{,}000 m^3/s$. The water level was higher than the one measured during the large flood of 1982–1983 due to excessive anthropic pressure on the floodplains (Paoli, 1997).

The increase in mean discharges and water levels since 1970 shows that the volume of water over the last three decades has increased with respect to similar periods in the past. Even if this condition is not permanent, it can be associated to the global climate change.

Statistical data on monthly minimum mean levels (month of September) and on the usual monthly maximum mean level (month of April) for the period 1970–1992 show a seasonal variation amplitude that decreases through time because flows have been

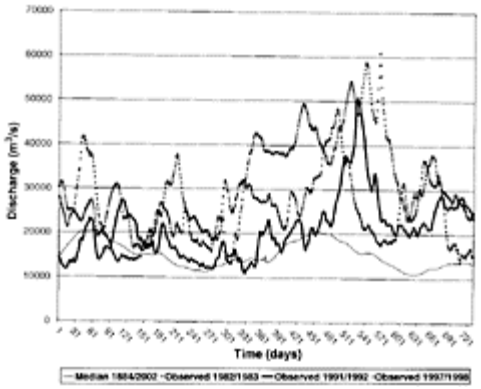

Figure 2. Discharges at Corrientes. Median and discharges associates with ENSO events.

regulated by many Brazilian hydroelectric dams in the upstream basin. The said amplitude reduction exerts a greater impact on low water levels than on high water levels. During severe floods the system's regulation capacity is negligible.

In the case of large rivers flowing in flatland valleys with low slopes, extreme floods can be predicted and forecasted by means of rainfall data in the basin's upstream and middle regions. It must be pointed that even if storm characteristics and conditions are critical, the magnitude of the flood will strongly depend on the previous humidity content in the basin. If the basin's soil is saturated, if the floodplains are waterlogged, and if the reservoirs are full, a storm with heavy rainfall will trigger a flooding disaster.

5 THE HYDROLOGICAL EARLY WARNING SYSTEM

A hydrological warning system provides the Civil Defence and Disaster Control authorities with anticipated information on exceptional hydrological events. Forecasts must be precise. If floods are not accurately predicted credibility is lost and the cost of emergency measures increases. If the flooding event is not predicted, disaster occurs. Precision and regularity of the forecasting system is of the utmost importance for the preservation of life and minimisation of material losses in affected areas.

As a result of the 1982/83 floods, the National Secretariat of Water Resources created a Hydrological Warning System for Plata River Basin, which is operated by the National Water Institute (Goniadzki, 1997). The severe flood of 1992 caused serious damages in the northeastern provinces of Argentina. The Inter American Bank for Reconstruction and Promotion (BIRF) has granted a loan for the flooding restoration program that is administered by the Ministry of the Interior. This agency has signed an agreement with the National Water Institute to improve the technological capacity of the Hydrological Warning System for the Plata River Basin.

The Hydrological Warning System must operate on a continuous basis because it forecasts not only floods but also low water levels strongly required for navigation purposes. In the cities of Rosario and Santa Fe the Paraná River's water level can be predicted more than twenty days in advance while in other cities (Formosa, Corrientes, Goya) prediction levels are different.

The flood of 1992, when INA's early warning system was already in operation, caused physical damages that amounted to approximately U$500 million. Water levels were considerably higher than in 1966; however, in spite of the fact that there was a remarkable increase in investments and in population density, there were less physical damages.

The Plata River Basin System comprises simulation and forecasting models for different real-time hydrological variables. A probabilistic focus is represented by multiple lineal regression models using a recursive estimation algorithm for the parameters with the Kalman filter. Deterministic hydrological models are represented by the Sacramento Model of the National Weather Service, calibrated for the downstream basin of the Iguazú River (24,000km^2), Chavasse and Seoane (1997).

The HEC-HMS precipitation-discharge transformation model developed by the U.S. Corps of Engineers has been calibrated and is used for the Uruguay River Basin. For floods along the Paraná River, a hydrodynamic translation model (Ezeiza V) has been developed by the National Water Institute (Menéndez, 1998).

The early warning system includes a series of tasks which range from rainfall monitoring (in different time scales) to short-and long-term rainfall forecasting in selected catchments. Main field tasks are: (a) estimation of rainfall areal distribution by means of satellite images combined with field data (real precipitation in the catchment); (b) areal distribution calculation with the "Hydroestimator" model; (c) assessment of different rainfall estimation techniques for use in several hydrological and neuronal models; (d) convective systems monitoring through satellite images (use of the FORTACC algorithm-FORecasting and Tracking for Active Cloud Clusters); and ε) mean areal precipitation forecasting (72 hours) at catchment level.

The catchment areas of the Southern Salado River (2001) and of the Salado River (2003) are examples of rainfall estimated with satellite images in cooperation with the National Environmental Data and Information Service (NESDIS/NOAA) from USA.

6 RECENT FLOODING OF THE CITY OF SANTA FE

During the last days of April and early in May 2003 the city of Santa Fe, subject to periodic flooding of the Paraná River, experienced a most devastating flood induced by a tributary of the Paraná River, called Salado River (which is not the Salado River that flows in the "Pampas" region of Buenos Aires, some 1,000km south).

The loss of more than twenty human lives, the large number of people evacuated, and the huge economic damages characterize this event as a disaster of catastrophic proportions. More than one third of the city's area, including strategic buildings such as schools, hospitals and an electric power plant, was suddenly inundated.

The downstream basin of the Salado River a typical flatland river is in the Province of Santa Fe. The upstream basin flow has little influence on maximum downstream flow

discharges. The Salado River flows into the Paraná River between the cities of Santa Fe and Santo Tome.

The Salado River mean discharge in the downstream region is 145,6m^3/s. Mean annual precipitation in the area ranged from 1,100mm in the east to 800mm in the west during the 1941/1970 period, and from 1,200mm to 900mm during the 1971/2000 period. The natural flatland landscape has been modified by anthropogenic activities (construction of roads, canals and land works). In the 1990s the Province of Santa Fe implemented diverse structural and non-structural measures such as Argentina's flood program, which was launched with World Bank financing after the big flood of 1992.

The 2003 flood was caused by heavy rains that fell within the southern basin and which lasted from April 22 to April 24 (saturation of the basin had been detected in January 2003). Most of the rainfall turned into surface flow.

The discharge measured at the railway bridge near the city of Santa Fe was Q=3,100m^3/s. Previous hydrological analyses (INA, 1998) estimated a discharge of 3,010m^3/s (some kilometres upstream from that section) for a recurrence period T=100 years. Fortunately, the mighty Salado River flood did not occur simultaneously with the Paraná River flood since the backwater effect would have further raised the Salado River water levels.

Some of the anthropogenic activities that contributed to the disaster were:

- A small part of the western protection, erected between 1994 and 1998, was not finished. It seems that this disaster could have been prevented if construction of the structure had been completed.
- The Santa Fe-Rosario highway bridge is narrow (155m) representing only 8% of the total valley's width (2,000m) in this section. During the flood the backwater effect raised the water level more than 80cm and overflowed the western protection 1,800m upstream from the bridge.
- Since March 2003 the Hydrological Warning System of the Plata River Basin had been reporting that the basin was saturated and that the region was being affected by severe storms. The flood wave translation was already known to the authorities because of the floods that affected small villages and caused bridge damages in the upstream region.
- Land use in the floodplains is not adequately regulated. Construction of permanent strategic buildings in floodplains should not be authorized.
- The city lacked a flood contingency plan for evacuation and social assistance during and after the event.

In conclusion, the vulnerability (from a physical point of view) of the city of Santa Fe is the result of the following major factors:

- Its geographical location: it is located between two big uncontrolled rivers and its large floodplains have been occupied due to urban expansion.
- Its flat topography: inadequate rainfall runoff, low-lands close to the rivers, and high groundwater table levels.
- It lacks comprehensive and consistent urban planning.
- Its roads and protection works: inadequate for the increasing severe water scenarios and poor operation and maintenance plans.

- People should be made aware of the fact that a protected area is still a risk area. The province failed to implement non-structural measures to supplement infra-structure works and to devise an explicit contingency plan.

The damages caused by the extraordinary rise of the Salado River are the result of both natural and anthropogenic vulnerability.

7 RESEARCH PRIORITIES

There are no infallible flood protection structures. A flood protection structure may overflow during its life cycle or have construction problems or be poorly maintained. Therefore, non-structural measures are a must.

It is worth pointing out that flood risk assessment and formulation of emergency plans are tasks involving many disciplines in which professionals in water sciences must participate using a holistic approach.

It should be borne in mind that integrated water resources management related to floods and rising water levels calls for the need to investigate the means to improve administrative and economic management. Some lines of research and development to be considered in the near future, always aiming at diminishing risks and economic losses during critical water events, are:

- Research to improve hydrological modelling in order to gain a better understanding of the selection criteria and of statistic function parameters required to define the flow-return period relationship. This must be supplemented with enhanced knowledge of mathematical modelling of rain-flow transformation processes in order to safely predict possible rated flows for protection works.
- Research to improve hydrodynamic flood modelling in watercourses. It is particularly important to obtain accurate basic data on floodplain topography in areas of low slope, bathymetries, gauging and water quality monitoring.
- Research to use at—a local scale—the results derived from climate prediction models (such as those used for the El Niño-Southern Oscillation phenomenon).
- Comprehensive water resources management studies related to rising water levels and to jurisdictional, economic and legal problems derived from flood protection structural and non-structural measures.
- Research to optimise hydraulic design of infrastructure waterworks.
- Specific research to solve water-related problems in urban areas (floods, waterlogging, and pollution).
- Research on sustainable water resources use to prevent future water disasters.
- Development of techniques that combine satellite information with forecasting and monitoring activities.

“Science and Technology must be useful to society”. This means that there must be an interaction between knowledge expansion and the society that will benefit from it, that boundary conditions must be taken into account so that society can profit from scientific production. The services rendered by a hydrological warning system is only one part of an overall process which should be fully operational to be meaningful.

8 CONCLUSIONS

The academic community, specialized agencies and decision-making bodies must interact in order to optimise human and material resources and generate greater benefits to society.

It is then crucial to develop, adapt and promote the use of modern hydro-meteorological technologies and to establish hydrological measurement networks. This can be achieved through the joint action of specialized state agencies that have shown an interest in working together. Cooperation links should be cemented, both formally and informally, across the institutions engaged in emergency response and mitigation activities. This is the only way to promote adequate and timely actions to withstand adversity.

One major problem specialists in this field currently face relates to dissemination of technological advances. Engineers, in particular, have always been and are still considered by the media as some sort of mercenaries reporting to a powerful client who puts the rest of the population at risk. Their voice and opinions are always questioned by professionals from other disciplines, by the journalists themselves, and by people that lack technological knowledge.

Moreover, decision-making bodies usually get conflicting messages about the benefits of some measures or projects from different actors. Such actors, who lack adequate scientific training, exert an influence and cause confusion about the priorities and critical activities that are required for an organized management of water resources.

Therefore, it will not be possible to integrate scientific and technological advances with social growth unless profound changes in management aspects are achieved. To this end, qualified specialists and professionals should have an active participation in the decision-making process and should not be involved with political bodies responsible for deciding on certain programs and processes.

These conclusions are supported by the chapter on “What is needed” in Kundzewicz, Szamalek & Kowalczak (1999). The catastrophic flood that hit Poland in 1997 has shown that local conclusions can help build up general concepts.

REFERENCES

Aisiks, E.G. 1984. La gran crecida del río Paraná de 1983, Organización Techint, Boletín Informativo, 232, Buenos Aires.

Amarasekera, K.N., Lee, R.F., Williams, E.R. & Eltahir, E.A. B. 1997. ENSO and natural variability in the flow of tropical rivers. J. Hydrol. 200, 24–39.

Chavasse, D. & Seoane, R. 1997. Asociación deterministicoestocastica para la predicción de caudales. Ingeniería del Agua. Vol. 4 N° 2, 55–64, España.

Goniadzki, D. 1997. Sistemas de información y alerta hidrológico. La prestación de un servicio esencial, Revista INA, Año, 1, N° 1, 21–23.

Kundzewicz, Z.W. & Takeuchi K. 1999. Flood protection and managements: quo vadimus?, Hydrological Sciences Journal, 44(3) 417–432.

Kundzewicz, Z.W. 1999. Flood protection—sustainability issues, Hydrological Sciences Journal, 44(4) 559–572.

Kundzewicz, Z.W., Szamalek, K. & Kowalczak, P. 1999. The great flood of 1997 in Poland, Hydrological Sciences Journal, 44(6) 855–870.

Menéndez, A. 1998. La comprensión de la fenomenología de las inundaciones como requisito para su control, Revista INA, Año II, diciembre, 25–28.
Paoli, C. 1997. Inundaciones en ríos con creciente ocupación, Revista INA, N° 1, 78–81.
Soldano, F.A. 1947. Régimen y aprovechamiento de la red fluvial argentina, Editorial Cimera, Buenos Aires.

Flood management and control in an urban environment—Diakoniaris case study

E.I.Daniil, S.Michas, G.Bouklis, P.L.Lazaridou & L.S.Lazarides

HYDROEXIGIANTIKI, L.S.Lazarides & Co.Consulting Engineers, Marousi, Greece

River Flow 2004—Greco, Carravetta & Della Morte (eds.)

ABSTRACT: In this paper the implementation of general design considerations for flood management and control in an urban environment and their application to Diakoniaris project is presented. Diakoniaris river is located near Patra city, Peloponnese, Greece. It has ephemeral flow, flows from south to north and for the last 5km before its outlet to the sea flows through the west suburbs of the city of Patra. Presently only 1km, just before the outlet, is trained with a closed section, running under the main avenue of the area. According to city planning this avenue is proposed to be extended to the north to meet the highway circumventing Patra city, currently under construction. The design was based on an integrated watershed management approach, including works in the upstream mountainous area and consideration of the impact of proposed diversions on adjacent basins. Sediment control dams upstream and a sedimentation basin downstream of the new highway are proposed. Parallel to the closed concrete section, which will have to be extended upstream under the new part of the road, additional culverts running parallel to the existing one will be constructed.

1 INTRODUCTION

Integrated decision making for watershed management is not a simple task. Currently, different tools and approaches are proposed by researchers, and a trend for public involvement is evident in many countries. As the state of the art is far from complete understanding of the processes involved, many times, custom solutions, taking into consideration cultural and other local features, should be preferred.

Diplas (2002) notes that although significant attention has been paid recently on the impact that maninduced changes have on the environment, this has been a well known fact for a very long time, dating back to Plato. While the concept of land use change is

not new, the rate, scale, and kind of changes that have been taking place over the last hundred years or so have been unprecedented. Real progress in predicting the modifications caused by human activities within a watershed will require further disciplinary work, research at the interface between disciplines, and improved dynamic interaction of the processes occurring in the abiotic and biotic systems.

General design considerations and principles for flood protection and related stormwater drainage system design, based on an integrated environmental approach, involving less technical works and preservation of the physical condition of streams and creeks in urbanized areas have been presented (Daniil et al. 2000, Lazaridou et al. 2002). Special topics to be taken into consideration include sediment control through check dams and selection of design return period. The design period should be selected depending on the specific location, the associated design of the receiving stream or water body, and considering the consequences of a bigger flood than the one used for the design. It should always be kept in mind that the selected design should be implemented starting from the downstream end and special care should be used in main road crossings.

1.1 *General design principles*

For flood protection design, regulation and management of streams passing through urban areas, an integrated environmental approach should be implemented and many factors taken into account (Daniil et al. 2000). Design considerations to be used as guidelines for practical use are mentioned below.

- Streams should remain in their physical condition, wherever possible. Channelization gains effectiveness by increasing channel slope and reducing bed resistance. This augments the velocity of flow and enables a channel to capacitate greater discharges without overbank flow and consequent flooding. However, rivers are not passive and their morphological structure responds to channelisation by changing configuration, with undesirable and even detrimental effects (Parker & Andres 1976).
- Technical works should be designed with environment friendly materials and adapted to the natural architecture.
- The design return period should be selected depending on the specific location, the associated design of the receiving stream or water body, and considering the consequences of a bigger flood than the one used for the design. Designing upstream reaches for higher return periods than the downstream reaches may have disastrous effects due to intense flooding.
- Special effort should be made to locate possible sites for the construction of dams or reservoirs for upstream flood control in order to avoid designing a more costly stormwater drainage system.
- Alternative solutions should be evaluated to examine if existing insufficient storm sewers can be used as part of the new design system in their whole or even partly instead of being destroyed and rebuilt.
- Sediment transport calculations and measures for its control in populated areas are necessary.
- Geological mapping and assessment of possible hydrological flushing is also indispensable.

2 HYDROLOGY CONSIDERATIONS

Singh & Woolhiser (2002) in the 150 year anniversary hydrology paper discuss many aspects of mathematical modeling in watershed hydrology, illustrating the complexity of the problems involved.

In the case of complex basins and drainage systems, the use of hydrographs should be preferred over the rational method, that is widely used, but cannot easily give the spatial distribution of discharges over time.

Design for a given return period is not uniquely defined and may vary considerably depending on the selection of the parameters and methodologies involved: choice of appropriate intensity-duration-frequency (idf) curve, rainfall distribution, rainfall height and duration, unit hydrograph type. Implementing the worst profile distribution may result in twice the design discharge, compared to the one resulting from rainfall heights computed by the idf curve without redistribution (Daniil & Lazaridis 2003). Yen (2000) notes that part of the misunderstanding comes from inadequate appreciation of probability and that the more serious problem is that the X-year return period of what is not clearly specified.

2.1 *Rainfall duration*

A common recommendation is that the storm duration should be sufficiently long so that the entire drainage area is contributing to runoff, as a result it should exceed the time of concentration and it is suggested that it should be 3 to 4 times the concentration time. Concentration time can be severely shortened due to urbanization and river training works.

In the USA the National Weather Service reports that the most frequent duration of runoff-producing rainfall is about 12 hours. Levy & McCuen (1999), based on observed data in Maryland, show that 24 hr is a good hypothetical storm. Storm types provided by the Soil Conservation Service (SCS) for different areas in the US have a 24 hr duration. The choice of rainfall duration, as a result, depends largely on the designer's interpretation of the data and the significance of the project.

2.2 *Rainfall distribution*

Alternating block method distribution and Worst profile distribution tend to become popular in recent years. The alternating block method distribution produces a center-loaded storm, while the worst profile distribution produces the highest peak discharge for a given total rainfall height and unit hydrograph.

Levy & McCuen (1999) report that actual data from six Maryland watersheds ($5<A<135 km^2$) suggest that center-loaded design storms are appropriate. Packman & Kidd (1980) also reported that center-loaded hyetograph was most appropriate based on the analysis of data from the United Kingdom.

The concern on the effect of rainfall distribution is also reflected in recent editions of commercially available software packages. HEC-HMS (USACE 2000) for example provides the user in the case of the frequency storm with the choice of placing the hydrograph peak at 25–33–50–67–75% of the storm duration. In every case the user has

to give rainfall heights at predetermined times according to the idf curve and the program performs the redistribution. No option for the worst profile scenario is given and the 50% is usually considered the standard. Although the above choices do not give exactly the worst profile scenario, the user can determine the one that gives the highest peak.

Eventually, a frequency or return period should be associated with rainfall distribution patterns, or alternatively certain patterns should be adopted for given return periods of rainfall.

2.3 *Unit hydrograph selection*

Determining an appropriate design hydrograph in ungaged basins becomes almost an art and depends largely on the experience of the design engineer. It involves choices of many parameters including rainfall distribution, once a type of unit hydrograph is selected.

In the third edition of Design of Small Dams (US Dept. of the Interior, Bureau of Reclamation 1987) six types of dimensionless hydrographs are presented based on 162 reconstructed flood hydrographs. The Sierra Nevada type and the Rocky Mountain Thunderstorms seem applicable to some Greek mountainous basins and have been used by the authors in recent studies.

In order to apply these dimensionless hydrographs, lag time has to be determined, based on the geometric characteristics of the basin and a parameter, Kn. Kn is an average Manning's n value representing the hydraulic characteristics of the drainage network. For Kn higher values are considered appropriate for developing flood hydrographs of more common frequency than, say the 100 yr event.

Lag time was originally defined by Horner & Flynt as the "…time difference between…center of mass of rainfall and center of mass of runoff…". Bureau of Reclamation uses the following definition in conjunction with the dimensionless hydrograph technique: Lag time is the time from the midpoint of the unit rainfall excess to the time that 50% of the volume of unit runoff from the drainage basin has passed the concentration point.

$$L_g = C\left(\frac{L\,L_{ca}}{S^{0.5}}\right)^N \qquad (1)$$

Lg is the unit hydrograph time in hours, C, N are constants N=0.33,C=26Kn, L is the longest watercourse from the point of concentration to the boundary of the drainage basin in miles. The point of concentration is the location on the watercourse where a hydrograph is desired, Lca is the length along the longest watercourse from the point of concentration to a point opposite the centroid of the drainage basin in miles, and S is the overall slope of the longest watercourse (along L) in feet per mile.

Unit hydrographs by the Soil Conservation Service (SCS) can also be used and they are offered as an option in mathematical modeling programs (e.g. HEC-HMS), contrary to the aforementioned hydrographs given in the Design of Small Dams. A critical parameter again is the time to peak.

2.4 *Design discharge—return period*

Design for a given return period is not uniquely defined and may vary considerably depending on the selection of the parameters and methodologies involved: choice of appropriate idf curve, rainfall distribution, rainfall height and duration and unit hydrograph type.

Idf curves derived from a limited time series cannot usually be extrapolated to predict rainfall depth at very high return periods. Koutsoyiannis & Baloutsos (2000) have demonstrated that the General Extreme Value (GEV) distribution appears to be suitable for the analysis of annual maximum rainfall, its predictions for large return periods agree with the probable maximum precipitation estimated by the statistical method (Hershfield 1961, 1965) and an idf curve with a wide range of applicability can be derived.

Koutsoyiannis' (1999) methodology provides at the same time a rainfall distribution even at those high return periods and no additional assumptions are needed. Equations of this type should be used wherever possible.

The scale of the catchment area is also important in determining peak discharge, which is not directly proportional to the catchment area. Odgen & Dawdy (2003) based on data from an experimental watershed, 21.2km^2, report that on the average, individual runoff event peak discharges are described by a power law function of a catchment area. They also found that flood quantiles in nearly all subbasin are self-similar as described by a simple scaling theory.

Finally, another consideration is the impact of stormwater on the water quality of the receiving water body. In some countries, environmental regulations exist that impose strict standards for water quality and measures preventing pollution due to stormwater inflow have to be taken. Calabro (2004) presents an interesting study and shows that design storms with triangular or Chicago shape and duration similar to the time of concentration of the catchment are in most case the worst regarding the water quality impact and can be used in the design.

For complex drainage systems, computational platforms, such as HEC-HMS should be used, as they facilitate determination of time and spatial distribution of discharges.

3 DIAKONIARIS PROJECT

Diakoniaris river is located near Patra city, Peloponnese, Greece (Fig. 1). It has ephemeral flow and flows from south to north. For the last 5km before its outlet in the sea flows through the west suburbs of the city of Patra. Presently only 1km, just before the outlet to the sea is trained with a closed section, running under the main avenue of the area. According to city planning this avenue is proposed to be extended to the north to meet the highway circumventing Patra city (PCH), currently under construction.

3.1 *Background*

Diakoniaris river (Fig. 2) and its tributaries, Malamamoutis, Panagitsa, Romanos etc, used to have a total drainage area upstream of the new highway of ~19.5km^2 in the 70's, when part of Elekystra's (~9.6km^2) basin was diverted through an open diversion channel

to Glaykos river. The remaining basin ~9.8km^2 develops on the west side of Panachaikos mountain from elevation +150 to+1150m along a 5.2km.

In December 2001 a flood resulted in human losses, drawing public awareness to the problem and a new

Figure 1. Location of the project.

study of the project. The project in its introductory and preliminary stage was assigned to Hydroexigiantiki by the Ministry of the Environment, Planning and Public Works. Hydrology of the area, including idf relations and design discharges, was reevaluated.

In the mountainous area geological instabilities and erosion are observed in the area of neogenic formations. This is considered the main source for sediment production. Main sediment producing areas are located within Diakoniaris and Panagitsa catchment areas. Sediment transport rate has not been determined from systematic measurements. However, based on field reconnaissance and on site observations after the December 2001 flood, it can be concluded that sediment yield is high, possibly more than 1000m^3/km^2/yr. This value may be more than doubled for certain years. The river bed upstream of the city limits is wide and flows through a forested area. Within the city limits urban development has limited the width of the river bed and the floodplain has been inhabited.

Sediment control upstream from PCH (Patra Circumventing Highway) is crucial for the design of Diakoniaris training works. Based on this realization a final design study was performed for Diakoniaris and downstream drainage network covering ~11km^2 drainage area, under the assumption that the area upstream of PCH will be diverted to Glaykos river. Implementing this design the existing close section was constructed with a 2×6×2 closed conduit section running for 400 m from the outlet to the sea and upstream simple box culvert 6.0×2.6 and 7.5×2.6 up to station 1+100.

Assuming that no significant sediment depositions reducing the conveyance of the system will take place, the existing structure can convey ~90m^3/s.

The proposed Diakoniaris diversion to Glaykos was never constructed, with the exception of small area ~1km^2 between Elekystra diversion and PCH. The rest of the watercourses continued to follow their natural course.

3.2 *Intensity—duration -frequency curves*

The following idf curve determined in the old study (1984) and adopted with a fit for return period term in the hydraulic design of the new highway (PCH)

$$i=20.31T^{0.25}t^{-0.59}=\alpha t^{-0.59} \quad (2)$$

where i intensity in mm/hr, t rainfall duration in hrs, T return period in years.

The idf curve was compared to the one used in Xerias River Corinth, also in northern Peloponnese (Lazaridou et al., 2003).

The idf curve adopted for Xerias river, constructed based on Koutsoyiannis methodology, was:

$$i(d,T)=\frac{50.44\left(T^{0.16}-0.636\right)}{\left(d+0.0679\right)^{0.732}} \quad (3)$$

where d is the rainfall duration in hours, i the rainfall intensity in mm/h and T the return period in years.

The comparison of the two curves is given in graphical form in figure 3.

Comparison of hydrographs for the return periods considered gave no significant difference in peak discharge between the two idf curves and consequently eq. (2), used for the design of other works in the area was used in modeling of Diakoniaris basin.

The rainfall distribution resulting from the idf curve was also compared to the SCS synthetic storm hyetographs proposed for use in the USA for storms of 6 and 24 hours duration (Chow et al. 1988). Types I, IA are for the Pacific maritime climate with wet winters and dry summers. Type is is quite close to the alternating block method distribution applied to eq. (2) as shown in figure 4.

3.3 *Design discharge—return period*

A return period of 50 years was specified as the lower acceptable return period in the environmental permit relating to the extension of Diakoniaris Avenue. Due to the complexity of the system it was deemed appropriate to model it in a HEC-HMS environment. Diakoniaris basin was modeled in great detail. Elekystra basin and part of Glaykos basin were also included

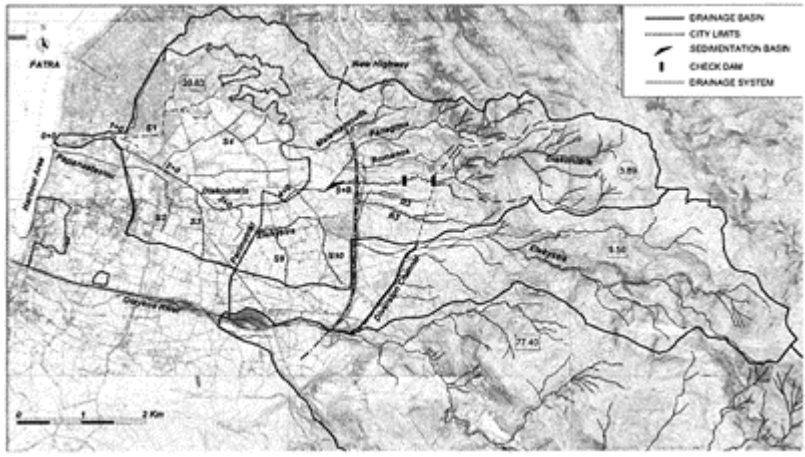

Figure 2. General layout of Diakoniaris basin and drainage system.

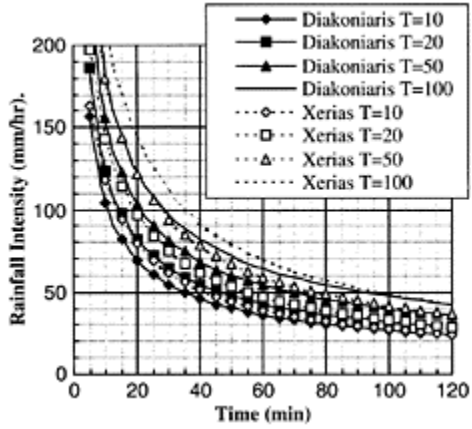

Figure 3. Comparison of idf curves.

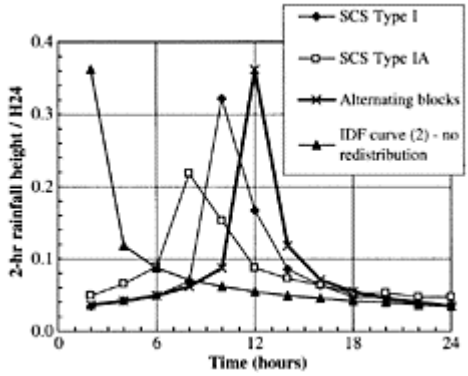

Figure 4. Variation of peak discharge along Diakoniaris river for T=10, 20, 50, 100 years.

in the model, but not with the same detail, in order to determine the impact of the proposed diversions.

Information from geologic and land resource maps was used for the determination of CN to appropriately include infiltration losses. In the upstream area there is a small part of pseudoalpine zone and fir zone. The largest part of the area just upstream of the city limits is covered by the broadleaved evergreen zone and cultivated land and near the city limits there is a deciduous oak zone. Near the sea we encounter alluvium and tertiary deposits.

In their majority the soils can be considered to be in category C with the exception of the area downstream of Elekystra diversion channel that falls in category B.

Finally, for the modeling three CN curve numbers were implemented: CN=80 for the upstream Diakoniaris basin, CN=75 for the areas outside the city limits and CN=85 for the areas within the city limits.

3.4 *Hydrologic modeling*

For the Diakoniaris project the drainage area (~20km^2) was modeled with HEC-HMS software. For the mountain area of the basin, hydrographs were also developed according to the design of Small Dams and compared to the SCS hydrographs obtained within the HEC-HMS environment. Many scenarios were run with different idf relations, return periods of 10, 20, 50 and 100 years and different rainfall distributions. Using the developed model many alternatives were examined: diversions both in the mountainous area, involving tunnels and open channels, and closed conduits in the urbanized area.

The whole drainage system was modeled using HEC-HMS (Hydrologic Engineering Center—Hydrologic Modeling System). Modeling in the HEC-HMS environment includes three components.

The basin model where the watersheds or basins are represented and hydrologic elements connected in a dendritic network to simulate runoff process. In this part losses, runoff transformations and open channel routing are selected.

The meteorological model where precipitation to be used is given and the method for its distribution selected.

The control specifications, where the duration and time step of the modeling is defined.

3.5 *Hydrologic modeling parameters*

The whole drainage system was modeled using HEC-HMS with the following parameter selection:

- Hydrographs according to SCS
- SCS curve number loss model
- Lag time was determined using data from hydrographs given in Design of Small Dams and estimated flow velocities in concrete culverts in the order of 6m/s
- Flood routing through trained sections with the Muskingam—Cunge standard method.

The final design discharges were determined for a 12-hour—center-loaded storm.

For the Sierra Nevada type hydrograph, that is considered applicable to Diakoniaris area,

$$t_p=0.75(L_g+\tfrac{1}{2}D)=0.75L_g+0.375D \tag{4}$$

where tp is the time to peak, D is the unit rainfall duration and Lg is the lag time.

For a small unit duration, as assumed in HEC-HMS simulations

$$t_p\approx 0.75L_g \tag{5}$$

This value was used as time to peak for the SCS hydrographs.

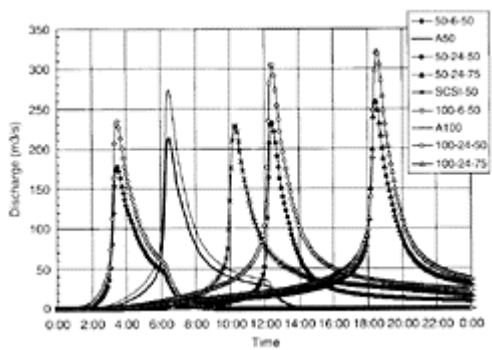

Figure 5. Hydrographs at Diakoniaris outlet for various rainfall duration and distribution for T=50, 100 years.

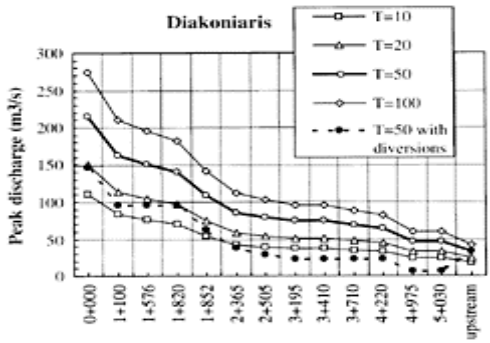

Figure 6. Variation of peak discharge along Diakoniaris river for T=10, 20, 50, 100 years.

In figure 5 hydrographs at Diakoniaris outlet, without any diversions, for T=50, 100 yrs, durations of 6, 12, 24 hrs and peak located at 50% (center-loaded) or 75% (closer to the worst profile), along with SCS Storm Profile I are given.

In figure 6 the variation of peak discharge for Diakoniaris watercourse for T=10, 20, 50, 100 yrs without any diversions and for T=50 yrs with the proposed diversions is presented.

4 SEDIMENT TRANSPORT

Geological and land resource maps along with new geological studies performed for the study area and especially the upstream sediment producing area, were used for estimating sediment transport conditions in the area.

Sediment production is high in the area causing depositions in the closed sections and the outlet.

Figure 7. Existing sediment control drop structures in the mountainous area filled with sediment.

Figure 8. Existing sediment control structure upstream of the highway crossing.

Average sediment transport in the area is estimated at 2200$m^3/km^2/yr$ while there is an very active area upstream where 23,000$m^3/km^2/yr$ sediment production rate is reported in the literature. Therefore, sediment control structures are absolutely necessary.

Sediment control drop structures have been constructed in the past in the mountainous area, but the have been filled with sediment (Fig. 7). A newer sediment control structure exists upstream of the highway crossing (Fig. 8). This structure was filled with sediment during the December 2001 flood and subsequently cleared out.

A sedimentation basin in the natural confluence of Diakoniaris and Panagitsa tributary was designed. This involved a special design. In the main conduit under the road, a spillway was placed so that for discharges up to the design discharge is routed through the sedimentation basin, while for higher discharges it acts as emergency spillway. This special structure will be studied in a model before construction. Check dams to

Figure 9. Existing Diakoniaris outlet structure to the sea.

be used for sediment control, combined with upstream diversions were also proposed.

Additionally two sediment control dams were proposed. The upstream one can be combined with the diversion of the upstream Diakoniaris basin to Elekystra Diversion Channel.

5 DIAKONIARIS TRAINING WORKS

The training works and diversion were designed for the 50-year flood according to the environmental permit. The existing closed section can only convey about $90m^3/s$ and possible additional culverts running parallel to the existing one, due to space limitations, can handle only a maximum additional $60m^3/s$.

The downstream closed sections were checked for higher discharges in order to locate critical points. The estimated discharge without any diversions is $215m^3s$ while with a combination of diversions upstream and in the city area, the discharge at the outlet can be limited to $150m^3/s$.

Higher discharges were assumed to be combined with unfavorable conditions at the outlet, thus creating pressurized flow towards the outlet and the pressure gradient was determined. It was desired that the pressure grade line remains below the ground, so that manhole covers are not affected.

The following possibilities were examined:

– Diversion of the upstream Diakoniaris basin, $A=3.89km^2$.
– Diversion of sewer basins S9 and S10 to “Perimetriki”, i.e. a sewer running under the new road running around Patra suburbs.
– Diversion of sewer basins S2 and S3 to Papanastasiou, a road running parallel to Diakoniaris axis and reaching the harbor area. In the harbor area (under construction) a channel running parallel to the sea front and receiving all sewers flowing towards that area will be constructed. The proposed Papanastasiou diversion will also flow in this channel, close to the outlet, with appropriate outlet modification.
– Diversions of local creeks R2 and R3 to Glaykos through the storm sewer system of the new highway.

Various combinations of all the above were simulated with the HEC-HMS model and results for the discharge at the outlet are presented in Table 1.

It should be noted that in modeling the future conditions, with full development of the city and the drainage system, were represented. With the existing conditions, with minimal development of the drainage system, concentration times are expected to be longer and consequently peak discharges lower. This was taken into account in scheduling the construction of the proposed works. As a result construction of the closed conduit upstream of the existing closed section can start before the addition of parallel conduits to the existing structure.

Figure 10. View of the river bed and pedestrian crossings within the city limits, to be trained.

Provision is made in the design for big surface openings (~2–3×6–8 m), appropriately fenced, that would facilitate aeration and cleaning by mechanical means of the closed section. Additionally, holes in the bottom of the conduit are provided for water table recharge.

Proposed training works for Diakoniaris main course are summarized in Table 2.

Table 1. Peak discharge at Diakoniaris outlet for T=10, 20, 50, 100 years (12 hr, center-loaded storm).

Scenario	Scenario name	Diakoniaris upstream diversion	R2 & R3 diversion	Perimetriki diversion (S9 & S10)	Papanastasiou diversion (S2 & S3)	Panagitsa, Romanos upstream diversion	Q10 (m^3/s)	Q20 (m^3/s)	Q50 (m^3/s)	Q100 (m^3/s)
1	(A)	–	–	–	–	–	111	151	214	274
2	(D)	X	–	–	–	–	105	142	200	256
3	(DPAP)	X	–	–	X	–	92	125	178	228

4	(DTX)	X	X	–	–	–	101	136	193	246
5	(DPP)	X	–	X	X	–	81	109	155	198
6	(DPPT)	X	X	X	X	–	77	104	147	187
7	(PP)	–	–	X	X	–	87	119	169	217
8	(DTPAP)	X	X	–	X	–	88	120	170	217
9	(DPER)	X	–	X	–	–	94	126	177	226
10	(TX)	–	X	–	–	–	107	145	206	263
11	(PPT)	–	X	X	X	–	83	109	161	206
12	(PAP)	–	–	–	X	–	98	135	193	248
13	(PER)	–	–	X	–	–	100	135	191	244
14	(PED)	–	–	X	X*	–	84	111	**154**	195
15	(OREI)	X	X	–	–	X	102	137	194	248
16	**PPN**	**–**	**X****	**X****	**X****	**–**	**79**	**107**	**152**	**195**

*Part of Diakoniaris discharge (26.4 out of 63.7m^3/s) is assumed to be diverted to S10, while the 37.3m^3/s continue to flow through the main course.
**In this scenario drainage areas have been revised so that Perimetriki is the divide.

Table 2. Diakoniaris training works.

Reach	Description—cross section
0+000/0+050	open cross section/outlet modification
0+050/0+400	existing section 2×(6.0×2.0)—slope 5.2%$_0$ addition of two conduits 4×2
0+400/0+908	existing section (6.0×2.6)—slope 11.0%$_0$ addition of two conduits 4×2.6
0+908/1+110	existing section (7.5×2.6)—slope 11.5%$_0$ addition of two conduits 3.25×2.6
1+110/1+852	8.50×3.0
1+852/2+365	6.0×3.0
2+365/3+412	5.0×3.0
3+412/5+028	4.0×3.0
5+028/5+084	4.0×3.0 (C30/35 concrete)

Special structures are designed at stations 0+400 and 1+100, where the number of opening changes. A cascade structure is designed at the entrance of the upstream basin in the downstream trained reach, where there is a significant elevation difference due to the construction of the highway.

5.1 *Time planning of training works*

Training works are planned in two stages, taking advantage of the existing situation, i.e. not fully developed urbanization and stormwater drainage system in the area, that results in lower discharges than the ones estimated under the assumption of fully developed drainage system and city layout.

6 CONCLUSIONS

Flood management and control in an urban environtnent should follow an integrated watershed management plan, but is restricted from existing city planning and development.

In the examined case of Diakoniaris river in Patra, Peloponnese, Greece, a combination of diversions upstream and within the city limits and sediment control measures was used in order to achieve sufficient flood protection in the catchment.

ACKNOWLEDGEMENT

Special thanks to Stella Michailidou for preparing the general layout figure and maps.

REFERENCES

Calabro, P.S. 2004. Design storms and water quality control. *J. Hydrologic Eng.* 9(1):28–34.

Chow, V.T., Maidment, D.R. & Mays, L.W. 1988. *Applied Hydrology,* McGraw-Hill.

Daniil, E.I., Bouklis, G.D., Lazaridou, P.L. & Lazaridis, L.S. 2000. Integrated Approach for Environmental Flood Protection for northern suburbs of Athens, Greece. *Building Partnerships,* ASCE, Proc. of the 2000 Joint Conf. on Water Resources on CD, Minneapolis, MN, USA, 2000.

Daniil, E.I. & Lazaridis, L.S. 2003. Designer's concerns on the effect of rainfall distribution on dam and diversion works sizing, *IAHR XXX Congress*, Thessaloniki, GREECE, 24–29 August 2003, Theme B: 95–102.

Diplas, P. 2002. Integrated Decision Making for Watershed Management: *Introduction. Journal of the American Water Resources Association.* 38(2):337–340.

Hershfield, D.M. 1961. Estimating the probable maximum precipitation, ASCE, *J. Hydraul Div.* 87(HY5): 99–106.

Hershfield, D.M. 1965. Method for estimating probable maximum precipitation, *Journal of American Waterworks Association.* 57:965–972.

Koutsoyiannis, D. 1999. A probabilistic view of Hershfield's method for estimating probable maximum precipitation, *Water Resources Research.* 35(4):1313–1322.

Koutsoyiannis, D. & Baloutsos, G. 2000. Analysis of a long record of annual maximum rainfall in Athens, Greece and design rainfall inferences, *Natural Hazards.* 29:29−8.

Lazaridou, P.L., Daniil, E.I., Michas, S.N., Papanicolaou, P.N. & Lazarides, L.S. 2002. Integrated Environmental and Hydraulic Design of Training Works for major Watercourses, *Proceedings of the Int. Conf. Protection and Restoration of the Environment VI,* Skiathos, Greece, July 2002, A.G. Kungolos et al (eds), Vol. I:175–182.

Lazaridou, P.L., Daniil, E.I., Michas, S.N., Papanicolaou, P.N. & Lazarides, L.S. 2003. Integrated environmental and hydraulic design of Xerias river, Corinthos, Greece, training works, *Water, Air, Pollution: Focus/Protection and restoration of the environment, Kluwer Academic* (in press).

Levy, B. & McCuen, R. 1999. Assessment of Storm Duration for Hydrologic Design, *J. Hydrologic Eng.* 4(3): 209–213.

National Environmental Research Council (NERC), Flood Studies Report, Institute of Hydrology, Wallingford, 1975.

Odgen, F.L. & Dawdy, D.R. 2003. Peak discharge scaling in small Hortonian watershed. *J. Hydrologic Eng.* 8(2): 64−73.

Packman, J.C. & Kidd, C.H.R. 1980. A logical approach to the design storm concept. *Water Resour. Res.* 16(6): 994–1000.

Parker, G. & Andres, D. 1976. Detrimental Effects of River Channelization, *ASCE Proceedings of the Symposium on Inland Waters for Navigation, Flood Control & Water Diversions,* Colorado State University, August 10–12: 1248–1266.

Singh, V.J. & Woolhiser, W. 2002. Mathematical Modeling of Watershed Hydrology, *J. Hydrologic Eng.,* 7(3):270–292.

Stedinger, J.R., Heath, D.C. & Thompson, K. Risk Analysis for Dam Safety Evaluation: Hydrologic Risk, U.S. Army Corps of Engineers, Institute for Water Resources, IWR REPORT 96-R-13, March 1996.

US Army Corps of Engineers, Hydrologic Engineering Center. 2000. *Hydrologic Modeling System, HEC-HMS, Technical Reference.*

US Department of the Interior, Bureau of Reclamation 1987. *Design of Small Dams,* 3rd edition, US Government Printing Office, Denver, CO.

Yen, B.C. 2000. 100-Year Return Period of what?, *Building Partnerships,* ASCE, Proceedings, Minneapolis, MN, USA.

Flood mitigation planning related to land use

Y.Takeuchi

Kawasaki Geological Engineering Co., Ltd, Tokyo, Japan
M.Takezawa

Nihon University, Tokyo, Japan

River Flow 2004—Greco, Carravetta & Della Morte (eds.)

ABSTRACT: The present study proposes a new comprehensive flood mitigation system that considers the current stage of land development. The proposal includes the distribution of a flood mitigation guidebook to affected residents, followed by a medium-scale implementation of measures involving the construction of readily achievable structures such as one-sided dikes or unenclosed ring dikes. The project would then extend to a large-scale consultation and the implementation of comprehensive flood mitigation measures.

The present study also presents a unique economic analysis method to increase the relative economic value of a flood migration project by combining previously independent structures like river, highway and railroad dikes and eliminating unnecessary construction. The concept of "time and regional extended effects" is also introduced as an assessment technique for determining the economic value of flood mitigation projects.

1 INTRODUCTION

Many flood mitigation plans for alluvial basins around the world have not been implemented because of problems associated with the economic analyses or the measures themselves. In many cases, failure to implement the flood mitigation measures has lead to an area being under-utilized. In some instances, mitigation projects are not followed through due to plan implementation difficulties, which have often been drawn up without consideration of current levels of development and land usage or the financial capacity of the concerned countries or regions. In other cases, the projects have not been started because the estimated economic value of flood mitigation is insufficient, when

implementation of the measures may in fact increase the economic efficiency significantly.

Flood mitigation projects should be designed so as to correspond with target area conditions. The present study proposes a new comprehensive flood mitigation sy stem that considers the current stage of land development. The proposal includes the distribution of a flood mitigation guidebook to the residents concerned, followed by medium-scale implementation involving the construction of readily achievable structures, such as one-side dikes or unenclosed ring dikes. The project would subsequently extend to large-scale consultation and the implementation of comprehensive flood mitigation measures.

The present study also presents a unique economic analysis method that increases the relative economic value of a flood migration project by combining structures, such as previously independent structures like rivers, highways and railroad dikes and eliminating unnecessary construction. The concept of “time and regional extended effects” is also introduced as an economic value assessment of flood mitigation projects, which also ensures that the scope and efficiency of the project is optimized. This measure is calculated based on an existing standard method employed in feasibility studies. The “time extended effect” concept identifies how flood mitigation infrastructures allow the development of property and capital, with accumulated benefits over long periods. Thus, when properties are protected against floods, new properties and capital will accumulate without destruction and confidence will increase. The “regional extended effect” of flood mitigation projects refers to the influence on increased economic activity of a region, locally, nationally and throughout the world.

2 COMPREHENSIVE FLOOD DAMAGE MITIGATION SYSTEM

A comprehensive flood damage mitigation system consists of three main sub-systems that simultaneously

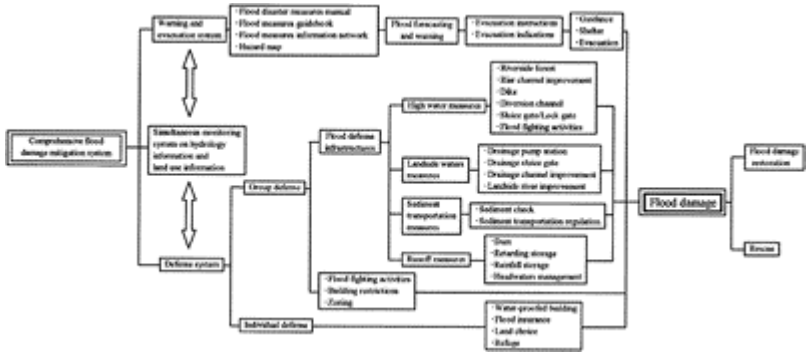

Figure 1. Comprehensive flood damage mitigation system.

monitor hydrology and land use information, warning and evacuation systems and defense systems, as shown in Figure 1. The warning and evacuation sub-system consists of a flood disaster measures manual, a flood measures guidebook, a flood measures information network and hazard map. The defense sub-system consists of individual defense and group defense. Individual defense consists of waterproofed buildings, flood insurance, land choice and refuge availability. Group defense consists of flood mitigation infrastructures, flood fighting activities, building restrictions and zoning.

A comprehensive flood damage mitigation system is based on the assumption that flood damage inevitably happens, regardless of the strength of flood mitigation measures. To minimize flood damage, which includes restoration costs, flood mitigation measures should always be systematically combined with the development stage of engineering, economics and regional land use.

A comprehensive flood damage mitigation system should give priority to the development of linked soft wares of flood mitigation related to land use as a first step in land development. These soft wares include flood disaster measures manuals, flood measures guidebooks, flood measures information networks, hazard maps and flood forecasting and warning systems, which give the highest priority to saving human life with evacuation instructions and evacuation indicators as guidance.

The flood mitigation measures of individual defense include waterproofed buildings, flood insurance, land development choices and refuge availability. In an intensive stage of land development, hard wares of flood measures, such as high water measures, landside water measures, sediment transportation measures and runoff measures become necessary.

3 ECONOMIC ESTIMATION OF DIKE CONSTRUCTION WORKS JOINTED PROJECTS

Some projects were judged infeasible due to low economic effect. If the construction costs of dike combined with flood mitigation and highway infrastructure costs are distributed across each project, higher accuracy economic estimations become feasible. In this case study, the Apure River Flood Mitigation Project is presented.

The flood mitigation project in the Apure River Basin, Venezuela, was subdivided into the following three projects, shown in Figure 2.

Project A: construction of a 187km-long dike on the right bank of the Portuguese River

Project B: construction of a 145km-long dike on the right bank of the Guanare River

Project C: construction of a 155km-long dike on the left bank of the Apure River.

Table 1 shows the dike length, project costs and benefit-cost ratio of these projects. The design life of each dike is 50 years.

The benefit-cost ratio of Project A, Project B, Project C and total projects are 1.39, 1.45, 0.82,

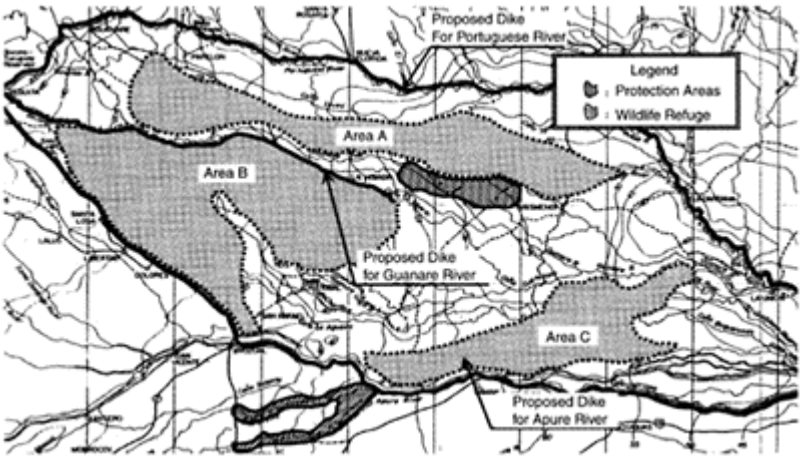

Figure 2. Flood mitigation plan of the Apure River Basin.

1.15, respectively. The total project was economically judged feasible because its benefit-cost ratio was above 1. The tops of the project dikes were designed for use as gravel-paved roads, however, the benefit-cost ratios did not include the road construction benefits. If these were counted in the benefit-cost ratios, the benefits of dike construction would have increased.

4 SEPARATION OF INESTIMABLE CONSTRUCTION WORKS FROM A FLOOD MITIGATION PROJECT

The Action Plan of the Chama River Basin Conservation Project in Venezuela was economically estimated as a large-category disaster prevention project in a basin that includes sub-projects in different areas and with different objectives. The Action Plan consists of

Table 1. Comparison of economic efficiency.

Project	Dike length (km)	Project cost US $ (millions)	Benefit/ cost
Project A	187	34.19	1.38
Project B	145	25.55	1.45
Project C	155	34.11	0.82
Total	487	93.85	1.15

the Lower Basin Project to protect the alluvial fan region from El Vijia to the Lake Maracaibo and the Upper Basin Project from El Vijia to the mountain regions. The

Lower Basin Project was subdivided into river improvement works on the lower reaches from El Vijia and sediment control works on the upper reaches from El Vijia to the mountain regions. The main sediment control works in the Lower Basin Project, which aim to control sediment load, consisted of 3 high dams, 18 low dams and 340 retaining walls.

The river improvement works of the action plan from El Vijia to Lake Maracaibo are the same as those of Master Plan, which consist of the construction of a 24.7km-long one-sided dike, a 10.4km-long dike on the right side bank and a 10.3km-long dike on the left side bank, and the strengthening of a 12km long of existing one-side dikes on the left bank, as shown in Figure 3. Consequently, if the Action Plan were implemented, 36.7km of one-sided dikes would be installed in the 53.4 km between El Vijia to the Lake of Maracaibo.

The costs of the Action Plan are shown in Table 2. The project costs and the benefit-cost ratio of the Action Plan were estimated in 2000 to be US $27.58 million and 1.58, respectively. The economic benefits of executing the Action Plan Project were considerable.

If only 24.7km of one-sided dikes and 12km of strengthening works were executed, the project would

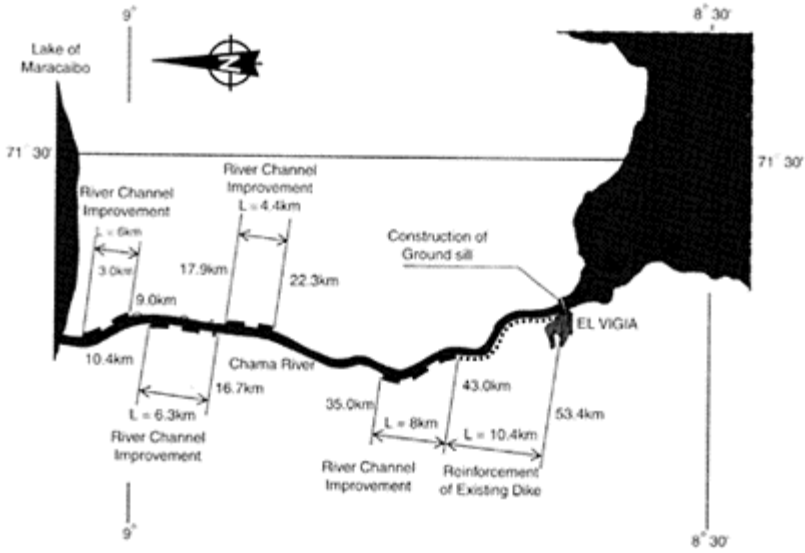

Figure 3. River improvement works from El Vijia to Lake Maracaibo.

Table 2. Project cost of action plan.

No.	Project name	B/C	Project cost (US $ millions)
1	River improvement works on the lower reaches from El	2.65	12.93

	Vijia			
2	Sediment control works on the upper reaches from El Vijia		13.45	
3	Lower basin=(1)+(2)		26.38	
4	Upper basin			1.20
5	Total=(3)+(4)	1.58	27.58	

be more profitable with US $12.93 million in project costs and a 2.65 benefit-cost ratio.

5 “TIME EXTENDED EFFECT”

The “time extended effect” is the effect of flood mitigation infrastructures that allow the development of properties and capital with benefits accumulated over long periods. Thus, economic development, in the form of property and capital accumulation, is impossible in an area submerged by flood every year and the “effect” is the benefits accrued from the enabled development.

Conventional economic assessments of flood mitigation projects have counted direct and indirect damage to inhabited properties. The deprived potential for new property development due to flooding was not counted with the losses of old properties and capital in the flooded areas. In other words, if properties are protected from flooding, new properties are produced and capital is accumulated without potential for destruction. The effect of producing new properties and capital is defined here as the “time extended effect” of flood mitigation infrastructures over long periods.

It is currently difficult to quantitatively calculate the “time extended effect”. However, the “time extended effect” of constructing the Okakoi Dike, Japan, in the early 17th century was studied as follows. A 50 km-long of dike was constructed on the left bank of the Kiso River from Inuyama to Yatomi in 1610 as shown in Figure 4. As a result, the height of the left bank was 0.9m higher than that of the right for approximately 280 years, until 1887. In the 400 years since 1610, there has not been a flood on the left-side plain of the Kiso River, while many floods have occurred on the right-side plain.

Before 1610, both plains were closely connected with the river and their natural, social and economic conditions were almost identical. Economic capital formation in the side plains has been different since the construction of the left-side dike. In the Bisai District of Aichi Prefecture on the left-side plain, from the early

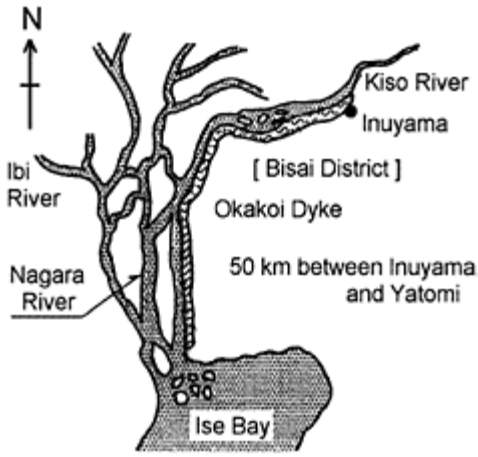

Figure 4. Location of Okakoi Dike.

17th to the early 19th, cotton textiles were produced, in addition to the existing silk textiles. Textile industries developed, which encouraged engineering and capital accumulation, and enabled the production of high quality wool textiles, creating the industrial infrastructure to produce weapons, cars and aircrafts in the whole of Aichi Prefecture until the 1920s. In 1999, industrial production per person in Aichi Prefecture, on the left-side plain, was 1,960 thousand yen and that in Gifu Prefecture, on the right-side plain, was 96 thousand yen. This difference in industrial production per person between the two prefectures is thought to be influenced by the difference in bank height between both sides due to the dike construction.

The difference in flood damage between Aichi Prefecture on the left-side plain and Gifu Prefecture on the right-side plain in the probable flood area of the Kiso River was analyzed in 1953, as shown in Table 1. The inhabitants of Aichi Prefecture were richer in domestic property than those in Giju Prefecture. If the indicators included the industrial and agricultural properties and products, the difference in economic power between the two prefectures would be even more evident. The “time extended effect” from the flood mitigation project was qualitatively proven through the case study of the Okakoi Dike on the left bank of the Kiso River, in which the capital accumulated properties were protected against floods and produced new capital, as listed in Table 3. If this case study were surveyed in detail over several historical stages, a qualitative study of the “time extended effect” would be possible.

6 “REGIONAL EXTENDED EFFECT"

The “regional extended effect” of flood mitigation projects is the influence on economic activities not

Table 3. Difference of flood damage between Aichi Prefecture and Gifu Prefecture in the probable flood area of the Kiso River.

	Aichi prefecture	Gifu prefecture
A: Building (million yen)	159,818	16,374
B: Property except building (million yen)	103,500	11,731
C=A+B	263,313	38,105
D: Family	151,828	16,592
E: Population (person)	725,261	90,304
F: Inundated area (ha.)	48,859	79,999
C/D(10 thousand yen/family)	173.4	169.4
C/D(10 thousand yen/person)	36.3	31.1
C/D(10 thousand yen/ha.)	538.9	351.4
E/F (person/ha.)	14.8	11.3

(price in 1951).

only in the region adjacent to the flooded area, but also in the country and in the world. For example, if the center of Manila is flooded, indirect damage is caused not only in Manila City, but also on the whole Luzon Island, in all of the Philippines and in the world.

On September 12, 2000 the Shinkawa River, Japan, was flooded because of a dike failure. Several car factories in Toyota City, 30km south-east of the river, stopped working due to the resulting insufficient supply of parts. However, the determination of the "regional extended effect" and the "time extended effect" has not been an objective of the economic evaluations for flood mitigation projects.

We propose to measure the decreases in land prices due to floods, instead of measuring indirect damage from the "regional extended effect" of floods, because the indirect damage is very difficult to measure. If the "regional extended effect" was assessed in the Flood Control and Drainage Project in metropolitan Manila, the Philippines, as an example, the priority between the following two subprojects would be reversed. The Japan International Cooperation Agency (JICA) study selected the Mangahan Drainage Improvement Project as more feasible than the Pasig River Improvement Project, with a higher economic efficiency, as summarized in Table 4.

The SM-2 district of the Pasig River Improvement Project is the center core area in metropolitan Manila, as in shown Figure 5. Land use in the SM-2 district was developed in 1986 and if the Pasig River Improvement Project were executed, a high dense commercial and residential area would be developed in 4.4 km^2 by 2020, as in shown Table 5.

The WM-1 district was planned as the development of 2.86km^2 of the largest high-density commercial

Table 4. Economic efficiency.

	High dense commercial and house areas	
A.D.	1986	2020
SM-2 District in the Pasig River Improvement Project	3.97km^2	4.41km^2
WM-1 District in the Mangahan Drainage Project	0.00km^2	2.86km^2

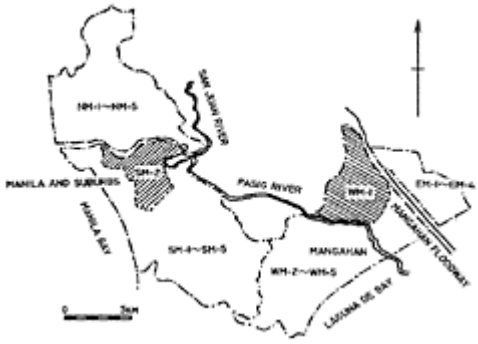

Figure 5. Location of SM-2 district and WM-1 district.

Table 5. Land use conditions.

	Mangahan drainage improvement project	Pasig river improvement project
Total project cost	132.0 million US$	65.8 million US$
Mean annual decreased damage	20.2 million US$	9.3 million US$
B/C: benefitcost ratio	1.11	1.07
Internal rate of return	16.80%	16.10%

and residential area in the Mangahan Drainage area (as shown in Figure 5 and Table 5).

Each district in the Flood Control and Drainage Project in metropolitan Manila was at a different landdevelopment stage. The capacity for land development in the underdeveloped areas of the Mangahan Drainage Project area was larger than that in the developed area of the Pasig River Improvement Project.

As a consequence of these capacities, the Pasig River Improvement Project, in the center of metropolitan Manila, was determined to have less economic efficiency than the Mangahan Drainage Project in the marshland suburbs of Manila. The "regional extended effect" was taken into account when planning the economic evaluation, and the economic efficiencies of developing the projects were reversed.

Through the metropolitan Manila Flood Control and Drainage Project case study, issues such as the "regional extended effect" were studied qualitatively. If land prices decreased by actual flood damage were measured over time and in several districts, it would be possible to quantitatively study the regional extended effects.

The integrated efficiency of the total project was increased by making the area with the higher regional extended effect safer from floods than the lower effect area. The area with a high regional extended effect is the district that would sustain greater indirect flood damage per unit squared than the other area, the highly developed land use area, with high land prices, and the central core cites in the basin with the collective transportation areas such as highways, railways, ports and airports.

The success of a flood mitigation project in regional development depends on the cooperation of social, economic and cultural infrastructures, which are essential in attracting able inhabitants.

7 CONCLUSIONS

The process of executing a flood mitigation project should be related to the stage of land development in the study area. The new basic concept explained in the present paper clarified problems with existing plans. Flood mitigation projects should be designed so as to relate to the land use conditions of the target area.

A comprehensive flood damage mitigation system that considers the current stages of land development should initiate the distribution of flood mitigation guidebooks to the residents concerned, followed by the medium-scale implementation of mitigation measures, involving the construction of readily achievable structures, such as one-sided dikes or unenclosed ring dikes. Subsequently, a large-scale consultation and implementation of comprehensive flood mitigation measures would be implemented.

Depending on the potential for flood and the need for flood mitigation in the area, some flood mitigation projects could not be easily executed without investment, approval of residents and their government. In these areas, the economic effects were often assessed lower than the actual costs. Consequently, it is very important to show the true economic effects. If a river dike is constructed as part of a highway or railway infrastructure, and the inestimable construction works are separated from the flood mitigation project, the economic effects increase and the project would be smoothly implemented.

The "time and regional extended effects" of a flood mitigation project were assessed, in addition to the existing economic evaluation of the direct and indirect damage by flood, to give a project more economic feasibility. These effects were defined as the benefits of capital accumulation due to the construction of flood mitigation infrastructure in the long term, enabling investment in new industrial projects, as shown in the Kiso River Improvement Project case study from the early 17th century.

The “regional extended effect” is the accumulated indirect benefit from flood mitigation infrastructure in a wide area that would be directly impacted by flooding.

To increase the economic benefits of a flood mitigation project, it is important to give the total project a more integrated efficiency by making the higher regional extended effect area safer from floods than the lower effect area. The area that has a high regional extended effect is the district that causes more indirect flood damage per unit squared in another area, with highly developed land use, high-priced land, central core cites in the basin or collective transportation facilities, such as highways, railways, ports and airports.

REFERENCES

Japan International Cooperation Agency. 1990. *Study of Chama River Basin Conservation Project.* 1–16. Final Report: JICA.

Japan International Cooperation Agency. 1990. *The Study of Flood Contol and Drainage Project in Metropolitan Manila Philippines:* S1–13. Main Report: JICA.

Japan International Cooperation Agency. 1993. *Study on Comprehensive Improvement of the Apure River Basin.* 1–4. Figure 25. Final Report, Volume II Main Report: JICA.

Oriental Economic Weekly Review. 1999. *General View of Regional Economy in Japan:* 169: Oriental Economic Weekly Review.

The Asahi Newspaper 1961. *The Kiso River.* 86: The Asahi Newspaper.

Yoichi, T. 1964. *Difference of Flood Damage Between Aichi Prefecture and Gifu Prefecture in the Probable Flood Area of the Kiso River*.

Yoichi, T. 1976. *The Kisosansen:* 5–11, Proceedings of The Seminar on Escape and Typhoon Commitee in Tokyo.

Yoichi, T. & Kyozo, S. 1999. *Study of the Economic Effects on Chama River Basin Conservation Project in Venezuela:* Proceedings of E11 on CD-ROM, XXVIII IAHR CONGRESS: IAHR.

Yoichi, T., Kyozo, S. & Mitsuo, T. 2002. *Time and Regional Extended Effects by Flood Mitigation Project:* 13th APD-IAHR Vol. 1, 520–523: APD-IAHR.

Yoichi, T., Kyozo, S. & Mitsuo, T. 2002. *One-sided Dikes,* CD-ROM of Global Solutions for Urban Drainage: 9ICUD: ASCE.

Modeling floodplain flow on lower Deer Creek, CA

M.L.MacWilliams, Jr., R.L.Street & P.K.Kitanidis

Environmental Fluid Mechanics Laboratory, Department of Civil and Environmental Engineering, Stanford University, Stanford, CA

River Flow 2004—Greco, Carravetta & Della Morte (eds.)

ABSTRACT: Three-dimensional hydrodynamic modeling of flow in complex river-floodplain systems offers the potential to increase the current understanding of stream stability, channel morphology, and flood conveyance in natural channels. A three-dimensional hydrodynamic model is applied to lower Deer Creek, CA to simulate a large flood event that resulted in levee failure. A description of the numerical model and the development of the model grid and boundary conditions are presented. Simulation results show good agreement with high water surveys and demonstrate the important features influencing flow on the lower Deer Creek floodplain. Simulation results provide detailed information about the capacity of floodplain pathways and demonstrate the value of detailed hydrodynamic modeling as a tool to understand and quantify flow on complex floodplain systems. These results will be used to help guide the planning and implementation of future flood management strategies on lower Deer Creek.

1 INTRODUCTION

Deer Creek is one of the last drainages in the Sacramento River system that supports spring-run Chinook salmon, which have recently been added to the federal list of endangered species. As a result, Deer Creek has been recognized as a priority for habitat restoration by the CALFED Bay-Delta Program (CALFED 2000). A geomorphic study (DCWC 1998) concluded that habitat in Deer Creek is limited mostly because of effects of the existing flood control project. These effects include a lack of habitat diversity and riparian vegetation due to channel maintenance and clearing, and a lack of suitable spawning material due to the high shear stresses which occur in the channel when high flows are constrained within the existing levees.

Various proposals have been put forth to enhance salmon habitat and passage on Deer Creek, including maintaining minimum base flows, artificial addition of smaller gravel for spawning, and planting of riparian trees to address the relative lack of vegetation on the banks of most of lower Deer Creek (CALFED 2000). The CALFED Strategic Plan for Ecosystem Restoration (2000) notes that many of the restoration efforts planned for Deer Creek are treatments of the symptoms of the current flood management strategy and do not address the underlying problems. Their proposed management alternative suggests that if the style of flood management were changed to set levees back, permit overbank flooding, and eliminate channel clearing, Deer Creek would, in the course of one or more floods, reestablish a more natural channel form with better habitat.

The California Department of Water Resources (DWR) is currently considering flood management alternatives for lower Deer Creek which would incorporate the proposed CALFED management strategies. As noted in the Lower Deer Creek Flood Management Study Draft Scope of Work (Cepello 2000): "The opportunity exists through a combination of redesigning existing flood control features and encouraging appropriate land use to restore the reliability of the flood control project, reclaim a large portion of the historic floodplain, and incorporate natural distributary channels into an overflow bypass system for lower Deer Creek. These actions would also help natural stream processes occur and would be the most effective ecological strategy to restoring the terrestrial and aquatic habitats of lower Deer Creek."

A detailed understanding of river stage, flow velocities, bed shear stresses, inundation areas, levy capacity and floodplain storage will be essential to understand the response of the system to various flood discharges and provide information necessary for developing further project objectives. Commonly used one-dimensional hydraulic models are not suitable for assessing complex flow systems that will result from the proposed flood management strategy, which includes reclamation of the historic floodplain and the incorporation of historic distributary channels. This study utilizes a robust and efficient three-dimensional hydrodynamic model, UnTRIM, to simulate a large flood event which occurred on lower Deer Creek in January, 1997. This modeling effort provides much more detailed information about channel conveyance, flow variability within the river channel, floodplain storage, the capacity of the natural distributary channels and existing culverts for overflow bypass, and the effects of potential levee modifications on the flow system than could be obtained from existing one-dimensional models. Through collaboration with California DWR and the Deer Creek Watershed Conservancy, this information will be used to help guide the implementation of the proposed flood management strategy on lower Deer Creek.

1.1 *Site description*

Deer Creek originates on the west slope of Mount Lassen and ultimately flows into the Sacramento River near Vina, CA. The watershed encompasses approximately 590km^2 and ranges in elevation from 2400m to less than 100m above mean sea level. Historical aerial photographs taken in 1939 show that the lower portion of Deer Creek was highly sinuous, with small-scale bends, point bars, and alternating pools and riffles (CALFED 2000). During floods, Deer Creek would regularly overflow its banks and inundate adjacent floodplains, providing water and nutrients to adjacent riparian zones. Under

natural conditions, lower Deer Creek exhibited the multiple channels characteristic of alluvial fans. During floods, water flowed across the floodplain and into some of the multiple distributary channels on the alluvial fan.

The Deer Creek Flood Control Project, authorized by the 1944 Flood Control Act, was completed by the U.S. Army Corps of Engineers in 1953 and transferred to the jurisdiction of the State Reclamation Board in 1956 (Cepello 2000). About 16km of levees were built along lower Deer Creek by the U.S. Army Corps of Engineers to control flooding, and the channel was straightened and cleared (CALFED 2000). As a result of this work, the role of the natural distributary channels was disrupted and the riparian zone was limited to a small band within the constructed levees.

Although the average flow rate on Deer Creek is only about $9m^3/s$, Deer Creek experiences a high snowmelt flow virtually every year, and large floods often result from warm winter rains on snow. Large floods have occurred in January 1997 ($680m^3/s$), 1970 ($530m^3/s$), December 1964 ($570m^3/s$), 1940 ($610m^3/s$), and 1937 ($675m^3/s$) (CALFED 2000). Although the 1997 flood experienced flows greater than 7500% of the average flow rate, frequency analysis indicates that this is only considered a 25-year recurrence interval flow event (CALFED 2000). Under the pressure of such floods, maintenance of the stream channel and levee system has been an expensive undertaking. Major levee repair work was undertaken by the Corps of Engineers following the flood of February 1986 and by the National Resources Conservation Service and Tehama County after the January 1997 flood (Cepello 2000).

During the January 1997 flood, Deer Creek breached its levee and flowed across the floodplain for several kilometers. The areas which were flooded during the 1997 flood were predominantly agricultural land, including orchards, grazing land, and farms. Based on field observations following the flood and eyewitness accounts, a conceptual model of the January 1997 flood on lower Deer Creek has been developed by the California DWR. This conceptual model, shown in Figure 1, demonstrates the importance of the role of the floodplain for providing flood storage and the importance of the natural distributary channels in influencing the flow of water on the floodplain. In particular, Delaney Slough (top right) and China Slough (bottom center) play an important role in the natural hydrology of Deer Creek and served as conduits for water on the floodplain during the 1997 flood.

The conceptual model of the 1997 flood on lower Deer Creek provides a valuable resource for identifying the features on the floodplain which had a significant effect on floodplain hydrodynamics; however the conceptual model does not provide any quantifiable information about flow on the lower Deer Creek floodplain. The collection of data during large flood events is not practical, and thus limited quantifiable information is available to help guide efforts to redesign the flood management strategy. The application of a three-dimensional hydrodynamic model to lower Deer Creek provides an opportunity to quantify floodplain storage and the capacity of specific pathways on the floodplain to convey bypass flow.

2 METHODS

2.1 *Model description*

This study applies the three-dimensional non-hydrostatic hydrodynamic model for free-surface flows on unstructured grids, UnTRIM, described in Casulli and Zanolli (2002). The model solves the three-dimensional Navier-Stokes equations on an unstructured grid in the horizontal plane. A structured grid is used in the vertical direction, such that the domain is divided into vertical layers of uniform, but not necessarily equal, thickness. Volume conservation is expressed by the incompressible continuity equation, and the free-surface is calculated by integrating the continuity equation over the depth and using a

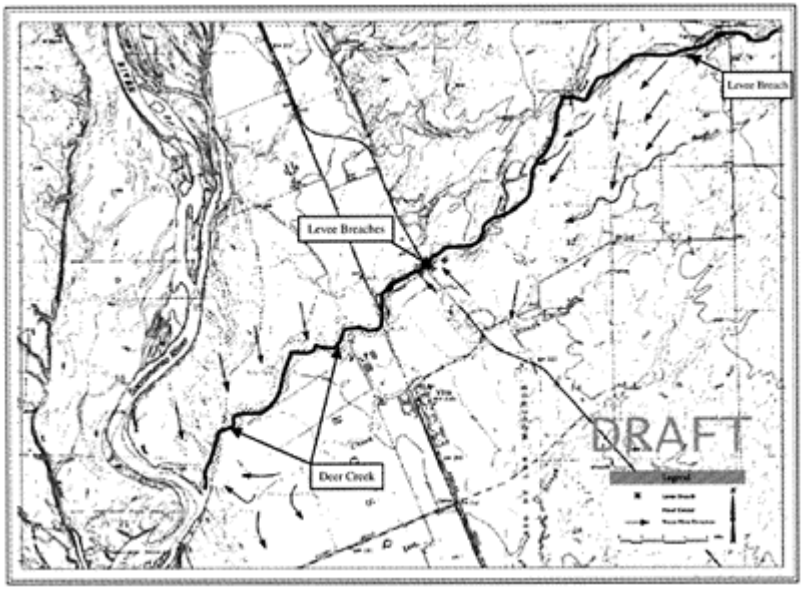

Figure 1. DWR conceptual model of the January 1997 flood. The Sacramento River flows from top left to bottom left, and Deer Creek flows from top right to lower left. The levee breach occurred on the upper right portion of the figure. The breaches shown in the center served to allow water back into the main channel. Note

the influence of Delaney Slough and China Slough in influencing the flow of water on the floodplain (*Source:* California DWR).

kinematic condition at the free-surface as described in Casulli and Cheng (1992). The governing equations are discretized using a finite difference—finite volume algorithm. The numerical model accounts for bottom friction, wind stress, convective and viscous acceleration, gravitational acceleration, and vertical eddy viscosity. For the work presented in this study, several additional enhancements were added to the model presented by Casulli and Zanolli (2002). An inflow boundary condition for volume and momentum, a radiation outflow boundary condition, a modified formulation of bed drag and vertical eddy viscosity, and a method for modeling hydraulic structures were added, as described in MacWilliams (2004). The modified UnTRIM code was applied to simulate flow on lower Deer Creek.

2.2 *Grid development*

One of the limitations of using three-dimensional models is the capacity to accurately specify complex topography (Lane *et al.* 1999). At the Deer Creek site, high resolution photogrammetric data had already been collected, and this photogrammetric topography was available in digital form. Photogrammetry was completed as part of the Lower Deer Creek Flood Management Study and includes detailed (0.6m contours) topography for the lower Deer Creek study area (approximately 75km^2) based on photography and ground control data provided by the Department of Water Resources. Processing of aerial photography and terrestrial and bathymetric surveys into detailed topography was completed by the U.S. Army Corps of Engineers and the California DWR under the Sacramento and San Joaquin River Basins Comprehensive Study. This terrain and bathymetric data was obtained from California DWR and used in the development of the grids used in UnTRIM. Using this detailed topography it was possible to minimize the difficulties associated with specifying channel geometry and generate a high resolution grid consistent with the actual topography at the site.

An orthogonal unstructured grid was generated over the horizontal domain for use with the UnTRIM model. The grid was generated in two sections using the mesh generation program TRIANGLE (Shewchuck 1996). The first section of the grid was generated for the portion of lower Deer Creek which is bounded by the levees on each side of the channel, shown in Figure 2. In this portion of the grid, the grid was constrained such that the levees and the low water waterlines were aligned with cell edges in the grid mesh. Where no distinct levees were present, the grid is bounded by the local topographic break along the edge of the floodplain. This was done to ensure that the topographic high associated with the levees was captured in the grid, and to delineate the area within the low flow channel as a distinct portion within the grid. Because the topography for lower Deer Creek was obtained through photogrammetric mapping, the topographic data extend

only to the edge of the wetted channel on the date which the photogrammetry was collected. No bathymetric data were available for the low water channel.

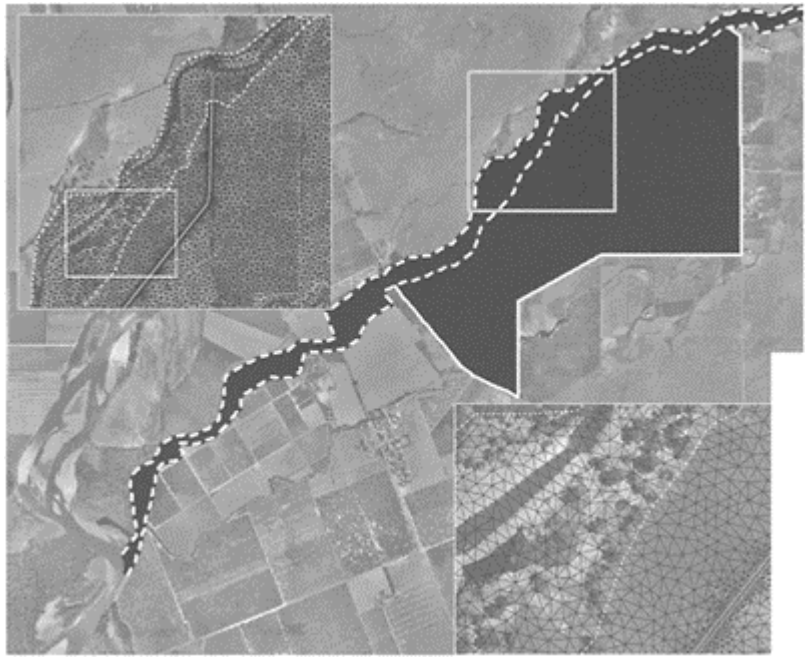

Figure 2. Model grid for lower Deer Creek (black). The grid for the channel of lower Deer Creek is bounded by the levees or high topography (shown as two “parallel” white dotted lines from top right to bottom left). The floodplain grid is bounded predominantly by bordering roads (solid white). The top inset shows a portion of the grid with the low flow channel and the South-Main Canal highlighted. The lower inset shows a close-up view of the area identified in the top inset, again showing a portion of the low flow channel and the South-Main Canal (bottom right). The model

grid extends approximately 5km
upstream of the area shown.

The bathymetry of the low water channel was estimated through a series of model calibrations. The aerial photogrammetry for lower Deer Creek was completed on May 11, 1999. On this day, the average daily flow in Deer Creek was measured to be $11 m^3/s$. A series of UnTRIM simulations was made by assuming an initial bathymetry where the bed was set to be 1m below the observed water surface in the low flow channel. A constant flow rate of $11 m^3/s$ was applied and the downstream water surface elevation was set to be 51.5m, which is the water surface elevation observed in the photogrammetric data at the mouth of Deer Creek on May 11, 1999. By comparing the predicted water surface throughout the low flow channel to the water surface observed in the photogrammetric survey, the low flow channel bathymetry was adjusted and the procedure was iteratively repeated. Although this method is not expected to provide a highly accurate estimate of low flow bathymetry, visual comparison of calibration results and channel morphology visible on the aerial photographs suggests that this calibration procedure produced a reasonable bathymetric profile for the low flow channel. Because the flow capacity of the low flow channel is only $11 m^3/s$, it is not expected that errors associated with this bathymetric calibration will introduce significant effects on modeling flood flows on the order of $500 m^3/s$. Additionally, it is believed that this approach is more consistent with the other available topographic data than conducting a present-day bathymetric survey on the low flow channel, which has been altered since 1999 and since the pre-flood 1997 bathymetry.

A grid of the upper portion of the lower Deer Creek floodplain was also developed using TRIANGLE. The western boundary of the floodplain grid was constrained so that the grid sides aligned with the edge of the levee-bounded grid. Additionally, the edges of the South-Main Canal, which flows across the floodplain, were identified and preserved in the floodplain grid. The floodplain grid is bounded by a series of roads which are topographic highs and serve as hydraulic barriers. Highway CA-99 runs along the southwestern edge of the floodplain grid. The merged grid consisting of the levee-bounded grid and the upper floodplain grid, shown in Figure 2, contains 45,668 triangular elements in the horizontal grid and over two and a half million computational cells. As seen in Figure 2, the model grid follows the topography such that the levees, low flow channel, and South-Main Canal are all aligned with grid cell faces. This ensures that the elevations associated with these features are captured in the model grid, because grid elevations are located on the center of each cell side. The resolution of the model grid surrounding the South-Main canal, as seen in the lower offset is on the order of 5m. The grid spacing on the majority of the floodplain is typically on the order of 25m, and a slightly finer resolution of approximately 20m is typically used between the levees and in the low flow channel. A uniform vertical grid spacing of 1m was used.

2.3 *Boundary conditions*

The simulation of the 1997 flood on lower Deer Creek requires the specification of an inflow hydrograph and a downstream water surface elevation. Additional boundary conditions are applied to model hydraulic structures on the floodplain.

A USGS gauging station is located on Deer Creek, approximately 14.5km upstream of its confluence with the Sacramento River, and approximately 2.5km upstream of the upstream end of the model domain. This gauge reports river stage, and a stage-discharge relationship exists for this station. Using the USGS stage-discharge relationship with the measured stage data predicts two flood peaks of 564 and 680m^3/s. It is known that the second peak resulted in levy failure on Deer Creek and that the first peak did not exceed the capacity of the levees.

Preliminary simulations, an analysis of previous levee failures, and a one-dimensional model indicate that the magnitude of both of these flood peaks exceeds the capacity of the levee system. Annual peak discharge data are available for lower Dear Creek from 1912 through 1997. Comparing the yearly peak discharge with the years in which levee failure occurred indicates that flows greater than 450m^3/s consistently resulted in levee failure. This suggests that the two peaks predicted by the USGS rating curve are not accurate because if the first flood peak was actually more than 560m^3/s, as predicted by the measured stage data and the USGS rating curve, levee failure almost certainly would have occurred.

The measured stage for the second flood peak is only 0.33m greater than the stage measured for the first peak. This small difference in measured stage is inconsistent with eyewitness accounts of river stage near the breach location. Additionally, the measured stage for the second flood peak varies by less than 0.06m during the seven hours surrounding the peak. This flat stage measurement at the flood peak suggests that the stage for the flood peak has exceeded the height which can be measured at the gauge and that the actual stage at the gauge was greater during the peak than was reported at the station.

By assuming that the actual stage for the second flood peak exhibited a similar shape to the stage measured for the first peak, the flat stage data for the second peak were augmented by an appropriate filter. Using this filter, the difference in stage between the first and second flood peaks was increased from 0.33 to 0.91m. A new stage-discharge relationship was developed, as shown in Figure 3, which maintained the discharge at the augmented peak stage to be identical to the discharge at the original peak stage for the second flood peak. However, the discharge associated with the first peak in flood stage is reduced relative to the original rating curve. Using the modified stage data and the new stage-discharge relationship, the discharge associated with the second flood peak remained at 680m^3/s, while the first flood peak was calculated to be 450m^3/s, which is within the capacity of the levee system. This hydrograph is shown in Figure 4 and was used as the inflow boundary condition. Based on observational information about stage and breach timing, an analysis of past levee failures, one-dimensional simulations and preliminary simulations using the three-dimensional model, this hydrograph is a more appropriate estimate of the hydrograph for the January 1997 flood than the hydrograph calculated from the raw stage data using the USGS stage-discharge relationship (MacWilliams 2004).

The downstream boundary is specified using the river stage on the Sacramento River measured at DWR Woodson-Vina gauging station at Woodson Bridge, shown in Figure 4. The Woodson Bridge gauge is approximately 1.7km downstream of the mouth of Deer Creek. Based on the photogrammetric data and the DWR stage data at Woodson Bridge, the stage at the mouth of Deer Creek is estimated to be 0.3m above the stage observed at

the Woodson-Vina Bridge gauge. This estimate is used to calculate the downstream boundary stage and is based on the assumption that the water surface slope on this reach of the Sacramento

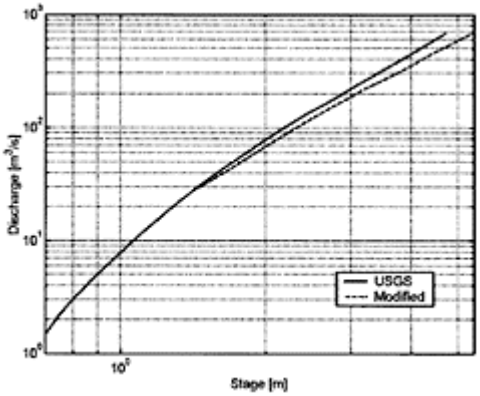

Figure 3. Original USGS stage-discharge relationship and modified stage-discharge relationship.

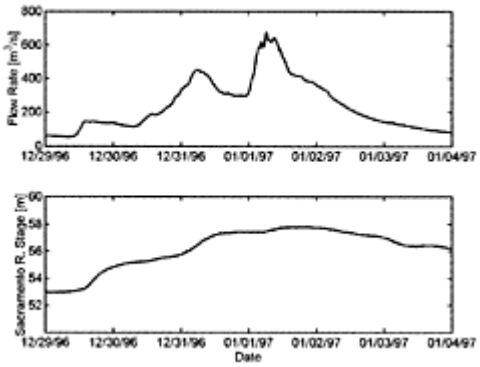

Figure 4. Hydrograph for lower Deer Creek (top) used for inflow boundary condition and Sacramento River stage elevation (bottom) used as downstream boundary condition.

River does not change significantly during higher flows.

In addition to the upstream and downstream boundary conditions, culvert rating curves were developed for three hydraulic structures that are important conduits for flow on the lower Deer Creek floodplain. The rating curves were developed using HEC-RAS based

on field measurements of the culvert dimensions for each of the three culverts. The rating curves used assume free-flow conditions at the outlet, which provides the largest possible flow through the culvert based on the set of rating curves developed.

Using these boundary conditions and rating curves, UnTRIM was used to simulate the 1997 flood on lower Deer Creek. A period of six days was simulated using a time step of 1 second. The bottom roughness was specified over the domain using a roughness height of 1×10^{-3}m in the channel and on the floodplain values of 1×10^{-2} and 1×10^{-1}m were specified for areas delineated as grazing lands and orchards, respectively. The roughness parameters on the floodplain were calculated from the tables of Chow (1959) by converting the appropriate roughness coefficient to a roughness height using the approach described in MacWilliams (2004).

The levee failure resulted in a significant change in local geometry at the location of the levee breach and a section of levee was washed out. To capture this effect in the flood simulations, a similar adjustment is made to the model grid by removing a section of levee at the breach location at the time in the simulation when significant levee topping occurs.

3 RESULTS

Because no data were collected during the 1997 flood, there is only a limited capacity to quantitatively validate the model results. However, efforts have been made to gather as much quantitative or qualitative information as possible about the 1997 flood to perform an assessment of model performance.

Following the 1997 flood, high water mark surveys were conducted on January 13–16, 1997. The data from these surveys were obtained through the California Department of Water Resources Northern District Office. Eighteen high water marks were surveyed on the east levee of Deer Creek and twenty high water marks were surveyed on the west levee of Deer Creek. At each survey point, the high water mark (HWM) was photographed, sketched relative to surrounding features, and surveyed. Using the information available in the survey notes, each of the HWM survey stations within the study area was identified and located on the model grid. The predicted HWM was calculated to be the maximum water surface at the survey location during the flood simulation. The differences between predicted and measured HWM along the Deer Creek levees for the January 1997 flood are shown in Figure 5. All of the predicted HWM elevations are higher than the observed HWM elevations, which suggests that the modeled peak discharge may exceed the actual peak flood discharge. The average difference between the predicted and observed HWM is 0.36m. This difference can also be attributed to error associated with the field HWM survey elevations, error in the photogrammetric topography, error in the simulated hydrograph, and model accuracy. The error associated with the topographic data are on the order of 0.15m; a slightly higher error is associated with the HWM surveys. Based on this, the model results show good agreement with the surveyed HWM elevations within the accuracy of the available data.

In addition to the high water mark surveys, the other primary sources for model validation come from the

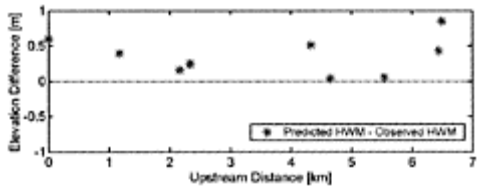

Figure 5. Difference between predicted and observed high water marks at stations surveyed by DWR following the January 1997 flood.

DWR conceptual model of lower Deer Creek flood actions, shown in Figure 1, and from post-flood aerial photographs. The post-flood aerial photographs give a good indication of flooded areas and flow direction based on disruption of floodplain vegetation and deposition sediment on the floodplain. A comparison between the inundation area predicted by UnTRIM at the time of maximum floodplain inundation and the inundation area incorporated in the DWR conceptual model is shown in Figure 6. As seen in this figure, the results from the UnTRIM simulation show good agreement with the conceptual model both in terms of inundation areas and flow direction on the floodplain.

Figure 7 shows a comparison between post-flood aerial photographs, the DWR conceptual model and the UnTRIM predictions in the section of the floodplain containing the South-Main Canal. The orientation of the conceptual model and the UnTRIM results have been rotated to match the boundaries of the aerial photographs. As seen in this figure, there is good agreement between the inundation areas predicted by UnTRIM and the flooded areas shown by the conceptual model. The grey areas in the UnTRIM model (top left of the right panel) which designate portions of the model grid which remain dry agree well with the areas in the aerial photograph which show no evidence of sediment deposition and thus are assumed to have been above the elevation of the flood waters. One of the major flow pathways back into the main channel is shown crossing the irrigation canal in the top center of each panel on Figure 7 and then entering the main

Figure 6. DWR conceptual model of January 1997 flood (left) shown with UnTRIM model predictions during

maximum floodplain inundation (right). Lightly hatched area on conceptual model indicates flooded areas; flooded area on the model results shown as light-colored area overlaid by velocity vectors. Arrows on the conceptual model show flow pathways but are not scaled to flow magnitude or velocity. Arrows on the model predictions show surface velocity vectors for a subset of the computational cells.

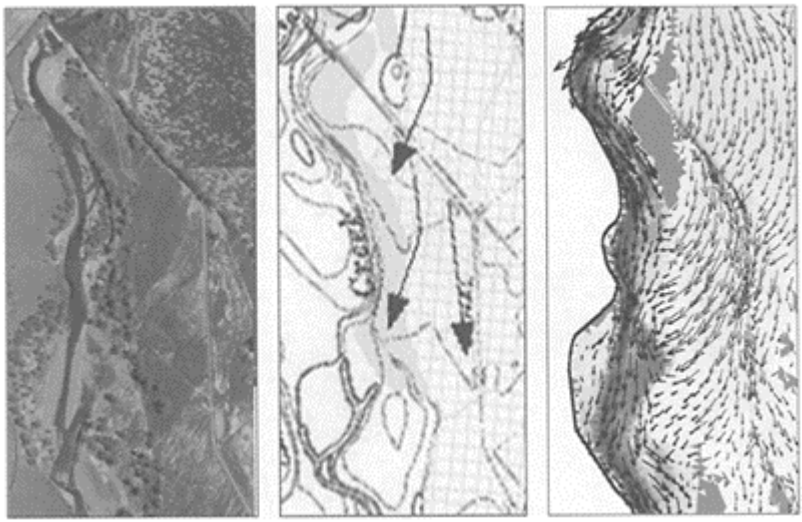

Figure 7. Post-flood aerial photograph showing sediment deposited along flow pathways (left) shown with conceptual model of January 1997 (center) and UnTRIM model predictions during maximum floodplain inundation (right). Arrows on the conceptual model show flow pathways. Arrows on the model predictions show surface velocity

vectors for a subset of the computational cells.

channel in the bottom half of each panel. On the aerial photograph, the sediment deposition pattern between the South-Main Canal and the main channel of Deer Creek indicate the significance of this flow pathway. A similar pathway is observed in the UnTRIM results and is shown in the conceptual model. In the aerial photograph, a significant amount of headcut erosion into the floodplain is visible at the location where flow re-enters the main channel. This is consistent with model results which indicate a large fraction of the flow on the floodplain re-enters the main channel in this reach. Overall these comparisons suggest the UnTRIM model is providing a reasonable estimate of flow on the floodplain for the January 1997 flood.

A schematic of the primary flow pathways on the Deer Creek floodplain for the January 1997 flood is shown in Figure 8. The primary levee breach on lower Deer Creek occurred approximately 0.5km downstream of Leininger Bridge. The majority of the water traveling across the floodplain re-entered the main channel at two locations, downstream of the Stanford-Vina diversion dam, and immediately upstream of highway CA-99. Figure 9 shows the hydrographs for the flow contained between the levees at Leininger Bridge, the Stanford-Vina diversion dam, and at the highway CA-99 Bridge. These hydrographs are

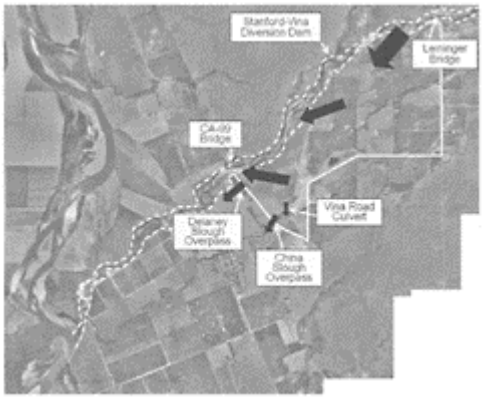

Figure 8. Schematic of primary flood pathways on lower Deer Creek during January 1997 flood. The boundaries of the main channel (white dashed lines) and the boundaries of the floodplain grid (white solid line) are indicated for reference. The dark arrows show primary flow pathways. Text boxes and white arrows identify the locations

corresponding to the channel and hydraulic structure hydrographs shown in Figures 9–10.

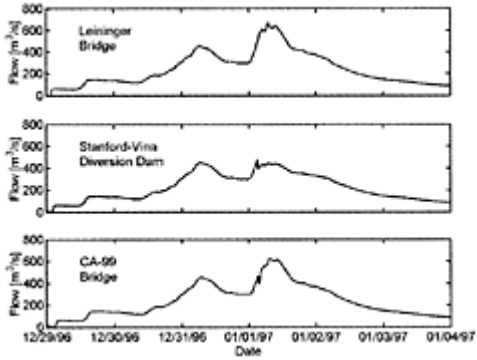

Figure 9. Predicted hydrographs in the main channel of lower Deer Creek at three locations identified on figure 8.

obtained by calculating the total flow through each of these channel cross-sections during each time step during the simulation. As seen in Figure 9, the levee breach truncates the second flood peak at the Stanford-Vina diversion dam due to the flow across the floodplain. The peak discharge predicted at the Stanford-Vina diversion during the first flood peak was 450m^3/s. The discharge predicted at the Stanford-Vina diversion at the time of the levee breach was approximately 475m^3/s and following the levee breach the maximum discharge predicted was 450m^3/s. This reduction in maximum discharge results because, following the breach, a larger amount of water is diverted onto the floodplain and the effective downstream conveyance capacity of the main channel at the breach is truncated. Downstream of Stanford-Vina diversion dam, the floodplain elevation is sufficiently above the main channel that no significant levees were constructed. As a result, water from the floodplain can freely flow back into the main channel of lower Deer Creek. A significant fraction of the flow on the floodplain during the 1997 flood re-entered the main channel at this location (as seen in Figure 7). The remaining water flowed down the floodplain until it reached highway CA-99. At the highway, which is elevated significantly above the surrounding floodplain, the water backed up until the levees were breached to allow the water to flow back into the main channel immediately above the CA-99 highway bridge. As seen in Figure 9, the hydrograph at the CA-99 Bridge shows a flood peak similar to the hydrograph at Leininger Bridge, which indicates that the majority of water has re-entered the main channel by the time Deer Creek flows under CA-99. The simulation results predict a peak discharge of 670m^3/s at Leininger Bridge and a peak discharge of 620m^3/s at CA-99.

The balance of water which does not re-enter the main channel upstream of CA-99 flows under the highway at overpasses located on Delaney Slough and

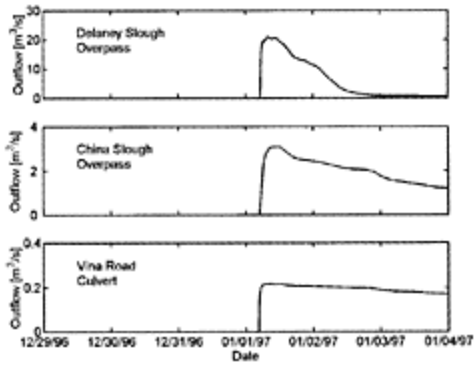

Figure 10. Predicted hydrographs through the hydraulic structures at the locations identified on figure 8.

China Slough. The flow hydrographs for these two structures, and the hydrograph for the culvert under Vina Road which connects the main area of the floodplain with China Slough, are shown in Figure 10. The culvert under Vina Road is quite small and based on the large discharge predicted through the end of the simulation it is evident that this culvert is limiting flow into China Slough. The culvert on China Slough under CA-99 provides a larger conveyance capacity but also shows a significant flow rate following the initial flood pulses. If a substantial flow is to be routed through China Slough as is suggested in the Lower Deer Creek Flood Management Study, this culvert would also need to be resized to increase its capacity.

4 DISCUSSION

The three-dimensional simulation of the January 1997 flood on lower Deer Creek provides valuable quantifiable information about water levels, flow velocities, inundation areas, flow pathways on the floodplain, and the performance of existing floodplain hydraulic structures. Coupled with the knowledge provided by the DWR conceptual model of the 1997 flood on lower Deer Creek, this information can serve as a valuable tool in planning future restoration strategies on lower Deer Creek.

The implementation of flood management alternatives that will change the style of flood management to set levees back, permit overbank flooding, and incorporate natural distributary channels back into the floodplain system depends on an adequate understanding of hydrodynamics on the floodplain during large flood events. This understanding is necessary in order to help improve the reliability of the existing flood management system and to help foster the restoration of the terrestrial and aquatic habitats of lower Deer Creek by allowing natural stream processes to occur.

Kondolf (2000) argues that “aquatic and riparian habitat for salmon and other organisms is, in effect, a by-product of the channel geomorphology, which, in alluvial reaches, largely reflects the prevailing flow and sediment regimes, as well as effects of

riparian vegetation and human modifications." As a result, a detailed understanding of the flow regime on lower Deer Creek during floods is necessary for the proper evaluation of future restoration efforts on Deer Creek.

Restoration projects, such as that on the Cosumnes River, CA, have demonstrated the benefit of breaching and setting back levees. Based on the result of a levee breach on the Cosumnes River it was concluded that "if the natural process of flooding is allowed to take place, the river can reforest its old flood plain and restore fish and wildlife habitat quickly and effectively. When natural processes are allowed to shape the landscape on a large scale, the habitat becomes very diverse, enabling many species to live together in a balanced ecosystem" (Cosumnes 2003). A similar opportunity exists on lower Deer Creek to setback levees and reclaim a large portion of the historic floodplain. Deer Creek remains one of the least altered streams in the Central Valley and still supports all four runs of Chinook salmon, as well as mns of steelhead. As a result, the preservation of this resource is a high priority.

Using the model developed in this study as a starting point, it is possible to simulate the potential effects of various structural modifications to the floodplain using UnTRIM. Information about flood inundation and frequency under the proposed management plan can be used to recommend sensitive areas that should be obtained through purchase or land-easements to ensure the reliability of the proposed flood management strategy. An analysis of the hydraulic effects of levee setbacks, allowing inundation of the natural floodplain, and the incorporation of natural distributary channels into the flood management strategy, can be used to recommend appropriate modifications to the levee system that will allow natural channel and floodplain processes to occur while still providing adequate protection to existing structures. As a result, the extension of this modeling study can be used to provide information that will help to maximize the effectiveness of the proposed management strategy. Funds spent on this type of planning study can help prevent much larger expenditures on projects that would prove to be ineffective or unnecessary (Kondolf 2000).

5 CONCLUSIONS

These results demonstrate the ability of detailed hydrodynamic modeling to simulate flooding on a large-scale complex river floodplain. Through the application of a newly-developed three-dimensional hydrodynamic model, this study made use of available topographic, and hydrologic data to quantify the major flow pathways on the lower Deer Creek floodplain. In the absence of detailed field measurements during the flood, model results were validated against postflood high water mark surveys, a conceptual model of the flood developed by California DWR, and postflood aerial photographs. The UnTRIM simulations provide good overall agreement with these available data sources.

The simulation of the January 1997 flood on lower Deer Creek provides a state-of-the-art analysis of the capacity of the levee system on lower Deer Creek and the important flow pathways on the floodplain. If used in guiding future management decisions, this work has the potential to have a lasting impact on the management and conservation practices in the Deer Creek watershed. The implementation of these management practices through the collaboration of the California DWR and CALFED will provide a

unique opportunity within the Central Valley to preserve one of the regions most important salmon habitats, and demonstrate the capacity of innovative flood management strategies to preserve the watershed's ecological and agricultural resources.

ACKNOWLEDGEMENTS

The authors would like to acknowledge the collaboration of Stacy Cepello from the California Department of Water Resources and G.Mathias Kondolf from the University of California, Berkeley. The UnTRIM code was provided by Prof. V.Casulli of the University of Trento, Italy. This work was funded in part through a Conserving California Landscapes Initiative Grant by the David and Lucile Packard Foundation (CCLI Grant #00–14780) and by a grant from the National Science Foundation (Grant EAR-0087842, Program Manager: Dr. L.Douglas James). Additional funding was provided to MLM by a Stanford Graduate Fellowship and a NSF Graduate Research Fellowship.

REFERENCES

CALFED Bay-Delta Program 2000. *Ecosystem Restoration Progrsam Plan. Volume 3: Strategic Plan for Ecosystem Restoration.* July. Sacramento, CA.

Casulli, V. & Cheng, R.T. 1992. Semi-implicit finite difference methods for three-dimensional shallow water flow. *International Journal for Numerical Methods in Fluids* 15:629–648.

Casulli, V. & Zanolli, P. 2002. Semi-implicit numerical modeling of non-hydrostatic free-surface flows for environmental problems. *Mathematical and Computer Modeling* 36:1131–1149.

Cepello, S. 2000. Lower Deer Creek Flood Management Study Preliminary Hydrology and Engineering Draft Scope of Work. Red Bluff, CA: California Department of Water Resources.

Chow, V.T. 1959. *Open-channel Hydraulics.* New York: McGraw-Hill.

Cosumnes 2003. http://www.cosumnes.org/project.htm

DCWC, 1998. (Deer Creek Watershed Conservancy). Deer Creek Watershed Management Plan. Vina, CA.

Kondolf, G.M. 2000. Some suggested guidelines for geomorphic aspects of anadromous salmonid habitat restoration proposals. *Restoration Ecology* 8(1): 48–56.

Lane, S.N., Bradbrook, K.F., Richards, K.S., Biron, P.A. & Roy, A.G. 1999. The application of computational fluid dynamics to natural river channels: three-dimensional versus two-dimensional approaches. *Geomorphology* 29:1–20.

MacWilliams, M.L. 2004. Three-dimensional hydrodynamic simulation of river channels and floodplains. Ph.D. Dissertation, Stanford University.

Shewchuck, J.R. 1996. Triangle: Engineering a 2D Quality Mesh Generator and Delaunay Triangulator. In Lin, M.C. & Manocha, M. (eds.). *Applied Computa-tional Geometry: Towards Geometric Engineering,* Lecture Notes in Computer Science Vol. 1148:203–222. Berlin: Springer-Verlag.

C.4. Integration of telemetry and GIS

Estimating hydraulic parameters and geometric characteristics of a river from remote sensing data using optimization methods

H.Roux & D.Dartus

Institut de Mécanique des Fluides, Toulouse, France

River Flow 2004—Greco, Carravetta & Della Morte (eds.)

ABSTRACT: The necessity of an improvement of flood risk management has been emphasized by the importance of the damages caused by several disastrous floods in recent years. An obligatory way to better understand and forecast these events is to be able to accurately simulate the water transport in the river. Application of numerical models requires parameter calibration, even when in situ measurements are available. Here is presented an exploration of the possibility of estimating these parameters from observations provided by telemetry implementing optimization techniques. The originality of this study is to reconstitute information about the geometry of the river and the hydraulic characteristics of the considered event from top sights. Application examples on two different rivers are presented.

1 INTRODUCTION

Recent floods in Europe have had catastrophic consequences from a human but also economic and historic point of view. The total damages have emphasized the need of an accurate prevision of these floods to improve the risk management (Plate, 2002). Huge progresses have been recently realized in the modelling of the hydrodynamic of the flow in the river but also on the floodplain areas (Bates & de Roo, 2000), (Stewart et al., 1999), (Marks & Bates, 2000). However, hydrological modelling requires a thorough knowledge of the river to be able to map flood extents for risk analysis purpose. Some models contain conceptual parameters that usually cannot be assessed by measurements in the field; on the contrary, distributed, physically based models use only parameters that can be assessed from in-situ data. But it is often a long and expensive procedure, sometimes difficult to implement and in practice, it is not possible to determine the parameters at each computational point grid (Madsen, 2003). Therefore, both type of

models need calibration and the problem is even more pronounced in the case of ungauged rivers.

New generations of satellite are equipped with sensors of metric resolution, 1m in panchromatic for IKONOS-2, launched by the USA in 1999 and 2.5m in panchromatic for SPOT-5, launched by France in 2002. Air photo techniques have also developed quickly and compared to the satellite telemetry, they offer a better reactivity in front of the events. Indeed, satellite images taken during a flood remain rare as it needs the concomitancy of the event with the satellite track.

This study starts from these two facts: the need of a thorough knowledge of the river for both model calibration and running and the increasing potential of telemetry as a source of information. Data assimilation methods allow to combine data provided by the model with data provided by space observation to identify information about the river. The formulation of flowstate equations to ascertain the value of the parameters embedded in the simulation process is referred to as an inverse problem (Khatibi et al., 2001). There is no exact solution but it is possible to estimate the best one in a mathematical sense using optimization techniques.

This paper focuses on the identification of parameters necessary to simulate open-channel flows by resolution of the one-dimensional Saint-Venant equations. That is to say discharge, Manning roughness coefficient or geometric characteristics of the channel. A preliminary study (Roux et al., 2004) has shown that the minimization of an error criterion gives satisfactory results for this purpose. This method has then been implemented using two different approaches. Both estimate parameters such as discharge, Manning roughness coefficients and a downstream condition, but they differ in their way of identifying the geometry of the cross-section. The first approach consists in identifying an equivalent river: a hypothesis is made on the geometry of the cross-section and the characteristics of this geometry are then estimated. It has been implemented on the river Lèze (South-West of France). The second approach consists in taking into account the topography of the overbanks in the assimilation process. This topography may also be provided by telemetry. In the cross-section, only the geometry of the main channel is then identified. This method has been implemented on the river Aisne (North of France).

2 METHODOLOGY

2.1 *Optimization techniques*

The scope of data assimilation is to make the best estimate of the model state using observations and a numerical model.

If $\mathbf{X^t}$ is the true state of the system at a given time (Ide et al., 1997), an observation $\mathbf{y^o}$ of $\mathbf{X^t}$ can be written as (Hoteit, 2001):

$$\mathbf{y^o}=F(\mathbf{X^t})+\boldsymbol{\varepsilon} \quad (1)$$

where F is an operator linking state space with observation space, called observation operator. It allows to calculate the model equivalent $F(\mathbf{X^t})$ of the observations. $\boldsymbol{\varepsilon}$ is a random vector with zero mean and covariance matrix **R,** modelling an observation noise.

The best estimate $\mathbf{X^a}$ of the model state $\mathbf{X^t}$ can be obtained by minimization of the sum of a distance to an a priori estimate (often a prevision) of the model state $\mathbf{X^f}$ and a distance to the observations $\mathbf{y^o}$.

$$\mathbf{\Phi}=(\mathbf{X}-\mathbf{X^f})^{\mathbf{T}}\mathbf{P}^{-1}(\mathbf{X}-\mathbf{X^f})+(\mathbf{y^o}-F(\mathbf{X}))^{\mathbf{T}}\mathbf{R}^{-1}(\mathbf{y^o}-F(\mathbf{X})) \quad (2)$$

$\mathbf{P}$ is the covariance matrix of the error made in estimating $\mathbf{X^t}$ by $\mathbf{X^f}$.

The numerical calculus of the analysis state $\mathbf{X^a}$ can be very expensive, in terms of computation time, if the size of the vector is big. Several methods have been developed, using simplification hypothesis. They can be divided into two categories: statistical methods calculate $\mathbf{X^a}$ directly using its analytic expression and formulating statistical hypothesis on the form of the matrix $\mathbf{P}$ (Kalman, 1960). Variational methods minimize the cost function Φ in an iterative way, using minimization algorithms (PALM Team, 1998).

These techniques have very different numerical properties. Their equivalence stops as soon as some underlying hypotheses are not verified, like the linearization of the observation operator for instance (Carlier, 1982). A preliminary study (Roux et al., 2004) has shown that the minimization of an error criterion gives satisfactory results for the purpose of this study.

In the case of hydraulic parameter identification, there is no prevision of the model state and therefore no a priori estimate $\mathbf{X^f}$. That's why the cost function only takes into account the distance to gauged data.

2.2 *Model description*

The model that has been developed solves the steady-state one-dimensional Saint-Venant equations (Horritt & Bates, 2002):

$$\begin{cases} \dfrac{dQ}{dx} = q_L \\ \dfrac{dH}{dx} = \dfrac{S_0 - S_f - 2Fr^2 \dfrac{Sq_L}{BQ}}{1-Fr^2} \end{cases} \quad (3)$$

where Q is the discharge, q_L the lateral inflow, H the water depth, S_0 the bed slope, S_f the friction slope: $S_f=n^2Q^2/R_H^{4/3}S^2$ (Graf, 1996), n the Manning coefficient, R_H the hydraulic radius, S the cross-sectional area, Fr the Froude number: $Fr=(Q^2B/gS^3)^{1/2}$, B the flow top width and x the distance along the channel. This study will only deal with subcritical flows (Fr< 1). Therefore only one downstream boundary condition on the water depth and one on the discharge are necessary to solve (3).

The chosen compound channel modelling supposes the equality of the friction slopes as well as the equality of the velocities in all the cross-sectional subdivisions (Carlier, 1982), (U.S.A.C.E., 1997). It allows to calculate a composite coefficient of roughness n_{comp}, function of the water depth (4).

$$n_{comp}(H) = \left(\frac{\sum_i (P_{w,i} n_i^{3/2})}{P_w} \right)^{2/3} \quad (4)$$

where P_w is the wetted perimeter of the entire channel, $P_{w,i}$ is the wetted perimeter of subdivision i and n_i is the friction coefficient of subdivision i (Figure 1).

Equations (3) are integrated by means of order four Runge-Kutta's method. The resolution requires:

– The definition of the geometry of the cross-section
– The determination of the Manning roughness coefficient for each subdivision of the cross-section
– The determination of the boundary conditions.

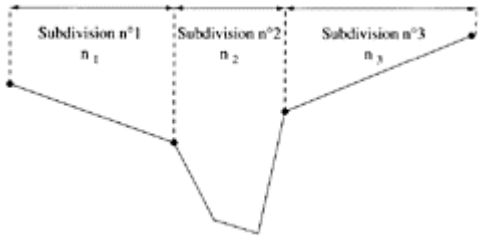

Figure 1. Compound channel.

The purpose of this study is to explore the possibility to determine these data using optimization techniques and the information provided by telemetry. Such a method would be useful for the determination of all the parameters for ungauged or poorly gauged rivers but also for the determination of non-directly measurable parameters, such as the Manning coefficient for instance.

3 IDENTIFICATION OF AN EQUIVALENT RIVER

A 4km reach of the river Lèze, in the South of France, between the cities of Lagardelle-sur-Lèze and Labarthe-sur-Lèze was considered (Figure 2).

Data concerning this site have been provided by the DIREN Midi-Pyrénées (DIREN Midi-Pyrénées, 2001). They consist in two synthetic flood events, one 15-year event and one exceptional event determined by geomorphology (Figure 3), and two real floods, one occurred in 1977 and the other one in June 2000. Figure 4 shows the extent of the flooded area for each event. The two real floods can be considered as exceptional events, indeed their extents are larger than the one of the exceptional event in some places.

3.1 *Identification from one flood event*

Figure 5 represents the hypothesis made on the geometry of the cross-section. The identified parameters are: the discharge at the downstream boundary, a local inflow as there is a local stream draining into the river, the stage at the downstream boundary, two Manning roughness coefficients, one for the main channel and one for the overbanks, and the characteristics of the

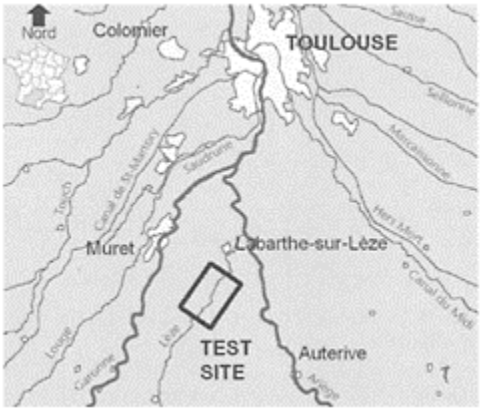

Figure 2. Location map of the test site (from Agence de l'eau Adour-Garonne, 1998/1999).

geometry of the cross-section (Figure 5), that is to say main channel depths, cross bank and overbank slopes. These geometric parameters are estimated for each side of the river and for each cross-section. Cross-sections are distant of about 70m.

In addition to the width of the flooded area for each event, the main channel width, that is to say the river bed, was also available as it can be seen in Figure 4.

The most known error criterion in hydrology is the sum of square of errors (Nash & Sutcliffe, 1970), the objective function Φ to be minimized in the assimilation process is then chosen as the sum of square of

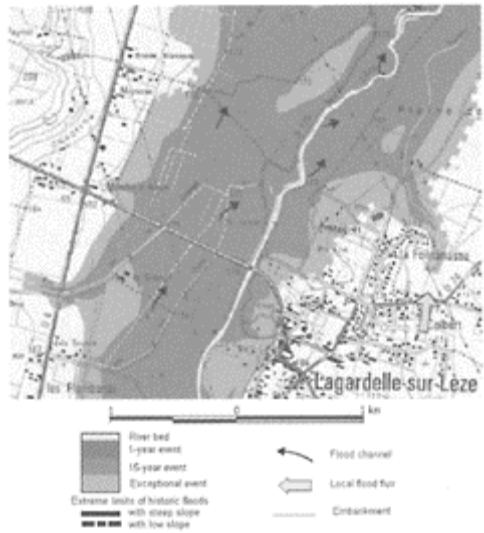

Figure 3. Cartography of the possible floodplains of the river Lèze provided by the DIREN Midi-Pyrénées (from DIREN Midi-Pyrénées, 2001).

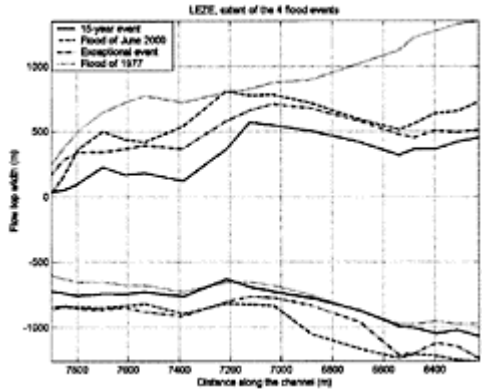

Figure 4. Extent of the 4 studied flood events.

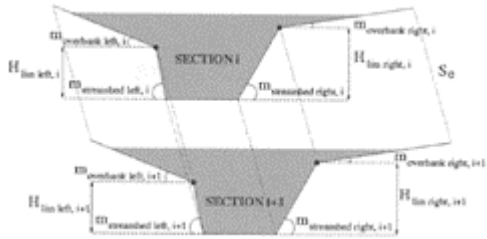

Figure 5. Geometric characteristics of the cross-section.

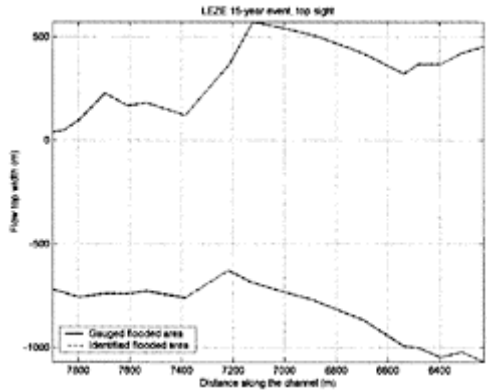

Figure 6. Comparison between gauged and identified flow top widths, 15-year event.

errors between the observed flow top width B_{Obs} and the simulated one B_{Sim}. In order to take into account the asymmetry of the flooded area, the minimised cost function (5) represents the distance between gauged flow top widths and simulated flow top widths for each bank (Roux et al., 2003b).

$$\Phi = \sum_{\text{cross-sections}} \left((B_{Obs} - B_{Sim})^2_{\text{left bank}} + (B_{Obs} - B_{Sim})^2_{\text{right bank}} \right) \quad (5)$$

The minimization is carried out using traditional algorithms based on the non-linear least square technique (Madsen, 2003).

Figure 6 shows the flow top width simulated with the parameters identified from the 15-year event. The result is satisfactory, nevertheless this approach needs a validation: the equivalent geometry (Figure 7) has been identified with only one event, it is necessary to ascertain that it also suits for others events.

The parameters listed above have been identified for each available flood event. Table 1 gives the values found for the hydraulic parameters by minimization of the cost function (5) for each event.

Knowing these values and the geometry, it is then possible to simulate the flow top width for each event. Figure 8 compares the flooded area of the event of

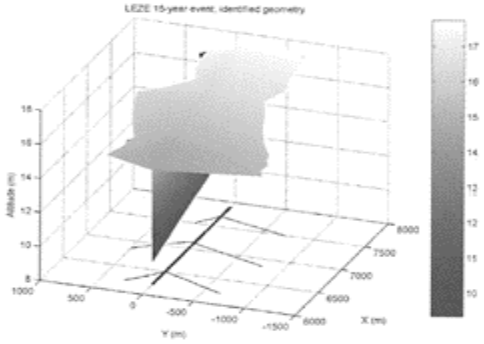

Figure 7. Geometry identified from the 15-year event.

Table 1. Identified value of the hydraulic parameters.

	15-year event	Exceptional event	Flood of June 2000
Discharge at the downstream boundary	122.5m^3/s	259.0m^3/s	285.8m^3/s
Lateral inflow	9.43m^3/s	12.8m^3/s	17.3m^3/s
Stage at the downstream boundary	5.86m	6.39m	6.64m

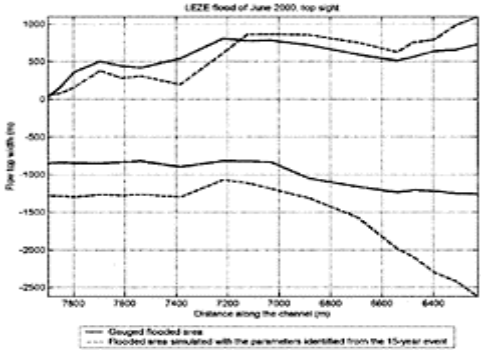

Figure 8. Comparison between gauged and simulated flow top widths for the flood of June 2000.

June 2000 with the flooded area simulated using the geometry identified from the 15-year event.

As these events have very different hydraulic characteristics, the flooded area of the exceptional event

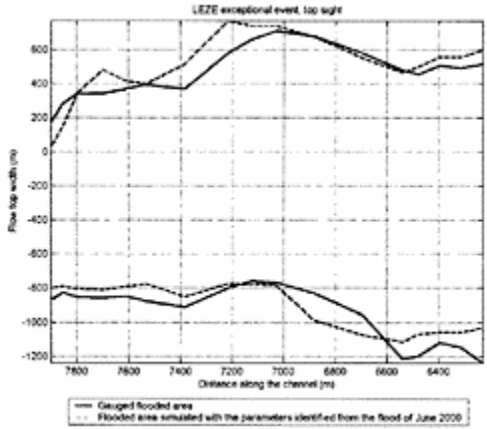

Figure 9. Comparison between gauged and simulated flow top widths for the exceptional event.

obtained by resolution of the Saint-Venant equations with the geometry identified from the 15-year event doesn't correspond to the observed one: the average error on the flow top width is of ±170m for the right bank and ±580m for the left bank which corresponds to a average relative error of 37%. But if the two events have closer hydraulic characteristics, like the exceptional event and the flood of June 2000 for instance, the result is better as it can be seen in Figure 9. Indeed, the average error on the flow top width is of ±70m for the right bank and ±200m for the left bank, that is to say a relative error of 19%.

Moreover, it is reasonable to say that the relevance of the identification can be improved by introducing more sets of gauged data into the assimilation process (Werner, 2001).

3.2 *Identification from several flood events*

3.2.1 *Simultaneous minimization*

The methodology is the same as in the previous paragraph 3.1 but the cost function (6) represents the distance to several flood events:

$$\Phi=\Phi_{15-year}+\Phi_{2000}+\Phi_{1977} \quad (6)$$

with

$$\Phi_{\text{each event}} = \sum_{\text{cross section}} \left((B_{Obs} - B_{Sim})^2_{\text{left bank}} + (B_{Obs} - B_{Sim})^2_{\text{right bank}} \right)$$

Discharge, lateral inflow and stage at the downstream boundary are supposed to be known (Table 1) and only the geometric characteristics of the transversal bed profile (Figure 5) are estimated by minimization of the cost function (6). A comparison between the

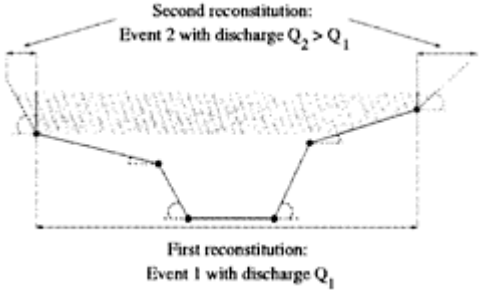

Figure 10. Gradual building of the cross-section bed profile.

gauged flooded areas for the three events and the simulated ones shows that the average relative error on the flow top width is of 14% for the 15-year event, 9.7% for the flood of June 2000 and 7.4% for the exceptional event. Consequently, the use of several flood events to identify an equivalent river actually leads to an improvement of the results. Indeed, the identified geometry allows to simulate the flooded area of the three events with an average error of less than 14%, compare to up to 37% with a reconstitution using only one event. Moreover, it is also possible to add points in the cross-section in order to better adapt the shape to the magnitude of the considered event.

3.2.2 *Gradual building of the cross-section*

The implemented method consists in a gradual building of the transversal bed profile (Figure 10). A first minimization considering an event of discharge Q_1 will estimate the characteristics of a transversal bed profile with four cross-sectional slopes (Figure 5). These points will then be considered as known. The introduction of another event of discharge Q_2, greater than Q_1 will allow to determine a change in the slope of the overbanks.

In the case of the river Lèze, the first minimization considers the 15-year event. The flood of June 2000 and the exceptional event are then introduced into the assimilation process in order to estimate the location of the change of slope and the second slope of the overbank, for each side of the river. Consequently, in this second step, there are 4 new parameters to estimate for each cross-section.

Figure 11 compares the extent of the 1977 flood with the flooded area obtained by simulation of the Saint-Venant equations with the geometry identified using the method

of gradual building. The average error on the flow top width is now of ±50m for the right bank and ±30m for the left bank, that is to say a relative error of about 4.9% against 19% using only one event as for Figure 9, or 7.4% using several events simultaneously. Hence, there is an important improvement of the portability of the identified geometry.

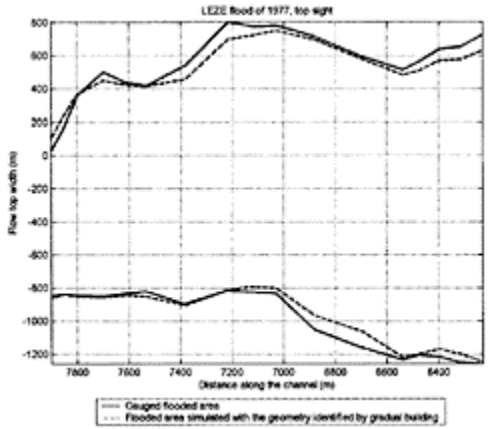

Figure 11. Comparison between gauged and simulated flow top widths, flood of 1977.

Next step will be to compare the flooded area simulated using the equivalent geometry with the one simulated using transversal bed profiles from in situ measurements.

4 UTILISATION OF THE OVERBANK TOPOGRAPHY

A 5km reach of the river Aisne, located in the north of France, between the cities of Soisson and Compiègne, was considered (Figure 12). Data concerning this event have been provided by the Cemagref of Montpellier. Flow top widths have been extracted from several air photos taken during the flood of December 1993 (Raclot, 2003). Another set of air photos, taken in low water period, provides the main channel width and the flow axe. This additional information can be integrated with profit into the assimilation process. Except the bridges and the locks, the studied flood plain presents few structures that can influence the flow, therefore it suits well the one-dimensional choice for the resolution of the Saint-Venant equations. However, only one set of gauged data is available.

Overbanks topography information (Figure 13) has been obtained by photogrammetry. The precision of this information is supposed to be sufficient for hydraulic simulation purpose (Raclot et al., 2000). However, measurement points are distant of fifty meters approximately in both horizontal directions.

The objective function Φ to be minimized is the same as in the previous case (5). The identified parameters are: the discharge, which is taken constant along the channel reach,

the stage at the downstream boundary, two Manning roughness coefficients, one for the main channel and one for the overbanks, and

Figure 12. Location map of the river Aisne reach (from Conseil Régional de Picardie, 2003).

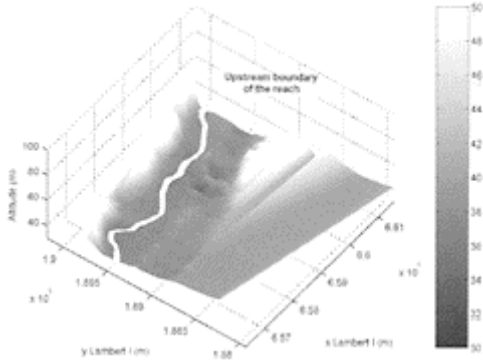

Figure 13. Topography of the overbanks provided by photogrammetry.

the characteristics of the geometry of the main channel (Figure 14), that is to say altitudes of the bottom of the main channel and cross bank slopes. The geometric parameters are estimated for each side of the river and for each cross-section. Cross-sections are distant of 100m.

Figure 15 compares the gauged flooded area and the simulated one. The result is satisfactory for the right bank, the lower one on the figure. The simulated flow top width of the other bank does not correspond to the gauged flooded area.

This is probably due to the fact that, as it can be easily seen on Figure 15, the left overbank is uneven. As the hydraulic simulation of Saint-Venant equations used to obtain the flow top width is strictly one-dimensional, there is no way for the flow to bypass the obstacles. The incapacity of the model to simulate flows around an elevated part of the floodplain and

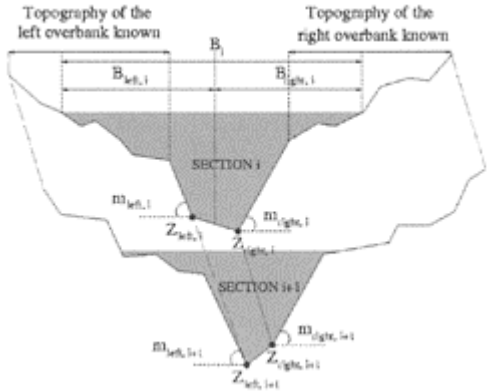

Figure 14. Cross-section geometry.

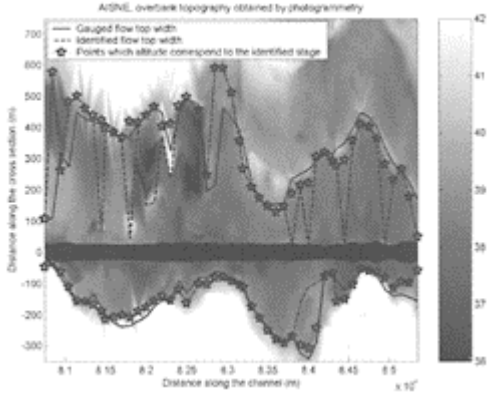

Figure 15. Top sight of the overbanks topography with the limits of both gauged and identified flooded areas and the points which altitude corresponds to the identified stage.

therefore separated from the main channel, explains the peaks of the identified flooded area: the water is stuck behind the topography obstacles (Roux et al., 2003 a). Indeed, a bidimensional simulation implemented with Telemac2D (developed by Electricité de France, (Galland et al., 1991)) using the identified parameters calculates a flooded area that doesn't present these peaks. Furthermore, this flooded area better corresponds to the observed one (Figure 16).

Searching for the points beyond the topography obstacles, which altitude corresponds to the identified stage, gives a better approximation of the gauged flooded area (Figure 15), as the 2D simulation already did. This result obviously does not take into account flows around the obstacles of the floodplain. Nevertheless, it shows that the identified altitude is satisfactory (Figure 17). Even if the flow discharge in the areas separated from the main channel is low, this test has

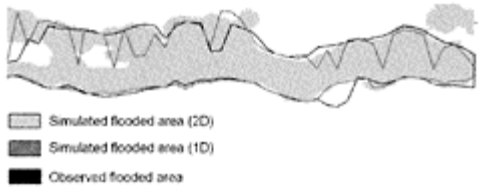

Figure 16. Flooded area simulated with Telemac2D (Chorda & Maubourguet, 2000).

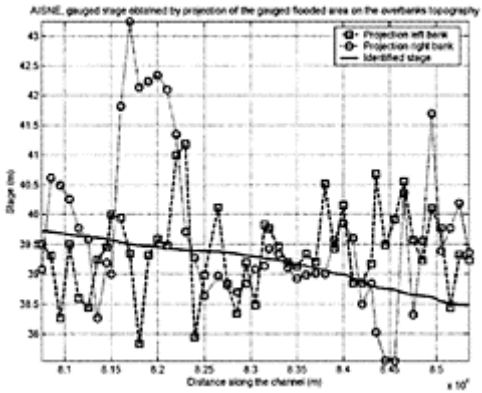

Figure 17. Comparison between the identified stage and the stages obtained by projection of the limits of the flooded area on the overbank topography.

emphasizes the importance of introducing the possibility of bypassing the topography obstacles in the resolution of the Saint-Venant equations, which is now being implemented.

Another observation that can be made from Figure 17 is that the difference of water surface elevation between the two banks can rise up to 5m, which is obviously incompatible with hydraulic requirements. Therefore a more accurate topography is needed to proceed the study in this direction.

5 CONCLUSIONS

The first approach of hydraulic parameter identification using an equivalent river has given satisfactory results for one set of observation. Adding information by introducing more events in the assimilation process allows to build gradually the transversal bed profile which increases the relevance of the estimated parameters. Indeed, geometric parameters identified from two or three events allow to simulate the flooded area of a third event with a satisfactory precision.

Concerning the introduction of the overbank topography in the assimilation process, it has been shown that the results can be satisfactory provided that the topography is known with a sufficient precision. According to (Alquier et al., 2000), an horizontal accuracy of 2m and a vertical accuracy of 0.5m are needed to simulate correctly the hydrodynamics of the flow on the overbanks and to determine the stage with a precision sufficient for flood risk management. Concerning the determination of the flooded areas, a very good knowledge of the topography is necessary, as local bumps or holes can radically modify the flood inundation conditions. Indeed, (Bates & Anderson, 1996) has demonstrated that a small change in topography (±10cm) may have complex and non negligible influence on the model prediction. The case of the river Aisne has emphasised the necessity of the introduction of the modelling of flows separated from the main channel in the resolution of the Saint-Venant equations (Roux et al., 2003a), even if in these areas, the discharge is relatively low because of their high roughness and their low depth.

Moreover, the methodology of this study is easily adaptable to the new sorts of data that the progresses in telemetry are going to make available in a few years (Smith, 1997). Indeed, satellite altimetry (TOPEX/POSEIDON launched in August 1992, or ENVISAT launched in March 2002) has been able to measure time series of water levels on very large rivers, such as the Amazon (Koblinsky et al., 1993), (Birkett, 1998), the Paraná or the Gange. If water levels were also available, the assimilation problem could be formulated in a multi-objective context in which different cost functions those measure different distances, one related to the water level and one related to the flow top width for instance, can be optimised simultaneously. In this framework, the calibration will be tailored to the specific model application being considered (Madsen, 2003).

REFERENCES

Agence de l'eau Adour-Garonne 1998/1999. Qualité des eaux superficielles en Haute-Garonne. http://www.eau-adourgaronne.fr/telechargement/dpt31/31.pdf.

Alquier, M, Chorda, J., Dartus, D., Estupina, V., Guennec, B.L. & Maubourguet, M.-M. 2000. Contribution des données d'observation de la terre a la cartographie de l'aléa. Rapport d'étude ADEMA, Institut de Mécanique des Fluides de Toulouse.

Bates, P.D. & Anderson, M.G. 1996. A preliminary investigation into the impact of initial conditions on flood inundation predictions using a time/space distributed sensitivity analysis. *Catena* 26:115–134.

Bates, P.D. & de Roo, A.P. J. 2000. A simple raster-based model for flood inundation simulation. *J. of Hydrology* 236:54–77.

Birkett, C.M. 1998. Contribution of the TOPEX NASA radar altimeter to the global monitoring of large rivers and wetlands. *Water Resources Research* 34(5):1223–1239.

Carlier, M. 1982. Hydraulique générale et appliquée.

Chorda, J. & Maubourguet, M.-M. 2000. Flood propagation. EDF-SOGREAH, *7th TELEMAC user club workshop, Grenoble, France*.

Conseil regional de Picardie 2003. La Picardie, le relief et l'hydrographie. http://www.cr-picadie.fr/fr/page.cfm?pageref=environnement~picardie~hydro.

DIREN Midi-Pyrénées 2001. Cartographie informative des zones inondables de Midi-Pyrénées. http://www.environnement.gouv.fr/midi-pyrenees/.

Galland, J.C., Goutal, N. & Hervouet, J.-M. 1991. TELEMAC-a new numerical-model for solving shallow-water equations. *Advances in Water Resources* 14(3): 138–148.

Graf, W.H. 1996. Hydraulique fluviale.

Horritt, M.S. & Bates, P.D. 2002. Evaluation of 1D and 2D numerical models for predicting river flood inundation. *J. of Hydrology* 268:87–99.

Hoteit, I. 2001. Filtres de Kalman réduits et efficaces pour l'assimilation de données en océanographie. PhD Thesis, Université de Grenoble I, Grenoble, France.

Ide, K., Courtier, P., Ghil, M. & Lorenc, A.C. 1997. Unified Notation for Data Assimilation: Operational, Sequential and Variational. *J. Meteo. Soc. Japan* 75 1(B): 181–189.

Kalman, R.E. 1960. A new approach to linear filtering and prediction problems. *J. Phys. Oceanogr.* 23:2541–2566.

Khatibi, R.H., Wormleaton, P.R. & Williams, J.J. R 2001. Parameter quality conditions in open-channel inverse problems. *J. Hydr. Res.* 38(6):447–458.

Koblinsky, C.J., Clarke, R.T., Brenne, A.C. & Frey, H. 1993. Measurement of river level variations with satellite altimetry. *Water Resources Research* 29(6):1839–1848.

Madsen, H. 2003. Parameter estimation in distributed hydrological catchment modelling using automatic calibration with multiple objectives. *Advances in WaterResources* 26: 205–216.

Marks, K. & Bates, P.D. 2000. Integration of high resolution topographic data with floodplain models. *Hydrological Processes* 14:2109–2122.

Nash, J.E. & Sutcliffe, J.V. 1970. River flow forecasting through conceptual models. Part I—A discussion of principles. *J. of Hydrology* 10:282–290.

Palm Team 1998. Etude de faisabilité du projet PALM. Rapport interne, CERFACS.

Plate, E.J. 2002. Flood risk and flood management. *J. of Hydrology* 267:2–11.

Raclot, D. 2003. Méthodologie d'exploitation quantitative des photographies aériennes d'inondation de plaine. PhD Thesis, Université Montpellier II, Sciences et Techniques du Languedoc, Montpellier, France.

Raclot, D., Puech, C., Blin, C. & Cornet, J.-M. 2000. Guide methodologique: integration des photos aériennes d'inondation dans les modelès hydrauliques. Rapport d'étude, Cemagref/Engref, CETMEF.

Roux, H., Raclot, D. & Dartus, D. 2004. Méthodes d'assimilation de données appliquées a la reconstitution de paramètres hydrauliques. *Société Française de Photogmmmétrie et Télédétection:* in press.

Roux, H., Raclot, D., Dartus, D. & Puech, C. 2003a. Hydraulic Parameter Identification using Aerial Photographs. IEEE, *International Geoscience and Remote Sensing Symposium, Toulouse, France*.

Roux, H., Raclot, D., Dartus, D. & Puech, C. 2003b. Hydraulic Parameter Identification using Satellite Earth Imagery. European Geophysical Society, *EGS-AGU-EUG Joint Assembly, Nice, France.*

Smith, L.C. 1997. Satellite remote sensing of river inundation area, stage, and discharge: a review. *Hydrol Process*. 11: 1427–1439.

Stewart, M.D., Bates, P.D., Anderson, M.G., Price, D.A. & Burt, T.P. 1999. Modelling floods in hydrologically complex lowland river reaches. *J. of Hydrology* 223: 85–106.

U.S.A.C.E. 1997. HEC-RAS River Analysis System. U.S. Army Corps of Engineers, Hydrologic Engineering Center.

Werner, M. 2001. Uncertainty in flood extent estimation due to uncertain parameters. *XXIX IAHR Congress Proceedings, Beijing, China.*

River Flow 2004-Greco, Carravetta & Della Morte (eds.) *ISBN 90 5809 658 0*

Author Index